BIOLOGICAL CONTROL SYSTEMS AND DISEASE MODELLING

EDITED BY: Babatunde Ogunnaike, David Bogle, Robert Parker and Julio R. Banga

PUBLISHED IN: Frontiers in Bioengineering and Biotechnology, Frontiers in Neuroscience, Frontiers in Physiology and Frontiers in Genetics

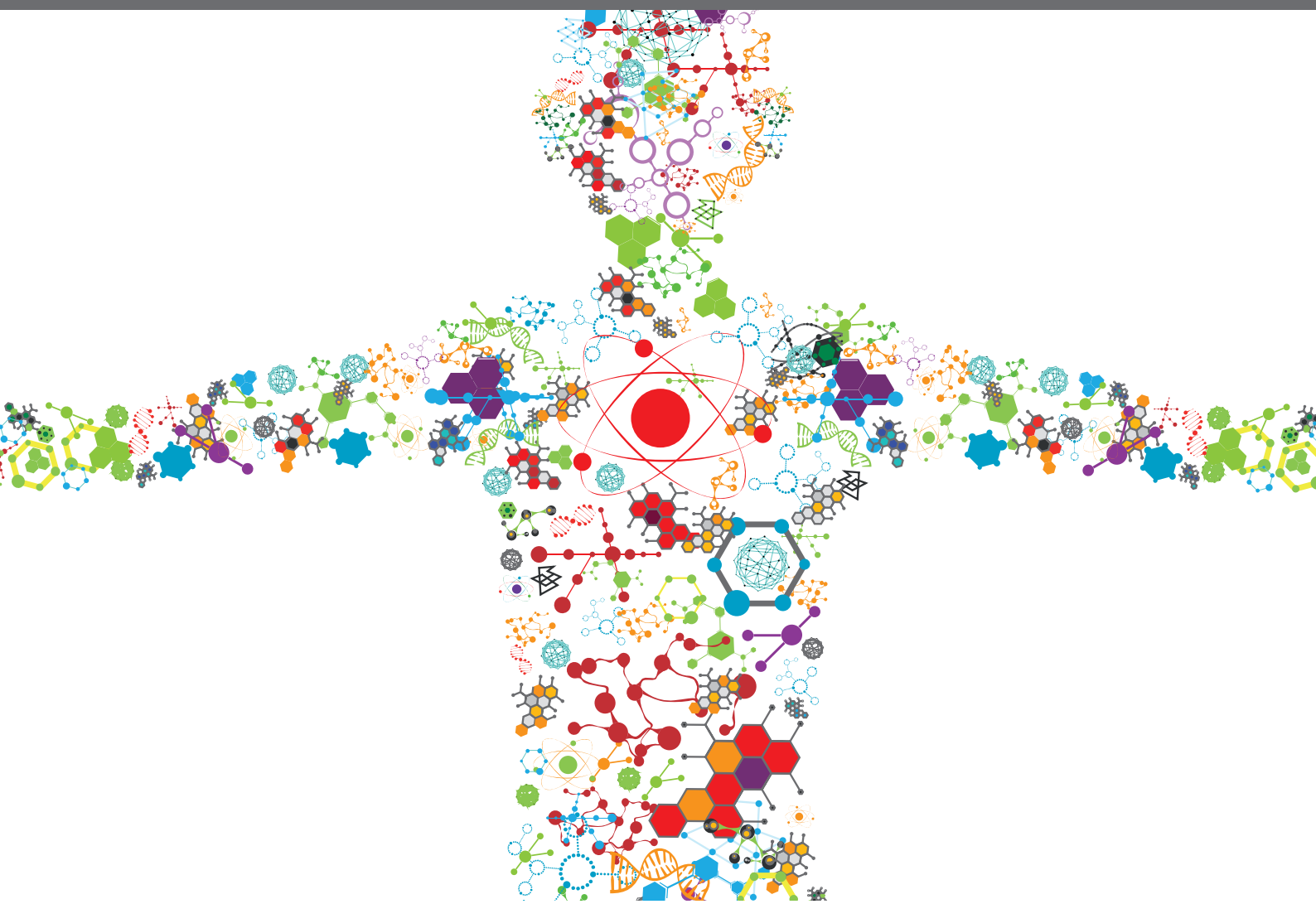

frontiers Research Topics

frontiers

Frontiers eBook Copyright Statement

The copyright in the text of individual articles in this eBook is the property of their respective authors or their respective institutions or funders. The copyright in graphics and images within each article may be subject to copyright of other parties. In both cases this is subject to a license granted to Frontiers.

The compilation of articles constituting this eBook is the property of Frontiers.

Each article within this eBook, and the eBook itself, are published under the most recent version of the Creative Commons CC-BY licence. The version current at the date of publication of this eBook is CC-BY 4.0. If the CC-BY licence is updated, the licence granted by Frontiers is automatically updated to the new version.

When exercising any right under the CC-BY licence, Frontiers must be attributed as the original publisher of the article or eBook, as applicable.

Authors have the responsibility of ensuring that any graphics or other materials which are the property of others may be included in the CC-BY licence, but this should be checked before relying on the CC-BY licence to reproduce those materials. Any copyright notices relating to those materials must be complied with.

Copyright and source acknowledgement notices may not be removed and must be displayed in any copy, derivative work or partial copy which includes the elements in question.

All copyright, and all rights therein, are protected by national and international copyright laws. The above represents a summary only. For further information please read Frontiers' Conditions for Website Use and Copyright Statement, and the applicable CC-BY licence.

ISSN 1664-8714
ISBN 978-2-88966-851-9
DOI 10.3389/978-2-88966-851-9

About Frontiers

Frontiers is more than just an open-access publisher of scholarly articles: it is a pioneering approach to the world of academia, radically improving the way scholarly research is managed. The grand vision of Frontiers is a world where all people have an equal opportunity to seek, share and generate knowledge. Frontiers provides immediate and permanent online open access to all its publications, but this alone is not enough to realize our grand goals.

Frontiers Journal Series

The Frontiers Journal Series is a multi-tier and interdisciplinary set of open-access, online journals, promising a paradigm shift from the current review, selection and dissemination processes in academic publishing. All Frontiers journals are driven by researchers for researchers; therefore, they constitute a service to the scholarly community. At the same time, the Frontiers Journal Series operates on a revolutionary invention, the tiered publishing system, initially addressing specific communities of scholars, and gradually climbing up to broader public understanding, thus serving the interests of the lay society, too.

Dedication to Quality

Each Frontiers article is a landmark of the highest quality, thanks to genuinely collaborative interactions between authors and review editors, who include some of the world's best academicians. Research must be certified by peers before entering a stream of knowledge that may eventually reach the public - and shape society; therefore, Frontiers only applies the most rigorous and unbiased reviews.
Frontiers revolutionizes research publishing by freely delivering the most outstanding research, evaluated with no bias from both the academic and social point of view. By applying the most advanced information technologies, Frontiers is catapulting scholarly publishing into a new generation.

What are Frontiers Research Topics?

Frontiers Research Topics are very popular trademarks of the Frontiers Journals Series: they are collections of at least ten articles, all centered on a particular subject. With their unique mix of varied contributions from Original Research to Review Articles, Frontiers Research Topics unify the most influential researchers, the latest key findings and historical advances in a hot research area! Find out more on how to host your own Frontiers Research Topic or contribute to one as an author by contacting the Frontiers Editorial Office: frontiersin.org/about/contact

BIOLOGICAL CONTROL SYSTEMS AND DISEASE MODELLING

Topic Editors:
Babatunde Ogunnaike, University of Delaware, United States
David Bogle, University College London, United Kingdom
Robert Parker, University of Pittsburgh, United States
Julio R. Banga, Consejo Superior de Investigaciones Científicas (CSIC), Spain

Citation: Ogunnaike, B., Bogle, D., Parker, R., Banga, J. R., eds. (2021). Biological Control Systems and Disease Modelling. Lausanne: Frontiers Media SA. doi: 10.3389/978-2-88966-851-9

Table of Contents

05 ***Editorial: Biological Control Systems and Disease Modeling***
Babatunde Ogunnaike, Julio R. Banga, David Bogle and Robert Parker

08 ***A Novel Prognostic Index Based on Alternative Splicing in Papillary Renal Cell Carcinoma***
Zhipeng Wu, Jinhui Liu, Rui Sun, Dongming Chen, Kai Wang, Changchun Cao and Xianlin Xu

23 ***Multiple Pathways Involved in Palmitic Acid-Induced Toxicity: A System Biology Approach***
Daniel Osorio, Andrés Pinzón, Cynthia Martín-Jiménez, George E. Barreto and Janneth González

37 ***Simplified Model of PKCγ Signaling Dysregulation and Cytosol-to-Membrane Translocation Kinetics During Neurodegenerative Spinocerebellar Ataxia Type 14 (SCA14)***
Naveed Aslam and Farah Alvi

52 ***Conducting a Virtual Clinical Trial in HER2-Negative Breast Cancer Using a Quantitative Systems Pharmacology Model With an Epigenetic Modulator and Immune Checkpoint Inhibitors***
Hanwen Wang, Richard J. Sové, Mohammad Jafarnejad, Sondra Rahmeh, Elizabeth M. Jaffee, Vered Stearns, Evanthia T. Roussos Torres, Roisin M. Connolly and Aleksander S. Popel

68 ***A Novel Synthetic Model of the Glucose-Insulin System for Patient-Wise Inference of Physiological Parameters From Small-Size OGTT Data***
Sebastián Contreras, David Medina-Ortiz, Carlos Conca and Álvaro Olivera-Nappa

82 ***Model-Based Simulation of Maintenance Therapy of Childhood Acute Lymphoblastic Leukemia***
Felix Jost, Jakob Zierk, Thuy T. T. Le, Thomas Raupach, Manfred Rauh, Meinolf Suttorp, Martin Stanulla, Markus Metzler and Sebastian Sager

95 ***Early Diagnosis of Hepatocellular Carcinoma Using Machine Learning Method***
Zi-Mei Zhang, Jiu-Xin Tan, Fang Wang, Fu-Ying Dao, Zhao-Yue Zhang and Hao Lin

104 ***Quantitative Modeling Extends the Antibacterial Activity of Nitric Oxide***
Darshan M. Sivaloganathan and Mark P. Brynildsen

119 ***Optimized and Personalized Phlebotomy Schedules for Patients Suffering From Polycythemia Vera***
Patrick Lilienthal, Manuel Tetschke, Enrico Schalk, Thomas Fischer and Sebastian Sager

138 ***Agent-Based Models Predict Emergent Behavior of Heterogeneous Cell Populations in Dynamic Microenvironments***
Jessica S. Yu and Neda Bagheri

160 ***Mathematical Details on a Cancer Resistance Model***
James M. Greene, Cynthia Sanchez-Tapia and Eduardo D. Sontag

187 ***An Integrated Spatial Dynamics—Pharmacokinetic Model Explaining Poor Penetration of Anti-retroviral Drugs in Lymph Nodes***
Aditya Jagarapu, Michael J. Piovoso and Ryan Zurakowski

202 ***Experimental Control of Macrophage Pro-Inflammatory Dynamics Using Predictive Models***
Laura D. Weinstock, James E. Forsmo, Alexis Wilkinson, Jun Ueda and Levi B. Wood

217 ***Modeling Pathway Dynamics of the Skeletal Muscle Response to Intravenous Methylprednisolone (MPL) Administration in Rats: Dosing and Tissue Effects***
Alison Acevedo, Debra DuBois, Richard R. Almon, William J. Jusko and Ioannis P. Androulakis

235 ***Computational Modeling of Fructose Metabolism and Development in NAFLD***
Yunjie Liao, Nathan A. Davies and I. David L. Bogle

249 ***Chronic Undernutrition Differentially Changes Muscle Fiber Types Organization and Distribution in the EDL Muscle Fascicles***
Erika E. Rodriguez-Torres, Jorge Viveros-Rogel, Kenia López-García, Enrique Vázquez-Mendoza, Gonzalo Chávez-Fragoso, Salvador Quiroz-González and Ismael Jiménez-Estrada

266 ***Progesterone Receptor Signaling Selectively Modulates Cytokine-Induced Global Gene Expression in Human Cervical Stromal Cells***
Douglas A. Kniss and Taryn L. Summerfield

283 ***An Introductory Overview of Image-Based Computational Modeling in Personalized Cardiovascular Medicine***
Thanh Danh Nguyen, Olufemi E. Kadri and Roman S. Voronov

309 ***Effective Biophysical Modeling of Cell Free Transcription and Translation Processes***
Abhinav Adhikari, Michael Vilkhovoy, Sandra Vadhin, Ha Eun Lim and Jeffrey D. Varner

323 ***Metabolic Modeling Combined With Machine Learning Integrates Longitudinal Data and Identifies the Origin of LXR-Induced Hepatic Steatosis***
Natal A. W. van Riel, Christian A. Tiemann, Peter A. J. Hilbers and Albert K. Groen

frontiers in Bioengineering and Biotechnology

EDITORIAL
published: 09 April 2021
doi: 10.3389/fbioe.2021.677976

Editorial: Biological Control Systems and Disease Modeling

Babatunde Ogunnaike[1], Julio R. Banga[2], David Bogle[3] and Robert Parker[4]*

[1] Department of Chemical & Bimolecular Engineering, University of Delaware, Newark, NJ, United States, [2] Consejo Superior de Investigaciones Científicas (CSIC), Madrid, Spain, [3] Department of Chemical Engineering, University College London, London, United Kingdom, [4] Department of Chemical and Petroleum Engineering, University of Pittsburgh, Pittsburgh, PA, United States

Keywords: systems biology, mathematical modeling, biological control systems, precision medicine, disease modeling

Editorial on the Research Topic

Biological Control Systems and Disease Modeling

INTRODUCTION

The mammalian organism maintains stable, efficient, and "near-optimal" performance and *homeostasis* in the face of external and internal perturbations via distinct biological systems ranging from the large-scale *physiological* (nervous, endocrine, immune, circulatory, respiratory, etc.), to the *cellular* (growth and proliferation regulation, DNA damage repair, etc.), and the *sub-cellular* (gene expression, protein synthesis, metabolite regulation, etc). "Biological Control Systems," the application of control theory and practice to biological systems, arises from a control engineering perspective of the function, organization, and coordination of these multi-scale biological systems and the control mechanisms that enable them to carry out their functions effectively. A direct consequence of this engineering perspective is that many diseases are seen as arising when one (or more) of these biological control systems malfunctions or fails completely. For example, hypertension results from a malfunctioning blood pressure control system, hypocalcemia from a malfunctioning calcium homeostasis system, and Type 1 diabetes from a failure of the blood glucose control system. A natural corollary therefore is that appropriate treatment regimens consist of ways of restoring (for example via pharmaceutical drugs) the functions lost by the malfunctioning components, or, where full functional restoration is not possible, the introduction of external means of supplementing or replacing the malfunctioning biological component (for example, the "artificial pancreas" for treating Type-I diabetes). Such a perspective places emphasis on a rigorous *quantitative* approach to three tasks: (i) the analysis of biological systems for insight; (ii) the identification of the root cause of pathologies and potential treatment targets; and (iii) the rational design (and implementation) of effective interventions.

OVERVIEW

This collection of twenty papers seeks to provide—under a single cover—a broad spectrum of research results showcasing this quantitative perspective of the physiological processes that subtend life, the diseases that occur when these systems malfunction, and the design of effective treatments for these diseases, specifically using mathematical modeling and principles of systems engineering. For obvious reasons of space limitation, the collection is naturally representative rather than exhaustive.

Nevertheless, the papers address a wide variety of diseases including non-alcoholic fatty liver disease; hepatic steatosis; cancers of various types (liver, blood, breast, leukemia, papillary renal cell carcinoma); immune system dysregulation; neurodegeneration diseases; and such "classics"

OPEN ACCESS

Edited and reviewed by:
Richard D. Emes, University of Nottingham, United Kingdom

****Correspondence:***
Babatunde Ogunnaike
ogunnaike@udel.edu

Specialty section:
This article was submitted to Computational Genomics, a section of the journal Frontiers in Bioengineering and Biotechnology

Received: *08 March 2021*
Accepted: *16 March 2021*
Published: *09 April 2021*

Citation:
Ogunnaike B, Banga JR, Bogle D and Parker R (2021) Editorial: Biological Control Systems and Disease Modeling. Front. Bioeng. Biotechnol. 9:677976. doi: 10.3389/fbioe.2021.677976

as diabetes and HIV. Some of the papers focus on entire physiological processes, such as the cardiovascular system, or the specialized process of parturition—how babies are delivered vaginally following pregnancy; others focus on cellular and signaling sub-processes that subtend the physiological manifestation of diseases. Viewed from another vantage point, some papers are concerned with how the physiological control systems function endogenously while others focus on how to design effective external interventions, such as designing optimal personalized treatments for blood cancer patients, or the use of the engineering technique of model predictive control (MPC) to control macrophage polarization. Also, the approaches represented in this collection cover the entire length scale from the genetic and cellular to the tissue and physiological. Also, while some of the results are strictly theoretical, a significant number of these results have been validated experimentally, while some are entirely experimental in nature. On many levels, therefore, the papers are sufficiently complementary to provide a good representation of the broad and expanding landscape of quantitative biomedicine viewed through the lens of biological control systems.

UNIFYING THEME

While the diseases and physiological processes encountered here are richly diverse, the common unifying thread holding the 20 papers together is the use of a mathematical model—of one type or another—to quantify the phenomenon in question and employing such a quantitative description to answer a wide variety of questions for many different applications. For example, in this collection: mathematical models are used for disease diagnosis; for rational identification of treatment targets; for design, analysis, and implementation of optimal treatment regimens; for prognosis; and even as a surrogate for clinical trials. In addition, the papers collectively illustrate the diversity of mathematical models *themselves* and the versatility with which they can be developed, validated, deployed, and utilized, depending on the actual application in question. Consequently, in addition to the standard ordinary differential equation (ODE) models with which most readers will likely be familiar, one will find in this collection, such exemplars of mechanistic models as partial differential equation models used to capture spatial variations when these are important, or steady state metabolic flux models. At the other end of the spectrum, one will also find models based entirely on data, employing techniques such as support vector machines, data mining, and machine learning to develop the appropriate data-based model best suited to the problem at hand. Hybrid models, which occupy the vast domain in between these two ends of the modeling spectrum, are also represented here. This class of models arise by combining mechanistic principles appropriately with empirical data in proportions typically dictated by which is more readily available in the desired amount—first principles knowledge, or data. There are also in this collection a handful of applications of other techniques with which the average reader may not be familiar, such as fractals, or agent-based models, presented here as systematic frameworks best suited to studying complex and heterogenous systems (e.g., tumor microenvironments and microbiomes) that would otherwise be virtually impossible to study systematically. The variety of mathematical model forms represented in this collection, when overlaid onto the myriad applications and diseases to which they have been applied, underscores the depth of penetration of mathematical modeling into modern physiology and medicine, and the effectiveness of quantitative techniques in providing heretofore unimaginable solutions.

KEY IMPLICATIONS OF RESULTS

With the exception of the lone review/perspective paper (on image-based computational modeling for non-invasive acquisition of the crucial measurements required for personalized cardiovascular medicine), every paper in this collection *by itself* contributes important results that add to the growing consensus of the role of quantitative analysis in the understanding of biological systems at all length scales, the rational deduction of the sources and emergence of diseases, and the determination of *optimal* treatment regimens—how best to intervene to treat these diseases while minimizing side effects. Taken together as an ensemble, here are some of the most significant implications of the results in this collection:

- *Growing indispensability of mathematical modeling in biomedicine*: The importance and scope of mathematical modeling in understanding diseases as complex systems, and in designing rational treatment regimens, continues to grow, underscored and exemplified by the novel implementation of a virtual clinical trial in HER2-Negative Breast Cancer, with major implications for personalized medicine at reasonable cost.
- *Novel extraction and utilization of germane actionable information from data*: Beyond the traditional role as the basis for data-based model development, appropriately acquired data sets and the judicious extraction of the information contained therein have the potential to enable modern biomedicine in unprecedented ways, ranging from early—and reliable—diagnosis of liver cancer; more accurate prognosis of papillary renal cell carcinoma; and the identification of effective therapeutic targets based on gene networks deduced from gene expression data.
- *Effective disease treatment as a control problem*: The implementation of appropriate treatments for some diseases can be formulated as an engineering control problem, which then allows one to invoke principles and established results from that engineering field and modify and/or extend them appropriately for use in designing optimal treatment regimens for diseases. The implementation of such an approach is exemplified here with specific applications ranging from theoretical analysis of drug resistance in cancer chemotherapy, leading to *à-priori* design of patient specific optimal therapies; controlling macrophage polarization using model predictive control (MPC); or personalized optimization of blood cancer treatment.

In conclusion, we believe that the message in this collection of papers is both relevant and timely. With attention currently focused on precision (more appropriately *personalized*) medicine, the approaches discussed and illustrated by these papers should contribute significantly to how the grand vision of personalizing disease diagnosis and treatment will be realized in the future. Consequently, we are pleased to present this collection to the community with the belief that it will be useful to the beginner (to obtain a broad overview of the evolving landscape) as well as to the expert who might find therein a useful stepping stone to the next contribution that will further extend the frontier of knowledge in the subject of biological control systems.

AUTHOR CONTRIBUTIONS

All authors listed have made a substantial, direct and intellectual contribution to the work, and approved it for publication.

Conflict of Interest: The authors declare that the research was conducted in the absence of any commercial or financial relationships that could be construed as a potential conflict of interest.

Copyright © 2021 Ogunnaike, Banga, Bogle and Parker. This is an open-access article distributed under the terms of the Creative Commons Attribution License (CC BY). The use, distribution or reproduction in other forums is permitted, provided the original author(s) and the copyright owner(s) are credited and that the original publication in this journal is cited, in accordance with accepted academic practice. No use, distribution or reproduction is permitted which does not comply with these terms.

frontiers in Genetics

ORIGINAL RESEARCH
published: 29 January 2020
doi: 10.3389/fgene.2019.01333

A Novel Prognostic Index Based on Alternative Splicing in Papillary Renal Cell Carcinoma

Zhipeng Wu[1†], *Jinhui Liu*[2†], *Rui Sun*[2†], *Dongming Chen*[1], *Kai Wang*[1], *Changchun Cao*[1*] *and Xianlin Xu*[1*]

[1] Department of Urology, Sir Run Run Hospital, Nanjing Medical University, Nanjing, China, [2] Department of Gynecology, The First Affiliated Hospital of Nanjing Medical University, Nanjing, China

OPEN ACCESS

Edited by:
Julio R. Banga,
Spanish National Research Council (CSIC), Spain

Reviewed by:
Zheng Xia,
Oregon Health & Science University, United States
Yuriy L. Orlov,
First Moscow State Medical University, Russia

***Correspondence:**
Xianlin Xu
xianlinxu@njmu.edu.cn
Changchun Cao
caochangchun@njmu.edu.cn

[†]These authors have contributed equally to this work

Specialty section:
This article was submitted to Bioinformatics and Computational Biology, a section of the journal Frontiers in Genetics

Received: 25 August 2019
Accepted: 05 December 2019
Published: 29 January 2020

Citation:
Wu Z, Liu J, Sun R, Chen D, Wang K, Cao C and Xu X (2020) A Novel Prognostic Index Based on Alternative Splicing in Papillary Renal Cell Carcinoma. Front. Genet. 10:1333. doi: 10.3389/fgene.2019.01333

Background: Papillary renal cell carcinoma (pRCC) is a heterogeneous multifocal or isolated tumor with an invasive phenotype. Previous studies presented that alternative splicing, as a crucial posttranscriptional regulator in gene expression, is associated with tumorigenesis. However, the association between alternative splicing and pRCC has not been clarified

Methods: The RNA sequencing data and clinical information were downloaded from The Cancer Genome Atlas database and mRNA splicing profiles from TCGASpliceSeq. The percent spliced in data of alternative splicing merged with survival information was firstly calculated by univariate Cox regression analysis to screen for survival-associated alternative splicing events, and survival-associated alternative splicing events were then analyzed by Gene Ontology categories using Kyoto Encyclopedia of Genes and Genomes. Meanwhile, the least absolute shrinkage and selection operator Cox analysis and multivariate Cox analysis were performed to calculate the prognostic index for each alternative splicing type. In addition, clinical factors were introduced to assess the performance of prognostic index.

Results: A total of 4,084 candidate survival-associated alternative splicing events in 2,558 genes were screened out. Patients were divided into the low-risk group and the high-risk group based on the median prognostic index value. The Kaplan-Meier survival analysis ($p < 0.05$) and receiver operating characteristics curves (AUC>0.9) indicated that prognostic index was effective and stable for predicting the prognosis of pRCC patients. Furthermore, a regulatory network was constructed incorporating alternative splicing events and survival-associated splicing factors.

Conclusion: Our study provides new insights into the mechanism of alternative splicing events in tumorigenesis and their clinical potential for pRCC.

Keywords: alternative splicing, prognostic index, papillary renal cell carcinoma, splicing factor, The Cancer Genome Atlas

INTRODUCTION

Papillary renal cell carcinoma (pRCC), which accounts for up to 15% of renal cell carcinoma, is the second most common histological subtype of kidney cancer (Jonasch et al., 2014; Malouf et al., 2016). PRCC emerges as either indolent localized tumor or aggressive metastatic cancer (Delahunt and Eble, 1997), but the biological basis for this difference remains unidentified. Vascular endothelial growth factor (VEGF) pathway has been proven to be involved in metastatic pRCC (Armstrong et al., 2016), but we still speculate that multiple mechanisms lie behind these pRCC with diverse presentations. Thus, we designed this systematic and comprehensive analysis to drill into the oncogenic mechanism of pRCC.

High-throughput sequencing has revolutionized human genomics and the research in this field. The current number of human genes is still controversial. Up to now, people's statistics on the number of genes are constantly changing (Pertea and Salzberg, 2010; Pertea et al., 2018). The GENCODE (Frankish et al., 2019) genome maintained by EBI currently counts 19,965 protein-coding genes, 17,910 long noncoding RNA genes, and 7,576 small noncoding genes in human (https://www.gencodegenes.org/human/stats.html). The database RefSeq (O'Leary et al., 2016), managed by the National Center for Biotechnology Information, lists 20,203 protein-coding genes and 17,871 noncoding genes. Regardless of the specific number of genes, given the limited number of human genes, alternative splicing (AS) serves as a key mechanism producing myriads of proteins (Tang et al., 2013; Bowler et al., 2018). AS is regulated by spliceosome, a large and highly dynamic protein complex constructed by nearly 200 protein components and five small nuclear ribonucleic acids (Agrawal et al., 2018). Dysregulation of splicing factors (SFs) can distort mRNA splicing programs, which could result in cancer development and progression (Grosso et al., 2008). Studies have also shown that aberrant AS events during transcription, which are tissue-specific and stage-specific, can evoke tumorigenesis (Wang et al., 2008; Kahles et al., 2018; Wan et al., 2019).

In this study, to clarify the AS events and its clinical implications in pRCC, AS events and complete clinical information from the TCGA database were analyzed. A prognostic model was formed to predict the prognosis of pRCC according to the survival information. Meanwhile, a regulatory network was constructed to evaluate the correlation between AS events and SFs, and identify several key factors which might exert important functions in occurrence and development of pRCC.

MATERIALS AND METHODS

Data Collection of AS Events

RNA sequencing data (level 3) and clinical information of The Cancer Genome Atlas (TCGA) KIRP cohorts were obtained from the TCGA data portal (https://portal.gdc.cancer.gov/). Analysis of mRNA splicing profiles in pRCC was conducted with the aid of SpliceSeq (Ryan et al., 2016), java that explicitly quantifies RNA-Seq reads and identifies its possible functional changes as a consequence of AS in the context of transcript splice graphs. AS events were divided into seven types including exon skip (ES), mutually exclusive exons (ME), retained intron (RI), alternate promoter (AP), alternate terminator (AT), alternate donor site (AD), and alternate acceptor site (AA) (**Figure 1**). Meanwhile, we downloaded the Percent Spliced In (PSI) value

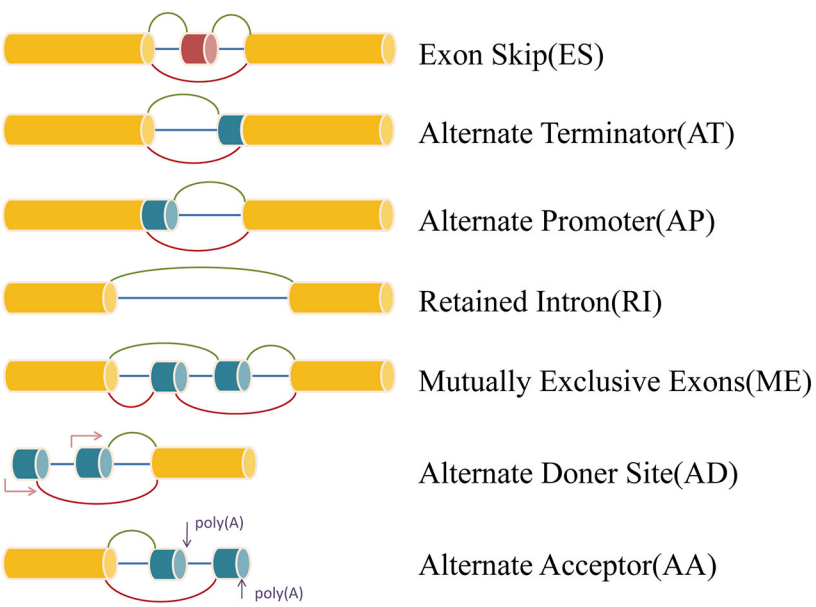

FIGURE 1 | Representative model of seven types of alternative splicing.

(>75%) for pRCC patients. The PSI value, ranging from zero to one, was used in quantifying AS events.

Identification of Survival-Associated AS Events

A total of 32 adjacent normal tissues and 289 pRCC tissues were collected from TCGA. The number of AS events and genes involved was showed by UpSet plot using "UpSetR" package in R (Conway et al., 2017). Univariate Cox regression analysis was used to screen out the candidate AS events ($P < 0.05$).

Functional Annotation

The parent genes of survival-associated AS events were subjected to functional enrichment analyses. Gene ontology (GO) term enrichment analysis and Kyoto Encyclopedia of Genes and Genomes (KEGG) pathway analysis were performed using "clusterProfiler" package in R (Yu et al., 2012). A p-value and q-value both smaller than 0.05 in GO and KEGG was considered significant.

Survival Analysis

The result of univariate Cox regression analysis in identifying survival-associated AS events was shown by Volcano plot using "ggplot2" in R (**Figure 4A**). Seven types of AS events were revealed by Bubble chart respectively. Each chart contained the top 20 significant survival-associated AS events of corresponding types. LASSO method was then employed for the regression of high-dimensional predictors. LASSO Cox regression model was used to determine the ideal coefficient for each prognostic feature and to estimate the deviance likelihood via 1-standard error (SE) criteria. The coefficients and partial likelihood deviance were calculated with the "glmnet" package in R (Friedman et al., 2010).

Construction and Validation of a Prognostic Model

The result of LASSO Cox regression was then submitted to multivariate Cox analysis to evaluate the independent prognostic value of each gene and construct an independent prognosis model.

The risk score model for prediction based on survival-associated AS events were calculated by multiplying the PSI values of prognostic indictors and the regression coefficient calculated by the multivariate Cox regression analysis.

$$\text{Risk Score based on eventes(patient)} = \sum_i \text{Coefficient}(\text{mRNA}_i) \times \text{PSI value}(\text{mRNA}_i)$$

The specific calculation formula was shown in **Table 1**. Patients were then divided into two groups based on the median levels of risk score. This prognostic model and patient survival information were merged. Kaplan-Meier survival curves were conducted to identify the prognostic ability of prediction models. Area under the curve (AUC) value for the ROC curves of each prognostic model was calculated by survivalROC package in R. Besides, univariate and multivariate analysis were performed containing the risk score of prognostic models and important clinical features for pRCC. Patients with incomplete clinical information and less than 90 days of OS were excluded, and only 129 samples were deemed qualified. Finally, a nomogram was constructed using the "rms" package on R. The calibration of this nomogram was assessed by calibration curves.

Correlation Network of SF and Survival-Associated AS Events

The data of SFs was obtained from SpliceAid 2 (Piva et al., 2012). SF files and patient survival information were merged and calculated by univariate Cox regression analysis to get survival-associated SFs. Correlation network was constructed using the gene expression of SFs and PSI values of prognosis-related AS events with the conditions of P value less than 0.001 and Pearson correlation coefficient more than 0.7. The correlation network was plotted by Cytoscape (version 3.6.1).

The risk score model based on survival-associated SFs was the sum of each optimal prognostic mRNA expression level multiplying relative regression coefficient weight calculated from the multivariate Cox regression model.

$$\text{Risk Score based on SFs(patient)} = \sum_i \text{Coefficient}(\text{mRNA}_i) \times \text{Expression}(\text{mRNA}_i)$$

RESULTS

Overview of AS Events in pRCC

We collected 41,673 AS events from 10,026 genes in 32 adjacent normal tissues and 289 pRCC tissues. The numbers of the genes showing seven types of AS events were plotted by UpSet plot (**Figure 2A**). Several genes only have one kind of AS event, ES was found in 1,699 genes (the largest number) and ME in 36 genes (the smallest number). The plot also showed that one gene might involve two or more AS events, leading to multiple transcripts from one gene. AS data was merged with clinical survival data and calculated by univariate Cox regression analysis. As a result, 4,084 AS events in 2,558 genes were deemed associated with the overall survival (OS) ($p < 0.05$). The result was also shown by UpSet plot (**Figure 2B**).

Functional and Pathway Enrichment Analysis

Based on survival-associated AS events, GO (**Figure 3A**), and KEGG (**Figure 3B**) were conducted by "clusterProfiler" package in R. The involved functions and pathways included "ciliary basal body-plasma membrane docking," "purine ribonucleotide metabolic process," and "organelle localization by membrane tethering" in biological process (BP), "adherens junction," "focal adhesion," and "cell-substrate adherens junction" in cellular component (CC), "cadherin binding," "cell cadherin molecule binding," and "retinoic acid receptor binding" in molecular function (MF). Besides, these genes were mainly enriched in "MAPK signaling pathway," "thermogenesis," and "human

TABLE 1 | Prognostic signatures for papillary renal cell carcinoma.

Type	Formula	AUC
AA	FKBP8|48446|AA*−8.261326216+ITGB1BP1|52617|AA*−3.645087449+FAM213A|12365|AA*−3.591154025+MYL6|22381|AA*−16.63167012+PILRB|80930|AA*4.461677112+TRPT1|16579|AA*−28.05557115+RPS24|12297|AA*−2.123512398+ENTPD6|58863|AA*−4.538790703+SPATA20|42429|AA3.809741969	0.967
AD	TCEB1|84216|AD*−3.227392376+ATP5J|60266|AD*−6.409262477+IRF3|51027|AD*−5.374919151+CFL2|27169|AD*−4.984160824+ATP6V1H|83836|AD*−14.79100606+AKT1S1|51111|AD*−6.962315249+PQBP1|89029|AD*−2.068032636	0.861
AP	UNG|24277|AP*4.194935004+NHS|88586|AP*−2.822266615+DYNC1I2|55939|AP*−6.138633492+LIMA1|21688|AP*3.922489143+PMEPA1|59946|AP*1.640017308+RNF220|2555|AP*−4.636337467	0.961
AT	CLDN11|67616|AT*1.439647629+SLC25A48|73462|AT*-3.684109126+KIF4A|89373|AT*2.503402505+RBM39|59235|AT*−22.33853542+BCAM|50347|AT*3.282115813+LARP1B|70567|AT*−3.356001505	0.959
ES	YIF1A|17008|ES*−20.56958015+RPS24|12295|ES*−1.999160275+C16orf13|265882|ES*−2.503302918+ARHGEF10|82562|ES*−2.479391656+PAX8|55049|ES*−7.098738552+MUM1|46457|ES*2.479075665	0.928
ME	AMT|64866|ME*−11.67288726+C14orf2|29528|ME*2.439891378+CBWD5|86504|ME*−9.123153517+MEF2A|32717|ME*−5.089591595+FAIM|67014|ME*−3.726223934+CERS5|21668|ME*−2.23329899+STK36|57557|ME*−15.49762863+FBLN5|28892|ME*10.43894503+GLOD4|123198|ME*−4.401329099	0.901
RI	TMUB1|82347|RI*−4.817625749+ELP5|38889|RI*−5.149262596+ZSWIM7|39393|RI*−6.043747899+LRRC29|36982|RI*4.739092712+ZNF276|38138|RI*6.294309106+SNX5|58749|RI*−4.792058193+TTLL3|63208|RI*4.305033369	0.963
All	SEC31A|69730|ES*−3.130605352+RPS24|12295|ES*−2.37334211+FKBP8|48446|AA*−10.11459992+UNG|24277|AP*4.542255311+ARHGEF10|82562|ES*−3.009037952	0.968

Example: "FKBP8|48446|AA−8.261326216," "FKBP8" is the gene name, "48446" is the AS id, "AA" is the type of AS event, "FKBP8|48446|AA" mean the PSI value of AA event in FKBP8, and "−8.261326216" is the regression coefficient calculated by the multivariate Cox regression analysis.*

cytomegalovirus infection" in KEGG. AS events generating from these genes might influence the occurrence and development of pRCC through interfering with the above BPs and pathways.

Prognostic Model for pRCC

Among the survival-associated AS events (**Figure 4A**), the top 20 significant AS events were shown by bubble chart (**Figures 4B–H**). These AS events were further treated with LASSO Cox analysis (**Figures 5A–G**). LASSO Cox analysis of all AS events (ALL) was also shown (**Figure 5H**). Next, multivariate Cox analysis was performed to construct an independent model with PI. The formula was showed in **Table 1**. Patients were divided into the low-risk group and the high-risk group based on the median risk score. With the increasing risk score, the patient's survival became worse. The risk plot of ALL AS events was shown in **Figure 6**. **Figure 6C** with high resolution were affiliated in the **Supplementary Figure 1**. The separate risk plots of seven AS event were affiliated in **Supplementary Figure 2**. The Kaplan-Meier survival analysis suggested that a pRCC patient with a higher risk score might show a worse survival (**Figures 7A–H**). An AUC value of more than 0.9 was found in all the seven types of AS in pRCC except AD (0.861), which validated the efficiency of these signatures in predicting prognosis. To assess whether this model was an independent predictor of pRCC, univariate analyses was performed between clinical factors and risk score. The results showed that this model could distinguish pRCC patients ($p < 0.001$) (**Table 2**). Furthermore, by using multivariate analyses, this prognostic model was proved to serve as a moderate and independent prognostic indicator in the AS events of AA, AD, AP, AT, and RI. (**Figures 8A–H**). Finally, to provide a clinically associated quantitative method, we tried to construct a nomogram incorporating riskscore and clinical factors to predict the probabilities of 3- and 5-year OS in pRCC. Since the predict model based on AA event showed the best performance among AS events that proved to serve as a moderate and independent prognostic indicator (AUC = 0.967), the nomogram was constructed based on AA event (**Figure 9A**). The Harrel's concordance index (C-index) for OS prediction was 0.963, which showed a fairly high prediction accuracy of this nomogram. The calibration curves for the 3- (**Figure 9B**) OS rates showed good agreement between the prediction and the actual observation, but not so good in 5-year (**Figure 9C**).

A Survival-Associated Network Incorporating SFs and AS Events

SFs play an important part in the occurrence and development of AS events via changing exon selection and splicing site. Therefore, it is necessary to uncover the correlation between SFs and AS events. Survival analyses based on TCGA data was performed to screen out potential SFs. And then, correlation network was constructed using the expression value of SFs and PSI values of prognosis-related AS events (**Figure 10A**). **Figure 10A** with high resolution were affiliated in the **Supplementary Figure 3**. To highlight the key players in this network, we performed LASSO Cox analysis on those SFs (**Figure 10B**). CDK12, CDK10, SF3A2, SNRNP35, and SNRNA were screened out by multivariate Cox regression analysis (**Figure 10C**).

Risk score = the expression of CDK12 * 0.260889 + the expression of CDK10 * (−0.06669) + the expression of SF3A2 * 0.041459 + the expression of SNRNP35 * (−0.21053) + the expression of SNRPA * 0.087523

The model formed by these five SFs showed outstanding prognostic efficiency as evidenced by the Kaplan-Meier survival curves (**Figure 10D**) and ROC curve (**Figure 10E**). With clinical information, we further analyzed the five key genes with multivariate analyses (**Figure 10F**). In additionally, only CDK12 and SF3A2 were deemed significant statistically

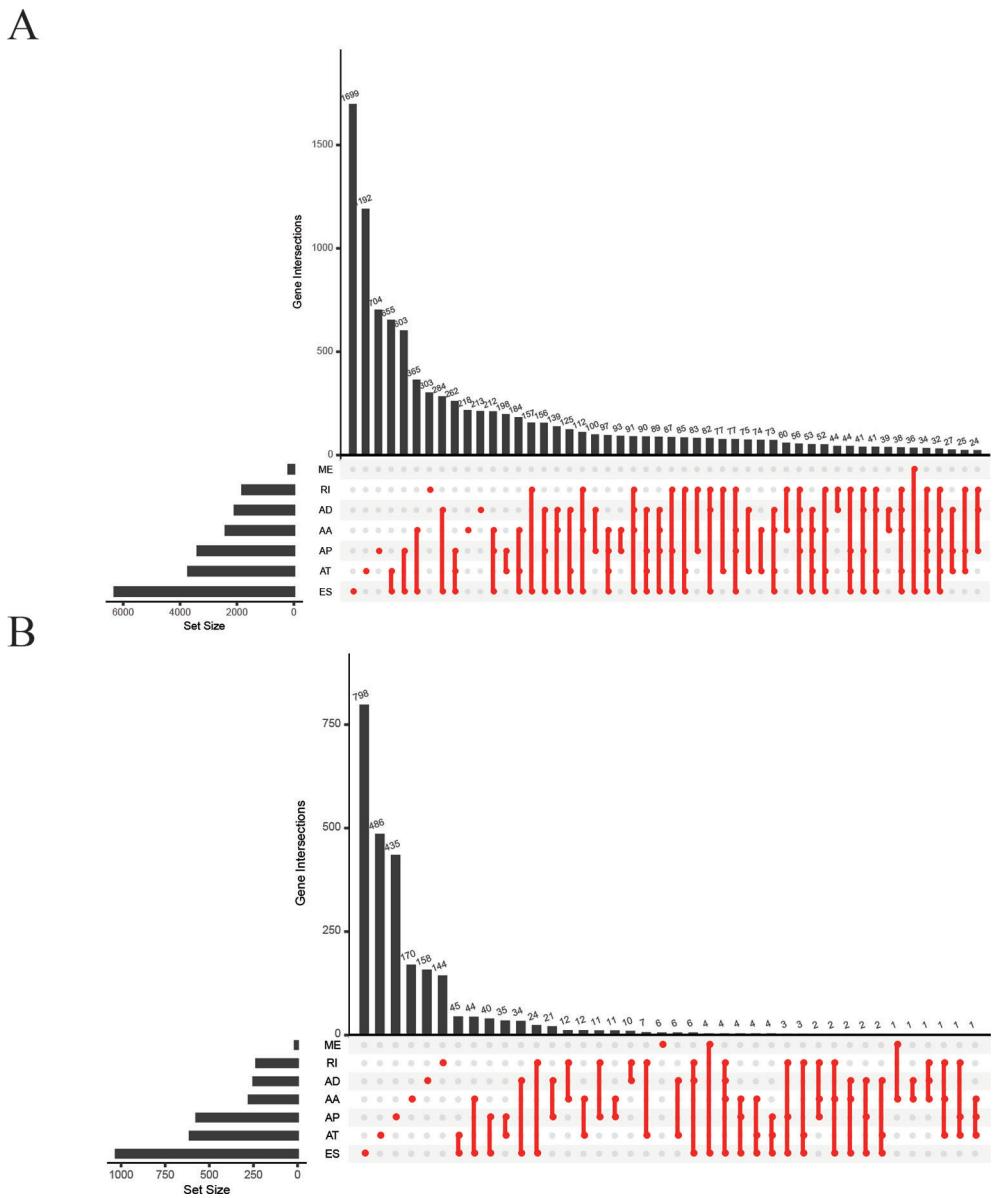

FIGURE 2 | UpSet plots of alternative splicing (AS) events in papillary renal cell carcinoma (pRCC). **(A)** Summary of AS events in pRCC. **(B)** Survival-associated AS events from univariate Cox regression analysis. AA, alternate acceptor; AD, alternate donor; AP, alternate promoter; AT, alternate terminator; ES, exon skip; ME, mutually exclusive exons; RI, retained intron.

($p < 0.05$). The HR values of CDK12 and SF3A2 in multivariate analyses were all greater than 1, suggesting that CDK12 and SF3A2 may associate with the poor survival of pRCC patients.

DISCUSSION

Previous studies have presented that AS is a crucial posttranscriptional regulation leading to structural transcript variation and proteome diversity (Zhang and Manley, 2013). Abnormal AS is associated with tumorigenesis (Grosso et al., 2008). To the best of our knowledge, few systematic AS-related research has been conducted. Prior to our research, Yang XJ et al. identified pRCC into two classes using comparative genomic microarray analysis, one associated with excellent survival and the other with poor prognosis (Yang et al., 2005). Wach S et al. classified pRCC subtypes using microRNA profiles (Wach et al., 2013). Recently, machine learning models have been used to classify stages of PRCC pRCC patients, showing a best performance with area under Precision Recall curve of 0.804, Matthews Correlation Coefficient of 0.711, and accuracy of 88% with Shrunken Centroid classifier on a test dataset based on 80

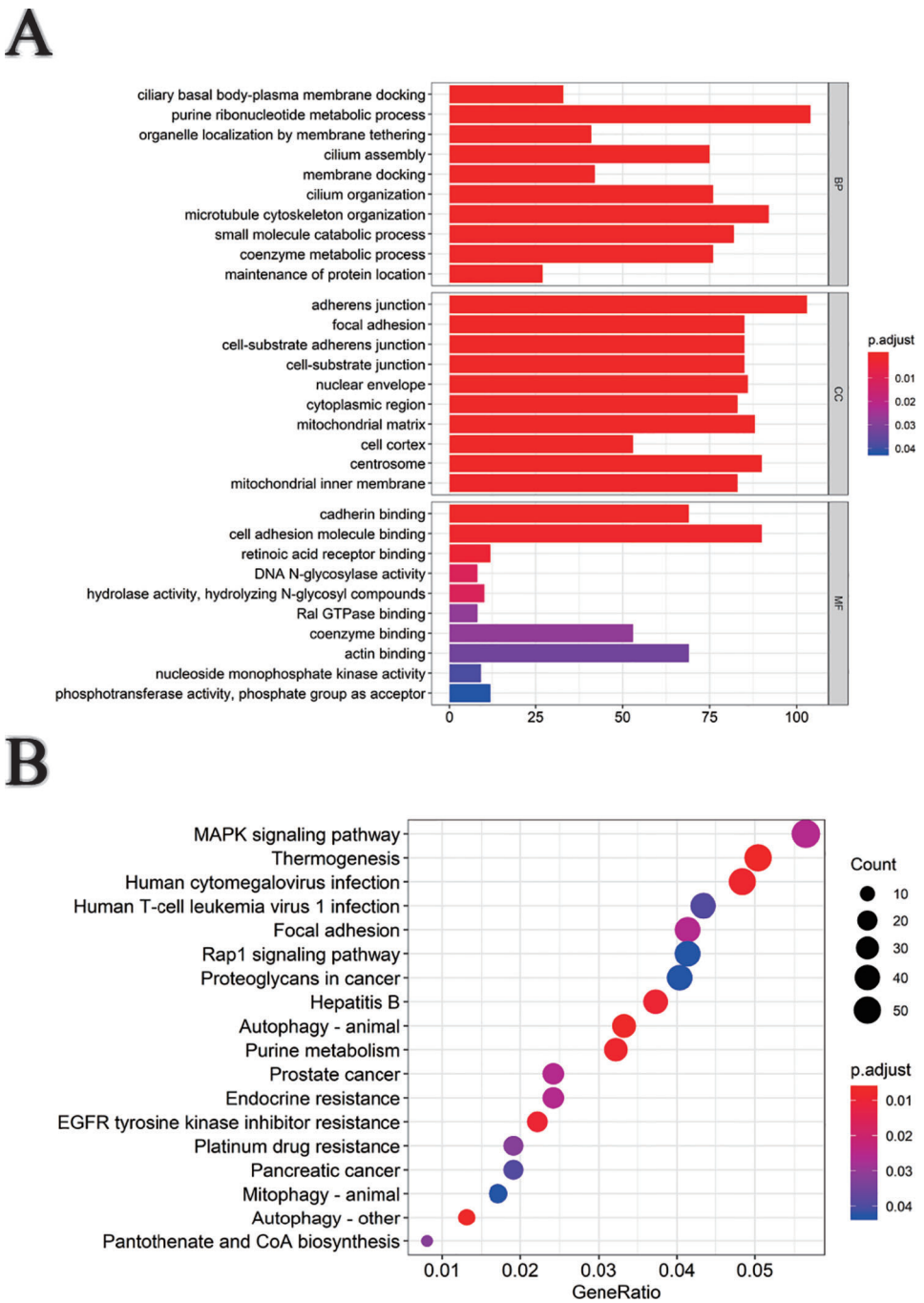

FIGURE 3 | Functional and pathway enrichment analysis. **(A)** Gene ontology analysis of genes with survival-associated alternative splicing events. **(B)** Kyoto Encyclopedia of Genes and Genomes (KEGG) pathway analysis of genes with survival-associated alternative splicing events.

selected genes (Singh et al., 2018). Therefore, this study is the first systematic analysis on pRCC-survival-associated AS events. The analysis showed that 4,084 AS events in 2,558 genes were associated with the overall survival (OS) of pRCC patients.

The parent genes of survival-associated AS events were subjected to functional enrichment analyses, and 18 potential pathways were enriched. Among which, MAPK signaling pathway was the top 1 in the list (**Figure 3B**). Targeted therapy against VEGF was a traditional medical treatment for renal cell carcinoma. Zhang Y et al. reported RKTG to inhibit angiogenesis by suppressing MAPK-mediated autocrine VEGF signaling (Zhang et al., 2010), and MAPK

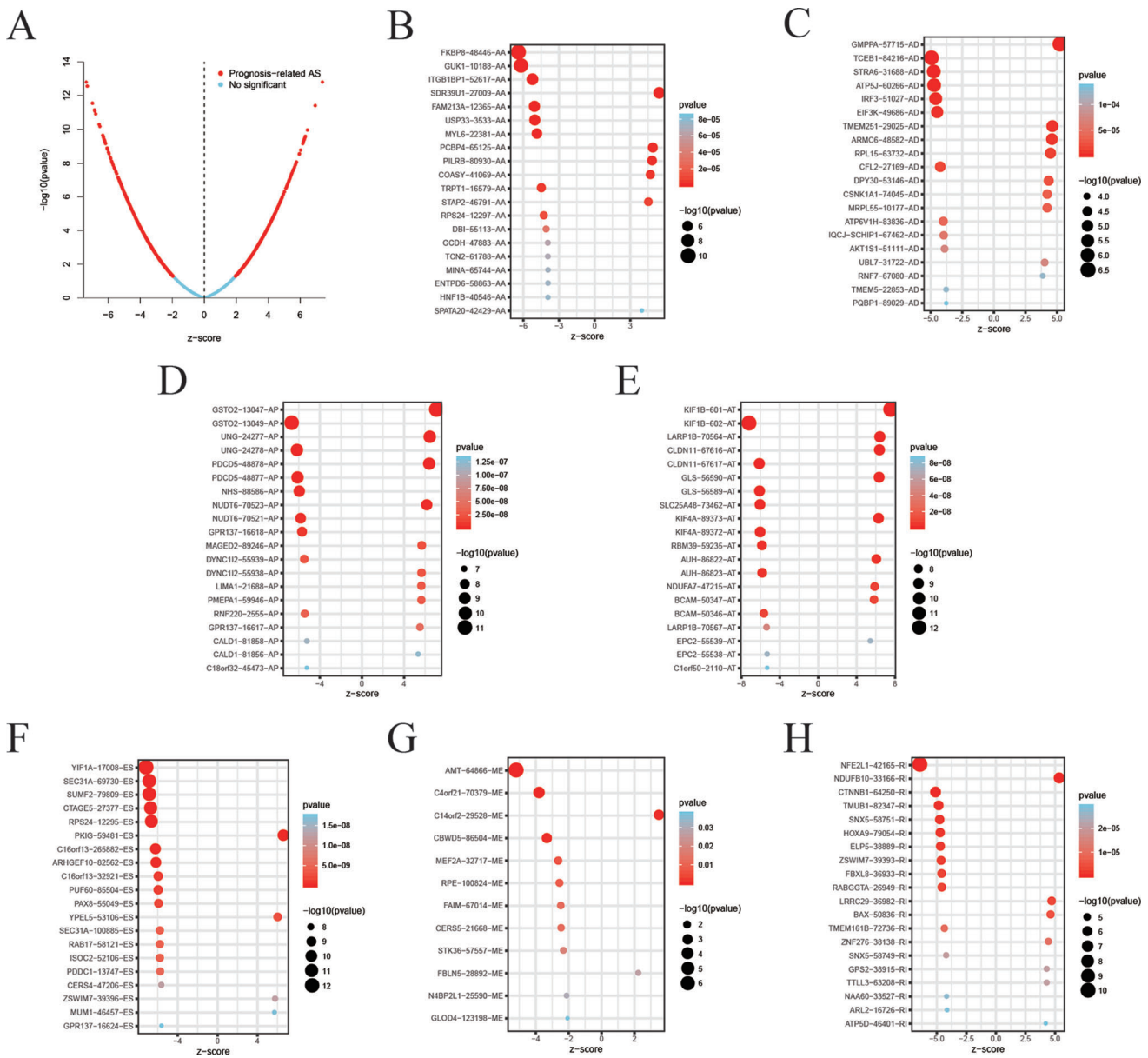

FIGURE 4 | Top 20 most significant alternative splicing (AS) events in papillary renal cell carcinoma (pRCC). **(A)** Volcano plot demonstrating result of univariate Cox regression analysis, red dots represent survival-associated genes and blue dots represent irrelevant genes. The top 20 AS events correlated with clinical outcome based on alternate acceptor (AA) **(B)**, alternate donor (AD) **(C)**, alternate promoter (AP) **(D)**, alternate terminator (AT) **(E)**, exon skip (ES) **(F)**, mutually exclusive exons (ME) **(G)**, and retained intron (RI) **(H)**. The value in the x-axis z-score is the coefficients of univariate cox regression analysis.

signaling pathway has also been reported to be involved in the development of renal cell carcinoma by some other molecular regulation (Huang et al., 2008; Huang et al., 2016; Li et al., 2017). AS is closely related to tumor resistance to drugs (Wang et al., 2017; Martinez-Montiel et al., 2018; Siegfried and Karni, 2018). In the pathway that genes enriched, "EGFR tyrosine kinase inhibitor resistance" and "platium drug resistance" were involved. EGFR (Wei et al., 2013; Robichaux et al., 2018) and platium (Vaughn et al., 2009; Teo et al., 2017; Pal et al., 2018) have been reported to be involved in the treatment of cancer, and through these enriched genes we may be able to discover specific mechanisms of drug resistance.

In this paper, we formed prognostic models by these survival-associated AS events. Before our research, Yang XJ et al performed microarray-based microRNA (miRNA) expression profiling of primary ccRCC and pRCC cases, and finally five miRNAs (miR-145, -200c, -210, -502-3p, and let-7c) were screened out to identify the samples with high accuracy (86.5%

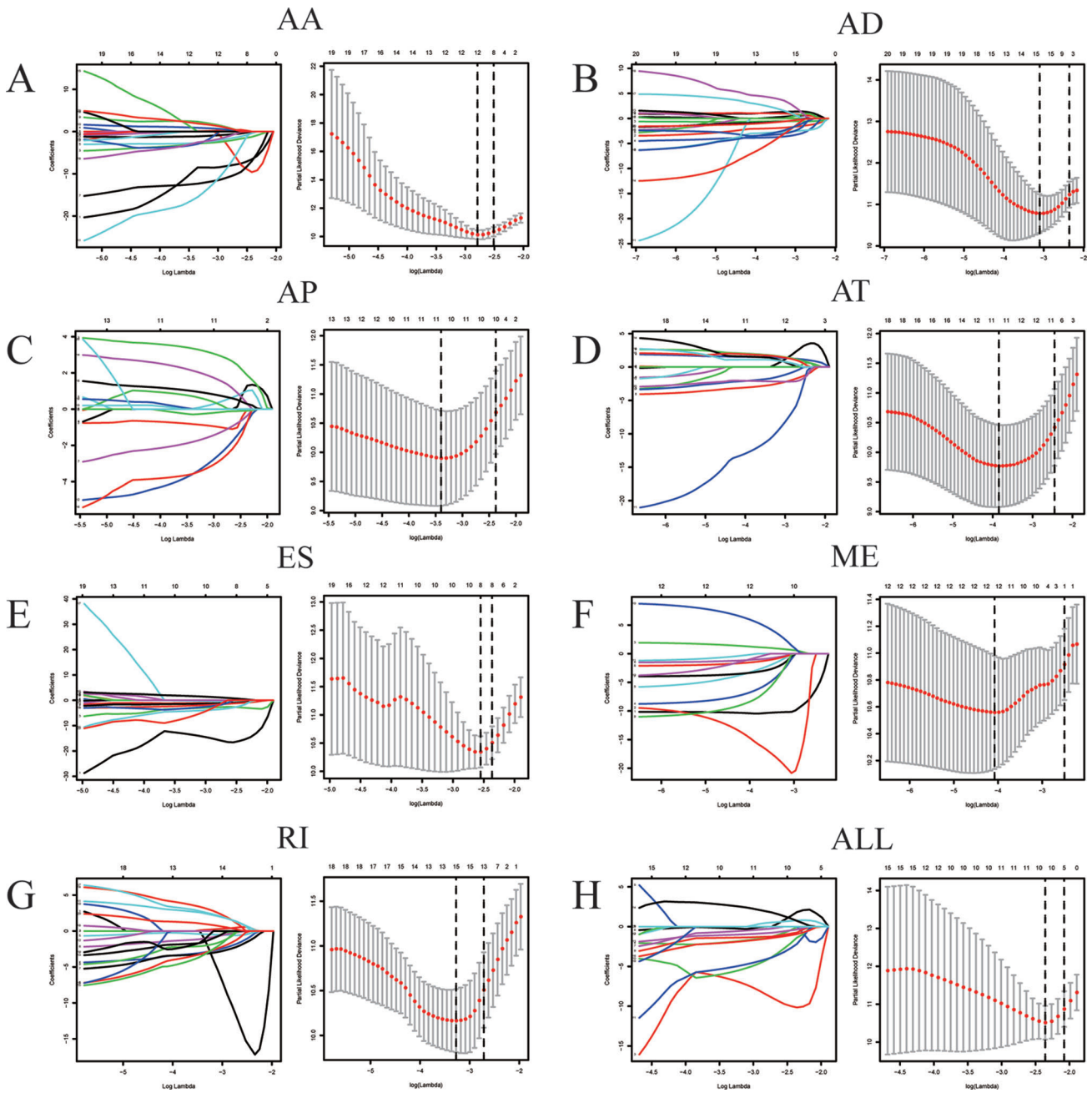

FIGURE 5 | LASSO Cox analysis of alternative splicing (AS) events. LASSO Cox regression model with 10-fold cross-validation was constructed using the top significant survival-associated AS events to screen the key AS features in AA **(A)**, AD **(B)**, AP **(C)**, AT **(D)**, ES **(E)**, ME **(F)**, RI **(G)** and all AS events **(H)**.

in tumor/normal classification, 77.6% in ccRCC/pRCC classification, and 86.4% in pRCC type 1/2 classification); Wach S et al. used machine learning models to classify stages of PRCC pRCC patients, showing a good performance with area under Precision Recall curve of 0.804, Matthews Correlation Coefficient of 0.711 and accuracy of 88% with Shrunken Centroid classifier on a test dataset based on 80 selected genes. As for the prognostic models in our research, firstly, Kaplan-Meier survival curves suggested that these models were appropriate methods to stratify pRCC patients into groups of different survivals ($p < 0.01$). Secondly, either single AS event or combined seven AS events performed well in predicting overall survival of pRCC patients (AUC > 0.9) with an exception of AUC = 0.861 in AD. Meanwhile, PI was proved to be independent in AA, AD, AP, AT, and RI by univariate and multivariate analyses. Compared with previous studies, using the

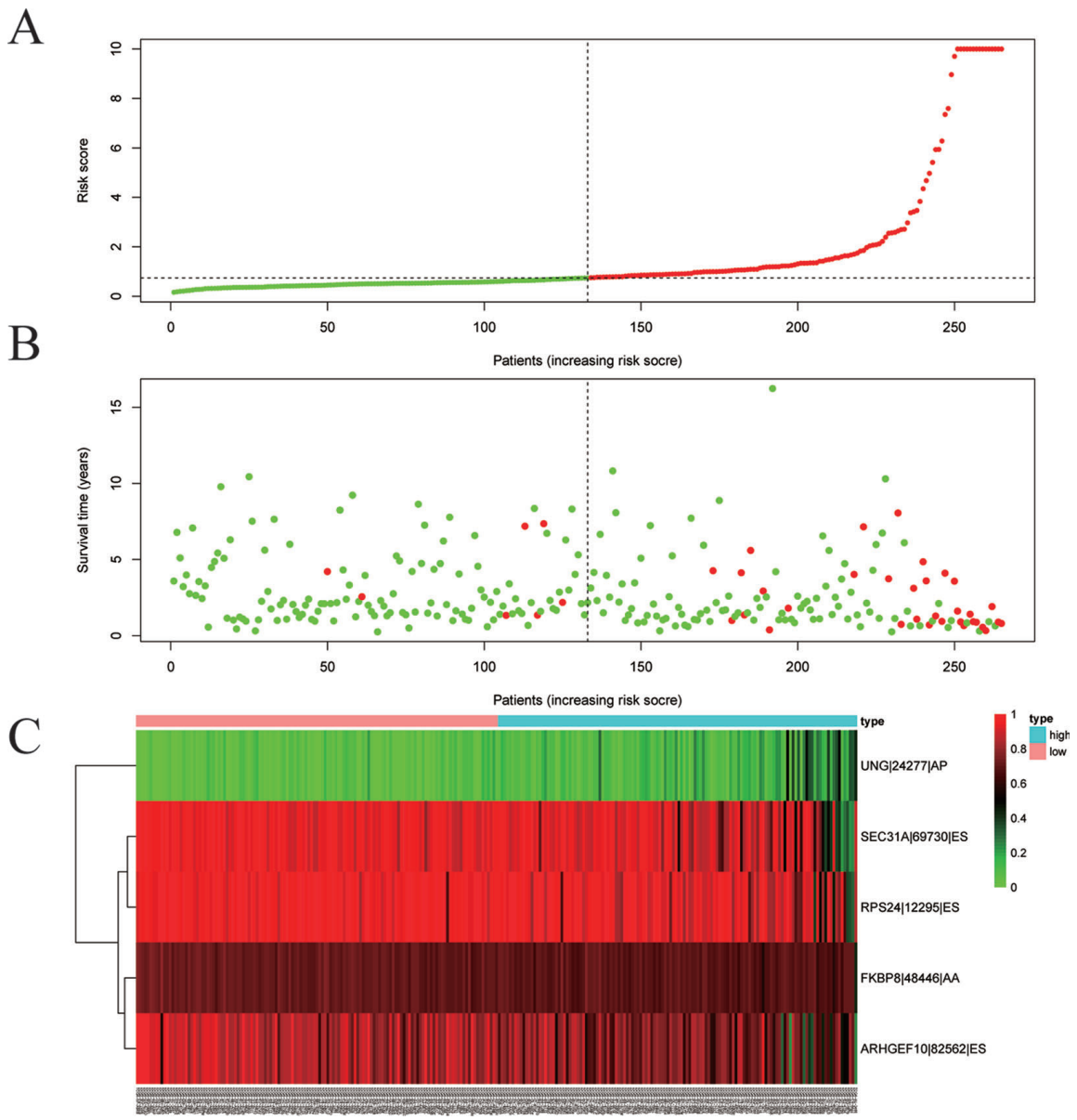

FIGURE 6 | Development of the prognostic index. Risk plot of ALL alternative splicing (AS) event. **(A)** Rank of prognostic index and distribution of groups. Patients with papillary renal cell carcinoma (pRCC) were divided into low- and high-risk subgroups based on the median value of the risk score calculated. **(B)** The survival status and survival time of patients with pRCC ranked by risk score. In **(A)** and **(B)**, green dots represent for patients with a low level of risk score and red dots represent for patients with a high level of risk score. **(C)** Heatmap of included AS event in ALL. Patients were divided into two groups according to risk score. The color from green to red means the Percent Spliced In (PSI) value from 0 to 1.

PSI value of AS events to predict patient's outcome is theoretically more systematic and accurate. At the same time, by searching for articles, we found that there were also related studies based on AS events in other tumors like uteri corpus endometrial carcinoma (Gao et al., 2019) and papillary thyroid cancer (Lin et al., 2019). However, based on the value of AUC in the prognostic model, it seems that the prognostic model based on AS events is more suitable for pRCC. We also built a nomogram for clinical application and validation.

By searching scientific literature, we found that some genes that make up PI have been reported to play an important role in tumors. For example, in the PI model of AT AS events, CLDN11, SLC25A48, KIF4A, RBM39, BCAM, and LARP1B were involved (**Table 1**, AT). It was reported that inactivation of CLDN11 could promote cell migration in nasopharyngeal carcinoma (Li et al., 2018). KIF4A were identified as prognostic gene or key gene involved in the metastasis of renal cell carcinoma in recent survey (Gu et al., 2017; Wei et al., 2019). Anticancer

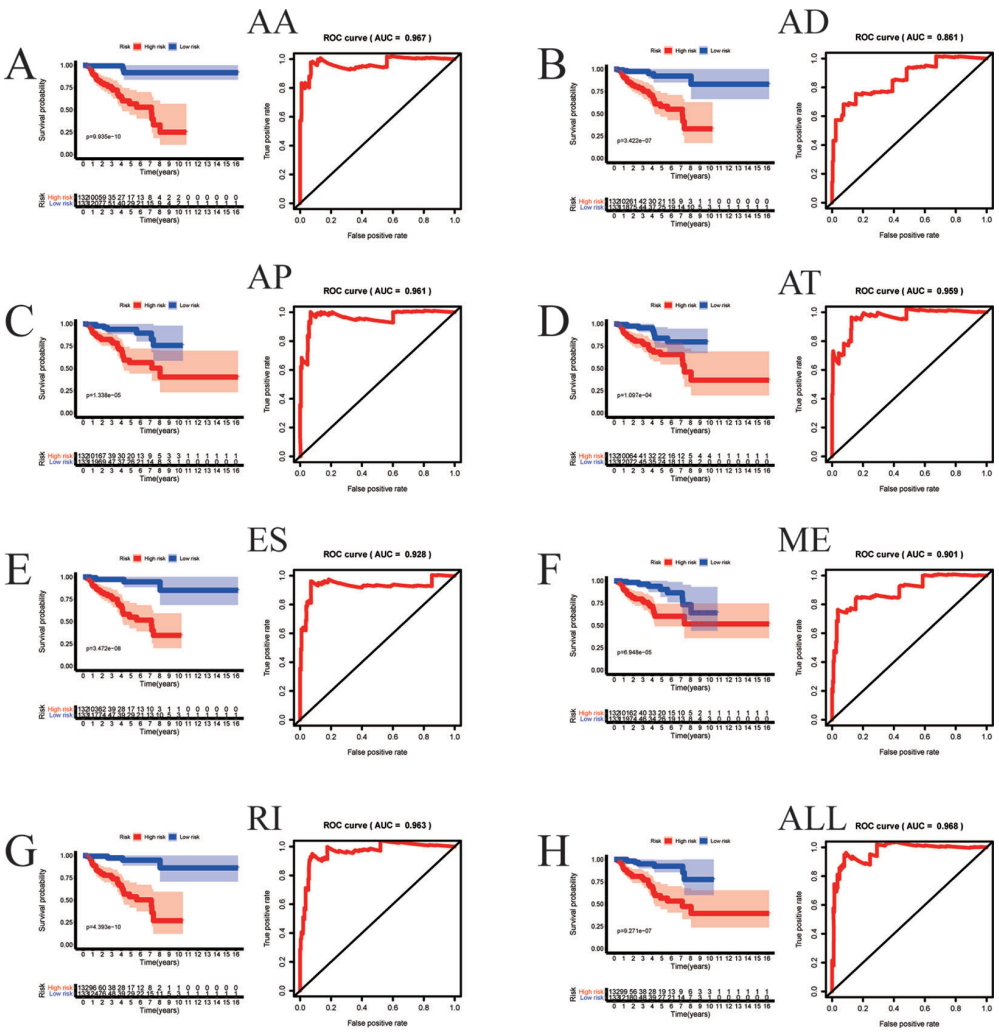

FIGURE 7 | The prognostic value of PI presented by overall survival (OS) and ROC curves. Kaplan-Meier plot depicting the survival probability over time for prognostic predictor of seven types of AS events **(A–G)** and all AS event **(H)** with high (red) and low (blue) risk group, respectively. The ROC curve to which the respective model belongs is located to the right of the KM curve.

TABLE 2 | Univariate analysis between clinical parameters and alternative splicing (AS) events in The Cancer Genome Atlas (TCGA) cohort of papillary renal cell carcinoma (pRCC) patients.

id	HR	HR.95L	HR.95H	pvalue
Age	1.8095854	0.8102357	4.041539	0.1479857
Gender	0.7549775	0.3182836	1.7908277	0.5236151
Stage	12.273306	5.4549378	27.614253	**1.36E-09**
T(Tumor)	5.3163151	2.4726062	11.430533	**1.89E-05**
M(Metastasis)	41.108075	12.143928	139.15381	**2.33E-09**
N (Lymph Node)	12.51509	5.7257522	27.354916	**2.39E-10**
Risk score based on AA	1.0053074	1.0032742	1.0073448	**2.98E-07**
Risk score based on AD	1.0162305	1.0078678	1.0246627	**0.0001341**
Risk score based on AP	1.0088837	1.0050934	1.0126883	**4.12E-06**
Risk score based on AT	1.0223319	1.0147675	1.0299526	**5.58E-09**
Risk score based on ES	1.0106936	1.0065517	1.0148524	**3.84E-07**
Risk score based on ME	1.0523824	1.0325915	1.0725527	**1.36E-07**
Risk score based on RI	1.0257308	1.0171857	1.0343477	**2.65E-09**
Risk score based on ALL	1.0076827	1.0039129	1.0114666	**6.28E-05**

Font bold indicates P < 0.05.

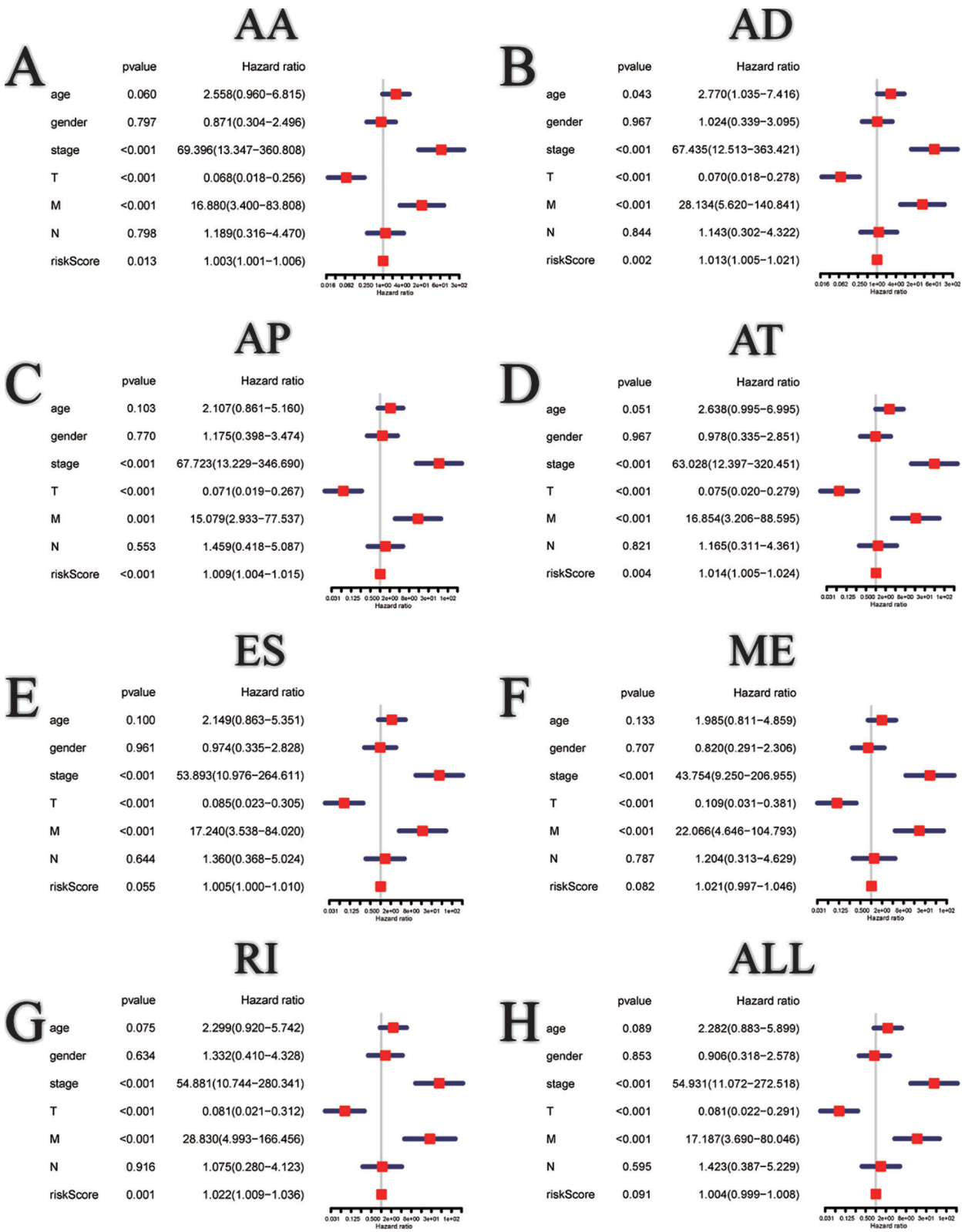

FIGURE 8 | Multivariate Cox regression analysis of clinical parameters and different PI models constructed by AA **(A)**, AD **(B)**, AP **(C)**, AT **(D)**, ES **(E)**, ME **(F)**, RI **(G)** and all AS events **(H)** in pRCC patients.

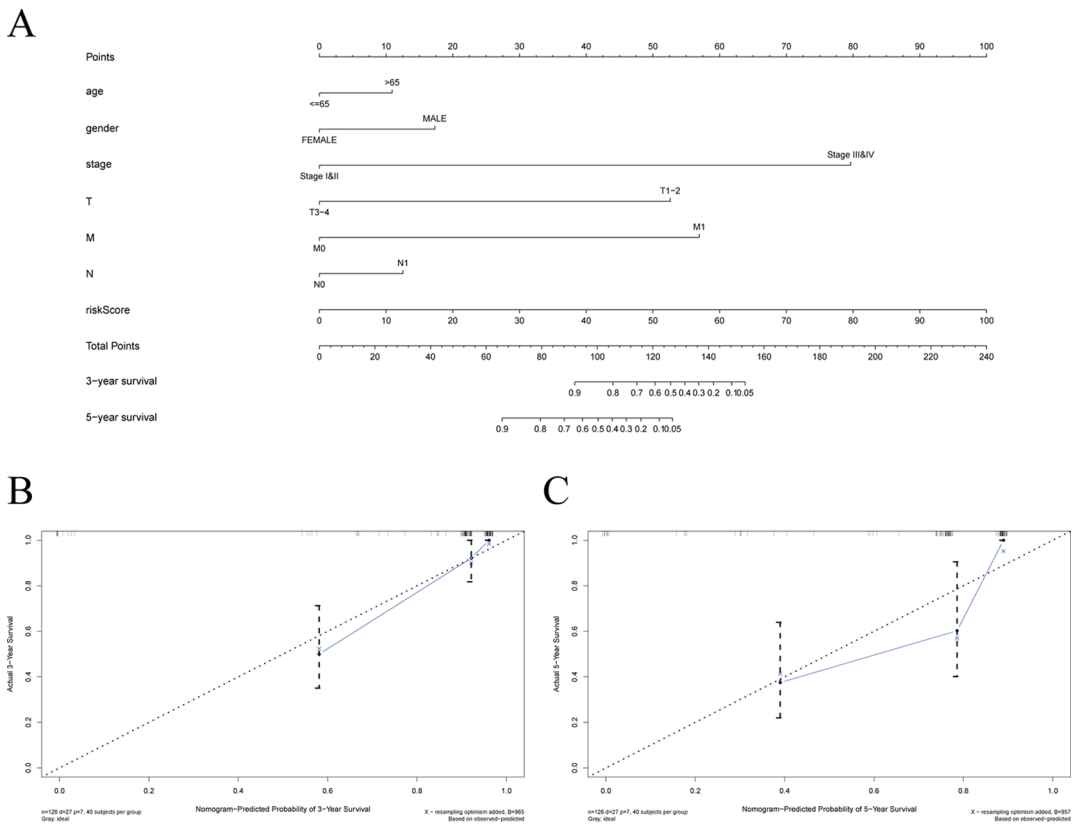

FIGURE 9 | Establishment of the overall survival (OS) nomogram for papillary renal cell carcinoma (pRCC) patients based on alternate acceptor (AA) event. **(A)** Nomogram for predicting OS of pRCC. There were seven factors containing age, gender, stage, T, N, M, and riskscore in the nomogram. Each of them generates points according to the line drawn upward. And the total points of the seven components of an individual patient lie on "Total Points" axis which corresponds to the probability of 3-year and 5-year OS rate plotted on the two axes below. **(B–C)** The calibration plots for predicting patient 3- or 5- year OS.

sulfonamides functions by inducing RBM39 degradation (Anticancer Sulfonamides Induce Splicing Factor RBM39 Degradation, 2017; Han et al., 2017). BCAM was reported to mediate recognition between tumor cells and the endothelium in KRAS-Mutant colorectal cancer. In the present study, the role of SLC25A48 and LARP1B was still unclear, and our analysis may guide the direction of future research on pRCC.

SFs are implicated in the process of alternative mRNA splicing (Venables et al., 2009). Splicing abnormalities arise owing to aberrant expression and/or mutations of SFs (Venables, 2006). Hence, SFs have a tight link with AS events. In this paper, survival-associated SFs were screened out by survival analyses. Correlation network was then formed to describe the interactions between SFs and AS events. Both positive and negative correlations were observed between one SF and multiple survival-associated AS events, or between one survival-associated AS event and multiple SFs. By performing LASSO Cox analysis and multivariate Cox regression analysis, CDK12, CDK10, SF3A2, and SNRNA were screened out. However, only CDK12 and SF3A2 were deemed significant statistically ($p < 0.05$) according to multivariate analyses. CDK12 contains an arginine–serine-rich (RS) domain, and can regulate the splicing of a minigene construct (Chen et al., 2006). CDK12 may be inactivated in patients with metastatic castration-resistant prostate cancer, and may make tumors more responsive to PD-1 inhibitors (CDK12 Changes Telling in Prostate Cancer, 2018). According to the regulatory network in our research, we found a negative correlation between CDK12 and SP100-57896-AT. It has been reported that SP100 could reduce malignancy of human glioma cells (Held-Feindt et al., 2011). The HR value of SF3A2 was 1.051, and SF3A2 was also reported to be associated with the metastasis and recurrence of osteosarcoma (Zhang et al., 2019). These results indicated that these altered SFs, as independent molecules, can construct a regulatory network in the carcinogenesis and progression in pRCC. However, this network may be optimized with more molecules. Besides, only 129 pRCC patients were involved in our analysis due to the restricted standard of OS time more than 90 days and requirement for complete clinical data. PI was proved to be independent in AA, AD, AP, AT, and RI by univariate and multivariate analyses in this paper, but when we brought all the AS events together, $p > 0.05$ in multivariate analyses (**Figure 8H**) which indicted that there were still some key factors that were not considered in our analysis and certain errors were inevitable due to the heterogeneity of patients.

In conclusion, our study created an efficient prognostic model based on survival-associated AS events for pRCC, which may

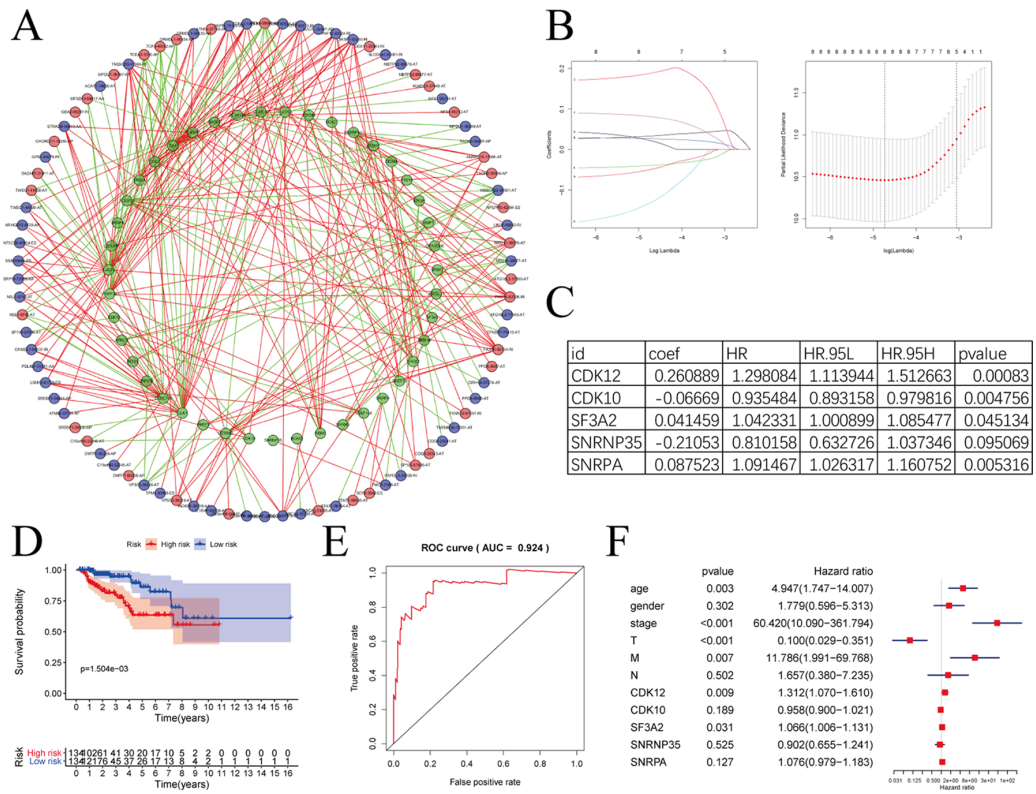

FIGURE 10 | The correlation network between alternative splicing (AS) events and splicing factors in papillary renal cell carcinoma (pRCC). **(A)** Correlation network between filtered AS events and survival-associated splicing factors (SFs). Green dots were survival associated splicing factors. Red/blue dots were favorable/adverse AS events. Red/green lines represent positive/negative correlations between substances. **(B)** LASSO Cox analysis of involved SFs. **(C)** Multivariate Cox regression analysis of LASSO result. **(D–E)** The prognostic value of SFs presented by overall survival (OS) and ROC curves. **(F)** Multivariate analyses containing clinical factors and five key genes.

help clinicians in selecting reliable prognostic indicators and understanding the mechanism of pRCC.

DATA AVAILABILITY STATEMENT

Publicly available datasets were analyzed in this study. This data can be found here: https://portal.gdc.cancer.gov/repository. AS files could be downloaded from TCGASpliceSeq: https://bioinformatics.mdanderson.org/TCGASpliceSeq/.

AUTHOR CONTRIBUTIONS

Conception and design: XX and CC. Collection and assembly of data: ZW and JL. Data analysis and interpretation: RS and DC. Manuscript writing: ZW and KW. Final approval of manuscript: All authors.

ACKNOWLEDGMENTS

The authors would like to thank the TCGA databases and TCGASpliceseq for the availability of the data.

SUPPLEMENTARY MATERIAL

The Supplementary Material for this article can be found online at: https://www.frontiersin.org/articles/10.3389/fgene.2019.01333/full#supplementary-material

REFERENCES

Agrawal, A. A., Yu, L., Smith, P. G., and Buonamici, S. (2018). Targeting splicing abnormalities in cancer. *Curr. Opin. Genet. Dev.* 48, 67–74. doi: 10.1016/j.gde.2017.10.010

Anticancer Sulfonamides Induce Splicing Factor RBM39 Degradation. (2017). *Cancer Discovery*. doi: 10.1158/2159-8290.CD-RW2017-08

Armstrong, A. J., Halabi, S., Eisen, T., Broderick, S., Stadler, W. M., Jones, R. J., et al. (2016). Everolimus versus sunitinib for patients with metastatic non-clear cell renal cell carcinoma (ASPEN): a multicentre, open-label, randomised phase 2 trial. *Lancet Oncol.* 17 (3), 378–388. doi: 10.1016/S1470-2045(15)00515-X

Bowler, E., Porazinski, S., Uzor, S., Thibault, P., Durand, M., Lapointe, E., et al. (2018). Hypoxia leads to significant changes in alternative splicing and elevated

expression of CLK splice factor kinases in PC3 prostate cancer cells. *BMC Cancer* 18 (1), 355. doi: 10.1186/s12885-018-4227-7

CDK12 Changes Telling in Prostate Cancer. (2018). *Cancer Discovery* 8, 1055. doi: 10.1158/2159-8290.CD-NB2018-093

Chen, H. H., Wang, Y. C., and Fann, M. J. (2006). Identification and characterization of the CDK12/cyclin L1 complex involved in alternative splicing regulation. *Mol. Cell Biol.* 26 (7), 2736–2745. doi: 10.1128/MCB.26.7.2736-2745.2006

Conway, J. R., Lex, A., and Gehlenborg, N. (2017). UpSetR: an R package for the visualization of intersecting sets and their properties. *Bioinformatics* 33 (18), 2938–2940. doi: 10.1093/bioinformatics/btx364

Delahunt, B., and Eble, J. N. (1997). Papillary renal cell carcinoma: a clinicopathologic and immunohistochemical study of 105 tumors. *Mod. Pathol.* 10 (6), 537–544.

Frankish, A., Diekhans, M., Ferreira, A. M., Johnson, R., Jungreis, I., Loveland, J., et al. (2019). GENCODE reference annotation for the human and mouse genomes. *Nucleic Acids Res.* 47 (D1), D766–D773. doi: 10.1093/nar/gky955

Friedman, J., Hastie, T., and Tibshirani, R. (2010). Regularization Paths for Generalized Linear Models via Coordinate Descent. *J. Stat. Softw.* 33 (1), 1–22.

Gao, L., Xie, Z. C., Pang, J. S., Li, T. T., and Chen, G. (2019). A novel alternative splicing-based prediction model for uteri corpus endometrial carcinoma. *Aging (Albany NY)* 11 (1), 263–283. doi: 10.18632/aging.101753

Grosso, A. R., Martins, S., and Carmo-Fonseca, M. (2008). The emerging role of splicing factors in cancer. *EMBO Rep.* 9 (11), 1087–1093. doi: 10.1038/embor.2008.189

Gu, Y., Lu, L., Wu, L., Chen, H., Zhu, W., and He, Y. (2017). Identification of prognostic genes in kidney renal clear cell carcinoma by RNAseq data analysis. *Mol. Med. Rep.* 15 (4), 1661–1667. doi: 10.3892/mmr.2017.6194

Han, T., Goralski, M., Gaskill, N., Capota, E., Kim, J., Ting, T. C., et al. (2017). Anticancer sulfonamides target splicing by inducing RBM39 degradation via recruitment to DCAF15. *Science* 356. doi: 10.1126/science.aal3755

Held-Feindt, J., Hattermann, K., Knerlich-Lukoschus, F., Mehdorn, H. M., and Mentlein, R. (2011). SP100 reduces malignancy of human glioma cells. *Int. J. Oncol.* 38 (4), 1023–1030. doi: 10.3892/ijo.2011.927

Huang, D., Ding, Y., Luo, W. M., Bender, S., Qian, C. N., Kort, E., et al. (2008). Inhibition of MAPK kinase signaling pathways suppressed renal cell carcinoma growth and angiogenesis *in vivo*. *Cancer Res.* 68 (1), 81–88. doi: 10.1158/0008-5472.CAN-07-5311

Huang, B., Fu, S. J., Fan, W. Z., Wang, Z. H., Chen, Z. B., Guo, S. J., et al. (2016). PKCepsilon inhibits isolation and stemness of side population cells via the suppression of ABCB1 transporter and PI3K/Akt, MAPK/ERK signaling in renal cell carcinoma cell line 769P. *Cancer Lett.* 376 (1), 148–154. doi: 10.1016/j.canlet.2016.03.041

Jonasch, E., Gao, J., and Rathmell, W. K. (2014). Renal cell carcinoma. *BMJ* 349, g4797. doi: 10.1136/bmj.g4797

Kahles, A., Lehmann, K. V., Toussaint, N. C., Huser, M., Stark, S. G., Sachsenberg, T., et al. (2018). Comprehensive analysis of alternative splicing across tumors from 8,705 patients. *Cancer Cell* 34 (2), 211–224, e216. doi: 10.1016/j.ccell.2018.07.001

Li, J. K., Chen, C., Liu, J. Y., Shi, J. Z., Liu, S. P., Liu, B., et al. (2017). Long noncoding RNA MRCCAT1 promotes metastasis of clear cell renal cell carcinoma via inhibiting NPR3 and activating p38-MAPK signaling. *Mol. Cancer* 16 (1), 111. doi: 10.1186/s12943-017-0681-0

Li, H. P., Peng, C. C., Wu, C. C., Chen, C. H., Shih, M. J., Huang, M. Y., et al. (2018). Inactivation of the tight junction gene CLDN11 by aberrant hypermethylation modulates tubulins polymerization and promotes cell migration in nasopharyngeal carcinoma. *J. Exp. Clin. Cancer Res.* 37 (1), 102. doi: 10.1186/s13046-018-0754-y

Lin, P., He, R. Q., Huang, Z. G., Zhang, R., Wu, H. Y., Shi, L., et al. (2019). Role of global aberrant alternative splicing events in papillary thyroid cancer prognosis. *Aging (Albany NY)* 11 (7), 2082–2097. doi: 10.18632/aging.101902

Malouf, G. G., Su, X., Zhang, J., Creighton, C. J., Ho, T. H., Lu, Y., et al. (2016). DNA methylation signature reveals cell ontogeny of renal cell carcinomas. *Clin. Cancer Res.* 22 (24), 6236–6246. doi: 10.1158/1078-0432.CCR-15-1217

Martinez-Montiel, N., Rosas-Murrieta, N. H., Anaya Ruiz, M., Monjaraz-Guzman, E., and Martinez-Contreras, R. (2018). Alternative Splicing as a Target for Cancer Treatment. *Int. J. Mol. Sci.* 19 (2). doi: 10.3390/ijms19020545

O'leary, N. A., Wright, M. W., Brister, J. R., Ciufo, S., Haddad, D., Mcveigh, R., et al. (2016). Reference sequence (RefSeq) database at NCBI: current status, taxonomic expansion, and functional annotation. *Nucleic Acids Res.* 44 (D1), D733–D745. doi: 10.1093/nar/gkv1189

Pal, S. K., Hoffman-Censits, J., Zheng, H., Kaiser, C., Tayama, D., and Bellmunt, J. (2018). Atezolizumab in platinum-treated locally advanced or metastatic urothelial carcinoma: clinical experience from an expanded access study in the United States. *Eur. Urol.* 73 (5), 800–806. doi: 10.1016/j.eururo.2018.02.010

Pertea, M., and Salzberg, S. L. (2010). Between a chicken and a grape: estimating the number of human genes. *Genome Biol.* 11. doi: 10.1186/gb-2010-11-5-206

Pertea, M., Shumate, A., Pertea, G., Varabyou, A., and Salzberg, S. (2018). Thousands of large-scale RNA sequencing experiments yield a comprehensive new human gene list and reveal extensive transcriptional noise.

Piva, F., Giulietti, M., Burini, A. B., and Principato, G. (2012). SpliceAid 2: a database of human splicing factors expression data and RNA target motifs. *Hum. Mutat.* 33 (1), 81–85. doi: 10.1002/humu.21609

Robichaux, J. P., Elamin, Y. Y., Tan, Z., Carter, B. W., Zhang, S., Liu, S., et al. (2018). Mechanisms and clinical activity of an EGFR and HER2 exon 20-selective kinase inhibitor in non-small cell lung cancer. *Nat. Med.* 24 (5), 638–646. doi: 10.1038/s41591-018-0007-9

Ryan, M., Wong, W. C., Brown, R., Akbani, R., Su, X., Broom, B., et al. (2016). TCGASpliceSeq a compendium of alternative mRNA splicing in cancer. *Nucleic Acids Res.* 44 (D1), D1018–D1022. doi: 10.1093/nar/gkv1288

Siegfried, Z., and Karni, R. (2018). The role of alternative splicing in cancer drug resistance. *Curr. Opin. Genet. Dev.* 48, 16–21. doi: 10.1016/j.gde.2017.10.001

Singh, N. P., Bapi, R. S., and Vinod, P. K. (2018). Machine learning models to predict the progression from early to late stages of papillary renal cell carcinoma. *Comput. Biol. Med.* 100, 92–99. doi: 10.1016/j.compbiomed.2018.06.030

Tang, J. Y., Lee, J. C., Hou, M. F., Wang, C. L., Chen, C. C., Huang, H. W., et al. (2013). Alternative splicing for diseases, cancers, drugs, and databases. *ScientificWorldJournal* 2013, 703568. doi: 10.1155/2013/703568

Teo, M. Y., Bambury, R. M., Zabor, E. C., Jordan, E., Al-Ahmadie, H., Boyd, M. E., et al. (2017). DNA damage response and repair gene alterations are associated with improved survival in patients with platinum-treated advanced urothelial carcinoma. *Clin. Cancer Res.* 23 (14), 3610–3618. doi: 10.1158/1078-0432.CCR-16-2520

Vaughn, D. J., Srinivas, S., Stadler, W. M., Pili, R., Petrylak, D., Sternberg, C. N., et al. (2009). Vinflunine in platinum-pretreated patients with locally advanced or metastatic urothelial carcinoma: results of a large phase 2 study. *Cancer* 115 (18), 4110–4117. doi: 10.1002/cncr.24460

Venables, J. P., Klinck, R., Koh, C., Gervais-Bird, J., Bramard, A., Inkel, L., et al. (2009). Cancer-associated regulation of alternative splicing. *Nat. Struct. Mol. Biol.* 16 (6), 670–676. doi: 10.1038/nsmb.1608

Venables, J. P. (2006). Unbalanced alternative splicing and its significance in cancer. *Bioessays* 28, 378–386. doi: 10.1002/bies.20390

Wach, S., Nolte, E., Theil, A., Stohr, C., T, T. R., Hartmann, A., et al. (2013). MicroRNA profiles classify papillary renal cell carcinoma subtypes. *Br. J. Cancer* 109 (3), 714–722. doi: 10.1038/bjc.2013.313

Wan, L., Yu, W., Shen, E., Sun, W., Liu, Y., Kong, J., et al. (2019). SRSF6-regulated alternative splicing that promotes tumour progression offers a therapy target for colorectal cancer. *Gut* 68 (1), 118–129. doi: 10.1136/gutjnl-2017-314983

Wang, E. T., Sandberg, R., Luo, S., Khrebtukova, I., Zhang, L., Mayr, C., et al. (2008). Alternative isoform regulation in human tissue transcriptomes. *Nature* 456 (7221), 470–476. doi: 10.1038/nature07509

Wang, B. D., Ceniccola, K., Hwang, S., Andrawis, R., Horvath, A., Freedman, J. A., et al. (2017). Alternative splicing promotes tumour aggressiveness and drug resistance in African American prostate cancer. *Nat. Commun.* 8, 15921. doi: 10.1038/ncomms15921

Wei, Y., Zou, Z., Becker, N., Anderson, M., Sumpter, R., Xiao, G., et al. (2013). EGFR-mediated Beclin 1 phosphorylation in autophagy suppression, tumor progression, and tumor chemoresistance. *Cell* 154 (6), 1269–1284. doi: 10.3892/ol.2019.10130

Wei, W., Lv, Y., Gan, Z., Zhang, Y., Han, X., and Xu, Z. (2019). Identification of key genes involved in the metastasis of clear cell renal cell carcinoma. *Oncol. Lett.* 17 (5), 4321–4328. doi: 10.1016/j.cell.2013.08.015

Yang, X. J., Tan, M. H., Kim, H. L., Ditlev, J. A., Betten, M. W., Png, C. E., et al. (2005). A molecular classification of papillary renal cell carcinoma. *Cancer Res.* 65 (13), 5628–5637. doi: 10.1158/0008-5472.CAN-05-0533

Yu, G., Wang, L. G., Han, Y., and He, Q. Y. (2012). clusterProfiler: an R package for comparing biological themes among gene clusters. *OMICS* 16 (5), 284–287. doi: 10.1089/omi.2011.0118

Zhang, J., and Manley, J. L. (2013). Misregulation of pre-mRNA alternative splicing in cancer. *Cancer Discovery* 3 (11), 1228–1237. doi: 10.1158/2159-8290.CD-13-0253

Zhang, Y., Jiang, X., Qin, X., Ye, D., Yi, Z., Liu, M., et al. (2010). RKTG inhibits angiogenesis by suppressing MAPK-mediated autocrine VEGF signaling and is downregulated in clear-cell renal cell carcinoma. *Oncogene* 29 (39), 5404–5415. doi: 10.1038/onc.2010.270

Zhang, Y., Zhao, H., Xu, W., Jiang, D., Huang, L., and Li, L. (2019). High expression of PQBP1 and low expression of PCK2 are associated with metastasis and recurrence of osteosarcoma and unfavorable survival outcomes of the patients. *J. Cancer* 10(9), 2091–2101. doi: 10.7150/jca.28480

Conflict of Interest: The authors declare that the research was conducted in the absence of any commercial or financial relationships that could be construed as a potential conflict of interest.

Copyright © 2020 Wu, Liu, Sun, Chen, Wang, Cao and Xu. This is an open-access article distributed under the terms of the Creative Commons Attribution License (CC BY). The use, distribution or reproduction in other forums is permitted, provided the original author(s) and the copyright owner(s) are credited and that the original publication in this journal is cited, in accordance with accepted academic practice. No use, distribution or reproduction is permitted which does not comply with these terms.

frontiers in Neuroscience

ORIGINAL RESEARCH
published: 31 January 2020
doi: 10.3389/fnins.2019.01410

Multiple Pathways Involved in Palmitic Acid-Induced Toxicity: A System Biology Approach

Daniel Osorio[1], Andrés Pinzón[2], Cynthia Martín-Jiménez[3]*, George E. Barreto[4,5] and Janneth González[3]**

[1] Department of Veterinary Integrative Biosciences, Texas A&M University, College Station, TX, United States, [2] Laboratorio de Bioinformática y Biología de Sistemas, Universidad Nacional de Colombia, Bogotá, Colombia, [3] Departamento de Nutrición y Bioquímica, Facultad de Ciencias, Pontificia Universidad Javeriana, Bogotá, Colombia, [4] Department of Biological Sciences, University of Limerick, Limerick, Ireland, [5] Health Research Institute, University of Limerick, Limerick, Ireland

Inflammation is a complex biological response to injuries, metabolic disorders or infections. In the brain, astrocytes play an important role in the inflammatory processes during neurodegenerative diseases. Recent studies have shown that the increase of free saturated fatty acids such as palmitic acid produces a metabolic inflammatory response in astrocytes generally associated with damaging mechanisms such as oxidative stress, endoplasmic reticulum stress, and autophagic defects. In this aspect, the synthetic neurosteroid tibolone has shown to exert protective functions against inflammation in neuronal experimental models without the tumorigenic effects exerted by sexual hormones such as estradiol and progesterone. However, there is little information regarding the specific mechanisms of tibolone in astrocytes during inflammatory insults. In the present study, we performed a genome-scale metabolic reconstruction of astrocytes that was used to study astrocytic response during an inflammatory insult by palmitate through Flux Balance Analysis methods and data mining. In this aspect, we assessed the metabolic fluxes of human astrocytes under three different scenarios: healthy (normal conditions), induced inflammation by palmitate, and tibolone treatment under palmitate inflammation. Our results suggest that tibolone reduces the L-glutamate-mediated neurotoxicity in astrocytes through the modulation of several metabolic pathways involved in glutamate uptake. We also identified a set of reactions associated with the protective effects of tibolone, including the upregulation of taurine metabolism, gluconeogenesis, cPPAR and the modulation of calcium signaling pathways. In conclusion, the different scenarios studied in our model allowed us to identify several metabolic fluxes perturbed under an inflammatory response and the protective mechanisms exerted by tibolone.

Keywords: tibolone, astrocytes, inflammatory response, flux balance analysis, palmitic acid, genome-scale reconstruction, systems biology

OPEN ACCESS

Edited by:
Julio R. Banga, Spanish National Research Council (CSIC), Spain

Reviewed by:
Peng Zhong, Wuhan University, China
Shivendra Gajraj Tewari, Biotechnology HPC Software Applications Institute (BHSAI), United States

****Correspondence:***
Daniel Osorio
dcosorioh@tamu.edu
Cynthia Martín-Jiménez
martin.c@javeriana.edu.co; cynthialexa@hotmail.com
Janneth González
janneth.gonzalez@javeriana.edu.co

Specialty section:
This article was submitted to Systems Biology, a section of the journal Frontiers in Neuroscience

Received: *20 August 2019*
Accepted: *12 December 2019*
Published: *31 January 2020*

Citation:
Osorio D, Pinzón A, Martín-Jiménez C, Barreto GE and González J (2020) Multiple Pathways Involved in Palmitic Acid-Induced Toxicity: A System Biology Approach. Front. Neurosci. 13:1410. doi: 10.3389/fnins.2019.01410

INTRODUCTION

Astrocytes are the most abundant cells in the human brain. In the last years, it has been shown that they are of paramount importance for different essential functions in central nervous system (CNS). For instance, the homeostatic regulation of the central nervous system (Takuma et al., 2004), tissue repair, modulation of synaptic activity through the release of gliotransmitters and glycogen

storage (Lange et al., 2012). Additionally, astrocytes protect neurons against the glutamate-induced excitotoxicity through the astrocyte-specific sodium-dependent glutamate transporters such as GLT-1 and GLAST (Bélanger and Magistretti, 2009). On the other hand, astrocytes are important modulators of inflammation (Sofroniew, 2014). Their main response to inflammation happens through the activation of the complex process of reactive gliosis, which is an important process for CNS during injuries and diseases (Dowell et al., 2009; Barreto et al., 2011; Sofroniew, 2014). For these reasons, a great number of studies have shown that the dysregulation of astrocytic functions is highly correlated with the development of neurodegenerative processes, (Takuma et al., 2004; Kumar Jha et al., 2016).

Different works have shown that astrocytes are key mediators in the brain lipid homeostasis and B-oxidation of fatty acid (Panov et al., 2014). Interestingly, saturated free fatty acids, including stearic acid, lauric acid, and palmitic acid, are closely associated with neurodegenerative processes such as traumatic brain injury (TmBI), dementia, stroke, epilepsy, spinal cord injury, Parkinson's disease (PD) reactive gliosis, neuroinflammation, and Alzheimer's disease (AD) (Bruce-Keller et al., 2001, 2009; White et al., 2009; Gupta et al., 2012; Little et al., 2012; González-Giraldo et al., 2019). Additionally, both palmitic acid and stearic acid were shown to increase the secretion of Aβ amyloid peptide in an AD cellular model (Amtul et al., 2011). Recent studies in human populations also point an inverse correlation between clinical obesity and neuroinflammation (Barnard et al., 2014; Reichelt et al., 2017; Melo et al., 2019), suggesting that long-term consumption of high fat diets is associated with pathological mechanisms in the brain (Melo et al., 2019). Moreover, the increase of saturated free fatty acids during metabolic inflammation activates IKKβ kinase and its downstream effector NF-κβ, which in turn impairs leptin and insulin hormonal signaling and triggers the production and release of reactive oxygen species (ROS) and pro-inflammatory cytokines like TNF-α and IL-6 from glial cells (Purkayastha and Cai, 2013).

In this aspect, tibolone is a synthetic steroid (Kloosterboer, 2001), with estrogenic, progestogenic, and weak androgenic actions (González-Giraldo et al., 2019). It has been used for the treatment of climacteric symptoms and osteoporosis in post-menopausal women (Rymer et al., 1994; Rymer, 1998) and has also shown beneficial antidepressant effects in menopausal women (Kulkarni et al., 2015). It has been shown that tibolone exerts its neuroprotective effects through the activation of the Akt/GSK3ß signaling pathway which in turns causes the reduction of Tau phosphorylation in the hippocampus and cerebellum of ovariectomized rats, the increase in antioxidant activity in primary neuronal cultures and the increase in the expression of the antiapoptotic protein Bcl-2 (Genazzani et al., 2006; Belenichev et al., 2012; Pinto-Almazán et al, 2012; Avila-Rodriguez et al., 2014). Nevertheless, there is little information regarding the effects of tibolone in astrocytes or the metabolic pathways related with its neuroprotective mechanisms (Avila-Rodriguez et al., 2014; González-Giraldo et al., 2019).

In that sense, genome-scale metabolic reconstructions are a compilation of all the stoichiometric reactions and pathways that can describe the entire cellular metabolism of an organism (Vodovotz et al., 2008; Thiele et al., 2013). In recent years, they have become an indispensable tool for the understanding of complex biological phenomena, including neurodegenerative diseases and inflammation processes (Cakir et al., 2007; Swainston et al., 2013; Sertbaş et al., 2014; Martín-Jiménez et al., 2017). Moreover, genomic-scale reconstructions are builder from a system biology approach that allows the integration of several sources of information, such as biological data bases, high-throughput omic data, and experimental evidence, in order to improve the development of novel pharmacological treatments (Najafi et al., 2014).

Having in account the importance of astrocytes for brain inflammation, and the promising effects of tibolone for astrocytic and neuronal protection (Crespo-Castrillo et al., 2018), we developed a genomic-scale metabolic model of astrocytes, with the purpose of enlighten the metabolic pathways modulated by tibolone during an inflammatory response caused by the increased uptake of palmitate. We focused or attention, in the identification of metabolic changes related with the modulation of cytokines, the release of gliotransmitters and the neuroprotective effects mediated by tibolone in an inflammatory scenario (Wojtal et al., 2006). Our results suggest that tibolone exerts its neuroprotective effects through the reduction of neurotoxicity mediated by L-glutamate in astrocytes. We also found a tibolone-associated increase in the biomass growth rate that is consistent with previous reports concerning the side effects of neurosteroids in other human cell types.

MATERIALS AND METHODS

Tissue Specific Model Construction

The tissue specific model construction process started with the identification of all enzyme-coding genes expressed in healthy human astrocytes indexed in the GEO database (Swainston et al., 2013) as GSE73721. Gene identifier conversion from GeneCards (Rebhan et al., 1997) to ENTREZ (Maglott et al., 2011) was performed through "UniProt.ws" R Package. Reactions associated with the identified genes were mapped from the Human Genome-Scale Metabolic Reconstruction RECON 2.04 (Thiele et al., 2013) as downloaded from the VMH Lab (Swainston et al., 2016)[1] and further enriched with metabolic information obtained from KEGG (Kanehisa and Goto, 2000). Additionally, we developed the R package "g2f" available in CRAN (Hornik, 2012; Botero et al., 2016) to identify and fill the gaps using all the reactions with an uncorrelated gene expression included in RECON 2.04, as well as to select and remove all blocked reactions from our reconstruction.

All the reactions involved in the conversion of extracellular glutamate, glycine, cysteine and glucose to extracellular glutamine, glycine, serine-D, reduced glutathione, lactate, and ATP were added, as they are essential for the normal astrocytic

[1] https://vmh.uni.lu

metabolism (Barreto et al., 2011; Souza et al., 2019). Exchange reactions were limited to components of the Dulbecco's Modified Eagle Medium (DMEM) as an input, and the gliotransmitters, glutamine, D-serine, ATP and glutamate, reduced glutathione, lactate, glucose, nitric oxide, prostaglandins and leukotrienes as output, in accordance with previous experimental studies from our group (Avila-Rodriguez et al., 2016; Cabezas et al., 2018; González-Giraldo et al., 2019). Finally, we developed the R Package "MinVal" to validate the syntax of the model, the mass-charge and the creation of SBML files (Osorio et al., 2017).

Reaction limits (upper and lower bounds) were constrained proportionally to the mean gene expression reported for genes included in Gene-Protein-Reaction (GPR) (Thiele and Palsson, 2010) associated to each reaction in samples of male and female human patients from 47 to 63 years old, using the "exp2flux" R package available in CRAN (Hornik, 2012; Osorio et al., 2017). All Flux Balance Analysis (FBA) were performed using the "sybil" (Gelius-Dietrich et al., 2013) R Package running under R 3.3.1 (Gelius-Dietrich et al., 2013; R Development Core Team, 2016).

Flux Balance Analysis

Flux balance analysis is a linear optimization method for simulating the metabolic reactions of a cell or an organism that allows the identification of the set of reactions involved in the production of a biological response within the metabolic model (Orth et al., 2010). The metabolic reactions are represented internally as a stoichiometric matrix (S), of size m×n, where m represents the metabolites and n the reactions. The entries in the matrix are the stoichiometric coefficients of the metabolites that take part in a reaction. The flux through all of the reactions in a network is represented by the vector v, which has a length of n. The concentrations of all metabolites are represented by the vector x, with length m.

The systems of mass balance equations at steady state are defined by:

$$\frac{d_x}{d_t} = 0 \text{ or } S \times v = 0. \text{ FBA}$$

This expression seeks to maximize or minimize an objective function, which can be any linear combination of fluxes to obtain a flux for each reaction, indicating how much each reaction contributes to the objective function (Orth et al., 2010). The FBA for the studied scenarios was resolved using GLPK 4.60[2], setting the generic human biomass reaction included in RECON 2.04 as default, and each one of the reactions described in **Table 1** as objective functions. Models for each scenario were analyzed by comparing their specific fluxes, metabolite's production rate and a sensitivity analysis.

Identifying Flux Changes Between Scenarios

The measurement of flux change for each reaction between metabolic scenarios is a task generally carried out manually and oriented directly toward the research objective. However, at system level this process can become laborious. The *flux Differences function* calculates the fold change for each common reaction between metabolic scenarios.

TABLE 1 | Set of objective functions used to evaluate the protective effects of tibolone in the inflammatory scenario.

ID	Formula reaction	Description
Glu2Gln	1 glu_L[e] → 1 gln_L[e]	Glutamate – Glutamine cycle
Gly2SerD	1 gly[e] → 1 ser_D[e]	Glycine to D-serine conversion
Glc2Lac	1 glc_D[e] → 2 lac_L[e]	Lactate production from glucose
Glc2ATP	1 glc_D[e] → 36 atp[e]	ATP production from glucose
Cys2GTHRD	1 cys_L[e] + 1 glu_L[c] + 1 gly[c] → 1 gthrd[e]	Catch of cysteine to produce reduced glutathione

Fold change is a measure that describes how much a quantity changes going from an initial to a final value. The implemented algorithm in the *flux Differences function* is described in Eq. 1:

$$foldChange : \mathbb{R} \times \mathbb{R} \to \mathbb{R}$$

$$(rFluxModel1,\ rFluxModel2) \mapsto$$

$$\begin{cases} rFluxModel2, & rFlux\ Model1 = 0; \\ \dfrac{rFluxModel1 - rFluxModel2}{\left|rFluxModel1\right|}, & \text{Other cases} \end{cases} \tag{1}$$

Here, the function takes as argument two valid models for the "sybil" R package and a customizable threshold value to filter functions to be reported.

In this aspect, we chose an arbitrary threshold value greater or equal to 2-fold times for reactions with an absolute change between the unconstrained and constrained metabolic scenarios, as reported in previous models (Hausen et al., 2015; Banos et al., 2017).

Metabolic Scenarios

To test the protective effects of tibolone during metabolic inflammation in astrocytes we defined three different metabolic scenarios: (1) A "healthy" scenario, where the rate of palmitate uptake was set freely by the optimizer. This scenario emulates the normal conditions of astrocytes metabolism (**Supplementary Data Sheet 1**), without any inflammatory response (Seeger et al., 2016). (2) An "induced inflammation by palmitate" scenario, where the uptake rate of palmitate was forced to be stable in the mean of the half maximal inhibitory concentration (IC_{50}) value for all the objective functions included in **Table 1**. In this aspect, IC_{50} values were calculated through a robustness analysis performed using uptake of palmitate ('EXhdca(e)' in RECON 2.04) as control and 1000 points in the range from 0 to 1 mMgDW–1h–1 for each objective function. Uptake values where each objective function reached IC_{50} was selected and subsequently averaged. Moreover, the modeled inhibitory effects

[2]https://sourceforge.net/projects/winglpk/files/winglpk/GLPK-4.60/

TABLE 2 | Set of reactions added to recreate the "Tibolone treatment" scenario for the astrocytic model.

ID	Formula reaction	Description
T1	Tibolone[e] ↔	Tibolone exchange reaction
T2	Tibolone[e] ↔ a3OHtibolone[e]	3*a*hidroxytibolone interconvertion
T3	Tibolone[e] ↔ b3OHtibolone[e]	3*b*hidroxytibolone interconvertion
T4	Tibolone[e] → d4tibolone[e]	D4tibolone isomer formation
T5	b3OHtibolone[e] → d4tibolone[e]	D4tibolone isomer formation from 3*b*-hidroxytibolone
T6	a3OHtibolone[e] → estradiol[c]	Estradiol receptor agonist action mechanism of 3*a*-hidroxytibolone
T7	b3OHtibolone[e] → estradiol[c]	Estradiol receptor agonist action mechanism of 3*b*-hidroxytibolone
T8	d4tibolone[e] → prgstrn[c] + tststerone[c]	Progesterone and androgen receptor activation by tibolone D^4 isomer
T9	a3OHtibolone[e] ↔ a3SOtibolone[e]	3*a*hidroxytibolone interconvertion to sulfated inactive compounds
T10	a3SOtibolone[e] →	Tibolone inactive form in blood

Tibolone reactions affecting the astrocytic metabolism were based on Kloosterboer (2004).

are in congruence with the reported damaging effects of palmitate in astrocytes (Gupta et al., 2012; González-Giraldo et al., 2019). Finally, a "Tibolone treatment under inflammation" scenario was defined as an "inflammatory scenario" which included 279 additional reactions associated with the metabolic effects exerted by estradiol and derivates compounds obtained in KEGG (Kanehisa et al., 2014), and ten specific reactions associated with tibolone metabolism (Kloosterboer, 2004) not included in RECON 2.04, which are described in **Table 2**.

Metabolic Changes

Flux differences for each reaction between optimized scenarios were measured using the fold change as described in the following equation:

$$foldChange = \frac{valueModel2 - valueModel1}{|valueModel1|} \quad (2)$$

Mechanisms of Associated Enzymes With Pro-inflammatory, Anti-inflammatory and Tibolone Effects

Enzymes involved in pro-inflammatory and anti-inflammatory responses during palmitic acid damage and upon tibolone treatment were identified through a sensitivity analysis as follows: Pro-inflammatory enzymes are those that catalyze reactions that allow the increase of the objective function value when knocked out. Anti-inflammatory enzymes are those associated with reactions that have a fold-change greater or equal to 2, and that once being knocked out reduces the objective function value. Tibolone associated enzymes are those that catalyze reactions that produce a total inhibition of the metabolic effects of tibolone when knocked out.

RESULTS AND DISCUSSION

Astrocytic Metabolic Model

We reconstructed an FBA based astrocytic tissue-specific model composed by 1262 unique genes, 1956 metabolites and 2747 biochemical reactions of which 1607 were intracellular reactions, 60 were exchange reactions, and 1080 were transport reactions (**Figure 1A**). Reactions were classified based on their enzymatic activity according to their EC (Enzyme Commission) numbers (**Figure 1B**), and sub-cellular localization (**Figure 1C**).

Based on the enzymatic classification (**Figure 1B**), 33.2% of total reactions are catalyzed by a transferase enzyme, 15.8% by an oxidoreductase, 14.4% by a hydrolase, 6.2% by a lyase, 2.3% by a ligase, 1.9% by an isomerase and 25.3% of them are spontaneous reactions without an associated enzyme or gene associated. Regarding subcellular localization, cytosolic and mitochondrial reactions contributed to 60% of the total reactions in the model. The remaining 40% of reactions are distributed in six subcellular compartments as follows: 8.7% in Golgi apparatus, 8.5% in peroxisome, 6.9% in endoplasmic reticulum, 6.3% in lysosome, 4.2% in nucleus, and finally 5.5% are transport reactions from the extracellular space (**Figure 1C**).

The reactions included in the model are associated with 113 metabolic pathways reported in the KEGG database (Kanehisa and Goto, 2000). Almost 50% of reactions are associated to 10 main metabolic pathways of paramount importance for astrocytic metabolism and neuronal support such as oxidative phosphorylation, purine metabolism, glycolysis and gluconeogenesis, and pentose and glucuronate interconversions. The distribution of reactions in metabolic pathways is shown in **Figure 2**. These results are similar to those previously reported astrocytic models (Fitch and Silver, 1997; Ciccarelli et al., 2001; Çakir et al., 2007; Giaume et al., 2010; Sertbaş et al., 2014; Martín-Jiménez et al., 2017; Sá et al., 2017). For example, Martín-Jiménez et al. (2017) developed a genome-scale metabolic reconstruction of human astrocyte, comprising of 5.659 reactions (237 exchange reactions and 1.948 transport reactions), 3.765 genes, 862 enzymes, 5.007 metabolites. Regarding the subcellular distribution of reactions, cytosolic and mitochondrial reaction accounted for 59% of the total reactions, while 23% belonged to peroxisome, lysosome, endoplasmic reticulum, golgi apparatus and nucleus. Finally, transport reactions represented 18% of the total reactions, making them highly similar to our model.

Healthy Scenario (Basal Conditions)

Our metabolic simulation predicts a slow growth rate for astrocytes (0.37 mMgWD-1h-1) under normal conditions using DMEM medium as metabolic supply[3]. This result is in agreement with the study of Das et al. (2010) which reported that Human Normal Astrocyte cells (HNA) are able to grow in DMEM culture medium supplemented with 2% FBS (Das et al., 2010). Moreover, astrocytes activated 52% of model reactions (**Figure 3**) and preferentially use a glucose-based metabolism. Our model also shows that glucose is catabolized and constitutively released by astrocytes as lactate without any

[3]http://himedialabs.com/TD/AT068.pdf

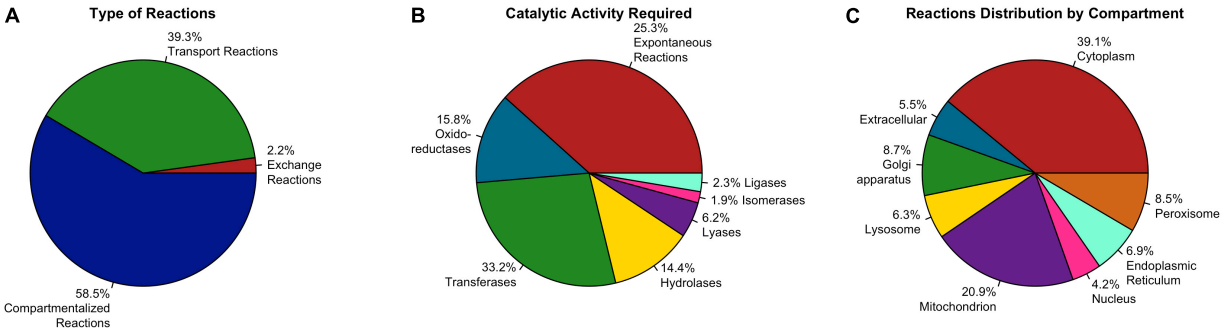

FIGURE 1 | Distribution of enzymes included in the astrocyte metabolic model. Classification is based in **(A)** Type of reaction, **(B)** Catalytic activity and **(C)** Associated compartment of the enzyme (subcellular location).

stimuli similar (Le Foll and Levin, 2016), in agreement with Cakir et al. (2007) and Bhowmick et al. (2015) whom reported a lactate release rate of 8.9% from the glucose flux in resting conditions (Çakir et al., 2007; Bhowmick et al., 2015). As previously stated, astrocytes in physiological conditions release large amounts of lactate to the extracellular space (Mangia et al., 2009), which can be used by neurons to supply their energetic requirements (Kumar Jha et al., 2016). Moreover, our simulations show that ATP and glutamate are synthesized and released by astrocytes only under the metabolic alterations present in the inflammatory and tibolone treatment scenarios which were analyzed through the evaluated objective functions of our model (**Table 1**). Metabolite release rate and biomass growth were used as references for the comparative changes between the three metabolic scenarios (**Figures 3**, **4**).

Inflammatory Scenario

In this scenario, we simulated an inflammatory microenvironment by increasing the cellular concentration of palmitic acid in astrocytes (Liu et al., 2013; González-Giraldo et al., 2019). The calculated IC_{50} for palmitic acid (**Table 1**) was 0.208 ± 0.024 $mMgDW^{-1}h^{-1}$, similar to the study by Liu et al. (2013) which used a concentration of 0.2 mM of palmitic acid to induce astrogliosis in primary rat cortical astrocytes (Liu et al., 2013). Upon palmitic acid, astrocytes increased the uptake of L-asparagine, L-aspartate, iron, D-glucose, L-glutamate, histidine and L-serine and the release of L-glutamine and lactate (**Figure 3**). This response is usual in reactive astrocytes under neuroinflammation, which leads to homeostatic disturbances, including an increased uptake in iron in CNS cells (Kumar Jha et al., 2016). Iron accumulation is present in several neurodegenerative diseases such as AD, and PD, promoting microglial pro-inflammatory activity, altering mitochondrial function, and inducing ROS production (Williams et al., 2012). An increase in histidine uptake was previously reported as a biomarker for metabolic inflammation during obesity (Niu et al., 2012). In this aspect, histidine acts as a free-radical scavenger that might reduce IL-6, TNF-α, and CRP levels, and inhibit the secretion of $H_2O^-_2$ and TNF-α induced by IL-8 (Lee et al., 2005; Son et al., 2005). Aspartate, present in the brain as *N*-Acetyl-L-aspartate (NAA), is synthesized and stored in neurons but is hydrolyzed in glial cells (Baslow, 2003). NAA act as an anti-proliferative, antiangiogenic, and anti-inflammatory molecule by inducing the decrease of prostaglandin E2 (PGE2) in astrocytes (Rael et al., 2004). L-Asparagine, in turn, acts as a regulator of ammonia toxicity through the increase of Na^+ intracellular concentration when is co-transported within astrocytes (Chaudhry et al., 1999). Moreover, asparagine induces a Ca^{2+} response comparable to GABA-induced Ca^{2+} transients in a dose-dependent manner (Doengi et al., 2009).

L-serine and L-asparagine uptake increase may be related to a cell survival process that switches cellular metabolism to be highly dependent of non-essential amino acids available in extracellular space such as glutamine, serine, glycine, arginine, and asparagine (Green et al., 2014). Moreover, under the inflammatory scenario, our astrocyte model released a limited amount of prostaglandin D2 (<1e-6 mMgDW-1h-1), a mediator of inflammation. It has been shown that reactive astrocytes express the DP_1 receptor of prostaglandin D2, and that the inhibition of this receptor resulted in reactive gliosis suppression in mice (Mohri et al., 2006).

In the inflammatory scenario, astrocytes modified the flux rate of 586 reactions when compared with the unstimulated scenario. Main metabolic changes are present in oxidative phosphorylation, histidine metabolism, and fatty acid degradation pathways, as well as the inactivation of TCA and glycolysis pathways (**Figure 5**). Inflammation affects all metabolic objective functions evaluated (**Table 1**) except for the release of D-serine. In this aspect, it was observed that there was a decrease of 15.6% in the growth rate of astrocytes compared with the normal scenario, a decrease of 59.3% in the intake of cysteine related to reduced glutathione production, a decrease of 72% in glucose degradation to ATP 72%, and to lactate in 74.4%. Finally, the conversion of extracellular glutamate to glutamine was reduced by 67.7% (**Figure 6**).

Based on the sensibility analysis, we identified two pro-inflammatory candidate reactions that were knocked out (**Table 3**). These reactions are associated with the formimidoyl-transferase cyclodeaminase (FTCD) and mitochondrial water transport, which has been associated with aquaporin-9 (Potokar et al., 2016). Following the inhibition of these reactions, it was observed an increase of the objective function above the maximum value set for the inflammatory scenario (11.45

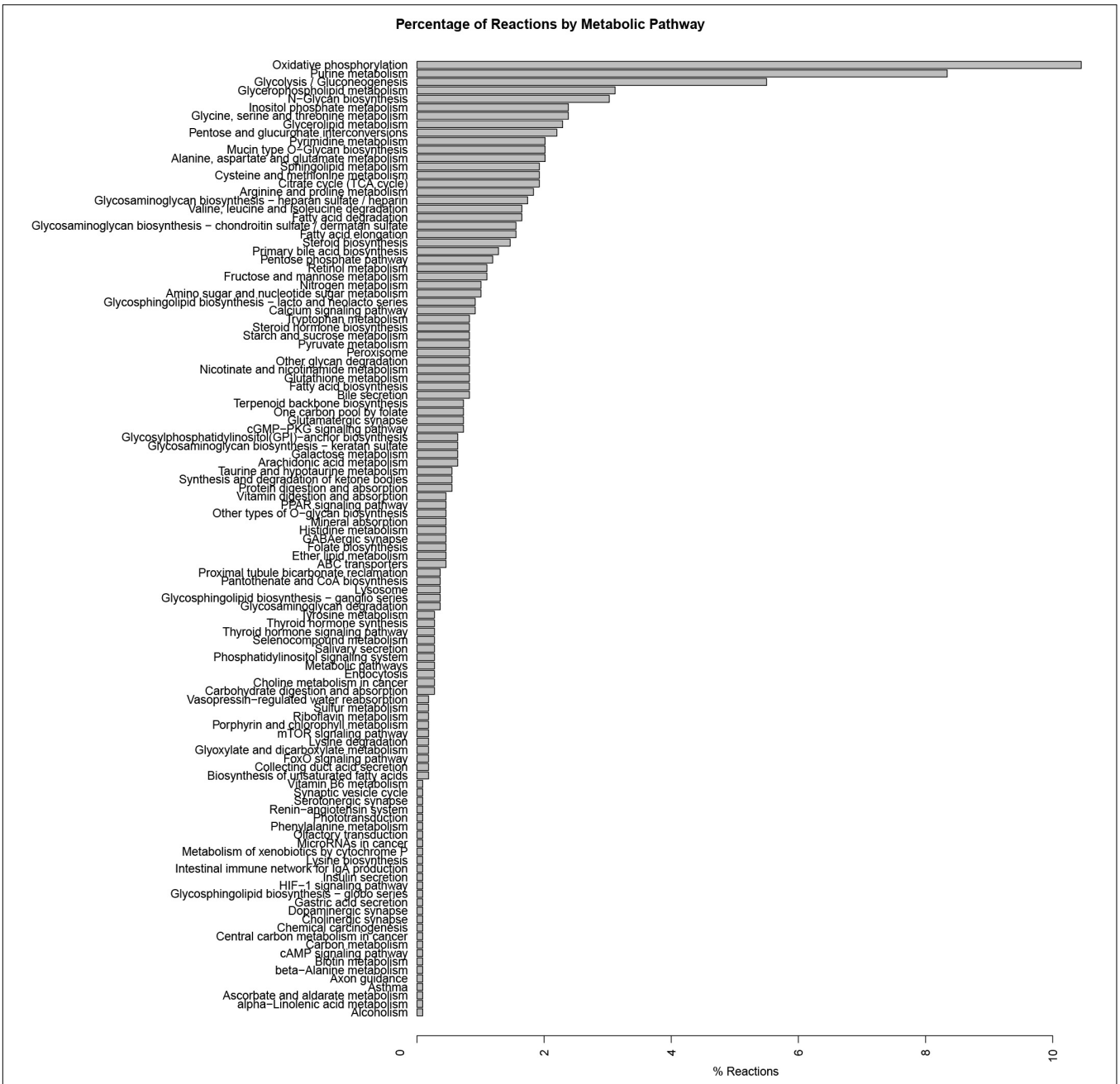

FIGURE 2 | Summary of pathways associated with biochemical reactions included in the genome-scale metabolic model for astrocytes. Pathway association was assigned based in the metabolic categories used in the KEGG database.

and 5.14%, respectively). In this aspect, it has been shown that FTCD is overexpressed in high-fat diets (Fernando et al., 2013) and contributes with one-carbon units from histidine degradation to the folate pool (Väremo et al., 2015) and glutamate synthesis. Moreover, this enzyme has been associated with working memory performance in young adults (Greenwood et al., 2018). On the other hand, six isoforms of aquaporins (AQP 1, 3, 4, 5, 8, 9) have been reported in glial cells, performing important functions like water transport, regulation of the cerebrospinal fluid (CSF), synaptic remodeling, formation of brain edemas and inflammatory processes (Saparov et al., 2007; Te Velde et al., 2008; Albertini and Bianchi, 2010; Nagahara et al., 2010). Aquaporin 9 (AQP9) is highly expressed in the inner mitochondrial membrane of astrocytes (Potokar et al., 2016). Different studies have shown that AQP9 is permeable to many solutes including glycerol, purines, pyrimidines and urea, suggesting its importance for diffusion and energetic metabolism in astrocytes

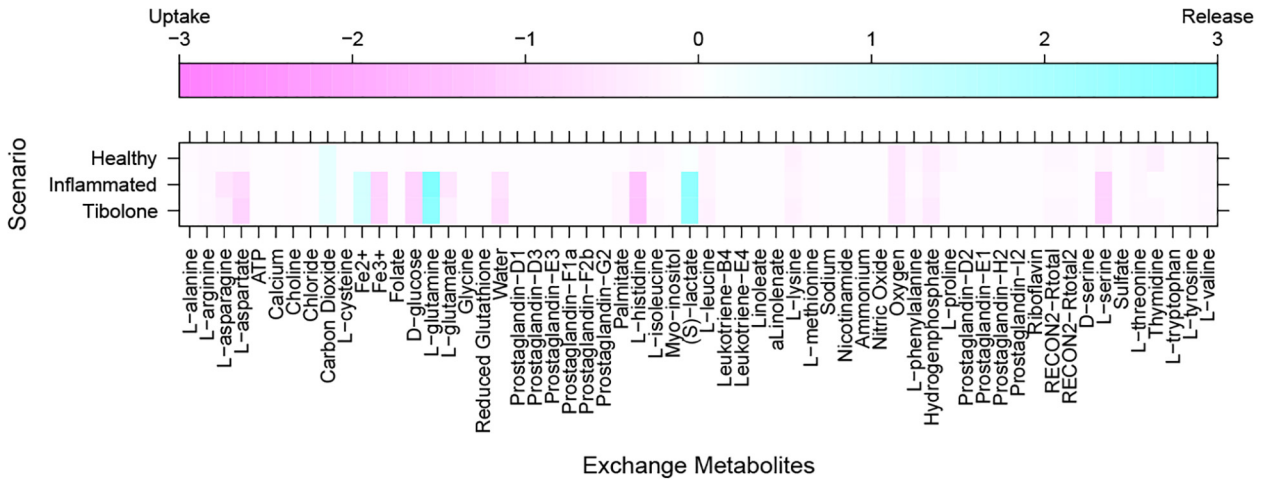

FIGURE 3 | Exchange rate of metabolites between the different metabolic scenarios using the generic biomass reaction included in RECON 2.04, as the objective function.

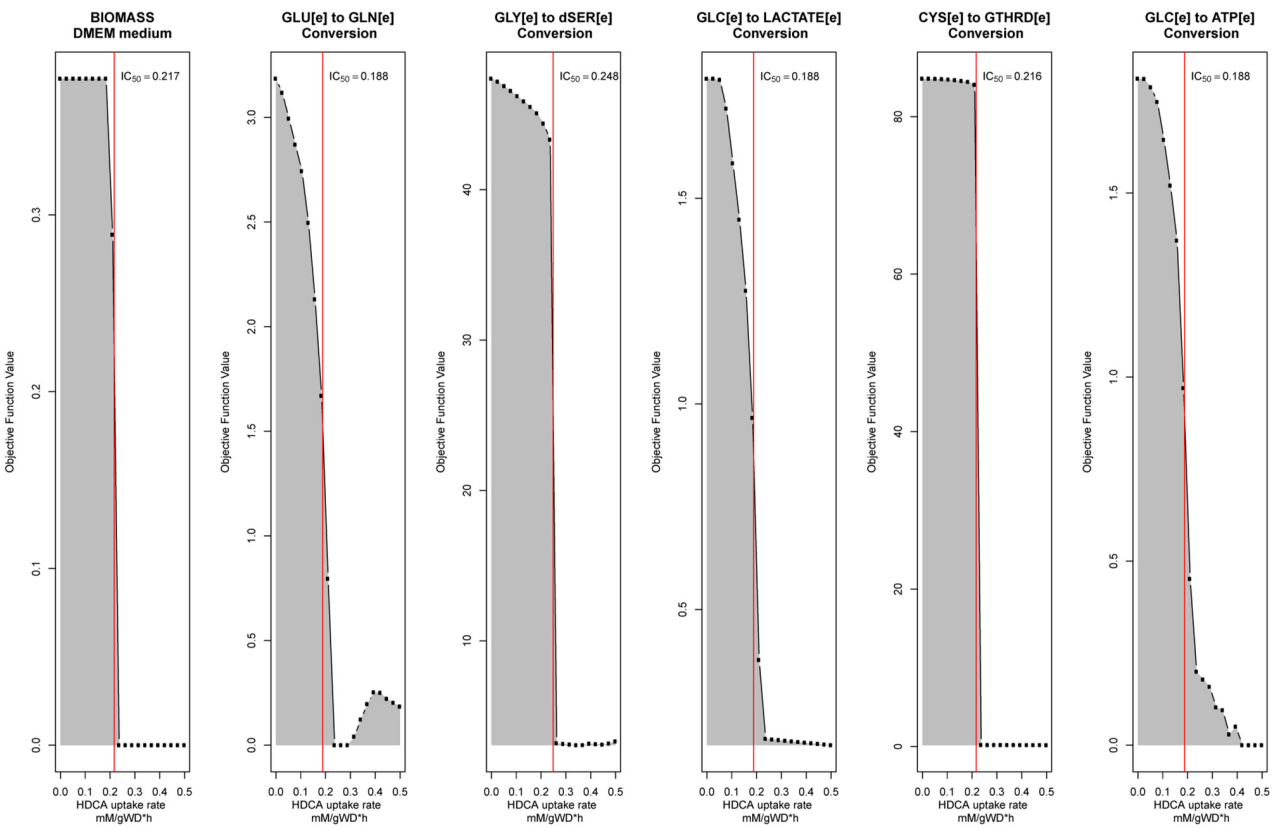

FIGURE 4 | Robustness analysis to calculate palmitate-induced IC_{50} value for each objective function described in **Table 1**. The red line represents the calculated IC_{50} value.

(Albertini and Bianchi, 2010; Badaut et al., 2012; Potokar et al., 2016). Moreover, silencing of AQP9 in murine astrocytes decreased glycerol uptake and increased glucose and oxidative metabolism, suggesting its importance for astrocyte metabolism (Badaut et al., 2012). Finally, a study by Nagahara et al. (2010) showed that in synovial tissues from osteoarthritic patients (OA), TNFα regulated AQP9 mRNA and protein expression, thus suggesting that AQP9 could be a biomarker for inflammatory

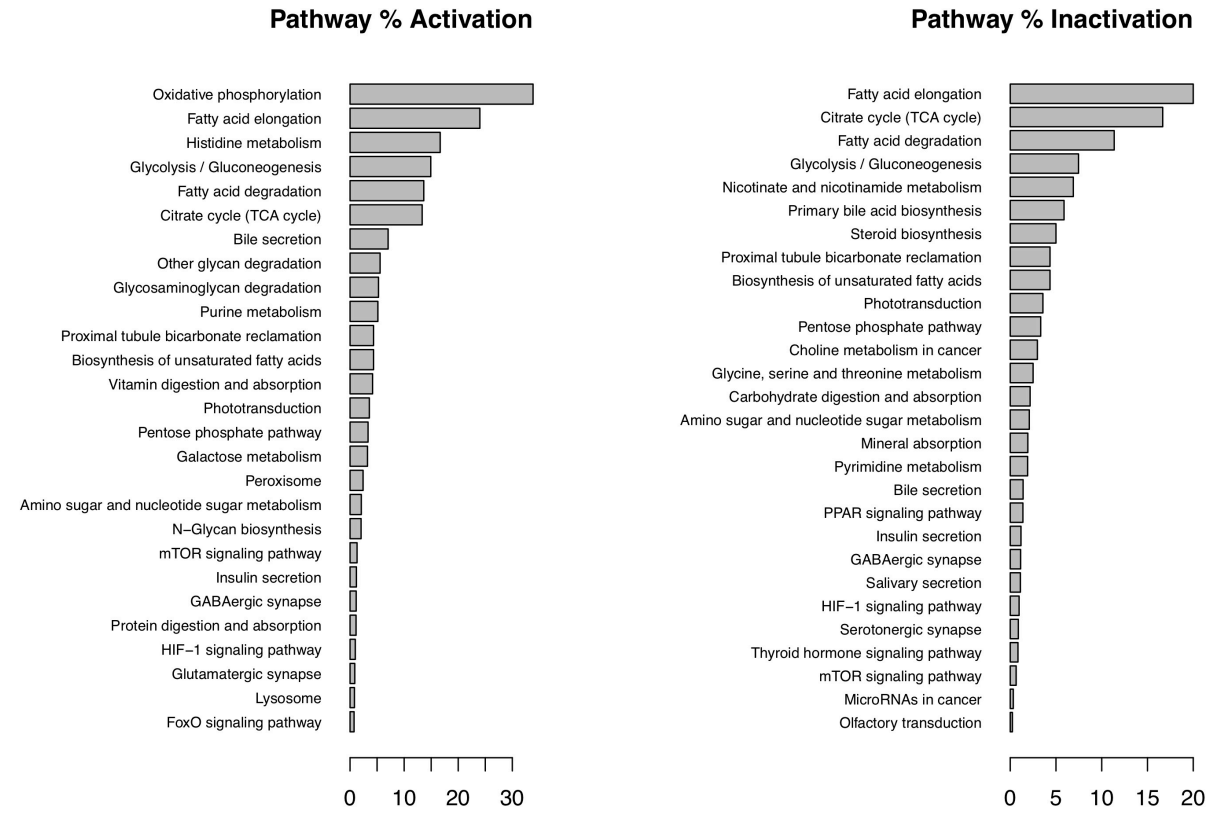

FIGURE 5 | Metabolic pathways affected during metabolic inflammation by palmitate. Percentage of activation and inactivation was calculated compared with genes associated with each pathway in the KEGG database.

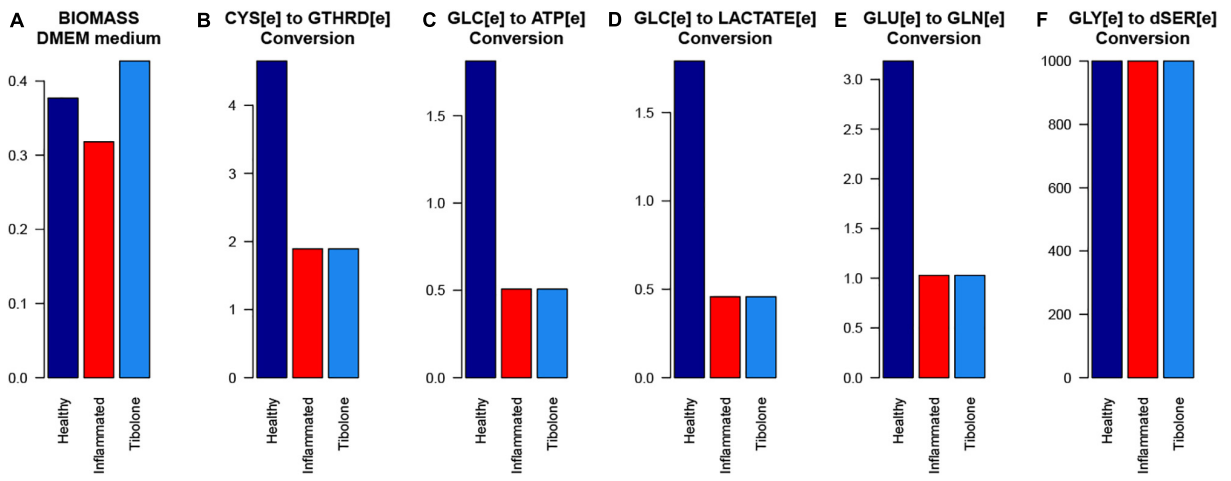

FIGURE 6 | The response of the main astrocytes metabolic capabilities to different modeled scenarios. **(A)** Biomass with DMEm medium, **(B)** Cystenine to reduced glutathione conversion, **(C)** Glucose to ATP conversion, **(D)** Glucose to lactate conversion, **(E)** Glutamate to Glutamine conversion, and **(F)** Glycine to D-serine conversion.

processes (Nagahara et al., 2010). It is possible that a similar mechanism could be present in astrocytes under inflammation; however, additional experimental studies are needed in order to address this issue.

Finally, 8 anti-inflammatory reactions were found to have a change equal or greater that 2-fold when knocked-out in the model (**Table 4**). 6 of these reactions (r0639, r0653, r0714, r0716, r0718, and r0720) are involved in fatty acid elongation in

TABLE 3 | Set of reactions with pro-inflammatory potential, identified through a sensibility analysis for the inflammatory scenario.

ID	Reaction description	H. Flux	I. Flux	Fold change
FTCD	Formimidoyltransferase cyclodeaminase	0.39	1.28	2.28
H2Otm	H2O transport mitochondrial	−0.26	2.44	10.44

Fluxes for healthy scenario (H. Flux) and inflammatory scenario (I. Flux) are compared.

mitochondria through their association with acyl-CoA (Saparov et al., 2007). This elongation system is responsible for the addition of two carbon units to the carboxyl end of a fatty acid chain, and plays an important role in the maintenance of membrane lipid composition, and in the generation of cell signaling precursors (such as eicosanoids and sphingosine-1 phosphate), energy production, and other unknown pathways related with cancer growth (Murphy et al., 1988; Te Velde et al., 2008).

Our data also showed that AKGMALtm (α-ketoglutarate/malate transporter) experienced a fold change of −6.85 when knocked out (**Table 4**). This transporter is important for the glutamate/glutamine cycle in astrocytes, which prevents the excessive accumulation of glutamate in the extracellular space and the subsequent excitotoxicity (Hertz, 2013). Finally, the mitochondrial NADH lactate dehydrogenase (LDH) allows lactate use in ATP production in astrocytes during oxidative phosphorylation (Lemire et al., 2008). Recently, it was shown that LDH in murine lymphocyte T cells is important for the T-cell effector functions by increasing histone acetylation and the pro-inflammatory IFN-γ transcription, thus suggesting that LDH could be a therapeutic target in autoinflammatory diseases (Peng et al., 2016). Further *in vivo* and *in vitro* experiments are needed in order to assess this mechanism in astrocytes.

Tibolone Treatment Scenario

In our "Tibolone treatment" scenario, tibolone affected the flux rate of 948 reactions in comparison with the inflammatory scenario. We found important metabolic changes associated with the activation of several protective pathways in astrocytes (Schuller-Levis and Park, 2003). These include taurine metabolism, which has been shown to protect against oxidative injury in different *in vitro* and *in vivo* models including lung cells, leucocytes, rat macrophages and neuronal cells (Schuller-Levis and Park, 2003), gluconeogenesis which facilitates the conversion of fatty acids into ketone bodies under steroid-mediated effects (Amen-Ra, 2006), calcium, and PPAR signaling path-ways (**Figure 7**). Interestingly, PPAR gamma has been shown to antagonize the actions of pro-inflammatory transcription factors nuclear factor-κB (NF-κB) and activator protein 1 (AP-1) in human aortic smooth muscle cells and in primary human hepatocytes (Delerive et al., 2000; Daynes and Jones, 2002). These results suggest that tibolone exerts a significative modulation on inflammatory reactions through the activation of several protective pathways, which is agreement with previous experimental results from our group (Avila-Rodriguez et al., 2014, 2016; González-Giraldo et al., 2019).

The "tibolone treatment" scenario also increased the demand for L-aspartate and in turn, decreased the demand for L-asparagine, L-glutamate and the release of L-glutamine when compared with the inflammatory scenario (**Figure 3**). The reduction on the L-glutamate and L-glutamine uptake/release rate mediated by tibolone could be associated with a neuroprotective effect through the reduction in neurotoxicity mediated by L-glutamate in astrocytes (Petrelli and Bezzi, 2016). In this aspect, it has been shown that the excess in L-glutamate is a contributing factor in neuronal damage induced by inflammation in pathologies like TBI stroke, PD and AD (Ahlemeyer et al., 2002). However, it is important to perform additional simulations in our model to assess supplementary metabolic mechanisms that are associated to the induced inflammation in astrocytes (Shi et al., 2009). Against our initial hypothesis, tibolone treatment did not show actions over reactions affected by inflammation and associated with neuronal support (**Table 1**). However, tibolone increased cellular growth by 13.26% compared with basal conditions (**Figure 6**), suggesting an increase either on cell viability or in astrocytic proliferation (Feist and Palsson, 2010). Interestingly, this proliferative potential was not observed in the inflammatory scenario, suggesting that the observed proliferation in our model could be important for cellular homeostasis (Heimann et al., 2017). In this aspect, previous studies have shown that estrogen stimulates the differentiation and proliferation of neural stem cells into neurons, astrocytes, and oligodendrocytes (Okada et al., 2010). There is no evidence of increased proliferation

TABLE 4 | Set of reactions with anti-inflammatory potential, identified through a sensibility analysis on the inflammatory scenario with palmitate.

ID	Reaction description	H. Flux	I. Flux	Fold change
AKGMALtm	*a*-ketoglutarate/malate transporter	−0.17	−1.3	−6.85
NADH2_u10 m	NADH dehydrogenase mitochondrial	0.12	0.37	2.17
r0639	Lauroyl-CoA: acetyl-CoA C-acyltransferase	0.02	0.09	4.04
r0653	cMyristoyl-CoA: acetyl-CoA C-myristoyl transferase	0.02	0.09	4.04
r0714	(S)-3-Hydroxyhexadecanoyl-CoA: NAD^+ oxidoreductase	0.02	0.09	4.04
r0716	(S)-3-Hydroxyhexadecanoyl-CoA hydrolyase	0.02	0.09	4.04
r0718	(S)-3-Hydroxytetradecanoyl-CoA: NAD+ oxidoreductase	0.02	0.09	4.04
r0720	(S)-3-Hydroxytetradecanoyl-CoA hydrolyase	0.02	0.09	4.04

Fluxes for healthy Scenario (H. Flux) and inflammatory scenario (I. Flux) are compared.

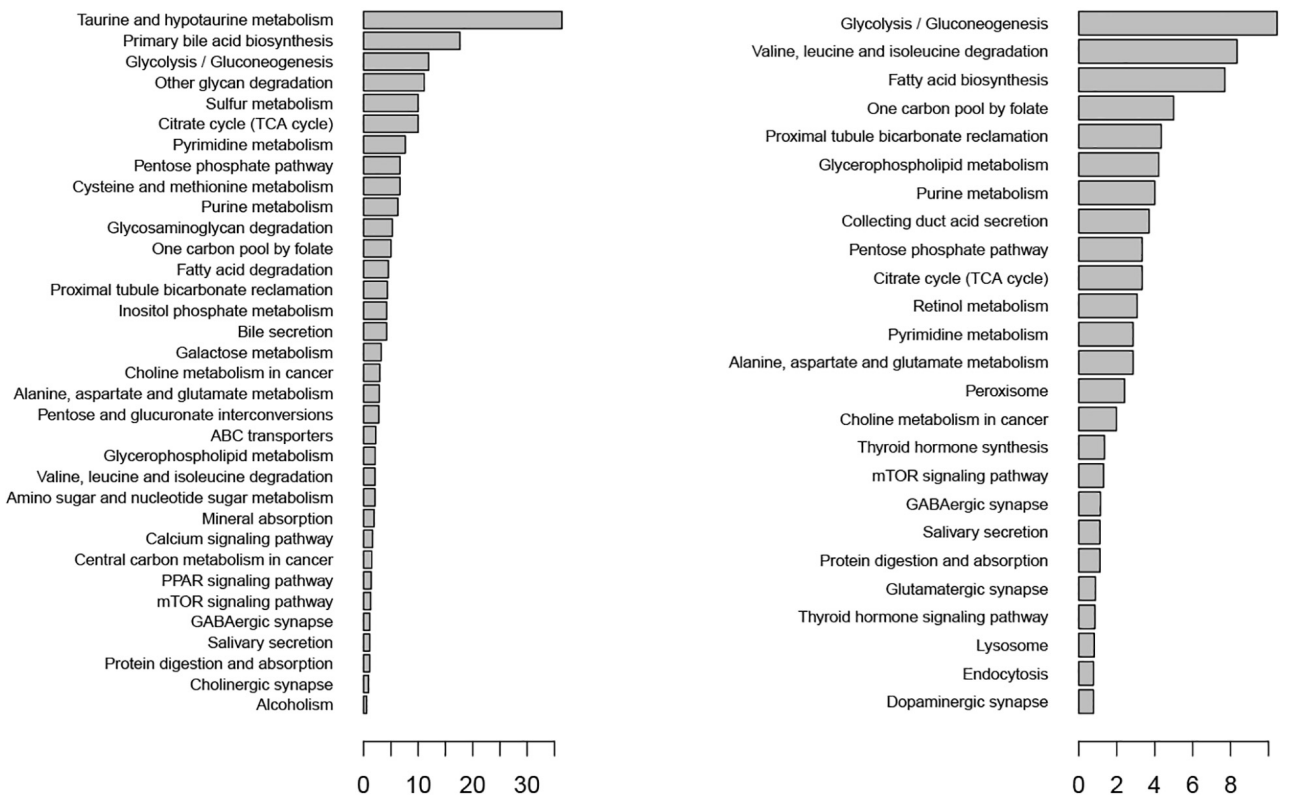

FIGURE 7 | Metabolic pathways affected by tibolone over an inflammatory scenario. Activation and inactivation percentage was measured in comparison with genes associated to each pathway in the KEGG database.

TABLE 5 | Set of reactions associated with tibolone, involved in the protective effects of the drug.

ID	Reaction description	Genes in astrocyte data
r0739	Alcohol Dehydrogenase	ADH4, ADH5, ADH7
r2518	ATP-binding Cassette (ABC)	ABCD3
RE1804M	Cholestanetriol 26-monooxygenase	CYP27A1
RE1807M	Cholestanetriol 26-monooxygenase	CYP27A1

Reactions were identified through a sensibility analysis, carried out in the "Tibolone treatment" scenario.

by tibolone under palmitate insult, probably due to the experimental and technical challenges associated with an accurate measurement of cell proliferation (Frago et al., 2017; González-Giraldo et al., 2019).

Based on a sensibility analysis performed over 289 reactions associated with tibolone and estradiol-derived compounds, we identified a set of four reactions that after being individually knocked out, completely blocked tibolone effects in our model (**Table 5**). The identified reactions are catalyzed by an alcohol dehydrogenase (E.C. 1.1.1.1) and cholestanetriol 26-monooxygenase associated with cytochrome P450 and the PPAR signaling pathway (Mast et al., 2017). Both enzymes were previously reported to be associated with a reduction in ROS production through redox reactions mediated by alcohol dehydrogenase (ADH) and cytochrome P450 (Colditz et al., 1995; Pessayre et al., 2001). Moreover, a recent study in knockout mice showed that cholestanetriol 26-monooxygenase deficiency is associated with early atherosclerosis, osteoporosis, and progressive neurological deterioration associated with AD (Mast et al., 2017). Altogether, these results suggest the importance of tibolone in the regulation of multiple protective mechanisms in the brain.

CONCLUSION

In this work, we developed a tissue-specific metabolic network for human astrocytes that was simulated under three different scenarios. The model allowed us to identify the metabolic changes between a healthy, an inflammatory and a tibolone treatment scenario. In our model, the adverse effects associated with the increase of palmitic acid uptake in astrocytes were described based on exchange fluxes, metabolite production, and metabolic pathways perturbed under the inflammatory response. Moreover, this model was consistent with previous experimental studies showing that tibolone exerts multiple protective effects against

inflammation, oxidative stress and metabolic dysregulation (Liu et al., 2013; Avila-Rodriguez et al., 2014, 2016; González-Giraldo et al., 2019. In this aspect, a "Tibolone treatment" scenario was modeled, based on previous works describing the neuroprotection induced by this synthetic compound on astrocytes under a variety of anti-inflammatory stimuli.

Our results suggest that tibolone exerts its protective effects through multiple mechanisms, including the reduction of neurotoxicity mediated by L-glutamate in astrocytes, the activation of inflammatory modulators like PPAR gamma, and the increase in the metabolism of antioxidative molecules like taurine. We also found a tibolone-associated increase in biomass growth rate, which is similar to previously reported studies of the tumorigenic effects exerted by this compound in breast cancer (Colditz et al., 1995). On the other hand, the identified enzymes and reactions associated with tibolone mechanisms are highly consistent with previous results from our lab (Avila-Rodriguez et al., 2014, 2016).

Finally, a sensitivity analysis performed through constrained-based modeling approaches and FBA allowed us to recognize two possible reactions with their associated enzymes, susceptible to be knocked out in order to reduce the inflammatory perturbations of palmitic acid in astrocytes.

In summary, constraint-based models are valuable tools for the study of the protective effects mediated by pharmacological molecules in astrocytes, and provide a detailed insight into high-throughput data analysis. Further experiments are needed in to confirm the involvement of tibolone in the regulation of inflammatory mediators in astrocytic animal and cellular models.

DATA AVAILABILITY STATEMENT

The datasets generated for this study are available on request to the corresponding author.

AUTHOR CONTRIBUTIONS

DO and AP developed the theory, performed the model, contributed to the design and implementation of the research, the analysis of the results, and writing of the manuscript. CM-J and DO performed the simulations and wrote the manuscript with input from all authors. DO, GB, AP, and JG designed the model and the computational framework and analyzed the data. All authors discussed the results and contributed to the final manuscript.

FUNDING

This research is the result of the master's thesis presented by DO. This work was supported by the Pontificia Universidad Javeriana, Bogotá, Colombia, and Colciencias IDs 7425, 7714, and 7740 to JG.

SUPPLEMENTARY MATERIAL

The Supplementary Material for this article can be found online at: https://www.frontiersin.org/articles/10.3389/fnins.2019.01410/full#supplementary-material

REFERENCES

Ahlemeyer, B., Kolker, S., Zhu, Y., Hoffmann, G. F., and Krieglstein, J. (2002). Increase in glutamate-induced neurotoxicity by activated astrocytes involves stimulation of protein kinase C. *J. Neurochem.* 82, 504–515. doi: 10.1046/j.1471-4159.2002.00994.x

Albertini, R., and Bianchi, R. (2010). Aquaporins and glia. *Curr. Neuropharmacol.* 8, 84–91. doi: 10.2174/157015910791233178

Amen-Ra, N. (2006). Humans are evolutionarily adapted to caloric restriction resulting from ecologically dictated dietary deprivation imposed during the Plio-Pleistocene period. *Med. Hypotheses.* 66, 978–984. doi: 10.1016/j.mehy.2005.11.013

Amtul, Z., Westaway, D., Cechetto, D. F., and Rozmahel, R. F. (2011). Oleic acid ameliorates amyloidosis in cellular and mouse models of Alzheimer's disease. *Brain Pathol.* 21, 321–329. doi: 10.1111/j.1750-3639.2010.00449

Avila-Rodriguez, M., Garcia-Segura, L. M., Cabezas, R., Torrente, D., Capani, F., Barreto, G. E., et al. (2014). Tibolone protects T98G cells from glucose deprivation. *J. Steroid Biochem. Mol. Biol.* 144(Pt B), 294–303. doi: 10.1016/j.jsbmb.2014.07.009

Avila-Rodriguez, M., Garcia-Segura, L. M., Hidalgo-Lanussa, O., Baez, E., Gonzalez, J., and Barreto, G. E. (2016). Tibolone protects astrocytic cells from glucose deprivation through a mechanism involving estrogen receptor beta and the upregulation of neuroglobin expression. *Mol. Cell. Endocrinol.* 433, 35–46. doi: 10.1016/j.mce.2016.05.024

Badaut, J., Brunet, J. F., Guérin, C., Regli, L., and Pellerin, L. (2012). Alteration of glucose metabolism in cultured astrocytes after AQP9-small interference RNA application. *Brain Res.* 1473, 19–24. doi: 10.1016/j.brainres.2012.07.041

Banos, D. T., Trébulle, P., and Elati, M. (2017). Integrating transcriptional activity in genome-scale models of metabolism. *BMC Syst. Biol.* 11(Suppl 7):134. doi: 10.1186/s12918-017-0507-0

Barnard, N. D., Bunner, A. E., and Agarwal, U. (2014). Saturated and trans fats and dementia: a systematic review. *Neurobiol. Aging* 35, S65–S73. doi: 10.1016/J.NEUROBIOLAGING.2014.02.030

Barreto, G. E., Gonzalez, J., Torres, Y., and Morales, L. (2011). Astrocytic-neuronal crosstalk:implications for neuroprotection from brain injury. *Neurosci. Res.* 71, 107–113. doi: 10.1016/j.neures.2011.06.004

Baslow, M. H. (2003). *N*-acetylaspartate in the vertebrate brain: metabolism and function. *Neurochem. Res.* 28, 941–953. doi: 10.1023/A:1023250721185

Bélanger, M., and Magistretti, P. J. (2009). The role of astroglia in neuroprotection. *Dialogues Clin. Neurosci.* 11, 281–295.

Belenichev, O. V., Odnokoz, S. V., and Pavlov, O. I. (2012). The neuroprotective activity of tamoxifen and tibolone during glutathione depletion in vitro. *Neurochem. J.* 6:202. doi: 10.1134/s181971241203004x

Bhowmick, R., Subramanian, A., and Sarkar, R. R. (2015). Exploring the differences in metabolic behavior of astrocyte and glioblastoma: a flux balance analysis approach. *Syst. Synthetic Biol.* 9, 159–177. doi: 10.1007/s11693-015-9183-9

Botero, K., Osorio, D., Gonzalez, J., and Pinzon, A. (2016). *Exp2flux: Convert Gene EXPression Data to FBA FLUXes Importer. R Package Version 0.1.* Available at: https://cran.r-project.org/web/packages/exp2flux/README.html (accessed January 8, 2020).

Bruce-Keller, A. J., Barger, S. W., Moss, N. I., Pham, J. T., Keller, J. N., Nath, A. (2001). Pro-inflammatory and pro-oxidant properties of the HIV protein Tat in a microglial cell line: attenuation by 17beta-estradiol. *J. Neurochem.* 78, 1315–1324.

Bruce-Keller, A. J., Keller, J. N., Morrison, C. D. (2009). Obesity and vulnerability of the CNS. *Biochim. Biophys. Acta* 1792, 395–400.

Cabezas, R., Vega-Vela, N. E., González-Sanmiguel, J., González, J., Esquinas, P., Echeverria, V., et al. (2018). PDGF-BB preserves mitochondrial morphology, attenuates ROS production, and upregulates neuroglobin in an astrocytic model under rotenone insult. *Mol. Neurobiol.* 55, 3085–3095. doi: 10.1007/s12035-017-0567-6

Cakir, T., Alsan, S., Saybaşili, H., Akin, A., and Ulgen, K. O. (2007). Reconstruction and flux analysis of coupling between metabolic pathways of astrocytes and neurons: application to cerebral hypoxia. *Theor. Biol. Med. Model.* 4:48. doi: 10.1186/1742-4682-4-48

Çakir, T., Alsan, S., Saybaşili, H., Akin, A., and Ülgen, K. Ö. (2007). Reconstruction and flux analysis of coupling between metabolic pathways of astrocytes and neurons: application to cerebral hypoxia. *Theor. Biol. Med. Model.* 4:48 doi: 10.1186/1742-4682-4-48

Chaudhry, F. A., Reimer, R. J., Krizaj, D., Barber, D., Storm-Mathisen, J., Copenhagen, D. R., et al. (1999). Molecular analysis of system N suggests novel physiological roles in nitrogen metabolism and synaptic transmission. *Cell* 99, 769–780. doi: 10.1016/S0092-8674(00)81674-8

Ciccarelli, R., Ballerini, P., Sabatino, G., Rathbone, M. P., D'Onofrio, M., Caciagli, F., et al. (2001). Involvement of astrocytes in purine-mediated reparative processes in the brain. *Int. J. Dev. Neurosci.* 19, 395–414. doi: 10.1016/S0736-5748(00)00084-8

Colditz, G. A., Hankinson, S. E., Hunter, D. J., Willet, W. C., Manson, J. E., Stampfer, M. J., et al. (1995). The use of estrogens and progestins and the risk of breast cancer in postmenopausal women. *Obstet. Gynecol. Surv.* 50, 789–791. doi: 10.1097/00006254-199511000-00017

Crespo-Castrillo, A., Yanguas-Casás, N., Arevalo, M. A., Azcoitia, I., Barreto, G. E., Garcia-Segura, L. M., et al. (2018). The synthetic steroid tibolone decreases reactive gliosis and neuronal death in the cerebral cortex of female mice after a stab wound injury. *Mol. Neurobiol.* 55:8651. doi: 10.1007/s12035-018-1008-x

Das, A., Banik, N. L., and Ray, S. K. (2010). Flavonoids activated caspases for apoptosis in human glioblastoma T98G and U87MG cells but not in human normal astrocytes. *Cancer* 116, 164–176. doi: 10.1002/cncr.24699

Daynes, R. A., and Jones, D. C. (2002). Emerging roles of PPARs in inflammation and immunity. *Nat. Rev. Immunol.* 2, 748–759. doi: 10.1038/nri912

Delerive, P., Gervois, P., Fruchart, J. C., and Staels, B. (2000). Inductionof IκBα expression as a mechanism contributing to the antiinflammatory activities of peroxisome proliferator-activated receptor-α activators. *J. Biol. Chem.* 275, 36703–36707.

Doengi, M., Hirnet, D., Coulon, P., Pape, H.-C., Deitmer, J. W., and Lohr, C. (2009). GABA uptake-dependent Ca^{2+} signaling in developing olfactory bulb astrocytes. *Proc. Natl. Acad. Sci. U.S.A.* 106, 17570–17575. doi: 10.1073/pnas.0809513106

Dowell, J. A., Johnson, J. A., and Li, L. (2009). Identification of astrocyte secreted proteins with a combination of shotgun proteomics and bioinformatics. *J. Proteome Res.* 8, 4135–4143. doi: 10.1021/pr900248y

Feist, A. M., and Palsson, B. O. (2010). The biomass objective function. *Curr. Opin. Microbiol.* 13, 344–349. doi: 10.1016/j.mib.2010.03.003

Fernando, H., Wiktorowicz, J. E., Soman, K. V., Kaphalia, B. S., Khan, M. F., and Shakeel Ansari, G. A. (2013). Liver proteomics in progressive alcoholic steatosis. *Toxicol. Appl. Pharmacol.* 266, 470–480. doi: 10.1016/j.taap.2012.11.017

Fitch, M. T., and Silver, J. (1997). Activated macrophages and the blood-brain barrier: inflammation after CNS injury leads to increases in putative inhibitory molecules. *Exp. Neurol.* 148, 587–603. doi: 10.1006/exnr.1997.6701

Frago, L. M., Canelles, S., Freire-Regatillo, A., Argente-Arizón, P., Barrios, V., Argente, J., Garcia-Segura, L. M. et al. (2017). Estradiol uses different mechanisms in astrocytes from the hippocampus of male and female rats to protect against damage induced by palmitic acid. *Front. Mol. Neurosci.* 10:330. doi: 10.3389/fnmol.2017.00330

Gelius-Dietrich, G., Desouki, A. A., Fritzemeier, C. J., and Lercher, M. J. (2013). Sybil - Efficient constraint-based modelling in R. *BMC Syst. Biol.* 7:125. doi: 10.1186/1752-0509-7-125

Genazzani, A. R., Pluchino, N., Bernardi, F., Centofanti, M., and Luisi, M. (2006). Beneficial effect of tibolone on mood, cognition, well-being, and sexuality in menopausal women. *Neuropsychiatr. Dis. Treat.* 2, 299–307. doi: 10.2147/nedt.2006.2.3.299

Giaume, C., Koulakoff, A., Roux, L., Holcman, D., and Rouach, N. (2010). Astroglial networks: a step further in neuroglial and gliovascular interactions. *Nat. Rev. Neurosci.* 11, 87–99. doi: 10.1038/nrn2757

González-Giraldo, Y., Forero, D. A., Echeverria, V., Garcia-Segura, L. M., and Barreto, G. E. (2019). Tibolone attenuates inflammatory response by palmitic acid and preserves mitochondrial membrane potential in astrocytic cells through estrogen receptor beta. *Mol. Cell. Endocrinol.* 486, 65–78. doi: 10.1016/j.mce.2019.02.017

Green, D. R., Galluzzi, L., and Kroemer, G. (2014). Metabolic control of cell death. *Science* 345:1250256. doi: 10.1126/science.1250256

Greenwood, P., Schmidt, K., Lipsky, R., Parasuraman, R., and Jankord, R. (2018). A Functional promoter variant of the human formimidoyltransferase cyclodeaminase (FTCD) gene is associated with working memory performance in young but not older adults. *Neuropsychology* 32, 973–984. doi: 10.1037/neu0000470

Gupta, S., Knight, A. G., Gupta, S., Keller, J. N., and Bruce-Keller, A. J. (2012). Saturated long-chain fatty acids activate inflammatory signaling in astrocytes. *J. Neurochem.* 120, 1060–1071 doi: 10.1111/j.1471-4159.2012.07660.x

Hausen, J., Otte, J. C., Strähle, U., Hammers-Wirtz, M., Hollert, H., Keiter, S. H., et al. (2015). Fold-change threshold screening: a robust algorithm to unmask hidden gene expression patterns in noisy aggregated transcriptome data. *Environ. Sci. Pollut. Res.* 22:16384. doi: 10.1007/s11356-015-5019-0

Heimann, G., Canhos, L. L., Frik, J., Jäger, G., Lepko, T., Ninkovic, J., Götz, M., Sirko, S. (2017). Changes in the proliferative program limit astrocyte homeostasis in the aged post-traumatic murine cerebral cortex. *Cereb. Cortex* 27, 4213–4228. doi: 10.1093/cercor/bhx112

Hertz, L. (2013). The glutamate-glutamine (GABA) cycle: importance of late postnatal development and potential reciprocal interactions between biosynthesis and degradation. *Front. Endocrinol.* 4:59. doi: 10.3389/fendo.2013.00059

Hornik, K. (2012). The comprehensive R archive network. *Wiley Interdiscip. Rev. Comput. Stat.* 4, 394–398. doi: 10.1002/wics.1212

Kanehisa, M., and Goto, S. (2000). KEGG: kyoto encyclopedia of genes and genomes. *Nucleic Acids Res.* 28, 27–30.

Kanehisa, M., Goto, S., Sato, Y., Kawashima, M., Furumichi, M., and Tanabe, M. (2014). Data, information, knowledge and principle: back to metabolism in KEGG. *Nucleic Acids Res.* 42, D199–D205. doi: 10.1093/nar/gkt1076

Kloosterboer, H. J. (2001). Tibolone: a steroid with a tissue-specific mode of action. *J. Steroid Biochem. Mol. Biol.* 76, 231–238. doi: 10.1016/S0960-0760(01)00044-9

Kloosterboer, H. J. (2004). "Tissue-selectivity: the mechanism of action of tibolone," in *Maturitas*, Ed. M. Rees (Amsterdam: Elsevier). doi: 10.1016/j.maturitas.2004.02.012

Kulkarni, J., Gavrilidis, E., Wang, W., Worsley, R., Fitzgerald, P. B., Gurvich, C., Burger, H. (2015). Estradiol for treatment-resistant schizophrenia: a large-scale randomized-controlled trial in women of child-bearing age. *Mol. Psychiatry* 20, 695–702. doi: 10.1038/mp.2014.33

Kumar Jha, M., Ho Park, D., Kook, H., Lee, I.-K., Lee, W.-H., and Suk, K. (2016). Metabolic control of glia-mediated neuroinflammation. *Curr. Alzheimer Res.* 13, 387–402. doi: 10.2174/1567205013666151116124755

Lange, S. C., Lasse, K., Bak, H. S., Waagepetersen, H. S., Schousboe, A., and Norenberg, M. D. (2012). Primary cultures of astrocytes: their value in understanding astrocytes in health and disease. *Neurochem. Res.* 37, 2569–2588. doi: 10.1007/s11064-012-0868-0

Le Foll, C., and Levin, B. E. (2016). Fatty acid-induced astrocyte ketone production and the control of food intake. *Am. J. Physiol.* 310, R1186–R1192. doi: 10.1152/ajpregu.00113.2016

Lee, Y. T., Hsu, C. C., Lin, M. H., Liu, K. S., and Yin, M. C. (2005). Histidine and carnosine delay diabetic deterioration in mice and protect human low density lipoprotein against oxidation and glycation. *Eur. J. Pharmacol.* 513, 145–150. doi: 10.1016/j.ejphar.2005.02.010

Lemire, J., Mailloux, R. J., and Appanna, V. D. (2008). Mitochondrial lactate dehydrogenase is involved in oxidative-energy metabolism in human astrocytoma cells (CCF-STTG1). *PLoS One* 3:e1550. doi: 10.1371/journal.pone.0001550

Little, J. P., Madeira, J. M., and Klegeris, A. (2012). The saturated fatty acid palmitate induces human monocytic cell toxicity toward neuronal cells: exploring a possible link between obesity-related metabolic impairments and

neuroinflammation. *J. Alzheimers Dis.* 2, S179–S183. doi: 10.3233/JAD-2011-111262

Liu, L., Martin, R., and Chan, C. (2013). Palmitate-activated astrocytes via serine palmitoyltransferase increase BACE1 in primary neurons by sphingomyelinases. *Neurobiol. Aging* 34, 540–550. doi: 10.1016/j.neurobiolaging.2012.05.017

Maglott, D., Ostell, J., Pruitt, K. D., and Tatusova, T. (2011). Entrez gene: gene-centered information at NCBI. *Nucleic Acids Res.* 39, D52–D57. doi: 10.1093/nar/gkq1237

Mangia, S., Simpson, I. A., Vannucci, S. J., and Carruthers, A. (2009). The in vivo neuron-to-astrocyte lactate shuttle in human brain: evidence from modeling of measured lactate levels during visual stimulation. *J. Neurochem.* 109(Suppl 1), 55–62. doi: 10.1111/j.1471-4159.2009.06003.x

Martín-Jiménez, C. A., Salazar-Barreto, D., Barreto, G. E., and González, J. (2017). Genome-scale reconstruction of the human astrocyte metabolic network. *Front. Aging Neurosci.* 9:23. doi: 10.3389/fnagi.2017.00023

Mast, N., Anderson, K. W., Lin, J. B., Li, Y., Turko, I. V., Tatsuoka, C., et al. (2017). Cytochrome P450 27A1 deficiency and regional differences in brain sterol metabolism cause preferential cholestanol accumulation in the cerebellum. *J. Biol. Chem.* 292, 4913–4924. doi: 10.1074/jbc.M116.774760

Melo, H. M., Santos, L. E., and Ferreira, S. T. (2019). Diet-derived fatty acids, brain inflammation, and mental health. *Front. Neurosci.* 13:265. doi: 10.3389/fnins.2019.00265

Mohri, I., Taniike, M., Taniguchi, H., Kanekiyo, T., Aritake, K., Inui, T., et al. (2006). Prostaglandin D2-mediated microglia/astrocyte interaction enhances astrogliosis and demyelination in twitcher. *J. Neurosci.* 26, 4383–4393. doi: 10.1523/JNEUROSCI.4531-05.2006

Murphy, S., Pearce, B., Jeremy, J., and Dandona, P., (1988). Astrocytes as eicosanoid−producing cells. *Glia* 1, 241–245. doi: 10.1002/glia.440010402

Nagahara, M., Waguri-Nagaya, Y., Yamagami, T., Aoyama, M., Tada, T., Inoue, K., et al. (2010). TNF-alpha-induced aquaporin 9 in synoviocytes from patients with OA and RA. *Rheumatology* 49, 898–906. doi: 10.1093/rheumatology/keq028

Najafi, A., Bidkhori, G., Bozorgmehr, J. H., Koch, I., and Masoudi-Nejad, A. (2014). Genome scale modeling in systems biology: algorithms and resources. *Curr. Genomics* 15, 130–159. doi: 10.2174/1389202915666140319002221

Niu, Y. C., Feng, R. N., Hou, Y., Li, K., Kang, Z., Wang, J., et al. (2012). Histidine and arginine are associated with inflammation and oxidative stress in obese women. *Br. J. Nutr.* 108, 57–61. doi: 10.1017/S0007114511005289

Okada, M., Makino, A., Nakajima, M., Okuyama, S., Furukawa, S., and Furukawa, Y. (2010). Estrogen stimulates proliferation and differentiation of neural stem/progenitor cells through different signal transduction pathways. *Int. J. Mol. Sci.* 11, 4114–4123. doi: 10.3390/ijms11104114

Orth, J. D., Thiele, I., and Palsson, B. Ø. (2010). What is flux balance analysis? *Nat. Biotechnol.* 28, 245–248. doi: 10.1038/nbt.1614

Osorio, D., González, J., and Pinzón, A. (2017). minval: an R package for MINimal VALidation of stoichiometric reactions. *R. J.* 9, 114–123.

Panov, A., Orynbayeva, Z., Vavilin, V., and Lyakhovich, V. (2014). Fatty acids in energy metabolism of the central nervous system. *Biomed. Res. Int.* 2014:472459. doi: 10.1155/2014/472459

Peng, M., Yin, N., Chhangawala, S., Xu, K., Leslie, C. S., and Li, M. O. (2016). Aerobic glycolysis promotes T helper 1 cell differentiation through an epigenetic mechanism. *Science* 354, 481–484. doi: 10.1126/science.aaf6284

Pessayre, D., Berson, A., Fromenty, B., and Mansouri, A. (2001). Mitochondria in steatohepatitis. *Semin. Liver Dis.* 21, 57–69 doi: 10.1055/s-2001-12929

Petrelli, F., and Bezzi, P. (2016). Novel insights into gliotransmitters. *Curr. Opin. Pharmacol.* 26, 138–145. doi: 10.1016/j.coph.2015.11.010

Pinto-Almazán, R., Calzada-Mendoza, C., Campos-Lara, M., and Guerra-Araiza, C. (2012). Effect of chronic administration of estradiol, progesterone, and tibolone on the expression and phosphorylation of glycogen synthase kinase-3á and themicrotubule-associated protein tau in the hippocampus and cerebellum of female rat. *J. Neurosci. Res.* 90, 878–886. doi: 10.1002/jnr.22808

Potokar, M., Jorgačevski, J., and Zorec, R. (2016). Astrocyte aquaporin dynamics in health and disease. *Int. J. Mol. Sci.* 17:1121. doi: 10.3390/ijms17071121

Purkayastha, S., and Cai, D. (2013). Neuroinflammatory basis of metabolic syndrome. *Mol. Metab.* 2, 356–363. doi: 10.1016/j.molmet.2013.09.005

R Development Core Team, (2016). *R: A Language and Environment for Statistical Computing*. Vienna: R Development Core Team. doi: 10.1007/978-3-540-74686-7

Rael, L. T., Thomas, G. W., Bar-Or, R., Craun, M. L., and Bar-Or, D. (2004). An anti-inflammatory role for N-acetyl aspartate in stimulated human astroglial cells. *Biochem. Biophys. Res. Commun.* 319, 847–853. doi: 10.1016/j.bbrc.2004.04.200

Rebhan, M., Chalifa-Caspi, V., Prilusky, J., and Lancet, D. (1997). GeneCards: integrating information about genes, proteins and diseases. *Trends Genet.* 13:163. doi: 10.1016/S0168-9525(97)01103-7

Reichelt, A. C., Westbrook, R. F., and Morris, M. J. (2017). Editorial: impact of diet on learning, memory and cognition. *Front. Behav. Neurosci.* 11:96. doi: 10.3389/fnbeh.2017.00096

Rymer, J. M. (1998). The effects of tibolone. *Gynecol. Endocrinol.*12, 213–220. doi: 10.3109/09513599809015548

Rymer, J., Chapman, M. G., and Fogelman, I. (1994). Effect of tibolone on postmenopausal bone loss. *Osteoporos. Int.* 4, 314–319. doi: 10.1007/BF01622189

Sá, J. V., Kleiderman, S., Brito, C., Sonnewald, U., Leist, M., Teixeira, A.P., and Alves, P. M. (2017). Quantification of metabolic rearrangements during neural stem cells differentiation into astrocytes by metabolic flux analysis. *Neurochem. Res.* 42, 244–253. doi: 10.1007/s11064-016-1907-z

Saparov, S. M., Liu, K., Agre, P., and Pohl, P. (2007). Fast and selective ammonia transport by aquaporin-8. *J. Biol. Chem.* 282, 5296–5301. doi: 10.1074/jbc.M609343200

Schuller-Levis, G. B., and Park, E. (2003). Taurine: new implications for an old amino acid. *FEMS Microbiol. Lett.* 226, 195–202. doi: 10.1016/S0378-1097(03)00611-6

Seeger, D. R., Murphy, C. C., and Murphy, E. J. (2016). Astrocyte arachidonate and palmitate uptake and metabolism is differentially modulated by dibutyryl-cAMP treatment. *Prostagland. Leukotr. Essential Fatty Acids* 110, 16–26. doi: 10.1016/j.plefa.2016.05.003

Sertbaş, M., Ulgen, K., and Cakır, T. (2014). Systematic analysis of transcription-level effects of neurodegenerative diseases on human brain metabolism by a newly reconstructed brain-specific metabolic network. *FEBS Open Bio.* 4, 542–553. doi: 10.1016/j.fob.2014.05.006

Shi, M., Caudle, W. M., and Zhang, J. (2009). Biomarker discovery in neurodegenerative diseases: a proteomic approach. *Neurobiol. Dis.* 35, 157–164. doi: 10.1016/j.nbd.2008.09.004

Sofroniew, M. V. (2014). Multiple roles for astrocytes as effectors of cytokines and inflammatory mediators. *Neuroscientist* 20, 160–172. doi: 10.1177/1073858413504466

Son, D. O., Satsu, H., and Shimizu, M. (2005). Histidine inhibits oxidative stress- and TNF-α-induced interleukin-8 secretion in intestinal epithelial cells. *FEBS Lett.* 579, 4671–4677. doi: 10.1016/j.febslet.2005.07.038

Souza, D. G., Almeida, R. F., Souza, D. O., and Zimmer, E. R. (2019). The astrocyte biochemistry. *Semin. Cell Dev. Biol.* 95, 142–150. doi: 10.1016/j.semcdb.2019.04.002

Swainston, N., Fleming, R. M., Hoppe, A., Sahoo, S., Aurich, M. K., Haraldsdottir, H., et al. (2013). A community-driven global reconstruction of human metabolism. *Nat. Biotechnol.* 31, 419–425. doi: 10.1038/nbt.2488

Swainston, N., Smallbone, K., Hefzi, H., Dobson, P. D., Brewer, J., Hanscho, M., et al. (2016). Recon 2.2: from reconstruction to model of human metabolism. *Metabolomics* 12:109. doi: 10.1007/s11306-016-1051-4

Takuma, K., Baba, A., and Matsuda, T. (2004). Astrocyte apoptosis: implications for neuroprotection. *Prog. Neurobiol.* 72, 111–127. doi: 10.1016/j.pneurobio.2004.02.001

Te Velde, A. A., Pronk, I., De Kort, F., and Stokkers, P. C. F. (2008). Glutathione peroxidase 2 and aquaporin 8 as new markers for colonic inflammation in experimental colitis and inflammatory bowel diseases: an important role for H2O2? *Eur. J. Gastroenterol. Hepatol.* 20, 555–560. doi: 10.1097/MEG.0b013e3282f45751

Thiele, I., and Palsson, B. Ø. (2010). A protocol for generating a high-quality genome-scale metabolic reconstruction. *Nat. Protoc.* 5, 93–121. doi: 10.1038/nprot.2009.203

Thiele, I., Swainston, N., Fleming, R. M. T., Hoppe, A., Sahoo, S., Aurich, M. K., et al. (2013). A community-driven global reconstruction of human metabolism. *Nat. Biotechnol.* 31, 419–425. doi: 10.1038/nbt.2488

Väremo, L., Scheele, C., Broholm, C., Mardinoglu, A., Kampf, C., Asplund, A., et al. (2015). Proteome- and transcriptome-driven reconstruction of the human myocyte metabolic network and its use for identification of markers for diabetes. *Cell Rep.* 11, 921–933. doi: 10.1016/j.celrep.2015.04.010

Vodovotz, Y., Csete, M., Bartels, J., Chang, S., and An, G. (2008). Translational systems biology of inflammation. *PLoS Comput. Biol.* 4:e1000014. doi: 10.1371/journal.pcbi.1000014

White, C. L., Pistell, P. J., Purpera, M. N., Gupta, S., Fernandez-Kim, S. O., Hise, T. L., et al. (2009). Effects of high fat diet on Morris maze performance, oxidative stress, and inflammation in rats: contributions of maternal diet. *Neurobiol. Dis.* 35, 3–13. doi: 10.1016/j.nbd.2009.04.002

Williams, R., Buchheit, C. L., Berman, N. E. J., and Levine, S. M. (2012). Pathogenic implications of iron accumulation in multiple sclerosis. *J. Neurochem.* 120, 7–25. doi: 10.1111/j.1471-4159.2011.07536.x

Wojtal, K., Trojnar, M. K., and Czuczwar, S. J. (2006). Endogenous neuroprotective factors: neurosteroids. *Pharmacol. Rep.* 58, 335–340.

Conflict of Interest: The authors declare that the research was conducted in the absence of any commercial or financial relationships that could be construed as a potential conflict of interest.

Copyright © 2020 Osorio, Pinzón, Martín-Jiménez, Barreto and González. This is an open-access article distributed under the terms of the Creative Commons Attribution License (CC BY). The use, distribution or reproduction in other forums is permitted, provided the original author(s) and the copyright owner(s) are credited and that the original publication in this journal is cited, in accordance with accepted academic practice. No use, distribution or reproduction is permitted which does not comply with these terms.

frontiers in Neuroscience

ORIGINAL RESEARCH
published: 31 January 2020
doi: 10.3389/fnins.2019.01397

Simplified Model of PKCγ Signaling Dysregulation and Cytosol-to-Membrane Translocation Kinetics During Neurodegenerative Spinocerebellar Ataxia Type 14 (SCA14)

Naveed Aslam[1,2]* *and Farah Alvi*[1,3]

[1] BioSystOmics, Bellaire, TX, United States, [2] Department of Chemistry and Chemical Engineering, Lahore University of Management Sciences, Lahore, Pakistan, [3] Department of Physics, COMSATS University Islamabad, Islamabad, Pakistan

OPEN ACCESS

Edited by:
Babatunde Ogunnaike,
University of Delaware, United States

Reviewed by:
Filippo Tempia,
University of Turin, Italy
Ilya Bezprozvanny,
UT Southwestern Medical Center,
United States

***Correspondence:**
Naveed Aslam
naveed.aslam@biosystomics.com

Specialty section:
This article was submitted to Systems Biology, a section of the journal Frontiers in Neuroscience

Received: 02 August 2019
Accepted: 11 December 2019
Published: 31 January 2020

Citation:
Aslam N and Alvi F (2020) Simplified Model of PKCγ Signaling Dysregulation and Cytosol-to-Membrane Translocation Kinetics During Neurodegenerative Spinocerebellar Ataxia Type 14 (SCA14). Front. Neurosci. 13:1397. doi: 10.3389/fnins.2019.01397

Spinocerebellar ataxia type 14 (SCA14) is an autosomal neurodegenerative disease clinically characterized by progressive ataxia in the patient's gait, accompanied by slurred speech and abnormal eye movements. These symptoms are linked to the loss of Purkinje cells (PCs), which leads to cerebellar neurodegeneration. PC observations link the mutations in PRKCG gene encoding protein kinase C γ (PKCγ) to SCA14. Observations also show that the link between PKCγ and SCA14 relies on a gain-of-function mechanism, and, in fact, both positive and negative regulation of PKCγ expression and activity may result in changes in cellular number, size, and complexity of the dendritic arbors in PCs. Here, through a systems biology approach, we investigate a key question relating to this system: why is PKCγ membrane residence time reduced in SCA14 mutant PCs compared to wild-type (WT) PCs? In this study, we investigate this question through two contrasting PKCγ signaling models in PCs. The first model proposed in this study describes the mechanism through which PKCγ signaling activity may be regulated in WT PCs. In contrast, the second model explores how mutations in PKCγ signaling affect the state of SCA14 in PCs. Numerical simulations of both models show that, in response to extracellular stimuli-induced depolarization of the membrane compartment, PKCγ and diacylglycerol kinase γ (DGKγ) translocate to the membrane. Results from our computational approach indicate that, for the same set of parameters, PKCγ membrane residence time is shorter in the SCA14 mutant model compared to the WT model. These results show how PKCγ membrane residence time is regulated by diacylglycerol (DAG), causing translocated PKCγ to return to the cytosol as DAG levels drop. This study shows that, when the strength of the extracellular signal is held

constant, the membrane lifetime of mutant PKCγ is reduced. This reduction is due to the presence of constitutively active mutant PKCγ in the cytosol. Cytosolic PKCγ, in turn, leads to phosphorylation and activation of DGKγ while it is still residing in the cytosol. This effect occurs even during the resting conditions. Thus, the SCA14 mutant model explains that, when both DAG effector molecules are active in the cytosol, their interactions in the membrane compartment are reduced, critically influencing PKCγ membrane residence time.

Keywords: PKCγ translocation kinetics, dysregulated signaling, spinocerebellar ataxia, neurodegeneration, mutant

INTRODUCTION

Clinically, the term "ataxia" describes abnormal limb movements and poor limb coordination (Shimobayashi, 2016). The most common form of ataxia is cerebellar ataxia, which can be linked to dysfunction either within the cerebellum or the cerebellar connecting pathways (Shimobayashi, 2016). Spinocerebellar ataxia (SCA) is a disease that manifests as dysfunction in the spinocerebellum, the part of the cerebellar cortex that receives somatosensory input from the spinal cord (Soong and Paulson, 2007; Carlson et al., 2009; Paulson, 2009). SCA14 is a rare form of SCA that can be inherited through autosomal dominance (Duenas et al., 2006; Shimobayashi, 2016). SCA14 has been linked to missense point mutations, deletions, or splice site mutations in the PRKCG coding region of PKCγ (Yamashita et al., 2000). Previous studies have linked almost 30 types of deletions or missense mutations in the PRKCG gene to SCA14-related symptoms (Shimobayashi, 2016). PKCγ is principally expressed in the central nervous system (CNS) and predominantly found in PCs (Saito et al., 1988; Saito and Shirai, 2002; Schrenk et al., 2002; Yabe et al., 2003). PKCγ is considered one of the key factors that control cerebellar development. SCA14 disease onset ranges from childhood to late adulthood, and usually does not result in a shorter lifespan. Generally, clinical symptoms of SCA14 include ataxia, dysarthria, oculomotor dysfunction, vertigo, facial myokymia, and myoclonus (Shimobayashi, 2016). Post-mortem neurohistological–pathological studies of patients with SCA14 have shown a pronounced reduction in the number of cerebellar Purkinje cells (PCs), as well a reduction in cellular size and complexity of the dendritic arbor (Brkanac et al., 2002).

An interesting possibility, supported by previous experimental observations, is that SCA14 might be linked to increases in PKCγ activity (Metzger and Kapfhammer, 2000; Adachi et al., 2008; Shimobayashi, 2016; Wong et al., 2018). Studies have shown that PMA-induced chronic PKCγ activation in cerebellar slice cultures drastically inhibits the growth and development of the PC dendritic tree (Metzger and Kapfhammer, 2000). This result could indicate that degeneration of the PC dendritic tree during SCA14 may be caused by increased PKCγ activity (Verbeek et al., 2005). Furthermore, 19 out of 20 spontaneous mutations found in the PKCγ gene of SCA14 patients showed increased constitutive PKCγ activity (Adachi et al., 2008). How constitutively active PKCγ may contribute to neurodegeneration is not clear. However, there is evidence that, despite an enhanced basal activity of the PKCγ isoform, there may be a deficit recruitment or regulation of downstream targets linked to a loss of specific cerebellar functions.

One possibility may be related to the membrane residence duration of PKCγ (Adachi et al., 2008; Shuvaev et al., 2011; Wong et al., 2018). In order to achieve precise regulation of PKCγs' downstream targets, its membrane residence time must be exquisitely regulated (Adachi et al., 2008; Shuvaev et al., 2011; Shimobayashi, 2016). If the amount of time PKCγ spends in the membrane compartment is altered, this may lead to aberrant regulation and/or recruitment of downstream signaling molecules. Previous observations suggest that in PCs, the PKCγ membrane residence time is controlled by the amplitude and duration of DAG signaling. Experimental observation in Chinese hamster ovary (CHO) cells indicate that DAG signaling could contribute to a functional coupling of PKCγ and its regulator DGKγ (Yamaguchi et al., 2006; Goto and Kondo, 1999; Mérida et al., 2008). These results show (Yamaguchi et al., 2006) that in the membrane compartment, DGKγ regulates the activity of PKCγ through phosphorylating DAG, and thus inducing its metabolism. Our previous work elucidated the role of this functional coupling and showed how the timing of DGKγ and PKCγ colocalization in the membrane compartment is important for DAG signaling regulation in both CHO cells and PCs (Aslam and Alvi, 2017, 2019).

In addition, previous data indicate that, compared to wild-type, mutant PKCγ has higher basal level activity, but reduced membrane compartment residence time (Shuvaev et al., 2011). This may explain aberrant downstream signaling in mutant models of PKCγ. For example, one study revealed a decrease in PKCγ signaling, measured by canonical transient receptor potential channel (TRPC3) phosphorylation, when a PKCγ mutant remained at the membrane for significantly less time than wild-type PKCγ (Adachi et al., 2008). Altered PKCγ phosphorylation or recruitment may contribute to cerebellar dysfunction and apoptosis in PCs.

The purinergic receptors belong to a class of plasma membrane molecules that have been critically implicated in the regulation of physiological and pathological responses such as learning memory, inflammation, motor control, and sleep. They are classified into P_1 (adenosine-activated) and P_2 (ATP-activated) subfamilies. Among the P_2 subfamily, the P_2X subgroup is ionotropic and the P_2Y subgroup is metabotropic nucleotide receptor. The P_2Y subfamily has

eight members and are expressed in cells of the nervous system. Among this subgroup, P_2Y_1, P_2Y_2, P_2Y_4, P_2Y_6, and P_2Y_{11} receptors are coupled to G_q-protein (Weisman et al., 2012; Guzman and Gerevich, 2016). The activation of this group by general currency in energy conversion, i.e., adenosine triphosphate (ATP) or nucleotide, uridine-5′-triphosphate (UTP), induces the G_q-dependent activation of phospholipase C (PLC), which promotes the hydrolysis of plasma membrane phospholipid phosphatidylinositol 4,5, bisphosphate (PIP_2) to generate second messenger DAG and inositol 1,4,5 triphosphate (IP_3). Both these second messengers are critical for the release of intracellular Ca^{+2} from stores, exchange of Ca^{+2} with extracellular pools, and activation of PKCγ and DGKγ.

This work explores why PKCγ membrane residence time is reduced in PCs in the mutant model, despite higher kinase activity. The following experimental observations provide the basis for this study: (1) Depolarization-induced activation of mGluR1 pathways leads to the membrane translocation of both mutant and wild-type PKCγ (Shuvaev et al., 2011; Shimobayashi, 2016). (2) Mutant PKCγ is constitutively active (Adachi et al., 2008; Shuvaev et al., 2011; Shimobayashi, 2016). (3) During a depolarization-induced activation event, the wild-type PKCγ membrane residence time is 19 s. The mutant PKCγ membrane residence time is 6 s (Shuvaev et al., 2011). (4) Depolarization-induced stimulation of both mutant and wild-type PKCγ results in rapid membrane translocation followed by a slow return to the cytosol (Adachi et al., 2008; Shuvaev et al., 2011; Shimobayashi, 2016). (5) In response to ATP stimulation, PKCγ and DGKγ form a subtype-specific functional coupling, which regulates DAG signaling in the membrane compartment in the CHO cell system (Yamaguchi et al., 2006). (6) Observations in post-mortem SCA14 cerebellum and human patient-derived induced pluripotent stem cells (iPSCs) show that, when activated, wild-type PKCγ is distributed in the membrane and cytosolic compartment, whereas mutant PKCγ tends to localize in cytosol (Wong et al., 2018), thus indicating that mutant PKCγ is impaired in its ability to translocate, or be retained at, the plasma membrane. (7) Additional observations from SCA14 iPSCs and SCA14 PCs indicate that mutant PKCγ present in cytosol is in hyperactive state (Wong et al., 2018). (8) Moreover, this molecule leads to a robust increase in PKCγ substrate phosphorylations as observed by increase in PKCγ substrate antibody and its well-established target, i.e., myristoylated alanine-rich C-kinase substrate (MARCKS) in SCA14 cerebellum (Wong et al., 2018). In this work, we test the hypothesis that due to reduced local signaling, the lifetime of mutant PKCγ is reduced in the membrane compartment.

This work tests this hypothesis by constructing two contrasting models (WT and mutant). The simulations mimicking mutant model includes a constitutively active PKCγ in the cytosol (Adachi et al., 2008; Shuvaev et al., 2011; Shimobayashi, 2016; Wong et al., 2018), which, in turn, phosphorylates and activates DGKγ even during basal conditions. The simulations representing the wild-type model includes inactive and dormant PKCγ and DGKγ in the cytosol during basal conditions and models translocation to the membrane compartment upon stimulation. The wild-type model shows membrane activation of DGKγ in a stimulation-dependent manner, whereas the mutant model relies on stimulation-independent cytosolic DGKγ activation. Both models are numerically perturbed by the same stimulation strength levels. For both models, all kinetic rate constants and translocation parameters are set at the identical numerical values. The overall goal of this study is to compare the effects on PKCγ membrane residence duration in the mutant and wild-type models through numerical experimentation, with all other parameters held constant. Here, we show that, despite higher activity levels membrane residence, duration for PKCγ in the mutant model is three times shorter than the wild-type. We also show that, when a stimulation pulse is applied to mimic depolarization-induced activation of mGluR1, PKCγ translocation from the cytosol to the membrane is induced. The manner and time scale of this induction is consistent with experimental observations (Shuvaev et al., 2011). Depolarization-induced local DAG generation in the membrane compartment also induces DGKγ translocation from the cytosol to the membrane, where the molecule acts as a key negative regulator of DAG levels in the membrane compartment.

Experimental results suggest that despite the constitutively active nature of mutant molecule, the impaired translocation and shorter membrane residence time result in lower PKCγ concentrations in the membrane compartment of PCs (Shuvaev et al., 2011; Wong et al., 2018). This observation could be linked to the association of mutant PKCγ with large EPSC amplitudes in PCs (Shuvaev et al., 2011). Our simulations are consistent with these observations, as the maximum membrane-to-cytosol (M/C) ratio in the mutant model is half of the ratio in the wild-type model. This indicates that reductions in PKCγ concentration in the membrane compartment may be linked to impaired PC functionality.

MATERIALS AND METHODS

Biochemical Reactions

The following model describes a mutant PKCγ signaling model in PCs. This simulation models mutant and active PKCγ and DGKγ molecules. These biochemical interactions describe how local DAG generation leads to a signaling loop between PKCγ and DGKγ in our mutant models of PCs. The simulated interactions of molecules within the PKCγ and DKCγ loop (**Figure 1**) are based on standard Michaelis–Menten kinetics. The following sets of biochemical reactions are used to describe the molecular interactions that occur within the PKCγ and DKCγ loop. The dynamic variables are DAG, DGKγ, and PKCγ. Subscript I represents the concentration in the first compartment, the plasma membrane. Subscript II denotes the concentration in the second compartment, which represents the cytosol. The superscript Active represents the activated form of a molecule and the subscript P represents the phosphorylated

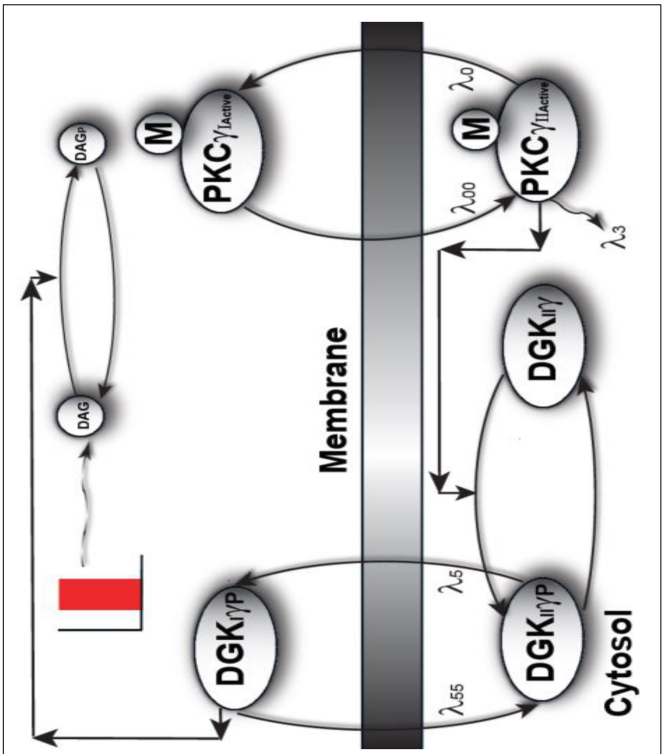

FIGURE 1 | A proposed regulatory model of mutant PKCγ, translocation in the SCA14-associated Purkinje cells of the cerebellum. This is a two-compartment model where one compartment is cytosol, whereas the other compartment is plasma membrane. This model provides the mechanistic basis of how the translocation of mutant PKCγ and DGKγ molecules could be regulated in SCA14 disease. This model suggests that in diseases associated with cPCs, the mutant PKCγ is constitutively active and resides in the cytosol. In turn, this constitutively active molecule induces the phosphorylation and activation of the cytosolic DGKγ molecule even during the basal or unstimulated conditions. In contrast, to the wild-type model, the current model suggests that both PKCγ and DGKγ are active and cytosolic even during basal conditions. Depolarization-induced activation of purinergic receptor leads to the local generation of DAG and, in turn, induces the translocation of both mutant PKCγ and DGKγ from cytosol to membrane. Once in the plasma membrane compartment, the already active DGKγ molecule directly converts DAG to PA through DAG phosphorylation.

form of a molecule. The subscript Mutant represents the mutant form of a molecule. The phosphatase P is approximated as a fixed parameter. The parameter S1 denotes purinergic receptor stimulation, which leads to the rapid generation of DAG molecules.

$$\mathrm{PKC^{Active}}\,\gamma_{\mathrm{II.Mutant}} \xrightarrow{\lambda_0} \mathrm{PKC^{Active}}\,\gamma_{\mathrm{IMutant}} \quad (1)$$

$$\mathrm{PKC^{Active}}\,\gamma_{\mathrm{IMutant}} \xrightarrow{\lambda_{00}} \mathrm{PKC^{Active}}\,\gamma_{\mathrm{II\ Mutant}} \quad (2)$$

$$\mathrm{DGK}\gamma_{\mathrm{IIP}} \xrightarrow{\lambda_5} \mathrm{DGK}\,\gamma_{\mathrm{1P}} \quad (3)$$

$$\mathrm{DGK}\gamma_{\mathrm{IP}} \xrightarrow{\lambda_{55}} \mathrm{DGK}\gamma_{\mathrm{IIP}} \quad (4)$$

$$\mathrm{S_1} \xrightarrow{k_1} \mathrm{DAG} \quad (5)$$

$$\mathrm{DGK}\gamma_{\mathrm{II}} + \mathrm{PKC^{Active}}\gamma_{\mathrm{IIMutant}} \underset{k_3}{\overset{k_2}{\rightleftarrows}} \mathrm{C_1} \xrightarrow{k_4} \mathrm{DGK}\gamma_{\mathrm{IP}} + \mathrm{PKC^{Active}}\,\gamma_{\mathrm{IIMutant}} \quad (6)$$

$$\mathrm{DGK}\gamma_{\mathrm{IIp}} + \mathrm{P} \xrightarrow{k_5} \mathrm{DGK}\gamma_{\mathrm{II}} + \mathrm{P} \quad (7)$$

$$\mathrm{DAG} + \mathrm{DGK}\gamma_{\mathrm{IP}} \underset{k_7}{\overset{k_6}{\rightleftarrows}} \mathrm{C_2} \xrightarrow{k_8} \mathrm{DGK}\gamma_{\mathrm{IP}} + \mathrm{DAG_P} \quad (8)$$

$$\mathrm{DAG_P} \xrightarrow{k_g} \mathrm{P.A} \quad (9)$$

$$\mathrm{PKC_{II}}\gamma^{\,\mathrm{Active}}\,\mathrm{mutant} \xrightarrow{\lambda 3} [\,] \quad (10)$$

The signaling described in the above model starts during basal conditions. The constitutively active cytosolic mutant PKCγ molecule leads to phosphorylation and activation of DGKγ in the cytosol. This event is described by Equation (6). A pulse stimulation that mimics depolarization-induced stimulation of the pathway leads to DAG generation at the plasma membrane. This local event, causing generation of a second messenger, is described in Equation (5). DAG generation then stimulates the migration of dormant and active mutant $\mathrm{PKC}\gamma_{\mathrm{II}}$ and $\mathrm{DGK}\gamma_{\mathrm{II}}$ from the cytosol to the plasma membrane. These migration events are described by Equations (1) and (3). Here, the migration rates "λ_0" and "λ_5" are described through functions that are directly proportional to DAG concentrations, but with different slopes. Then, the active γ-molecules in the plasma membrane compartment re-translocate to the cytosol with fixed migration rates, "λ_{00}" and "λ_{55}," as described by Equations (2) and (4). Once at the plasma membrane, $\mathrm{DGK}\gamma_{\mathrm{I}}$ causes DAG metabolism through its phosphorylation, as described by Equation (8). Phosphorylated DAG is converted to phosphatidic acid (PA) as shown in Equation (9). PA is another key signaling lipid that may function directly as a key regulatory molecule. The dephosphorylation event of $\mathrm{DGKII}\gamma_{\mathrm{P}}$ is described by Equation (7).

Induction

During simulations, the membrane depolarization-induced activation of purinergic receptor is mimicked through the application of a brief pulse. The local biosynthesis of second messenger DAG is modulated through a 1.0-min pulse stimulation. DAG generation in the membrane compartment induces the translocation and activation of its effector molecules.

Temporal Dynamics

The differential equations resulting from the above interactions [Equations (1) to (9)] were integrated through nonlinear solvers using MATLAB (MathWorks). The dynamical coefficients' values were estimated from limited experimental data (Shuvaev et al., 2011). Unknown rate constants were scaled to obtain dynamics that were comparable to experimental values (Shuvaev et al., 2011). Unless otherwise stated, all of the molecular concentrations in the model are expressed as pg/ml and time is represented in seconds.

RESULTS

Comparative Models Describing DAG Signaling in Mutant and Wild-Type PCs

The DAG signaling model we propose for mutant PCs (**Figure 1**) in cerebellar PCs is composed of two molecular components. The first component is mutant PKCγ, which can be active and cytosolic ($PKC^{Active}\gamma_{II\text{-}Mutant}$) or active and membrane ($PKC^{Active}\gamma_{I\text{-}Mutant}$). The second component is DGKγ, which can be cytosolic and inactive ($DGK_{II}\gamma$); cytosolic, active, and phosphorylated ($DGK_{II}\gamma_P^A$); or active and phosphorylated in the membrane compartment ($DGK_I\gamma_P{}^A$). In the mutant signaling model, PKCγ is constitutively active and leads to phosphorylation and activation of DGKγ in the cytosolic compartment. This occurs even during basal conditions. In this model, depolarization-induced stimulation leads to local DAG generation in the membrane compartment. This leads to cytosol-to-membrane translocation of active PKCγ and DGKγ. Once in the membrane compartment, already active and phosphorylated DGKγ stimulates DAG metabolism. DAG levels are quickly reduced by the molecule's conversion to PA. Once DAG levels in the membrane drop, both molecules relocate back to the cytosol.

In contrast, **Figure 2** shows that PKCγ can reside in one of four states in the wild-type model (**Supplementary Material S2**: Biochemical Reactions describing fast kinetics wild-type model). The four states are cytosolic dormant ($PKC\gamma_{II}$), inactive membrane ($PKC\gamma_I$), active membrane ($PKC\gamma_I{}^A$), and active cytosolic ($PKC\gamma_{II}{}^A$). In the mutant cascade, PKCγ exists in only two distinct forms. This is because PKCγ is inactive in the wild-type model in its dormant cytosolic state, but constitutively active in the mutant model while residing in the cytosol. This difference leads to a reduced PKCγ cycle in the mutant model (**Figures 1**, **2**). Interestingly, cytosolic DGKγ in the wild-type model is inactive, and only phosphorylated and activated in the membrane compartment. In contrast, in the mutant model, it is activated and phosphorylated in the cytosol by constitutively active PKCγ. The two-state mutant model and four-state wild-type model of PKCγ (**Figure 2**) are only simplistic descriptions of a complex PKCγ cycling process. A more realistic, complex PKCγ cycling model should account for molecular events like translocation, binding, activation, and re-translocation of active PKCγ to the cytosol. In addition, it should include deactivation of PKCγ back to its dormant form in the cytosol. While the processes modeled in this manuscript are complex, this study approximates the processes using simpler biochemical kinetic events that preserve key qualitative features. Cytosol-to-membrane translocation of both PKCγ and DGKγ in these mutant and wild-type simulations is described through proportionality functions of DAG concentrations. In addition, this study assumes non-negligible basal levels of $PKC^{Active}\gamma_{II\text{-}Mutant}$ (100 pg/ml) and $DGK_{II}\gamma$ (100 pg/ml) in the mutant and $PKC\gamma_{II}$ (100 pg/ml) and $DGK_{II}\gamma$ (100 pg/ml) in the wild-type model. In contrast, the basal concentration of all other forms of PKCγ and DGKγ is negligible. The biochemical reaction and translocation rates of this molecular loop were obtained by fitting the depolarization-induced temporal dynamics of PKCγ translocation and re-translocation obtained from PCs in cerebellar slices as described in previously published studies (Shuvaev et al., 2011).

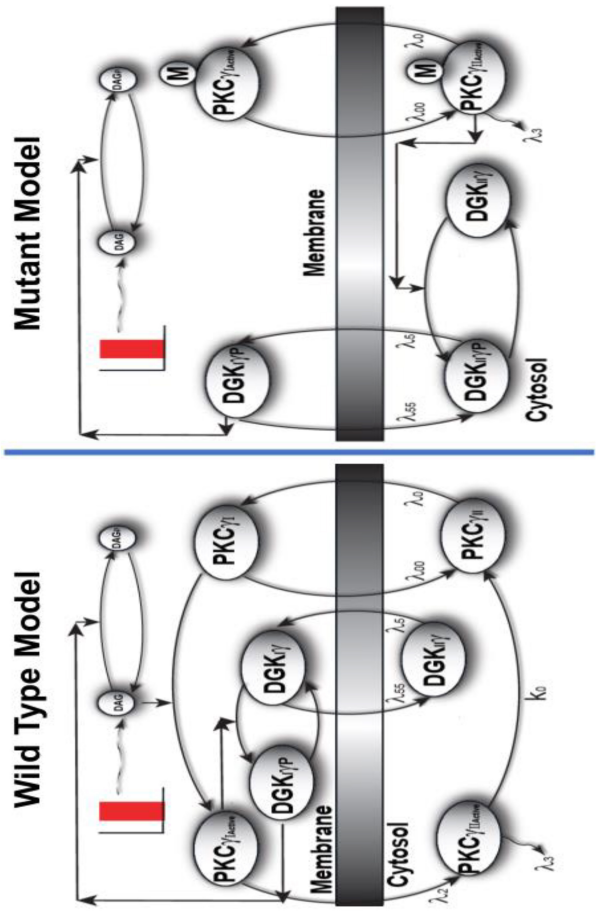

FIGURE 2 | The comparison of two-compartment, wild-type, and mutant models of local DAG signaling in PCs. Depolarization-induced local generation of DAG in PCs, in turn, leads to the functional coupling between PKCγ and DGKγ molecules. The wild-type model is characterized by dormant and inactive PKCγ molecule residing in cytosol, whereas the mutant model is characterized by active PKCγ isoform in the cytosol. In the wild-type model, the depolarization-induced activation of purinergic receptor and local generation of DAG stimulates the translocation of PKCγ and DGKγ molecules from cytosol to membrane compartments. Once in the membrane compartment, the DAG binds with PKCγ and activates it, which, in turn, activates DGKγ through phosphorylation. In the membrane compartment, the phosphorylated and active DGKγ molecule stimulates the DAG metabolism, thus restricting its own activation. Once DAG is converted to PA in membrane compartment, both these molecules return to their dormant forms in cytosol. In contrast, the signaling in the mutant model is reduced as in the mutant model of PCs; the PKCγ is in constitutively active state and leads to the phosphorylation and activation of DGKγ in the cytosol even during unstimulated conditions. On stimulation, as DAG is generated in the membrane compartment, both these molecules migrate to membrane where the already activated DGKγ molecule converts DAG to PA. It seems that signaling in the mutant model is reduced due to the constitutively active form of PKCγ in cytosol.

In both the mutant and wild-type models, DGKγ inhibits its own translocation and that of PKCγ by converting DAG into PA

at the plasma membrane. Our models show that depolarization-induced stimulation in the membrane compartment leads to DAG generation. DAG generation, in turn, stimulates the DGKγ and PKCγ translocation. In the mutant model, once the already active DGKγ is at the plasma membrane, it directly induces DAG metabolism. In contrast, in the wild-type model, DGKγ undergoes an activation event before becoming competent to metabolize DAG. These events restore DAG homeostasis, thus reducing migration to the membrane compartment. In both these models, local DAG generation is counterbalanced by DGKγ-assisted metabolism in the membrane compartment.

Regulation of depolarization-induced activation of G protein-coupled receptor (GPCR) pathways is a complex process (Shuvaev et al., 2011). GPCR agonist mGluR1 stimulates PLC-mediated hydrolysis of phosphatidylinositol 4,5-biphosphate to produce inositol triphosphate (IP_3) and DAG (Shuvaev et al., 2011). In this study, although we are primarily focusing on the downstream signaling of the purinergic receptor pathway, we modeled local DAG biosynthesis in both the mutant and wild-type models by using a brief pulse of variable intensity. This pulse is used to mimic the effects of GPCR agonist mGluR1. This approach is simple in that it ignores the details of purinergic receptor-induced DAG biosynthesis. Since our primary focus is regulation of DAG homeostasis, and not DAG biosynthesis, this study employs this simple approach.

Comparison of PKCγ and DGKγ Translocation Characteristics in Mutant and Wild-Type PC Models Through Numerical Simulations

Next, the translocation characteristics of PKCγ and DGKγ in the mutant and wild-type models were compared through numerical simulations. Translocation characteristics were determined by measuring two key properties. First, translocation kinetics from cytosol to membrane were measured. Next, the membrane-to-cytosol (M/C) ratio was measured. The kinetics of translocation are determined by measuring the time that both DAG effector molecules spend in the membrane compartment. During the course of simulations, the M/C ratio is measured by computing the total amount of DAG effector molecules in the membrane and cytosolic compartment at every time step and then taking the ratio. In simulations mimicking the post depolarization-induced receptor activation, the speed of translocation response is described using kinetic parameters. In contrast, during these numerical experiments, the intensity of this response is described using the M/C ratio of PKCγ and DGKγ in the membrane and cytosolic compartments. In simulations mimicking both the mutant and wild-type models, the mGluR1-induced activation of GPCR and subsequent DAG generation were implemented using a brief 1-min pulse, as described in the previous section. The strength of pulse is described by an arbitrary parameter S_1. S_1 was set at an arbitrary level of 20. In the absence of a pulse (**Figure 3**, solid blue lines), there is no *de novo* DAG biosynthesis and the system is fixed in its basal state. In the basal state, both molecules reside in the cytosol with no possibility of translocation.

The stimulation-induced temporal dynamics of PKCγ in the mutant (**Figure 3A**, dashed green line) and wild-type (**Figure 3A**, dashed red line) models show two phases of translocation. The first is an early phase, in which PKCγ migrates from the cytosol to the membrane. The second phase that follows is a resolution phase in which PKCγ relocates back to the cytosol. These results show that, for the same level of stimulation pulse, the translocation of PKCγ from the cytosol to the membrane is faster in the mutant model compared to wild-type. In contrast, the translocation intensity, measured by the M/C ratio of PKCγ, is lower in the mutant model compared to wild-type (**Figure 3A**, dashed green and red line). These results show that cytosolic-to-membrane molecular migration in both models is dependent on local DAG concentration at the plasma membrane and is linked to *de novo* DAG biosynthesis. In both the mutant and wild-type models, DAG concentration can be controlled through the duration and amplitude of pulse stimulation at the plasma membrane compartment.

In both models, the PKCγ translocation rate is a directly proportional function of DAG concentration (**Supplementary Material S1: Table S1** and **Supplementary Material S3: Table S2**). When the mutant model was perturbed with different levels of stimulation, the results indicate that when stimulation strength is set at moderate levels (**Figure 4A**, inset; pulse strength parameter $S_1 = 20$), only a small pool of DAG is generated at the plasma membrane. This induces a low-intensity migration event reflected by a maximal M/C ratio. The M/C ratio is linked to pulse strength (**Figure 4A**). Higher levels of stimulation generate (**Figure 4A**, inset; pulse strength parameter $S_1 = 40$ and 60) much larger pools of DAG at the plasma membrane. This induces migration of a large pool of PKCγ to the membrane. Interestingly, perturbation of the wild-type model (**Figure 4B**) also generates the same pattern with regard to the M/C ratio of PKCγ. However, at higher stimulation strengths, the maximal M/C ratio of PKCγ in the wild-type model is five-times more than the ratio at moderate stimulation. In contrast, it is 10-times more at even higher stimulation strength, showing the effects of DAG generation on translocation of PKCγ from the cytosol to the membrane.

In this study, DGKγ translocation is spatially similar, but temporally distinct, from PKCγ. The migration of DGKγ is also controlled by DAG concentrations at the plasma membrane. The sensitivity of this migratory event is different from that of PKCγ. DGKγ translocation is also described by a proportionality function (**Supplementary Material S1: Table S1** and **Supplementary Material S3: Table S2**) of DAG concentration at the plasma membrane. Compared to PKCγ, however, the slope of this function is much smaller. This means that DGKγ migration from the cytosol to the plasma membrane requires a much larger increase in DAG concentration at the plasma membrane. This approach was adopted so that the proposed models align with previous experimental observations showing different translocation sensitivities of PKCγ and DGKγ to Ca^{+2} concentrations (Yamaguchi et al., 2006). These observations suggest that both PKCγ and DGKγ possess DAG-sensitive C_1 and Ca^{+2}-sensitive C_2 domain. Interestingly, nanomolar elevation in

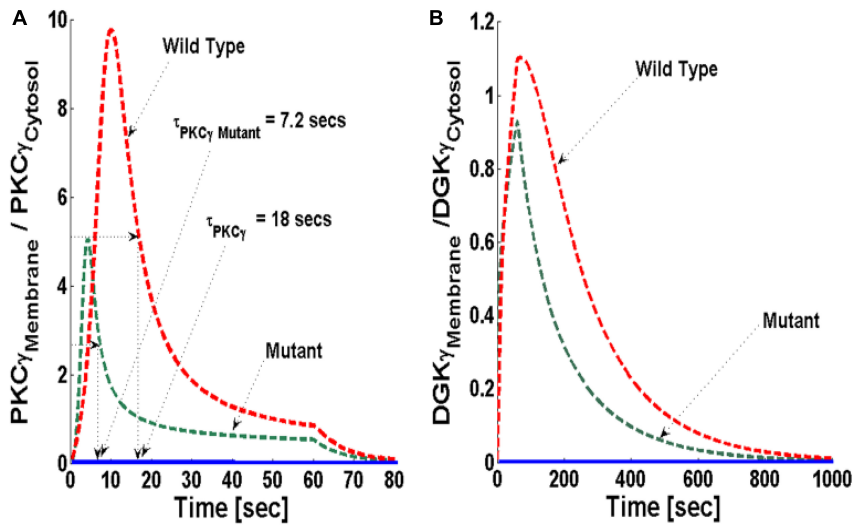

FIGURE 3 | The simulations mimicking the comparison of depolarization-induced translocation of PKCγ and DGKγ molecules in the mutant and wild-type models of PCs. These results show the membrane-to-cytosol (M/C) ratio of PKCγ and DGKγ molecules in response to a brief 1-min pulse, which leads to the rapid generation of DAG in the membrane compartment. Here, the strength of stimulation is controlled by setting the pulse parameter "S_1" at 20. The generation of the second messenger, in turn, stimulates the translocation of both PKCγ and DGKγ from cytosol to membrane. Here, the solid line represents the non-stimulation and the dashed line represents the stimulation condition (green dashed line, mutant; red dashed line, wild-type PCs). **(A)** The translocation characteristics of the PKCγ molecule in both mutant and wild-type models. These results suggest that for identical strength and duration of stimulation, the cytosol-to-membrane migration kinetics of PKCγ molecule are much faster in mutant models compared to wild-types. Compared to wild-types, the membrane residence time of PKCγ molecule is shorter in mutant models, i.e., 7.2 s for mutant and 18 s for wild-type models. **(B)** The translocation characteristics of the DGKγ molecule in both mutant and wild-type models. These results show that the membrane residence time of the DGKγ molecule is shorter in mutant models compared to models representing wild-type PCs.

Ca^{+2} concentration was enough to warrant PKCγ translocation, whereas DGKγ translocation required micromolar increase in Ca^{+2}concentration (Yamaguchi et al., 2006).

At the plasma membrane, the coupling between PKCγ and DGKγ can be quantified by measuring colocalization time between these two molecules. Colocalization time is defined as the duration for which these molecules may interact with each other. This time interval also determines the duration during which a negative feedback loop is functional and effectively facilitating DAG metabolism. Colocalization time depends on DAG concentration in the plasma membrane, re-translocation rates of the inactive molecules, the remigration rate of active PKCγ, the activation rate and DAG binding activity of PKCγ, and activation and phosphorylation of DGKγ.

In order to estimate the parameters of proposed PKCγ and DGKγ interaction in PCs, we fixed the membrane residence duration of PKCγ in both mutant and wild-type models well within the experimentally reported ranges (Shuvaev et al., 2011) and determined the unknown parameters of molecular loop as well as the translocation and remigration rates of DGKγ. We also assumed that, similar to the CHO cell model, the sensitivity of PKCγ translocation to DAG concentration is higher than DGKγ (**Supplementary Material S1: Table S1** and **Supplementary Material S3: Table S2**). We calibrated our models by matching the ranges of membrane residence duration of PKCγ in mutant and wild-type models of cPCs (Shuvaev et al., 2011). This ad hoc approach could be questioned, but in the absence of direct translocation data of DGKγ migration and remigration in PCs, we believe that this is a reasonable approximation. The assumption made here should be tested directly and the translocation rate of DGKγ should be measured directly in PCs. However, it is unlikely that the overall structure of this model and the conclusion drawn from this model will be significantly different based on these assumptions.

Simulations Mimicking the Effect of the Rate of DAG Phosphorylation on the Translocation Characteristics of PKCγ in Mutant and Wild-Type Models of PCs

The residence time of PKCγ at the membrane is modulated by DAG levels. DAG metabolism at the membrane is regulated by active and phosphorylated DGKγ. DGKγ leads to DAG phosphorylation, an essential step for the conversion of DAG to PA. It is possible that the molecular events involved in DAG phosphorylation may influence the residence time of PKCγ at the membrane. This study addresses the question of how the DAG phosphorylation rate, "k_6" in the mutant model and "k_8" in the wild-type model, might influence the intensity and translocation of PKCγ and DGKγ from the cytosol to the membrane. The parameter "k_6" in the mutant and "k_8" in the wild-type model describe the feed forward rate constant of DAG phosphorylation by DGKγP. This study tested the hypothesis that how an increase in parameters k_6 and k_8 could influence the translocation as well as membrane residence duration of PKCγ. The simulations compared three difference cases: (a) baseline k_6 and k_8 (k_6 = 0.95

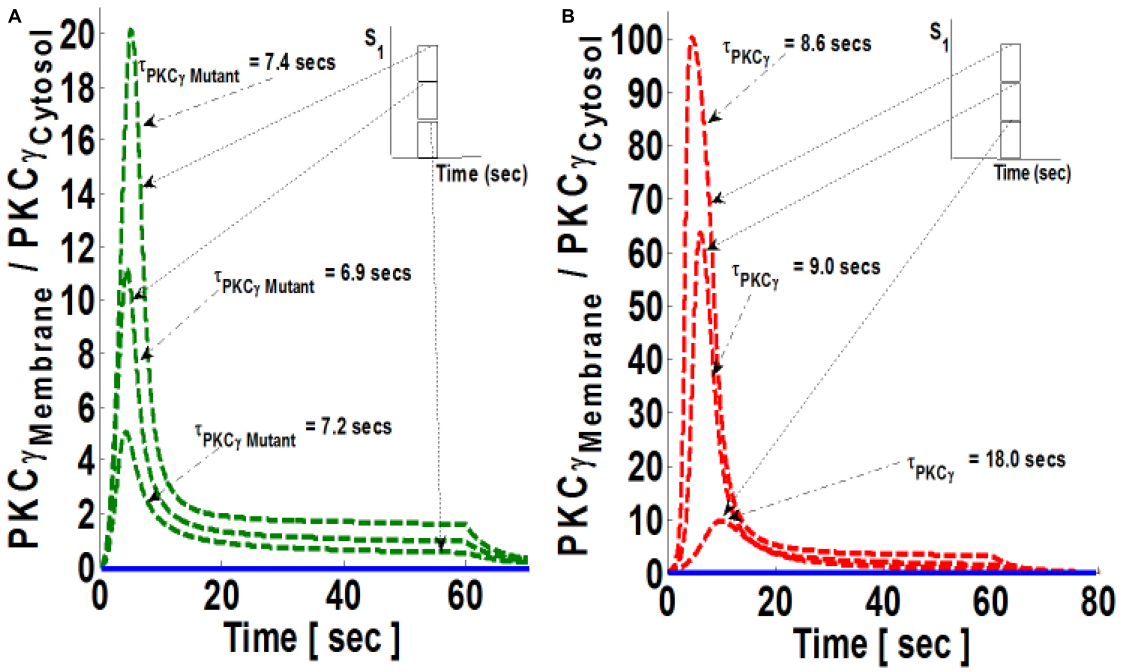

FIGURE 4 | The simulations mimicking the effect of stimulation strength on the comparative translocation kinetics of PKCγ isoform in the mutant and wild-type models of PCs. Here, the strength of stimulation is controlled by setting the pulse parameter "S_1" at different levels. The parameter S_1 is set at arbitrary values of 20, 40, and 60 (inset). The duration of pulse for all these three cases is 1 min. Here, the solid line represents the non-stimulation and the dashed line represents the stimulation condition (green dashed line, mutant; red dashed line, wild-type PCs). **(A)** Translocation characteristics of PKCγ in the mutant model. Here, results show that maximum levels of M/C ratio of PKCγ increases with increase in the strength of parameter "S_1"; however, the residence time of mutant PKCγ first decreases and then increases with pulse strength (S_1 = 20, leads to maximum M/C levels of 5 and $\tau_{PKC_\gamma\ mutant}$ = 7.2 s; S_1 = 40, leads to maximum M/C levels of 11 and $\tau_{PKC_\gamma\ mutant}$ = 6.9 s; S_1 = 60, leads to maximum M/C levels of 20 and $\tau_{PKC_\gamma\ mutant}$ = 7.4 s). **(B)** Translocation characteristics of PKCγ in the wild-type models. Here, results show that maximum levels of the M/C ratio of PKCγ increases with increase in the strength of parameter "S_1," and the residence time of wild-type PKCγ decreases with pulse strength (S_1 = 20, leads to maximum M/C levels of 10 and τ_{PKC_γ} = 18 s; S_1 = 40, leads to maximum M/C levels of 64 and τ_{PKC_γ} = 9 s; S_1 = 60, leads to maximum M/C levels of 100 and τ_{PKC_γ} = 8.6 s).

$pM^{-1}\ s^{-1}$ and k_8 = 0.95 $pM^{-1}\ s^{-1}$); (b) 25-times increase in the k_6 and k_8; (c) 100-times increase in the k_6 and k_8. The results show that increasing the parameter k_6 not only reduces the intensity of translocation but also the membrane residence time of PKCγ in the mutant model (**Figure 5A**). A 25-fold increase in k_6 causes the maximum M/C ratio to decrease 10%. In contrast, membrane residence time decreased 13% in the mutant model (**Figure 5A**). Interestingly, increasing k_6 from 25- to 100-fold had no effect on translocation or membrane residence duration for PKCγ in the mutant model (**Figure 5A**). The results from the wild-type model show that a 25-fold increase in k_8 reduces PKCγ translocation intensity to almost 40%. In contrast, membrane residence time is reduced by only 11% (**Figure 5B**). Furthermore, an increase in k_8 from 25- to 100-fold had an almost negligible influence on membrane residence duration and the magnitude of translocation (**Figure 5B**).

Next, this study investigated how blocking DAG phosphorylation influences the magnitude of PKCγ translocation as well as PKCγ membrane residence duration in both the mutant and wild-type models. Our results indicate that blocking parameter k_6 in the mutant model increases both the magnitude and membrane residence duration of PKCγ (**Figure 6**). Our results show that 90 and 95% blocking of k_6 in the mutant model leads to maximum M/C ratios of 8.8 and 12.2, respectively. In contrast, PKCγ membrane residence duration times are 10.5 and 14.5 s, respectively (**Figure 6A**). These results indicate that 95% blocking in the mutant model leads to an almost twofold increase in the magnitude of translocation and membrane residence duration of PKCγ (**Figure 6A**). Similarly, our results indicate that blocking the DAG phosphorylation parameter, k_8, in wild-type models also increases translocation intensity and membrane residence duration (**Figure 6B**). Our results show that 90 and 95% blocking of k_8 in the wild-type model leads to 3 and 5-fold increases in the magnitude of translocation (**Figure 6B**; measured as maximum in M/C ratio). In contrast, only 5 and 10% increases in membrane residence duration were observed for the wild-type model of PKCγ in cPCs (**Figure 6B**).

Simulations Mimicking the Influence of the DGKγ Activation Rate on the Translocation Characteristics of PKCγ

DGKγ phosphorylation and activation play key roles in regulating DAG homeostasis in the mutant and wild-type models. In the mutant model, DGKγ activation takes place in the cytosol. In contrast, activation takes place in the

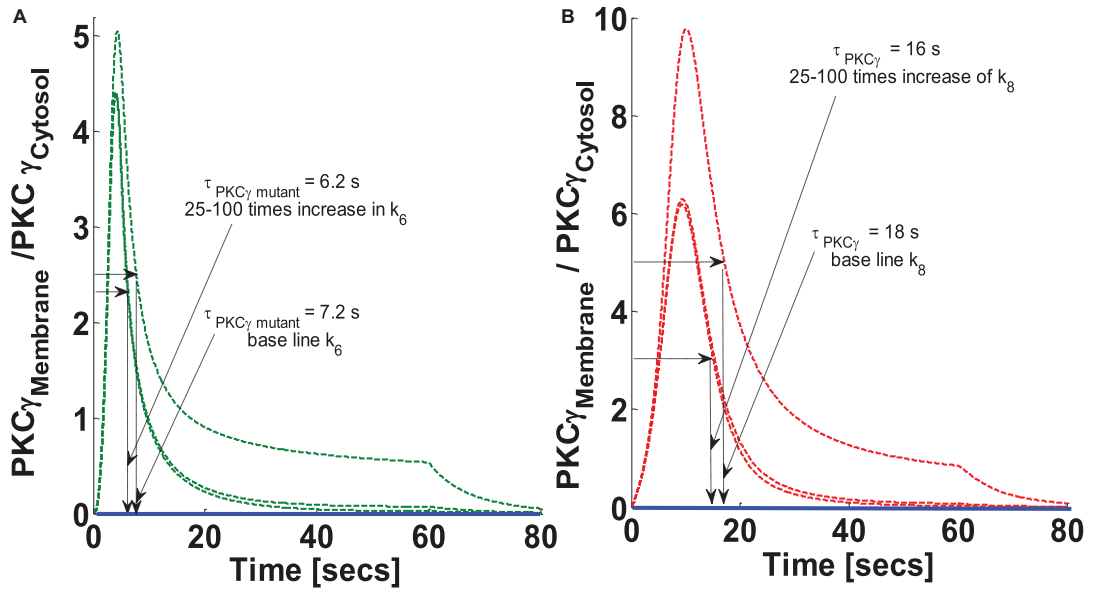

FIGURE 5 | The simulations mimicking the effect of feed forward rate constant of DAG phosphorylation by $DGK\gamma_P$ on the comparative translocation kinetics of PKCγ molecule in the mutant and wild-type models of PCs. Parameter k_6 represent this rate constant in mutant models, whereas in wild-types, it is represented by k_8. Here, the strength of stimulation is controlled by setting the pulse parameter "S_1" at 20. The duration of pulse is set for 1 min. Here, the solid line represents the non-stimulation and the dashed line represents the stimulation condition (green dashed line, mutant; red dashed line, wild-type PCs). **(A)** Translocation characteristics of PKCγ in the mutant model. Here, results show that increasing the parameter k_6 in the mutant model reduces the membrane residence time of PKCγ (at baseline, k_6, $\tau_{PKC_{\gamma\ mutant}}$ = 7.2 s; and 25–100 times increase in k_6 leads to $\tau_{PKC_{\gamma\ mutant}}$ = 6.2 s). **(B)** Translocation characteristics of PKCγ in the wild-type models. Here, results show that increasing the parameter k_8 in the wild-type model reduces the membrane residence time of PKCγ (at baseline, k_8, τ_{PKC_γ} = 18 s; and 25–100 times increase in k_8 leads to τ_{PKC_γ} = 16 s).

membrane compartment in the wild-type model. Next, through numerical simulations, this study investigated how reducing DGKγ activation and phosphorylation rates may influence the magnitude of translocation and the membrane residence duration of PKCγ in the mutant and wild-type models. Our results show that blocking parameter k_4 in the mutant model reduces the magnitude of PKCγ translocation, but increases membrane residence duration (**Figure 7A**). The results show that 80% blocking results in a 70% reduction in translocation magnitude and a near 2.5-fold increase in membrane residence time (**Figure 7B**). Furthermore, 90% blocking results in an 80% reduction in the magnitude of translocation and an almost threefold increase in membrane residence time of PKCγ (**Figure 7A**). Interestingly, the results from the wild-type model show that 80% blocking increases magnitude by fivefold and reduces membrane residence time by 33% (**Figure 7B**). Furthermore, 90% blocking increases magnitude by 12-fold and reduces duration by 22% (**Figure 7B**) compared to the baseline case of no blocking.

How Can the PKCγ-to-DGKγ Expression Ratio Influence the Translocation Characteristics of PKCγ?

The formulation of both models indicates that DAG levels, after stimulation, are controlled through a net negative feedback loop between its effector molecules PKCγ and DGKγ. One intriguing and still-unanswered question is how the relative expression of these molecules may influence negative feedback efficacy. In this simulation, it was assumed that both DAG effector molecules are equally expressed in the cytosol (choice of equal expressions is empirical and is chosen here to have a balanced effect on negative feedback loop). This study tested how changes in the expression ratio of PKCγ and DGKγ may influence the magnitude of PKCγ translocation, as well as its residence time, in the membrane compartment. We selected three different ratios to test. The ratios were PKCγ:DGKγ 1:1, PKCγ:DGKγ 1:0.5, and PKCγ:DGKγ 1:0.3. In both models, the systems are perturbed by a brief pulse (S_1 = 7) which leads to rapid DAG generation in the membrane compartment. Our results show that reducing DGKγ expression in the mutant model increases the magnitude of PKCγ translocation as well as the membrane residence time (**Figure 8A**). It is possible that reducing DGKγ expression in the mutant model reduces the efficacy of negative feedback. Furthermore, our results indicate that reducing DGKγ expression in the wild-type models also reduces the efficacy of negative feedback. This results in increased translocation magnitude as well as increased membrane residence time of PKCγ (**Figure 8B**).

DISCUSSION

Recent evidence links mutations in the C_1 domain of PKCγ (Yabe et al., 2003; Shimobayashi, 2016) to cerebellar neurodegeneration in SCA14 disease. It is likely that a gain of function is the mechanism causing the observed neuronal degeneration that

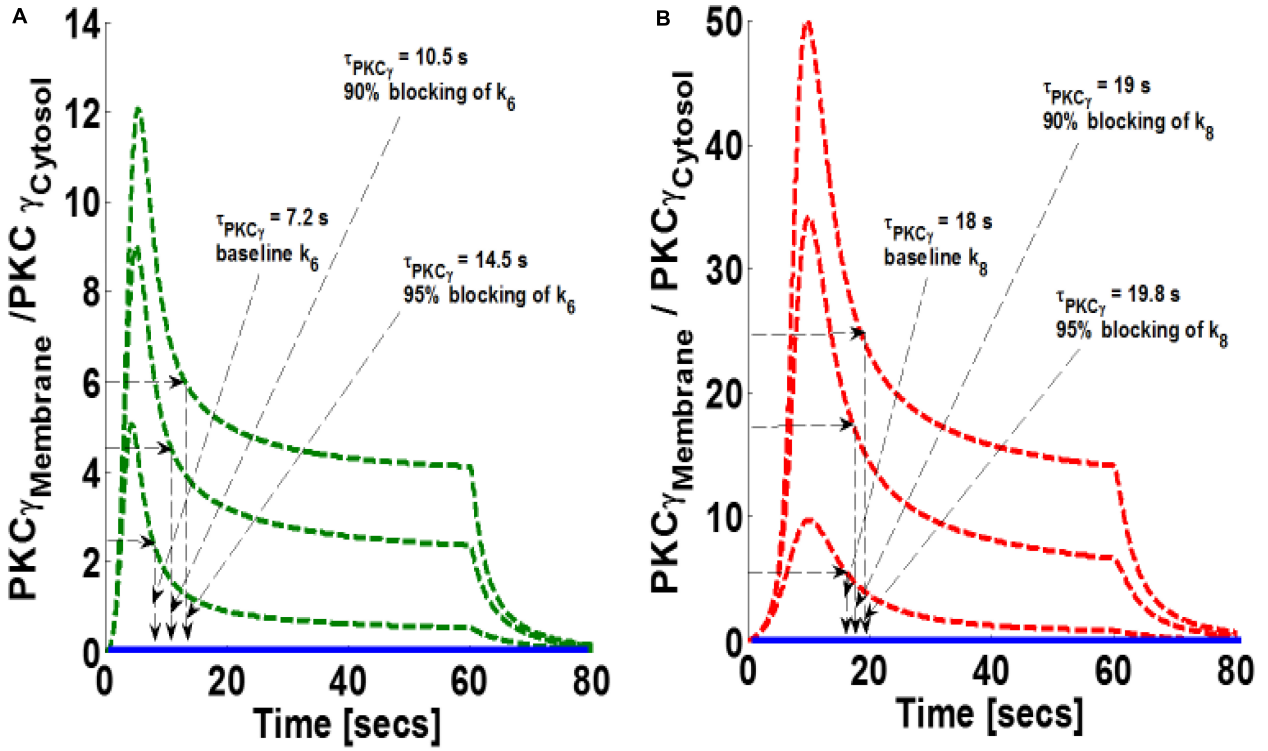

FIGURE 6 | The simulations mimicking the effect of blocking of forward rate constant of DAG phosphorylation by $DGK\gamma_P$ on the comparative translocation kinetics of PKCγ molecule in the mutant and wild-type models of PCs. Parameter k_6 represent this rate constant in mutant models, whereas in wild-types, it is represented by k_8. Here, the strength of stimulation is controlled by setting the pulse parameter "S_1" at 20. The duration of pulse is set for 1 min. Here, the solid line represents the non-stimulation and the dashed line represents the stimulation condition (green dashed line, mutant; red dashed line, wild-type PCs). **(A)** Translocation characteristics of PKCγ in the mutant model. Here, results show that blocking the parameter k_6 in the mutant model increases the membrane residence time of PKCγ (baseline, k_6, $\tau_{PKC\gamma\ mutant}$ = 7.2 s; 90% blocking of k_6 leads to $\tau_{PKC\gamma\ mutant}$ = 10.5 s; 95% blocking of k_6 leads to $\tau_{PKC\gamma\ mutant}$ = 14.5 s). **(B)** Translocation characteristics of PKCγ in the wild-type models. Here, results show that blocking the parameter k_8 in the wild-type model enhances the membrane residence time of PKCγ (baseline, k_8, $\tau_{PKC\gamma}$ = 18 s; 90% blocking leads to $\tau_{PKC\gamma}$ = 19 s; 95% blocking leads to $\tau_{PKC\gamma}$ = 19.8 s).

occurs during SCA14. It is likely because the PKCγ knock-out failed to exhibit cerebellar degeneration and only showed slight ataxia (Chen et al., 1995; Kano et al., 1995). This was probably due to the loss of the pruning process at the PF-PC synapses. Evidence also suggests that mutations in the C_1 domain could alter the activation and translocation profiles of PKCγ (Adachi et al., 2008; Shuvaev et al., 2011; Wong et al., 2018). It could be that these alterations in the enzymological properties of PKCγ and its regulator DGKγ are responsible for the dysregulation of Ca^{+2} homeostasis during SCA14 disease pathology. This disruption of Ca^{+2} equilibrium is probably due to altered gating characteristics of $TRPC_3$ channels. One possible cause of $TRPC_3$ gating dysregulation may be the inability of mutant molecules to completely phosphorylate $TRPC_3$ channels. In this case, the Ca^{+2} influx during disease-related PCs was only partially blocked. Consequently, the intracellular accumulation of Ca^{+2} in PCs is probably an underlying cause of observed neurodegeneration in SCA14 patients (Shuvaev et al., 2011). Thus, in order to understand the mechanisms of SCA14 disease, it is essential to study the associated changes in the enzymological properties of its key molecular players (Yamaguchi et al., 2006).

This study focuses on analyzing the enzymological properties of PKCγ and DGKγ in the context of SCA14 disease. Here, through a computational approach, we compare the signaling interactions of PKCγ and DGKγ in wild-type and mutant cells. Experimental evidence shows that despite the increase in activity, the membrane residence time of PKCγ is reduced in mutant models of PCs compared to wild-type models (Adachi et al., 2008; Shuvaev et al., 2011). Interestingly, another set of observations indicate that despite constitutive activity in cytosol, the activity of mutant PKCγ is reduced in the membrane compartment (Verbeek et al., 2008). In turn, this reduction in membrane residence duration or activity of PKCγ is believed to be linked to insufficient phosphorylation of $TRPC_3$. This causes a disruption in Ca^{+2} homeostasis (Adachi et al., 2008; Henning, 2011; Shuvaev et al., 2011). Here, we investigate the key question of why membrane residence time of PKCγ decreases in SCA14 disease. This study investigates this question by proposing and numerically evaluating two contrasting signaling models of depolarization-induced DAG generation and regulation in both wild-type and mutant PCs. The models compare the possible signaling cascades of DAG both in the SCA14 mutant and in wild-type PCs through simulations.

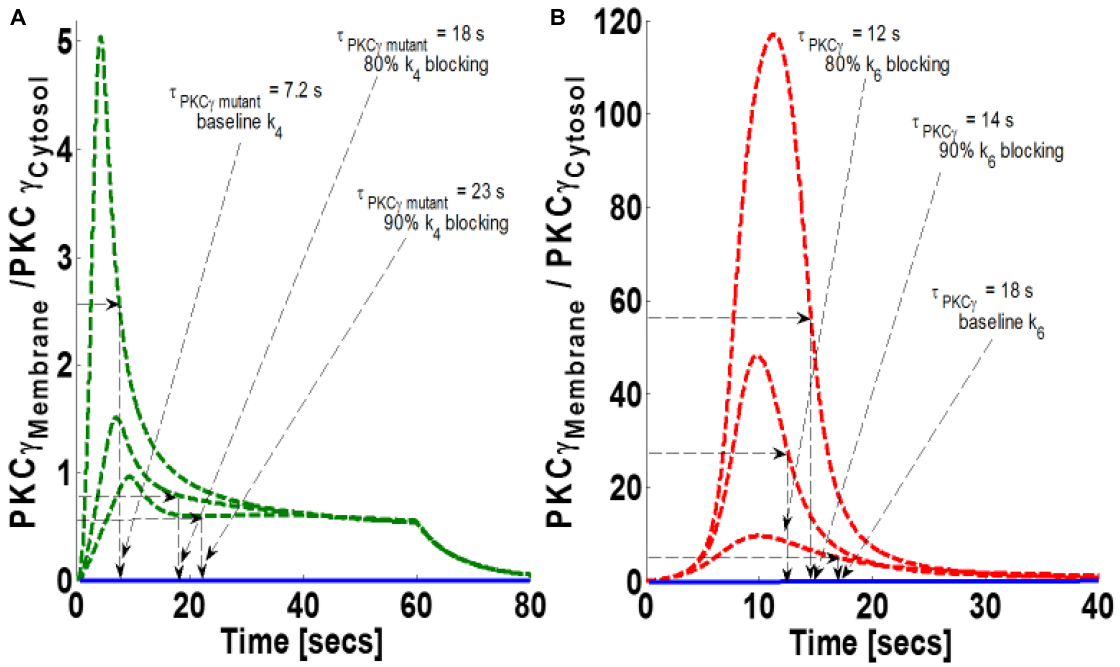

FIGURE 7 | The simulations mimicking the effect of blocking the rate constant of DGKγ phosphorylation to DGKγP on the comparative translocation kinetics of PKCγ molecule in the mutant and wild-type models of PCs. Parameter k_4 represents this rate constant in mutant models, whereas in wild-types, it is represented by k_6. Here, the strength of stimulation is controlled by setting the pulse parameter "S_1" at 20. The duration of pulse is set for 1 min; the solid line represents the non-stimulation and the dashed line represents the stimulation condition (green dashed line, mutant; red dashed line, wild-type PCs). **(A)** Translocation characteristics of PKCγ in the mutant model. Here, results show that blocking the parameter k_4 in the mutant model increases the membrane residence time of PKCγ (baseline, k_4, $\tau_{PKC_{\gamma\ mutant}}$ = 7.2 s; 80% blocking of k_4 leads to $\tau_{PKC_{\gamma\ mutant}}$ = 18 s; 90% blocking of k_4 leads to $\tau_{PKC_{\gamma\ mutant}}$ = 23 s). **(B)** Translocation characteristics of PKCγ in the wild-type models. Here, results show that blocking the parameter k_6 in the wild-type model reduces the membrane residence time of PKCγ (baseline, k_6, τ_{PKC_γ} = 18 s; 80% blocking leads to τ_{PKC_γ} = 12 s; 90% blocking leads to τ_{PKC_γ} = 14 s).

Precise modulation of $TRPC_3$ gating is essential for the viability of PCs and their characteristically dense dendritic tree (Shuvaev et al., 2011; Henning, 2011). Evidence also suggests that, in a single PC, the $TRPC_3$ channels are by far the most abundant molecule compared to the other members of the TRPC family (Henning, 2011). $TRPC_3$ proteins are mainly found in the PC soma and dendrites (Henning, 2011). These channels are regulated downstream of $mGluR_1$ pathways and play a key role in the maintenance of calcium homeostasis in cPCs (Henning, 2011). Furthermore, experimental evidence suggests that precise gating of the $TRPC_3$ channel is modulated by PKCγ in the membrane compartment (Henning, 2011; Shuvaev et al., 2011; Shimobayashi, 2016). Evidence also suggests that PKCγ may modulate phosphorylation and hence inactivation of the $TRPC_3$ channel. Thus, membrane residence duration of PKCγ may play a critical role in regulating channel gating mechanisms. The membrane residence time of PKCγ is regulated by DAG, and, as DAG is converted to PA by DGKγ, membrane-bound PKC returns to the cytosol (Shuvaev et al., 2011).

The simulations in this study focused on the key question of how reduced membrane residence time of mutant PKCγ is based on comparing mutant and wild-type models under the same conditions. The wild-type model within this study is based on stimulation-induced translocation and activation of PKCγ and DGKγ. The mutant model, however, is based on constitutively active PKCγ in the cytosol (Wong et al., 2018) and activation and phosphorylation of DGKγ even during basal conditions. In the mutant model, stimulation-induced translocation of both active molecules from the cytosol to the plasma membrane leads to quick and direct metabolism of DAG in the plasma membrane compartment. Here, all the parameters in both models are set at the same numerical values and both the models are perturbed with a similar strength pulse. The goal of this is to test what happens to the membrane residence duration within two different signaling topologies. If all the kinetics, translocation, and stimulation strength parameters are kept the same, how does τ_{PKC_γ} change in the wild-type and mutant models of cPCs? Here, τ_{PKC_γ} is the membrane residence time of PKCγ and is defined as average residence duration during which 50% of membrane PKCγ has re-translocated back to cytosol. Interestingly, the results show that τ_{PKC_γ} = 18 s for the wild-type model and τ_{PKC_γ} = 7.2 s for the mutant model. Indeed, these results elucidate that alteration of topological structure between two models could lead to differences in membrane residence time. The results here indicate that PKCγ residence time in the mutant model is approximately threefold shorter than in the wild-type. These results are consistent with previous experimental recordings in PCs from cerebellar slices (τ_{PKC_γ} = 19 s for wild-type cells and 6.0 s for mutant cells) (Shuvaev et al., 2011). These results support the hypothesis

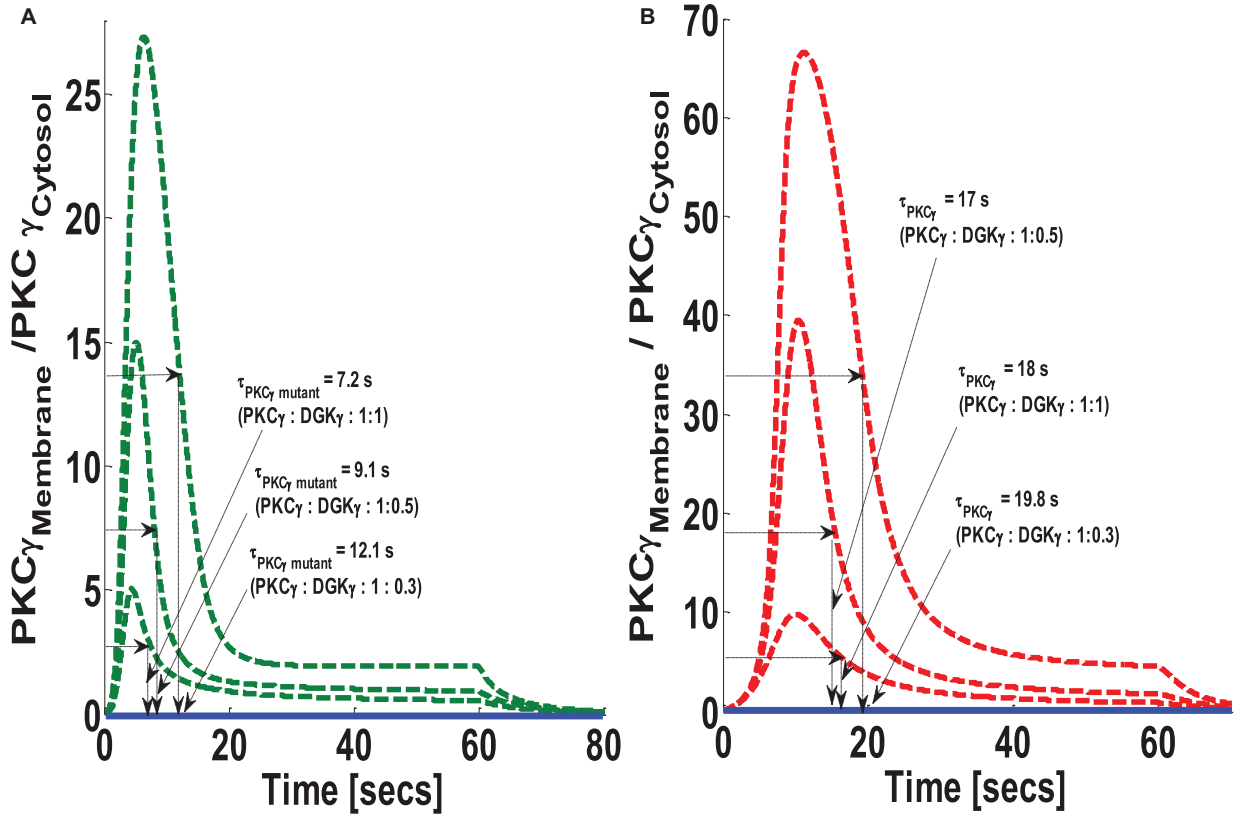

FIGURE 8 | The simulations mimicking the effect of PKCγ to DGKγ expression ratio on the comparative translocation kinetics of PKCγ molecule in the mutant and wild-type models of PCs. Three different levels of expression ratios are used (PKCγ:DGKγ: 1:1; PKCγ:DGKγ: 1:0.5; PKCγ:DGKγ: 1:0.3). Here, the strength of stimulation is controlled by setting the pulse parameter "S_1" at 20. The duration of pulse is set for 1 min; the solid line represents the non-stimulation and the dashed line represents the stimulation condition (green dashed line, mutant; red dashed line, wild-type PCs). **(A)** Translocation characteristics of PKCγ in the mutant model. Here, results indicate that reducing the PKCγ:DGKγ expression ratio increases the membrane residence time of mutant γ isoform (PKCγ:DGKγ: 1:1, $\tau_{PKC_\gamma\ mutant}$ = 7.2 s; PKCγ:DGKγ: 1:0.5, $\tau_{PKC_\gamma\ mutant}$ = 9.1 s; PKCγ:DGKγ: 1:0.3, $\tau_{PKC_\gamma\ mutant}$ = 12.1 s). **(B)** Translocation characteristics of PKCγ in the wild-type model. Here, results indicate that reducing the PKCγ:DGKγ expression ratio first decreases and then increases the membrane residence time of γ isoform (PKCγ:DGKγ: 1:1, τ_{PKC_γ} = 18 s; PKCγ:DGKγ: 1:0.5, $\tau_{PKC_\gamma\ mutant}$ = 17 s; PKCγ:DGKγ: 1:0.3, $\tau_{PKC_\gamma\ mutant}$ = 19.8 s).

that constitutively active PKCγ may have shorter membrane residence duration in a mutant model of cPCs, despite higher activity levels (Adachi et al., 2008; Shuvaev et al., 2011; Wong et al., 2018).

In this study, we explore the mechanisms that might control membrane residence time of PKCγ. Our results suggest that the formation of a local signalosome in the membrane compartment is key in regulating the membrane residence time of PKCγ (Yamaguchi et al., 2006). Furthermore, our results show that, in the case of the wild-type model, the local signalosome is formed in the membrane compartment. In the case of the mutant model, the signalosome is formed in the cytosol. It seems that in the wild-type model, the depolarization-induced stimulation leads to membrane translocation of inactive PKCγ and DGKγ. Once in the membrane compartment, these molecules organize themselves into a local signalosome, which, in turn, leads to DAG metabolism and eventual disassembly of this local signaling machine. It also leads to return of both DAG effector molecules to the cytosol. Our results suggest that, in the mutant model, the signalosome between PKCγ and DGKγ is formed in the cytosol. This occurs independent of DAG and even under basal conditions.

Our results propose that, in the case of the wild-type model, the molecular processes involved in the assembly, anchoring, and disassembly of the signalosome may provide enough time for PKCγ to tightly modulate the activation, inactivation, or recruitment of its key substrates, TRPC3 channels in PCs. In contrast, our simulations suggest that, in the mutant model, signalosome is not assembled at the membrane. Instead, the PKCγ and DGKγ molecular pair interact with each other in the cytosol under basal and DAG-independent conditions. Furthermore, the results reflect that reduced residence time of PKCγ in the mutant model could be due to the lack of signalosome assembly at the membrane. This is because depolarization-induced translocation of active DGKγ molecule from the cytosol to the membrane could lead to direct metabolism of DAG into PA, without undergoing the formation of a molecular complex at the membrane. Consequently, this results in faster DAG conversion to PA and quicker return of effector molecules

to the cytosol. These results support the idea that reduced membrane residence time of PKCγ is mainly linked to its constitutive activity in the cytosol (Wong et al., 2018), which, in turn, may result in differences in PKCγ and DGKγ interaction in the cytosol.

A critical assumption of this study is based on the possibility of a functional coupling between DAG effector molecules in PCs. This assumption could be disputed, as we do not have a direct evidence that such a coupling exists in PCs and is functional during the depolarization-induced translocation and activation events. We borrowed the idea of this functional interaction between DAG effector molecules from a previous experimental observation focusing on the PKCγ and DGKγ interactions in CHO cells and our previous modeling work of this system (Yamaguchi et al., 2006; Aslam and Alvi, 2019). We assumed that a similar signaling cascade could be functional in PCs. This similarity of CHO model cell and PCs could be disputed, as there may be differences in translocation dynamics of DGKγ in these cell systems. However, another set of direct observations in PCs indicate the quick degradation of DAG, cyctosol-to-membrane translocation kinetics of PKCγ, remigration dynamics of PKCγ to cytosol after purinergic receptor activation, and membrane residence duration in both mutant and wild-type models (Shuvaev et al., 2011). Based on these observations, we argue that during membrane depolarization-induced events in PCs, a coupling between DAG effector molecules could be present and functional. In the absence of a net negative feedback effect generated through PKCγ and DGKγ interactions, DAG might persist at membrane, leading to the prolonged membrane residence duration of PKCγ, which at least is not the case, as observed in some previous studies (Adachi et al., 2008; Shuvaev et al., 2011; Wong et al., 2018). In fact, the mutant PKCγ molecule is linked to shorter membrane residence duration (Adachi et al., 2008; Shuvaev et al., 2011). Additional observations in the SCA14 mutant model (Wong et al., 2018) suggest the mislocalization of PKCγ in cytosol with hyperactivity and the possibility of phosphorylating/activating its substrates in the cytosol.

Besides exploring depolarization-induced translocation characteristics of PKCγ and DGKγ molecules in mutant and wild-type models of PCs, we have also studied the influence of stimulation strength (amplitude of pulse mimicking depolarization event) on the translocation characteristics and membrane residence time of PKCγ (**Figures 4A,B**). Our results indicate that, in mutant models, the maximum M/C ratio of PKCγ increases fourfold with a threefold increase in stimulation strength. In contrast, the increase is 10-fold for the same increase in stimulation strength for models representing wild-type PCs. Interestingly, the membrane residence time of PKCγ in the mutant model first decreases and then increases with increasing stimulation strength. The corresponding residence and translocation characteristics of DGKγ shows decreases in membrane residence but increases in the maximum M/C ratio for this molecule with increasing stimulation strength (**Supplementary Figure S1**).

Furthermore, our results show that a 25- to 100-fold increase in the DAG metabolism rate leads to a 1-s reduction in membrane residence duration for the mutant and a 2-s reduction for the wild-type model. The maximum M/C ratio is reduced 10% in the mutant and 40% in the wild-type model (**Figure 5**). This occurs because enhancing DAG metabolism results in decreased membrane translocation and faster remigration to the cytosol. Interestingly, blocking second messenger metabolism has an opposite effect on membrane residence duration, as well as the translocation characteristics of PKCγ (**Figure 6**). This occurs because blocking metabolism will result in DAG accumulation at the membrane compartment, thus enhancing the membrane residence duration, as well as the M/C ratio of PKCγ. Interestingly, our results show that the effects of metabolism blocking are much more pronounced on membrane residence duration in mutant PKCγ (95% blocking of DAG metabolism results in a twofold increase in residence time) compared to the wild-type model (95% blocking results only in a 10% increase in residence time) (**Figure 6**). However, in the case of a maximum M/C ratio, 95% blocking of second messenger metabolism in the wild-type model results in a 5-fold increase. This increase is only 2-fold in the mutant model (**Figure 6**). The corresponding residence and translocation characteristics of DGKγ shows increase in the maximum M/C ratio for this molecule in the wild-type model with increase in blocking of DAG metabolism rate (**Supplementary Figure S2**).

Our results also indicate a role for DGKγ expression on the membrane residence duration and translocation characteristics of PKCγ (**Figure 8**). Recent experimental results that use the GFP-tagged PKCγ in CHKO cells indicate that the membrane residence of PKCγ could be modulated by negative feedback effects of DGKγ on the activity of PKCγ through regulating DAG metabolism (Yamaguchi et al., 2006). However, these results are based on a wild-type system. It is not understood how this negative feedback loop is affected in mutant systems when PKCγ is constitutively active. In addition, how might this influence the membrane residence time, as well as the M/C ratio of mutant PKCγ? These models assume equally proportional DGKγ expression is necessary for its negative influence on PKCγ activity. The results indicate that any changes in expression ratios of PKCγ and DGKγ will have a strong influence on the membrane residence time and M/C ratio of PKCγ and DGKγ (**Figure 8** and **Supplementary Figure S3**). These results are consistent with previous observations (Yamaguchi et al., 2006) showing a fourfold increase in membrane residence time of PKCγ. However, the key difference between the kinetics reported in previous experimental findings and the results reported here is that the current results are based on depolarization-induced stimulation in PCs (Shuvaev et al., 2011) and experimental observations mentioned above are based on ATP-induced stimulation in CHO cells (Yamaguchi et al., 2006).

In our models, we did not attempt to simulate cytosol-to-membrane translocation and re-translocation back to the cytosol in a detailed manner (Imai et al., 2002, 2004; Luo et al., 2003a,b). This study only represented the whole complex process by introducing two first-order functions of DAG concentration. These functions describe the cytosol-to-membrane migration rates of PKCγ and DGKγ as a linear function of DAG

concentration (**Supplementary Material S1: Table S1** and **Supplementary Material S3: Table S2**). The slope of the PKCγ function is higher compared to DGKγ and adjusted to account for differential sensitivity of these molecules to DAG and calcium concentrations (Yamaguchi et al., 2006). We are not aware if there is any model proposed to describe the PKCγ and DGKγ translocation in PCs. Clearly, a complete model should account for events like DAG and IP_3 generation, DAG binding, DAG-induced activation of TRPC3, and Ca^{+2} influx due to TRPC3 opening. In addition, there is IP_3 diffusion into cytosol, Ca^{+2} diffusion from membrane to cytosol, Ca^{+2} release from intracellular stores, binding of Ca^{+2} with dormant PKCγ, and translocation of PKCγ and DGKγ from the cytosol to the membrane (Nishizuka, 1988, 1992, 1995; Newton, 2001, 2003; Oancea and Meyer, 1998). In addition, diffusion in the membrane occurs. However, this is beyond the scope of this study. Similarly, the models presented in this study assume that the complex process of DAG generation in response to depolarization-induced activation of the mGluR1 pathway can be simply represented by a brief pulse with certain duration and amplitude. This study has not modeled the complex processes involved in the generation of DAG and IP_3 after the activation of the G-protein-coupled phospholipase. Rather, we have used a simplistic approach to describe these complex processes.

Some of the assumptions we made to construct these models may be disputed. This study was not able to find data points linking the effect of PKCγ mutations to the extent of its activity. Do these mutations lead to maximal activation or only partial activation of PKCγ in the cytosol? Here, we assume that mutations in PKCγ lead to maximum basal activation, which, in turn, leads to the maximum phosphorylation and activation of DGKγ in the cytosol, even during resting conditions. According to our mutant model, depolarization-induced local generation of DAG in the membrane compartment stimulates the translocation of its already-active effector molecules from the cytosol to the membrane. Active and phosphorylated DGKγ is in the membrane compartment and stimulates the DAG metabolism. This assumption may be disputed, and additional data should be generated to evaluate the DAG-binding capacity of constitutively active mutant molecule. Here, this study assumes that DAG metabolism in the mutant model is fast, and as soon DAG levels drop, both molecules relocate back to the cytosol.

Based on our wild-type and mutant models, it appears that activation and phosphorylation of DGKγ could critically influence the magnitude of translocation as well as the membrane residence duration of PKCγ in both these models (**Figure 7**). The blocking of DGKγ activation in the mutant model clearly shows that the magnitude of translocation and the membrane residence time of PKCγ are increased (**Figure 7A**). However, the same blocking in the wild-type model shows that though the translocation intensity increases, membrane residence time decreases with increase in blocking levels (**Figure 7B**). This is rather counterintuitive, as one would expect the increase in membrane residence duration with blocking of DGKγ activation in wild-type models too. Interestingly, as the parameter k_6 was further blocked, we noticed that 99 and 99.95% blocking resulted in an increase not only in the magnitude of translocation but also in membrane residence duration (**Supplementary Figure S4**). Thus, these results indicate that reducing the activation of DGKγ reduces the efficacy of negative feedback loop.

CONCLUSION

Through a computational approach, we show that enhanced PKCγ activity is linked to reduced membrane residence duration in the SCA14 mutant model. This work provides the very first simple mechanistic understanding and comparison of PKCγ temporal dynamics in wild-type and mutant models. We propose that SCA14 mutation causes the shift of PKCγ signaling from membrane compartment to cytosol, thus resulting in reduced membrane lifetime. The mechanistic nature of this work provides possibilities to increase the membrane residence duration of PKCγ through specific interventions, exquisitely targeting biochemical interactions such as blocking the DAG metabolism rate. An integrated model describing the calcium homeostasis in PCs involving DAG effector molecules and TRPC3 channels is under development and could further enhance the insights of DAG signaling in PCs.

DISCLOSURE

The corresponding author is part of a non-profit, i.e., BioSystOimcs, focusing on the basic R&D in drug target identification and development with no commercial plans and interests.

DATA AVAILABILITY STATEMENT

The datasets generated for this study are available on request to the corresponding author.

AUTHOR CONTRIBUTIONS

NA came up with the idea, carried out modeling and wrote the manuscript. FA reviewed data and helped in polishing ideas.

ACKNOWLEDGMENTS

Special thanks to Mrs. Bushria Aslam for support and inspiration.

SUPPLEMENTARY MATERIALS

The Supplementary Material for this article can be found online at: https://www.frontiersin.org/articles/10.3389/fnins.2019.01397/full#supplementary-material

REFERENCES

Adachi, N., Kobayashi, T., Takahashi, H., Kawasaki, T., Shirai, Y., Ueyama, T., et al. (2008). Enzymological analysis of mutant protein kinase Cγ causing spinocerebellar ataxia type 14 and dysfunction in Ca2+ homeostasis. *J. Biol. Chem.* 283, 19854–19863. doi: 10.1074/jbc.m801492200

Aslam, N., and Alvi, F. (2017). How the cytosol-to-membrane translocation kinetics and signaling of PKCγ are dysregulated in the neurodegenerative spinocerebellar ataxia type14 (SCA14). *FASEB J.* 31:183.

Aslam, N., and Alvi, F. (2019). How the PKCγ activity is regulated in the neurodegenerative spinocerebellar ataxia type 14 (SCA14)? *FASEB J.* 30:1179.

Brkanac, Z., Bylenok, L., Fernandez, M., Matsushita, M., Lipe, H., Wolff, J., et al. (2002). A new dominant spinocerebellar ataxia linked to chromosome 19q13.4-*qter*. *Arch. Neurol.* 59, 1291–1295.

Carlson, K. M., Andresen, J., and Orr, H. T. (2009). Emerging pathogenic pathways in the spinocerebellar ataxias. *Curr. Opin. Genet. Dev.* 19, 247–253. doi: 10.1016/j.gde.2009.02.009

Chen, C., Kano, M., Abeliovich, A., Chen, L., Bao, S., Kim, J. J., et al. (1995). Impaired motor coordination correlates with persistent multiple climbing fiber innervation in PKC gamma mutant mice. *Cell* 29, 1233–1242. doi: 10.1016/0092-8674(95)90148-5

Duenas, A. M., Goold, R., and Giunti, P. (2006). Molecular pathogenesis of spinocerebellar ataxias. *Brain* 129, 1357–1370. doi: 10.1093/brain/awl081

Goto, K., and Kondo, H. (1999). Diacylglycerol kinase in the central nervous system molecular heterogeneity and gene expression. *Chem. Phys. Lipids* 98, 109–117. doi: 10.1016/s0009-3084(99)00023-7

Guzman, S. J., and Gerevich, Z. (2016). P2Y receptors in synaptic transmission and plasticity: therapeutic potential in cognitive dysfunction. *Neural Plast.* 2016:1207393. doi: 10.1155/2016/1207393

Henning, H. A. (2011). *Synaptic Signaling by mGluR1 and TRPC3 in Spiny Dendrites of Cerebellar Purkinje Cells*. Ph.D. Dissertation, Technische Universitat Munchen, Munchen.

Imai, S., Kai, M., Yamada, K., Kanoh, H., and Sakane, F. (2004). The plasma membrane translocation of diacylglycerol kinase δ1 is negatively regulated by conventional protein kinase C-dependent phosphorylation at Ser-22 and Ser-26 within the pleckstrin homology domain. *Biochem. J.* 382, 957–966. doi: 10.1042/bj20040681

Imai, S., Sakane, F., and Kanoh, H. (2002). Phorbol ester-regulated oligomerization of diacylglycerol kinase δ linked to its phosphorylation and translocation. *J. Biol Chem.* 278, 39542–39547.

Kano, M., Hashimoto, K., Chen, C., Abeliovich, A., Aiba, A., Kurihara, H., et al. (1995). Impaired synapse elimination during cerebellar development in PKC gamma mutant mice. *Cell* 83, 1223–1231. doi: 10.1016/0092-8674(95)90147-7

Luo, B., Prescott, S. M., and Topham, M. K. (2003a). Association of diacylglycerol kinase ζ with protein kinase C α spatial regulation of diacylglycerol signaling. *J. Cell Biol.* 160, 929–937.

Luo, B., Prescott, S. M., and Topham, M. K. (2003b). Protein Kinase Cα Phosphorylates and Negatively Regulates Diacylglycerol Kinase ζ. *J. Biol. Chem.* 278, 39542–39547. doi: 10.1074/jbc.m307153200

Mérida, I., Avila-Flores, A., and Merino, E. (2008). Diacylglycerol kinases: at the hub of cell signaling. *Biochem. J.* 409, 1–18. doi: 10.1042/bj20071040

Metzger, F., and Kapfhammer, J. P. (2000). Protein kinase C activity modulates dendritic differentiation of rat Purkinje cells in cerebellar slice cultures. *Eur. J. Neurosci* 12, 1993–2005. doi: 10.1046/j.1460-9568.2000.00086.x

Newton, A. C. (2001). Protein kinase C: structural and spatial regulation by phosphorylation, cofactors, and macromolecular interactions. *Chem. Rev.* 101, 2353–2364. doi: 10.1021/cr0002801

Newton, A. C. (2003). Regulation of the ABC kinases by phosphorylation: protein kinase C as a paradigm. *Biochem. J.* 370, 361–371. doi: 10.1042/bj20021626

Nishizuka, Y. (1988). The molecular heterogeneity of protein kinase C and its implications for cellular regulation. *Nature* 334, 661–665. doi: 10.1038/334661a0

Nishizuka, Y. (1992). Intracellular signaling by hydrolysis of phospholipids and activation of protein kinase C. *Science* 258, 607–614. doi: 10.1126/science.1411571

Nishizuka, Y. (1995). Protein kinase C and lipid signaling for sustained cellular responses. *FASEB J.* 9, 484–496. doi: 10.1096/fasebj.9.7.7737456

Oancea, E., and Meyer, T. (1998). Protein kinase C as a molecular machine for decoding calcium and diacylglycerol signals. *Cell* 95, 307–318. doi: 10.1016/s0092-8674(00)81763-8

Paulson, H. L. (2009). The spinocerebellar ataxias. *J. Neuroophthalmol.* 29, 227–237. doi: 10.1097/WNO0b013e3181b416de

Saito, N., Kikkawa, U., Nishizuka, Y., and Tanaka, C. (1988). Distribution of protein kinase C like immunoreactive neurons in rat brain. *J. Neurosci.* 8, 369–382. doi: 10.1523/jneurosci.08-02-00369.1988

Saito, N., and Shirai, Y. (2002). Protein kinase Cγ (PKCγ): function of neuron specific isotype. *J. Biochem.* 132, 683–687. doi: 10.1093/oxfordjournals.jbchem.a003274

Schrenk, K., Kapfhammer, J. P., and Metzger, F. (2002). Altered dendritic development of cerebellar Purkinje cells in slice cultures from protein kinase Cgamma-deficient mice. *Neuroscience* 110, 675–689. doi: 10.1016/s0306-4522(01)00559-0

Shimobayashi, E. (2016). *Mechanisms of PKC Gamma-Mediated Inhibition of Dendritic Growth in Cerebellar Purkinje Cells*. Ph.D. Dissertation, Universität Basel, Basel.

Shuvaev, A. N., Horiuchi, H., Seki, T., Goenawan, H., Irie, T. I., Iizuka, A., et al. (2011). Mutant PKCγ in spinocerebellar ataxia type 14 disrupts synapse elimination and long-term depression in purkinje cells *In Vivo*. *J. Neurosci.* 30, 14324–14334. doi: 10.1523/jneurosci.5530-10.2011

Soong, B. W., and Paulson, H. L. (2007). Spinocerebellar ataxias: an update. *Curr. Opin. Neurol.* 20, 438–446. doi: 10.1097/wco.0b013e3281fbd3dd

Verbeek, D. S., Goedhart, J., Bruinsma, L., Sinke, R. J., and Reits, E. A. (2008). PKC gamma mutations in spinocerebellar ataxia type 14 affect C1 domain accessibility and kinase activity leading to aberrant MAPK signaling. *J. Cell Sci.* 121(Pt 14), 2339–2349. doi: 10.1242/jcs.027698

Verbeek, D. S., Knight, M. A., Harmison, G. G., Fischbeck, K. H., and Howell, B. W. (2005). Protein kinase C gamma mutations in spinocerebellar ataxia 14 increase kinase activity and alter membrane targeting. *Brain* 128, 436–442. doi: 10.1093/brain/awh378

Weisman, G. A., Camden, J. M., Peterson, T. S., Ajit, D. V., Woods, L. T., and Erb, L. (2012). Receptors for extracellular nucleotides in the central nervous system: role of P2X7 and P2Y2 receptor interactions in neuroinflammation. *Mol. Neurobiol.* 46, 96–113. doi: 10.1007/s12035-012-8263-z

Wong, M. M. K., Hoekstra, S. D., Vowles, J., Waston, L. M., Fuller, G., Nemeth, A. H., et al. (2018). Neurodegeneration in SCA14 is associated with increased PKCγ kinase activity, mislocalization and aggregation. *Acta Neuropathol. Commun.* 6:99.

Yabe, I., Sasaki, H., Chen, D. H., Raskind, W. H., Bird, T. D., Yamashita, I., et al. (2003). Spinocerebellar ataxia type 14 caused by a mutation in protein kinase C gamma. *Arch. Neurol.* 60, 1749–1751.

Yamaguchi, Y., Shirai, Y., Matsubara, T., Sanse, K., Kuriyama, M., Oshiro, N., et al. (2006). Phosphorylation and Up-regulation of diacylglycerol kinase γ via its interaction with protein kinase Cγ. *J. Biol. Chem.* 281, 31627–31637. doi: 10.1074/jbc.m606992200

Yamashita, I., Sasaki, H., Yabe, I., Fukazawa, T., Nogoshi, S., Komeichi, K., et al. (2000). A novel locus for dominant cerebellar ataxia (SCA14) maps to a 10.2-cM interval flanked by D19S206 and D19S605 on chromosome 19q13.4- qter. *Ann. Neurol.* 48, 156–163. doi: 10.1002/1531-8249(200008)48:2<156::aid-ana4>3.0.co;2-9

Conflict of Interest: The authors declare that the research was conducted in the absence of any commercial or financial relationships that could be construed as a potential conflict of interest.

Copyright © 2020 Aslam and Alvi. This is an open-access article distributed under the terms of the Creative Commons Attribution License (CC BY). The use, distribution or reproduction in other forums is permitted, provided the original author(s) and the copyright owner(s) are credited and that the original publication in this journal is cited, in accordance with accepted academic practice. No use, distribution or reproduction is permitted which does not comply with these terms.

frontiers in Bioengineering and Biotechnology

ORIGINAL RESEARCH
published: 25 February 2020
doi: 10.3389/fbioe.2020.00141

Conducting a Virtual Clinical Trial in HER2-Negative Breast Cancer Using a Quantitative Systems Pharmacology Model With an Epigenetic Modulator and Immune Checkpoint Inhibitors

Hanwen Wang[1], Richard J. Sové[1], Mohammad Jafarnejad[1], Sondra Rahmeh[1], Elizabeth M. Jaffee[2,3], Vered Stearns[2], Evanthia T. Roussos Torres[2†], Roisin M. Connolly[2,3†] and Aleksander S. Popel[1,2]*

[1] Department of Biomedical Engineering, Johns Hopkins University School of Medicine, Baltimore, MD, United States, [2] Department of Oncology, The Sidney Kimmel Cancer Center, Johns Hopkins University School of Medicine, Baltimore, MD, United States, [3] Viragh Center for Pancreatic Clinical Research and Care, Bloomberg Kimmel Institute for Immunotherapy, Johns Hopkins University School of Medicine, Baltimore, MD, United States

The survival rate of patients with breast cancer has been improved by immune checkpoint blockade therapies, and the efficacy of their combinations with epigenetic modulators has shown promising results in preclinical studies. In this prospective study, we propose an ordinary differential equation (ODE)-based quantitative systems pharmacology (QSP) model to conduct an *in silico* virtual clinical trial and analyze potential predictive biomarkers to improve the anti-tumor response in HER2-negative breast cancer. The model is comprised of four compartments: central, peripheral, tumor, and tumor-draining lymph node, and describes immune activation, suppression, T cell trafficking, and pharmacokinetics and pharmacodynamics (PK/PD) of the therapeutic agents. We implement theoretical mechanisms of action for checkpoint inhibitors and the epigenetic modulator based on preclinical studies to investigate their effects on anti-tumor response. According to model-based simulations, we confirm the synergistic effect of the epigenetic modulator and that pre-treatment tumor mutational burden, tumor-infiltrating effector T cell (Teff) density, and Teff to regulatory T cell (Treg) ratio are significantly higher in responders, which can be potential biomarkers to be considered in clinical trials. Overall, we present a readily reproducible modular model to conduct *in silico* virtual clinical trials on patient cohorts of interest, which is a step toward personalized medicine in cancer immunotherapy.

Keywords: immuno-oncology, immune checkpoint inhibitor, computational model, systems biology, epigenetic modulator, quantitative systems pharmacology, virtual clinical trial

OPEN ACCESS

Edited by:
Babatunde Ogunnaike, University of Delaware, United States

Reviewed by:
Mohit Kumar Jolly, Indian Institute of Science (IISc), India
Shankar Suman, The Ohio State University, United States

****Correspondence:***
Hanwen Wang
hwang163@jhmi.edu

†Present address:
Evanthia T. Roussos Torres, Division of Hematology/Oncology, Department of Medicine, Norris Comprehensive Cancer Center, University of Southern California, Los Angeles, CA, United States
Roisin M. Connolly, College of Medicine and Health, Cork University Hospital, University College Cork, Cork, Ireland

Specialty section:
This article was submitted to Bioinformatics and Computational Biology, a section of the journal Frontiers in Bioengineering and Biotechnology

Received: *05 December 2019*
Accepted: *11 February 2020*
Published: *25 February 2020*

Citation:
Wang H, Sové RJ, Jafarnejad M, Rahmeh S, Jaffee EM, Stearns V, Torres ETR, Connolly RM and Popel AS (2020) Conducting a Virtual Clinical Trial in HER2-Negative Breast Cancer Using a Quantitative Systems Pharmacology Model With an Epigenetic Modulator and Immune Checkpoint Inhibitors. Front. Bioeng. Biotechnol. 8:141. doi: 10.3389/fbioe.2020.00141

INTRODUCTION

Although in clinical trials immunotherapies using anti-PD-1 and anti-PD-L1 antibodies and their combinations with other types of therapies have improved the overall response rate and progression-free survival rate in patients with breast cancer, more than half of patients developed progressive disease (Emens, 2018). To improve the efficacy of checkpoint inhibitors, multiple strategies are being developed to facilitate antigen release, T cell activation and homing, and improve tumor microenvironment, such as cancer vaccines and anti-OX40 antibody therapy (Hu-Lieskovan and Ribas, 2017). In March 2019, the Food and Drug Administration (FDA) granted an accelerated approval for the immunotherapy anti-PD-L1 drug, atezolizumab, in combination with chemotherapy drug, nanoparticle albumin–bound paclitaxel (nab-paclitaxel), for the initial treatment of some women with advanced triple-negative breast cancer (TNBC). Among the ongoing clinical trials in breast cancer, a phase I trial using a triple combination of anti-CTLA-4 and anti-PD-1 antibodies, and a small-molecule epigenetic modulator, entinostat, tests safety, efficacy and impact on the ratio of tumor-specific effector T cell (Teff) to regulatory T cell (Treg) (NCT02453620).

Entinostat, also called MS-275, was originally developed as an antitumor agent, which inhibits histone deacetylases (HDAC) and induces a shift of cell cycle from S phase to G_1 phase (Saito et al., 1999). There is emerging evidence that it can alter the immune-suppressive microenvironment in the tumor (Connolly et al., 2017; Christmas et al., 2018). Preclinical studies also suggest that the alteration of the tumor microenvironment can improve the efficacy of checkpoint blockade therapy (Kato et al., 2014; Pili et al., 2017). In an *in vivo* experiment by Kim et al., the addition of entinostat significantly reduced tumor volume in 4T1 and CT26 mouse models under anti-PD-1 and anti-CTLA-4 antibody treatment (Kim et al., 2014). In a recent study, combining entinostat with anti-PD-1, anti-CTLA-4, or both significantly improved tumor-free survival in the HER-2/neu transgenic breast cancer mouse model (Christmas et al., 2018).

The success of entinostat treatment in preclinical studies has also drawn the attention to myeloid-derived suppressor cells (MDSCs) in the breast tumor microenvironment. In breast cancer patients, MDSC level is correlated to cancer stages and metastasis (Gonda et al., 2017). As a major contributor of the immune suppression in peripheral lymphoid tissues, the inhibitory effect of MDSCs is also found to be augmented in the tumor microenvironment, such as Treg expansion and inhibition of Teff functions (Kumar et al., 2016). Although a number of mechanisms are considered to be the potential causes of their inhibitory effects, recent studies suggest that Arginase I (Arg-I) and nitric oxide (NO) are the major immune-suppressive molecules secreted by MDSCs (Alotaibi et al., 2018; Park et al., 2018; Sheikhpour et al., 2018). Due to their significant inhibition of adaptive immune response in the tumor microenvironment, MDSCs have been suggested as a target for breast cancer treatment (Markowitz et al., 2013).

Besides the significant reduction of tumor volume, entinostat is also suggested to alter MDSC levels both in blood and in the tumor microenvironment; to change the proportions of T cell subsets; and to increase tumor sensitivity to CTL-mediated lysis (Kim et al., 2014; Gameiro et al., 2016; Orillion et al., 2017; Christmas et al., 2018). Experiments detected a significant reduction of tumor-infiltrating $FoxP3^+$ Treg and granulocytic MDSC (G-MDSCs) (vs. monocytic MDSC, M-MDSC) in mice receiving entinostat treatment (Kim et al., 2014; Christmas et al., 2018). A separate preclinical study also observed the enhanced antitumor immune response with significantly decreased $FoxP3^+$ expression in circulating Tregs and increased tumor-infiltrating G-MDSCs in syngeneic mouse cancer models under entinostat and anti-PD-1 antibody treatment (Orillion et al., 2017). Although preclinical studies have provided somewhat controversial conclusions on how entinostat alters the composition of T cell subsets and MDSCs in the tumor microenvironment, they all suggest that entinostat reverses the inhibitory effects of MDSCs (Kim et al., 2014; Orillion et al., 2017; Christmas et al., 2018).

Due to the promising efficacy of entinostat treatment in preclinical studies, the effects of entinostat were investigated with exemestane/placebo in locally advanced or metastatic hormone receptor-positive breast cancer (Yardley et al., 2013; Tomita et al., 2016; Yeruva et al., 2018). In a phase II trial, both progression-free survival and overall survival rates were significantly higher in the entinostat-treated cohort. These results have led to a phase III trial (E2112, NCT02115282) that aims to validate the preclinical and clinical evidence supporting the role of HDAC inhibitors in improving outcomes for patients with advanced breast cancer (Yeruva et al., 2018). In addition, the synergistic effect of entinostat in combination therapy with anti-PD-1 antibody, nivolumab, has been reported in melanoma patients. Patients who had stable or progressive disease in previous checkpoint blockade therapy were converted to responders with entinostat treatment (Agarwala et al., 2018).

Since the characteristics of patients who are likely to benefit from epigenetic modulation are still unknown, we propose an expanded quantitative systems pharmacology (QSP) model based on our previous steps (Jafarnejad et al., 2019; Milberg et al., 2019; Wang et al., 2019). It is built with a detailed MDSC module and pharmacokinetics and pharmacodynamics of entinostat, to investigate the effect of entinostat and its combination with nivolumab and ipilimumab by conducting an *in silico* virtual clinical trial. Virtual clinical trials aim to generate virtual patient cohorts with physiologically plausible parameters and predict efficacies of treatments of interest using *in silico* simulations with a QSP model (Allen et al., 2016; Cheng et al., 2017; Rieger et al., 2018). Due to the heterogeneity of patient cohorts enrolled in clinical trials and wide range of treatment strategies, *in silico* simulations using a virtual patient cohort that resembles the desired clinical population can provide insights into the potential therapeutic outcome even before the therapy begins. In this study, we will conduct an *in silico* virtual clinical trial to explore the effects of different factors and patients' characteristics prospectively, ahead of the results of the ongoing clinical trial (NCT02453620).

MATERIALS AND METHODS

Model Overview

The proposed QSP model has a general structure similar to the model introduced in our previous studies (Jafarnejad et al., 2019; Wang et al., 2019). It comprises four compartments: central, peripheral, tumor, and tumor-draining lymph node (TDLN). The central and the peripheral compartments represent the total volume of blood and peripheral tissues, respectively. The TDLN compartment represents a lumped lymph node assuming that the antibody and T cell activation is evenly distributed among a number of TDLNs. The tumor compartment represents the total tumor volume, which is calculated at each time step as the addition of the total volume of proliferating and dead cancer cells, T cells, and other cells and tumor interstitium. Tumor diameter is calculated using total tumor volume assuming a spherical tumor, which is an estimate of mean lesion size for each virtual patient.

The model comprises multiple modules, each of which describes the dynamics of one of the major species (i.e., effector T cells, regulatory T cells, MDSCs, cancer cells, antigen-presenting cells (APCs), antigens, checkpoint ligands and receptors, and therapeutic agents); each module is built separately using MATLAB (MathWorks, Natick, MA, United States) scripts. The modular structure of this model greatly facilitates modifications and expansions for future applications. The model used in this study comprises eight modules, 210 parameters, 120 ordinary differential equations (ODEs) and 39 algebraic equations, which are implemented using the SimBiology toolbox in MATLAB. The dynamics of the major species in the model are illustrated in **Figure 1**. Full lists of model parameters, reactions, algebraic equations, and cellular and molecular species are included in the **Supplementary Tables S1–S6**.

Pharmacokinetics and Pharmacodynamics (PK/PD) of Entinostat

Since there is no published population-based pharmacokinetic model for entinostat, we propose a model structure for this oral-administered drug based on four published clinical PK studies of entinostat, and the PK parameters are optimized using data reported in these studies (Ryan et al., 2005; Gojo et al., 2007; Kummar et al., 2007; Gore et al., 2008). Parameter optimization is performed using pattern search in the MATLAB Global Optimization Toolbox. Multi-compartment PK model structures are tested using similar methods from Gasthuys et al. (2018) and the final diagram of our proposed PK model structure is demonstrated in **Figure 2A**. As shown in the figure, a portion of the dose is immediately absorbed by the patients via zero-order buccal absorption over a time duration D_0 into the buccal compartment, and the rest of the dose is absorbed after a time period T_{lag} via first-order gastrointestinal absorption into the gastrointestinal compartment. The drug in buccal and gastrointestinal compartments are then absorbed into the central compartment via first-order absorption and diffuse into the peripheral and the tumor compartments. For pharmacodynamics of entinostat, it is known to induce cell cycle arrest in cancer cells, reduce their viability, and significantly reduce the level of immune-suppressive cytokines in the tumor (Lee et al., 2001; Bouchain et al., 2003; Choo et al., 2010, 2013; Ryu et al., 2019). In the current module, we assume that the major mechanisms of action for entinostat are inhibitions of cancer cell proliferation and production of monocyte chemoattractant protein-1 (MCP-1/CCL2) and nitric oxide, by which entinostat has shown to reverse the immune-suppressive effects of MDSCs (Kim et al., 2014; Orillion et al., 2017; Christmas et al., 2018). The PD parameters of entinostat are listed in **Supplementary Table S7**, and its anti-proliferative effect on breast cancer cells is shown in **Supplementary Figure S1**. Since the effect of entinostat on MDSC level and T cell subsets are still under investigation, it is assumed not to have direct impact on any species other than cancer cells in the model (Kim et al., 2014; Orillion et al., 2017; Christmas et al., 2018). In addition, the PK/PD of checkpoint blockade antibodies are implemented using the same equations as in our previous model based on published clinical data (Feng et al., 2014; Bajaj et al., 2017; Wang et al., 2019).

MDSC Module

In addition to the mechanisms from our previous model (Jafarnejad et al., 2019), a new MDSC module is implemented to describe the immune-suppressive mechanisms of MDSC including Treg expansion and inhibition of effector T cell function. MDSCs are recruited into the tumor compartment by CCL2 secreted by cancer cells in addition to a baseline recruitment, and the predicted CCL2 expression and migration indices are fitted to TNBC data (**Supplementary Figure S3**; Huang et al., 2007; Dutta et al., 2018). The factors secreted by MDSCs as the major contributors of their inhibitory effects are assumed to be Arg-I and NO, whose expression rates are estimated based on *in vitro* experiments on breast cancer cells (**Supplementary Figure S2**; Serafini et al., 2008). Since only the enzymatic activity of Arg-I is measured in enzyme unit, mU, we use mU as a placeholder of Arg-I concentration in the model, assuming that the protein concentration is proportional to the enzymatic activity. The unit of its production rate is then set to be mU*(microliter)/cell/day to estimate the amount of Arg-I produced by MDSCs per day. The unit of production rates of NO and CCL2 is set to be nanomole/cell/day. While both Arg-I and NO inhibit cytotoxic killing of cancer cells by effector T cells, only Arg-I facilitates Treg expansion in the tumor (Serafini et al., 2008). The effective concentrations are estimated based on *in vitro* experiments and listed in **Supplementary Table S7** with references.

Mechanisms of Anti-CTLA-4 Activity

Checkpoint Activity of CTLA-4

Dynamics of CTLA-4 related checkpoint molecules are modeled based on the previously published model by Jansson et al. (2005), and cross-arm binding of monoclonal anti-CTLA-4 antibody to CTLA-4 is incorporated similar to that of anti-PD-1 antibody to PD-1 in our previous model (Harms et al., 2014; Jafarnejad et al., 2019). Briefly, CD28 and CTLA-4 on naïve T cells are assumed to bind CD80 and CD86 on APCs. CD28 is a co-stimulatory signal that enhances the activation

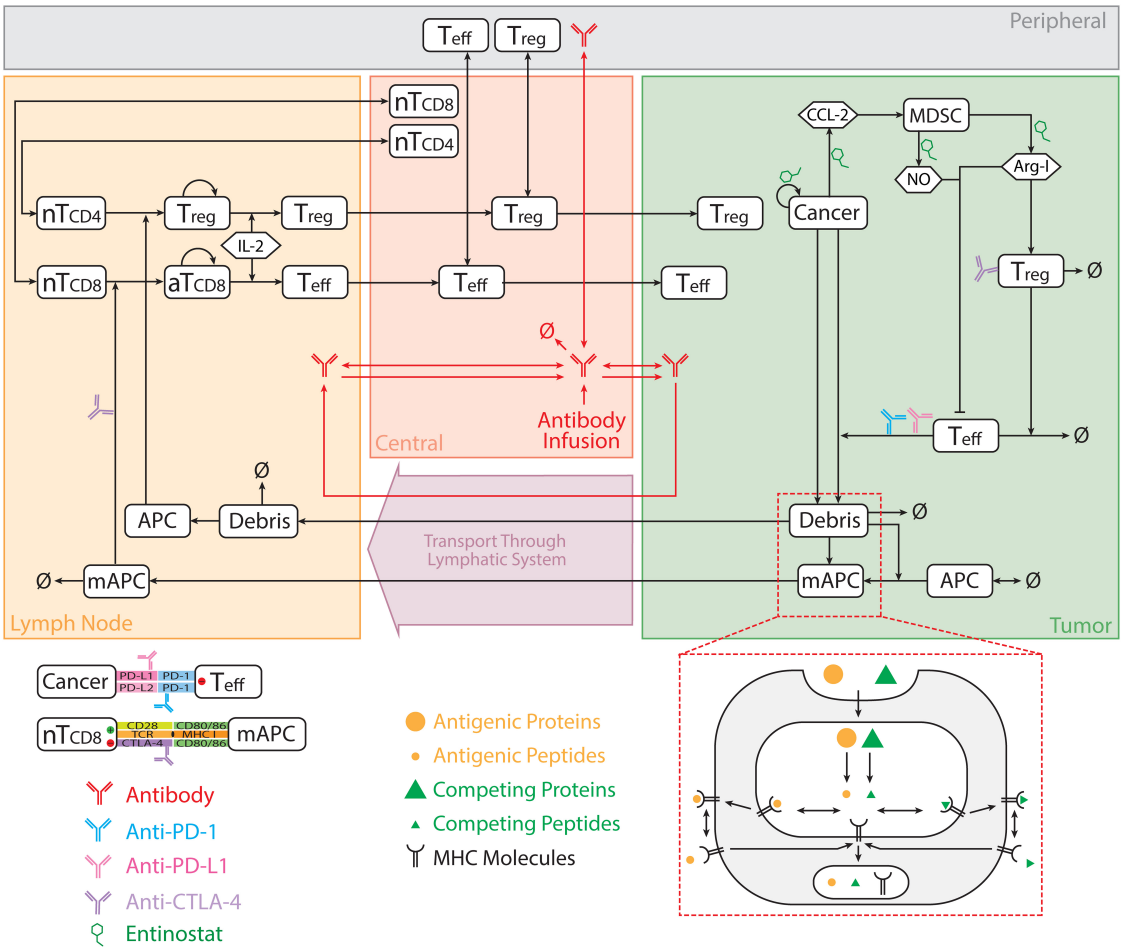

FIGURE 1 | Model diagram. The model is comprised of four compartments: central, peripheral, tumor, and tumor-draining lymph node, which describe cycles of immune activation in lymph nodes, T cell trafficking to the tumor, killing of cancer cells, immune evasion, and antigen release and lymphatic transport. Anti-CTLA-4 antibody blocks interaction between CD80/86 and CTLA-4 on mAPC and naïve T cell, respectively, in lymph nodes, and induces ADCC-mediated Treg depletion in the tumor. Anti-PD-1 antibody blocks interaction between PD-1 and PD-L1/2 on Teff and cancer cell, respectively, in the tumor. nT, naïve T cell; aT, activated T cell; NO, nitric oxide; Arg-I, arginase I; Treg, regulatory T cell; Teff, effector T cell; mAPC, mature antigen presenting cell. The figure is adapted from Jafarnejad et al. (2019).

of naïve T cells resulting in higher levels of proliferating T cells. Higher affinity of CTLA-4 for CD80/CD86 results in the depletion of CD28 ligands for T cell activation, and blockade of CTLA-4 restores ligand availability for CD28 that leads to enhanced T cell activation and proliferation. Furthermore, the binding of CD80 on APC to PD-L1 on T cells was included to compete with the interactions of PD-1 and CTLA-4 related axes (Sugiura et al., 2019). All the reactions are assumed to happen in the two-dimensional synapse compartment between the respective cells and the details of the reactions are included in the **Supplementary Material**. The biochemical parameters of this module are mostly measured experimentally and reported in the literature (Jansson et al., 2005).

Anti-CTLA4-Mediated Antibody-Dependent Cellular Cytotoxicity (ADCC)

In addition to the checkpoint activity of CTLA-4, ADCC is shown to be a potential mechanism of action for antibodies targeting CTLA-4 (Arce Vargas et al., 2018). Regulatory T cells express higher levels of CTLA-4 compared to effector T cells, and anti-CTLA-4 antibodies enhance Treg depletion through ADCC (Arce Vargas et al., 2018). It should be noted that the importance of this mechanism in human has been questioned by clinical observations (Sharma et al., 2019). In this model, anti-CTLA4-mediated ADCC is incorporated as Treg depletion through binding between the anti-CTLA-4 antibody and CTLA-4 on Treg in the tumor. The maximal Treg depletion rate is estimated based on *in vitro* experiments (Richards et al., 2008).

Simulation Settings

Although the model is used to simulate PK/PD for all the immune checkpoint antibodies (i.e., anti-CTLA-4, anti-PD-1, and anti-PD-L1) and entinostat in monotherapy and combination therapies, we focus on the particular clinical trial (NCT02453620), in which nivolumab and entinostat are administered to 26 HER2-negative breast cancer patients with

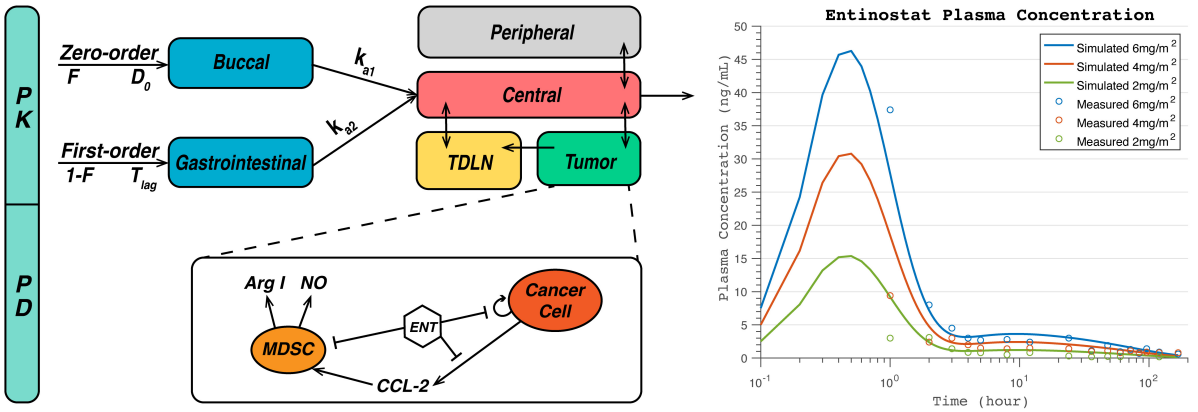

FIGURE 2 | Diagram of pharmacokinetic/pharmacodynamic (PK/PD) module for entinostat **(A)** and simulated and measured plasma concentration at doses of 2, 4, 6 mg/m^2 **(B)**. A fraction of dose, F, is immediately absorbed by the patients via zero-order buccal absorption over a time duration D_0 into the buccal compartment, and the rest of the dose, 1-F, is absorbed after a time period T_{lag} via first-order gastrointestinal (GI) absorption into the gastrointestinal compartment. The drug in buccal and gastrointestinal compartments are then absorbed into the central compartment via first-order absorption, and transported into the peripheral and the tumor compartments via passive diffusion. For pharmacodynamics of entinostat, it inhibits nitric oxide (NO) and arginase I (Arg-I) production by myeloid-derived suppressor cells (MDSCs), CCL2 production by cancer cells, Arg-I activity, and cancer cell proliferation.

or without ipilimumab. The breast cancer-specific parameters, including cancer cell diameter, the number of tumor-draining lymph nodes, tumor growth rate, volume fractions, and steady-state MDSC and Treg levels are estimated based on literature data. The baseline parameter values are estimated using TNBC data, and the parameter ranges are estimated using both TNBC and estrogen-positive/HER2-negative breast cancer data to describe the heterogeneity of HER2-negative patients. Both baseline parameter values and their ranges are listed with references in **Supplementary Tables S1–S6**.

For each individual as a potential patient, a simulation is performed starting from a single cancer cell with a plausible characteristic parameter set of the patient drawn from our assumed distributions. Due to the lack of patients' information of their initial tumor diameters at the beginning of the therapy from the clinical trial, an initial tumor diameter is randomly selected for the virtual patient based on our assumed distribution. These preselected initial tumor diameters are then used to calculate the initial tumor volume assuming a spherical tumor as the pre-treatment tumor volume (i.e., preselected initial tumor volume) for the virtual patient. Once the tumor reaches the preselected initial tumor volume, the values of all the species are saved and substituted into the model for further simulations of the therapy of interest. If the tumor has not been able to reach the preselected initial tumor volume, the corresponding individual is considered to not develop a tumor, possibly due to a strong immune response given by the plausible parameter set. These individuals are not included in the post-simulation analysis. The initial conditions and dynamic solutions are calculated using the ode15s solver in MATLAB, and the tumor growth is simulated for 400 days after therapy begins. The absolute tolerance and relative tolerance are set to be 10^{-12} (day) and 10^{-6}, respectively. In SimBiology, absolute tolerance controls the largest absolute error allowed for the ODE solver at any step in the simulation, while relative tolerance controls the tolerable error relative to the state vector at each step.

In silico Virtual Clinical Trial and Sensitivity Analysis

For virtual clinical trials, a plausible characteristic parameter set is selected for each potential patient to represent the inter-individual variabilities, such as the cancer killing rate by effector T cells, steady-state Treg and MDSC density in the tumor, antigen binding affinity, cytokine expressions, and tumor mutational burden (TMB), which is measured as the total number of mutations per tumor genomic region and is defined in our model as the number of tumor-specific T cell clones in TDLNs (Li et al., 2016; Yarchoan et al., 2017). The values of selected parameters are assigned using Latin Hypercube Sampling (LHS) based on our estimated distribution and plugged in as input. Among all the simulations, virtual patients who reach the preselected initial tumor volumes are used to calculate the overall response rate and the Partial Rank Correlation Coefficient (PRCC) between post-treatment observations (e.g., end tumor volume, tumor-infiltrating Treg and effector T cell density) and parameters of interest for sensitivity analysis (e.g., cancer cell growth rate, tumor antigen affinity, TMB) (Marino et al., 2008).

Statistical Analysis

The overall response rate is predicted as the proportion of patients with complete response (CR) or partial response (PR) based on RECIST v1.1, and the 95% Agresti-Coull confidence interval (CI) is estimated based on normal approximation for the binomial distribution. For comparison of model observations between responders and non-responders and that among virtual patients in various therapeutic regimens, Wilcoxon test is performed using ggpubr package in RStudio v1.2 (Kassambara, 2019).

RESULTS

Prediction of Entinostat Concentration in Tumor

Figure 2B, demonstrates the simulated plasma concentration of entinostat together with the clinical measurements at dose levels of 2, 4, and 6 mg/m^2 assuming a body surface area of 1.7 m^2 (Gore et al., 2008). The simulated peak concentrations are 15.4, 30.8, and 46.3 ng/mL, and the areas under the curve are calculated to be 105.5, 211.0, and 316.8 ng h/mL for doses of 2, 4, and 6 mg/m^2, respectively. The time t_{max} at the peak concentrations is estimated to be 0.5 h for all doses. To further test the interindividual variability of entinostat concentration, we varied the values of absorption rates and clearance rates of entinostat in the sensitivity analysis. The results are represented by a heatmap below with other parameters of interest, and show that non-linear clearance rate of entinostat has a significant inverse correlation with its anti-proliferative effect on cancer cells.

Efficacy of Anti-PD-1 Monotherapy and Its Combination With Entinostat

The model is first used to simulate the overall anti-tumor response to anti-PD-1 monotherapy in breast cancer. Among the 1500 simulations, 1196 virtual patients reach the preselected initial tumor volume. It should be noted that the ratio 1196/1500 reflects our method of generating the initial conditions and does not reflect the actual fraction of individuals who develop tumors. Thus, it should be considered a methodological detail rather than a reflection of a biological process. The parameter sets of the 1196 virtual patients are saved to simulate anti-tumor response to all the following therapeutic regimens and statistical analysis. Once the tumor diameter has reached its preselected value, 3 mg/kg nivolumab is administered every 2 weeks. The time-dependent percentage change of the tumor size (spider plot) is plotted in **Figure 3A**, based on RECIST criteria (Eisenhauer et al., 2009). Overall, 265 virtual patients have a partial or complete response (22.2%), and 37 virtual patients have stable disease (3.1%); the remaining 894 patients had progressive disease (74.8%). A waterfall plot of changes from baseline in model-predicted tumor diameter is shown in **Figure 3B**.

To further investigate the effect of entinostat on the overall response rate and tumor microenvironment, we simulate the overall anti-tumor response to a double combination therapy using 3 mg/kg nivolumab every 2 weeks and weekly doses of 5 mg entinostat. The parameter sets and initial conditions of the same 1196 virtual patients who reached preselected initial tumor volume are saved and used to perform a virtual trial with combination of entinostat and nivolumab. Of the 1196 virtual patients, 320 have a partial or complete response (26.8%), and 52 have stable disease (4.4%), the remaining 824 patients had progressive disease (68.9%). Thus, the predicted increase of the response rate from 22.2% for nivolumab alone to 26.8% for the combination of nivolumab and entinostat. The time-dependent percentage change of the tumor size (spider plot) and the waterfall plot are shown in **Figures 3C,D**. We can now apply these simulation results to the actual clinical trial in which each dose regimen involves less than 15 patients. By randomly sampling 15 virtual patients 100,000 times, we obtain a 95% percentile bootstrap confidence interval of (6.67%, 46.7%) for our estimate of the overall response rate in the double combination therapy. Thus, even though these results are dependent of the space of parameters for the virtual patients, we note that the predicted confidence interval is very wide.

Model-Predicted Anti-tumoral Effect in Triple Combination Therapy

Now that the efficacy of entinostat on improving anti-tumoral effect of anti-PD-1 monotherapy has been simulated, the model is used to investigate the effect of the addition of anti-CTLA-4 antibody. Four doses of 1 mg/kg ipilimumab are administered every 6 weeks with weekly 5 mg entinostat and 3 mg/kg nivolumab every 2 weeks. While the number of responders remains the same, the mean post-treatment tumor volume is lower than that in the double combination therapy. This slight increase of anti-tumor response is due to the ADCC-mediated Treg depletion by ipilimumab, which significantly increase Teff to Treg ratio in the tumor. The total virtual population is then divided into six subgroups based on their pre-treatment tumor-infiltrating Teff, Treg, and MDSC density, Teff to Treg ratio, TMB, and tumor-specific antigen binding affinity by their medians. The response rates of all subgroups with 95% confidence intervals are shown in **Figure 4**. The confidence intervals for subgroups MDSC density, TMB, tumor-infiltrating Teff density, and Teff to Treg ratio show significantly different response rates in these subgroups, while those for other subgroups overlap. The 95% percentile bootstrap confidence interval for our estimate of the overall response rate in the triple combination therapy is calculated to be (6.67%, 53.3%) for a sample size of 15, using the same methods in the previous section. 100 out of the 1196 virtual patients are randomly selected to illustrate their changes from baseline in model-predicted tumor diameter with parameters of interest, as shown in **Figures 5A–D**. While a large portion of responders correspond to patients with high TMB and low PD-L1 expression on cancer cells, antigen binding affinity and initial tumor diameter are evenly distributed between responders and non-responders.

To further investigate the effect of combination therapy using immune checkpoint inhibitors and the epigenetic modulator, we plot the changes of Teff/Treg density and ratio, and tumor volume as post- to pre-treatment ratio using the five therapeutic regimens from the clinical trial as shown in **Figure 6**. The significant increase of Teff to Treg ratio when higher doses of nivolumab are administered in the double combination therapy corresponds to the significant increase of tumor-infiltrating Teffs, as nivolumab blocks inhibitory signals on cancer cells and restores Teff functionality. On the other hand, the increases of Teff to Treg ratio by addition of entinostat and ipilimumab correspond more to the decrease of Tregs than to the increase of tumor-infiltrating Teffs. This phenomenon is due to the immune modulation by entinostat that inhibits Treg expansion, as well as the Treg depletion effect by anti-CTLA-4 antibody.

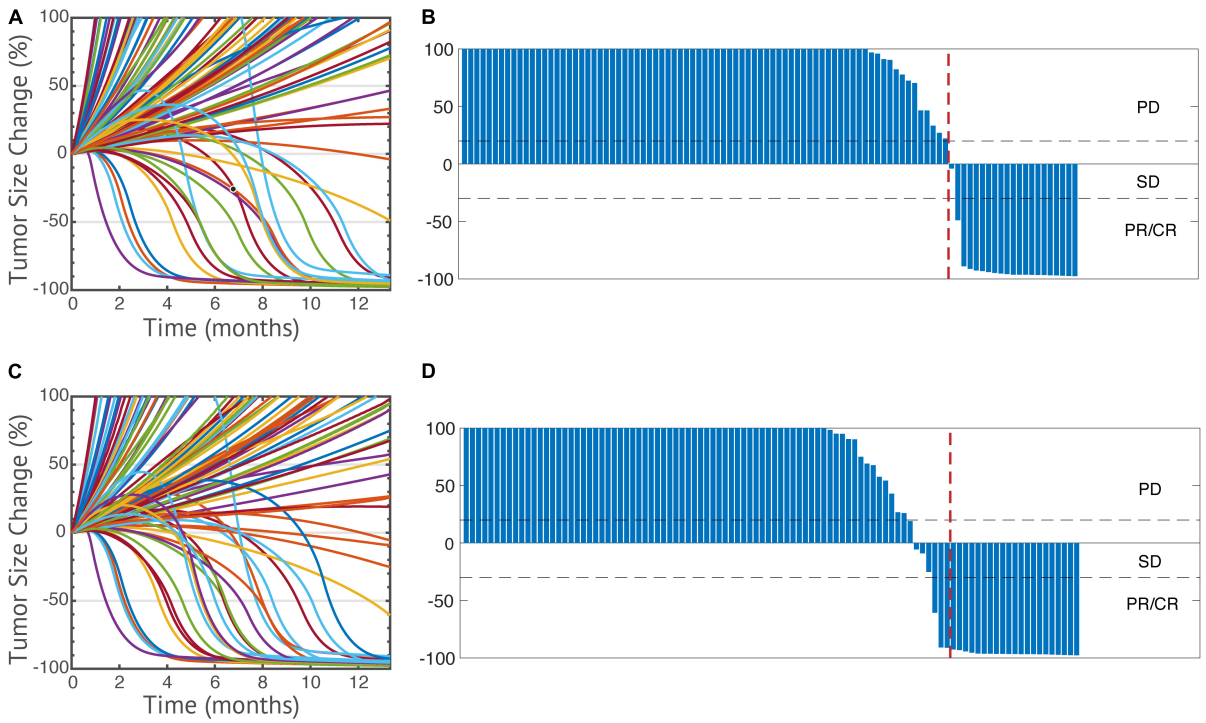

FIGURE 3 | Spider plots of 100 randomly selected virtual patients **(A,C)** and change from baseline in model-predicted tumor diameter assessed by RECIST v1.1 **(B,D)** in anti-PD-1 monotherapy **(A,B)** and its combination with entinostat **(C,D)**. PD, progressive disease; SD, stable disease; PR, partial response; CR, complete response.

Anti-tumor Response as Affected by Parameters of Interest

In **Figure 7**, a heatmap of global uncertainty and sensitivity analysis shows that among 32 parameters, tumor growth rate, T cell exhaustion, cancer killing rate by T cells, TMB, initial tumor diameter, steady-state MDSC density, PD-L1 expression on cancer cells, and inhibitory effect of Arg-I on T cells are significantly correlated with end tumor volume. The sensitivity of these responses to parameters is further illustrated in **Figure 8**. In the above simulations based on the reference values of model parameters, we predicted certain response rate at 400 days, e.g., in a combination of nivolumab and entinostat 26.8% have a partial or complete response, 4.4% have stable disease, and 68.9% have progressive disease. However, these percentages are affected by the parameters of the patient cohort, and results of a trial may be different depending on the parameters of the patients within the cohort. **Figure 8**, illustrates the effects of variation of parameters on the patients' response according to RECIST criteria for 9 parameters selected from the global sensitivity results. TMB, tumor growth rate, steady-state MDSC density, the number of PD-L1 molecules on cancer cell, and effective concentration of Arg-I on Teff inhibition show strong impacts on tumor size change, which corroborates their statistical significance suggested by PRCC analysis and emphasizes a need for accurate estimation of these parameters for personalized simulations.

Identification and Performance of Potential Predictive Biomarkers

From sensitivity analysis and overall response table presented above, we identify several potential predictive biomarkers for the triple combination therapy in this virtual clinical trial. As shown in **Figure 9**, the distributions of pre-treatment tumor-infiltrating Teff and Treg density, Teff to Treg ratio, and TMB are significantly higher in responders when compared with those in non-responders, while MDSC density is significantly higher in non-responders, possibly due to its strong immune-suppressive activity in the tumor microenvironment. We further investigate the performance of these potential biomarkers on prediction of anti-tumor response to the triple combination therapy through binary classification. As shown in **Figure 10**, the Sensitivity and 1-Specificity values from each cutoff were plotted as ROC curves. TMB, tumor-infiltrating Teff and Teff to Treg ratio have higher AUCs (0.872, 0.766, and 0.740, respectively) than intra-tumoral MDSC density (0.652), further implicating their potential to be predictive biomarkers for this triple combination regimen.

DISCUSSION

Based on our previously published QSP model and our first attempt to make personalized predictions of anti-tumor response to immunotherapy using immune checkpoint inhibitors (Milberg et al., 2019; Wang et al., 2019), a more recent model with

	N	ORR	95% CI
Overall	1196	26.8	(24.3, 29.3)
MDSC density			
< 9.4e4 cell/mL tumor	598	36.0	(32.2, 39.9)
≥ 9.4e4 cell/mL tumor	598	17.6	(14.7, 20.8)
Ag binding affinity			
< 37.5 nM	598	29.1	(25.6, 32.9)
≥ 37.5 nM	598	24.4	(21.1, 28.0)
TMB (T cell clones)			
< 100	598	4.0	(2.7, 5.9)
≥ 100	598	49.5	(45.5, 53.5)
Teff/Treg ratio			
< 33	598	11.4	(9.1, 14.2)
≥ 33	598	42.1	(38.2, 46.1)
Teff density			
< 2.2e4 cell/mL tumor	598	12.4	(10.0, 15.3)
≥ 2.2e4 cell/mL tumor	598	41.1	(37.3, 45.1)
Treg density			
< 577 cell/mL tumor	598	25.6	(22.2, 29.2)
≥ 577 cell/mL tumor	598	27.9	(24.5, 31.7)

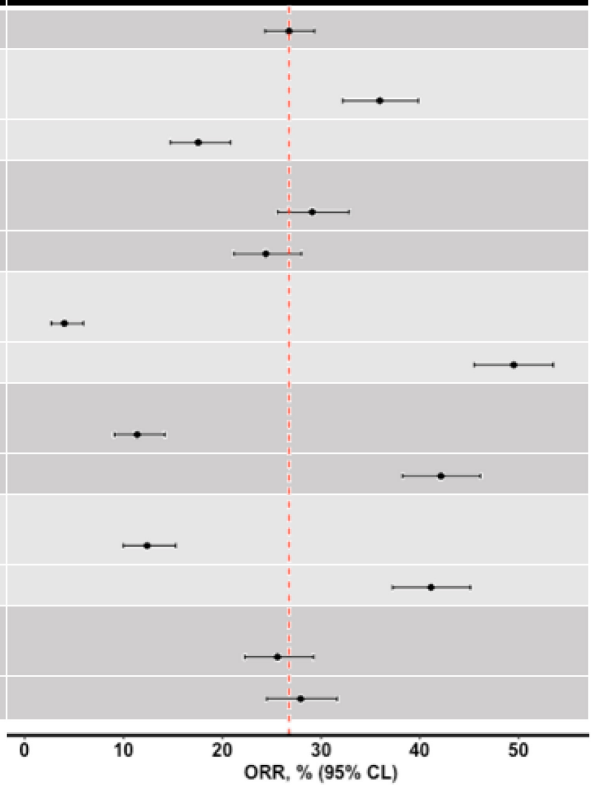

FIGURE 4 | Anti-tumor activity of triple combination therapy in virtual patient cohort. Total 1196 virtual patients in triple combination of entinostat, nivolumab, and ipilimumab are divided into subgroups based on the population medians, and the objective response rates in each subgroup are calculated with 95% Agresti-Coull confidence intervals. MDSC, myeloid-derived suppressor cell; Ag, tumor antigen; TMB, tumor mutational burden (tumor-specific T cell clones in lymph nodes); Teff, effector T cell; Treg, regulatory T cell.

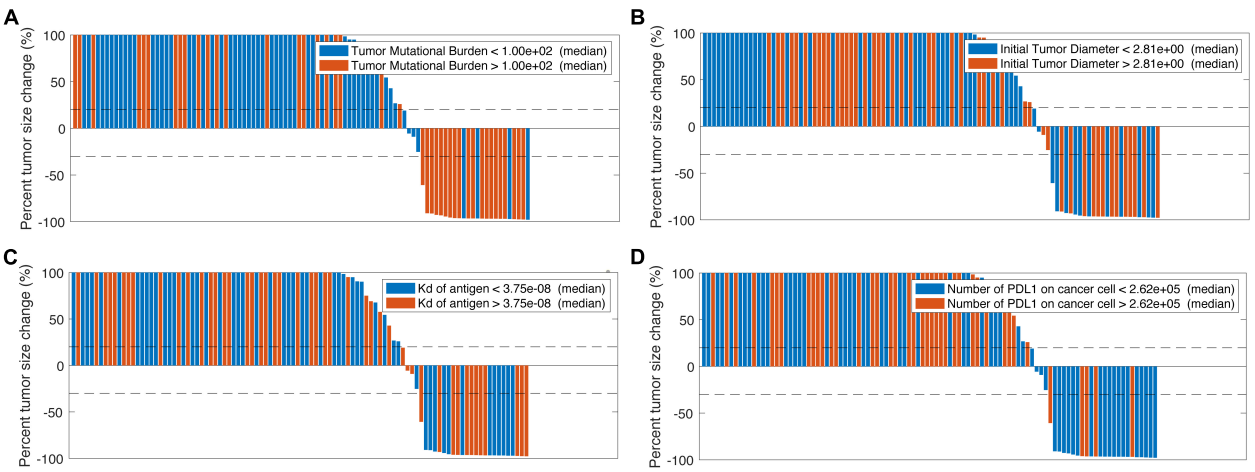

FIGURE 5 | Change from baseline in model-predicted tumor diameter assessed by RECIST v1.1 based on tumor mutational burden **(A)**, initial tumor diameter **(B)**, tumor antigen binding affinity **(C)**, and number of PD-L1 molecules on cancer cells **(D)**.

reduced number of ODEs has been published by Jafarnejad et al. (2019) through simplification of certain processes, such as T cell trafficking and the kinetics of T cell priming in the lymph nodes. In this study, we present a further developed model to: modularize each species of interest and individually calibrate the modules based on literature data;

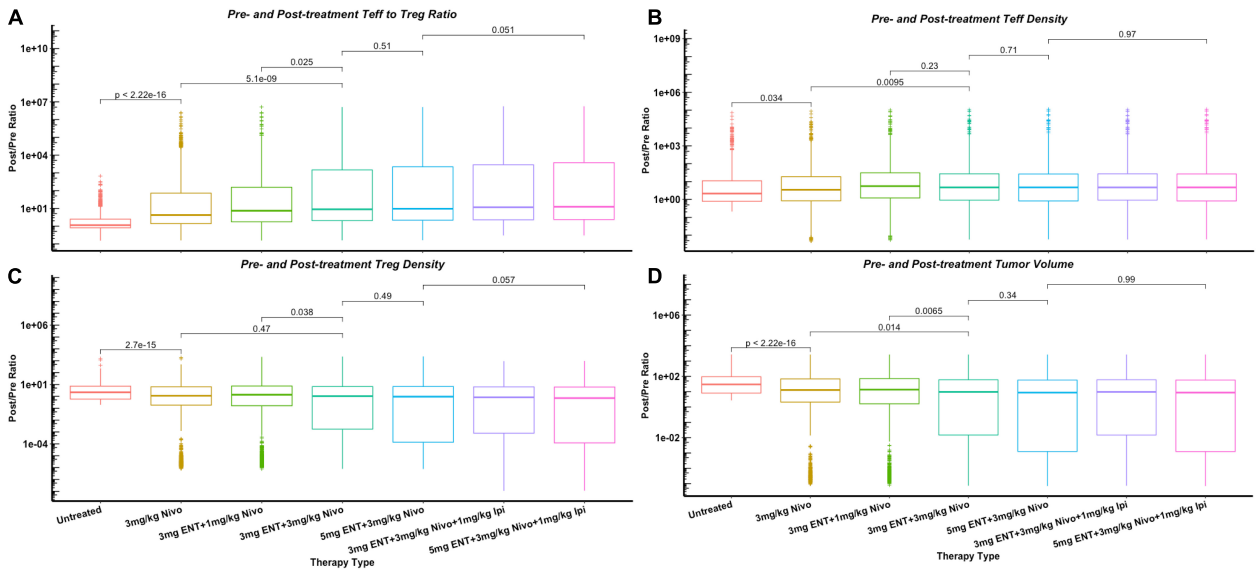

FIGURE 6 | Changes of cell density and tumor volume in dose escalation as post- to pre-treatment ratios, including Teff to Treg ratio **(A)** and their densities in tumor **(B,C)**, and tumor volume **(D)**. *p*-values are calculated using Wilcoxon test.

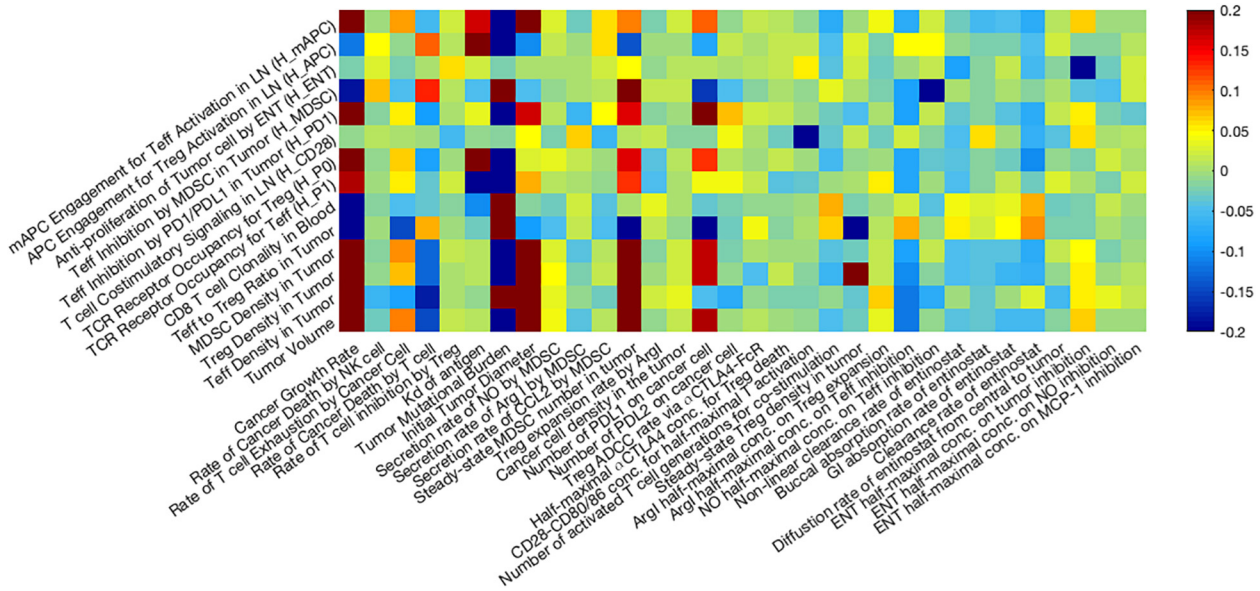

FIGURE 7 | Global uncertainty and sensitivity analysis. Thirty two parameters are assigned using Latin Hypercube Sampling (LHS) based on our estimated distribution, and the Partial Rank Correlation Coefficient (PRCC) between selected post-treatment observations and input parameters are presented as a heatmap. Among 32 parameters, tumor growth rate, T cell exhaustion, cancer killing rate by T cells, TMB, initial tumor diameter, steady-state MDSC density, PD-L1 expression on cancer cells, and inhibitory effect of Arg-I on T cells are significantly correlated with post-treatment tumor volume.

add a MDSC module; investigate the mechanisms of action for the epigenetic modulator and checkpoint inhibitors with limited and/or controversial preclinical results; and conduct a virtual clinical trial of a combination therapy using anti-PD-1, anti-CTLA-4 antibodies and an epigenetic modulator, entinostat. The modularized model can be readily reproduced, and additional modules can be added in future studies if the dynamics of other molecular and cellular species are of interest.

While T cell trafficking equations and the PK/PD module of checkpoint inhibitors remained unchanged compared to our previous models (Jafarnejad et al., 2019; Wang et al., 2019), we adopted a new mechanism of T cell activation by mature APCs (mAPCs) (Lever et al., 2014). Tumor antigens are released from

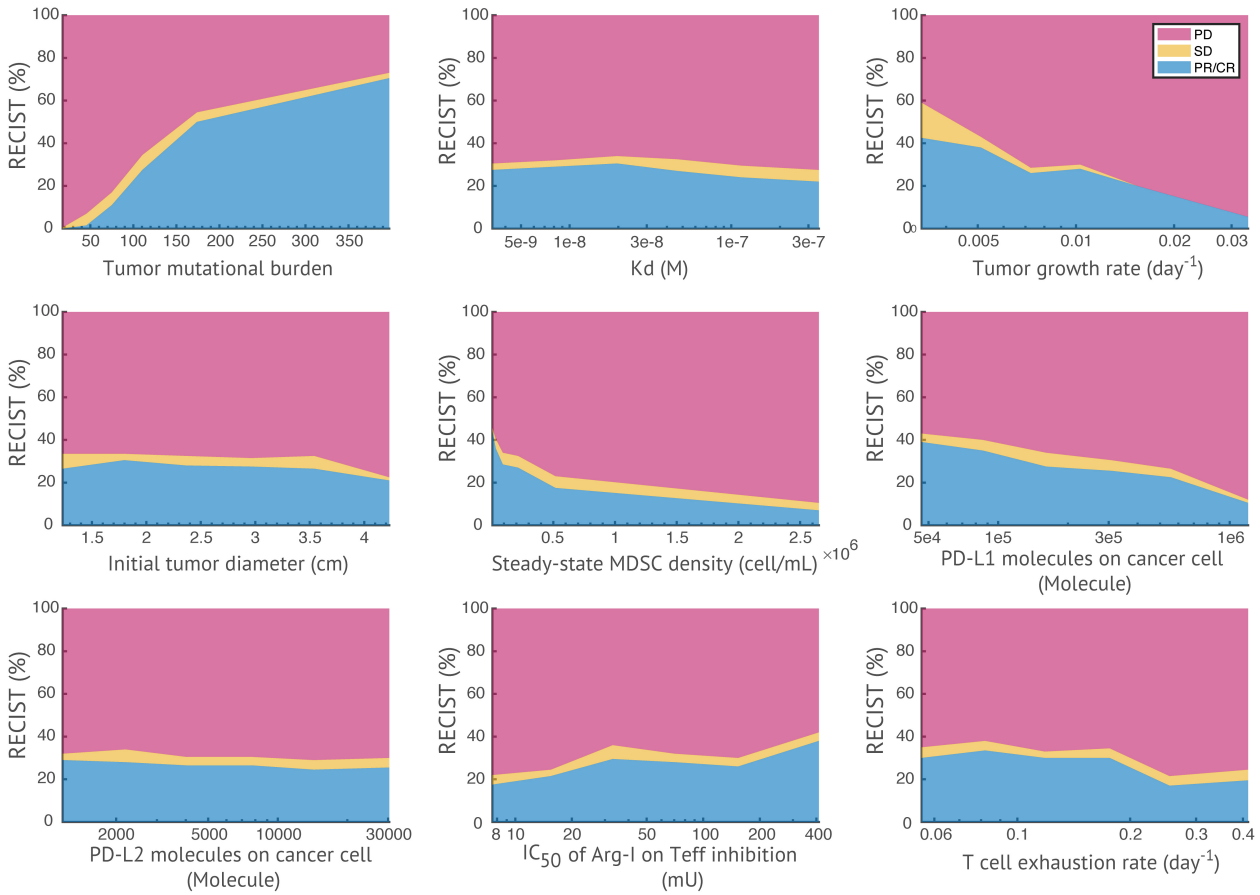

FIGURE 8 | Effects of parameters on patients' response. For each parameter of interest, virtual patients are sorted by their corresponding parameter values in ascending order, and evenly divided into six subgroups. The response status of each subgroup is plotted against the median parameter values in each subgroup. TMB and effective concentration of Arg-I on Teff inhibition show positive correlations with response rate, while tumor growth rate, steady-state MDSC density, and the number of PD-L1 molecules on cancer cell show negative correlations (i.e., with a >15% increase/decrease of response rates in subgroups).

dying cancer cells and transported to TDLNs. Virtual patients with higher TMB would generate higher levels of tumor antigens, which can be recognized by higher levels of tumor-specific naïve T cells in TDLNs. Activation of tumor-specific naïve T cells in TDLNs is modeled by a kinetic proofreading module with limited signaling based on TMB, binding affinity of tumor antigens and concentration of mAPCs (Lever et al., 2014). The activated T cells proliferate through a calculated number of generations based on T cell receptor signaling, co-stimulatory signaling, and cytokine signaling before returning to quiescence, while they simultaneously differentiate into effector T cells (Marchingo et al., 2014). In addition, simulations also start from a single cancer cell to capture the initial conditions at the preselected initial tumor volumes. This way, we take into account the virtual patients whose adaptive immune response is strong enough to eliminate the cancer cells before developing into a tumor. Using this method, we no longer observe the strong correlation between tumor volume and initial tumor diameter (**Figure 8**) as we did in previous study (Wang et al., 2019). By starting model simulation from a single cancer cell, larger initial tumor size is more likely to acquire higher number of pre-treatment tumor-infiltrating T cells, which results in a similar T cell density to smaller sizes. Thus, anti-tumor response is less dependent on its initial size.

According to our model analysis, a positive correlation between PD-L1 expression on cancer cell and end tumor volume is observed. That is, patients with small number of PD-L1 molecule on cancer cell are likely to have strong anti-tumor response. This is due to our assumption that Teff function is not inhibited by cancer cells without PD-L1 expression, opposite to our previous model, where we assume that Teffs are inhibited by other inhibitory pathways if not by PD-L1 on cancer cells (Wang et al., 2019). Both of the assumptions aim to explain the correlation between PD-L1 status and anti-tumor response observed in clinical trials (Vikas et al., 2018). To further investigate the implication of PD-L1 positivity in patients with breast cancer, its expression on both cancer cells and immune cells should be implemented in future studies with appropriate assumptions of their functionality based on clinical evidence (Marra et al., 2019; Matikas et al., 2019). For example, PD-L1 expression on macrophages plays an important role

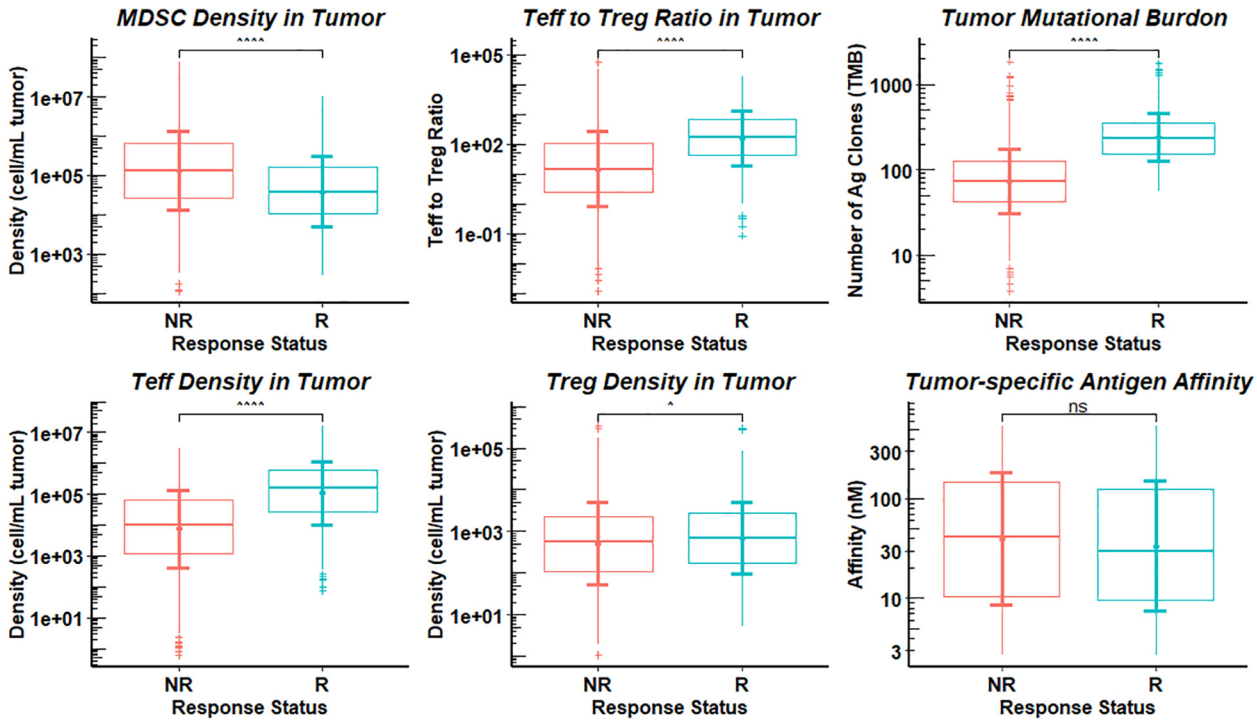

FIGURE 9 | Distributions of Potential Biomarkers in Responders and Non-responders. The response in the 1196 simulations was divided into responders (R) and non-responders (NR), and statistical comparisons are presented between the two groups for pre-treatment observations. Statistical significance is calculated by Wilcoxon test. ^p-values ≤ 0.05; ^^^^p-values ≤ 0.0001; non-significance (ns), p-values > 0.05.

in macrophage polarization and antitumor cytokine secretion (Hartley et al., 2018). In addition, PD-L1 expression on cancer cells shows correlations with tumor metastasis and suppression of effector T cells, which is regulated by epithelial-to-mesenchymal transition of cancer cells (Chen et al., 2014; Terry et al., 2017). Therefore, a macrophage module can be added to investigate the interactions between macrophages and cancer cells and the resulting effects on the tumor microenvironment (Mahlbacher et al., 2018; Li et al., 2019; Zhao et al., 2019).

In our previous model (Wang et al., 2019), we suggested that the MDSC level in the tumor was significantly related to anti-tumor response to combination checkpoint blockade therapy, assuming that the inhibition of effector T cells by MDSCs was mainly dependent on their checkpoint expression and that intratumoral Treg level remained a constant fraction of MDSCs. In the present model, we further expand the mechanisms of MDSCs to include both the secretion of Arg-I and NO by MDSCs, which inhibit Teff cytotoxicity and induce Treg expansion, and CCL2 secretion by breast cancer cells, which facilitates MDSC recruitment into the tumor. As shown in the sensitivity analysis (**Figure 7**), the addition of detailed MDSC mechanisms does not lead to an overestimated inhibition of the immune response, as the efficacy of the combination therapy is significantly correlated to not only MDSC-related parameters but also to other immune-suppressive factors.

To study the efficacy of entinostat, we proposed a pharmacokinetic model to estimate the transport parameters based on the plasma concentration measured by Gore et al. (2008). The simulated peak concentration and area under the plasma concentration curve for different doses are compared with other published PK analysis data of entinostat (Ryan et al., 2005; Gojo et al., 2007; Kummar et al., 2007). Although most of our simulated concentrations fall within the range of their clinically measured values, the small sample sizes and the large differences in means and ranges reported in all the four studies suggest that additional clinical measurements are needed to improve our prediction of entinostat concentration in patients with breast cancer. For pharmacodynamics of entinostat, it is assumed to inhibit proliferation of breast cancer cells and the cytokine secretion by MDSCs, reversing their inhibitory effects on T cell subsets. Interestingly, the effective concentrations of entinostat on its anti-proliferative activity are dependent on the subtypes (i.e., HS-578t, MCF-7, ZR-75, and SKBR3), and it also reduces cell viability in some subtypes of breast cancer, including MCF-7, ZR-75, and SKBR3 cells (Lee et al., 2001). The discrepancy of the efficacy of combination therapy using immune checkpoint inhibitors and epigenetic modulator among different cancer types might result from this difference in effective concentrations (Gallagher et al., 2017).

For mechanism of action of anti-CTLA-4 antibody, it was assumed in our previous model that the efficacy of anti-CTLA-4 therapy observed in clinical trials is mainly mediated by blocking CTLA-4 and CD80/86 interactions and thus restoring co-stimulatory signaling in T cell activation in TDLNs

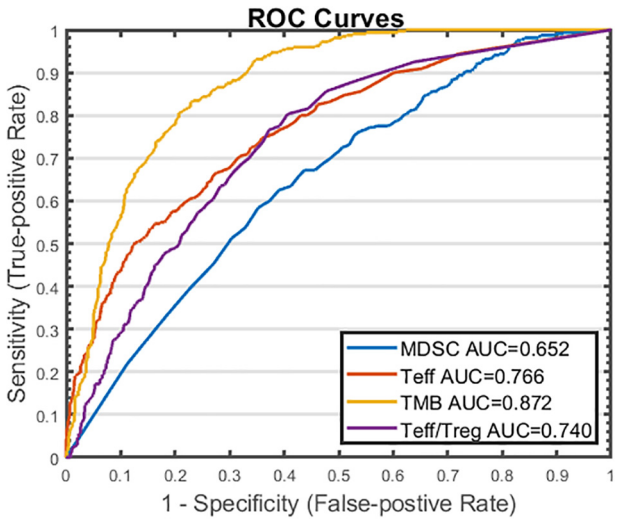

FIGURE 10 | ROC Analysis of Potential Predictive Biomarkers in Triple Combination Therapy. Cutoff values are selected based on the range of pre-treatment amounts of myeloid-derived suppressor cell (MDSC) density, effector T cell (Teff) density, tumor mutational burden (TMB), and Teff to regulatory T cell (Treg) ratio. For each cutoff value, response status (R vs. NR) is predicted for each virtual patient by comparing the pre-treatment amount of the potential biomarker to the cutoff value. Sensitivity (true positive rate) is plotted against 1 – specificity (true negative rate) for each biomarker. R, responders; NR, non-responders.

(Wei et al., 2018). In addition, recent studies suggest that Fc domain of the anti-CLTA-4 antibody is required for efficacy in mouse tumor models, which is critical to induce Fc-mediated depletion of regulatory T-cells (Arce Vargas et al., 2018; Ingram et al., 2018; Tang et al., 2018). However, this newly proposed mechanism of anti-CTLA-4 antibody has shown controversial results from clinical studies (Romano et al., 2015; Sharma et al., 2019). While both mechanisms are implemented in the present model to investigate their roles in anti-tumoral activity in breast cancer, the major mechanism of action of anti-CTLA-4 antibody that contributes to its efficacy has yet to be determined by future studies, which might also be cancer type-dependent.

By conducting a prospective virtual clinical trial, we aim to make predictions of the anti-tumor activities and biomarkers for an ongoing trial that has not yet been completed. Starting from the nivolumab monotherapy, we predict the response rate of 1196 virtual patients with breast cancer. A 22.2% response rate is predicted given our set of parameters of interest with assumed distributions. Based on our assumptions on the mechanisms of action, our predicted response rate falls within the reported range of response rate of anti-PD-1 monotherapy using pembrolizumab in patients with TNBC or estrogen-positive/HER2-negative metastatic breast cancer (Emens, 2018; Planes-Laine et al., 2019), which demonstrate the ability of the present model to perform virtual clinical trials and make reasonable qualitative predictions on anti-tumor response. When combined with entinostat, the response rate of checkpoint therapy increases to 26.8%. However, it is challenging to quantify the improvement of anti-tumor response to checkpoint blockade therapy by the addition of entinostat, since the PK parameters and the effective concentrations are only roughly estimated for entinostat. Although combination therapy of entinostat and anti-PD-1 antibody has shown promising results in patients with anti-PD-1-resistant melanoma and non-small cell lung cancer, the effect of cancer type and patients' characteristics on the improved efficacy has yet to be determined (Agarwala et al., 2018; Hellmann et al., 2018). Furthermore, the simulations show that the addition of four doses of anti-CTLA-4 antibody ipilimumab does not significantly improve the performance of the combination therapy, even though Teff to Treg ratio is significantly increased due to ADCC. This result is also suggested by our previous model (Wang et al., 2019), and higher doses of the ipilimumab might be required to improve the T cell activation and thus anti-tumor response; however, in the clinic, higher doses of ipilimumab are limited by toxicity. Overall, the model suggests that TMB, tumor-infiltrating Teff density, and Teff to Treg ratio can be predictive biomarkers in this triple combination therapy. The efficacy of all the tested therapies shows strong correlation with these model observations, which is also supported by their clinical significance in anti-tumor response and overall survival in breast cancer (Adams et al., 2014; Asano et al., 2016; Takada et al., 2018; Thomas et al., 2018).

Notably, the predictions of anti-tumor response and predictive biomarkers are strongly affected by our assumptions on mechanism of action for all therapeutics and distribution of physiological parameters for virtual patient cohort (Cassidy and Craig, 2019). The expected response rate of the ongoing clinical trial simulated in this study, as suggested by the 95% percentile bootstrap confidence intervals, could fall into a wide range. Due to the variations of selection criteria and settings in clinical trials, the distribution of patient parameters can be largely different and in fact only a few of the parameters that are necessary as inputs for the model are clinically measured; most of the parameters remain unknown for each particular patient or a cohort that results in uncertainty of model predictions. For example, the generally lower overall response rate reported in previously treated TNBC patients might result from their changes of physiological parameters in previous therapy when compared with previously untreated patients (Adams et al., 2019a,b). In this case, our model proposes to consider high TMB, tumor-infiltrating Teff density, and Teff to Treg as potential biomarkers, which might improve anti-tumor response in previously treated patients (Alva et al., 2019). Importantly, ongoing clinical trials may provide insights on the effect of entinostat and ipilimumab on the immune system and resistance mechanism in breast cancer development, which would allow us to make step-by-step modification of the model and its parameters and improve its predictive power (Pitt et al., 2016; Darvin et al., 2018; Eladdadi et al., 2018; Mahlbacher et al., 2019). Our goal is to understand the dynamic interactions between drugs and the immune system in cancer as a whole, to update our assumptions on drug/tumor-immune dynamics through comparison between model predictions and clinical observations, and thereby to guide drug development and clinical trial design (Cheng et al., 2017; Nijsen et al., 2018; Bai et al., 2019; Bradshaw et al., 2019).

DATA AVAILABILITY STATEMENT

The authors confirm that the data supporting the findings of this study are available within the article and the **Supplementary Material**. MATLAB scripts for model and data generation for this study will be made available by the corresponding author, without undue reservation, to any qualified researcher on request.

AUTHOR CONTRIBUTIONS

HW, AP, RC, and ET designed and planned the project. AP supervised the project and critically edited the manuscript. MJ, RS, HW, and SR built and modified the model structure. HW performed all simulations, analyzed the simulation data, and prepared a draft of the manuscript. EJ, VS, ET, and RC critically revised the manuscript. All authors have read and approved the final manuscript.

FUNDING

This work was supported by the NIH grants R01CA138264 and U01CA212007.

SUPPLEMENTARY MATERIAL

The Supplementary Material for this article can be found online at: https://www.frontiersin.org/articles/10.3389/fbioe.2020.00141/full#supplementary-material

FIGURE S1 | Antiproliferative effect of entinostat (ENT) on Breast Cancer Cell. 1-Hill function of inhibitory effect of ENT vs. its concentration **(A)**, and number of cancer cells vs. time **(B)**. Experimental data is from Lee et al. (2001) (PMID: 11221885). WT, wild type. Exp, experiment. Sim, simulation.

FIGURE S2 | Arginase I and nitric oxide expression. The error bars represent the range of arginase I **(A)** and nitric oxide **(B)** in virtual patient cohort, fitted to experimental data from Serafini et al., 2008 (PMID: 18593947).

FIGURE S3 | MCP-1/CCL2 Expression **(A)** and Recruitment of MDSC **(B)**. Range of CCL2 expression is fitted to data from Dutta et al. (2018) (PMID: 29594759), and effective concentration of CCL2 on recruitment of MDSC into the tumor is optimized to match the migration index reported by Huang et al., 2007 (PMID: 17257744).

TABLE S1 | Model Compartment Name, Capacity, Unit, and Description.

TABLE S2 | Model Parameter Name, Value, Unit, and Description.

TABLE S3 | Model Reaction, Reaction Rate, and Description.

TABLE S4 | Model Algebraic Equations (Model Rules).

TABLE S5 | Model Species Name, Initial Amount, Unit, Location, and Description.

TABLE S6 | Model Events.

TABLE S7 | Model Parameters used in MDSC Module.

REFERENCES

Adams, S., Gray, R. J., Demaria, S., Goldstein, L., Perez, E. A., Shulman, L. N., et al. (2014). Prognostic value of tumor-infiltrating lymphocytes in triple-negative breast cancers from two phase III randomized adjuvant breast cancer trials: ECOG 2197 and ECOG 1199. *J. Clin. Oncol.* 32, 2959–2966. doi: 10.1200/JCO.2013.55.0491

Adams, S., Loi, S., Toppmeyer, D., Cescon, D. W., De Laurentiis, M., Nanda, R., et al. (2019a). Pembrolizumab monotherapy for previously untreated, PD-L1-positive, metastatic triple-negative breast cancer: cohort B of the phase II KEYNOTE-086 study. *Ann. Oncol.* 30, 405–411. doi: 10.1093/annonc/mdy518

Adams, S., Schmid, P., Rugo, H. S., Winer, E. P., Loirat, D., Awada, A., et al. (2019b). Pembrolizumab monotherapy for previously treated metastatic triple-negative breast cancer: cohort A of the phase II KEYNOTE-086 study. *Ann. Oncol.* 30, 397–404. doi: 10.1093/annonc/mdy517

Agarwala, S. S., Moschos, S. J., Johnson, M. L., Opyrchal, M., Gabrilovich, D., Danaher, P., et al. (2018). Efficacy and safety of entinostat (ENT) and pembrolizumab (PEMBRO) in patients with melanoma progressing on or after a PD-1/L1 blocking antibody. *J. Clin. Oncol.* 36, 9530–9530. doi: 10.1200/JCO.2018.36.15_suppl.9530

Allen, R. J., Rieger, T. R., and Musante, C. J. (2016). Efficient generation and selection of virtual populations in quantitative systems pharmacology models. *CPT Pharmacomet. Syst. Pharmacol.* 5, 140–146. doi: 10.1002/psp4.12063

Alotaibi, M. R., Hassan, Z. K., Al-Rejaie, S. S., Alshammari, M. A., Almutairi, M. M., Alhoshani, A. R., et al. (2018). Characterization of apoptosis in a breast cancer cell line after IL-10 silencing. *Asian Pac. J. Cancer Prev.* 19, 777–783. doi: 10.22034/APJCP.2018.19.3.777

Alva, A. S., Mangat, P. K., Garrett-Mayer, E., Halabi, S., Alvarez, R. H., Calfa, C. J., et al. (2019). Pembrolizumab (P) in patients (pts) with metastatic breast cancer (MBC) with high tumor mutational burden (HTMB): results from the targeted agent and profiling utilization registry (TAPUR) Study. *J. Clin. Oncol.* 37, 1014–1014. doi: 10.1200/JCO.2019.37.15_suppl.1014

Arce Vargas, F., Furness, A. J. S., Litchfield, K., Joshi, K., Rosenthal, R., Ghorani, E., et al. (2018). Fc effector function contributes to the activity of human anti-CTLA-4 antibodies. *Cancer Cell* 33, 649–663.e4. doi: 10.1016/j.ccell.2018.02.010

Asano, Y., Kashiwagi, S., Goto, W., Kurata, K., Noda, S., Takashima, T., et al. (2016). Tumour-infiltrating CD8 to FOXP3 lymphocyte ratio in predicting treatment responses to neoadjuvant chemotherapy of aggressive breast cancer. *Br. J. Surg.* 103, 845–854. doi: 10.1002/bjs.10127

Bai, J. P. F., Earp, J. C., and Pillai, V. C. (2019). Translational quantitative systems pharmacology in drug development: from current landscape to good practices. *AAPS J.* 21:72. doi: 10.1208/s12248-019-0339-5

Bajaj, G., Wang, X., Agrawal, S., Gupta, M., Roy, A., and Feng, Y. (2017). Model-based population pharmacokinetic analysis of nivolumab in patients with solid tumors. *CPT Pharmacometr. Syst. Pharmacol.* 6, 58–66. doi: 10.1002/psp4.12143

Bouchain, G., Leit, S., Frechette, S., Khalil, E. A., Lavoie, R., Moradei, O., et al. (2003). Development of potential antitumor agents. Synthesis and biological evaluation of a new set of sulfonamide derivatives as histone deacetylase inhibitors. *J. Med. Chem.* 46, 820–830. doi: 10.1021/jm020377a

Bradshaw, E. L., Spilker, M. E., Zang, R., Bansal, L., He, H., Jones, R. D. O., et al. (2019). Applications of quantitative systems pharmacology in model-informed drug discovery: perspective on impact and opportunities. *CPT Pharmacometr. Syst. Pharmacol.* 8, 777–791. doi: 10.1002/psp4.12463

Cassidy, T., and Craig, M. (2019). Determinants of combination GM-CSF immunotherapy and oncolytic virotherapy success identified through in silico treatment personalization. *PLoS Comput. Biol.* 15:e1007495. doi: 10.1371/journal.pcbi.1007495

Chen, L., Gibbons, D. L., Goswami, S., Cortez, M. A., Ahn, Y. H., Byers, L. A., et al. (2014). Metastasis is regulated via microRNA-200/ZEB1 axis control of tumour cell PD-L1 expression and intratumoral immunosuppression. *Nat. Commun.* 5:5241. doi: 10.1038/ncomms6241

Cheng, Y., Thalhauser, C. J., Smithline, S., Pagidala, J., Miladinov, M., Vezina, H. E., et al. (2017). QSP toolbox: computational implementation of integrated

workflow components for deploying multi-scale mechanistic models. *AAPS J.* 19, 1002–1016. doi: 10.1208/s12248-017-0100-x

Choo, Q. Y., Ho, P. C., Tanaka, Y., and Lin, H. S. (2010). Histone deacetylase inhibitors MS-275 and SAHA induced growth arrest and suppressed lipopolysaccharide-stimulated NF-kappaB p65 nuclear accumulation in human rheumatoid arthritis synovial fibroblastic E11 cells. *Rheumatology* 49, 1447–1460. doi: 10.1093/rheumatology/keq108

Choo, Q. Y., Ho, P. C., Tanaka, Y., and Lin, H. S. (2013). The histone deacetylase inhibitors MS-275 and SAHA suppress the p38 mitogen-activated protein kinase signaling pathway and chemotaxis in rheumatoid arthritic synovial fibroblastic E11 cells. *Molecules* 18, 14085–14095. doi: 10.3390/molecules181114085

Christmas, B. J., Rafie, C. I., Hopkins, A. C., Scott, B. A., Ma, H. S., Cruz, K. A., et al. (2018). Entinostat converts immune-resistant breast and pancreatic cancers into checkpoint-responsive tumors by reprogramming tumor-infiltrating MDSCs. *Cancer Immunol. Res.* 6, 1561–1577. doi: 10.1158/2326-6066.CIR-18-0070

Connolly, R. M., Rudek, M. A., and Piekarz, R. (2017). Entinostat: a promising treatment option for patients with advanced breast cancer. *Future Oncol.* 13, 1137–1148. doi: 10.2217/fon-2016-2526

Darvin, P., Toor, S. M., Sasidharan Nair, V., and Elkord, E. (2018). Immune checkpoint inhibitors: recent progress and potential biomarkers. *Exp. Mol. Med.* 50:165. doi: 10.1038/s12276-018-0191-191

Dutta, P., Sarkissyan, M., Paico, K., Wu, Y., and Vadgama, J. V. (2018). MCP-1 is overexpressed in triple-negative breast cancers and drives cancer invasiveness and metastasis. *Breast Cancer Res. Treat.* 170, 477–486. doi: 10.1007/s10549-018-4760-8

Eisenhauer, E. A., Therasse, P., Bogaerts, J., Schwartz, L. H., Sargent, D., Ford, R., et al. (2009). New response evaluation criteria in solid tumours: revised RECIST guideline (version 1.1). *Eur. J. Cancer* 45, 228–247. doi: 10.1016/j.ejca.2008.10.026

Eladdadi, A., Pillis, L. D., and Kim, P. (2018). Modelling tumour–immune dynamics, disease progression and treatment. *Lett. Biomath.* 5, S1–S5. doi: 10.1080/23737867.2018.1483003

Emens, L. A. (2018). Breast cancer immunotherapy: facts and hopes. *Clin. Cancer Res.* 24, 511–520. doi: 10.1158/1078-0432.CCR-16-3001

Feng, Y., Masson, E., Dai, D., Parker, S. M., Berman, D., and Roy, A. (2014). Model-based clinical pharmacology profiling of ipilimumab in patients with advanced melanoma. *Br. J. Clin. Pharmacol.* 78, 106–117. doi: 10.1111/bcp.12323

Gallagher, S. J., Shklovskaya, E., and Hersey, P. (2017). Epigenetic modulation in cancer immunotherapy. *Curr. Opin. Pharmacol.* 35, 48–56. doi: 10.1016/j.coph.2017.05.006

Gameiro, S. R., Malamas, A. S., Tsang, K. Y., Ferrone, S., and Hodge, J. W. (2016). Inhibitors of histone deacetylase 1 reverse the immune evasion phenotype to enhance T-cell mediated lysis of prostate and breast carcinoma cells. *Oncotarget* 7, 7390–7402. doi: 10.18632/oncotarget.7180

Gasthuys, E., Vermeulen, A., Croubels, S., Millecam, J., Schauvliege, S., van Bergen, T., et al. (2018). Population pharmacokinetic modeling of a desmopressin oral lyophilisate in growing piglets as a model for the pediatric population. *Front. Pharmacol.* 9:41. doi: 10.3389/fphar.2018.00041

Gojo, I., Jiemjit, A., Trepel, J. B., Sparreboom, A., Figg, W. D., Rollins, S., et al. (2007). Phase 1 and pharmacologic study of MS-275, a histone deacetylase inhibitor, in adults with refractory and relapsed acute leukemias. *Blood* 109, 2781–2790. doi: 10.1182/blood-2006-05-021873

Gonda, K., Shibata, M., Ohtake, T., Matsumoto, Y., Tachibana, K., Abe, N., et al. (2017). Myeloid-derived suppressor cells are increased and correlated with type 2 immune responses, malnutrition, inflammation, and poor prognosis in patients with breast cancer. *Oncol. Lett.* 14, 1766–1774. doi: 10.3892/ol.2017.6305

Gore, L., Rothenberg, M. L., O'Bryant, C. L., Schultz, M. K., Sandler, A. B., Coffin, D., et al. (2008). A phase I and pharmacokinetic study of the oral histone deacetylase inhibitor, MS-275, in patients with refractory solid tumors and lymphomas. *Clin. Cancer Res.* 14, 4517–4525. doi: 10.1158/1078-0432.CCR-07-1461

Harms, B. D., Kearns, J. D., Iadevaia, S., and Lugovskoy, A. A. (2014). Understanding the role of cross-arm binding efficiency in the activity of monoclonal and multispecific therapeutic antibodies. *Methods* 65, 95–104. doi: 10.1016/j.ymeth.2013.07.017

Hartley, G. P., Chow, L., Ammons, D. T., Wheat, W. H., and Dow, S. W. (2018). Programmed cell death ligand 1 (PD-L1) signaling regulates macrophage proliferation and activation. *Cancer Immunol. Res.* 6, 1260–1273. doi: 10.1158/2326-6066.CIR-17-0537

Hellmann, M., Jänne, P., Opyrchal, M., Hafez, N., Raez, L., Gabrilovich, D., et al. (2018). OA05.*01* efficacy/safety of entinostat (ENT) and pembrolizumab (PEMBRO) in NSCLC patients previously treated with anti-PD-(L)1 therapy. *J. Thorac. Oncol.* 13:S330. doi: 10.1016/j.jtho.2018.08.257

Huang, B., Lei, Z., Zhao, J., Gong, W., Liu, J., Chen, Z., et al. (2007). CCL2/CCR2 pathway mediates recruitment of myeloid suppressor cells to cancers. *Cancer Lett.* 252, 86–92. doi: 10.1016/j.canlet.2006.12.012

Hu-Lieskovan, S., and Ribas, A. (2017). New combination strategies using programmed cell death 1/programmed cell death ligand 1 checkpoint inhibitors as a backbone. *Cancer J.* 23, 10–22. doi: 10.1097/PPO.0000000000000246

Ingram, J. R., Blomberg, O. S., Rashidian, M., Ali, L., Garforth, S., Fedorov, E., et al. (2018). Anti-CTLA-4 therapy requires an Fc domain for efficacy. *Proc. Natl. Acad. Sci. U.S.A.* 115, 3912–3917. doi: 10.1073/pnas.1801524115

Jafarnejad, M., Gong, C., Gabrielson, E., Bartelink, I. H., Vicini, P., Wang, B., et al. (2019). A computational model of neoadjuvant PD-1 inhibition in non-small cell lung cancer. *AAPS J.* 21:79. doi: 10.1208/s12248-019-0350-x

Jansson, A., Barnes, E., Klenerman, P., Harlen, M., Sorensen, P., Davis, S. J., et al. (2005). A theoretical framework for quantitative analysis of the molecular basis of costimulation. *J. Immunol.* 175, 1575–1585. doi: 10.4049/jimmunol.175.3.1575

Kassambara, A. (2019). *Ggpubr: 'ggplot2' Based Publication Ready Plots. R Package Version 0.2.2.*

Kato, Y., Yoshino, I., Egusa, C., Maeda, T., Pili, R., and Tsuboi, R. (2014). Combination of HDAC inhibitor MS-275 and IL-2 increased anti-tumor effect in a melanoma model via activated cytotoxic T cells. *J. Dermatol. Sci.* 75, 140–147. doi: 10.1016/j.jdermsci.2014.04.014

Kim, K., Skora, A. D., Li, Z., Liu, Q., Tam, A. J., Blosser, R. L., et al. (2014). Eradication of metastatic mouse cancers resistant to immune checkpoint blockade by suppression of myeloid-derived cells. *Proc. Natl. Acad. Sci. U.S.A.* 111, 11774–11779. doi: 10.1073/pnas.1410626111

Kumar, V., Patel, S., Tcyganov, E., and Gabrilovich, D. I. (2016). The nature of myeloid-derived suppressor cells in the tumor microenvironment. *Trends Immunol.* 37, 208–220. doi: 10.1016/j.it.2016.01.004

Kummar, S., Gutierrez, M., Gardner, E. R., Donovan, E., Hwang, K., Chung, E. J., et al. (2007). Phase I trial of MS-275, a histone deacetylase inhibitor, administered weekly in refractory solid tumors and lymphoid malignancies. *Clin. Cancer Res.* 13(18 Pt 1), 5411–5417. doi: 10.1158/1078-0432.CCR-07-0791

Lee, B. I., Park, S. H., Kim, J. W., Sausville, E. A., Kim, H. T., Nakanishi, O., et al. (2001). MS-275, a histone deacetylase inhibitor, selectively induces transforming growth factor beta type II receptor expression in human breast cancer cells. *Cancer Res.* 61, 931–934.

Lever, M., Maini, P. K., van der Merwe, P. A., and Dushek, O. (2014). Phenotypic models of T cell activation. *Nat. Rev. Immunol.* 14, 619–629. doi: 10.1038/nri3728

Li, B., Li, T., Pignon, J. C., Wang, B., Wang, J., Shukla, S. A., et al. (2016). Landscape of tumor-infiltrating T cell repertoire of human cancers. *Nat. Genet.* 48, 725–732. doi: 10.1038/ng.3581

Li, X., Jolly, M. K., George, J. T., Pienta, K. J., and Levine, H. (2019). Computational modeling of the crosstalk between macrophage polarization and tumor cell plasticity in the tumor microenvironment. *Front. Oncol.* 9:10. doi: 10.3389/fonc.2019.00010

Mahlbacher, G., Curtis, L. T., Lowengrub, J., and Frieboes, H. B. (2018). Mathematical modeling of tumor-associated macrophage interactions with the cancer microenvironment. *J. Immunother. Cancer* 6:10. doi: 10.1186/s40425-017-0313-317

Mahlbacher, G. E., Reihmer, K. C., and Frieboes, H. B. (2019). Mathematical modeling of tumor-immune cell interactions. *J. Theor. Biol.* 469, 47–60. doi: 10.1016/j.jtbi.2019.03.002

Marchingo, J. M., Kan, A., Sutherland, R. M., Duffy, K. R., Wellard, C. J., Belz, G. T., et al. (2014). T cell signaling. Antigen affinity, costimulation, and cytokine inputs sum linearly to amplify T cell expansion. *Science* 346, 1123–1127. doi: 10.1126/science.1260044

Marino, S., Hogue, I. B., Ray, C. J., and Kirschner, D. E. (2008). A methodology for performing global uncertainty and sensitivity analysis in systems biology. *J. Theor. Biol.* 254, 178–196. doi: 10.1016/j.jtbi.2008.04.011

Markowitz, J., Wesolowski, R., Papenfuss, T., and Brooks, T. R. (2013). Myeloid-derived suppressor cells in breast cancer. *Breast Cancer Res. Treat.* 140, 13–21. doi: 10.1007/s10549-013-2618-2617

Marra, A., Viale, G., and Curigliano, G. (2019). Recent advances in triple negative breast cancer: the immunotherapy era. *BMC Med.* 17:90. doi: 10.1186/s12916-019-1326-1325

Matikas, A., Zerdes, I., Lovrot, J., Richard, F., Sotiriou, C., Bergh, J., et al. (2019). Prognostic implications of PD-L1 expression in breast cancer: systematic review and meta-analysis of immunohistochemistry and pooled analysis of transcriptomic Data. *Clin. Cancer Res.* 25, 5717–5726. doi: 10.1158/1078-0432.CCR-19-1131

Milberg, O., Gong, C., Jafarnejad, M., Bartelink, I. H., Wang, B., Vicini, P., et al. (2019). A QSP model for predicting clinical responses to monotherapy, combination and sequential therapy following CTLA-4, PD-1, and PD-L1 checkpoint blockade. *Sci. Rep.* 9:11286. doi: 10.1038/s41598-019-47802-47804

Nijsen, M., Wu, F., Bansal, L., Bradshaw-Pierce, E., Chan, J. R., Liederer, B. M., et al. (2018). Preclinical QSP modeling in the pharmaceutical industry: an IQ consortium survey examining the current landscape. *CPT Pharmacometr. Syst. Pharmacol.* 7, 135–146. doi: 10.1002/psp4.12282

Orillion, A., Hashimoto, A., Damayanti, N., Shen, L., Adelaiye-Ogala, R., Arisa, S., et al. (2017). Entinostat neutralizes myeloid-derived suppressor cells and enhances the antitumor effect of PD-1 inhibition in murine models of lung and renal cell carcinoma. *Clin. Cancer Res.* 23, 5187–5201. doi: 10.1158/1078-0432.CCR-17-0741

Park, M. J., Lee, S. H., Kim, E. K., Lee, E. J., Baek, J. A., Park, S. H., et al. (2018). Interleukin-10 produced by myeloid-derived suppressor cells is critical for the induction of Tregs and attenuation of rheumatoid inflammation in mice. *Sci. Rep.* 8:3753. doi: 10.1038/s41598-018-21856-21852

Pili, R., Quinn, D. I., Hammers, H. J., Monk, P., George, S., Dorff, T. B., et al. (2017). Immunomodulation by entinostat in renal cell carcinoma patients receiving high-dose interleukin 2: a multicenter, single-arm, phase I/II Trial (NCI-CTEP#7870). *Clin. Cancer Res.* 23, 7199–7208. doi: 10.1158/1078-0432.CCR-17-1178

Pitt, J. M., Vetizou, M., Daillere, R., Roberti, M. P., Yamazaki, T., Routy, B., et al. (2016). Resistance mechanisms to immune-checkpoint blockade in cancer: tumor-intrinsic and -extrinsic factors. *Immunity* 44, 1255–1269. doi: 10.1016/j.immuni.2016.06.001

Planes-Laine, G., Rochigneux, P., Bertucci, F., Chretien, A. S., Viens, P., Sabatier, R., et al. (2019). PD-1/PD-L1 targeting in breast cancer: the first clinical evidences are emerging. a literature review. *Cancers* 11:1033. doi: 10.3390/cancers11071033

Richards, J. O., Karki, S., Lazar, G. A., Chen, H., Dang, W., and Desjarlais, J. R. (2008). Optimization of antibody binding to FcgammaRIIa enhances macrophage phagocytosis of tumor cells. *Mol. Cancer Ther.* 7, 2517–2527. doi: 10.1158/1535-7163.MCT-08-0201

Rieger, T. R., Allen, R. J., Bystricky, L., Chen, Y., Colopy, G. W., Cui, Y., et al. (2018). Improving the generation and selection of virtual populations in quantitative systems pharmacology models. *Prog. Biophys. Mol. Biol.* 139, 15–22. doi: 10.1016/j.pbiomolbio.2018.06.002

Romano, E., Kusio-Kobialka, M., Foukas, P. G., Baumgaertner, P., Meyer, C., Ballabeni, P., et al. (2015). Ipilimumab-dependent cell-mediated cytotoxicity of regulatory T cells ex vivo by nonclassical monocytes in melanoma patients. *Proc. Natl. Acad. Sci. U.S.A.* 112, 6140–6145. doi: 10.1073/pnas.1417320112

Ryan, Q. C., Headlee, D., Acharya, M., Sparreboom, A., Trepel, J. B., Ye, J., et al. (2005). Phase I and pharmacokinetic study of MS-275, a histone deacetylase inhibitor, in patients with advanced and refractory solid tumors or lymphoma. *J. Clin. Oncol.* 23, 3912–3922. doi: 10.1200/JCO.2005.02.188

Ryu, Y., Kee, H. J., Sun, S., Seok, Y. M., Choi, S. Y., Kim, G. R., et al. (2019). Class I histone deacetylase inhibitor MS-275 attenuates vasoconstriction and inflammation in angiotensin II-induced hypertension. *PLoS One* 14:e0213186. doi: 10.1371/journal.pone.0213186

Saito, A., Yamashita, T., Mariko, Y., Nosaka, Y., Tsuchiya, K., Ando, T., et al. (1999). A synthetic inhibitor of histone deacetylase, MS-27-275, with marked in vivo antitumor activity against human tumors. *Proc. Natl. Acad. Sci. U.S.A.* 96, 4592–4597. doi: 10.1073/pnas.96.8.4592

Serafini, P., Mgebroff, S., Noonan, K., and Borrello, I. (2008). Myeloid-derived suppressor cells promote cross-tolerance in B-cell lymphoma by expanding regulatory T cells. *Cancer Res.* 68, 5439–5449. doi: 10.1158/0008-5472.CAN-07-6621

Sharma, A., Subudhi, S. K., Blando, J., Vence, L., Wargo, J., Allison, J. P., et al. (2019). Anti-CTLA-4 immunotherapy does not deplete FOXP3(+) regulatory T cells (Tregs) in human cancers-response. *Clin. Cancer Res.* 25, 3469–3470. doi: 10.1158/1078-0432.CCR-19-0402

Sheikhpour, E., Noorbakhsh, P., Foroughi, E., Farahnak, S., Nasiri, R., and Neamatzadeh, H. (2018). A survey on the role of interleukin-10 in breast cancer: a narrative. *Rep. Biochem. Mol. Biol.* 7, 30–37.

Sugiura, D., Maruhashi, T., Okazaki, I. M., Shimizu, K., Maeda, T. K., Takemoto, T., et al. (2019). Restriction of PD-1 function by cis-PD-L1/CD80 interactions is required for optimal T cell responses. *Science* 364, 558–566. doi: 10.1126/science.aav7062

Takada, K., Kashiwagi, S., Goto, W., Asano, Y., Takahashi, K., Takashima, T., et al. (2018). Use of the tumor-infiltrating CD8 to FOXP3 lymphocyte ratio in predicting treatment responses to combination therapy with pertuzumab, trastuzumab, and docetaxel for advanced HER2-positive breast cancer. *J. Transl. Med.* 16:86. doi: 10.1186/s12967-018-1460-1464

Tang, F., Du, X., Liu, M., Zheng, P., and Liu, Y. (2018). Anti-CTLA-4 antibodies in cancer immunotherapy: selective depletion of intratumoral regulatory T cells or checkpoint blockade? *Cell. Biosci.* 8:30. doi: 10.1186/s13578-018-0229-z

Terry, S., Savagner, P., Ortiz-Cuaran, S., Mahjoubi, L., Saintigny, P., Thiery, J. P., et al. (2017). New insights into the role of EMT in tumor immune escape. *Mol. Oncol.* 11, 824–846. doi: 10.1002/1878-0261.12093

Thomas, A., Routh, E. D., Pullikuth, A., Jin, G., Su, J., Chou, J. W., et al. (2018). Tumor mutational burden is a determinant of immune-mediated survival in breast cancer. *Oncoimmunology* 7:e1490854. doi: 10.1080/2162402X.2018.1490854

Tomita, Y., Lee, M. J., Lee, S., Tomita, S., Chumsri, S., Cruickshank, S., et al. (2016). The interplay of epigenetic therapy and immunity in locally recurrent or metastatic estrogen receptor-positive breast cancer: correlative analysis of ENCORE 301, a randomized, placebo-controlled phase II trial of exemestane with or without entinostat. *Oncoimmunology* 5:e1219008. doi: 10.1080/2162402X.2016.1219008

Vikas, P., Borcherding, N., and Zhang, W. (2018). The clinical promise of immunotherapy in triple-negative breast cancer. *Cancer Manag. Res.* 10, 6823–6833. doi: 10.2147/CMAR.S185176

Wang, H., Milberg, O., Bartelink, I. H., Vicini, P., Wang, B., Narwal, R., et al. (2019). In silico simulation of a clinical trial with anti-CTLA-4 and anti-PD-L1 immunotherapies in metastatic breast cancer using a systems pharmacology model. *R. Soc. Open Sci.* 6:190366. doi: 10.1098/rsos.190366

Wei, S. C., Duffy, C. R., and Allison, J. P. (2018). Fundamental mechanisms of immune checkpoint blockade therapy. *Cancer Discov.* 8, 1069–1086. doi: 10.1158/2159-8290.CD-18-0367

Yarchoan, M., Hopkins, A., and Jaffee, E. M. (2017). Tumor mutational burden and response rate to PD-1 inhibition. *N. Engl. J. Med.* 377, 2500–2501. doi: 10.1056/NEJMc1713444

Yardley, D. A., Ismail-Khan, R. R., Melichar, B., Lichinitser, M., Munster, P. N., Klein, P. M., et al. (2013). Randomized phase II, double-blind, placebo-controlled study of exemestane with or without entinostat in postmenopausal women with locally recurrent or metastatic estrogen receptor-positive breast cancer progressing on treatment with a nonsteroidal aromatase inhibitor. *J. Clin. Oncol.* 31, 2128–2135. doi: 10.1200/JCO.2012.43.7251

Yeruva, S. L. H., Zhao, F., Miller, K. D., Tevaarwerk, A. J., Wagner, L. I., Gray, R. J., et al. (2018). E2112: randomized phase iii trial of endocrine therapy plus entinostat/placebo in patients with hormone receptor-positive advanced breast cancer. *NPJ Breast Cancer* 4:1. doi: 10.1038/s41523-017-0053-53

Zhao, C., Mirando, A. C., Sove, R. J., Medeiros, T. X., Annex, B. H., and Popel, A. S. (2019). A mechanistic integrative computational model of macrophage polarization: implications in human pathophysiology. *PLoS Comput. Biol.* 15:e1007468. doi: 10.1371/journal.pcbi.1007468

Conflict of Interest: RC has received research grants to institution from Novartis, Puma Biotechnology, Merck, Merrimack, Genentech, Macrogenics, and travel expenses from Genentech.

The remaining authors declare that the research was conducted in the absence of any commercial or financial relationships that could be construed as a potential conflict of interest.

Copyright © 2020 Wang, Sové, Jafarnejad, Rahmeh, Jaffee, Stearns, Torres, Connolly and Popel. This is an open-access article distributed under the terms of the Creative Commons Attribution License (CC BY). The use, distribution or reproduction in other forums is permitted, provided the original author(s) and the copyright owner(s) are credited and that the original publication in this journal is cited, in accordance with accepted academic practice. No use, distribution or reproduction is permitted which does not comply with these terms.

frontiers in Bioengineering and Biotechnology

ORIGINAL RESEARCH
published: 13 March 2020
doi: 10.3389/fbioe.2020.00195

A Novel Synthetic Model of the Glucose-Insulin System for Patient-Wise Inference of Physiological Parameters From Small-Size OGTT Data

Sebastián Contreras[1], *David Medina-Ortiz*[1,2], *Carlos Conca*[1] *and Álvaro Olivera-Nappa*[1,2]*

[1] *Centre for Biotechnology and Bioengineering (CeBiB), University of Chile, Santiago, Chile,* [2] *Department of Chemical Engineering, Biotechnology and Materials, Faculty of Physical and Mathematical Sciences, University of Chile, Santiago, Chile*

OPEN ACCESS

Edited by:
Julio R. Banga, Spanish National Research Council, Spain

Reviewed by:
Pavel Loskot, Swansea University, United Kingdom
Pasquale Palumbo, University of Milano-Bicocca, Italy

***Correspondence:**
Álvaro Olivera-Nappa
aolivera@ing.uchile.cl

Specialty section:
This article was submitted to Bioinformatics and Computational Biology, a section of the journal Frontiers in Bioengineering and Biotechnology

Received: *20 December 2019*
Accepted: *27 February 2020*
Published: *13 March 2020*

Citation:
Contreras S, Medina-Ortiz D, Conca C and Olivera-Nappa Á (2020) A Novel Synthetic Model of the Glucose-Insulin System for Patient-Wise Inference of Physiological Parameters From Small-Size OGTT Data. Front. Bioeng. Biotechnol. 8:195. doi: 10.3389/fbioe.2020.00195

Existing mathematical models for the glucose-insulin (G-I) dynamics often involve variables that are not susceptible to direct measurement. Standard clinical tests for measuring G-I levels for diagnosing potential diseases are simple and relatively cheap, but seldom give enough information to allow the identification of model parameters within the range in which they have a biological meaning, thus generating a gap between mathematical modeling and any possible physiological explanation or clinical interpretation. In the present work, we present a synthetic mathematical model to represent the G-I dynamics in an Oral Glucose Tolerance Test (OGTT), which involves for the first time for OGTT-related models, Delay Differential Equations. Our model can represent the radically different behaviors observed in a studied cohort of 407 normoglycemic patients (the largest analyzed so far in parameter fitting experiments), all masked under the current threshold-based normality criteria. We also propose a novel approach to solve the parameter fitting inverse problem, involving the clustering of different G-I profiles, a simulation-based exploration of the feasible set, and the construction of an information function which reshapes it, based on the clinical records, experimental uncertainties, and physiological criteria. This method allowed an individual-wise recognition of the parameters of our model using small size OGTT data (5 measurements) directly, without modifying the routine procedures or requiring particular clinical setups. Therefore, our methodology can be easily applied to gain parametric insights to complement the existing tools for the diagnosis of G-I dysregulations. We tested the parameter stability and sensitivity for individual subjects, and an empirical relationship between such indexes and curve shapes was spotted. Since different G-I profiles, under the light of our model, are related to different physiological mechanisms, the present method offers a tool for personally-oriented diagnosis and treatment and to better define new health criteria.

Keywords: mathematical modeling, glucose-insulin control, OGTT, inverse problems, personalized medicine

INTRODUCTION

Disequilibriums in the glucose-insulin (G-I) dynamics, as in diabetes, insulin resistance, glucose intolerance, among others, are a widespread condition in modern society (Cobelli et al., 2009; Ajmera et al., 2013; Hu et al., 2015; Toniolo et al., 2018). For this reason, the mathematical modeling of the G-I control system has been frequently visited, as shown by the wide variety of models presented in numerous reviews published to date (Bergman, 2005; Boutayeb and Chetouani, 2006; Makroglou et al., 2006; Palumbo et al., 2013; Cobelli et al., 2014).

For modeling purposes, we may understand the G-I dynamics as follows. The digestion of macronutrients generates glucose (among others nutrients), which enterocytes absorb into the bloodstream in the upper intestinal tract. The blood glucose concentration increase caused by glucose absorption induces pancreatic β-cells to secrete insulin in different timescales: early insulin release, signaled by the incretin hormones (secreted from intestinal enterocytes), is achieved by emptying the contents of the vacuoles in the β-cells. After that source is depleted, insulin production follows a saturable dynamics. Insulin signals the uptake of glucose from peripheral tissues (mainly muscle and adipose tissue), which metabolize it to obtain energy or to synthesize storage macromolecules, and the decrease of glucose release from the liver. If blood glucose levels are too low, pancreatic glucagon-induced hepatic glucose release restores the steady-state homeostatic level.

Some typical routine tests employed for the diagnosis of G-I-related dysregulations are the Oral Glucose Tolerance Test (OGTT) and the Meal Test (MT), which are widely used given their clinical simplicity and low cost. In OGTT, a fasting patient ingests a 75 g-controlled dose of liquid glucose (Bartoli et al., 2011), while in MT a controlled meal with known glycemic index (such as rice) is given to a patient. In both tests, glycemia is measured at different times. Typically, such measurements take place at time 0 (fasting) and 2 h after the ingestion of glucose, but more temporal resolution might be required, or other physiological variables measured, depending on how strict clinical criteria are. Moreover, efforts have been made to modify and standardize the temporal resolution and duration of the tests (Bergman et al., 2018). Besides the clinical interpretation of the OGTT and MT values, some model-derived indexes can be obtained, as is the case of the Insulin Sensitivity S_I, derived from the very well known Minimal Model (Bergman et al., 1979). The insulin sensitivity S_I quantifies the ability of insulin to increase the effect of glucose on its own disappearance in a steady state. From Bergman's Minimal Model, mathematical models of the G-I dynamics have evolved, increasing their complexity and aiming to different objectives.

Stumvoll et al. (2000) presented an empirical approach based on correlations to determine S_I from OGTT curves. Mari et al. (2001) proposed a parametric approach to obtain this index, studying a population of 104 individuals with different clinical classification. High correlations between results for S_I calculated from the model vs. direct measurement for the full patient sample suggested the applicability of the OGTT to obtain clinically relevant parameters and perform large scale studies. Caumo et al. (2000) and Dalla Man et al. (2002, 2004, 2006) focused their efforts on modeling glucose absorption from the digestive system into the bloodstream, making differences between OGTT and MT. However, parametric identifiability in their models required the *a priori* knowledge of average values of some parameters of the sample, assumed equal and constant for all individuals. The number of patients (88) in Dalla Man et al. (2004) allowed to determine the non-Gaussian distributions of some of the parameters. Later, Dalla Man et al. (2007) presented a nested sub-systems model, fitting its parameters to a population of 204 clinically healthy individuals that underwent a MT. Reflecting on its complexity, the authors suggested to use this model only as a simulator. Following the trend of previous minimal models, this model also leaves out equations for other regulatory hormones such as glucagon, epinephrine, growth hormone, and incretins, which regain importance in other works (Brubaker et al., 2007; Silber et al., 2010; Mari et al., 2013).

Salinari et al. (2011) presented a model in which the intestinal absorption of glucose is obtained as a solution of a transport partial differential equation, where glucose is progressively absorbed while passing through the intestine, and stomach emptying is assumed to be exponential. Subsequently, De Gaetano et al. (2013) presented an extension of the classic minimal model, modeling the gastrointestinal tract as four compartments, coupled with first-order kinetics. Besides, the authors proposed fixed forms for hepatic glucose production and incretin action, without clear physiological justification or supporting background, and in disagreement with the state of the art (Silber et al., 2010). The patient sample analyzed in De Gaetano et al. (2013) comprised 78 patients with different clinical classifications, and parameters were fitted to whole groups of patients according to each clinical criterion, reporting statistical differences for insulin sensitivity between different groups.

The importance of the development of mathematical models for the study of the G-I control system lies in the potential to serve as support for clinical diagnostic tools in the detection of type II diabetes, insulin resistance, glucose intolerance, among other dysregulations of the G-I control system. However, at present, these models do not manage to effectively capture the differences that exist between patients in the way of achieving glycemic control (reflected as morphological variations in OGTT response curves), and do not represent it as a difference in the involved parameters that can be interpreted according to clinical criteria. Additionally, the more complex models mentioned above have not been used to infer physiological parameters for an individual patient from an OGTT, since they have only been used to calculate average parameters in a group of patients, or required special clinical setups to obtain the data needed for fitting them. This is partly due to the intrinsic complexity of the models and the number of parameters involved, but also to the lack of a numerical procedure for parameter fitting. Therefore, a mathematical model capable of accounting for different physiological states and applicable as a tool for clinical diagnosis becomes necessary for personalized medicine.

In the present work, we present a synthetic mathematical model to represent the G-I dynamics in OGTT using Delay Differential Equations (DDE), in which each parameter describes a single physiological phenomenon. To the best knowledge of the authors, this is the first DDE model involved in describing OGTT dynamics, including the mutual interrelation between glucose and insulin. The structure of the model allowed for representation of every observed qualitative dynamic behavior in our cohort, regardless of the number, height or location of the glucose and insulin peaks. Using a novel information-based approach we achieved an individual-wise parameter fitting using the five glycemia and insulinemia points of a routine OGTT directly, for a cohort of 407 patients that underwent a 75-g OGTT, which is the largest cohort analyzed so far for this end. We also show that there are different controlling behaviors within the clinical normality thresholds, accounting for different physiological mechanisms to achieve glycemic control. Given that parameter fitting is individual, it would be possible to classify each patient within different groups, suggesting that different dysregulated mechanisms require different corrections, thus transforming the proposed model and fitting procedure into a tool for preventive clinical diagnosis and personalized medicine.

MATERIALS AND METHODS

A cohort of 407 volunteers was used for testing the capabilities of our model and our patient-wise parameter recognition methodology. All volunteers gave their informed consent to use their OGTT data in this study. All volunteers in this sample were clinically healthy according to criteria used in Chile, in strict clinical settings to characterize normoglycemic patients. According to these criteria, a patient who has basal (stable overnight) glycemia lower than 100 mg/dL, basal insulinemia lower than 15 μU/mL, glycemia values not exceeding 160 mg/dL at any time and not persisting at values higher than 140 mg/dL over 2 h, and insulinemia not persisting at values higher than 60 μU/mL for a continuous time period of 120 min, would be classified as normal. Approximately 80% of the cohort corresponded to female patients, with ages ranging between 18 and 65 years-old. Nevertheless, no statistical sex-related difference was found within the cohort. Every patient underwent an OGTT with five measurements for both glycemia and insulinemia: fasting (basal state) and every 30 min, for 2 h. Further description of the data, as statistical properties, histograms of the measurements at every time and of the age distribution are presented in Supplementary Material (**Table S1** and **Figures S1**, **S2**, respectively).

We identified many radically different G-I profiles among the population. Examples of them are hypoglycemic individuals, single/double peak patients, and those with practically invariant G-I profiles, as shown in **Figure 1**. In **Figure 1**, the solid lines correspond to a spline interpolation of the experimental measurements, which are marked with solid diamonds of the same color. These different OGTT profiles could account for diverse physiological states related to gastric emptying, intestinal absorption, or other components of the glycemic control system, masking pre-disease conditions under the concept of normality. Therefore, as currently defined, to identify the physiological background behind a clinically healthy or unhealthy individual seems to be an ill-posed inverse problem.

The implementation of the mathematical model and resolution of the parameter-fitting inverse problem was performed in Matlab version R2017a, using the Global Optimization Toolbox. All scripts and routines for parameter fitting were run on the Chilean National Laboratory for High-Performance Computation (NLHPC) servers, using BASH-based control scripts.

RESULTS

Synthetic OGTT Glycemia-Insulinemia Model

The synthetic model proposed in this work considers five main variables. Four of them represent the amount or concentration of glucose in different compartments: in the stomach S, in the upper intestinal tract J (jejunum) and L (ileum), and in the bloodstream (glycemia) G. The last variable accounts for the insulinemia I. These different variables interact as illustrated in the box diagram of **Figure 2**, in ways that will be further detailed in this section. We follow the notation of De Gaetano et al. (2013), but our model also considers the contributions of other works (Dalla Man et al., 2007; Salinari et al., 2011; De Gaetano et al., 2013), together with our own developments.

Figure 2 shows the interdependence of the different variables of the model. The gastrointestinal sections are decoupled from the blood G-I dynamics, which, as we will see, are connected in a very non-linear fashion. To obtain the G-I profiles of a particular individual, given all the parameters involved, it is necessary to solve the system of differential equations that we propose to model it. All the proposed constitutive equations may be found in this section, together with their physiological background and the reasons behind its mathematical formulation. A summary of the model is presented in the last subsection and a detailed list of its parameters and variables can be found in **Tables S2**, **S3**.

Gastrointestinal System

To mathematically represent the stomach emptying for a liquid bolus, we assume its rate $v_s = \frac{dS}{dt}$ to be directly proportional to the content of glucose at every time, $S(t)$, as Equation (1) shows:

$$\frac{dS}{dt} = -k_{js}S, \qquad S(0) = D, \tag{1}$$

where k_{js} is a first-order kinetic constant, D the ingested glucose bolus in an OGTT (75 g), and the minus sign accounts for the disappearance of glucose, hence the emptying of the stomach. The glucose that leaves the stomach appears in the jejunum J, being a source term in the rate (Equation 2).

As absorption of glucose may take place in this section of the small intestine, we may close the mass balance noting that the glucose that is not absorbed will continue its way, being transported to the ileum L.

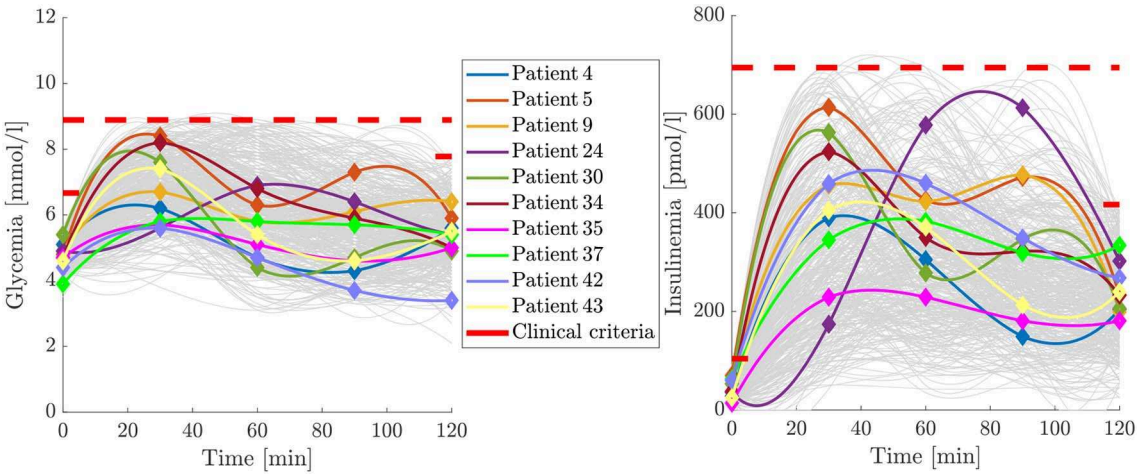

FIGURE 1 | Some of the different G-I profiles encompassed under the clinical normality criterion. Continuous curves are spline interpolations of the diamond marked experimental trends. Note that similar glycemia curves are not necessarily associated with similar insulinemia curves, and a single-peak profile in glycemia is not necessarily associated with a single-peak insulinemia profile. Upper clinical normality criteria are represented as red limits for the basal and last points and for the entire OGTT time span.

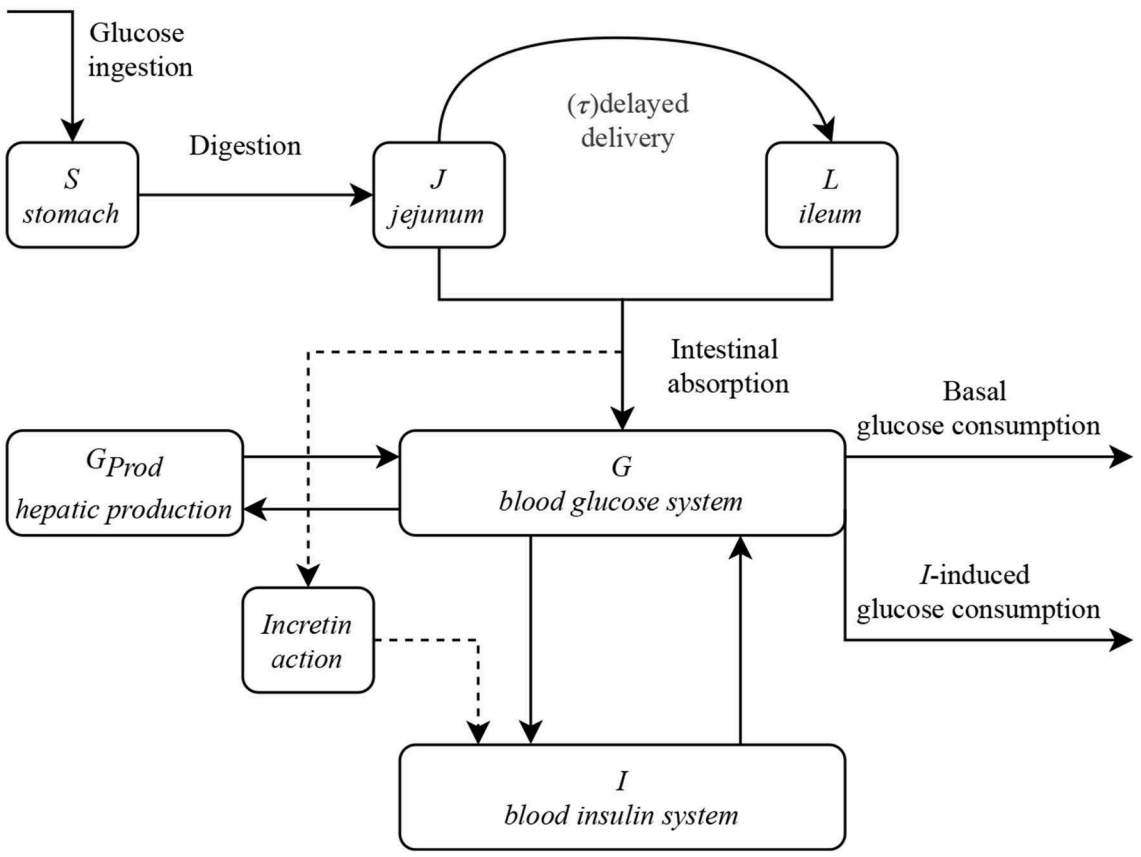

FIGURE 2 | Box diagram of the proposed model and the interactions between the different compartments and variables. The gastrointestinal tract, namely variables *S*, *J*, and *L*, are decoupled from the blood G-I dynamics.

$$\frac{dJ}{dt} = \underbrace{k_{js}S}_{\text{Stomach delivery}} - \underbrace{k_{gj}J}_{\text{Absorption into the bloodstream}} - \underbrace{k_{jl}J}_{\text{Delivery to } L}, \quad J(0) = 0 \tag{2}$$

The structure of our model, from this point and further, is significantly different from the one presented in De Gaetano et al. (2013). De Gaetano et al. (2013) suggested that to represent the effect of intestinal transit between jejunum and ileum, a virtual compartment R can be added in between, where absorption does not occur. Nevertheless, the equations proposed to reach such objective are not entirely appropriate for representing different curve shapes, especially those curves with delayed 2-peak dynamics with equal peak height and width or a higher second peak (see **Figure 1**).

Here we decided to follow the formalism presented by Salinari et al. (2011) to represent intestinal transit. Taking into account the peristalsis-driven intestinal transit mechanism, we can assume there is no mixing in the axial axis. Hence, we model the flow through the intestine as a plug-flow reactor with uniform velocity U. To represent the distribution of glucose transporters along the small intestine, we assume that absorption occurs in two separated areas of the intestine, the jejunum and the ileum, located at a distance l, so the time it takes for the ileum to receive glucose transiting from the jejunum is $\tau := l/U$. Consequently, instead of having a spatial partial differential equation for intestinal absorption, we have two ordinary differential equations, one for the jejunum (Equation 2) and one for the ileum, the last one having a $\tau-$delayed forcing function (Equation 3).

$$\frac{dL}{dt} = \underbrace{k_{jl}\varphi(t)}_{\text{Delayed contribution from } J} - \underbrace{k_{gl}L(t)}_{\text{Absorption into the bloodstream}}, \qquad \varphi(t) = \begin{cases} 0, & \text{if } t < \tau \\ J(t-\tau), & \text{if } t \geq \tau \end{cases} \tag{3}$$

where k_{jl} and k_{gl} are first-order kinetic constants, respectively, accounting for the rate of jejunal glucose delivery and the glucose absorption into the bloodstream.

Blood Glucose Dynamics

To represent variations in glycemia, our model contemplates the following control mechanisms. As source terms in the glycemia equation, we considered the intestinal absorption of glucose adjusted by glucose bioavailability (η), following the form presented in Dalla Man et al. (2002), and the hepatic contribution to glucose homeostasis (G_{prod}), which indirectly accounts for the action of glucagon. The sink terms in the equation represent glucose uptake by insulin-insensitive tissues and renal excretion, which is proportional to G, and insulin-driven consumption of glucose, taking place in insulin-sensitive tissues, which is proportional to GI. Equation (4) represents mathematically the glycemia dynamics.

$$\frac{dG}{dt} = \underbrace{-k_{xg}G}_{\text{Basal uptake}} - \underbrace{k_{xgi}GI}_{\text{Insulin-sensitive uptake}} + \underbrace{G_{\text{prod}}}_{\text{Hepatic delivery}} + \underbrace{\eta\left(k_{gj}J + k_{gl}L\right)}_{\text{Intestinal absorption}}, \qquad G(0) = G_b \tag{4}$$

where k_{xg} is the insulin-independent glucose uptake rate, k_{xgi} is the uptake rate of insulin-sensitive tissues, η is the bioavailability of the intestinal absorbed glucose, and G_{prod} is the rate of hepatic glucose production.

Hepatic Glucose Production Function

We implicitly incorporated the effect of glucagon into a hepatic glucose production function, which is an always positive term that contributes to the equation of blood glucose dynamics. Previous works model this contribution with exponential functions (De Gaetano et al., 2013; Erlandsen et al., 2018), without a solid physiological background but rather a mathematical convenience. However, when analyzing the functional nature of such expressions, we realize that the differential mechanism is not entirely clear since the function derivative cannot be written as a function of itself. Therefore, no reliable physiological mechanism supports the form of such rate functions. We propose G_{prod} as the complement of a Monod-like equation, which is typically used to model problems of saturable growth, production, enzymatic reaction and receptor/ligand interaction or transport:

$$G_{\text{prod}} = \frac{k_\lambda}{k_2 + G}, \tag{5}$$

As defined above, G_{prod} is also the solution of the mechanism given by Equation (6), which represents a logistic hyperbolic production with an asymptotic maximum rate (see derivation in **Supplementary Material**).

$$\frac{dG_{\text{prod}}}{dG} = -\frac{G_{\text{prod}}}{G}\left(1 - \frac{k_2}{k_\lambda}G_{\text{prod}}\right), \tag{6}$$

By imposing steady-state conditions $G_{\text{prod}}(G_b) = G^0_{\text{prod}}$, k_2 can be written as a function of the other variables, resulting in Equation (7), i.e., a saturable Michaelis-Menten-like kinetics much more representative of the physiological background of cellular processes. Noticeably, even though the rate Equation (6) does not include any set point, the integrated steady-state hepatic glucose production (Equation 7) explicitly depends on the difference between glycemia and its base level (see derivation in **Supplementary Material**).

$$G_{\text{prod}} = \frac{k_\lambda}{\frac{k_\lambda}{G^0_{\text{prod}}} + (G - G_b)}. \tag{7}$$

Blood-Insulin Dynamics

For the blood-insulin system, following the model in De Gaetano et al. (2013), we propose a Hill's dynamics for pancreatic secretion (Goutelle et al., 2008), and an I-proportional degradation term. Noteworthy, these dynamics exhibit a saturation behavior since it is formulated exclusively for OGTT circumstances. However, we corrected the mathematical form of the incretin action suggested in De Gaetano et al. (2013). De Gaetano et al. (2013) assumed that incretin secretion is proportional to glucose levels within the intestinal lumen. Nonetheless, it has been shown that it rather depends on the rate of absorption of glucose from the intestinal lumen (Silber et al., 2010). Therefore, we corrected this in Equation (8):

$$\tilde{G} = G + f_{gj}(k_{gj}J + k_{gl}L). \tag{8}$$

Equation (8) makes sense from a physiological point of view since intestinal epithelial cells are not able to sense the absolute amount of glucose in the intestine due to the lack of glucose sensor proteins, but their internal metabolic rates are directly dependent on the steady-state cytoplasmic concentration of glucose, which is proportional to glucose membrane transport through the cell. In this equation, f_{gj} is a conversion factor that indirectly links glucose absorption rate to insulin secretion rate through incretin action, thus representing the relative power of incretin action vs. direct glycemic action on the pancreas. Under these assumptions, Equation (9) gives the final expression for the insulin dynamics:

$$\frac{dI}{dt} = k_{xi}I_b\left(\frac{\beta^\gamma + 1}{\beta^\gamma\left(\frac{G_b}{\tilde{G}}\right)^\gamma + 1} - \frac{I}{I_b}\right) \tag{9}$$

where k_{xi} is a first-order kinetic constant for the insulin degradation in target tissues, β and γ are parameters for half saturation and acceleration of the insulin production, which account for first and second phase pancreatic secretion, $\tilde{G}$ the apparent G, enhanced by incretin action, and G_b, I_b the steady-state value of such variables.

Insulin Action on Glycemia and Insulin Sensitivity

Former mathematical models including insulin action were divided in models that considered a direct action of blood insulin on tissues to regulate glucose uptake and more complex models that considered an additional intermediate compartment. Such compartment represented the interstitial fluid in peripheral tissues, into which insulin was absorbed from the bloodstream following a first-order kinetics, and only then could exert its action. Mathematically, the effect of this formulation in the more complex models was the introduction of a small delay and a proportionality constant between concentrations in the bloodstream and the interstitial fluid, which caused a small decrease in peak height and slight broadening of peak width for insulin in the intermediate compartment compared to the bloodstream. Application of these models to experimental data demonstrated a minimal delay, in the range of a few minutes, between concentrations in the bloodstream and the intermediate active compartment. Taking into account that usual OGTT experiments take measures every 30 min and the registered G-I dynamics occur in the order of hours, this small delay was not included in the formulation of our model, because the time resolution might result too coarse to accurately calibrate such parameters. In this way, we only consider a direct action of blood insulin on target tissues. From a mathematical and practical point of view, this decision also resulted in a more compact model with fewer parameters to fit experimental data.

Insulin sensitivity S_I, formally introduced by Bergman et al. (1979) and mathematically defined by Equation (10), accounts for the quantitative influence of insulin to increase the effect of glucose on its own disappearance, in steady state.

$$S_I = \frac{\partial E}{\partial I}, \qquad E = -\frac{\partial\left(dG/dt\right)}{\partial G} \tag{10}$$

In our mathematical model, we adopted the term $k_{xgi}GI$ and $k_{xg}G$ of De Gaetano et al. (2013) to represent the glucose-mediated effect of insulin on glucose disappearance from the bloodstream and glucose uptake by insulin-independent tissues, respectively. However, contrary to the equations of De Gaetano et al. (2013), in our model parameter k_{xgi} is a true insulin sensitivity value. This was achieved by the redefinition of G_{prod}, resulting in such a way that no additional terms appeared in the mathematical calculation of the insulin sensitivity according to Equation (10).

Summary of the Model

Collecting the different expressions derived in the previous sections for the constitutive compartments of our model, we can summarize it in the following system of differential equations:

$$\begin{aligned}
&\frac{dS}{dt} = -k_{js}S, \qquad S(0) = D\\
&\frac{dJ}{dt} = k_{js}S - k_{gj}J - k_{jl}J, \qquad J(0) = 0\\
&\frac{dL}{dt} = k_{jl}\varphi(t) - k_{gl}L(t), \qquad \varphi(t) = \begin{cases} 0, & \text{if } t < \tau \\ J(t-\tau), & \text{if } t \geq \tau \end{cases}\\
&\frac{dG}{dt} = -(k_{xg} + k_{xgi}I)G + G_{\text{prod}} + \eta\left(k_{gj}J + k_{gl}L\right), \qquad G(0) = G_b\\
&\frac{dI}{dt} = k_{xi}I_b\left(\frac{\beta^\gamma + 1}{\beta^\gamma\left(\frac{G_b}{\tilde{G}}\right)^\gamma + 1} - \frac{I}{I_b}\right)
\end{aligned}$$

Parameter Fitting Strategy

During a 5-point OGTT, five experimental measures of both glucose and insulin are captured, generating vectors G_{exp} and I_{exp}. By protocol, measurements are taken at 0, 30, 60, 90, and 120 min after glucose ingestion, giving a time vector $T_{\text{exp}} = [0\ 30\ 60\ 90\ 120\ ]$. The model detailed in the previous sections was used to represent and interpolate these points continuously. Let $G_{\text{num}}(\vec{\theta})$, $I_{\text{num}}(\vec{\theta})$ be its solution for the G-I dynamics, with

parameters $\vec{\theta}$. The traditional way of formulating the parametric fitting problem is by minimization of a cost function J_{exp} that accounts for the difference between the modeled curve and experimental measurements. Generally, this function is proportional to the mean squared error *MSE*,

$$J_{\text{exp}}(\vec{\theta},\alpha) = \frac{1}{5\,(G_{\max}-G_{\min})^2}\sum_{i=1}^{5}\left(G_{\text{exp}}(i)-G_{\text{num}}(T_i)\right)^2 + \frac{\alpha}{5\,(I_{\max}-I_{\min})^2}\sum_{i=1}^{5}\left(I_{\text{exp}}(i)-I_{\text{num}}(T_i)\right)^2, \tag{11}$$

where α is a constant that connects the contribution of the insulin curve to *MSE* and $(G_{\max}-G_{\min})^2$ is a scaling factor. This problem consists of finding the values of all 13 parameters of the model from 10 experimental measures obtained during a routine 5-point OGTT for a given patient, which is a slightly underdetermined problem. However, we can exploit the knowledge we have about the nature of the physiological G-I response, accumulated in more than 40 years of routine testing and modeling, to gain in robustness and identifiability of the parameter set for each patient. We identified and used the following strategies for improvement:

- Increasing data density through the use of interpolators, to favor smoothness and regularity of the solutions, and to penalize nonphysiological oscillations.
- Simulation-based regularization for clusters of similar curves.
- Nested sub-problems and sequential approximations to build a robust initial guess.
- Incorporation of information in the cost function and the delimitation of the feasible set.
- Algorithm choice for the parameter recognition problem and final shaping of the feasible set.

Increasing Data Density

Given the nature of the equations presented in our model, non-physiological high-frequency oscillatory solutions might appear. Taking into account (a) the nature of the physiological G-I control system, (b) the oscillations measured experimentally in the literature, and (c) the 30-min apart measurements taken during a 5-point OGTT, we know that high-frequency oscillations –relative to the sampling time– should not be observable in our solution. Therefore, we propose to favor those solutions that only have low-frequency oscillations, somehow forcing the it to resemble the experimental data in a smooth way. For this, we propose to increase the density of putative measured points using a soft interpolant to connect the experimental measurement points. Without loss of generality, for *G*, the interpolant $\hat{G}$ used to increase the data density is defined by Equation (12):

$$\hat{G} = \phi G_{\text{spline}} + (1-\phi)G_{\text{pol}}, \tag{12}$$

that is a convex combination between a cubic spline and a low-degree polynomial interpolator. We can define a new component of the error function, J_{spline}, based on the *MSE* between $\hat{G}$ and G_{num}, following the structure of Equation (11). It is important to point out that this contribution has no greater effect than favoring those solutions that are smooth and regular. Introducing this component into the curve fitting procedure adds information because the optimizer would not only look for those solutions whose numerical profiles match the experimental data points, but for those whose profiles also do not drift considerably from the expected trend.

Simulation-Based Regularization for Clusters of Similar Curves

Taking into account the physiological and molecular mechanisms involved in the G-I dynamics and the experimental values obtained in typical OGTT measurements, we determined plausible lower and upper bounds ($\theta_{i,\min}$ and $\theta_{i,\max}$, respectively) for each parameter θ_i. In a first stage, we may define the feasible set F_0 considering such thresholds,

$$F_0 = \bigotimes_{i=1}^{13}\left[\theta_{i,\min},\,\theta_{i,\max}\right], \tag{13}$$

where the operator $\otimes$ represents the Cartesian product between the intervals defined by the lower and upper thresholds of each parameter. We performed a simulation stage to explore the nature of F_0, in which we simulated 10^8 values of $\vec{\theta}^* \in F_0$, and studied the $G_{\text{num}}(\vec{\theta}^*)$ and $I_{\text{num}}(\vec{\theta}^*)$ profiles obtained. If such profiles fulfilled the clinical normality criteria, they were assigned to groups of experimental profiles based on their similarities, aiming to build a set of initial guesses for the parameters corresponding to such individuals. Once we had enough $\vec{\theta}^*$ for each group of curves, a fourth component for the global cost function (Equation 16) was added, accounting for the contribution of local regularization near $\vec{\theta}_j^*$ characteristic of the *j*'th group.

Nested Sub-problems and Sequential Approximations

We followed a staged approach for the construction of initial guesses for the inverse problem, summarized in the following algorithm:

Steps one and two aim to build an appropriate initial guess for the parameter fitting problem, solved in step three. This step does not include further assumptions on the nature of the solutions, but only the model equations.

Incorporation of Information in the Cost Function

Given that the *a priori* identifiability of the model is not guaranteed (De Gaetano et al., 2013), we corrected the cost function presented in the previous section to incorporate more information. Without making any assumption concerning the parameters, we incorporated information from clinical records and from the test itself. In particular. we added terms that account for: (i) experimental errors, associated with sampling time and laboratory techniques, and (ii) expected extreme values (maxima and minima), inferred from the experimental measurements and based on clinical criteria.

Algorithm 1: Sequential approximation to the initial guess

Data:
$\vec{\theta}_j^*$: Initial guess, built from the simulation-based parametric pool of group j;
G_{num}, I_{num} : Model derived G-I profiles, with temporal resolution t_{num};
$\hat{G}$, $\hat{I}$: Interpolation of the experimental G-I profiles at t_{num};
Result: Initial guess $\vec{\theta}_0$ for the parametric recognition inverse problem of a particular patient
foreach *individual in the cohort* **do**
  Find the most similar simulated curve, and set $\vec{\theta}_0 = \vec{\theta}_j^*$.
  Fit the glycemia-related parameters, using $I = \hat{I}$ (Equation 12) as a known forcing function on Equation (4), minimizing $J_{\text{exp}}(\vec{\theta}, 0)$.;
  Update the glycemia-related components of $\vec{\theta}_0$.
  Fit the insulinemia-related parameters, using $G = \hat{G}$ (Equation 12) as a known forcing function on Equation (4), minimizing $J_{\text{exp}}(\vec{\theta}, \alpha)$, considering only insulinemia ($\alpha \to \infty$).;
  Update the insulinemia-related components of $\vec{\theta}_0$.
  Set $\vec{\theta}_0$ as initial guess for the parameter fitting inverse problem.
end

Algorithm 2: Incorporation of experimental errors in the cost function

Data:
x_{exp} : experimental glycemia or insulinemia value at time t_{exp};
t_{exp} : sampling time, element from T_{exp};
λ : penalizing factor, $\lambda > 1$;
Result: J_{error}
Set $J_{\text{error}} = 0$;
foreach $t_{exp} \in T_{exp}$, $x = \{G, I\}$ **do**
  Calculate $\mathcal{E}$, ellipse centered in $(t_{\text{exp}}, x_{\text{exp}}(t_{\text{exp}}))$, with semi-axes $a = 2\Delta_t$, $b = 2\Delta_x$.;
  Calculate $c = x_{\text{num}}([t_{\text{exp}} - \Delta_t, t_{\text{exp}} + \Delta_t])$, image of the major semi-axe through function x_{num}.;
  Calculate d, the distance between $\mathcal{E}$ and c.;
  if $d = 0$ **then**
    Calculate d', the distance between c and the center of $\mathcal{E}$;
    Find θ', angle of the point of minimum distance;
    Calculate $r(\theta')$, ellipse radius at $\theta = \theta'$;
    Update $J_{\text{error}} = J_{\text{error}} + \lambda \left(\frac{d'}{r(\theta')}\right)$;
  else
    Update $J_{\text{error}} = J_{\text{error}} + \lambda(d + 1)$;
  end
end

Regarding the first term, associated with experimental errors in both time and measurement, such 2− D variability transformed each data point into an ellipse in the (t, G) or (t, I) space, centered on the experimentally determined value G_{exp} or I_{exp}, at time T_{exp}. We used a constant $\Delta_t = \pm 3$ min as a scale for the temporal uncertainty (horizontal semi-axis of the ellipse), meanwhile a proportional contribution (to the G_{exp} or I_{exp} values) was chosen for the vertical axis. The weight of this error source in the total cost function was calculated based on a polar probability density of $\rho(r, \theta)$, as described in algorithm 2. Note that when considering together J_{exp} and J_{error}, the algorithm can be significantly simplified, as the calculations for the case $d = 0$ may be skipped only giving a greater weight to the contribution of J_{exp}.

Regarding the second term, its derivation was—in a mathematical sense—more complicated. Given the characteristics of the 5-point OGTT considered on this work, it seems reasonable to expect that the maximum value of the modeled glycemia curve should be of the same order of the maximum of the experimental profile. Consequently, we will have an idea of the time $t^* \sim T_{\text{exp}}(i)$ when our model reaches such value. Furthermore, considering a sequence of experimental measurements H_i recorded at times T_i, which approximate a $\mathcal{C}^1$ function $h(t)$. If for certain i_0 it is fulfilled that

$$\left(H_{i_0} - H_{i_0-1}\right)\left(H_{i_0+1} - H_{i_0}\right) < 0, \tag{14}$$

there exists a time $t^* \in \left[T_{i_0-1},\ T_{i_0+1}\right]$ where $h'(t^*) = 0$. Note that this can happen more than once for a sequence of experimental measurements so that we may have more equations of the form $h'(t_j^*) = 0$. For our case, as the OGTT data consists of five glucose and five insulin measurements, the maximum number of additional equations we can have is 6.

The classical way of solving the direct problem of finding maximum/minimum values of a function $h(t)$ is finding a time t^* in which $h'(t^*) = 0$ and a sign change occurs in the same point. Then, $h_{\text{opt}} = h(t^*)$. This same reasoning can be applied to glycemia, using Equation (4) and imposing $\frac{dG}{dt} = 0$ to obtain Equation (15):

$$G^{\text{opt}} = \frac{G^*_{\text{prod}} + \eta\left(k_{gj}J^* + k_{gl}L^*\right)}{k_{xg} + k_{xgi}I^*}, \tag{15}$$

where G^{opt} is the maximum glycemia, and I^*, G^*_{prod}, J^*, L^* are, respectively, the insulin concentration, hepatic glucose production rate, and the amount of glucose in the jejunum and ileum at time t^* (when G^{opt} is reached). Note that the formulation is general, and it serves for any point of derivative equal to zero (which we can estimate from the clinical exam trends). We can indeed follow and apply the same idea for the insulin equation (Equation 9). If we do this for all critical points we will have n linearly independent equations, since the times t^* and optimal values of G, I will be different. We can think of each equation as the $i-$ th component of a function $F(\vec{\theta}) = \sum_{i=1}^{n} f_i\vec{e}_i$. Note that around $\vec{\theta}^*$ where $F(\vec{\theta}^*) = 0$, the parameters can be expressed as implicit functions of the known variables

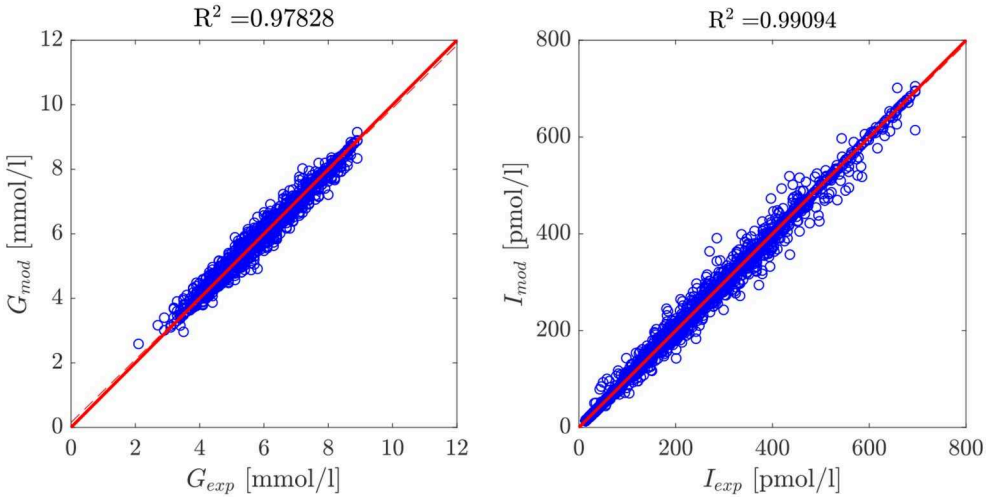

FIGURE 3 | Scatter plot of model-predicted glycemia and insulinemia vs. experimental measurements for the entire cohort of 407 patients. The data cloud lies in the identity zone, without significant deviations from it, accounting for a good fit.

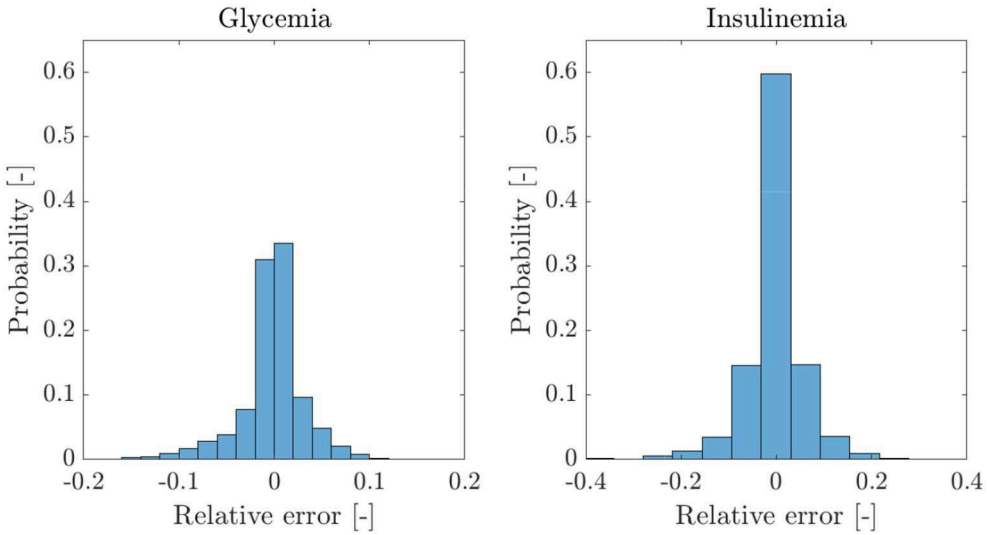

FIGURE 4 | Probability histograms of relative errors of the model predictions for the cohort of 407 patients and five data points per patient. Given the Gaussian nature of the residues of both variables, we can safely discard the presence of bias.

(such as $G_{i,max}$ and $I_{i,max}$). These equations will define different loci for the fitted parameters. The problem that appears directly after this definition is that known variables, in reality, are only approximately known within a confidence interval $I_{c,i}$. Then, when incorporating them, we will have manifolds (of loci). More specifically, we say that $\vec{\theta}$ satisfies the equation i, if there are $G^*_{i,max}$, $I^*_{i,max}$, $t^* \in I_{c,i}$ such that $f_i(\vec{\theta}) = \vec{0}$. We then build an information function, which conditions the shape of the feasible set, tagging as unfeasible the solutions $\vec{\theta}$ such that $F(\vec{\theta}) = \sum_{i=1}^{n} f_i(\vec{\theta})\vec{e}_i \neq \vec{0}$. Thus, we will have a new feasible set for our solutions and a new approach to the problem.

Settings of the Inverse Problem: Functions, Algorithms, and Thresholds

Finally, including all the contributions mentioned above, the parameter-fitting problem can be formulated as:

$$\underbrace{\min_{\vec{\theta}\in F_0 | F(\vec{\theta})=\vec{0}}}_{\text{Information function}} \underbrace{\lambda_1 J_{\text{exp}}(\vec{\theta},\alpha)}_{\text{Experimental data}} + \underbrace{\lambda_2 J_{\text{spline}}(\vec{\theta},\alpha)}_{\text{Interpolator}} + \underbrace{\lambda_3 J_{\text{error}}(\vec{\theta},\alpha)}_{\text{Experimental errors}} + \underbrace{\epsilon\|\vec{\theta}-\vec{\theta}^*_j\|}_{\text{Local regularization}}, \tag{16}$$

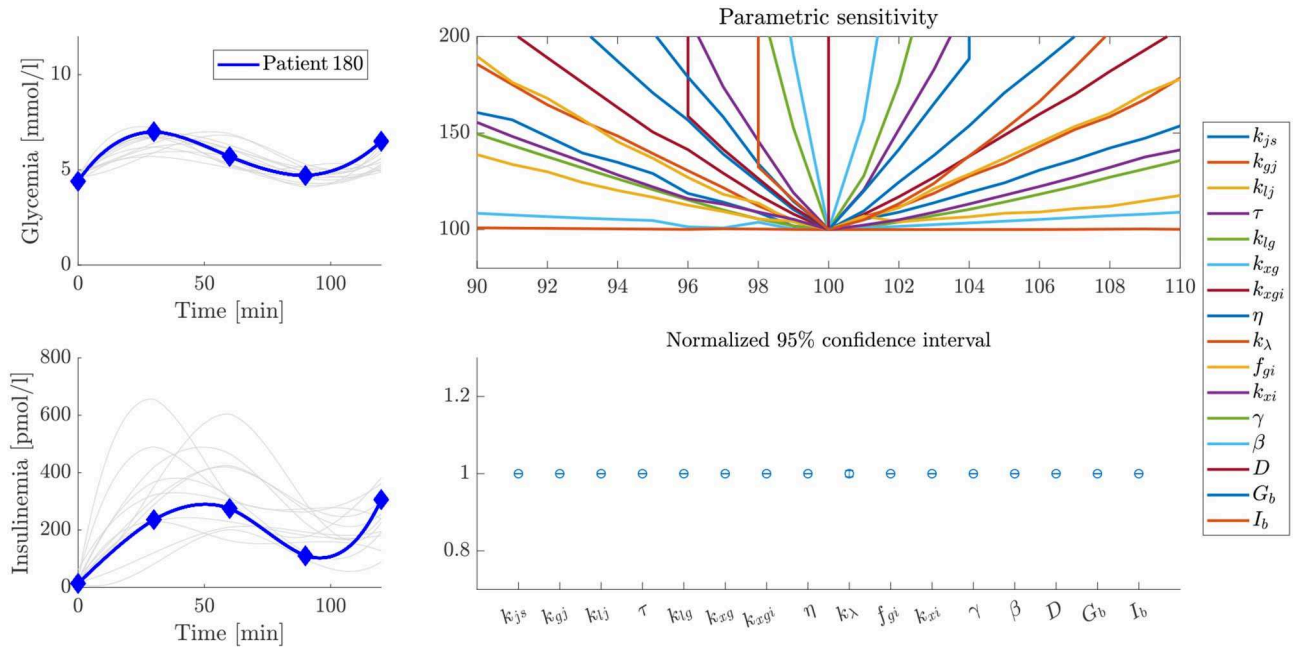

FIGURE 5 | Sensitivity and stability analysis of fitted parameters for patient 180. The figure shows the glycemia and insulinemia profiles of the patient in the frame of patients that have similar glycemic curves (upper and lower left plots, respectively). A volcano plot, as described in the text, is presented in the upper right plot, and a representation of the width of the 95% confidence interval for each parameter is presented in the lower right plot. In this example, even though some parameters have a low slope over the studied interval, the variability of their values, expressed as the width of the 95% confidence interval, is almost negligible.

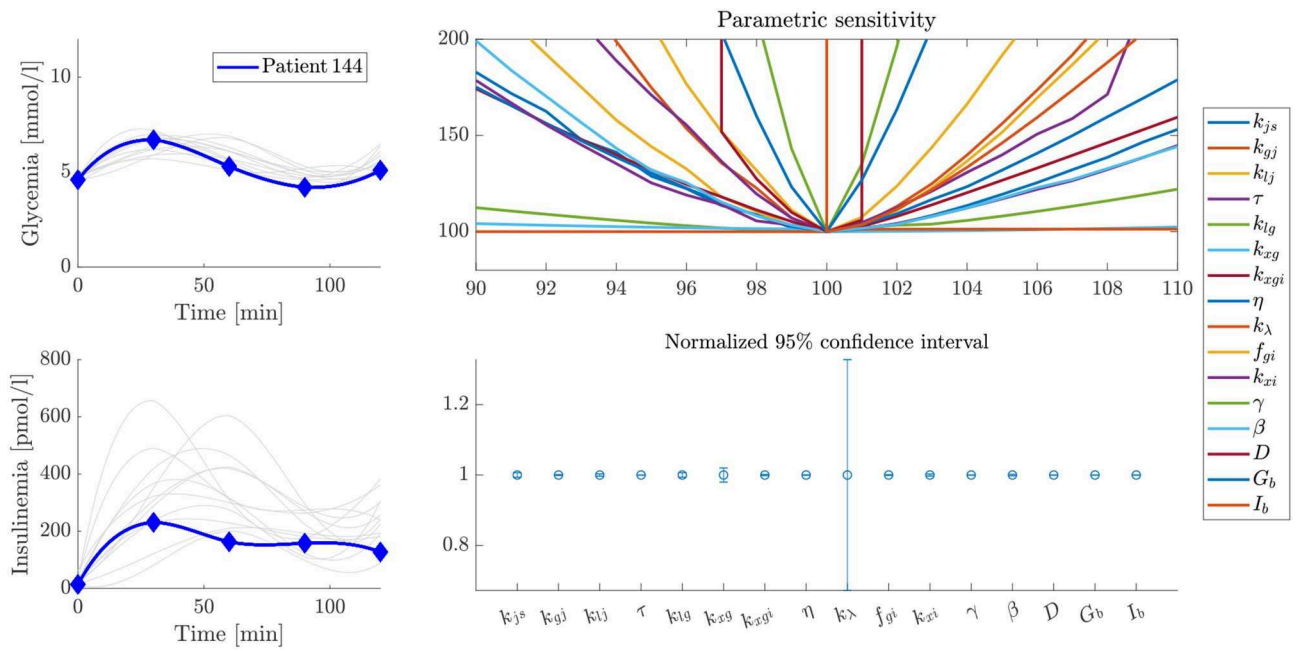

FIGURE 6 | Sensitivity and stability analysis of fitted parameters for patient 144. The figure shows the glycemia and insulinemia profiles of the patient in the frame of patients that have similar glycemic curves (upper and lower left plots, respectively). A volcano plot, as described in the text, is presented in the upper right plot, and a representation of the width of the 95% confidence interval for each parameter is presented in the lower right plot. In this example, the variability of the k_λ parameter is considerably higher than in the case of **Figure 5**, probably because of differences in the experimental profiles.

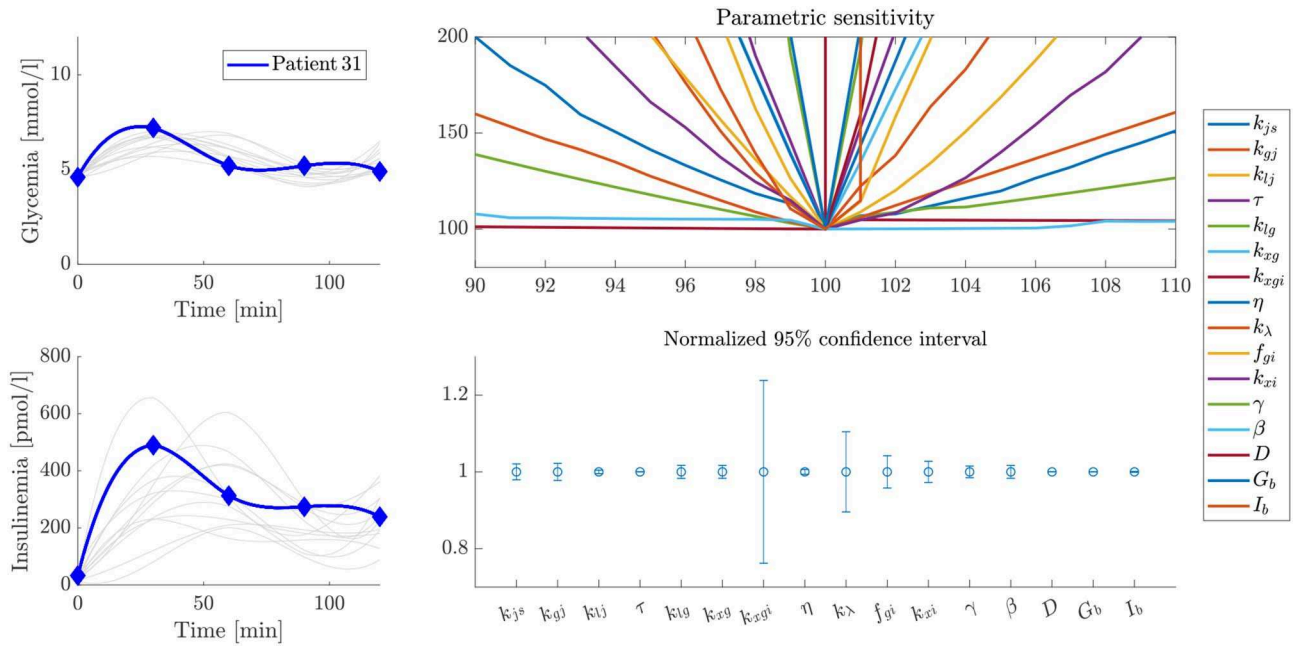

FIGURE 7 | Sensitivity and stability analysis of fitted parameters for patient 31. The figure shows the glycemia and insulinemia profiles of the patient in the frame of patients that have similar glycemic curves (upper and lower left plots, respectively). A volcano plot, as described in the text, is presented in the upper right plot, and a representation of the width of the 95% confidence interval for each parameter is presented in the lower right plot. In this example, the variability of some parameter values is not negligible.

with ϵ arbitrarily small, and which solution is the set of parameters that characterize the glycemic-insulinemic control for each patient. The resolution of the minimization problem 16 at every stage was achieved by combining deterministic methods (gradient search) and heuristic methods such as simulated annealing and pattern search, available in the Matlab Global Optimization Toolbox. Parameters were obtained for the whole studied cohort.

DISCUSSION

Goodness of Fit

Applying the parameter recognition procedure presented in previous sections, it was possible to fit our model to the experimental OGTT glycemia and insulinemia profiles of the whole studied cohort, thus obtaining the physiological parameters that control the observed trends for each patient.

To evaluate the performance of our model and the proposed parameter recognition procedure, we studied the quality of their predictions for both glycemia and insulinemia. **Figure 3** shows the scatter plots of experimental vs. predicted values for glycemia and insulinemia for all 407 patients, where both predicted variables follow the expected trend. The data point cloud lies in the identity zone, without significant deviations, and the variables show high correlation. The probability-normalized residues histogram of both variables had a Gaussian nature, as depicted in **Figure 4**, with low variance. In sum, prediction errors are normally distributed and unbiased, while predictions are highly correlated to experimental measures, which demonstrates the goodness of fit of our model and method.

Sensitivity Analysis

Parameter sensitivity was evaluated for each patient by analyzing how variations in parameter values affected the error between predicted and experimental values (the cost function defined by Equation 16). Some particular examples are shown by the volcano plots in **Figures 5–7**. In these figures, the greater the slope around the central point, the more sensitive the patient is to variations of that parameter. Therefore, a more sensitive parameter suggests higher confidence in its fitted value. We also performed ten different parameter fitting experiments for each patient, starting from different initial values and using the deterministic and heuristic procedures described above. With these results, we calculated a 95% confidence interval for the parameters of each patient, as shown in **Figures 5–7**. Following our former reasoning, all parameters with high slopes around the central point in the volcano plot have very narrow confidence intervals, but unexpectedly some parameters with low sensitivity in volcano plots have also very narrow confidence intervals in fitting experiments. This observation demonstrates that parameter accuracy following our fitting method is higher than expected from analyzing parameter sensitivity around a central point.

Analyzing differences between patients, our results show that this sensitivity analysis differs for each case, since different curve shapes suggest different physiological ways to achieve glycemic

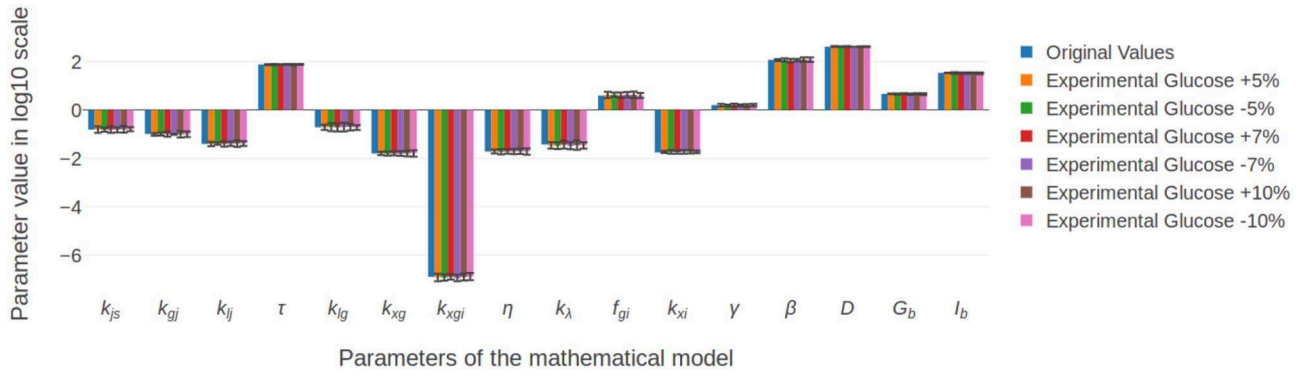

FIGURE 8 | Parameter stability in response to small perturbations in the experimental glucose measurements. Random noise of at most 10% of the reported measurement was added to the original values, and the inverse problem was solved. Results show that, even for the maximum percentage of variation, the difference between the original and final values remained non significant.

control. Hence, the relative importance of each parameter on the control mechanism, and the reliability of their values, can be considered proportional to their sensitivity or the extension of their confidence interval. As the most sensitive parameters are those that determine the shape of the control profile, understanding their individual and collective meaning may give valuable information about the health status of each patient, highlighting the physiological background of the observed trend.

We present some examples of these observations in **Figures 5**–**7**, which feature a special kind of graph that we will address as a volcano plot. In a volcano plot, we analyze the impact that small variations in the parameters, relative to their optimal value, have on the value of the error functional J_T. The x-axis represents the percent variation of the optimal value of the parameter, and the y-axis, the variation of the error, normalized by its minimum value, which is the optimal. Therefore, the point $(100, 100)$ is the center and global minimum of all curves in the plot.

Figure 5 shows the sensitivity and stability analysis of the parameters for patient 180. Out of the whole set, the parameter k_λ shows the more significant variability, which is very small and almost negligible. On the other hand, **Figure 6** shows the same analysis for patient 144, which has a very similar glycemic profile, but whose k_λ is somehow unreliable. Despite sharing almost the same glycemic profile, they have essential differences in their insulinemic trends. The above demonstrates the importance of analyzing both glycemia and insulinemia for having a reliable indicator of the health status of an individual, given that glycemia alone might not be enough. Furthermore, patient 31, who shares little or no properties with the glycemic and insulinemic profile of the other two patients studied above (see **Figure 7**), has a different sensitivity footprint, proving the relationship between curve shape and parameter reliability.

Stability of the Solutions in Response to Experimental Errors

After obtaining final values for every parameter, we evaluated their stability in response to small perturbations in the fitted experimental measures. Starting from the experimental OGTT points for a fixed individual $(G_{\text{exp}}, I_{\text{exp}})$, we simulated a set of virtual patients with OGTT curves $(G_{\text{sim}}, I_{\text{sim}})$ whose measurements resulted of adding random noise to $(G_{\text{exp}}, I_{\text{exp}})$, and solved the parameter fitting problem, considering as a starting point the parameters fitted to the original patient. Different amounts of noise were added to the experimental points in all patients. The effects of these variations on all parameter values are shown in **Figure 8** for one patient example. All parameters in all generated variations show no significant differences in comparison to the original data, showing that the model allows margins of error associated to both experimental error or time lags at the moment of taking samples without compromising the accuracy of the solution. This invariability is related to the inclusion in the fitting procedure of a component accounting for experimental error, acting as a mathematical buffer, which demonstrates the utility of this approach for individual parameter fitting.

CONCLUSIONS

We presented a new synthetic mathematical model for the G-I dynamics in an Oral Glucose Tolerance Test. Our model only includes parameters with a coherent physiological meaning and, to the best knowledge of the authors, is the first approach which involves Delay Differential Equations (DDE) presented in the literature. The new model can represent radically different G-I behaviors observed in the studied population, including hypoglycemiant individuals, single/double peak patients, and those with practically invariant G-I profiles. In this way, we demonstrate that these unexpected G-I profiles are not experimental errors, but are the result of particular combinations of physiological processes.

We have proposed and numerically implemented a novel strategy for the resolution of the curve-fitting problem, exploiting existing knowledge about the function of the G-I control system, leading to the correct recognition of the individual parameters for the studied cohort of 407 individuals. Our

methodology showed to be robust, as the dimensionality of the problem can be dramatically decreased by reshaping the feasible set with the incorporation of an information function and splitting the problem into sequential approaches, thus allowing a correct fitting of the model parameters for each patient. As suggested by the simulations, and afterwards verified by our results, we observed consistency between differences in glycemic and insulinemic OGTT curves and differences in parameter values. The parameters obtained for each and every patient showed to be stable under small perturbations of the experimental measurements, and their sensitivity varied from one patient to another, giving physiological and patient-wise insights of the mechanistic background of the observed trends. This can be asserted particularly by the fact that each parameter in the proposed model represents a unique physiological phenomenon.

Finally, since our model can represent the different forms of control observed so far, to characterize them through parameters with a physiological meaning, and to identify those parameters using a robust methodology for the inverse problem solving, we propose it as a tool for patient evaluation, review of health criteria, and re-definition of clinical normality. Understanding that under the current clinical normality definition there are different ways to achieve glycemic control, parametric analysis of patients would allow the development of individual-oriented treatments, contributing significantly to the preventive and personalized diagnosis of relevant pathophysiological events in the control system. In accordance to this, our future work will include a thorough analysis of parameter values in normal and pathological patients under current definitions and their statistical distributions in broader patient samples, in order to define clinical meaning, normality and pathological criteria for each parameter, which falls out of the scope and length of the present work.

DATA AVAILABILITY STATEMENT

The datasets generated for this study are available on request to the corresponding author.

ETHICS STATEMENT

The studies involving human participants were reviewed and approved by the Ethics Committee of the San Cristobal Medical Center, Santiago, Chile. The patients/participants provided their written informed consent to participate in this study.

AUTHOR CONTRIBUTIONS

SC, DM-O, ÁO-N, and CC: conceptualization, writing, review, and editing. SC, ÁO-N, and CC: methodology. SC and DM-O: validation. SC, DM-O, and ÁO-N: investigation. SC and ÁO-N: supervision. ÁO-N: project administration and funding.

FUNDING

This research has been financed mainly by the Centre for Biotechnology and Bioengineering - CeBiB (PIA project FB0001, Conicyt, Chile). DM-O gratefully acknowledges Conicyt, Chile, for Ph.D. fellowship 21181435. Powered@NLHPC: This research was partially supported by the supercomputing infrastructure of the National Laboratory for High-Performance Computing, NLHPC (ECM-02), Chile.

SUPPLEMENTARY MATERIAL

The Supplementary Material for this article can be found online at: https://www.frontiersin.org/articles/10.3389/fbioe.2020.00195/full#supplementary-material

REFERENCES

Ajmera, I., Swat, M., Laibe, C., Le Novere, N., and Chelliah, V. (2013). The impact of mathematical modeling on the understanding of diabetes and related complications. *CPT Pharmacometr. Syst. Pharmacol.* 2, 1–14. doi: 10.1038/psp.2013.30

Bartoli, E., Fra, G., and Schianca, G. C. (2011). The oral glucose tolerance test (OGTT) revisited. *Eur. J. Int. Med.* 22, 8–12. doi: 10.1016/j.ejim.2010.07.008

Bergman, M., Jagannathan, R., Buysschaert, M., Pareek, M., Olsen, M. H., Nilsson, P. M., et al. (2018). Lessons learned from the 1-hour post-load glucose level during OGTT: current screening recommendations for dysglycaemia should be revised. *Diabetes Metab. Res. Rev.* 34:e2992. doi: 10.1002/dmrr.2992

Bergman, R. N. (2005). Minimal model: perspective from 2005. *Hormone Res. Paediatr.* 64(Suppl. 3):8–15. doi: 10.1159/000089312

Bergman, R. N., Ider, Y. Z., Bowden, C. R., and Cobelli, C. (1979). Quantitative estimation of insulin sensitivity. *Amer. J. Physiol. Endocrinol. Metab.* 236:E667. doi: 10.1152/ajpendo.1979.236.6.E667

Boutayeb, A., and Chetouani, A. (2006). A critical review of mathematical models and data used in diabetology. *Biomed. Eng. Online* 5:43. doi: 10.1186/1475-925X-5-43

Brubaker, P. L., Ohayon, E. L., D'Alessandro, L. M., and Norwich, K. H. (2007). A mathematical model of the oral glucose tolerance test illustrating the effects of the incretins. *Ann. Biomed. Eng.* 35, 1286–1300. doi: 10.1007/s10439-007-9274-1

Caumo, A., Bergman, R. N., and Cobelli, C. (2000). Insulin sensitivity from meal tolerance tests in normal subjects: a minimal model index. *J. Clin. Endocrinol. Metab.* 85, 4396–4402. doi: 10.1210/jcem.85.11.6982

Cobelli, C., Dalla Man, C., Pedersen, M. G., Bertoldo, A., and Toffolo, G. (2014). Advancing our understanding of the glucose system via modeling: a perspective. *IEEE Trans. Biomed. Eng.* 61, 1577–1592. doi: 10.1109/TBME.2014.2310514

Cobelli, C., Dalla Man, C., Sparacino, G., Magni, L., De Nicolao, G., and Kovatchev, B. P. (2009). Diabetes: models, signals, and control. *IEEE Rev. Biomed. Eng.* 2:54. doi: 10.1109/RBME.2009.2036073

Dalla Man, C., Camilleri, M., and Cobelli, C. (2006). A system model of oral glucose absorption: validation on gold standard data. *IEEE Trans. Biomed. Eng.* 53, 2472–2478. doi: 10.1109/TBME.2006.883792

Dalla Man, C., Caumo, A., Basu, R., Rizza, R., Toffolo, G., and Cobelli, C. (2004). Minimal model estimation of glucose absorption and insulin sensitivity from oral test: validation with a tracer method. *Am. J. Physiol. Endocrinol. Metab.* 287, E637–E643. doi: 10.1152/ajpendo.00319.2003

Dalla Man, C., Caumo, A., and Cobelli, C. (2002). The oral glucose minimal model: estimation of insulin sensitivity from a meal test. *IEEE Trans. Biomed. Eng.* 49, 419–429. doi: 10.1109/10.995680

Dalla Man, C., Rizza, R. A., and Cobelli, C. (2007). Meal simulation model of the glucose-insulin system. *IEEE Trans. Biomed. Eng.* 54, 1740–1749. doi: 10.1109/TBME.2007.893506

De Gaetano, A., Panunzi, S., Matone, A., Samson, A., Vrbikova, J., Bendlova, B., et al. (2013). Routine OGTT: a robust model including incretin effect for precise identification of insulin sensitivity and secretion in a single individual. *PLoS ONE* 8:e70875. doi: 10.1371/journal.pone.0070875

Erlandsen, M., Martinussen, C., and Gravholt, C. H. (2018). Integrated model of insulin and glucose kinetics describing both hepatic glucose and pancreatic insulin regulation. *Comput. Methods Prog. Biomed.* 156, 121–131. doi: 10.1016/j.cmpb.2017.12.009

Goutelle, S., Maurin, M., Rougier, F., Barbaut, X., Bourguignon, L., Ducher, M., et al. (2008). The hill equation: a review of its capabilities in pharmacological modelling. *Fundament. Clin. Pharmacol.* 22, 633–648. doi: 10.1111/j.1472-8206.2008.00633.x

Hu, F. B., Satija, A., and Manson, J. E. (2015). Curbing the diabetes pandemic: the need for global policy solutions. *JAMA* 313, 2319–2320. doi: 10.1001/jama.2015.5287

Makroglou, A., Li, J., and Kuang, Y. (2006). Mathematical models and software tools for the glucose-insulin regulatory system and diabetes: an overview. *Appl. Numer. Math.* 56, 559–573. doi: 10.1016/j.apnum.2005.04.023

Mari, A., Bagger, J. I., Ferrannini, E., Holst, J. J., Knop, F. K., and Vilsbøll, T. (2013). Mechanisms of the incretin effect in subjects with normal glucose tolerance and patients with type 2 diabetes. *PLoS ONE* 8:e73154. doi: 10.1371/journal.pone.0073154

Mari, A., Pacini, G., Murphy, E., Ludvik, B., and Nolan, J. J. (2001). A model-based method for assessing insulin sensitivity from the oral glucose tolerance test. *Diab. Care* 24, 539–548. doi: 10.2337/diacare.24.3.539

Palumbo, P., Ditlevsen, S., Bertuzzi, A., and De Gaetano, A. (2013). Mathematical modeling of the glucose–insulin system: a review. *Math. Biosci.* 244, 69–81. doi: 10.1016/j.mbs.2013.05.006

Salinari, S., Bertuzzi, A., and Mingrone, G. (2011). Intestinal transit of a glucose bolus and incretin kinetics: a mathematical model with application to the oral glucose tolerance test. *Am. J. Physiol. Endocrinol. Metab.* 300, E955–E965. doi: 10.1152/ajpendo.00451.2010

Silber, H. E., Frey, N., and Karlsson, M. O. (2010). An integrated glucose-insulin model to describe oral glucose tolerance test data in healthy volunteers. *J. Clin. Pharmacol.* 50, 246–256. doi: 10.1177/00912700093 41185

Stumvoll, M., Mitrakou, A., Pimenta, W., Jenssen, T., Yki-Järvinen, H., Van Haeften, T., et al. (2000). Use of the oral glucose tolerance test to assess insulin release and insulin sensitivity. *Diab. Care* 23, 295–301. doi: 10.2337/diacare.23.3.295

Toniolo, A., Cassani, G., Puggioni, A., Rossi, A., Colombo, A., Onodera, T., et al. (2018). The diabetes pandemic and associated infections: suggestions for clinical microbiology. *Rev. Med. Microbiol.* 30, 1–17. doi: 10.1097/MRM.0000000000000155

Conflict of Interest: The authors declare that the research was conducted in the absence of any commercial or financial relationships that could be construed as a potential conflict of interest.

Copyright © 2020 Contreras, Medina-Ortiz, Conca and Olivera-Nappa. This is an open-access article distributed under the terms of the Creative Commons Attribution License (CC BY). The use, distribution or reproduction in other forums is permitted, provided the original author(s) and the copyright owner(s) are credited and that the original publication in this journal is cited, in accordance with accepted academic practice. No use, distribution or reproduction is permitted which does not comply with these terms.

frontiers in Physiology

ORIGINAL RESEARCH
published: 18 March 2020
doi: 10.3389/fphys.2020.00217

Model-Based Simulation of Maintenance Therapy of Childhood Acute Lymphoblastic Leukemia

*Felix Jost[1], Jakob Zierk[2], Thuy T. T. Le[1], Thomas Raupach[2], Manfred Rauh[2], Meinolf Suttorp[3], Martin Stanulla[4], Markus Metzler[2] and Sebastian Sager[1,5]**

[1] Department of Mathematics, Institute of Mathematical Optimization, Otto-von-Guericke University Magdeburg, Magdeburg, Germany, [2] Department of Paediatrics and Adolescent Medicine, University Hospital Erlangen, Erlangen, Germany, [3] Pediatric Hematology and Oncology, University Hospital "Carl Gustav Carus", Dresden, Germany, [4] Department of Pediatric Hemato-Oncology, Hannover Medical School, Hanover, Germany, [5] Health Campus "Immunology, Infectiology and Inflammation (GC-I^3)", Otto-von-Guericke University, Magdeburg, Germany

Acute lymphoblastic leukemia is the most common malignancy in childhood. Successful treatment requires initial high-intensity chemotherapy, followed by low-intensity oral maintenance therapy with oral 6-mercaptopurine (6MP) and methotrexate (MTX) until 2–3 years after disease onset. However, intra- and inter-individual variability in the pharmacokinetics (PK) and pharmacodynamics (PD) of 6MP and MTX make it challenging to balance the desired antileukemic effects with undesired excessive myelosuppression during maintenance therapy. A model to simulate the dynamics of different cell types, especially neutrophils, would be a valuable contribution to improving treatment protocols (6MP and MTX dosing regimens) and a further step to understanding the heterogeneity in treatment efficacy and toxicity. We applied and modified a recently developed semi-mechanistic PK/PD model to neutrophils and analyzed their behavior using a non-linear mixed-effects modeling approach and clinical data obtained from 116 patients. The PK model of 6MP influenced the accuracy of absolute neutrophil count (ANC) predictions, whereas the PD effect of MTX did not. Predictions based on ANC were more accurate than those based on white blood cell counts. Using the new cross-validated mathematical model, simulations of different treatment protocols showed a linear dose-effect relationship and reduced ANC variability for constant dosages. Advanced modeling allows the identification of optimized control criteria and the weighting of specific influencing factors for protocol design and individually adapted therapy to exploit the optimal effect of maintenance therapy on survival.

Keywords: childhood acute lymphoblastic leukemia, maintenance therapy, 6-mercaptopurine, methotrexate, neutropenia, non-linear mixed-effects modeling, population pharmacokinetics/pharmacodynamics

OPEN ACCESS

Edited by:
Babatunde Ogunnaike, University of Delaware, United States

Reviewed by:
Alexey Goltsov, Abertay University, United Kingdom
Noriko F. Hiroi, Tokyo University of Science Yamaguchi, Japan

***Correspondence:**
Sebastian Sager
sager@ovgu.de

Specialty section:
This article was submitted to Systems Biology, a section of the journal Frontiers in Physiology

Received: *07 November 2019*
Accepted: *25 February 2020*
Published: *18 March 2020*

Citation:
Jost F, Zierk J, Le TTT, Raupach T, Rauh M, Suttorp M, Stanulla M, Metzler M and Sager S (2020) Model-Based Simulation of Maintenance Therapy of Childhood Acute Lymphoblastic Leukemia. Front. Physiol. 11:217. doi: 10.3389/fphys.2020.00217

1. INTRODUCTION

Acute lymphoblastic leukemia (ALL), characterized by malignant white blood cells (WBCs) and displacement of normal hematopoiesis, is the most common childhood malignancy (Hoffbrand et al., 2016). The treatment of childhood ALL is based on combination chemotherapy and begins with intensive, high-dose treatment for approximately 6 months (the so-called induction and consolidation therapy) followed by less-intensive, low-dose treatment [so-called maintenance

therapy (MT)] that lasts for 2–3 years after disease onset. The goal of induction and consolidation therapy is to achieve remission via lymphoblast elimination below the limit of detection, and the high intensity of these therapy elements limits further therapy intensification using conventional chemotherapy. Subsequent MT is essential to prevent disease relapse, and aims to maintain prolonged antileukemic activity against residual lymphoblasts, with minimal adverse events. MT includes daily oral 6-mercaptopurine (6MP) and weekly oral methotrexate (MTX). Both drugs cause myelosuppression through their metabolized active forms (Schmiegelow et al., 2014). Blood count tests are performed regularly to ensure adequate WBC and absolute neutrophil count (ANC) suppression as a surrogate marker for antileukemic activity, without unintended excessive myelotoxicity. However, there exists no international consensus for MT dosing strategies and target levels for WBC and ANC suppression (i.e., what dose to start with, and when and how to increase or decrease chemotherapy). Empirical evaluation of different MT strategies using randomized clinical trials would be extremely challenging, due to the probably moderate effect size, the length of MT, the latency of clinically relevant endpoints, and the risk of compromising the current overall favorable outcome of childhood ALL. However, certain levels of WBC and ANC are established factors for survival, relapse or death, and other adverse events (e.g., infection), respectively. Therefore, a simulation model of childhood ALL MT could support the development of future MT strategies by identifying those strategies that achieve established survival factors best while avoiding established risk factors. Mathematical models describing the pharmacokinetics (PK) of 6MP and MTX and their pharmacodynamic (PD) effects on neutrophils may help clarify the drug-exposure relationship, predict the ANC dynamics, adapt subsequent dosing amounts, and stratify patients into groups with different drug responses. Several PK models for 6MP (Hawwa et al., 2008; Jayachandran et al., 2014, 2015) and MTX (Godfrey et al., 1998; Panetta et al., 2002, 2010; Nagulu et al., 2010; Rühs et al., 2012; Korell et al., 2013; Hui et al., 2019) have been published, but not all have been developed with low-dosage treatments and validated in the pediatric population. To the best of our knowledge, there are only three publications (Jayachandran et al., 2014; Le et al., 2018; Karppinen et al., 2019) in which some of the PK models or their simplifications were linked to transient PD compartment models (Upton and Mould, 2014). The models were individually fitted to WBC counts and different prediction and optimization studies were conducted.

Here, we developed a population PK/PD model for maintenance treatment of ALL in children based on the approach used by Le et al. (2018) with a modified underlying PK model. As ANCs are the best established risk and survival factors, we adapted the model to predict ANCs instead of WBCs. The model was fitted to and validated on a dataset consisting of weekly ANC measurements obtained from 116 patients treated with daily oral 6MP and weekly oral MTX over an average of 459 (range, 200–581) days. We started our investigations with a PK/PD model considering 6MP and MTX but the constant administration ratio hampered the identification of separate PD effects. Further, the PK of MTX had no significant impact on the improvement of the model fitting, similar to the mathematical approach in Karppinen et al. (2019) and the clinical findings of *NUDT15* genetics conferring 6MP but no MTX sensitivities (Tsujimoto et al., 2018). Thus, the final model only contains the PK of 6MP. We come back to this issue in the discussion. Then, for each patient, we simulated different therapy protocols (6MP dosing regimens), and compared the resulting predictions.

2. PATIENTS AND METHODS

2.1. Data

The data used in this study were obtained retrospectively from 116 children who were diagnosed with de novo ALL at university hospitals in Erlangen and Dresden and treated according to the AIEOP-BFM 2000 and 2009 protocols. A subset of this data set (WBC counts from nine patients) was used and described similarly in a previous study (Le et al., 2018). Patients were eligible if they were diagnosed with precursor B-cell or T-cell ALL, negative for the BCR-ABL- and MLL-AF4 translocations, and started MT (i.e., did not experience relapse before the end of consolidation therapy and did not undergo stem cell transplantation). During MT administered according to the AIEOP-BFM 2000 and 2009 protocols, patients received oral chemotherapy with daily 6MP and once-weekly MTX until 2 years after ALL diagnosis. During MT, chemotherapy was applied to achieve antileukemic activity against lymphoblasts below the limit of detection. As a surrogate for antileukemic activity, WBC and ANC were measured regularly, with ANC <2 G/L, being correlated to a significantly better relapse-free survival (Schmiegelow et al., 2014), and ANC <0.5 G/L being an indicator of excessive myelosuppression. The target range for the WBC count was 1.5–3 G/L. The chemotherapeutic dose was reduced when cell counts fell below the lower limits (WBC count <1.5 G/L, ANC <0.5 G/L, lymphocyte count <0.3 G/L, and platelet count <0.05 G/L) or liver toxicity was suspected. For each patient included in the analysis, data regarding the following variables were recorded: gender, age, weight, height, body surface area (BSA), prescribed 6MP and MTX dosages (absolute and per BSA), WBC count, platelet count, lymphocyte and neutrophil counts, and therapy interruptions. In this study, we focused on 5897 ANCs and 6640 WBC counts, disregarding measurements of other cell types. We used both WBC counts and ANC separately and compared the accuracy of the resulting mathematical models. In all, 1150 ANC and 1289 WBC count measurements were excluded due to concurrent high C-reactive protein (CRP) levels indicating periods in which patients probably suffered from an infection. More precisely, we excluded measurements in the interval from 2 weeks before until 2 weeks after CRP levels of >5 mg/L were recorded. Among the remaining 4747 ANC measurements 56% were below the ANC threshold of 2 G/L, only 2% were below 0.5 G/L, and 54% were in the ANC target range 0.5–2 G/L. The demographic and clinical characteristics of the pediatric ALL population are shown in **Table 1**.

TABLE 1 | Characteristics (median and range) of the pediatric ALL population consisting of 116 (64 male and 52 female) patients.

Characteristic	Unit	Median	Range
Age	Year	4.75	1.1–17.1
Weight	kg	22	10–90
Height	cm	112.45	80–182.7
Body surface area	m^2	0.82	0.47–1.98
6MP daily dose	mg	40	5–150
MTX weekly dose	mg	15	1.25–60
ANC	G/L	1.8	0.0–19.9

The body surface area was calculated using the Mosteller formula.

2.2. Non-linear Mixed-Effects Modeling and Parameter Estimation

The non-linear mixed-effects (NLME) modeling (Bonate and Steimer, 2011) was based on the PK/PD model of Le et al. (2018). It describes the absorption of both drugs, 6MP and MTX, through the gastrointestinal (GI) tract into the plasma after oral administration and their metabolization to their active forms. The MTX metabolites $MTXPG_2$ to $MTXGP_7$ inhibit several enzymes responsible for DNA synthesis (Panetta et al., 2002). The active form of 6MP, 6-thioguanine nucleotides (6-TGNs), is incorporated into the DNA (Hawwa et al., 2008). Thus, both drugs negatively affect the hematopoiesis of neutrophils. During the model development, we replaced the 6MP PK model of Jayachandran et al. (2014) with the PK model described by Hawwa et al. (2008) to obtain a better response to 6MP dosage. The PK model of Jayachandran et al. (2014) was validated on concentration data of eight patients (adults) from Hindorf et al. (2006). However, the simulated 6-TGN concentrations coincided with data from pediatric patients reported by Hawwa et al. (2008); hence, it was a priori unclear which would give better results. Both compartment models have a comparable representation of the absorption and metabolic pathway of 6MP but the model of Hawwa et al. (2008) describes the metabolic transformations by first order kinetics instead of Michaelis–Menten kinetics. Further, the clearance is described by a BSA-dependent term, thus providing individualized PK profiles through patient characteristics. We also tested the influence of weekly MTX administration by either ignoring or considering the administrations and their resulting concentrations through the MTX PK model with a second PD parameter during model fitting. Additionally, we tested the myelosuppression model from Jayachandran et al. (2014), which contained a different feedback term for ANC recovery, but the accuracy decreased and this line of research was not further investigated.

As a result, we identified one PK/PD model which described the clinical data best. This model was formulated as a system of ordinary differential equations (ODEs):

$$\begin{aligned}
\dot{x}_{6mp}^{gut}(t) &= -k_a\, x_{6mp}^{gut}(t) + F\, u(t),\\
\dot{x}_{6mp}(t) &= \quad k_a\, x_{6mp}^{gut}(t) - k_{20}\, x_{6mp}(t),\\
\dot{x}_{6tgn}(t) &= \mathrm{FM}_3\, k_{me}\, x_{6mp}(t) - \mathrm{CL}_{6tgn}(\mathrm{BSA})\, x_{6tgn}(t)\\
\dot{x}_{pr}(t) &= k_{tr}\, x_{pr}(t)\,(1 - E_{drug})\left(\frac{Base}{x_{ma}(t)}\right)^{\gamma} - k_{tr}\, x_{pr}(t),\\
\dot{x}_{tr1}(t) &= k_{tr}\,(x_{pr}(t) - x_{tr1}(t)),\\
\dot{x}_{tr2}(t) &= k_{tr}\,(x_{tr1}(t) - x_{tr2}(t)),\\
\dot{x}_{tr3}(t) &= k_{tr}\,(x_{tr2}(t) - x_{tr3}(t)),\\
\dot{x}_{ma}(t) &= k_{tr}\, x_{tr3}(t) - k_{ma}\, x_{ma}(t)
\end{aligned} \tag{1}$$

with the BSA-dependent clearance

$$\mathrm{CL}_{6tgn}(\mathrm{BSA}) = 0.00914\,(\mathrm{BSA})^{1.16}, \tag{2}$$

the linear pharmacodynamic effect

$$E_{drug} = \mathrm{slope}\, x_{6tgn}, \tag{3}$$

and the patient-specific bioavailable 6MP amount $F\,u(t)$ of 6MP (implemented as point administration in NONMEM). The PK of 6MP is described by a three compartment model altered from Hawwa et al. (2008). A fraction of the orally administered 6MP dosage enters the GI tract where bioavailable 6MP is absorbed to the central compartment with the first order rate k_a. In the central compartment, 6MP is eliminated by k_{20}. The elimination also comprises metabolization of 6MP with the rate k_{me} out of which a fraction FM_3 is metabolized to the active form 6-TGN. 6-TGN is then cleared by the BSA-dependent clearance term CL_{6tgn}. The hematopoiesis of neutrophils is described via a chain of five compartments with equivalent transition rates k_{tr} representing the mean maturation time of the neutrophils (De Souza et al., 2018). The proliferation rate of hematopoietic stem cells k_{prol} is equivalent to the transition rate k_{tr} guaranteeing homeostasis (De Souza et al., 2018). Deviations from the neutrophil baseline *Base* are compensated by the feedback regulation $(Base/x_{ma})^{\gamma}$ reflecting the granulocyte colony-stimulating factor (GCSF) controlled proliferation of neutrophils (Friberg et al., 2002; Quartino et al., 2012; Henrich et al., 2017; Jost et al., 2019). As the active forms of both drugs affect the proliferation process, the PD effect is modeled via a linear term with one joint parameter *slope* multiplied to the feedback-regulated first order proliferation rate constant. Other modeling approaches for the incorporation of the PD effect previously showed worst results in model fitting such that we focused on the described term which is additionally more plausible regarding the PD effect, i.e. an impaired proliferation through the incorporation of the metabolized drug into the DNA (Jost et al., 2019). Matured neutrophils die by the process of apoptosis with the rate k_{ma}. A schematic representation of the model is shown in **Figure 1** and model constants are listed in **Table 2**. As no PK biomarkers were measured in the examined dataset, we relied on published PK models and individualized the PD models with respect to individual sets of PD parameters.

In the following, we describe the NLME parameter estimation approach. Therefore, we summarize model (1) for patient i as

$$\dot{x}_i(t) = f(x_i(t), \theta_i, u_i(t))$$

with $u_i(t)$ the individual treatment schedule and $\theta_i = (Base_i, k_{tr,i}, \gamma_i, slope_i)^T$ the patient specific parameter values of

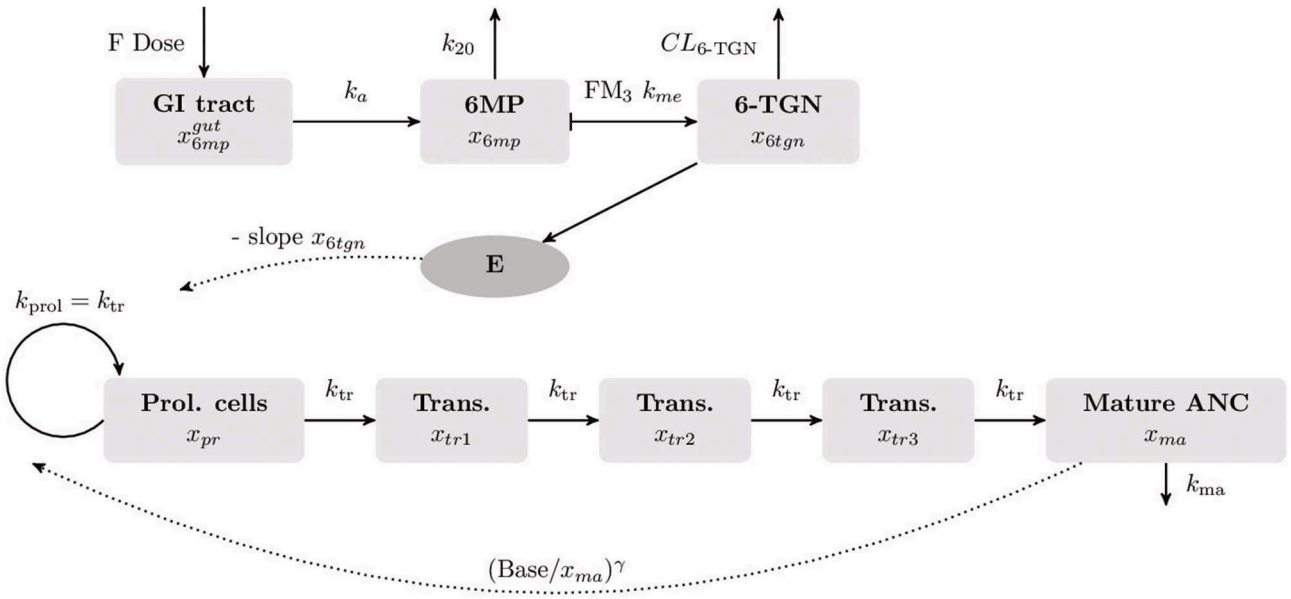

FIGURE 1 | Visualization of the final compartment model used for the population PK/PD analysis. The underlying mathematical models for the PK of 6MP and the myelosuppression were published by Hawwa et al. (2008), respectively (Le et al., 2018). The PK of orally administered 6MP is described as a three compartment model. A fraction of the 6MP dosage (6MP dose multiplied with the bioavailability factor F) enters the gastrointestinal (GI) tract where bioavailable 6MP is absorbed into the central compartment by the rate k_a. In the central compartment, 6MP is eliminated with the first order kinetics k_{20}. The elimination rate also comprises metabolization of 6MP to its active form 6-thioguanine nucleotide (6-TGN) with the rate FM_3 k_m. The hematopoiesis of neutrophils is described by a chain of five compartments. The first compartment represents the hematopoietic stem cells proliferating with the rate k_{prol}. The maturation process with equivalent transition rates k_{tr} is represented by three intermediate compartments after which matured cells enter the circulating blood (last compartment). Matured cells die by the process of apoptosis with the rate k_{ma}. The neutrophil baseline *Base* is maintained by the feedback term $(B/x_{ma})^{\gamma}$. As 6-TGN is incorporated into the DNA leading to cell apoptosis, the proliferation process is negatively affected by a linear PD function E.

the steady state of neutrophils *Base*, the transition rate k_{tr}, the feedback term γ, and the PD effect *slope*. The vector θ_i contains the fixed effect parameters $Base, k_{tr}, \gamma$ and *slope* for all patients and the individual realizations $\eta_i \in \mathbb{R}^4, i = 1, \ldots, 116$ of the random variable

$$\eta = (\eta_{Base}, \eta_{k_{tr}}, \eta_{\gamma}, \eta_{slope})^T \sim \mathcal{N}(0, \Omega) \tag{4}$$

with the mean $0 \in \mathbb{R}^4$ and the diagonal variance matrix $\Omega \in \mathbb{R}^{4\times4}$ with the diagonal vector $\omega^2 = (\omega_1^2, \omega_2^2, \omega_3^2, \omega_4^2)^T$. Interindividual variability (IIV) was assumed as log-normally distributed for all four parameters resulting in the following relation between fixed and random effects:

$$Base_i = Base\ exp(\eta_{i,Base}) \tag{5}$$
$$k_{tr,i} = k_{tr}\ exp(\eta_{i,k_{tr}}) \tag{6}$$
$$\gamma_i = \gamma\ exp(\eta_{i,\gamma}) \tag{7}$$
$$slope_i = slope\ exp(\eta_{i,slope}) \tag{8}$$

summarized as $\theta_i = g(\theta, \eta_i)$ and for the description of the residual variability a proportional error model was used

$$y_{ij} = x_{ma}(t_{ij}) + x_{ma}(t_{ij})\ \varepsilon \quad i = 1, \ldots, 116, \quad j = 1, \ldots, n_i \tag{9}$$

with a normally distributed measurement error $\varepsilon \sim \mathcal{N}(0, \sigma^2)$ and ANC count measurements y_{ij}.

The parameters were estimated using the first order conditional estimation (FOCE) method with η-ε interaction. This approximation method results in the parameter estimation method

$$\begin{aligned}
\min_{x_i(t),\theta,\omega^2,\sigma^2,\eta_i} \quad & \sum_{i=1}^{116} \mathcal{L}_{i,outer}^{\text{FOCEi}}(x_i(t), u_i(t), \theta, \omega^2, \sigma^2, \eta_1^*, \ldots, \eta_N^*) \\
& \forall\, t \in [0, t_f^i],\ i = 1, \ldots, 116 \\
\text{s.t.} \quad \eta_i^* &= \text{argmin}_{\eta_i} = \mathcal{L}_{MAP}^{\text{FOCEi}}(x_i(t), u_i(t), \theta, \omega^2, \sigma^2, \eta_i) \\
& \forall\, t \in [0, t_f^i],\ i = 1, \ldots, 116 \\
\text{s.t.} \quad \dot{x}_i(t) &= f(t, x_i(t), u_i(t), \theta_i) \\
& \forall\, t \in [0, t_f^i],\ i = 1, \ldots, 116 \\
x_i(t_{0,i}; \theta_i) &= x_{0,i}(\theta_i) \\
& \forall\, t \in [0, t_f^i],\ i = 1, \ldots, 116 \\
\theta_i &= g(\theta, \eta_i) \\
& \forall\, t \in [0, t_f^i],\ i = 1, \ldots, 116
\end{aligned} \tag{10}$$

consisting of two nested optimization problems and t_f^i being the time point of patient *i*'s last ANC measurement. The two parameter estimation problems (estimating $\theta, \omega^2, \sigma^2$ with fixed η_i and vice versa) are iteratively solved until a convergence criterion is fulfilled (Bae and Yim, 2016). For the detailed derivation of the FOCE method with η-ε interaction and the

TABLE 2 | Model constants of the pharmacokinetic model of 6MP and its metabolite 6-TGN from Hawwa et al. (2008), death rate constant of matured neutrophils, and initial conditions of the model (1).

Constant	Value	Unit	Description/comment
F	0.22		Bioavailability factor
k_a	31.2	1/day	Absorption rate constant of 6MP
k_{20}	12.72	1/day	Elimination rate constant of 6MP
FM_3	0.019		Fractional metabolic transformation into 6TGN
k_{me}	9.9216	1/day	Metabolic transformation rate constant of 6MP into either 6TGN or 6MPN
$CL_{6tgn}(BSA)$	$0.219\ (BSA)^{1.16}$	L/day	Body surface area (BSA) dependent clearance of metabolite 6-TGN
k_{ma}	2.3765	1/day	Death rate of matured neutrophils/leukocytes
$u(t_i)$		mg	6MP amount at time point t_i
$x_{6mp}^{gut}(0)$	0	mg	Same initial value for $x_{6mp}(0)$
$x_{6tgn}(0)$	0	mg/L	
$x_{pr}(0)$	$(Base\ k_{ma})/k_{tr}$	G/L	Same initial value for $x_{tr1}(0) = x_{tr2}(0) = x_{tr3}(0)$
x_{ma}	*Base*	G/L	

formulation of the resulting objective functions $\mathcal{L}_{i,outer}^{\text{FOCEi}}$ and $\mathcal{L}_{MAP}^{\text{FOCEi}}$ we refer the interested reader to Wang (2007) and Demidenko (2013) as we confine our analysis on the application of the parameter estimation method.

2.3. Out-of-Sample Validation

The reliability of the final population PK/PD model was tested via out-of-sample cross-validation. For each patient, the first 70% of ANC measurements were used for parameter estimation and the final 30% were used to evaluate the model predictions. Model accuracy and predictability were evaluated using the root mean squared error (RMSE) and the mean absolute error (MAE).

2.4. Simulation Study

We compared individual simulated minimal, median, and maximal ANCs resulting from the application of different dosing regimens (MT dosage over time). The choice of the different doses described in **Table 3** was based on ALL treatment protocols (AIEOP-BFM 2009 with EudraCT number 2007-004270-43, NOPHO-ALL 2008-003235-20, and UKALL 2010-020924-22). In particular, we sought to investigate the relationship between an increased total amount of chemotherapy (higher dosage) and plausibly reduced ANC in the *in silico* simulations. Throughout, we used the fitted models (estimated model parameters) from section 2.2 and only varied the chemotherapy dosage. The simulated ANC values were obtained from the individual actual measurement time points.

2.5. Software

The population PK/PD analysis was performed with the NLME modeling program NONMEM 7.4 (ICON Plc., Dublin, Irland) (Beal et al., 2009). There exist several other software packages

TABLE 3 | Different dosing protocols for our *in silico* simulation study.

Nr	Description	Short
1	Collected clinical data	(ClinicalData)
2	Fitted model based on patient's actual dosing	(FittedModels)
3	Daily 6MP administration of 25 mg/m^2 (50% of AIEOP dosis)	(25 mg/m^2)
4	Daily 6MP administration of 50 mg/m^2 (AIEOP dosis)	(50 mg/m^2)
5	Daily 6MP administration of 75 mg/m^2 (NOPHO/UK dosis)	(75 mg/m^2)
6	Daily 6MP administration of 100 mg/m^2 (200% of AIEOP dosis)	(100 mg/m^2)

Identical protocols for the administration of 6MP for ClinicalData and FittedModels with a median of the patient-individual average daily dosages of 43.15 ± 10.5 mg/m^2 (minimum 15.8 mg/m^2, maximum 72.9 mg/m^2).

for parameter estimation of NLME models providing the same or similar algorithms. A variety of algorithms are provided in R Core Team (2019, version 3.6.1). The software Monolix (version 2019R1. Antony, France: Lixoft SAS, 2019) and Diffmem (see https://bitbucket.org/tomhaber/diffmem/src/master/, Melicher et al., 2017) are based on the stochastic approximation expectation maximization algorithm and the recently published package Pumas (based on Julia, see https://pumas.ai/) contains several deterministic and stochastic algorithms. Standard errors were computed with the $COVARIANCE step in NONMEM. Pirana (Certara, Princeton, USA) was used for the generation of the visual predictive check with *auto_bin* option. The simulations in section *out-of-sample validation* and *simulation study* were performed with the ODE integrator CVodes (Sundials, Lawrence Livermore National Laboratory, Livermore) (Hindmarsh et al., 2005) interfaced to CasADi (Optimization in Engineering Center [OPTEC], K.U. Leuven) (Andersson et al., 2019).

3. RESULTS

3.1. Mathematical Model

Table 4 shows RMSEs, MAEs, and final objective function values for four different parameter estimations. Here, we compared the usage of different PK/PD models and parameter estimations based on either WBC counts or ANCs. First, the explicit consideration of MTX within the PK/PD model of Le et al. (2018) only had a minimal/non-significant effect on the model accuracy, so we fixed it to the ratio 2.5:1 between 6MP and MTX and neglected the PK of MTX in the following. Second, our results showed that the use of the PK model of Hawwa et al. (2008) increased the sensitivity of the PD effect and the model accuracy compared to the 6MP PK model of Jayachandran et al. (2014). Third, ANC measurements resulted in higher accuracy than did WBC measurements.

3.2. Parameter Estimation

Figure 2 shows the comparisons of observed clinical and simulated ANCs derived from the final PK/PD model (1) after parameter estimation for three exemplary chosen patients

TABLE 4 | Results of parameter estimations for different models.

	Model 1	Model 2	Model 3	Model 3
Data	ANC	ANC	ANC	WBC
PK 6MP	Jayachandra	Jayachandra	Hawwa	Hawwa
PK MTX	Panetta	–	–	–
MAE	1.068 (1.65)	1.045 (1.92)	0.9571 (4.31)	1.315 (2.92)
RMSE	1.033 (0.492)	1.022 (0.539)	0.9783 (0.678)	1.147 (0.579)
FinalOBJ	7003	7094	6550	9746*

*Shown are model characteristics [data based on absolute neutrophil count (ANC) or white blood cell (WBC) count and PK models for 6MP and MTX], median and standard deviation in parentheses of individual root mean squared errors (RMSE), mean absolute errors (MAE), and final objective function values (FinalOBJ). Medians and final objective function values are rounded off to four and the standard deviations in parentheses to three significant figures. *Objective value is not comparable to first three values due to different dataset.*

presented in rows 1,3 and 5. For each patient, the individual 6-mercaptopurine (6MP [mg]) dosing protocol is presented in rows 2, 4 and 6, indicating dose changes for efficacy adjustments. The model simulations represented the clinical ANCs quite well in the average and captured trends toward larger or smaller ANC values. However, they did not oscillate as strongly as the measured values. Persistent oscillations of neutrophils often occur in chemotherapy-treated hematopoietic diseases inducing cyclic myelosuppression (see Knauer et al., 2019 and references therein). Several othter reasons were responsible for the observed ANC oscillations such as aberrant hematopoiesis, chemotherapeutic dose adaptations, infections or measurement errors. This exemplary behavior was representative of the entire data set of 116 patients. The visual predictive check plot in **Figure 3** shows the good agreement of model response and measurements for the median (solid line) and

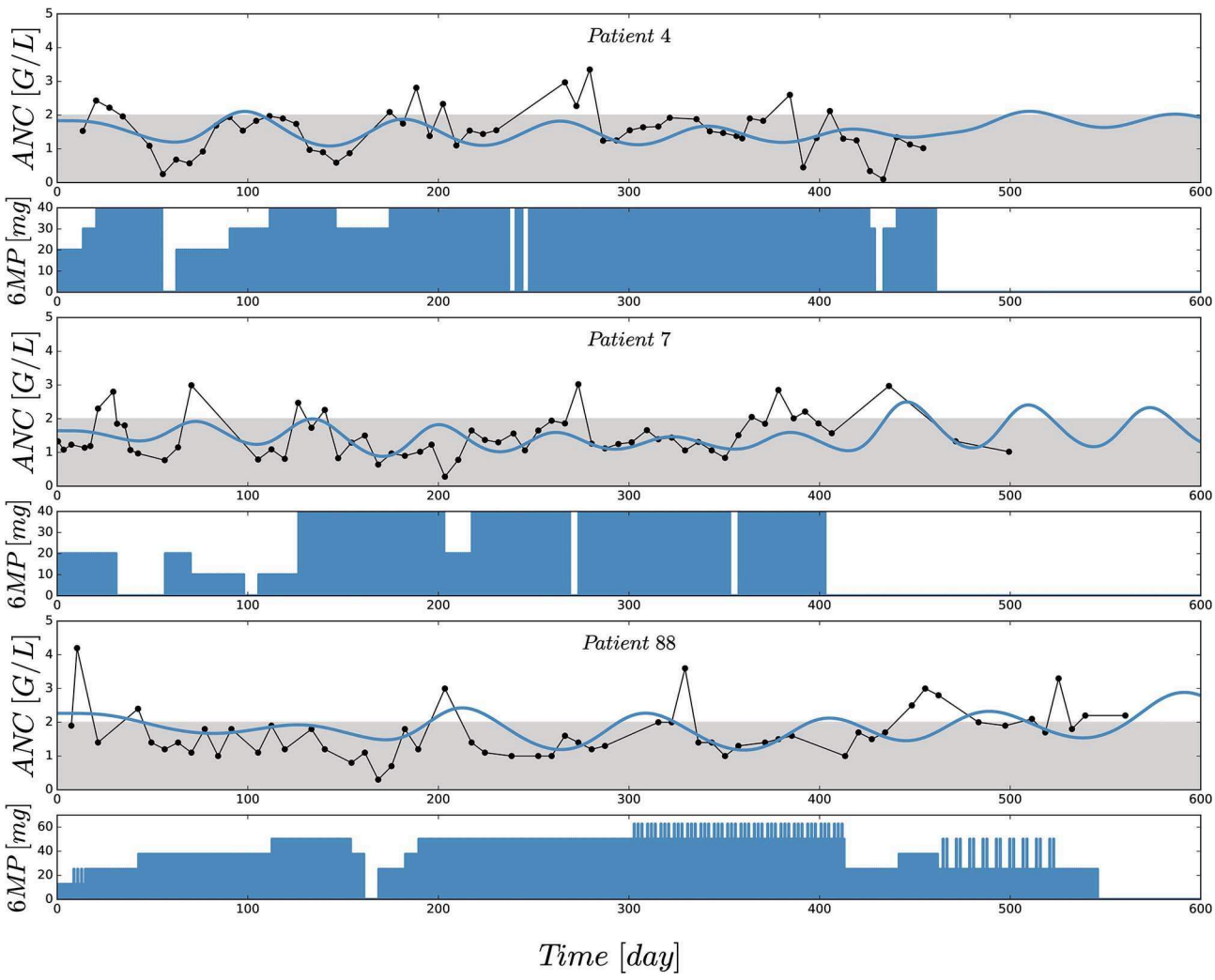

FIGURE 2 | Comparisons of observed (black) and individually simulated (blue) absolute neutrophil counts (ANCs) [G/L] for three exemplary chosen patients presented in rows 1,3 and 5. Simulations of the ANCs (x_{ma}) were performed with the newly proposed mathematical model (1) after nonlinear mixed-effects parameter estimation. Based on a visual assessment, the model captures the trends of the chemotherapy induced myelosuppression (compared with the indicators in **Table 4**). For each patient, the individual 6-mercaptopurine (6MP [mg]) dosing protocol is presented in rows 2, 4 and 6, indicating dose changes for efficacy adjustments. The daily oral 6MP administration, ranging from 10 to 60 mg for the three patients, are presented as filled areas and corresponds to the control function $u(t)$ in model (1).

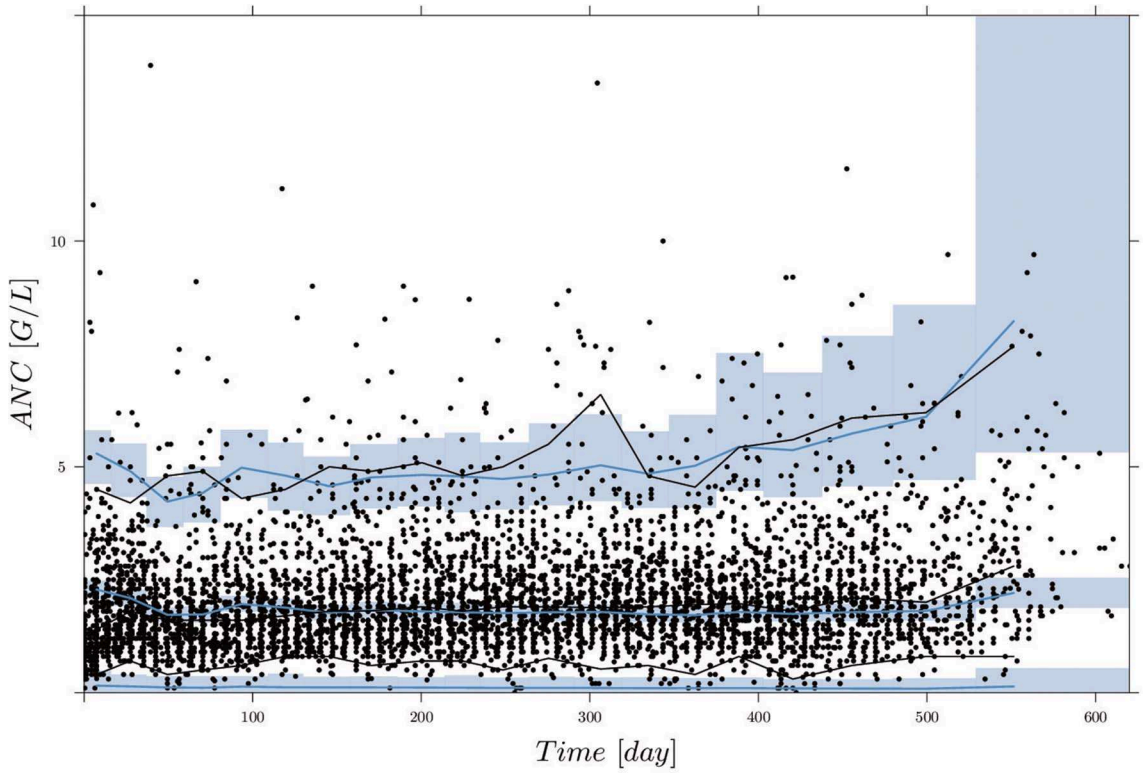

FIGURE 3 | Visual predictive check (VPC), derived by 1,000 simulations with the final parameter estimates from the first column of **Table 5**, for circulating ANCs (G/L) vs. time (days). Black dots are the measured ANCs. Black and blue lines show the median and 2.5th and 97.5th percentiles of measurements and model predictions, respectively. The shaded areas represent the 95% confidence intervals around the 2.5, 50, and 97.5th percentiles of the model predictions. Two ANC outliers (19.9 and 17.8) at time points 285.42 and 340.42 days are not shown.

97.5th percentile (dashed line) with a slight underprediction of the model for low ANC values. The 95% confidence interval of the model simulation median was very thin, indicative of high prediction accuracy. The fixed effect estimate for the ANC steady state was slightly higher than the target range limit of 2 G/L. The estimated transition rate of 0.148 resulted in a mean maturation time (MMT = n_{tr}/k_{tr}) of 487 h (20.3 days) (De Souza et al., 2018). The interindividual variability and residual error were within reasonable ranges.

The goodness-of-fit plot in **Supplemental Data** shows the results of out-of-sample cross-validation. It reflected reasonable model accuracy for fitted (blue) and predicted (red) ANC measurements with spreading around the line of identity because the model was not able (and not intended) to hit the lower and upper peaks of the measurements. The values of estimated model parameters both for the in-sample and out-of-sample calculations are shown in **Table 5**. The parameter values for *slope* and *Base* were reduced and the value of γ was slightly increased for the estimates based on 70% of the ANC. The interindividual variability (IIV) for the *slope* was significantly larger whereas the IIV of k_{tr} was smaller. To evaluate the model accuracy, we calculated the median and standard deviation of the individual MAEs and RMSEs, showing the expected decrease in accuracy for out-of-sample predictions.

3.3. Simulation

Figure 4 shows boxplot results for an *in silico* simulation study based on the 6 different treatment protocols (including the real clinical data) from **Table 3**. We want to stress three main observations.

First, a comparison of the first two entries of the three boxplots confirmed an already known result. The personalized models could reproduce the clinical ANC data on average quite well, with the exception of extreme values quantitatively confirming the observation made in **Figure 2**. Given the similarity of simulated and observed median values, we continued with an objective comparison only of the simulated results (protocols 2–6).

Second, a comparison of the protocols 3–6 (25, 50, 75, and 100 mg/m^2 BSA 6MP) showed a significant and linear dosage-effect relationship with respect to the total amount of 6MP administered, which is, of course, proportional to the daily dose. All (minimal, median and maximal) ANC values decreased linearly, when daily dosing was increased linearly.

Third, a comparison of protocol 2 (the simulation of the real treatment) and protocols 3 and 4 (which gave lower and upper bounds on the total amount of administered 6MP in protocol 2, respectively) showed that the median ANC value of protocol 2 was indeed bounded by the two other values, however, for significantly lower minimal and higher maximal ANC values. **Figure 5** shows an exemplary comparison of

TABLE 5 | Results of parameter estimations of the final model using all (in-sample) or 70% (out-of-sample) of the ANC values.

Data	In-sample	Out-of-sample
Fixed effect parameters		
Base	2.34 (1)	2.06 (0.1)
k_{tr}	0.148 (0.4)	0.146 (0.2)
slope	0.242 (0.2)	0.103 (0.2)
γ	0.769 (0.1)	0.866 (0.2)
Interindividual variability as coefficients of variation		
Base	23.1 (20)	27.5 (10)
k_{tr}	16.5 (30)	7.19 (3)
slope	44.9 (5)	67.8 (1)
γ	10.7 (0.5)	16.5 (0.4)
Proportional additive error	0.226 (2)	0.226 (FIXED)
Parameter estimation errors		
Mean absolute error	0.957 (4)	1.47 (500)
Root mean squared error	0.978 (0.7)	1.21 (7)

Shown are parameter estimates of fixed effects, interindividual variability as coefficient of variation, proportional additive error as variance, and median errors of the parameter estimations rounded off to three significant figures. For the mean absolute and root mean squared errors all ANC measurements are used. Relative standard errors are shown in parentheses rounded off to one significant figure.

protocols 2–6 for one patient, highlighting lower peak values and smaller drug-induced steady state values when the dosing is linearly increased from 25 mg/m^2 to 100 mg/m^2. The actual dosage administered to the patient (blue) ranged between the 25 mg/m^2 and 50 mg/m^2 protocols and resulted in similar ANC dynamics. At approximately day 240, the actual dosing was stopped for a short period, inducing stronger ANC oscillations in the subsequent treatment period and revealing a significant impact of the dosing regimen on the ANCs. This observation is even stronger regarding the proliferating cells as well as cells in the first transit compartment. Similar plots for all 116 patients are provided in the **Supplemental Data**.

4. DISCUSSION

4.1. Mathematical Model

We developed and fitted a population PK/PD model to assess the ANC dynamics during 6MP/MTX treatment, get a better understanding of dose adjustments, and identify solutions to the challenges that arise throughout MT. During the model development process we also fitted the model to WBC measurements. The resulting MAEs and RMSEs were worse compared to the values resulting from ANC measurements. This is probably due to the fact that WBCs comprise different cell lineages, with additional physiological effects that are not accounted for in the mathematical model. In future studies, the current model might be extended to further cell lineages. The models brought forth by Quartino et al. (2012) and Fornari et al. (2019) might serve as a basis and drive the modeling process from a semi-mechanistic approach toward a more mechanistic one.

In addition to using a population estimation approach and applying it to ANC instead of WBC, two modifications brought forth by Le et al. (2018) were shown to yield better results. First, the 6MP PK model of Jayachandran et al. (2014) was replaced by that of Hawwa et al. (2008). The first order kinetics in the PK model of Hawwa et al. (2008) compared to the Michaelis–Menten terms in the PK model of Jayachandran et al. (2014) resulted in more significant concentration changes with altered drug amounts consequently in a more sensitive PD effect. Second, the MTX PK model was completely omitted as the constant ratio of administered 6MP and MTX prevents a differentiation of separate PD effects. Further studies with measurements of drug concentrations, metabolites and clinical effects as cell counts would push forward the development of a mathematical model additionally including the PK of MTX to provide two distinct PD effects and to account for varying ratios of 6MP to MTX. For the currently available data, our new model, which indirectly agglomerates the effects of 6MP and MTX, appears to be a good choice (compare for **Table 4**).

4.2. Model Parameter Estimates

Looking at the resulting model parameter estimates listed in **Table 5**, the question arises as to how these values relate to known biological properties of hematopoiesis and myelosuppression and to other values from the literature. The estimated ANC steady state value *Base* was below the normal ANC range for children, but still higher than the desired ANC range of 0.5–2 G/L. Without treatment, the model-based ANCs would increase to normal patient-specific steady states. Thus, low ANC values were induced via MT or some of the aforementioned external events.

The estimated fixed-effects parameter value of the transition rate $k_{tr} = 0.148$ was comparable with the published mean value ($\bar{k_{tr}} = 0.1431$) obtained from eight pediatric ALL patients from Riley Hospital for Children in Indianapolis (Jayachandran et al., 2014). For better interpretability, the transition rate parameter k_{tr} can be transformed to the MMT (n_{tr}/k_{tr}) of the neutrophils. The estimated MMT in our study, as well as the MMT from Jayachandran et al., are extremely high and do not coincide with biological findings of 3.9 days obtained by Hearn et al. (1998). This mismatch is a large disadvantage of the model as it fails to comply with biological properties, leading to falsely characterized physiological mechanisms and thus reduced model reliability. Jayachandran et al. did not discuss this issue, but a similar observation was made by Craig et al. (2016) who determined an estimated proliferation time of 26 days (Craig et al., 2016). In their work, the authors further presented model modifications to obtain a more realistic maturation time of 3.9 days. For this value we performed two parameter estimations with either *Base* as a parameter or fixed to 5 resulting in promising dynamics but worse RMSEs and MAEs. In future studies, the falsely determined MMT and possible model limitations for continuous low-dose treatments should be further investigated.

The feedback parameter (γ) is significantly higher compared with published values (Friberg et al., 2002), indicating a stronger feedback mechanism during the daily chemotherapy over a long

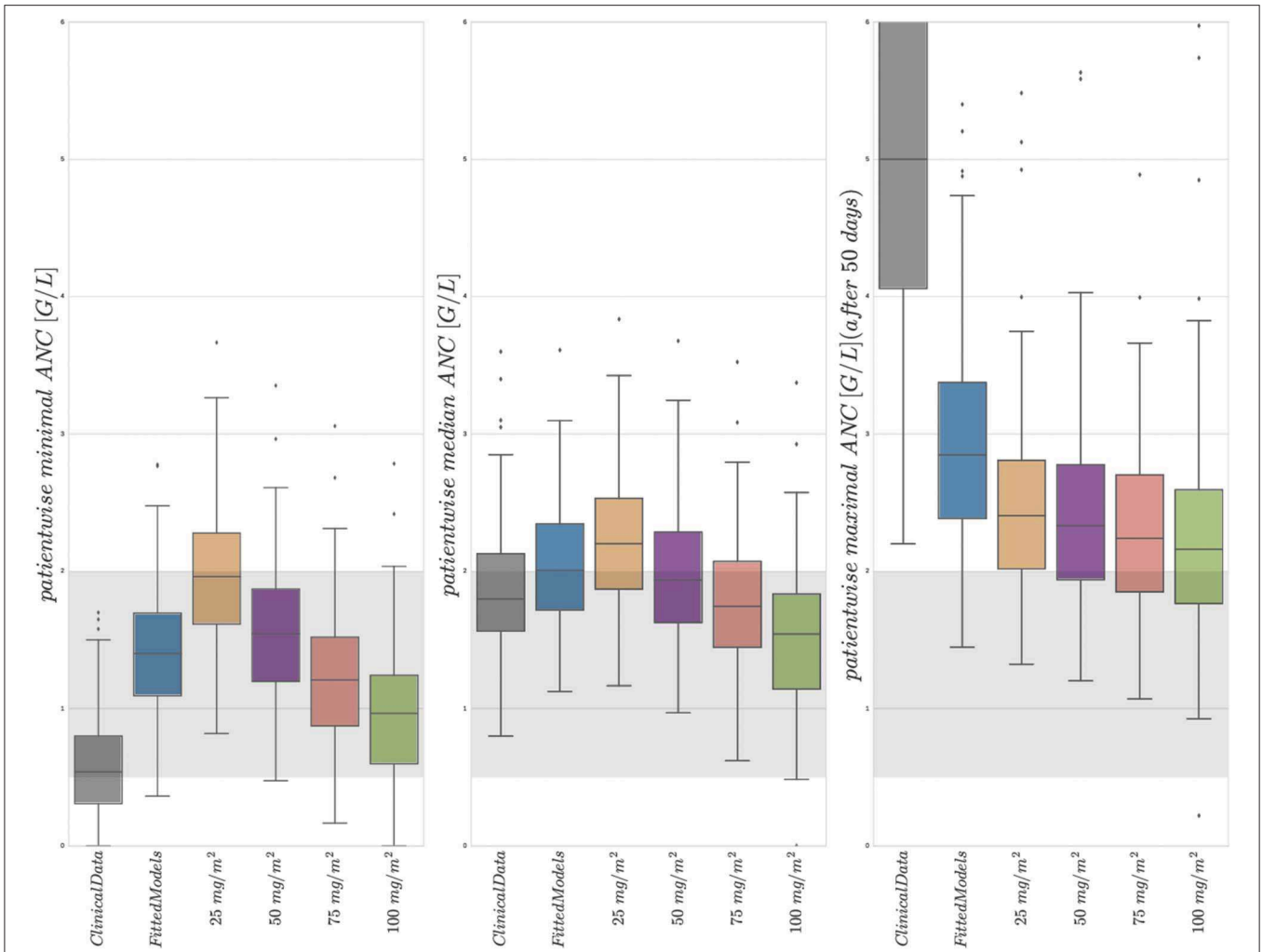

FIGURE 4 | Boxplots of minimal, median, and maximal (from left to right) individual ANCs for all 116 patients. Shown are values for the 6 different protocols from **Table 3**, observed for the first column and simulated for protocols 2–6. The target range (0.5–2.0 G/L) of the NOPHO/UK treatment protocol is shown as the gray background. Horizontal lines within the boxes are the medians, the upper and lower box limits are the first and third quartiles of the data, respectively. The whiskers indicate an even larger confidence region of these quartiles plus/minus 1.5-times the interquartile range. Beyond the whiskers, data are considered as outliers and are plotted as individual points. For the columns representing 25 mg/m^2 to 100 mg/m^2, the total amount of 6MP administered is increasing. The median average individual daily doses actually administered for protocols 1 and 2 were 43.15 ± 10.5 mg/m^2.

period. This is the first time estimated *slope* values of the linear PD function from the PK model of Hawwa et al. (2008) are presented; thus there are no available comparisons.

4.3. Simulation Results

The newly developed mathematical model enables us to perform a virtual comparison of different treatment protocols. The boxplots in **Figure 4** show several interesting results.

First, the median and standard deviation of actual ANC measurements were very accurately matched by the simulation using the estimated parameters (compare the first two entries in the middle boxplot of **Figure 4**). Concerning the patientwise observed and simulated minimal and maximal ANC values, the model demonstrates a corresponding weakened chemotherapy-induced myelosuppression, respectively overproduction of ANCs compared to the high measured variability. This variability is biologically and clinically very plausible due to the aforementioned external events and uncertainties, although periods of severe infections were already excluded. The reproducibility of the median and avoidance of over-fitting of the extreme values are in our opinion good properties of a mathematical model. Given this good correspondence between cross-validated data and simulations, we felt encouraged to compare simulations of different treatment protocols as specified in **Table 3**. Note, however, that generalizations of mathematical models personalized for data from one protocol to another have to be considered with extreme care (compare the discussion for acute myeloid leukemia models by Jost et al., 2019). Further, we want to highlight that the current model is not intended to describe the ANC extrema such that the results of the simulation

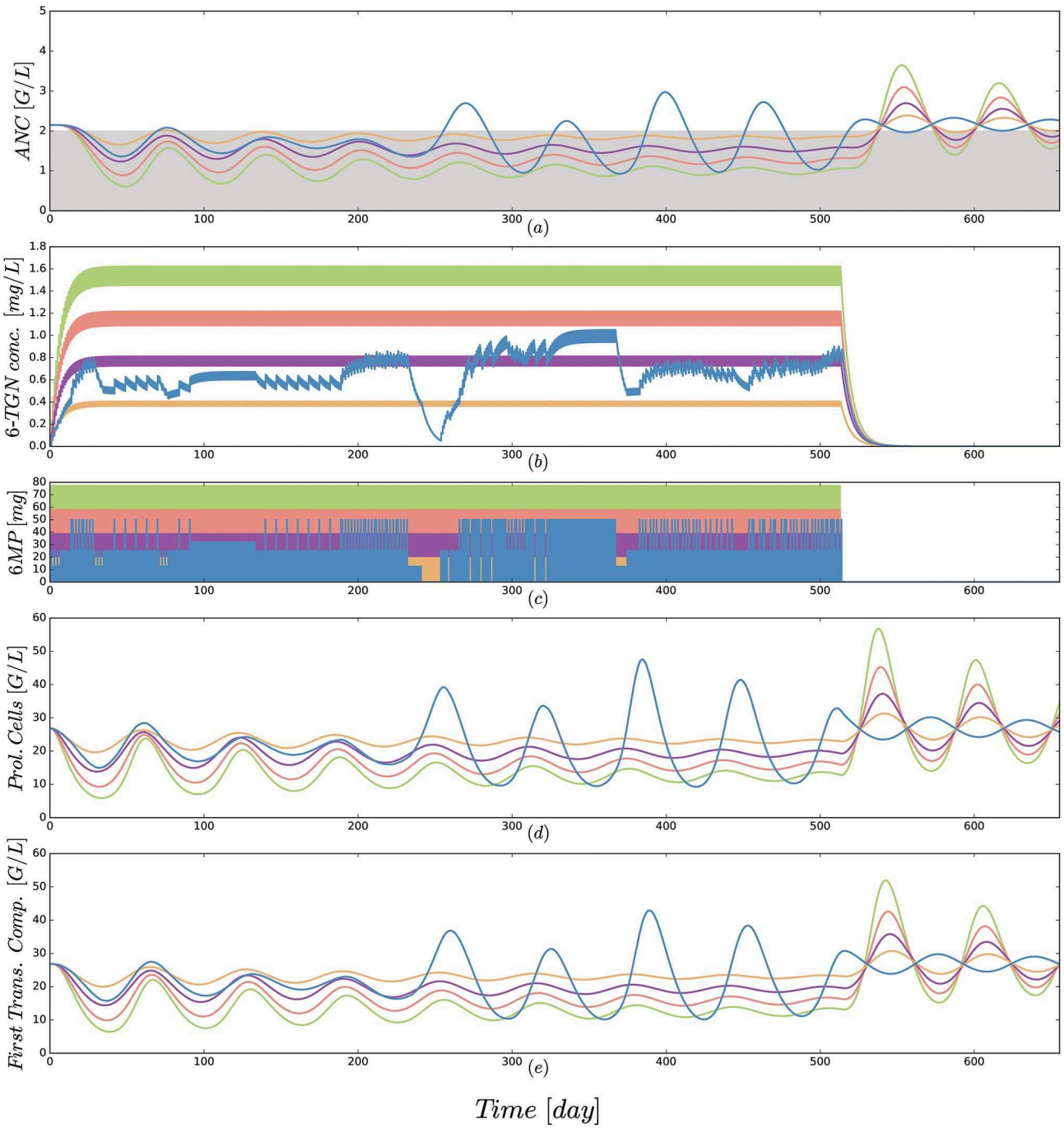

FIGURE 5 | (a) Simulated absolute neutrophil count (ANC) dynamics [equal to x_{ma} in Equation (1)], **(b)** concentration of the active form 6-TGN [equal to x_{6tgn} in Equation (1)], **(c)** 6MP dosing amount [control function $u(t)$ in Equation (1)], **(d)** dynamics of proliferating cells [equal to x_{pr} in Equation (1)] and **(e)** cells of the first transition compartment [equal to x_{tr1} in Equation (1)] for 5 different protocols from **Table 3** and an exemplary patient. Colors of the trajectories are identical to those used in **Figure 4**. The linear increase in dosing from 25 to 100 mg/m^2 forces the neutrophils (ANC) to lower peak values and a smaller drug-induced steady state value at the end of treatment. The actual dosage administered to the patient (blue) ranged between the 25 mg/m^2 and 50 mg/m^2 protocols and resulted in similar ANC dynamics. At approximately day 240, the actual dosing was stopped for a short period, inducing stronger ANC oscillations in the subsequent treatment period. This observation is even stronger regarding the proliferating cells as well as cells in the first transit compartment. Interestingly, these oscillations also continued for some time after the end of treatment. Due to the long simulation horizon, the 6-TGN dynamics are squeezed such that the concentrations between two administrations are not visible.

study have to be treated with caution. The results shall serve as a preliminary assessment of the dose-effect relationship which has to be confirmed in future studies. The relationship might be stronger compared to the current model predictions and demonstrated by the clinical data in **Figure 5**. The impact of model variations on the outcome of simulation studies is usually significant. We tested the value of fixing the k_{tr} parameter to represent a biologically plausible MMT of 3.9 days. This decreased the model accuracy (which is why the results are not included here), but still led qualitatively to the same subsequent effects.

Second, an approximately linear decrease in minimal, median and maximal values could be observed as the dosage increased linearly from 25 to 100 mg/m^2 with a slightly reduced decrease of the maximal ANC values. Again, this linear dose-effect relationship seems biologically plausible. For most of the simulations such as those shown in **Figure 5**, the maximal ANC value decreased. However, for other simulations (see **Supplementary Material**) stronger myelosuppression led to identical maximal ANC values. This effect is due to a feedback mechanism that may lead to increased proliferation for reduced ANC which leads to larger ANC values after some delay.

Third, a tendency for higher oscillations for treatments with pauses and changes in dosage was seen in a comparison of the simulated actual treatment protocol 2 and the constant administrations of protocols 3 and 4, which used lower/higher total amounts of 6MP. Again, an example of this can be seen in **Figure 5**. We believe that in the future adapted dosing schedules might take advantage of the chemotherapy-induced oscillations for an optimized dosing regimen. In the consolidation therapy of acute myeloid leukemia it was shown *in silico* that the timing of the treatment start can have a beneficial influence on the reduction of myelosuppression (Jost et al., 2019). However, high dose chemotherapy administered every 3 to 4 weeks provokes stronger periodic oscillations compared to the daily oral dosing which makes it more challenging to identify and capture the oscillations. For high dosage, previously a multi-compartment hematopoietic model was analayzed regarding Hopf bifurcation and an explicit analytical expression for the bifurcation point was provided depending on model parameters (Knauer et al., 2019). Oscillations of various blood cell populations have been observed in clinical data and partly investigated for different hematological disorders (Haurie et al., 1998; Colijn et al., 2006). The exact mechanisms and interaction between (1) stem cell cycling, (2) hematological disorder, and (3) drug exposure are still not fully understood. In our case, for all 116 patients *in silico* simulations showed that the oscillations were damped (in 84 cases into a steady state) once the chemotherapy was stopped, albeit with long time ranges of up to one year (see **Supplemental Data** for examples). Therefore, we assume that the oscillations in the ANCs observed in our simulations could be attributed to the influence of chemotherapy on the nonlinear dynamics of hematopoiesis. The connection between *model-intrinsic* and *chemotherapy-induced* oscillations should be assessed in detail in future studies. A stability analysis (Edelstein-Keshet, 2005) of the steady state could be performed (e.g., similar to Stiehl, 2014; Tetschke et al., 2018) to assess the theoretical properties of the model and relate them to the physiological behavior of neutrophils.

5. CONCLUSION

We presented a novel NLME model describing myelosuppression for ALL MT among children who received 6MP and MTX and was cross-validated on a data set of 4747 ANC measurements obtained from 116 patients. A comparison with alternative modeling approaches and using WBC counts instead of ANCs showed the benefit of this model. We could show a linear dose-effect relationship superimposed with fluctuations of varying magnitude. Mathematical simulations and more mechanistic modeling approaches will allow to improve the understanding of intrinsic and extrinsic influence factors on the aberrant hematopoiesis and chemotherapy-induced myelosuppression of pediatric ALL patients. Therefore, the monitoring of individual PK profiles and a subsequent analysis of the PK/PD relationship are mandatory next steps for a better dose-effect correlation.

In the future, based on the conduction of further PK and PD experiments driving the development of more advanced mathematical models together with the individual determination of response-related genotyping (Tsujimoto et al., 2018), MT protocols might be developed *in silico*, leading to individualized treatment protocols with better clinical outcomes.

DATA AVAILABILITY STATEMENT

The datasets generated from the parameter estimation process can be found in the **Supplemental Material**.

AUTHOR CONTRIBUTIONS

FJ developed the population PK/PD models, performed the numerical computations, and wrote the first draft of the manuscript. JZ, TL, TR, MR, MM, and SS contributed to the model development, the study designs, and the interpretation of the results. MSu and MSt provided clinical data. All authors contributed to writing the final manuscript.

FUNDING

This project has received funding from the European Research Council (ERC, grant agreement No 647573) and from the European Regional Development Fund (grants SynMODEST and SynIsItFlutter) under the European Union's Horizon 2020 research and innovation program.

SUPPLEMENTARY MATERIAL

The Supplementary Material for this article can be found online at: https://www.frontiersin.org/articles/10.3389/fphys.2020.00217/full#supplementary-material

Goodness-of-fit plot presenting observed vs. individually calculated absolute neutrophil counts for 116 patients (see **Supplemental Data 1**).

Simulations of protocols 2–6 for all 116 patients, similar to **Figure 5** (see **Supplemental Data 1**).

Simulations of protocols 2 for all 116 patients to analyze the steady state behavior (see **Supplemental Data 2**).

The individual parameter estimates of the final PK/PD model are recorded in the file *finalParameterEstimates191221.csv*.

The individual 6-mercaptopurine (6MP) treatment schedules, the observed and calculated absolute neutrophil counts (ANCs) and the patient's weight, height and body surface area are recorded in the file *NONMEMresultsALL191221.csv*. The dataset contains the columns ID, TIME, DV, CMT, AMT, MDV, EVID, IPRED, WEIGHT, HEIGHT and BSA. ID serves as an identifier for the appropriate patient. TIME [day] either specifies the measurement times of ANCs or the time of oral 6MP administrations. DV [G/L] is the dependent variable, in our case the individual ANC measurements. The column CMT specifies the compartment in which a dosing or observation event occurs. AMT [mg] defines the amount of oral 6MP administration. The column MDV allows the user to inform NONMEM whether or not the value in the DV field is missing, but in our case the datasets do not contain missing measurements. The column EVID explicitly declares to NONMEM the type of the current record. EVID=0 defines the record as an observation event and EVID=1 defines the record as a dose event. The column IPRED contains the calculated ANCs derived by the PK/PD model after parameter estimation.

REFERENCES

Andersson, J. A., Gillis, J., Horn, G., Rawlings, J. B., and Diehl, M. (2019). Casadi: a software framework for nonlinear optimization and optimal control. *Math. Prog. Comput.* 11, 1–36. doi: 10.1007/s12532-018-0139-4

Bae, K.-S., and Yim, D.-S. (2016). R-based reproduction of the estimation process hidden behind nonmem® part 2: first-order conditional estimation. *Transl. Clin. Pharmacol.* 24, 161–168. doi: 10.12793/tcp.2016.24.4.161

Beal, S., Sheiner, L., Boeckmann, A., and Bauer, R. (2009). *Nonmem User's Guides (1989–2009)*. Ellicott City, MD: Icon Development Solutions.

Bonate, P. L., and Steimer, J.-L. (2011). *Pharmacokinetic-Pharmacodynamic Modeling and Simulation*. New York, NY: Springer.

Colijn, C., Fowler, A. C., and Mackey, M. C. (2006). High frequency spikes in long period blood cell oscillations. *J. Math. Biol.* 53, 499–519. doi: 10.1007/s00285-006-0027-9

Craig, M., Humphries, A. R., and Mackey, M. C. (2016). A mathematical model of granulopoiesis incorporating the negative feedback dynamics and kinetics of g-csf/neutrophil binding and internalization. *Bull. Math. Biol.* 78, 2304–2357. doi: 10.1007/s11538-016-0179-8

De Souza, D. C., Craig, M., Cassidy, T., Li, J., Nekka, F., Bélair, J., et al. (2018). Transit and lifespan in neutrophil production: implications for drug intervention. *J. Pharmacokinet. Pharmacodyn.* 45, 59–77. doi: 10.1007/s10928-017-9560-y

Demidenko, E. (2013). *Mixed Models: Theory and Applications With R*. New Jersey, NJ: John Wiley & Sons.

Edelstein-Keshet, L. (2005). *Mathematical Models in Biology*. Philadelphia, PA: SIAM.

Fornari, C., O'Connor, L. O., Pin, C., Smith, A., Yates, J. W., Amy Cheung, S., et al. (2019). Quantifying drug-induced bone marrow toxicity using a novel haematopoiesis systems pharmacology model. *Pharmacometr. Syst. Pharmacol.* 8, 858–868. doi: 10.1002/psp4.12459

Friberg, L., Henningsson, A., Maas, H., Nguyen, L., and Karlsson, M. (2002). Model of chemotherapy-induced myelosuppression with parameter consistency across drugs. *J. Clin. Oncol.* 20, 4713–4721. doi: 10.1200/JCO.2002.02.140

Godfrey, C., Sweeney, K., Miller, K., Hamilton, R., and Kremer, J. (1998). The population pharmacokinetics of long-term methotrexate in rheumatoid arthritis. *Brit. J. Clin. Pharmacol.* 46, 369–376. doi: 10.1046/j.1365-2125.1998.t01-1-00790.x

Haurie, C., Dale D. C., Mackey, M. C. (1998). Cyclical neutropenia and other periodic hematological disorders: a review of mechanisms and mathematical models. *Blood* 92, 2629–2640.

Hawwa, A. F., Collier, P. S., Millership, J. S., McCarthy, A., Dempsey, S., Cairns, C., et al. (2008). Population pharmacokinetic and pharmacogenetic analysis of 6-mercaptopurine in paediatric patients with acute lymphoblastic leukaemia. *Brit. J. Clin. Pharmacol.* 66, 826–837. doi: 10.1111/j.1365-2125.2008.03281.x

Hearn, T., Haurie, C., and Mackey, M. C. (1998). Cyclical neutropenia and the peripheral control of white blood cell production. *J. Theor. Biol.* 192, 167–181. doi: 10.1006/jtbi.1997.0589

Henrich, A., Joerger, M., Kraff, S., Jaehde, U., Huisinga, W., Kloft, C., et al. (2017). Semimechanistic bone marrow exhaustion pharmacokinetic/pharmacodynamic model for chemotherapy-induced cumulative neutropenia. *J. Pharmacol. Exp. Ther.* 362, 347–358. doi: 10.1124/jpet.117.240309

Hindmarsh, A., Brown, P., Grant, K., Lee, S., Serban, R., Shumaker, D., et al. (2005). SUNDIALS: suite of nonlinear and differential/algebraic equation solvers. *ACM Trans. Math. Softw.* 31, 363–396. doi: 10.1145/1089014.1089020

Hindorf, U., Lindqvist, M., Peterson, C., Söderkvist, P., Ström, M., Hjortswang, H., et al. (2006). Pharmacogenetics during standardised initiation of thiopurine treatment in inflammatory bowel disease. *Gut* 55, 1423–1431. doi: 10.1136/gut.2005.074930

Hoffbrand, A. V., Higgs, D. R., Keeling, D. M., and Mehta, A. B. (2016). *Postgraduate Haematology*. John Wiley & Sons.

Hui, K. H., Chu, H. M., Fong, P. S., Cheng, W. T. F., and Lam, T. N. (2019). Population pharmacokinetic study and individual dose adjustments of high-dose methotrexate in chinese pediatric patients with acute lymphoblastic leukemia or osteosarcoma. *J. Clin. Pharmacol.* 59, 566–577. doi: 10.1002/jcph.1349

Jayachandran, D., Laínez-Aguirre, J., Rundell, A., Vik, T., Hannemann, R., Reklaitis, G., et al. (2015). Model-based individualized treatment of chemotherapeutics: Bayesian population modeling and dose optimization. *PLoS ONE* 10:e0133244. doi: 10.1371/journal.pone.0133244

Jayachandran, D., Rundell, A. E., Hannemann, R. E., Vik, T. A., and Ramkrishna, D. (2014). Optimal chemotherapy for leukemia: a model-based strategy for individualized treatment. *PLoS ONE* 9:e109623. doi: 10.1371/journal.pone.0109623

Jost, F., Schalk, E., Rinke, K., Fischer, T., and Sager, S. (2019). Mathematical models for cytarabine-derived myelosuppression in acute myeloid leukaemia. *PLoS ONE* 14:e0204540. doi: 10.1371/journal.pone.0204540

Karppinen, S., Lohi, O., and Vihola, M. (2019). prediction of leukocyte counts during paediatric acute lymphoblastic leukaemia maintenance therapy. *Sci. Rep.* 9, 1–11. doi: 10.1038/s41598-019-54492-5

Knauer, F., Stiehl, T., and Marciniak-Czochra, A. (2019). Oscillations in a white blood cell production model with multiple differentiation stages. *J. Math. Biol.* 1–26. doi: 10.1007/s00285-019-01432-6

Korell, J., Stamp, L. K., Barclay, M. L., Dalrymple, J. M., Drake, J., Zhang, M., et al. (2013). A population pharmacokinetic model for low-dose methotrexate and its polyglutamated metabolites in red blood cells. *Clin. Pharmacokinet.* 52, 475–485. doi: 10.1007/s40262-013-0052-y

Le, T. T., Jost, F., Raupach, T., Zierk, J., Rauh, M., Suttorp, M., et al. (2018). A mathematical model of white blood cell dynamics during maintenance therapy of childhood acute lymphoblastic leukemia. *Math. Med. Biol.* 36, 471–488. doi: 10.1093/imammb/dqy017

Melicher, V., Haber, T., and Vanroose, W. (2017). Fast derivatives of likelihood functionals for ode based models using adjoint-state method. *Comput. Stat.* 32, 1621–1643. doi: 10.1007/s00180-017-0765-8

Nagulu, M., Kiran, V. U., Nalini, Y., Reddy, Y. N., and Krishna, D. R. (2010). Population pharmacokinetics of methotrexate in indian cancer patients. *Asian Pac. J. Cancer Prevent.* 11, 403–407. Available online at: http://journal.waocp.org/article_25216_c66d07759a9ccdf9e27b3c46c5450c48.pdf

Panetta, J., Yanishevski, Y., Pui, C.-H., Sandlund, J. T., Rubnitz, J., Rivera, G. K., et al. (2002). A mathematical model of *in vivo* methotrexate accumulation in acute lymphoblastic leukemia. *Cancer Chemother. Pharmacol.* 50, 419–428. doi: 10.1007/s00280-002-0511-x

Panetta, J. C., Sparreboom, A., Pui, C.-H., Relling, M. V., and Evans, W. E. (2010). Modeling mechanisms of *in vivo* variability in methotrexate accumulation and folate pathway inhibition in acute lymphoblastic leukemia cells. *PLoS Comput. Biol.* 6:e1001019. doi: 10.1371/journal.pcbi.1001019

Quartino, A., Friberg, L., and Karlsson, M. (2012). A simultaneous analysis of the time-course of leukocytes and neutrophils following docetaxel administration using a semi-mechanistic myelosuppression model. *Investigat. New Drugs* 30, 833–845. doi: 10.1007/s10637-010-9603-3

R Core Team (2019). *R: A Language and Environment for Statistical Computing*. Vienna: R Foundation for Statistical Computing.

Rühs, H., Becker, A., Drescher, A., Panetta, J. C., Pui, C.-H., Relling, M. V., etal. (2012). Population PK/PD model of homocysteine concentrations after high-dose methotrexate treatment in patients with acute lymphoblastic leukemia. *PLoS ONE* 7:e46015. doi: 10.1371/journal.pone.0046015

Schmiegelow, K., Nielsen, S. N., Frandsen, T. L., and Nersting, J. (2014). Mercaptopurine/methotrexate maintenance therapy of childhood acute lymphoblastic leukemia: clinical facts and fiction. *J. Pediatr. Hematol. Oncol.* 36:503. doi: 10.1097/MPH.0000000000000206

Stiehl, T.-P. (2014). *Mathematical modeling of stem cell dynamics in acute leukemias*. (Ph.D. thesis). Ruprecht-Karls-Universität Heidelberg.

Tetschke, M., Lilienthal, P., Pottgiesser, T., Fischer, T., Schalk, E., and Sager, S. (2018). Mathematical modeling of RBC count dynamics after blood loss. *Processes* 6, 157–185. doi: 10.3390/pr6090157

Tsujimoto, S., Osumi, T., Uchiyama, M., Shirai, R., Moriyama, T., Nishii, R., et al. (2018). Diplotype analysis of nudt15 variants and 6-mercaptopurine sensitivity in pediatric lymphoid neoplasms. *Leukemia* 32:2710. doi: 10.1038/s41375-018-0190-1

Upton, R., and Mould, D. (2014). Basic concepts in population modeling, simulation, and model-based drug development: part 3—introduction to pharmacodynamic modeling methods. *CPT Pharmacometr. Syst. Pharmacol.* 3, 1–16. doi: 10.1038/psp.2013.71

Wang, Y. (2007). Derivation of various nonmem estimation methods. *J. Pharmacokinet. Pharmacodyn.* 34, 575–593. doi: 10.1007/s10928-007-9060-6

Conflict of Interest: The authors declare that the research was conducted in the absence of any commercial or financial relationships that could be construed as a potential conflict of interest.

Copyright © 2020 Jost, Zierk, Le, Raupach, Rauh, Suttorp, Stanulla, Metzler and Sager. This is an open-access article distributed under the terms of the Creative Commons Attribution License (CC BY). The use, distribution or reproduction in other forums is permitted, provided the original author(s) and the copyright owner(s) are credited and that the original publication in this journal is cited, in accordance with accepted academic practice. No use, distribution or reproduction is permitted which does not comply with these terms.

frontiers in Bioengineering and Biotechnology

ORIGINAL RESEARCH
published: 27 March 2020
doi: 10.3389/fbioe.2020.00254

Early Diagnosis of Hepatocellular Carcinoma Using Machine Learning Method

*Zi-Mei Zhang, Jiu-Xin Tan, Fang Wang, Fu-Ying Dao, Zhao-Yue Zhang and Hao Lin**

Key Laboratory for Neuro-Information of Ministry of Education, School of Life Sciences and Technology, Center for Informational Biology, University of Electronic Science and Technology of China, Chengdu, China

Hepatocellular carcinoma (HCC) is a serious cancer which ranked the fourth in cancer-related death worldwide. Hence, more accurate diagnostic models are urgently needed to aid the early HCC diagnosis under clinical scenarios and thus improve HCC treatment and survival. Several conventional methods have been used for discriminating HCC from cirrhosis tissues in patients without HCC (CwoHCC). However, the recognition successful rates are still far from satisfactory. In this study, we applied a computational approach that based on machine learning method to a set of microarray data generated from 1091 HCC samples and 242 CwoHCC samples. The within-sample relative expression orderings (REOs) method was used to extract numerical descriptors from gene expression profiles datasets. After removing the unrelated features by using maximum redundancy minimum relevance (mRMR) with incremental feature selection, we achieved "11-gene-pair" which could produce outstanding results. We further investigated the discriminate capability of the "11-gene-pair" for HCC recognition on several independent datasets. The wonderful results were obtained, demonstrating that the selected gene pairs can be signature for HCC. The proposed computational model can discriminate HCC and adjacent non-cancerous tissues from CwoHCC even for minimum biopsy specimens and inaccurately sampled specimens, which can be practical and effective for aiding the early HCC diagnosis at individual level.

Keywords: hepatocellular carcinoma, early diagnosis, cirrhosis, REOs, mRMR, support vector machine

OPEN ACCESS

Edited by:
Meng Zhou,
Wenzhou Medical University, China

Reviewed by:
Lei Deng,
Central South University, China
Shaherin Basith,
Ewha Womans University, South Korea

***Correspondence:**
Hao Lin
hlin@uestc.edu.cn

Specialty section:
This article was submitted to Bioinformatics and Computational Biology, a section of the journal Frontiers in Bioengineering and Biotechnology

Received: *02 January 2020*
Accepted: *12 March 2020*
Published: *27 March 2020*

Citation:
Zhang Z-M, Tan J-X, Wang F, Dao F-Y, Zhang Z-Y and Lin H (2020) Early Diagnosis of Hepatocellular Carcinoma Using Machine Learning Method. Front. Bioeng. Biotechnol. 8:254. doi: 10.3389/fbioe.2020.00254

INTRODUCTION

Liver cancer is the fourth leading cause of death in patients with malignant cancerous (Indhumathy et al., 2018; Villanueva, 2019). Hepatocellular carcinoma (HCC), which accounts for approximately 90% of all liver cancer cases, is frequently diagnosed at a late stage and has a poor prognosis. Thus, the early HCC diagnosis is significant to improve the prognosis and survival of patients (Asia-Pacific Working Party on Prevention of Hepatocellular Carcinoma, 2010). At present, diagnosis of HCC is based on laboratory investigations and imaging techniques (El-Serag, 2011; Hartke et al., 2017). Nevertheless, for HCC, especially for early HCC, current serum biomarkers and tools, such as α-fetoprotein (AFP) and imaging techniques, displayed poor diagnostic sensitivity and specificity (Sun et al., 2015). Liver biopsy is regarded as a good diagnostic choice in clinical practice only when

Abbreviations: CwHCC, cirrhosis tissues in patients with HCC; CwoHCC, cirrhosis tissues in patients without HCC; HCC, hepatocellular carcinoma; IFS, incremental feature selection; mRMR, maximum redundancy minimum relevance; REOs, relative expression orderings; SVM, support vector machine.

imaging techniques cannot provide accurate identification of HCC (Russo et al., 2018). However, the biopsy location is usually inaccurate, which might result in inaccurately sampling and thus decrease the diagnosis successful rate (Forner et al., 2008). Therefore, it is necessary to design new methods or discovery new diagnostic signatures to assist the pathologists in the identification of early HCC using biopsy specimens, even inaccurately sampled biopsy specimens. It is likely that the adjacent non-cancerous tissues (cirrhosis tissues in patients with HCC or normal tissues in patients with HCC) can be affected by cancerous tissues, so that they may obtain some similar molecular characteristics of cancerous tissues (Budhu et al., 2006; Wei et al., 2014).

The existed diagnostic signatures are mainly on the basis of risk scores obtained from signature genes' expression (Wurmbach et al., 2007; Archer et al., 2009; Zhou et al., 2015, 2017; Qu et al., 2019), which are highly sensitive to measurement batch effects (Guan et al., 2018) and are hardly applied in clinical settings. Luckily the relative expression orderings (REO)-based strategy (Zhang et al., 2013; Zhou et al., 2013; Wang et al., 2015; Li et al., 2016), which was firstly proposed by Eddy et al. (2010), is highly robust against experimental batch effects (Cai et al., 2015; Ao et al., 2016; Zhao et al., 2016) and platform differences (Guan et al., 2016), partial RNA degradation (Chen et al., 2017; Liao et al., 2017, 2018; Tang et al., 2018) and uncertain sampling sites within the same cancer tissue (Cheng et al., 2017). And thus the REOs have been used in the early diagnosis of HCC (Ao et al., 2018), gastric cancer (Yan et al., 2019) and colorectal cancer (Guan et al., 2019). In 2018, Ao et al. (2018) obtained 19 gene pairs by using the within-sample REOs. These genes could improve early HCC diagnosis using biopsy specimens, even inaccurately sampled biopsy specimens. However, the rule to identify HCC based on REOs is so simply that some intrinsic relationships among these genes are not revealed. Moreover, the accuracy for HCC diagnosis should still be improved.

Machine learning method is a good choice to uncover underlying patterns (Stephenson et al., 2019). It has been widely employed in bioinformatics (Cao et al., 2017; Bao et al., 2019; Conover et al., 2019; Moritz et al., 2019; Stephenson et al., 2019; Zou and Ma, 2019; Sun et al., 2020). The current work aims to develop a machine learning based method to diagnose HCC within-sample REOs. By removing redundant REOs using minimum redundancy maximum relevance (mRMR), a diagnostic signature consisting of 11 gene pairs was obtained. These signatures were also applied in some independent datasets for examining the performance of these gene pairs for HCC identification. High accuracies were obtained, suggesting that the obtained 11-gene-pair signature based on mRMR is better than the existed 19-gene-pair signature gained by Ao et al. (Ao et al., 2018).

MATERIALS AND METHODS

Data Collection and Preprocessing

The gene expression profiles datasets were freely gained from GEO (Barrett et al., 2005) and TCGA (Tomczak et al., 2015) database. Firstly, according to the type and sampling method of samples, the training datasets were derived from biopsy samples of HCC (D1), surgery samples of HCC (D2), biopsy samples of CwoHCC (D3), and surgery samples of CwoHCC (D4), respectively. To objectively evaluate the model, we separated the samples of each type (D1, D2, D3, and D4) mentioned above into two data subsets: training (80% samples of each type) and testing datasets (20% samples of each type). Finally, the training datasets contained 1091 HCC samples (112 biopsy samples of HCC and 979 surgery samples of HCC) and 242 CwoHCC samples (70 biopsy samples of CwoHCC and 172 surgery samples of CwoHCC). The testing datasets contained 73 biopsy samples (29 HCC samples and 44 CwoHCC samples) and 263 surgery samples (245 HCC samples and 18 CwoHCC samples). The independent datasets, which was comprised of surgical resection samples and biopsy samples, was used to evaluate the performance signature. We used the R package of TCGAbiolinks (Colaprico et al., 2016) to download the gene expression data which including 371 HCC and 50 normal tissues in patients from TCGA data resource[1] (up to October 19, 2019). The details have been listed in **Supplementary Table S1**.

For the raw data (.CEL files) detected by the Affymetrix platform, the RMA (Robust Multi-array Average) algorithm was used for background adjustment. If a gene was matched to multiple probes, the arithmetic mean expression value was used as the gene expression level. For the data sets detected by the Illumina platforms, we directly used the processed expression data.

The Within−Sample Relative Expression Orderings

Within a sample, the REOs of two genes (a and b) is expressed as $Ea > Eb$ (or $Ea < Eb$) if gene a has higher (or lower) expression level than gene b. The REOs pattern of a gene pair is regarded as stable if the REOs kept in at least 95% of the samples. A reversal gene pair is a gene pair with stable REOs in both cirrhosis tissues in patients without HCC (CwoHCC) samples and HCC samples, but the REOs patterns are reversed in the second group ($Ea < Eb$ or $Ea > Eb$ in CwoHCC samples but $Ea > Eb$ or $Ea < Eb$ in HCC samples). Here, the reversal gene pairs are selected as the candidate REOs signature for the identification of HCC. Then we obtained the common genes between training datasets and validation datasets and its corresponding gene expression profile. Subsequently, based on the gene expression profiles and reversal gene pairs, we generate a new profile by using 1, 0, and −1 to represent $Ea > Eb$, $Ea < Eb$, and other cases (Ea or Eb do not exist), respectively.

Feature Selection Through mRMR and IFS Methods

Based on the new profiles, mRMR (minimum Redundancy Maximum Relevance) (Peng et al., 2005) was applied to ranking the gene pairs based on the conditions of maximum relevance with the disease type along with minimum redundancy with other gene pairs.

[1]https://portal.gdc.cancer.gov/repository

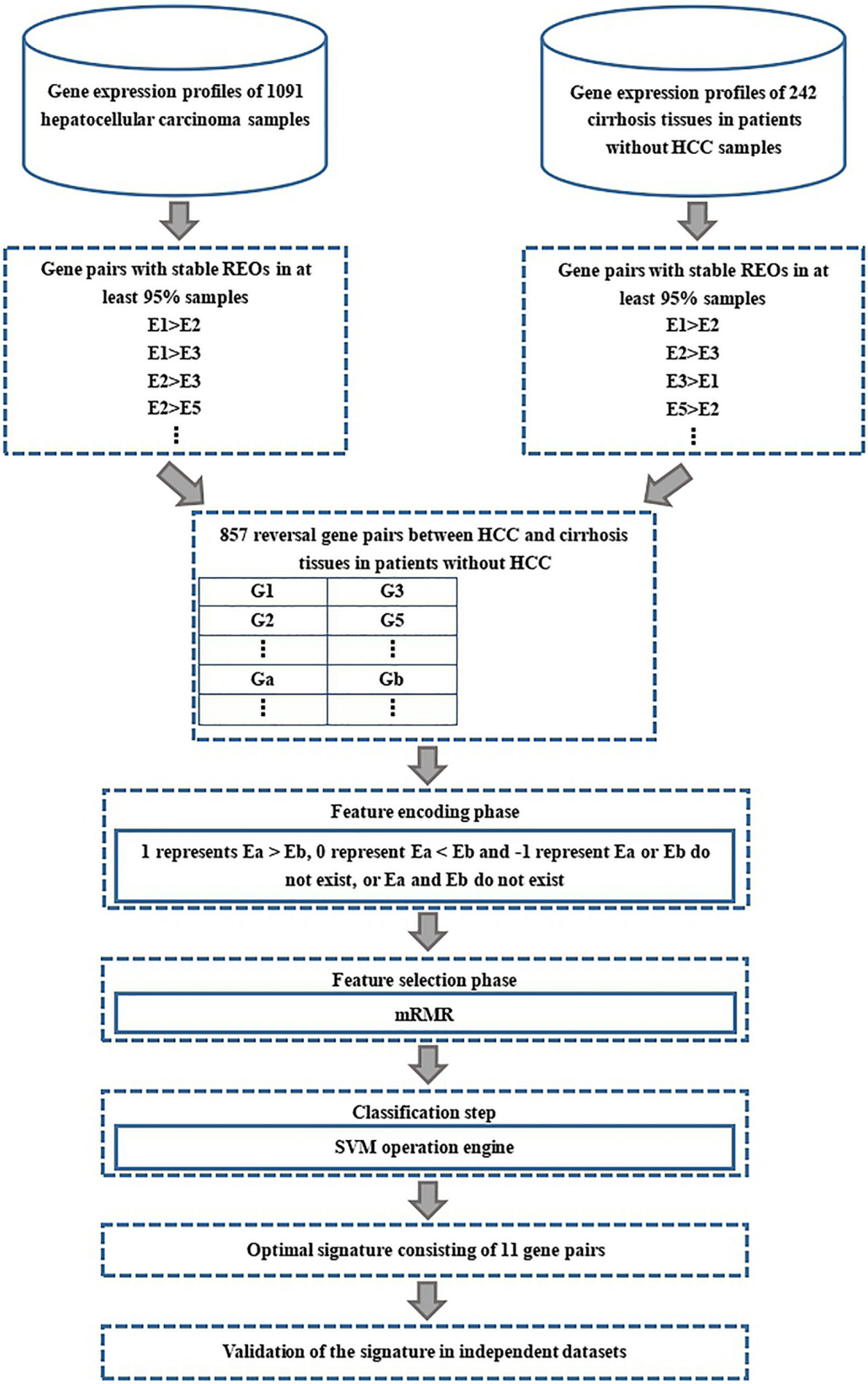

FIGURE 1 | Flowchart presenting the process of developing and validating the HCC diagnostic signature.

Here, Ω represents all 857 gene pairs, *gi* is a gene pair from the 857 gene pairs and *T* is the disease type. The mutual information (*I*) can be formulated as:

$$I(g_i, T) = \int p(g_i, T) \ln \left(\frac{p(g_i, T)}{p(g_i)p(T)}\right) dg_i dT. \quad (1)$$

The mRMR function:

$$mRMR = \frac{1}{|\Omega|} \sum_{g_i \in \Omega} I(g_i, T) - \frac{1}{|\Omega|^2} \sum_{g_i g_j \in \Omega} I(g_i, g_j) \quad (2)$$

where *I(gi, T)* is mutual information between the *gi* gene pair and disease type *T*, *I(gi, gj)* is mutual information between *gi* and *gj*. Then we used incremental feature selection (IFS) (Tan et al., 2019; Yang et al., 2019) method to select the optimal gene pairs from 857 mRMR gene pairs as diagnostic signature. The details about IFS can be found in (Dao et al., 2019).

Classification Through SVM

Support Vector Machine (SVM) is a powerful classification method which has been used extensively in the fields of biological data mining (Cao et al., 2014; Manavalan and Lee, 2017; Manavalan et al., 2017, 2018b, 2019c,d; Tang et al., 2017; Bu et al., 2018; Zhang et al., 2018; Chao et al., 2019a,b; Wang et al., 2019). Here, the free package LibSVM (version 3.23) (Chang and Lin, 2011) was downloaded to implement SVM. Due to its good performance on non-linear problem, RBF (radial basis function) was utilized. The values of two parameters *C* and γ for SVM are determined by the use of grid search with fivefold cross-validation. In present work, the optimal values are $C = 0.125$ and $\gamma = 0.5$, respectively.

Performance Metrics

The sensitivity, specificity and accuracy (Basith et al., 2019; Manavalan et al., 2018a,c, 2019a,b) was applied to evaluating the performance of prediction methods. Here, HCC samples were regarded as positive samples; CwoHCC samples were negative samples. Mathematical representation of the above mentioned measures are calculated as:

$$\begin{cases} \text{Sensitivity} = \frac{\text{TP}}{\text{TP} + \text{FN}} \\ \text{Specificity} = \frac{\text{TN}}{\text{TN} + \text{FP}} \\ \text{Accuracy} = \frac{\text{TP} + \text{TN}}{\text{TP} + \text{FP} + \text{TN} + \text{FN}} \end{cases} \quad (3)$$

where TP, FN, TN, and FP denotes the number of true positives, false negatives, true negatives, and false positives, respectively. Additionally, the ROC curve and AUC are commonly used to test the balance between true positive rate and false positive rate.

RESULTS

Identification of the Diagnostic Signature

The flow diagram for identifying and validating the diagnostic signature is shown in **Figure 1**. Firstly, total of 13,586,043 stable gene pairs which have an identical REOs in at least 95% of the 1091 HCC samples were recognized. Similarly, we also identified 14,475,509 stable gene pairs which have an identical REOs in at least 95% of the 242 CwoHCC samples. Then, we obtained 857 reversal gene pairs between the HCC samples and CwoHCC samples in the training data (see section "Materials and Methods"). Based on the new profiles (see section "Materials and Methods"), 11 gene pairs shown in **Table 1** were picked out by using mRMR with SVM and regarded as the diagnostic signature. The 11-gene-pair could produce the accuracy of 100% on training data for HCC identification. **Figure 2** showed the IFS process (blue curve).

Examination of the Diagnostic Signature on Independent Datasets

Subsequently, we used biopsy and surgically resected samples to estimate the performance of the 11-gene-pair (see **Table 2**). For 73 biopsy samples in the testing datasets, it yielded accuracy of 100%, sensitivity of 100%, specificity of 100%. For 263 surgically resected samples in the testing datasets, its accuracy is 100%, sensitivity 100%, specificity 100%. In the data set GSE121248, all (100.0%) of the 70 HCC samples were correctly recognized as HCC. For surgically resected samples, 79.79% of the 475 HCC samples from 3 datasets (GSE109211, GSE112790, and GSE102079) were correctly classified. Moreover, the 11-gene-pair based model could correctly identify the 371 HCC and the 50 normal tissues in patients with HCC (NwHCC) samples measured by RNA-seq, in which no RNA-seq information was included (**Table 2**). These results demonstrated that the 11-gene-pair signature could distinguish HCC from non-cancerous liver tissues and the signature was robust to clinicopathological variations. For the 1190 HCC samples and 62 CwoHCC samples, the sensitivity, specificity, and AUC are 91.93%, 100%, and 0.9597 [95% CI (confidence intervals) is 0.9519–0.9674; see in **Figure 3**], respectively.

For biopsy samples, all of 80 cirrhosis tissues in patients with HCC (CwHCC) samples in GSE54236 and all of 97 NwHCC biopsy tissues from 2 datasets (GSE64041 and GSE121248) were

TABLE 1 | The 11−gene−pair signature for early diagnosis of HCC.

Signature	Gene *a*	Gene *b*
pair1	TRMT112	SF3B1
pair2	MFSD5	COLEC10
pair3	FDXR	APC2
pair4	LAMC1	CHST4
pair5	UBE4B	HGF
pair6	NCAPH2	APC2
pair7	HSPH1	MTHFD2
pair8	TMEM38B	AGO3
pair9	PLGRKT	COLEC10
pair10	HNF1A	APC2
pair11	ARPC2	SF3B1

Gene a has a higher expression level than Gene b in HCC patients compared with CwoHCC patients.

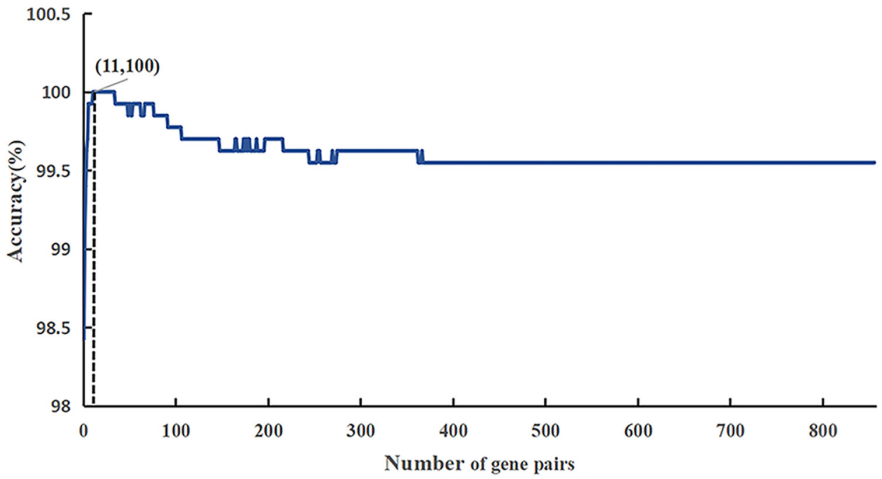

FIGURE 2 | A plot showing the IFS procedure for identifying HCC. When the top 857 features optimized by mRMR were used to perform prediction, the overall success rate reaches an IFS peak of 100% in fivefold cross validation. The solid line represents the ROC curve. The dotted line represents the strategy of randomly guess.

TABLE 2 | The performance of the signature in the validation datasets.

Datasets	NSnHCC	NSpCwoHCC
Testing datasets (biopsy)	100% (29/29)	100% (44/44)
Testing datasets (surgery)	100% (245/245)	100% (18/18)
GSE109211	31.43% (44/140)	–
GSE112790	100% (183/183)	–
GSE102079	100% (152/152)	–
GSE121248	100% (70/70)	–
TCGA	100% (371/371)	–

NSnHCC, number (sensitivity) of HCC samples; NSpCwoHCC, number (specificity) of CwoHCC samples.

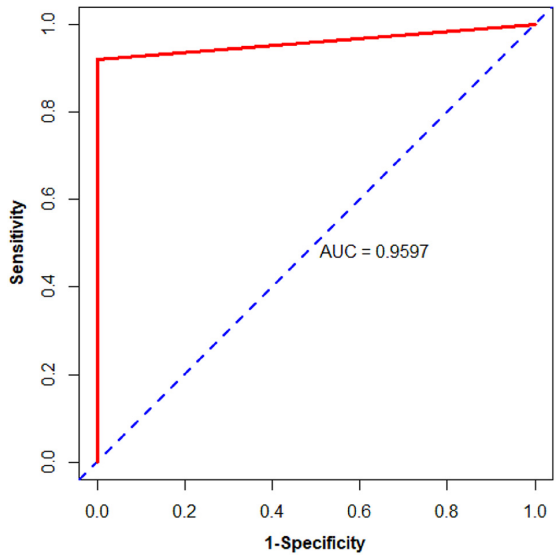

FIGURE 3 | Area under the receiver operating characteristic curve (AUC) of the validation data from public databases of biopsy and surgically resected HCC and CwoHCC samples. The solid line represents the ROC curve. The dotted line represents the strategy of randomly guess.

correctly classified to HCC. The results proved again that, the 11-gene-pair still displayed good performance that most of HCC adjacent non-cancerous patients (CwHCC and NwHCC) can be correctly recognized, even for the inaccurate samples from biopsy specimens. For surgically resected samples, 93.7% of the 254 CwHCC samples and 100% of the 644 NwHCC samples can be accurately identified (see in **Table 3**). All above results demonstrated again that the obtained 11-gene-pair could be regarded as key biological signatures to diagnose HCC patients.

Comparison With Existing Methods

To further demonstrate the performance of our proposed signatures, we compared our method with 19-gene-pair-based models and recorded results in **Table 3**. An earlier work done by Ao et al. (2018) found that 19-gene-pair can be regarded as diagnostic signature to discriminate HCC and adjacent non-cancerous tissues (cirrhosis or normal) from CwoHCC. Their model could produce 99.69% of accuracy which is lower than that of our 11-gene-pair based model.

For biopsy samples, our proposed model could correctly identify the 70 HCC samples in GSE121248 and the 97 NwHCC biopsy tissues from 2 datasets (GSE64041 and GSE121248) with the accuracy of 100%. Moreover, all 80 CwHCC samples in GSE54236 can be predicted as HCC. Compared with the accuracy (77.5%) of 19-gene-pair based model, the accuracy of 11-gene-pare model could increase to 100%.

For surgically resected samples, based on the predictor of 11-gene-pair, 79.8% of the 475 HCC samples from 3 datasets (GSE109211, GSE112790, and GSE102079) and 93.7% of the 254 CwHCC samples from 5 datasets (GSE6764, GSE17548, GSE25097, GSE17967, and GSE63898) can be corrected as HCC. Moreover, the model can accurately predict the 644 NwHCC biopsy tissues integrated from 7 datasets (GSE25097,

TABLE 3 | Comparison of 11 gene pairs with existing methods on independent datasets.

Dataset	11-gene-pair			19-gene-pair		
	NSnHCC	NACwHCC	NANwHCC	NSnHCC	NACwHCC	NANwHCC
Datasets from surgical resection						
GSE6764	–	10/10 (100.0%)	–	–	10/10 (100.0%)	–
GSE17548	–	18/20 (90.0%)	–	–	18/20 (90.0%)	–
GSE17967	–	16/16 (100.0%)	–	–	8/16 (50.0%)	–
GSE63898	–	168/168 (100.0%)	–	–	168/168 (100.0%)	–
GSE25097	–	40/40 (100.0%)	243/243 (100.0%)	–	40/40 (100.0%)	243/243 (100.0%)
GSE62232	–	–	10/10 (100.0%)	–	–	10/10 (100.0%)
GSE36376	–	–	193/193 (100.0%)	–	–	172/193 (89.1%)
GSE39791	–	–	72/72 (100.0%)	–	–	71/72 (98.6%)
GSE41804	–	–	20/20 (100.0%)	–	–	20/20 (100.0%)
GSE112790	183/183 (100.0%)	–	15/15 (100.0%)	183/183 (100.0%)	–	15/15 (100.0%)
GSE102079	152/152 (100.0%)	–	91/91 (100.0%)	152/152 (100.0%)	–	91/91 (100.0%)
GSE109211	44/140 (31.4%)	–	–	37/140 (26.4%)	–	–
Total	379/475 (79.8%)	238/254 (93.7%)	644/644 (100.0%)	372/475 (79.3%)	244/254 (96.1%)	622/644 (96.6%)
Datasets from biopsy						
GSE121248	70/70 (100.0%)	–	37/37 (100.0%)	70/70 (100.0%)	–	37/37 (100.0%)
GSE64041	–	–	60/60 (100.0%)	–	–	60/60 (100.0%)
GSE54236	–	80/80 (100.0%)	–	–	62/80 (77.5%)	–
Total	70/70 (100.0%)	80/80 (100.0%)	97/97 (100.0%)	70/70 (100.0%)	62/80 (77.5%)	97/97 (100.0%)

NACwHCC, number (accuracy) of cirrhosis tissues in patients with HCC samples to HCC; NANwHCC, number (accuracy) of normal tissues in patients with HCC samples to HCC.

GSE62232, GSE36376, GSE39791, GSE41804, GSE112790, and GSE102079). Also, the sensitivity of HCC samples increases to 79.8% (19-gene-pair: 79.3%) and the accuracy of NwHCC samples to HCC increases to 100% (19-gene-pair: 96.6%). It can be seen from **Table 3** that in the identification of both HCC and adjacent non-cancerous tissues (CwHCC and NwHCC) from CwoHCC by surgically resected samples, the 11-gene-pair based model displayed better performance than the 19-gene-pair based model, demonstrating that the 11-gene-pair-based model is quite promising in generating reliable results for the early HCC diagnosis.

The above results showed that the proposed 11-gene-pair-based model is powerful on both training datasets and independent datasets. This achievement can be attribute to using within-sample REOs and SVM.

DISCUSSION

Clinical practice has demonstrated that diagnosing the tumors in early stages is key to improve the survival of patient. Although pathology is used as a gold standard for HCC diagnosis, the histological analysis of the HCC biopsy specimen is influenced by the sampling location and tissue amount. In present work, a set of diagnostic signature including 11-gene-pair consisting of 18 genes was identified, which can be used to discriminate HCC and adjacent non-cancerous tissues (CwHCC and NwHCC) from CwoHCC individuals for the early HCC diagnosis.

Ten genes in the signature set, including LAMC1, UBE4B, HSPH1, HNF1A, SF3B1, APC2, CHST4, HGF, MTHFD2, and AGO3, might have a vital role during the hepatocarcinogenesis and are key genes for cancer. For instance, LAMC1 mRNA can promote the development of HCC by competing with miR-124 and supporting the excretion of CD151 (Yang et al., 2017). UBE4B can be used as a potential prognostic marker for HCC treatment due to its carcinogenic effect in human primary HCC (Zhang et al., 2016). Additionally, HNF1A is closely associated with HCC because the number of HNF1A increase when non-cancerous liver develops into high differentiate HCC (Wang et al., 1998). SF3B1 is a highly conserved spliceosomal protein in evolution (Eilbracht and Schmidt-Zachmann, 2001) and its expression increases significantly in liver HCC tissues. Serum anti-SF3B1 autoantibody is a potential diagnostic marker for HCC patients (Hwang et al., 2018). Reportedly, HSPH1 (Yang et al., 2015), APC2 (Ghosh et al., 2016), CHST4 (Gao et al., 2015), HGF (Unic et al., 2018), MTHFD2 (Liu et al., 2016), and AGO3 (Kitagawa et al., 2013) are closely related to HCC.

Subsequently, the 18 genes (11-gene-pair) were used for functional enrichment analysis by using Metascape[2] (Tripathi et al., 2015) on the KEGG (Kyoto Encyclopedia of Genes and Genomes) pathways and GO (Gene Ontology) terms. In order to determine the significant terms, p-value < 0.05 and the number of enriched genes ≥ 3 were used as the statistical standard. Finally, 18 genes were significantly enriched in the "ribonucleoprotein complex biogenesis," "positive regulation of cellular component biogenesis," "lymphocyte activation," and "chemotaxis" terms based on GO analysis, as well as "Pathways in cancer" according to KEGG analysis. The above analysis showed that the genes of the 11-gene-pair might have vital roles in the development and progression of HCC.

[2]http://metascape.org

In current study, we showed that 11 gen pairs can be applied to accurately diagnose the tumors found in the liver. Further, we shall try to establish a user-friendly web-server for the proposed "11-gene-pair" model. In the future, we will apply other feature selection techniques and algorithms to further improve the diagnosis of cancers.

DATA AVAILABILITY STATEMENT

The datasets used in this study can be freely download from the GEO (https://www.ncbi.nlm.nih.gov/geo/) and TCGA (https://portal.gdc.cancer.gov/repository) repository.

AUTHOR CONTRIBUTIONS

HL designed the study and revised the manuscript. Z-MZ carried out all the data collection and drafted the manuscript. Z-MZ, J-XT, FW, F-YD, and Z-YZ performed the data analysis. All authors approved the final manuscript.

FUNDING

This work was supported by the National Nature Scientific Foundation of China (61772119) and Sichuan Provincial Science Fund for Distinguished Young Scholars (20JCQN0262).

SUPPLEMENTARY MATERIAL

The Supplementary Material for this article can be found online at: https://www.frontiersin.org/articles/10.3389/fbioe.2020.00254/full#supplementary-material

REFERENCES

Ao, L., Song, X., Li, X., Tong, M., Guo, Y., Li, J., et al. (2016). An individualized prognostic signature and multiomics distinction for early stage hepatocellular carcinoma patients with surgical resection. *Oncotarget* 7, 24097–24110. doi: 10.18632/oncotarget.8212

Ao, L., Zhang, Z., Guan, Q., Guo, Y., Guo, Y., Zhang, J., et al. (2018). A qualitative signature for early diagnosis of hepatocellular carcinoma based on relative expression orderings. *Liver Int.* 38, 1812–1819. doi: 10.1111/liv.13864

Archer, K. J., Mas, V. R., David, K., Maluf, D. G., Bornstein, K., and Fisher, R. A. (2009). Identifying genes for establishing a multigenic test for hepatocellular carcinoma surveillance in hepatitis C virus-positive cirrhotic patients. *Cancer Epidemiol. Biomarkers Prev.* 18, 2929–2932. doi: 10.1158/1055-9965.EPI-09-0767

Asia-Pacific Working Party on Prevention of Hepatocellular Carcinoma (2010). Prevention of hepatocellular carcinoma in the Asia-Pacific region: consensus statements. *J. Gastroenterol. Hepatol.* 25, 657–663. doi: 10.1111/j.1440-1746.2009.06167.x

Bao, S., Zhao, H., Yuan, J., Fan, D., Zhang, Z., Su, J., et al. (2019). Computational identification of mutator-derived lncRNA signatures of genome instability for improving the clinical outcome of cancers: a case study in breast cancer. *Brief. Bioinform.* doi: 10.1093/bib/bbz118 [Epub ahead of print].

Barrett, T., Suzek, T. O., Troup, D. B., Wilhite, S. E., Ngau, W. C., Ledoux, P., et al. (2005). NCBI GEO: mining millions of expression profiles–database and tools. *Nucleic Acids Res.* 33, D562–D566. doi: 10.1093/nar/gki022

Basith, S., Manavalan, B., Shin, T. H., and Lee, G. (2019). SDM6A: a web-based integrative machine-learning framework for predicting 6mA sites in the rice genome. *Mol. Ther. Nucleic Acids* 18, 131–141. doi: 10.1016/j.omtn.2019.08.011

Bu, H. D., Hao, J. Q., Guan, J. H., and Zhou, S. G. (2018). Predicting enhancers from multiple cell lines and tissues across different developmental stages based on SVM method. *Curr. Bioinform.* 13, 655–660. doi: 10.2174/1574893613666180726163429

Budhu, A., Forgues, M., Ye, Q. H., Jia, H. L., He, P., Zanetti, K. A., et al. (2006). Prediction of venous metastases, recurrence, and prognosis in hepatocellular carcinoma based on a unique immune response signature of the liver microenvironment. *Cancer Cell* 10, 99–111. doi: 10.1016/j.ccr.2006.06.016

Cai, H., Li, X., Li, J., Ao, L., Yan, H., Tong, M., et al. (2015). Tamoxifen therapy benefit predictive signature coupled with prognostic signature of post-operative recurrent risk for early stage ER+ breast cancer. *Oncotarget* 6, 44593–44608. doi: 10.18632/oncotarget.6260

Cao, R., Freitas, C., Chan, L., Sun, M., Jiang, H., and Chen, Z. (2017). ProLanGO: protein function prediction using neural machine translation based on a recurrent neural network. *Molecules* 22:1732. doi: 10.3390/molecules22101732

Cao, R., Wang, Z., Wang, Y., and Cheng, J. (2014). SMOQ: a tool for predicting the absolute residue-specific quality of a single protein model with support vector machines. *BMC Bioinformatics* 15:120. doi: 10.1186/1471-2105-15-120

Chang, C. C., and Lin, C. J. (2011). LIBSVM: a library for support vector machines. *ACM Trans. Intell. Syst. Technol.* 2:27.

Chao, L., Jin, S., Wang, L., Guo, F., and Zou, Q. (2019a). AOPs-SVM: a sequence-based classifier of antioxidant proteins using a support vector machine. *Front. Bioeng. Biotechnol.* 7:224. doi: 10.3389/fbioe.2019.00224

Chao, L., Wei, L., and Zou, Q. (2019b). SecProMTB: a SVM-based classifier for secretory proteins of *Mycobacterium tuberculosis* with imbalanced data set. *Proteomics* 19:e1900007.

Chen, R., Guan, Q., Cheng, J., He, J., Liu, H., Cai, H., et al. (2017). Robust transcriptional tumor signatures applicable to both formalin-fixed paraffin-embedded and fresh-frozen samples. *Oncotarget* 8, 6652–6662. doi: 10.18632/oncotarget.14257

Cheng, J., Guo, Y., Gao, Q., Li, H., Yan, H., Li, M., et al. (2017). Circumvent the uncertainty in the applications of transcriptional signatures to tumor tissues sampled from different tumor sites. *Oncotarget* 8, 30265–30275. doi: 10.18632/oncotarget.15754

Colaprico, A., Silva, T. C., Olsen, C., Garofano, L., Cava, C., Garolini, D., et al. (2016). TCGAbiolinks: an R/bioconductor package for integrative analysis of TCGA data. *Nucleic Acids Res.* 44:e71. doi: 10.1093/nar/gkv1507

Conover, M., Staples, M., Si, D., Sun, M., and Cao, R. (2019). AngularQA: protein model quality assessment with LSTM networks. *Comput. Math. Biophys.* 7, 1–9. doi: 10.1515/cmb-2019-0001

Dao, F. Y., Lv, H., Wang, F., Feng, C. Q., Ding, H., Chen, W., et al. (2019). Identify origin of replication in *Saccharomyces cerevisiae* using two-step feature selection technique. *Bioinformatics* 35, 2075–2083. doi: 10.1093/bioinformatics/bty943

Eddy, J. A., Sung, J., Geman, D., and Price, N. D. (2010). Relative expression analysis for molecular cancer diagnosis and prognosis. *Technol. Cancer Res. Treat.* 9, 149–159. doi: 10.1177/153303461000900204

Eilbracht, J., and Schmidt-Zachmann, M. S. (2001). Identification of a sequence element directing a protein to nuclear speckles. *Proc. Natl. Acad. Sci. U.S.A.* 98, 3849–3854. doi: 10.1073/pnas.071042298

El-Serag, H. B. (2011). Hepatocellular carcinoma. *N. Engl. J. Med.* 365, 1118–1127. doi: 10.1056/NEJMra1001683

Forner, A., Vilana, R., Ayuso, C., Bianchi, L., Sole, M., Ayuso, J. R., et al. (2008). Diagnosis of hepatic nodules 20 mm or smaller in cirrhosis: prospective validation of the noninvasive diagnostic criteria for hepatocellular carcinoma. *Hepatology* 47, 97–104. doi: 10.1002/hep.21966

Gao, F., Liang, H., Lu, H., Wang, J., Xia, M., Yuan, Z., et al. (2015). Global analysis of DNA methylation in hepatocellular carcinoma by a liquid hybridization

capture-based bisulfite sequencing approach. *Clin. Epigenetics* 7:86. doi: 10.1186/s13148-015-0121-1

Ghosh, A., Ghosh, A., Datta, S., Dasgupta, D., Das, S., Ray, S., et al. (2016). Hepatic miR-126 is a potential plasma biomarker for detection of hepatitis B virus infected hepatocellular carcinoma. *Int. J. Cancer* 138, 2732–2744. doi: 10.1002/ijc.29999

Guan, Q., Chen, R., Yan, H., Cai, H., Guo, Y., Li, M., et al. (2016). Differential expression analysis for individual cancer samples based on robust within-sample relative gene expression orderings across multiple profiling platforms. *Oncotarget* 7, 68909–68920. doi: 10.18632/oncotarget.11996

Guan, Q., Yan, H., Chen, Y., Zheng, B., Cai, H., He, J., et al. (2018). Quantitative or qualitative transcriptional diagnostic signatures? A case study for colorectal cancer. *BMC Genomics* 19:99. doi: 10.1186/s12864-018-4446-y

Guan, Q., Zeng, Q., Yan, H., Xie, J., Cheng, J., Ao, L., et al. (2019). A qualitative transcriptional signature for the early diagnosis of colorectal cancer. *Cancer Sci.* 110, 3225–3234. doi: 10.1111/cas.14137

Hartke, J., Johnson, M., and Ghabril, M. (2017). The diagnosis and treatment of hepatocellular carcinoma. *Semin. Diagn. Pathol.* 34, 153–159. doi: 10.1053/j.semdp.2016.12.011

Hwang, H. M., Heo, C. K., Lee, H. J., Kwak, S. S., Lim, W. H., Yoo, J. S., et al. (2018). Identification of anti-SF3B1 autoantibody as a diagnostic marker in patients with hepatocellular carcinoma. *J. Transl. Med.* 16:177. doi: 10.1186/s12967-018-1546-z

Indhumathy, M., Nabhan, A. R., and Arumugam, S. (2018). A weighted association rule mining method for predicting HCV-human protein interactions. *Curr. Bioinform.* 13, 73–84. doi: 10.2174/1574893611666161123142425

Kitagawa, N., Ojima, H., Shirakihara, T., Shimizu, H., Kokubu, A., Urushidate, T., et al. (2013). Downregulation of the microRNA biogenesis components and its association with poor prognosis in hepatocellular carcinoma. *Cancer Sci.* 104, 543–551. doi: 10.1111/cas.12126

Li, X., Cai, H., Zheng, W., Tong, M., Li, H., Ao, L., et al. (2016). An individualized prognostic signature for gastric cancer patients treated with 5-Fluorouracil-based chemotherapy and distinct multi-omics characteristics of prognostic groups. *Oncotarget* 7, 8743–8755. doi: 10.18632/oncotarget.7087

Liao, Z., Li, D., Wang, X., Li, L., and Zou, Q. (2018). Cancer diagnosis from isomiR expression with machine learning method. *Curr. Bioinform.* 13, 57–63. doi: 10.2174/1574893611666160609081155

Liao, Z., Wang, X., Lin, D., and Zou, Q. (2017). Construction and identification of the RNAi recombinant lentiviral vector targeting human DEPDC7 gene. *Interdiscip. Sci.* 9, 350–356. doi: 10.1007/s12539-016-0162-y

Liu, X., Huang, Y., Jiang, C., Ou, H., Guo, B., Liao, H., et al. (2016). Methylenetetrahydrofolate dehydrogenase 2 overexpression is associated with tumor aggressiveness and poor prognosis in hepatocellular carcinoma. *Dig. Liver Dis.* 48, 953–960. doi: 10.1016/j.dld.2016.04.015

Manavalan, B., Basith, S., Shin, T. H., Choi, S., Kim, M. O., and Lee, G. (2017). MLACP: machine-learning-based prediction of anticancer peptides. *Oncotarget* 8, 77121–77136. doi: 10.18632/oncotarget.20365

Manavalan, B., Basith, S., Shin, T. H., Lee, D. Y., Wei, L., and Lee, G. (2019a). 4mCpred-EL: an ensemble learning framework for identification of DNA N^4-methylcytosine sites in the mouse genome. *Cells* 8:1332. doi: 10.3390/cells8111332

Manavalan, B., Basith, S., Shin, T. H., Wei, L., and Lee, G. (2019b). AtbPpred: a robust sequence-based prediction of anti-tubercular peptides using extremely randomized trees. *Comput. Struct. Biotechnol. J.* 17, 972–981. doi: 10.1016/j.csbj.2019.06.024

Manavalan, B., Basith, S., Shin, T. H., Wei, L., and Lee, G. (2019c). mAHTPred: a sequence-based meta-predictor for improving the prediction of anti-hypertensive peptides using effective feature representation. *Bioinformatics* 35, 2757–2765. doi: 10.1093/bioinformatics/bty1047

Manavalan, B., Basith, S., Shin, T. H., Wei, L., and Lee, G. (2019d). Meta-4mCpred: a sequence-based meta-predictor for accurate DNA 4mC site prediction using effective feature representation. *Mol. Ther. Nucleic Acids* 16, 733–744. doi: 10.1016/j.omtn.2019.04.019

Manavalan, B., and Lee, J. (2017). SVMQA: support-vector-machine-based protein single-model quality assessment. *Bioinformatics* 33, 2496–2503. doi: 10.1093/bioinformatics/btx222

Manavalan, B., Shin, T. H., and Lee, G. (2018a). DHSpred: support-vector-machine-based human DNase I hypersensitive sites prediction using the optimal features selected by random forest. *Oncotarget* 9, 1944–1956. doi: 10.18632/oncotarget.23099

Manavalan, B., Shin, T. H., and Lee, G. (2018b). PVP-SVM: sequence-based prediction of phage virion proteins using a support vector machine. *Front. Microbiol.* 9:476. doi: 10.3389/fmicb.2018.00476

Manavalan, B., Subramaniyam, S., Shin, T. H., Kim, M. O., and Lee, G. (2018c). Machine-learning-based prediction of cell-penetrating peptides and their uptake efficiency with improved accuracy. *J. Proteome Res.* 17, 2715–2726. doi: 10.1021/acs.jproteome.8b00148

Moritz, S., Pfab, J., Wu, T., Hou, J., Cheng, J., Cao, R., et al. (2019). Cascaded-CNN: deep learning to predict protein backbone structure from high-resolution cryo-EM density maps. *BioRxiv [Preprint]* doi: 10.1038/s41598-020-60598-y

Peng, H., Long, F., and Ding, C. (2005). Feature selection based on mutual information: criteria of max-dependency, max-relevance, and min-redundancy. *IEEE Trans. Pattern Anal. Mach. Intell.* 27, 1226–1238. doi: 10.1109/TPAMI.2005.159

Qu, K. Y., Gao, F., Guo, F., and Zou, Q. (2019). Taxonomy dimension reduction for colorectal cancer prediction. *Comput. Biol. Chem.* 83:107160. doi: 10.1016/j.compbiolchem.2019.107160

Russo, F. P., Imondi, A., Lynch, E. N., and Farinati, F. (2018). When and how should we perform a biopsy for HCC in patients with liver cirrhosis in 2018? A review. *Dig. Liver Dis.* 50, 640–646. doi: 10.1016/j.dld.2018.03.014

Stephenson, N., Shane, E., Chase, J., Rowland, J., Ries, D., Justice, N., et al. (2019). Survey of machine learning techniques in drug discovery. *Curr. Drug Metab.* 20, 185–193. doi: 10.2174/1389200219666180820112457

Sun, J., Zhang, Z., Bao, S., Yan, C., Hou, P., Wu, N., et al. (2020). Identification of tumor immune infiltration-associated lncRNAs for improving prognosis and immunotherapy response of patients with non-small cell lung cancer. *J. Immunother. Cancer* 8:e000110. doi: 10.1136/jitc-2019-000110

Sun, W., Liu, Y., Shou, D., Sun, Q., Shi, J., Chen, L., et al. (2015). AFP (alpha fetoprotein): who are you in gastrology? *Cancer Lett.* 357, 43–46. doi: 10.1016/j.canlet.2014.11.018

Tan, J. X., Li, S. H., Zhang, Z. M., Chen, C. X., Chen, W., Tang, H., et al. (2019). Identification of hormone binding proteins based on machine learning methods. *Math. Biosci. Eng.* 16, 2466–2480. doi: 10.3934/mbe.2019123

Tang, H., Cao, R. Z., Wang, W., Liu, T. S., Wang, L. M., and He, C. M. (2017). A two-step discriminated method to identify thermophilic proteins. *Int. J. Biomath.* 10:1750050. doi: 10.1142/s1793524517500504

Tang, W., Wan, S., Yang, Z., Teschendorff, A. E., and Zou, Q. (2018). Tumor origin detection with tissue-specific miRNA and DNA methylation markers. *Bioinformatics* 34, 398–406. doi: 10.1093/bioinformatics/btx622

Tomczak, K., Czerwinska, P., and Wiznerowicz, M. (2015). The cancer genome atlas (TCGA): an immeasurable source of knowledge. *Contemp. Oncol.* 19, A68–A77. doi: 10.5114/wo.2014.47136

Tripathi, S., Pohl, M. O., Zhou, Y., Rodriguez-Frandsen, A., Wang, G., Stein, D. A., et al. (2015). Meta- and orthogonal integration of influenza "OMICs" data defines a role for UBR4 in virus budding. *Cell Host Microbe* 18, 723–735. doi: 10.1016/j.chom.2015.11.002

Unic, A., Derek, L., Duvnjak, M., Patrlj, L., Rakic, M., Kujundzic, M., et al. (2018). Diagnostic specificity and sensitivity of PIVKAII, GP3, CSTB, SCCA1 and HGF for the diagnosis of hepatocellular carcinoma in patients with alcoholic liver cirrhosis. *Ann. Clin. Biochem.* 55, 355–362. doi: 10.1177/0004563217726808

Villanueva, A. (2019). Hepatocellular carcinoma. *N. Engl. J. Med.* 380, 1450–1462. doi: 10.1056/NEJMra1713263

Wang, H., Sun, Q., Zhao, W., Qi, L., Gu, Y., Li, P., et al. (2015). Individual-level analysis of differential expression of genes and pathways for personalized medicine. *Bioinformatics* 31, 62–68. doi: 10.1093/bioinformatics/btu522

Wang, W., Hayashi, Y., Ninomiya, T., Ohta, K., Nakabayashi, H., Tamaoki, T., et al. (1998). Expression of HNF-1 alpha and HNF-1 beta in various histological differentiations of hepatocellular carcinoma. *J. Pathol.* 184, 272–278. doi: 10.1002/(sici)1096-9896(199803)184:3<272::aid-path4>3.0.co;2-k

Wang, Y., Shi, F. Q., Cao, L. Y., Dey, N., Wu, Q., Ashour, A. S., et al. (2019). Morphological segmentation analysis and texture-based support vector machines classification on mice liver fibrosis microscopic images. *Curr. Bioinform.* 14, 282–294. doi: 10.2174/1574893614666190304125221

Wei, L., Lian, B., Zhang, Y., Li, W., Gu, J., He, X., et al. (2014). Application of microRNA and mRNA expression profiling on prognostic biomarker discovery

for hepatocellular carcinoma. *BMC Genomics* 15(Suppl. 1):S13. doi: 10.1186/1471-2164-15-S1-S13

Wurmbach, E., Chen, Y. B., Khitrov, G., Zhang, W., Roayaie, S., Schwartz, M., et al. (2007). Genome-wide molecular profiles of HCV-induced dysplasia and hepatocellular carcinoma. *Hepatology* 45, 938–947. doi: 10.1002/hep.21622

Yan, H., Li, M., Cao, L., Chen, H., Lai, H., Guan, Q., et al. (2019). A robust qualitative transcriptional signature for the correct pathological diagnosis of gastric cancer. *J. Transl. Med.* 17:63. doi: 10.1186/s12967-019-1816-4

Yang, W., Zhu, X. J., Huang, J., Ding, H., and Lin, H. (2019). A brief survey of machine learning methods in protein sub-Golgi localization. *Curr. Bioinform.* 14, 234–240. doi: 10.2174/1574893613666181113131415

Yang, Z., Zhuang, L., Szatmary, P., Wen, L., Sun, H., Lu, Y., et al. (2015). Upregulation of heat shock proteins (HSPA12A, HSP90B1, HSPA4, HSPA5 and HSPA6) in tumour tissues is associated with poor outcomes from HBV-related early-stage hepatocellular carcinoma. *Int. J. Med. Sci.* 12, 256–263. doi: 10.7150/ijms.10735

Yang, Z. P., Ma, H. S., Wang, S. S., Wang, L., and Liu, T. (2017). LAMC1 mRNA promotes malignancy of hepatocellular carcinoma cells by competing for MicroRNA-124 binding with CD151. *IUBMB Life* 69, 595–605. doi: 10.1002/iub.1642

Zhang, L., Hao, C., Shen, X., Hong, G., Li, H., Zhou, X., et al. (2013). Rank-based predictors for response and prognosis of neoadjuvant taxane-anthracycline-based chemotherapy in breast cancer. *Breast Cancer Res. Treat.* 139, 361–369. doi: 10.1007/s10549-013-2566-2

Zhang, N., Yu, S., Guo, Y., Wang, L., Wang, P., and Feng, Y. (2018). Discriminating ramos and jurkat cells with image textures from diffraction imaging flow cytometry based on a support vector machine. *Curr. Bioinform.* 13, 50–56. doi: 10.2174/1574893611666160608102537

Zhang, X. F., Pan, Q. Z., Pan, K., Weng, D. S., Wang, Q. J., Zhao, J. J., et al. (2016). Expression and prognostic role of ubiquitination factor E4B in primary hepatocellular carcinoma. *Mol. Carcinog.* 55, 64–76. doi: 10.1002/mc.22259

Zhao, W., Chen, B., Guo, X., Wang, R., Chang, Z., Dong, Y., et al. (2016). A rank-based transcriptional signature for predicting relapse risk of stage II colorectal cancer identified with proper data sources. *Oncotarget* 7, 19060–19071. doi: 10.18632/oncotarget.7956

Zhou, M., Guo, M., He, D., Wang, X., Cui, Y., Yang, H., et al. (2015). A potential signature of eight long non-coding RNAs predicts survival in patients with non-small cell lung cancer. *J. Transl. Med.* 13:231. doi: 10.1186/s12967-015-0556-3

Zhou, M., Zhao, H., Xu, W., Bao, S., Cheng, L., and Sun, J. (2017). Discovery and validation of immune-associated long non-coding RNA biomarkers associated with clinically molecular subtype and prognosis in diffuse large B cell lymphoma. *Mol. Cancer* 16:16. doi: 10.1186/s12943-017-0580-4

Zhou, X., Li, B., Zhang, Y., Gu, Y., Chen, B., Shi, T., et al. (2013). A relative ordering-based predictor for tamoxifen-treated estrogen receptor-positive breast cancer patients: multi-laboratory cohort validation. *Breast Cancer Res. Treat.* 142, 505–514. doi: 10.1007/s10549-013-2767-8

Zou, Q., and Ma, Q. (2019). The application of machine learning to disease diagnosis and treatment. *Math. Biosci.* 320:108305. doi: 10.1016/j.mbs.2019.108305

Conflict of Interest: The authors declare that the research was conducted in the absence of any commercial or financial relationships that could be construed as a potential conflict of interest.

Copyright © 2020 Zhang, Tan, Wang, Dao, Zhang and Lin. This is an open-access article distributed under the terms of the Creative Commons Attribution License (CC BY). The use, distribution or reproduction in other forums is permitted, provided the original author(s) and the copyright owner(s) are credited and that the original publication in this journal is cited, in accordance with accepted academic practice. No use, distribution or reproduction is permitted which does not comply with these terms.

frontiers in Physiology

ORIGINAL RESEARCH
published: 17 April 2020
doi: 10.3389/fphys.2020.00330

Quantitative Modeling Extends the Antibacterial Activity of Nitric Oxide

Darshan M. Sivaloganathan[1] *and Mark P. Brynildsen*[2]*

[1] *Program in Quantitative and Computational Biology, Princeton University, Princeton, NJ, United States,* [2] *Department of Chemical and Biological Engineering, Princeton University, Princeton, NJ, United States*

Numerous materials have been developed to try and harness the antimicrobial properties of nitric oxide (NO). However, the short half-life and reactivity of NO have made precise, tunable delivery difficult. As such, conventional methodologies have generally relied on donors that spontaneously release NO at different rates, and delivery profiles have largely been constrained to decaying dynamics. In recent years, the possibility of finely controlling NO release, for instance with light, has become achievable and this raises the question of how delivery dynamics influence therapeutic potential. Here we investigated this relationship using *Escherichia coli* as a model organism and an approach that incorporated both experimentation and mathematical modeling. We found that the best performing delivery mode was dependent on the NO payload, and developed a mathematical model to quantitatively dissect those observations. Those analyses suggested that the duration of respiratory inhibition was a major determinant of NO-induced growth inhibition. Inspired by this, we constructed a delivery schedule that leveraged that insight to extend the antimicrobial activity of NO far beyond what was achievable by traditional delivery dynamics. Collectively, these data and analyses suggest that the delivery dynamics of NO have a considerable impact on its ability to achieve and maintain bacteriostasis.

Keywords: *Escherichia coli*, Hmp, flavohemoglobin, NO, respiration, bacteriostatic

OPEN ACCESS

Edited by:
Julio R. Banga, Spanish National Research Council, Spain

Reviewed by:
Yu Luo, University of Delaware, United States
Chunguang Yang, Institute of Metals Research (CAS), China

***Correspondence:**
Mark P. Brynildsen
mbrynild@princeton.edu

Specialty section:
This article was submitted to Systems Biology, a section of the journal Frontiers in Physiology

Received: *17 December 2019*
Accepted: *20 March 2020*
Published: *17 April 2020*

Citation:
Sivaloganathan DM and Brynildsen MP (2020) Quantitative Modeling Extends the Antibacterial Activity of Nitric Oxide. Front. Physiol. 11:330. doi: 10.3389/fphys.2020.00330

INTRODUCTION

Nitric oxide (NO) is a diatomic, hydrophobic, free radical gas with a wide array of antimicrobial properties (Fang, 2004; Thomas et al., 2008). When present at concentrations in the micromolar (μM) range and above, NO can directly impair enzyme activity by irreversibly damaging iron-sulfur cluster residues and inhibit cellular respiration by binding heme groups within cytochrome oxidases (Wink and Mitchell, 1998; Thomas et al., 2008; Radi, 2018). Additionally, it is capable of reacting with oxygen and superoxide spontaneously to generate even more deleterious species that can cause protein damage, through thiol and tyrosine nitrosylation, DNA damage through base deamination, and damage to membranes and lipid structures through lipid peroxidation (Hogg and Kalyanaraman, 1999; O'Donnell and Freeman, 2001; Vázquez-Torres and Fang, 2005; Toledo and Augusto, 2012). These diverse cytotoxic effects can ultimately impair bacterial metabolism, inhibit growth, and cause cell death.

Within the context of innate immunity, phagocytic cells harness NO to combat and eliminate invading pathogens (Fang, 2004; Flannagan et al., 2009; Henard and Vázquez-Torres, 2011). The importance of NO to pathogen virulence has been demonstrated by the large number of

bacteria that require NO detoxification systems for survival (Poole and Hughes, 2000; Poole, 2005). For example, *Salmonella enterica* lacking the flavohemoglobin Hmp were found to be more susceptible to killing by macrophages (Stevanin et al., 2002; Bang et al., 2006). Similarly, deletion of Hmp in uropathogenic *E. coli* was found to significantly impair its ability to colonize the urinary tract (Svensson et al., 2010). In addition, the inability to produce NO in a murine model, through deletion of inducible nitric oxide synthase (iNOS), has been linked to increased likelihood of infection by *Mycobacterium tuberculosis*, *Listeria monocytogenes*, and *Leishmania* spp. (MacMicking et al., 1995). Conversely, increased iNOS expression has been associated with reduced malaria symptoms, as well as the decreased possibility of relapse (Kun et al., 2001; Hobbs et al., 2002).

The potent and broad-spectrum antimicrobial properties of NO have led to the development of numerous NO therapeutics (Kim et al., 2014; Yang et al., 2015). Many small chemical compounds and functional moieties have been developed to exogenously produce NO in response to heat, pH, and enzymatic catalysis. Some of the most widely used and studied NO-releasing moieties include diazeniumdiolates (NONOates) and S-nitrosothiols (Riccio and Schoenfisch, 2012; Sadrearhami et al., 2018). In recent years, different materials and delivery vehicles have been designed to take advantage of the release properties of these chemistries. Polymer scaffolds, gels, and coatings represent one large class of such materials (Kim et al., 2014; Liang et al., 2015). Examples include NO-releasing polymer coatings (Ho et al., 2017), NO-releasing sol-gels (Nablo et al., 2005), and NO-releasing chitosan oligosaccharides (Lu et al., 2014). Ho and colleagues demonstrated that exposure of *P. aeruginosa* or *S. aureus* to NONOate coatings significantly reduce bacterial adhesion and biofilm formation (Ho et al., 2017). Moreover, NONOate based sol-gels have been evaluated as potential coatings for orthopedic devices, where coated medical grade steel was effective at inhibiting *P. aeruginosa*, *S. aureus*, and *S. epidermidis* adhesion (Nablo et al., 2005). Lu and colleagues designed NONOate-based chitosan oligosaccharides that were extremely effective at penetrating biofilms and killing *P. aeruginosa*, while providing essentially no toxicity to mouse fibroblast cells (Lu et al., 2014). Another significant class of NO delivery vehicles are nanoparticles (Quinn et al., 2015). Kafshgari and coworkers devised porous silica-based nanoparticles conjugated to S-nitrosothiols and S-nitrosogluthatione and showed that they have significant antimicrobial activity against *E. coli* and *S. aureus* (Hasanzadeh Kafshgari et al., 2016). Overall, there has been sustained, growing interest in developing NO materials and delivery vehicles capable of harnessing the antimicrobial properties of NO. The examples mentioned above represent only a fraction of such compounds.

Despite the development of numerous NO materials, few have been evaluated for therapeutic purposes or have translated to clinical settings (Liang et al., 2015; Yang et al., 2015). One of the issues is associated with poor control of NO release. Low stability and rapid release of NO make it difficult to deliver NO for extended periods of time, maintain concentrations within desirable ranges, and provide tissue-specific activity. Traditional materials are loaded with a payload of NO donor that spontaneously dissociates when exposed to water or other conditions. As such, NO dynamics have largely been constrained to rapid accumulation of NO at the onset of delivery followed by progressive decay. Not only are these dynamics restricted, but they are in stark contrast to the way NO is delivered naturally within phagosomes. During an immune response, NO is delivered for extended periods of time, in which the rates of NO delivery have been suggested to peak hours after phagocytosis (Reichner et al., 1999; Vazquez-Torres et al., 2000; Pfeiffer et al., 2001). Recently, our group established a relationship between bolus payload and release kinetics, where at lower payloads faster dissociation rates led to greater antimicrobial activity, while at higher payloads slower dissociation rates were favored (Robinson et al., 2014b). However, the restricted set of delivery dynamics evaluated and their discordance with the way NO is delivered in physiological environments, raises the question of how this design criterion may impact the development of future NO-based therapeutics.

In recent years, the possibility of finely controlling delivery has become achievable with the development of light controlled, photoactivated compounds (Sortino, 2010; Choi et al., 2016; Sadrearhami et al., 2018). In particular, metal-nitrosyl complexes have gained significant attention, as alternative NO releasing moieties, because of their ability to induce NO release upon exposure to specific wavelengths of light (Tfouni et al., 2012; Xiang et al., 2017). The Mascharak group developed manganese-nitrosyl sol-gel coatings that released NO upon exposure to near infrared light (NIR) and led to significant reduction of *S. aureus*, *E. coli* and *A. baumannii* bacterial loads (Heilman and Mascharak, 2013). Similarly, Evans and colleagues developed manganese-nitrosyl based polymer microparticles that release NO upon exposure to NIR (Evans et al., 2018). Roveda and coworkers designed polyamidoamine dendrimers modified with ruthenium nitrosyl moieties, which could be activated upon UV irradiation (Roveda et al., 2014). In addition to light-activated compounds, enzymatic pro-drug systems represent another methodology to finely tune delivery rates through the control of enzymes or substrates. Jones and colleagues developed a NO probiotic patch in which *Lactobacilli* fermentation of glucose lead to NO production from nitrite (Jones et al., 2010). The Zhao group generated a unique methylated galactose NONOate conjugate that was only recognizable by a mutant beta galactosidase enzyme from *Thermus thermophilus* (Hou et al., 2019). NONOate release was restricted to environments containing the selective beta galactosidase and by co-delivering the enzyme and pro-drug, which allowed localization of NO release to specific tissues and reduced systemic toxicity.

The capability of precisely controlling NO delivery raises several interesting questions, such as, how delivery dynamics influence the antimicrobial potency of NO; and what is the best way to deliver a given payload of NO? To begin to address these questions, we used an approach that integrated experiments and computational modeling to assess, analyze, and predict how NO delivery dynamics influence the duration of nitrosative stress in *E. coli* cultures. Using fed-batch bioreactors, we evaluated four basic modes of delivery, one of which was a traditional bolus delivery, and observed that dosing outcome

differed drastically depending on the payload administered. That data was used to train a computational model of the *E. coli* NO stress network, which was able to accurately predict the NO concentration profiles and clearance times when larger payloads were administered. Quantitative analysis of those results suggested that maintaining respiratory inhibition was a major driver of delivery outcome, which was a prediction confirmed by further experimentation. Finally, with the model as a guide, we constructed delivery regimes capable of maintaining steady state NO concentrations at levels sufficient to inhibit cellular respiration, and this led to dosing schedules that were far more effective than any other tested delivery schemes. Collectively, the data and analyses presented here demonstrate the importance of dosing dynamics when designing NO-based treatments.

RESULTS

Bioreactor Configuration to Modulate NONOate Delivery

In this study, we sought to investigate the impact of delivery dynamics on the antimicrobial potency of NO. To do this, we constructed a system capable of finely tuning delivery of NO releasing compounds (NONOates) (**Figure 1A**). Specifically, our system is composed of a fed-batch bioreactor, in which the input flowrates of NONOate and its balance stream (NONOate solvent) can be programmed and automated using a low flow control system. We elected a drip system to eliminate the possibility of back flow, which was a concern due to the low flowrates we planned to use (as low as 10 μL/min). We are able to measure and monitor several outputs, such as the concentration of NO and O_2 present in the bioreactor, as well as temperature and culture turbidity.

We chose to begin our investigation by evaluating four principle modes of delivery. In particular, we examined the dynamics of linearly increasing (ramp up), linearly decreasing (ramp down) and constant delivery regimes and compared them to the traditional delivery method, which is a bolus (**Figure 1B**). Delivery schemes were implemented over 1 h with a total payload of 6 μmol PAPA NONOate delivered (**Figure 1C**). To maintain identical volumes with the different schema as a function of time, a secondary drip system delivered a balance stream, which was 10 mM NaOH (solvent for PAPA NONOate). In the control case of bolus delivery, both reservoirs were programmed to deliver 10 mM NaOH over 1 h. **Figure 1D** depicts the differing NO dynamics in cell-free systems for these four modes of delivery.

Type of Delivery Mode Influences the Duration of NO Stress in a Payload-Dependent Manner

To begin exploring NO detoxification under different delivery schema, aerobic cultures of *E. coli* were grown to mid-exponential phase and inoculated into a bioreactor at an optical density at 600 nm (OD_{600}) of 0.05 before being treated with 6 μmol of PAPA NONOate, delivered using each of the four modes, over 1 h, with the exception of bolus which was introduced at the onset. Our metric of interest to evaluate different delivery modes is NO clearance time (t_{clear}), which is the time during which the concentration of NO ([NO]) is greater than or equal to 0.5 μM. This concentration was chosen because NO at μM concentrations or above exerts nitrosative stress (Thomas et al., 2008).

At a payload of 6 μmol PAPA NONOate, bolus delivery led to an [NO] peak of 10.32 ± 0.37 μM (**Figure 2A**) and NO was cleared from the culture by 0.686 ± 0.016 h. In contrast, the other delivery schemes failed to reach 0.5 μM, and thus did not result in nitrosative stress. Interestingly, dosing higher payloads (18 μmol), led to strikingly different dynamics (**Figure 2B**). All four delivery schema produced nitrosative stress, with constant delivery being the most effective dosing scheme with an NO clearance time of 1.411 ± 0.029 h, which was a thirty percent increase in t_{clear} compared to bolus delivery of the same payload. This result suggested that the ability of NO to cause nitrosative stress depends both on the payload and the dynamics of how it is delivered.

Computational Modeling of NO Stress

To quantitatively explore the relationship between delivery dynamics and antimicrobial efficacy, we trained a kinetic model of NO stress in *E. coli* using the data obtained at 6 and 18 μmol. The model was developed in previous studies (Robinson and Brynildsen, 2013, 2015, 2016a,b; Robinson et al., 2014a,b; Sacco et al., 2017) and expanded upon here. Specifically, the model was adjusted to comply with fed-batch systems and cellular growth was incorporated and assumed to depend on the availability of aerobic cytochrome oxidases for respiration. Uncertain parameters were trained using a non-linear least squared optimization algorithm, followed by a Markov Chain Monte Carlo (MCMC) procedure. Parameter sets were accepted based on Evidence Ratios (ER) and ensembles of models were generated (section Materials and Methods). A complete list of species, reactions, and kinetic parameters can be found in **Supplementary Tables S1–S3**.

Model Adjustments for Fed-Batch Operation

To simulate our microfluidic drip system, continuous NONOate delivery and extracellular species dilution were incorporated into an existing kinetic model of NO metabolism (Robinson and Brynildsen, 2016b). Specifically, an input term was added to the rate equation for the NONOate species balance to capture influx of NONOate. The input term had four functional forms, depending on the delivery mode implemented (section Materials and Methods and **Supplementary Methods**). A volume dependent dilution term was also included to capture dilution of extracellular species, as a result of volume expansion within the bioreactor during operation (section Materials and Methods and **Supplementary Methods**).

Incorporation of Cellular Growth

Previous iterations of the model used in this study did not account for cellular growth but rather focused on the period of NO stress. This was done because NO is bacteriostatic, and thus under NO stress cells are non-growing. However, as

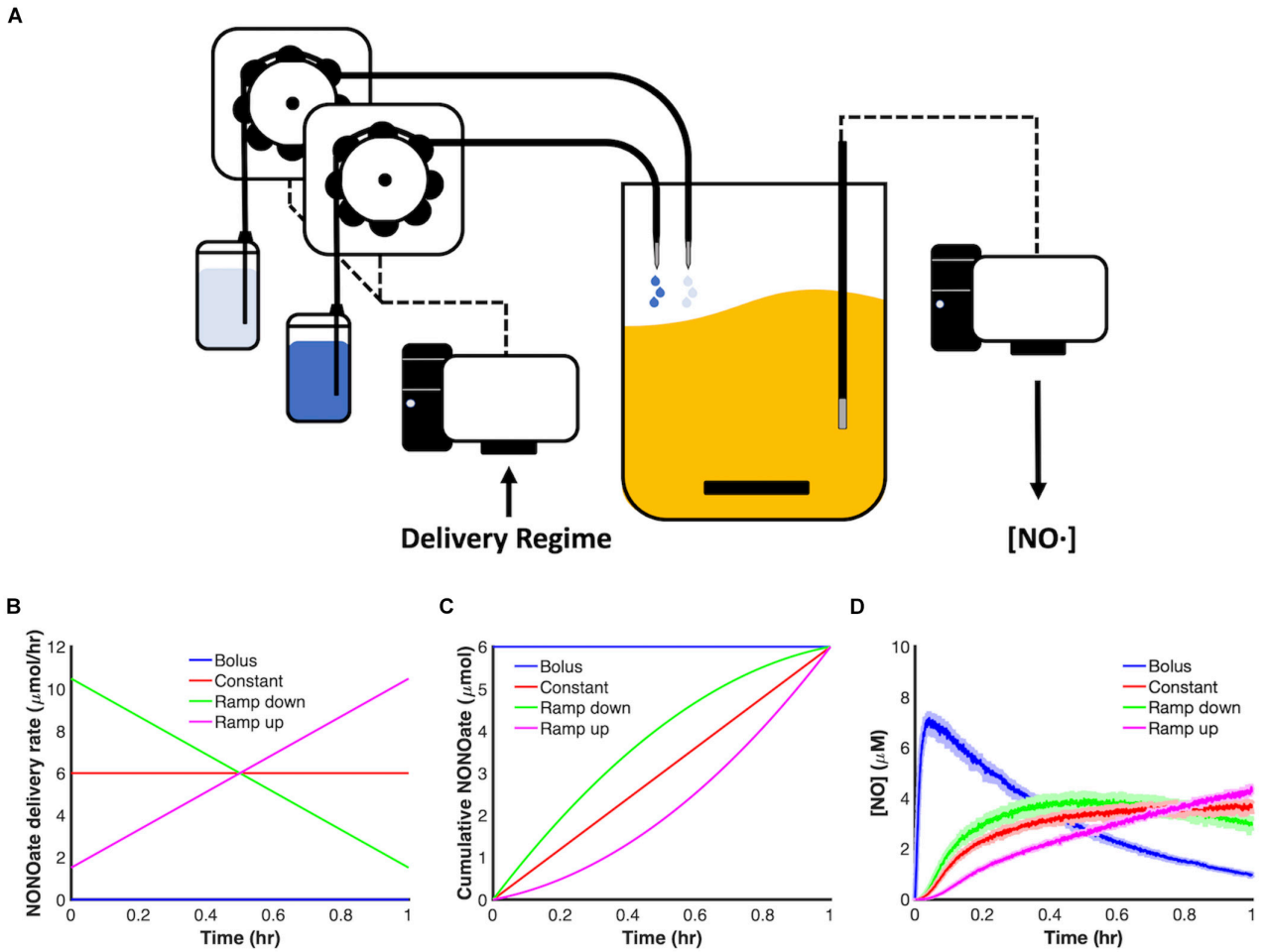

FIGURE 1 | Control of NONOate delivery dynamics. **(A)** Schematic of a computer-controlled, fed-batch bioreactor used to deliver NONOate. Delivery schedules were programmed using a computer-controlled low flow drip system. Once initiated, individual peristaltic pumps drew solutions from two reservoirs: PAPA NONOate solution (dark blue) and 10 mM NaOH (light blue), which then dripped into a bioreactor containing 50 mL MOPS minimal media. [NO] was continuously measured in the bioreactor using an electrochemical probe. **(B,C)** 6 μmol PAPA NONOate was delivered over an hour in four modes: bolus (blue), constant (red), ramp down (green), ramp up (pink). **(D)** Measured [NO] dynamics, for each mode, during delivery of 6 μmol PAPA NONOate over an hour in the absence of cells. Solid lines represent the mean of three replicates, whereas the lightly shaded areas represent the standard error of the mean.

depicted for three of the 6 μmol delivery modes (constant, ramp up, ramp down) and one of the 18 μmol schemes (ramp up), long periods of time without NO stress were present, and OD_{600} measurements revealed that cells were growing during those periods (**Supplementary Figures S1B,D**). Growth rate was modeled as a 1st order Hill-type function.

$$\mu = \mu_{max} \cdot \frac{[Cytochrome_{bo}] + [Cytochrome_{bd}]}{K_\mu + [Cytochrome_{bo}] + [Cytochrome_{bd}]} \quad (1)$$

Where μ_{max} is the maximum specific growth rate and K_μ represents the concentration of cytochromes required to reach half the maximum growth specific rate. Under aerobic conditions, the majority of ATP production in *E. coli* is accounted for by cellular respiration (Baron, 1996; Trotter et al., 2011; Soria et al., 2013) and therefore we chose to define the specific growth rate equation as a function of freely available terminal cytochrome *bo* and *bd*-I oxidases. A set of 16 uncertain respiratory parameters (section Materials and Methods and **Supplementary Table S5**), were trained on $[O_2]$ and OD_{600} data obtained from aerobic, mid-exponential phase *E. coli* treated with three concentrations of KCN (0, 50, and 1000 μM) (**Supplementary Figure S2**). The ensemble of models could accurately capture O_2 consumption and cell density at all three concentrations of KCN. Additionally, growth-dependent dilution terms were incorporated into rate equations for cellular species to capture the expansion of intracellular volume that occurs with growth (section Materials and Methods). Further, in previous iterations (Robinson and Brynildsen, 2016b) the protein translation rate was modeled as a function of $[O_2]$, a reflection of energy production through O_2 consumption by terminal cytochromes; however, here we adjusted that rate expression so that translation was directly related to growth (Materials & Methods).

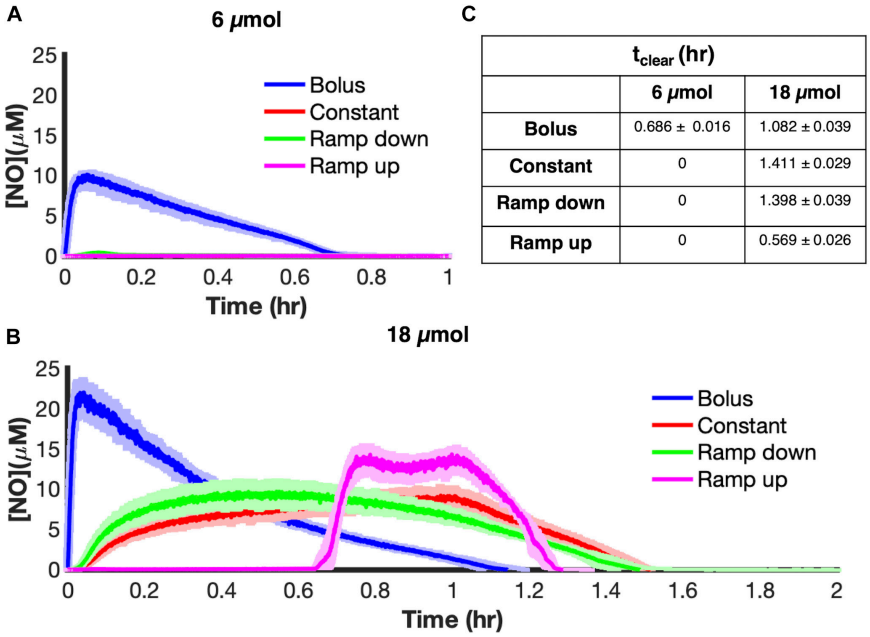

C

t_{clear} (hr)		
	6 μmol	18 μmol
Bolus	0.686 ± 0.016	1.082 ± 0.039
Constant	0	1.411 ± 0.029
Ramp down	0	1.398 ± 0.039
Ramp up	0	0.569 ± 0.026

FIGURE 2 | Delivery outcome is payload dependent. *E. coli* cultures were grown to exponential phase and inoculated in a bioreactor at an OD_{600} of 0.05. Five minutes after inoculation, PAPA NONOate was delivered over an hour in one of four ways (bolus-blue; constant-red; ramp down-green; ramp up-pink) at payloads of **(A)** 6 μmol or **(B)** 18 μmol. [NO] was measured continuously using an ISO-NOP probe. Solid lines represent the mean of three independent experiments, whereas the lightly shaded areas represent the standard error of the mean. **(C)** The duration of nitrosative stress (t_{clear}) was measured at 6 μmol and 18 μmol for each delivery scheme (calculated as the time for which [NO] ≥ 0.5 μM). Values represent the average value ± the standard error of the mean.

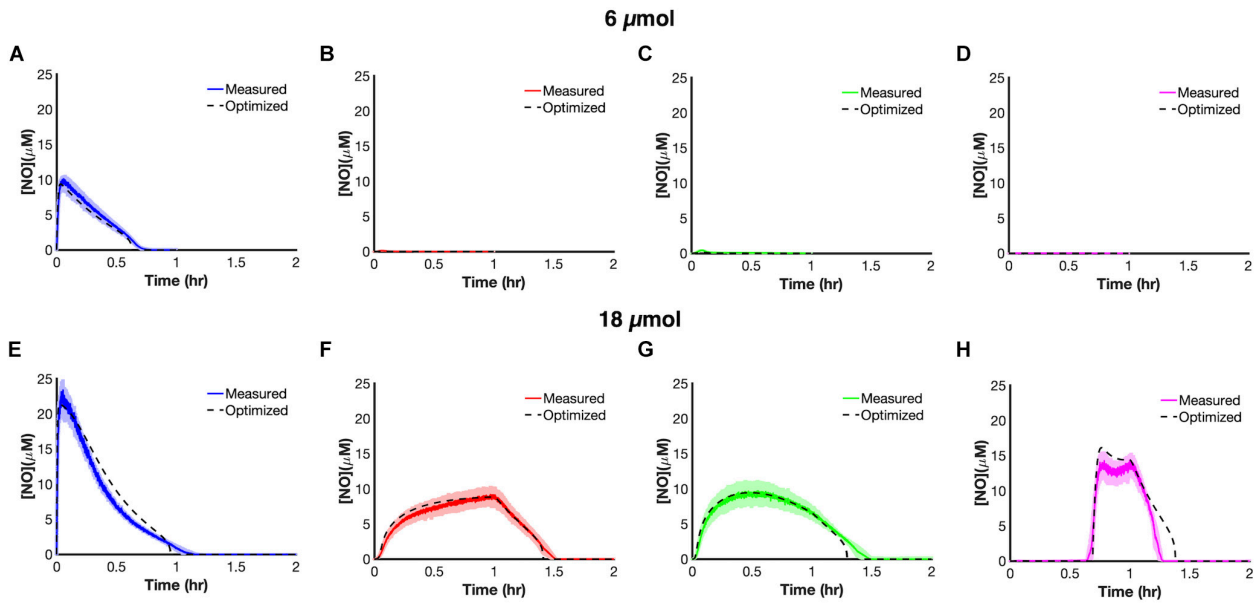

FIGURE 3 | Model training and optimization on NO dynamics observed at 6 μmol **(A–D)** and 18 μmol **(E–H)** for the four principle dosing modes (refer to **Supplementary Table S6** for a list of optimized parameters). Cultures of *E. coli* were grown to exponential phase and inoculated in a bioreactor at an OD_{600} of 0.05. Five minutes after inoculation, PAPA NONOate was delivered over an hour in one of four ways (bolus- blue; constant-red; ramp down-green; ramp up-pink). Solid lines represent the mean of three independent experiments, whereas the lightly shaded areas represent the standard error of the mean. Dashed black lines represent simulation results using the ensemble of parameter sets (ER < 10, 28 sets in total) trained on the data presented in this figure. Simulations from the ensemble members greatly overlapped, thus resembling a single line.

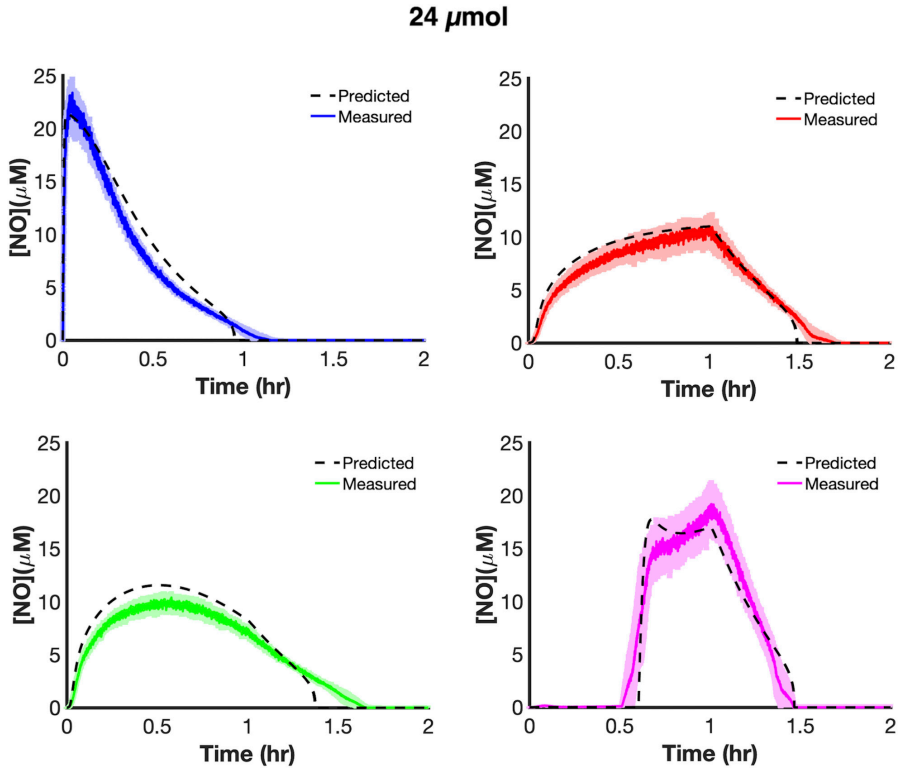

FIGURE 4 | Model extrapolation and predictions at 24 μmol payloads. Dashed black lines represent predicted [NO] dynamics using the ensemble of parameter sets (ER < 10, 28 sets in total). Simulations from the ensemble members greatly overlapped, thus resembling a single line. Colored lines represent measured [NO] dynamics (bolus- blue; constant-red; ramp down-green; ramp up-pink). The solid lines represent the mean of three independent experiments, whereas the lightly shaded areas represent the standard error of the mean.

Model Training and Experimental Validation

We trained uncertain parameters related to cellular NO consumption on all [NO] and [O_2] data measured at 6 and 18 μmol (21 parameters in total, **Supplementary Table S6**). Simulations for the ensembles of models did a good job of capturing data at both 6 and 18 μmol for the different delivery modes (**Figure 3**). To assess the utility of the model, we tested its predictive power by simulating each delivery mode at 24 μmol. The model predicted that bolus delivery should lead to a t_{clear} of 0.957 h and that it would be outcompeted by ramp down and constant modes, with t_{clear} of 1.359 and 1.462 h, respectively, whereas it should still be more effective than ramp up with a t_{clear} of 0.859 h. Experimental measurements agreed well with those forward predictions from the model (**Figure 4**). This confirmed that the model could accurately extrapolate to conditions outside its training data, which gave confidence that it could be used to quantitatively analyze NO stress in *E. coli* cultures.

Evaluating NO Clearance by Varying the Delivery Time

We sought to evaluate the dynamics of three of the principle dosing modes by varying an additional parameter, duration of delivery. The analysis focused on 24 μmol payloads and the total time to achieve that dosage. As depicted in **Figures 5A–C**, extending the delivery period lengthened t_{clear} for constant (red trend line) and ramp-down (green trend line) delivery modes to such an extent that their t_{clear} exceeded that of bolus delivery (t_{clear} = 0.957 h) by more than twofold, whereas the most effective delivery periods for ramp up (purple trend line) were less than an hour. In addition, simulations revealed that each delivery mode displayed distinct discontinuities when plotting t_{clear} against delivery period. Evaluation of the cumulative NO consumption flux profiles (**Figures 5D–F**), suggested that the discontinuities were associated with failures to inhibit cellular respiration, which led to higher translation rates and ultimately higher concentrations of Hmp (**Supplementary Figures S3–S5**), which is the main NO detoxification enzyme under aerobic conditions (Gardner and Gardner, 2002; Corker and Poole, 2003; Robinson and Brynildsen, 2013, 2016b). Noticeably, the ramp-up delivery mode contains two discontinuities, where the first was due to an initial failure to inhibit cellular respiration which allowed increased translation and Hmp protein expression. This led to cellular NO consumption rates that balanced NO delivery rates. However, near the end of the delivery period, the increasing delivery rates began to exceed cellular consumption, which led to a sudden rise in [NO]. While the second discontinuity, was similarly due to a failure to inhibit cellular respiration, and cellular consumption invariably balanced NO influx throughout delivery. Experiments were performed to assess the accuracy

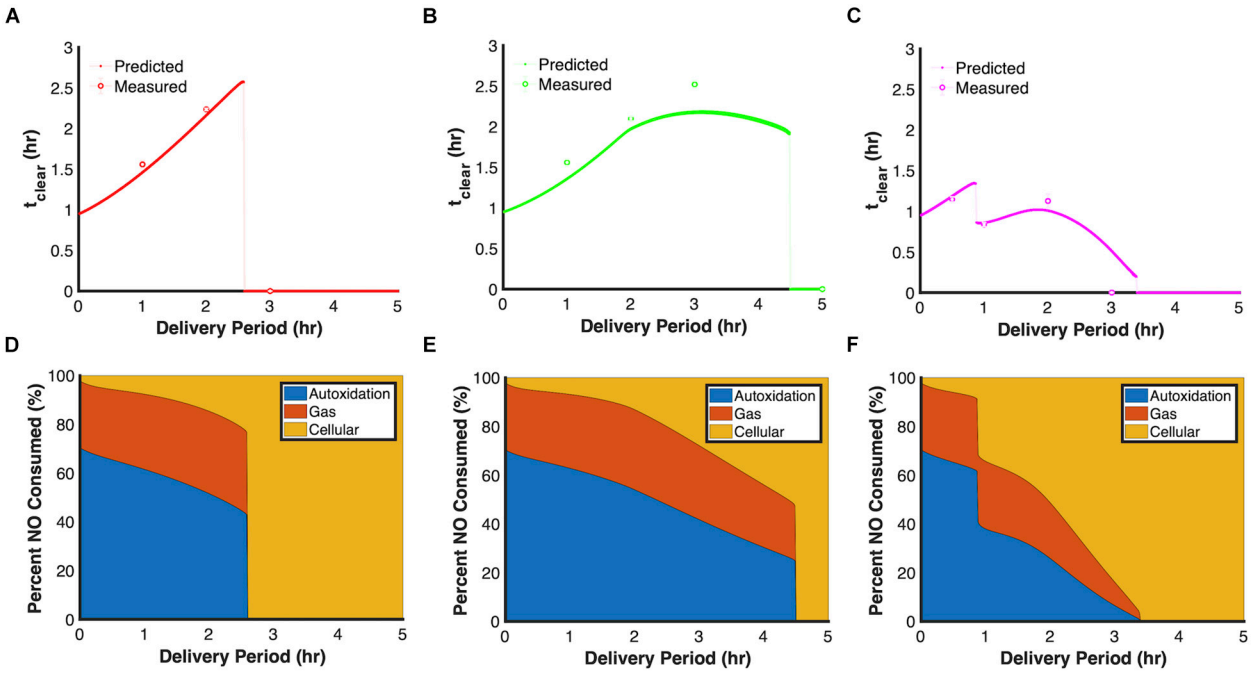

FIGURE 5 | Relationship between t_{clear} and delivery period. Model simulations using the ensemble of parameter sets (ER < 10, 28 sets in total) were performed by delivering 24 μmol PAPA NONOate and varying the delivery period between 0 and 5 h and calculating t_{clear} for each simulation. **(A)** Constant, **(B)** ramp down, **(C)** ramp up. Solid lines represent predicted relationship between t_{clear} and delivery period, while dashed lines represent discontinuities in the curves. Circles represent mean t_{clear} values from at least three experiments and error bars represent the standard error of the mean. Predicted NO cumulative distribution profiles using the optimal parameter set (ER = 1, minimum SSR, 1 set) up to the end of the delivery period or when [NO] dropped below 0.5 μM, whichever was greater for constant **(D)**, ramp-down **(E),** and ramp-up **(F)** delivery schedules. The three major NO consumption pathways are autoxidation (blue), transport to gas phase (red), and cellular consumption (yellow).

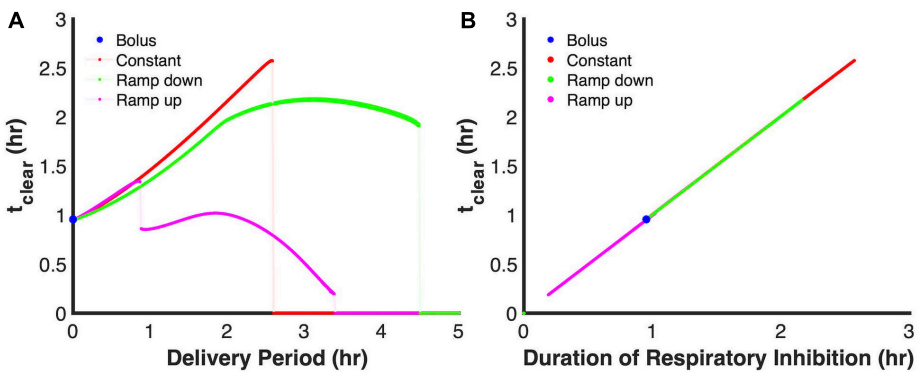

FIGURE 6 | Duration of respiratory inhibition is a strong predictor of t_{clear}. **(A)** Model predictions using the ensemble of parameter sets (ER < 10, 28 sets in total) for t_{clear} as a function of delivery period when a 24 μmol PAPA NONOate payload is delivered. Solid lines represent the predicted relationship between t_{clear} and delivery period (bolus- blue; constant-red; ramp down-green; ramp up-pink), while the lightly shaded lines represent discontinuities in the curves. **(B)** Plot of duration for respiratory inhibition vs. t_{clear}. Duration of respiratory inhibition was defined as the length of time for which the percentage of NO bound cytochromes ≥ 99%.

of these predictions, and as depicted by the colored dots in **Figures 5A–C**, data agreed well with model predictions, including the approximate delivery times that corresponded to the discontinuities.

Given the central role of respiratory inhibition in defining the delivery periods at which the principle modes become ineffective (or less effective for the first discontinuity of the ramp up mode), we plotted t_{clear} as a function of the duration during which respiration is inhibited. We considered respiratory inhibition, as the time for which 99% or more of terminal cytochrome oxidase were NO bound. As depicted in **Figure 6**, all of the simulations, regardless of delivery mode, fall onto a single line. This suggested that the duration of NO stress is strongly associated with the ability to achieve and maintain respiratory inhibition.

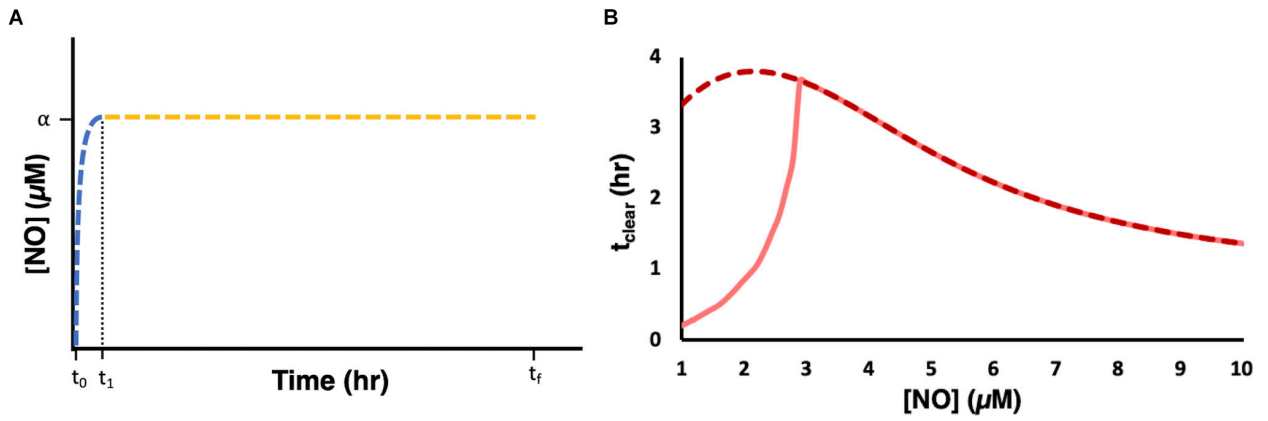

FIGURE 7 | Designing and implementing delivery schemes to maintain steady state [NO]. **(A)** For a desired NO concentration α and payload ω, a bolus delivery was introduced at t_0 such that the [NO] profile (blue dashed line) peaked at [NO] = α at t_1. At t_1 a dosing regime was implemented to maintain $d[NO]/dt = 0$ and [NO] = α up until t_f (yellow dashed line), at which point the payload ω was exhausted. **(B)** Steady state dosing regimes were simulated at [NO] between 1 and 10 μM for a payload of 24 μmol and t_{clear} was measured (dark red dashed line). The light shaded solid red line represent the relationship between t_{clear} and [NO] when implementing a step function delivery approximation. All simulations were performed using the optimal parameter set (ER = 1, minimum SSR, 1 set).

Maintaining Respiratory Inhibition to Maximize the Duration of NO Stress

We used the model to evaluate the relationship between [NO] and respiratory inhibition and found that NO concentrations slightly above 1 μM (∼1.2 μM) corresponded to 99% NO bound cytochrome (**Supplementary Figure S6**). We hypothesized that, for a given payload, a dosing regimen that could raise and maintain NO at concentrations of 1.2 μM or greater, would extend t_{clear} beyond that which could be achieved with bolus administration or any of the principal modes. Using the model, we designed delivery schema capable of maintaining steady state concentrations of NO. Specifically, this was accomplished by constructing composite delivery schemes (**Figure 7A**). First, a bolus was introduced to raise NO to the desired steady state concentration. Then when [NO] had reached its peak value a dosing scheme was solved for, using the remainder of the payload, to deliver NO at a rate that balanced NO consumption, as predicted by the model, and maintain d[NO]/dt equal to zero. Composite delivery schemes were designed in this manner for various concentrations of NO greater than or equal to 1 μM. The model predicted that the optimal composite dosing regime was achieved by maintaining NO at approximately 2.2 μM. Model simulations suggested that a bolus payload of 0.8 μmol would lead to an NO profile that peaked at 2.2 μM and that implementing a dosing schedule to maintain NO at 2.2 μM, with the remaining 23.2 μmol, could extend t_{clear} to over 3.8 h. Experimental application of the composite dosing regimen failed to recapitulate the predicted NO dynamic (**Supplementary Figure S7A**), and severely underperformed (t_{clear} = 0.2 h) compared to the predicted t_{clear}. A deeper analysis revealed that this inaccurate prediction was due to physical limitations of our experimental system. Specifically, the pumping system required us to approximate dosing schedules with piecewise step functions (**Supplementary Figure S7B**). Taking into account this source of error, the model predicted that t_{clear} was not robust to these variations until the steady NO concentration exceeded approximately 3 μM (**Figure 7B**). Therefore, we chose to implement a delivery regime to maintain [NO] at 4 μM, which is well within the regime where simulations with the piece-wise step function agree well with the continuous delivery function. Simulations revealed that a 4 μM [NO] peak was achieved by a bolus payload of 1.7 μmol. The remaining 22.3 μmol were delivered to maintain [NO] at 4 μM (**Figures 8A,B**). Simulations suggested that it was possible to extend t_{clear} to over 3 h by delivering in this manner, which would be over threefold higher than bolus administration of 24 μmol. The delivery scheme was implemented experimentally and the measured [NO] profile agreed well with simulations (**Figure 8C**). This dosing schedule proved to be far more effective than any of the principle delivery modes, and more specifically, it led to a threefold increase in t_{clear} when compared to a bolus delivery of the same payload (**Figure 8D**).

DISCUSSION

Nitric oxide is a potent antibacterial harnessed by macrophages of the innate immune response (Radtke and O'Riordan, 2006; Haas, 2007; Bowman et al., 2011). The potential of NO as an antimicrobial treatment has led to the development of numerous materials capable of directly delivering NO to infection sites (Seabra and Durán, 2010; Schairer et al., 2012a). For example, Martinez and coworkers demonstrated that delivery of silica-based nanoparticle into skin lesions of MRSA-infected mice, led to significant reductions of bacterial burden when compared to untreated infections (Martinez et al., 2009). Nablo and colleagues developed silicone elastomer implants coated with NONOate sol-gels that led to an 82% reduction in the number of *S. aureus* infected implants when compared to uncoated implants in a rat model (Nablo et al., 2005). Notably, these animal studies were

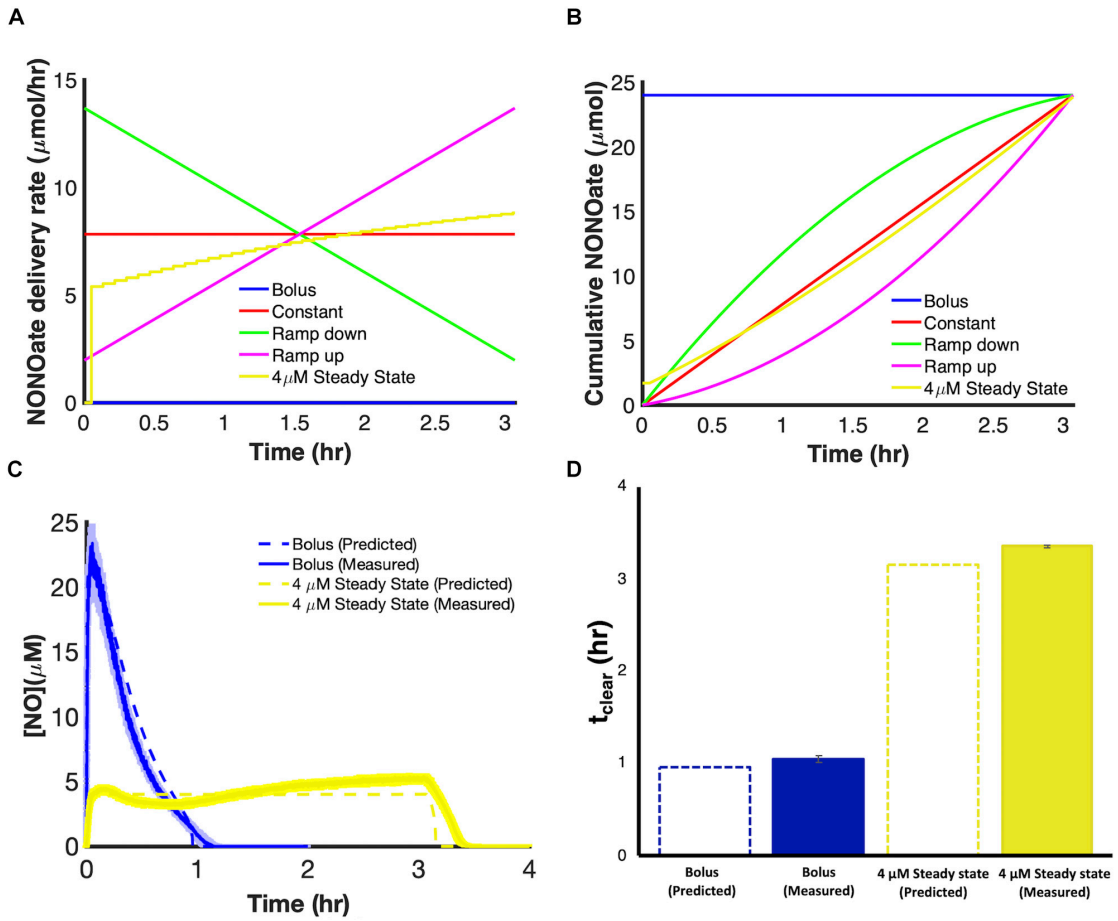

FIGURE 8 | Implementation of a delivery schedule to maintain [NO] at 4 μM steady state with a payload of 24 μmol. Comparison of delivery rate **(A)** and cumulative NONOate **(B)** profiles for a 4 μM steady state dosing schedule and the principle delivery modes over identical delivery periods. Comparison of the predicted and measured [NO] profiles **(C)** and t_{clear} values **(D)** for a 4 μM steady state dosing scheme compared to a bolus delivery. Dashed colored lines represent predicted [NO] dynamics using the optimal parameter set (ER = 1, minimum SSR, 1 set). Solid colored lines represent the mean of three independent experiments, while lightly shaded areas represent the standard error of the mean.

conducted with materials that would spontaneously release NO with a decaying rate. The limited control over NO release has led to restricted NO dynamics, in which NO profiles exhibit high initial levels that decline as a function of time. Given the advent of materials with increasingly tunable NO delivery, such as photo controllable and enzyme pro-drug systems, the question of whether other modalities of NO release could influence therapeutic outcomes arises.

We began by constructing a system capable of tuning NO delivery and measured how cultures of *E. coli* responded to treatment. In particular, we explored three primary modes of delivery (linearly increasing, decreasing, and constant modes) and compared them to bolus. At lower payloads, we observed that bolus delivery was the only effective method. While at higher payloads delivery outcome was quite different with all four delivery schedules providing periods of nitrosative stress (t_{clear}) and two of the four outcompeting bolus. With the observation that the efficacies of delivery regimens were a function of payload, we sought to develop a computational model that could predict NO dynamics under different delivery scenarios. Using the data obtained at both payloads (6 and 18 μmol), we trained a model of the NO biochemical network and showed that the model was effective at extrapolating to higher payloads (24 μmol) and predicting the outcome.

We continued our analysis by exploring how delivery period, as a variable, influenced antimicrobial activity. The model predicted that by extending the delivery period it was possible to extend t_{clear} to be greater than twofold of a bolus of the same payload. Moreover, the model predicted sudden changes in t_{clear}, for each principle mode, as the delivery period was extended beyond specific thresholds. The model predicted that these sudden changes were due to delivery rates that failed to inhibit cellular respiration and thereby led to increased Hmp protein expression in growing cells. Experiments confirmed the trends predicted by the model, which led us to define a metric representative of the length of time under respiratory inhibition. A model-facilitated analysis revealed that the longer cells were unable to respire, the longer it took cells to detoxify NO,

and when t_{clear} was plotted against the duration of respiratory inhibition, all of the delivery modalities collapsed onto a single line. This led us to hypothesize that dosing regimens that maintained respiratory inhibiting concentrations of NO, for as long as possible, would extend dose efficacy beyond what we observed with the principal modes. To test this hypothesis, we used the model to design dosing schedules capable of maintaining NO concentrations at and above the threshold to inhibit cellular respiration. When we tested predictions that maintained NO at 4 μM, we were able to extend dose efficacy to over threefold what it would have been with a bolus administration of the same payload. Further, that dosing schedule also outperformed all of the other principal modes at that payload. Looking forward, it is worth noting that future work to extend bacterial NO stress could benefit from formulating the task as an optimization problem. As a first pass at this, we considered delivery schedules that conformed to third order polynomials and used an optimization algorithm to identify coefficients that maximized the amount of time cultures were exposed to NO concentrations that were inhibitory to respiration (Materials and Methods). Although that attempt at optimization did not yield solutions better than the steady-state approach we presented, there are many different ways to formulate an optimization problem and numerous algorithms to identify best solutions. We believe that future work on optimization frameworks with this application could reveal novel strategies that outperform the methodologies used in the present study.

The data presented in this study suggest that the dosing method of NO can have a significant impact on its antibacterial capabilities. Further, this work suggests that maintaining NO concentrations at levels that inhibit cellular respiration is a critical parameter for inhibiting the propagation of *E. coli* under aerobic conditions, such as those found in the urinary tract (Svensson et al., 2010; Spiro et al., 2015). Many microbes contain similar detoxification networks, generate protein homologs similar to Hmp, and thrive under oxygenated conditions (Gardner, 2005, 2012; Stern and Zhu, 2014). Therefore, inhibiting cytochrome oxidase activity may be an important variable to maximize dose efficacy of NO-releasing materials across a wide range of bacteria. We envision that such knowledge could be employed with feed-back control devices that maintain local NO levels at infection sites, such as dermal wounds, at concentrations that yield respiratory inhibition. Such delivery platforms could be important for the eventual application of these materials since NO is also deleterious to mammalian cells and there is a restricted concentration window where it is antibacterial and non-toxic to our cells, which argues against the use of bolus delivery schemes (Hurford, 2005; Friedman et al., 2011; Schairer et al., 2012a; Sun et al., 2012). However, it should be noted that one limitation of this study is associated with its time scales, which are on the order of several hours due to constraints associated with our experimental system (Materials and Methods). With an eye toward clinical applications, time scales of 24 h or longer need to be tested in order to assess whether what was found to be important at a few hours is also important over a few days (Martinez et al., 2009; Jones et al., 2010; Schairer et al., 2012b).

MATERIALS AND METHODS

Bacterial Strains

All experiments performed in this study were conducted with *E. coli* K-12 MG1655 (Brynildsen et al., 2013).

Chemicals and Growth Media

Growth media used in all experiments was MOPS minimal media with 10 mM glucose as the sole carbon source. The NO donor used, (Z)-1-[N-(3-aminopropyl)-N-(n-propyl)amino]diazen-1-ium-1,2-diolate (PAPA NONOate), was dissolved in 10 mM NaOH and stored on ice during delivery. Potassium cyanide (KCN) was dissolved in autoclaved Milli-Q water at a concentration of 1 M. Luria-Bertani (LB) broth was made from dissolving LB powder (40% Tryptone, 20% Yeast extract, 40% Sodium Chloride per gram of solid) in Milli-Q water and autoclaving the solution.

Fed-Batch Bioreactor

Sterile 250 mL conical tubes (Nunc) were used as batch bioreactors for experiments. The bioreactor contained 50 mL of MOPS media, as well as a 0.5″ magnetic stir bar to facilitate mixing. The bioreactor was suspended in a water bath, maintained at 37°C, using a magnetic stirrer hot plate (Fisher Scientific). PAPA NONOate was delivered using a 2 channel, 8 roller, Ismatec REGLO ICC Digital Peristaltic Pump (Cole Palmer). 30-gauge, regular bevel, stainless steel needles (Covidien) were fastened into the ends of the tubing to create a drip system to facilitate delivery into the bioreactor. Delivery schedules were programmed using the associated software on a Dell Latitude E7440 with an Intel Core i5 CPU processor at 2.50 GHz. One channel was programmed to deliver NONOate and the second channel was programmed to deliver 10 mM NaOH, to maintain a constant volume delivered per unit time across delivery schema (5 mL/h). Prior to delivery, each channel was run for 2 min at a flow rate of 50 μL/min, to ensure that tubing had been primed and loaded with their respective solutions (approximately 8 equivalent volumes of fluid through the tubing). We note that experiments on this system were performed for up to a few hours. When longer time periods were assessed (e.g., 24 h), considerable volume loss due to evaporation from bioreactor was observed (50% or more), and delivery of 10 mM NaOH solutions over those time periods resulted in much higher media pH levels (e.g., above 9). These constraints limited experiments that were performed to several hours.

[NO] and [O_2] Measurements

NO concentrations were measured continuously using a 2 mm NO sensing probe (WPI). The probe was calibrated daily using the manufacturer's instructions. Briefly, this was accomplished by delivering increasing doses of *S*-nitroso-*N*-acetyl-d,l-penicillamine (SNAP) (Cayman Chemical) to a 10 mM copper chloride (II) solution. A proportionality factor of 0.457 molecules of NO per molecule of SNAP (Chou and Brynildsen, 2019) was used to convert the raw signal generated (pico Amps) to units of NO concentration (μM). For NO assays where

pico Amp measurements following clearance fell slightly below baseline, [NO] data were set to zero.

O_2 concentration present in the bioreactor was continuously monitored using OXROB10 robust O_2 probe (Pyroscience) attached to a FireStingO_2 fiber-optic O_2 meter (Pyroscience). Temperature was continuously monitored using TDIP15 temperature sensor (Pyroscience) and the probe signal automatically compensated for temperature fluctuations. The probe was calibrated daily using the manufacturer's instructions.

Absorbance Measurements (OD_{600}, NO_2^- and NO_3^-)

Cell density was measured during experiments by sampling 300 μL of solution from bioreactors and measuring absorbance at 600 nm using a microplate reader.

NO_2^- and NO_3^- concentrations were measured using a Nitrate/Nitrite Colorimetric Assay Kit (Cayman). Samples consisted of biological triplicates that were each measured in technical triplicates. The NO_2^- concentration in samples was estimated by adding Griess reagents to samples, which converted them to Azo products. Following this, absorbance was measured at 540 nm using a microplate reader. A calibration curve was constructed using various concentrations of an NO_2^- standard solution. A similar process was used to measure total NO_2^- and NO_3^- concentration in samples. However, an additional step, involving the addition of nitrate reductase and cofactors, was used to convert NO_3^- to NO_2^-. Similarly, a calibration curve was constructed using various concentrations of an NO_3^- standard solution. NO_3^- concentration was calculated by subtracting the NO_2^- concentration that was measured from the combined NO_2^- and NO_3^- concentration measurement. For more details on the procedure, refer to the manufacturer's instructions.

NO Consumption Assays

E. coli were taken from a −80°C stock, inoculated into a test tube with 1 ml of LB broth and incubated for 4 h at 37°C and 250 rpm. Following this, 10 μL were extracted from the test tube and transferred to a second test tube containing 1 mL of MOPS minimal media. The second test tube was incubated for 16 h at 37°C and 250 rpm. After 16 h, the overnight culture was used to inoculate a 250 mL baffled flask with 20 mL MOPS media at an OD_{600} of 0.01. The flask culture was grown to mid-exponential phase (OD_{600} = 0.2) and transferred to a pre-warmed (37°C) 50 mL falcon tube. The falcon tube was centrifuged at 4000 rpm, for 10 min at 37°C. Following this, 16 mL of MOPS were removed from the falcon tube, carefully avoiding the pellet of cells. The pellet was re-suspended in the remaining 4 mL and 1 mL was transferred to four separate pre-warmed (37°C) microcentrifuge tubes. The tubes were then centrifuged at 15,000 rpm for 3 min. Nine hundred and eighty microliter of media was removed from each microcentrifuge tube and the cell pellets were resuspended in 1 mL of pre-warmed MOPS media. The resuspended culture was used to inoculate a bioreactor with 50 mL MOPS media at an OD_{600} of 0.05. Five minutes after inoculation, NONOate delivery was initiated, either as bolus or through a delivery scheme implemented using the digital peristaltic pump.

Mathematical Modeling

Model Construction

The model was constructed and used in previous studies (Robinson and Brynildsen, 2013, 2015, 2016b; Robinson et al., 2014b). In brief, the mathematical model is a system of ordinary differential equations that describes the change in concentration of numerous biochemical species, upon exposure to NO, within the cell as well as the extracellular environment, as a function of reaction rates and stoichiometric coefficients.

$$\frac{d\vec{C}}{dt} = \hat{\boldsymbol{S}} \cdot \vec{r}_I - \boldsymbol{d} \cdot \vec{C} \tag{2}$$

Where $\vec{C}$ represents a vector of species concentrations. $\hat{\boldsymbol{S}}$ is a scaled reaction stoichiometry matrix and $\vec{r}_I$ is a vector of intensive reaction rates, which itself is a function of species concentrations and kinetic parameters. $\boldsymbol{d}$ represents a diagonal matrix of species-specific dilution terms as a result of volume expansion during NONOate delivery and cellular growth. The model was partitioned into extracellular and intracellular compartments, assuming rapid diffusion of NO and O_2 across the cell membrane. This was done to facilitate parameter optimization and model validation. Initial species concentrations, reaction rates and reaction structures were derived from the literature or trained on experimental data. MATLAB 2017b was used to run all simulations. For more information, on model construction and the specific reactions and species relevant to the model, refer to (**Supplementary Methods** and **Supplementary Tables S1–S3**).

Incorporation of NONOate Delivery Module

Delivery was incorporated into the differential equation for [NONOate] by including a delivery function, capable of taking one of four functional forms.

$$N_{NONOate_{|t=0}} + \int_0^{t_f} f_{del}\, dt = \omega \tag{3}$$

Where $N_{NONOate_{|t=0}}$ represents the number of moles of NONOate introduced as a bolus at the onset of delivery. f_{del} is the NONOate delivery function (μmol/h); t_f represents the duration of delivery (h); ω represents the total payload delivered (μmol). For more details, refer to (**Supplementary Methods**).

Incorporation of Bacterial Growth

Bacterial growth was modeled as a function of cell density:

$$\frac{dX}{dt} = \mu \cdot X \tag{4}$$

Where μ represents the specific growth rate and X represents cell density. X was assumed to vary linearly with optical density at 600 nm (OD_{600}), such that $k \cdot X = OD_{600}$ (Myers et al., 2013). μ was modeled as a 1st order Hill-type equation that depended on the concentrations of available cytochromes *bo* and *bd*:

$$\mu = \mu_{max} \cdot \frac{\left[Cytochrome_{bo}\right] + \left[Cytochrome_{bd}\right]}{K_\mu + \left[Cytochrome_{bo}\right] + \left[Cytochrome_{bd}\right]} \tag{5}$$

Incorporation of Growth-Dependent Translation Rate

Previously, we had chosen to model the rate of protein production as a function of mRNA transcripts with the inclusion of an $[O_2]$ dependency, such that increased $[O_2]$ led to increased translation rate (Robinson and Brynildsen, 2016b). The inspiration for this was that cells grew faster at higher O_2 tensions, and translation is known to vary closely with specific growth rate (Neidhardt and Magasanik, 1960; Roller et al., 2016; Dai et al., 2017; Zhu and Dai, 2018).

$$\frac{d\,[Protein]}{dt} = k_{translate} \cdot [mRNA] \cdot \left(1 + k_{act,O_2} \cdot \frac{[O_2]}{K_{O_2} + [O_2]}\right) - k_{deg} \cdot [Protein] \quad (6)$$

Where "Protein" represents either Hmp, NorV, or NrfA. mRNA represents the associated mRNA for each protein ($mRNA_{Hmp}$, $mRNA_{NorV}$, $mRNA_{NrfA}$). However, with the addition of growth to the model, we replaced the $[O_2]$ dependency term with a growth dependency term, which more explicitly exemplifies the connection between specific growth rate and translation rate.

$$\frac{d\,[Protein]}{dt} = k_{translate} \cdot [mRNA] \cdot \left(1 + k_{growth} \cdot \frac{\mu}{\mu_{max}}\right) - k_{deg} \cdot [Protein] \quad (7)$$

Where protein production is modeled with a growth dependency term as opposed to an O_2 dependency term. Substituting Equation (5) into Equation (7), protein production can be re-written as a function of terminal cytochrome oxidases.

$$\frac{d\,[Protein]}{dt} = k_{translate} \cdot [mRNA] \cdot \left(1 + k_{growth} \cdot \frac{[Cytochrome_{bo}] + [Cytochrome_{bd}]}{K_\mu + [Cytochrome_{bo}] + [Cytochrome_{bd}]}\right) - k_{deg} \cdot [Protein] \quad (8)$$

Where protein production in Equation (8) is a function of terminal cytochrome oxidases *bo* and *bd*, as opposed to a function of $[O_2]$. This modified form represents a direct relationship between translation and cellular respiration, where the larger the concentration of uninhibited cytochromes, the greater the rates of respiration, which leads to faster cellular growth rates and accelerated rates of protein production.

Incorporation of Extracellular and Intracellular Dilution

Previously, the model assumed a fixed volume in the bioreactor during the course of experiments, and that changes in concentration of individual species were only a result of consumption and production. However, with the implementation of the low flow drip system, the volume of the bioreactor continuously changed during delivery. As a result, species relevant to the extracellular environment were continuously diluted. In a similar vein, with the addition of growth, we could no longer assume a fixed cellular volume as a function of time. As cells grow, so does the cellular volume in the reactor, and species relevant to the intracellular environment are diluted in growing cells. Therefore, in the rate equation for each species, we incorporated a term to account for dilution:

$$d = \frac{\frac{dV_i}{dt}}{V_i} \quad (9)$$

Where V_i represents the volume compartment in which the species exists, where i can be extracellular, intracellular, or total. For more details, regarding model compartmentalization and derivation of the dilution term refer to (**Supplementary Methods**).

Parameter Optimization

Uncertain model parameters were fitted to experimental data, using the MATLAB function *lsqcurvefit*. Specifically, the algorithm involves a non-linear least squares optimization algorithm that searched for optimal parameter sets by minimizing the variance weighted sum of squared residuals between experimental NO (and/or O_2) curves and model simulations. Due to the compartmentalization of the model, different sets of unknown parameters were estimated independently using specific experimental conditions. The uncertain parameters fall into three categories: parameters relevant to NO reactions in the extracellular environment, parameters relevant to growth and cellular respiration, and parameters relevant to NO reactions in the cellular environment.

Estimating Extracellular Parameters

The product of the O_2 mass transfer coefficient and surface area to volume ratio of the media in the bioreactor ($k_{L_{O_2}} \cdot \frac{A}{V}$) was estimated from O_2 curves generated after purging O_2 with N_2 gas from bioreactors containing 50 and 55 mL MOPS media (**Supplementary Figure S8**). The rate of autoxidation, PAPA NONOate degradation rate, and rate of NO loss to the gas phase were trained simultaneously on both [NO] and $[O_2]$ curves generated from bolus delivery of 6 and 18 μmol of PAPA NONOate in cell-free media (**Supplementary Figure S9**). For more information on the parameters included in the optimization, refer to (**Supplementary Methods** and **Supplementary Table S4**).

Estimating O_2 Respiratory Parameters

Parameters relevant to cellular respiration, namely cellular growth, ubiquinol-oxygen oxidoreduction, and ubiquinone reduction (16 parameters in total), were trained on $[O_2]$ and OD_{600} data generated from monitoring cells seeded at an OD_{600} of 0.025 and treated with 0, 50 and 1000 μM KCN (**Supplementary Figure S2**), which inhibits respiration and halt growth. For more information on the parameters included in the optimization, refer to (**Supplementary Table S5**).

Estimating NO Cellular Parameters

Uncertain cellular parameters related to NO detoxification (21 parameters in total) were optimized on 8 sets of [NO] and $[O_2]$ data obtained for bolus, constant, ramp down, and ramp up delivery regimens at 6 and 18 μmol. We note that a variety of training protocols could have been employed. We elected to use all four delivery dynamics at both 8 and 16 μmol for training because of the distinct outcomes observed in different conditions (e.g., immediate cessation of growth, lack of cessation of growth,

delayed cessation of growth). We considered this diversity to be important for the ability of the model to extrapolate to conditions that it was not trained on, such as the 24 μmol dataset. For more information on the parameters included in the optimization, refer to (**Supplementary Table S6**).

Model Discrimination

Parameter sets were compared using Evidence Ratios (ER), which represent the likelihood of a given parameter set relative to the best set identified. Parameter sets with ER > 10, representing a less than 10% likelihood, were discarded. All parameters sets with ER < 10 were retained and used as initial points for an out-of-equilibrium adaptive Metropolis Markov Chain Monte Carlo (MCMC) process to further explore parameter space. If the MCMC algorithm generated a parameter set such that the initial point had an ER > 10 relative to the new minimum, the process was repeated using the best parameter set obtained from MCMC as the initial point. For more information on the model selection process, refer to (Robinson and Brynildsen, 2016b).

Algorithm to Identify Composite Dosing Schedules

For specified NO concentrations above 1 μM, the following algorithm was applied to identify dosing schema to maintain steady state levels, subject to the constraint of a total 24 μmol payload. Initial boluses (α) were determined such that simulated [NO] peaks equaled desired steady state concentrations. The vectors of species concentrations at the time of those peaks were used as initial conditions for secondary simulations where at each time step the concentrations of NONOate were solved to maintain d[NO]/dt = 0. The output of this simulation was a vector of NONOate concentrations at each time point, which was used to compute vectors of values corresponding to d[NONOate]/dt, and the rates of loss of NONOate (through decay and dilution) at each time point. These three vectors were added together, which yielded a vector corresponding to the NONOate delivery rate (f_{del}) required to maintain steady state.

$$f_{del} = \frac{d\,[NONOate]}{dt} + k_{deg} \cdot [NONOate] + d_{NONOate} \quad (10)$$

Lastly, f_{del} was truncated at t = T, such that $\int_0^T f_{del} dt = 24 - \alpha$.

In addition to determining dosing schedules to maintain [NO] at specified steady state levels, we attempted to enhance the antibacterial activity of NO by formulating the task as an optimization problem. Specifically, we attempted to maximize the amount of time [NO] was at or above the threshold to inhibit 99% of cytochromes (∼1.2 μM) by using the MATLAB optimization function *fmincon*. For this purpose, we considered dosing schedules that could be captured by third order polynomials. Parameters that were allowed to vary during the optimization were the coefficients of the polynomial and the total delivery time, and solutions were similarly constrained to cumulative payloads of 24 μmol. We tried two different approaches for initialization. In the first, the polynomial coefficients and delivery time were obtained from a least-squares fitting to the 2.2 μM steady state dosing scheme (best predicted scheme from steady state approach). The optimization algorithm then used those values and α from the steady state solution as a jumping off point to maximize the amount of time at or above ∼1.2 μM NO. This enabled a focused search around the best steady state solution for better performing schedules. In the second initialization approach, we used 100 sets of randomly selected polynomial coefficients and values of α subject to a total payload of 24 μmol, which effectively set the total delivery time for each initialization. The optimization algorithm then used those values as initial points to maximize the amount of time at or above ∼1.2 μM NO. This allowed a broader swath of parameter space to be searched for solutions better than the best steady state solution. For both types of initialization, the optimization procedure did not yield solutions that were better than the best dosing schedule from the steady state approach. This could have occurred due to the algorithm getting trapped in local optima or third order polynomials giving insufficient flexibility to reach globally optimal solutions. Given the depth and breadth of potential algorithms and optimization formulations there remains the possibility that better solutions than that provided by the steady state approach could be found in future studies.

DATA AVAILABILITY STATEMENT

The datasets generated for this study are available on request to the corresponding author.

AUTHOR CONTRIBUTIONS

Experiments and analyses were designed by DS and MB. DS performed the experiments and analyzed the data. The manuscript was written by DS and MB.

FUNDING

This work was supported by the National Science Foundation (CBET-1453325), the Natural Sciences and Engineering Research Council of Canada (NSERC), and Princeton University (Helen Shipley Hunt Fund and Forese Family Fund for Innovation).

ACKNOWLEDGMENTS

We thank Wen Kang Chou and Xuanqing (Mike) Wan for assistance. Parameter optimizations were performed using the Terascale Infrastructure for Groundbreaking Research in Science and Engineering (TIGRESS) high performance computer center at Princeton University, which is jointly supported by the Princeton Institute for Computational Science and Engineering (PICSciE) and the Princeton University Office of Information Technology's Research Computing department.

SUPPLEMENTARY MATERIAL

The Supplementary Material for this article can be found online at: https://www.frontiersin.org/articles/10.3389/fphys.2020.00330/full#supplementary-material

REFERENCES

Bang, I.-S., Liu, L., Vazquez-Torres, A., Crouch, M.-L., Stamler, J. S., and Fang, F. C. (2006). Maintenance of nitric oxide and redox homeostasis by the *Salmonella* flavohemoglobin hmp. *J. Biol. Chem.* 281, 28039–28047. doi: 10.1074/jbc.M605174200

Baron, S. (ed.) (1996). "Chapter 4: Bacterial metabolism," in *Medical Microbiology* (Galveston, TX: University of Texas Medical Branch at Galveston).

Bowman, L. A. H., McLean, S., Poole, R. K., and Fukuto, J. M. (2011). The diversity of microbial responses to nitric oxide and agents of nitrosative stress. *Adv. Microb. Physiol.* 59, 135–219. doi: 10.1016/B978-0-12-387661-4.00006-9

Brynildsen, M. P., Winkler, J. A., Spina, C. S., MacDonald, I. C., and Collins, J. J. (2013). Potentiating antibacterial activity by predictably enhancing endogenous microbial ROS production. *Nat. Biotechnol.* 31, 160–165. doi: 10.1038/nbt.2458

Choi, H. W., Kim, J., Kim, J., Kim, Y., Song, H. B., Kim, J. H., et al. (2016). light-induced acid generation on a gatekeeper for smart nitric oxide delivery. *ACS Nano* 10, 4199–4208. doi: 10.1021/acsnano.5b07483

Chou, W. K., and Brynildsen, M. P. (2019). Loss of DksA leads to multi-faceted impairment of nitric oxide detoxification by *Escherichia coli*. *Free Radic. Biol. Med.* 130, 288–296. doi: 10.1016/j.freeradbiomed.2018.10.435

Corker, H., and Poole, R. K. (2003). Nitric oxide formation by *Escherichia coli*: dependence on nitrite reductase, the no-sensing regulator Fnr, and flavohemoglobin hmp. *J. Biol. Chem.* 278, 31584–31592. doi: 10.1074/jbc.M303282200

Dai, X., Zhu, M., Warren, M., Balakrishnan, R., Patsalo, V., Okano, H., et al. (2017). Reduction of translating ribosomes enables *Escherichia coli* to maintain elongation rates during slow growth. *Nat. Microbiol.* 2:16231. doi: 10.1038/nmicrobiol.2016.231

Evans, M. A., Huang, P.-J., Iwamoto, Y., Ibsen, K. N., Chan, E. M., Hitomi, Y., et al. (2018). Macrophage-mediated delivery of light activated nitric oxide prodrugs with spatial, temporal and concentration control. *Chem. Sci.* 9, 3729–3741. doi: 10.1039/C8SC00015H

Fang, F. C. (2004). Antimicrobial reactive oxygen and nitrogen species: concepts and controversies. *Nat. Rev. Microbiol.* 2, 820–832. doi: 10.1038/nrmicro1004

Flannagan, R. S., Cosío, G., and Grinstein, S. (2009). Antimicrobial mechanisms of phagocytes and bacterial evasion strategies. *Nat. Rev. Microbiol.* 7, 355–366. doi: 10.1038/nrmicro2128

Friedman, A., Blecher, K., Sanchez, D., Tuckman-Vernon, C., Gialanella, P., Friedman, J. M., et al. (2011). Susceptibility of Gram-positive and -negative bacteria to novel nitric oxide-releasing nanoparticle technology. *Virulence* 2, 217–221. doi: 10.4161/viru.2.3.16161

Gardner, A. M., and Gardner, P. R. (2002). Flavohemoglobin detoxifies nitric oxide in aerobic, but not anaerobic, *Escherichia coli*: evidence for a novel inducible anaerobic nitric oxide-scavenging activity. *J. Biol. Chem.* 277, 8166–8171. doi: 10.1074/jbc.M110470200

Gardner, P. (2005). Nitric oxide dioxygenase function and mechanism of flavohemoglobin, hemoglobin, myoglobin and their associated reductases. *J. Inorg. Biochem.* 99, 247–266. doi: 10.1016/j.jinorgbio.2004.10.003

Gardner, P. R. (2012). Hemoglobin: a nitric-oxide dioxygenase. *Scientifica* 2012, 1–34. doi: 10.6064/2012/683729

Haas, A. (2007). The phagosome: compartment with a license to kill. *Traffic* 8, 311–330. doi: 10.1111/j.1600-0854.2006.00531.x

Hasanzadeh Kafshgari, M., Delalat, B., Harding, F. J., Cavallaro, A., Mäkilä, E., Salonen, J., et al. (2016). Antibacterial properties of nitric oxide-releasing porous silicon nanoparticles. *J. Mater. Chem. B* 4, 2051–2058. doi: 10.1039/C5TB02551F

Heilman, B., and Mascharak, P. K. (2013). Light-triggered nitric oxide delivery to malignant sites and infection. *Philos. Trans. R. Soc. Math. Phys. Eng. Sci.* 371:20120368. doi: 10.1098/rsta.2012.0368

Henard, C. A., and Vázquez-Torres, A. (2011). Nitric oxide and *Salmonella* pathogenesis. *Front. Microbiol.* 2:84. doi: 10.3389/fmicb.2011.00084

Ho, K. K. K., Ozcelik, B., Willcox, M. D. P., Thissen, H., and Kumar, N. (2017). Facile solvent-free fabrication of nitric oxide (NO)-releasing coatings for prevention of biofilm formation. *Chem. Commun.* 53, 6488–6491. doi: 10.1039/C7CC02772A

Hobbs, M. R., Udhayakumar, V., Levesque, M. C., Booth, J., Roberts, J. M., Tkachuk, A. N., et al. (2002). A new NOS2 promoter polymorphism associated with increased nitric oxide production and protection from severe malaria in Tanzanian and Kenyan children. *Lancet* 360:8.

Hogg, N., and Kalyanaraman, B. (1999). Nitric oxide and lipid peroxidation. *Biochim. Biophys. Acta BBA Bioenerg.* 1411, 378–384. doi: 10.1016/S0005-2728(99)00027-24

Hou, J., Pan, Y., Zhu, D., Fan, Y., Feng, G., Wei, Y., et al. (2019). Targeted delivery of nitric oxide via a 'bump-and-hole'-based enzyme–prodrug pair. *Nat. Chem. Biol.* 15, 151–160. doi: 10.1038/s41589-018-0190-195

Hurford, W. E. (2005). Nitric oxide as a bactericidal agent: is the cure worse than the disease? *Respir. Care* 50, 1428–1429.

Jones, M. L., Ganopolsky, J. G., Labbé, A., and Prakash, S. (2010). A novel nitric oxide producing probiotic patch and its antimicrobial efficacy: preparation and in vitro analysis. *Appl. Microbiol. Biotechnol.* 87, 509–516. doi: 10.1007/s00253-010-2490-x

Kim, J., Saravanakumar, G., Choi, H. W., Park, D., and Kim, W. J. (2014). A platform for nitric oxide delivery. *J. Mater. Chem. B* 2, 341–356. doi: 10.1039/C3TB21259A

Kun, J. F., Mordmüller, B., Perkins, D. J., May, J., Mercereau-Puijalon, O., Alpers, M., et al. (2001). Nitric oxide synthase 2 lambaréné (G-954C), increased nitric oxide production, and protection against malaria. *J. Infect. Dis.* 184, 330–336. doi: 10.1086/322037

Liang, H., Nacharaju, P., Friedman, A., and Friedman, J. M. (2015). Nitric oxide generating/releasing materials. *Future Sci. OA* 1:FSO54. doi: 10.4155/fso.15.54

Lu, Y., Slomberg, D. L., and Schoenfisch, M. H. (2014). Nitric oxide-releasing chitosan oligosaccharides as antibacterial agents. *Biomaterials* 35, 1716–1724. doi: 10.1016/j.biomaterials.2013.11.015

MacMicking, J. D., Nathan, C., Hom, G., Chartrain, N., Fletcher, D. S., Trumbauer, M., et al. (1995). Altered responses to bacterial infection and endotoxic shock in mice lacking inducible nitric oxide synthase. *Cell* 81, 641–650. doi: 10.1016/0092-8674(95)90085-90083

Martinez, L. R., Han, G., Chacko, M., Mihu, M. R., Jacobson, M., Gialanella, P., et al. (2009). Antimicrobial and healing efficacy of sustained release nitric oxide nanoparticles against staphylococcus aureus skin infection. *J. Invest. Dermatol.* 129, 2463–2469. doi: 10.1038/jid.2009.95

Myers, J. A., Curtis, B. S., and Curtis, W. R. (2013). Improving accuracy of cell and chromophore concentration measurements using optical density. *BMC Biophys.* 6:4. doi: 10.1186/2046-1682-6-4

Nablo, B. J., Rothrock, A. R., and Schoenfisch, M. H. (2005). Nitric oxide-releasing sol–gels as antibacterial coatings for orthopedic implants. *Biomaterials* 26, 917–924. doi: 10.1016/j.biomaterials.2004.03.031

Neidhardt, F. C., and Magasanik, B. (1960). Studies on the role of ribonucleic acid in the growth of bacteria. *Biochim. Biophys. Acta* 42, 99–116. doi: 10.1016/0006-3002(60)90757-90755

O'Donnell, V. B., and Freeman, B. A. (2001). Interactions between nitric oxide and lipid oxidation pathways: implications for vascular disease. *Circ. Res.* 88, 12–21. doi: 10.1161/01.RES.88.1.12

Pfeiffer, S., Lass, A., Schmidt, K., and Mayer, B. (2001). Protein tyrosine nitration in cytokine-activated murine macrophages: involvement of a peroxidase/nitrite pathway rather than peroxynitrite. *J. Biol. Chem.* 276, 34051–34058. doi: 10.1074/jbc.M100585200

Poole, R. K. (2005). Nitric oxide and nitrosative stress tolerance in bacteria. *Biochem. Soc. Trans.* 33, 176–180. doi: 10.1042/BST0330176

Poole, R. K., and Hughes, M. N. (2000). New functions for the ancient globin family: bacterial responses to nitric oxide and nitrosative stress. *MicroReview. Mol. Microbiol.* 36, 775–783. doi: 10.1046/j.1365-2958.2000.01889.x

Quinn, J. F., Whittaker, M. R., and Davis, T. P. (2015). Delivering nitric oxide with nanoparticles. *J. Control. Rel.* 205, 190–205. doi: 10.1016/j.jconrel.2015.02.007

Radi, R. (2018). Oxygen radicals, nitric oxide, and peroxynitrite: redox pathways in molecular medicine. *Proc. Natl. Acad. Sci. U.S.A.* 115, 5839–5848. doi: 10.1073/pnas.1804932115

Radtke, A. L., and O'Riordan, M. X. D. (2006). Intracellular innate resistance to bacterial pathogens. *Cell. Microbiol.* 8, 1720–1729. doi: 10.1111/j.1462-5822.2006.00795.x

Reichner, J. S., Meszaros, A. J., Louis, C. A., Henry, W. L., Mastrofrancesco, B., Martin, B.-A., et al. (1999). Molecular and metabolic evidence for the restricted expression of inducible nitric oxide synthase in healing wounds. *Am. J. Pathol.* 154, 1097–1104. doi: 10.1016/S0002-9440(10)65362-X

Riccio, D. A., and Schoenfisch, M. H. (2012). Nitric oxide release: Part I. *Macromolecular scaffolds*. *Chem. Soc. Rev.* 41:3731. doi: 10.1039/c2cs15272j

Robinson, J., and Brynildsen, M. (2016a). Construction and experimental validation of a quantitative kinetic model of nitric oxide stress in enterohemorrhagic *Escherichia coli* O157:H7. *Bioengineering* 3:9. doi: 10.3390/bioengineering3010009

Robinson, J. L., Adolfsen, K. J., and Brynildsen, M. P. (2014a). Deciphering nitric oxide stress in bacteria with quantitative modeling. *Curr. Opin. Microbiol.* 19, 16–24. doi: 10.1016/j.mib.2014.05.018

Robinson, J. L., Miller, R. V., and Brynildsen, M. P. (2014b). Model-driven identification of dosing regimens that maximize the antimicrobial activity of nitric oxide. *Metab. Eng. Commun.* 1, 12–18. doi: 10.1016/j.meteno.2014.08.001

Robinson, J. L., and Brynildsen, M. P. (2013). A kinetic platform to determine the fate of nitric oxide in *Escherichia coli*. *PLoS Comput. Biol.* 9:e1003049. doi: 10.1371/journal.pcbi.1003049

Robinson, J. L., and Brynildsen, M. P. (2015). An ensemble-guided approach identifies ClpP as a major regulator of transcript levels in nitric oxide-stressed *Escherichia coli*. *Metab. Eng.* 31, 22–34. doi: 10.1016/j.ymben.2015.06.005

Robinson, J. L., and Brynildsen, M. P. (2016b). Discovery and dissection of metabolic oscillations in the microaerobic nitric oxide response network of *Escherichia coli*. *Proc. Natl. Acad. Sci. U.S.A.* 113, E1757–E1766. doi: 10.1073/pnas.1521354113

Roller, B. R. K., Stoddard, S. F., and Schmidt, T. M. (2016). Exploiting rRNA operon copy number to investigate bacterial reproductive strategies. *Nat. Microbiol.* 1:16160. doi: 10.1038/nmicrobiol.2016.160

Roveda, A. C., Papa, T. B. R., Castellano, E. E., and Franco, D. W. (2014). PAMAM dendrimers functionalized with ruthenium nitrosyl as nitric oxide carriers. *Inorganica Chim. Acta* 409, 147–155. doi: 10.1016/j.ica.2013.07.009

Sacco, S. A., Adolfsen, K. J., and Brynildsen, M. P. (2017). An integrated network analysis identifies how ArcAB enables metabolic oscillations in the nitric oxide detoxification network of *Escherichia coli*. *Biotechnol. J.* 12:1600570. doi: 10.1002/biot.201600570

Sadrearhami, Z., Nguyen, T.-K., Namivandi-Zangeneh, R., Jung, K., Wong, E. H. H., and Boyer, C. (2018). Recent advances in nitric oxide delivery for antimicrobial applications using polymer-based systems. *J. Mater. Chem. B* 6, 2945–2959. doi: 10.1039/C8TB00299A

Schairer, D. O., Chouake, J. S., Nosanchuk, J. D., and Friedman, A. J. (2012a). The potential of nitric oxide releasing therapies as antimicrobial agents. *Virulence* 3, 271–279. doi: 10.4161/viru.20328

Schairer, D. O., Martinez, L. R., Blecher, K., Chouake, J. S., Nacharaju, P., Gialanella, P., et al. (2012b). Nitric oxide nanoparticles: pre-clinical utility as a therapeutic for intramuscular abscesses. *Virulence* 3, 62–67. doi: 10.4161/viru.3.1.18816

Seabra, A. B., and Durán, N. (2010). Nitric oxide-releasing vehicles for biomedical applications. *J. Mater. Chem.* 20, 1624–1637. doi: 10.1039/B912493B

Soria, S., de Anda, R., Flores, N., Romero-Garcia, S., Gosset, G., Bolívar, F., et al. (2013). New insights on transcriptional responses of genes involved in carbon central metabolism, respiration and fermentation to low ATP levels in *Escherichia coli*: new insights on transcriptional responses of genes in *E. coli*. *J. Basic Microbiol.* 53, 365–380. doi: 10.1002/jobm.201100525

Sortino, S. (2010). Light-controlled nitric oxide delivering molecular assemblies. *Chem. Soc. Rev.* 39:2903. doi: 10.1039/b908663n

Spiro, S., Zhang, M. Q., Mehta, H. H., and Liu, Y. (2015). Genome-wide analysis of the response to nitric oxide in uropathogenic *Escherichia coli* CFT073. *Microb. Genomics* 1:e000031. doi: 10.1099/mgen.0.000031

Stern, A. M., and Zhu, J. (2014). An introduction to nitric oxide sensing and response in bacteria. *Adv. Appl. Microbiol.* 87, 187–220. doi: 10.1016/B978-0-12-800261-2.00005-0

Stevanin, T. M., Poole, R. K., Demoncheaux, E. A. G., and Read, R. C. (2002). Flavohemoglobin Hmp protects *Salmonella enterica* Serovar *Typhimurium* from nitric oxide-related killing by human macrophages. *Infect. Immun.* 70, 4399–4405. doi: 10.1128/IAI.70.8.4399-4405.2002

Sun, B., Slomberg, D. L., Chudasama, S. L., Lu, Y., and Schoenfisch, M. H. (2012). Nitric oxide-releasing dendrimers as antibacterial agents. *Biomacromolecules* 13, 3343–3354. doi: 10.1021/bm301109c

Svensson, L., Poljakovic, M., Säve, S., Gilberthorpe, N., Schön, T., Strid, S., et al. (2010). Role of flavohemoglobin in combating nitrosative stress in uropathogenic *Escherichia coli* – Implications for urinary tract infection. *Microb. Pathog.* 49, 59–66. doi: 10.1016/j.micpath.2010.04.001

Tfouni, E., Truzzi, D. R., Tavares, A., Gomes, A. J., Figueiredo, L. E., and Franco, D. W. (2012). Biological activity of ruthenium nitrosyl complexes. *Nitric Oxide* 26, 38–53. doi: 10.1016/j.niox.2011.11.005

Thomas, D. D., Ridnour, L. A., Isenberg, J. S., Flores-Santana, W., Switzer, C. H., Donzelli, S., et al. (2008). The chemical biology of nitric oxide: implications in cellular signaling. *Free Radic. Biol. Med.* 45, 18–31. doi: 10.1016/j.freeradbiomed.2008.03.020

Toledo, J. C., and Augusto, O. (2012). Connecting the chemical and biological properties of nitric oxide. *Chem. Res. Toxicol.* 25, 975–989. doi: 10.1021/tx300042g

Trotter, E. W., Rolfe, M. D., Hounslow, A. M., Craven, C. J., Williamson, M. P., Sanguinetti, G., et al. (2011). Reprogramming of *Escherichia coli* K-12 metabolism during the initial phase of transition from an anaerobic to a micro-aerobic environment. *PLoS One* 6:e25501. doi: 10.1371/journal.pone.0025501

Vázquez-Torres, A., and Fang, F. C. (2005). Nitric oxide in *Salmonella* and *Escherichia coli* infections. *Ecosal Plus* 1:84. doi: 10.1128/ecosalplus.8.8.8

Vazquez-Torres, A., Jones-Carson, J., Mastroeni, P., Ischiropoulos, H., and Fang, F. C. (2000). Antimicrobial actions of the nadph phagocyte oxidase and inducible nitric oxide synthase in experimental Salmonellosis. I. effects on microbial killing by activated peritoneal macrophages in vitro. *J. Exp. Med.* 192, 227–236. doi: 10.1084/jem.192.2.227

Wink, D. A., and Mitchell, J. B. (1998). Chemical biology of nitric oxide: insights into regulatory, cytotoxic, and cytoprotective mechanisms of nitric oxide. *Free Radic. Biol. Med.* 25, 434–456. doi: 10.1016/S0891-5849(98)00092-6

Xiang, H.-J., Guo, M., and Liu, J.-G. (2017). Transition-metal nitrosyls for photocontrolled nitric oxide delivery: transition-metal nitrosyls for photocontrolled nitric oxide delivery. *Eur. J. Inorg. Chem.* 2017, 1586–1595. doi: 10.1002/ejic.201601135

Yang, Y., Qi, P. K., Yang, Z. L., and Huang, N. (2015). Nitric oxide based strategies for applications of biomedical devices. *Biosurf. Biotribol.* 1, 177–201. doi: 10.1016/j.bsbt.2015.08.003

Zhu, M., and Dai, X. (2018). On the intrinsic constraint of bacterial growth rate: *M. tuberculosis*'s view of the protein translation capacity. *Crit. Rev. Microbiol.* 44, 455–464. doi: 10.1080/1040841X.2018.1425672

Conflict of Interest: The authors declare that the research was conducted in the absence of any commercial or financial relationships that could be construed as a potential conflict of interest.

Copyright © 2020 Sivaloganathan and Brynildsen. This is an open-access article distributed under the terms of the Creative Commons Attribution License (CC BY). The use, distribution or reproduction in other forums is permitted, provided the original author(s) and the copyright owner(s) are credited and that the original publication in this journal is cited, in accordance with accepted academic practice. No use, distribution or reproduction is permitted which does not comply with these terms.

frontiers in Physiology

ORIGINAL RESEARCH
published: 17 April 2020
doi: 10.3389/fphys.2020.00328

Optimized and Personalized Phlebotomy Schedules for Patients Suffering From Polycythemia Vera

Patrick Lilienthal[1*†], *Manuel Tetschke*[1†], *Enrico Schalk*[2], *Thomas Fischer*[2] *and Sebastian Sager*[1]

[1] *Institute for Mathematical Optimization, Otto-von-Guericke-University Magdeburg, Magdeburg, Germany,* [2] *Department of Hematology and Oncology, Medical Center, Otto-von-Guericke-University Magdeburg, Magdeburg, Germany*

Polycythemia vera (PV) is a slow-growing type of blood cancer, where the production of red blood cells (RBCs) increase considerably. The principal treatment for targeting the symptoms of PV is bloodletting (phlebotomy) at regular intervals based on data derived from blood counts and physician assessments based on experience. Model-based decision support can help to identify optimal and individualized phlebotomy schedules to improve the treatment success and reduce the number of phlebotomies and thus negative side effects of the therapy. We present an extension of a simple compartment model of the production of RBCs in adults to capture patients suffering from PV. We analyze the model's properties to show the plausibility of its assumptions. We complement this with numerical results using exemplary PV patient data. The model is then used to simulate the dynamics of the disease and to compute optimal treatment plans. We discuss heuristics and solution approaches for different settings, which include constraints arising in real-world applications, where the scheduling of phlebotomies depends on appointments between patients and treating physicians. We expect that this research can support personalized clinical decisions in cases of PV.

Keywords: polycythemia vera, optimal control, modeling, numerical simulation, therapy scheduling, mixed-integer non-linear optimization, cancer, decision support

OPEN ACCESS

Edited by:
Julio R. Banga, Spanish National Research Council, Spain

Reviewed by:
Alexey Goltsov, Abertay University, United Kingdom
Francesco Passamonti, University of Insubria, Italy
Matthew Joseph Simpson, Queensland University of Technology, Australia

***Correspondence:**
Patrick Lilienthal
patrick-marcel.lilienthal@ovgu.de

†These authors have contributed equally to this work

Specialty section:
This article was submitted to Systems Biology, a section of the journal Frontiers in Physiology

Received: *21 December 2019*
Accepted: *20 March 2020*
Published: *17 April 2020*

Citation:
Lilienthal P, Tetschke M, Schalk E, Fischer T and Sager S (2020) Optimized and Personalized Phlebotomy Schedules for Patients Suffering From Polycythemia Vera. Front. Physiol. 11:328. doi: 10.3389/fphys.2020.00328

1. INTRODUCTION

The disease polycythemia vera (PV) belongs to chronic myeloproliferative neoplasms, meaning that an excess of blood cells are produced. In particular, red blood cells (RBCs) are affected (Lichtman et al., 2006). With an increasing number of RBCs in the human body, there is increased risk of thromboembolic events (Marchioli, 2005). To prevent patients from suffering serious events, such as strokes, heart attacks, or pulmonary embolisms, the density of the blood must be reduced. In moderate cases of the disease, this can be achieved with blood-letting (phlebotomy) at regular intervals (Tefferi et al., 2018).

In those cases, therapy schedules based on blood image data are proposed by physicians. However, those schedules might not be optimal for each individual (Finazzi and Barbui, 2007). These patients benefit considerably from a therapeutic strategy, that is able to predict the optimal treatment time for the next phlebotomy. In this paper, therefore, the data-driven model for erythropoiesis by Tetschke et al. (2018), verified for use on the data of healthy subjects, is extended to include amplified cell production by PV. Model analysis is applied to derive properties that

emphasize the model's plausibility for this disease. Clinical data from PV patients and *in silico* data derived from healthy subjects are used to evaluate and compare different optimization strategies for computing individual patient treatment schedules. Such strategies are for the most part capable of including constraints that appear in clinical applications, including reasonable clinical treatment times.

Using our results, it might be possible to enable physicians to schedule therapies individually based on a set of parameters unique to each patient. Thus, on the one hand, the probability of severe complications will decrease, when the time until the next measurement is assumed to be too long. On the other hand, in cases where the frequency of two consecutive measurements is assumed to be too low, the patient will benefit from not needing to go to a hematologist and the patient will be spared additional blood withdrawals.

To our knowledge there is neither a published mathematical model of erythropoiesis, that considers the disease PV, nor a study discussing optimal treatment schedules for PV patients by phlebotomy.

The paper is organized as follows: first, in chapter 2, we present the materials and methods used for this research. In chapter 3 we display the results of the modeling and the optimization approaches. Finally, we summarize and discuss our findings in chapter 4. Given the interdisciplinary nature of this research project, literature surveys are included in the corresponding subsections of this paper.

2. MATERIALS AND METHODS

In this section, we present the concepts and methods for modeling PV and for computing optimal treatment schedules. First, biological properties necessary for the modeling process are summarized. Then, a published compartment model for erythropoiesis in healthy subjects is reviewed. Afterwards, the acquisition of data from real and artificial patients is presented. Finally, computational methods for verifying the proposed model and for generating treatment schedules are discussed.

2.1. Biological Background

Understanding the relevant biological processes is crucial for the following modeling process. To this end, basic information about the physiological processes of erythropoiesis and of PV are summarized in this section.

2.1.1. Summary of Erythropoiesis

The supply of oxygen from the lungs to tissues and the transport of carbon dioxide back from tissues is central for the maintenance of vital functions in the human body. This exchange of substances is realized by erythrocytes (i.e., RBCs), which are biconcave discoid cells in the blood stream containing the protein complex hemoglobin. This protein complex binds the substances and enables the RBCs to their part. At any given time, a healthy adult human has a total of $2–3{\cdot}10^{13}$ erythrocytes, with men and women having about 5–6 million and 4–5 million erythrocytes per microliter of blood, respectively.

Erythropoiesis is the process by which RBCs are produced in the bone marrow. Beginning with stem cells, multi-potent stem cells are matured through several levels of erythroid progenitor cells, i.e., the Blast Forming Unit-Erythroid (BFU-E) and Colony Forming Unit-Eryhroid (CFU-E), and several levels of erythroblasts to bone marrow reticulocytes. These are then released into the blood circulation as blood reticulocytes, which then quickly grow into mature erythrocytes. During this process, which takes ∼20 days, the cell undergoes major changes including the removal of nuclei, organelles, and mitochondria to provide more room for hemoglobin. This process is displayed in **Figure 1** in a simplified scheme. The mature RBC has no nucleus, and it is incapable of cell division and regeneration of cell tissue. Damaged cells are removed by phagocytes to prevent clogging. This determines the mean life expectancy of RBCs in the blood stream, which is ∼120 days in healthy adults (Jandl, 1987). Sufficient iron concentration in the blood stream is necessary for successful erythropoiesis.

The hormone erythropoietin (EPO) is mainly responsible for the response of the body to changes in the amount of RBCs. It acts like a negative feedback mechanism for erythropoiesis. The EPO concentration in the blood circulation is inversely related to the concentration of hemoglobin. High EPO concentrations result in an increase to the RBC proliferation rate in the bone marrow. Several precursor cell types are affected, especially CFU-E production. This short summary can be complemented by a more detailed overview of erythropoiesis in Lichtman et al. (2006).

2.1.2. The Disease Polycythemia Vera

Polycythemia vera, also called primary polycythemia, is a chronic myeloproliferative neoplasm. That is, the production of blood cells increase to pathological levels. Most prominently, erythrocytes (i.e., RBCs) are affected. This causes the main symptoms of the patients: if the ratio of erythrocytes to the total blood volume—which, in medical terms, is called the hematocrit (*Hct*)—exceeds a certain threshold, the blood cells can clot. This can cause thromboembolic events, which can lead to strokes, myocardial infarctions, vein/arterial thrombosis, or pulmonary embolisms. These events can also often be located in atypical sides (Kiladjian et al., 2008; Dentali et al., 2014). While RBCs are mainly responsible for the clotting, also leukocytes and platelets as well as inflammatory mechanisms have an impact on the thromboembolic events (Falanga and Marchetti, 2014; Koschmieder et al., 2016).

If untreated, the mean life expectancy of patients suffering from PV is only ∼18 months (Marchioli, 2005; Lichtman et al., 2006). On the other hand, with treatment, a normal life span can be assumed (c.f. Rozman et al., 1991).

Other symptoms of the disease are not fatal, but can strongly reduce the quality of life of the patient. Most prominently, aquagenic pruritus, a severe itching that patients experience from

Abbreviations: B&B, branch and bound; BFU-E, blast forming unit-hematopoietic; CFU-E, colony forming unit-hematopoietic; DP, dynamic programming; EPO, erythropoietin; Hct, hematocrit; MCH, mean corpuscular hemoglobin; MIOCP, mixed-integer optimal control problem; OCP, optimal control problem; PV, polycythemia vera; RBC, red blood cell; SUR, sum up rounding; tHb, total hemoglobin mass.

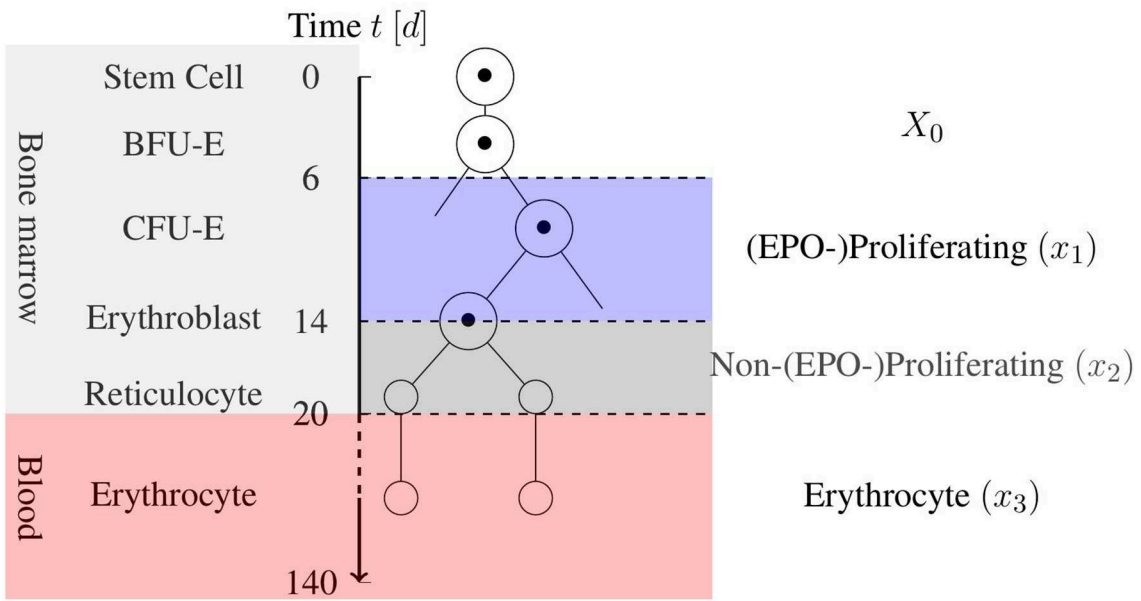

FIGURE 1 | Simplified schematic view of erythropoiesis. Certain cell stages over the age of the cell in days are displayed with a corresponding cell partition based on the model by Tetschke et al. (2018).

contact with water, is observed in up to 70% of cases (Siegel et al., 2013). Furthermore, patients suffer from headaches, hypertonia, fatigue, weight loss, and night sweats (Policitemia, 1995; Scherber et al., 2011). Also splenomegaly can be observed in PV patients. As described in Marchioli (2005), PV patients have a higher risk of developing other types of blood cancer over time, such as acute myeloid leukemia or myelofibrosis. This risk is associated with the age of the patient and the duration of the disease. After eight years, the disease evolves into secondary post-polycythaemic myelofibrosis in 15% of the cases (35% after 15 years, c.f. Alvarez-Larrán et al., 2009). In 20% of these cases, the patients develop acute myeloid leukemia (Mesa et al., 2005).

In low-risk cases, the basic therapy for PV is blood-letting (phlebotomy): ∼500 ml of blood on a regular basis (Tefferi et al., 2018). As the body is compensating for blood loss through blood plasma within a short amount of time yet requires several weeks to produce new RBCs, the *Hct* can be temporarily reduced using this treatment. In severe cases, this procedure is insufficient and there is the need for cytoreductive therapy (or a combination of both). It is currently unknown, how the frequency and volume of phlebotomies should be calculated to give an optimal outcome for the patient (Marchioli, 2005).

The most important clinical parameter for the planning of the treatment ist *Hct*. Additionally, counts of leukocytes, platelets, size of the spleen and other symptoms are taken into account (Barbui et al., 2011, 2018). In clinical practice, a phlebotomy is executed in a PV patient if the *Hct* is above 45% (Lichtman et al., 2006). According to Finazzi and Barbui (2007), this threshold might be inappropriate, because these findings were based on retrospective studies with small sample sizes and methodological shortcomings. They were unable to associate severe implications with *Hct* values between 40 and 55% in a larger prospective study. Contrarily, in a more recent study (Marchioli et al., 2013) showed that the rate of major thromboembolic events was significantly higher, if a target *Hct* of 45–50% was used. They recommend a target *Hct* of below 45%. Due to these conflicting results, the complementation of the *Hct* treatment criterion by additional information regarding individual patients might yield additional insights. To the best of our knowledge, no such approach to doing so exists.

The regulation of erythropoiesis no longer works in patients suffering from PV. The underlying process has yet to be fully understood, although there are plausible assumptions about it. In the investigation by Eaves and Eaves (1978), it was observed that in PV patients there is a partition in the CFU-E population. In the first fraction of cells, EPO exerts a normal influence when controlling the population, and in the second fraction, the cells proliferate unbounded, even at extremely low levels of EPO. In most (but not all) PV patients, a mutation of the JAK2V617F gene is present (Pardanani et al., 2007). This is associated with an uncontrolled proliferation of the progenitor cells (Lichtman et al., 2006). However, the direct influence of the mutation on erythropoiesis in PV is not fully understood. The JAK2V617F allele burden, i.e., the fraction of genes affected by that mutation, can be measured. More thorough understanding of JAK mutations has recently led to an increasing influence on therapy decisions in other hematopoietic diseases (Vainchenker et al., 2008). However, it does not seem to have a direct impact on Hct or the number of treatments (Silver et al., 2011).

2.2. Data-Driven Model for Erythropoiesis in Healthy Subjects

A mathematical model of erythropoiesis in healthy adults was developed in Tetschke et al. (2018). This simple compartment

model focuses on the system dynamics after blood loss, and it should be capable of capturing the relevant mechanisms in the case of a phlebotomy in a PV patient. Using the model, a suitable choice of model parameters was made such that the model reflected the subjects individually. The simulation results using this parameter set were verified using high-quality clinical data. In addition, the identifiability of the model parameters was positively investigated.

Basically, the model consists of three ordinary differential equations, that characterize the maturation and differentiation of a stem cell into an RBC until its death. Instead of incorporating EPO directly, the model uses an indirect approach with the help of the feedback function $Fb(\cdot)$. Thus, a decrease in the number of RBCs in x_3 results in an increased proliferation in x_1.

The three compartment model for erythropoiesis by Tetschke et al. (2018) is given by

$$\begin{aligned} \dot{x}_1(t) &= \beta \cdot \big(X_0 - k_1 \cdot x_1(t)\big) + Fb(x_3(t)) \cdot x_1(t) \\ \dot{x}_2(t) &= \beta \cdot \big(k_1 \cdot x_1(t) - k_2 \cdot x_2(t)\big) \\ \dot{x}_3(t) &= \beta \cdot \big(k_2 \cdot x_2(t) - \alpha \cdot x_3(t)\big) \\ Fb(x_3(t)) &= \gamma \cdot \left(1 - \frac{x_3(t)}{B}\right) \end{aligned} \tag{1}$$

with the following model components:

- The compartments x_1 [1] and x_2 [1] reflect certain precursor cells in the bone marrow, that are committed to the erythrocyte lineage. x_1 includes CFU-E and early erythroblasts, which are highly affected by EPO in the blood circulation. x_2 denotes late erythroblasts and reticulocytes, which are unaffected or only slightly affected by EPO.
- The compartment x_3 [g] contains the mass of mature erythrocytes in the blood stream.
- X_0 [d^{-1}] denotes a constant inflow from the stem cell compartment into the erythroid lineage.
- β [1] is a factor for EPO-independent proliferation. This is assumed to be unique to the patient.
- γ [d^{-1}] is a factor for EPO-dependent proliferation of early precursor cells. This is also assumed to be unique to the patient.
- k_1 [d^{-1}], k_2 [d^{-1}] and α [$(gd)^{-1}$] are the transition and apoptosis rates given by the literature (Tetschke et al., 2018). It remains unclear whether these transition rates are dependent on EPO. Here, they are assumed to be EPO-independent and set to $\frac{1}{8}$, $\frac{1}{6}$, and $\frac{1}{120}$, respectively, based on the literature values.
- In the case of healthy erythropoiesis, the existence of an average normal erythrocyte level can be assumed, when environmental conditions do not change drastically. The average value is denoted by B [g].
- $Fb(\cdot)$ [1] is a negative feedback function based on the fractional loss in x_3 , meaning, that the function decreases with increasing values of x_3 and vice versa. This indirectly incorporates the EPO dependency of the first compartment. By only using this function as a feedback, it was implicitly assumed that this is the only proliferation amplification factor from blood loss. This assumption is reasonable, provided that the blood loss is not too high, as, for example, in the case of severe where anemia emergency reactions like the release of stress reticulocytes (Lichtman et al., 2006) occur.

Blood removal of at most $V_{\max}$ ml of blood can be realized in a discrete way by removing $u(t) \cdot \frac{V_{\max}}{V_{\text{pat}}} \cdot x_3$ from the third compartment or in a continuous way by modifying the equation for $\dot{x}_3$:

$$\dot{x}_3(t) = \beta \cdot \big(k_2 \cdot x_2(t) - \alpha \cdot x_3(t)\big) - u(t) \cdot \frac{V_{\max}}{V_{\text{pat}}} \cdot x_3(t) \tag{2}$$

Here, V_{pat} is the subject's total blood volume in ml, and $u(t) \in [0, 1]$ accounts for the application of (fractional) blood removal. The unique steady state of (1) was shown to be

$$\bar{x} := (\bar{x}_1, \bar{x}_2, \bar{x}_3) = \left(\frac{k_1}{\alpha}, \frac{k_2}{\alpha}, 1\right) \cdot B \tag{3}$$

given that x_1, x_2 and x_3 are positive and $X_0 := \alpha \cdot B$.

The model was verified using data from Pottgiesser et al. (2008). There, blood loss of 500 ml in healthy adult subjects with sufficient iron concentrations was taken into account. In Tetschke et al. (2018), sufficient data from one re-saturation cycle after a blood donation could personalize the variables β and γ of the model. The estimation of B further improves the quality of the estimations, but in most cases this was not possible, as more data was needed. Details regarding model assumptions, clinical data, and numerical results can be found in Tetschke et al. (2018).

2.3. Data

The clinical parameter *Hct*, which is used to determine necessary treatment in clinical practice, suffers from serious drawbacks in measurements. This is mainly from plasma volume deviations, which can be significant in short amounts of time (Pottgiesser et al., 2008; Otto et al., 2017). Further, *Hct* only reflects a relative amount of solid blood particles. Rather, absolute values are needed to compute the effect of phlebotomies.

Indeed, our models need to take into account the absolute amount of erythrocytes in the body. As blood counts only provide information relative to the withdrawn amount, the total blood volume is needed for this computation. As described by Ertl et al. (2007), most measurement techniques for blood volume are invasive, and formulae for such estimations are imprecise. Thus, in Tetschke et al. (2018) the total hemoglobin mass (*tHb*) was used, which indirectly reflects the absolute amount of erythrocytes. This is advantageous insofar as much more accurate measurements can be made. In what follows, we use *tHb*, rather than *Hct* or the number of erythrocytes.

2.3.1. Clinical Data

In cooperation with the Department of Hematology and Oncology at the University Hospital Magdeburg, Germany, we retrospectively collected data from patients suffering from PV. The institutional ethics committee at the University of Magdeburg endorsed the study procedures. Each subject gave written informed consent before participation in this study. Unfortunately, the data were gathered according to routine

TABLE 1 | Details about three clinical patients used in 2.3.1.

ID	Sex	Age	Time since diagnosis (years)	Treatment
01	Male	45	6	Phlebotomy, chemotherapy since 5 years
02	Female	45	9	Phlebotomy only
03	Female	79	15	Phlebotomy, chemotherapy since 3 years

clinical practice, meaning the quality of the data for use in an optimization study was poor: when treating patients, physicians aim to see patients only when necessary. Thus, the density of the data was quite low. Moreover, only standard blood counts are regularly conducted. Such data suffers the effect of plasma volume deviations and corresponding measurement errors, as described above. Another problem arises with treatment. Phlebotomy is the method of choice, as long as the disease is not too severe. In severe cases, additional therapies with drugs are adopted. For specific medication, a model of the pharmacokinetics and pharmacodynamics of the drug would be helpful. This is beyond the scope of this study, however.

Ultimately, we were able to identify three patient data sets with a reasonable data density and quantity. In **Table 1** details about the three patients are displayed. Available data included the relative number of erythrocytes (*Ery* in $\left[Tpt/l\right]$), the mean corpuscular hemoglobin (*MCH* in $\left[pg\right]$), and covariates like the height, weight, and sex of the patient. With the help of Nadler's formula (Nadler et al., 1962) an (error-prone) estimation of the total blood volume in $\left[l\right]$ was made. Then, *tHb* was computed as the product of *Ery*, *MCH*, and the total blood volume. We excluded data gathered in cases where the patient started a complementary therapy with drugs.

As many patients are treated for several years, two of the three data sets cover more than five years. One of the assumptions of the model in Tetschke et al. (2018) was that subject-individual parameters are only valid for a certain amount of time. Thus, entire data sets should not be inspected. Instead, we identified periods of time during which there were no drastic changes. This was achieved with change-point analysis and the so-called moving-sum approach by Cho et al. (2018).

2.3.2. Generation of *in silico* Test Data

Owing to the described problems arising from the collection of clinical data, we used data from Pottgiesser et al. (2008) and the resulting parameter sets β and γ obtained in Tetschke et al. (2018), based on a prospective study with 29 healthy adult male subjects using a measurement technique for obtaining *tHb* measurements. Of the data, 28 data sets were used, as one set was excluded in Tetschke et al. (2018).

For the artificial generation of parameters for PV patients from those of healthy subjects, the rejection sampling method (von Neumann, 1963) was used to obtain suitable λ_{PV}. These λ_{PV} are suitable, if treatments are necessary and possible with reasonable frequency. For that, a random λ_{PV} was drawn from a uniform distribution on $[0, 1]$. With the heuristic approach without constraints 2.4.2, a number of necessary treatments within 365 days is generated. A λ_{PV} where that number of treatments is in $[1, 26]$ is accepted. Otherwise, the value is rejected. The interpretation is that the PV patient should be so much affected by the disease that treatment with phlebotomy at least once in a year is necessary. However, it should not be needed more often than twice a month. For patients that are even more sick, physicians proceed with chemotherapy anyway. This process was repeated until, for each subject, five distinct λ_{PV} were found.

This process yielded 140 artificially generated parameter sets of PV patients. The generated values for the five λ_{PV} for each subject were on average in the interval $\left[0.34(\pm 0.12), 0.6(\pm 0.16)\right]$ with an overall average number of treatments of 15.56 ± 6.56. The subject parameters with generated λ_{PV} can be found in **Table 2**.

TABLE 2 | Parameter sets of subjects from Tetschke et al. (2018) with five *in silico* parameters $\lambda_{\mathrm{PV}} = \lambda_i$ for each subject as detailed in Section 2.3.2.

ID	γ	β	B	V_{pat}	λ_1	λ_2	λ_3	λ_4	λ_5
01	0.769	1.650	865.45	5530.04	0.405	0.418	0.512	0.513	0.521
02	0.388	0.867	885.42	4666.08	0.385	0.498	0.558	0.706	0.709
03	0.510	1.617	863.97	5265.93	0.326	0.393	0.413	0.480	0.549
04	0.323	0.424	854.15	5984.70	0.522	0.544	0.604	0.878	0.888
05	0.061	1.381	971.67	7734.16	0.192	0.321	0.334	0.367	0.419
06	0.590	2.615	1001.42	5096.65	0.290	0.331	0.343	0.354	0.415
07	0.262	1.518	964.59	7270.17	0.343	0.349	0.370	0.424	0.480
08	0.324	2.676	704.42	4091.19	0.216	0.243	0.340	0.371	0.433
09	0.356	0.891	958.55	9282.78	0.366	0.555	0.559	0.602	0.605
10	0.089	2.557	851.70	4588.62	0.199	0.207	0.298	0.391	0.396
11	0.243	0.925	1006.45	4610.27	0.384	0.385	0.533	0.615	0.652
12	1.003	1.409	932.51	6127.49	0.528	0.541	0.567	0.581	0.631
13	0.057	0.879	647.98	4017.69	0.198	0.369	0.428	0.506	0.583
14	0.762	0.460	1081.34	8260.98	0.639	0.743	0.767	0.787	0.845
15	0.344	2.132	939.61	6778.40	0.289	0.334	0.387	0.397	0.408
16	0.141	1.661	753.24	7102.67	0.226	0.339	0.349	0.350	0.379
17	0.470	0.544	900.53	5832.50	0.514	0.541	0.691	0.705	0.758
18	0.525	0.631	841.61	4872.18	0.529	0.661	0.689	0.695	0.847
19	0.423	1.525	786.47	5109.69	0.393	0.401	0.451	0.512	0.540
20	0.661	2.798	765.99	8486.20	0.328	0.334	0.341	0.342	0.360
21	0.686	1.943	908.60	5725.97	0.345	0.389	0.404	0.408	0.463
22	0.613	3.142	893.06	5438.46	0.278	0.303	0.305	0.337	0.342
23	0.421	1.528	695.05	4989.05	0.318	0.502	0.518	0.533	0.563
24	0.863	2.078	768.83	6182.47	0.435	0.454	0.469	0.476	0.479
25	0.414	1.172	687.85	5733.62	0.408	0.559	0.575	0.600	0.625
26	0.635	0.836	925.62	6168.52	0.659	0.681	0.682	0.708	0.746
27	0.952	1.596	869.00	6351.31	0.440	0.444	0.466	0.490	0.555
28	0.805	1.486	809.18	5987.13	0.472	0.497	0.507	0.527	0.551

Patient-specific parameters γ and β are given, along with the B value used in that study and the calculated blood volume V_{pat}.

2.4. Computational Methods

In this section, the numerical methods and optimization approaches are described. First, a parameter estimation problem is solved on the available clinical data for proof-of-concept simulations. Then, optimization approaches for the generation of

treatment schedules for PV patients are presented and discussed. The software used to evaluate the approach is stated in the corresponding subsection. The most relevant parts of the code are available on GitHub (https://github.com/tetschke/PVschedule).

One main focus in this paper is the generation of optimal treatment schedules for phlebotomies of PV patients. Important properties of a suitable treatment schedule include the following:

1. **Respecting an upper bound**: the principle goal of treatment is to decrease the density of RBCs in the blood (measured in *Hct*) to reduce the symptoms of the disease and to reduce the risk of fatal complications. For this purpose, with the help of physicians, an upper limit for *tHb* ($X_{3,\mathrm{up}}$) is identified, which should not be exceeded.
2. **Minimizing the number of treatments**: with a good choice of dates for when treatments will be performed, one might reduce the number of necessary treatments without violating the proposed critical thresholds. This reduces the amount of days in which the patient might have side effects because of the treatment.
3. **Incorporating restrictions of the physician**: procedures in hospitals or medical practices should be limited to regular working hours. That is, weekends and night times should not be regarded as feasible in an optimal schedule. Other restrictions of the physicians can also be incorporated into the schedule.
4. **Varying the volume of a phlebotomy**: in clinical practice, a standard amount (500 ml) of blood is typically withdrawn in a phlebotomy (Lichtman et al., 2006). This restriction can be replaced with an interval of possible volumes, which can be chosen individually for each patient.
5. **Incorporating preferences of the patient**: a patient suffering from PV usually has a normal life span and can live a normal live with all its obligations. Thus, it might be advantageous to give the patient the means to prioritize possible time slots for therapy. For instance, job-related appointments or a vacation can be included in the planning with the help of a weighted objective function.

The focus of this work lies on the first three properties. Properties 1 and 3 will be incorporated as constraints of the optimization problem. The minimization of the number of treatments is reflected in the objective function J. This can have the structure

$$J = \int_0^T u(t)dt \tag{4}$$

in the case of a continuous problem formulation. In the integer case it is

$$J = \sum_{i \in \mathcal{T}} U_i, \tag{5}$$

where $\mathcal{T}$ is a subset of the used time discretization. A phlebotomy is a continuous process in a very short amount of time compared to the relevant time horizon for treatment planning. Therefore, the interpretation as an integer control is physiologically sensible. In contrast, the continuous objective function formulation corresponds to a minimization of the removed blood volume. Nevertheless, the latter one enables us to thoroughly analyze the structure of the resulting optimal control and yields insights into model properties. This justifies the use of these continuous solutions for the generation of integer solutions with low computational cost, as detailed in the next subsections.

For improved readability, the schedules generated by the methods presented in the following sections are abbreviated as follows:

- **H-Schedule**: Heuristic approach without constraints given by the test case (section 2.4.2).
- **HC-Schedule**: Heuristic approach with constraints given by the test case (section 2.4.2).
- **C-Schedule**: Solution of continuous optimal control problem (OCP) (section 2.4.3).
- **IP-Schedule**: Integer programming approach (section 2.4.4).
- **SUR-Schedule**: Sum up rounding (SUR) (section 2.4.5).
- **BB-Schedule**: Rounding via branch and bound (B&B) (section 2.4.6).
- **DP-Schedule**: Dynamic programming (DP) (section 2.4.7).

The number of treatments for such a schedule is then abbreviated by n_*, where $*$ is the one-, two-, or three-letter code of the corresponding method. For example, n_H describes the number of treatments according to the heuristic approach without constraints. This indexing with the respective letter code also holds for other occurring variables.

As a general test setup for evaluating the optimization methods, a time horizon of 365 days (October 1st to September 30th) is considered. Treatments are possible from Monday to Friday, where the first of October is considered a Monday. In addition, restrictions of the clinic are included as blocked times on days 81–95 and days 280–301. The interpretation of these blocked times is that, around the winter and summer holidays, there are reduced personnel in the clinic, such that routine treatments are not performed. In **Figure 2** an illustration of the restrictions can be found.

The evaluations were performed on 140 *in-silico*-generated PV patients, as described in section 2.3.2. All computations were performed on a server with 8 cores (Intel Xeon E5-2640 v3, 2.6 GHz) and 64 GB of RAM, running Ubuntu 18.04.3 LTS. Time measurements were performed using the "clock()" function from the Python package "time," which, on Unix systems, displays the used CPU time without interruptions by other processes.

To present the following methods, it is sufficient to have a model based on ordinary differential equations, that characterizes PV. In section 3.1.1, the model f_{PV} is presented. For our purposes, it here suffices to state that the model includes a fraction λ_{PV} of affected progenitor cells, which influence the severity of the disease. The model dynamics have the following structure:

$$\dot{x}(t) = f_{\mathrm{PV}}(t, x(t), \lambda_{\mathrm{PV}}, u). \tag{6}$$

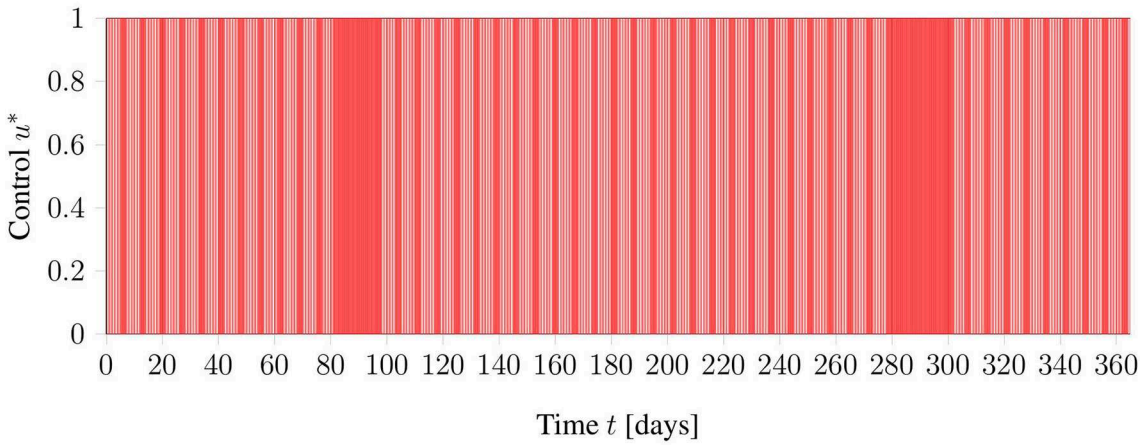

FIGURE 2 | Graphical view on the general test setup including restrictions of the clinic in red. Phlebotomies are only allowed during times denoted in white.

2.4.1. Proof-of-Concept Simulations

To get a first impression regarding the validity of the extended model in 3.1.1, the data sets of PV patients presented in 2.3.1 were used to obtain patient specific parameter vectors p. This parameter vector includes the formerly relevant model parameters β and γ as well as the fraction λ_{PV} introduced by the model extension.

The following parameter estimation problem with the least-squares objective is formulated:

$$\min_{p} \quad \frac{1}{2}\sum_{i=0}^{n_\eta} \frac{\left(\eta_i - x_3(t_i)\right)^2}{\sigma_i^2} + \phi(p) \tag{7}$$

$$s.t. \quad \dot{x}(t) = f_{\mathrm{PV}}(x(t), \lambda_{\mathrm{PV}}, p, u(t)) \tag{8}$$

$$x(0) = \left(x_1^0, x_2^0, \eta_0\right) \tag{9}$$

where

- $\{t_0 = 0, t_1, \ldots, t_{n_\eta}\}$ are the time points where *tHb* measurements were taken.
- η_i is the measurement value of *tHb* at time t_i.
- $x_3(t_i)$ is the corresponding model response at time t_i.
- σ_i is the standard deviation of the measurement at time t_i. As all considered data were collected by the same method under similar conditions, $\sigma_1 = 1$ for all measurements.
- p is the chosen parameter vector with n_p entries (including x_1^0 and x_2^0).

and the regularization ϕ is selected as

$$\phi(p) = \sum_{i=1}^{n_p} \left(\frac{p_i - p_i^{\mathrm{prior}}}{p_i^{\mathrm{prior}}} \right)^2 \tag{10}$$

Here, $\phi(p)$ is a term that can be used to incorporate a priori information. In our setting, regularization to known parameter values for healthy subjects was taken from Tetschke et al. (2018). The initial base value B was computed as the average over all *tHb* measurements with a corresponding *Hct* value of 45% or lower. This optimization problem is solved formulated as a deterministic OCP using ampl_mintoc, a package for mixed-integer optimal control problems (MIOCP), based on AMPL (Fourer et al., 2002) and using IPOPT (3.12.10, Wächter and Biegler, 2006).

2.4.2. Heuristic Approach

As displayed in 2.1.2 the aim of the treatment is to keep the patient's *Hct* level below 45%. To realize this, the standard procedure in clinical practice is the following. The *Hct* value of the patient is checked at regular intervals, selected in a fashion that ensures the critical threshold is not exceeded. As soon as the value becomes too high, a phlebotomy of constant volume takes place. Transferring this idea into algorithmic notation yields the following:

Algorithm 1: Heuristic approach

Set initial value X_0 ▷ (Initialization)
for $i \in \mathcal{I} \setminus \{0\}$ **do**
  $X_i = X_{i-1} + \mathcal{F}(X_{i-1}, f_{\mathrm{PV}}, \Delta_t)$ ▷ (Integration)
  if $X_{i,3} > X_{3,\mathrm{up}}$: **then** ▷ (Check for violation)
    if $i \in \mathcal{T}$: **then** ▷ (Treatment if allowed)
      $X_{i,3} = X_{i,3} - \frac{V_{\max}}{V_{\mathrm{pat}}} \cdot X_{i,3}$
    else ▷ (Shift treatment)
      Find largest $i^* \in \mathcal{T}$ with $i^* + i_{\mathrm{dwell}} < i$ and
      Set $i = i^*$
      $X_{i,3} = X_{i,3} - \frac{V_{\max}}{V_{\mathrm{pat}}} \cdot X_{i,3}$

where

- $\mathcal{I} = \{0, \ldots, N\}$ is the index set corresponding to the equidistant integration grid with step size Δt.
- $\mathcal{T} \subset \mathcal{I}$ denotes the integration points in which a treatment is possible.

- $\mathcal{F}$ is the forward quadrature scheme (here, the Runge-Kutta-scheme of order 4) with regard to Model (16).
- $V_{\max}$ and V_{pat} are the constant blood volume per treatment and total blood volume of the patient, respectively.
- i_{dwell} is the dwell time of the system, which represents the minimal distance between two treatments.

For $\mathcal{I} = \mathcal{T}$, heuristic treatment schedules without test constraints are generated (H-Schedules). Using $\mathcal{T}$ as in the general test case described above, HC-Schedules are computed. One major advantage to this approach is that both types of treatment plans can be computed quickly (within a few seconds). However, the treatment plans are not guaranteed to be optimal. Moreover, this heuristic does not take the lower bound $X_{3,\text{lo}}$ into account. Therefore, it is necessary to inspect other approaches.

2.4.3. Continuous Optimal Control Problem

Another point of view is to see the desired treatment schedule as a solution to an OCP. To apply the solution in clinical practice, we are interested in a mixed integer solution. The next two sections deal with the generation of feasible and optimal integer solutions. First, we showcase the relaxed OCP and generate continuous treatment schedules (C-Schedules). An interpretation of these schedules is that a phlebotomy can be done arbitrarily often with arbitrarily withdrawn blood volumes. An exemplary illustration of a continuous solution with the corresponding *tHb* trajectory is displayed in **Figure 3**. Some of the rounding strategies in the following sections are based on these relaxed solutions. Further, the theoretical investigation of the solution structure can yield insights into the underlying structure of the problem.

The continuous OCP for minimizing the number of phlebotomies while allowing fractional treatments reads as follows:

$$\begin{aligned} \min_{u(.)} \quad & \int_0^T u(t)\mathrm{d}t \\ s.t. \quad & \dot{x}(t) = f_{\text{PV}}(x(t), \lambda_{\text{PV}}) \quad t \in [0,T] \\ & x(0) = x_0 \\ & X_{3,\text{lo}} \le x_3(t) \le X_{3,\text{up}} \quad t \in [0,T] \\ & u(t) \in [0,1] \qquad\qquad t \in [0,T] \end{aligned} \tag{11}$$

The objective function only indirectly accounts for the number of necessary treatments. Actually, this formulation minimizes the amount of withdrawn blood over the time horizon. A theoretical analysis of the problem solution is given in **Appendix A**. This analysis yields unique optimal control u^* of the structure:

$$u^*(t) = \begin{cases} 0 & , x_3(t) < X_{3,\text{up}} \\ u_{\text{path}}(t) & , x_3(t) = X_{3,\text{up}} \end{cases} \tag{12}$$

This optimal control is intuitive in the sense that no treatment is applied when unnecessary. Alternatively, phlebotomies are reduced to a minimum, such that they approach the threshold $X_{3,\text{up}}$. The existence of this solution shows that, in general, the OCP is solvable. Computationally, this problem is solved with a non-linear programming formulation in CasADi (3.5.1) (Andersson et al., 2019) using IPOPT (3.12.3, Wächter and Biegler, 2006).

2.4.4. End Time Optimization Using Integer Approach on Non-linear Program

Continuous blood withdrawal, as seen in the case of the relaxed problem, can not be performed in clinical practice with currently available tools. To find an approach that is closer to clinical practice, an MIOCP with a discrete formulation is used. Let $U = \{U_1, ..., U_N\}$ and $X = \{X_1, ..., X_N\}$. Then the discrete formulation is given by

$$\begin{aligned} \min_{U,X} \quad & \sum_{i \in \mathcal{T}} U_i \\ s.t. \quad & X_{i+1} = \left(1 - U_{i+1} \cdot \frac{V_{\max}}{V_{\text{pat}}}\right) \\ & \cdot \left(X_i + \mathcal{F}(X_i, f(X_i), \Delta t)\right) \qquad \forall i \in \mathcal{I} \setminus \{N\} \\ & X_{3,\text{lo}} \le X_{i+1,3} \le X_{3,\text{up}} \qquad \forall i \in \mathcal{I} \setminus \{N\} \\ & X_0 = x_0 \\ & U_i \in \{0,1\} \qquad\qquad \forall i \in \mathcal{T} \\ & U_i = 0 \qquad\qquad \forall i \in \mathcal{I} \setminus \mathcal{T} \end{aligned} \tag{13}$$

Here, $\mathcal{I}, \mathcal{T}, \mathcal{F}, V_{\max}$, and V_{pat} are the same as in subsection 2.4.2.

Using this objective function, the system solution is not unique. In fact, a solution with $\sum U_i = \min_{U,X} \sum U_i$ does not take into account when the next treatment will take place after the end of the time horizon. A possible extension to avoid this problem is to include the time point of the next necessary treatment T_f after the end of the schedule. Although it is possible to combine those two objectives, it is unclear how exactly the individual components should be weighted. To circumvent this problem, an iterative approach is proposed.

Using the heuristic approach with schedule constraints $\mathcal{T}$ leads to a feasible treatment schedule, which gives an upper bound u_{up} for the necessary number of treatments. Starting with u_{up}, we fix the number of treatments in the optimization problem and maximize T_f. We decrement the number of treatments and repeat, until there are no more feasible solutions. The optimization problem that needs iterative solving is

$$\begin{aligned} \min_{U,X,X_{N+1},...,X_{N_T},T_f} \quad & -T_f \\ s.t. \quad & X_{i+1} = \left(1 - U_{i+1} \cdot \frac{V_{\max}}{V_{\text{pat}}}\right) \\ & \cdot \left(X_k + \mathcal{F}(X_i, f(X_i), \Delta t)\right) \qquad \forall i \in \mathcal{I}_{T_f} \setminus \{N_{T_f}\} \\ & X_{3,\text{lo}} \le X_{i+1,3} \le X_{3,\text{up}} \qquad \forall i \in \mathcal{I}_{T_f} \setminus \{N_{T_f}\} \\ & X_0 = x_0 \\ & X_{N_T} = X_{3,\text{up}} \\ & U_i \in \{0,1\} \qquad\qquad \forall i \in \mathcal{T} \\ & \sum_{i \in \mathcal{T}} U_i = u_{\text{sum}} \\ & U_i = 0 \qquad\qquad \forall i \in \mathcal{I} \setminus \mathcal{T} \end{aligned} \tag{14}$$

Here, $\mathcal{I}_{T_f} = \mathcal{I} \cup \{N+1, \ldots, N_{T_f}\}$ is an expansion of the former integration index set $\mathcal{I}$ for additional integration points after

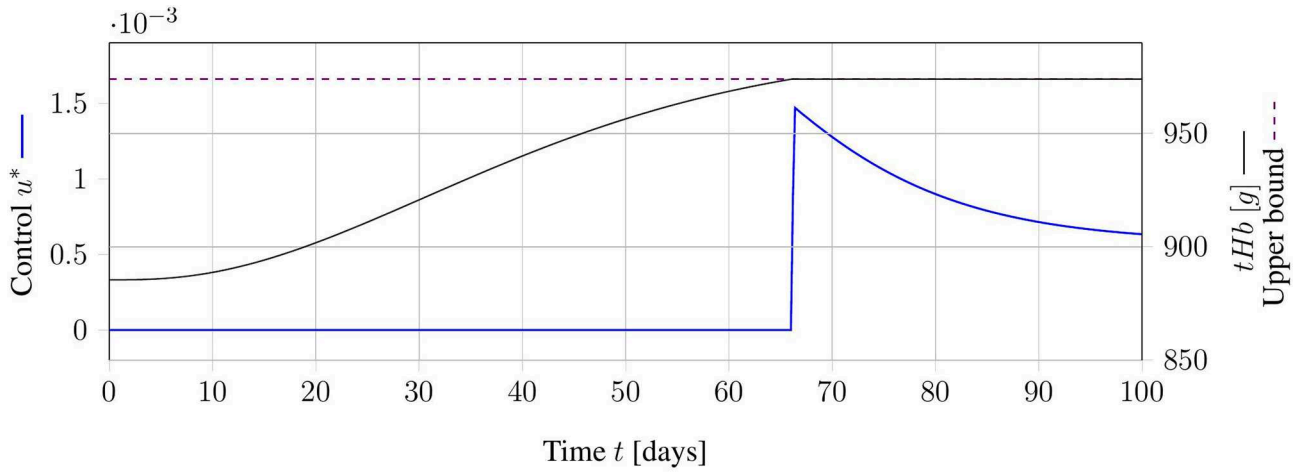

FIGURE 3 | Exemplary result for an optimal relaxed treatment schedule. The continuous control function u (blue) is zero, as long as the *tHb*-value (black) is below the upper bound (dashed, purple). As soon as the upper bound is reached, the control function increases exactly as much as necessary to keep the *tHb*-value at the upper bound.

the times where controls are possible. Thus, $\mathcal{T} \subset \mathcal{I}$ is selected such that $\forall i \in \mathcal{T} : i \leq N$. The objective of minimizing $-T_f$ reflects the aim of postponing for as long as possible the first phlebotomy after the end of the schedule with the given number of treatments. The algorithm, then, is as follows:

Algorithm 2: Mixed Integer OCP with T_f

1: Solve the heuristic algorithm (1) and set u_{up} to objective
2: $u_{\text{sum}} = u_{\text{up}}$
3: Solve (14)
4: **while** feasible **do**
5: $\quad u_{\text{sum}} = u_{\text{sum}} - 1$
6: $\quad$ Solve (14)

This problem is solved with BONMIN (Bonami et al., 2008) using a non-linear programming formulation in CasADi. Integer schedules (IP-Schedules) derived using this MIOCP formulation have the advantage of being realizable in clinical practice while still including the main ideas for optimal treatment. However, this problem leads to an MIOCP, that is computationally expensive. In general, MIOCP problems are NP-hard. This already holds true for the linear, discretized version of this problem class (Kannan and Monma, 1978). Thus, for large $|\mathcal{T}|$ in particular, the problem is difficult to handle. For rather small $|\mathcal{T}|$, this approach can be investigated and compared to the heuristic approach presented in subsection 2.4.2. In addition, using BONMIN on a non-linear problem does not guarantee global optimality. The performance of the software depends on the options used. In this paper, we used the following options: *variable_selection* = *most-fractional*, and *tree_search_strategy* = *dive*.

2.4.5. Sum-Up Rounding

Owing to the size of the MIOCP, as described in the previous subsection, computations with standard solvers are only feasible for a rather small number of possible integer control points. Larger problem sizes might be more relevant. Indeed, more control points per week or longer overall time horizons can be included. Thus, it is worthwhile to inspect rounding strategies and to compare them to the heuristic approach.

The SUR approach (Sager, 2005) exclusively uses the optimal solution of the relaxed problem (11) to compute a binary treatment schedule. Basically, the idea is to collect the relaxed control in time and set the integer solution to one, as soon as a certain threshold u^T is reached. This collection is then reduced by one, and, afterwards, the previous process is repeated.

We use the multiple shooting method on an equidistant time grid for the computation of the relaxed solution u^*. The integer solution at the discretization point t_i using SUR can then be computed as follows:

$$U_i = \begin{cases} 1 & \text{, if } \sum_{j=0}^{i} u_j^* - \sum_{j=0}^{i-1} U_j \geq u^T \\ 0 & \text{, else} \end{cases} \tag{15}$$

In the standard SUR approach, u^T is set to $\frac{1}{2}$. Owing to the problem structure, we instead use $u^T = \varepsilon$ for SUR-Schedules, where $\varepsilon > 0$ is close to zero. This is necessary because only the relaxed solution is non-zero. If the upper bound $X_{3,\text{up}}$ is already reached, treatment must be done immediately.

This approach has the advantage that it is easy to implement and the computations are extremely fast, once the relaxed problem is solved. Moreover, if the relaxed problem includes blocked times t_j, $u^*(t_j)$ will be zero and $U_j = 0$ automatically.

The big disadvantage to SUR is that it is not obvious how to include path constraints. The strategy only takes into account

the relaxed solution. There is no guarantee that the upper bound $X_{3,\mathrm{up}}$ will be respected.

To summarize, although fast and intuitive to implement, SUR-Schedules risk endangering the patient, owing to violations of the treatment aim. Therefore, in clinical applications, the use of this approach should be combined with safety strategies, such as the use of a stricter upper bound $X_{3,\mathrm{sumup,\,up}} < X_{3,\mathrm{up}}$.

2.4.6. Rounding via Combinatorial Integral Approximation

Another approach to generating integer solutions from the relaxed solution is to adopt so-called combinatorial integral approximation (Sager et al., 2011). For this, we used open-source software called pycombina (Buerger et al., 2019). Here, a B&B algorithm is implemented, that is able to include combinatorial constraints with regard to binary controls. The standard B&B tree is organized in a fashion, that branches forward in time.

Originally, the algorithm was designed to approximate relaxed controls with binary ones. For this purpose, it does not need to take into account the actual states. Therefore, it is unable to deal with path constraints and suffers from the same disadvantage as the SUR approach.

This is why we adapted the algorithm to take into account the states (and especially x_3) in each iteration through forward integration. If at time point t_i one of the conditions $X_{3,\mathrm{lo}} \leq x_3(t_i) \leq X_{3,\mathrm{up}}$ is violated, the corresponding branch of the tree is no longer feasible and can be disregarded. This not only helps to include path constraints, but also decreases the size of the B&B tree.

This modified B&B version is able to generate feasible solutions, if we also fix the control u to zero when no treatments are possible. We used the prefixing option in pycombina to include this into our problem formulation.

The overall quality of BB-Schedules generated by this approach depends on the maximum number of iterations. As the B&B tree tends to become very large, relatively few iterations search through only part of that tree. This can lead to instances where no solution can be determined, however, even though we implemented the additional pruning of the tree for infeasible solutions. Nevertheless, a large number of iterations leads to very large run times. For our numerical results, we used the default of five million iterations.

2.4.7. Dynamic Programming

A completely different algorithmic idea for the solution of (13) is to generate treatment schedules by dynamic programming (DP-Schedules). Here, discretization is done not only in time, but also in the state space. This approach goes back to Bellman (1957). Details can be found in Bertsekas (2012).

First, we introduce an equidistant grid $x^0 < x^1 < \cdots < x^{n_x}$ with resolution Δ_x in state space and tabulate state transitions: for each possible combination of a state value and a possible control value, the corresponding result of an integration over the next time interval must be stored. The result of the integration usually does not match one of the grid points. This is why rounding toward a valid grid point is necessary.

In our provided code this tabulation is stored with the help of indices. Thus, the rounding is done in the following fashion: Let i be a fractional value of a result of an integration. This value is a convex combination of the two grid points closest to the result. The value i is then rounded toward a valid grid point i^*, if $-0.5 \cdot \Delta_x \leq i - i^* - o \cdot \Delta_x \leq 0.5 \cdot \Delta_x$ holds. For the offset $o = 0.0$, rounding half up is applied, whereas for $o > 0$, a more conservative rounding is applied. We test both $o = 0.0$ and $o = 0.4$.

The tabulation is then used to compute a so-called cost-to-go function. For each time point and state grid point this function indicates the best possible choice from that state and that time onwards. This is computed backwards in time. The last step is the computation of the optimal control starting in suitable grid points close to x_0 with the help of the tabulation.

This approach is globally optimal with regard to the grid used, as every possible combination of states and controls is evaluated. However, this approach suffers from practical drawbacks, when systems with many states are used, or when there are too many grid points for each state. In the case of the MIOCP (13), only three states have to be regarded and we consider only binary control. For this reason, the algorithm might be a good choice. We used 400 grid points for each of the three states.

After the initial tabulation, the algorithm has a linear complexity in the time discretization. Therefore, this approach is especially suited for schedule generation with large time horizons. It is also easy to include constraints. In our implementation, we worked with sparse matrix structures to account for the exponential growth of the state transition tabulation.

3. RESULTS

In this section, the results based on the previously introduced methods are presented. The model proposed by Tetschke et al. (2018) is extended, and we discuss necessary assumptions for the biological process. The plausibility of this extended model is then examined with both steady-state analysis and numerical proof-of-concept simulations using clinical data from PV patients. Then, the numerical results from heuristic generations of treatment schedules are compared to those of other numerical approaches on *in silico* patient configurations.

3.1. Mathematical Modeling of Erythropoiesis in PV Patients

The three-compartment model by Tetschke et al. (2018) captures the basic physiological processes of healthy erythropoiesis in adults. We extend this model to capture PV as well. The small number of free parameters in the original model also motivated its suitability for this purpose: the amount of clinical data describing PV patients is usually insufficient for large models.

In this section, we describe the proposed model for PV, analyze its properties, and discuss simulation results using clinical data. We generated suitable treatment plans using heuristic and optimization-based approaches. The overall goal of treatment

was to ensure the safety of the patient, while aiming to improve quality of life.

3.1.1. Model Extension

Here, we discuss our extension of the model (1) to reflect the relevant dynamics of erythropoiesis in PV patients. For this, we follow the idea in Eaves and Eaves (1978) stated in subsection 2.1.1. According to this study, a fraction of CFU-E cells proliferates at a maximal rate, independent of EPO or fractional blood loss. We introduce a parameter λ_{PV}, which corresponds to this fraction and can take values between $[0, 1]$. Correspondingly, there is a fraction of cells $1-\lambda_{\mathrm{PV}}$ that responds in a normal way to EPO. A person not affected by PV will correspond to $\lambda_{\mathrm{PV}} = 0$, whereas higher values give means to quantify the severeness of the disease. As the compartment x_1 mainly consists of CFU-E cells, an intuitive model extension of (1) is given as follows:

$$\begin{aligned} \dot{x}_1 &= \beta \cdot \left(X_0 - k_1 \cdot x_1\right) + (1-\lambda_{\mathrm{PV}}) \cdot Fb(x_3) \cdot x_1 \\ &\quad + \lambda_{\mathrm{PV}} \cdot \gamma^* \cdot x_1 \\ \dot{x}_2 &= \beta \cdot \left(k_1 \cdot x_1 - k_2 \cdot x_2\right) \\ \dot{x}_3 &= \beta \cdot \left(k_2 \cdot x_2 - \alpha \cdot x_3\right) \\ Fb(x_3) &= \gamma \cdot \left(1 - \frac{x_3}{B}\right) \end{aligned} \tag{16}$$

with γ^* denoting the growth rate of affected cells in x_1. A phlebotomy can be incorporated in the same way as Equation (2) in section 2.2.

The model components are here discussed with respect to their plausibility in the case of PV.

- β, k_1, k_2, γ: using this model extension by cell partition with λ_{PV} leads to the assumption that cells affected by PV only proliferate faster in x_1, and otherwise behave like a healthy cell. We note that there might be physiological processes not covered by this model that affect other components, such as the transition times between the compartments. However, we assume that this is not the case and use the model variables β, k_1, k_2, and γ as in Tetschke et al. (2018).
- α: there are conflicting studies regarding the average life span of erythrocytes in PV patients. Depending on the investigation, the average life span is either shortened or normal (see London et al., 1949; Huff et al., 1950; Berlin et al., 1951). We will not discuss this further here. We used $\alpha = \frac{1}{120}$ as in the healthy case. We note that α might be different in PV patients and might depend, for example, on progression of the disease, reflected by λ_{PV}, or on patient-specific factors. This could be inspected in a follow-up investigation, once suitable clinical data are available.
- γ^*: the model variable γ^* has a significant impact on proliferation in PV patients, especially in those with a higher number of affected cells described by high values of λ_{PV}. To our knowledge, however, no study has investigated the proliferation rate of CFU-E in PV patients based on the fraction of affected cells. Therefore, an accurate guess for the value of γ^* is not possible. In case of unknown model variables, a numerical estimation based on suitable data is optimal. However, there are many unknown patient-specific variables, such as β, γ, λ_{PV}, and (in most cases) B. The additional estimation of γ^* is unreasonable, given that data of exceptional quality and quantity are unavailable. As the available data do not often meet these criteria, one might opt for a heuristic approach by assuming a dependency of γ^* on other model variables, such as γ or β. By definition, γ reflects a proliferation amplification of EPO-affected cells, such that the use of the EPO-independent factor β seems more intuitive. For our investigation, we used $\gamma^* = \frac{\beta}{10}$.
- X_0: the model variable X_0 reflects the inflow from hematopoietic stem cells to the erythrocyte lineage. As the proliferation rate of PV-affected stem cells might also be increased, one might assume X_0 to be higher and to be dependent on λ_{PV}. We assumed that a potentially enhanced stem cell inflow is compensated by the proliferation rate γ^*, and we used X_0 as in Tetschke et al. (2018).

3.1.2. Steady State Analysis

In most cases, the system's steady state for the erythrocyte mass $\bar{x}_3 = B_{\mathrm{PV}}$ of PV patients should be at sufficiently high levels such that long, before it is reached, treatment is administered to prevent possibly fatal complications. However, deriving information about the system's steady states often yields useful information about the system's properties. In this case, we inspected the relation between the new steady state erythrocyte mass B_{PV} and the steady state erythrocyte mass B without the model extension.

Following the calculations in **Appendix B**, the steady state erythrocyte mass B_{PV} is given by

$$B_{\mathrm{PV}}(\lambda_{\mathrm{PV}}) = B \cdot \begin{cases} -\frac{\beta \cdot k_1 - (1-\lambda_{\mathrm{PV}}) \cdot \gamma - \lambda_{\mathrm{PV}} \cdot \gamma^*}{2 \cdot (1-\lambda_{\mathrm{PV}}) \gamma} & \text{for } \lambda_{\mathrm{PV}} < 1 \\ + \sqrt{\left(\frac{\beta \cdot k_1 - (1-\lambda_{\mathrm{PV}}) \cdot \gamma - \lambda_{\mathrm{PV}} \cdot \gamma^*}{2 \cdot (1-\lambda_{\mathrm{PV}}) \gamma}\right)^2 + \frac{\beta \cdot k_1}{(1-\lambda_{\mathrm{PV}}) \cdot \gamma}}, & \\ \frac{\beta \cdot k_1}{\beta \cdot k_1 - \gamma^*}, & \text{for } \lambda_{\mathrm{PV}} = 1 \end{cases} \tag{17}$$

As described in the **Appendix**, we also found that this function (using $\gamma^* = \frac{\beta}{10}$) is continuous for $\lambda_{\mathrm{PV}} \in [0, 1]$, such that only the case where $\lambda_{\mathrm{PV}} = 1$ must be thoroughly investigated. With similar calculations, one can also show that $B_{\mathrm{PV}}(\lambda_{\mathrm{PV}})$ increases monotonously for $\lambda_{\mathrm{PV}} \in [0, 1]$.

To summarize the results, B_{PV} is a continuous, monotonously increasing function with $B_{\mathrm{PV}}(\lambda_{\mathrm{PV}}) \in [B, 5 \cdot B]$ for $\lambda_{\mathrm{PV}} \in [0, 1]$. This means that an increasing fraction of affected cells can indeed lead to physiological complications, as the system tends to reach critical erythrocyte levels. This is consistent with the main physiological assumptions about the process.

3.2. Numerical Results

In this section, the numerical results using the proposed model are presented. First, clinical data are evaluated in a proof-of-concept simulation. Then, the computed treatment schedule given by the heuristic method in section 2.4.2 is compared to schedules computed by the other approaches given in 2.4.

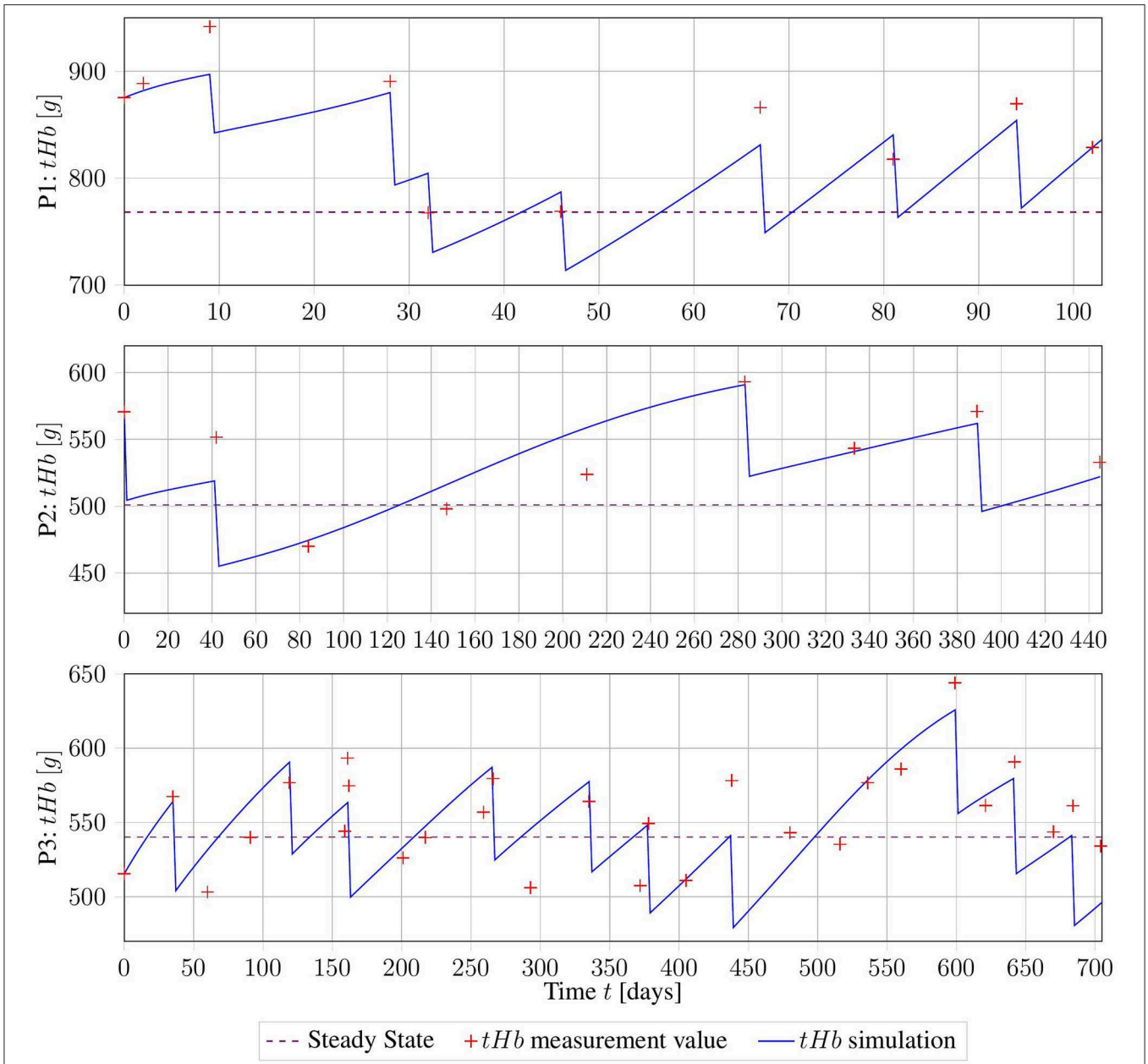

FIGURE 4 | Erythrocyte trajectories as a result of parameter estimation on three clinical data sets. The computed measurement values are given in red, and the healthy base value B is displayed in purple.

In 22 of the available 140 test cases, no H-Schedules could be generated, owing to the constraints. The remaining 118 H-Schedules were thus compared to the schedules from other methods.

3.2.1. Proof of Concept Simulation

The three data sets of patients suffering from PV presented in section 2.3.1 were used to assess the applicability of the model to real-world data. The method described in section 2.4.1 was used to obtain the patient-specific parameter vector $p = (\beta, \gamma, \lambda_{\mathrm{PV}})$. The results are displayed in **Figure 4** and summarized in **Table 3**.

Taking into account all the problems with the collected data, the fits of the trajectories appear satisfying from visual inspection. Objectively, the R^2 value of the three fits was 0.7. However, for subjects 02 and 03, the parameters β and γ were both equal to the lower bound set, owing to numerical restrictions. This might be a sign of errors in the assumption of B, or in the calculation of tHb values from Hct. More precise information about those factors will drastically improve the numerical performance of the method.

The good fit achieved by this method suggests that our proposed model captures the essential dynamics of this

TABLE 3 | Results of proof-of-concept simulation of clinical data from three patients.

Patient ID	β	γ	λ_{PV}	B	B^{PV}	R^2
01	0.6	0.3	0.89	768.25	1314.20	0.89
02	0.2	0.1	0.62	501.04	607.02	0.76
03	0.2	0.1	0.61	540.17	650.21	0.45

TABLE 4 | Results of integer approach run time demonstration.

Days per week	n_H	n_{HC}	n_{IP}	$\Delta_{Tf}[d]$	CPU time MIOCP (s)
1	4	5	5	0	954.8
2	4	5	5	0	17960.4
3	4	5	5	0	72239.5
4	4	5	5	0	195409.4

process. However, this must be verified using higher-quality clinical data.

3.2.2. Evaluation of Integer Approach

In this section, we compare the HC-Schedules and the IP-Schedules of the MIOCP approach in Algorithm 2. For demonstration purposes, the IP-Schedule was compared to the corresponding H-Schedule and HC-Schedule in one modified test case. For this test case, subject 20 with $\lambda_{PV} = \lambda_2$ was used with a time horizon of $T = 103$ days. Per allowed day, one time point for treatment was possible. Four sets of test restrictions on weekdays were tested: treatments were exclusively allowed on Monday (Mo), Monday and Wednesday (Mo, Wed), Monday, Wednesday, and Friday (Mo, Wed, Fri), or Monday, Wednesday, Friday, and Sunday (Mo, Wed, Fri, Sun)—beginning the simulation with the first day being a Monday. An integrator step size of $\frac{1}{6}$ days was used. The results are displayed in **Table 4**.

Here, $\Delta_{Tf}[d] = Tf_{HC} - Tf_{IP}$, where both Tf_{HC} and Tf_{IP} are computed as the respective time points in which the first treatment after the observed time horizon occurs. In the documentation, we set $\Delta_{Tf} := 0$ when $|\Delta_{Tf}| < \frac{1}{6}$. The interpretation is that a time deviation below this step size is irrelevant, and small numerical differences should not be incorporated.

In this test case, the results of the IP-Schedules and HC-Schedules were without notable differences. However, whereas the generation of HC-Schedules had a constant run time of only a few seconds, the run time of IP-Schedules dramatically increased (up to 2.3 days for the largest test case). This demonstrates that the MIOCP approach is only suitable for very small test cases. Therefore, applications for this approach to the general test case in subsection 2.3.2 are unfeasible.

To compare the heuristic approach with the MIOCP approach further, both algorithms were applied to a modified version of the test case. It was modified with a smaller end time $T = 103$ permitting treatments only on 1 day per week (Mo) and only at one time point per day.

In three cases, the MIOCP approach did not produce a feasible solution. In all other cases, the number of treatments n_{IP} and n_{HC} were equal. In those cases, differences only occurred with different Δ_{Tf}. In two of the latter cases, the MIOCP schedules were worse by $\overline{|\Delta_{Tf}|} = 3.62 \pm 0.911$ days. In five other treatment schedules, the heuristic solution produced better results by $\overline{|\Delta_{Tf}|} = 0.402 \pm 0.1$. Another six subjects were excluded, as no treatment was necessary owing to the shortened time horizon. In the other 124 cases, no significant differences between the two approaches were found.

Exemplary results from three patient configurations are displayed in **Figure 5**. Patient 01 with $\lambda_{PV} = 0.51$ is an example of the general case, in which both generated treatment schedules were identical. By contrast, for patient 02 with $\lambda_{PV} = 0.56$, the IP-Schedule was worse, owing to a treatment at approximately $t = 84$ days. As solutions generated using BONMIN can be especially sensitive to the algorithmic options, this results could likely be improved by testing more configurations. There are also examples where the IP-Schedule was slightly better, such as the case of patient 26 with $\lambda_{PV} = 0.71$.

The MIOCP optimization approach using BONMIN only rarely yielded an improvement over the heuristic approach. The original problem size (see subsection 2.3.2) had to be reduced by a factor of 17 in terms of the number of integer variables, to produce results in a reasonable amount of time. Nonetheless, the run-times were long (920.22 ± 845.71 s). Therefore, the use of standard integer optimization solvers seems inappropriate for this problem. This motivated the investigation of other heuristic approaches, such as rounding schemes, for generating treatment plans.

3.2.3. Sum-Up Rounding

In this section, the HC-Schedules and the SUR-Schedules are compared. One relevant property is the difference in the number of treatments $n_{diff} = n_{HC} - n_{SUR}$ of the schedules. The sum-up method does not directly take into account the critical threshold $X_{3,up}$. Therefore, we evaluated the number of days in which the threshold was violated (d_{viol}).

In all 140 test cases, SUR-Schedules were successfully computed. In 118 cases where the heuristic also found a feasible solution, the sum-up approach on average had a lower objective function value than the respective HC-Schedules, by an average of $\bar{n}_{diff} = 1.15 \pm 3.92$ treatments. However, using these 118 treatment SUR-Schedules, the patients *tHb* was above the critical level for $\bar{d}_{viol} = 58.93 \pm 70.81$ days of that year. This was also the case for the 22 SUR-Schedules, with which the heuristic method did not find a valid solution ($\bar{d}_{viol} = 74.53 \pm 38.4$). There was no case in which the SUR-Schedule was better (by having fewer treatments or being the only approach that worked), with zero days of violation.

We investigated the reduction in treatment n_{diff} by the sum-up method and plotted it over the respective days of violation d_{viol} (see **Figure 6**). The data show that violations by the method increased with further reduction in the number of treatments. This was emphasized by a linear regression with a positive slope ($d_{viol,reg}(n_{diff}) = 17.61 \cdot n_{diff} + 30.04[days]$ with $R^2 = 0.42$). The

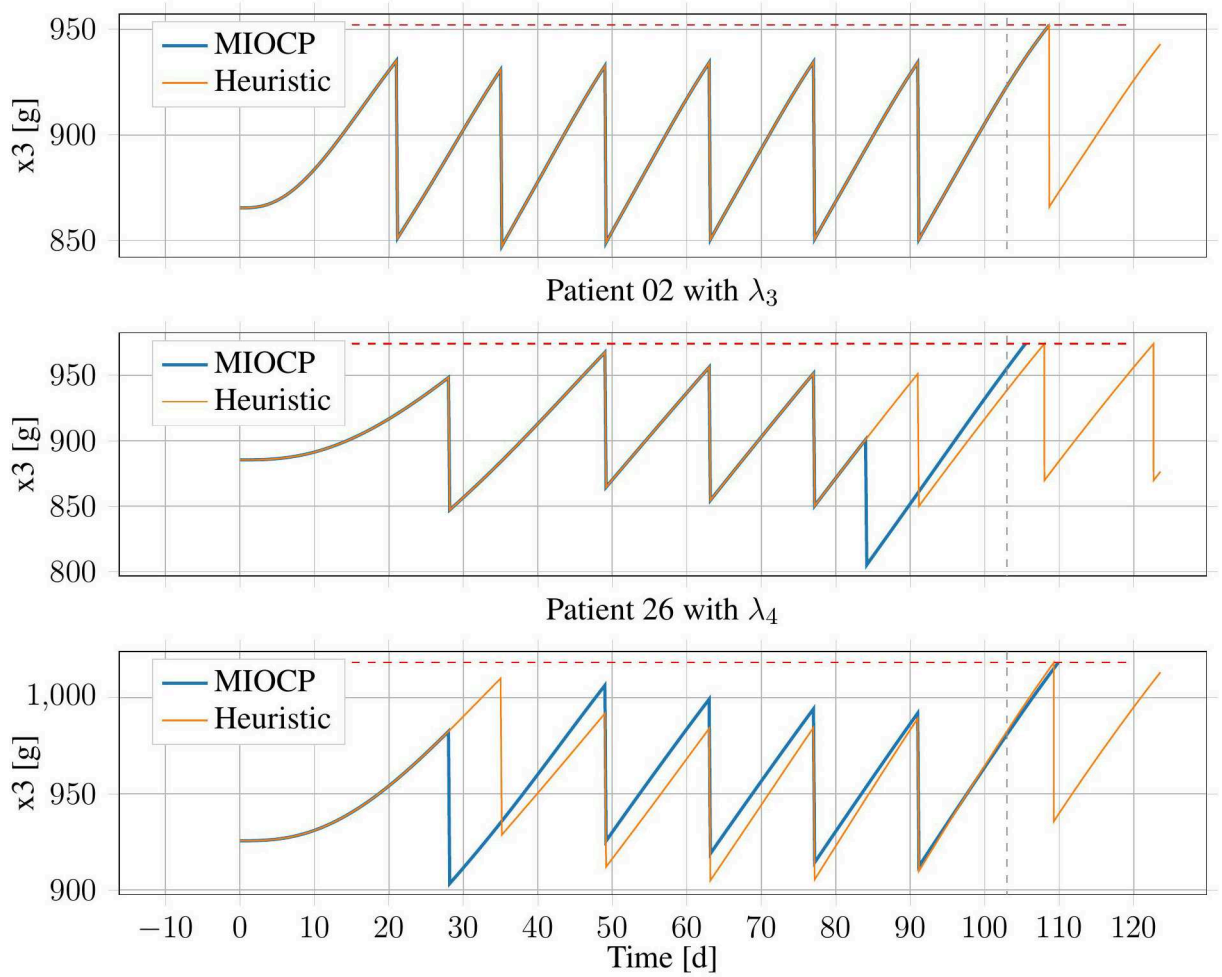

FIGURE 5 | Erythrocyte trajectories of three exemplary patients using IP-Schedules and HC-Schedules. The upper threshold (red, dashed) and the end of the time horizon at $T = 103$ days (gray, dashed) are marked.

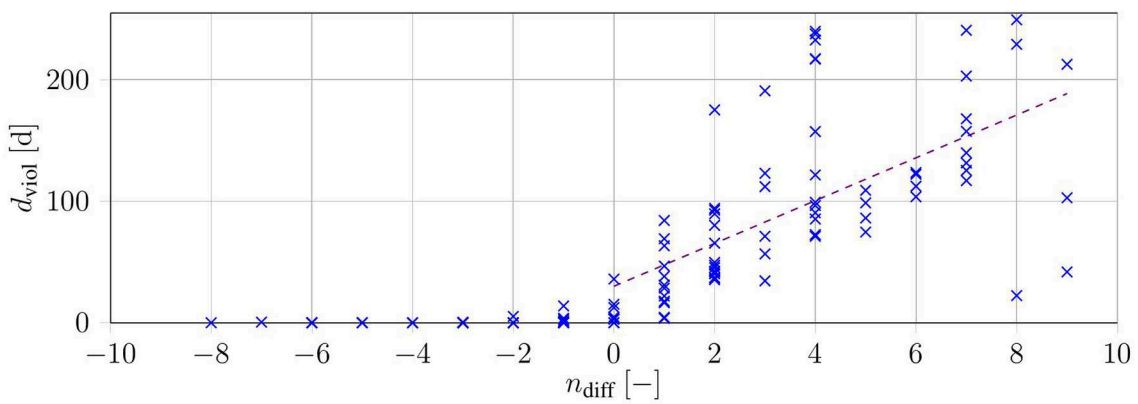

FIGURE 6 | Duration of constraint violation d_{viol} over the difference in the number of treatments for each of the 140 test cases (blue). The purple dashed line shows a linear regression over all instances with $n_{\text{diff}} \geq 0$.

TABLE 5 | Results of BB-Schedule in comparison to HC-Schedule.

Method	# Successful	$\bar{n}_*$	Average CPU time (s)
HC	118	15.78 ± 7.34	7.3 ± 13.3
BB small	111	15.47 ± 7.21	26.9 ± 3.54
BB large	112	15.54 ± 7.21	7.3 ± 13.3

regression only considered the instances with a lower objective function value in the SUR-Schedules.

In summary, the SUR-Schedules either had fewer treatments than the respective HC-Schedules, with considerable endangerment to the patient, or were similar or worse than schedules with only slight endangerment in most cases. To overcome these constraint violations, we can decrease the critical threshold $X_{3,\,\mathrm{up}}$, although this would lead to more treatments. Based on our investigation, the sum-up method performed considerably worse, because it did not directly take the upper bound into account.

3.2.4. Rounding via Branch and Bound

The BB-Schedule was considered as a rounding approach. In contrast to the SUR-Schedule, the BB-Schedule respects constraints. As a complete B&B tree grows exponentially in the number of variables, the computations were run with a maximal number of iterations. In **Table 5** we present the default results of pycombina (5 million iterations) and results from decreasing that number to half a million iterations, which increased the speed of the computations by a factor of nearly 10, omitting the time for the solution of the C-Schedule (on average 26.48 s).

In comparison to the HC-Schedule, the results of the approach are similar: 22 cases were not feasible with either approach. Additionally, the BB-Schedule failed to find a feasible solution with six patients in the version with a large iteration number (and with seven patients in the faster version). In both cases, there were 13 cases where the heuristic saved one phlebotomy, and two cases where even two phlebotomies were saved in comparison to the BB-schedule.

The results for the BB-Schedule can be improved by increasing the permitted number of iterations even further, although this would increase the average computation time.

3.2.5. Dynamic Programming

The DP approach generates treatment schedules by exploring all possible schedules on a chosen grid. Those DP-Schedules were compared to the corresponding HC-Schedules. Relevant properties were the difference in the number of treatments $n_{\mathrm{diff},0} = n_{\mathrm{HC}} - n_{\mathrm{DP},0}$ and $n_{\mathrm{diff},0.4} = n_{\mathrm{HC}} - n_{\mathrm{DP},0.4}$, and the number of failed attempts for both rounding offsets. Moreover, the computation time and the used RAM were documented. The latter was the limiting factor of the approach.

Of all 140 patient data sets, the system memory was exceeded in four configurations of subject 08 ($\lambda_1, \lambda_2, \lambda_4$, and λ_5) for both offsets. Therefore, only the results for the other 136 data sets were available. The system memory per configuration in most cases was close to the maximum available memory ($\sim$50 GB). The results are presented in **Figure 7**.

Using the conservative rounding rule with offset $o = 0.4$, in an additional 12 cases, no DP-Schedule could be produced. The remaining 124 schedules on average were worse than the heuristic schedules by $\bar{n}_{\mathrm{diff},0.4} = -3.06 \pm 1.71$ treatments, with an average violation of $\bar{d}_{\mathrm{viol}} = 0.2 \pm 0.89$ days. There was no case in which a DP-Schedule needed fewer treatments than its respective HC-Schedule.

For the commercial rounding rule with $o = 0.0$, in five data sets, no feasible solution was produced by the DP method. However, this approach was successful in four cases, in which no HC-Schedule could be generated. For the 126 cases in which both approaches succeeded, an average improvement of the DP-Schedules by $\bar{n}_{\mathrm{diff},0.0} = 0.076 \pm 1.69$ treatments was achieved with an average cost of $\bar{d}_{\mathrm{viol}} = 9.09 \pm 8.52$ days of violation. For the four cases in which the heuristic rule did not produce a schedule, the DP method had an average violation of $\bar{d}_{\mathrm{viol}} = 5.08 \pm 1.17$ days.

There was no case in which an improvement from the DP method had zero days of violation. However, in some cases, DP-Schedules with only minor violations and a significant reduction in the number of treatments were generated. For example, for subject 02 with λ_1, there was a violation of $d_{\mathrm{viol}} = 32.33$ days with very small offset from the upper bound, which then reached its B_{PV}, slightly below that threshold. As that threshold would probably be selected with some safety region, this subject might not need any treatment at all. Following the HC-Schedule, three treatments were applied, because the upper bound must be strictly respected. A similar case was inspected for subject 04 with λ_2, where the number of treatments was reduced by one when $d_{\mathrm{viol}} = 5.5$ days of violation were tolerated. There were also some cases in which the DP-Schedules were clearly sub-optimal (see subject 25 with λ_1).

Using DP with $o = 0.4$ often produced solutions, which were feasible, but on average significantly worse than the heuristic schedules. Using commercial rounding with $o = 0.0$ provided the opportunity of finding better schedules, which only slightly endangered the patient but increased the quality of life of the patient. Therefore, this approach seems suitable for producing alternative treatment schedules, which, in clinical practice, can be compared to one another.

4. DISCUSSION

4.1. Model

To our knowledge, this is the first time that erythropoiesis in PV patients has been described in a framework that can simulate the dynamics of the disease. This is a first step toward clinical decision support, with which medical doctors can use simulation results to predict follow-up treatments. Such a framework has the potential to improve the treatment of PV patients significantly, while decreasing the work-load of clinical personnel by reducing the number of necessary appointments.

There are some drawbacks to the proposed model, however, and these will be addressed in future work. First, the different stages of erythropoiesis are simplified and summarized in few

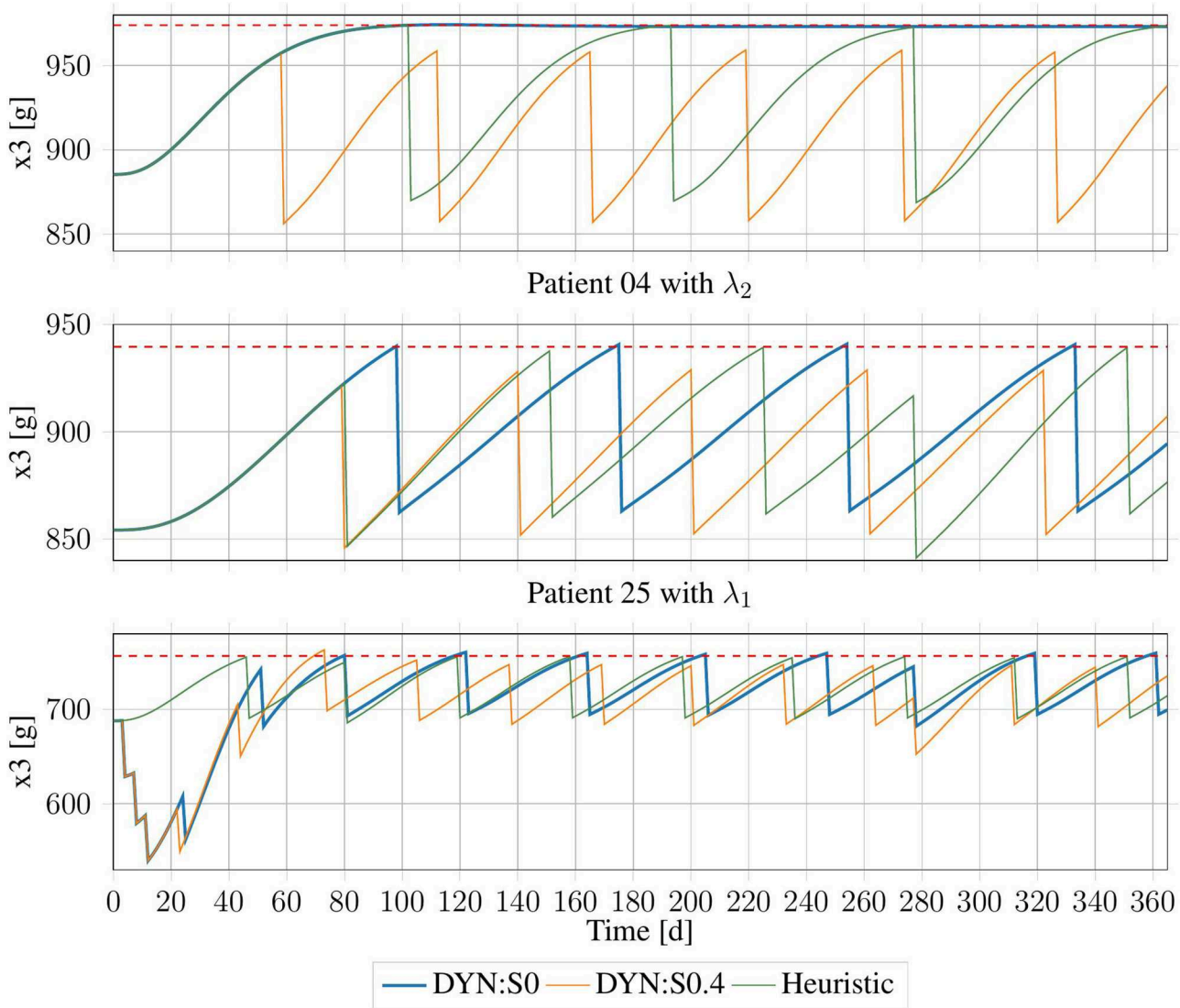

FIGURE 7 | Erythrocyte trajectories using DP-Schedules for both rounding approaches and HC-Schedules for three exemplary patients. $X_{3,up}$ is shown as the red dashed line.

compartments. One can argue that too much information is lost through the agglomeration of complex underlying phenomena.

Second, further investigation in this area is limited by the data available. As PV is a rather rare disease, data sets are difficult to come by. In addition, clinical measurements are performed using *Hct*, rather than with more precise values, such as *tHb*. The inclusion of *tHb* measurements in the clinical routine would drastically improve the results provided by a modeling framework, as discussed in Tetschke et al. (2018). Overall, the use of more patient data with higher density and more precise measurement techniques is necessary for the success of model-based decision support.

Finally, PV is not yet fully understood. This makes the modeling process difficult, as more black-box components must be introduced. However, the modeling framework can support medical research in this field. For example, investigations are warranted regarding the shortened life span of RBCs which often occurs in PV patients, and regarding the connection between the fraction of affected cells λ_{PV} and the JAK2V617F allele burden. Additional medical parameters might be introduced into this model framework for this purpose, which can, in combination with more clinical data, lead to new insights into the disease.

4.2. Optimization

In the second part of this paper, we evaluated different methods of generating treatment schedules for PV patients based on the proposed model. An overview over the results is given in **Table 6**.

TABLE 6 | Summary of relevant properties of the investigated methods for generating treatment schedules.

Schedule	H	HC	C	IP	SUR	BB	DP (0.0/0.4)
Integer solution	✓	✓	x	✓	✓	✓	✓
No constraint violation	✓	✓	✓	✓	x	✓	x
Respecting restrictions of clinic	x	✓	✓	✓	✓	✓	✓
Extension for weighted dates	x	x	✓	✓	✓	(✓)	(✓)
Run time practicable	✓	✓	✓	x	✓	(✓)	(✓)
Memory practicable	✓	✓	✓	✓	✓	✓	x
# Computed schedules (of 140)	140	118	140	0	140	112	136/136
# Feasible instances (of 140)	140	118	140	0	33	112	8/94

Fields with a ✓ show that the respective method fulfills this property. In cases of a ✓ in brackets, the method has this feature formally but with practical drawbacks. Unfulfilled properties are marked with an "x".

The heuristic method of generating schedules follows the intuitive treatment design practiced by medical doctors. The resulting H-Schedules and HC-Schedules can be derived quickly and the schedules are integer solutions by design. Unfortunately, the heuristic is less flexible with regard to the inclusion of new features. As this method was sub-optimal in a formal sense, the quality of this approach was evaluated in comparison to formally derived optimization methods.

The investigated methods led to treatment schedules that in most cases had an equal or higher number of treatments in the observed time horizon, or included violations of safety constraints. Both the I-Schedules and the BB-Schedules were often similar to the respective HC-Schedules. The BB-Schedules were in a few cases even slightly better than the HC-Schedules. However, those approaches are difficult to realize, owing to high run times. The generation of I-Schedules is only possible for very limited time horizons and reduced treatment options. BB-Schedules can be generated relatively quickly, but need a higher run time for an increased rate of successful computation.

It is crucial to respect safety constraints to prevent endangering patients. Therefore, the SUR-Schedules and the DP-Schedules, which do not respect these safety constraints, must be used carefully. The SUR-Schedules were in most cases worse than the corresponding HC-Schedules, and often had significant violations of the constraints. Any strategy that uses this approach will require tighter safety constraints. Consequently, this might lead to feasible treatment schedules, but they would be significantly worse than the HC-Schedules. Therefore, the sum-up approach is not recommended for generating treatment schedules. By contrast, DP-Schedules in many cases demonstrated comparable quality, without any or with only minor constraint violations. There were even cases in which the acceptance of a minor violation led to considerably improved treatment plans. The major drawback here is that the order of magnitude of the violations depends on the selected discretization. This considerably influences memory consumption. Although DP-Schedules can be used in conjunction with the corresponding HC-Schedules, the high demand for system memory renders the approach difficult to realize.

Based on our investigation using a test configuration, the heuristic method with its HC-Schedules seemed to be the method of choice for generating treatment schedules. However, the heuristic method is difficult to extend when the properties of the treatments change. For example, as a quality-of-life feature for the patient, day-based weights might be introduced, assigning more weight to inconvenient days that are preferably avoided. This would give the patient the opportunity to realize treatment on more convenient days—offering more flexibility than a strictly optimal treatment schedule. The patient can thus avoid appointments that conflict with personal commitments. Such day-based weights can be incorporated into all of the other investigated methods. This would make BB-Schedules, DP-Schedules, and (in smaller instances) IP-Schedules desirable suggestions for patient treatment. In all cases, treatment schedules can be used to support decision-making by medical doctors when planning therapy.

Continuous treatment schedules were briefly discussed, but only as a foundation for other approaches, such as the sum-up method and the B&B method. Currently, continuous phlebotomy is technologically impractical in clinics, which makes C-Schedules inapplicable. With increasing technological progress, however, such a method might be derived in the future. Based on the results of this paper, this would lead to superior treatment compared to discrete approaches.

4.3. Conclusion

In this paper, a novel compartment model for PV patients was derived from the data-driven model in Tetschke et al. (2018). Theoretical model analysis and proof-of-concept simulations on clinical data emphasize that this model delivers a plausible description of changes in erythropoiesis from PV.

This gives the opportunity to simulate the disease patient individually and to provide phlebotomy schedules based on this information. Due to the model structure this can be achieved using tools of mathematical optimization. Thus, in the future many different further aspects of the clinical practice can be included in the treatment design. For example, also a treatment with chemotherapy could be included into the model to also capture more severe cases of the disease. This is a first step toward clinical decision support in the case of the disease PV.

DATA AVAILABILITY STATEMENT

All datasets generated for this study are included in the article/**Supplementary Material**.

ETHICS STATEMENT

The studies involving human participants were reviewed and approved by Ethics Committee of the Otto von-Guericke University at the Medical Faculty and at the University Hospital Magdeburg. The patients/participants provided their written informed consent to participate in this study.

AUTHOR CONTRIBUTIONS

PL and MT developed the model, performed the analysis and experiments, and wrote the paper. TF and ES contributed to the design of the research, provided clinical data for the experiments, and analyzed the data. SS contributed to the design of the research and to the discussion of the mathematical model.

FUNDING

This project has received funding from the European Research Council (ERC, grant agreement No 647573), from the European Regional Development Fund (grants SynMODEST and SynIsItFlutter) under the European Union's Horizon 2020 Research and Innovation Program, from the Deutsche Forschungsgemeinschaft (DFG, German Research Foundation) (No. 314838170), GRK 2297 MathCoRe and was supported by a research grant from the International Max Planck Research School (IMPRS) for Advanced Methods in Process and System Engineering in Magdeburg, which we gratefully acknowledge.

ACKNOWLEDGMENTS

We would like to thank Mirko Hahn and Clemens Zeile from the Mathopt Group of the Faculty of Mathematics at Otto-von-Guericke University Magdeburg for their support with the implementation of the branch and bound method in pycombina. We also express our gratitude to Phillip Klein from the Institute of Mathematical Stochastics of the Faculty of Mathematics at Otto-von-Guericke University Magdeburg for his assistance with the realization of the moving sum approach with clinical data. We would like to thank Editage (www.editage.com) for English language editing.

SUPPLEMENTARY MATERIAL

The Supplementary Material for this article can be found online at: https://www.frontiersin.org/articles/10.3389/fphys.2020.00328/full#supplementary-material

REFERENCES

Alvarez-Larrán, A., Bellosillo, B., Martínez-Avilés, L., Saumell, S., Salar, A., Abella, E., et al. (2009). Postpolycythaemic myelofibrosis: frequency and risk factors for this complication in 116 patients. *Br. J. Haematol.* 146, 504–509. doi: 10.1111/j.1365-2141.2009.07804.x

Andersson, J. A., Gillis, J., Horn, G., Rawlings, J. B., and Diehl, M. (2019). Casadi: a software framework for nonlinear optimization and optimal control. *Math. Program. Comput.* 11, 1–36. doi: 10.1007/s12532-018-0139-4

Barbui, T., Barosi, G., Birgegard, G., Cervantes, F., Finazzi, G., Griesshammer, M., et al. (2011). Philadelphia-negative classical myeloproliferative neoplasms: critical concepts and management recommendations from european leukemianet. *J. Clin. Oncol.* 29, 761–770. doi: 10.1200/JCO.2010.31.8436

Barbui, T., Tefferi, A., Vannucchi, A., Passamonti, F., Silver, R., Hoffman, R., et al. (2018). Philadelphia chromosome-negative classical myeloproliferative neoplasms: revised management recommendations from european leukemianet. *Leukemia* 32, 1057–1069. doi: 10.1038/s41375-018-0077-1

Bellman, R. (1957). *Dynamic Programming. 6th Edn*. Princeton, NJ: University Press.

Berlin, N. I., Lawrence, J. H., and Lee, H. C. (1951). The life span of the red blood cell in chronic leukemia and polycythemia. *Science* 114, 385–387. doi: 10.1126/science.114.2963.385

Bertsekas, D. (2012). *Dynamic Programming and Optimal Control, Volume 2, 4th Edn*. Belmont, MA: Athena Scientific.

Bonami, P., Biegler, L. T., Conn, A. R., Cornuéjols, G., Grossmann, I. E., Laird, C. D., et al. (2008). An algorithmic framework for convex mixed integer nonlinear programs. *Discrete Optimiz.* 5, 186–204. doi: 10.1016/j.disopt.2006.10.011

Buerger, A., Zeile, C., Altmann-Dieses, A., Sager, S., and Diehl, M. (2019). Design, implementation and simulation of an mpc algorithm for switched nonlinear systems under combinatorial constraints. *Process Control* 81, 15–30. doi: 10.1016/j.jprocont.2019.05.016

Cho, H., Kirch, C., and Meier, A. (2018). *Mosum: A Package for Moving Sums in Change Point Analysis*. Working paper. Bristol: University of Bristol.

Dentali, F., Ageno, W., Rumi, E., Casetti, I., Poli, D., Scoditti, U., et al. (2014). Cerebral venous thrombosis and myeloproliferative neoplasms: results from two large databases. *Thromb. Res.* 134, 41–43. doi: 10.1016/j.thromres.2014.03.040

Eaves, C. J., and Eaves, A. C. (1978). Erythropoietin (ep) dose-response curves for three classes of erythroid progenitors in normal human marrow and in patients with polycythemia vera. *Blood* 52, 1196–1210. doi: 10.1182/blood.V52.6.1196.1196

Ertl, A. C., Diedrich, A., and Raj, S. R. (2007). Techniques used for the determination of blood volume. *Am. J. Med. Sci.* 334, 32–36. doi: 10.1097/MAJ.0b013e318063c6d1

Falanga, A., and Marchetti, M. (2014). Thrombosis in myeloproliferative neoplasms. *Semin. Thromb. Hemost.* 40, 348–358. doi: 10.1055/s-0034-1370794

Finazzi, G., and Barbui, T. (2007). How i treat patients with polycythemia vera. *Blood* 109, 5104–5111. doi: 10.1182/blood-2006-12-038968

Fourer, R., Gay, D., and Kernighan, B. (2002). *AMPL: A Modeling Language for Mathematical Programming*. Evaston, IL: Duxbury Press; Northwestern University.

Huff, R., Hennessy, T. G., Austin, R., Garcia, J., Roberts, B., and Lawrence, J. (1950). Plasma and red cell iron turnover in normal subjects and in patients having various hematopoietic disorders. *J. Clin. Invest.* 29, 1041–1052. doi: 10.1172/JCI102335

Jandl, J. H. (1987). *Blood. 1st Edn*. Boston: Little Brown.

Kannan, R., and Monma, C. L. (1978). "On the computational complexity of integer programming problems," in *Optimization and Operations Research*, eds R. Henn, B. Korte, and W. Oettli (Berlin; Heidelberg: Springer Berlin Heidelberg), 161–172.

Kiladjian, J.-J., Cervantes, F., Leebeek, F. W. G., Marzac, C., Cassinat, B., Chevret, S., et al. (2008). The impact of JAK2 and MPL mutations on diagnosis and prognosis of splanchnic vein thrombosis: a report on 241 cases. *Blood* 111, 4922–4929. doi: 10.1182/blood-2007-11-125328

Koschmieder, S., Mughal, T., Hasselbalch, H., Barosi, G., Valent, P., Kiladjian, J.-J., et al. (2016). Myeloproliferative neoplasms and inflammation: whether to target the malignant clone or the inflammatory process or both. *Leukemia* 30, 1018–1024. doi: 10.1038/leu.2016.12

Lichtman, M. A., Beutler, E., Kipps, T. J., Seligsohn, U., Kaushansky, K., and Prchal, J. T. (2006). *Williams Hematology*. New York, NY: McGraw-Hill.

London, I. M., Shemin, D., West, R., and Rittenberg, D. (1949). Heme synthesis and red blood cell dynamics in normal humans and in subjects with polycythemia vera, sickle-cell anemia, and pernicious anemia. *J. Biol. Chem.* 179, 463–484.

Marchioli, R. (2005). Vascular and neoplastic risk in a large cohort of patients with polycythemia vera. *J. Clin. Oncol.* 23, 2224–2232. doi: 10.1200/JCO.2005.07.062

Marchioli, R., Finazzi, G., Specchia, G., Cacciola, R., Cavazzina, R., Cilloni, D., et al. (2013). Cardiovascular events and intensity of treatment in polycythemia vera. *N. Engl. J. Med.* 368, 22–33. doi: 10.1056/NEJMoa1208500

Mesa, R. A., Li, C.-Y., Ketterling, R. P., Schroeder, G. S., Knudson, R. A., and Tefferi, A. (2005). Leukemic transformation in myelofibrosis with myeloid metaplasia: a single-institution experience with 91 cases. *Blood* 105, 973–977. doi: 10.1182/blood-2004-07-2864

Nadler, S. B., Hidalgo, J. H., and Bloch, T. (1962). Prediction of blood volume in normal human adults. *Surgery* 51, 224–232.

Otto, J. M., Plumb, J. O., Clissold, E., Kumar, S. B., Wakeham, D. J., Schmidt, W., et al. (2017). Hemoglobin concentration, total hemoglobin mass and plasma volume in patients: implications for anemia. *Haematologica* 102, 1477–1485. doi: 10.3324/haematol.2017.169680

Pardanani, A., Lasho, T., Finke, C., Hanson, C., and Tefferi, A. (2007). Prevalence and clinicopathologic correlates of jak2 exon 12 mutations in jak2v617f-negative polycythemia vera. *Leukemia* 21, 1960–1963. doi: 10.1038/sj.leu.2404810

Policitemia, G. I. S. (1995). Polycythemia vera: the natural history of 1213 patients followed for 20 years. *Ann. Intern. Med.* 123, 656–664. doi: 10.7326/0003-4819-123-9-199511010-00003

Pottgiesser, T., Specker, W., Umhau, M., Dickhuth, H.-H., Roecker, K., and Schumacher, Y. O. (2008). Recovery of hemoglobin mass after blood donation. *Transfusion* 48, 1390–1397. doi: 10.1111/j.1537-2995.2008.01719.x

Rozman, C., Feliu, E., Giralt, M., Rubio, D., and Cortés, M.-T. (1991). Life expectancy of patients with chronic nonleukemic myeloproliferative disorders. *Cancer* 67, 2658–2663. doi: 10.1002/1097-0142(19910515)67:10<2658::AID-CNCR2820671042>3.0.CO;2-C

Sager, S. (2005). *Numerical Methods for Mixed-Integer Optimal Control Problems*. Der andere Verlag, Tönning, Lübeck, Marburg.

Sager, S., Jung, M., and Kirches, C. (2011). Combinatorial integral approximation. *Math. Methods Oper. Res.* 73, 363–380. doi: 10.1007/s00186-011-0355-4

Scherber, R., Dueck, A. C., Johansson, P., Barbui, T., Barosi, G., Vannucchi, A. M., et al. (2011). The myeloproliferative neoplasm symptom assessment form (MPN-SAF): international prospective validation and reliability trial in 402 patients. *Blood* 118, 401–408. doi: 10.1182/blood-2011-01-328955

Siegel, F. P., Tauscher, J., and Petrides, P. E. (2013). Aquagenic pruritus in polycythemia vera. *Am. J. Hematol.* 88, 665–669. doi: 10.1002/ajh.23474

Silver, R. T., Vandris, K., Wang, Y. L., Adriano, F., Jones, A. V., Christos, P. J., et al. (2011). Jak2v617f allele burden in polycythemia vera correlates with grade of myelofibrosis, but is not substantially affected by therapy. *Leuk. Res.* 35, 177–182. doi: 10.1016/j.leukres.2010.06.017

Tefferi, A., Vannucchi, A., and Barbui, T. (2018). Polycythemia vera treatment algorithm 2018. *Blood Cancer J.* 8:3. doi: 10.1038/s41408-017-0041-8

Tetschke, M., Lilienthal, P., Pottgiesser, T., Fischer, T., Schalk, E., and Sager, S. (2018). Mathematical modeling of RBC count dynamics after blood loss. *Processes* 6, 157–185. doi: 10.3390/pr6090157

Vainchenker, W., Dusa, A., and Constantinescu, S. N. (2008). Jaks in pathology: role of janus kinases in hematopoietic malignancies and immunodeficiencies. *Semin. Cell Dev. Biol.* 19, 385–393. doi: 10.1016/j.semcdb.2008.07.002

von Neumann, J. (1963). Various techniques used in connection with random digits. *Collect. Works* 5, 768–770.

Wächter, A., and Biegler, L. (2006). On the implementation of an interior-point filter line-search algorithm for large-scale nonlinear programming. *Math. Program.* 106, 25–57. doi: 10.1007/s10107-004-0559-y

Conflict of Interest: The authors declare that the research was conducted in the absence of any commercial or financial relationships that could be construed as a potential conflict of interest.

Copyright © 2020 Lilienthal, Tetschke, Schalk, Fischer and Sager. This is an open-access article distributed under the terms of the Creative Commons Attribution License (CC BY). The use, distribution or reproduction in other forums is permitted, provided the original author(s) and the copyright owner(s) are credited and that the original publication in this journal is cited, in accordance with accepted academic practice. No use, distribution or reproduction is permitted which does not comply with these terms.

frontiers in Bioengineering and Biotechnology

TECHNOLOGY AND CODE
published: 11 June 2020
doi: 10.3389/fbioe.2020.00249

Agent-Based Models Predict Emergent Behavior of Heterogeneous Cell Populations in Dynamic Microenvironments

Jessica S. Yu[1] *and Neda Bagheri*[1,2,3,4,5]*

[1] Chemical and Biological Engineering, Northwestern University, Evanston, IL, United States, [2] Northwestern Institute on Complex Systems, Northwestern University, Evanston, IL, United States, [3] Center for Synthetic Biology, Northwestern University, Evanston, IL, United States, [4] Biology, University of Washington, Seattle, WA, United States, [5] Chemical Engineering, University of Washington, Seattle, WA, United States

OPEN ACCESS

Edited by:
Robert Parker,
University of Pittsburgh, United States

Reviewed by:
Pinyi Lu,
Biotechnology HPC Software Applications Institute (BHSAI), United States
Yaroslav Ispolatov,
Universidad de Santiago de Chile, Chile

***Correspondence:**
Neda Bagheri
nbagheri@uw.edu

Specialty section:
This article was submitted to Bioinformatics and Computational Biology, a section of the journal Frontiers in Bioengineering and Biotechnology

Received: 17 July 2019
Accepted: 10 March 2020
Published: 11 June 2020

Citation:
Yu JS and Bagheri N (2020) Agent-Based Models Predict Emergent Behavior of Heterogeneous Cell Populations in Dynamic Microenvironments. Front. Bioeng. Biotechnol. 8:249. doi: 10.3389/fbioe.2020.00249

Computational models are most impactful when they explain and characterize biological phenomena that are non-intuitive, unexpected, or difficult to study experimentally. Countless equation-based models have been built for these purposes, but we have yet to realize the extent to which rules-based models offer an intuitive framework that encourages computational and experimental collaboration. We develop ARCADE, a multi-scale agent-based model to interrogate emergent behavior of heterogeneous cell agents within dynamic microenvironments and demonstrate how complexity of intracellular metabolism and signaling modules impacts emergent dynamics. We perform *in silico* case studies on context, competition, and heterogeneity to demonstrate the utility of our model for gaining computational and experimental insight. Notably, there exist (i) differences in emergent behavior between colony and tissue contexts, (ii) linear, non-linear, and multimodal consequences of parameter variation on competition in simulated co-cultures, and (iii) variable impact of cell and population heterogeneity on emergent outcomes. Our extensible framework is easily modified to explore numerous biological systems, from tumor microenvironments to microbiomes.

Keywords: agent-based model, cell population dynamics, computational modeling, emergent behavior, microenvironment

1. INTRODUCTION

Computational models are *in silico* tools used to represent a system or phenomenon of interest, with wide ranging applications in both experimental and clinical settings (Winslow et al., 2012; Brodland, 2015). With increasingly high resolution and high throughput experimental techniques, computational models become essential for summarizing, integrating, and exploring high dimensional data sets. While reactive data-driven computational models are ubiquitous—from simple, single equations fitting population level aggregate metrics to more complex differential equation systems—we have yet to realize the full impact of proactive models to provide *de novo* insights in cases where experimental techniques are inadequate or insufficient. Computational modeling has the potential to overcome experimental limitations in three major areas: spatial and temporal resolution, intra- and intercellular heterogeneity, and environmental context.

First, biological systems exhibit spatial and temporal variation as observed in cell fate commitment during development, cell state commitment in pattern formation, and circadian-regulated gene expression (Zernicka-Goetz, 2004; Zhang et al., 2014; Manukyan et al., 2017). Models that are able to capture such behavior with high temporal and spatial resolution allow rigorous systems analysis and hypothesis testing that is often not possible experimentally.

Second, biological systems are highly heterogeneous, both between and within cell types. The immune system, for example, is composed of a number of different cell types, each with its own unique role. Studies have demonstrated remarkable phenotypic variation within tumor cell populations (Dagogo-Jack and Shaw, 2017) and highly diverse species within microbial communities (Eckburg, 2005). Homogeneous experimental systems fail to account for this diversity and its role in shaping behavior. In addition, heterogeneity within a computational model can be measured and tuned precisely whereas the same quantification and control in an experimental setting is much more difficult.

Finally, biological systems exist within diverse environmental contexts. The tumor microenvironment, for instance, has received significant attention as a major contributor to disease prognosis (Balkwill et al., 2012; Quail and Joyce, 2013). Cells cultured in 2D vs. 3D matrices display notable differences in growth and behavior (Baker and Chen, 2012; Stock et al., 2016). Studying cell population dynamics without the environmental context may lead to inaccurate conclusions; computational models provide a method for exploring cell behavior within precisely controlled, dynamic environments.

Agent-based models (ABMs) are particularly well-suited for addressing these areas to explore how complex, heterogeneous interactions at the cellular level result in the emergence of spatial and temporal dynamics at the cell population level (Thorne et al., 2007; Yu and Bagheri, 2016). ABMs are a bottom-up modeling technique in which autonomous agents follow a set of rules that define their actions and interactions with each other and their environment (Bonabeau, 2002). Specifically, ABMs can readily incorporate agent heterogeneity and environmental dynamics with high precision and resolution. Classically used in the social sciences, ABMs have become increasingly popular for studying emergent behavior in biological systems, including bacterial biofilms and infection (Segovia-Juarez et al., 2004; Gorochowski et al., 2012), tumor growth (Enderling et al., 2009; Mehdizadeh et al., 2013; Walpole et al., 2015; Norton et al., 2017), and immune interactions (Folcik et al., 2007; Pienaar et al., 2015).

In this study, we introduce an extensible ABM framework designed to interrogate heterogeneous cell systems within dynamic environments with high spatial and temporal resolution. A key feature of the model is flexibility in defining agents and environments through interfaces and modular intracellular components. We use the presented ABM to investigate emergent dynamics in three relevant case studies: (i) to compare cell population dynamics between colony and tissue contexts, (ii) to explore competition between cell populations, and (iii) to investigate the impact of heterogeneity on clonal evolution and emergent dynamics.

2. RESULTS

ARCADE (Agent-based Representation of Cells And Dynamic Environments) is built in Java, using the MASON library for multi-agent scheduling and simulation (Luke et al., 2005) along with a custom, extensible, interface-based framework for defining agents and environments. At the start of a simulation, selected agents and environments are added. MASON then runs the simulation by stepping through agent rules at each time step (representing 1 min, called ticks). A single simulation of 14 days (20,160 ticks) requires 5–10 min of CPU time on a computer with Intel® Core i7 Processor (8x 3.40 GHz) and 19.5 GB of RAM.

2.1. Interfaces Provide an Extensible Modeling Approach

Java interfaces act as contracts between the underlying model framework and the implementing classes, guaranteeing that a certain set of methods are provided. By abstracting out how an agent interacts with its environment, the model is agnostic to a specific system and can be easily extended and customized.

Broadly, the model comprises three main packages—simulation (`sim`), agents (`agent`), and environments (`env`)—as well as visualization (`vis`) and utility (`util`) packages (**Figure 1A**). The simulation package handles the processing of inputs into simulation series, running the simulations, and saving simulation results to output.

There are three types of agents. First, `Cell` agents represent the physical cells within the system, such as tissue, immune, or bacterial cells (**Figure 1B**). These agents are introduced into the simulation and at each tick, they follow their rules defining how they interact with their surroundings. Second, `Module` agents are subcellular entities that represent a certain function or behavior within a cell, such as metabolism, signaling, and angiogenesis (**Figure 1B**). Finally, `Helper` agents provide a mechanism for (i) outside perturbations to the system, such as the introduction of new cell agents or a wound, and (ii) time delayed behaviors by `Cell` agents, such as division or movement.

The environment is divided into three distinct layers, all of which are integrated through a `Location` object. The `Grid` is an abstract layer on which cell agents are contained and can be defined in a variety of geometries (**Figure 1B**). Each `Lattice` layer tracks nutrients or molecules of interest, such as glucose or oxygen, and can also be defined in a variety of geometries (**Figure 1B**). The geometry of the `Lattice` layers does not necessarily need to match the geometry of the `Grid`, allowing flexibility in how the environment is defined. Finally, `Component` layers provide a mechanism for (i) changes in the `Lattice` layers, such as diffusion or introduction of a drug, and (ii) physical entities within the environment, such as a capillary bed or matrix scaffolding.

2.2. Modeling Pipeline Emphasizes Flexible Inputs and High-Resolution Outputs

The model can be run both in GUI form, for real-time visualization of the simulation, or directly through command line for rapid simulation (**Figure 1C**). Simulations are defined using an XML (`.xml`) file describing one or more simulation

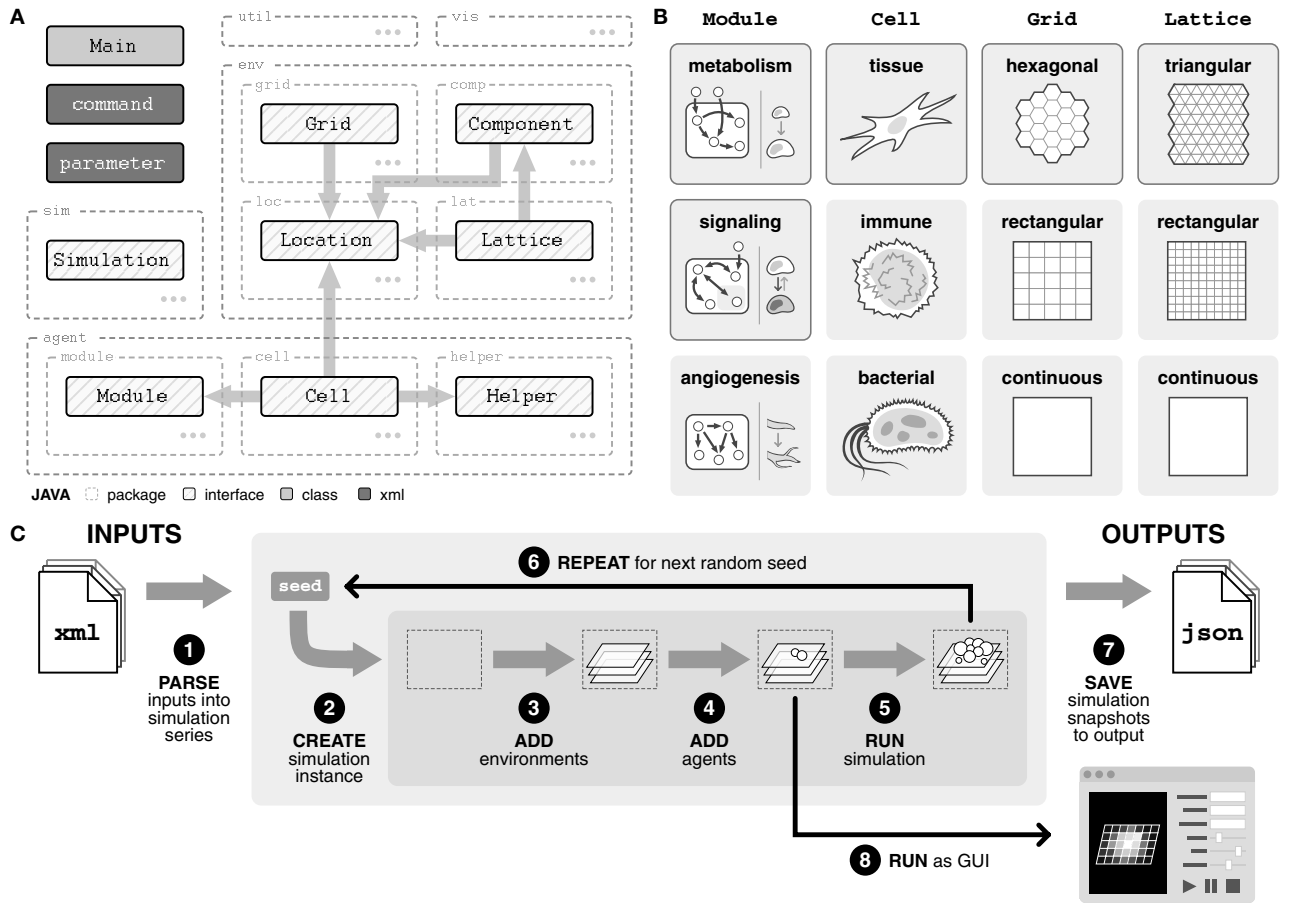

FIGURE 1 | Overview of agent-based model framework. **(A)** Diagram of package structure and interfaces. Agents include `Cell`, `Module`, and `Helper` and environments include `Grid`, `Lattice`, `Component`, and `Location`. By importing an interface, a class is guaranteed a certain set of methods with which it can interact with objects of the imported interface. **(B)** Interfaces can be implemented into concrete classes in a variety of ways, depending on the system of interest. Classes with solid border are implemented in our model. **(C)** Overview of the modeling pipeline. Inputs, defined with an XML (`.xml`) file, are parsed to create a simulation series. Within the simulation series, for each random seed, a simulation instance is created. Environments and agents are added to the simulation instance. The simulation is stepped, and data is output to a JSON (`.json`) file. Alternatively, the simulation can be run in GUI mode.

series (**Supplementary Figure 1A**). Simulations within a series only differ in random seed, analogous to experimental replicates, and multiple series can be defined within a single input file.

Each series is created by parsing the input file for three tags: (i) `simulation`, which specifies model size as well as any profilers for capturing simulation data, (ii) `agents`, which describes the composition and parameters of cell agent populations, and (iii) `environment` which defines environment parameters (**Figure 1C**, **Supplementary Figure 1A**). For each seed, a simulation instance is created. Environments and agents are added into the simulation instance, and then the simulation is run for the defined number of ticks. This process is repeated for all random seeds in the series. Alternatively, if the GUI version is selected, the simulation is run through the GUI interface once environments and agents have been added.

Simulation outputs are saved as JSON (`.json`) files, a common, lightweight file format that uses human-readable text to store data (**Supplementary Figure 1B**). Each output file includes a summary of the input file, full parameter lists for every cell population, and location and cell information for all cells at selected timepoints during the simulation.

2.3. Tissue Cell Implementation Exhibits Representative Growth Dynamics

With the framework and pipeline in place, specific classes for tissue cell agents are implemented within a hexagonal and triangular environment (**Supplementary Figure 2A**). Each tissue cell agent contains a metabolism and signaling module (described in the following section) and can be in one of seven states: apoptotic, necrotic, quiescent, migratory, proliferative, senescent, and undecided (Methods). At each tick, each agent steps through specific decisions based on its current state (**Figure 2A**). Briefly, a cell agent increases in age and evaluates if its age is greater than the defined lifespan. If so, it becomes apoptotic. The metabolism module is simulated to update energy and volume of the cell. If the cell is nutrient starved, it becomes necrotic; if there is

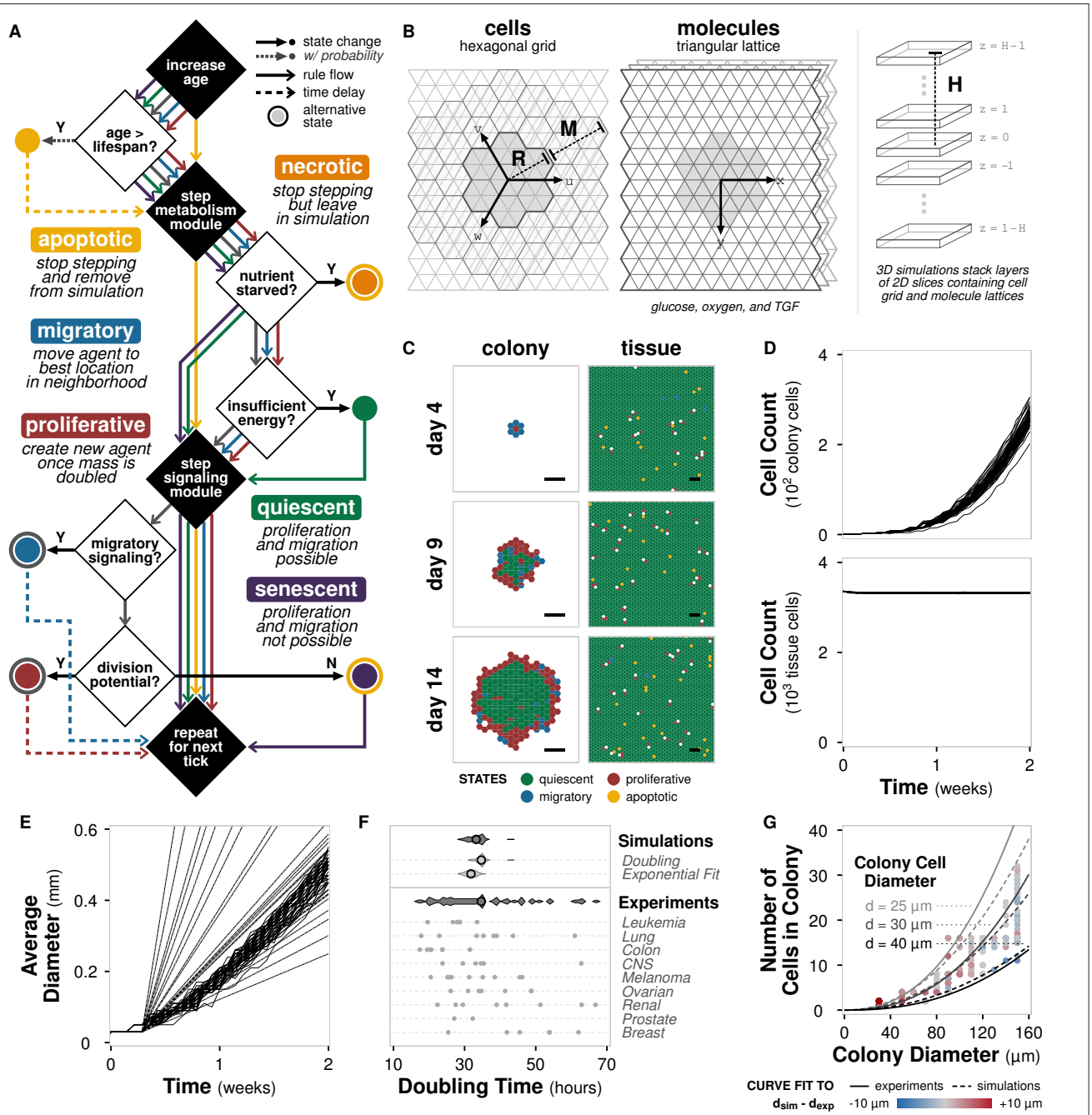

FIGURE 2 | Tissue cell implementation. **(A)** Flowchart outlining tissue cell agent states and the rules governing transitions between them at each tick of the simulation. **(B)** Diagram of the simulation environment structure comprising a hexagonal grid for cells and triangular lattices for molecules. Environment size is defined by radius *R* from the center hexagon and a margin *M* between the cell grid and the molecule lattices. For 3D simulations, layers of 2D simulations are stacked at a height *H* from the center layer. **(C)** Spatial distribution of cell states for colony (left) and tissue (right) growth for a single example replicate (random seed 0) at different timepoints during the simulation. Scale bars represent 100 μm. **(D)** Plot of total cell count for colony (top) and tissue (bottom) growth for each of $n = 50$ replicate simulations of the model with default parameters and settings. Each line shows the trajectory for a single simulation. **(E)** Plot of average colony diameter for each of $n = 50$ replicate simulations of the model with default parameters and settings. Each line shows the trajectory for a single simulation. Dashed and dotted lines indicate experimentally observed diameters (Conger and Ziskin, 1983; Brú et al., 2003), respectively. **(F)** Violin plots of doubling times for the simulation ($n = 50$) calculated using (i) cell count doublings at $t = 7$ days and (ii) exponential curve fit to the first 7 days of growth compared to doubling times of the cancer cell lines in the NCI-60 panel (Alley et al., 1988), both aggregated and separated by pathology. Black circle indicates mean. **(G)** Scatter plot of colony diameter and number of cells in the colony for colonies less than 160 μm in diameter across $n = 50$ replicate simulations. Solid lines show the relationship between colony diameter, number of cells in the colony, and diameter of a colony cell using an equation fit to experimental data (Meyskens et al., 1984). Dotted lines show the same relationship for an equation of the same form fit to the simulation results. Colors indicate the difference between the cell diameter calculated directly from the simulation data and the cell diameter predicted by the experimental fit.

insufficient energy, it becomes quiescent. The signaling module is simulated to decide between migratory and proliferative states for undecided cells. Cells who have reached their division limit become senescent. This process repeats for all cell agents at the current tick, and then for each tick of the simulation. Default cell parameters are derived from literature (**Supplementary Table 1**). In addition, we develop a null model for comparison in which agents simulate their metabolism and signaling modules, but instead randomly select a cell state (**Supplementary Figure 2B**).

The environment comprises a hexagonal grid containing the cell agents and three triangular lattices in which glucose, oxygen, and a signaling molecule TGFα diffuse (**Figure 2B**). Each hexagon is 30 μm in diameter (side-to-side) and contains, on average, 2-3 cells depending on total cell volume. The grid is $R = 34$ hexagons in radius with an $M = 6$ hexagon margin, for a total environment diameter of approximately 2 mm, which is consistent with experimental observations of the limiting radius for non-vascularized tumors (Heymach et al., 2010). Because the hexagonal grid and triangular lattices explicitly account for volume, the 2D simulations are representative of a 3D cross section. Simulations in 3D ($H > 1$) utilize layers of these 2D simulations, with alternating cell grid offsets to prevent vertical cell stacking. Default environmental parameters are derived from literature (**Supplementary Table 2**).

With high temporal and spatial resolution, we monitor a number of features over the course of the simulation. We ran sample growth simulations of colony and tissue growth for 14 days with $n = 50$ replicates (i.e., different random seeds) and timepoints taken every 12 h with default, untuned parameters (**Supplementary Table 3**). The colony growth simulations are initialized with a single cell agent, whereas the tissue growth simulations are initialized with one agent in every location.

For a single simulation, we can capture the spatial distribution of cell states (**Figure 2C**). For colony growth, as observed experimentally, there is a rim of active cells—proliferative and migratory—surrounding the inactive, quiescent core (Freyer and Sutherland, 1986; Brú et al., 2003). The rim spans approximately $2 - 4$ hexagonal locations (equivalent to $60 - 120$ μm), consistent with literature measurements, which span $25 - 100$ μm across a variety of glucose and oxygen concentrations (Freyer and Sutherland, 1986). For tissue growth, there exists tissue homeostasis with the majority of cells in a quiescent state. Neither the distribution of the cell states nor the thickness of the rim are specified in the model. Instead, these biologically relevant behaviors emerge directly from agent and environment interactions. In contrast, the null model, initialized with a single cell agent as well as multiple cell agents, fails to show the observed emergent spatial behavior (**Supplementary Figure 2C**). Instead, the cells begin with an equal distribution of all cell states and quickly fall into irreversible terminal states (necrotic, apoptotic, and senescent) whereas the full rule set maintains active cell states (**Supplementary Figure 2D**).

The total number of cells over time are shown in **Figure 2D**. Fitting an exponential curve to the number of colony cells for the first 7 days gives $r^2 = 0.98 \pm 0.01$ across the replicates, indicating clear early exponential growth. The number of cells in tissue growth quickly reaches a steady state, further indicating tissue homeostasis. The diameter growth rate of the colony cells is 1.45 ± 0.09 $\mu\text{m} \cdot \text{h}^{-1}$, which falls well within the experimentally reported range of 3.78 ± 3.14 $\mu\text{m} \cdot \text{h}^{-1}$ for 15 *in vitro* cell lines (Brú et al., 2003) and 1.89 ± 1.09 $\mu\text{m} \cdot \text{h}^{-1}$ for 8 *in vitro* tumor spheroids (Conger and Ziskin, 1983). The linear increase in diameter and early exponential increase in cell number, both experimentally observed behaviors (Brú et al., 2003; Talkington and Durrett, 2015), emerge without explicitly defining these growth dynamics in the model.

Finally, we consider emergent phenomena at the single cell level. The average doubling time of cells in the simulation, calculated at 7 days, is 34.6 ± 1.5 or 31.8 ± 1.4 h depending on calculation method, is well within literature values of doubling time for human cancer cell lines (**Figure 2E**) (Alley et al., 1988). We also find that relationship between colony diameter, cell number, and cell diameter match the literature reported relationship between these features for tumor populations (**Figure 2F**) (Meyskens et al., 1984). Again, we note that the model was never trained to meet these objectives; doubling time and the cell size relationships emerge *de novo*.

For the following case studies, we consider temporal, spatial, and parametric emergent phenomena quantified using three metrics: growth rate, symmetry, and cell cycle length, respectively (Methods). Note that cell cycle length is not equivalent to doubling time; cycle length is the amount of time a cell takes to complete its cell cycle and is tracked per cell while doubling time is calculated based on change in population cell counts between two timepoints. Model parameters are not specifically tuned or derived to provide these specific emergent outcomes. In addition, these metrics are not a function of initial state conditions, which allows us to compare results between simulations.

2.4. Module Complexity and Model Resolution Impact Emergent Population Dynamics

To determine how the complexity of subcellular modules, and thus model resolution, impacts emergent cell population dynamics, we introduce metabolism and signaling modules with complex, medium, simple, and random mechanistic detail. Here, we consider simulations for every combination of metabolism and signaling module. Note that for case study simulations, the complex metabolism and complex signaling modules are used.

The metabolism module governs changes in cell energy and volume as a function of external nutrient availability and internal cell state (**Figure 3A**; Methods). Complex metabolism explicitly accounts for both glycolysis and oxidative phosphorylation pathways and produces an internal pyruvate intermediate. Glucose uptake is based on cell surface area, which acts as a proxy for the number of glucose receptors. Medium metabolism implicitly accounts for glycolysis and oxidative phosphorylation and glucose uptake is based on cell volume. Both complex and medium metabolism use autophagy to regulate cell size. Simple metabolism assumes constant glucose uptake, energy production, and growth rate. Random metabolism takes up a random fraction of the external nutrients and uses a random fraction of internal

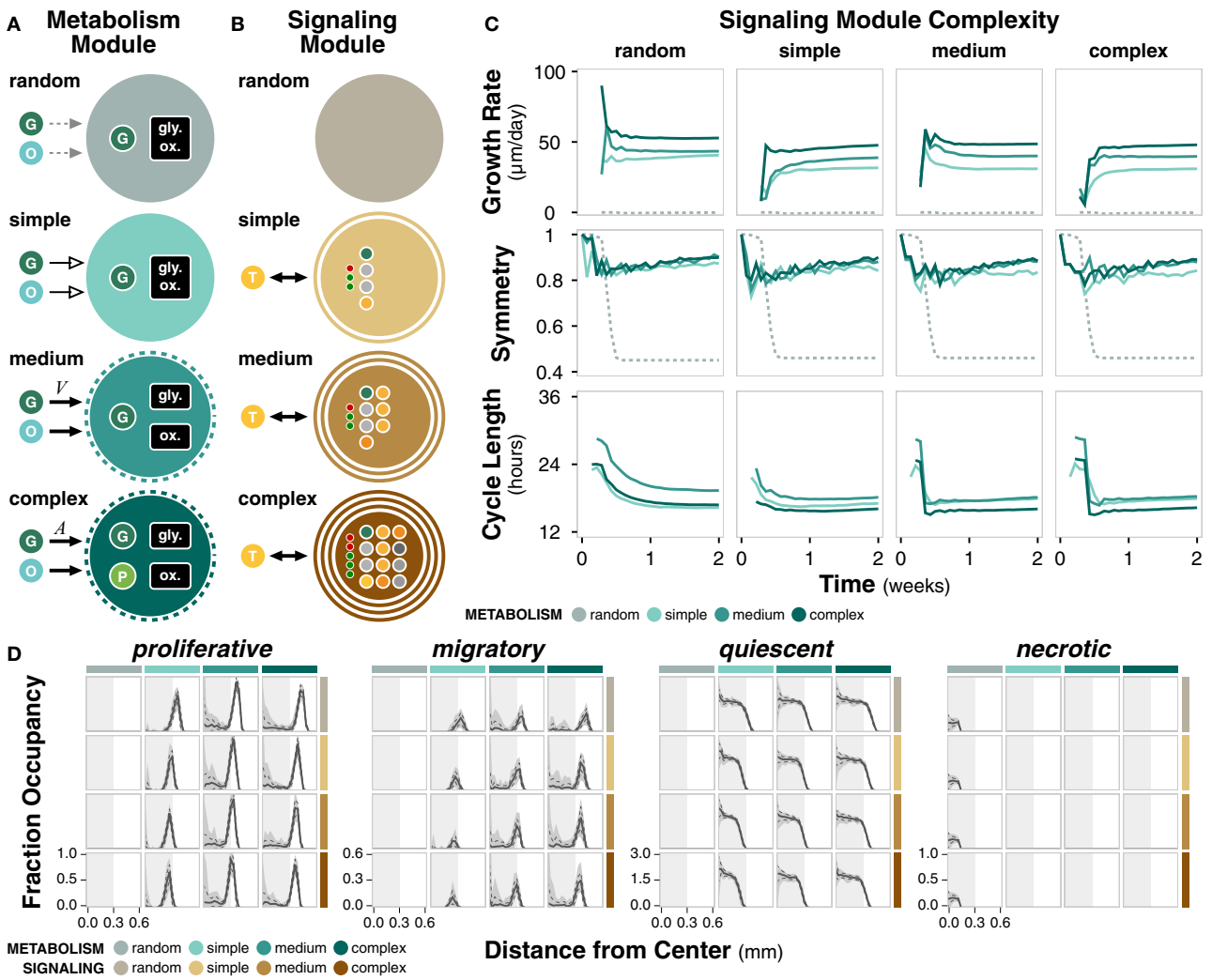

FIGURE 3 | Metabolism and signaling module complexity. **(A)** Diagram summarizing the differences between complexities of the metabolism module. All modules uptake glucose (G) and oxygen (O) from the environment through various mechanisms. Cell size regulation by autophagy is indicated by dotted ring. Only complex metabolism explicitly accounts for a pyruvate (P) intermediate. Nutrient uptake can be variable (solid, black arrow), constant (solid, empty arrow), or random (dotted, gray arrow). **(B)** Diagram summarizing the differences between complexities of the signaling module. The non-random modules interact with extracellular TGFα (T). Number of rings indicate how many cellular compartments (i.e., membrane, cytoplasm, and/or nucleus) are explicitly included in the signaling network. Large dots denote molecular species within the network and small dots denote regulatory interactions. **(C)** Time course of growth rate, symmetry, and cycle length for different complexities of the metabolism and signaling modules, grouped by signaling module complexity. **(D)** Distribution of cell states as a function of distance from the center of the colony at $t = 2$ weeks. Solid line, dotted line, and shaded area denote the mean, standard deviation, and range across $n = 20$ replicates. Light gray rectangle is a visual reference for a distance of 0.3 mm from the center across all cell states.

glucose to produce cell mass. Metabolism module parameters are derived from literature (**Supplementary Table 4**).

The signaling module governs the decision between proliferative and migratory states as a function of the change in concentration of active PLCγ (**Figure 3B**; Methods). Complex signaling is a simplification of an established EGFR signaling network (Zhang et al., 2007) consisting of 12 species and five regulatory edges, spanning the nucleus, cytoplasm, and cell membrane. Medium signaling does not explicitly include the nuclear compartment, resulting in a network with seven species and three regulatory edges. Simple signaling further removes the cell membrane compartment for a network with four species and three regulatory edges. Random signaling is uncoupled to external TGFα and selects between the two states with a certain probability. Signaling module parameters are derived from literature (**Supplementary Table 5**).

We first consider the effect of these modules on the external concentrations of glucose, oxygen, and TGFα, independent of cell state and cell decision processes. Cell agents, fixed in a quiescent state with no rules, are introduced into the environment. When these agents contain only the metabolism module, both glucose and oxygen consumption decrease with

increasing metabolism complexity (**Supplementary Figure 3A**, left). With random metabolism, glucose and oxygen consumption are similar to complex metabolism given the parameterization, suggesting that a correctly parameterized simplification may be sufficient if only external nutrient concentrations are of interest. There are no time dependent effects; glucose and oxygen consumption quickly reach a steady state.

However, when these fixed state agents contain only the signaling module, TGFα shows time dependent effects (**Supplementary Figure 3A**, right). Complex signaling exhibits an early spike in TGFα before returning to equilibrium whereas medium and simple signaling both exhibit a dip in TGFα and establish new equilibriums. The major difference between complex and simple/medium signaling modules is the number of regulatory edges, emphasizing the importance of regulation in biological systems. As expected, (i) TGFα is unaffected when agents contain only the metabolism module and (ii) glucose and oxygen are unaffected when agents contain only the signaling module.

For agents fixed in a quiescent state with pairwise combinations of modules, there are no significant differences compared to simulating the modules in isolation (**Supplementary Figure 3B**, left). When the full rule set is added to cell agents, glucose and oxygen consumption become more dependent on module complexities (**Supplementary Figure 3B**, right).

We ran simulations for every combination of metabolism and signaling module (**Supplementary Table 3**). Simulations reflect 14 days of growth (timepoints taken every 12 h) and reflect outcomes across 20 replicates. Growth rate increases with higher non-random metabolism complexity, suggesting more efficient utilization of nutrients to meet energetic and growth requirements (**Figure 3C**). For a given metabolism module complexity, signaling complexity changes early growth rate dynamics (**Supplementary Figure 3C**), perhaps due to an early compromise between the proliferation and migration governed by PLCγ. The random metabolism module is unable to meet energetic demands, resulting in negligible cell growth. Symmetry increases slightly with increasing metabolism complexity for a given signaling complexity or decreasing signaling complexity for a given metabolism complexity (**Figure 3C**; **Supplementary Figure 3C**). Overall, long term symmetry is unaffected by module complexity, except in simulations with random metabolism in which symmetry is significantly lower. Cell cycle length ranges between 16 and 24 h. Higher metabolism complexity generally results in shorter cell cycles; cells are able to more effectively utilize nutrients to produce cell mass necessary for division (**Figure 3C**; **Supplementary Figure 3C**). Within a given metabolism module, higher complexity signaling results in a slightly shorter early cell cycle (**Supplementary Figure 3C**).

All combinations of modules except those with random metabolism produce cell colonies with a quiescent core surrounded by a proliferative and migratory rim (**Figure 3D**). There is a distribution of apoptotic cells for all cases except for random metabolism, which results in a necrotic core (**Figure 3D**; **Supplementary Figure 3D**). This difference further highlights that the random metabolism module is unable to regulate nutrient usage to produce sufficient energy for the cell.

Overall, we observe key spatial and temporal behaviors that only occur at certain levels of module complexity. For example, extracellular TGFα concentration profiles are highly dependent on the complexity of the signaling module and a necrotic core emerges without a minimal complexity of the metabolism module. Identifying such relationships offer guidelines on the resolution of a computational model necessary to capture specific behaviors in a given biological system.

2.5. Case Study 1: Cell Population Dynamics Differ Between Colony and Tissue Contexts

In vitro studies are ubiquitous in biological research, but they remain limited in their ability to replicate the rich context of the microenvironment (Kim et al., 2004; Hickman et al., 2014). This limitation can result in misleading conclusions that are not relevant or consistent *in vivo* (Fràter-Schröder et al., 1987; Toledo and Wahl, 2006) or even in three-dimensional *in vitro* culture (Wang et al., 1998). Our model can be used to identify differences in emergent behavior as a function of context. In doing so, we are able to (i) distinguish between cases where the difference is irrelevant or negligible and assume observations made *in vitro* hold *in vivo*, and vice versa, as well as (ii) guide experimental design to avoid or compensate in cases where the difference is significant. Here, we simulate cells with variations in three parameters (crowding tolerance, metabolic preference, and migratory threshold) in both colony and tissue contexts, representing *in vitro* and *in vivo* experiments, respectively (**Figure 4A**; Methods).

Growth rate is non-linearly sensitive to changes in crowding tolerance and somewhat linearly sensitive to changes in metabolic preference and migratory threshold (**Figure 4B**; **Supplementary Figure 4A**). Large decreases in crowding tolerance ($< -40\%$) leads to a significant drop in growth rate as cells are unable to successfully divide due to physical constraints. No migratory threshold (-100%) also results in a drop in growth rate as cells are unable to become proliferative. Symmetry diminishes with both decreased crowding tolerance and migratory threshold, but is essentially unaffected by metabolic preference (**Supplementary Figure 4A**). Cell cycle length is sensitive to crowding tolerance, and, to a lesser degree, migratory threshold (**Supplementary Figure 4A**). Overall, the sensitivities of different metrics to changes in parameter values are variable, with crowding tolerance exhibiting highly non-linear trends.

We define the three representative cell populations based on known cancerous phenotypes: `A` (crowding tolerance at $+50\%$ of baseline), `B` (metabolic preference at $+50\%$ of baseline), and `C` (migratory threshold at -50% of baseline). We also define an unmodified cell population `X` (all parameters at baseline). Each population exhibits distinct trends in population fraction over time when simulated in combinations. The relative fraction of population `X` generally decreases, confirming that all the

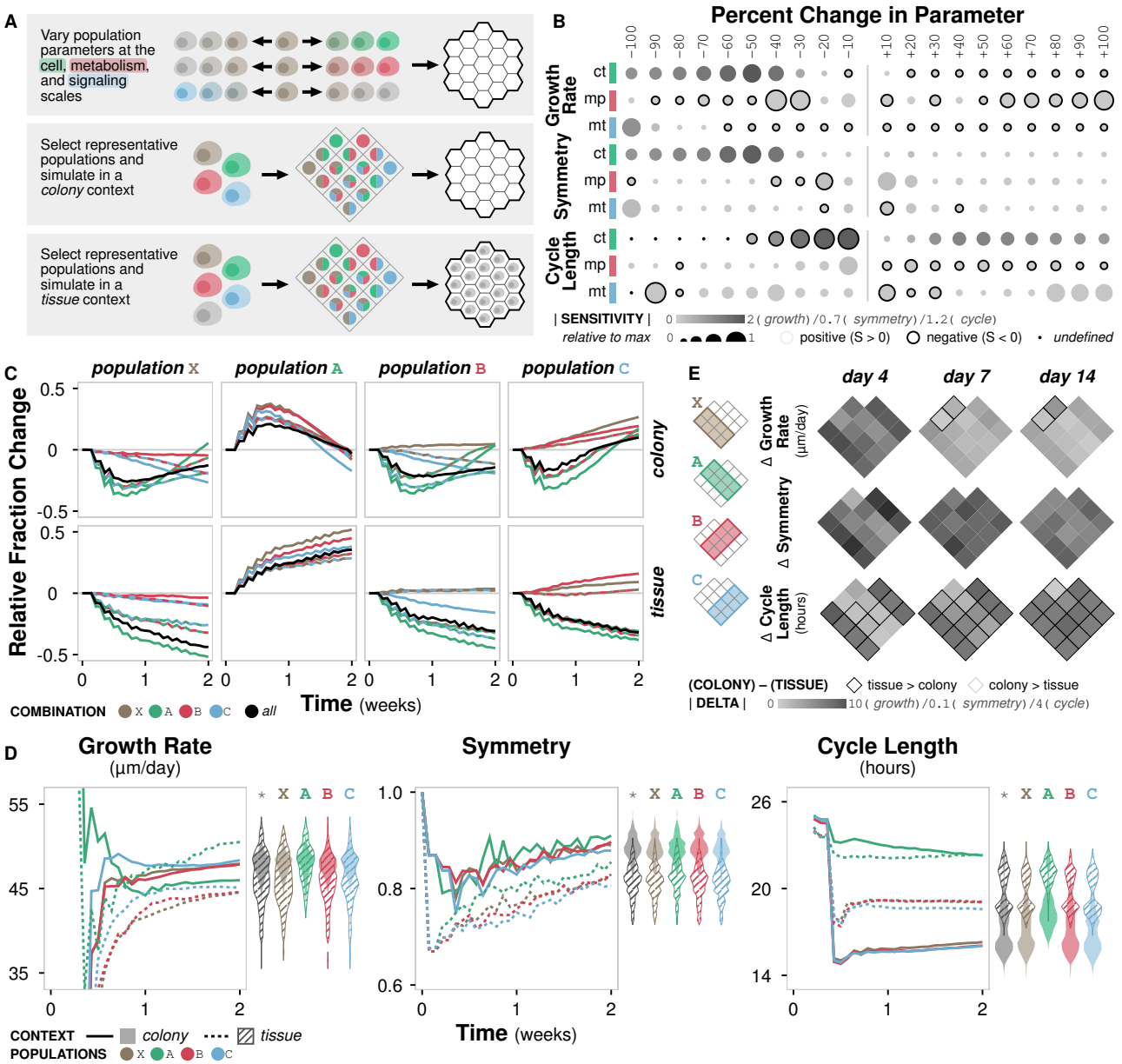

FIGURE 4 | Case study 1: Context. **(A)** Diagram of the three sets of simulations. First, three parameters at the cell, metabolism, and signaling scales (crowding tolerance, metabolic preference, and migratory threshold, respectively) were varied +/− 100% (increments of 10%) and initialized onto an empty environment. Second, combinations of representative cell populations (A, B, C, and X) were initialized onto an empty environment to represent a colony context. Third, combinations of representative cell populations (A, B, C, and X) were initialized onto an environment containing a generic cell population to represent a tissue context. **(B)** Sensitivity of three metrics to variation in the three parameters calculated as $(y - y_0)x_0/(x - x_0)y_0$ where y is the metric value and x is the parameter value. Circle size indicates relative fold change in sensitivity to the maximum for a given metric and parameter, circle color indicates absolute sensitivity, and inverse relationships are indicated by a black border. **(C)** Relative change in population fraction for each of the four representative populations over time across all combinations under colony and tissue contexts. Color indicates the other populations included in the simulation; black indicates all three other populations where included. **(D)** Time course of metric values for the four representative populations under colony and tissue contexts. Violin plots show distribution of the metric value between contexts at time $t = 2$ weeks for all population combinations (*) or for population combinations including the indicated population. **(E)** Heat map of the change in metric value between the (colony) − (tissue) contexts at different timepoints for all population combinations.

modified populations (A, B, and C) have growth advantages over the unmodified population (**Figure 4C**). The relative fraction of population A generally increases (**Figure 4C**). Populations B and C show variable changes in fraction depending on which other populations are present; they are able to outgrow population X but not population A, and population C is able to outgrow

population B (**Figure 4C**). These colony trends for populations X, B, and C hold in the tissue context, but the early increase then gradual return to the initial fraction for population A seen in the colony context is not observed in the tissue context (**Figure 4C**).

With the addition of the generic background cell population in the tissue simulations, increased tolerance for crowding becomes a more valuable phenotype, resulting in a growth rate comparable to that in the colony simulations (**Figure 4D**). In the colony context, the advantage of increased crowding tolerance (population A) becomes less important after the initial burst of growth (**Figure 4D**). In the tissue context, there is significantly lower symmetry for all populations (A, B, C, and X) and higher cycle times for all populations, except A (**Figure 4D**). While symmetry and cell cycle length show clear separation in trajectories between the colony and tissue contexts, growth rate exhibits overlap between contexts, suggesting that growth rate is less sensitive overall to the addition of a generic background population.

In general, when simulating combinations of the four representative populations in a colony context, the resulting overall population symmetry and cycle length are near the average of the constituent populations (**Supplementary Figure 4B**). However, growth rate tends to be higher than the average of the constituent populations when population A is included, even though population A alone has the lowest growth rate. This behavior suggests a synergy in cases where population A is grown with other populations. In the tissue context, population growth rate and symmetry are near the average of the constituent populations, but cycle length is more likely to favor one of the constituent populations, demonstrating that the addition of a generic background population changes the emergent dynamics of the system such that certain phenotypic modifications become more or less advantageous (**Supplementary Figure 4B**).

Growth rate is generally higher in colony contexts, though the increase depends on the constituent populations and decreases over time (**Figure 4E**). Symmetry is consistently higher in colony contexts. Cell cycle length is higher in tissue contexts, except for combinations containing population A, where cycle length is essentially equal between the two contexts during early growth (**Figure 4E**).

Overall, we observe significant differences between the colony and tissue simulation contexts across all three metrics of emergent phenomena. The tissue context simulations generally exhibit lower growth rates, decreased symmetry, and higher cell cycle lengths, though population-dependent effects do exist. These differences might help explain observations in cell culture that are not consistent in animal models and highlights the importance of context when designing both computational and experimental models of biological systems.

2.6. Case Study 2: Cell and Module Parameters Govern Competitive Fitness Between Cell Populations

Biological systems rarely contain only a single population of cells; they comprise complex cell-cell interactions that drive emergent dynamics of the system. Cellular competition has been shown to impact dynamics in a variety of contexts including development, aging, and cancer (Gregorio et al., 2016; Merino et al., 2016). Co-culture systems have been used to study such phenomena (Kirkpatrick et al., 2011; Goers et al., 2014). Several variables must be considered—cell composition, relative seeding and spatial separation, culture dimensionality and local environment—all of which affect temporal and spatial observations and present challenges for data acquisition (Kirkpatrick et al., 2011; Goers et al., 2014). Our model provides a platform for *in silico* co-culture in which these variables can be easily and precisely tuned and controlled. Here, we simulate a modified population along with an unmodified, basal population to specifically interrogate the how differences in cell phenotype and relative seeding affect competitive fitness (**Figure 5A**; Methods).

The crowding tolerance parameter significantly impacts the fraction and dominance of the modified population in co-culture simulations (**Figure 5B**). Significant decreases in crowding tolerance (−30, −40, and −50%) lead to a decrease in the fraction of modified population relative to the initial fraction. Any increase (+10, +20, +30, +40, and +50%) or, unexpectedly, slight negative decrease (−10% and −20%) to crowding tolerance leads to an increase in the fraction of the modified population.

Changes in the metabolic preference parameter result in non-linear changes in the fraction of the modified population (**Figure 5B**). Modifying the migratory threshold parameter follows a linear trend; an increase or decrease in parameter values results in a decrease or increase in the fraction of modified population, respectively (**Figure 5B**). The non-linear trend of metabolic preference indicates that the fraction of energy derived from glycolysis has a complex relationship to population fitness whereas the linear trend of migratory threshold suggests that a cell more likely to commit to migration instead of proliferation is a more competitive phenotype relative to the basal population. For crowding tolerance, the multimodal responses indicate that both an increased and decreased (to a certain limit) tolerance to crowding can be advantageous.

The trends observed in changes in modified population fraction as a function of modified parameter are reflected in emergent behavior (**Figure 5C**). Differences in growth rate due to changes in crowding tolerance are more prominent for higher initial modified population (**Supplementary Figure 5A**). Variations in the crowding tolerance parameter represent different tolerances to mechanical stress during the competition for space (Merino et al., 2016). The modified population with an increased crowding tolerance is able to pack more densely in the core of the cell colony whereas the population with a slightly decreased tolerance is incentivized to grow outward; both strategies are sufficient to outcompete the basal population (**Figure 5D**; **Supplementary Figure 5B**).

Symmetry, a function of spatial distribution, is mostly unaffected by competition, except with a decrease due to decrease in crowding tolerance at high initial modified population (**Figure 5C**; **Supplementary Figure 5A**). Cell colonies that look spatially similar may have distinctly different composition at the subcellular level (**Supplementary Figure 5C**). For example, tumors may appear spatially homogeneous despite being

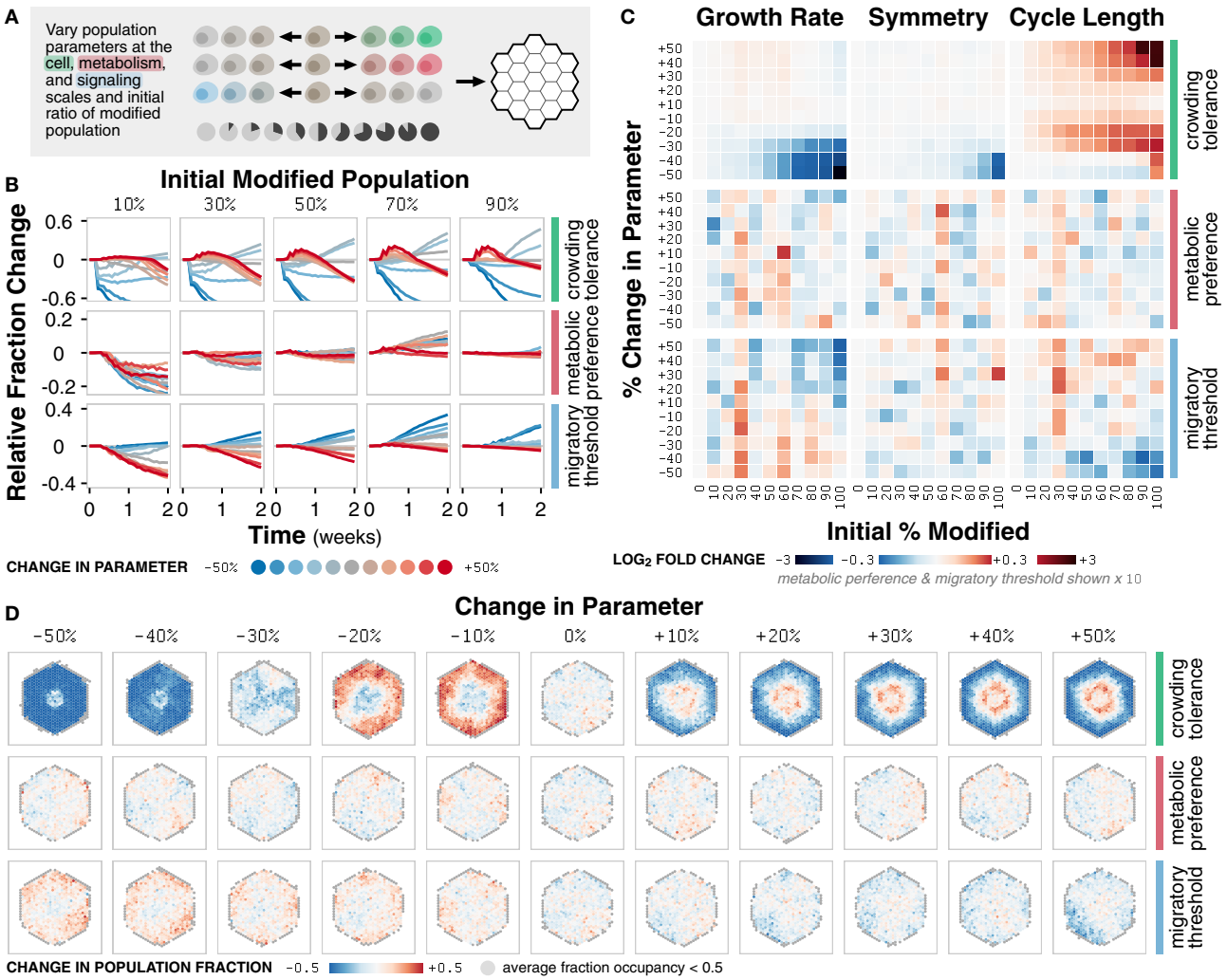

FIGURE 5 | Case study 2: Competition. **(A)** Diagram of the set of simulations. Three parameters at the cell, metabolism, and signaling scales (crowding tolerance, metabolic preference, and migratory threshold, respectively) were varied +/− 50% (increments of 10%) and initialized in ratios of 0 to 100% (increments of 10%) with a basal, unmodified cell population onto an empty environment. **(B)** Relative change in population fraction for the modified population over time for different changes in parameter at selected initial ratios of the modified population. **(C)** Heat maps of fold change in metric value across $n = 20$ replicates for different changes in parameter and initial ratios relative to a 0% change in parameter at $t = 2$ weeks. **(D)** Spatial distribution of change in fraction of the modified population at $t = 2$ weeks across $n = 20$ replicates for simulations initialized with an equal mixture of the modified and basal cell populations. Locations with less than 0.5 fraction occupancy across replicates are shown in gray.

composed of highly diverse subpopulations; a biopsy may only represent a small fraction this diversity (Poleszczuk et al., 2015). Similarly, microbial colonies, which are largely indistinguishable spatially, may contain highly diverse mixtures of the component cells in which competition is driven by cell morphology (Smith et al., 2016).

Cell cycle length is also essentially unaffected for metabolic preference and migratory threshold (**Figure 5C**). However, increased and slightly decreased crowding tolerance leads to increased cell cycle length (**Figure 5C**; **Supplementary Figure 5A**). The increased tolerance for crowding results in greater competition for nutrients, requiring more time for cell growth before division. However, the benefit of increased tolerance for mechanical stress outweighs the disadvantage of a slower cell cycle; this tradeoff allows the modified population to outcompete the basal population and highlights the relative (and arguably non-intuitive) contributions of different modes of competition.

Overall, we observe both linear (migratory threshold), non-linear (metabolic preference) and multimodal (crowding tolerance) relationships between the parameter values of the modified population and the emergent behavior of the system. The high temporal and spatial resolution of our simulations, in combination with parametric sensitivity analysis, help identify when, where, and how the modified population is able to outcompete the basal population. In addition, identifying the linearity and transition points of these relationships provide insight into the mechanisms of the underlying cell-cell

interactions. The multimodal relationship between modifications in crowding tolerance and growth dynamics, for example, demonstrates that there exist two separate mechanisms by which cells with an increased or decreased tolerance for mechanical stress can successfully outcompete another population.

2.7. Case Study 3: Intra- and Intercellular Heterogeneity Impact Clonal Evolution and Emergent Dynamics

Cell heterogeneity is an intrinsic property of biological systems, even within clonal populations (Raser, 2004; Lidstrom and Konopka, 2010; Marusyk et al., 2012). Advancements in experimental approaches have enabled observation and quantification of heterogeneity at the single cell level (Schmid et al., 2010; Walling and Shepard, 2011). However, while heterogeneity can be measured, it cannot be systematically varied. Given the ubiquitous nature of heterogeneity, it remains important to distinguish between functional variation that selectively arises to improve evolutionary fitness from intrinsic variation that arises from random fluctuations (Altschuler and Wu, 2010). Our model allows for explicit control of differences between cell populations, variation in cell parameters, and probabilities of stochastic processes. Here, we simulate growth in both colony and tissue contexts to explore how heterogeneity within and between cell populations impacts emergent responses (**Figure 6A**; Methods).

Growth rate increases with increasing heterogeneity in colony and tissue simulations (**Figure 6B**; **Supplementary Figure 6A**). Higher background heterogeneity corresponds to lower growth rate for all populations (A, B, C, and X) (**Supplementary Figure 6B**). Symmetry generally decreases for any increase in heterogeneity or background heterogeneity (**Figure 6B**; **Supplementary Figures 6A,B**). Interestingly, the change in growth rate and symmetry as heterogeneity increases is not consistent across different background heterogeneities, which suggests that background heterogeneity can mask the effects of heterogeneity in the population of interest (**Figure 6B**). Cell cycle length increases with increasing heterogeneity for most populations; population A is minimally affected (**Figure 6B**; **Supplementary Figure 6A**). Background heterogeneity does not have a clear relationship to cycle length; this emergent behavior appears to be less context-dependent and more population-dependent, as previously noted (**Supplementary Figure 6B**).

In general, regardless of context, population A increases and population X decreases in fraction when simulated in combination with other populations (**Figure 6C**). Population A persists best in colony contexts at higher heterogeneity ($H \geq 20$) and persists best in tissue contexts at lower heterogeneity ($H < 20$) (**Figure 6C**). Change in population A fraction is unaffected by background heterogeneity (**Supplementary Figure 6C**). Populations X, B, and C do not have clear background heterogeneity trends, but generally exhibit better population fraction outcomes in tissue contexts as heterogeneity increases (**Figure 6C**).

The crowding tolerance parameter (**Supplementary Table 1**), which is already higher in population A, is one of the internal cell parameters now subject to heterogeneity in all four representative populations. The increased heterogeneity in the other populations, which are normally less competitive in tissue contexts than population A, provides a mechanism by which they can select for cells with a higher crowding tolerance. This hypothesis is further supported by the observation that populations B and C persist better in colony contexts, where there is a weaker selective pressure for higher crowding tolerance (**Figure 6C**). In addition, the distribution of the average value of the crowding tolerance parameter across the replicates shows a clear evolution toward a higher value (**Figure 6D**; **Supplementary Figure 6D**).

The metabolic preference parameter (**Supplementary Table 4**) shows a minor evolution toward a lower value in the tissue context for population B, in which the parameter was increased (**Figure 6D**). There is minimal evolution of the metabolic preference parameter in the other cell populations, suggesting that the basal value of metabolic preference was optimal for the given environment conditions in these simulations and that there exists a stronger selective pressure in the tissue context (**Supplementary Figure 6D**). The migratory threshold parameter (**Supplementary Table 5**) shows a minor increase toward a larger value at very high heterogeneity (**Supplementary Figure 6D**) for all populations. In almost all cases, the variance of the distribution in average parameter value across replicates increases from the initial distribution (**Supplementary Figure 6E**).

The changes in metrics between simulated colony and tissue contexts with the addition of heterogeneity generally match trends seen without heterogeneity for symmetry and cycle length: symmetry is higher and cycle length is lower in the colony context (**Figure 6E**). Growth rate shows a significant dependence on the degree of both heterogeneity and background heterogeneity. There exist critical values of heterogeneity and background heterogeneity for which growth rate in colony and tissue contexts are comparable (**Figure 6E**). In this system, background heterogeneity matters when growth rate and symmetry are of interest, but is less important for cycle length (Altschuler and Wu, 2010).

Overall, we observe heterogeneity-dependent emergent behavior in both colony and tissue contexts. Higher heterogeneity generally corresponds to higher growth rate, lower symmetry, and longer cycle lengths, though there are population-dependent effects as well. As a consequence of heterogeneity, cell populations evolve toward certain parameter values such as higher crowding tolerance. Exploring such trends identify how heterogeneity within and between populations shapes emergent population dynamics.

3. DISCUSSION

Computational models are critical for understanding biological systems (Brodland, 2015; Yu and Bagheri, 2016). Agent-based modeling in particular has seen increasing applications in biology

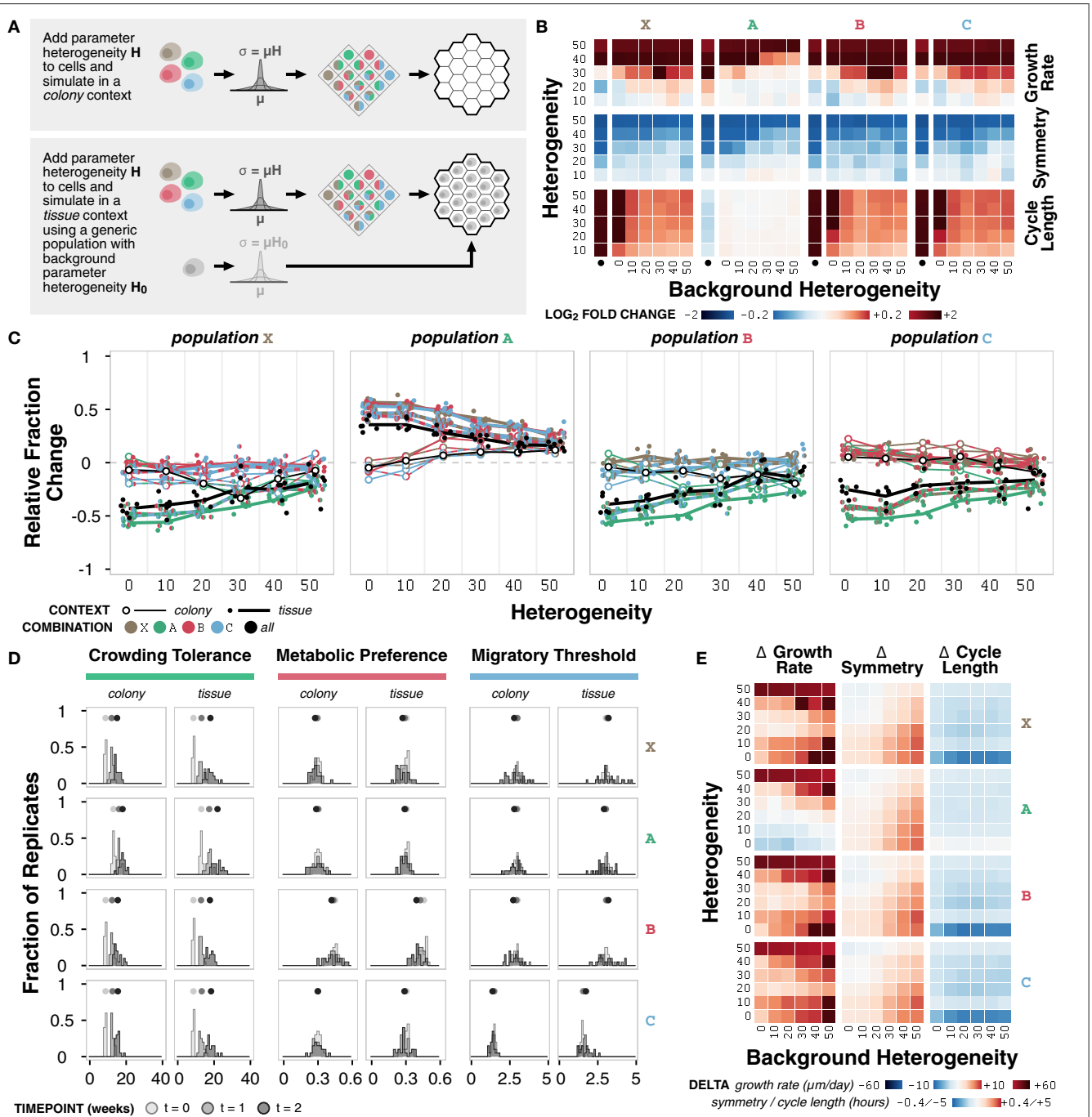

FIGURE 6 | Case study 3: Heterogeneity. **(A)** Diagram of the two sets of simulations. First, combinations of representative cell populations (A, B, C, and X) with heterogeneity H varied at 0, 10, 20, 30, 40, and 50% were initialized onto an empty environment to represent a colony context. Second, combinations of representative cell populations (A, B, C, and X) with heterogeneity H varied at 0, 10, 20, 30, 40, and 50% were initialized onto an environment containing a generic cell population with background heterogeneity H_0 varied at 0, 10, 20, 30, 40, and 50% to represent a tissue context. **(B)** Heat maps of fold change in metrics for each representative cell population across different amounts of heterogeneity relative to the non-heterogeneous ($H = 0$) case at $t = 2$ weeks. The colony context (no background population) is indicated by the bullet (•). **(C)** Relative change in population fraction for each of the four representative populations for all combinations as a function of heterogeneity at $t = 2$ weeks. Color indicates the other populations included in the simulation; black indicates all three other populations where included. Lines connect average values for the colony context (thin) and averages across values for different background heterogeneities for the tissue context (thick) for each combination. **(D)** Distributions parameter means across $n = 20$ replicates at different timepoints under colony and tissue contexts for representative cell populations with $H = H_0 = 40$. **(E)** Heat maps of change in metric value between the (colony with heterogeneity) – (tissue with heterogeneity) contexts for representative cell populations at $t = 2$ weeks.

(An et al., 2009; Gorochowski, 2016). A number of agent-based modeling platforms exist, including Chaste (Mirams et al., 2013), CompuCell3D (Swat et al., 2012), and FLAME (Holcombe et al., 2012). We develop the first ABM that uses interfaces custom-built to formalize the interactions within and among cells and their environment.

We implemented a tissue cell system within the framework and demonstrate that, with literature-derived parameters and no additional parameter fitting, we produce biologically realistic growth dynamics that are agnostic to a specific cell population. Three case studies investigating cellular context, competition, and heterogeneity demonstrate how our model provides unique insight into biological systems in a manner that is infeasible to probe experimentally.

First, we analyze the impact of specific cell parameters and simulate representative populations in colony and tissue contexts. Second, we systematically vary cell population parameters and initial conditions of simulated co-culture experiments to evaluate cellular competition. Finally, we introduce tunable cell heterogeneity, both within the representative populations and between the representative and background populations. Tracking temporal, spatial, and single-cell data of each simulation across multiple replicates identifies non-linear trends and non-intuitive relationships. These observations offer hypotheses on the underlying mechanisms that could be validated experimentally.

Our framework is readily extensible across many biological systems, with applications in a variety of areas including drug development, personalized medicine, and synthetic biology. The model can be tuned to a specific disease or patient population context by varying cell parameters and altering the simulation environment. For example, we could simulate a highly glycolytic cancer growing in a patient with diabetes by increasing the metabolic preference for glycolysis parameter and setting a higher basal concentration of glucose in the simulation environment. We can then test how various perturbations, such as excision combined with radiation compared to excision alone, affects the growth of the tumor. Here, the model acts as an *testbed* with which to interrogate new strategies for drug design and treatment.

This framework can also catalyze a new approach to translational and personalized therapy by matching the model to biopsy and imaging data from a patient. Here, the model acts as a *proxy* with which to rapidly, inexpensively, and safely simulate a wide variety of possible interventions to develop patient-specific treatment regimes that offer more successful outcomes.

Finally, with the advent of engineered cell therapy (Kitada et al., 2018), this framework can uniquely redirect efforts in synthetic biology by predicting emergent outcomes. New agents, representing engineered immune cells with modules specific to their method of action, can be introduced to the model. Varying parameters and rules of the these agents, such as receptor density, binding strength, or target specificity, and observing the emergent response of the system can identify key design targets for effective cell therapy. Here, the model acts as a *tool* with which to predict novel system response in order to generate experimentally testable hypotheses.

In conclusion, our framework offers a new computational approach to interrogate the complexity and emergence of cell populations *de novo*. The intuitive nature of ABMs, in which rules can be explained with natural language and parameters are derived from literature values, helps bridge the gap between computational theory and experimental application and provides an opportunity for interdisciplinary collaboration (Cvijovic et al., 2014). We do not present a "whole cell" model nor seek to diminish the utility of reactive, equation-based approaches. Rather, we acknowledge the inherently multi-scale nature of biology and have designed a proactive, rule-based modeling framework to encourage the development of constituent parts by experts, and the investigation of their impact on emergent behavior in a variety of systems. This framework can serve as an invaluable resource that disrupts the status quo of current research efforts.

4. METHODS

All source code for ARCADE is available on GitHub at `https://github.com/bagherilab/ARCADE`. MASON, a multi-agent simulation library required by the model, is available at `https://cs.gmu.edu/~eclab/projects/mason/`.

4.1. Model Agents

For the tissue cell implementation, seven cell states were defined: quiescent, migratory, proliferative, apoptotic, necrotic, senescent, and undecided. The state defines which rules the agent follows at each timepoint (**Figure 2A**). The undecided state acts as a transition state; undecided cells decide between migratory and proliferative states based on active PLCγ and the migratory threshold (`MIGRA_THRESHOLD`) through the signaling module (Zhang et al., 2007). Each cell agent is initialized with a volume drawn from a normal distribution (mean = `CELL_VOL_AVG`, standard deviation = `CELL_VOL_RANGE`) and an age drawn from a uniform distribution (between 0 and `DEATH_AGE_RANGE`).

4.1.1. Quiescent

Cells can enter quiescence through a variety of mechanisms (Valcourt et al., 2012; Yao, 2014). Proliferating cells might become quiescent without completing the cell cycle due to contact inhibition (Gos et al., 2005), which occurs when (i) there are no neighboring locations into which it can divide or (ii) cell size exceeds the available space. Migratory cells might also become quiescent through contact inhibition (Abercrombie and Heaysman, 1953). Cells unable to meet energetic requirements become quiescent (Valcourt et al., 2012). Tissue cell agents exit quiescence through external growth signals, such as apoptosis of a neighboring cell inducing compensatory proliferation or the removal of contact inhibition (Valcourt et al., 2012; Yao, 2014).

4.1.2. Migratory

Cells that decide to migrate create a helper agent that is called after a time delay corresponding to the distance the cells needs to move (`HEX_SIZE`) and its movement speed (`MIGRA_RATE`).

The cell identifies all neighboring locations, including its current location, meeting the following criteria: (i) adding the new agent does not increase the total cell volume over the volume of the location (HEX_VOLUME), (ii) each agent, with the addition, exists at a height lower than their tolerable height (MAX_HEIGHT), and (iii) there are no more than 6 agents in the new location. To enforce normal cell density, no more than one healthy (H) cell agent is allowed in a location; the cancerous (C) and cancer stem cell (S) subtypes do not follow this additional constraint. To represent chemotactic movement (Zhang et al., 2007), each location i is assigned a score $\mathcal{S}$ based on glucose concentration $\mathcal{G}_i$:

$$\mathcal{S} = \alpha \frac{R - r_i + 1}{2} + (1 - \alpha)\left[\beta \frac{\mathcal{G}_i}{\mathcal{G}^\circ} + (1 - \beta)u\right]$$

where α is affinity (AFFINITY), R is the distance from the center of the migrating cell, r is the radial distance of location i from the center of the environment, β is accuracy (ACCURACY), $\mathcal{G}^\circ$ is the source concentration of glucose (CONC_GLUC), and u is a random number drawn from a uniform distribution $U([0, 1])$. If there are no locations that meet the criteria, the cell becomes quiescent, representing contact inhibition (Abercrombie and Heaysman, 1953).

4.1.3. Proliferative

Cells that decide to proliferate create a helper agent that is stepped along with the rest of the agents until proliferation is complete or the cell is no longer able to proliferate. At each tick, the helper agent checks if (i) the cell is no longer proliferative, (ii) the cell no longer exists at a tolerable height, or (iii) there are no locations into which the cell can divide. For the latter two, the cell becomes quiescent, representing contact inhibition (Gos et al., 2005). Once (i) the cell has doubled in size, which is controlled by the metabolism module, and (ii) sufficient time for DNA synthesis has passed (SYNTHESIS_TIME), the helper creates a new cell agent by dividing the parent cell volume and module contents by 50% ± 5%. The division count for both cells is then incremented.

4.1.4. Apoptotic

Cells that reach an age above the average life span (DEATH_AGE_AVG) have an increasingly high probability of undergoing apoptosis (Elmore, 2007), defined by a cumulative normal distribution (mean = DEATH_AGE_AVG, standard deviation = DEATH_AGE_RANGE). Cells that become apoptotic create a helper that is called after a time delay corresponding to the duration of apoptosis (DEATH_TIME). The helper removes the cell from the schedule and the grid—it is no longer stepped and it no longer occupies space in the environment—which represents the removal of cell debris and regulated nature of apoptosis (Edinger and Thompson, 2004). Compensatory proliferation is also mediated by the helper, which selects a quiescent neighbor of the cell and sets it to proliferate (Fan and Bergmann, 2008; Ryoo and Bergmann, 2012).

4.1.5. Necrotic

Cells under sustained energy deficits (ENERGY_THRESHOLD) undergo necrosis (Edinger and Thompson, 2004; Zong, 2006). These cells also have a probability of undergoing apoptosis instead (NECRO_FRAC), to reflect the more continuous nature of the decision between, and morphology of, necrosis and apoptosis (Zong, 2006). Necrotic cells are removed from the schedule but remain in the grid—it is no longer stepped, but continues to occupy space—which represents the more disorganized nature of necrosis (Edinger and Thompson, 2004).

4.1.6. Senescent

Cells that reach a replicative limit (DIVISION_POTENTIAL) have a probability (SENES_FRAC) of becoming senescent or apoptotic, due to uncertainty about what drives the decision between the two states (Childs et al., 2014). Senescent cells remain on the schedule and in the simulation, but are no longer able to proliferate (Campisi and d'Adda di Fagagna, 2007). Senescent cells might later become apoptotic/necrotic due to nutrient deficiency (Wang et al., 2016), but will not apoptose due to age (Campisi and d'Adda di Fagagna, 2007).

4.2. Model Environment

4.2.1. Coupled Hexagonal and Triangular Grids

Cell agents exist on a hexagonal grid of radius R using a hexagonal coordinate system (u, v, w, z) such that $(0, 0, 0, 0)$ is the center of the environment (**Figure 2B**). For three dimensional models (height $H > 1$), each hexagonal grid layer ($z = 1 - H, ..., H - 1$) has alternating offsets: offset a in the $(-u, +w)$ and offset b in the $(+u, -v)$ direction. The offsets prevent the cell agents from stacking in columns when simulated in 3D. Layer $z = 0$ always has no offset, offset a always has offset b above, and offset b always has no offset above. Given a location with coordinates (u, v, w, z), there are six equidistant neighboring locations in the same layer: $(0, +1, -1, 0)$, $(0, -1, +1, 0)$, $(-1, +1, 0, 0)$, $(+1, -1, 0, 0)$, $(-1, 0, +1, 0)$, $(+1, 0, -1, 0)$; three equidistant locations above: $(0, 0, 0, +1)$, $[(+1, 0, -1, +1)$, $(-1, +1, 0, +1)$, $(0, -1, +1, +1)]$, $[(0, +1, -1, +1), (-1, 0, +1, +1), (+1, -1, 0, +1)]$; and three equidistant locations below: $(0, 0, 0, -1)$, $[(-1, +1, 0, -1)$, $(0, -1, +1, -1)$, $(+1, 0, -1, -1)]$, $[(0, +1, -1, -1)$, $(-1, 0, +1, -1)$, $(+1, -1, 0, -1)]$ where brackets indicate the offset of the layer: [no offset, offset a, and offset b].

Each molecule (oxygen, glucose, and TGFα) diffuses on triangular lattices using rectangular coordinate system (x, y, z) associated with the main hexagonal grid (**Figure 2B**). Glucose and oxygen are introduced from constant sources (CONC_GLUC and CONC_OXY). Each hexagonal location corresponds to six triangular lattice locations, indexed clockwise from the upper center triangle by position p. When cell agents interact with their local environment, average concentration across the six triangular locations is used.

4.2.2. Molecule Diffusion

Diffusion of each molecule is calculated using a reaction-diffusion equation:

$$\frac{\partial C}{\partial t} = \mathscr{D}\nabla^2 C + R_a + R_s$$

where C is the concentration, $\mathscr{D}$ is diffusivity of the molecule in the environment (DIFF_GLUC, DIFF_OXY, or DIFF_TGF), R_a is the rate of consumption/production of the molecule by the cell

agents, and R_s is the rate of production by the vasculature sources. Consumption and production of molecules (R_a) and the source production (R_s) are separately managed by cell agents and a sites component, respectively, which leaves:

$$\frac{\partial C}{\partial t} = \mathscr{D}\nabla^2 C$$

A finite difference approximation for this equation in triangular geometry (Huiskamp, 1991) is solved at each tick t to update the lattice concentrations for the next tick $t + \Delta t$:

$$C^{t+\Delta t} = C^t + \frac{4\mathscr{D}\Delta t}{3\Delta s^2}\left(\sum_{i=1}^{3} C_i^t - 3C^t\right) + \delta\frac{2\mathscr{D}\Delta t}{\Delta z^2}\left(\sum_{j=1}^{2} C_j^t - 2C^t\right)$$

where Δt is the time step (1 s), Δs is the distance between two adjacent triangular locations (half of HEX_SIZE), Δz is the distance between layers (MAX_HEIGHT), i indexes across the three triangular neighbors in a layer, j indexes across the two neighbors above and below the layer, and δ is 0 if $H = 1$ and 1 otherwise.

To check stability of the finite difference approximation, we perform a von Neumann stability analysis:

$$\lambda = 4\mathscr{D}\Delta t\left(\frac{1}{\Delta s^2} + \delta\frac{1}{\Delta z^2}\right)$$

For stability, $0 \leq \lambda < 1$. If not satisfied, we use a pseudo-steady state approximation:

$$C^{t+\Delta t} = \frac{1}{3 + \delta\frac{3\Delta s^2}{\Delta z^2}}\left[\sum_{i=1}^{3} C_i^t + \delta\frac{3\Delta s^2}{2\Delta z^2}\sum_{j=1}^{2} C_j^t\right]$$

4.3. Metabolism Modules

All metabolism modules except for random metabolism account for glycolysis and oxidative phosphorylation pathways for producing energy (ATP) from glucose and oxygen with a metabolic preference μ for glycolysis over oxidative phosphorylation (META_PREF). The complex metabolism module explicitly accounts for a pyruvate intermediate and glucose/oxygen utilization is based on actual energy requirements for the given tick. The medium metabolism module maintains utilization based on actual energy requirements, but does not use a pyruvate intermediate. The simple metabolism module assumes utilization based on constant ATP production rate. Default parameter values are given in **Supplementary Table 4**.

Several stoichiometric ratios are defined:

- S_{glyc} = ATP produced per glucose from glycolysis (2 ATP/glucose)
- S_{oxphos} = ATP produced per pyruvate from oxidative phosphorylation (15 ATP/pyruvate)
- S_{PG} = pyruvate per glucose in glycolysis (2 pyruvate/glucose)
- S_{OP} = oxygen per pyruvate in oxidative phosphorylation (3 oxygen/pyruvate)

4.3.1. Determine Nutrient Availability

At each tick (representing one minute), for each cell agent, the external glucose G_{ext} and oxygen O_{ext} are calculated from the environmental glucose $\mathcal{G}$ and oxygen $\mathcal{O}$ concentrations:

$$G_{ext}^t = \mathcal{G}^t \cdot \mathcal{V}$$
$$O_{ext}^t = \mathcal{O}^t \cdot \mathcal{V} \cdot \rho$$

where $\mathcal{V}$ is the volume of the hexagonal location (HEX_VOLUME) and ρ is the solubility of oxygen in tissue (OXY_SOLU_TISSUE).

4.3.2. Consume Energy

Energy consumed E_{cons} is given by:

$$E_{cons} = \nu(E_0 + E_{pr} \cdot x_{pr} + E_{mi} \cdot x_{mi})$$

where E_0 is basal energy consumption (BASAL_ENERGY), E_{pr} and E_{mi} are additional energy consumed for proliferation (PROLIF_ENERGY) and migration (MIGRA_ENERGY), respectively, and x_{pr} and x_{mi} are cell state flags (mi = migratory, pr = proliferative) which can be on (1) or off (0).

Energy requirement E_{req} for the current timepoint includes E_{cons} and any additional energy $\mathcal{E}$ requirement remaining from the previous time step:

$$E_{req} = E_{cons} + \mathcal{E}^{t-1}$$

4.3.3. Uptake Glucose

Internal glucose G_{int} increases by glucose uptake:

$$G_{int}^t = G_{int}^{t-1} + G_{uptake}$$

where glucose uptake G_{uptake} varies by module complexity.

For random metabolism:

$$G_{uptake} = G_{ext}^t \cdot X_{GU}$$

where X_{GU} = random number drawn from a uniform distribution $U([0.005, 0.015])$.

For simple metabolism:

$$G_{uptake} = k_U \cdot \left(\frac{G_{ext}^t}{\mathcal{V}} - \frac{G_{int}^{t-1}}{\nu}\right)$$

where k_U = constant glucose uptake rate (CONS_GLUC_UPTAKE).

For medium metabolism:

$$G_{uptake} = k_P \cdot \nu \cdot \left(\frac{G_{ext}^t}{\mathcal{V}} - \frac{G_{int}^{t-1}}{\nu}\right) \cdot \left(\frac{1}{S_{avg}}\right)$$

where k_P = ATP production rate (ATP_PRODUCTION_RATE) and S_{avg} = average ATP produced per glucose calculated as $\mu \cdot S_{glyc} + (1 - \mu) \cdot S_{oxphos} \cdot S_{PG}$.

For complex metabolism:

$$G_{uptake} = k_G \cdot A \cdot \left(\frac{G_{ext}^{t}}{\mathcal{V}} - \frac{G_{int}^{t-1}}{v} \right)$$

where k_G = glucose uptake rate (GLUC_UPTAKE_RATE) and A = cell agent surface area based on the cell volume.

4.3.4. Calculate Nutrient Requirements

The amount of glucose required G_{req}, amount of pyruvate required P_{req} (complex only), and oxygen uptake O_{uptake}, can be calculated depending on module complexity.

For random metabolism:

$$G_{req}^{glyc} = X_{GR}$$
$$O_{uptake} = O_{ext}^{t} \cdot X_{OU}$$

where X_{GR} is a random number drawn from a uniform distribution $U([0.2, 0.4])$ and X_{OU} is a random number drawn from a uniform distribution $U([0.2, 0.5])$.

For simple metabolism:

$$G_{req}^{glyc} = \frac{\mu \cdot \alpha}{S_{glyc}}$$
$$G_{req}^{oxphos} = \frac{(1-\mu) \cdot \alpha}{S_{oxphos} \cdot S_{PG}}$$
$$O_{uptake} = \mathbf{min}(O_{ext}, G_{req}^{oxphos} \cdot S_{PG} \cdot S_{OP})$$

where α is the constant ATP production rate (CONS_ATP_PRODUCTION).

For medium metabolism:

$$G_{req}^{glyc} = \frac{\mu \cdot E_{req}}{S_{glyc}}$$
$$G_{req}^{oxphos} = \frac{(1-\mu) \cdot E_{req}}{S_{oxphos} \cdot S_{PG}}$$
$$O_{uptake} = \mathbf{min}(O_{ext}, G_{req}^{oxphos} \cdot S_{PG} \cdot S_{OP})$$

For complex metabolism:

$$G_{req} = \frac{\mu \cdot E_{req}}{S_{glyc}}$$
$$P_{req} = \frac{(1-\mu) \cdot E_{req}}{S_{oxphos}}$$
$$O_{uptake} = \mathbf{min}(O_{ext}, P_{req} \cdot S_{OP})$$

4.3.5. Generate Energy

Energy is generated through oxidative phosphorylation and glycolysis based on internal glucose or pyruvate, depending on the module complexity.

For oxidative phosphorylation with random, simple, and medium metabolism, the amount of glucose needed in terms of oxygen G_O is calculated as $G_O = O_{uptake}/(S_{PG} \cdot S_{OP})$.

If $G_{int} > G_O$:

$$E_{gen}^{oxphos} = G_O \cdot S_{oxphos} \cdot S_{PG}$$
$$G_{int} = G_{int} - G_O$$

If $G_{int} \leq G_O$:

$$E_{gen}^{oxphos} = G_{int} \cdot S_{oxphos} \cdot S_{PG}$$
$$G_{int} = 0$$
$$O_{uptake} = G_{int} \cdot S_{PG} \cdot S_{OP}$$

For oxidative phosphorylation with complex metabolism, the amount of pyruvate needed in terms of oxygen P_O is calculated as $P_O = O_{uptake}/S_{OP}$.

If $P_{int} > P_O$:

$$E_{gen}^{oxphos} = P_O \cdot S_{oxphos}$$
$$P_{int} = P_{int} - P_O$$

If $P_{int} \leq P_O$:

$$E_{gen}^{oxphos} = P_{int} \cdot S_{oxphos}$$
$$P_{int} = 0$$
$$O_{uptake} = P_{int} \cdot S_{OP}$$

For glycolysis with random, simple, and medium metabolism:

If $G_{int} > G_{req}^{glyc}$:

$$E_{gen}^{glyc} = G_{req}^{glyc} \cdot S_{glyc}$$
$$G_{int} = G_{int} - G_{req}^{glyc}$$

If $G_{int} \leq G_{req}^{glyc}$:

$$E_{gen}^{glyc} = G_{int} \cdot S_{glyc}$$
$$G_{int} = 0$$

For glycolysis with complex metabolism:

If $G_{int} > G_{req}$:

$$E_{gen}^{glyc} = G_{req} \cdot S_{glyc}$$
$$G_{int} = G_{int} - G_{req}$$
$$P_{int} = P_{int} + G_{req} \cdot S_{PG}$$

If $G_{int} \leq G_{req}$:

$$E_{gen}^{glyc} = G_{int} \cdot S_{glyc}$$

$$G_{int} = 0$$
$$P_{int} = P_{int} + G_{int} \cdot S_{PG}$$

Note that for complex and medium metabolism, between oxidative phosphorylation and glycolysis, additional glucose can be diverted through glycolysis to compensate for an energy deficit ($\mathcal{E} < 0$ and $G_{int} > 0$) in cases where there is not enough oxygen for complete oxidative phosphorylation. The two pathways do not occur sequentially in real systems so this step ensures that the glycolysis pathway can be used to produce energy under hypoxic conditions.

$$G_{req} = \mathbf{max}\left(G_{req}, \frac{-(\mathcal{E} - E_{cons} + E_{gen}^{oxphos})}{S_{glyc}}\right)$$

4.3.6. Update Energy

The final energy level, for all complexities, is given by:

$$\mathcal{E}^t = \mathcal{E}^{t-1} + E_{gen} - E_{cons}$$

where $E_{gen} = E_{gen}^{oxphos} + E_{gen}^{glyc}$ for complex metabolism.

4.3.7. Generate Cell Mass

Cells will generate cell mass m during (i) proliferation and (ii) size maintenance, depending on module complexity, when not under an energy deficit ($\mathcal{E} \geq 0$). Cells use a fraction of their internal glucose and pyruvate f_m (`FRAC_MASS`) to produce cell mass. The cell aims to main a critical mass m_{crit}.

For random metabolism where ($x_{pr} = 1$ and $m < 2m_{crit}$):

$$\Delta m = X_U \left[\frac{G_{int}}{\phi}\right]$$
$$G_{int} = G_{int} - X_U \cdot G_{int}$$

where X_U is a random number drawn from a uniform distribution $U([0, 1])$ and ϕ is the glucose recovered from cell mass (`MASS_TO_GLUC`).

For simple metabolism where ($x_{pr} = 1$ and $m < 2m_{crit}$ and $G_{int} > k_M \cdot \rho \cdot \phi$):

$$\Delta m = k_M \cdot \rho$$
$$G_{int} = G_{int} - k_M \cdot \rho \cdot \phi$$

where k_M is a constant growth rate (`CONS_GROWTH_RATE`) and ρ is cell density (`CELL_DENSITY`).

For medium metabolism where ($x_{pr} = 1$ and $m < 2m_{crit}$) or ($m < 0.99m_{crit}$):

$$\Delta m = f_m \left[\frac{G_{int}}{\phi}\right]$$
$$G_{int} = G_{int} \cdot (1 - f_m)$$

For complex metabolism where ($x_{pr} = 1$ and $m < 2m_{crit}$) or ($m < 0.99m_{crit}$):

$$\Delta m = f_m \left[\frac{\lambda \cdot G_{int}}{\phi} + \frac{(1-\lambda) \cdot P_{int}}{S_{PG} \cdot \phi}\right]$$
$$G_{int} = G_{int} \cdot (1 - f_m \cdot \lambda)$$
$$P_{int} = P_{int} \cdot (1 - f_m \cdot (1 - \lambda))$$

where λ is the relative contribution of glucose and pyruvate to cell mass (`RATIO_GLUC_TO_PYRU`).

4.3.8. Consume Cell Mass

For complex and medium metabolism, a cell consumes cell mass through autophagy (Glick et al., 2010) when (i) it is under an energy deficit and is larger than the minimum viable mass ($\mathcal{E} < 0$ and $m > m_{min}$) or (ii) it is not under and energy deficit, is above its desired size, and it not proliferating ($\mathcal{E} \geq 0$ and $m > 1.01m_{crit}$ and $x_{pr} = 1$):

$$m = m - k_A$$
$$G_{int} = G_{int} + k_A \cdot \phi$$

where m_{min} is the minimum mass the cell agent tolerates (`MIN_MASS_FRAC`) and k_A is the rate of autophagy (`AUTOPHAGY_RATE`). Simple and random metabolism do not have a mechanism to consume mass.

4.3.9. Update Cell and Environment

Cell volume is updated from cell mass m using cell density ρ as $v = m/\rho$. For complex metabolism, interval pyruvate is removed through conversion to lactate at rate k_L (`LACTATE_RATE`):

$$P_{int} = (1 - k_L) \cdot P_{int}$$

The external glucose and oxygen environments are updated based on final uptake by the cell:

$$\mathcal{G}^{t+1} = \mathcal{G}^t \cdot \left(1 - \frac{G_{uptake}}{G_{ext}^t}\right)$$
$$\mathcal{O}^{t+1} = \mathcal{O}^t \cdot \left(1 - \frac{O_{uptake}}{O_{ext}^t}\right)$$

4.4. Signaling Modules

The complex signaling module is based on a published EGFR gene-protein interaction network (Athale et al., 2005; Zhang et al., 2007). The medium and simple signaling modules are further simplifications of this network. For the random signaling module, cells become migratory with a certain probability (`MIGRA_PROB`). Default parameter values are given in **Supplementary Table 5**.

At each tick (representing 1 min), for each agent, the external TGFα concentration is determined from the lattice. The system of equations is iteratively solved using a forward Euler method with time steps of 1 s. The external TGFα concentration in the lattice is then set to the new value. Cell agent state is defined by the relative fold change Δ in active PLCγ:

$$\Delta = \frac{\mathbf{max}([\text{PLC}\gamma]^t, [\text{PLC}\gamma]^{t-1})}{\mathbf{min}([\text{PLC}\gamma]^t, [\text{PLC}\gamma]^{t-1})}$$

where t is the current tick. Cells in an undefined state with Δ greater than migratory threshold θ (MIGRA_THRESHOLD) become migratory; otherwise they become proliferative:

$$\left\{ \begin{array}{l} \Delta > \theta : \ x_{mi} = 1 \ x_{pr} = 0 \\ \Delta \leq \theta : \ x_{mi} = 0 \ x_{pr} = 1 \end{array} \right\}$$

where x is the cell state flag (mi = migratory, pr = proliferative).

4.4.1. Regulatory Weighting

Regulatory interactions are simplified into weights w of the following form:

$$w_k = 1 \pm \frac{X_i}{\mathrm{WK} + X_i}$$

where i indicates the regulatory species, $\pm$ indicates an increase ($+$) or decrease ($-$) in rate, and WK is the corresponding weighting parameter given in **Supplementary Table 5**.

4.4.2. Uptake and Transport

For simple signaling, extracellular TGFα (X_1) forms a complex with EGFR and is internalized into cytoplasmic TGFα-EGFR (X_2). Membrane EGFR is not explicitly considered. Inactive PLCγ (X_3) converts to active PLCγ (X_4) and vice versa (Athale et al., 2005; Zhang et al., 2007).

$$\begin{aligned} \frac{dX_1}{dt} &= k_6 - k_1 X_1 w_G w_C - k_3 X_1 \\ \frac{dX_2}{dt} &= k_1 X_1 w_G w_C - k_2 X_2 \\ \frac{dX_3}{dt} &= k_5 X_4 - k_4 (1 - X_4) w_P \\ \frac{dX_4}{dt} &= k_4 (1 - X_4) w_P - k_5 X_4 \end{aligned}$$

For medium signaling, extracellular TGFα (X_1) and membrane EGFR (X_2) form a TGFα-EGFR complex (X_3) that autophosphorylates into p-TGFα-EGFR (X_4) (Athale et al., 2005; Zhang et al., 2007). Unlike complex signaling, the translation of TGFα and EGFR are no longer explicitly included; TGFα secretion and EGFR insertion occur at constant rates. The complex is internalized into cytoplasmic TGFα-EGFR (X_5), which can then dissociate. Inactive PLCγ (X_6) converts to active PLCγ (X_7) and vice versa (Athale et al., 2005; Zhang et al., 2007).

$$\begin{aligned} \frac{dX_1}{dt} &= k_{-1} X_3 - k_1 X_1 X_2 - k_7 X_1 + k_{11} \\ \frac{dX_2}{dt} &= k_{-1} X_3 - k_1 X_1 X_2 - k_6 X_2 + k_{10} \\ \frac{dX_3}{dt} &= 2k_1 X_1 X_2 - 2k_{-1} X_3 - k_2 X_3 w_G + k_{-2} X_4 w_C - k_3 X_3 \\ \frac{dX_4}{dt} &= k_2 X_3 w_G - k_{-2} X_4 w_C - k_4 X_4 \\ \frac{dX_5}{dt} &= k_3 X_3 + k_4 X_4 - k_5 X_5 \\ \frac{dX_6}{dt} &= k_9 X_7 - k_8 (1 - X_7) w_P \\ \frac{dX_7}{dt} &= k_8 (1 - X_7) w_P - k_9 X_7 \end{aligned}$$

For complex signaling, extracellular TGFα (X_1) and membrane EGFR (X_2) form a TGFα-EGFR complex (X_3) that autophosphorylates into p-TGFα-EGFR (X_4) (Athale et al., 2005; Zhang et al., 2007). The complex is internalized into cytoplasmic TGFα-EGFR (X_5), which can then dissociate into cytoplasmic EGFR (X_6) and TGFα (X_7). Both EGFR and TGFα are translated from EGFR RNA (X_8) and TGFα RNA (X_9), respectively (Athale et al., 2005; Zhang et al., 2007). Inactive PLCγ (X_{10}) converts to active PLCγ (X_{11}) and vice versa (Athale et al., 2005; Zhang et al., 2007). EGFR RNA and TGFα RNA are generated from a nucleotide pool (X_{12}) (Athale et al., 2005; Zhang et al., 2007).

$$\begin{aligned} \frac{dX_1}{dt} &= k_{-1} X_3 - k_1 X_1 X_2 + k_9 X_7 - k_{11} X_1 \\ \frac{dX_2}{dt} &= k_{-1} X_3 - k_1 X_1 X_2 + k_8 X_6 - k_{-8} X_2 - k_{10} X_2 \\ \frac{dX_3}{dt} &= 2k_1 X_1 X_2 - 2k_{-1} X_3 - k_2 X_3 w_G + k_{-2} X_4 w_C - k_3 X_3 \\ \frac{dX_4}{dt} &= k_2 X_3 w_G - k_{-2} X_4 w_C - k_4 X_4 \\ \frac{dX_5}{dt} &= k_3 X_3 + k_4 X_4 + 2k_{-5} X_6 X_7 - 2k_5 X_5 \\ \frac{dX_6}{dt} &= k_5 X_5 - k_{-5} X_6 X_7 + k_{14} X_8 - k_6 X_6 - k_8 X_6 + k_{-8} X_2 \\ \frac{dX_7}{dt} &= k_5 X_5 - k_{-5} X_6 X_7 + k_{15} X_9 - k_7 X_7 - k_9 X_7 \\ \frac{dX_8}{dt} &= k_{16} X_{12} w_E - k_{18} X_8 \\ \frac{dX_9}{dt} &= k_{17} X_{12} w_T - k_{19} X_9 \\ \frac{dX_{10}}{dt} &= k_{13} X_{11} - k_{12} (1 - X_{11}) w_P \\ \frac{dX_{11}}{dt} &= k_{12} (1 - X_{11}) w_P - k_{13} X_{11} \\ \frac{dX_{12}}{dt} &= -k_{16} X_{12} w_E - k_{17} X_{12} w_T + k_{18} X_8 + k_{19} X_9 \end{aligned}$$

4.4.3. Initial Concentrations and Regulatory Species

For simple metabolism, initial concentrations (in nM) are $X_6 = 0.333$, and $X_7 = 0.667$. Extracellular TGFα (X_1) is given by CONC_TGF. All other species are initially at 0. Regulatory species are internal glucose (determined from the metabolism module) for G, X_4 for C, and X_2 for P.

For medium metabolism, initial concentrations (in nM) are $X_2 = 25$, $X_6 = 0.333$, and $X_7 = 0.667$. Extracellular TGFα (X_1) is given by CONC_TGF. All other species are initially at 0. Regulatory species are internal glucose (determined from the metabolism module) for G, X_7 for C, and X_4 for P.

For complex metabolism, initial concentrations (in nM) are $X_2 = 25$, $X_6 = X_7 = 5$, $X_8 = X_9 = 2.5$, $X_{10} = 0.333$, $X_{11} = 0.667$, and $X_{12} = 5$. Extracellular TGFα (X_1) is given by CONC_TGF. All other species are initially at 0. Regulatory species

are internal glucose (determined from the metabolism module) for G, X_{11} for C, and X_4 for E, T, and P.

4.5. Simulation Data Analysis

4.5.1. Doubling Time

Doubling time is given by $(t_b - t_a) \cdot \ln 2 / \ln (N_b/N_a)$ where t is time and N is the number of cells. Doubling time is calculated for each seed at 7 days ($a = 0$ and $b = 7$) across $n = 50$ replicates. Doubling time is also calculated by $\ln 2/r$ where r is obtained by fitting an exponential curve $N = N_0 \exp(t \cdot r)$ to each seed for the first 7 days across $n = 50$ replicates.

4.5.2. Colony Diameter

Colony diameter D is calculated as the average of the diameter across the three hexagonal axes using $D = \mathcal{C}\left[\max(u_{max} - u_{min} + 1, 0) + \max(v_{max} - v_{min} + 1, 0) + \max(w_{max} - w_{min} + 1, 0)\right]/3$ where subscripts *max* and *min* refer to the maximum and minimum, respectively, of the given hexagonal coordinate across all cell locations at a given timepoint, and $\mathcal{C}$ is a scaling factor of 30 $\mu\text{m} \cdot \text{hex}^{-1}$ (`HEX_SIZE`). Colony diameter is calculated at each timepoint for $n = 50$ replicates.

4.5.3. Cell Diameter

Assuming a cylindrical cell whose volume v is calculated as $v = \pi r^2 h$ where r is radius and h is height, cell diameter d is given by $d = 2\sqrt{v/\pi h}$ using an average height of $h = 4.35$, which is calculated as half the max cell height (`MAX_HEIGHT`).

4.5.4. Fraction Occupancy

At a given seed and timepoint, the fraction occupancy at a radius r from the center is given by n/N_r where n is the number of agents of the state or population of interest and N_r is the maximum possible number of locations at radius r in a hexagonal grid. Note that fraction occupancy can exceed 1 as there can be more than a single agent per location.

4.5.5. Relative Fraction Change

For simulations in which there are multiple populations, the relative change in the fraction of a given population is calculated as $(x - x_0)/s$ where x is the fraction of the population, x_0 is the initial fraction of the population, and s is a scaling factor equal to $1 - x_0$ or x_0 if the change $(x - x_0)$ is positive or negative, respectively. For simulations using the tissue context, the healthy background population is not included in the calculation.

4.6. Emergent Behavior Metrics

4.6.1. Growth Rate

Growth rate quantifies the temporal emergence of colony diameter over time, in units of $\mu\text{m} \cdot \text{day}^{-1}$. For each time index i in [2, 2.5, ..., 14] days, a least squares linear fit between timepoints $[1, 1.5, ..., t_i]$ and colony diameters $[D_1, D_{1.5}, ..., D_i]$ is performed (Python, function `polyfit` from package `numpy` with degree of 1). The growth rate is taken as the slope of this line.

4.6.2. Symmetry

Symmetry quantifies the spatial emergence of colony shape at a given timepoint, ranging from 0 (not symmetric) to 1 (perfectly symmetric). In hexagonal coordinates, the colony is perfectly symmetric if for each location (`u, v, w`), the corresponding five locations (`-w, -u, -v`), (`v, w, u`), (`-u, -v, -w`), (`w, u, v`), and (`-v, -w, -u`) are all occupied. For a given seed and timepoint, for each unique occupied location i, the number of unoccupied corresponding locations n_i is determined. Duplicate locations are not counted. Symmetry is calculated as:

$$1 - \frac{1}{N}\sum_{i}^{N}\frac{n_i}{5}$$

where N is the number of unique occupied locations.

4.6.3. Cycle Length

Cycle length quantifies the parametric emergence of cell cycle length, in units of hours. Each cell agent tracks the number of ticks (minutes) between when it switches to a proliferative state and when it successfully divides to create a daughter cell agent. For a given seed and timepoint, cycle lengths are first averaged per agent, then averaged across all agents.

4.7. Data Fitting

4.7.1. Colony Size

For **Figure 2G**, an equation relating number of cells n, cell diameter d, and colony diameter D given by:

$$n = a\left(D^b/d^c\right)$$

with parameters a, b, and c (Meyskens et al., 1984), was fit to simulated data using non-linear least squares (Python, function `curve_fit` from package `scipy.optimize`).

4.7.2. Parameter Statistics

The average value x of each cell parameter across all cells at each timepoint is calculated for $n = 20$ replicates. The mean (μ) and standard deviation (σ) of these averages are estimated using:

$$\mu = \frac{1}{n}\sum_{i=1}^{n} x_i \quad \sigma = \sqrt{n^{-1}\sum_{i=1}^{n}(x_i - \mu)^2}$$

The distribution of average parameter values across replicates at a given timepoint is compared to the initial distribution of averages at $t = 0$ using a t-test with paired samples (Python, function `ttest_rel` from package `scipy.stats`). The variance of average parameter values across replicates at a given timepoint is compared to the variance of the initial distribution at $t = 0$ using Levene's test (Python, function `levene` from package `scipy.stats`).

4.8. Case Study Simulations

First, we select three parameters to reflect common cancerous cell phenotypes: (i) crowding tolerance (`MAX_HEIGHT`), which captures a cell's tolerance for crowding (**Supplementary Table 1**); (ii) metabolic preference (`META_PREF`), which controls a cell's preference for using glycolysis over oxidative phosphorylation to produce energy (**Supplementary Table 4**); and (iii) migratory threshold (`MIGRA_THRESHOLD`), which

governs a cell's tendency to migrate instead of proliferate (**Supplementary Table 5**). The crowding tolerance parameter quantifies the sensitivity of cells to contact inhibition, a phenomenon where cells stop growing even with sufficient nutrients when they reach a certain level of confluency (Swat et al., 2009). Cancerous cells exhibit reduced, or lack of, contact inhibition (Hanahan and Weinberg, 2011). The Warburg effect, in which cancerous cells predominantly produce energy through glycolysis rather than oxidative phosphorylation even in the presence of sufficient oxygen, is captured by the metabolic preference parameter (Heiden et al., 2009; Hanahan and Weinberg, 2011) Finally, cancer cell motility is an important factor in metastasis. We use the migratory threshold parameter to control the cell agent decision between migratory and proliferative states (Zhang et al., 2007).

Input options used to run the simulations are summarized in **Supplementary Table 3**.

4.8.1. Case Study 1: Context

We perform a sensitivity analysis on these parameters by varying the parameter value +/− 100% in increments of 10%. For each parameter and modification, cells were seeded in isolation and simulated for 14 days with 20 replicates and timepoints taken every 12 h. Four representative populations were selected: `A` (crowding tolerance at +50% of baseline), `B` (metabolic preference at +50% of baseline), `C` (migratory threshold at −50% of baseline), `X` (all parameters at baseline). All four representative populations have the ability to exit quiescence without external stimulation; in contrast, the generic background population used for tissue context simulations is unable to exit quiescence without stimulation. These populations, and combinations thereof, were simulated in isolation (colony, representing an *in vitro* context) and in an environment containing a generic background cell population (tissue, representing an *in vivo* context). Simulations were run for 15 days with the representative populations introduced at t = 1 day. All simulations were run with 20 replicates with timepoints taken every 12 h.

4.8.2. Case Study 2: Competition

A modified population is created by varying one of the three parameters (crowding tolerance, metabolic preference, and migratory threshold) between −50% and +50% in increments of 10%. This modified population is initialized into the simulation along with an unmodified, basal population in different ratios and simulated for 14 days. All simulations contain 20 replicates with timepoints taken every 12 h.

Note that we specifically focus on interactions between two populations, as is common with most co-culture studies (Goers et al., 2014). Including additional populations in our simulation is straightforward (one can introduce an additional cell agent or modify the parameters of an existing cell agent). However, including additional populations in an experimental setting is more difficult and may not necessarily form a more accurate representation of system; for example, a co-culture model of the blood-brain barrier system performed better than the mono- and tri-culture models (Hatherell et al., 2011; Goers et al., 2014). This counter-intuitive observation further motivates the need for a computational model with which to interrogate population interactions. In this case, our framework can be used to guide experimental design by identifying the minimal number of populations necessary to model a system.

4.8.3. Case Study 3: Heterogeneity

Within the model, certain cell parameters (such as initial cell volume and age) are derived from a distribution. However, the internal cell parameters are constant among cell agents within a given population. To add heterogeneity to these parameters, each cell agent was modified to draw its parameter values from truncated normal distributions with means equal to the defined parameter values and variances dictated by a new heterogeneity parameter (`HETEROGENEITY`, **Supplementary Table 1**). Daughter cells of the agent use the parent parameter values as the mean of the truncated normal distributions from which it draws its parameter values, enabling clonal evolution in which population means can tend toward more "fit" values.

We vary the heterogeneity within representative cell populations and simulate their evolution in both colony and tissue contexts. For the colony context, the generic background population also contains heterogeneity H_0, termed background heterogeneity, whose value is not necessarily equal to that of the representative populations. Simulations were run for 15 days with the representative populations introduced at t = 1 day. All simulations contain 20 replicates with timepoints taken every 12 h.

DATA AVAILABILITY STATEMENT

The datasets generated for this study are available on request to the corresponding author.

AUTHOR CONTRIBUTIONS

JY and NB: Conceptualization, Writing – Original Draft, and Writing – Review & Editing. JY: Software, Formal Analysis, and Visualization. NB: Supervision.

FUNDING

This work was supported by National Science Foundation Graduate Research Fellowship Program award DGE-1842165 to JY, National Science Foundation CAREER award CBET-1653315 to NB, and the Northwestern University Robert R. McCormick School of Engineering and Applied Science.

ACKNOWLEDGMENTS

This research was supported in part through the computational resources and staff contributions provided for the Quest

high performance computing facility at Northwestern University which is jointly supported by the Office of the Provost, the Office for Research, and Northwestern University Information Technology.

SUPPLEMENTARY MATERIAL

The Supplementary Material for this article can be found online at: https://www.frontiersin.org/articles/10.3389/fbioe.2020.00249/full#supplementary-material

REFERENCES

Abercrombie, M., and Heaysman, J. E. (1953). Observations on the social behaviour of cells in tissue culture. *Exp. Cell Res.* 5, 111–131. doi: 10.1016/0014-4827(53)90098-6

Alley, M. C., Scudiero, D. A., Monks, A., Hursey, M. L., Czerwinski, M. J., Fine, D. L., et al. (1988). Feasibility of drug screening with panels of human tumor cell lines using a microculture tetrazolium assay. *Cancer Res.* 48, 589–601.

Altschuler, S. J., and Wu, L. F. (2010). Cellular heterogeneity: do differences make a difference? *Cell* 141, 559–563. doi: 10.1016/j.cell.2010.04.033

An, G., Mi, Q., Dutta-Moscato, J., and Vodovotz, Y. (2009). Agent-based models in translational systems biology. *Wiley Interdiscipl. Rev. Syst. Biol. Med.* 1, 159–171. doi: 10.1002/wsbm.45

Athale, C., Mansury, Y., and Deisboeck, T. S. (2005). Simulating the impact of a molecular 'decision-process' on cellular phenotype and multicellular patterns in brain tumors. *J. Theor. Biol.* 233, 469–481. doi: 10.1016/j.jtbi.2004.10.019

Baker, B. M., and Chen, C. S. (2012). Deconstructing the third dimension–how 3d culture microenvironments alter cellular cues. *J. Cell Sci.* 125, 3015–3024. doi: 10.1242/jcs.079509

Balkwill, F. R., Capasso, M., and Hagemann, T. (2012). The tumor microenvironment at a glance. *J. Cell Sci.* 125, 5591–5596. doi: 10.1242/jcs.116392

Bonabeau, E. (2002). Agent-based modeling: methods and techniques for simulating human systems. *Proc. Natl. Acad. Sci. U.S.A.* 99(Suppl. 3), 7280–7287. doi: 10.1073/pnas.082080899

Brodland, G. W. (2015). How computational models can help unlock biological systems. *Semin. Cell Dev. Biol.* 47–48, 62–73. doi: 10.1016/j.semcdb.2015.07.001

Brúu, A., Albertos, S., Subiza, J. L., García-Asenjo, J. L., and Brú, I. (2003). The universal dynamics of tumor growth. *Biophys. J.* 85, 2948–2961. doi: 10.1016/S0006-3495(03)74715-8

Campisi, J., and d'Adda di Fagagna, F. (2007). Cellular senescence: when bad things happen to good cells. *Nat. Rev. Mol. Cell Biol.* 8, 729–740. doi: 10.1038/nrm2233

Childs, B. G., Baker, D. J., Kirkland, J. L., Campisi, J., and van Deursen, J. M. (2014). Senescence and apoptosis: dueling or complementary cell fates? *EMBO Rep.* 15, 1139–1153. doi: 10.15252/embr.201439245

Conger, A. D., and Ziskin, M. C. (1983). Growth of mammalian multicellular tumor spheroids. *Cancer Res.* 43, 556–560.

Cvijovic, M., Almquist, J., Hagmar, J., Hohmann, S., Kaltenbach, H.-M., Klipp, E., et al. (2014). Bridging the gaps in systems biology. *Mol. Genet. Genomics* 289, 727–734. doi: 10.1007/s00438-014-0843-3

Dagogo-Jack, I., and Shaw, A. T. (2017). Tumour heterogeneity and resistance to cancer therapies. *Nat. Rev. Clin. Oncol.* 15, 81–94. doi: 10.1038/nrclinonc.2017.166

Eckburg, P. B. (2005). Diversity of the human intestinal microbial flora. *Science* 308, 1635–1638. doi: 10.1126/science.1110591

Edinger, A. L., and Thompson, C. B. (2004). Death by design: apoptosis, necrosis and autophagy. *Curr. Opin. Cell Biol.* 16, 663–669. doi: 10.1016/j.ceb.2004.09.011

Elmore, S. (2007). Apoptosis: a review of programmed cell death. *Toxicol. Pathol.* 35, 495–516. doi: 10.1080/01926230701320337

Enderling, H., Hlatky, L., and Hahnfeldt, P. (2009). Migration rules: tumours are conglomerates of self-metastases. *Br. J. Cancer* 100, 1917–1925. doi: 10.1038/sj.bjc.6605071

Fan, Y., and Bergmann, A. (2008). Apoptosis-induced compensatory proliferation. The cell is dead. Long live the cell! *Trends Cell Biol.* 18, 467–473. doi: 10.1016/j.tcb.2008.08.001

Folcik, V. A., An, G. C., and Orosz, C. G. (2007). The basic immune simulator: an agent-based model to study the interactions between innate and adaptive immunity. *Theor. Biol. Med. Model.* 4:39. doi: 10.1186/1742-4682-4-39

Fràter-Schröder, M., Risau, W., Hallmann, R., Gautschi, P., and Böhlen, P. (1987). Tumor necrosis factor type α, a potent inhibitor of endothelial cell growth *in vitro*, is angiogenic *in vivo*. *Proc. Natl. Acad. Sci. U.S.A.* 84, 5277–5281. doi: 10.1073/pnas.84.15.5277

Freyer, J. P., and Sutherland, R. M. (1986). Proliferative and clonogenic heterogeneity of cells from emt6/ro multicellular spheroids induced by the glucose and oxygen supply. *Cancer Res.* 46, 3513–3520.

Glick, D., Barth, S., and Macleod, K. F. (2010). Autophagy: cellular and molecular mechanisms. *J. Pathol.* 221, 3–12. doi: 10.1002/path.2697

Goers, L., Freemont, P., and Polizzi, K. M. (2014). Co-culture systems and technologies: taking synthetic biology to the next level. *J. R. Soc. Interface* 11:20140065. doi: 10.1098/rsif.2014.0065

Gorochowski, T. E. (2016). Agent-based modelling in synthetic biology. *Essays Biochem.* 60, 325–336. doi: 10.1042/EBC20160037

Gorochowski, T. E., Matyjaszkiewicz, A., Todd, T., Oak, N., Kowalska, K., Reid, S., et al. (2012). BSim: an agent-based tool for modeling bacterial populations in systems and synthetic biology. *PLoS ONE* 7:e42790. doi: 10.1371/journal.pone.0042790

Gos, M., Miloszewska, J., Swoboda, P., Trembacz, H., Skierski, J., and Janik, P. (2005). Cellular quiescence induced by contact inhibition or serum withdrawal in c3h10t1/2 cells. *Cell Prolif.* 38, 107–116. doi: 10.1111/j.1365-2184.2005.00334.x

Gregorio, A. D., Bowling, S., and Rodriguez, T. A. (2016). Cell competition and its role in the regulation of cell fitness from development to cancer. *Dev. Cell* 38, 621–634. doi: 10.1016/j.devcel.2016.08.012

Hanahan, D., and Weinberg, R. A. (2011). Hallmarks of cancer: the next generation. *Cell* 144, 646–674. doi: 10.1016/j.cell.2011.02.013

Hatherell, K., Couraud, P.-O., Romero, I. A., Weksler, B., and Pilkington, G. J. (2011). Development of a three-dimensional, all-human *in vitro* model of the blood–brain barrier using mono-, co-, and tri-cultivation transwell models. *J. Neurosci. Methods* 199, 223–229. doi: 10.1016/j.jneumeth.2011.05.012

Heiden, M. G. V., Cantley, L. C., and Thompson, C. B. (2009). Understanding the warburg effect: the metabolic requirements of cell proliferation. *Science* 324, 1029–1033. doi: 10.1126/science.1160809

Heymach, J. V., Sledge, G. W. Jr., and Jain, R. K. (2010). *Chapter 11:Tumor Angiogenesis*. Shelton, CT: People's Medical Publishing House, 149.

Hickman, J. A., Graeser, R., de Hoogt, R., Vidic, S., Brito, C., Gutekunst, M., et al. and consortium, I. P. (2014). Three-dimensional models of cancer for pharmacology and cancer cell biology: Capturing tumor complexity *in vitro/ex vivo*. *Biotechnol. J.* 9, 1115–1128. doi: 10.1002/biot.201300492

Holcombe, M., Adra, S., Bicak, M., Chin, S., Coakley, S., Graham, A. I., et al. (2012). Modelling complex biological systems using an agent-based approach. *Integr. Biol.* 4, 53–64. doi: 10.1039/C1IB00042J

Huiskamp, G. (1991). Difference formulas for the surface laplacian on a triangulated surface. *J. Comput. Phys.* 95, 477–496. doi: 10.1016/0021-9991(91)90286-T

Kim, J. B., Stein, R., and O'Hare, M. J. (2004). Three-dimensional *in vitro* tissue culture models of breast cancer-a review. *Breast Cancer Res. Treat.* 85, 281–291. doi: 10.1023/B:BREA.0000025418.88785.2b

Kirkpatrick, C. J., Fuchs, S., and Unger, R. E. (2011). Co-culture systems for vascularization —learning from nature. *Adv. Drug Deliv. Rev.* 63, 291–299. doi: 10.1016/j.addr.2011.01.009

Kitada, T., DiAndreth, B., Teague, B., and Weiss, R. (2018). Programming gene and engineered-cell therapies with synthetic biology. *Science* 359:eaad1067. doi: 10.1126/science.aad1067

Lidstrom, M. E., and Konopka, M. C. (2010). The role of physiological heterogeneity in microbial population behavior. *Nat. Chem. Biol.* 6, 705–712. doi: 10.1038/nchembio.436

Luke, S., Cioffi-Revilla, C., Panait, L., Sullivan, K., and Balan, G. (2005). MASON: a multiagent simulation environment. *Simulation* 81, 517–527. doi: 10.1177/0037549705058073

Manukyan, L., Montandon, S. A., Fofonjka, A., Smirnov, S., and Milinkovitch, M. C. (2017). A living mesoscopic cellular automaton made of skin scales. *Nature* 544, 173–179. doi: 10.1038/nature22031

Marusyk, A., Almendro, V., and Polyak, K. (2012). Intra-tumour heterogeneity: a looking glass for cancer? *Nat. Rev. Cancer* 12, 323–334. doi: 10.1038/nrc3261

Mehdizadeh, H., Sumo, S., Bayrak, E. S., Brey, E. M., and Cinar, A. (2013). Three-dimensional modeling of angiogenesis in porous biomaterial scaffolds. *Biomaterials* 34, 2875–2887. doi: 10.1016/j.biomaterials.2012.12.047

Merino, M. M., Levayer, R., and Moreno, E. (2016). Survival of the fittest: essential roles of cell competition in development, aging, and cancer. *Trends Cell Biol.* 26, 776–788. doi: 10.1016/j.tcb.2016.05.009

Meyskens, F. L., Thomson, S. P., and Moon, T. E. (1984). Quantitation of the number of cells within tumor colonies in semisolid medium and their growth as oblate spheroids. *Cancer Res.* 44, 271–277.

Mirams, G. R., Arthurs, C. J., Bernabeu, M. O., Bordas, R., Cooper, J., Corrias, A., et al. (2013). Chaste: An open source c++ library for computational physiology and biology. *PLoS Comput. Biol.* 9:e1002970. doi: 10.1371/journal.pcbi.1002970

Norton, K.-A., Wallace, T., Pandey, N. B., and Popel, A. S. (2017). An agent-based model of triple-negative breast cancer: the interplay between chemokine receptor CCR5 expression, cancer stem cells, and hypoxia. *BMC Syst. Biol.* 11:1. doi: 10.1186/s12918-017-0445-x

Pienaar, E., Cilfone, N. A., Lin, P. L., Dartois, V., Mattila, J. T., Butler, J. R., et al. (2015). A computational tool integrating host immunity with antibiotic dynamics to study tuberculosis treatment. *J. Theor. Biol.* 367:166–179. doi: 10.1016/j.jtbi.2014.11.021

Poleszczuk, J., Hahnfeldt, P., and Enderling, H. (2015). Evolution and phenotypic selection of cancer stem cells. *PLoS Comput. Biol.* 11:e1004025. doi: 10.1371/journal.pcbi.1004025

Quail, D. F., and Joyce, J. A. (2013). Microenvironmental regulation of tumor progression and metastasis. *Nat. Med.* 19, 1423–1437. doi: 10.1038/nm.3394

Raser, J. M. (2004). Control of stochasticity in eukaryotic gene expression. *Science* 304, 1811–1814. doi: 10.1126/science.1098641

Ryoo, H. D., and Bergmann, A. (2012). The role of apoptosis-induced proliferation for regeneration and cancer. *Cold Spring Harb. Perspect. Biol.* 4:a008797. doi: 10.1101/cshperspect.a008797

Schmid, A., Kortmann, H., Dittrich, P. S., and Blank, L. M. (2010). Chemical and biological single cell analysis. *Curr. Opin. Biotechnol.* 21, 12–20. doi: 10.1016/j.copbio.2010.01.007

Segovia-Juarez, J. L., Ganguli, S., and Kirschner, D. (2004). Identifying control mechanisms of granuloma formation during *M. tuberculosis* infection using an agent-based model. *J. Theor. Biol.* 231, 357–376. doi: 10.1016/j.jtbi.2004.06.031

Smith, W. P. J., Davit, Y., Osborne, J. M., Kim, W., Foster, K. R., and Pitt-Francis, J. M. (2016). Cell morphology drives spatial patterning in microbial communities. *Proc. Natl. Acad. Sci. U.S.A.* 114, E280–E286. doi: 10.1073/pnas.1613007114

Stock, K., Estrada, M. F., Vidic, S., Gjerde, K., Rudisch, A., Santo, V. E., et al. (2016). Capturing tumor complexity *in vitro*: comparative analysis of 2d and 3d tumor models for drug discovery. *Sci. Rep.* 6:28951. doi: 10.1038/srep28951

Swat, A., Dolado, I., Rojas, J. M., and Nebreda, A. R. (2009). Cell density-dependent inhibition of epidermal growth factor receptor signaling by p38α mitogen-activated protein kinase via sprouty2 downregulation. *Mol. Cell. Biol.* 29, 3332–3343. doi: 10.1128/MCB.01955-08

Swat, M. H., Thomas, G. L., Belmonte, J. M., Shirinifard, A., Hmeljak, D., and Glazier, J. A. (2012). Multi-scale modeling of tissues using CompuCell3D. *Comput. Methods Cell Biol.* 110, 325–366. doi: 10.1016/B978-0-12-388403-9.00013-8

Talkington, A., and Durrett, R. (2015). Estimating tumor growth rates *in vivo*. *Bull. Math. Biol.* 77, 1934–1954. doi: 10.1007/s11538-015-0110-8

Thorne, B. C., Bailey, A. M., and Peirce, S. M. (2007). Combining experiments with multi-cell agent-based modeling to study biological tissue patterning. *Brief. Bioinformatics* 8, 245–257. doi: 10.1093/bib/bbm024

Toledo, F., and Wahl, G. M. (2006). Regulating the p53 pathway: *in vitro* hypotheses, *in vivo* veritas. *Nat. Rev. Cancer*, 6, 909–923. doi: 10.1038/nrc2012

Valcourt, J. R., Lemons, J. M., Haley, E. M., Kojima, M., Demuren, O. O., and Coller, H. A. (2012). Staying alive. *Cell Cycle* 11, 1680–1696. doi: 10.4161/cc.19879

Walling, M. A., and Shepard, J. R. E. (2011). Cellular heterogeneity and live cell arrays. *Chem. Soc. Rev.* 40, 4049. doi: 10.1039/c0cs00212g

Walpole, J., Chappell, J. C., Cluceru, J. G., Gabhann, F. M., Bautch, V. L., and Peirce, S. M. (2015). Agent-based model of angiogenesis simulates capillary sprout initiation in multicellular networks. *Integr. Biol.* 7, 987–997. doi: 10.1039/C5IB00024F

Wang, D., Liu, Y., Zhang, R., Zhang, F., Sui, W., Chen, L., et al. (2016). Apoptotic transition of senescent cells accompanied with mitochondrial hyper-function. *Oncotarget* 7, 28286–28300. doi: 10.18632/oncotarget.8536

Wang, F., Weaver, V. M., Petersen, O. W., Larabell, C. A., Dedhar, S., Briand, P., et al. (1998). Reciprocal interactions between β1-integrin and epidermal growth factor receptor in three-dimensional basement membrane breast cultures: a different perspective in epithelial biology. *Proc. Natl. Acad. Sci. U.S.A.* 95, 14821–14826. doi: 10.1073/pnas.95.25.14821

Winslow, R. L., Trayanova, N., Geman, D., and Miller, M. I. (2012). Computational medicine: Translating models to clinical care. *Sci. Transl. Med.* 4:158rv11. doi: 10.1126/scitranslmed.3003528

Yao, G. (2014). Modelling mammalian cellular quiescence. *Interface Focus* 4, 20130074. doi: 10.1098/rsfs.2013.0074

Yu, J. S., and Bagheri, N. (2016). Multi-class and multi-scale models of complex biological phenomena. *Curr. Opin. Biotechnol.* 39, 167–173. doi: 10.1016/j.copbio.2016.04.002

Zernicka-Goetz, M. (2004). First cell fate decisions and spatial patterning in the early mouse embryo. *Semin. Cell Dev. Biol.* 15, 563–572. doi: 10.1016/j.semcdb.2004.04.004

Zhang, L., Athale, C. A., and Deisboeck, T. S. (2007). Development of a three-dimensional multiscale agent-based tumor model: simulating gene-protein interaction profiles, cell phenotypes and multicellular patterns in brain cancer. *J. Theor. Biol.* 244, 96–107. doi: 10.1016/j.jtbi.2006.06.034

Zhang, R., Lahens, N. F., Ballance, H. I., Hughes, M. E., and Hogenesch, J. B. (2014). A circadian gene expression atlas in mammals: Implications for biology and medicine. *Proc. Natl. Acad. Sci. U.S.A.* 111, 16219–16224. doi: 10.1073/pnas.1408886111

Zong, W.-X. (2006). Necrotic death as a cell fate. *Genes Dev.* 20, 1–15. doi: 10.1101/gad.1376506

Conflict of Interest: The authors declare that the research was conducted in the absence of any commercial or financial relationships that could be construed as a potential conflict of interest.

Copyright © 2020 Yu and Bagheri. This is an open-access article distributed under the terms of the Creative Commons Attribution License (CC BY). The use, distribution or reproduction in other forums is permitted, provided the original author(s) and the copyright owner(s) are credited and that the original publication in this journal is cited, in accordance with accepted academic practice. No use, distribution or reproduction is permitted which does not comply with these terms.

frontiers in Bioengineering and Biotechnology

ORIGINAL RESEARCH
published: 17 June 2020
doi: 10.3389/fbioe.2020.00501

Mathematical Details on a Cancer Resistance Model

James M. Greene[1], *Cynthia Sanchez-Tapia*[2] *and Eduardo D. Sontag*[3,4]*

[1] Department of Mathematics, Clarkson University, Potsdam, NY, United States, [2] Department of Mathematics and Center for Quantitative Biology, Rutgers University, Piscataway, NJ, United States, [3] Department of Electrical and Computer Engineering, Department of Bioengineering, Northeastern University, Boston, MA, United States, [4] Laboratory of Systems Pharmacology, Program in Therapeutic Science, Harvard Medical School, Boston, MA, United States

One of the most important factors limiting the success of chemotherapy in cancer treatment is the phenomenon of drug resistance. We have recently introduced a framework for quantifying the effects of induced and non-induced resistance to cancer chemotherapy (Greene et al., 2018a, 2019). In this work, we expound on the details relating to an optimal control problem outlined in Greene et al. (2018a). The control structure is precisely characterized as a concatenation of bang-bang and path-constrained arcs via the Pontryagin Maximum Principle and differential Lie algebraic techniques. A structural identifiability analysis is also presented, demonstrating that patient-specific parameters may be measured and thus utilized in the design of optimal therapies prior to the commencement of therapy. For completeness, a detailed analysis of existence results is also included.

Keywords: drug resistance, chemotherapy, phenotype, optimal control theory, singular controls

OPEN ACCESS

Edited by:
Julio R. Banga, Consejo Superior de Investigaciones Científicas (CSIC), Spain

Reviewed by:
Sebastian Sager, Otto von Guericke University Magdeburg, Germany
James William Thomas Yates, AstraZeneca, United Kingdom

***Correspondence:**
Eduardo D. Sontag
sontag@sontaglab.org

Specialty section:
This article was submitted to Bioinformatics and Computational Biology, a section of the journal Frontiers in Bioengineering and Biotechnology

Received: *30 January 2020*
Accepted: *29 April 2020*
Published: *17 June 2020*

Citation:
Greene JM, Sanchez-Tapia C and Sontag ED (2020) Mathematical Details on a Cancer Resistance Model. Front. Bioeng. Biotechnol. 8:501. doi: 10.3389/fbioe.2020.00501

1. INTRODUCTION

The ability of cancer chemotherapies to successfully eradicate cancer populations is limited by the presence of drug resistance. Cells may become resistant through a variety of cellular and micro-environmental mechanisms (Gottesman, 2002). These mechanisms are exceedingly complex and diverse, and remain to be completely understood. Equally complex is the manner in which cancer cells obtain the resistant phenotype. Classically resistance was understood to be conferred by random genetic mutations; more recently, the role of epigenetic phenotype switching was discovered as another mediator of resistance (Pisco et al., 2013). Importantly, both of these phenomena were seen as drug-independent, so that the generation of resistance is functionally separate from the selection mechanism (e.g., the drug). However, experimental studies from the past ten years suggest that drug resistance in cancer may actually be induced by the application of chemotherapy (Sharma et al., 2010; Pisco et al., 2013; Goldman et al., 2015; Doherty et al., 2016; Shaffer et al., 2017).

In view of the multitude of ways by which a cancer cell may become chemoresistant, we have previously introduced a mathematical framework to differentiate drug-independent from drug-dependent resistance (Greene et al., 2019). In that work, we demonstrated that induced resistance may play a crucial role in therapy outcome, and also discussed methods by which a treatment's induction potential may be identified via biological assays. An extension of the work was outlined in the conference paper (Greene et al., 2018a), where a formal optimal control problem was introduced and an initial mathematical analysis was performed. The aim of this work is to formalize the parameter identifiability properties of our theoretical model, to establish the existence of the optimal control introduced in Greene et al. (2018a), and to precisely classify the

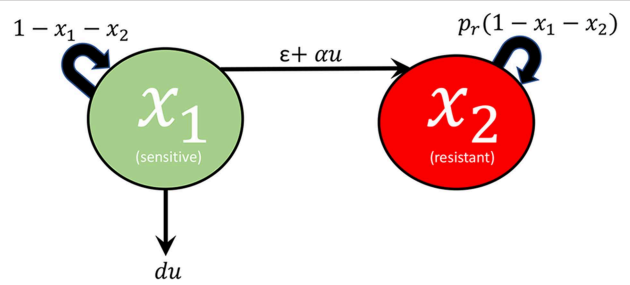

FIGURE 1 | Visualization of interactions considered in system (1).

optimal control structure utilizing the Pontryagin Maximum Principle and differential-geometric techniques. A numerical investigation of both the control structure and corresponding objective is also undertaken as a function of patient-specific parameters, and clinical conclusions are emphasized.

The work is organized as follows. In section 2, we briefly review the mathematical model together with the underlying assumptions. Section 3 restates the optimal control problem, and the Maximum Principle is analyzed in section 4. A precise theoretical characterization of the optimal control structure is summarized in section 5. In section 6, we compare theoretical results with numerical computations, and investigate the variation in control structure and objective as a function of parameters. Conclusions are presented in section 8. We also include additional properties, including details on structural identifiability and existence of optimal controls, in Section 7.

2. MATHEMATICAL MODELING OF INDUCED DRUG RESISTANCE

We briefly review the model presented in Greene et al. (2019) and analyzed further in Greene et al. (2018a). In that work, we have constructed a simple dynamical model which describes the evolution of drug resistance through both drug-independent (e.g., random point mutations, gene amplification, stochastic state switching) and drug-dependent (e.g., mutagenicity, epigenetic modifications) mechanisms. Drug-induced resistance, although experimentally observed, remains poorly understood. It is our hope that a mathematical analysis will provide mechanistic insight and produce a more complete understanding of this process by which cancer cells inhibit treatment efficacy.

A network diagram of the model under consideration is provided in **Figure 1**. Specifically, we assume that the tumor being studied is composed of two types of cells: sensitive (x_1) and resistant (x_2). For simplicity, the drug is taken as completely ineffective against the resistant population, while the log-kill hypothesis (Traina and Norton, 2011) is assumed for the sensitive cells. Complete resistance is of course unrealistic, but can serve as a reasonable approximation, especially when toxicity constraints may limit the total amount of drug that may be administered. Furthermore, this assumption permits a natural metric on treatment efficacy that may not exist otherwise (see section 3). The effect of treatment is considered as a control agent $u(t)$, which we assume is a locally bounded Lebesgue measurable function taking values in $\mathbb{R}_+$. Here $u(t)$ is directly related to the applied drug dosage $D(t)$, and in the present work we assume that we have explicit control over $u(t)$. Later, during the formulation of the optimal control problem (section 3), we will make precise specifications on the control set U. Even though an arbitrary dosage schedule is unrealistic as a treatment strategy, our objective in this work is to understand the fundamental mathematical questions associated with drug-induced resistance, so we believe the simplification is justified. Furthermore, our results in section 5 suggest that the applied optimal treatment should take a relatively simple form, which may be approximated with sufficient accuracy in a clinical setting. Sensitive and resistant cells are assumed to compete for resources in the tumor microenvironment; this is modeled via a joint carrying capacity, which we have scaled to one. Furthermore, cells are allowed to transition between the two phenotypes in both a drug-independent and drug-dependent manner. All random transitions to the resistant phenotype are modeled utilizing a common term, ϵx_1, which accounts for both genetic mutations and epigenetic events occurring independently of the application of treatment. Drug-induced deaths are assumed of the form $du(t)x_1$, where d is the drug cytotoxicity parameter relating to the log-kill hypothesis. Drug-induced transitions are assumed to be of the form $\alpha u(t)x_1$, which implies that the per-capita drug-induced transition rate is directly proportional to the dosage [as we assume full control on $u(t)$, i.e. pharmacokinetics are ignored]. Of course, other functional relationships may exist, but since the problem is not well-studied, we consider it reasonable to begin our analysis in this simple framework. The above assumptions then yield the following system of ordinary differential equations (ODEs):

$$\begin{aligned} \frac{dx_1}{dt} &= \left(1 - (x_1 + x_2)\right) x_1 - (\epsilon + \alpha u(t))x_1 - du(t)x_1 \\ \frac{dx_2}{dt} &= p_r \left(1 - (x_1 + x_2)\right) x_2 + (\epsilon + \alpha u(t))x_1. \end{aligned} \tag{1}$$

All parameters are taken as non-negative, and $0 \leq p_r < 1$. The restriction on p_r emerges due to (1) already being non-dimensionalized, as p_r represents the relative growth rate of the resistant population with respect to that of the sensitive cells. The condition $p_r < 1$ thus assumes that the resistant cells divide more slowly than their sensitive counterparts, which is observed experimentally (Shackney et al., 1978; Lee, 1993; Brimacombe et al., 2009). As mentioned previously, many simplifying assumptions are made in system (1). Specifically, both types of resistance (random genetic and epigenetic) are modeled as dynamically equivalent; both possess the same division rate p_r and spontaneous (i.e., drug-independent) transition rate ϵ. Thus, the resistant compartment x_2 denotes the total resistant subpopulation.

The region

$$\Omega = \{(x_1, x_2) \,|\, 0 \leq x_1 + x_2 \leq 1,\, x_1, x_2 \geq 0\} \tag{2}$$

in the first quadrant is forward invariant for any locally bounded Lebesgue measurable treatment function $u(t)$ taking values in $\mathbb{R}_+$. Furthermore, if $\epsilon > 0$, the population of (1) becomes asymptotically resistant:

$$\begin{pmatrix} x_1(t) \\ x_2(t) \end{pmatrix} \xrightarrow{t\to\infty} \begin{pmatrix} 0 \\ 1 \end{pmatrix}. \tag{3}$$

For a proof, see Theorem 2 in SI A in Greene et al. (2019). Thus in our model, the phenomenon of drug resistance is inevitable. However, we may still implement control strategies which, for example, may increase patient survival time. Such aspects will inform the objective introduced in section 3. For more details on the formulation and dynamics of system (1), we refer the reader to Greene et al. (2019).

3. OPTIMAL CONTROL FORMULATION

As discussed in section 2, all treatment strategies $u(t)$ result in an entirely resistant tumor: $\bar{x} := (\bar{x}_1, \bar{x}_2) = (0, 1)$ is globally asymptotically stable for all initial conditions in region Ω. Thus, any chemotherapeutic protocol will eventually fail, and a new drug must be introduced (not modeled in this work, but the subject of future study). Therefore, selecting an objective which minimizes tumor volume $(x_1 + x_2)$ or resistant fraction $[x_2/(x_1 + x_2)]$ at a fixed time horizon would be specious for our modeling framework. However, one can still combine therapeutic efficacy and clonal competition to influence transient dynamics and possibly prolong patient life, as has been shown clinically utilizing real-time patient data (Gatenby et al., 2009).

Toxicity as well as pharmacokinetic constraints limit the amount of drug to be applied at any given instant. Thus, we assume that there exists some number $M > 0$ such that $u(t) \leq M$ for all $t \geq 0$. Any Lebesgue measurable treatment regime $u(t)$ is considered, so that the control set is $U = [0, M]$ and the set of admissible controls $\mathcal{U}$ is

$$\mathcal{U} = \{u : [0, \infty) \to [0, M] \mid u \text{ is Lebesgue measurable}\}. \tag{4}$$

Recall that all cellular populations have been normalized to remain in $[0, 1]$. We assume that there is a *critical tumor volume* V_c, at which treatment, by definition, has failed. Our interpretation is that a tumor volume larger than V_c interferes with normal biological function, while $x_1 + x_2 \leq V_c$ indicates a clinically acceptable state. Different diseases will have different V_c values. For technical reasons needed in section 5 we assume that $V_c < 1 - \epsilon$. This is a mild assumption, since genetic mutation rates ϵ are generally small (Loeb et al., 1974), and our interest is on the impact of induced resistance. Thus

$$V_c \in (0, 1 - \epsilon). \tag{5}$$

Define t_c as the time at which the tumor increases above size V_c for the first time. To be precise,

$$t_c(u) := \max\{T \mid x_1(t) + x_2(t) \leq V_c \text{ for all } t \in [0, T]\}. \tag{6}$$

Since all treatments approach the state $(0, 1)$, $t_c(u)$ is well-defined for each treatment $u(t)$. For simplicity, denote $t_c = t_c(u)$ in the remainder of the work. The time t_c is then a measure of treatment efficacy, and our goal is then to find those controls u_* which maximize t_c. Writing in standard form as a minimization problem, we have the following objective:

$$\min_{u\in\mathcal{U}}\{J(u)\} = \min_{u\in\mathcal{U}}\left\{ -\int_0^{t_c} 1\, dt \right\}. \tag{7}$$

We are thus seeking a control $u_*(t) \in \mathcal{U}$ which *maximizes* t_c, i.e. solves the time-optimal minimization problem (7) restricted to the dynamic state equations given by the system described in (1) and the condition $x_1(t) + x_2(t) \leq V_c$ for all $0 \leq t \leq t_c$. Note that the above is formulated (using the negative sign) as a *minimization* problem to be consistent with previous literature and results related to the Pontryagin Maximum Principle (PMP) (Ledzewicz and Schättler, 2012). Note that maximization is still utilized in section 7.2 and section 4.1, and we believe that the objective will be clear from context. To be consistent with notation utilized later, we denote the system (1) as

$$\dot{x} = f(x) + u(t)g(x), \tag{8}$$

where

$$f(x) = \begin{pmatrix} (1 - (x_1 + x_2))x_1 - \epsilon x_1 \\ p_r(1 - (x_1 + x_2))x_2 + \epsilon x_1 \end{pmatrix}, \tag{9}$$

$$g(x) = \begin{pmatrix} -(\alpha + d) \\ \alpha \end{pmatrix} x_1 \tag{10}$$

and $x(t) = (x_1(t), x_2(t))$. By continuity of solutions, the time t_c must satisfy the terminal condition $(t_c, x(t_c)) \in N$, where N is the line $x_1 + x_2 = V_c$ in Ω, i.e.,

$$N = \psi^{-1}(0) \cap \Omega, \tag{11}$$

where

$$\psi(x_1, x_2) := x_1 + x_2 - V_c. \tag{12}$$

With this notation, the path-constraint

$$\psi(x_1(t), x_2(t)) \leq 0 \tag{13}$$

must also hold for $0 \leq t \leq t_c$. Equation (13) ensures that the tumor remains below critical volume V_c for the duration of treatment. Equivalently, the dynamics are restricted to lie in the set $\Omega_c \subseteq \Omega$, where

$$\Omega_c := \{(x_1, x_2) \mid 0 \leq x_1 + x_2 \leq V_c,\, x_1, x_2 \geq 0\}, \tag{14}$$

for all times t such that $t \in [0, t_c]$. The initial state

$$x_0 = (x_1^0, x_2^0) \tag{15}$$

is also assumed to lie in Ω_c. Except for section 7.1 where we restrict to the case $x_2^0 = 0$, the remainder of the work allows for arbitrary $x_2^0 \in [0, V_c)$.

4. MAXIMUM PRINCIPLE

We dedicate the present section to characterize the optimal control utilizing the Pontryagin Maximum Principle (PMP). The subsequent analysis is strongly influenced by the Lie-derivative techniques introduced by Sussmann (1982, 1987a,b,c). For an excellent source on both the general theory and applications to cancer biology, see the textbooks by Ledzewicz and Schättler (2012) and Schättler and Ledzewicz (2015).

Before starting our analysis of the behavior and response of system (1) to applied treatment strategies $u(t)$ utilizing geometric methods, we would like to mention that we have not found a reference for existence of optimal controls for a problem such as this, due perhaps to the non-standard character of it (maximization of time, path constraints). For this reason, we have added a self-contained proof of regarding existence in section 7.2.

4.1. Elimination of Path Constraints

We begin our analysis by separating interior controls from those determined by the path-constraint (13) (equivalently, $x \in N$). The following theorem implies that outside of the one-dimensional manifold N, the optimal pair (x_*, u_*) solves the same local optimization problem without the path and terminal constraints. More precisely, the necessary conditions of the PMP (see section 4.2) at states not on N are exactly the conditions of the corresponding maximization problem with no path or terminal constraints.

Theorem 1. *Suppose that x_* is an optimal trajectory. Let t_1 be the first time such that $x_*(t) \in N$. Fix $\delta > 0$ such that $t_1 - \delta > 0$, and*

$$\xi = x_*(t_1 - \delta). \tag{16}$$

Define $z(t) := x_*(t)|_{t\in[0,t_1-\delta]}$. Then the trajectory z is a local solution of the corresponding time maximization problem t_c with boundary conditions $x(0) = x^0$, $x(t_c) = \xi$, and no additional path constraints. Hence at all times t, the path z (together with the corresponding control and adjoint) must satisfy the corresponding unconstrained Pontryagin Maximum Principle.

Proof: We first claim that z satisfies the path-constrained maximization problem with boundary conditions $x(0) = x^0, x(t_c) = \xi$. This is a standard dynamic programming argument: if there exists a trajectory $\bar{z}$ such that $\bar{z}(\tau) = \xi$, $\tau > t_1 - \delta$, concatenate $\bar{z}(t)|_{t\in[0,\tau]}$ with $x_*(t)|_{t\in[\tau,t_c]}$ at $t = \tau$ to obtain a feasible trajectory satisfying all constraints. This trajectory then has total time $\tau + \delta + t_c - t_1 > t_c$, contradicting the global optimality of x_*.

Recall that t_1 was the first time such that $x_*(t) \in N$. Since z is compact, we can find a neighborhood of z that lies entirely in $\{x \,|\, x \notin N\}$. As the Maximum Principle is a local condition with respect to the state, this completes the proof. □

Theorem 1 then tells us that for states $x = (x_1, x_2)$ such that $x_1 + x_2 < V_c$, the corresponding unconstrained PMP must be satisfied by any extremal lift of the original problem. (Recall that an extremal lift of an optimal trajectory is obtained by adding the Lagrange multipliers, or adjoint variables, to the control and state; see details in Definition 2.2.4, page 95, Chapter 2 of Ledzewicz and Schättler, 2012). We have now demonstrated that the optimal control consists of concatenations of controls obtained from the unconstrained necessary conditions and controls of the form (18). In the next section, we analyze the Maximum Principle in the region $x_1 + x_2 < V_c$. Furthermore, the constraint (13) has generic order one. In other words,

$$L_g\psi = \nabla\psi \cdot g \neq 0. \tag{17}$$

Therefore, the feedback control (also known as the constrained control) can be found by differentiating the function (12) to insure that trajectories remain on the line N:

$$u_p(x_1, x_2) = \frac{1}{d}\frac{(1 - (x_1 + x_2))(x_1 + p_r x_2)}{x_1}. \tag{18}$$

Its existence however does not imply its feasibility, which is discussed below. Specifically, u_p can be shown to be a decreasing function of x_1 which is feasible on the portion of N satisfying $x_1^* \leq x_1 \leq V_c$, where x_1^* is given in (20), and infeasible elsewhere. This is proven in Proposition 3, and the geometric structure is depicted in **Figure 2**. Propositions 4 and 5 provide characterizations of the volume dynamics in certain regions of phase space, and are included here for completeness.

Proposition 2. *Suppose that the maximal dosage M satisfies*

$$M > \frac{(1 - V_c)(1 - p_r)}{d}. \tag{19}$$

and the point $x^* = (x_1^*, x_2^*) \in N$ with coordinates

$$\begin{aligned} x_1^* &= \frac{p_r(1 - V_c)V_c}{dM - (1 - V_c)(1 - p_r)}, \\ x_2^* &= V_c\left(1 - \frac{p_r(1 - V_c)}{dM - (1 - V_c)(1 - p_r)}\right). \end{aligned} \tag{20}$$

Denote by $Y(x) = f(x) + Mg(x)$ the vector field corresponding to the maximal allowed dosage M [here, f and g are the functions defined in (9), (10)]. The Lie derivative, for any $x \in N$, of the volume function $V(x) = x_1 + x_2$ with respect to Y is

(a) positive if $x_1 < x_1^*$,
(b) zero at (x_1^*, x_2^*), and
(c) negative if $x_1 > x_1^*$.

Proof: We verify the above claims with a direct calculation. Let $L_Y V(x)$ denotes the Lie derivative of $V(x)$ with respect to Y. Thus, for $x \in N$,

$$L_Y V(x) = \nabla V(x) \cdot Y(x)$$

$$= \begin{pmatrix} 1 \\ 1 \end{pmatrix} \cdot \begin{pmatrix} [1 - V_c - \epsilon - (\alpha + d)M]x_1 \\ \\ [\epsilon + \alpha M - p_r(1 - V_c)]x_1 + p_r(1 - V_c)V_c \end{pmatrix}$$

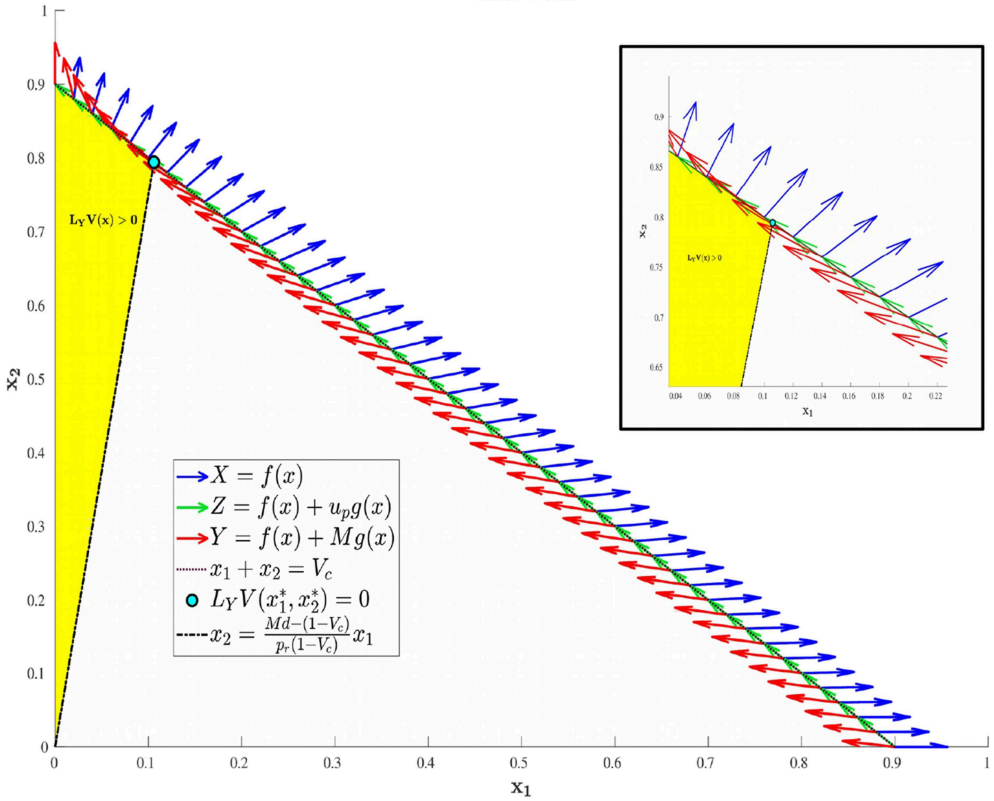

FIGURE 2 | Region in Ω_c where $L_Y V(x)$ is guaranteed to be positive. That is, applying the maximal dosage M results in an increasing cancer population in the yellow-shaded region of phase-space.

$$
\begin{aligned}
&= [1 - V_c - \epsilon - (\alpha + d)M]x_1 \\
&+ [\epsilon + \alpha M - p_r(1 - V_c)]x_1 \\
&+ p_r(1 - V_c)V_c \\
\\
&= [(1 - V_c)(1 - p_r) - dM]x_1 + p_r(1 - V_c)V_c.
\end{aligned}
$$

Assuming $M > \frac{(1-V_c)(1-p_r)}{d}$, the sign of $L_Y V(x)$ is as in the statement of the proposition. □

Proposition 2 implies that if the allowable dosage is large enough (Equation 9), treatment can at least decrease the tumor in certain regions of phase space. If this condition was not met, then the applied drug would generally be ineffective in reducing the tumor volume V, and hence not be utilized in a clinical scenario.

Proposition 3. *Let x be a point on the line N. The feedback control u_p is unfeasible if $x_1 \in (0, x_1^*)$, and is feasible if $x_1 \in (x_1^*, V_c)$*

Proof: For $x \in N$ we compute

$$u_p(x) = \frac{(1 - V_c)(1 - p_r)}{d} + \frac{(1 - V_c)p_r V_c}{dx_1} \geq 0.$$

It is straightforward to check that $u_p > M$ if $x_1 < x_1^*$. In addition, the feedback control, when restricted to points in N, is a decreasing function with respect to x_1. Thus, it is feasible for $x \in N$ if $x_1 \in (x_1^*, V_c)$. □

Proposition 4. *For $x = (x_1, x_2) \in \Omega_c$ with*

$$x_2 > \frac{dM - (1 - V_c)}{p_r(1 - V_c)} x_1, \tag{21}$$

the Lie derivative $L_Y V(x)$ is positive.

Proof: As in Proposition 2, we compute $L_Y V(x)$ directly:

$$
\begin{aligned}
L_Y V(x) &= (1 - (x_1 + x_2))(x_1 + p_r x_2) - dMx_1 \\
&\geq (1 - V_c)(x_1 + p_r x_2) - dMx_1 \\
&= [(1 - V_c) - dM]x_1 + p_r(1 - V_c)x_2 \\
&> [(1 - V_c) - dM]x_1 + p_r(1 - V_c)\frac{dM - (1 - V_c)}{p_r(1 - V_c)} x_1 \\
&= 0,
\end{aligned}
$$

where the first inequality utilizes $V \leq V_c$, and the second relies on (21) □

Proposition 5. *For*

$$M > \frac{1-\epsilon}{\alpha+d},$$

trajectories corresponding to the maximal dosage M have a decreasing sensitive cellular population.

Proof: For $u(t) \equiv M$, the corresponding sensitive trajectory is given by

$$\begin{aligned}\dot{x_1} &= (1-(x_1+x_2))x_1 - \epsilon x_1 - (\alpha+d)Mx_1 \\ &< (1-(x_1+x_2))x_1 - \epsilon x_1 - (1-\epsilon)x_1 \\ &= -(x_1+x_2)x_2 \leq 0\end{aligned}$$

Note that we are assuming here that the maximal dosage M satisfies $M > \frac{1-\epsilon}{\alpha+d}$. □

4.2. Maximum Principle and Necessary Conditions at Interior Points

Necessary conditions for the optimization problem discussed in section 3 without path or terminal constraints are derived from the Pontryagin Maximum Principle (Pontryagin, 1987; Ledzewicz and Schättler, 2012). The corresponding Hamiltonian function H is defined as

$$H(\lambda_0, \lambda, x, u) = -\lambda_0 + \langle \lambda, f(x) \rangle + u\Phi(x, \lambda), \tag{22}$$

where $\lambda_0 \geq 0$ and $\lambda \in \mathbb{R}^2$. Here $\langle \cdot, \cdot \rangle$ denotes the standard inner product on $\mathbb{R}^2$ and, since the dynamics are affine in the control u, $\Phi(x, \lambda)$ is the switching function:

$$\Phi(x, \lambda) = \langle \lambda, g(x) \rangle. \tag{23}$$

The Maximum Principle then yields the following theorem:

Theorem 6. *If the extremal (x_*, u_*) is optimal, there exists $\lambda_0 \geq 0$ and a covector (adjoint) $\lambda : [0, t_c] \to (\mathbb{R}^2)^*$, such that the following hold:*

1. *$(\lambda_0, \lambda(t)) \neq 0$ for all $t \in [0, t_c]$.*
2. *$\lambda(t) = (\lambda_1(t), \lambda_2(t))$ satisfies the second-order differential equation*

$$\begin{aligned}\dot{\lambda}(t) = &\begin{pmatrix} 2x_1 + x_2 + \epsilon - 1 & p_r x_2 - \epsilon \\ x_1 & p_r(2x_2 + x_1 - 1) \end{pmatrix} \lambda(t) \\ &+ u(t) \begin{pmatrix} \alpha + d & -\alpha \\ 0 & 0 \end{pmatrix} \lambda(t)\end{aligned} \tag{24}$$

3. *$u_*(t)$ minimizes H pointwise over the control set U:*

$$H(\lambda_0, \lambda, x_*(t), u_*(t)) = \min_{v \in U} H(\lambda_0, \lambda, x_*(t), v).$$

Thus, the control $u_*(t)$ must satisfy

$$u_*(t) = \begin{cases} 0 & \Phi(t) > 0, \\ M & \Phi(t) < 0. \end{cases} \tag{25}$$

where

$$\Phi(t) := \Phi(x_*(t), \lambda(t)). \tag{26}$$

4. *The Hamiltonian H is identically zero along the extremal lift $(x_*(t), u_*(t), \lambda(t))$:*

$$H(\lambda_0, \lambda(t), x_*(t), u_*(t)) \equiv 0. \tag{27}$$

Proof: Most statements of Theorem 6 follow directly from the Maximum Principle, so proofs are omitted. In particular, items (1), (2), and the first part of (3) are immediate consequences (Ledzewicz and Schättler, 2012). Equation (25) follows directly since we minimize the function H, which is affine in u (see Equation 22). The Hamiltonian vanishes along $(x_*(t), u_*(t), \lambda(t))$ since it is independent of an explicit time t dependence and the final time t_c is free, the latter being a consequence of the transversality condition. □

Proposition 7. *For all $t \in [0, t_c]$, the adjoint $\lambda(t)$ corresponding to the extremal lift $(x_*(t), u_*(t), \lambda(t))$ is nonzero.*

Proof: This is a general result relating to free end time problems. We include a proof here for completeness. Suppose that there exists a time $t \in [0, t_c]$ such that $\lambda(t) = 0$. By (22), the corresponding value of the Hamiltonian is $H(\lambda_0, \lambda(t), x_*(t), u_*(t)) = -\lambda_0$. By item (4) in Theorem 6, $H \equiv 0$, which implies that $\lambda_0 = 0$. This contradicts item (1) in Theorem 6. Hence, $\lambda(t) \neq 0$ on $[0, t_c]$. □

4.3. Geometric Properties and Existence of Singular Arcs

We now undertake a geometric analysis of the optimal control problem utilizing the affine structure of system (8) for interior states (i.e., controls which satisfy Theorem 6). We call such controls *interior extremals*, and all extremals in this section are assumed to be interior. The following results depend on the independence of the vector fields f and g, which we use to both classify the control structure for abnormal extremal lifts (extremal lifts with $\lambda_0 = 0$), as well as characterize the switching function dynamics via the Lie bracket.

Proposition 8. *For all $x_1 \in \Omega, x_1 > 0$, the vector fields $f(x)$ and $g(x)$ are linearly independent.*

Proof: Define $A(x) = A(x_1, x_2)$ to be the matrix

$$\begin{aligned}A(x) &= \begin{pmatrix} f(x) & g(x) \end{pmatrix} \\ &= \begin{pmatrix} (1-(x_1+x_2)-\epsilon)x_1 & -(\alpha+d)x_1 \\ p_r(1-(x_1+x_2))x_2 + \epsilon x_1 & \alpha x_1 \end{pmatrix}.\end{aligned} \tag{28}$$

The determinant of A can calculated as

$$\det A(x) = \alpha x_1^2 \kappa(x) + p_r(\alpha+d)x_2 x_1 \kappa(x) + \epsilon d x_1^2 \tag{29}$$

where

$$\kappa(x) := 1 - (x_1 + x_2). \tag{30}$$

As $x_1(t) + x_2(t) \leq 1$ for all $t \geq 0$, $\kappa(x(t)) \geq 0$, and we see that $\det A(x) = 0$ in Ω if and only if $x_1 = 0$, completing the proof. □

The line $x_1 = 0$ is invariant in Ω, and furthermore the dynamics in the set are independent of the control $u(t)$. Conversely, $x_1^0 > 0$ implies that $x_1(t) > 0$ for all $t \geq 0$. We concern our analysis only in this latter case, and so without loss of generality, **$\mathbf{f(x)}$ and $\mathbf{g(x)}$ are linearly independent in the region of interest Ω_c.**

We begin by showing that abnormal extremal lifts are easily characterized. We recall that an extremal lift is abnormal if $\lambda_0 = 0$, i.e., if the Hamiltonian is independent of the objective.

Theorem 9. *Abnormal extremal lifts at interior points, i.e., extremal lifts corresponding to $\lambda_0 = 0$, are constant and given by the maximal (M) or minimal (0) dosage.*

Proof: Assume that u_* switches values at some time t. From (25), we must have that $\Phi(t) = 0$. Since $\lambda_0 = 0$ and $\Phi(t) = \langle \lambda(t), g(x_*(t)) \rangle$, Equation (22) reduces to

$$H(t) = \langle \lambda(t), f(x_*(t)) \rangle = 0. \tag{31}$$

Thus, $\lambda(t)$ is orthogonal to both $f(x_*(t))$ and $g(x_*(t))$. Since f and g are linearly independent (Proposition 8), this implies that $\lambda(t) = 0$. But this contradicts Proposition 7. Hence, no such time t exists, and $u_*(t)$ is constant. The constant sign of Φ thus corresponds to $u = 0$ or $u = M$ (see Equation 25). □

The control structure for abnormal extremal lifts is then completely understood via Theorem 9. To analyze the corresponding behavior for normal extremal lifts, without loss of generality we assume that $\lambda_0 = 1$. Indeed, $\lambda(t)$ may be rescaled by $\lambda_0 > 0$ to yield an equivalent version of Theorem 6. We thus assume that the Hamiltonian $H(t)$ evaluated along $(\lambda(t), x_*(t), u_*(t))$ is of the form

$$H(t) = -1 + \langle \lambda(t), f(x_*(t)) \rangle + u_*(t)\Phi(t) \equiv 0. \tag{32}$$

We recall the Lie bracket as the first-order differential operator between two vector fields X_1 and X_2:

$$[X_1, X_2](z) = DX_2(z)X_1(z) - DX_1(z)X_2(z), \tag{33}$$

where, for example, $DX_2(z)$ denotes the Jacobian of X_2 evaluated at z. As f and g are linearly independent in Ω, there exist $\gamma, \beta \in C^\infty(\Omega)$ such that

$$[f, g](x) = \gamma(x)f(x) + \beta(x)g(x), \tag{34}$$

for all $x \in \Omega$. Explicitly, we compute γ and β:

$$\gamma(x) = -\frac{(\alpha + d)x_1^2}{\det A(x)} \left(ax_1 + bx_2 - c \right), \tag{35}$$

$$\beta(x) = \frac{x_1^2}{\det A(x)} \Big(\alpha(1 - p_r)\kappa(x)(\kappa(x) - \epsilon) + \epsilon d(x_1 + p_r x_2 + \kappa(x) - \epsilon) \Big), \tag{36}$$

where

$$a = \alpha \left((1 - p_r) + \frac{d}{\alpha + d} \right), \tag{37}$$

$$b = \alpha(1 - p_r) + dp_r, \tag{38}$$

$$c = \alpha(1 - p_r) + \epsilon d. \tag{39}$$

Clearly, for parameter values of interest (recall $0 < p_r < 1$), $a, b, c > 0$. The assumption (5) guarantees that $\beta(x) > 0$ on $0 < x_1 + x_2 < V_c$.

From (25), the sign of the switching function Φ determines the value of the control u_*. As λ and x_* are solutions of differential equations, Φ is differentiable. The dynamics of Φ can be understood in terms of the Lie bracket $[f, g]$:

$$\dot{\Phi}(t) = \frac{d}{dt} \langle \lambda(t), g(x_*(t)) \rangle \tag{40}$$

$$= \gamma(x_*(t)) \langle \lambda(t), f(x_*(t)) \rangle + \beta(x_*(t))\Phi(t). \tag{41}$$

The last lines of the above follow from (34) as well as the linearity of the inner product. We are then able to derive an ODE system for x_* and Φ. Equation (32) allows us to solve for $\langle \lambda(t), f(x_*(t)) \rangle$:

$$\langle \lambda(t), f(x_*(t)) \rangle = 1 - u_*(t)\Phi(t). \tag{42}$$

Substituting the above into (41) then yields the following ODE for $\Phi(t)$, which we view as coupled to system (8) via (25):

$$\dot{\Phi}(t) = \gamma(x_*(t)) + \Big(\beta(x_*(t)) - u_*(t)\gamma(x_*(t)) \Big)\Phi(t). \tag{43}$$

The structure of the optimal control at interior points may now be characterized as a combination of bang-bang and singular arcs. We recall that the control (or, more precisely, the extremal lift) u_* is singular on an open interval $I \subset [0, t_c]$ if the switching function $\Phi(t)$ and all its derivatives are identically zero on I. On such intervals, Equation (25) does not determine the value of u_*, and a more thorough analysis of the zero set of $\Phi(t)$ is necessary. Indeed, for a problem such as ours, aside from controls determined by the path constraint $\psi(x_1(t), x_2(t)) \leq 0$, singular arcs are the only candidates for optimal controls that may take values outside of the set $\{0, M\}$. Conversely, times t where $\Phi(t) = 0$ but $\Phi^{(n)}(t) \neq 0$ for some $n \geq 1$ denote candidate bang-bang junctions, where the control may switch between the vertices 0 and M of the control set U. Note that the parity of the smallest such n determines whether a switch actually occurs: n odd implies a switch, while for n even u_* remains constant. Equation (43) allows us to completely characterize the regions in the (x_1, x_2) plane where singular arcs are attainable, as demonstrated in the following proposition.

Proposition 10. *Singular arcs are only possible in regions of the (x_1, x_2) plane where $\gamma(x) = 0$. Furthermore, as $x_1(t) > 0$ for all $t \geq 0$, the region $\left\{ x \in \mathbb{R}^2 \mid \gamma(x) = 0 \right\} \cap \Omega$ is the line*

$$ax_1 + bx_2 - c = 0, \tag{44}$$

where a, b, c are defined in (37–39).

Proof: As discussed prior to the statement of Proposition 10, a singular arc must occur on a region where both $\Phi(t)$ and $\dot{\Phi}(t)$ are identically zero (as well as all higher-order derivatives). Denoting

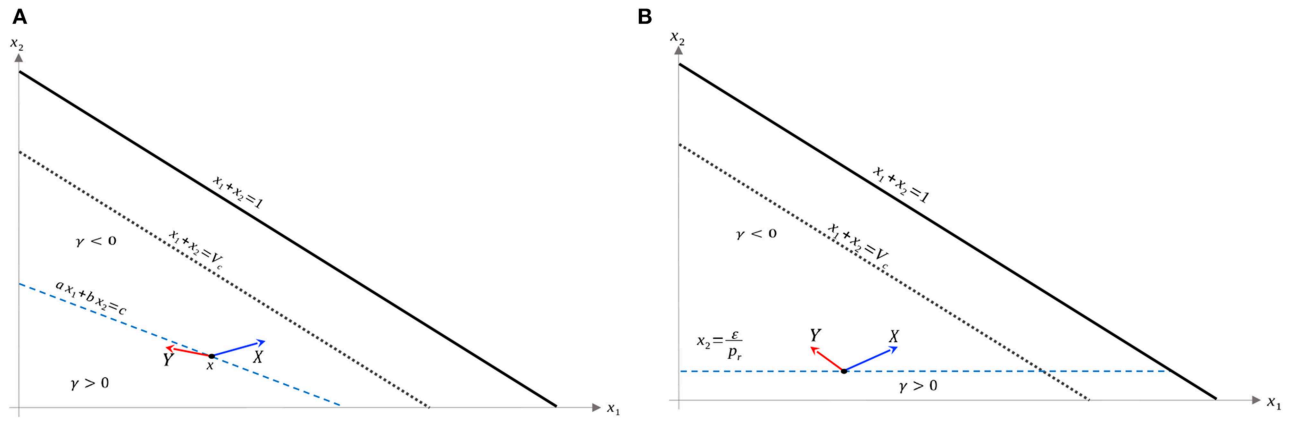

FIGURE 3 | Domain in (x_1, x_2) plane. **(A)** Region where γ changes sign. We see that inside the triangular region $x_1 + x_2 \leq 1$ of the first quadrant, γ changes sign only along the line $ax_1 + bx_2 - c = 0$. For this line to be interior to Ω_c as depicted, we must be in the parameter regime indicated in (49). X and Y vector fields corresponding to vertices of control set U. For singular controls to lie in U, X and Y must point to opposite sides along $\mathcal{L}$. **(B)** Same as in **(A)**, but with $\alpha = 0$.

by $x_*(t)$ the corresponding trajectory in the (x_1, x_2) phase plane, we may calculate $\dot{\Phi}(t)$ from equation (43):

$$\dot{\Phi}(t) = \gamma(x_*(t)). \tag{45}$$

Note we have substituted the assumption $\Phi(t) = 0$. Clearly we must also have that $\gamma(x_*(t)) = 0$, thus implying that $x_*(t) \in \gamma^{-1}(0)$, as desired. The last statement of the proposition follows immediately from Equation (35). □

Proposition 10 implies that singular solutions can only occur along the line $ax_1 + bx_2 - c = 0$. Thus, define regions in the first quadrant as follows:

$$\Omega_c^+ := \{x \in \Omega \mid \gamma(x) > 0\}, \tag{46}$$
$$\Omega_c^- := \{x \in \Omega \mid \gamma(x) < 0\}, \tag{47}$$
$$\mathcal{L} = \{x \in \Omega \mid \gamma(x) = 0\}. \tag{48}$$

Recall that Ω_c is simply the region in Ω prior to treatment failure, i.e., $0 \leq V \leq V_c, x_1, x_2 \geq 0$. From (35), Ω_c is partitioned as in **Figure 3B**. From (35) and (37–39), $\mathcal{L}$ is a line with negative slope $-b/a$. Furthermore, necessary and sufficient conditions for $\mathcal{L}$ to lie interior to Ω_c are $\frac{c}{a}, \frac{c}{b} \leq V_c$. From (37)–(39), this occurs if and only if

$$\epsilon \leq \min\left\{\frac{\alpha}{\alpha+d} - \frac{1-V_c}{d}\left(\alpha(1-p_r) + \frac{\alpha d}{\alpha+d}\right), \right.$$
$$\left. p_r - \frac{1-V_c}{d}\left(\alpha(1-p_r) + dp_r\right)\right\}. \tag{49}$$

As we have assumed that ϵ is small, and that $V_c \approx 1$, this inequality is not restrictive, and we assume it is satisfied for the remainder of the work. We note an important exception below: when $\alpha = 0$ the inequality is never satisfied with $\epsilon > 0$; for such parameter values, line $\mathcal{L}$ is horizontal (**Figure 3B**). We note that this does not change the qualitative results presented below. Of course, other configurations of the line $ax_1 + bx_2 = c$ and hence precise optimal syntheses may exist, but we believe the situation illustrated in **Figure 3A** is sufficiently generic for present purposes.

With the existence of singular arcs restricted to the line $\gamma = 0$ by Proposition 10, we now investigate the feasibility of such solutions. Recall that the treatment $u(t)$ must lie in the control set $U = [0, M]$, for some $M > 0$ corresponding to the maximally tolerated applied dosage. Defining the vector field $X(x)$ and $Y(x)$ as the vector fields corresponding to the vertices of U,

$$\begin{aligned} X(x) &:= f(x), \\ Y(x) &:= f(x) + Mg(x), \end{aligned} \tag{50}$$

a singular control takes values in U at $x \in \mathcal{L}$ if and only if $X(x)$ and $Y(x)$ point in different directions along $\mathcal{L}$. More precisely, the corresponding Lie derivatives $L_X\gamma(x)$ and $L_Y\gamma(x)$ must have opposite signs (see **Figure 3A**). The following proposition determines parameter values where this occurs.

Proposition 11. *Suppose that $\alpha > 0$, so that drug has the potential to induce resistance. Also, let the maximally tolerated dosage M satisfy*

$$M > \frac{\alpha+d}{\alpha(\alpha+d)+\alpha d}\left(d\left(\frac{\alpha}{\alpha+d} - \epsilon\right) + \epsilon d(p_r - \alpha)\right.$$
$$\left. - 2\alpha d(1-p_r)\right). \tag{51}$$

Then the following hold along $\mathcal{L}$:

1. $L_X\gamma < 0$,
2. $L_Y\gamma < 0$ *as* $(x_1, x_2) \to \left(0, \frac{c}{b}\right)$ *in* Ω,
3. $L_Y\gamma > 0$ *at* $(x_1, x_2) = \left(\frac{c}{a}, 0\right)$, *and*
4. $L_Y\gamma$ *is monotonically decreasing as a function of* x_1.

Thus, $\mathcal{L}$ contains a segment $\bar{L} \subset \mathcal{L}$ which is a singular arc. Note that $\bar{L}$ is precisely the region in $\mathcal{L}$ where $L_Y\gamma$ is positive.

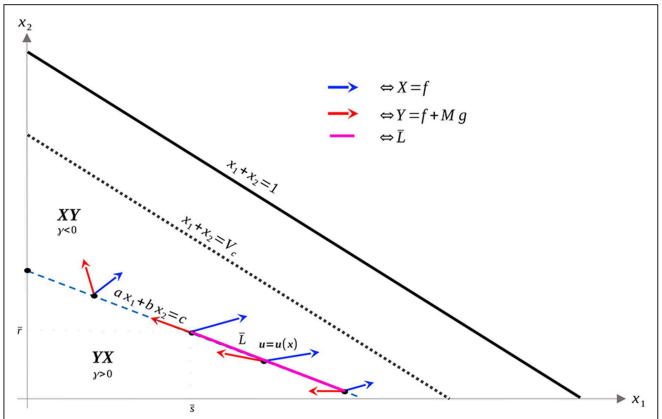

FIGURE 4 | Geometry of vector fields X and Y with $\alpha > 0$ and M satisfying (51). As in Proposition 11, this can be understood via the corresponding Lie derivatives of γ. Note that near $x_2 = 0$, X, and Y point to opposite sides of L, while at $(x_1, x_2) = (0, \frac{c}{b})$, both X and Y point away from $\gamma > 0$. The line $\bar{L}$ is the unique singular arc in Ω_c.

Proof: The proof is purely computational. □

Note that if inequality (51) is not satisfied, then singular arcs are not in the domain Ω_c.

The geometry of Proposition 11 is illustrated in **Figure 4**. Thus, assuming $\alpha > 0$ and M as in (51), singular arcs exist along the segment $\bar{L} \subset \mathcal{L}$. Furthermore, the corresponding control has a unique solution u_s, which may be computed explicitly. Indeed, as the solution must remain on the line $\mathcal{L}$, or equivalently, $ax_1 + bx_2 = c$, taking the time derivative of this equation yields $a\dot{x}_1 + b\dot{x}_2 = 0$, and substituting the expressions (1) we compute u_s as

$$u_s(t) = \frac{(1 - (x_1(t) + x_2(t)))\Big(ax_1(t) + p_r bx_2(t)\Big) + \epsilon(b - a)x_1(t)}{2\alpha(1 - p_r)dx_2(t)}, \tag{52}$$

where a, b, c are given by (37–39) and x_2 and x_1 satisfy $ax_1 + bx_2 = c$. As discussed previously, $x_1(t) > 0$ for $x_1^0 > 0$, so this formula is well-defined. Proposition 11 implies that it is possible to simplify Equation (52) as a function of x_1 (i.e. as a *feedback law*) for $x_1 \in (\bar{s}, \frac{c}{a})$, for some $\bar{s} > 0$, but since its value will not be needed, we do not provide its explicit form. Note that the maximal dose M is achieved precisely at $x_1 = \bar{s}$ where vector field Y is parallel to $\mathcal{L}$. Thus, at this $\bar{s}$, the trajectory must leave the singular arc, and enter the region Ω_c^-. As $\dot{x}_2 \geq 0$, trajectories must follow $\mathcal{L}$ in the direction of decreasing x_1 (see **Figure 4**). We summarize these results in the following theorem.

THEOREM 12. *If $\alpha > 0$, and M satisfies (51), a singular arc exists in the (x_1, x_2) plane as a segment of the line $\mathcal{L}$. Along this singular arc, the control is given by Equation (52), where $ax_1 + bx_2 = c$. Therefore, in this case the necessary minimum conditions on u_* from (25) can be updated as follows:*

$$u_*(t) = \begin{cases} 0 & \Phi(t) > 0, \\ M & \Phi(t) < 0, \\ u_s(t), & \Phi(t) \equiv 0 \text{ for } t \in I, \end{cases} \tag{53}$$

where I is an open interval. Recall again that this is the optimal control at points interior to Ω_c.

Proof: See the discussion immediately preceding Theorem 12. □

In the case $\alpha = 0$, the line $\mathcal{L}$ is horizontal, and as x_2 is increasing, no segment $\bar{L} \subseteq \mathcal{L}$ is admissible in phase space. Thus, the interior controls in this case are bang-bang; for a visualization (see **Figure 3B**).

THEOREM 13. *If $\alpha = 0$, there are no singular arcs for the optimal time problem presented in section 3. Thus, the interior control structure is bang-bang.*

Outside of the singular arc $\bar{L}$, the control structure is completely determined by (25) and (43). The precise result, utilized later for the optimal synthesis presented in section 5, is stated in the following theorem. We first introduce a convenient (and standard) notation. Let finite words on X and Y denote the concatenation of controls corresponding to vector fields X ($u \equiv 0$) and Y ($u \equiv M$), respectively. The order of application is read left-to-right, and an arc appearing in a word may not actually be applied (e.g. XY denotes an X arc followed by a Y arc or a Y arc alone).

THEOREM 14. *Consider an extremal lift $\Gamma = ((x, u), \lambda)$. Trajectories x remaining entirely in Ω_c^+ or Ω_c^- can have at most one switch point. Furthermore, if $x \in \Omega_c^+$, then the corresponding control is of the form YX. Similarly, $x \in \Omega_c^-$ implies that $u = XY$. Hence multiple switch points must occur across the singular arc $\bar{L}$.*

Proof: If τ is a switching time, so that $\Phi(\tau) = 0$, Equation (43) allows us to calculate $\dot{\Phi}(\tau)$ as

$$\dot{\Phi}(\tau) = \gamma(x(\tau)). \tag{54}$$

Thus, in Ω_c^+ where $\gamma > 0$, $\dot{\Phi}(\tau) > 0$, and hence Φ must increase through τ. The expression for the control (25) then implies that a transition from a Y-arc to an X-arc occurs at τ (i.e., a YX arc). Furthermore, another switching time cannot occur unless x leaves Ω_c^+, since otherwise there would exist a $\bar{\tau} > \tau$ such that $\Phi(\bar{\tau}) = 0, \dot{\Phi}(\bar{\tau}) < 0$ which is impossible in Ω_c^+. Similarly, only XY-arcs are possible in Ω_c^-. □

The structure implied by Theorem 14 is illustrated in **Figure 4**. Note that inside the sets Ω_c^+, Ω_c^-, and $\bar{L}$, extremal lifts are precisely characterized. Furthermore, the results of section 4.1 (and particularly Equation 18) yield the characterization on the boundary N. What remains is then to determine the synthesis of these controls to the entire domain Ω_c, as well as to determine the local optimality of the singular arc $\bar{L}$. The latter is addressed in the following section.

4.4. Optimality of Singular Arcs

We begin by proving that the singular arc is extremal, i.e. that it satisfies the necessary conditions presented in section 4.2 (note that it is interior by assumption). This is intuitively clear from **Figure 4**, since X and Y point to opposite sides along $\bar{L}$ by the definition of $\mathcal{L}$.

Theorem 15. *The line segment $\bar{L} \subset \mathcal{L}$ is a singular arc.*

Proof: We find an expression for $u = u(x)$ such that the vector $f(x)+u(x)g(x)$ is tangent to $\bar{L}$ at x, i.e. we find the unique solution to

$$L_{f+ug}(\gamma) = 0 \tag{55}$$

Note that we can invert (50):

$$\begin{aligned} f(x) &= X(x) \\ g(x) &= \frac{1}{M}\big(Y(x) - X(x)\big) \end{aligned} \tag{56}$$

so that $f + ug = \left(1 - \frac{u}{M}\right) X + \frac{u}{M} Y$. Thus,

$$L_{f+ug}(\gamma) = \left(1 - \frac{u}{M}\right) L_X\gamma + \frac{u}{M} L_Y\gamma$$

Setting the above equal to zero, and solving for $u = u(x)$ yields

$$u(x) = M\frac{L_X\gamma(x)}{L_X\gamma(x) - L_Y\gamma(x)} \tag{57}$$

As $L_X\gamma < 0$ and $L_Y\gamma > 0$ on $\bar{L}$ by Proposition 11, we see that $0 < u(x) < M$. We must also verify that the associated controlled trajectory (57) is extremal by constructing a corresponding lift. Suppose that $x(t)$ solves

$$\begin{aligned} \dot{x} &= f(x) + u(x)g(x), \\ x(0) &= q, \end{aligned}$$

for $q \in \bar{L}$. Let $\phi \in (\mathbb{R}^2)^*$ such that

$$\langle \phi, g(q)\rangle = 0, \qquad \langle \phi, f(q)\rangle = 1.$$

Let $\lambda(t)$ solve the corresponding adjoint Equation (24) with initial condition $\lambda(0) = \phi$. Then the extremal lift $\Gamma = ((x,u),\lambda)$ is singular if $\Phi(t) = \langle \lambda(t), g(x(t))\rangle \equiv 0$. By construction of $u(x)$, the trajectory remains on $\bar{L}$ on some interval containing zero, and we can compute $\dot{\Phi}$ as [using (34)]

$$\begin{aligned} \dot{\Phi}(t) &= \langle \lambda(t), [f,g](x(t))\rangle \\ &= \gamma(x(t))\langle \lambda(t), f(x(t)\rangle + \beta(x(t))\langle \lambda(t), g(x(t))\rangle \\ &= \beta(x(t))\Phi(t), \end{aligned}$$

Note that we have used (43) and the fact that $\gamma = 0$ by our choice of u. Since $\Phi(0) = 0$ by hypothesis, this implies that $\Phi(t) \equiv 0$, as desired. □

The above then verifies that $\bar{L}$ is a singular arc. Note that an explicit expression for $u = u(x)$ was given in (52), which can be shown to be equivalent to (57).

Having shown that the singular arc $\bar{L}$ is extremal, we now investigate whether it is locally optimal for our time-optimization problem. The singular arc is of intrinsic order k if the first $2k-1$ derivatives of the switching function are independent of u and vanish identically on an interval I, while the 2kth derivative has a linear factor of u. We can compute [this is standard for control-affine systems (8)] that

$$\Phi^{2k}(t) = \langle \lambda(t), \mathrm{ad}_f^{2k}(g)(x(t))\rangle + u(t)\langle \lambda(t), [g, \mathrm{ad}_f^{2k-1}(g)](x(t))\rangle, \tag{58}$$

where ad_Z is the adjoint endomorphism for a fixed vector field Z:

$$\mathrm{ad}_Z(V) = [Z, V], \tag{59}$$

and powers of this operator are defined as composition. Fix an extremal lift $\Gamma = ((x,u),\lambda)$ of a singular arc of order k. The Generalized Legendre-Clebsch condition (also known as the Kelley condition) (Ledzewicz and Schättler, 2012) states that a necessary condition for Γ to satisfy a minimization problem with corresponding Hamiltonian H is that

$$(-1)^k \frac{\partial}{\partial u}\frac{d^{2k}}{dt^{2k}}\frac{\partial H}{\partial u}(\lambda_0, \lambda(t), x(t), u(t)) \geq 0 \tag{60}$$

along the arc. Note that $\frac{\partial H}{\partial u} = \Phi$, so that the above is simply the u coefficient of the $2k$-th time derivative of the switching function (multiplied by $(-1)^k$). The order of the arc, as well as the Legendre-Clebsch condition, are addressed in Theorem 16.

Theorem 16. *The singular control is of order one. Furthermore, for all times t such that $x(t) \in \bar{L}$, $\langle \lambda(t), [g,[f,g]](x(t))\rangle > 0$. Thus, the Legendre-Clebsch condition is violated, and the singular arc $\bar{L}$ is not optimal.*

Proof: Along singular arcs we must have $\Phi(t), \dot{\Phi}(t), \ddot{\Phi}(t) \equiv 0$, and we can compute these derivatives using iterated Lie brackets as follows:

$$\begin{aligned} \Phi(t) &= \langle \lambda(t), g(x(t))\rangle, \\ \dot{\Phi}(t) &= \langle \lambda(t), [f,g](x(t))\rangle, \\ \ddot{\Phi}(t) &= \langle \lambda(t), [f+ug, [f,g]](x(t))\rangle. \end{aligned} \tag{61}$$

The final of the above in (61) can be simplified as

$$\ddot{\Phi}(t) = \langle \lambda(t), [f,[f,g]](x(t))\rangle + u(t)\langle \lambda(t), [g,[f,g]](x(t))\rangle \equiv 0, \tag{62}$$

which is precisely (58) for $k = 1$. Order one is then equivalent to being able to solve this equation for $u(t)$. Thus, $\langle \lambda(t), [g,[f,g]](x(t))\rangle > 0$ will imply that the arc is singular of order one. We directly compute $\langle \lambda(t), [g,[f,g]](x(t))\rangle = \langle \lambda(t), [g, \mathrm{ad}_f(g)](x(t))\rangle$. Using Equation (34) and recalling properties of the singular arc [$\gamma = 0$ and the remaining relations

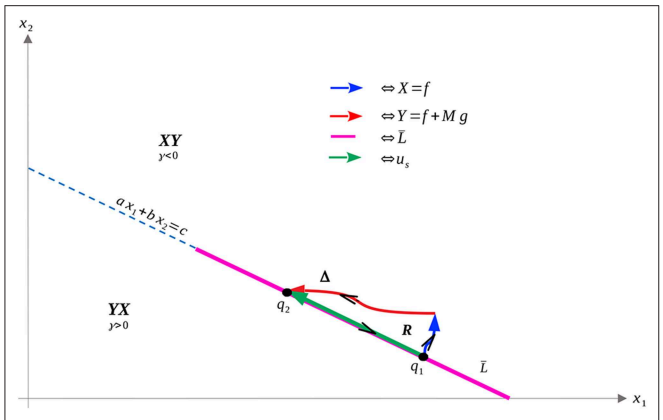

FIGURE 5 | Both *XY* and singular trajectories taking q_1 to q_2.

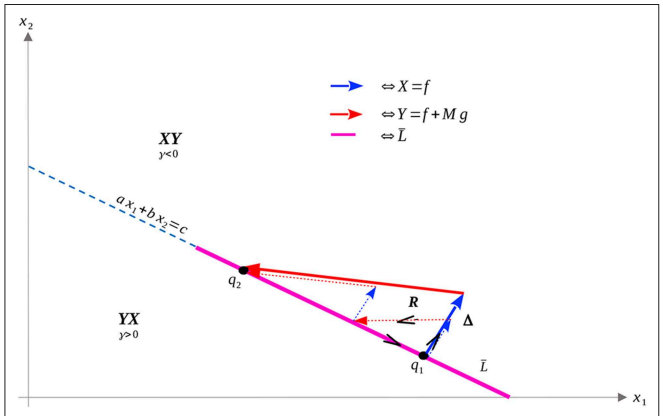

FIGURE 6 | *XY* (solid) and *XYXY* (dashed) trajectories taking q_1 to q_2 in the region $\gamma > 0$. The time difference between the two trajectories can again be related to the surface integral in the region *R*, where $\gamma < 0$. The *XY* trajectory can then be seen to be slower in comparison.

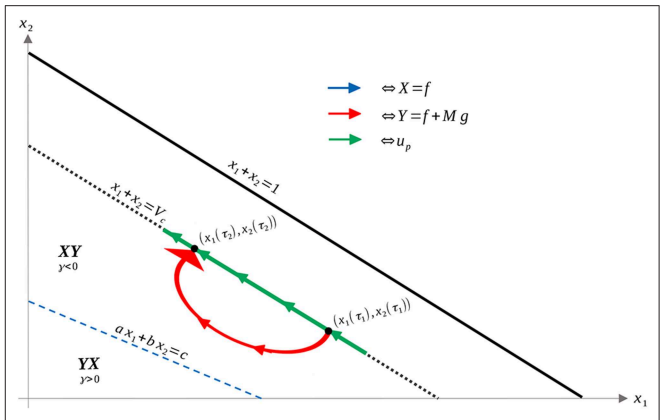

FIGURE 7 | Comparison of $u_p Y u_p$ arc and an arc that remains on *N* (hence $u \equiv u_p$) between the points $[S(\tau_1), R(\tau_1)]$ and $[S(\tau_2), R(\tau_2)]$, assuming that u_p remains feasible (that is, $u_p \in [0, M]$). Note that $\gamma < 0$ in the area of interest, and that a switching of a *Y* to an *X* arc is prohibited via the Maximum Principle. Thus, the only possibility is the curve illustrated, which leaves the boundary *N* for a *Y* arc before u_p becomes infeasible.

TABLE 1 | Parameter values and initial conditions used throughout section 6, unless stated otherwise.

Parameters	Interpretation	Value
x_1^0	Initial sensitive population	10^{-2}
x_2^0	Initial resistant population	0
α	Induced resistance rate due to the presence of the drug	10^{-2}
d	Drug cytotoxicity parameter	1
ϵ	Drug-independent resistance rate	10^{-6}
p_r	Resistant growth fraction	0.2
t_0	Initial time	0
M	Maximum drug dosage	5
V_c	Tumor volume defining treatment failure	0.9

in (61), as well as basic "product rule" properties of the Lie bracket], we can show that

$$[g,[f,g]] = (L_g\gamma)f - \gamma[f,g] + (L_g\beta)g. \tag{63}$$

Recall that for an extremal lift along the arc $\bar{\mathcal{L}}$,

$$\begin{aligned} \langle\lambda(t), g(x(t))\rangle &\equiv 0, \\ \langle\lambda(t), [f,g](x(t))\rangle &\equiv 0 \\ \langle\lambda(t), f(x(t))\rangle &\equiv 1. \end{aligned} \tag{64}$$

The first two of the above follow from $\Phi, \dot{\Phi} \equiv 0$, and the third is a consequence of $H \equiv 0$ [see (22)]. Equations (63) and (64) together imply that

$$\begin{aligned} \langle\lambda(t), [g,[f,g]](x(t))\rangle &= L_g\gamma\,\langle\lambda(t), f(x(t))\rangle - \gamma\,\langle\lambda(t), [f,g](x(t))\rangle \\ &\quad + L_g\beta\,\langle\lambda(t), g(x(t))\rangle \\ &= L_g\gamma(x(t)) \\ &= \frac{1}{M}\left(L_Y\gamma(x(t)) - L_X\gamma(x(t))\right). \end{aligned} \tag{65}$$

The last equality follows from the representation in (56). As $L_Y\gamma > 0$ and $L_X\gamma < 0$ along $\bar{L}$ (Proposition 11), $\langle\lambda(t), [g,[f,g]](x(t))\rangle > 0$, as desired. Furthermore,

$$-\langle\lambda(t), [g,[f,g]](x(t))\rangle < 0, \quad \text{or equivalently} \tag{66}$$

$$(-1)^1 \frac{\partial}{\partial u}\frac{d^2}{dt^2}\frac{\partial H}{\partial u} < 0, \tag{67}$$

showing that (60) is violated (substituting $k = 1$). Thus, $\bar{L}$ is not optimal. □

Theorem 16 then implies that the singular arc is suboptimal, i.e. that $\bar{L}$ is "fast" with respect to the dynamics. In fact, we can compare times along trajectories using the "clock form," a one-form on Ω. As one-forms correspond to linear functionals on the tangent space, and f and g are linearly independent, there exists a unique $\omega \in (T\Omega)^*$ such that

$$\omega_x(f(x)) \equiv 1, \qquad \omega_x(g(x)) \equiv 0. \tag{68}$$

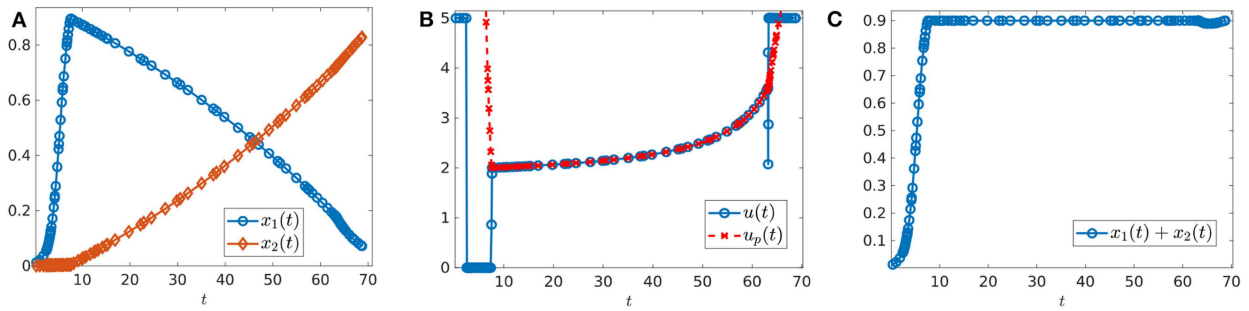

FIGURE 8 | Numerical solution of the optimal control problem with $d = 0.05$, $\alpha = 0.005$, and the remainder of parameters as in **Table 1**. **(A)** Sensitive (x_1) and resistant (x_2) temporal dynamics. **(B)** Control structure of form YXu_pY. **(C)** Volume dynamics. Note that the trajectory remains on the line $V = V_c$ for most times, with corresponding control $u = u_p$.

In fact, we compute it explicitly:

$$\omega_x = \frac{g_2(x)dx^1 - g_1(x)dx^2}{\det(f(x), g(x))}. \tag{69}$$

Then, along any controlled trajectory (x, u) defined on $[t_0, t_1]$, the integral of ω computes the time $t_1 - t_0$:

$$\begin{aligned}\int_x \omega &= \int_{t_0}^{t_1} \omega_{x(t)}(\dot{x}(t))\,\mathrm{d}t \\ &= \int_{t_0}^{t_1} \omega_{x(t)}(f(x(t)) + u(t)g(x(t)))\,\mathrm{d}t \\ &= \int_{t_0}^{t_1} \omega_{x(t)}(f(x(t))\,\mathrm{d}t + \int_{t_0}^{t_1} u(t)\omega_{x(t)}(g(x(t)))\,\mathrm{d}t \\ &= \int_{t_0}^{t_1} \mathrm{d}t \\ &= t_1 - t_0.\end{aligned} \tag{70}$$

We can then use ω and Stokes' Theorem to compare bang-bang trajectories with those on the singular arc. See **Figure 5** below for a visualization of a singular trajectory connecting $q_1, q_2 \in \bar{L}$ and the corresponding unique XY trajectory connecting these points in Ω_c^- (note that uniqueness is guaranteed as long as q_1 and q_2 are sufficiently close).

Let t_S denote the time spent along the singular arc, t_X the time spent along the X arc, and t_Y the time spent along the Y arc. Denote by Δ the closed curve traversing the X and Y arcs positively and the singular arc negatively, with R as its interior. As X and Y are positively oriented (they have the same orientation as f and g), Stokes' Theorem yields

$$t_X + t_Y - t_S = \int_\Delta \omega = \int_R d\omega \tag{71}$$

Taking the exterior derivative yields the two-form $d\omega$ see Chapter 2 of (Ledzewicz and Schättler, 2012):

$$d\omega = -\frac{\gamma}{\det(f, g)}. \tag{72}$$

As the determinant is everywhere positive (see the proof of Proposition 8), and R lies entirely in $\gamma < 0$, the integral on the right-hand side of (71) is positive, so that we have

$$t_S < t_X + t_Y \tag{73}$$

Thus, time taken along the singular arc is shorter than that along the XY trajectory, implying that the singular arc is locally suboptimal for our problem (recall that we want to maximize time). Since local optimality is necessary for global optimality, trajectories should never remain on the singular arc for a measurable set of time points. This reaffirms the results of Theorem 16. A completely analogous statement holds for YX trajectories in the region $\gamma > 0$. We can also demonstrate, utilizing the same techniques, that increasing the number of switchings at the singular arc speeds up the trajectory (see **Figure 6**). This again reinforces Theorem 16, and implies that trajectories should avoid the singular arc to maximize the time spent in Ω_c.

5. CHARACTERIZATION OF OPTIMAL CONTROL

The results of sections 4.1, 4.2, 4.3, and 4.4 may now be combined to synthesize the optimal control introduced in section 3.

THEOREM 17. *For any $\alpha \geq 0$, the optimal control to maximize the time to reach a critical time is a concatenation of bang-bang and path-constraint controls. In fact, the general control structure takes the form*

$$(YX)^n u_p Y \tag{74}$$

where $(YX)^n := (YX)^{n-1}YX$ for $n \in \mathbb{N}$, and the order should be interpreted as left to right. Here u_p is defined in (18).

Proof: Formula (74) is simply a combination of the results presented previously. Note that singular arcs are never (locally) optimal, and hence do not appear in the equation. We also observe that X arcs are not admissible once the boundary N has been obtained, as an X arc always increases V. A Y arc may bring

the trajectory back into int(Ω_c), but a YX trajectory is no longer admissible, as the switching structure in Ω_c^- is XY (Theorem 14).

The only aspect that remains is to show that once N is reached, the only possible trajectories are either u_p given by (18) or Y, with at most one switching occurring between the two. That is, a local arc of the form u_pYu_p is either sub-optimal or non-feasible (equivalently, outside of the control set U). Suppose that such an arc is feasible, i.e., that for all such points in phase space, $0 \leq u_p \leq M$ [recall that u_p is defined via feedback in (18)]. Denote by τ_1 and τ_2 the times at which the switch onto and off of Y occurs, respectively. Since u_p decreases with S, feasibility implies that $u_p(t) \leq M$ for all $t \in [\tau_1, \tau_2]$. Thus, we can consider the alternate feasible trajectory which remains on N between the points $(S(\tau_1), R(\tau_1))$ and $(S(\tau_2), R(\tau_2))$; see **Figure 7** for an illustration. Call τ the time for such a trajectory. Then, using the clock-form ω and the positively-oriented curve Δ which follows N first and Y (in the reverse direction) second, we obtain similarly to (71),

$$\tau - (\tau_2 - \tau_1) = -\int_R \frac{\gamma}{\det(f,g)}, \tag{75}$$

where $R := \text{int}(\Delta)$. Recalling that $\gamma < 0$ in R (see **Figure 4**), the previous equation implies that

$$\tau > \tau_1 - \tau_2, \tag{76}$$

i.e., a longer amount of time is achieved by remaining on the boundary N. Hence the arc u_pYu_p is sub-optimal if it is feasible, as desired.

The previous argument has one subtle aspect, as we used results from the Maximum Principle on the boundary set N, where technically it does not apply. However, the above still remains true, since we may approximate the boundary line $V = V_c$ with a curve interior to Ω_c which remains feasible. By continuity, the time along such a curve can be made arbitrarily close to τ, and hence is still greater than $\tau_2 - \tau_1$, implying that u_pYu_p is sub-optimal. □

Note that in Theorem 17, the switchings must occur across the singular arc $\bar{L}$, if it exists (recall that it is not admissible if $\alpha = 0$). The control u_p is determined along the boundary of Ω_c, and provides the synthesis between interior and boundary controls.

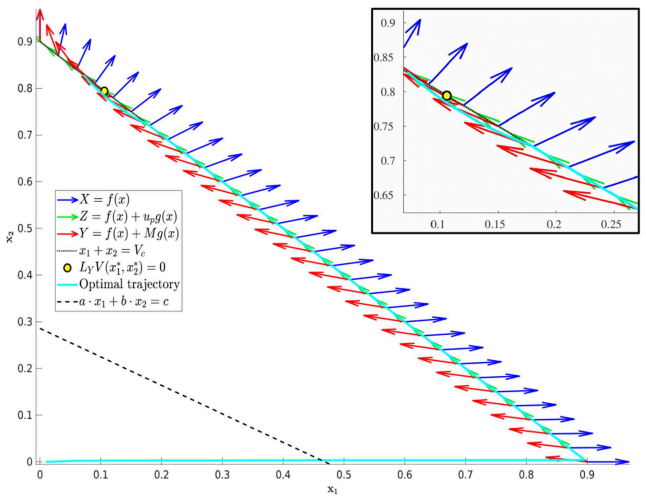

FIGURE 9 | Phase plane corresponding to **Figure 8**. Trajectory which optimal control is of the form YXu_pY with parameter values as in **Table 1** except for $\alpha = 0.005$ and $d = 0.05$. The yellow dot in the figure represents the (x_1^*, x_2^*) point at which $Y(x)$ is tangent to the sliding surface. Here, $(x_1^*, x_2^*) = (0.1059, 0.7941)$. As proven in Proposition 2, for points on the line N, the tumor volume will decrease along the $Y(x)$ direction if $x_1 > 0.1059$ and will increase for $x_1 < 0.1059$.

TABLE 2 | Optimal time t_c for each of the computed controls appearing in **Figure 11**.

d	α = 0.001	α = 0.01	α = 0.1
0.001	6.91	7.28	15.83
0.01	7.87	8.34	17.66
0.1	162.53	72.14	30.09
0.5	246.56	140.93	61.81
1	281.25	172.26	82.13

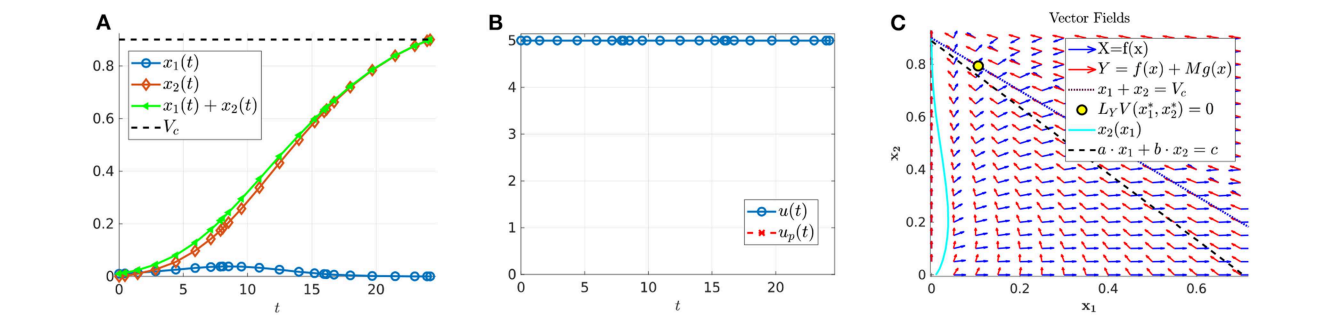

FIGURE 10 | Numerical solution of optimal control problem with $d = 0.05$, $\alpha = 0.1$, and the remainder of parameters as in **Table 1**. **(A)** Sensitive (x_1), resistant (x_2), and volume ($x_1 + x_2$) temporal dynamics. **(B)** Control structure of form Y, i.e., an entirely upper corner control. **(C)** Phase plane dynamics, plotted with relevant vector fields.

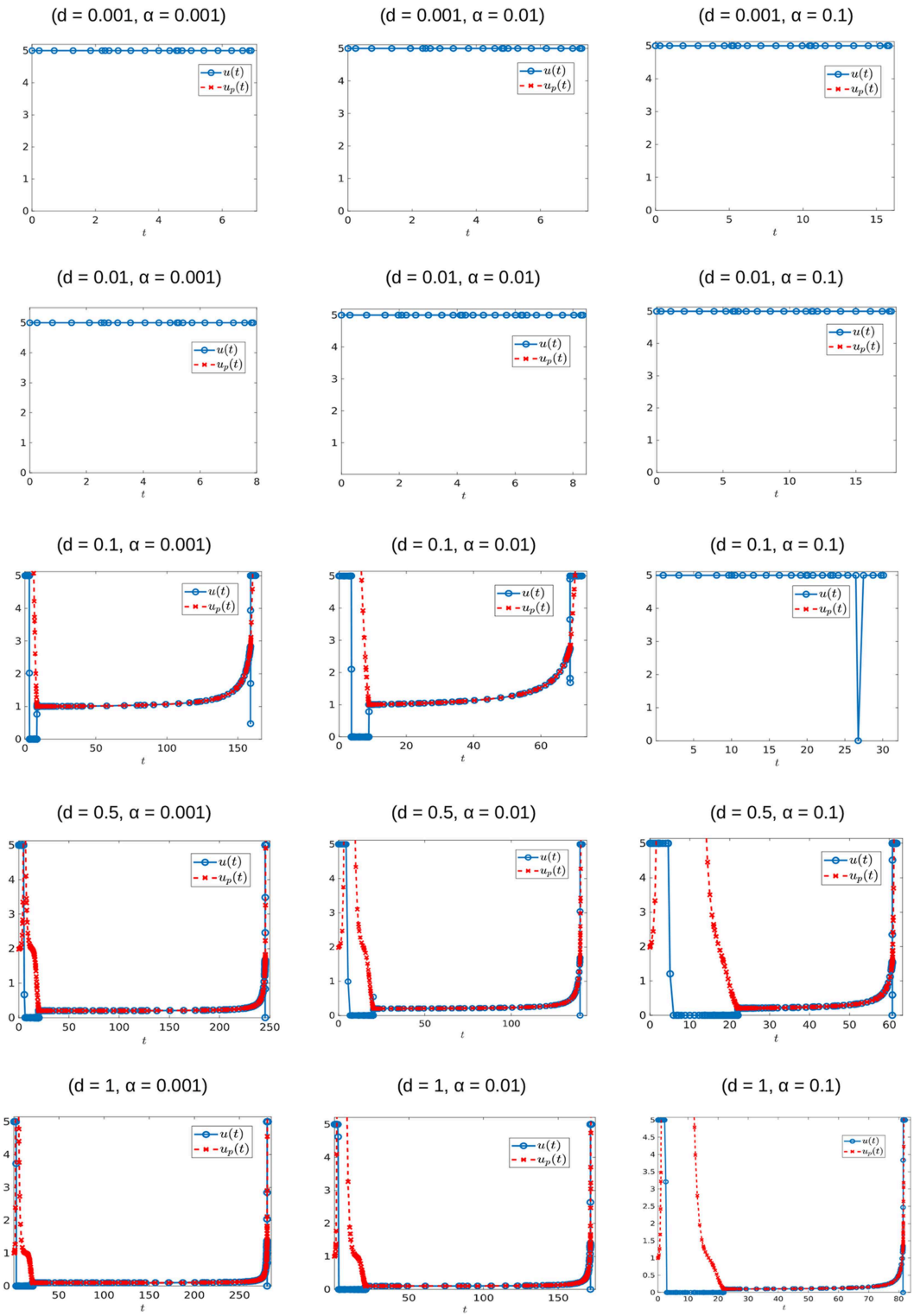

FIGURE 11 | Optimal control structures for different α and d values. The blue curve is the computed optimal control, while the red curve is the feedback control along on the boundary of N, which may or may not be optimal or even feasible.

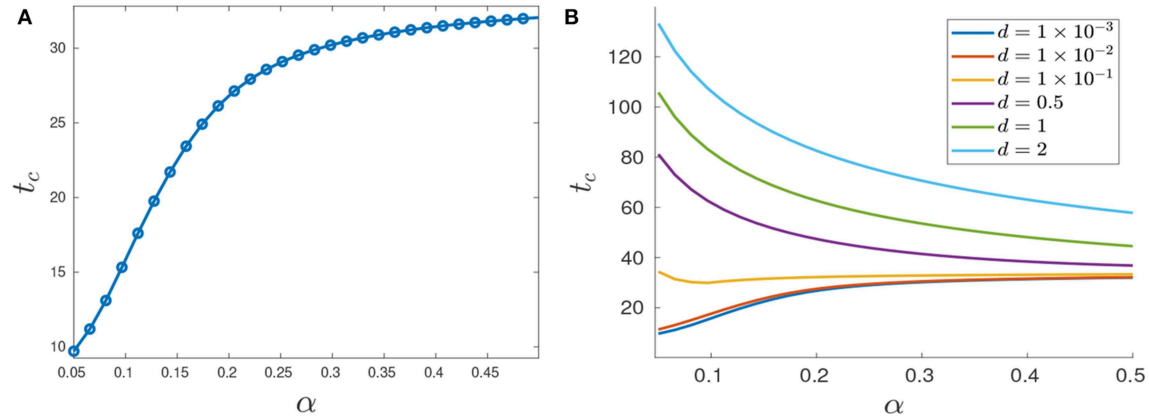

FIGURE 12 | Variation in t_c as a function of α. **(A)** Treatment success time t_c for $d = 0.001$ with varying α values. **(B)** Functional dependence of t_c on α for different d parameters. Note that for small d, t_c increases as a function of α, but that this trend is reversed if d is further increased.

We finally include a technical result, which eliminates the optimality of the constrained (boundary) control u_p in certain cases.

Proposition 18. *Assume that the maximal dose M is as in Proposition 2:*

$$M > \frac{(1 - V_c)(1 - p_r)}{d} \tag{77}$$

If the optimal control becomes maximal in Ω_c^- (i.e., $u = M$ in this region), then the control cannot take the boundary value u_p (Equation 18) on an interval. Equivalently, an optimal control cannot end in the form Yu_p.

Proof: Note that if $u_* = Y$ and reaches N at the point x, then the Lie derivative $L_Y V(x)$ must satisfy

$$L_Y V(x) \geq 0 \tag{78}$$

as V must be increasing along the Y vector field, since it reaches N. But by Proposition 2, this implies that

$$x_1 \leq x_1^*$$

Proposition 3 then implies that u_p is unfeasible in this region, completing the proof. □

6. NUMERICAL RESULTS

In this section, we provide numerical examples of the analytical results obtained in previous sections. All figures in this section were obtained using the GPOPS-II MATLAB software (Patterson and Rao, 2014). Parameters and initial values are given in **Table 1** shown below, unless stated otherwise.

Theorem 17 characterizes the qualitative form of the optimal control:

$$u_* = (YX)^n u_p Y, \tag{79}$$

where n is the number of interior switches, u_p the sliding control (18), and X and Y denote the lower and upper corner controls $u = 0$ and $u = M$, respectively. We begin by computing sample controls (see **Figures 8**, **10**). Note that the optimal control in **Figure 8B** takes the form YXu_pY, while that of **Figure 10B** is an upper corner control Y. The phase plane dynamics corresponding to **Figure 8** are also provided in **Figure 9**. In both cases the cytotoxic parameter was fixed at $d = 0.05$, while the induced rate of resistance α varies between $\alpha = 0.005$ in **Figure 8** and $\alpha = 0.1$ in **Figure 10**. Note that for the smaller value of α (**Figure 8**), a longer period of treatment success is observed, as the time to treatment failure is approximately 70 time units; compare this with $t_c = 24.2$ in **Figure 10**. This result is intuitive, as the treatment less likely to induce resistance is able to be more effective when optimally applied.

The generality of the previous statement is investigated in **Table 2** and **Figures 11**, **12**. The computed optimal times t_c suggest that when the cytotoxicity of the drug (d) is small, higher induction rates (α) actually increase treatment efficacy. For example, for $d = 0.001$ treatment response increases as α increases (**Figure 12A**). This could be explained from the fact that sensitive cells have a higher growth rate than resistant cells (assumption $p_r < 1$). Thus, when the chemotherapeutic drug has a low effectiveness (small d) a larger α value actually helps to reduce the sensitive population size, and therefore extends the time t_c at which the tumor volume exceeds its critical value V_c.

The situation is reversed when we consider larger values of d because in this case it would take more time for the tumor to grow to its critical volume V_c if the drug effectiveness is large enough; see for example the row $d = 0.5$ in **Table 2**, and the corresponding purple curve in **Figure 12B**. **Figure 12B** provides the critical time as a function of α for multiple cytotoxicities d; note the qualitative change in t_c as d increases.

Examining **Figure 11** and **Table 2** also suggests that as d increases, the feedback control u_p becomes optimal on an interval $[t_1, t_2]$ with $0 < t_1 < t_2 < t_c$. More numerical results are provided in section 7.3.

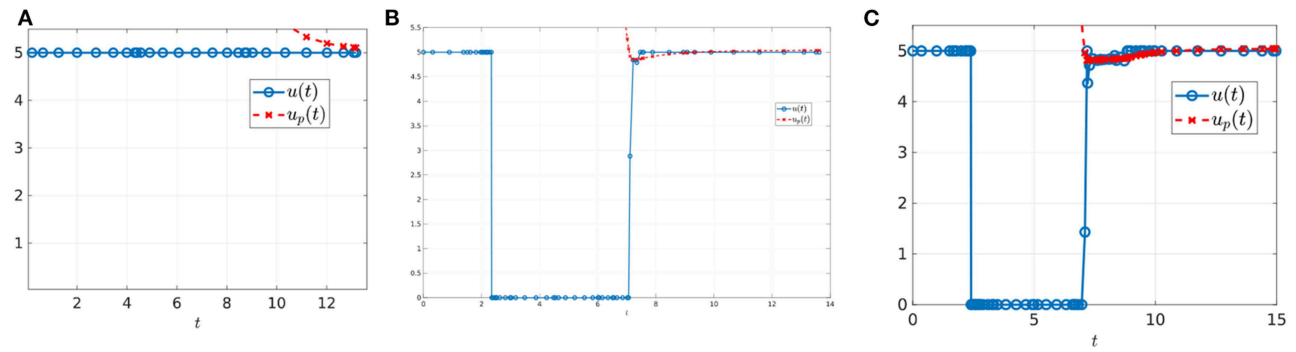

FIGURE 13 | Computed optimal controls for $\alpha = 0.005$ and **(A)** $d = 0.0206$, **(B)** $d = 0.020624489795918$, and **(C)** $d = 0.207959$. Note that the control in **(A)** takes the form Y, while that in **(B,C)** is of the form YXu_P.

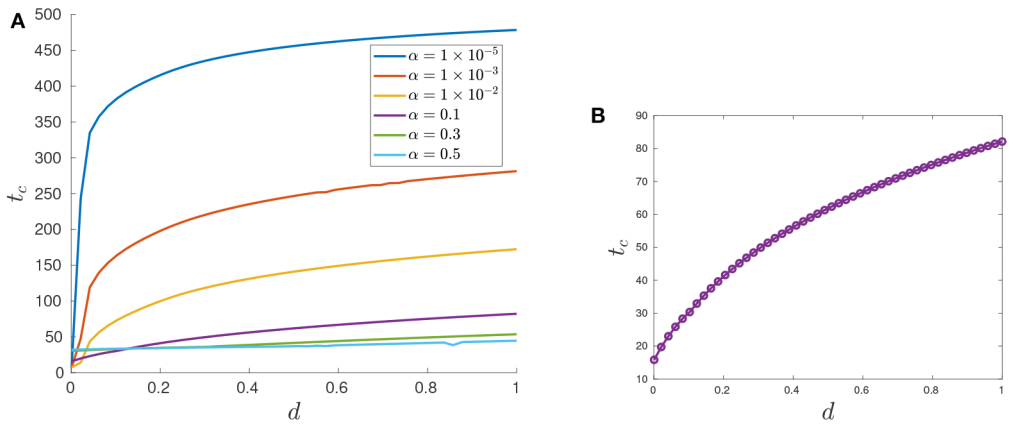

FIGURE 14 | Variation in t_c as a function of d. **(A)** t_c response for varying d values. Note that treatment efficacy generally increases with increasing d. **(B)** $\alpha = 0.1$.

7. ADDITIONAL RESULTS

7.1. Structural Identifiability

For completeness, we discuss the identifiability of system (1). As our focus in this work has been on control structures based on the presence of drug-induced resistance, we rely on the ability to determine whether, and to what degree, the specific chemotherapeutic treatment is generating resistance.

Ideally, we envision a clinical scenario in which cancer cells from a patient are cultured in an *ex vivo* assay (for example, see Silva et al., 2017) prior to treatment. Parameter values are then calculated from treatment response dynamics in the assay, and an optimal therapy regime is implemented based on the theoretical work described below. Thus, identifying patient-specific model parameters, specially the induced-resistance rate α, is a necessary step in determining the control structures to apply. In this section, we address this issue, and prove that all parameters are structurally identifiable, as well as demonstrate a specific set of controls that may be utilized to determine α. A self-contained discussion is presented; for more details on theoretical aspects, see Sontag (2017) and the references therein. Other recent works related to identifiability in the biological sciences (as well as *practical identifiability*) can be found in Eisenberg and Jain (2017) and Villaverde et al. (2016).

We first formulate our dynamical system, and specify the input and output variables. The treatment $u(t)$ is the sole input. Furthermore, we assume that the only clinically observable output is the net tumor volume $V(t)$:

$$V(t) := x_1(t) + x_2(t). \tag{80}$$

That is, we do not assume real-time measurements of the individual sensitive and resistant sub-populations. We note that in some instances, such measurements may be possible; however for a general chemotherapy, the precise resistance mechanism may be unknown *a priori*, and hence no biomarker with the ability to differentiate cell types may be available.

Treatment is initiated at time $t = 0$, at which we assume an entirely sensitive population:

$$x_1(0) = x_1^0, \qquad x_2(0) = 0. \tag{81}$$

Here $0 < x_1^0 < 1$, so that $(x_1(t), x_2(t)) \in \Omega$ for all $t \geq 0$. We note that $x_2(0) = 0$ is not restrictive, and similar results may derived under the more general assumption $0 \leq x_2(0) < 1$.

The condition $x_2(0) = 0$ is utilized both for computational simplicity and since $x_2(0)$ is generally small (assuming a non-zero detection time, and small drug-independent resistance parameter ϵ; see Greene et al., 2019 for a discussion).

As formulated in section 7.2.1, the above then allows us to formulate our system (1) in input/output form, where the input $u(t)$ appears affinely:

$$\begin{aligned} \dot{x}(t) &= f(x(t)) + u(t)g(x(t)), \\ x(0) &= x_0, \end{aligned} \tag{82}$$

where (as defined on Equations (9) and (10)) f and g are

$$f(x) = \begin{pmatrix} (1-(x_1+x_2))x_1 - \epsilon x_1 \\ p_r(1-(x_1+x_2))x_2 + \epsilon x_1 \end{pmatrix}, \tag{83}$$

$$g(x) = \begin{pmatrix} -(\alpha+d) \\ \alpha \end{pmatrix} x_1, \tag{84}$$

and $x(t) = (x_1(t), x_2(t))$. As is standard in control theory, the output is denoted by the variable y, which in this work corresponds to the total tumor volume:

$$\begin{aligned} y(t,p) &:= h(x(t), u(t), p) \\ &= x_1(t) + x_2(t). \end{aligned} \tag{85}$$

Note that $x_1(t), x_2(t)$ depend on both the input $u(t)$ and parameters p. A system in form (82) is said to be *uniquely structurally identifiable* if the map $(u(t), p) \mapsto (u(t), y(t,p))$ is injective almost everywhere (Meshkat and Seth, 2014; Eisenberg and Jain, 2017), where p is the vector of parameters to be identified. In this work,

$$p = (x_1^0, d, \alpha, \epsilon, p_r). \tag{86}$$

Local identifiability and *non-identifiability* correspond to the map being finite-to-one and infinite-to-one, respectively. Our objective is then to demonstrate unique structural identifiability for model system (82) [or equivalently (1)], and hence recover all parameter values p from only measurements of the tumor volume y. We also note that the notion of identifiability is closely related to that of *observability*; for details Anguelova (2004), Sontag (1979) are good references.

To analyze identifiability, we utilize results appearing in, for example (Hermann and Krener, 1977; Wang and Sontag, 1989; Sontag and Wang, 1991), and hence frame the issue from a differential-geometric perspective. Our hypothesis is that perfect (hence noise-free) input-output data is available and in particular, for differentiable controls, that we can compute y and its derivatives. We thus, for example, make measurements of

$$\begin{aligned} y(0) &= h(x(0)), \\ \dot{y}(0) &= \left.\frac{d}{dt}\right|_{t=0} h(x(t)) \end{aligned} \tag{87}$$

for appropriately chosen inputs, and relate their values to the unknown parameter values p. If there exist inputs $u(t)$ such that the above system of equations may be solved for p, the system is identifiable. The right-hand sides of (87) may be computed in terms of the Lie derivatives of the vector fields f and g in system (82). We recall the definition of Lie differentiation $L_X H$ of a C^ω function H by a C^ω (i.e. real-analytic) vector field X:

$$L_X H(x) := \nabla H(x) \cdot X(x). \tag{88}$$

Here the domain of both X and H is the first-quadrant triangular region Ω, seen as a subset of the plane, and the vector fields and output function are C^ω on an open set containing Ω (in fact, they are given by polynomials, so they extend as analytic functions to the entire plane). Iterated Lie derivatives are well-defined, and should be interpreted as function composition, so that for example $L_Y L_X H = L_Y(L_X H)$, and $L_X^2 H = L_X(L_X H)$.

More formally, let us introduce the observable quantities corresponding to the zero-time derivatives of the output $y = h(x)$,

$$Y(x_0, U) = \left.\frac{d^k}{dt^k}\right|_{t=0} h(x(t)), \tag{89}$$

where $U \in R^k$ is the value of the control $u(t)$ (without loss of generality, a polynomial of degree $k-1$) and its derivatives evaluated at $t = 0$: $U = \left(u(0), u^{'}(0), ..., u^{(k-1)}(0)\right)$. Here $k \geq 0$, indicating that the k^{th}-order derivative Y may expressed as a polynomial in the components of U (Sontag and Wang, 1991). The initial conditions x_0 appear due to evaluation at $t = 0$. The observation space is then defined as the span of the elements $Y(x_0, U)$:

$$F_1 := \text{span}_{\mathbb{R}}\{Y(x_0, U) \mid U \in \mathbb{R}^k, k \geq 0\}. \tag{90}$$

Conversely, we also define span of iterated Lie derivatives with respect to the output h and vector fields $f(x)$ and $g(x)$:

$$F_2 := \text{span}_{\mathbb{R}} \left\{ L_{i_1} \dots L_{i_k} h(x_0) \mid (i_1, \dots i_k) \in \{g,f\}^k, k \geq 0 \right\}. \tag{91}$$

Wang and Sontag (1989) proved that $F_1 = F_2$, so that the set of "elementary observables" may be considered as the set of all iterated Lie derivatives F_2. Hence, identifiability may be formulated in terms of the reconstruction of parameters p from elements in F_2. Parameters p are then identifiable if the map

$$p \mapsto \left(L_{i_1} \dots L_{i_k} h(x_0) \mid (i_1, \dots i_k) \in \{g,f\}^k, k \geq 0 \right) \tag{92}$$

is one-to-one. For the remainder of this section, we investigate the mapping defined in (92).

Computing the Lie derivatives and recalling that $x_0 = (S_0, 0)$ we can recursively determine the parameters p:

$$\begin{aligned} x_1^0 &= h(x_0), \\ d &= -\frac{L_g h(x_0)}{x_1^0}, \\ \alpha &= \frac{L_g^2 h(x_0)}{dx_1^0} - d, \\ \epsilon &= \frac{L_f L_g h(x_0)}{dx_1^0} + 1 - x_1^0, \\ p_r &= \frac{x_1^0}{1-x_1^0} + \frac{L_g L_f h(x_0)}{\alpha x_1^0 (1-x_1^0)} - \left(1 + \frac{d}{\alpha}\right)\left(1 - \frac{x_1^0}{1-x_1^0}\right). \end{aligned} \tag{93}$$

Since $F_1 = F_2$, all of the above Lie derivatives are observable via appropriate treatment protocols. For an explicit set of controls and corresponding relations to measurable quantities [elements of the form (89)], see Greene et al. (2019). Thus, we conclude that all parameters in system (1) are identifiable, which allows us to investigate optimal therapies dependent upon *a priori* knowledge of the drug-induced resistance rate α.

7.2. Existence Results

For the problem presented in section 3, we are going to verify that the supremum of times $t_c(u)$ for $u \in \mathcal{U}$ [with $t_c(u)$ as defined in Equation (6)] is obtained by some $u_* \in \mathcal{U}$, i.e., that an optimal control exists. This involves two distinct steps: (1) proving that the supremum is finite, and (2) that it is obtained by at least one admissible control. The following two subsections verify these claims.

7.2.1. Finiteness of the Supremum

We prove that

$$\sup_{u \in \mathcal{U}} t_c(u) < \infty \tag{94}$$

for the control system introduced in section 3. The result depends crucially on (3), and the fact that the globally asymptotically stable state $(0, 1)$ is disjoint from the dynamic constraint $x \in \Omega_c$ (see Equation (13)). That is, $V_c < 1$ is necessary for the following subsequent result to hold, and generally an optimal control will not exist if $V_c = 1$ or if the path constraint (13) is removed.

Our control system has the form

$$\dot{x} = f(x) + u(t)g(x), \tag{95}$$

where $x \in \Omega$, $u \in \mathcal{U}$, and the vector fields $f, g : \Omega \to \mathbb{R}^2$ are continuously differentiable. Note that the above vector field is affine (and thus continuous) in the control u. Fix the initial condition

$$x(0) = x_0, \tag{96}$$

with $x_0 \in \Omega$. Recall that all solutions of (95) and (96) approach the fixed point $\bar{x} := (0, 1) \in \Omega$. That is, for all $u \in \mathcal{U}$,

$$x_u(t) \xrightarrow{t \to \infty} \bar{x}. \tag{97}$$

Note that we explicitly denote the dependence of the trajectory on the control u, and the above point $\bar{x}$ is independent of the control u.

For any compact subset E of Ω such that $x_0 \in E, \bar{x} \notin E$, we associate to each control (and hence to its corresponding trajectory) a time $t_E(u)$ such that

$$t_E(u) = \max\{T \mid x_u(t) \in E \text{ for all } t \leq T\}. \tag{98}$$

The above is well-defined (as a maximum) for each control u, since by assumption $x_0 \in E$ and each trajectory asymptotically approaches $\bar{x} \notin E$, x_u is continuous, and E is compact.

Theorem 19. *Define*

$$T_* = \sup_{u \in \mathcal{U}} t_E(u). \tag{99}$$

With the above construction, T_* is finite.

Proof: Consider the sets $K, V \subset \mathbb{R}^2$, with V being an open neighborhood of the steady state $\bar{x} = (0, 1)$ and K a compact set in $\mathbb{R}^2$ such that

$$(0,1) \in V \subsetneq K \quad \text{and} \quad K \cap \{(x_1, x_2) \in \mathbb{R}^2 : x_1, x_2 \geq 0 \text{ and } 0 \leq x_1 + x_2 \leq V_c\} = \varnothing.$$

By contradiction, suppose that T_* is not finite, so we can find a sequence of controls $\{v_k\}_{k=1}^{\infty}$ in $\mathcal{U}$ satisfying

$$d_\infty\big(x(t, v_k), K\big) \geq \epsilon \qquad \text{for all } t \leq t_k, \text{ with } t_k \to \infty. \tag{100}$$

where d_∞ denotes the supremum metric and, for each $k \in \mathbb{N}$, $x(t, v_k)$ is the solution of the IVP:

$$\begin{aligned} \dot{x} &= f(x) + v_k(t)g(x), \\ x(0) &= x_0, \end{aligned} \tag{101}$$

Our aim is to find a control $u \in \mathcal{U}$ such that $x(t, u)$, solution of system (101), does not enter K for any $t > 0$. Recall that by the Banach-Alaoglu theorem, the ball

$$B\big(L^\infty([0,\infty))\big) = \{u \in L^\infty([0,\infty)) : \|u\|_\infty \leq M\} \tag{102}$$

is a compact set on the weak* topology and metrizable. Thus, the sequence $\{v_k\}_{k=1}^{\infty}$ must have a weak*−convergent subsequence $\{u_j\}_{j=1}^{\infty}$ which converges to a control $u \in L^\infty([0,\infty))$. In other words, for every $\psi \in L^1([0,\infty))$

$$\lim_{j \to \infty} \int_{[0,\infty)} \psi u_j d\mu = \int_{[0,\infty)} \psi u d\mu, \tag{103}$$

where μ is the usual Lebesgue measure. This means that the sequence $\{u_j\}_{j=1}^{\infty}$ converges to u with respect to the weak* topology on $L^\infty([0,\infty))$ as the dual of $L^1([0,\infty))$.

We next prove that $\lim_{j\to\infty} \|x(t,u) - x(t,u_j)\|_\infty = 0$ for all $t \in [t_{k-1}, t_k]$ and all $k \in \mathbb{N}$. In order to do so define

$$x_{k-1} = x_0 + \int_0^{t_{k-1}} [f(x(s)) + u(s)g(x(s))]ds$$

for any $t_{k-1} \in [0, \infty)$, where x solves the IVP

$$\begin{aligned} \dot{x} &= f(x) + v_k(t)g(x), \\ x(t_{k-1}) &= x_{k-1}. \end{aligned} \tag{104}$$

Notice that the fact that the equilibrium $(0,1)$ is globally asymptotically stable on $\{(x_1, x_2) \in \mathbb{R}^2 : x_1, x_2 \geq 0 \quad \text{and} \quad 0 < x_1 + x_2 \leq V_c\}$ implies that x_{k-1} is well-defined for any $k \in \mathbb{N}$.

The integral form of (104) is given by

$$F(t, x, v_k) = x_{k-1} + \int_{t_{k-1}}^{t} [f(x) + v_k(s)g(x)]ds. \tag{105}$$

With the help of the t_k's from (100) and assuming (without loss of generality) that t_k increases as k goes to infinity, we write the set $[0, \infty)$ as the countable union of finite closed intervals:

$$[0, \infty) = \bigcup_{k\in\mathbb{N}} [t_{k-1}, t_k] \qquad \text{where } t_0 = 0.$$

Let $w_{j,k}$ and w denote the functions u_j and u restricted to the interval $[t_{k-1}, t_k]$, respectively. Thus, the sequence $\{w_{j,k}\}_{j=1}^{\infty}$ converges weakly* to w on $[t_{k-1}, t_k]$:

$$\begin{aligned} &\lim_{j\to\infty} \|x(t,w) - x(t,w_{j,k})\|_\infty \\ &= \lim_{j\to\infty} \|F(t,x,w) - F(t,x,w_{j,k})\|_\infty \qquad (106) \\ &= \lim_{j\to\infty} \left\| \int_{t_{k-1}}^{t} w(s)g(x)ds - \int_{t_{k-1}}^{t} w_{j,k}(s)g(x)ds \right\|_\infty \qquad (107) \\ &= \lim_{j\to\infty} \left\| \int_{t_{k-1}}^{t} [w_{j,k}(s) - w(s)]g(x)ds \right\|_\infty \qquad (108) \\ &= 0 \qquad \text{for all } t \in [t_{k-1}, t_k]. \qquad (109) \end{aligned}$$

Since this result is independent of k, this implies that

$$d_\infty\big(x(t,u), K\big) = \lim_{j\to\infty} d_\infty\big(x(t,u_j), K\big) \geq \epsilon \quad \text{for all } t \in [t_{k-1}, t_k], \text{independently of } k \in \mathbb{N}. \tag{110}$$

The corresponding trajectory $x(t,u)$ thus never enters K, contradicting the the global stability of $\bar{x}$. Hence, T_* must be finite, as desired. □

For the system and control problem defined in sections 2 and 3, the above theorem implies that $\sup_{u\in\mathcal{U}} t_c(u)$ is finite by taking $E = \Omega_c$.

7.2.2. Supremum as a Maximum

Here we provide a general proof for the existence of optimal controls for systems of the form (95), assuming the set of maximal times is bounded above, which we have proven for our system in section 7.2.1. For convenience, we make the proof as self-contained as possible (one well-known result of Filippov will be cited), and state the results in generality which we later apply to the model of induced resistance. Arguments are adapted primarily from the textbook of Bressan and Piccoli (2007).

Consider again general control systems as in section 7.2.1. Solutions (or trajectories) of (95) will be defined as absolutely continuous functions for which a control $u \in \mathcal{U}$ exists such that $(x(t), u(t))$ satisfy (95) a.e., in their (common) domain $[a, b]$.

It is easier and classical to formulate existence with respect to differential inclusions. That is, define the multi-function

$$F(x) = \{f(x) + \omega g(x) \mid \omega \in U\}. \tag{111}$$

Thus, the control system (95) is clearly related to the inclusion

$$\dot{x} \in F(x). \tag{112}$$

The following theorem (see Filippov, 1967 for a proof) makes this relationship precise.

Theorem 20. *An absolutely continuous function $x : [a, b] \mapsto \mathbb{R}^2$ is a solution of (95) if and only if it satisfies (112) almost everywhere.*

We first prove a lemma demonstrating that the set of trajectories is closed with respect to the sup-norm $\|\cdot\|_\infty$ if all the sets of velocities $F(x)$ are convex.

Lemma 21. *Let x_k be a sequence of solutions of (95) converging to x uniformly on $[0, T]$. If the graph of $(t, x(t))$ is entirely contained in Ω, and all the sets $F(x)$ are convex, then x is also a solution of (95).*

Proof: By the assumptions on f, g, the sets $F(x)$ are uniformly bounded as (t, x) range in a compact domain, so that x_k are uniformly Lipschitz, and hence x is Lipschitz as the uniform limit. Thus x is differentiable a.e., and by Theorem 20, it is enough to show that

$$\dot{x}(t) \in F(x(t)) \tag{113}$$

for all t such that the derivative exists.

Assume not, i.e., that the derivative exists at some τ, but $\dot{x}(\tau) \notin F(x(\tau))$. Since $F(x(\tau))$ is compact and convex, and $\dot{x}(\tau)$ is closed, the Hyperplane Separation Theorem implies that there exists a hyperplane separating $F(x(\tau))$ and $\dot{x}(\tau)$. That is, there exists an $\epsilon > 0$ and a (without loss of generality) unit-vector $p \in \mathbb{R}^2$ such that

$$\langle p, y\rangle \leq \langle p, \dot{x}(\tau)\rangle - 3\epsilon, \tag{114}$$

for all $y \in F(x(\tau))$. By continuity, there exists $\delta > 0$ such that for $|x' - x(\tau)| \leq \delta$

$$\langle p, y \rangle \leq \langle p, \dot{x}(\tau) \rangle - 2\epsilon, \tag{115}$$

for all $y \in F(x')$. Since x is differentiable at τ, we can choose $\tau' > \tau$ such that

$$\begin{gathered} \left| \frac{x(\tau') - x(\tau)}{\tau' - \tau} - \dot{x}(\tau) \right| < \epsilon, \\ \left| x(t) - x(\tau) \right| < \delta, \end{gathered} \tag{116}$$

for all $t \in [\tau, \tau']$. Equation (116) and uniform convergence then implies that, as p is a unit vector,

$$\left\langle p, \frac{x_k(\tau') - x_k(\tau)}{\tau' - \tau} \right\rangle \xrightarrow{k \to \infty} \left\langle p, \frac{x(\tau') - x(\tau)}{\tau' - \tau} \right\rangle \geq \left\langle p, \dot{x}(\tau) \right\rangle - \epsilon. \tag{117}$$

On the other hand, since $\dot{x}(t) \in F(x')$ for $t \in [\tau, \tau']$, Equation (115) implies that for k sufficiently large,

$$\left\langle p, \frac{x_k(\tau') - x_k(\tau)}{\tau' - \tau} \right\rangle = \frac{1}{\tau' - \tau} \int_{\tau}^{\tau'} \left\langle p, \dot{x}(t) \right\rangle \mathrm{d}t \leq \left\langle p, \dot{x}(\tau) \right\rangle - 2\epsilon. \tag{118}$$

Clearly, (117) and (118) contradict one another, so that (113) must be true, as desired. □

We now restate the optimal control problem associated to (95). Let S denotes the set of admissible terminal conditions, $S \subset \mathbb{R} \times \mathbb{R}^2$, and $\phi : \mathbb{R} \times \mathbb{R}^2 \mapsto \mathbb{R}$ a cost function. We would like to maximize $\phi(T, x(T))$ over admissible controls with initial and terminal constraints:

$$\begin{gathered} \max_{u \in \mathcal{U}, T \geq 0} \phi(T, x(T, u)), \\ x(0) = x_0, \, (T, x(T)) \in S. \end{gathered} \tag{119}$$

We now state sufficient conditions for such an optimal control to exist.

Theorem 22. *Consider the control system (95) and corresponding optimal control problem (119). Assume the following:*

1. *The objective ϕ is continuous.*
2. *The sets of velocities $F(x)$ are convex.*
3. *The trajectories x remain uniformly bounded.*
4. *The target set S is closed.*
5. *A trajectory satisfying the constraints in (119) exists.*
6. *S is contained in some strip $[0, T] \times \mathbb{R}^2$, i.e. the set of final times (for free-endpoint problems) can be uniformly bounded.*

If the above items are all satisfied, an optimal control exists.

Proof: By assumption, there is at least one admissible trajectory reaching the target set S. Thus, we can construct a sequence of controls $u_k : [0, T_k] \mapsto U$ whose corresponding trajectories x_k satisfy

$$\begin{gathered} x_k(0) = x_0, \\ (T_k, x_k(T_k)) \in S, \\ \phi(T_k, x(T_k)) \xrightarrow{k \to \infty} \sup_{u \in \mathcal{U}, \bar{T} \geq 0} \phi(\bar{T}, x(\bar{T}, u)). \end{gathered} \tag{120}$$

Since $S \subset [0, T] \times \mathbb{R}^n$, we know that $T_k \leq T$ for all k. Each function x_k can then be extended to the entire interval $[0, T]$ by setting $x_k(t) = x_k(T_k)$ for $t \in [T_k, T]$.

The sequence x_k is uniformly Lipschitz continuous, as f is uniformly bounded on bounded sets. This then implies equicontinuity of $\{x_k\}_{k=1}^{\infty}$. By the Arzela-Ascoli Theorem, there exists a subsequence x_{n_k} such that $T_{n_k} \to T_*$, $T_* \leq T$, and $x_{n_k} \to x_*$ uniformly on $[0, T_*]$.

Lemma 21 implies that x_* is admissible, so that there exists a control $u_* : [0, T_*] \mapsto U$ such that

$$\dot{x}_*(t) = f(t, x_*(t), u_*(t)) \tag{121}$$

for almost all $t \in [0, T_*]$. Equations (120) imply that

$$\begin{gathered} x_*(0) = x_0 \\ (T_*, x_*(T_*)) = \lim_{n_k \to \infty} \phi(T_{n_k}, x_{n_k}(T_{n_k})) \in S. \end{gathered} \tag{122}$$

Note that the second of (122) relies on S being closed. Continuity of ϕ and (120) implies that

$$\phi(T_*, x_*(T_*)) = \lim_{n_k \to \infty} \phi(T_{n_k}, x_{n_k}(T_{n_k})) = \sup_{u \in \mathcal{U}, T_* \geq 0} \phi(T_*, x(T_*, u)). \tag{123}$$

Thus, u_* is optimal, as desired. □

For the model of drug-induced resistance, the control set U is the compact set $U = [0, M]$, and for such control-affine systems, convexity of $F(x)$ is implied by the convexity of U. Existence of a trajectory satisfying the constraints is clear; for example, take $u(t) \equiv 0$. Our objective is to maximize the time to not escape the set N. Note that N is a closed subset of $\mathbb{R}^2$, and that

$$\phi(\bar{T}, x(\bar{T}, u)) = \bar{T}. \tag{124}$$

is continuous. Lastly, we have seen that all solutions remain in the closure $\bar{\Omega}$, so that $|x(t)| \leq 1$ for all $u \in \mathcal{U}$ and hence solutions are uniformly bounded. Existence is then reduced to Item 6 in the previous theorem. Since the supremum of time t was shown to be finite, Theorem 22 together with Theorem 19 imply that the optimal control for the problem presented in section 3 exists.

7.3. Further Numerical Experiments

In this subsection, we present further numerical experiments (see section 6). Specifically, we study how the values of the relative resistant growth rate and critical volume influence the control structure. We also consider a regularized

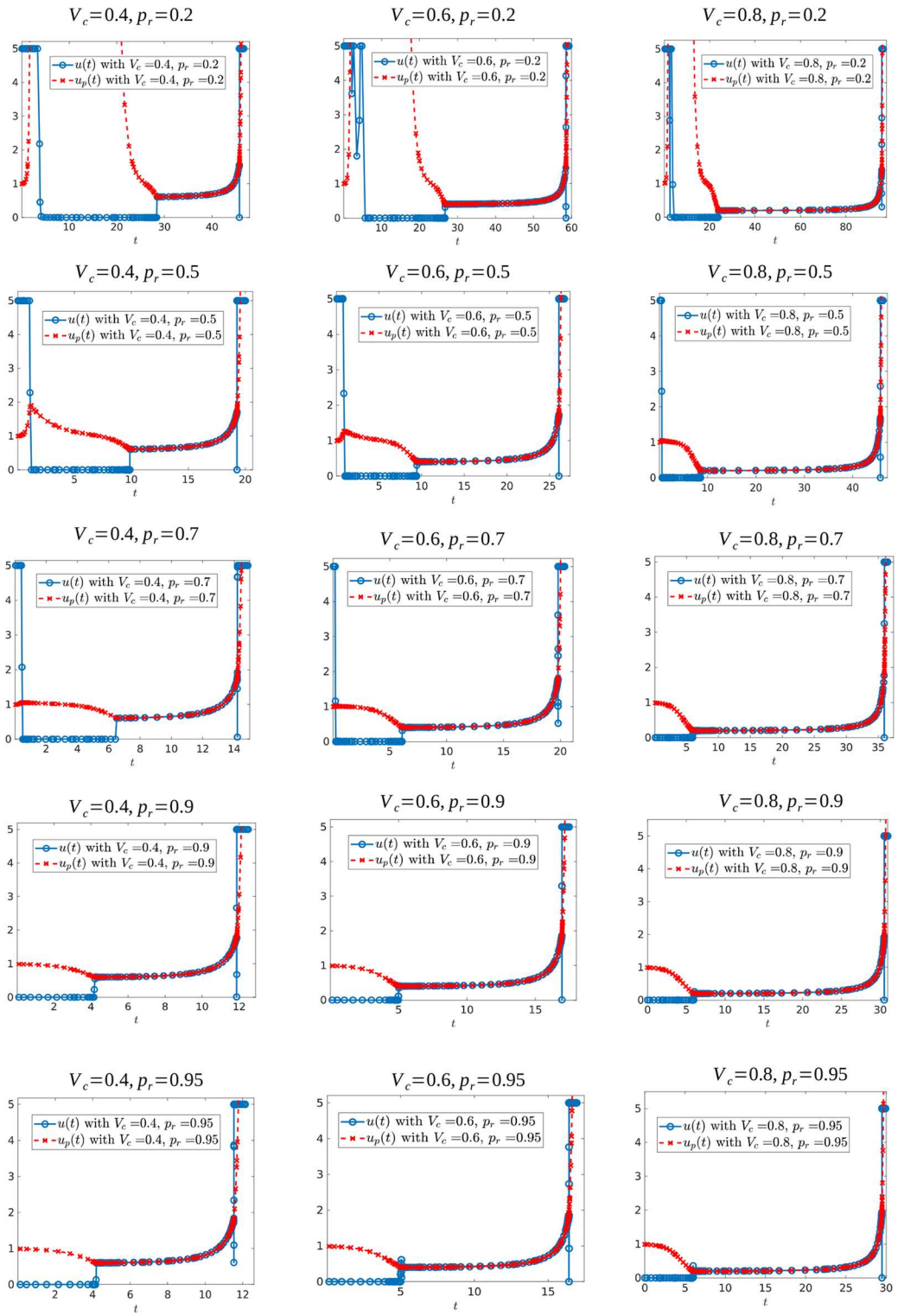

FIGURE 15 | Optimal control structures for different V_c and p_r values. The blue curve is the computed optimal control, while the red curve is the feedback control along on the boundary of N, which may or may not be optimal or even feasible.

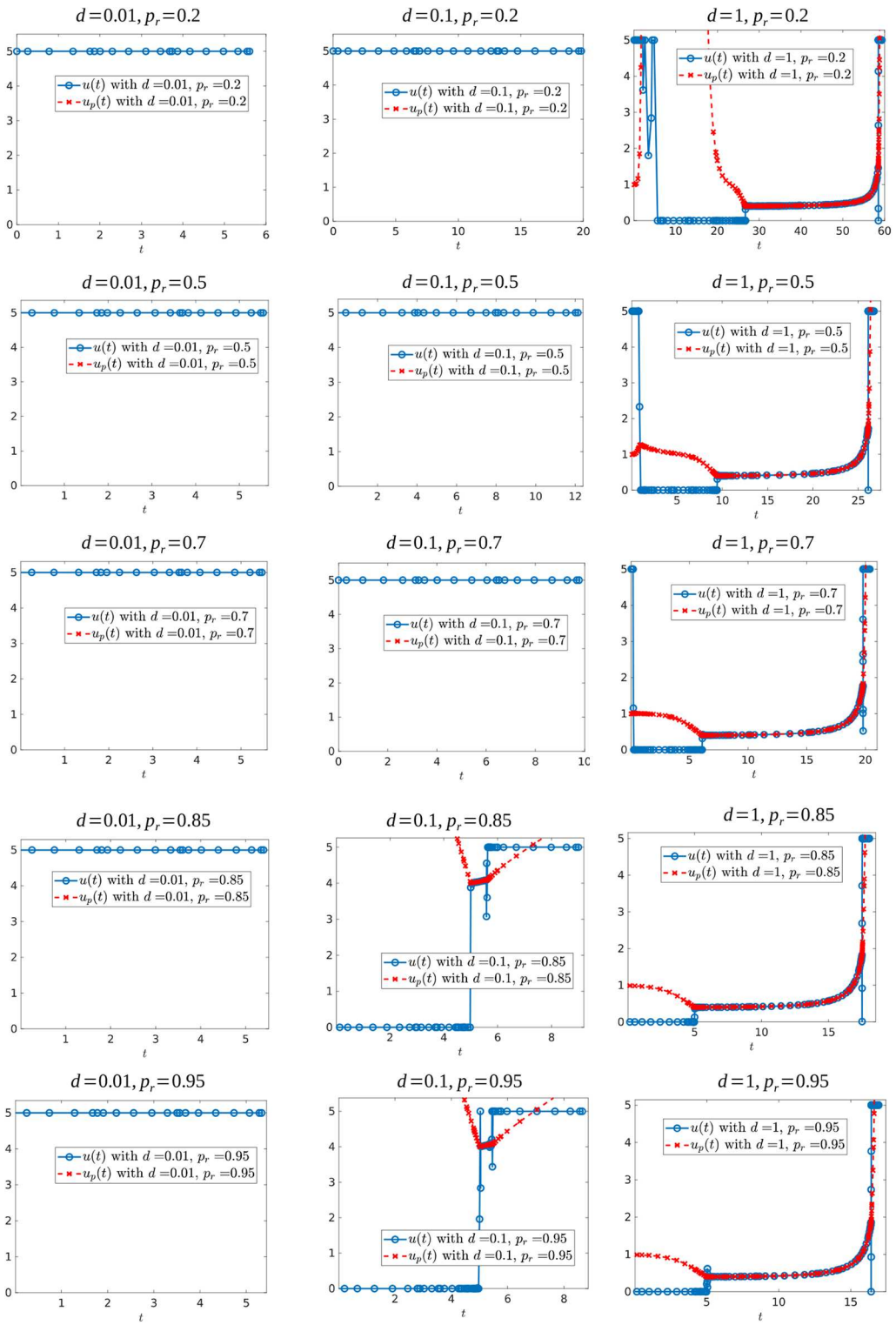

FIGURE 16 | Optimal control structures for $V_c = 0.6$, and different d and p_r values. The blue curve is the computed optimal control, while the red curve is the feedback control along on the boundary of N, which may or may not be optimal or even feasible.

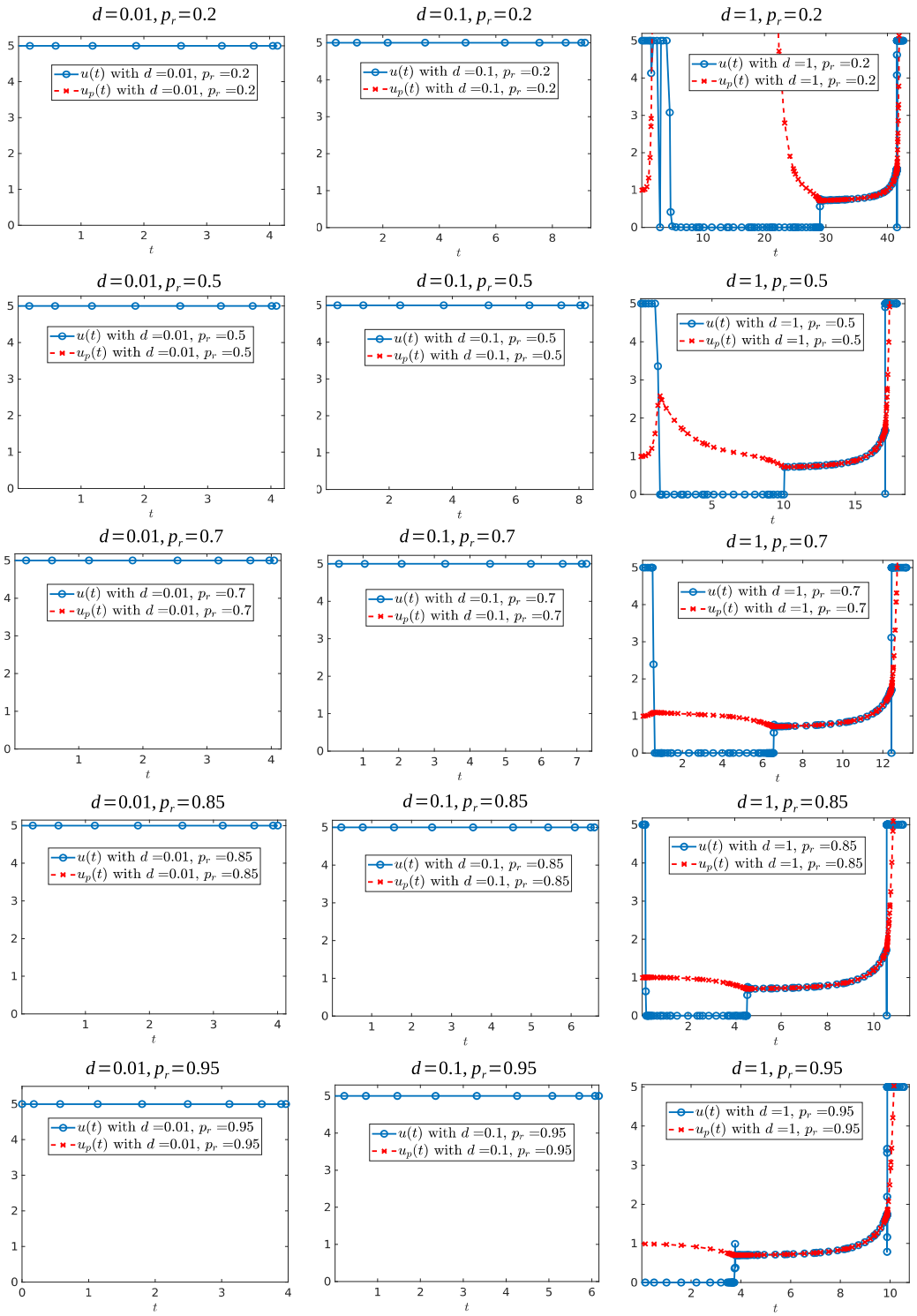

FIGURE 17 | Optimal control structures for $V_c = 0.3$, and different d and p_r values. The blue curve is the computed optimal control, while the red curve is the feedback control along on the boundary of N, which may or may not be optimal or even feasible.

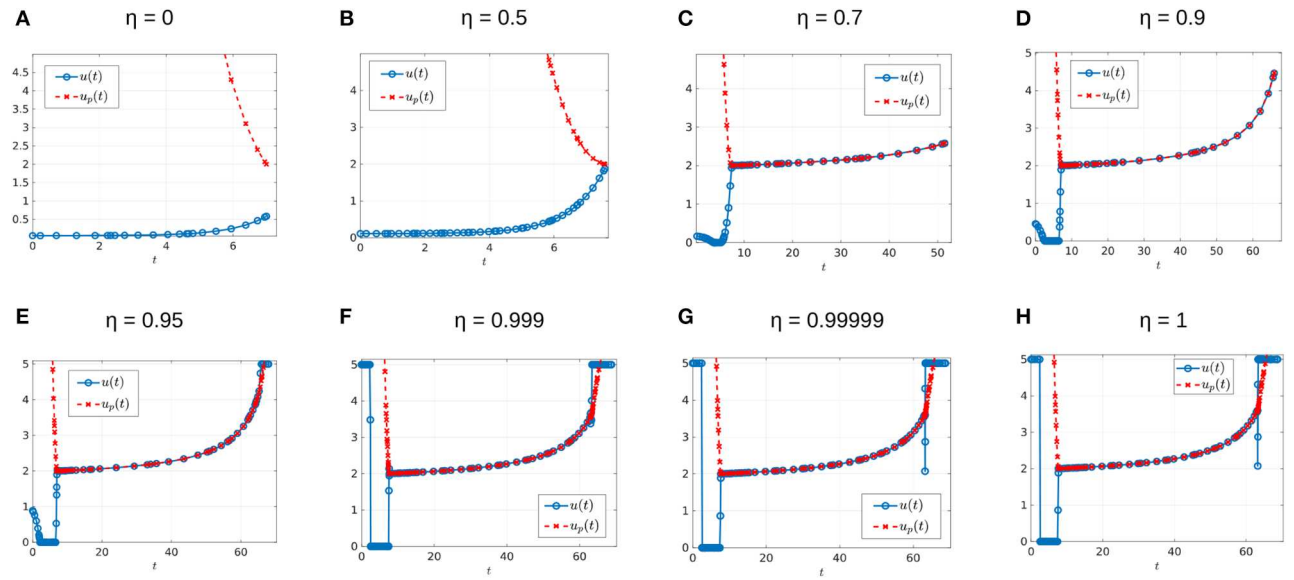

FIGURE 18 | Different perturbed controls for $\alpha = 0.005$ and $d = 0.05$. Here, from **(A–H)**, the value of η is 0, 0.5, 0.7, 0.9, 0.95, 0.999, 0.99999, and 1, respectively. The maximum relative error is of 4.0338×10^{-7} for figure $\eta = 0$, the remaining figures have a maximum relative error of 5.5727×10^{-7} or smaller.

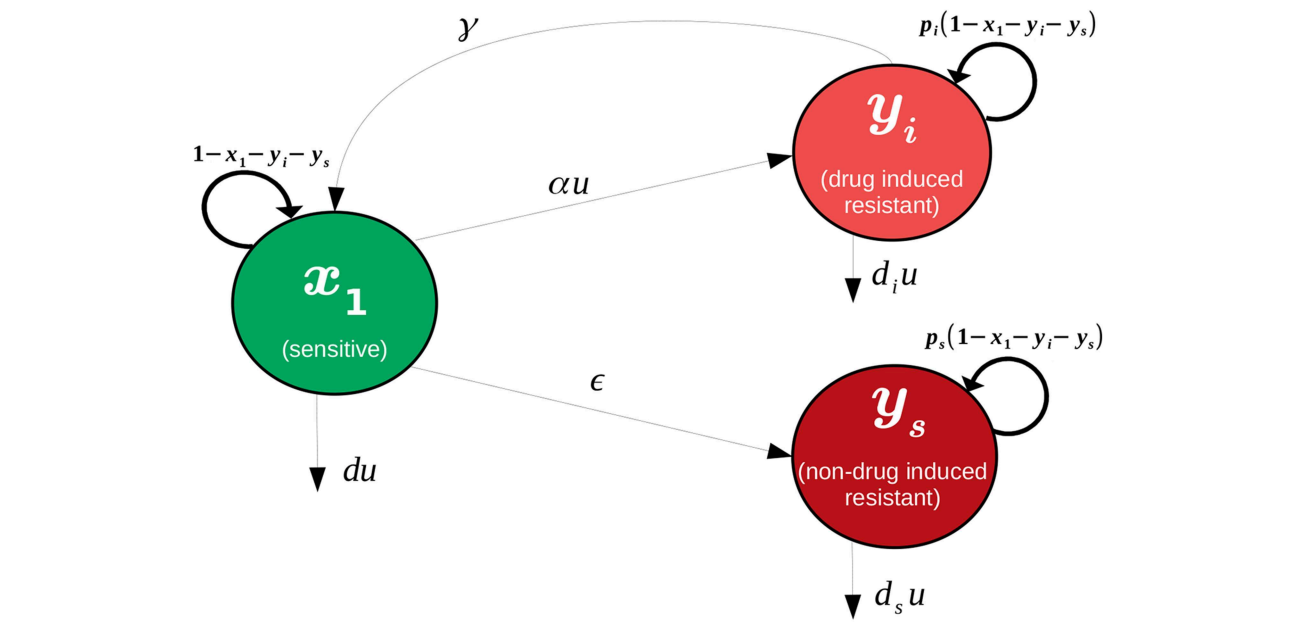

FIGURE 19 | Visualization of model that includes a reverse phenotype transition from resistant to sensitive. x_1 denotes the sensitive cancerous cell population, y_i the drug-induced resistant cancerous cell population, and y_s the non-drug-induced resistant cell population.

objective, which suggests that our numerical methods are converging to (at least local) solutions of the optimal control problem.

We first investigate the control structure and treatment outcome as a function of d for a fixed α; these results are presented in **Figures 13**, **14**. Here $\alpha = 0.005$ is fixed and d is varied on the interval $[0.001, 0.1]$. **Figure 13** presents three of these controls; although none of the controls is of the form YXY, the figure suggests that there may exist a $d^* \in (0.02062, 0.0207959)$ where the solution trajectory may intersect the boundary line N only at one point and subsequently switches into a Y arc, thus providing the existence of a YXY control. **Figure 14** suggests that increasing d for a fixed α increases the overall effectiveness of the treatment for all values of α, and that decreasing the induction rate α allows for longer tumor control. However, for small values of d,

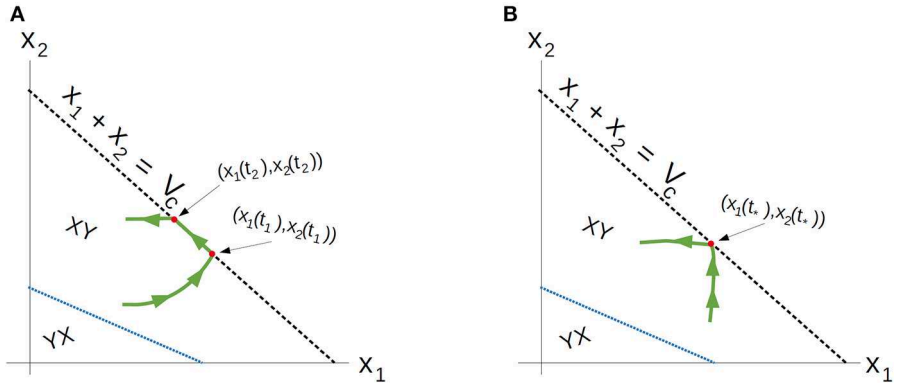

FIGURE 20 | (A) Example of an arc with feedback control with entry point $[x_1(t_1), x_2(t_1)]$ an exit point $[x_1(t_2), x_2(t_2)]$ the exit point **(B)** Example of an arc that does not slides but reaches the boundary $V = V_c$ at the contact point $(x_1(t_*), x_2(t_*))$.

increasing α may provide a better treatment outcome (see, for example, the intersection of the yellow and purple curves in **Figure 14**).

We also investigated how the shape of the optimal control changes for different values of the resistant growth fraction (p_r) and/or the critical tumor volume (V_c). We run several simulations for $V_c \in \{0.2, 0.25, 0.3, 0.4, 0.5, 0.6, 0.7, 0.8, 0.85, 0.9\}$ and $p_r \in \{0.2, 0.3, 0.5, 0.7, 0.85, 0.9, 0.95, 0.98, 0.99\}$. We found that when the reproduction rate of resistant cells is close to the reproduction rate of sensitive cells (p_r near 1), the best strategy is to not give any drug at the beginning of treatment. This is perhaps to prolong the appearance of fast-growing resistance cells which cannot be eliminated with treatment. A representative set of the controls for these simulations are shown in **Figure 15**.

We further simulated the following parameter sets: $V_c \in \{0.3, 0.6\}$, $d \in \{0.01, 0.05, 0.1, 0.5, 0.75, 1\}$ and $p_r \in \{0.2, 0.3, 0.5, 0.7, 0.85, 0.9, 0.95, 0.98, 0.99\}$. **Figure 16** shows some of the controls for these simulations for the case when $V_c = 0.6$, while **Figure 17** shows some of the controls for the case $V_c = 0.3$. In both figures, we observe that independently of the value of resistant growth rate p_r, if the chemotherapeutic drug has a low effectiveness (d small) then the best strategy is to give the maximum possible drug dosage during treatment. However, when d increases past $d = 0.1$, the control structure changes qualitatively. When $V_c = 0.6$ and the resistant reproduction rate is close to the reproduction rate of sensitive cells, the best strategy is to start with no drug treatment while for case $V_c = 0.3$ (independently of the value of p_r) the best strategy is to give the maximum drug dosage from the start.

Before ending this section, we would like to mention that to verify the performance of the numerical software, we approached the original problem by a sequence of regularized problems, which is done by adding a quadratic term to the Lagrangian. More precisely, we considered the perturbed performance index:

$$J_\eta[u] = -\int_0^{t_c} \left[1 - \frac{(1-\eta)}{2} u^2(t)\right] dt \qquad \text{for } \eta \in [0,1]. \quad (125)$$

Notice that Equation (125) represents a family of performance indexes parameterized by η. The original performance index corresponds to $\eta = 1$. Furthermore, for $\eta \neq 1$ the optimal control problem is regular and solvers such as GPOPS-II (used here) or SNOPT should provide accurate solutions. Thus, to test the accuracy to the case $\eta = 1$, we investigated the corresponding control structure in the limit $\eta \to 1$. An example of different controls, for η values $0, 0.5, 0.7, 0.9, 0.95, 0.999, 0.99999$, and 1, are shown on **Figure 18**. For each case we obtained different relative errors: the largest relative error of 4.0338×10^{-7} occurs for $\eta = 0$, with the remaining values of η having smaller relative errors. From the values $\eta = 0.95$, $\eta = 0.999$ and $\eta = 0.99999$ in **Figure 18** we can see that as $\eta \to 1$ the computed control approaches the solution to the original problem (case $\eta = 1$).

8. CONCLUSIONS

In this work, we have provided a rigorous analysis of the optimal control problem introduced in Greene et al. (2018a). That is, we have formally applied optimal control theory techniques to understand treatment strategies related to a model of induced drug resistance in cancer chemotherapy introduced in Greene et al. (2019). Although the model is relatively simple, it has recently been found to be highly successful in matching experimental data (Gevertz et al., 2019; Johnson et al., 2020), which we believe justifies the careful analysis presented here. An optimal control problem is then presented which maximizes a specific treatments therapy window. A formal analysis of the optimal control structure is performed utilizing the Pontryagin Maximum Principle and differential-geometric techniques. Optimal treatment strategies are realized as a combination of bang-bang and path-constrained arcs, and singular controls are proved to be sub-optimal. Numerical results are presented which verify our theoretical results, and demonstrate interesting and non-intuitive treatment strategies. We have also shown that a drug's level of resistance induction is identifiable, thus allowing for

the possibility of designing therapies based on individual patient-drug interactions (see section 7.1).

Under the assumption that sensitive cells have a higher growth rate than resistant cells, our results (section 6) indicate that when using a chemotherapeutic drug with low cytotoxicity, the time at which the tumor volume exceeds its critical value t_c would be larger when the transition rate of the drug is high (see for example **Table 2**, on cases $d = 0.001$ and $d = 0.01$, as α has larger values the end time t_c becomes larger). The situation is reversed when we consider larger values of drug effectiveness because in this case it would take more time for the tumor to grow to its critical volume whenever the drug effectiveness is large enough. Also, our simulations indicate that it is optimal to apply the maximal dosage M subsequent to sliding along the boundary $V = V_c$ (e.g., **Figure 9**), prior to treatment failure.

Clearly, further analysis is required in order to understand this phenomenon, and its implications for clinical scenarios. Although our model considers only an idealized scenario where resistance is unavoidable, we see that induced resistance dramatically alters therapy outcome, which underscores the importance of understanding its role in both cancer dynamics and designing chemotherapy regimes.

Other questions remain open for future work:

- ◊ Several studies indicate that drug-tolerance is a phenotypic property that appears transiently under the presence of the drug (Goldman et al., 2015). A next step to this research is to incorporate a reverse transition rate (from resistant to sensitive cells) that represents this phenotype-switching (see **Figure 19**).
- ◊ For controls where the trajectory remains on the boundary $V = V_c$ (u_p), the feedback control is optimal during a time interval $[t_1, t_2]$ with $0 \leq t_1 < t_2 < t_c$. It remains to understand the point of entry $[x_1(t_1), x_2(t_1)]$ and exit $[x_1(t_2), x_2(t_2)]$ (**Figure 20A**). What is the significance of the times t_1 and t_2 with respect to parameter values?
- ◊ Do there exist conditions, once the trajectory reaches V_c, under which the optimal trajectory no longer slides? Is it possible that at the time t_* the point $[x_1(t_*), x_2(t_*)]$ is a contact point (**Figure 20B**)? Some numerical results suggest that such a contact point may exist and give rise to a *YXY* control structure (**Figure 13**).
- ◊ We have shown that an optimal control can switch at most once in each of the regions Ω_c^+ and Ω_c^-. Numerically we did not observe any bang-bang controls of the form *YXY*, although its existence was strongly suggested. The existence of a bang-bang junction in Ω_c^- is therefore of interest.
- ◊ For all examples plotted in **Figure 11** with $d \geq 0.1$, the entry time occurs approximately at the same value $t_1 = 20.03$. Is this a coincidence? We would like to understand the dependence of the entry time t_1 and on parameters α, d, p_r, M, and/or ϵ.
- ◊ We would like to extend models to include multiple, possibly non-cross resistant, cytotoxic agents. Indeed, clinical practice generally includes multiple agents applied concurrently and sequentially, and we plan on investigating strategies when different types of drugs may be applied. For example, what control strategies arise when a targeted therapy exists which targets the resistant sub-population? What order should the agents be applied, and for how long? Are intermediate doses now optimal? Mathematically, all of these questions may be studied, and the results may be clinically relevant.

AUTHOR CONTRIBUTIONS

All authors listed have made a substantial, direct and intellectual contribution to the work, and approved it for publication.

FUNDING

This research was supported in part by NSF grants 1716623 and 1849588.

ACKNOWLEDGMENTS

We thank Dr. Anil Rao for technical suggestions regarding the optimization formulation and the use of GPOPS-II. This manuscript has been released as a pre-print at bioRxiv (Greene et al., 2018b).

REFERENCES

Anguelova, M. (2004). *Nonlinear Observability and Identifiability: General Theory and a Case Study of a Kinetic Model for S. cerevisiae*. Chalmers University of Technology.

Bressan, A., and Piccoli, B. (2007). Introduction to mathematical control theory. *AIMS Ser. Appl. Math. Philadelphia*

Brimacombe, K. R., Hall, M. D., Auld, D. S., Inglese, J., Austin, C. P., Gottesman, M. M., et al. (2009). A dual-fluorescence high-throughput cell line system for probing multidrug resistance. *Assay Drug Dev. Technol.* 7, 233–249. doi: 10.1089/adt.2008.165

Doherty, M., Smigiel, J., Junk, D., and Jackson, M. (2016). Cancer stem cell plasticity drives therapeutic resistance. *Cancers* 8:8. doi: 10.3390/cancers8010008

Eisenberg, M. C., and Jain, H. V. (2017). A confidence building exercise in data and identifiability: Modeling cancer chemotherapy as a case study. *J. Theor. Biol.* 431, 63–78.

Filippov, A. F. (1967). Classical solutions of differential equations with multi-valued right-hand side. *SIAM J. Control.* 5, 609–621.

Gatenby, R. A., Silva, A. S., Gillies, R. J., and Frieden, B. R. (2009). Adaptive therapy. *Cancer Res.* 69, 4894–4903. doi: 10.1158/0008-5472.CAN-08-3658

Gevertz, J. L., Greene, J. M., and Sontag, E. D. (2019). Validation of a mathematical model of cancer incorporating spontaneous and induced evolution to drug resistance. *bioRxiv*. doi: 10.1101/2019.12.27.889444

Goldman, A., Majumder, B., Dhawan, A., Ravi, S., Goldman, D., Kohandel, M., et al. (2015). Temporally sequenced anticancer drugs overcome adaptive resistance by targeting a vulnerable chemotherapy-induced phenotypic transition. *Nat. Commun.* 6:6139. doi: 10.1038/ncomms7139

Gottesman, M. (2002). Mechanisms of cancer drug resistance. *Annu. Rev. Med.* 53, 615–627. doi: 10.1146/annurev.med.53.082901.103929

Greene, J., Sanchez-Tapia, C., and Sontag, E. (2018b). Mathematical details on a cancer resistance model. *bioRxiv [preprint]*. doi: 10.1101/475533

Greene, J., Sanchez-Tapia, C., and Sontag, E. D. (2018a). Control structures of drug resistance in cancer chemotherapy. *Proc. IEEE Conf. Decis. Control*. doi: 10.1109/CDC.2018.8618653

Greene, J. M., Gevertz, J. L., and Sontag, E. D. (2019). Mathematical approach to differentiate spontaneous and induced evolution to drug resistance during cancer treatment. *JCO Clin. Cancer Inform*. 3, 1–20. doi: 10.1200/CCI.18.00087

Hermann, R., and Krener, A. (1977). Nonlinear controllability and observability. *IEEE Trans. Automatic Control* 22, 728–740. doi: 10.1109/TAC.1977.1101601

Johnson, K. E., Howard, G. R., Morgan, D., Brenner, E., Gardner, A. L., Durrett, R. E., et al. (2020). Integrating multimodal data sets into a mathematical framework to describe and predict therapeutic resistance in cancer. *bioRxiv [preprint]*. doi: 10.1101/2020.02.11.943738

Ledzewicz, U., and Schättler, H. (2012). *Geometric Optimal Control. Theory, Methods and Examples, 1st Edn*. New York, New York: Springer. doi: 10.1007/978-1-4614-3834-2

Lee, W.-P. (1993). The role of reduced growth rate in the development of drug resistance of hob1 lymphoma cells to vincristine. *Cancer Lett*. 73, 105–111. doi: 10.1016/0304-3835(93)90251-4

Loeb, L. A., Springgate, C. F., and Battula, N. (1974). Errors in DNA replication as a basis of malignant changes. *Cancer Res*. 34, 2311–2321.

Meshkat, N., and Seth, S. (2014). Identifiable reparametrizations of linear compartment models. *J. Symbolic Comput.* 63, 46–67.

Patterson, M. A., and Rao, A. V. (2014). GPOPS-II: A matlab software for solving multiple-phase optimal control problems using hp-adaptive Gaussian quadrature collocation methods and sparse nonlinear programming. *ACM Trans. Math. Softw*. 41:1. doi: 10.1145/2558904

Pisco, A. O., Brock, A., Zhou, J., Moor, A., Mojtahedi, M., Jackson, D., et al. (2013). Non-darwinian dynamics in therapy-induced cancer drug resistance. *Nat. Commun*. 4:2467. doi: 10.1038/ncomms3467

Pontryagin, L. S. (1987). *Mathematical Theory of Optimal Processes*. New York, NY; London, UK; Paris, Montreux, Tokyo: Gordon and Breach Science Publishers.

Schättler, H., and Ledzewicz, U. (2015). *Optimal Control for Mathematical Models of Cancer Therapies*. New York, NY: Springer. doi: 10.1007/978-1-4939-2972-6

Shackney, S. E., McCormack, G. W., and Cuchural, G. J. (1978). Growth rate patterns of solid tumors and their relation to responsiveness to therapy: an analytical review. *Ann. Intern. Med*. 89, 107-121. doi: 10.7326/0003-4819-89-1-107

Shaffer, S. M., Dunagin, M. C., Torborg, S. R., Torre, E. A., Emert, B., Krepler, C., et al. (2017). Rare cell variability and drug-induced reprogramming as a mode of cancer drug resistance. *Nature* 546:431. doi: 10.1038/nature22794

Sharma, S., Lee, D., Li, B., and Quinlan, M. E. A. (2010). A chromatin-mediated reversible drug-tolerant state in cancer cell subpopulations. *Cell* 141, 69–80. doi: 10.1016/j.cell.2010.02.027

Silva, A., Silva, M. C., Sudalagunta, P., Distler, A., Jacobson, T., Collins, A., et al. (2017). An *ex vivo* platform for the prediction of clinical response in multiple myeloma. *Cancer Res.* 77, 3336–3351.

Sontag, E. D. (1979). On the observability of polynomial systems, I: Finite-time problems. *SIAM J. Control Optimization.* 17, 139–151. doi: 10.1137/0317011

Sontag, E. D. (2017). Dynamic compensation, parameter identifiability, and equivariances. *PLoS Comput. Biol.* 13:e1005447.

Sontag, E. D., and Wang, Y. (1991). "I/O equations for nonlinear systems and observation spaces," in *Decision and Control, 1991., Proceedings of the 30th IEEE Conference on* (IEEE), 720–725.

Sussmann, H. (1982). "Time-optimal control in the plane," in *Feedback Control of Linear and Nonlinear Systems*, eds D. Hinrichsen and A. Isidori (Berlin, Heidelberg: Springer), 244–260. doi: 10.1007/BFb0006833

Sussmann, H. (1987a). Regular synthesis for time-optimal control of single-input real analytic systems in the plane. *SIAM J. Control Optim*. 25, 1145–1162. doi: 10.1137/0325062

Sussmann, H. (1987b). The structure of time-optimal trajectories for single-input systems in the plane: The C^∞ nonsingular case. *SIAM J. Control Optim*. 25, 433–465. doi: 10.1137/0325025

Sussmann, H. (1987c). The structure of time-optimal trajectories for single-input systems in the plane: the general real analytic case. *SIAM J. Control Optim*. 25, 868–904. doi: 10.1137/0325048

Traina, T. A., and Norton, L. (2011). "Log-kill hypothesis," in *Encyclopedia of Cancer*, ed M. Schwab (Berlin, Heidelberg: Springer), 2074–2075. doi: 10.1007/978-3-642-16483-5_3409

Villaverde, A. F., Barreiro, A., and Papachristodoulou, A. (2016). Structural identifiability of dynamic systems biology models. *PLoS Comput. Biol.* 12:e1005153. doi: 10.1371/journal.pcbi.1005153

Wang, Y., and Sontag, E. D. (1989). On two definitions of observation spaces. *Syst. Control Lett.* 13, 279–289.

Conflict of Interest: The authors declare that the research was conducted in the absence of any commercial or financial relationships that could be construed as a potential conflict of interest.

Copyright © 2020 Greene, Sanchez-Tapia and Sontag. This is an open-access article distributed under the terms of the Creative Commons Attribution License (CC BY). The use, distribution or reproduction in other forums is permitted, provided the original author(s) and the copyright owner(s) are credited and that the original publication in this journal is cited, in accordance with accepted academic practice. No use, distribution or reproduction is permitted which does not comply with these terms.

frontiers in Bioengineering and Biotechnology

ORIGINAL RESEARCH
published: 26 June 2020
doi: 10.3389/fbioe.2020.00667

An Integrated Spatial Dynamics—Pharmacokinetic Model Explaining Poor Penetration of Anti-retroviral Drugs in Lymph Nodes

Aditya Jagarapu[1], *Michael J. Piovoso*[2] *and Ryan Zurakowski*[1]*

[1] Department of Biomedical Engineering, University of Delaware, Newark, DE, United States, [2] Department of Electrical and Computer Engineering, University of Delaware, Newark, DE, United States

Although combined anti-retroviral therapy (cART) suppresses plasma HIV viremia below the limit of detection in a majority of HIV patients, evidence is emerging that the distribution of the anti-retroviral drugs is heterogeneous in tissue. Clinical studies measuring antiretroviral drug concentrations in lymph nodes (LNs) revealed lower concentrations compared to peripheral blood levels suggesting poor drug penetration properties. Our current study is an attempt to understand this poor anti-retroviral drug penetration inside lymph node lobules through integrating known pharmacokinetic and pharmacodynamic (PK/PD) parameters of the anti-retroviral drugs into a spatial model of reaction and transport dynamics within a solid lymph node lobule. Simulated drug penetration values were compared against experimental results whenever available or matched with data that is available for other drugs in a similar class. Our integrated spatial dynamics pharmacokinetic model reproduced the experimentally observed exclusion of antivirals from lymphoid sites. The strongest predictor of drug exclusion from the lymphoid lobule, independent of drug class, was lobule size; large lobules (high inflammation) exhibited high levels of drug exclusion. PK/PD characteristics associated with poor lymphoid penetration include high cellular uptake rates and low intracellular half-lives. To determine whether this exclusion might lead to ongoing replication, target CD4+ T cell, infected CD4+ T cell, free virus, and intracellular IC50 values of anti-retroviral drugs were incorporated into the model. Notably, for median estimates of PK/PD parameters and lobule diameters consistent with low to moderate inflammation, the model predicts no ongoing viral replication, despite substantial exclusion of the drugs from the lymphoid site. Monte-Carlo studies drawn from the prior distributions of the PK/PD parameters predicts increases in site-specific HIV replication in a small fraction of the patient population for lobule diameters greater than 0.2 mm; this fraction increases as the site diameter/ inflammation level increases. The model shows that cART consisting of two nRTIs and one PI is the most likely treatment combination to support formation of a sanctuary site, a finding that is consistent with clinical observations.

Keywords: HIV, lymph node, PK/PD modeling, sanctuary sites, inflammation, combined anti-retroviral therapy (cART)

OPEN ACCESS

Edited by:
Robert Parker,
University of Pittsburgh, United States

Reviewed by:
Chang Gong,
Johns Hopkins University, United States
Maria Rodriguez Martinez,
IBM Research - Zurich, Switzerland

***Correspondence:**
Ryan Zurakowski
ryanz@udel.edu

Specialty section:
This article was submitted to Computational Genomics, a section of the journal Frontiers in Bioengineering and Biotechnology

Received: *24 December 2019*
Accepted: *28 May 2020*
Published: *26 June 2020*

Citation:
Jagarapu A, Piovoso MJ and Zurakowski R (2020) An Integrated Spatial Dynamics—Pharmacokinetic Model Explaining Poor Penetration of Anti-retroviral Drugs in Lymph Nodes. Front. Bioeng. Biotechnol. 8:667. doi: 10.3389/fbioe.2020.00667

1. INTRODUCTION

Human Immunodeficiency Virus (HIV) is a retrovirus that attacks the CD4 T lymphocytes (CD4 Cells) of the immune system. Combination anti-retroviral (cART) therapy have tremendously reduced HIV associated morbidity and mortality. However, the virus will rebound during treatment interruptions in almost all patients. This is understood to be primarily due to the activation of long-lived, quiescent infected cells that persist during therapy and intermittently activate producing virus.

Recent studies have shown that antiretroviral drugs distribute heterogeneously in various tissues, which raises the possibility that drug concentrations in some tissues may be low enough to allow ongoing HIV replication even in treated patients, forming sanctuary sites. Non-human primate experiments revealed high concentrations of viral RNA and DNA in lymphoid tissues (particularly the spleen, lymph nodes, and gut tissues) compared to suppressed levels in plasma during treatment conditions (North et al., 2009). Pharmacokinetic measurements using positron emission tomography in rats revealed a two-fold decrease in drug concentration in spleen and submandibular lymph nodes, four-fold reduction in mesenteric lymph nodes and the testes, 25-fold reduction in the brain compartment compared to the blood compartment (Di Mascio et al., 2009). Similarly anti-retroviral drug concentrations in human subjects were studied (Fletcher et al., 2014) with multiple sampling of drug concentrations from lymph node, ileum, rectum and plasma compartments after initiation of cART; comparison of the average concentrations in lymph nodes to peripheral blood showed that Tenofovir-diphosphate (TVF-DP), Emtricitabine-triphosphate (FTC-TP), Atazanavir (ATV), Darunavir (DRV), and Efarivenz (EFV) were 80, 66, 100, 99, and 94% lower in the lymph nodes, respectively. These drug distribution studies in animal and human subjects reveal significantly lower drug concentrations in the lymphoid tissues.

Treatment intensification schemes with integrase inhibitor (Raltegravir) revealed a transient increase in 2-LTR circles which are markers of a failed linear DNA integration during viral replication in the host genome (Buzón et al., 2010). Approximately 29% of the HIV positive patients who were on cART with suppressed levels of viral load in peripheral blood compartment observed a transient increase in CD4+ T cells containing HIV 2-LTR following raltegravir intensification. Mathematical modeling on the formation of 2-LTR circles during treatment intensification studies explain that a rapid increase followed by a decrease in 2-LTR circles is evidence of significant levels of ongoing infection, rather than simple virus release from reservoir cells (Luo et al., 2013). This implies the presence of sanctuary sites in these patients.

In our previous work, we proposed a spatial dynamics mathematical model that predicted conditions under which the formation of a sanctuary site is possible inside a lymphoid lobule (Cardozo et al., 2014). Our previous model demonstrated that the 2-LTR dynamics under treatment intensification observed in the INTEGRAL study (Buzón et al., 2010) were possible only if inflammation had increased the size of, and consequently the T cell residence time in, the lymphoid lobule. In the previous study, reduced drug activity within the lobule was assumed, but the mechanisms of drug exclusion were not explored. The current study seeks to estimate the drug penetration for the most commonly used anti-retroviral drugs and understand their transport inside a lymphoid lobule. In order to understand drug transport inside lymph nodes, a model incorporating both reactive and transport mechanisms of cellular components and drugs is developed. Published PK/PD models for representative drugs from each class have been selected and integrated into the spatial dynamic model to evaluate drug penetration inside lymph nodes. Transport between extracellular and intracellular compartments, together with metabolism and degradation rates for each drug, use median published PK/PD parameters. Extracellular drug diffusion rates inside the lymph nodes are calculated using thermodynamic principles, and intracellular transport rates are based on measured T-cell kinetics within lymph nodes as described in our previous work.

2. BIOLOGICAL BACKGROUND

2.1. Transport Biology of the Lymph Node

Lymph nodes are surrounded by a fibrous capsule that is contiguous with the afferent and efferent lymphatic ducts, which connect the lymph node to the lymphatic capillary network. Directly under the surface of the fibrous capsule is a network of fluid lymph channels known as the lymphoid sinuses. The sinuses are open fluid channels that form a contiguous fluid path from the afferent lymphatic ducts to the efferent lymphatic ducts, as shown in **Figure 2A**. These are separated from the LN parenchyma by a fenestrated fibrous layer (**Figure 2C**). The parenchyma is subdivided by these fibrous boundaries and sinuses into several functional units called lobules. The lobule interior is densely populated with lymphocytes, which can move freely on a reticular fiber meshwork. The basal end of each lobule extends into the lymph node medulla, where it is adjacent to a large number of narrow sinus channels called the medullary sinuses, which facilitate drainage of the lobule into the sinus network and the efferent lymphatic duct (Willard-Mack, 2006). The entire LN lobule is vascularized by specialized post capillary venous channels called High Endothelial Venules (HEV) illustrated in **Figure 2B**. The HEV, as the name implies, have characteristically thick walls consisting of cuboidal endothelial cells bound by tight junctions. Similar in structure to the capillary walls of the blood-brain barrier, the HEV facilitates highly selective transport between the blood and the lymph node parenchyma.

Lymphocytes in the blood and peripheral tissue enter the LN through one of the two ways: either through specialized post capillary venous channels called High Endothelial Venules (HEV) located in the paracortex region, or through the afferent lymph vessel and the subcapsular sinus. HEV cells express specific adhesion molecules that facilitate efficient transport of the lymphocytes along the endothelial surface of the HEVs. Approximately 2% of the T cells are recruited through HEVs from the recirculating pool per day (Von Andrian and Mempel, 2003). The other cellular components of the lobule, such as macrophages, antigen bearing dendritic cells (DCs) and some

lymphocytes, enter from afferent lymphatic vessels, cross the sinus boundaries into the lobule, pass into the medullary sinuses, and eventually leave via the efferent lymphatic vessels.

T cells explore the LN lobule via random walk, and generate an immune response if they encounter antigen presenting cells (APCs) displaying their specific cognate antigen. T cells spend roughly 6–18 h exploring a particular lymph node in uninflamed conditions. However during inflammatory conditions, lymphocyte accumulation is markedly increased and their exit into the efferent lymphatics is transiently blocked (Cahill et al., 1976). This effect increases the probability of lymphocytes encountering presented antigen, by dramatically increasing the time spent exploring the inflamed lymph node. Those lymphocytes that do not encounter cognate antigen will exit the lobule and eventually the LN through the cortical sinus and the efferent lymph vessel (Von Andrian and Mempel, 2003).

2.1.1. Transport of Antiviral Drugs Within a Lymph Node

All antiretroviral drugs used in cART are taken orally, and rapidly transport across the intestinal walls to the bloodstream. The small molecule nature of the drugs facilitate their rapid transport into the lymphoid capillaries. The drugs are taken up into cells via active and passive transport mechanisms, and some of the drugs may undergo metabolic conversion from prodrug to active form. Transport of the drugs and their various metabolites into a lymphoid follicle can thereby occur through two major channels: the blood, through the HEV network, and the fluid lymph, through the sinus network. In both of these channels, the drug may enter the lymph node either as free drug or carried intracellularly by cells migrating into the lymphoid lobule.

2.1.2. cART Mechanisms of Action

HIV infects CD4+ T cells. Uninfected CD4+ T cells are infected by HIV at a mass-action rate forming infected CD4+ T cells. Intracellular HIV events result in the budding of new HIV particles. These infect more CD4 + T cells, continuing the cycle.

Combined anti-retroviral therapy (cART) consists of a combination of drugs that each block one or multiple stages of the viral life-cycle, preventing viral replication. Currently there are six different mechanistic classes of drugs.

HIV initially binds to the CD4 surface receptor and either the CCR5 or CXCR4 co-receptor on the CD4+ T cell. Drugs known as chemokine co-receptor antagonists (CCR5 antagonists) block the virus from binding to the co-receptor and prevent the entry of virus into the host cell (Danjuma, 2009).

After transfer of the viral RNA into the host cytoplasm, the reverse transcriptase enzyme converts the viral RNA into DNA in a process called reverse transcription. Nucleoside Reverse Transcriptase Inhibitor (nRTI) are incorporated into viral DNA instead of natural nucleotides during this stage, resulting in termination of the reverse transcription (Pau and George, 2014). Non-nucleoside Reverse Transcriptase Inhibitors (NNRTI) target and bind to the active catalytic site of the reverse transcriptase (RT) enzyme, preventing the reverse transcriptase enzyme from converting the viral RNA into DNA at the reverse transcription stage (Danjuma, 2009).

Successful reverse transcription produces viral DNA which is transported into the host nucleus for integration into the host genome by the viral integrase enzyme. Integrase strand transfer inhibitors (INSTI) bind to a specific complex between the viral DNA and integrase enzyme, blocking the integration of the viral DNA into the host genome. This results in the formation of episomal artifacts such as linear unintegrated DNA, 1-LTR, and 2-LTR circles which have been investigated as markers for ongoing viral replication (Arts and Hazuda, 2012).

After successful integration into the host genome, transcription and translation results in the production of non-functional polyproteins. The protease enzyme breaks these long chain proteins into functional matrix, capsid and nucleocapsid proteins. Protease Inhibitors (PI) bind to the protease enzyme and prevent the proteolytic cleavage of polyproteins, resulting in the formation of non-infectious viral particles (Arts and Hazuda, 2012).

Three different treatment combinations are most commonly prescribed to treatment-naive patients. Each combination includes two nRTI's which are referred as "backbone" drugs, plus one drug from the PI, INSTI, or NNRTI classes (Eron et al., 2008; Pau and George, 2014).

2.2. Integrated Pharmacokinetic-Spatial Dynamics (PKSD) Compartmental Model

2.2.1. Previous Models

Several different groups have introduced lymph node models, all focusing on lymphocyte circulation, migration between blood and lymph, T cell motility inside lymph nodes, and HIV induced immune response during inflammation (Kirschner et al., 2000; Baldazzi et al., 2009; Mirsky et al., 2011; Marinho et al., 2012). None of these focused on drug transport and exclusion or ongoing HIV replication. A recent study modeling persistent viral replication in HIV patients (Lorenzo-Redondo et al., 2016) used a simple two-compartment model assuming heterogeneity in the drug distribution between the two compartments to investigate the possibility of ongoing replication in a drug-privileged node; the simplicity of this model does not allow it to explore mechanisms of drug exclusion from the lymph node.

Our previous work in modeling lymph node consists of a spatial, N - compartmental model (N>2) of lymphoid lobules as sanctuary sites explaining viral dynamics in the presence of anti-retroviral drugs. We explored the behavior of these sanctuary sites across a wide range of parameter values and showed that the necessary conditions for low-level ongoing replication is a sanctuary site with large size and low drug efficacy inside it (Cardozo et al., 2014). This study assumed low drug concentrations in the sanctuary sites and did not investigate the mechanism of drug exclusion.

2.2.2. Model Description

In the current study we modified the previous spatial compartmental model to incorporate pharmacokinetic properties of frequently used anti-retroviral drugs. In this work, we model HIV, cell, and drug dynamics in blood, lymphoid sinuses, and lymphoid lobules, including the transport of cells, anti-retroviral drugs and virus between them. Published

pharmacokinetic parameters and experimental drug transport values have been used in the model to reflect realistic behavior behind drug transport and their efficacy inside the lobules. Monte-Carlo studies sampling from the published or inferred uncertainty in these parameters has been used to explore the variance and robustness in the behavior. Our results indicate that despite limited drug transport into the lymphoid lobule and resulting low drug efficacy conditions inside the lymphoid lobule, only a small subset of patients on cART will develop the necessary conditions for sanctuary site formation with ongoing HIV replication. The formation of sanctuary sites was far more likely when patients were on nRTI/PI cART compared to nRTI/INSTI or nRTI/NNRTIs cART, and the proportion of patients with ongoing replication increases as the size of the lobules increase.

The model developed in this paper is a reaction/diffusion model. The reaction dynamics describing HIV infection are adapted directly from the basic HIV model (Ho et al., 1995; Wei et al., 1995; Perelson et al., 1997; Nowak and May, 2000; Perelson and Ribeiro, 2013). Published pharmacokinetic studies have been used for modeling the dynamics of anti-retroviral drugs in both plasma and lymphoid lobule (Dixit and Perelson, 2004; Hurwitz et al., 2007; Arab-Alameddine et al., 2012; Habtewold et al., 2017). Modeling assumptions concerning transport of T cells and antiretroviral drugs are as follows:

- Transport of T cells and anti-retroviral drugs between lobule and blood/fluid lymph is assumed to be diffusion-like.
- Transport of T cells and anti-retroviral drugs inside the lobule is assumed to be diffusion-like.
- Free HIV particles are assumed to be blocked from entry into or exit from the lobule. Infected cells may carry HIV in or out.
- Transport between blood and lymphatic sinuses and recirculation within these compartments is assumed to be much faster than transport into and out of the lobule, so blood and lymphatic sinuses are modeled as a single well-stirred compartment.
- Transport between the blood/lymphatic sinus compartment and the lobule occurs primarily at the outer boundary of the lobule. Transport of drugs, lymphocytes and virus across HEV in the lobule interior has been neglected, as most vasculature is associated with the sinus boundaries, and transport of free drugs is expected to be extremely limited across the HEV due to their similarity to the blood-brain barrier (Engelhardt and Wolburg, 2004; Pfeiffer et al., 2008).
- The rate of elimination of the drugs within the lobule compartments is similar to the rate in the blood/lymph compartment.

Based on the above assumptions, the reaction diffusion system has been modeled into a set of compartmental diffusively-coupled ODEs as described in our previous study (Cardozo et al., 2014). The overall system consists of a main compartment that includes blood and the lymphatic sinuses communicating with N spherical domains representing all the lobules in the human body. These lobules are all connected to the blood/lymph compartment, but not to each other. Within each lobule the method of lines have been used to spatially discretize the reaction-diffusion PDE domain into n-1 concentric spherical shells, where only the outermost shell is in contact with the blood/lymph compartment. The total number of lobules $N = 20{,}000$, and the distribution volume of the blood/lymph compartment is 15 liters. Previous work in Cardozo et al. (2014) showed negligible variation in results for compartment numbers larger than 10, so $n = 10$ in this study. Each spherical shell has been denoted by a subscript s.

The basic viral dynamic model in the presence of anti-retroviral drugs has been previously described (Ho et al., 1995; Wei et al., 1995; Perelson et al., 1997; Nowak and May, 2000; Perelson and Ribeiro, 2013), and is summarized in **Figure 1** and Equations (1–3). The states within each compartment s are Uninfected/Target CD4+ T cells ($\mathbf{x_s}$), actively infected cells ($\mathbf{y_s}$), and free virus $\mathbf{v_s}Y_s$). Other viral dynamic parameters include λ, the regeneration rate of healthy T cells, d, the turnover rate of healthy T cells, β, the mass-action infection rate of T cells by HIV, a, the death rate of productively infected T cells, γ, the production of HIV virus from infected cells, ω, the decay rate of free virus, and y_e, the rate at which productively infected cells arise from the quiescent reservoir. These parameter values and their uncertainties have been previously estimated from treatment interruption trial data in Luo et al. (2012), and are detailed in **Table S1**.

The application of the nRTIs, NNRTIs, INSTIs, and PIs is represented as binary input variables u_n,u_{nn},u_i,and u_p, respectively. As an example, u_n=1, u_{nn}=1, u_i=1, u_p=0 indicates a drug combination consisting of an nRTI,NNRTI and an INSTI excluding PI. Since nRTIs, NNRTIs and INSTIs block the viral replication before viral integration, they reduce infectivity β with efficacies ϵ_n, ϵ_{nn}, and ϵ_i, respectively. Protease inhibitors reduce the effective virus production rate γ with efficacy ϵ_p. Usually a combination of drugs are used as treatment strategy for HIV (cART) comprising a total of three drugs selecting two from nRTIs and third one from either of the three class i.e., NNRTIs or INSTIs or PIs. The pharmacodynamic values of the drug efficacies are functions of the drug concentrations within the compartment, explained in greater detail in the next section.

$$\dot{x} = \lambda - d\mathbf{x} - \beta\mathbf{x}\mathbf{v}(1 - u_n\epsilon_n)(1 - u_{nn}\epsilon_{nn})(1 - u_i\epsilon_i) \quad (1)$$

$$\dot{y} = \beta\mathbf{x}\mathbf{v}(1 - u_n\epsilon_n)(1 - u_{nn}\epsilon_{nn})(1 - u_i\epsilon_i) - a\mathbf{y} + y_e \quad (2)$$

$$\dot{\boldsymbol{v}} = \gamma(1 - u_p\epsilon_p)\mathbf{y} - \omega\mathbf{v} \quad (3)$$

The HIV infection dynamics are reaction dynamics occurring between species in the same spatial compartment. Species also migrate between compartments following diffusion principles. The transport of lymphocytes, ARV drugs and HIV between compartments is shown in **Figure 2**. Compartment ($s = 1$) consisting of the blood and fluid lymph, is in contact with only the outermost shell ($s = 2$) of the lymphoid lobules which is further linked with other $n-1$ compartments in series as shown in **Figure 2**. Transport of cellular and molecular components between these compartments depends on their diffusive properties and their concentration differences between

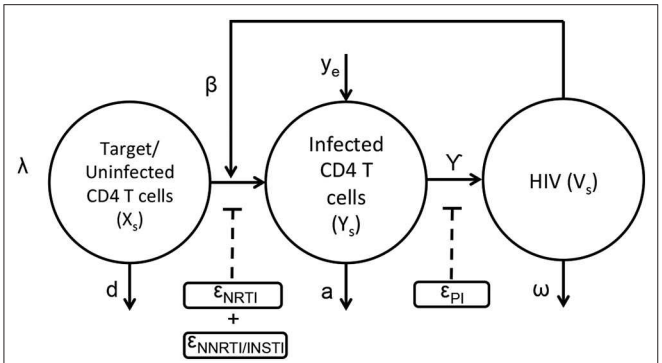

FIGURE 1 | Schematic representation of HIV dynamics in the presence of ART.

any two compartments. Equations (4–9) are the ODE equations resulting from the method of lines discretization of the reaction diffusion equations, including spatial transport mechanisms along with the HIV dynamics. Equations (4–6) represent transport between the blood/lymph ($s = 1$) with the outermost compartment ($s = 2$) of the lobule as discussed above. The rate of diffusive flux is directly proportional to concentration difference, surface area and inversely proportional to the volume and length between any two adjacent compartments. The set of indices for the compartments which are adjacent to compartment s is the set ψ_s. $A_{(i,s)}$, represents the surface area between any two adjacent compartments i and s in the lobule. $V_s, \frac{D_{(xi,s)}}{l} = \frac{D_{(yi,s)}}{l}$, $\frac{D_{(vi,s)}}{l}$ represents the volume, effective diffusivity of uninfected, infected CD4 T cells and virions of the layer between the i^{th} and s^{th} compartments. In this case, cART consisting of two NRTIs and a PI is modeled. The efficacies of the two NRTIs and the PI have been denoted as "ϵ_{NRTI1}," "ϵ_{NRTI2}," "ϵ_{PI}." The actual effectiveness is a function of the concentration of the drug within the compartment and the pharmacodynamics of the drug, which are discussed in the next section.

$$\dot{\mathbf{x}}_1 = \lambda - d\mathbf{x}_1 - \beta\mathbf{x}_1\mathbf{v}_1(1-\epsilon_{NRTI1,1})(1-\epsilon_{NRTI2,1}) + N\frac{D_{x1,2}}{l}\frac{A_{1,2}}{V_1}(\mathbf{x}_2 - \mathbf{x}_1) \quad (4)$$

$$\dot{\mathbf{y}}_1 = \beta\mathbf{x}_1\mathbf{v}_1(1-\epsilon_{NRTI1,1})(1-\epsilon_{NRTI2,1}) - a\mathbf{y}_1 + y_e + N\frac{D_{y1,2}}{l}\frac{A_{1,2}}{V_1}(\mathbf{y}_2 - \mathbf{y}_1) \quad (5)$$

$$\dot{\mathbf{v}}_1 = \gamma(1-\epsilon_{PI,1})\mathbf{y}_1 - \omega\mathbf{v}_1 + N\frac{D_{v1,2}}{l}\frac{A_{1,2}}{V_1}(\mathbf{v}_2 - \mathbf{v}_1) \quad (6)$$

Transport between adjacent compartments within the lobule is described in Equations (7–9).

$$\dot{\mathbf{x}}_s = \lambda - d\mathbf{x}_s - \beta\mathbf{x}_s\mathbf{v}_s(1-\epsilon_{NRTI1,s})(1-\epsilon_{NRTI2,s}) + \sum_{i\in\psi_s}\frac{D_{xi,s}}{l}\frac{A_{i,s}}{V_s}(\mathbf{x}_i - \mathbf{x}_s) \quad (7)$$

$$\dot{\mathbf{y}}_s = \beta\mathbf{x}_s\mathbf{v}_s(1-\epsilon_{NRTI1,s})(1-\epsilon_{NRTI2,s}) - a\mathbf{y}_s + y_e + \sum_{i\in\psi_s}\frac{D_{yi,s}}{l}\frac{A_{i,s}}{V_s}(\mathbf{y}_i - \mathbf{y}_s) \quad (8)$$

$$\dot{\mathbf{v}}_s = \gamma(1-\epsilon_{PI,s})\mathbf{y}_s - \omega\mathbf{v}_s + \sum_{i\in\psi_s}\frac{D_{vi,s}}{l}\frac{A_{i,s}}{V_s}(\mathbf{v}_i - \mathbf{v}_s) \quad (9)$$

2.2.3. Pharmacokinetic/Pharmacodynamic (PK/PD) Models

Efficacy (pharmacodynamics) for each drug is assumed to follow Hill dynamics as described in Equation (10). The terms IDC(t), IC_{50} and "n_{drug}" in Equation (10) denote the effective drug concentration (usually the intracellular concentration of the active form) at any time "t," amount of drug concentration required to produce a 50% inhibitory effect and the Hill coefficient for the drug, respectively. Drugs from each class were chosen based on the availability of published PK/PD models and their associated parameters. The following sub-sections describe the PK/PD models for the drugs used in the current study.

$$\epsilon_{\mathbf{drug}} = IDC(t)^{n_{drug}}/(IC_{50}^{n_{drug}} + IDC(t)^{n_{drug}}) \quad (10)$$

2.2.3.1. NRTI: nucleoside reverse transcriptase inhibitor (Tenofovir, Lamivudine)

The most commonly used nRTIs are tenofovir and abacavir, both of which are used in combinations with emtricitabine or lamivudine as the second nRTI. In our current simulations, we chose to use tenofovir and lamivudine as the two nRTI drugs in the antiretroviral repertoire. The intracellular pharmacokinetic models for these drugs have been adopted from Baheti et al. (2011), Dixit and Perelson (2004), and Hurwitz et al. (2007).

Tenofovir is usually administered in its monophosphorylated analog Tenofovir Disoproxil Fumarate (TDF) in doses of 300 mg/day. The pharmacokinetics of tenofovir are shown in **Figure 3**. After oral administration it is rapidly adsorbed into the plasma at a rate k_{Ta} with a bioavailability F_T and eliminated from the plasma compartment(T_p) at a rate k_{Te}. TDF binds minimally with the proteins by a factor f_{BT} in the extracellular space and starts to accumulate in the intracellular compartment at a rate k_{Tacell} across the cell boundary with a partition coefficient H_T. Once the monophosphate form of the drug reaches the intracellular space, it undergoes only two steps of phosphorylation to obtain the triphosphate anabolite unlike other nRTIs that undergo three steps of phosphorylation. The forward rate constants for the formation of TDF monophosphate and TDF diphosphate are k_{1f} and k_{2f} while the backward rate constants are k_{1b} and k_{2b}, respectively. All the intracellular components of the drug are eliminated at a rate k_{Tecell} from the cell. The intracellular concentrations of TDF, TDF monophosphate and TDF diphosphate are represented as T_c,T_{cmp}, and T_{cdp}, respectively.

The pharmacokinetic model for simulating lamivudine (3TC) has been adopted from Hurwitz et al. (2007) as shown in **Figure 4**. The extracellular pharmacokinetics have been described by a two compartment model (Plasma and Deep

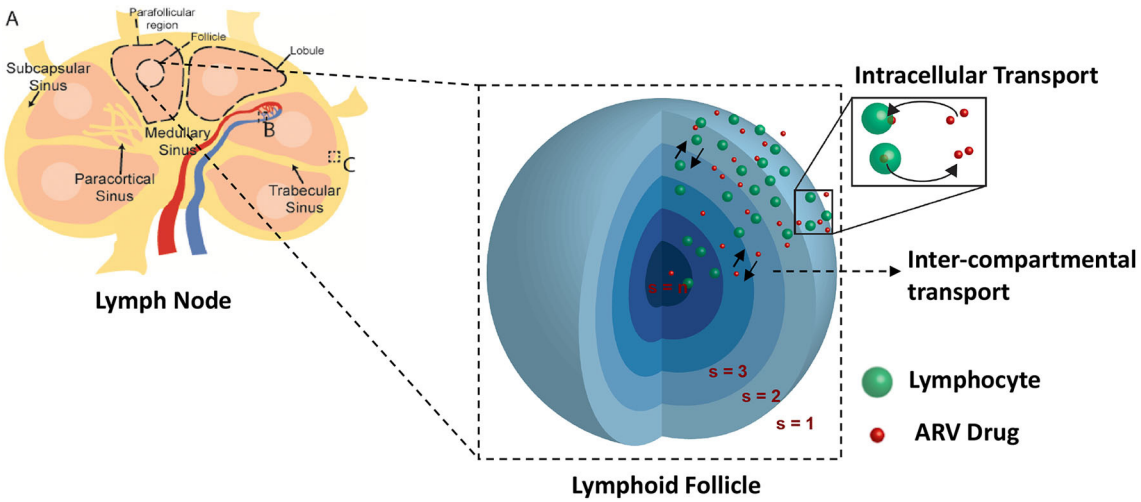

FIGURE 2 | Spatial compartmental model. Lymph node diagram **(A)** highlights the vascular interface **(B)**, and sinus interface **(C)**.

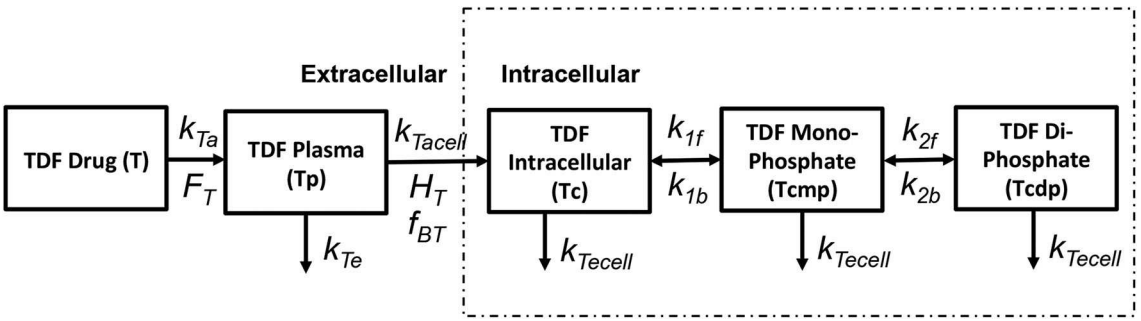

FIGURE 3 | Tenofovir pharmacokinetic model (Dixit and Perelson, 2004).

tissue), where the drug absorption into plasma was assumed to be a zero order process with input (F^*D/T_1) where "F" is the bioavailability of the drug, "D" is the drug dosage (150 mg twice daily) and "T_1" is the time period (1 or 3 h) for the zero order absorption. The plasma concentration (L_P) is further distributed between the deep tissue (L_{DT}) and the intracellular compartments (L_C). Drug elimination from the plasma compartment takes place at a rate k_{EP}. The inter-compartmental clearance rates k_{PT} and k_{TP} describe the rate at which the plasma concentration is transferred from plasma to tissue and vice versa. Rapid equilibrium is assumed to be achieved between the plasma concentration and intracellular concentration of 3TC due to action of equilibrative nucleoside transporters present on the cell membranes of lymphocytes as assumed in Hurwitz et al. (2007). Intracellular 3TC undergoes series of phosphorylation steps to form 3TC triphosphate (L_{CTP}). Formation of 3TC monophosphate (L_{CMP}) was assumed to be rate limiting and the conversion was modeled using Michaelis-Menten reaction with maximum rate (V_m) and Michaelis-Menten constant (K_M). Rapid equilibrium is assumed in-between phosphorylation steps with ratios $R_{DP/MP}$ and $R_{TP/DP}$ relating the concentrations between the 3TC-diphosphate to 3TC-monophosphate and 3TC-triphosphate to 3TC-diphosphate. Re-circulation of 3TC-triphosphate to 3TC-monophosphate was also considered with the formation of an intermediate metabolite (M) with $K_{CTP\text{-}M}$ as the rate of formation and $K_{M\text{-}CMP}$ as the rate of conversion of metabolite to 3TC-monophosphate.

2.2.3.2. NNRTI: non-nucleoside reverse transcriptase inhibitor (Efarvirenz)

Currently five different NNRTIs have been approved by FDA for antiretroviral therapy. For our current study we chose to use efarivenz due to the availability of a previously published intracellular pharmacokinetic model by Habtewold et al. (2017) as shown in **Figure 5**. Efarivenz (EFV) is usually prescribed once daily in doses of 600mg single pill. The pharmacokinetic model was described by a two-compartmental model with concentrations of EFV distributed between the plasma and peripheral blood mono-nuclear cells (PBMC). First order kinetics has been used to describe the transfer of drug from gastrointestinal tract (E) to plasma (E_p) at a rate k_{Ea} and from plasma (E_p) to the intracellular compartment

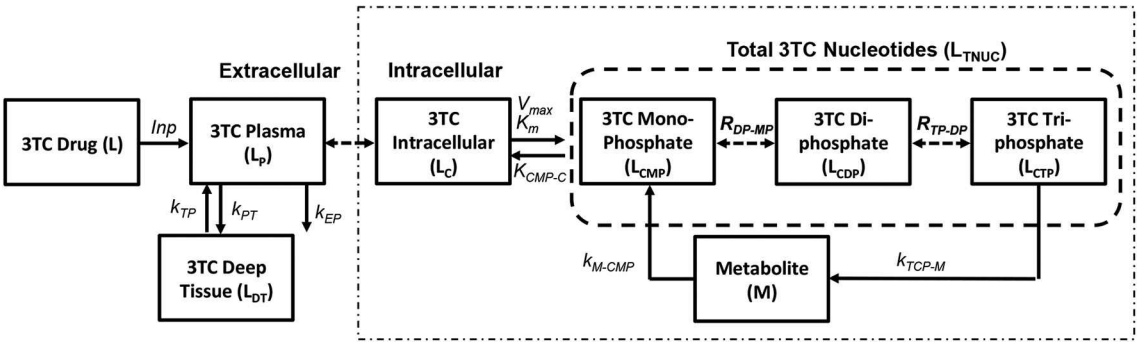

FIGURE 4 | Lamivudine pharmacokinetic model (Hurwitz et al., 2007).

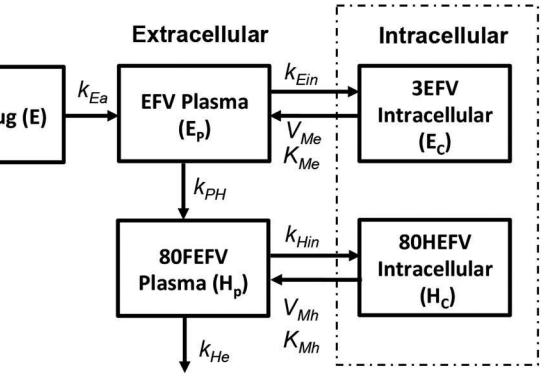

FIGURE 5 | Efarivenz pharmacokinetic model (Habtewold et al., 2017).

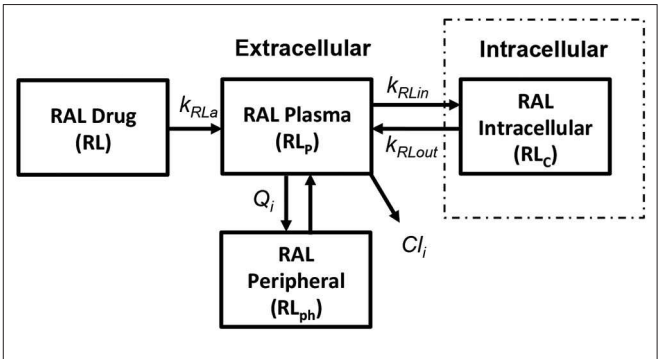

FIGURE 6 | Raltegravir pharmacokinetic model (Arab-Alameddine et al., 2012).

(E_c) at a rate k_{Ein}. Transport of drug from intracellular compartment (E_c) to plasma (E_p) has been assumed to follow a nonlinear saturating inter-compartmental clearance process with V_{Me} and K_{Me} as the maximum rate and Michaelis-Menten constant, respectively. EFV in plasma is further converted into its metabolite 80HEFV (H_p) at a rate k_{Ee} and the inter-compartmental clearance of 80HEFV was modeled with similar kinetics for forward and backward transport of EFV between plasma (H_p) and intracellular compartments (H_c). NNRTIs do not require phosphorylation like NRTIs to inhibit reverse transcriptase. Hence we used the concentration of EFV in the intracellular compartment to evaluate the instantaneous drug efficacy in Equation (10) for the viral dynamics in our reaction-diffusion model.

2.2.3.3. INSTI: integrase inhibitor (Raltegravir)

We use the integrase inhibitor Raltegravir (RAL) in this study; its pharmacokinetics were studied in both HIV-positive (HIV^+) and healthy individuals in Arab-Alameddine et al. (2012). A basic two compartmental model with first order absorption rate (k_{Ra}) from the gastrointestinal tract (R) to plasma (R_p) and with an inter-compartmental clearance (Q_i) between plasma (R_p) and peripheral compartment (R_{ph}) was described in their study as shown in **Figure 6**. The other parameters that were estimated in this population pharmacokinetic model include the apparent volumes of distribution for plasma (V_p) and peripheral compartment (V_{ph}) along with apparent clearance of drug from the plasma compartment (Cl_i). The above pharmacokinetic study did not evaluate the intracellular pharmacokinetics in their model. However, other studies estimated the cellular penetration values (ration of raltegravir concentration between intracellular and plasma compartments) as between 5% (Fayet Mello et al., 2011) to 11% (Wang et al., 2011). Using this range of penetration values, we assumed steady state conditions between plasma (R_p) and intracellular compartments (R_c) to estimate the forward (k_{Rin}) and backward (k_{Rout}) drug transfer constants across the cellular membrane for raltegravir. Recommended dosage of 400 mg twice daily for raltegravir has been used in our simulations.

2.2.3.4. PI: protease inhibitor (Ritonavir)

In order to obtain the intracellular drug concentrations for PI we chose to adopt the pharmacokinetic model on ritonavir used by Dixit and Perelson (2004) to evaluate its effect as monotherapy in viral dynamics, shown in **Figure 7**. A relatively simple model of drug transport from plasma (R_p) to intracellular compartment (R_c) has been discussed with k_{pa}, k_{pe}, k_{pacell}, k_{pecell} describing the rate of drug absorption from the drug compartment (R), rate of drug elimination from plasma compartment, rate of forward transport and backward transport

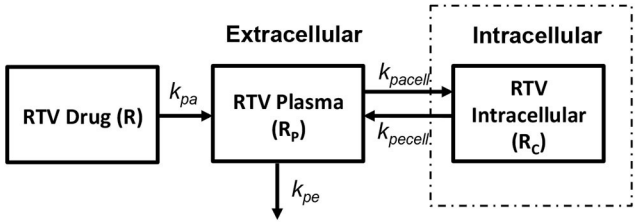

FIGURE 7 | Ritonavir pharmacokinetic model (Dixit and Perelson, 2004).

across the cellular membrane, respectively. *In vitro* studies suggest that the intracellular concentrations of ritonavir reach steady state very quickly describing that the cell membrane offers little resistance for ritonavir transport. However, the steady state concentrations are different across the cellular membrane which can be modeled using a non-unit partition coefficient. The non-unit partition coefficient was established from *in vitro* studies in Dixit and Perelson (2004) and included the protein binding fraction to estimate the concentration of intracellular ritonavir concentration as a ratio of the plasma concentration. We modified this transfer coefficient (partition coefficient along with protein binding effect) into a forward (k_{pacell}) and backward (k_{pecell}) rate constants by adjusting the ratios such that they give the same transfer coefficient as used in Dixit and Perelson (2004). This method was adopted to evaluate the time evolution of the intracellular ritonavir concentration for our simulations. Six hundred milligrams of pill with twice daily as dosage regimen has been chosen to evaluate the time evolution of the plasma and intracellular concentrations as used in Dixit and Perelson (2004).

2.3. Parameter Values and Uncertainties

All the parameters used in this study have been obtained from previously published works on HIV viral dynamics, experimental studies on drug transport and T cell motion inside the lymph node and population pharmacokinetic studies on drug distribution and metabolism in HIV patients. These parameters are known to have a significant degree of within-patient drift and between-patient variability. To investigate the range of behaviors consistent with the parameter heterogeneity, we undertook a Monte-Carlo analysis drawing from prior distributions for each uncertain parameter. For parameters that were published with experimental uncertainty intervals, we have used the published uncertainty values; for parameters without published uncertainty, we have imputed an uncertainty interval of ±20% of the published nominal value. The HIV dynamic parameters are highly correlated, and drawing independently from each parameter's prior can result in non-physiological behavior. Instead, we have drawn our HIV dynamic parameter values from the multi-dimensional distributions obtained by Bayesian model fits to interruption trial data from 12 HIV patients previously published in Luo et al. (2012). The exact parameter values used in this study, together with the uncertainty intervals used in the Monte-Carlo studies, can be found in **Tables S1–S8**.

2.3.1. Viral Dynamics

Parameters for viral dynamics have been obtained from parameter identification studies for HIV sampled from frequently sampled viral load data from ten patients enrolled in the published AutoVac HAART interruption study (Ruiz et al., 2000). The viral dynamic parameters have been estimated using a Bayesian Markov-Chain Monte-Carlo method. The posterior estimates on the parameters are based on the experimental data of HIV patients who had 3–5 treatment interruption cycles (Luo et al., 2012). The estimated parameters with confidence intervals that were used in the current study can be found in **Table S1**.

2.3.2. Diffusion Parameters

2.3.2.1. Effective diffusivity of T cells and virus

The effective diffusivity for T cells across the boundary between lymphoid lobule and the blood/lymph compartment is estimated as described in our previous work (Cardozo et al., 2014). Previous experimental studies have shown that lymph nodes with an average diameter of 1 mm in a mouse recruit approximately 2% of the circulating T cells in the absence of infection. Hence, the effective diffusivity of T cells across the boundary i.e., between the blood compartment and the outermost spherical compartment of the lymphoid lobule $D_{x_{b,LN}}/l$, $D_{y_{b,LN}}/l$ can be obtained from the equation $(D_{x_{b,LN}}/l)(A_{b,LN}/V_{b,LN})x_b = 0.02x_b$ where $A_{b,LN}$, $V_{b,LN}$ are the area and volume of the lymphoid lobule. The effective diffusivity $D_{x_{b,LN}}/l$ equals 1/300 mm/day when the lymph node diameter is 1 mm. Since the target CD4 cells and infected CD4 cells have similar effective diffusivity, the calculated values for $D_{x_{b,LN}}/l = D_{y_{b,LN}}/l$.

The effective diffusivity within the lymphoid lobule (i.e., between any two concentric compartments in our model) is equal to the average value of the experimentally observed motility coefficient of T-cells within lymphoid lobules which is 0.1 mm^2/day (Von Andrian and Mempel, 2003; Beltman et al., 2007; Mirsky et al., 2011; Girard et al., 2012) divided by the length of each layer $l = r/(n\text{-}1)$, where "r" is the radius of the lymphoid lobule and "n" is the total number of compartments in the model.

2.3.2.2. Effective diffusivity of drugs

Effective diffusivity of the drugs inside the lymphoid lobule has been calculated using the diffusion coefficients theoretically obtained from the Einstein-Stokes equation and the viscosity of fluid lymph. Effective viscosity within the lymph node will be higher due to the high density of cells and extracellular matrix components. Experiments tracking the motility of single-molecule chemokine AF647-tagged CXCL13 using high speed light microscopy system capable of millisecond sampling in an *ex vivo* native mouse lymph node environment allow for direct measurement of these values (Miller et al., 2018). The experimentally observed values were 22.7 times less than the values for fluid lymph; we adjusted our values by the same factor. The adjusted drug diffusion coefficients used in our simulations can be found in **Table S2**.

In order to evaluate the effective drug diffusivity across the boundary i.e., between the blood/ fluid lymph and lymphoid lobule, we calculate the ratio of effective diffusivity values for T cells between the boundary and the inner lobule (values

discussed in the previous section) and assume a similar ratio for effective diffusivities across the boundary and inner lobule for the antiretroviral drugs. Hence, we multiply this ratio (boundary/inner lobule for T cells) with the adjusted drug diffusivity inside the lymphoid lobule (obtained from Einstein stokes equation) to obtain the effective diffusivity across the boundary i.e., between blood/lymph and the lobule. For an average lymphoid lobule with a diameter of 0.2 mm with 10 total compartments, i.e., $n = 10$, the effective diffusivity (D/l) would be 9 mm/day. The ratio of effective diffusivity at the boundary to the inner lobule would be 1/2,700 which was used to estimate the effective diffusivity for the drugs at the boundary (**Table S3**). Recall that we are assuming that transport for most species is dominated by transport from the subcapsular sinus, which is separated from the lobule by a fibrous epithelial boundary—this ratio can be interpreted as the fraction of total surface area available for transport across this boundary.

2.3.3. Pharmacokinetic Parameters

All the reaction rate constants, elimination rate constants for each individual drug have been obtained from the published pharmacokinetic studies as mentioned above. Parameters for evaluating the instantaneous efficacy of the drug such as IC_{50} and hill coefficient "*n*," have been determined from the dose-response curves on antiretroviral drugs studied by Shen et al. (2008). Pharmacokinetic parameter estimates used in our current study can be found in **Tables S4–S8**.

2.4. Monte-Carlo Simulations

Integrating the above discussed population pharmacokinetic models along with the spatial compartmental model gives us the integrated pharmacokinetic spatial compartmental model to understand the drug transport and viral dynamics inside the lymphoid lobule of a HIV patient. In order to investigate the robustness of drug transport effects to parameter uncertainty and inter-patient variability, we employed Monte Carlo simulations by sampling random values from parameter distributions on viral dynamics and pharmacokinetics. The 95% confidence intervals from which we draw our Monte-Carlo samples are shown in the **Supplementary Tables**. Simulations were carried out on varying sizes of lymphoid lobule with diameters of 0.01, 0.05, 0.10, 0.20, 0.35, and 0.50 mm. Five thousand simulations were carried out on each diameter of the lobule under each of three treatment conditions, with cART consisting of two nRTIs as the backbone drugs along with either a PI, INSTI or an NNRTI. Simulations were carried out for a time period of 100 days, which was long enough to reach steady state.

3. RESULTS

3.1. Drug Penetration vs. Lobule Diameter

Drug penetration for various anti-retroviral drugs in the lymphoid lobules has been evaluated using our integrated spatial dynamic pharmacokinetic model, following the Monte-Carlo methods described above. The three cART regimens simulated were NNN (tenofovir, lamivudine, efavirenz), NNP (tenofovir, efavirenz, ritonavir), and NNI (tenofovir, lamivudine, raltegravir). These three drug combinations were simulated on lymphoid lobules with diameters of 0.01, 0.05, 0.10, 0.20, 0.35, and 0.50 mm. For each combination of drug regimen and lobule size, 5,000 sets of parameters were randomly drawn from the parameter distributions described in **Tables S1–S8**. Intracellular drug penetration ratios (DPR) between the lymphoid lobule and the plasma were calculated for each drug. The intracellular drug concentration inside the lobule is evaluated by averaging the concentration over the entire volume of the lobule. **Figures 8–12** show histograms of the predicted drug concentration ratio between lobule and plasma for the six different lobule sizes. Vertical dashed lines show experimentally measured ratios for drugs of the same class. The DPR consistently drops as the lobule size increases, though the strength of this effect varies from drug to drug. The posterior distributions depend on the uncertainty in the PK parameters for the individual drugs; lamivudine, in particular, has very broad posterior distributions due to a high published uncertainty in its PK parameters (**Figure 11**). The experimentally measured DPRs seem to correlate best with lobule sizes of approximately 0.2 mm in diameter, though this underestimates drug exclusion for efavirenz and ritonavir. A lobule diameter of 0.2 mm would correspond to a moderate state of inflammation consistent with treated HIV infection.

Assuming an average uninflamed lymphoid lobule to be of 0.2 mm in diameter, our model predicts median DPR between lobule and plasma of 10% for PI (Ritonavir, RTV), 25.40% for NNRTI (Efarivenz, EFV), 17.80% for nRTI (Tenofovir diphosphate, TFV-DP), 30.70% for nRTI (Lamivudine, LMV) and 27.67% for INSTI (Raltegravir, RAL). These results reproduce the experimentally reported median intracellular tissue (Lymph node) to plasma ratio values for nRTIs such as Tenofovir Diphosphate (TFV-DP) and Emtricitabine (FTC-TP) at 20 and 34%, respectively, INSTI such as Raltegravir (RAL) AT 17%, PI's such as Atazanavir (ATV) and Darunavir (DRV) at 0 and 1%, respectively and NNRTIs such as Efavirenz (EFV) at 6% (Fletcher et al., 2014). Lobules with diameters of 0.5 mm, which would correspond to extreme levels of inflammation, predicted median DPRs under 10% for all drugs. In the absence of inflammation (lobule diameter 0.1 mm or less), median predicted DPRs were over 50% for all drugs except ritonovir.

3.2. Sanctuary Site Formation vs. Treatment Combination

For each of the 5,000 simulations for each drug regimen and lobule size combination described above, HIV dynamics were also simulated in the blood/lymph compartment as well as in the lobule. For each simulation, the fold increase in viral replication inside the lobule relative to the blood lymph compartment was measured once the dynamics reached steady-state. **Figure 13** shows the percentage of the simulations with a fold increase of viral replication in the lobule at each order of magnitude relative to the blood, grouped by drug regimen. Our model predictions suggest no ongoing viral replication occurs in lobules with diameter 0.01, 0.05, and 0.10 mm during on treatment conditions across all treatment combinations. Less than 5% of the population showed a 10-fold increase in viral replication inside the sanctuary

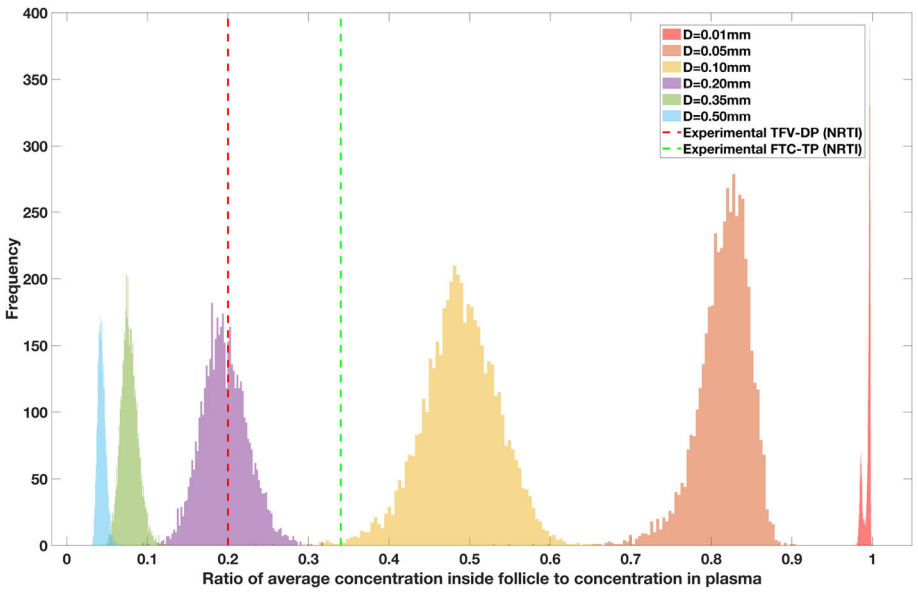

FIGURE 8 | Concentration ratio (lobule/plasma) of Tenofovir-diphosphate, TFV-DP (nRTI) with change in lobule diameter.

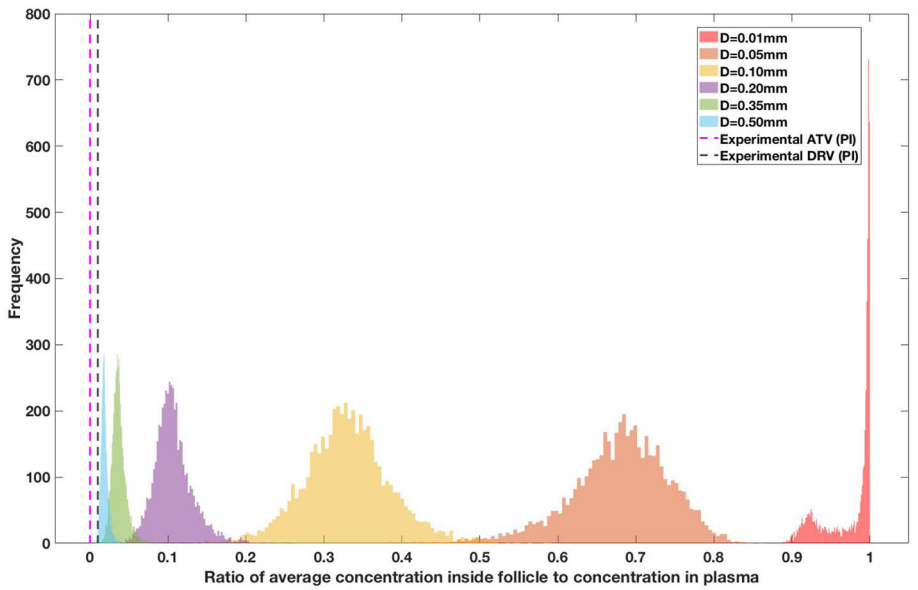

FIGURE 9 | Concentration ratio (lobule/plasma) of Ritonavir, RTV (PI) with change in lobule diameter.

site compared to plasma levels for patients on treatment with NNP (Two nRTIs and a PI) and NNI (Two nRTIs and a INSTI) for lobule size of 0.2 mm in diameter. The proportion of population with ongoing viral replication inside the lobule increases with increase in diameter of the lobule for both NNP and NNI treatment conditions, with NNP always having a higher percentage of population with ongoing replication compared to NNI. Treatment combination with NNRTIs i.e., NNN (two nRTIs with a NNRTI) did not show any sanctuary site formation for lobule diameters less than 0.5 mm. However, the proportion of population with ongoing replication under NNN combination is still less than 2% for a lobule size as large as 0.5 mm.

Our simulations suggest that the chances of sanctuary site formation are higher under NNP treatment combination compared to the other combinations. This result is consistent with the predicted drug penetration results because PIs are the most excluded drugs compared to the other class of drugs. Even though INSTIs and NNRTIs have similar penetration levels

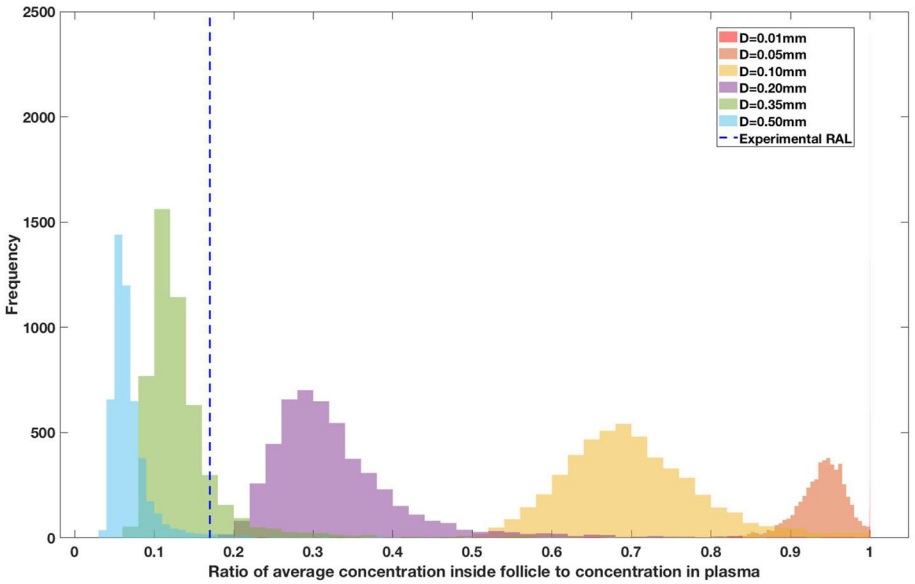

FIGURE 10 | Concentration ratio (lobule/plasma) of Raltegravir, RAL (INSTI) with change in lobule diameter.

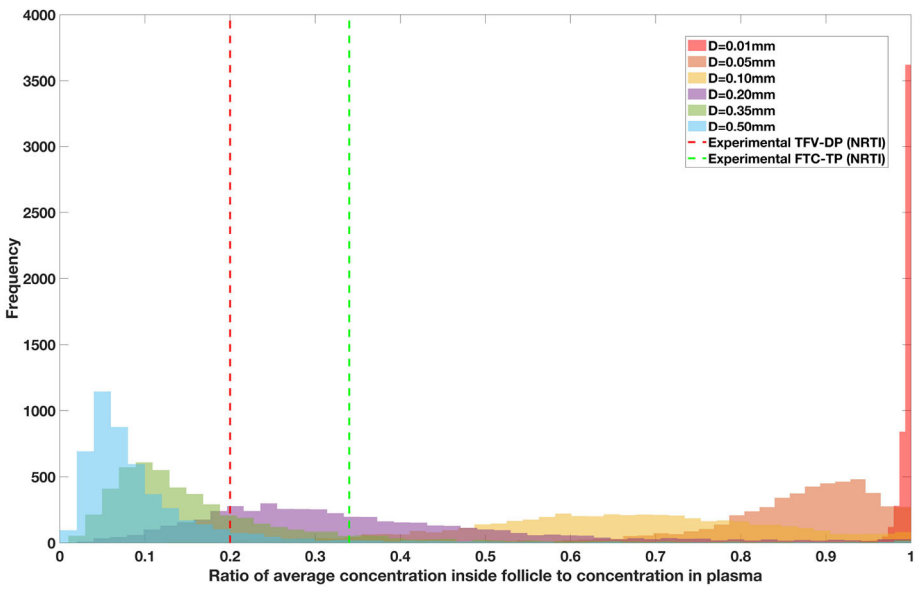

FIGURE 11 | Concentration ratio (lobule/plasma) of Lamivudine, LMV (nRTI) with change in lobule diameter.

inside the lobules, the proportion of population with sanctuary site formation is less in the case of NNRTI-containing regimens. This is likely due to the superior pharmacodynamic profile of NNRTIs, which have a low IC50 relative to their target dose and a higher Hill coefficient compared to INSTIs.

Our model predicts that sanctuary site formation while on cART is rare except under conditions where lymphoid lobules are very large. However, the proportion of population with sanctuary site formation increases with increase in lobule size, and NNP regimens are the most like to lead to sanctuary site formation.

4. DISCUSSION

In our current study, we integrated our previously published HIV dynamics spatial compartmental model with a pharmacokinetic model to evaluate the drug penetration inside a lymphoid lobule. Our predictions on antiviral drug concentrations inside the lobule suggest that drug penetration decreases with increase in lymphoid lobule size, with less than 50% of the drug reaching the interior regions for lobule diameters greater than 0.10 mm. PIs are the least penetrative drugs compared to INSTIs and

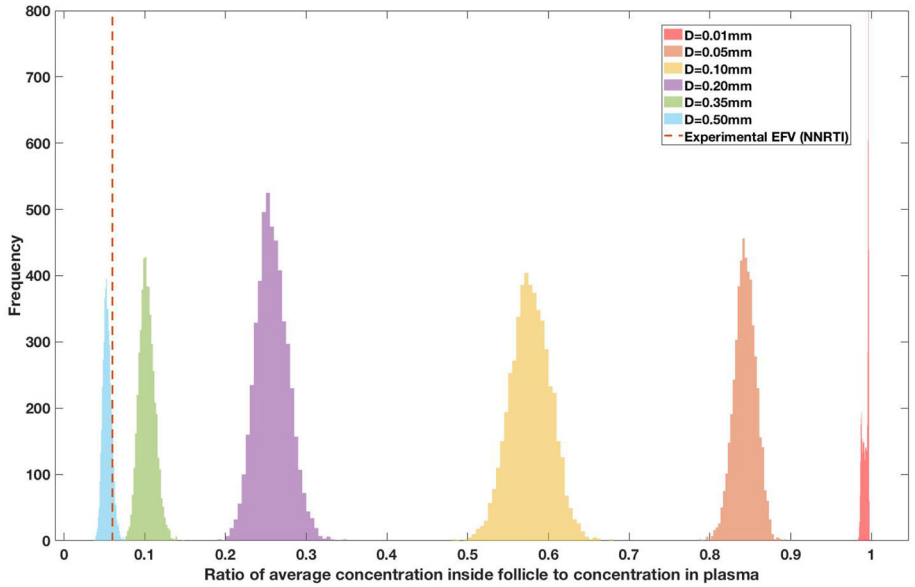

FIGURE 12 | Concentration ratio (lobule/plasma) of Efarivenz, EFV (NNRTI) with change in lobule diameter.

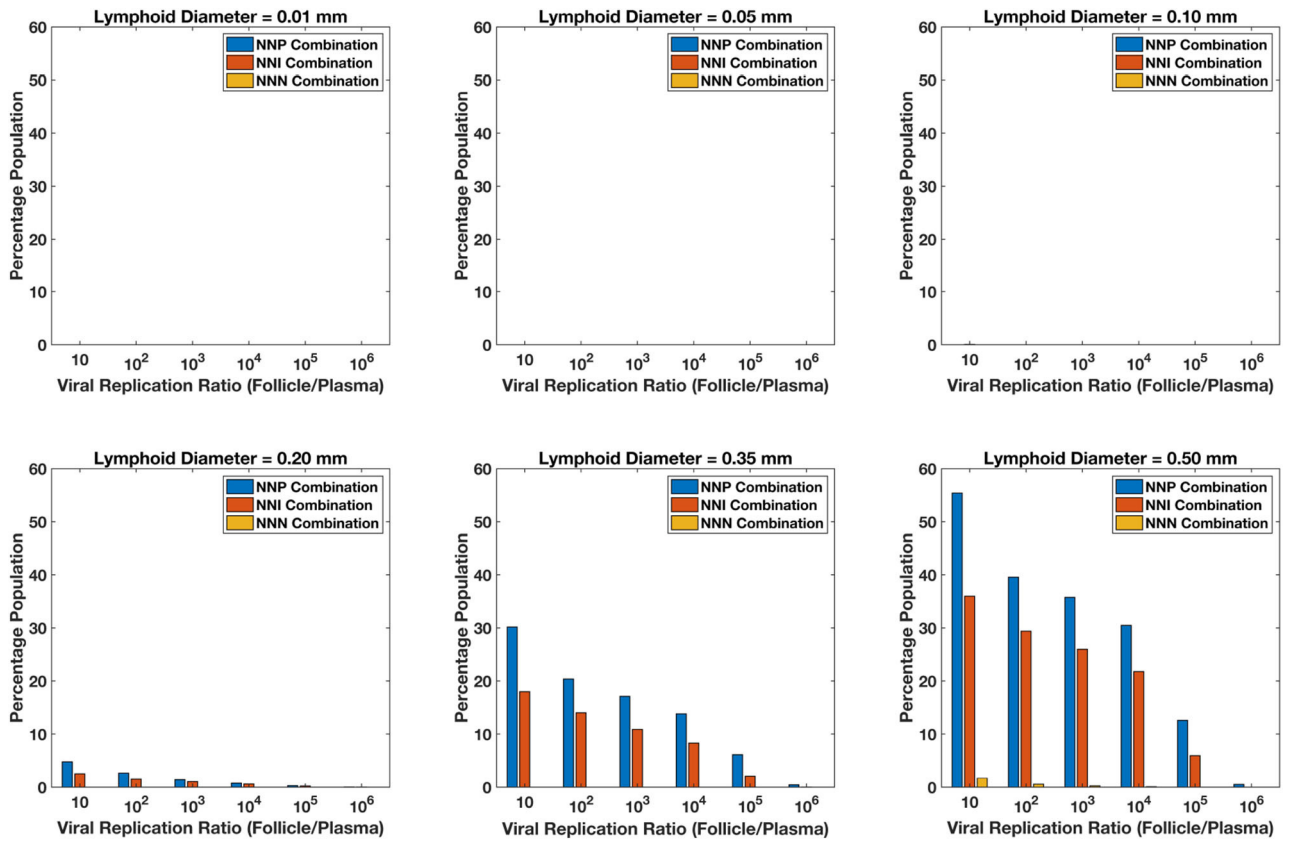

FIGURE 13 | Percentage sanctuary site formation with varying treatment combinations and lymphoid lobule diameter.

NNRTIs. Our model predictions on drug penetration were matched against previously published experimental observations for validation purposes (Fletcher et al., 2014). Drug penetration results for an average lymphoid lobule diameter of 0.2 mm match with the experimental drug penetration values. Our model does tend to underestimate the exclusion of PIs and NNRTIs compared to the experimental data. Our model incorporates only the most basic pharmacokinetic properties of the drugs in its transport model, and the two drugs in question have chemical properties that could significantly affect their transport rates across the lobule boundaries that are not captured in our model. Efavirenz is known to be unusually lipophilic, which will affect it transport rates across any plasma membrane boundary, and ritonavir is known to have a very high protein-bound fraction, which could significantly affect its transport rates across both the HEV and the lymphoid sinus boundaries. Future experiments could directly measure these transport rates. Furthermore, none of the experimental results contain information on the lobule size corresponding to their observed results. Since the drug penetration values are size-dependent as shown in our results, we suggest future experimental designs include determination of size and location for evaluating the drug penetration values experimentally.

The low drug penetration of PI results in a much higher proportion of virtual patients on NNP treatment regimens forming sanctuary sites compared to NNN and NNI combinations. Most patients, however, do not form sanctuary sites in our model. Formation of sanctuary sites (characterized by elevated viral replication in a treated patient) depends on the patient-specific drug transport dynamics, the PK/PD dynamics of the individual patient, the virus dynamics of the individual patient, and most strongly on the inflammation status of the lymphoid lobule in question. The limit of detection for increased viral activity in the lobule would probably be at least a 100-fold increase compared to the blood, and median parameter values never displayed this level of increase for any level of inflammation up to lobule diameters of 0.5 mm. Monte-Carlo studies exploring the range of parameter uncertainties revealed that sanctuary site behavior at the level of 100-fold increase does begin to emerge once lobules reach diameters of 0.2 mm, but only 3% of the population on NNP regimens and 2% of patients on NNI regimens would be expected to exhibit any sanctuary site activity at this level of inflammation. Increasing inflammation beyond this point does result in increased probability of sanctuary site formation, but lobules with diameters of 0.5 mm or larger likely represent pathological levels of lymphoid hyperplasia.

These predictions are broadly consistent with the clinical observations. The amount of viral replication in mono-nuclear cells inside lymph nodes is 10- to 100-fold greater, and the frequency of cells containing HIV DNA is 5- to 10-fold greater, than that in PBMC (Pantaleo et al., 1991, 1993). Furthermore, the absence of measurable viral load in the blood compartment does not rule out the possibility of ongoing low-level viral replication. It has been well-established that transport between the lymphoid sites and the blood is limited (Fletcher et al., 2014), which almost certainly limits the transport of infected cells and virus. Similarly, the lack of any observations on sequence evolution in HIV through experiments (Anderson et al., 2011; Evering et al., 2012) does not rule out the possibility of isolated ongoing replication; the small numbers of infected cells produced in the site, coupled with the limited transport between the site and the blood, mean that this would have to persist for a very long time to measurably influence the genetic distribution of the integrated HIV DNA in circulating cells. Furthermore, the low population incidence rates predicted by our model make it likely that this would be missed by all except the largest studies.

There is also some evidence of a positive feedback mechanism whereby viral activity in a lymphoid site causes physiological changes to the site that promote sanctuary site activity. Since the majority of the HIV infections are harbored in the paracortical site of the LN, an increase in traffic of CD4+ T cells to mount an immune response in the lymph node causes inflammation of the lymphoid lobule. As HIV infection progresses the histopathology of the LN changes toward hyperplasia in the beginning and eventually leading to follicular involution (Paiva et al., 1996; Cohen et al., 1997). As discussed above, increased lobule volume decreases anti-retroviral transport into the lobule, increases cell residence time, and enables localized viral replication. Marked collagen deposition in the paracortical T-cell zone of inguinal lymph nodes in HIV infected individuals has also been observed (Schacker et al., 2002). These observed changes in the architecture of the lymphatic tissue and the increase in size of the lobule due to immune activation might affect the penetration of anti-retroviral drugs during HIV infection. These effects are not captured in this model, but represent an avenue of future research.

DATA AVAILABILITY STATEMENT

The datasets generated for this study are available on request to the corresponding author.

AUTHOR CONTRIBUTIONS

AJ contributed to model development, code development, data generation and analysis, writing, and editing the manuscript. MP contributed to model development, data analysis, and editing the manuscript. RZ contributed to model development, data analysis, writing, and editing the manuscript.

FUNDING

Research reported in this publication was supported by the National Institute of Allergy And Infectious Diseases of the National Institutes of Health under Award Number R03AI136710. The content is solely the responsibility of the authors and does not necessarily represent the official views of the National Institutes of Health.

SUPPLEMENTARY MATERIAL

The Supplementary Material for this article can be found online at: https://www.frontiersin.org/articles/10.3389/fbioe.2020.00667/full#supplementary-material

REFERENCES

Anderson, J. A., Archin, N. M., Ince, W., Parker, D., Wiegand, A., Coffin, J. M., et al. (2011). Clonal sequences recovered from plasma from patients with residual HIV-1 viremia and on intensified antiretroviral therapy are identical to replicating viral RNAs recovered from circulating resting CD4+ T Cells. *J. Virol*. 85, 5220–5223. doi: 10.1128/JVI.00284-11

Arab-Alameddine, M., Fayet-Mello, A., Lubomirov, R., Neely, M., di Iulio, J., Owen, A., et al. (2012). Population pharmacokinetic analysis and pharmacogenetics of raltegravir in HIV-positive and healthy individuals. *Antimicrob. Agents Chemother*. 56, 2959–2966. doi: 10.1128/AAC.05424-11

Arts, E. J., and Hazuda, D. J. (2012). HIV-1 antiretroviral drug therapy. *Cold Spring Harbor Perspect. Med*. 2:a007161. doi: 10.1101/cshperspect.a007161

Baheti, G., Kiser, J. J., Havens, P. L., and Fletcher, C. V. (2011). Plasma and intracellular population pharmacokinetic analysis of tenofovir in HIV-1-infected patients. *Antimicrob. Agents Chemother*. 55, 5294–5299. doi: 10.1128/AAC.05317-11

Baldazzi, V., Paci, P., Bernaschi, M., and Castiglione, F. (2009). Modeling lymphocyte homing and encounters in lymph nodes. *BMC Bioinform*. 10:387. doi: 10.1186/1471-2105-10-387

Beltman, J. B., Marée, A. F., Lynch, J. N., Miller, M. J., and de Boer, R. J. (2007). Lymph node topology dictates t cell migration behavior. *J. Exp. Med*. 204, 771–780. doi: 10.1084/jem.20061278

Buzón, M., Massanella, M., Llibre, J. M., Esteve, A., Dahl, V., Puertas, M. C., et al. (2010). HIV-1 replication and immune dynamics are affected by Raltegravir intensification of HAART-suppressed subjects. *Nat. Med*. 16, 460–465. doi: 10.1038/nm.2111

Cahill, R., Frost, H., and Trnka, Z. (1976). The effects of antigen on the migration of recirculating lymphocytes through single lymph nodes. *J. Exp. Med*. 143, 870–888. doi: 10.1084/jem.143.4.870

Cardozo, E. F., Luo, R., Piovoso, M. J., and Zurakowski, R. (2014). Spatial modeling of HIV cryptic viremia and 2-LTR formation during Raltegravir intensification. *J. Theor. Biol*. 345, 61–69. doi: 10.1016/j.jtbi.2013.12.020

Cohen, O. J., Pantaleo, G., Lam, G. K., and Fauci, A. S. (1997). Studies on lymphoid tissue from HIV-infected individuals: implications for the design of therapeutic strategies. *Springer Semin. Immunopathol*. 18, 305–322. doi: 10.1007/BF00813500

Danjuma, M. I. (2009). Pharmacokinetics of HIV non-nucleoside reverse-transcriptase inhibitors. *HIV Therapy* 3, 625–632. doi: 10.2217/hiv.09.42

Di Mascio, M., Srinivasula, S., Bhattacharjee, A., Cheng, L., Martiniova, L., Herscovitch, P., et al. (2009). Antiretroviral tissue kinetics: *in vivo* 3imaging using positron emission tomography. *Antimicrob. Agents Chemother*. 53, 4086–4095. doi: 10.1128/AAC.00419-09

Dixit, N. M., and Perelson, A. S. (2004). Complex patterns of viral load decay under antiretroviral therapy: influence of pharmacokinetics and intracellular delay. *J. Theor. Biol*. 226, 95–109. doi: 10.1016/j.jtbi.2003.09.002

Engelhardt, B., and Wolburg, H. (2004). Mini-review: transendothelial migration of leukocytes: through the front door or around the side of the house? *Eur. J. Immunol*. 34, 2955–2963. doi: 10.1002/eji.200425327

Eron, J. J., Montaner, J. S. G., Cahn, P., Schooley, R. T., Walmsley, S., Jacobsen, D. M., et al. (2008). Antiretroviral treatment of adult HIV infection. *JAMA* 300:555. doi: 10.1001/jama.300.5.555

Evering, T. H., Mehandru, S., Racz, P., Tenner-Racz, K., Poles, M. A., Figueroa, A., et al. (2012). Absence of HIV-1 evolution in the gut-associated lymphoid tissue from patients on combination antiviral therapy initiated during primary infection. *PLoS Pathog*. 8:e1002506. doi: 10.1371/journal.ppat.1002506

Fayet Mello, A., Buclin, T., Franc, C., Colombo, S., Cruchon, S., Guignard, N., et al. (2011). Cell disposition of Raltegravir and newer antiretrovirals in HIV-infected patients: high inter-individual variability in Raltegravir cellular penetration. *J. Antimicrob. Chemother*. 66, 1573–1581. doi: 10.1093/jac/dkr151

Fletcher, C. V., Staskus, K., Wietgrefe, S. W., Rothenberger, M., Reilly, C., Chipman, J. G., et al. (2014). Persistent HIV-1 replication is associated with lower antiretroviral drug concentrations in lymphatic tissues. *Proc. Natl. Acad. Sci. U.S.A*. 111, 2307–2312. doi: 10.1073/pnas.1318249111

Girard, J.-P., Moussion, C., and Förster, R. (2012). HEVs, lymphatics and homeostatic immune cell trafficking in lymph nodes. *Nat. Rev. Immunol*. 12:762. doi: 10.1038/nri3298

Habtewold, A., Aklillu, E., Makonnen, E., Yimer, G., Bertilsson, L., Burhenne, J., et al. (2017). Population pharmacokinetic model linking plasma and peripheral blood mononuclear cell concentrations of efavirenz and its metabolite, 8-hydroxy-efavirenz, in HIV patients. *Antimicrob. Agents Chemother*. 61:e00207-17. doi: 10.1128/AAC.00207-17

Ho, D. D., Neumann, A. U., Perelson, A. S., Chen, W., Leonard, J. M., and Markowitz, M. (1995). Rapid turnover of plasma virions and CD4 lymphocytes in HIV-1 infection. *Nature* 373:123. doi: 10.1038/373123a0

Hurwitz, S. J., Asif, G., and Schinazi, R. F. (2007). Development of a population simulation model for hiv monotherapy virological outcomes using lamivudine. *Antiviral Chem. Chemother*. 18, 329–341. doi: 10.1177/095632020701800605

Kirschner, D., Webb, G. F., and Cloyd, M. (2000). Model of HIV-1 disease progression based on virus-induced lymph node homing and homing-induced apoptosis of CD4+ lymphocytes. *J. Acquir. Immune Defic. Syndr*. 24, 352–362. doi: 10.1097/00042560-200008010-00010

Lorenzo-Redondo, R., Fryer, H. R., Bedford, T., Kim, E.-Y., Archer, J., Pond, S. L. K., et al. (2016). Persistent HIV-1 replication maintains the tissue reservoir during therapy. *Nature* 530:51. doi: 10.1038/nature16933

Luo, R., Cardozo, E. F., Piovoso, M. J., Wu, H., Buzon, M. J., Martinez-Picado, J., et al. (2013). Modelling HIV-1 2-LTR dynamics following raltegravir intensification. *J. R. Soc. Interface* 10:20130186. doi: 10.1098/rsif.2013.0186

Luo, R., Piovoso, M. J., Martinez-Picado, J., and Zurakowski, R. (2012). HIV model parameter estimates from interruption trial data including drug efficacy and reservoir dynamics. *PLoS ONE* 7:e40198. doi: 10.1371/journal.pone.0040198

Marinho, E., Bacelar, F. S., and Andrade, R. (2012). A model of partial differential equations for hiv propagation in lymph nodes. *Phys. A Stat. Mech. Appl*. 391, 132–141. doi: 10.1016/j.physa.2011.08.023

Miller, H., Cosgrove, J., Wollman, A., O'Toole, P., Coles, M., and Leake, M. C. (2018). High-speed single-molecule tracking of CXCL13 in the B-follicle. *Front. Immunol*. 9:1073. doi: 10.3389/fimmu.2018.01073

Mirsky, H. P., Miller, M. J., Linderman, J. J., and Kirschner, D. E. (2011). Systems biology approaches for understanding cellular mechanisms of immunity in lymph nodes during infection. *J. Theor. Biol*. 287, 160–170. doi: 10.1016/j.jtbi.2011.06.037

North, T. W., Higgins, J., Deere, J. D., Hayes, T. L., Villalobos, A., Adamson, L., et al. (2009). Viral sanctuaries during highly active antiretroviral therapy in a nonhuman primate model for AIDS. *J. Virol*. 84, 2913–2922. doi: 10.1128/JVI.02356-09

Nowak, M., and May, R. M. (2000). *Virus Dynamics: Mathematical Principles of Immunology and Virology: Mathematical Principles of Immunology and Virology*. Oxford: Oxford University Press.

Paiva, D. D., Morais, J. C., Pilotto, J., Veloso, V., Duarte, F., and Lenzi, H. L. (1996). Spectrum of morphologic changes of lymph nodes in HIV infection. *Memorias do Instituto Oswaldo Cruz* 91, 371–379. doi: 10.1590/S0074-02761996000300023

Pantaleo, G., Graziosi, C., Butini, L., Pizzot, P. A., Schnittman, S. M., Kotler, D. P., et al. (1991). Lymphoid organs function as major reservoirs for human. *Proc. Natl. Acad. Sci. U.S.A*. 88, 9838–9842. doi: 10.1073/pnas.88.21.9838

Pantaleo, G., Graziosi, C., Demarest, J. F., Butinit, L., Montronit, M., Fox, C. H., et al. (1993). HIV infection is active and progressive in LT during the clinically latent stage of disease. *Nature* 10, 355–358. doi: 10.1038/362355a0

Pau, A. K., and George, J. M. (2014). Antiretroviral therapy: current drugs. *Infect. Dis. Clin. N. Am*. 28, 371–402. doi: 10.1016/j.idc.2014.06.001

Perelson, A., Essunger, P., and Ho, D. (1997). Dynamics of HIV-1 and CD4+ lymphocytes *in vivo*. *AIDS* 11:S17.

Perelson, A. S., and Ribeiro, R. M. (2013). Modeling the within-host dynamics of HIV infection. *BMC Biol*. 11:96. doi: 10.1186/1741-7007-11-96

Pfeiffer, F., Kumar, V., Butz, S., Vestweber, D., Imhof, B. A., Stein, J. V., et al. (2008). Distinct molecular composition of blood and lymphatic vascular endothelial cell junctions establishes specific functional barriers within the peripheral lymph node. *Eur. J. Immunol*. 38, 2142–2155. doi: 10.1002/eji.200838140

Ruiz, L., Martinez-Picado, J., Romeu, J., Paredes, R., Zayat, M. K., Marfil, S., et al. (2000). Structured treatment interruption in chronically HIV-1 infected patients after long-term viral suppression. *AIDS* 14, 397–403. doi: 10.1097/00002030-200003100-00013

Schacker, T. W., Nguyen, P. L., Beilman, G. J., Wolinsky, S., Larson, M., Reilly, C., et al. (2002). Collagen deposition in HIV-1 infected lymphatic tissues and T cell homeostasis. *J. Clin. Investig*. 110, 1133–1139. doi: 10.1172/JCI0216413

Shen, L., Peterson, S., Sedaghat, A. R., McMahon, M. A., Callender, M., Zhang, H., et al. (2008). Dose-response curve slope sets class-specific limits on inhibitory potential of anti-HIV drugs. *Nat. Med.* 14:762. doi: 10.1038/nm1777

Von Andrian, U. H., and Mempel, T. R. (2003). Homing and cellular traffic in lymph nodes. *Nat. Rev. Immunol.* 3, 867–878. doi: 10.1038/nri1222

Wang, L., Soon, G. H., Seng, K.-Y., Li, J., Lee, E., Yong, E.-L., et al. (2011). Pharmacokinetic modeling of plasma and intracellular concentrations of Raltegravir in healthy volunteers. *Antimicrob. Agents Chemother.* 55, 4090–4095. doi: 10.1128/AAC.00593-11

Wei, X., Ghosh, S. K., Taylor, M. E., Johnson, V. A., Emini, E. A., Deutsch, P., et al. (1995). Viral dynamics in human immunodeficiency virus type 1 infection. *Nature* 373:117. doi: 10.1038/373117a0

Willard-Mack, C. L. (2006). Normal structure, function, and histology of lymph nodes. *Toxicol. Pathol.* 34, 409–424. doi: 10.1080/01926230600867727

Conflict of Interest: RZ is named as an inventor on US Patent 9874563, Detecting and quantifying cryptic HIV replication.

The remaining authors declare that the research was conducted in the absence of any commercial or financial relationships that could be construed as a potential conflict of interest.

Copyright © 2020 Jagarapu, Piovoso and Zurakowski. This is an open-access article distributed under the terms of the Creative Commons Attribution License (CC BY). The use, distribution or reproduction in other forums is permitted, provided the original author(s) and the copyright owner(s) are credited and that the original publication in this journal is cited, in accordance with accepted academic practice. No use, distribution or reproduction is permitted which does not comply with these terms.

frontiers in Bioengineering and Biotechnology

ORIGINAL RESEARCH
published: 13 July 2020
doi: 10.3389/fbioe.2020.00666

Experimental Control of Macrophage Pro-Inflammatory Dynamics Using Predictive Models

Laura D. Weinstock[1,2], *James E. Forsmo*[2], *Alexis Wilkinson*[3], *Jun Ueda*[4] and *Levi B. Wood*[1,2,4]*

[1] Parker H. Petit Institute for Bioengineering & Bioscience, Georgia Institute of Technology, Atlanta, GA, United States, [2] The Wallace H. Coulter Department of Biomedical Engineering, Georgia Institute of Technology, Atlanta, GA, United States, [3] School of Chemical & Biomolecular Engineering, Georgia Institute of Technology, Atlanta, GA, United States, [4] George W. Woodruff School of Mechanical Engineering, Georgia Institute of Technology, Atlanta, GA, United States

Macrophage activity is a major component of the healthy response to infection and injury that consists of tightly regulated early pro-inflammatory activation followed by anti-inflammatory and regenerative activity. In numerous diseases, however, macrophage polarization becomes dysregulated and can not only impair recovery, but can promote further injury and pathogenesis, e.g., after trauma or in diabetic ulcers. Dysregulated macrophages may either fail to polarize or become chronically polarized, resulting in increased production of cytotoxic factors, diminished capacity to clear pathogens, or failure to promote tissue regeneration. In these cases, a method of predicting and dynamically controlling macrophage polarization will enable a new strategy for treating diverse inflammatory diseases. In this work, we developed a model-predictive control framework to temporally regulate macrophage polarization. Using RAW 264.7 macrophages as a model system, we enabled temporal control by identifying transfer function models relating the polarization marker iNOS to exogenous pro- and anti-inflammatory stimuli. These stimuli-to-iNOS response models were identified using linear autoregressive with exogenous input terms (ARX) equations and were coupled with non-linear elements to account for experimentally identified supra-additive and hysteretic effects. Using this model architecture, we were able to reproduce experimentally observed temporal iNOS dynamics induced by lipopolysaccharides (LPS) and interferon gamma (IFN-γ). Moreover, the identified model enabled the design of time-varying input trajectories to experimentally sustain the duration and magnitude of iNOS expression. By designing transfer function models with the intent to predict cell behavior, we were able to predict and experimentally obtain temporal regulation of iNOS expression using LPS and IFN-γ from both naïve and non-naïve initial states. Moreover, our data driven models revealed decaying magnitude of iNOS response to LPS stimulation over time that could be recovered using combined treatment with both LPS and IFN-γ. Given the importance of dynamic tissue macrophage polarization and overall inflammatory regulation to a broad number of diseases, the temporal control methodology presented here will have numerous applications for regulating immune activity dynamics in chronic inflammatory diseases.

Keywords: macrophages, dynamic systems and control, inflammation, trajectory planning, system identification, predictive model

OPEN ACCESS

Edited by:
Robert Parker,
University of Pittsburgh, United States

Reviewed by:
Mohit Kumar Jolly,
Indian Institute of Science (IISc), India
Guilherme De Alencar Barreto,
Federal University of Ceara, Brazil

***Correspondence:**
Levi B. Wood
levi.wood@me.gatech.edu

Specialty section:
This article was submitted to Computational Genomics, a section of the journal Frontiers in Bioengineering and Biotechnology

Received: *25 January 2020*
Accepted: *28 May 2020*
Published: *13 July 2020*

Citation:
Weinstock LD, Forsmo JE, Wilkinson A, Ueda J and Wood LB (2020) Experimental Control of Macrophage Pro-Inflammatory Dynamics Using Predictive Models. Front. Bioeng. Biotechnol. 8:666. doi: 10.3389/fbioe.2020.00666

INTRODUCTION

Healthy immune response during infection or injury is a dynamic process consisting of initial acute pro-inflammatory activation followed by anti-inflammatory/resolving activity, which is mediated in large part by macrophages (Sica and Mantovani, 2012; Decano and Aikawa, 2018). This temporally regulated response promotes pathogen and debris clearance followed by tissue regeneration and, ultimately, recovery of homeostasis (**Figure 1A**; Sica and Mantovani, 2012; Decano and Aikawa, 2018). Dysregulation can occur in several ways. First, a strong initial pro-inflammatory response within the affected tissue can lead to systemic inflammation that positively feeds back to sustain local inflammation. Second, a compensatory anti-inflammatory response (e.g., via regulatory T cells) can lead to aberrant immunosuppression, which impairs pathogen clearance and regeneration (Binkowska et al., 2015). Third, long-term dysregulation of immune response during chronic disease interferes with tissue regeneration and homeostasis, in turn further sustaining immune dysregulation. Indeed, chronic inflammatory dysfunction contributes to a breadth of diseases, including impaired wound healing after major trauma and multiple neurodegenerative diseases (**Figure 1A**; Ohashi et al., 2015; Oishi and Manabe, 2016), and chronically impaired immune response can lead to worsened outcomes after new insults (Wynn et al., 2013). However, broad ablation of immune response, e.g., via corticosteroids, can equally limit successful regeneration, and recovery of tissue homeostasis (Guo and Dipietro, 2010; Weekman et al., 2014; Oishi and Manabe, 2016; Hamelin et al., 2018).

Although the need for regulation of tissue immune response is well-recognized, identification of new strategies to intervene in tissue inflammation remains a major challenge. After trauma for example, treatment selection, dosing, and timing of administration are all crucial factors in determining patient outcome (Becelli et al., 2000). There has recently been a call for a better understanding of the complex and dynamic immune response post-injury in order to identify new strategies to regulate dynamic immune response and ultimately patient outcome (Galbraith et al., 2016).

The dynamic activity of macrophages is integral to both the early (<1 h) and continued (>1 month) response to infection and injury (Wynn et al., 2013; Hu et al., 2015). Without appropriate regulation of their activity, macrophages can drive the initiation and progression of many diseases (Wynn et al., 2013; Ohashi et al., 2015). In particular, loss of regulation can lead to insufficient pro-inflammatory activity, leading to incomplete clearance of pathogens and/or tissue debris, impaired pro-regenerative response, chronic inflammation, and infection (Guo and Dipietro, 2010; Oishi and Manabe, 2016). Recent efforts to regulate dysfunctional macrophages have focused on cell-based therapies, such as delivery of mesenchymal stem cells (MSCs) or macrophages conditioned *ex vivo* toward anti-inflammatory and pro-regenerative "M2" phenotypes. The underlying principal behind immunomodulatory cell therapies is that these cells will act as natural "controllers" of immune response through beneficial immunomodulatory signaling in the local environment (Pacini, 2014). However, these strategies are subject to a number of limitations. For example, MSCs are subject to variable efficacy between donors and batches (Wang et al., 2012; Pacini, 2014).

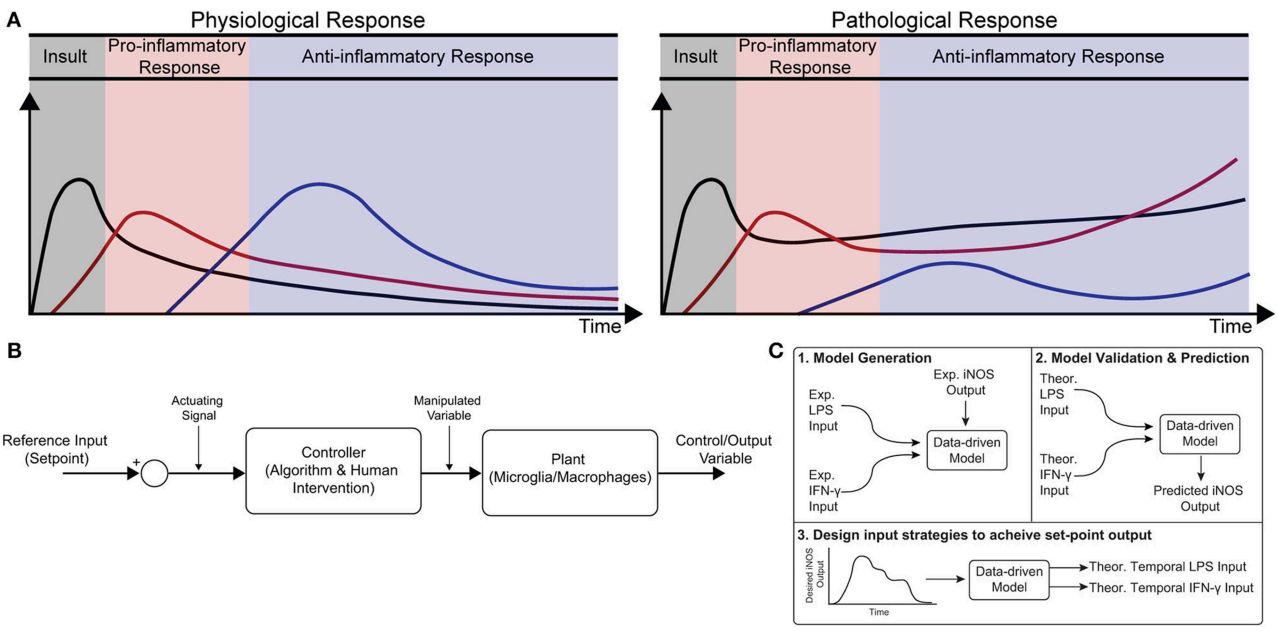

FIGURE 1 | Conceptual diagram of modeling immune response in health and disease. **(A)** Immune response as dynamically regulated in health (left) and dysfunctional in chronic conditions (right). **(B)** Block diagram with macrophages as the "system" or "plant" that is being controlled. **(C)** Identification, validation, and prediction of inflammatory response as a three-step process consisting of (1) design of an engineering model structure and fit of model parameters, (2) comparison of predicted and experimental results, and (3) use of the predictive model to design input strategies to obtain a desired response.

Other approaches seek to deliver *ex vivo* modified macrophages, but both mouse and human trials have had variable success and still face many challenges (Lee et al., 2016; Spiller and Koh, 2017). A new approach that actively regulates resident tissue macrophages would escape many challenges faced by current cell-based therapies.

Exogenous control of macrophage activity would provide an exciting new method to modulate immune response (Ohashi et al., 2015; Decano and Aikawa, 2018) that would steer the system through a desired trajectory of activity. Macrophages are an attractive target for regulating immune response because (i) they are involved in diverse immune functions essential for tissue protection and repair and (ii) they are highly plastic, with the ability to dynamically re-polarize for different functions based on external cues (Wynn et al., 2013). Since macrophage polarization is dynamic, a quantitative temporal model will enable design of exogenous input sequences capable of normalizing response (**Figures 1A,B**). The pathways governing macrophage polarization in response to stimuli have been comprehensively modeled, including receptor binding kinetics, downstream kinase signaling, and gene transcription (Salim et al., 2016). While mechanistically appealing, these models possess dozens of equations and hundreds of parameters, making it intractable to identify reliably predictive input-output relationships between exogenous stimulation and polarization in terms of these precise mechanistic models. Moreover, it has recently been argued that identification of viable strategies to intervene in immune activity will require rigorous integration of experimental data with computational modeling (Vodovotz et al., 2017). There is thus a need for an empirical input/output model that relates macrophage response to exogenous inputs in order to predict and control activation levels over time.

In the current study, we formulated a data-driven modeling approach, informed by an *in vitro* macrophage polarization assay and system identification theory, to identify the temporal dynamics of macrophage response to multiple exogenous pro-inflammatory stimuli. Specifically, we conditioned RAW 264.7 macrophages with M1 polarizing stimuli (LPS and IFN-γ) or an M2 polarizing stimulus (IL-4) and quantified response in terms of iNOS expression for 1–72 h post-stimulation. We then used least squares regression to fit a low-order autoregressive with exogenous terms (ARX) model together with non-linear elements to relate iNOS response to each input (**Figures 1C1**,**2**). The identified model predicted the dynamics of polarization in subsequent experiments in response to different concentrations and temporal trajectories (simultaneous vs. sequential) of each input (**Figure 1C3**). Finally, we used the identified model as part of an open-loop control framework to tailor input sequences to achieve desired temporal trajectories of macrophage polarization *in vitro*. To our knowledge, this is the first study to experimentally control immune cell dynamics using a predictive control framework. Given the importance of dynamic M1 and M2 polarization during tissue regeneration, the control methodology presented here defines a novel framework that will have diverse applications for treating chronic inflammatory diseases and promoting tissue regeneration.

RESULTS

Macrophage iNOS Expression Is Transient and Refractory to Repeated Stimulations

We first aimed to determine the temporal dynamics of macrophage response to single or repeated pro-inflammatory stimuli. As a model system, we used expression of the pro-inflammatory M1 marker inducible nitric oxide synthase (iNOS) by RAW 264.7 macrophages in response to the pro-inflammatory stimulus lipopolysaccharide (LPS). Using quantitative Western blot, we found that a single administration of 1 μg/mL LPS, but not IL-4 (**Supplementary Figure S1**), resulted in transient iNOS dynamics with a peak in iNOS expression at 24 h followed by a decay to baseline over the following 48 h (**Figure 2A**). Immunocytochemistry (ICC) confirmed this response (**Figures 2B,C**) and revealed that this temporal trajectory was (1) conserved given a range of lower doses of LPS and (2) that the magnitude of the response monotonically increased with the magnitude of the stimulation (**Supplementary Figure S2**). Intriguingly, although LPS was not removed from cultures, and thus represented a persistent step-like stimulus, the dynamics of iNOS expression followed a first order decay response (**Figures 2B,C**). In traditional engineered systems, this type of system response is usually obtained by stimulating the system with a finite impulse input (Ljung, 1999).

To test whether the observed decay in iNOS expression was due to LPS depletion from the culture medium, we re-administered 1 μg/mL LPS every 24 h. However, iNOS expression in response to repeated stimulation was comparable to that of a single LPS stimulation (**Figure 2D**), indicating suppression of response to continued stimulation, which is consistent with known auto-inhibitory mechanisms of macrophage response to LPS, such as induction of ATF3 (Lawrence and Natoli, 2011) and kinase phosphatases (Zhao et al., 2006; Sun et al., 2017). Although the dynamics of these auto-inhibitory processes have not been fully delineated, we next wanted to determine if we could identify a stimulation strategy that would increase sustained iNOS expression over the course of our 72 h culture experiments. Because we found an initial peak at 24 h in response to 1 μg/ml of LPS, we tested a recovery time period of 24 h between the initial peak and a potential second peak within the 72 h experimental treatment window. However, cycled re-stimulation did not alter iNOS expression dynamics (**Figure 2E**), suggesting that the dynamics of macrophage polarization to LPS stimulation consist of an initial response that is not sustained despite either continued or repeated LPS stimulation, during our experimental time window, i.e., the system becomes refractory. This refractory behavior resembles immune tolerance/fatigue observed in chronic disease conditions, such as type 2 diabetes and cancer (Geerlings and Hoepelman, 1999; Makkouk and Weiner, 2015).

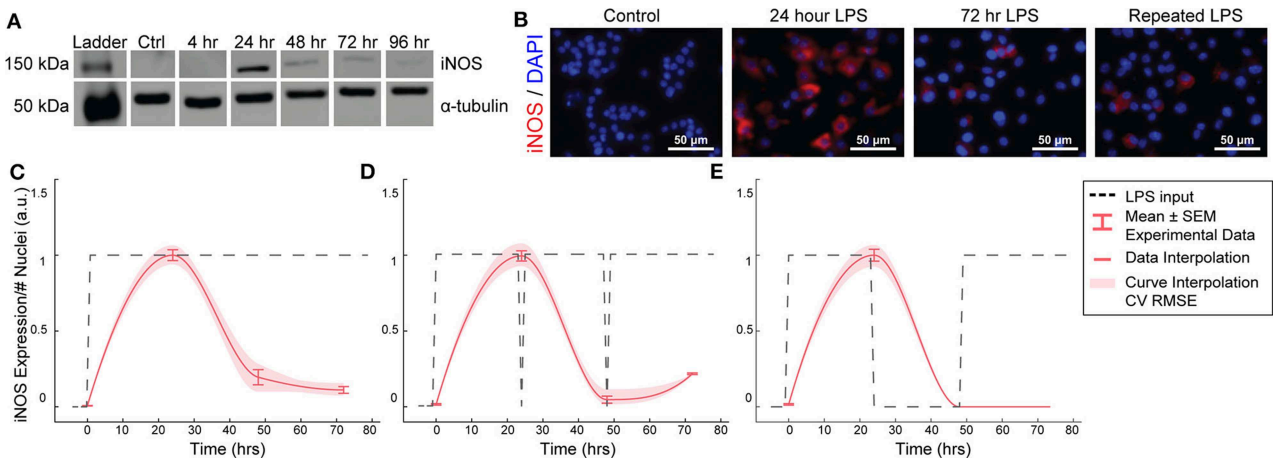

FIGURE 2 | RAW264.7 macrophages transiently express iNOS in response to constant or repeated LPS stimulation. **(A)** Representative Western blot for iNOS (140 kDa) and α-tubulin (55 kDa) after LPS treatment. **(B)** Representative ICC images showing iNOS response after LPS stimulation. **(C)** ICC quantification matches Western blot analysis of transient iNOS expression in response to a single administration of LPS. **(D)** Dynamics of iNOS expression are not modulated in response to multiple administrations of LPS or **(E)** after 24 h in basal medium before LPS re-stimulation (mean ± SEM, $N = 16$ at 0, 24, 48, and 72 h; red curves; interpolation ± RMS CV error).

Auto-Regressive Model With Exogenous Inputs Fits iNOS Dynamic Response to LPS Input

We next asked if a control systems engineering methodology could be used to design a temporal sequence of LPS stimulation that would enable us to recover or sustain iNOS expression, and, by extension, pro-inflammatory activation of RAW 264.7 cells. Control systems methodology requires a model that can be used to predict future system response given a known stimulation input. Diverse model structures are employed in engineering fields, ranging from high-order mechanistic models to input-output data-driven models. For this application, a mechanistic model encoding all of the genetic and protein interactions responsible for iNOS expression would suffer from reduced predictive capacity due to uncertainty in fitted parameters. Gray and black box models, which capture dominant response dynamics without specifying mechanistic details, are thus more appealing to relate iNOS dynamics to pro-inflammatory stimulation (Shin et al., 2012). We therefore sought to identify an optimized black box single input and single output (SISO) model relating LPS input to iNOS output (Shin et al., 2012; Rachad et al., 2015). A critical tradeoff must be considered when choosing model structure: maximize flexibility to best capture system dynamics while avoiding the need to have more model parameters than can be reliably identified from the data (Van den Hof et al., 1994). Autoregressive models with exogenous inputs (ARX) models are frequently used for black-box system identification because they can capture underlying system dynamics in diverse applications and because parameterization using the ARX (Materials and Methods, Equations 1–3) structure guarantees uniqueness of solution and identification of the global minimum of the error function (Liu and Allen, 2002; Zurakowski and Teel, 2006; Shin et al., 2012; Deshpande et al., 2014).

To identify the parameters of this model architecture, extensive experimental characterization of macrophage polarization dynamics with multiple input patterns and magnitudes was performed to generate a rich dataset to train and identify an input/output model of iNOS expression dynamics (**Figures 2C–E**, **Supplementary Figure S2**). We experimentally found that macrophages exhibited a monotonic LPS dose-to-iNOS response relationship within a physiologically relevant concentration range (**Supplementary Figure S2**), which is well-described using the linear ARX model structure. Above a high (1 μg/mL) concentration of LPS, response tapers off, potentially due to cell death or changes in intracellular signaling activity (Ziegler-Heitbrock et al., 1994). As such, we set 1 μg/mL LPS as the maximum concentration used in this study. To capture the post-LPS stimulation refractory period, we fit an ARX model (orders $n_a = 1$, $n_b = 2$, $n_k = 1$, Materials and Methods, Equations 1–3) to experimental time sequence input-output data from numerous experimental runs consisting of constant high input ($N = 38$), constant input for three lower concentrations (10, 100, and 500 ng/mL, $N = 4$), cyclic high input (**Figure 2E**, $N = 8$), and replenished high input (**Figure 2D**, $N = 8$) with model parameters estimated using least squares (Materials and Methods, Equation 4). The resulting model recapitulated this refractory pattern for a step input (**Figure 3A**). The model parameter estimates are given in **Supplementary Table S1** (three free coefficients) and returned a normalized Akaike's Information Criterion (AICc) model quality metric of 430.59 and minimized mean squared error (**Supplementary Table S3**). This model outperforms the related ARMAX (autoregressive-moving average with exogenous terms) model structure with similar numbers of parameters ($n_a = 1$, $n_b = 2$, number of moving average coefficients $n_c = 0$; AICc = 501.96). By estimating this input/output model (**Supplementary Tables S1, S2**), we can achieve both high descriptive and predictive capacities.

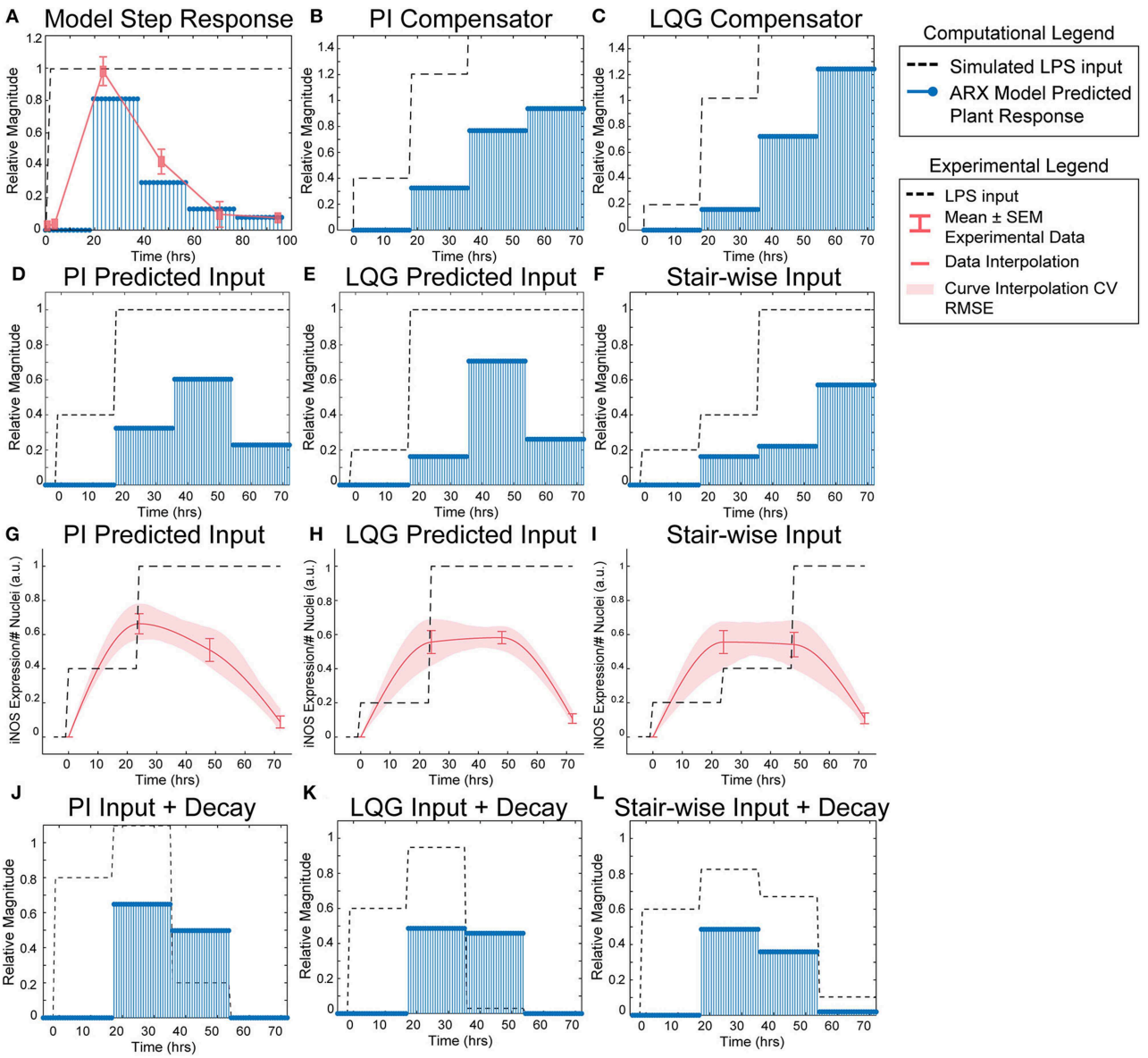

FIGURE 3 | SISO LPS/iNOS ARX model, controller design, and experimental MPC testing. **(A)** Identified ARX model of macrophage iNOS response to LPS has a characteristic step response that follows the experimentally quantified trajectory. Control system design identifies input strategy (dashed line) for a step reference that elicits a gradual increase in plant response (blue stems) using a **(B)** PI or **(C)** LQG controller. Model simulations given controller defined inputs but within experimental input constraints predict sustained outputs for **(D)** PI and **(E)** LQG controllers. **(F)** A heuristically defined three-step increase input strategy predicts an output that reaches a maximum at 72 h. Experimental implementation using cultured RAW 264.7 macrophages and **(G)** PI controller-, **(H)** LQG controller-, or **(I)** a heuristic combination of designed LPS input schema (dashed line) modulates temporal iNOS expression (red curves, mean ± SEM, $N = 16$; interpolated curve ± RMS CV error) but does not reach the unit reference nor sustain 72 h activity. Macrophage refractory response to repeated LPS input is captured (blue stems) by multiplying the **(J)** PI predicted, **(K)** LQG predicted, or **(L)** heuristically defined input sequences against a time-dependent exponential decay term (dashed lines).

Model Predictive Controller Identifies LPS Stimulation Sequence to Sustain iNOS Expression

Using the identified ARX system model, we sought to tune a controller (Control System Design Toolbox, MATLAB), placed upstream of the plant (**Figure 1B**), that would predict a temporally defined LPS input strategy to overcome the persistent decay in iNOS expression. We used two controller structures to design input strategies capable of achieving sustained iNOS expression. First, since our system dynamics (**Figure 2C**) indicated that the system model responds to the derivative of the input, we attempted to compensate for the derivative using a classical proportional-integral (PI) controller, which is commonly applied in engineering applications to minimize

steady-state error (Nise, 2015; **Supplementary Table S4**). Here, we used the PI controller (Materials and Methods, Equation 8) to control LPS-induced iNOS expression to the unit reference (1 a.u. iNOS relative expression, Materials and Methods). The controller predicted that a stair-wise delivery of LPS (**Figure 3B**, dashed line) would give rise to a more gradual but prolonged output response, *y*, that reached the reference by the control horizon of 72 h (**Figure 3B**, blue stems). Importantly, the second step in input exceeded the unit input value (corresponding *in vitro* to 1 μg/mL LPS), which was the upper bound of LPS concentration used in this study. When the controller was constrained to inputs between 0 and 1 (1 μg/mL LPS), no PI controller obtained by adjusting controller gains K_p and K_i (Materials and Methods), was capable of defining an input sequence that both maintained a $u \leq 1$ μg/mL and predicted *y* to reach the reference within the control time horizon.

Due to the inability of the PI controller to identify an input sequence capable of reaching or maintaining output levels at 72 h, we next decided to take advantage of our ARX system model to re-design the input sequence using a linear-quadratic Gaussian (LQG) controller (Materials and Methods, Equation 9; **Supplementary Table S4**), which can provide improved performance over conventional PID controllers for minimizing total error (Mohammadbagheri et al., 2011). This LQG controller designed a reduced magnitude for the original input followed by the unit max of LPS input (**Figure 3C**, dashed line) to achieve 80% of the reference point prior to exceeding the unit max stimulation input (**Figure 3C**, blue stems), which the PI controller-defined input could not achieve within LPS concentration constraints. However, this controller also required $u > 1$ μg/mL to reach the reference. When the input is constrained to $0 \leq u \leq 1$ μg/mL LPS, the model simulations predicted that progressive step increases in LPS would prolong the iNOS response but not sustain it at the unit reference value (**Figures 3D,E**). Finally, when the initial magnitudes of the LQG and PI predicted inputs were heuristically combined in a three-step increase strategy, simulations predicted a maximum response at 72 h (**Figure 3F**).

Experimental Implementation of Predicted LPS Input Temporarily Sustains Macrophage iNOS Activation

Each controller above defined a temporally increasing magnitude of the stimulus *u*, or LPS concentration, where the input is increased at each time step. Experimentally, the model predicted input values represent a fraction of the normalized maximum (high) LPS concentration, 1 μg/mL. For example, 0.2 is 20% of the maximum 1 μg/mL, or 200 ng/mL, and 0.4 is 400 ng/mL as in our data used for model fitting. To test the PI controller input strategy, RAW 264.7 macrophages were treated with 40 ng/mL of LPS for 24 h, followed by 1 μg/mL from hour 24 until fixation at 72 h (**Figure 3G**, dashed line). Despite the controller requiring *u* of 1.2, biologically this would have led to excessive cell death, likely changing the plant response. Thus, we tested the effect of the unit max of LPS in this stair-wise input scheme. The macrophage expression of iNOS peaked at approximately 70% of normalized maximum iNOS (defined by the 24 h expression level given 1 μg/mL LPS) at 24 h (**Figure 3G**, red curve). The subsequent increase in LPS concentration delivered did not sustain this level of iNOS, which declines through the 48 and 72 h time points, but does keep levels higher (∼50% max) at 48 h than an initially high level of LPS (**Figure 3G**, red curve).

The LQG controller predicted input, 24 h of 200 ng/mL followed by 48 h at 1 μg/mL LPS (**Figure 3H**, dashed line), realized an iNOS expression level ∼60% of the reference at 24 h (**Figure 3H**, red curve). Intriguingly, here the cells sustained this iNOS level through 48 h, but not through 72 h (**Figure 3H**, red curve). We next heuristically combined the input strategies defined by the PI and LQG controller to test whether iNOS expression at 72 h could be sustained (**Figure 3I**, dashed line). However, iNOS expression given this strategy reflected that of the LQG controller and did not keep activation high at 72 h (**Figure 3I**, red curve).

The refractory, or muted, iNOS response to either high, continued, or step-wise increases in LPS stimulation suggested a decaying efficacy of LPS regardless of input sequence. Reduced response to LPS is consistent with time-dependent compensatory downstream signaling (Kadelka et al., 2019), including increases in phosphatases that down-regulate LPS-induced phospho-protein signaling, e.g., MAP kinase phosphatase 1 and Protein phosphatase 2A; inhibition of pro-inflammatory transcription factors; or up-regulation of anti-inflammatory transcription factors, e.g., STAT6 inhibition of NF-κB (Zhao et al., 2006; Lawrence and Natoli, 2011; Ni et al., 2016; Sun et al., 2017).

Because prior work has shown that signaling proteins downstream of LPS respond with exponentially decaying dynamics (Kadelka et al., 2019), we next hypothesized that an exponential decay term would improve agreement between our dynamic model and experimental data. Indeed, when the input sequence terms were multiplied by a time-dependent exponential decay term (**Figures 3J–L**, dashed lines), the response magnitudes (**Figures 3J–L**, blue stems) reflected the experimentally obtained iNOS values for each input strategy. Although this single input system was unable to meet constant reference control specifications, the ability to qualitatively maintain elevated pro-inflammatory macrophage activation via our predictive control framework demonstrated an exciting feasibility of the approach that may be extendable to alternate strategies that can overcome the decaying efficacy of LPS stimulation.

IFN-γ Stimulation Increases Reachable iNOS Trajectories and Adds System Non-linearity

We found above that single or repeated stimulation with LPS was unable to indefinitely sustain iNOS expression and that sustained expression was only partially recovered by temporally modulating the input (**Figures 3D–I**), i.e., inflammatory activity was modulated but could not be prolonged indefinitely. In engineering systems, independent inputs increase the system rank and thereby increase state achievability. That is to say, adding a secondary stimulus that operates through separate,

orthogonal means, expands the internal states, and reachable output of a system (Hespanha, 2009). Therefore, we next hypothesized that a second pro-inflammatory input would improve controllability. To test this, we used IFN-γ, which signals largely independently of LPS (**Figure 4A**) as the second, orthogonal input because 100 ng/mL IFN-γ robustly increased iNOS levels despite prior LPS input (**Figures 4B–D**). Although we also considered TNF-α as the second pro-inflammatory stimulus, we found the iNOS response is more sensitive to IFN-γ within a physiologically relevant concentration range (**Supplementary Figure S3**). Given these findings, the use of multiple pro-inflammatory inputs is promising for toggling both the magnitude and duration of macrophage activity with greater reachability than can be achieved with a single input.

While IFN-γ recovered iNOS expression from LPS-induced tolerance, it also introduced a non-linear element to the dynamic response—supra-additivity. ARX and transfer function models require that the output of the sum of two inputs equal the sum of the output of each input. However, IFN-γ amplifies LPS-induced iNOS expression, where expression is greater than the sum of expression from each stimulus alone, whether added concomitantly or in series. In fact, supra-additivity for simultaneous conditioning is present across all time points and for a range of LPS and IFN-γ concentrations through 72 h of conditioning (**Figures 5A,B**, **Supplementary Figure S4**). The supra-additivity also lead to iNOS expression that was greater than the unit reference for 24 h of LPS (**Figures 5A,B**), so our predictive model needs to account for these non-linearities to avoid overshooting or behavior that does not settled to the desired reference (**Figure 4D**).

RAW 264.7 Macrophages Exhibit State Memory Based on Stimulation History

In disease, macrophages may exist in chronically activated or other non-naïve states, driven by local and systemic changes in signaling proteins, hormones, among other factors (Mosser and Edwards, 2008; Ohashi et al., 2015). Thus, having shown our ability to model macrophage pro-inflammatory dynamics

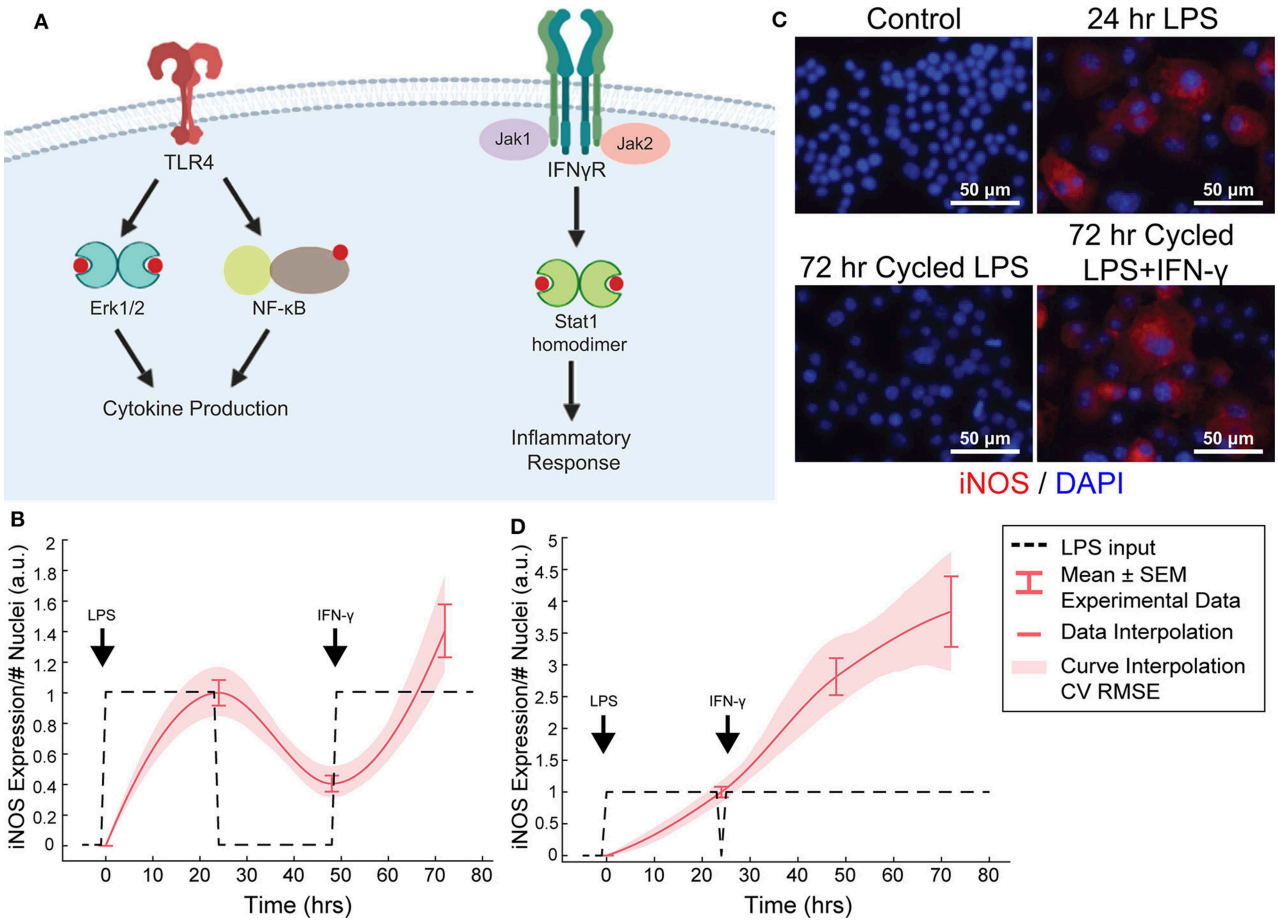

FIGURE 4 | Orthogonal stimuli maintained or magnified iNOS expression. **(A)** Signaling diagram for LPS and IFN-γ (created with BioRender). **(B)** 24 h of LPS treatment and delayed subsequent IFN-γ (dashed lines) treatment modulates iNOS expression (red curves, mean ± SEM, $N = 16$; interpolated curve ± RMS CV error), even at 72 h time point. **(C)** Representative ICC images showing cycled LPS and IFN-γ (input defined in **B**) induces iNOS expression comparable to 24 h of LPS alone while cycling only LPS in that same pattern (**Figure 2F**) does not maintain expression. **(D)** 24 h of LPS treatment and immediately subsequent IFN-γ (dashed lines) treatment modulates iNOS expression (red curves, mean ± SEM, $N = 16$; interpolated curve ± RMS CV error), even at 72 h time point.

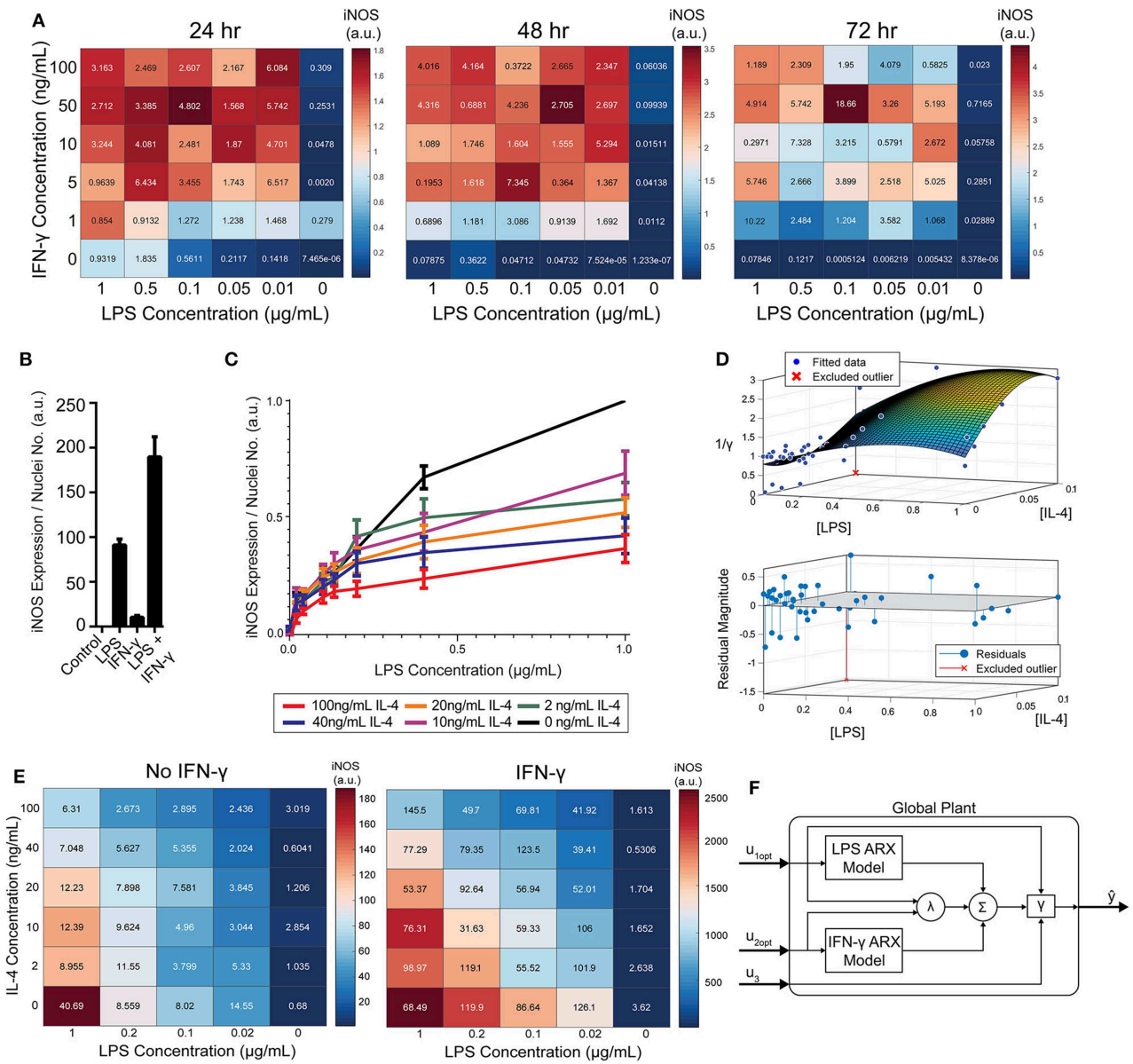

FIGURE 5 | RAW 264.7 macrophages are markedly affected by activation state-dependent hysteresis, which can be overcome using multiple pro-inflammatory inputs. **(A)** LPS and IFN-γ added simultaneously cause time dependent supra-additive expression of iNOS (color represents mean, SEM displayed numerically, $N = 2$). Data are normalized by 1 μg/mL LPS-only condition for each time-point. **(B)** Selected non-normalized data from **A** (24 h, highest concentration per stimulus) demonstrating that iNOS expression from combined conditions is greater than the linear addition of LPS or IFN-γ alone (mean ± SEM, $N = 2$). **(C)** Prior treatment with IL-4 attenuates LPS induced iNOS expression (24 h post-LPS treatment) in an IL-4 concentration-dependent manner (mean ± SEM, $N = 6$). **(D)** Interpolated attenuation factor gamma surface plot (top) and fit error (bottom). **(E)** Pretreating macrophages with 100 ng/mL IL-4 for 24 h prior to LPS stimulation reduced the magnitude of pro-inflammatory polarization measured by iNOS expression normalized to DAPI (color represents mean, SEM displayed numerically, $N = 4$). Combining 4 ng/mL of IFN-γ with LPS stimulates iNOS expression, overcoming the hysteretic effect dependent on the dose of LPS (color represents mean, SEM displayed numerically, $N = 4$). **(F)** Diagram of global plant, as implemented in control system (**Figure 1B**), of multiple input system with both linear and non-linear model elements. System predicted inputs u_1 (LPS) and u_2 (IFN-γ) are fed into respective identified SISO ARX models and supra-additive interaction term λ elements. Terms multiplied by weighting coefficients c (defined by multiple regression estimation; Equation 10) prior to summation (Σ) and hysteresis-dependent attenuation (γ). Note that u_3 accounts for IL-4 attenuation via γ.

and design input trajectories for naïve macrophages, we next wanted to determine whether the macrophage response to pro-inflammatory stimulation would be affected by pre-polarizing the cells toward an anti-inflammatory state.

To model RAW 264.7 cells starting in a non-naïve state, we pre-conditioned macrophages with IL-4 for 24 h prior to pro-inflammatory stimulation. Upon stimulation with LPS, we found that prior IL-4 conditioning attenuated expression

of iNOS after 24 h of treatment with LPS, but that iNOS still responded to LPS in a concentration dependent manner (**Figure 5C**). M2 polarization was validated by increased expression of Arg1 (data not shown). Further, an initial polarization toward a pro-inflammatory phenotype increased the magnitude of anti-inflammatory polarization that outweighed the IL-4 concentration given (**Supplementary Figure S5**), which is consistent with prior studies, including one study where AAV delivery of IFN-γ *in vivo* increased M2 gene expression, as well as M1 genes (Weekman et al., 2014). Together, these data suggest that macrophages exhibit hysteresis in their response to prior inputs, whereby prior M2 polarization attenuates future M1 response and prior M1 polarization sensitizes future M2 response. The M2 driven attenuation of M1 response reflects one aspect of how systemic immunosuppression poses a major risk to post-traumatic or surgical injury patients (Kimura et al., 2010; Islam et al., 2016).

Modeling Multi-Input Driven Hysteresis and Supra-Additivity

Since the dynamics of iNOS expression in RAW 264.7 cells were dependent on the polarization state history (i.e., hysteresis in non-naïve cells) and demonstrated supra-additivity in response to combinations of LPS and IFN-γ, we next sought to incorporate these elements into our iNOS response model. In terms of state history, quantification, and mathematical modeling of state-history dependence has previously been reported for cancer cell epithelial-mesenchymal transition (Celia-Terrassa et al., 2018; Tripathi et al., 2020). Here, we accounted for the hysteretic effects of prior treatment with IL-4 by defining an attenuation factor to account for the reduction in magnitude of iNOS expression in the next time step for the range of LPS and IL-4 concentrations described in **Figure 5C** relative to expression with no exposure to IL-4. Quantitatively, the attenuation factor γ (Materials and Methods) is equal to 1 for non-hysteretic systems and increases with higher prior concentrations of IL-4 such that $\frac{1}{\gamma}$ multiplied by iNOS expression for a given LPS concentration gives the iNOS response for that LPS concentration and an IL-4 pre-treatment concentration. A response plane for γ was fitted with 3rd order polynomials in [LPS] and [IL-4] to define a smoothed continuous response surface from which any attenuation due to anti-inflammatory induction is returned (**Figure 5D**).

To account for supra-additive effects of multiple pro-inflammatory inputs, as done for the hysteretic surface, we populated time-dependent interaction term (λ) surface curves for the defined ranges of co-addition of LPS and IFN-γ. Excitingly, the supra-additivity of IFN-γ with LPS demonstrated the ability to recover the attenuation effect induced by IL-4. Indeed, greater iNOS expression was observed across lower LPS concentrations and higher IL-4 concentrations when IFN-γ co-stimulation was used compared with LPS stimulation alone (**Figure 5E**, note that the scale of response is an order of magnitude greater in the heat map with IFN-γ). This interaction effect motivates the need for a system plant model that processes both M2 and M1 inputs.

The global plant model was constructed and is described schematically in **Figure 5F**. The system receives the concentration of LPS (u_1) and IFN-γ (u_2) which are passed into their respective identified ARX models (**Supplementary Table S2**), the supra-additivity of LPS and IFN-γ was accounted for using λ, the pro-inflammatory contributions are summed and applied as inputs to the hysteresis term γ, Finally, the output is the predicted iNOS output ($\hat{y}$) as a function of time *t* (**Figure 5F**).

Design of LPS and IFN-γ Temporal Input Trajectories With Global Plant Model Achieves Sustained iNOS Expression

Transfer functions were linearly combined with coefficients for supra-additivity (λ) and hysteresis (γ) acting as pre-processing filters, i.e., the terms were multiplied with each model's output, then added. The global regression of the function has the final form in Materials and Methods, Equation 10 [$R^2 = 0.748$; *p*-value (vs. constant model) = 1.34e-38]. Simultaneous administration of unit, high, inputs *in vitro* vastly overshot the unit value of iNOS and did not settle over the course of the experiment (**Figure 6A**), demonstrating that it is possible to obtain sustained iNOS response, but that more carefully crafted input sequences are needed to obtain constant, sustained expression of iNOS. We therefore next used the global model (**Figure 5F**) together with an MPC controller to design input trajectories for LPS (u_1) and IFN-γ (u_2) needed to obtain sustained constant iNOS expression over a 72 h control horizon (**Figure 6B**). Using these trajectories, the simulated plant reached the reference value by 24 h with a minor overshoot that settled by 72 h (**Figure 6C**). Including hysteresis in the plant controller estimation increases the predicted inputs magnitude needed to obtain the unit step reference (**Figure 6D**). Given the input sequence defined in **Figure 6D**, a hysteretic system was predicted to respond with relatively small overshoot and error (**Figure 6E**, red curve). Importantly, the model captures the large overshoot that would be expected from administering elevated input levels to a non-hysteretic system (**Figure 6E**, blue curve).

Next, the relative input magnitudes defined for a hysteretic plant (**Figure 6D**) were translated to concentrations of LPS and IFN-γ, which were administered as temporally defined to RAW 264.7 macrophages in culture. The macrophage iNOS expression trajectories reflected the model predicted response for both hysteretic, i.e., pretreatment with 100 ng/mL IL-4 (**Figure 6F**, red curve and **Figure 6G**) and non-hysteretic (**Figure 6F**, blue curve) cell conditions. Since this initial model only accounted for a static supra-additivity term, we next updated it to incorporate a dynamic supra-additivity λ term that updated with time based on our response data in **Figure 5A**. The updated model was simulated with inputs used experimentally (**Figure 6F**) and defined by the original model (**Figure 6D**). This 2nd generation model improved the predictive performance with results that recapitulated the overshoot seen in the hysteretic system (**Figure 6H**). Since we wanted to ultimately achieve a unit reference system response, our last step was to use the 2nd generation model to define new

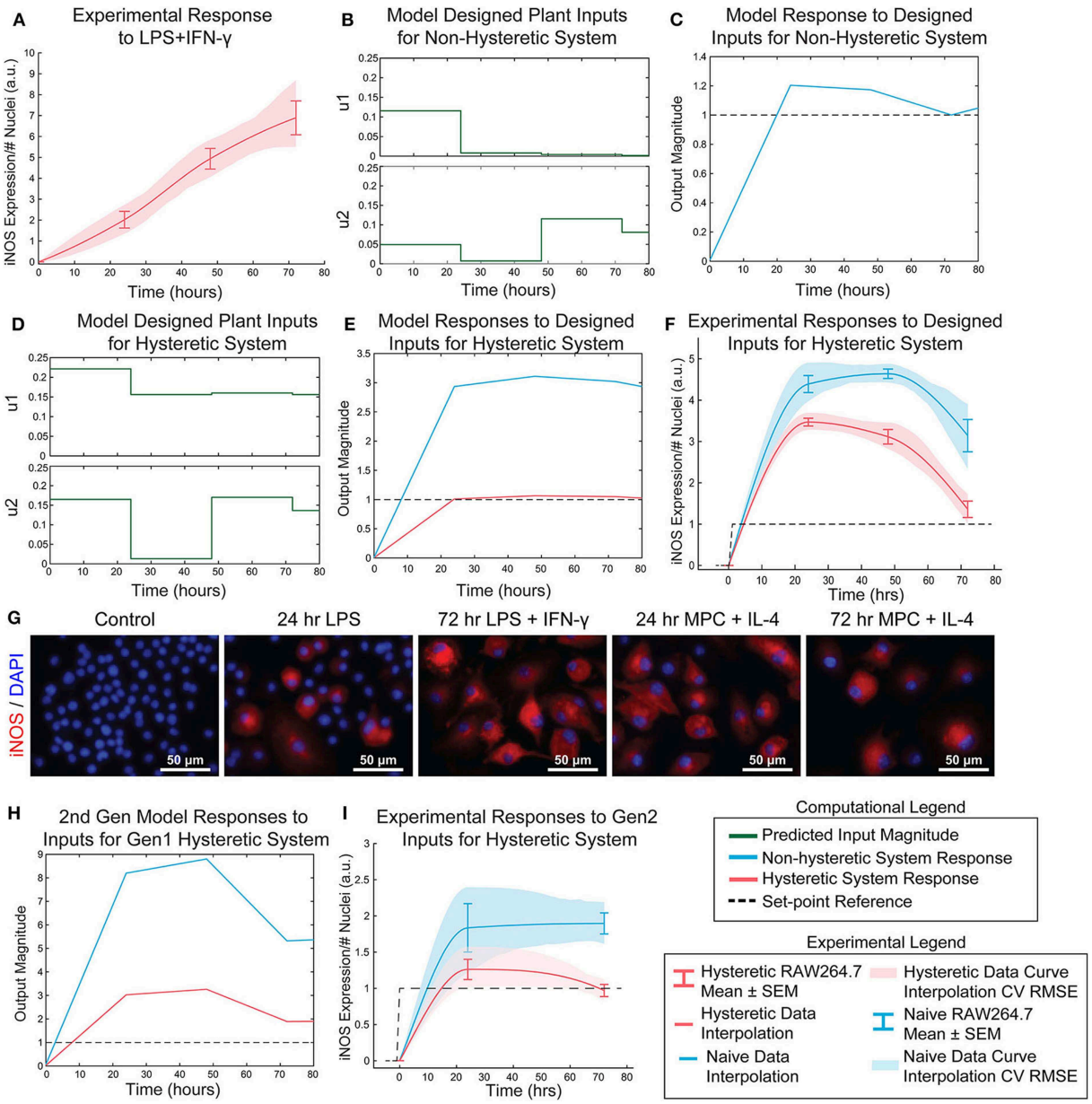

FIGURE 6 | Open-loop control of pro-inflammatory macrophage activity is experimentally achieved using a nested multiple regression. **(A)** RAW 264.7 macrophage temporal response to 1 μg/mL LPS and 100 ng/mL IFN-γ. **(B)** Model designed inputs u_1 and u_2 using hysteresis-free model, which reflects cells beginning in a naïve state. **(C)** Hysteresis-free model response to inputs defined in **(B)**. **(D)** Model designed inputs u_1 and u_2 using first generation model accounting for hysteresis, which reflects cells starting from a non-naïve 24 h IL-4 primed state. **(E)** Hysteretic model (red) and non-hysteretic model (blue) responses to inputs defined in **(D)**. **(F)** Experimental delivery of designed inputs in **(D)** reflects predicted control output **(E)** for both hysteretic IL-4 primed (red curve, mean ± SEM, $N = 16$; interpolated curve ± RMS CV error) and non-hysteretic (blue curve, mean ± SEM, $N = 16$; interpolated curve ± RMS CV error) RAW 264.7 macrophage cultures. **(G)** Representative images of iNOS staining in model predictive control experiments using the inputs in **(D)**. **(H)** Simulation of updated 2nd generation model with dynamic supra-additivity term in response to designed inputs **(D)** captures experimental RAW 264.7 iNOS expression for both hysteretic (red curve) and non-hysteretic (blue curve) systems. **(I)** Experimental validation of the second-generation global model. Delivery of inputs designed to maintain a constant unit output of iNOS in a hysteretic system using the new model (inputs shown in **Figure S6**) improves control output for both hysteretic IL-4 primed (red curve, mean ± SEM, $N = 8$; interpolated curve ± RMS CV error) and non-hysteretic (blue curve, mean ± SEM, $N = 8$; interpolated curve ± RMS CV error) macrophage cultures.

system inputs (**Supplementary Figure S6**) for the IL-4 pre-treated hysteretic system using the MPC controller. We then applied these temporal input sequences to both blank media and IL-4 pre-treated macrophages. Excitingly, this MPC designed input sequence improved macrophage iNOS expression dynamic response because the IL-4 pre-treated cells settled to the target

reference with minimal overshoot (**Figure 6I**). We also found that non-hysteretic (blank media pre-treated) cells overshot and did not settle to the reference by the control horizon (**Figure 6I**), as predicted by the model (**Figure 6E**).

In total, these experimental findings show that our global plant model predicts the dynamics macrophage pro-inflammatory response, including transient response to LPS, supra-additivity, and hysteresis. Moreover, we showed that this model could be used to define dual stimulation strategies that could prolong RAW 264.7 cell polarization as quantified by iNOS.

DISCUSSION

In this work, we developed a novel paradigm for engineering immune activity by defining predictive data-driven models of macrophage polarization and using them to define the dynamic delivery of pro-inflammatory factors to control the duration and magnitude of macrophage polarization. Rather than identifying detailed, highly parameterized mechanistic models, we applied a control theory framework to globally describe the pro-inflammatory activity of macrophages over time. Specifically, using expression of the canonical pro-inflammatory (M1) marker iNOS as an output, we defined a black-box transfer function to capture the dynamic response of macrophages given a temporal sequence of applied LPS and IFN-γ as system inputs. Our overall modeling framework coupled linear ARX models, which are uniquely identifiable, with non-linear elements that accounted for state-history dependent hysteresis and supra-additivity from multiple pro-inflammatory stimuli. Our global plant model structure not only predicted responses to different input sequences, but enabled design of new stimulation sequences that yielded a desired temporal iNOS response overcoming macrophage refractory behavior (**Figure 6**).

Immune dysregulation plays a central role in diverse diseases. Dysregulated activity of macrophages in particular can both hinder tissue repair and promote disease pathogenesis. However, macrophage functional diversity and broad distribution throughout the body also makes them excellent targets for modulating immune function to treat an array of diseases (Salim et al., 2016). Yet the vast majority of new immunomodulatory strategies, including inflammatory inhibitors and cell-based therapies, do not explicitly account for the temporal evolution of macrophage response needed to resolve the response to injury.

The importance of a temporally dynamic immune response has been highlighted by recent findings that long term resolution of inflammation depends on a sufficiently pro-inflammatory initial response followed by anti-inflammatory and resolving activity. Early pro-inflammatory macrophage response enables clearance of pathogens and damaged cells and subsequently triggers the anti-inflammatory and pro-regenerative response (Lee et al., 2016; Spiller and Koh, 2017; Ponzoni et al., 2018). Thus, in the current study, we sought to model and control macrophage pro-inflammatory activity, measured by iNOS expression. Using an ARX model structure, which is widely used for black-box system identification in engineering (Rachad et al., 2015) and biological systems (Liu and Allen, 2002; Zurakowski and Teel, 2006; Shin et al., 2012; Deshpande et al., 2014), we identified computational models able to predict and control temporal iNOS expression. This black-box approach enabled us to fit three parameters to model the dynamic LPS response and three more to fit the IFN-γ response, in contrast to dozens required in mechanistic differential equation models of macrophage polarization (Salim et al., 2016). A key feature of our black box modeling framework is that it is generalizable to broad inputs, outputs, and disease cases. Indeed, relationships between inputs and macrophage responses are quantitatively linked by experimental data, which can be extended beyond iNOS, LPS, and IFN-γ. This framework is therefore generalizable to inputs and outputs relevant to other diseases and markers of macrophage activity by experimentally tuning the model parameters to the new system.

Interestingly, when implementing model-predicted LPS input sequences, we observed that the time-dependent decay in the efficacy of LPS persisted. In fact, when the designed input magnitude was multiplied against a time-dependent decay term (**Figures 3J,L**, dashed lines), we were able to simulate the observed experimental response. This finding is consistent with macrophage auto-regulatory processes that prevent runaway inflammatory activity to LPS (Ziegler-Heitbrock et al., 1994).

The current work has some limitations that invite the need for future studies. First, we used murine RAW 264.7 immortalized macrophages, which is considered one of the best macrophage cell lines, for development of the methodology in this study, due to their high reproducibility between labs and studies (Taciak et al., 2018; Kong et al., 2019), but future work is needed to validate and tune the models for primary isolated macrophages. Further, to extend the utility of the model for disease therapeutics, it will be necessary to identify similarities and differences between primary macrophages, either bone-marrow derived or peritoneal, collected from wild type mice and mouse models of chronic inflammatory diseases. For example, macrophages are known to exhibit distinct inflammatory profiles from diabetic patients than from healthy individuals (Li et al., 2019), which will be reflected in the identified model parameters. Additionally, the methodology developed here lays a foundation for dynamic control of macrophage activation using a single polarization marker, but a wider panel of pro- and anti-inflammatory markers are needed to fully delineate macrophage activation state and effector function. Ultimately, the use of this methodology in *in vivo* models will be necessary to determine if it is possible to control immune activity for translational applications.

Together, our dynamic experimental and computational approach establishes a new way of conceptualizing and modulating macrophage activity by using a temporal sequence of input stimuli to shape the trajectory of inflammatory response. We experimentally validated the computational model predictions, extending previous theoretical work in model predictive control for patient-specific therapeutics (Day et al., 2010). We envision this framework having broad-reaching applications both *in vitro* an *in vivo*. Moreover, our ability to modulate macrophage activity suggests that design of temporally varying inputs has therapeutic potential for broad chronic inflammatory disorders.

MATERIALS AND METHODS

RAW 264.7 Macrophage Cell Culture and Conditioning

All studies in this work were performed using RAW 264.7 murine immortalized macrophages (ATCC TIB-71™). Macrophages were expanded, maintained, and cultured in basal macrophage medium, which is comprised of DMEM (Thermo Fisher Scientific; 12430062), 10% FBS (Thermo Fisher Scientific; 26140079), and 1% antibiotic/antimycotic (Sigma-Aldrich; A5955). Cells were cultured to 70% confluence before conditioning began. Cells were conditioned by addition of medium with lipopolysaccharide (LPS; Sigma-Aldrich; L2880 and Invitrogen; 00-4976-93), interferon gamma (IFN-γ; R&D Systems; 485-MI), or interleukin (IL)-4 (PeproTech; 214-14) as indicated. RAW 264.7 macrophages were conditioned with LPS or IFN-γ alone to quantify individual stimulus dynamic response, with LPS or IFN-γ sequentially to recover iNOS expression via orthogonal input, or with LPS or IFN-γ simultaneously to quantify supra-additivity and model predictive control strategy response. Pre-treatment, 24 h of 100 ng/mL IL-4 prior to addition of LPS or IFN-γ, was used to induce an anti-inflammatory, non-naïve state for experiments involving hysteretic effects.

Quantification of iNOS Expression via Immunofluorescence and Western Blot

For immunocytochemistry (ICC) experiments, macrophages were cultured in 96-well microplates. Macrophages were fixed in 4% PFA solution for 15 min and blocked with 5% BSA + 3% goat serum in PBS for 1 h. Cells were stained with α-iNOS antibody (Cell Signaling Technology; Cat. No. 13120; 1:400) and DAPI for normalization to nuclei count. Cells were imaged at 10X magnification (Zeiss Observer Z1). Image fluorescence was thresholded and total fluorescence above the threshold was normalized to nuclei number.

For Western blot experiments, cells were cultured in 6-well plates then lysed using RIPA buffer with PMSF (Sigma-Aldrich), and cOmplete Mini (Sigma-Aldrich). Membranes were probed for α-tubulin (Sigma-Aldrich, Cat. No. T6074; 1:4,000) and iNOS (1:1,000). Membranes were imaged on a LiCor Odyssey CLx machine and quantified in ImageStudio Lite. iNOS band intensity was normalized to α-tubulin intensity to yield iNOS expression.

Data Normalization and Dynamic iNOS Response Figure Generation

ICC and Western blot data were aggregated and iNOS expression for each independent experiment was normalized to the positive control with RAW 264.7 cells treated with 1 μg/mL LPS for 24 h. iNOS dynamics plots were generated using the Gramm package for MATLAB (Morel, 2018). Data at sampled time points (0, 24 48, and 72 h) were expressed as mean ± SEM for separated data ($N = 38$ for LPS single input experiments; $N = 8$ for LPS repeated input experiments; $N = 8$ for LPS cycled input experiments; $N = 32$ for IFN-γ single input experiments; $N = 16$ for IFN-γ repeated input experiments; $N = 16$ for IFN-γ cycled input experiments per each time point. Sample sizes used for model fits are indicated in figure legends). To generate interpolation curves, data were smoothed using the Savitzky-Golay (sgolay) option in the curve fitting toolbox. Shaded band on curve represents root mean squared (RMS) cross validation error on smoothed data (Morel, 2018).

SISO and MISO Linear ARX Model System Identification

LPS response data were compiled into a time-domain data object with experiments for all input concentrations and unique input sequences. Dynamic models were fit (**Supplementary Table S1**) to the autoregressive with exogenous inputs (ARX) model structure

$$A\left(z^{-1}\right) y\left(t\right) = B\left(z^{-1}\right) u\left(t - n_k\right) + \varepsilon\left(t\right) \quad (1)$$

where u(t) is the LPS stimulation input, n_k is the system dead time, y(t) is the iNOS response, and the model coefficients consist of

$$A\left(z^{-1}\right) = 1 + a_1 z^{-1} + a_2 z^{-2} + \ldots + a_n z^{-n_a} \quad (2)$$

$$B\left(z^{-1}\right) = b_0 + b_1 z^{-1} + b_2 z^{-2} + \ldots + b_{n_b} z^{-n_b} \quad (3)$$

with one pole (n_a), two zeros (n_b), an input-output delay of 1 time step corresponding to 24 h, and zero initial conditions (System Identification toolbox, MATLAB, 2018b). Parameters were estimated by solving the least squares problem

$$\left(\mathbf{W}^{\mathrm{T}}\mathbf{W}\right)\boldsymbol{\theta} = \mathbf{W}^{\mathbf{T}}\mathbf{y}_m \quad (4)$$

where $\mathbf{W}$ is the 4 × 4 regressor matrix consisting of given inputs, $\mathbf{y}_m = [y\,(0)\ y\,(1)\ y\,(2)\ y\,(3)]^T$ is the measured output vector, and the uniquely identified solution to the least squares parameter estimation is

$$\boldsymbol{\theta} = [a_1\ a_2\ \ldots\ a_{n_a}\ b_0\ b_1\ \ldots\ b_{n_b}\ ]^T \quad (5)$$

The sampling time step of the identified model was set to 24 h, which was equal to the data acquisition time step.

Realized for control design and flow diagram integration, the canonical state space equations for this ARX model are of the form Equations (6) and (7) with matrix coefficients listed in **Supplementary Table S2**.

$$\mathbf{x}(\mathrm{t}+1) = \mathbf{A}\mathbf{x}(\mathrm{t}) + \mathbf{B}\mathbf{u}(\mathrm{t}) \quad (6)$$

$$\mathbf{y}(\mathrm{t}) = \mathbf{C}\mathbf{x}(\mathrm{t}) + \mathbf{D}\mathbf{u}(\mathrm{t}) \quad (7)$$

where $\mathbf{A}$ is the 2 × 2 system matrix, $\mathbf{B}$ is the 2 × 1 input matrix, $\mathbf{C}$ is the 1 × 2 output matrix, $\mathbf{D}$ is the 1 × 1 feedthrough matrix, and t is discrete time. Model order was selected to minimize the small sample-size corrected Akaike's Information Criterion (AICc) (Ljung, 1999) and mean squared error (**Supplementary Table S3**). This process was repeated for a SISO IFN-γ model ($n_a = 1$, $n_b = 2$) and a multi-input single output (MISO) model with both LPS and IFN-γ inputs ($n_a = 1$, $n_b = 2$ for both inputs).

LPS System Controller Design

Controller design was carried out in the Control System Designer application (MATLAB, Mathworks) to find an input strategy capable of achieving the unit step response from a step reference. Since our estimated system dynamics indicated a continuous time zero at the origin, we selected a PI controller to compensate because it adds a continuous time pole at the origin and is widely used in engineered systems (Nise, 2015). A proportional-integral (PI) controller (Equation 8; Bellman, 1961), was designed with robust noise and quick response specifications (parameters given in **Supplementary Table S4**). In discrete time, the PI control law specifies the input in the current time step as a function of the current and prior errors (Ogata, 1995; Nise, 2015):

$$\mathbf{u}\,(\mathrm{t}) = \mathrm{K_p}\mathbf{e}\,(\mathrm{t}-1) + \mathrm{K}_i \sum_0^{\mathrm{t}-1} \mathbf{e}\,(\bar{\mathrm{t}}) \tag{8}$$

where K_p is the proportional gain associated with the error in the last time step and K_i is integral gain associated with the sum of errors in the prior time step. Additionally, since our system model (Equation 1), enabled state estimation, we implemented a third order linear-quadratic Gaussian (LQG) controller, defined to minimize $\tilde{J}$

$$\tilde{J} = \sum_{\mathrm{t}=0}^{\mathrm{N}-1} \left(\mathbf{x}(\mathbf{t})^T\mathbf{Q}\mathbf{x}(\mathbf{t}) + \mathbf{u}(\mathbf{t})^T\mathbf{R}\mathbf{u}(\mathbf{t})\right) + \mathbf{x}\,(\mathbf{N})^T\mathbf{Q}_F\mathbf{x}(\mathbf{N}) \tag{9}$$

The controller was tuned to be robust to noise and assuming moderate measurement noise (zero/pole/gain parameters in **Supplementary Table S4**). Where N is the time horizon, t is the time step, Q is the state cost matrix, Q_f is the final state cost matrix, and R is the input cost matrix. Q, Q_f, and R were defined internally by the system designer application.

Surface Interpolation for Non-linear Model Elements Parameterization

Supra-Additive Pro-Inflammatory Surface

Data matrices across concentration gradients of simultaneous LPS and IFN-γ addition were divided by the iNOS expression level given LPS only for each concentration to give the ratio by which each IFN-γ concentration amplified iNOS expression. The discrete matrix data were fit using cubic interpolation (Curve Fitting Toolbox) for each sampled time point. The cubic interpolation minimized the root mean square error between the fitted and actual values while avoiding outliers from overfitting for the supra-additivity matrix (**Supplementary Figure S7**; data used for interpolation are provided in **Supplementary Data 1**). Other curve fits sampled were linear interpolation, polynomial models, spline interpolation, and local linear regression (Lowess) but had greater error and were subject to overfitting. The resulting scaling factor, λ, was queried for intermediary concentrations of each input at each sampled time.

M2 Hysteresis Surface

For each LPS concentration, iNOS expression for non-M2 polarized LPS-only treated cells were divided by iNOS expression values from cells treated with an array of IL-4 concentrations for 24 h followed by 24 h of LPS. The matrix of LPS and IL-4 concentrations was interpolated using 3rd order polynomial linear regression, where parameters (**Supplementary Table S6**) were estimated by the least-squares method, which provided inverse of the continuous input concentration- dependent attenuation factor γ. Other models were assessed as above, considering overfitting via leave N out cross validation (with 10% of samples left out) and root mean square error minimization (**Supplementary Figure S7**).

Global System Model Architecture and Formulation

For our first nested model, we used a multiple regression with interaction terms to quantify the supra-additive effect of adding both IFN-γ and LPS. Simulations were run using SISO models for single- and double- stimuli experimental results to populate a table with predicted output levels for varying magnitudes of input. The linear dual-input (both IFN-γ and LPS for all time points) model predictions were used as the regression output y, and the single input (either IFN-γ or LPS) SISO model predictions were given as regression inputs to fit a model of relative contributions of time and input interactions (y'_{LPS} and $y'_{IFN\gamma}$). The terms that significantly predicted total iNOS output y were time-dependent LPS concentration, time-dependent IFN-γ concentration, and a combinatorial effect of both LPS and IFN-γ inputs (Equation 10). Weighting coefficients, c, for each term are given in **Supplementary Table S5**.

$$y = [c_1 t y'_{LPS} + c_2 t y'_{IFN\gamma}] + c_3 y'_{LPS} y'_{IFN\gamma} \tag{10}$$

We next sought to construct a second global model structure that handles time- and concentration-dependent supra-additive interaction terms. Here, experimentally obtained iNOS expression data given varying concentrations of LPS and IFN-γ was fit to a response surface, as described above, for each time point. This surface was used to define a table as above but with time and input-dependent dual-input model output predictions. A multiple linear regression on this prediction table similarly fit coefficients for time and input interaction terms (Equation 10, **Supplementary Table S5**). We accounted for this temporally shifting interaction term by implementing the multiple linear regression model with the output from the identified SISO transfer function models *and* time as inputs and the MISO transfer function output as multiple regression model output,

Global System Model MPC Controller Design and Prediction

The Model Predictive Control toolbox in MATLAB (2018b) was used to create the controller and define manipulated input sequences for the MISO "global" model. The SISO IFN-γ and LPS transfer functions with weighting coefficients derived from the multiple regression was given as the model object, referred to as the plant (Equation 11, **Figure 1B**). The plant model was defined with two manipulated variable inputs, one output, a control horizon of 72 h, and a prediction horizon of 120 h. Manipulated variables were constrained with a minimum of 0, a maximum of 1, and unconstrained rates of change. The default state estimator (Kalman filter) settings were used for the controller predictions (MATLAB). Closed loop simulations generated the inputs, u, needed to obtain the set reference

(unit step) over simulation time with the expected system output y. Plant performance was evaluated by running open-loop simulations given the predicted inputs from the closed-loop simulation. Optimal predicted input and output trajectories were validated using the mpcmove function.

$$G = [C_1Y_1,\ C_2Y_2] + C_3Y_1Y_2 \tag{11}$$

DATA AVAILABILITY STATEMENT

The datasets generated for this study are available on request to the corresponding author.

AUTHOR CONTRIBUTIONS

LDW and LBW designed the study. LDW, JF, and AW conducted experiments and data analysis. LDW conducted computational predictive modeling. JU conceptualized physical interpretation of control laws. LBW supervised the project. All authors contributed to the article and approved the submitted version.

FUNDING

This work was supported by startup funds from the George W. Woodruff School of Mechanical Engineering at the Georgia Institute of Technology. LDW was supported in part by the National Institutes of Health Cell and Tissue Engineering Biotechnology Training Grant (T32-GM008433).

ACKNOWLEDGMENTS

This manuscript has been released as a pre-print at bioRxiv, BIORXIV/2019/826966 (Weinstock et al., 2019).

SUPPLEMENTARY MATERIAL

The Supplementary Material for this article can be found online at: https://www.frontiersin.org/articles/10.3389/fbioe.2020.00666/full#supplementary-material

REFERENCES

Becelli, R., Renzi, G., Perugini, M., and Iannetti, G. (2000). Craniofacial traumas: immediate and delayed treatment. *J. Craniofac. Surg.* 11, 265–9. doi: 10.1097/00001665-200011030-00012

Bellman, R. (1961). *Adaptive Control Processes a Guided Tour*. Princeton, NJ: Princeton University Press. doi: 10.1515/9781400874668

Binkowska, A. M., Michalak, G., and, Slotwinski, R. (2015). Current views on the mechanisms of immune responses to trauma and infection. *Cent. Eur. J. Immunol.* 40, 206–216. doi: 10.5114/ceji.2015.52835

Celia-Terrassa, T., Bastian, C., Liu, D. D., Ell, B., Aiello, N. M., Wei, Y., et al. (2018). Hysteresis control of epithelial-mesenchymal transition dynamics conveys a distinct program with enhanced metastatic ability. *Nat. Commun.* 9:5005. doi: 10.1038/s41467-018-07538-7

Day, J., Rubin, J., and Clermont, G. (2010). Using nonlinear model predictive control to find optimal therapeutic strategies to modulate inflammation. *Math. Biosci. Eng.* 7, 739–763. doi: 10.3934/mbe.2010.7.739

Decano, J. L., and Aikawa, M. (2018). Dynamic macrophages: understanding mechanisms of activation as guide to therapy for atherosclerotic vascular disease. *Front. Cardiovasc. Med.* 5:97. doi: 10.3389/fcvm.2018.00097

Deshpande, S., Nandola, N. N., Rivera, D. E., and Younger, J. W. (2014). Optimized treatment of fibromyalgia using system identification and hybrid model predictive control. *Control Eng. Pract.* 33, 161–173. doi: 10.1016/j.conengprac.2014.09.011

Galbraith, N., Walker, S., Carter, J., and Polk, H. C. Jr. (2016). Past, present, and future of augmentation of monocyte function in the surgical patient. *Surg. Infect.* 17, 563–569. doi: 10.1089/sur.2016.014

Geerlings, S. E., and Hoepelman, A. I. (1999). Immune dysfunction in patients with diabetes mellitus (DM). *FEMS Immunol. Med. Microbiol.* 26, 259–265. doi: 10.1111/j.1574-695X.1999.tb01397.x

Guo, S., and Dipietro, L. A. (2010). Factors affecting wound healing. *J. Dent. Res.* 89, 219–229. doi: 10.1177/0022034509359125

Hamelin, L., Lagarde, J., Dorothee, G., Potier, M. C., Corlier, F., Kuhnast, B., et al. (2018). Distinct dynamic profiles of microglial activation are associated with progression of alzheimer's disease. *Brain* 141, 1855–1870. doi: 10.1093/brain/awy079

Hespanha, J. P. (2009). *Linear Systems Theory*. Princeton, NJ: Princeton University Press.

Hu, X., Leak, R. K., Shi, Y., Suenaga, J., Gao, Y., Zheng, P., et al. (2015). Microglial and macrophage polarization-new prospects for brain repair. *Nat. Rev. Neurol.* 11, 56–64. doi: 10.1038/nrneurol.2014.207

Islam, M. N., Bradley, B. A., and Ceredig, R. (2016). Sterile post-traumatic immunosuppression. *Clin. Transl. Immunol.* 5:e77. doi: 10.1038/cti.2016.13

Kadelka, S., Boribong, B. P., Li, L., and Ciupe, S. M. (2019). Modeling the bistable dynamics of the innate immune system. *Bull. Math. Biol.* 81, 256–276. doi: 10.1007/s11538-018-0527-y

Kimura, F., Shimizu, H., Yoshidome, H., Ohtsuka, M., and Miyazaki, M. (2010). Immunosuppression following surgical and traumatic injury. *Surg. Today* 40, 793–808. doi: 10.1007/s00595-010-4323-z

Kong, L., Smith, W., and Hao, D. (2019). Overview of RAW264.7 for osteoclastogensis study: Phenotype and stimuli. *J. Cell. Mol. Med.* 23, 3077–3087. doi: 10.1111/jcmm.14277

Lawrence, T., and Natoli, G. (2011). Transcriptional regulation of macrophage polarization: enabling diversity with identity. *Nat. Rev. Immunol.* 11, 750–761. doi: 10.1038/nri3088

Lee, S., Kivimae, S., Dolor, A., and Szoka, F. C. (2016). Macrophage-based cell therapies: the long and winding road. *J. Control Release* 240, 527–540. doi: 10.1016/j.jconrel.2016.07.018

Li, C., Menoret, A., Farragher, C., Ouyang, Z., Bonin, C., Holvoet, P., et al. (2019). Single cell transcriptomics based-MacSpectrum reveals novel macrophage activation signatures in diseases. *JCI Insight* 5:e126453. doi: 10.1172/jci.insight.126453

Liu, Y., and Allen, R. (2002). Analysis of dynamic cerebral autoregulation using an ARX model based on arterial blood pressure and middle cerebral artery velocity simulation. *Med. Biol. Eng. Comput.* 40, 600–5. doi: 10.1007/BF02345461

Ljung, L. (1999). *System Identification: Theory for the User, 2nd Edn*. Upper Saddle River, NJ: Prentice Hall.

Makkouk, A., and Weiner, G. J. (2015). Cancer immunotherapy and breaking immune tolerance: new approaches to an old challenge. *Cancer Res.* 75, 5–10. doi: 10.1158/0008-5472.CAN-14-2538

Mohammadbagheri, A., Zaeri, N., and Yaghoobi, M. (2011). "Comparison performance between PID and LQR controllers for 4-leg voltage-source inverters," in *International Conference on Circuits, System and Simulation* (Bangkok).

Morel, P. (2018). Gramm: grammar of graphics plotting in matlab. *J. Open Source Soft.* 3:568. doi: 10.21105/joss.00568

Mosser, D. M., and Edwards, J. P. (2008). Exploring the full spectrum of macrophage activation. *Nat. Rev. Immunol.* 8, 958–969. doi: 10.1038/nri2448

Ni, Y., Zhuge, F., Nagashimada, M., and Ota, T. (2016). Novel action of carotenoids on non-alcoholic fatty liver disease: macrophage polarization and liver homeostasis. *Nutrients* 8:391. doi: 10.3390/nu8070391

Nise, N. S. (2015). *Control Systems Engineering, 7th Edn*. Hoboken, NJ: Wiley.

Ogata, K. (1995). *Discrete-time Control Systems*. Hoboken, NJ: Prentice-Hall International.

Ohashi, W., Hattori, K., and Hattori, Y. (2015). Control of macrophage dynamics as a potential therapeutic approach for clinical disorders involving chronic inflammation. *J. Pharmacol. Exp. Ther.* 354, 240–250. doi: 10.1124/jpet.115.225540

Oishi, Y., and Manabe, I. (2016). Macrophages in age-related chronic inflammatory diseases. *NPJ Aging Mech. Dis.* 2:16018. doi: 10.1038/npjamd.2016.18

Pacini, S. (2014). Deterministic and stochastic approaches in the clinical application of mesenchymal stromal cells (MSCs). *Front. Cell. Dev. Biol.* 2:50. doi: 10.3389/fcell.2014.00050

Ponzoni, M., Pastorino, F., Di Paolo, D., Perri, P., and Brignole, C. (2018). Targeting macrophages as a potential therapeutic intervention: impact on inflammatory diseases and cancer. *Int. J. Mol. Sci.* 19:1953. doi: 10.3390/ijms19071953

Rachad, S., Nsiri, B., and Bensassi, B. (2015). System identification of inventory system using ARX and ARMAX models. *Int. J. Control Autom.* 8, 283–294. doi: 10.14257/ijca.2015.8.12.26

Salim, T., Sershen, C. L., and May, E. E. (2016). Investigating the role of TNF-alpha and IFN-gamma activation on the dynamics of iNOS gene expression in LPS stimulated macrophages. *PLoS ONE* 11:e0153289. doi: 10.1371/journal.pone.0153289

Shin, Y. J., Sayed, A. H., and Shen, X. (2012). Adaptive models for gene networks. *PLoS ONE* 7:e31657. doi: 10.1371/journal.pone.0031657

Sica, A., and Mantovani, A. (2012). Macrophage plasticity and polarization: *in vivo* veritas. *J. Clin. Invest.* 122, 787–795. doi: 10.1172/JCI59643

Spiller, K. L., and Koh, T. J. (2017). Macrophage-based therapeutic strategies in regenerative medicine. *Adv. Drug Deliv. Rev.* 122, 74–83. doi: 10.1016/j.addr.2017.05.010

Sun, L., Pham, T. T., Cornell, T. T., McDonough, K. L., McHugh, W. M., Blatt, N. B., et al. (2017). Myeloid-specific gene deletion of protein phosphatase 2A magnifies MyD88- and TRIF-dependent inflammation following endotoxin challenge. *J. Immunol.* 198, 404–416. doi: 10.4049/jimmunol.1600221

Taciak, B., Bialasek, M., Braniewska, A., Sas, Z., Sawicka, P., Kiraga, L., et al. (2018). Evaluation of phenotypic and functional stability of RAW 264.7 cell line through serial passages. *PLoS ONE* 13:e0198943. doi: 10.1371/journal.pone.0198943

Tripathi, S., Chakraborty, P., Levine, H., and Jolly, M. K. (2020). A mechanism for epithelial-mesenchymal heterogeneity in a population of cancer cells. *PLoS Comput. Biol.* 16:e1007619. doi: 10.1371/journal.pcbi.1007619

Van den Hof, P. M. J., Heuberger, P. S. C., and Bokor, J. (1994). "System identification with generalized orthonormal basis functions," in *Proceedings of 1994 33rd IEEE Conference on Decision and Control* (Lake Buena Vista, FL).

Vodovotz, Y., Xia, A., Read, E. L., Bassaganya-Riera, J., Hafler, D. A., Sontag, E., et al. (2017). Solving immunology? *Trends Immunol.* 38, 116–127. doi: 10.1016/j.it.2016.11.006

Wang, Y., Han, Z. B., Song, Y. P., and Han, Z. C. (2012). Safety of mesenchymal stem cells for clinical application. *Stem Cells Int.* 2012:652034. doi: 10.1155/2012/652034

Weekman, E. M., Sudduth, T. L., Abner, E. L., Popa, G. J., Mendenhall, M. D., Brothers, H. M., et al. (2014). Transition from an M1 to a mixed neuroinflammatory phenotype increases amyloid deposition in APP/PS1 transgenic mice. *J. Neuroinflammation* 11:127. doi: 10.1186/1742-2094-11-127

Weinstock, L. D., James, E. F., Alexis, W., Jun, U., and Wood, L. B. (2019). Experimental control of macrophage pro-inflammatory dynamics using predictive models. *bioRxiv [preprint]*. doi: 10.1101/826966

Wynn, T. A., Chawla, A., and Pollard, J. W. (2013). Macrophage biology in development, homeostasis and disease. *Nature* 496, 445–455. doi: 10.1038/nature12034

Zhao, Q., Wang, X., Nelin, L. D., Yao, Y., Matta, R., Manson, M. E., et al. (2006). MAP kinase phosphatase 1 controls innate immune responses and suppresses endotoxic shock. *J. Exp. Med.* 203, 131–140. doi: 10.1084/jem.20051794

Ziegler-Heitbrock, H. W., Wedel, A., Schraut, W., Strobel, M., Wendelgass, P., Sternsdorf, T., et al. (1994). Tolerance to lipopolysaccharide involves mobilization of nuclear factor kappa B with predominance of p50 homodimers. *J. Biol. Chem.* 269, 17001–17004.

Zurakowski, R., and Teel, A. R. (2006). A model predictive control based scheduling method for HIV therapy. *J. Theor. Biol.* 238, 368–382. doi: 10.1016/j.jtbi.2005.05.004

Conflict of Interest: The authors declare that the research was conducted in the absence of any commercial or financial relationships that could be construed as a potential conflict of interest.

Copyright © 2020 Weinstock, Forsmo, Wilkinson, Ueda and Wood. This is an open-access article distributed under the terms of the Creative Commons Attribution License (CC BY). The use, distribution or reproduction in other forums is permitted, provided the original author(s) and the copyright owner(s) are credited and that the original publication in this journal is cited, in accordance with accepted academic practice. No use, distribution or reproduction is permitted which does not comply with these terms.

frontiers in Bioengineering and Biotechnology

ORIGINAL RESEARCH
published: 14 July 2020
doi: 10.3389/fbioe.2020.00759

Modeling Pathway Dynamics of the Skeletal Muscle Response to Intravenous Methylprednisolone (MPL) Administration in Rats: Dosing and Tissue Effects

*Alison Acevedo[1], Debra DuBois[2,3], Richard R. Almon[2,3], William J. Jusko[2,3] and Ioannis P. Androulakis[1,4,5]**

[1] Department of Biomedical Engineering, Rutgers University, Piscataway, NJ, United States, [2] Department of Pharmaceutical Sciences, School of Pharmacy and Pharmaceutical Sciences, State University of New York at Buffalo, Buffalo, NY, United States, [3] Department of Biological Sciences, State University of New York at Buffalo, Buffalo, NY, United States, [4] Department of Chemical and Biochemical Engineering, Rutgers University, Piscataway, NJ, United States, [5] Department of Surgery, Rutgers Robert Wood Johnson Medical School, New Brunswick, NJ, United States

OPEN ACCESS

Edited by:
Babatunde Ogunnaike,
University of Delaware, United States

Reviewed by:
Le Shu,
University of California, Los Angeles, United States
Bin Du,
Google, United States

***Correspondence:**
Ioannis P. Androulakis
yannis@soe.rutgers.edu

Specialty section:
This article was submitted to Computational Genomics, a section of the journal Frontiers in Bioengineering and Biotechnology

Received: 08 December 2019
Accepted: 15 June 2020
Published: 14 July 2020

Citation:
Acevedo A, DuBois D, Almon RR, Jusko WJ and Androulakis IP (2020) Modeling Pathway Dynamics of the Skeletal Muscle Response to Intravenous Methylprednisolone (MPL) Administration in Rats: Dosing and Tissue Effects. Front. Bioeng. Biotechnol. 8:759. doi: 10.3389/fbioe.2020.00759

A model-based approach for the assessment of pathway dynamics is explored to characterize metabolic and signaling pathway activity changes characteristic of the dosing-dependent differences in response to methylprednisolone in muscle. To consistently compare dosing-induced changes we extend the principles of pharmacokinetics and pharmacodynamics and introduce a novel representation of pathway-level dynamic models of activity regulation. We hypothesize the emergence of dosing-dependent regulatory interactions is critical to understanding the mechanistic implications of MPL dosing in muscle. Our results indicate that key pathways, including amino acid and lipid metabolism, signal transduction, endocrine regulation, regulation of cellular functions including growth, death, motility, transport, protein degradation, and catabolism are dependent on dosing, exhibiting diverse dynamics depending on whether the drug is administered acutely of continuously. Therefore, the dynamics of drug presentation offer the possibility for the emergence of dosing-dependent models of regulation. Finally, we compared acute and chronic MPL response in muscle with liver. The comparison revealed systematic response differences between the two tissues, notably that muscle appears more prone to adapt to MPL.

Keywords: omics, corticosteroids, pathway analysis, methylprednisolone, dose comparison, tissue comparison

INTRODUCTION

Methylprednisolone (MPL) is a synthetic glucocorticoid (GC) widely used to treat a multitude of conditions including arthritis, blood disorders, severe allergic reactions, certain cancers, eye conditions, skin/kidney/intestinal/lung diseases, and immune system disorders. MPL, a typical corticosteroid, manages symptoms such as swelling, pain, and allergic-type reactions by decreasing the immune system's response (Swartz and Dluhy, 1978; Barnes, 1998). Mechanistic studies

of GCs in inflammation have identified two main modes of action: a direct consequence of glucocorticoid/glucocorticoid-receptor complex binding to gene targets, as well as by signaling through receptors in a manner independent of transcription (Schaaf and Cidlowski, 2002; Freishtat et al., 2010). Glucocorticoid effects are pervasive and involve multiple molecular mechanisms. Corticosteroids, including MPL, influence physiology at the regulatory level leading to systemic, multifactorial consequences further complicated by the observed differences in response dynamics to differing dosing regimens of glucocorticoid administration (Almon et al., 2007b; Yao et al., 2008). These changing dynamics are indicative of likely differences in regulatory mechanisms, further revealing that regulatory structures implied by acute administration are not consistent with regulatory structures implied by chronic MPL administration (Hazra et al., 2008; Yao et al., 2008; Nguyen et al., 2010). Acute administration of the drug is generally beneficial by reducing inflammation temporarily. However, chronic administration of corticosteroids, though necessary for chronic conditions, has deteriorative consequences including hyperglycemia, negative nitrogen balance, and fat redistribution leading to complications including diabetes, muscle wasting, osteoporosis (Morand and Leech, 1999; Liu et al., 2017). These consequences are notably observed in muscle where continuous use of corticosteroids leads to muscle atrophy and insulin resistance (Almon et al., 2005a; Schakman et al., 2013; Bodine and Furlow, 2015).

Earlier work has explored *in vivo* high-throughput transcriptomics to capture the tissue and dosing effects of MPL (Sun et al., 1998, 1999; Ramakrishnan et al., 2002a,b; Almon et al., 2005a,b, 2007a, 2008a; Hazra et al., 2007, 2008; Yang et al., 2008, 2009; Yao et al., 2008; Nguyen et al., 2010). We recently proposed a meta-analysis approach to further elaborate our understanding of liver's complex pharmacogenomic effects following acute and chronic dosing of MPL (Acevedo et al., 2019). The approach applies a pathway-based analysis, mapping transcriptomic data onto tissue- and organism-relevant pathways; characterizes the overall dynamic activity of the pathway; and uses a model-based assessment of activity to infer pathway dynamics. The approach was demonstrated using liver-specific genome-wide pharmacological time-series obtained from comparing alternative dosing regiments.

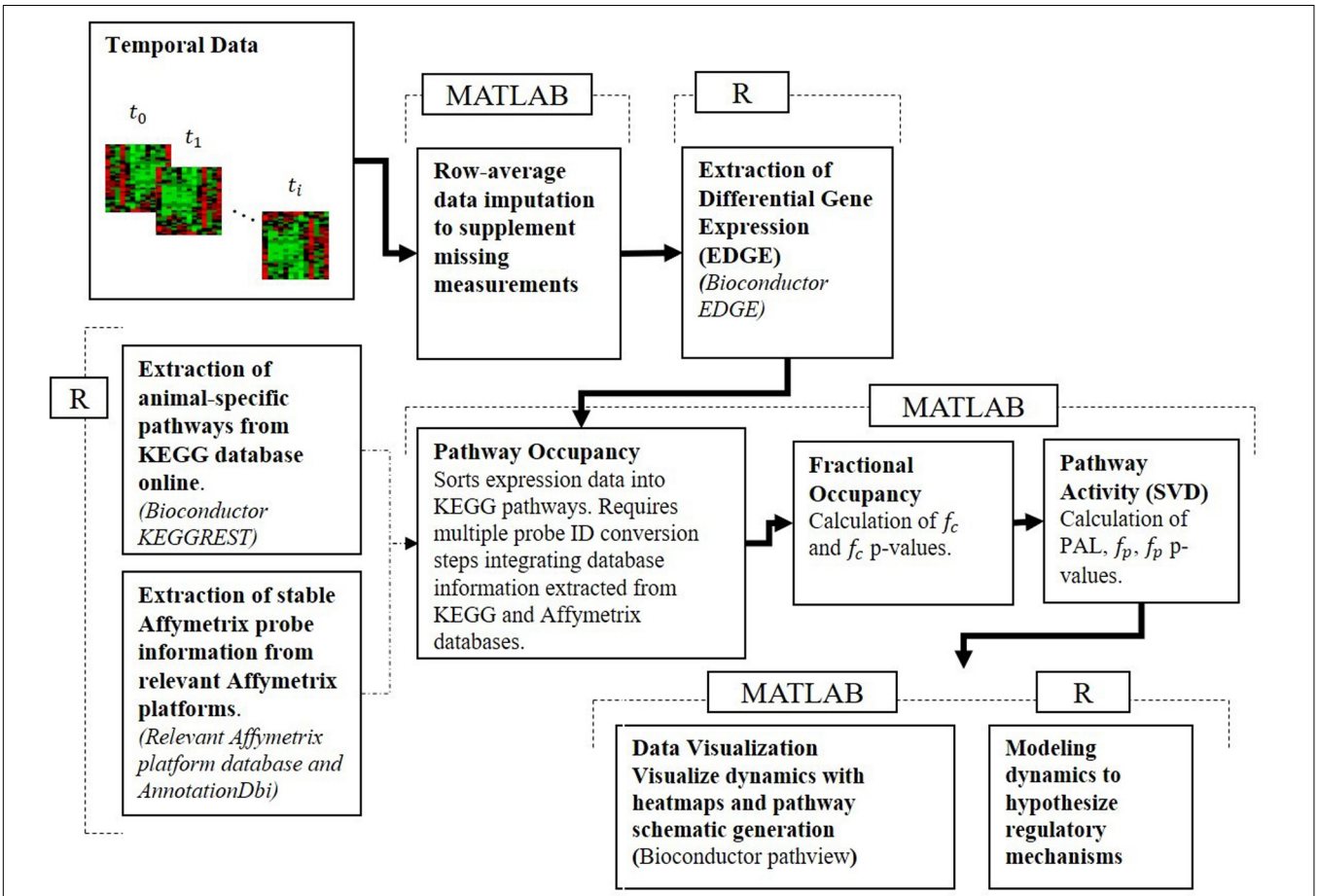

FIGURE 1 | Pathway activity analysis framework starts with the processing of the transcriptional data, maps differentially expressed AffyIDs to gene IDs, assigns those to KEGG pathway gene sets, populates KEGG pathways, assesses fractional occupancy, performs pathway activity to identify significant PALs, and develops dynamic models of regulatory controls of pathway activity.

Given that musculature contributes significantly to adverse glucocorticoid-induced effects, in the present study we employ our established pathway approach to study the acute and chronic MPL dosing effects in gastrocnemius muscle of male adrenalectomized rats, and characterize the dosing-dependent differences in the dynamic response of MPL-responsive pathways. To consistently compare across dosing-induced changes, a model-based approach for the assessment of pathway dynamics is employed extending the principles of pharmacokinetics and pharmacodynamics (PKPD) to characterize pathway activity. We hypothesize the emergence of dosing-dependent regulatory interactions to understand the mechanistic implications of MPL dosing in muscle. Our results indicate that key pathways including amino acid and lipid metabolism, signal transduction, endocrine regulation, regulation of cellular functions including growth, death, motility, transport, protein degradation, and catabolism, are all dependent on dosing. Finally, we compare acute and chronic MPL response across muscle with liver and observe systematic response differences between the two tissues. Notably, we observe that muscle appears more prone to developing tolerance to MPL.

MATERIALS AND METHODS

Animal Model and Experimental Data

The temporal transcriptomic data used for this analysis was collected from extracted gastrocnemius muscle in two temporal large rat studies presented here (Sun et al., 1999; Ramakrishnan et al., 2002a). For the generation of acute MPL response data, 39 adrenalectomized male (ADX) Wistar rats were treated with a bolus dose of 50 mg/kg MPL intravenously (Sun et al., 1999). This dose was established previously for identifying biomarkers for gene-mediated effects of glucocorticoids in liver tissue because of its induction of strong, but not saturating, effects on gene and protein expression and comparability with large doses in human upon scale-up (Boudinot et al., 1986). The animals

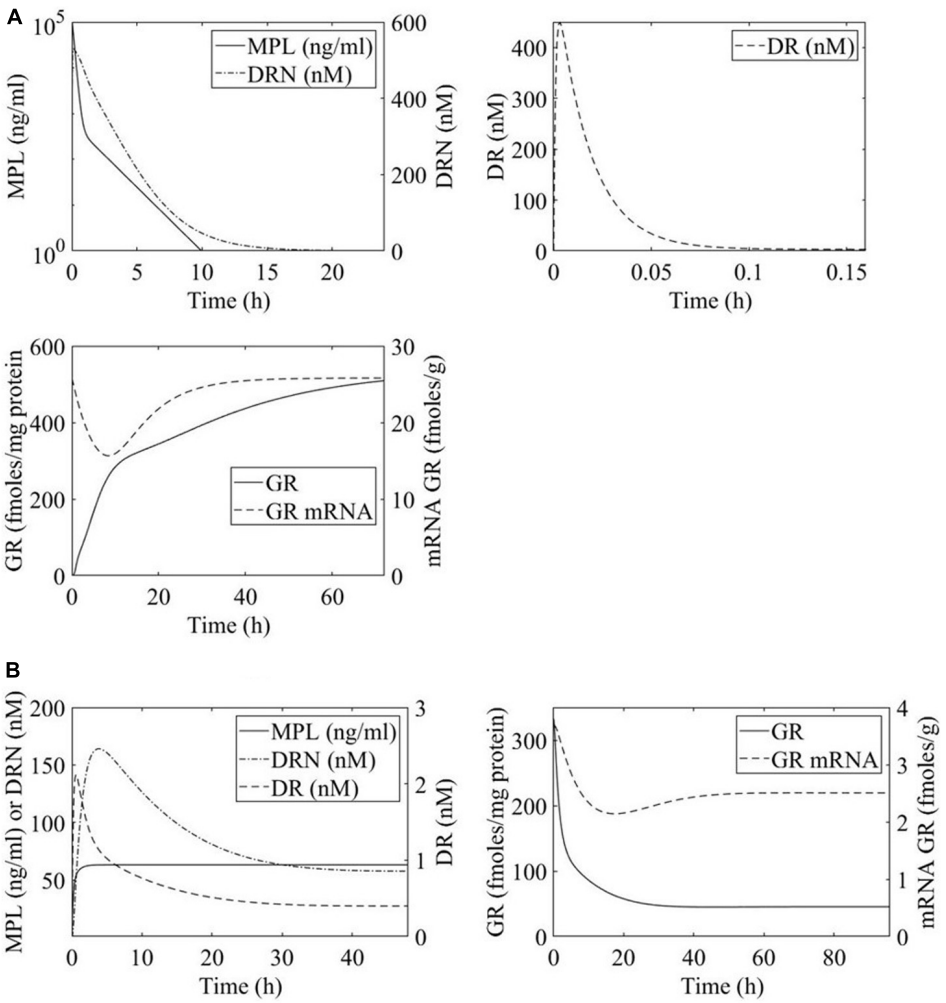

FIGURE 2 | Time profiles of methylprednisolone (MPL) pharmacokinetics and receptor dynamics for **(A)** acute 50 mg/mL bolus MPL dose and **(B)** chronic infusion of 0.3 mg/(kg·h) MPL. Methylprednisolone influence over transcription within the liver is dosing dependent and receptor mediated.

were sacrificed at 17 timepoints (n = 2–4) from 0 to 72 h post dosing and isolated RNA were hybridized with Affymetrix GeneChips Rat Genome U34A containing 8799 probes. Chronic MPL administration response data in muscle tissue was obtained from a longitudinal study in which 40 ADX male Wistar rats were administered 0.3 mg/kg·hr of MPL intravenously for 7 days (Nguyen et al., 2010). Animals were sacrificed at 11 time points over this period. Isolated RNA from excised gastrocnemius muscle tissue was hybridized with Affymetrix GeneChips Rat Genome 230A) containing 15,967 probes. Both the acute and chronic datasets have been submitted to GEO (acute: GSE490 and chronic: GSE5101) and we have previously presented analyses of the transcription responses (Sun et al., 1999; Almon et al., 2002, 2005a, 2008a,b; Ramakrishnan et al., 2002a; Yao et al., 2008; Fang et al., 2013; Nguyen et al., 2014).

Pathway Activity Analysis

To reconcile the temporal response of muscle tissue to acute and chronic MPL dosing, the datasets were processed using our pathway activity analysis described in depth in our previous publication analyzing dosing-dependent pathway activity in liver (Acevedo et al., 2019). The approach consists of a series of steps described briefly herein, moved beyond an individual gene-centric analysis, which seeks to characterize muscle response at the level of functional groups – at the level of pathways. For this analysis, pathways are defined as networks of molecular interactions and reactions designed to link genes in the genome to gene products through biochemical action. The steps are succinctly presented in **Figure 1**.

Microarray Data Preprocessing

Active genes are identified using differential expression analysis using the Extraction and Analysis of Gene Expression (EDGE) software (Storey et al., 2018). Differentially expressed profiles are then z-scored with respect to the individual profile mean and standard deviation.

Mapping Transcriptomic Data to Pathways

Differentially expressed genes are mapped onto pathways, defined as networks of molecular interactions and reactions designed to link genes in the genome to gene products. These pathways express layered and complementary activities, meaning pathways are groups of genes linked mechanistically that effect a signaling or biochemical action. Numerous databases exist defining pathways including the Kyoto Encyclopedia of Genes and Genomes (KEGG) (Aoki and Kanehisa, 2005) and Reactome (Fabregat et al., 2018). Without loss of generality, the present analysis is based on KEGG. As of February 2019, this database contains 326 pathways relevant to rat tissues and used for our analysis. Only pathways relevant to muscle tissue are analyzed resulting in 179 metabolic and signaling pathways for consideration in our analysis (**Supplementary Table A**). For the gene-to-pathway mapping, Affymetrix probe identifiers within the microarray template and are converted into KEGG IDs in order to be sorted into rat-relevant pathways from KEGG. Affymetrix probe identifiers are translated into their NCBI Entrez IDs and Gene Symbols using the Bioconductor packages for each Affymetrix Platform: Package rae230a.db containing the annotation data for Affymetrix Rat Expression Set 230A used with the chronic data; and Package rgu34a.db containing the annotation data for Affymetrix Rat Genome U34 Array annotation data used with the acute data. Following the gene-to-pathway assignment, the coverage of the KEGG pathways is assessed by evaluating the fractional coverage (f_c) of each pathway (Acevedo et al., 2019). This statistic is the fraction of genes within a pathway for which gene profiles are available. To assess the confidence in the fractional coverage, an associated p-value (f_c p-value) is determined using the 1-tail Fisher's Exact test such that the total rat genome is the set of unique rat genes in all KEGG's rat-relevant pathways (Acevedo et al., 2019). Pathways with low fractional occupancy yield inconclusive p-values as an artifact of the Fisher's Exact Test and were eliminated from the analysis.

TABLE 1 | Pharmacokinetic parameters for acute and chronic MPL administration (Ramakrishnan et al., 2002a).

Parameter	Definition	Acute	Chronic
$k_0\left(\frac{mg}{kg}h\right)$	Rate of drug infusion into central plasma compartment	0	220
$CL\left(\frac{L}{h\cdot kg}\right)$	Clearance	3.48	5.61
$V_p\left(\frac{L}{kg}\right)$	Central volume of drug distribution	0.73	0.82
$k_{12}\left(\frac{1}{h}\right)$	Drug distribution rate constant	0.98	0.32
$k_{21}\left(\frac{1}{h}\right)$	Drug distribution rate constant	1.78	0.68

TABLE 2 | Parameters for receptor-mediated effects of acute and chronic MPL administration (Hazra et al., 2008).

Parameter	Definition	Acute	Chronic
$k_{sRm}\left(\frac{fmol}{g\cdot h}\right)$	Receptor mRNA synthesis rate constant	3.15	0.45
$k_{dRm}\left(\frac{1}{h}\right)$	Receptor mRNA degradation rate constant	0.122	
$IC_{50Rm}\left(\frac{nmol}{L\cdot mg_{protein}}\right)$	DRN required for 50% inhibition of the synthesis rate of Rm	123.7	
$k_{sR}\left(\frac{nmol}{L\cdot mg_{protein}\cdot fmol_{Rm}\cdot g\cdot h}\right)$	Receptor synthesis rate	0.84	3.63
$k_{re}\left(\frac{1}{h}\right)$	Loss rate for drug receptor in the nucleus	0.402	
$k_{on}\left(\frac{1}{nmol\cdot h}\right)$	Association rate for receptor-drug binding	0.019	
$k_{dR}\left(\frac{1}{h}\right)$	Receptor loss/degradation rate	0.0403	
$k_T\left(\frac{1}{h}\right)$	Translocation of receptor into the nucleus	58.1	
R_f	Receptor recycling factor from nucleus to cytosol	0.69	

Pathway Activity Analysis

The presence of differentially expressed genes within a pathway does not guarantee that the pathway exhibits a coherent dynamic response (Kallio et al., 2011). In order to assess the emergence of activity patterns within a pathway we capitalize on our earlier work on pathway activity analysis (Ovacik et al., 2010; Euling et al., 2011, 2013) recently expanded in Acevedo et al. (2019). In brief, singular value decomposition (SVD) on the temporal transcriptomic data associated with each pathway, decomposes the overall pathway dynamics into constitutive elements (singular vectors referred to herein as pathway activity levels, PAL) reflecting coherence of expression among the genes of the pathway. The singular value associated with each singular vector expresses the fractional variability (f_p) captured by the corresponding PAL. In order to characterize the actual significance of a corresponding PAL, an associated f_p p-value is evaluated using bootstrapping of the original gene set (see **Supplementary Note**) (Acevedo et al., 2019). Finally, all pathways yielding fractional coverage f_c p-value $\leq$0.05 with at least one significant PAL profile f_p p-value $\leq$0.05 are defined as significant. These significance criteria indicate that the pathway is sufficiently represented by the transcriptomic data and that at least one global, non-random, trend has emerged from the pathway. It is important to emphasize that the activity analysis does not make any assumptions as to the nature of the dynamics of the activity across a pathway.

Evaluating Pathway Activity Dynamics

In order to capture the likely variability of the transcriptomic data bootstrapping is used to generate pathway gene sets likely to exist within the experimental variability. Each bootstrapped gene set is assessed for pathway activity, thus revealing a likely the range of activity a pathway in muscle tissue can produce in response to MPL administration. Briefly, each

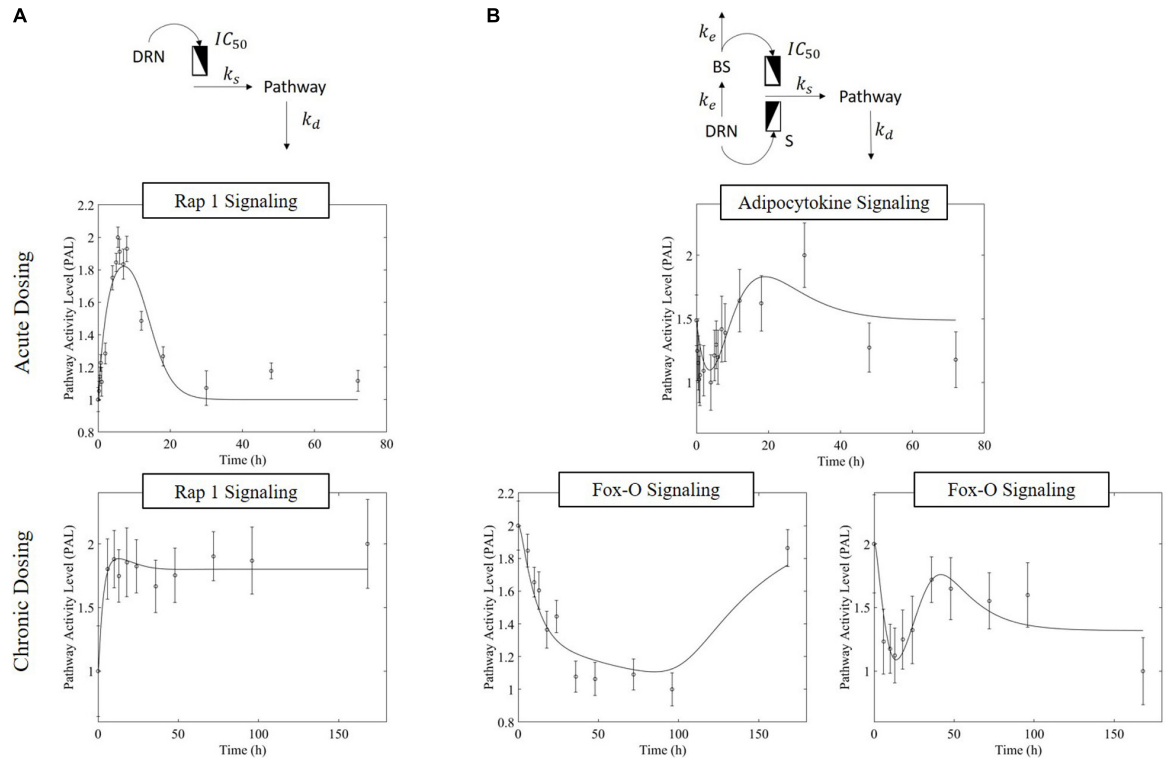

FIGURE 3 | Regulatory mechanism schematics for the **(A)** receptor-mediated regulation of PAL and **(B)** biosignal-mediated regulation of PAL. Methylprednisolone regulates transcription via binding to glucocorticoid receptors within the cytosol, transporting into the nucleus, and binding to a GRE element – thus initiating targeted transcription. (*Receptor-mediated dynamics*) Since the activity is driven by the levels of the active signal DRN, and this follows the PK of MPL, acute dosing the response dynamics should exhibit a major event with a subsequent return to pre-administration levels (exemplified by Acute Rap 1 Signaling), as the PK of MPL prescribes. Under chronic dosing, since the levels of DRN stabilize at a new steady state, the DRN effect should persist for as long as the levels of DRN are constant (exemplified by acute Rap 1 signaling response). (*Receptor-mediated and biosignal-mediated dynamics*) If the drug induces the release of a secondary biosignal (BS) this will induce a delayed secondary effect which, if competing with the effect of DRN, would lead to a "rebound"-type of response. As MPL clears, and both DRN and BS deplete, the system returns to pre-MPL level (exemplified by Adipocytokine signaling). Chronic administration can generate two distinct types of dynamics responses (the presence of the secondary biosignal BS can induce a secondary event, competing with that of DRN). BS can exercise its impact either in a delayed manner leading to a "tolerance-like" behavior (exemplified by Fox-O Signaling response, **A**) or through an incomplete rebound effect with the system relaxing eventually at a steady state other than the pre-MPL one (exemplified by Fox-O Signaling response, **B**). For each pathway, the significant bootstrapped PAL are clustered such that common activity patterns group together. PAL profiles plotted herein are plots of the centroids of these clusters (represented by the data points), fitted with models (represented by the fitted continuous profile). The error bars about the PAL central data points are defined by the standard deviation of all bootstrapped PAL that are captured within the cluster.

gene expression profile is bootstrapped assuming a normal distribution about the gene expression profile's mean. These bootstrapped genes are assembled into pathway gene sets. Thus, (N = 1000) bootstrapped pathway gene sets are generated from the original pathway gene set. These bootstrapped sets are decomposed with SVD, significant PAL profiles identified, and their corresponding f_p and f_p p-value statistics retained for each significant pathway. All PAL profiles extracted from these bootstrapped gene sets are assumed likely system behavior that would emerge if the rat experiments were repeated. Bootstrapped PAL within a pathway are subsequently clustered for the identification of common activity patterns. The MATLAB® function evalclusters.m is applied to assess optimal cluster number using the gap statistic and applying kmeans clustering (MATLAB, 2018) (see **Supplementary Note**). The finite set of PAL centroids identified indicate a finite list of activity patterns that emerge from each pathway, induced by MPL. Pathway activity analysis identifies a pathway's leading intrinsic dynamics as a result of application of its decomposition technique. We seek to compare pathway activities across non-overlapping gene sets and identified from data with different dosing regimens and time horizons. To this end, the dynamics of each dominant PAL is approximated using PKPD-driven models exploring alternative hypotheses for the mechanisms of regulation of a pathway, herein referred to as *pathway pharmacodynamics*.

Pharmacokinetics

The PK of MPL in both regimens was shown to be appropriately described by a two-compartment model, **Figure 2**, equations 1 and 2 (Ramakrishnan et al., 2002a; Hazra et al., 2008). A_p and A_t denote drug in the plasma and tissue compartments respectively. Term k_0 is the zero-order rate constant for drug input into the plasma, CL indicates clearance, V_p indicates plasma volume of distribution, and k_{12} and k_{21} are the intercompartmental distribution rate constants. In the case of acute MPL administration, k_0 = 0 indicating a bolus injection. Parameter values are adopted from Ramakrishnan et al. and presented in **Table 1** (Ramakrishnan et al., 2002a; Hazra et al., 2008).

$$\frac{dA_p}{dt} = k_0 + k_{21} \cdot A_t - \left(k_{12} + \frac{CL}{V_p}\right) \cdot A_p \quad (1)$$

$$\frac{dA_t}{dt} = k_{12} \cdot A_p - k_{21} \cdot A_t \quad (2)$$

Receptor Dynamics

MPL action is receptor-mediated as described in equations 3 through 6 and depicted in **Figure 2** (Ramakrishnan et al., 2002a; Hazra et al., 2008). Parameter values are adopted from Hazra et al. and presented in **Table 2** (Hazra et al., 2008). These parameter values are also used in previous analyses of dosing-dependence in liver (Acevedo et al., 2019). R_m indicates mRNA of the free cytosolic receptor, R indicates the free cytosolic receptor, DR indicates the cytosolic drug-receptor complex, and DRN indicates the drug-receptor complex in the nucleus (Ramakrishnan et al., 2002a). The concentration at which the synthesis rate of receptor mRNA drops to 50% of its baseline value is indicated by IC_{50Rm}, parameter k_{on} denotes a second-order rate constant for drug-receptor binding. Parameters k_T and k_{re} are first-order rates of receptor translocation between the nucleus and the cytosol (k_{re} : to the nucleus; k_{re} : recycling back to the nucleus) (Ramakrishnan et al., 2002a). The fraction of receptor recycled is indicated by parameter R_f. C_{MPL} corresponds to the concentration of free receptor in the cytosol and is given by $C_{MPL} = 0.43\frac{A_p}{V_p}$ (Ramakrishnan et al., 2002a; Hazra et al., 2008).

$$\frac{dRm}{dt} = k_{sRm} \cdot \left(1 - \frac{DRN}{IC_{50Rm} + DRN}\right) - k_{dRm} \cdot Rm \quad (3)$$

$$\frac{dR}{dt} = k_{sR} \cdot Rm + R_f \cdot k_{re} \cdot DRN - k_{on} \cdot C_{MPL} \cdot R - k_{dR} \cdot R \quad (4)$$

$$\frac{dDR}{dt} = k_{on} \cdot C_{MPL} \cdot R - k_T \cdot DR \quad (5)$$

$$\frac{dDRN}{dt} = k_T \cdot DR - k_{re} \cdot DRN \quad (6)$$

TABLE 3 | Counts of pathways that emerged as significant in response to acute and chronic MPL dosing in muscle.

Pathway subgroup	Pathway group	Significant acute response pathways	Significant chronic response pathways
Cell growth and death	Cellular processes	5	3
Cell motility	Cellular processes	1	1
Transport and catabolism	Cellular processes	3	6
Signal transduction	Environmental information processing	17	15
Signaling molecules and interaction	Environmental information processing	1	0
Folding, sorting and degradation	Genetic information processing	1	4
Transcription	Genetic information processing	0	1
Translation	Genetic information processing	0	1
Amino acid metabolism	Metabolism	2	6
Carbohydrate metabolism	Metabolism	0	9
Energy metabolism	Metabolism	0	2
Lipid metabolism	Metabolism	4	2
Metabolism of cofactors and vitamins	Metabolism	0	1
Metabolism of other amino acids	Metabolism	1	1
Nucleotide metabolism	Metabolism	1	0
Xenobiotics biodegradation and metabolism	Metabolism	1	0
Endocrine system	Organismal systems	12	8
Environmental adaptation	Organismal systems	0	1
	Total	**49**	**61**

*See **Supplementary Tables** for complete list of significant pathways and all calculated metrics.*

Pathway Pharmacodynamics

Pharmacogenomic models have been extensively used to model complex transcriptional dynamics (Almon et al., 2002; Ramakrishnan et al., 2002b; Jin et al., 2003; Yao et al., 2008; Ayyar et al., 2018), whereas we recently extended the concept to describe complex "pathways" pharmacodynamics (Acevedo et al., 2019). We hypothesize that transcriptional events are induced by the regulatory action of an MPL-receptor complex (DRN) binding to a GRE element in the nucleus. In order to capture more complex behaviors, such as tolerance and rebound, it has been hypothesized that the receptor complex can likely induce intermediate biosignal (BS) inducing complex responses (Sharma et al., 1998; Sharma and Jusko, 1998). By decomposing the pathway dynamics to its constitutive PALs, we aim to characterize the dosing-dependent activity in muscle, by hypothesizing that each PAL can be represented by an appropriate dynamic model. We thus compare PAL dynamics across dosing, and tissues, in the space of pathway pharmacodynamic models. PAL profiles were captured by our "receptor-mediated" or "biosignal-mediated" model types as previously discussed in the context of liver (Acevedo et al., 2019) and developed as an extension of the concepts presented in Hazra et al. (2008) and Yao et al. (2008).

The receptor-mediated model (**Figure 3A**, equation 7) indicates a mode of pathway regulation which assumes a saturable induction of the pathway activity driven primarily by the active MPL-receptor complex (k_s indicates the activation rate of pathway activity; IC_{50PAL} indicates the concentration of DRN responsible for 50% inhibition of the pathway activity activation rate; and k_d indicates the deactivation rate of pathway activity). This model captures the pathway activity response to intravenous MPL administration for both acute and chronic dosing, reflecting transient or persistent response types depending on dosing. Receptor-mediated response is expected to taper-off under acute administration since the dynamics of *PAL* should follow the dynamics of *DRN*. Under chronic dosing, and as *DRN* accumulates the influence should persist (**Figure 3**).

$$\frac{dPAL}{dt} = k_s\left(1 \pm \frac{DRN}{IC_{50PAL} + DRN}\right) - k_d \cdot PAL \qquad (7)$$

MPL regulation can be also mediated via an intermediate biosignal whose synthesis is directly related to DRN (Yao et al., 2008), equations 8 and 9 (k_e indicates the translation rate of BS; S is the stimulation constant for pathway activity due to DRN; IC_{50PAL} indicates the BS responsible for 50% inhibition of pathway activity activation rate; and γ indicates the factor of amplification of the influence of BS on the activation of pathway activity). Biosignal-mediated responses could either lead

Pathway	Pathway Category	Acute Type	Chronic Type
Prolactin signaling pathway	Endocrine system	monophasic	biphasic/tolerance
GnRH signaling pathway	Endocrine system	monophasic	biphasic/tolerance
FoxO signaling pathway	Signal transduction	monophasic	biphasic/tolerance
Arginine and proline metabolism	Amino acid metabolism	monophasic	monophasic/tolerance
Glutathione metabolism	Amino acid metabolism	monophasic	monophasic/tolerance
Apoptosis	Cell growth and death	monophasic	monophasic/tolerance
Cellular senescence	Cell growth and death	monophasic	monophasic/tolerance
Regulation of actin cytoskeleton	Cell motility	monophasic	monophasic/tolerance
Glucagon signaling pathway	Endocrine system	monophasic	monophasic/tolerance
Insulin signaling pathway	Endocrine system	monophasic	monophasic/tolerance
Oxytocin signaling pathway	Endocrine system	monophasic	monophasic/tolerance
PPAR signaling pathway	Endocrine system	monophasic	monophasic/tolerance
TGF-beta signaling pathway	Signal transduction	biphasic	monophasic/tolerance
cGMP-PKG signaling pathway	Signal transduction	monophasic	monophasic/tolerance
HIF-1 signaling pathway	Signal transduction	monophasic	monophasic/tolerance
PI3K-Akt signaling pathway	Signal transduction	monophasic	monophasic/tolerance
Rap1 signaling pathway	Signal transduction	monophasic	monophasic/tolerance
Peroxisome	Transport and catabolism	monophasic	monophasic/tolerance
Ferroptosis	Cell growth and death	monophasic	tolerance
Proteasome	Folding, sorting and degradation	biphasic	tolerance
Fatty acid degradation	Lipid metabolism	biphasic	tolerance
Thyroid hormone signaling pathway	Endocrine system	monophasic	tolerance
Fatty acid metabolism	Lipid metabolism	monophasic	tolerance
AMPK signaling pathway	Signal transduction	monophasic	tolerance
ErbB signaling pathway	Signal transduction	monophasic	tolerance
Autophagy - animal	Transport and catabolism	monophasic	tolerance
Adipocytokine signaling pathway	Endocrine system	monophasic/biphasic	tolerance
MAPK signaling pathway	Signal transduction	monophasic/biphasic	monophasic/tolerance
VEGF signaling pathway	Signal transduction	monophasic/biphasic	monophasic/tolerance

FIGURE 4 | Illustrated table capturing the summarized responses of each of the 29 significant pathways common to the acute and chronic muscle analyses. The consistent response types are indicative of likely common effects of MPL across metabolic and signaling pathways. The details of these dynamics are included in **Supplementary Table D**.

to "rebound" like behavior under acute dosing or, under chronic dosing, could lead to "tolerance"-like response or "rebound"-like eventually reaching a new steady state (**Figure 3**)

$$\frac{dBS}{dt} = k_e\,(DRN - BS) \tag{8}$$

$$\frac{dPAL}{dt} = k_s(1 \pm S \cdot DRN)\left(1 \mp \frac{BS^{\gamma}}{IC_{50PAL}^{\gamma} + BS^{\gamma}}\right) - k_d \cdot PAL \tag{9}$$

As previously discussed in Acevedo et al. (2019), the parameter estimation was performed using MATLAB's optimization toolkit in a series of optimization stages. In all stages, we sought to minimize the residual sum of squares between the model prediction and the cluster centroid profile. In the first stage, it is assumed that the system is non-linear and neither continuous nor differentiable for the entire parameter solution space. Therefore, as a rapid preliminary global search for a minimum, a stochastic direct method (simulated annealing) with bound constraints is employed. The result of this global search technique is taken as the initial parameter values for the second optimization stage using a direct pattern search method. In the final stage, a gradient-based method is used to probe this more limited space as the final optimization step. This stage uses the sequential quadratic programming as implemented through MATLAB's fmincon. The model which results from this optimization process is visually inspected.

RESULTS

Of the 179 pathways determined to be rat- and muscle- relevant, fractional coverage analysis yielded 51 represented pathways in the acute dataset and 61 in the chronic dataset. Pathway activity analysis examined these pathways to determine whether significant PALs emerged from each pathway. Pathways which yielded at least one significant PAL (f_p p-value $\leq$0.05) were considered active. For the acute dosing, 49 pathways emerged as significant while all 61 pathways emerged as significant for the chronic dosing (Significant pathways counts are listed by subgroup in **Table 3**, organized by subgroup. They are also listed in long form name with KEGG identification information in **Supplementary Tables STB, STC**), chronic dosing appears to engage relatively more of the amino acid and carbohydrate metabolism function of the tissue, whereas acute dosing appears to drive lipid metabolism and induce relatively more activity in endocrine and signaling functions. A subset of 29 pathways were identified as significant in both acute and chronic dosing (**Table 3** and **Figure 4**) comprising a collection of metabolic, signaling and endocrine functions. The dynamic profiles of all 29 pathways, in acute and chronic dosing, are presented in the **Supplementary Figures** and the pathways are listed in the **Supplementary Tables**. When compared against the list of significant pathways in liver, we identified a subset of pathways that were also significant in liver in response to acute and chronic MPL administration, detailed further in the "Discussion" section. Broadly, chronic dosing appears to engage relatively more amino acid and carbohydrate metabolism pathways compared to acute dosing.

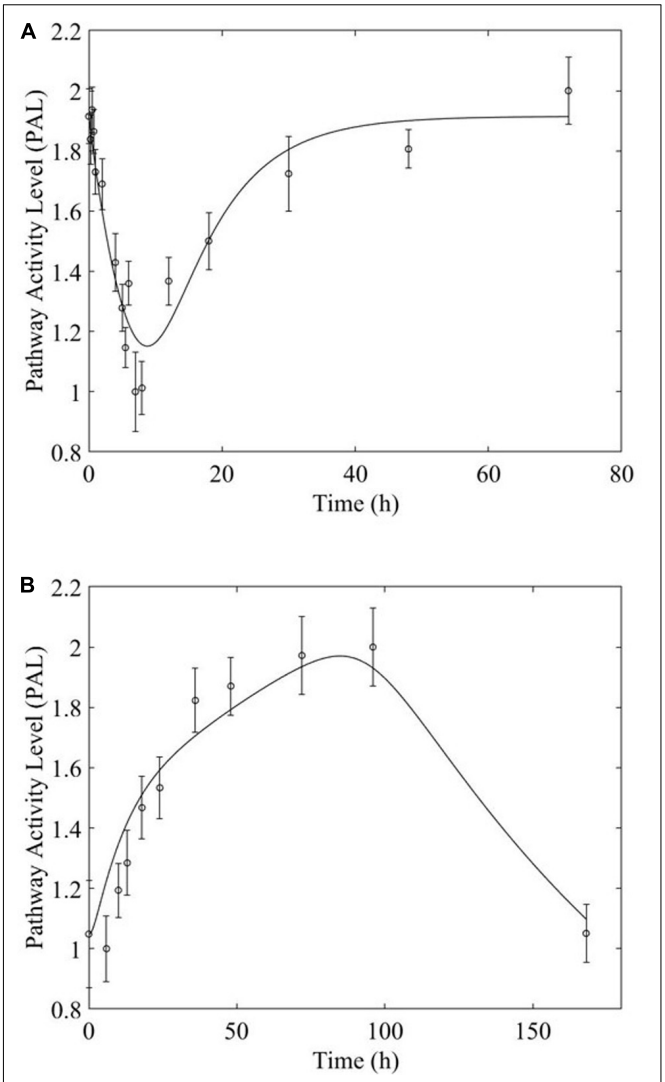

FIGURE 5 | AMPK signaling pathway response to **(A)** acute and **(B)** chronic MPL administration.

Overwhelmingly, muscle responds in a relatively direct way to acute dosing. Except for a handful of pathways, muscle response to acute dosing is receptor mediated. A transient response is observed in pathway profiles shortly after MPL dosing. This initial response is transient, and the pathway eventually resolves to the pre-administration levels. Characteristic examples of this response type are observed in AMPK, Fox-O, and PPAR signaling pathways (**Figures 5A**, **6A**, **7A**). These results are generally consistent with the observed PK of MPL since the drug clears within about 10 h (**Figure 2**).

Based on our earlier studies which determined that acute and chronic MPL exposure impact differentially liver (Acevedo et al., 2019), we hypothesize the drug to induce dosing-dependent and tissue-specific effects, as earlier transcriptomic analyses indicate (Ballard et al., 1974; Sun et al., 1999; Yao et al., 2008; Nguyen

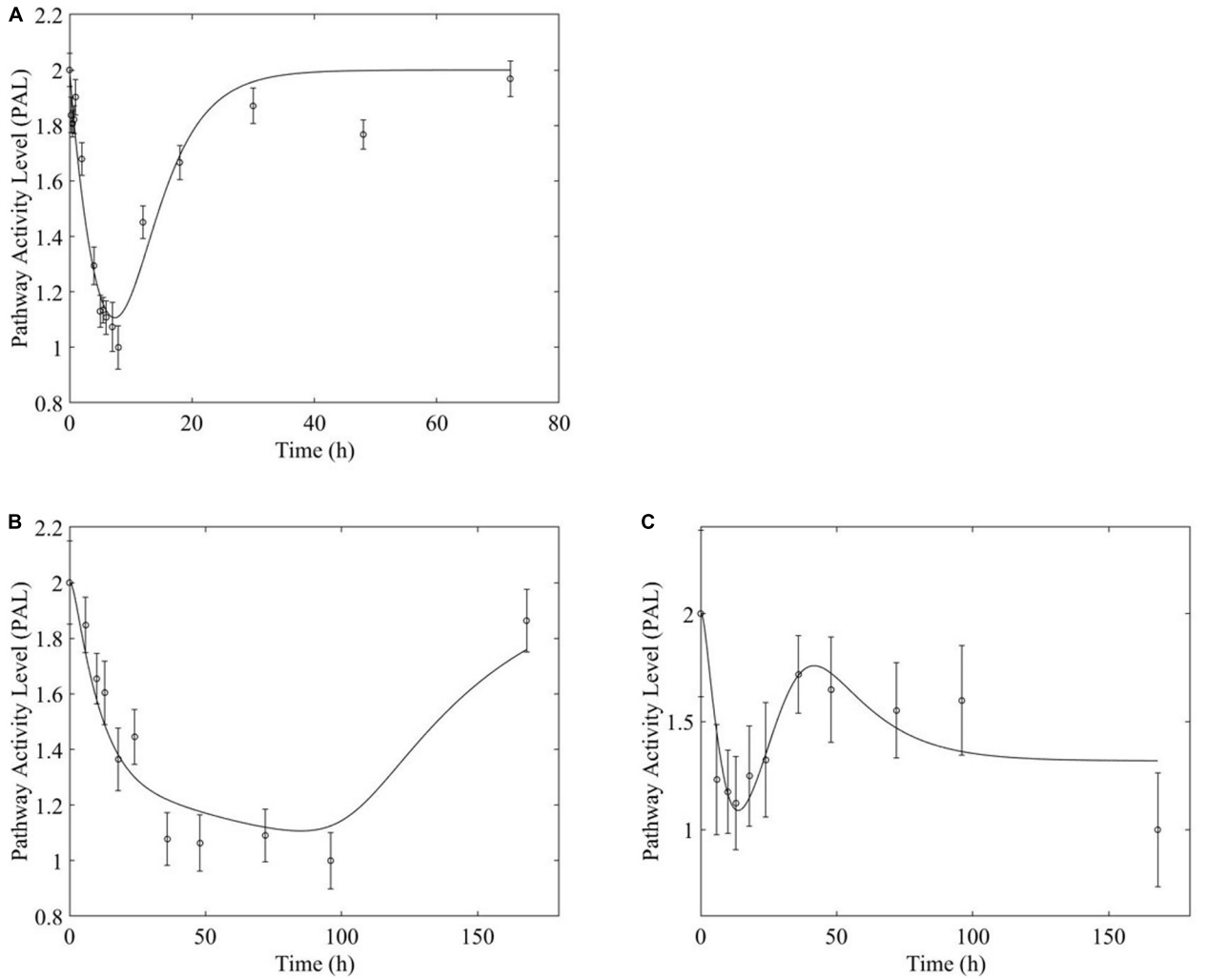

FIGURE 6 | Fox-O signaling pathway response to (**A**, top) acute and (**B,C**, bottom) chronic MPL administration.

et al., 2014). When comparing liver and muscle effects, we determine that acute dosing elicits comparable dynamics in liver and muscle, as exemplified in **Figure 8** for the peroxisome signaling pathway for which the dominant regulatory structure is receptor-mediated. However, chronic dosing appears to drive: (1) substantially different response dynamics in the two tissues, as exemplified with chronic administration of MPL impact to the PPAR signaling pathway (**Figure 9**); (2) simple(r) muscle dynamics but more complex liver dynamics, illustrated with fatty acid degradation pathway (**Figure 10**); and (3) leading dynamics manifested via tissue-specific regulation, or time scales (**Figure 11**).

Chronic MPL administration elicits complex behaviors in muscle. Despite a continuous infusion of the drug, the muscle-specific pathway dynamic responses relax over the 170 h experimental time course to either a new steady state or, via some mechanism of tolerance, returns to the pre-exposure condition. Examples of this tolerance behavior are described **Supplementary Table D** and depicted in greater detail in the **Supplementary Figures**. The new steady state is achieved via multiple mechanism options: (1) by the equilibrating roles of DRN and BS (AMPK, **Figure 5B**); (2) by a combination of the previous mechanism and a "rebound" effect leading to part of the pathway reaching a different steady state (Fox-O, **Figures 6B,C**); (3) by a combination of equilibration of the DRN and BS forces and the persistent regulatory driver toward a new steady state (PPAR, **Figures 7B,C**). One of the most striking observations of this analysis is that muscle appears to better "tolerate" chronic MPL exposure with a variety of mechanisms, enabling the tissue to recover to pre-exposure features of pathway dynamics.

DISCUSSION

MPL is a widely used anti-inflammatory and immune-suppressing drug. Like most drugs, its use can exhibit both deleterious and beneficial effects. Specifically with respect to

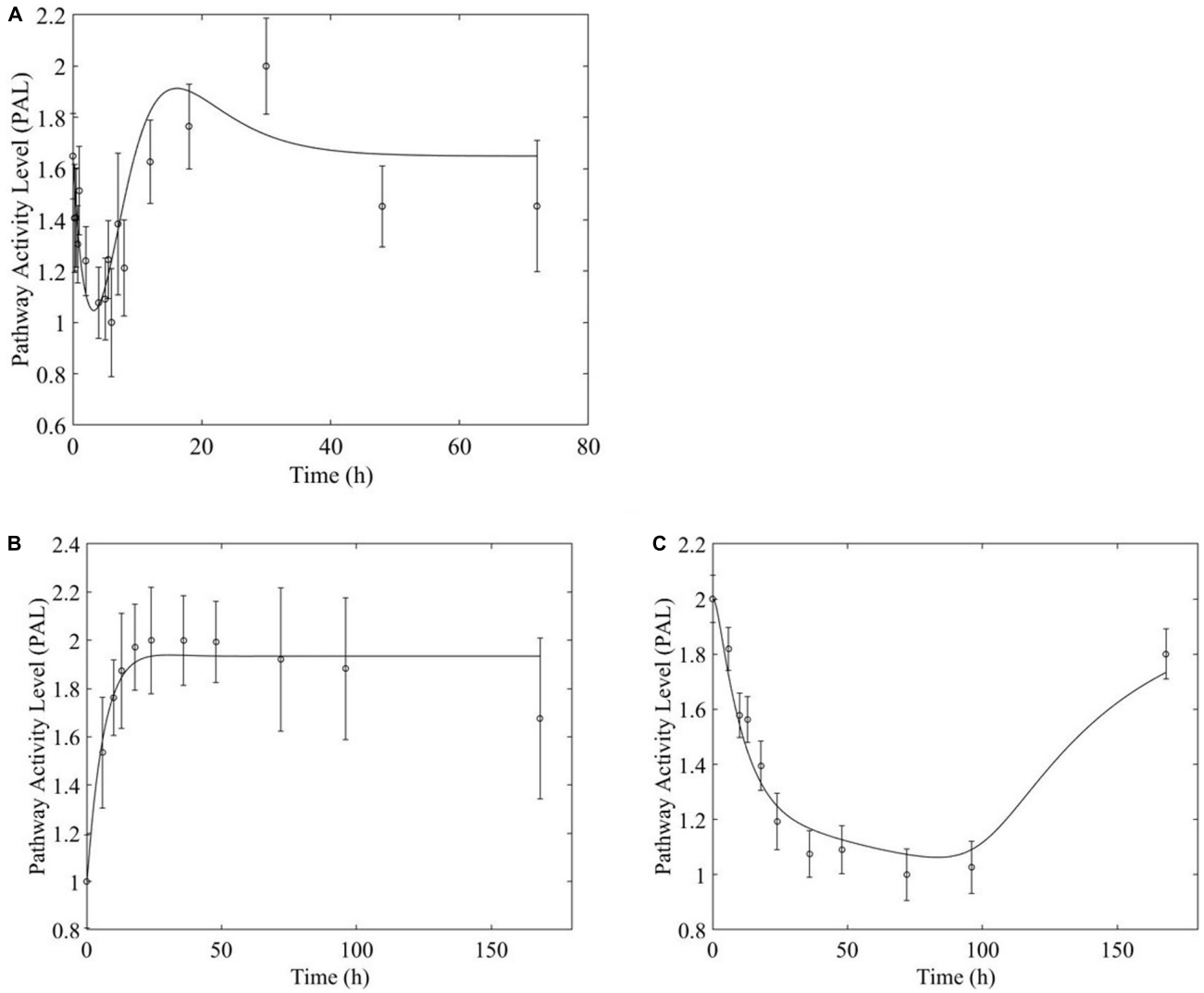

FIGURE 7 | PPAR signaling pathway response to (**A,** top) acute and (**B,C**, bottom) chronic MPL administration.

muscle, chronic use has been associated with muscle atrophy and insulin resistance (Schakman et al., 2013; Bodine and Furlow, 2015). Despite its continued use, the mechanistic details are not entirely characterized. Multiple dosing studies aim at probing the system differentially and as such hold promise in terms deciphering some of those complexities. Reconciling data from multiple studies that explore the influence of MPL is not straightforward, as data can potentially be collected using different experimental platforms, on different time scales, within different tissues, and across different dosing regimens (Ghosh et al., 2003; Ramasamy et al., 2008; Tseng et al., 2012).

Pathway activity analysis was explored to identify pathways that are significantly active in response to MPL. We view a (metabolic or signaling) pathway as a high-dimensional system whose decomposition identifies intrinsic trends. Using singular value decomposition (SVD), a pathway's dynamic is decomposed into constituent singular values and singular vectors. The singular vectors are linear combinations of the longitudinal transcriptional expression over time, thus capture trends in the activity of the pathway, defined as Pathway Activity Level (PAL). The fraction of variability of each PAL profile is calculated from the singular values and is defined as the fraction of pathway activity (f_p). Alternatively, a PAL profile can be thought of as the expression of a metagene over time, where the metagene is a representation of common trends in gene expression within a pathway. The emergence of multiple significant PALs indicates a codominance of activity patterns, and complex regulatory structures, within the pathway. To characterize these activity dynamics consistently, we extended the PD concept to describe the dynamics of a signaling or metabolic pathway's corticosteroid impact in muscle tissue. Models that describe receptor and biosignal-mediated regulation by MPL were fitted to PAL profiles. This step served to hypothesize likely modes of pathway regulation and is essential to enable comparison of drug

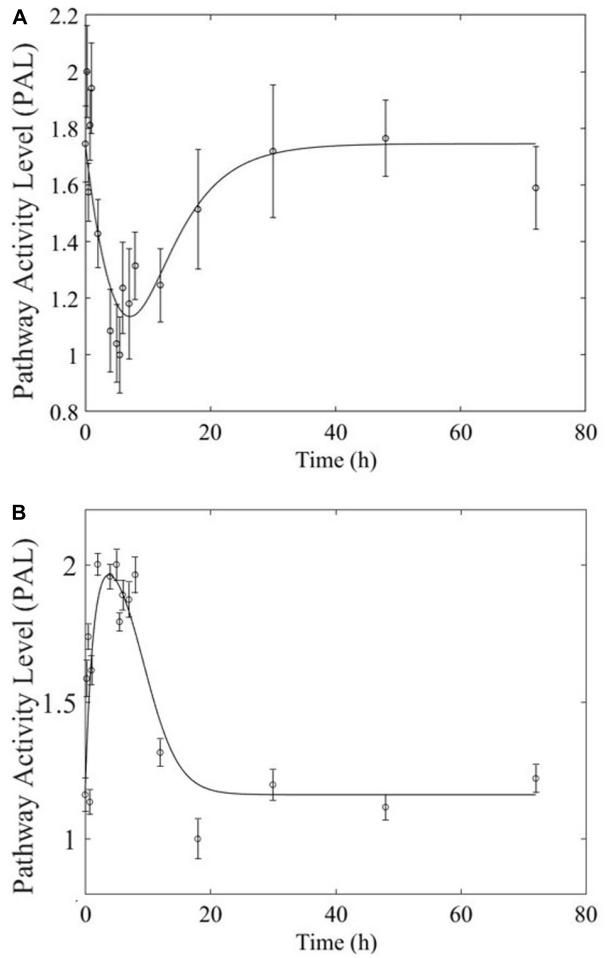

FIGURE 8 | Acute MPL administration in muscle **(A)** and liver **(B)**. Receptor mediated dynamics dominate acute administration in both tissues, as illustrated here for the peroxisome pathway.

response across experimental platforms, animals, tissues, dosing regimens, or time horizons. Overall, we observed strikingly consistent response profiles across pathways and within the same dosing regimen. We further observed that chronic administration yielded more complex pathway dynamics for most pathways, than did acute administration.

We first analyze the MPL response in each dosing regimen independently in the context of functional groups, i.e., pathways, and characterize this in the space of regulatory models. The authors would like to acknowledge that the acute platform is smaller than the microarray platform used to generate the chronic dataset. This detail of our data is consistent with our previous analysis in liver (Acevedo et al., 2019). The significant chronic pathways generally yield higher fractional coverage than the acute counterparts, and this is likely due to the difference in platforms. As a result of this, it may be true that the differences in gene content bias the pathway dynamics. However, the purpose of the fc p-value is to identify whether a pathway is sufficiently represented in our data and thus indicates whether we can trust a pathway to be represented in our solution set. It is this analysis step and statistic which enables us to retain as much data as possible for both studies in order to assess pathway dynamics without reducing one platform or the other to only a subset of genes common between the platforms. Further, because both acute and chronic studies capture the influence of MPL within muscle tissue, a consistent set of pathways is anticipated to emerge, and is observed (**Table 4**), when comparing these data, further discussed later in this section.

Forty nine pathways (see **Supplementary Table B**) were identified as active in the acute set. Interestingly, the dominant regulatory structure is receptor-mediated to acute MPL administration in muscle tissue with a consistent response of an initial peak in activity due to DRN action between 5 and 15 h followed by a return to baseline between 20 and 40 h. This response is consistent with the nature of the acute dosing–an MPL half-life of 0.33 h in ADX rats with total drug clearance observed after about 4.6 h (Hazra et al., 2007). Pathway families represented in this subset include: amino acid metabolism (Arginine and proline metabolism, Glutathione metabolism), pathways related to cell motility, cell growth and death, cellular events such folding, sorting, and degradation of genetic material and proteins, transport, and catabolism (Regulation of actin cytoskeleton, Apoptosis, Cellular senescence, Ferroptosis, Proteasome, Autophagy, Peroxisome), endocrine regulation (Signaling pathways for Glucagon, GnRH, Insulin, Oxytocin, Prolactin, PPAR, and Thyroid hormone), signal transduction (Signaling pathways for TGF-beta, AMPK, cGMP-PKG, ErbB, Fox-O, HIF-1, PI3K-Akt, and Rap1), and lipid metabolism (Fatty acid degradation and Fatty acid metabolism).

The chronic administration explored the Affymetrix microarray platform 230A and yielded 61 pathways as significantly active (**Supplementary Table C**). As in the acute response analysis, response to chronic administration yielded consistency in profile activity events across pathways. However, pathways varied in their complexity of response to chronic administration by exhibiting receptor and/or biosignal-mediated dynamics, often leading to tolerance, defined herein as a return to baseline despite continuous drug infusion. A tolerance profile is characterized by the receptor-mediated effects of *DRN* and the biosignal-mediated effects of *BS* regulating the activity of the pathway in opposite directions. The AMPK signaling pathway, Thyroid hormone signaling pathway, Autophagy, ErbB signaling pathway, Ferroptosis, and Fatty acid metabolism pathways yield strictly tolerance (biosignal-mediated) response to chronic MPL. The HIF-1 signaling pathway, Regulation of actin cytoskeleton, Oxytocin signaling pathway, PI3K-Akt signaling pathway, Apoptosis, Cellular senescence, Peroxisome, Insulin signaling pathway, Rap1 signaling pathway, Glucagon signaling pathway, cGMP-PKG signaling pathway, Arginine and Proline metabolism, Glutathione metabolism, PPAR signaling pathways exhibit both receptor, as well as biosignal-mediated responses to chronic MPL administration.

Chronic dosing appears to, disproportionately, impact metabolic processes, as indicated in **Table 3**. While the fraction of signaling pathways, whose activity is impacted by acute or chronic dosing is high for both, chronic dosing appears

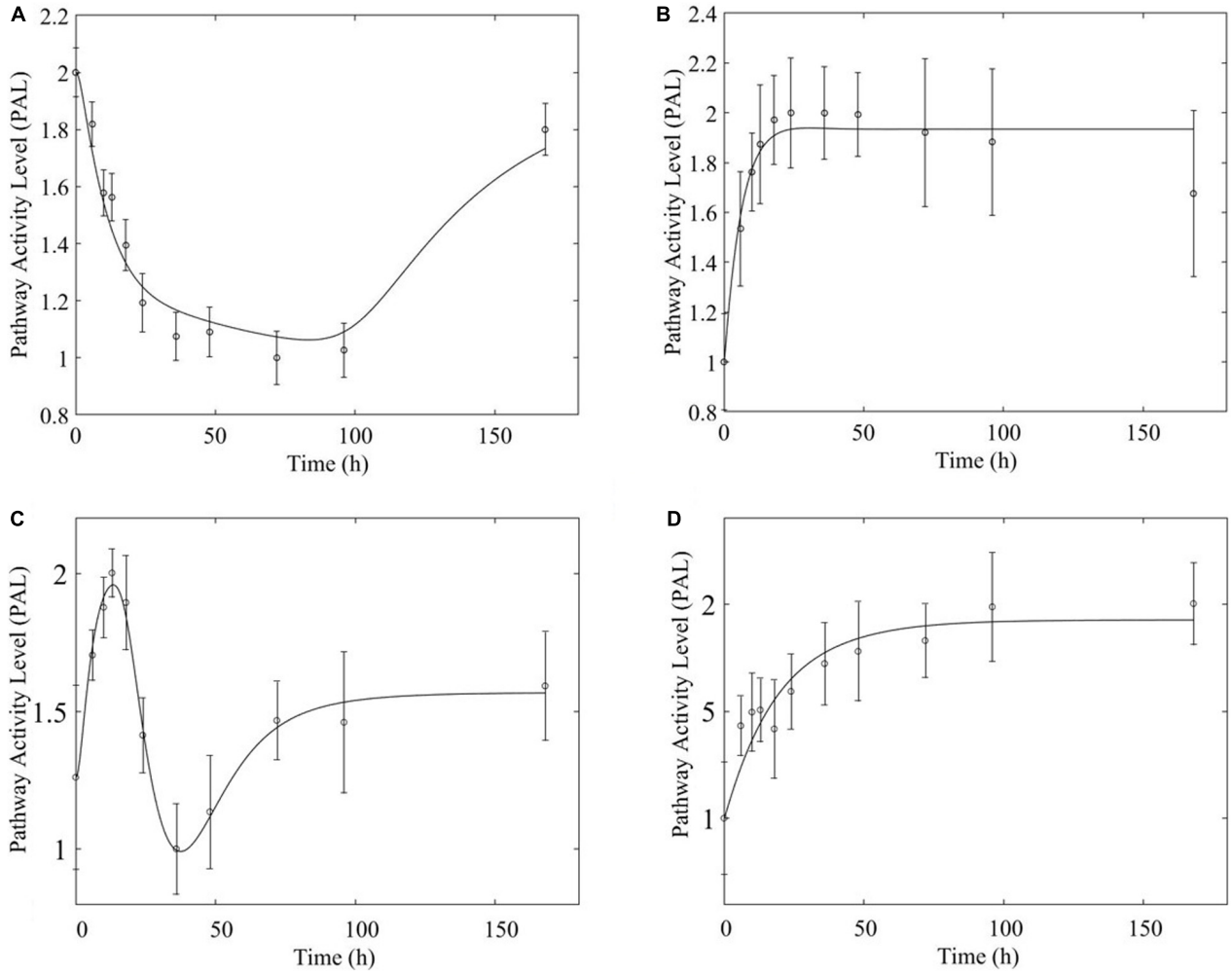

FIGURE 9 | Comparison of response to chronic MPL administration in muscle (**A,B**, top) and liver (**C,D**, bottom) for PPAR. Both tissues exhibit more complex behavior exhibiting a combination of biosignal-mediated (**A,C**, left) and receptor-mediated effects (**B,D,** right).

to engage amino acid and carbohydrate metabolism more actively. One of the most intriguing findings of the study is that the chronic MPL administration does not induce persistent effects on all pathways. This behavior is exemplified by the AMPK signaling pathway (**Figure 5**), an energy metabolism regulator responsible for inhibiting energy-consuming pathways (anabolic functions) and activating ATP-generating catabolic pathways. Activation of this pathway is unsurprising because it is previously observed that corticosteroid treatment causes mitochondrial dysfunction in muscle cells, which induces a state of ATP deprivation and subsequent activation of AMPK signaling to counteract this, ultimately leading to muscle atrophy (Liu et al., 2015). What is surprising is that in response to chronic MPL, the AMPK pathway yields a biosignal-mediated response. This is indicative of the development of tolerance to MPL because despite continuous administration of MPL over the course of the experiment, the pathway returns to baseline – at least for the duration of the experiment.

However, chronic MPL administration has the potential of yielding more complex behaviors. The Fox-O signaling pathway consists of a series of transcription factors that regulate multiple events within the cell including "apoptosis, cell-cycle control, glucose metabolism, oxidative stress resistance, and longevity (KEGG, 2019a)." Fox-O transcription factors including Foxo1 and Foxo3a are upregulated in response to the corticosteroid dexamethasone and are key regulators of gene expression leading to muscle atrophy (Waddell et al., 2008; Zhao et al., 2009; Schakman et al., 2013). In response to chronic MPL administration, the Fox-O pathway (**Figure 6A**) yields two formats of biosignal-mediated responses revealing an increased complexity across dosing studies, as well as an internal complexity to the pathway; subgroups of genes within this pathway respond differently to the same chronic dosing regimen. Part of the dominant pathway activity (**Figure 6B**) indicates the development of tolerance to MPL, marked by the observation that the system returns to baseline despite continued administration of MPL. An additional pathway activity exhibits

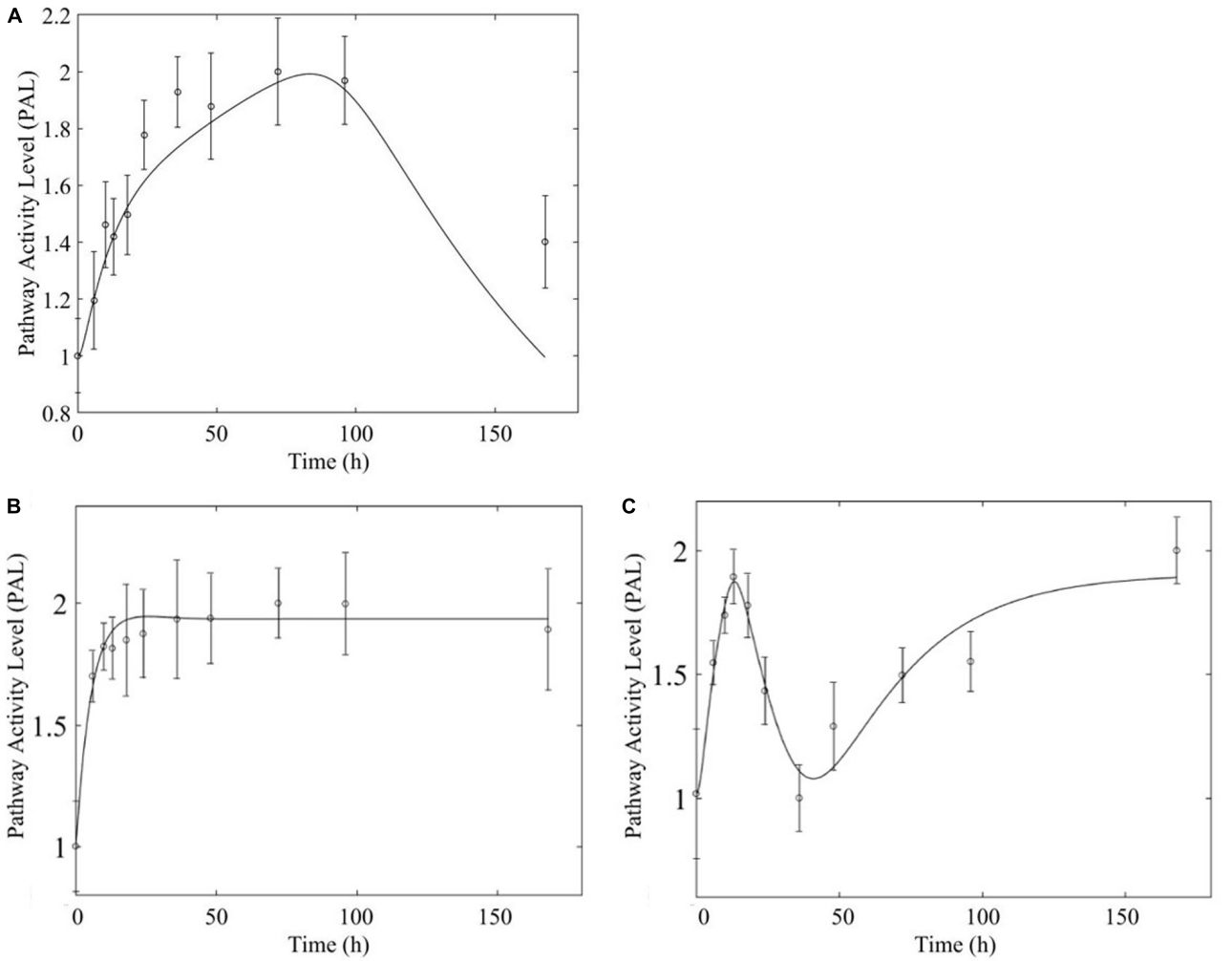

FIGURE 10 | Comparison of response to chronic MPL administration in muscle (**A,** top) and liver (**B,C**, bottom) of fatty acid degradation. The pathway analysis reveals a biosignal-mediated tolerance in muscle.

a biphasic response, eventually settling to a new steady state reflective of persistent MPL effects (**Figure 6C**). A different combination of the biosignal-mediated tolerance response and persistent receptor-mediated pathway activation is exemplified by the PPAR signaling pathway (**Figure 7**). This pathway assists in regulating lipid metabolism in liver and skeletal muscle (Burri et al., 2010; KEGG, 2019b) and is implicated in muscle atrophy in response to corticosteroid dexamethasone treatment via the mechanism of PPAR upregulation of Fox-O transcription factor expression in muscle (Castillero et al., 2013). Like Fox-O, PPAR develops two modes of response to chronic administration.

Liver and Muscle Response to MPL Administration

Acute Dosing

The most striking characteristic of muscle, compared to liver, pathway dynamics in response to acute MPL administration, is that muscle was found to be driven primarily by receptor mediated regulation, as opposed to liver which appears to reflect a balance between receptor and biosignal-mediated regulation (Acevedo et al., 2019). However, when the dynamics are driven by receptor binding, the timescale of the response appears to be comparable between the two tissues (**Figure 8**), likely due to the nature of MPL administration (*intravenous*).

Chronic Dosing

In comparing the response of chronic MPL dosing between liver and muscle, the most striking observation is that the tolerance response observed as a major constituent of muscle tissue was rarely observed in the liver (Acevedo et al., 2019). This suggests that in response to chronic MPL administration, muscle tissue can make functional adjustments to restore pre-administration levels, whereas liver is less likely to adjust and settles to a new set point, in most cases. However, intriguing responses do emerge. **Figure 9** depicts PPAR signaling dynamics, where a combination of receptor and biosignal regulation, and tolerance is observed,

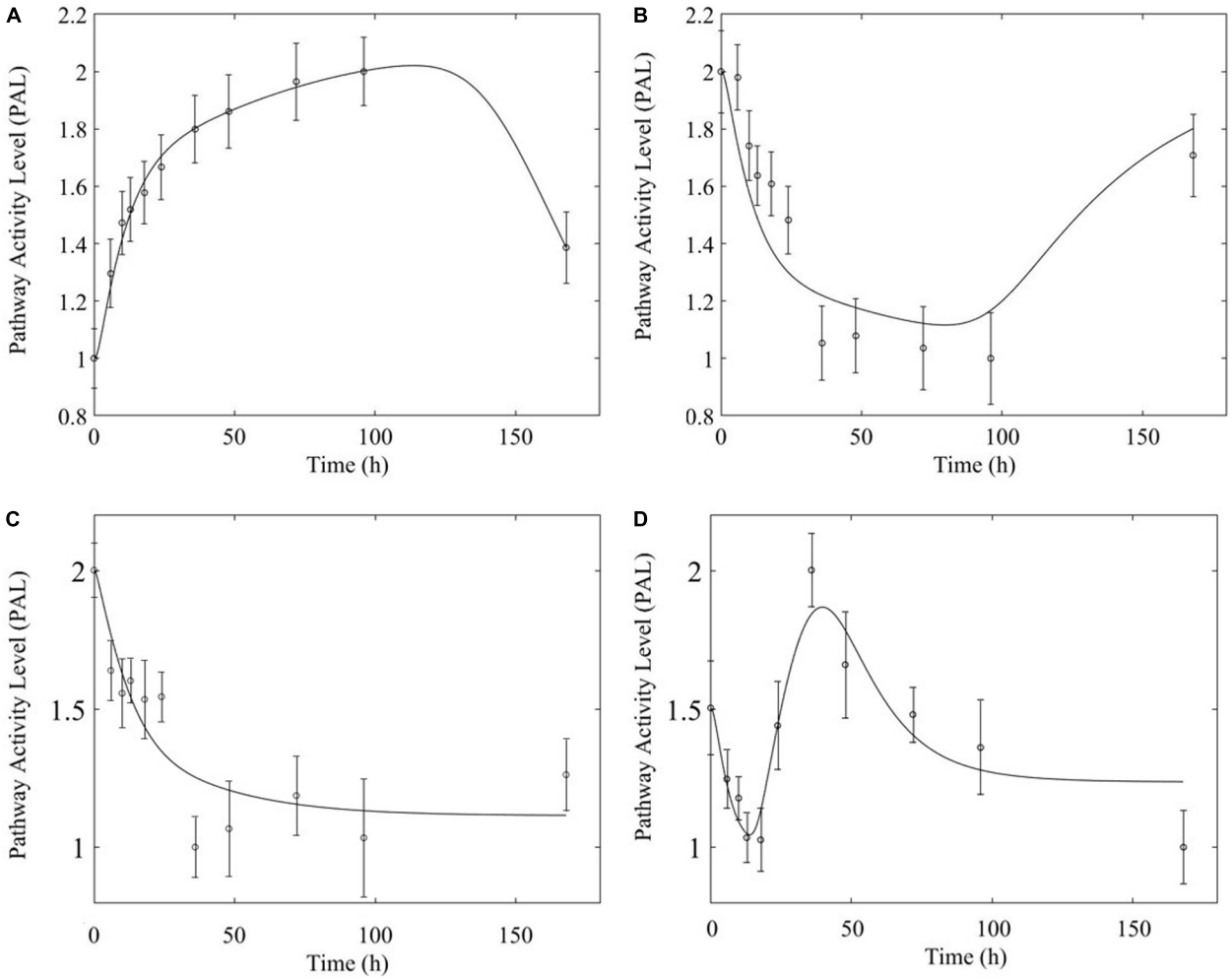

FIGURE 11 | Comparison of response to chronic MPL administration for arginine biosynthesis (left: **A,C**) and valine, leucine, isoleucine degradation (right: **B,D**). The top panels depict response in muscle while the bottom panels depict response in liver.

albeit through different mechanisms. In muscle, this biosignal-mediated response manifests as the tolerance-like behavior, whereas in liver a biphasic response emerges, as denoted by the two characteristic peaks in opposite directions corresponding to an initial receptor-mediated event primarily driven by DRN and subsequent rebound-like, secondary, action due to BS. However, both tissues appear to share a, common, second component of the pathway activity leading to a receptor-mediated displacement to a new steady state as MPL, and by extension *DRN*, equilibrates to its new steady state (**Figure 9**, right panels). Fatty acid degradation, depicted in **Figure 10**, is another characteristic example of tissue-specific regulation. In muscle (**Figure 10**, top) the dynamic response of the pathway under conditions of chronic exposure to MPL indicate a combination of receptor- and biosignal-regulation with a tolerance-like behavior. However, the acute response indicates a strictly receptor-mediated response (bottom left) in conjunction with a biosignal-mediated response (right). Furthermore, liver appears to adapt to a long-term response more gracefully, despite continuous presence of the drug. Particularly interesting are pathways that exhibit a single dominant dynamic in each tissue, which manifests in different ways. Two characteristic examples are the arginine biosynthesis and the valine, leucine, isoleucine degradation pathways (**Figure 11**). Arginine biosynthesis (**Figure 11**, left panels) reveals a biosignal mediated response in muscle (top) given a sharp increase in activity early on followed by a sharp decline at later times, whereas in liver (bottom) points to a receptor-mediated impact of MPL on the activity of the pathway. The valine, leucine, isoleucine degradation pathway (**Figure 11**, right panels), critical for protein metabolism, reported in both tissues (Nair et al., 1992; Holeček, 2002; Campos-Ferraz et al., 2013), points to yet another interesting tissue-specificity: most likely both tissues respond via a combination of receptor- and biosignal-mediated regulation. However, muscle (top) exhibits a more protracted response, whereas liver (right) indicates a much faster, rebound-like, dynamic.

Tissue-specificity is a recognized yet underutilized resource particularly in drug discovery (Yang et al., 2018; Yao et al., 2018;

TABLE 4 | Significant pathways common to acute and chronic MPL administration in muscle.

Pathway	rno ID	Genes in KEGG pathway	Acute				Chronic			
			Unique genes in pathway from dataset	Fractional pathway coverage (fc)	Total fraction of pathway activity (total fp)	Acute MPL response	Unique genes in pathway from dataset	Fractional pathway coverage (fc)	Total fraction of pathway activity (total fp)	Chronic MPL response
Amino acid metabolism										
Arginine and proline metabolism	rno00330	52	9	17%	42%	Receptor-mediated	17	33%	56%	Receptor-mediated/tolerance
Glutathione metabolism	rno00480	69	10	14%	69%	Receptor-mediated	22	32%	72%	Receptor-mediated/tolerance
Cell growth and death										
Apoptosis	rno04210	141	23	16%	61%	Receptor-mediated	38	27%	55%	Receptor-mediated/tolerance
Cellular senescence	rno04218	189	24	13%	57%	Receptor-mediated	44	23%	69%	Receptor-mediated/tolerance
Ferroptosis	rno04216	41	9	22%	49%	Receptor-mediated	15	37%	72%	Tolerance
Cell motility										
Regulation of actin cytoskeleton	rno04810	223	21	9%	47%	Receptor-mediated	48	22%	71%	Receptor-mediated/tolerance
Endocrine system										
Adipocytokine signaling pathway	rno04920	74	14	19%	57%	Receptor-mediated/ biosignal-mediated	20	27%	55%	Tolerance
Glucagon signaling pathway	rno04922	103	11	11%	65%	Receptor-mediated	32	31%	58%	Receptor-mediated/tolerance
GnRH signaling pathway	rno04912	94	12	13%	60%	Receptor-mediated	29	31%	76%	Biosignal-mediated/tolerance
Insulin signaling pathway	rno04910	138	18	13%	50%	Receptor-mediated	43	31%	73%	Receptor-mediated/tolerance
Oxytocin signaling pathway	rno04921	157	21	13%	58%	Receptor-mediated	40	25%	57%	Receptor-mediated/tolerance
PPAR signaling pathway	rno03320	82	15	18%	61%	Receptor-mediated	21	26%	61%	Receptor-mediated/tolerance
Prolactin signaling pathway	rno04917	74	13	18%	61%	Receptor-mediated	18	24%	48%	Biosignal-mediated/tolerance
Thyroid hormone signaling pathway	rno04919	118	21	18%	41%	Receptor-mediated	30	25%	55%	Tolerance
Folding, sorting and degradation										
Proteasome	rno03050	48	14	29%	62%	Biosignal-mediated	30	63%	87%	Tolerance
Lipid metabolism										
Fatty acid degradation	rno00071	47	11	23%	44%	Biosignal-mediated	18	38%	70%	Tolerance
Fatty acid metabolism	rno01212	59	12	20%	59%	Receptor-mediated	19	32%	68%	Tolerance
Signal transduction										
AMPK signaling pathway	rno04152	127	16	13%	50%	Receptor-mediated	36	28%	58%	Tolerance
cGMP-PKG signaling pathway	rno04022	172	19	11%	54%	Receptor-mediated	38	22%	53%	Receptor-mediated/tolerance
ErbB signaling pathway	rno04012	88	11	13%	70%	Receptor-mediated	23	26%	61%	Tolerance
FoxO signaling pathway	rno04068	134	16	12%	61%	Receptor-mediated	43	32%	68%	Biosignal-mediated/tolerance
HIF-1 signaling pathway	rno04066	107	16	15%	55%	Receptor-mediated	35	33%	67%	Receptor-mediated/tolerance
MAPK signaling pathway	rno04010	300	39	13%	59%	Receptor-mediated/ biosignal-mediated	68	23%	81%	Receptor-mediated/tolerance

(Continued)

TABLE 4 | Continued

Pathway	rno ID	Genes in KEGG Pathway	Acute				Chronic			
			Unique Genes in Pathway from Dataset	Fractional pathway coverage (fc)	Total fraction of pathway activity (total fp)	Acute MPL response	Unique genes in pathway from dataset	Fractional pathway coverage (fc)	Total fraction of pathway activity (total fp)	Chronic MPL response
PI3K-Akt signaling pathway	rno04151	349	45	13%	51%	Receptor-mediated	73	21%	56%	Receptor-mediated/tolerance
Rap1 signaling pathway	rno04015	213	28	13%	54%	Receptor-mediated	44	21%	67%	Receptor-mediated/tolerance
TGF-beta signaling pathway	rno04350	93	11	12%	47%	Biosignal-mediated	23	25%	54%	Receptor-mediated/tolerance
VEGF signaling pathway	rno04370	58	14	24%	57%	Receptor-mediated/ biosignal-mediated	20	34%	83%	Receptor-mediated/tolerance
Transport and catabolism										
Autophagy - animal	rno04140	134	16	12%	70%	Receptor-mediated	45	34%	59%	Tolerance
Peroxisome	rno04146	88	11	13%	47%	Receptor-mediated	24	27%	77%	receptor-mediated/tolerance

The pathways exhibit statistically significant fractional coverage (f_c p-value ≤ 0.05) and significant pathway activity (f_p p-value ≤ 0.05) in both the acute and chronic dosing. Detailed descriptions of the dynamics observed in all significant pathways are included in ***Supplementary Table D****.*

Ryaboshapkina and Hammar, 2019). The lack of a detailed understanding of the underlying gene regulation is clearly a major roadblock (Sonawane et al., 2017). The problem is easily stated: even though all tissues carry common genes not all genes perform the same functions or respond the same way. Our earlier studies have explored the co-expression – co-regulation premise to describe regulatory similarities and differences induced by MPL chronic and acute dosing in liver (Nguyen et al., 2010) and muscle (Nguyen et al., 2014). Interestingly, an emerging hypothesis posits that is that tissue-specific regulation is driven by regulatory paths (connections between target genes and transcription factors) rather than activation of tissue-specific transcription factors (Sonawane et al., 2017). Our results extend this concept to also account for dosing, i.e., the dynamics of the external signal presentation in the tissue. Even when considering genes at their functional rather than individual level, it appears as if distinct regulatory modes emerge. The interesting extension is that targeting a single gene may only provide part of the story. If the aim is to either modify or re-establish the functional characteristics of the tissue, the emphasis needs to shift from genes to functional groupings (metabolic and signaling pathways and/or drug modes of action). The proposed work is, we believe, a step in this direction.

DATA AVAILABILITY STATEMENT

The datasets for this study can be found in the GEO data base https://www.ncbi.nlm.nih.gov/geo/ using identifies for the acute (GSE490 and chronic (GSE5101) administration respectively.

AUTHOR CONTRIBUTIONS

AA developed the computational framework, conducted the studies, analyzed the results, co-wrote, and edited the manuscript. DD, RA, and WJ provided the experimental data, contributed to the analysis, and reviewed the manuscript. IA conceived the studies, contributed to the analysis, co-wrote, and edited the manuscript.

FUNDING

This work was supported in part by both the NIH Biotechnology Training Program (Award T32 GM008339), the U.S. Department of Education Graduate Assistance in Areas of National Need (GAANN) (P200A150131), the NIH GM24211 and GM131800.

SUPPLEMENTARY MATERIAL

The Supplementary Material for this article can be found online at: https://www.frontiersin.org/articles/10.3389/fbioe.2020.00759/full#supplementary-material

REFERENCES

Acevedo, A., Berthel, A., DuBois, D., Almon, R. R., Jusko, W. J., and Androulakis, I. P. (2019). Pathway-Based analysis of the liver response to intravenous methylprednisolone administration in rats: acute versus chronic dosing. *Gene Regulat. Syst. Biol.* 13:1177625019840282.

Almon, R. R., DuBois, D. C., Brandenburg, E. H., Shi, W., Zhang, S., Straubinger, R. M., et al. (2002). Pharmacodynamics and pharmacogenomics of diverse receptor-mediated effects of methylprednisolone in rats using microarray analysis. *J. Pharmacokinet. Pharmacodyn.* 29, 103–129.

Almon, R. R., Dubois, D. C., Jin, J. Y., and Jusko, W. J. (2005a). Temporal profiling of the transcriptional basis for the development of corticosteroid-induced insulin resistance in rat muscle. *J. Endocrinol.* 184, 219–232. doi: 10.1677/joe.1.05953

Almon, R. R., Lai, W., DuBois, D. C., and Jusko, W. J. (2005b). Corticosteroid-regulated genes in rat kidney: mining time series array data. *Am. J. Physiol. Endocrinol. Metab.* 289, E870–E882.

Almon, R. R., DuBois, D. C., and Jusko, W. J. (2007a). A microarray analysis of the temporal response of liver to methylprednisolone: a comparative analysis of two dosing regimens. *Endocrinology* 148, 2209–2225. doi: 10.1210/en.2006-2790

Almon, R. R., DuBois, D. C., Yao, Z., Hoffman, E. P., Ghimbovschi, S., and Jusko, W. J. (2007b). Microarray analysis of the temporal response of skeletal muscle to methylprednisolone: comparative analysis of two dosing regimens. *Physiol. Genomics* 30, 282–299. doi: 10.1152/physiolgenomics.00242.2006

Almon, R. R., DuBois, D. C., Piel, W. H., and Jusko, W. J. (2004). The genomic response of skeletal muscle to methylprednisolone using microarrays: tailoring data mining to the structure of the pharmacogenomic time series. *Pharmacogenomics* 5, 525–552. doi: 10.1517/14622416.5.5.525

Almon, R. R., Yang, E., Lai, W., Androulakis, I. P., DuBois, D. C., and Jusko, W. J. (2008a). Circadian variations in rat liver gene expression: relationships to drug actions. *J. Pharmacol. Exp. Ther.* 326, 700–716. doi: 10.1124/jpet.108.140186

Almon, R. R., Yang, E., Lai, W., Androulakis, I. P., Ghimbovschi, S., Hoffman, E. P., et al. (2008b). Relationships between circadian rhythms and modulation of gene expression by glucocorticoids in skeletal muscle. *Am. J. Physiol. Regulat. Integr. Comp. Physiol.* 295, R1031–R1047. doi: 10.1152/ajpregu.90399.2008

Aoki, K. F., and Kanehisa, M. (2005). Using the KEGG database resource. *Curr. Protoc. Bioinformatics* Chapter 1:Unit 1.12. doi: 10.1002/0471250953.bi0112s11

Ayyar, V. S., Sukumaran, S., DuBois, D. C., Almon, R. R., and Jusko, W. J. (2018). Modeling corticosteroid pharmacogenomics and proteomics in rat liver. *J. Pharmacol. Exp. Ther.* 367, 168–183. doi: 10.1124/jpet.118.251959

Ballard, P. L., Baxter, J. D., Higgins, S. J., Rousseau, G. G., and Tomkins, G. M. (1974). General presence of glucocorticoid receptors in mammalian tissues. *Endocrinology* 94, 998–1002. doi: 10.1210/endo-94-4-998

Barnes, P. J. (1998). Anti-inflammatory actions of glucocorticoids: molecular mechanisms. *Clin. Sci.* 94, 557–572. doi: 10.1042/cs0940557

Bodine, S. C., and Furlow, J. D. (2015). "Glucocorticoids and skeletal muscle," in *Glucocorticoid Signaling*, eds J.-C. Wang, and C. Harris (Berlin: Springer), 145–176. doi: 10.1007/978-1-4939-2895-8_7

Boudinot, F. D., D'Ambrosio, R., and Jusko, W. J. (1986). Receptor-mediated pharmacodynamics of prednisolone in the rat. *J. Pharm. Biopharm.* 14, 469–493. doi: 10.1007/bf01059656

Burri, L., Thoresen, G. H., and Berge, R. K. (2010). The role of PPAR activation in liver and muscle. *PPAR Res.* 2010:542359.

Campos-Ferraz, P. L., Bozza, T., Nicastro, H., and Lancha, A. H. Jr. (2013). Distinct effects of leucine or a mixture of the branched-chain amino acids (leucine, isoleucine, and valine) supplementation on resistance to fatigue, and muscle and liver-glycogen degradation, in trained rats. *Nutrition* 29, 1388–1394. doi: 10.1016/j.nut.2013.05.003

Castillero, E., Alamdari, N., Aversa, Z., Gurav, A., and Hasselgren, P.-O. (2013). PPARβ/δ regulates glucocorticoid-and sepsis-induced FOXO1 activation and muscle wasting. *PLoS One* 8:e59726. doi: 10.1371/journal.pone.0059726

Euling, S. Y., White, L., Ovacik, A. M., Makris, S. L., Sen, B., Androulakis, I. P., et al. (2011). An approach to using toxicogenomic data in risk assessment: dibutyl phthalate case study. *Environ. Mol. Mutagen.* 52, S16–S16.

Euling, S. Y., White, L. D., Kim, A. S., Sen, B., Wilson, V. S., Keshava, C., et al. (2013). Use of genomic data in risk assessment case study: II. Evaluation of the dibutyl phthalate toxicogenomic data set. *Toxicol. Appl. Pharmacol.* 271, 349–362. doi: 10.1016/j.taap.2011.06.014

Fabregat, A., Jupe, S., Matthews, L., Sidiropoulos, K., Gillespie, M., Garapati, P., et al. (2018). The reactome pathway knowledgebase. *Nucleic Acids Res.* 46, D649–D655. doi: 10.1093/nar/gkx1132

Fang, J., Sukumaran, S., DuBois, D. C., Almon, R. R., and Jusko, W. J. (2013). Meta-modeling of methylprednisolone effects on glucose regulation in rats. *PLoS One* 8:e81679. doi: 10.1371/journal.pone.0081679

Freishtat, R. J., Nagaraju, K., Jusko, W., and Hoffman, E. P. (2010). Glucocorticoid efficacy in asthma: is improved tissue remodeling upstream of anti-inflammation. *J. Investig. Med.* 58, 19–22. doi: 10.2310/JIM.0b013e3181b91654

Ghosh, D., Barette, T. R., Rhodes, D., and Chinnaiyan, A. M. (2003). Statistical issues and methods for meta-analysis of microarray data: a case study in prostate cancer. *Funct. Integr. Genom.* 3, 180–188. doi: 10.1007/s10142-003-0087-5

Hazra, A., DuBois, D. C., Almon, R. R., Snyder, G. H., and Jusko, W. J. (2008). Pharmacodynamic modeling of acute and chronic effects of methylprednisolone on hepatic urea cycle genes in rats. *Gene Regul. Syst. Biol.* 2, 1–19.

Hazra, A., Pyszczynski, N., DuBois, D. C., Almon, R. R., and Jusko, W. J. (2007). Pharmacokinetics of methylprednisolone after intravenous and intramuscular administration in rats. *Biopharm. Drug Dispos.* 28, 263–273. doi: 10.1002/bdd.551

Holeček, M. (2002). Relation between glutamine, branched-chain amino acids, and protein metabolism. *Nutrition* 18, 130–133. doi: 10.1016/s0899-9007(01)00767-5

Jin, J. Y., Almon, R. R., DuBois, D. C., and Jusko, W. J. (2003). Modeling of corticosteroid pharmacogenomics in rat liver using gene microarrays. *J. Pharmacol. Exp. Ther.* 307, 93–109. doi: 10.1124/jpet.103.053256

Kallio, A., Vuokko, N., Ojala, M., Haiminen, N., and Mannila, H. (2011). Randomization techniques for assessing the significance of gene periodicity results. *BMC Bioinformatics* 12:330. doi: 10.1186/1471-2105-12-330

KEGG (2019a). *FoxO signaling pathway (Pathway: rno04068)". (KEGG Online Database: Kyoto Encyclopedia of Genes and Genomes)*.Kyoto: KEGG.

KEGG (2019b). *PPAR signaling pathway (Pathway: rno03320)". (KEGG Online Database: Kyoto Encyclopedia of Genes and Genomes)*. Kyoto: KEGG.

Liu, J., Peng, Y., Wang, X., Fan, Y., Qin, C., Shi, L., et al. (2015). Mitochondrial dysfunction launches dexamethasone-induced skeletal muscle atrophy via AMPK/FOXO3 signaling. *Mol. Pharm.* 13, 73–84. doi: 10.1021/acs.molpharmaceut.5b00516

Liu, Y.-Z., Wang, Y.-X., and Jiang, C.-L. (2017). Inflammation: the common pathway of stress-related diseases. *Front. Hum. Neurosci.* 11:316. doi: 10.3389/fnhum.2017.00316

MATLAB (2018). *MATLAB and Statistics Toolbox Release 2014a*. Natick, Massachusetts: The MathWorks, Inc.

Morand, E., and Leech, M. (1999). Glucocorticoid regulation of inflammation: the plot thickens. *Inflamm. Res.* 48, 557–560. doi: 10.1007/s000110050503

Nair, K. S., Schwartz, R., and Welle, S. (1992). Leucine as a regulator of whole body and skeletal muscle protein metabolism in humans. *Am. J. Physiol. Endocrinol. Metab.* 263, E928–E934.

Nguyen, T. T., Almon, R. R., DuBois, D. C., Jusko, W. J., and Androulakis, I. P. (2010). Comparative analysis of acute and chronic corticosteroid pharmacogenomic effects in rat liver: transcriptional dynamics and regulatory structures. *BMC Bioinformatics* 11:515. doi: 10.1186/1471-2105-11-515

Nguyen, T. T., Almon, R. R., Dubois, D. C., Sukumaran, S., Jusko, W. J., and Androulakis, I. P. (2014). Tissue-specific gene expression and regulation in liver and muscle following chronic corticosteroid administration. *Gene Regul. Syst. Biol.* 8, 75–87. doi: 10.4137/GRSB.S13134

Ovacik, M. A., Sukumaran, S., Almon, R. R., DuBois, D. C., Jusko, W. J., and Androulakis, I. P. (2010). Circadian signatures in rat liver: from gene expression to pathways. *BMC Bioinformatics* 11:540. doi: 10.1186/1471-2105-11-540

Ramakrishnan, R., DuBois, D. C., Almon, R. R., Pyszczynski, N. A., and Jusko, W. J. (2002a). Fifth-generation model for corticosteroid pharmacodynamics: application to steady-state receptor down-regulation and enzyme induction patterns during seven-day continuous infusion of methylprednisolone in rats. *J. Pharmacokinet. Pharmacodyn.* 29, 1–24.

Ramakrishnan, R., DuBois, D. C., Almon, R. R., Pyszczynski, N. A., and Jusko, W. J. (2002b). Pharmacodynamics and pharmacogenomics of methylprednisolone during 7-day infusions in rats. *J. Pharmacol. Exp. Ther.* 300, 245–256. doi: 10.1124/jpet.300.1.245

Ramasamy, A., Mondry, A., Holmes, C. C., and Altman, D. G. (2008). Key issues in conducting a meta-analysis of gene expression microarray datasets. *PLoS Med.* 5:e184. doi: 10.1371/journal.pmed.0050184

Ryaboshapkina, M., and Hammar, M. (2019). Tissue-specific genes as an underutilized resource in drug discovery. *Sci. Rep.* 9:7233. doi: 10.1038/s41598-019-43829-43829

Schaaf, M. J., and Cidlowski, J. A. (2002). Molecular mechanisms of glucocorticoid action and resistance. *J. Steroid Biochem. Mol. Biol.* 83, 37–48. doi: 10.1016/s0960-0760(02)00263-7

Schakman, O., Kalista, S., Barbé, C., Loumaye, A., and Thissen, J.-P. (2013). Glucocorticoid-induced skeletal muscle atrophy. *Int. J. Biochem. Cell Biol.* 45, 2163–2172. doi: 10.1016/j.biocel.2013.05.036

Sharma, A., Ebling, W. F., and Jusko, W. J. (1998). Precursor-dependent indirect pharmacodynamic response model for tolerance and rebound phenomena. *J. Pharm. Sci.* 87, 1577–1584. doi: 10.1021/js980171q

Sharma, A., and Jusko, W. J. (1998). Characteristics of indirect pharmacodynamic models and applications to clinical drug responses. *Br. J. Clin. Pharmacol.* 45, 229–239. doi: 10.1046/j.1365-2125.1998.00676.x

Sonawane, A. R., Platig, J., Fagny, M., Chen, C. Y., Paulson, J. N., Lopes-Ramos, C. M., et al. (2017). Understanding tissue-specific gene regulation. *Cell Rep.* 21, 1077–1088. doi: 10.1016/j.celrep.2017.10.001

Storey, J., Leek, J., and Bass, A. (2018). *edge: Extraction of Differential Gene Expression". R package*.

Sun, Y. N., DuBois, D. C., Almon, R. R., and Jusko, W. J. (1998). Fourth-generation model for corticosteroid pharmacodynamics: a model for methylprednisolone effects on receptor/gene-mediated glucocorticoid receptor down-regulation and tyrosine aminotransferase induction in rat liver. *J. Pharmacokinet. Biopharm.* 26, 289–317.

Sun, Y. N., McKay, L. I., DuBois, D. C., Jusko, W. J., and Almon, R. R. (1999). Pharmacokinetic/Pharmacodynamic models for corticosteroid receptor down-regulation and glutamine synthetase induction in rat skeletal muscle by a Receptor/Gene-mediated mechanism. *J. Pharmacol. Exp. Ther.* 288, 720–728.

Swartz, S. L., and Dluhy, R. G. (1978). Corticosteroids: clinical pharmacology and therapeutic use. *Drugs* 16, 238–255. doi: 10.2165/00003495-197816030-00006

Tseng, G. C., Ghosh, D., and Feingold, E. (2012). Comprehensive literature review and statistical considerations for microarray meta-analysis. *Nucleic Acids Res.* 40, 3785–3799. doi: 10.1093/nar/gkr1265

Waddell, D. S., Baehr, L. M., Van Den Brandt, J., Johnsen, S. A., Reichardt, H. M., Furlow, J. D., et al. (2008). The glucocorticoid receptor and FOXO1 synergistically activate the skeletal muscle atrophy-associated MuRF1 gene. *Am. J. Physiol. Endocrinol. Metab.* 295, E785–E797.

Yang, E., Almon, R. R., Dubois, D. C., Jusko, W. J., and Androulakis, I. P. (2008). Extracting global system dynamics of corticosteroid genomic effects in rat liver. *J. Pharmacol. Exp. Ther.* 324, 1243–1254. doi: 10.1124/jpet.107.133074

Yang, E. H., Almon, R. R., DuBois, D. C., Jusko, W. J., and Androulakis, I. P. (2009). Identification of global transcriptional dynamics. *PLoS One* 4:e5992. doi: 10.1371/journal.pone.0005992

Yang, R. Y., Quan, J., Sodaei, R., Aguet, F., Segrè, A. V., Allen, J. A., et al. (2018). A systematic survey of human tissue-specific gene expression and splicing reveals new opportunities for therapeutic target identification and evaluation. *bioRxiv [Preprint]* doi: 10.1101/311563

Yao, F., Madani Tonekaboni, S. A., Safikhani, Z., Smirnov, P., El-Hachem, N., Freeman, M., et al. (2018). Tissue specificity of in vitro drug sensitivity. *J. Am. Med. Inform. Assoc.* 25, 158–166. doi: 10.1093/jamia/ocx062

Yao, Z., Hoffman, E. P., Ghimbovschi, S., Dubois, D. C., Almon, R. R., and Jusko, W. J. (2008). Mathematical modeling of corticosteroid pharmacogenomics in rat muscle following acute and chronic methylprednisolone dosing. *Mol. Pharm.* 5, 328–339. doi: 10.1021/mp700094s

Zhao, W., Qin, W., Pan, J., Wu, Y., Bauman, W. A., and Cardozo, C. (2009). Dependence of dexamethasone-induced Akt/FOXO1 signaling, upregulation of MAFbx, and protein catabolism upon the glucocorticoid receptor. *Biochem. Biophys. Res. Commun.* 378, 668–672. doi: 10.1016/j.bbrc.2008.11.123

Conflict of Interest: The authors declare that the research was conducted in the absence of any commercial or financial relationships that could be construed as a potential conflict of interest.

Copyright © 2020 Acevedo, DuBois, Almon, Jusko and Androulakis. This is an open-access article distributed under the terms of the Creative Commons Attribution License (CC BY). The use, distribution or reproduction in other forums is permitted, provided the original author(s) and the copyright owner(s) are credited and that the original publication in this journal is cited, in accordance with accepted academic practice. No use, distribution or reproduction is permitted which does not comply with these terms.

frontiers in Bioengineering and Biotechnology

ORIGINAL RESEARCH
published: 22 July 2020
doi: 10.3389/fbioe.2020.00762

Computational Modeling of Fructose Metabolism and Development in NAFLD

Yunjie Liao[1,2], *Nathan A. Davies*[2] *and I. David L. Bogle*[1]*

[1] Department of Chemical Engineering, Center for Process Systems Engineering, University College London, London, United Kingdom, [2] Division of Medicine, Institute for Liver and Digestive Health, University College London, London, United Kingdom

Non-alcohol fatty liver disease (NAFLD) is a common disorder that has increased in prevalence 20-fold over the last three decades. It covers a spectrum of conditions resulting from excess lipid accumulation in the liver without alcohol abuse. Among all the risk factors, over-consumption of fructose has been repeatedly reported in both clinical and experimental studies to be highly associated with the development of NAFLD. However, studying *in vivo* systems is complicated, time consuming and expensive. A detailed kinetic model of fructose metabolism was constructed to investigate the metabolic mechanisms whereby fructose consumption can induce dyslipidaemia associated with NAFLD and to explore whether the pathological conditions can be reversed during the early stages of disease. The model contains biochemical components and reactions identified from the literature, including ∼120 parameters, 25 variables, and 25 first order differential equations. Three scenarios were presented to demonstrate the behavior of the model. Scenario one predicts the acute effects of a change in carbohydrate input in lipid profiles. The results present progressive triglyceride accumulations in the liver and plasma for three diets. The rate of accumulation was greater in the fructose diet than that of the mixed or glucose only models. Scenario two explores the variability of metabolic reaction rate within the general population. Sensitivity analysis reveals that hepatic triglyceride concentration is most sensitive to the rate constant of pyruvate kinase and fructokinase. Scenario three tests the effect of one specific inhibitor that might be potentially administered. The simulations of fructokinase suppression provide a good model for potentially reversing simple steatosis induced by high fructose consumption, which can be corroborated by experimental studies. The predictions in these three scenarios suggest that the model is robust and it has sufficient detail to present the kinetic relationship between fructose and lipid in the liver.

Keywords: fructose metabolism, NAFLD, computational modeling, triglyceride, systems biology

OPEN ACCESS

Edited by:
Dapeng Wang,
University of Leeds, United Kingdom

Reviewed by:
Andrew Dellinger,
Elon University, United States
Pavel Loskot,
Swansea University, United Kingdom

***Correspondence:**
I. David L. Bogle
d.bogle@ucl.ac.uk

Specialty section:
This article was submitted to Computational Genomics, a section of the journal Frontiers in Bioengineering and Biotechnology

Received: *24 February 2020*
Accepted: *16 June 2020*
Published: *22 July 2020*

Citation:
Liao Y, Davies NA and Bogle IDL (2020) Computational Modeling of Fructose Metabolism and Development in NAFLD. Front. Bioeng. Biotechnol. 8:762. doi: 10.3389/fbioe.2020.00762

INTRODUCTION

Non-alcoholic fatty liver disease (NAFLD) is the most common chronic liver dysfunction worldwide (Miele et al., 2009). It covers a spectrum of conditions resulting from excess lipid accumulation in the liver without excessive alcohol consumption. The pathologic manifestations of NAFLD develop from simple steatosis (intrahepatic lipid deposition) to non-alcoholic

steatohepatitis (NASH), an advanced stage that combines steatosis with inflammation. NASH can then further progress to fibrosis (excess fibrous connective tissues) and cirrhosis (a late stage of scarring), and potentially to hepatocellular carcinoma (Ouyang et al., 2008; Cohen et al., 2011). Among these conditions, steatosis and NASH are reversible, while fibrosis and cirrhosis are often considered irreversible (Maldonado et al., 2018). Over the last three decades NAFLD has increased in its prevalence 20-fold, mainly linked with obesity, diabetes, and many other metabolic disorders. Currently it is globally affecting 20–30% of the general population (Nomura and Yamanouchi, 2012; Younossi et al., 2016). It has been estimated that between 2016 and 2030, NAFLD levels would continue to grow at a steady rate of up to ∼30% (Estes et al., 2018). However, the molecular mechanisms causing NAFLD are multifactorial and remain poorly understood, which results in the absence of effective therapeutic interventions.

Although overnutrition and a sedentary lifestyle have often been blamed as the cause of NAFLD, recent clinical and experimental studies repeatedly suggest that the climbing consumption of fructose may also be an important factor (Jensen et al., 2018). Fructose, along with glucose and galactose, is one of three primary dietary monosaccharides. Between 1900 and 1950, ∼20 g fructose (5% of total energy) was consumed in the daily meals, mainly from fruits and honey (Douard and Ferraris, 2008). Nowadays, fructose has become a ubiquitous ingredient that accounts for a large proportion of energy intake (approaching 15–25% of total energy) (Softic et al., 2016; Jensen et al., 2018). A 30% increase in total fructose consumption has been observed in recent decades (Ventura et al., 2011). The average fructose intake for the whole population in America has been reported as 49 g/day in 2004 (Douard and Ferraris, 2013) and 54.7 g/day in 2008 (Vos and Lavine, 2013). For the age groups 15–18 and 19–22, a reported total of 75 g fructose is consumed per day (Douard and Ferraris, 2013). Refined and processed fructose is responsible for this dramatic rise. Sucrose and high fructose corn syrup (HFCS) have become the main sources of fructose consumption, with a fructose/glucose ratio of 50/50 and 55/45, respectively (Ventura et al., 2011; Jensen et al., 2018). HFCS, a key component of sugar sweetened beverages, has been considered as an inexpensive substitute for other simple sugars in the food industry, accounting for 40% of all added sugars (Bray et al., 2004). Recently, this sweetener has been targeted by public health campaigns (e.g., sugar reduction programme in UK) and with a sugar tax levy in several countries (Jones, 2016; Briggs et al., 2017; Hashem et al., 2019).

Despite the fact that historically fructose was proposed as a beneficial sweetener and recommended for the obese and for patients with diabetes, high-fructose intake has been reported to be associated with a series of health issues such as metabolic syndrome, obesity, type 2 diabetes, and NAFLD (Basaranoglu et al., 2013). It is proposed that fructose is strongly associated with these chronic health issues due to its unique and distinct metabolic pathways which exclusively take place within the liver. It is known that, in contrast to glucose, fructose initiates its metabolism via the enzyme fructokinase after uptake by liver cells (hepatocytes), bypassing the crucial rate-limiting step of glycolysis and delivering abundant high energy substrates for subsequent metabolism (Ouyang et al., 2008). Growing evidence suggests that a high-fructose diet contributes to the enhancement of *de novo* lipogenesis, decreasing β-oxidation as well as increasing plasma levels of both triglyceride and very-low-density lipoprotein (VLDL) (Koo et al., 2008; Lim et al., 2010). Consequently, these metabolic effects would lead to hepatic lipid accumulation, insulin resistance and an increased inflammatory response which in turn contributes to NAFLD (Duarte et al., 2019). However, it is still controversial as to whether and how dietary fructose makes a unique contribution to the development of NAFLD in humans. The primary purpose of this paper is to investigate the effect of dietary fructose on hepatic energy metabolism and the consequences of its over-consumption in the development of NAFLD using models of known metabolic functions.

Studying *in vivo* systems is complicated, time consuming and expensive. A computational model based upon a systems biology approach is an attractive option to acquire a more comprehensive insight into the potential pathophysiological mechanisms involved.

With the benefit of extensive studies in modeling human metabolism over the last 20 years and with a systems biology approach called human genome-scale metabolic networks (GEMNs), reconstructions have been introduced. Three well-known reconstructed human metabolic networks have been established to incorporate complex metabolic pathways and biochemical reactions in humans (Duarte et al., 2007; Ma et al., 2007; Gille et al., 2010). Among these, the model "HepatoNet1" developed by Gille et al. (2010) mainly examines liver function at a system scale. It contains 777 components and over 2,500 reactions in order to explore ammonia detoxification rates and the synthesis of bile acids under starvation conditions. However, the major limitation of these stoichiometry-based reconstructed models is that their static predictions failed to represent the dynamic flows of metabolic reactions.

Applying a kinetic model to study liver energy metabolism has been investigated since the 1970s. The first model of metabolic regulation was introduced by Garfinkel (1971), which listed 34 dynamic chemical expressions to conduct the TCA cycle simulation. In recent decades a majority of hepatic models are focusing on the regulation of glucose homeostasis. Relevant *in silico* simulations have been reported, including glucose absorption and transportation, hormonal regulation, zonation effects, and the relationship between glucose intake and high-intensity exercise, lipid metabolism in addition to metabolic diseases (Chalhoub et al., 2007a,b; Hetherington et al., 2012; König et al., 2012; Sumner et al., 2012; Ashworth et al., 2016; Naftalin, 2016; Noorman et al., 2019). Irrespective of the fact that abundant studies have highlighted the important role fructose metabolism plays in metabolic diseases, only a few models have placed emphasis on the fructose metabolism and none of these have reflected the potentially dynamic changes (Allen and Musante, 2017, 2018; Maldonado et al., 2018).

Therefore, here we present a detailed kinetic model of fructose metabolism to investigate the metabolic mechanism whereby fructose consumption can induce changes to lipid metabolism

associated with NAFLD, and to explore whether the pathological conditions can be reversed during the early stages of disease.

METHODS

Model Description

A kinetic model of the fructose metabolism was developed based on modified Michaelis-Menten and Hill equations. This model comprises ∼120 parameters, 25 variables, and 25 first order differential equations. As shown in **Figure 1**, variables and equations were divided into three sections representing hepatocytes (SH), hepatic bloodstream (SHB), and bloodstream of the rest of the body (SBC). The model parameters were determined and refined by comparison with values reported in the literature (see **Table S1**). Hepatic fatty acids (FA) and hepatic triglycerides (TG) are selected to be the major outputs in this model as they are the most important indices reflecting lipid accumulation in the liver. Plasma free fatty acids (FFA) and plasma triglycerides are also predicted as they are the most directly measurable matching indices recorded in clinical and experimental data. The equations are reported in this section.

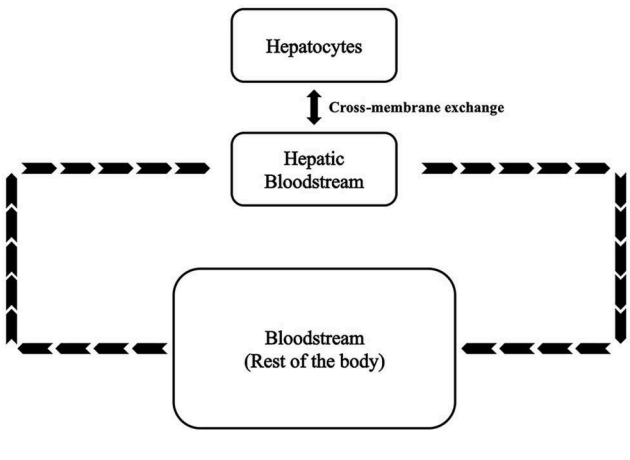

FIGURE 1 | Basic framework of the fructose metabolism modeling.

Hepatocytes–Fructose Metabolism

Since the metabolic activities of fructose mainly take place in the liver parenchyma, hepatocyte metabolism is the primary focus in this paper. As mentioned above, the most common assumption is to link fructose with NAFLD due to its unique metabolic processes. As fructokinase (also known as ketohexokinase, KHK), aldolase B, and triokinase are three specialized enzymes for fructose metabolism, the chemical reactions related to these three enzymes were first included to initiate the model construction. Substantial evidence leads to the proposition that high fructose consumption is attributable to enhancing *de novo* lipogenesis, suppressing β-oxidation and facilitating triglyceride synthesis (Koo et al., 2008; Lim et al., 2010; Tappy and Lê, 2010;

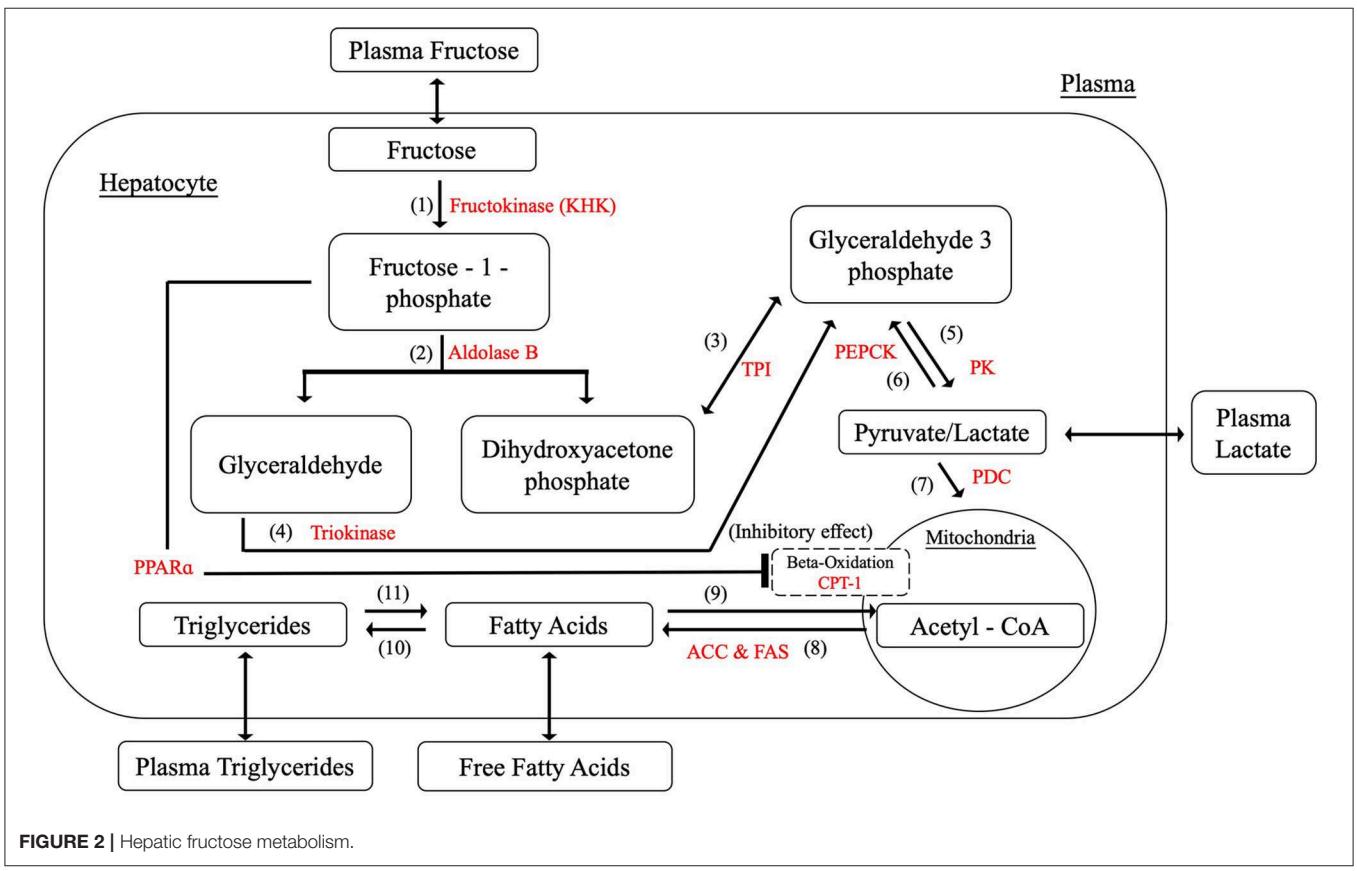

FIGURE 2 | Hepatic fructose metabolism.

Nomura and Yamanouchi, 2012). The model therefore was developed to incorporate these pathways. However, not every single component in the liver metabolism has been included. Pyruvate, acetyl-CoA, fatty acids and triglycerides were selected as they are identified as the most common intermediates and ultimate metabolites within the carbohydrate metabolic process associated with lipid deposition (Mayes, 1993; Sun and Empie, 2012; Laughlin, 2014). Also, they are considered to be the key components and they are assessable in clinical experiments, which allows the related parameters be tuned and validated during model development. Indeed, the reactions between these key metabolites in the human body are more complicated than that which is presented in the model. However, rate-determining enzymes among the biochemical processes were selected to simplify the reactions yet provide adequate details to represent realistic reaction rates.

As a result, **Figure 2** summarizes the biochemical components and reactions identified in the literature that are constructed within the model, including fructolysis, *de novo* lipogenesis (DNL), beta-oxidation, and triglyceride synthesis. **Table 1** presents the rate equations for the hepatic variables used in this section.

TABLE 1 | The rate equations for the hepatic variables in section Hepatocytes (SH).

Hepatic variables	Abbreviation	Rate equations
Fructose	Fru	$\frac{dFru}{dt} = T_{Fru} - \mathbb{R}_{KHK}$
Fructose-1-Phosphate	F1P	$\frac{dF1P}{dt} = \mathbb{R}_{KHK} - \mathbb{R}_{aldB}$
Dihydroxyacetone phosphate	DHAP	$\frac{dDHAP}{dt} = \mathbb{R}_{aldB} - \mathbb{R}_{TPI_{DHAP}} + \mathbb{R}_{TPI_{GA3P}}$
Glyceraldehyde	GA	$\frac{dGA}{dt} = \mathbb{R}_{aldB} - \mathbb{R}_{Tri}$
Glyceradehyde-3-phosphate	GA3P	$\frac{dGA3P}{dt} = \mathbb{R}_{TPI_{DHAP}} - \mathbb{R}_{TPI_{GA3P}} + \mathbb{R}_{Tri} - \mathbb{R}_{PK} + \mathbb{R}_{PEPCK}$
Pyruvate/lactate	Pyr	$\frac{dPyr}{dt} = T_{Lac} + \mathbb{R}_{PK} - \mathbb{R}_{PDC} - \mathbb{R}_{PEPCK}$
Acetyl-CoA	ACoA	$\frac{dACoA}{dt} = \mathbb{R}_{PDC} - 8\,\mathbb{R}_{FAS} + 8\,\mathbb{R}_{boxi}$
Fatty acids (palmitate)	FA	$\frac{dFA}{dt} = T_{FFA} + \mathbb{R}_{FAS} - \mathbb{R}_{boxi} - 3\,\mathbb{R}_{TGS} + 3\,\mathbb{R}_{Lply}$
Triglycerides	TG	$\frac{dTG}{dt} = T_{TG} + \mathbb{R}_{TGS} - \mathbb{R}_{Lply}$

The Distinctive Fructose Metabolic Pathways

The most significant distinction between glucose metabolism and fructose metabolism is their phosphorylation processes. After entering the hepatocyte, dietary fructose is swiftly phosphorylated by KHK to produce fructose-1-phosphate which bypasses the key rate-controlling regulatory enzyme (phosphofructokinase) of glycolysis in the glucose metabolism. Fructose-1-phosphate is then converted to dihydroxyacetone-phosphate (DHAP) and glyceraldehyde (GA) by aldolase B, providing intermediates for further glycolysis processes. Triokinase, the third essential enzyme, functions by phosphorylating GA to form glyceraldehyde-3-phosphate (GA3P), which also produces intermediates for subsequent reactions. The pathways of glucose and fructose metabolism then merge at the triose phosphate stage (as GA3P) and become the same from this point on (Havel, 2005; Rutledge and Adeli, 2007; Ouyang et al., 2008; Laughlin, 2014). Key enzymes and detailed reactions were demonstrated as follows. The corresponding metabolic functions are listed in **Table 2**.

(1) Hepatic fructokinase (KHK)

$$Fructose + ATP \xrightarrow{KHK} Fructose - 1 - phosphate + ADP$$

Hepatic fructokinase (KHK, EC 2.7.1.3), one of the three characteristic enzymes in human fructose metabolism, converts fructose into fructose-1-phosphate (F1P) by transferring one phosphate group from adenosine triphosphate (ATP). In contrast to glucose phosphorylation, there is no feedback inhibition for fructose which indicates that the activity of KHK is essentially free of regulatory control. Consequently, when sufficient fructose is available a significant amount of F1P enters subsequent metabolic reactions. Also, since the Michaelis constant (Km) of KHK is lower than glucokinase, it has been shown that KHK is effectively 10-times faster than glucokinase in substrate phosphorylation (Patel et al., 2015). In terms of energy transport, even though guanosine triphosphate (GTP) can also be utilized in a similar way to ATP for this initial phosphorylation reaction, it is only responsible for a minor proportion of the total process and the effect of GTP can be ignored in this equation.

(2) Aldolase B

$$Fructose - 1 - phosphate \xrightarrow{AldolaseB} Dihydroxyacetone\ phosphate + Glyceraldehyde$$

After phosphorylation, fructose-1-phosphate (F1P) undergoes further breakdown into two three-carbon components, namely dihydroxyacetone phosphate (DHAP) and glyceraldehyde (GA) by aldolase B. Aldolase B (E.C.4.1.2.13) is a liver-specific aldolase which can be considered the rate-limiting enzyme of hepatic fructose metabolism. Since little is known about the mechanism of aldolase B regulation, no strong allosteric control has yet been identified for this enzyme.

(3) Triose Phosphate Isomerase (TPI)

$$Dihydroxyacetone\ phosphate \xleftrightarrow{TPI} GA3P$$

DHAP is isomerised to glyceradehyde-3-phosphate (GA3P) by triose phosphate isomerase (TPI) (E.C.5.3.1.1) rapidly and reversibly.

(4) Triokinase

$$Glyceraldehyde + ATP \xrightarrow{Triokinase} GA3P + ADP$$

The primary pathway for the GA metabolism is through GA3P catalyzed by triokinase (E.C.2.7.1.28). This reaction requires one phosphate molecule from ATP, releasing adenosine diphosphate (ADP). The activity of triokinase is allosterically activated by ATP-Mg^{-2} and inhibited by both ATP and ADP, suggesting

TABLE 2 | The processes of metabolic reactions and rate functions in the fructose model.

	Key enzymes/reactions	Abbreviation	Rate functions
(1)	Fructokinase	KHK	$\mathbb{R}_{KHK} = V_{KHK} * \frac{Fru^{nFru}}{Km_{KHK}{}^{nFru} + Fru^{nFru}} * \frac{ATP^{nATP}}{Km_{ATP}{}^{nATP} + ATP^{nATP}}$
(2)	Aldolase B	aldB	$\mathbb{R}_{aldB} = V_{aldB} * \frac{F1P^{niF1P}}{Km_{F1P}{}^{niF1P} + F1P^{niF1P}}$
(3)	Triose phosphate isomerase	TPI	$\mathbb{R}_{TPI_DHAP} = V_{TPI_DHAP} * \frac{DHAP^{nDHAP}}{Km_{DHAP}{}^{nDHAP} + DHAP^{nDHAP}}$ $\mathbb{R}_{TPI_GA3P} = V_{TPI_GA3P} * \frac{GA3P^{nGA3P}}{Km_{TPIGA3P}{}^{nGA3P} + GA3P^{nGA3P}}$
(4)	Triokinase	Tri	$\mathbb{R}_{Tri} =$ $V_{Tri} * \frac{GA^{nGA}}{Km_{GA}{}^{nGA} + GA^{nGA}} * \frac{ATP_{Mg^{2-}}{}^{nATP_{Mg^{2-}}}}{Km_{ATP_{Mg^{2-}}}{}^{nATP_{Mg^{2-}}} + ATP_{Mg^{2-}}{}^{nATP_{Mg^{2-}}}} * \left(1 - \beta_{ATP} \frac{ATP}{K_i^{ATP} + ATP}\right) \left(1 - \beta_{ADP} \frac{ADP}{K_i^{ADP} + ADP}\right)$
(5)	Pyruvate kinase	PK	$\mathbb{R}_{PK} = V_{PK} * \frac{GA3P^{nGA3P}}{Km_{GA3P}{}^{nGA3P} + GA3P^{nGA3P}} * \frac{ADP^{nADPpk}}{Km_{ADPpk}{}^{nADPpk} + ADP^{nADPpk}} * \left(1 - \beta_{ACoA-PK} \frac{ACoA}{K_i^{ACoA-PK} + ACoA}\right)$
(6)	Phosphoenolpyruvate carboxykinase	PEPCK	$\mathbb{R}_{PEPCK} = V_{PEPCK} * \frac{Pyr}{K_m^{PEPCK} + Pyr} * \frac{ATP}{K_m^{ATPpepck} + ATP} * \frac{GTP}{K_m^{GTP} + GTP}$
(7)	Pyruvate oxidation	PDC	$\mathbb{R}_{PDC} = V_{PDC} * \frac{Pyr}{K_m^{Pyr} + Pyr} * \left(1 - \beta_{ACoA-PDC} \frac{ACoA}{ACoA + k_i^{CoA-pyr}}\right)$
(8)	Fatty acid synthesis	FAS	$\mathbb{R}_{FAS} = V_{FAS} * \frac{ACoA}{K_m^{ACoA} + ACoA} * \frac{ATP}{K_m^{ATPfas} + ATP} * \left(1 - \beta_{FA} \frac{FA}{FA + k_i^{FA-inhib}}\right)$
(9)	Beta-oxidation	boxi	$\mathbb{R}_{boxi} = V_{boxi} * \frac{FA}{K_m^{boxi} + FA} * \frac{ATP}{K_m^{ATPboxi} + ATP} * \left(1 - \beta_{boxi} \frac{ACoA}{ACoA + k_i^{CoA-boxi}}\right) * \left(1 - \beta_{PPARa} \frac{F1P}{F1P + k_i^{F1P-inhib}}\right)$
(10)	Triglyceride synthesis	TGS	$\mathbb{R}_{TGS} = V_{TGS} * \frac{FA}{K_m^{FA} + FA} * \frac{GA3P}{K_m^{TGSGA3P} + GA3P}$
(11)	Lipolysis	Lply	$\mathbb{R}_{Lply} = V_{Lply} * \frac{TG}{K_m^{TG} + TG}$

that this hepatic triokinase is regulated by the phosphorylation potential in the cytoplasm. Under normal conditions triokinase is fully activated.

(5) Pyruvate Kinase (PK)

$$GA3P + 2ADP + 2Pi \xrightarrow{PK} Pyruvate/Lactate + 2ATP$$

As pyruvate can be converted to lactate swiftly and reversibly, only one variable is used to denote this in the model. The pathways for glucose and fructose metabolism merge at the triose phosphate stage and become the same from this point onwards. GA3P is broken down to pyruvate relying on a series of enzyme reactions. The rate limiting enzyme in this process is pyruvate kinase (PK; E.C.2.7.1.40). Here we simplify the whole six-step conversion of GA3P to pyruvate by using PK. The phosphate in the GA3P and an additional free inorganic phosphate are combined with ADP molecules to produce two ATP molecules in this process. It should be noted that there are two GA3P molecules generated from one fructose molecule in the previous metabolic step, four ATP and two pyruvate molecules are therefore produced in the current reaction. Pyruvate kinase is allosterically controlled by acetyl-CoA.

(6) Phosphoenolpyruvate carboxykinase (PEPCK)

$$Pyruvate/Lactate + 2ATP + GTP \xrightarrow{PEPCK} GA3P + 2ADP + GDP + 2Pi$$

Phosphoenolpyruvate carboxykinase (PEPCK) (E.C.4.1.1.32) is rate limiting in the conversion from pyruvate to GA3P, consuming two ATPs and one guanosine triphosphate (GTP). There is no identified allosteric regulation for PEPCK while numerous metabolites, such as insulin and fatty acids, are able to stimulate its production. Over-expression of PEPCK is believed to be associated with high production of glucose and the development of type 2 diabetes (Beale et al., 2007).

(7) Pyruvate Dehydrogenase Complex (PDC)

$$Pyruvate/Lactate + NAD^{+} \xrightarrow{PDC} Acetyl - CoA + NADH$$

Pyruvate oxidation is regulated by the pyruvate dehydrogenase complex (PDC). This complex contains three enzymes that catalyze the conversion of pyruvate to acetyl-CoA. PDC is allosterically inhibited in a feedback mechanism by acetyl-CoA to prevent its over-production, which could result in mitochondrial stress.

(8) Fatty acid synthesis

$$8\,Acetyl - CoA + 7\,ATP \xrightarrow{ACC\&FAS} Fatty\ acid\ \left(Palmitate\right) + 7\,ADP + 7Pi$$

Lipogenesis describes the process of fatty acid synthesis and triglyceride synthesis. With the mediation of acetyl-CoA carboxylase (ACC) (E.C.6.4.1.2) and fatty acid synthase (FAS) (E.C.2.3.1.85), acetyl-CoA is converted into malonyl-CoA. Malonyl-CoA provides the two-carbon structure for producing both short and long chain fatty acids. There are two isoforms of ACC found in the hepatic metabolism as ACC1 contributes to lipogenesis and ACC2 to beta-oxidation. Palmitate (16:0), as the most common saturated fatty acid, has been chosen to represent fatty acids in this model for the purpose of simplification. Thus, eight acetyl-CoA molecules are consumed to synthesize one palmitate molecule. High concentrations of fatty acids are able to suppress this process allosterically.

(9) Beta-oxidation

$$Fatty\ acid\ \left(Palmitate\right) + 2ATP \xrightarrow{CPT-1(PPAR\alpha)} 8Acetyl-CoA + AMP + ADP + 3Pi$$

Hepatic carnitine palmitoyltransferase I (CPT-1) (E.C.2.3.1.21) is the rate-controlling enzyme of beta-oxidation. The metabolic process breaks down fatty acids to generate acetyl-CoA (Lim et al., 2010). Since malonyl-CoA is the main inhibitor for CPT-1, it supresses beta-oxidation allosterically. To simplify the equation, the inhibitory effect of malonyl-CoA is substituted by acetyl-CoA as the pathway of acetyl-CoA to produce malonyl-CoA is unidirectional. By contrast, it has been discovered recently that peroxisome proliferator-activated receptors (PPARs) promote beta-oxidation by upregulating the expression of CPT1 (Kersten, 2014). However, this regulation can be prevented by the production of fructose-1-phosphate (Nomura and Yamanouchi, 2012). Therefore, fructose-1-phosphate is also considered to be an allosteric inhibitor in the process of beta-oxidation.

(10) Triglyceride Synthesis

$$3\ Fatty\ acids\ \left(Palmitate\right) + 3\ ATP \xrightarrow{Glycerol-3-phosphate} Triglyceride + 3AMP + 7Pi$$

During triglyceride synthesis, three fatty acid molecules and one glycerol backbone from glycerol-3-phosphate are combined to produce triglyceride under the influence of coenzyme A (CoA) and several acyltransferases. Glycerol-3-phosphate is denoted as GA3P due to the rapid exchange rate between these two molecules. Triglyceride synthesis is regulated by insulin and glucagon.

(11) Lipolysis

$$Triglyceride \xrightarrow{Triacylglycerollipase} Glyceraldehyde + 3Fatty\ acids\ \left(Palmitate\right)$$

Three fatty acids are released when one triglyceride breaks down. The rate-determining enzyme during this process is triacylglycerol lipase (E.C.3.1.1.3). The concentration of hepatic triglyceride is regulated by insulin and glucagon under normal circumstances.

Hepatic Bloodstream: Cross-Membrane Exchange

The hepatic blood flow is maintained by hepatic arteries, portal veins, central veins, and bile ducts which allow hepatocytes to be exposed to nutrients, hormones (insulin and glucagon), and oxygen (Hijmans et al., 2014). As applied in König et al. (2012) and Ashworth et al. (2016), an altered Michaelis–Menten equation is employed for cross-membrane exchange. For unidirectional transportation, the model considers the components in the Hepatic Bloodstream as substrates and the corresponding molecules in the hepatocytes as products. For bidirectional exchange the equation for transport (T) is:

$$T_{SHB\rightarrow SH} = \frac{V_{max}(S_{SHB} - S_{SH})}{K_m + S_{SHB} + S_{SH}}$$

where the (section) Hepatic Bloodstream is denoted as SHB and (section) Hepatocytes denoted as SH.

The transportation and exchange rates of fructose, pyruvate/lactate, fatty acids, and triglyceride between SHB and SH are summarized in **Table 3**. The constant $R_{HE} = 4$ is used to represent the ratio of the total number of hepatocytes to the volume of the hepatic bloodstream as described in Ashworth et al. (2016). The rate equations in SHB are listed in **Table 5** combined with the rate equations for the section Bloodstream Circulation: Rest of the Body.

Fructose is absorbed from the gut lumen and transported across the brush border membrane into the hepatic portal vein via an energy-dependent process involving glucose transporter 5 (GLUT5) and glucose transporter 2 (GLUT2), in which GLUT 5 has a high specificity to fructose (Douard and Ferraris, 2008). After fructose uptake from the gut, plasma fructose is observed experimentally to rise only by micromolar levels, implying that hepatocytes have the capacity to uptake the majority of fructose during the first-pass through the liver (Tappy and Lê, 2010). Therefore, both GLUT2 and GLUT5 are included in the model where the Michaelis–Menten constant of GLUT2 has a lower value than that of GLUT5 as reported previously (Wright et al., 2012). In addition, GLUT 8 has also been mentioned in terms of hepatic fructose transportation (Manolescu et al., 2007; DeBosch et al., 2014). However, as the expression of GLUT8 is relatively low in mice in comparison to GLUT5 and GLUT2 even with high-fructose exposure, and the fact that the exact mechanism of this transporter in humans remains largely unknown, the effect of GLUT8 is considered negligible in the current model (Ferraris et al., 2018).

Bloodstream Circulation-Rest of the Body

Since circulation of the bloodstream around the body takes ∼1 min to complete, the rate of blood flow circulation is set to be $R_{BS} = 1/60 \approx 0.167\ s^{-1}$. Also, as the blood volume of the whole body and the liver are considered to be ∼5 and 0.8 L, respectively, in an average person, the ratio of the rest of body to the liver R_{RL} is set as:

$$R_{RL} = \frac{5 - 0.8}{0.8} \approx 5.25$$

(Arias et al., 1994; Davy and Seals, 1994; Critchley and Critchley, 1999; Eipel et al., 2010; Ashworth et al., 2016).

The equation representing the blood circulation (C) from (section) Hepatic Bloodstream (SHB) to (section) Bloodstream Circulation (SBC) is in the following form:

$$C_{SBC\rightarrow SHB} = \frac{R_{BS} * (C_{SBC} - C_{SHB})}{R_{RL}}$$

TABLE 3 | The transport and exchange rates between Section Hepatic Bloodstream (SHB) and Section Hepatocytes (SH).

Transport variables	Rate functions for cross-membrane transportation
Fructose	$T_{Fru} = V_{GLUT2}^{pump} * \frac{Fru_{SHB}}{K_m^{GLUT2-pump} + Fru_{SHB}} + V_{GLUT2}^{ex} * \frac{Fru_{SHB} - Fru_{SH}}{K_m^{GLUT2-ex} + Fru_{SHB} + Fru_{SH}} + V_{GLUT5}^{pump} * \frac{Fru_{SHB}}{K_m^{GLUT5-pump} + Fru_{SHB}} + V_{GLUT5}^{ex} * \frac{Fru_{SHB} - Fru_{SH}}{K_m^{GLUT5-ex} + Fru_{SHB} + Fru_{SH}}$
Pyruvate/lactate [simplified from Ashworth et al. (2016)]	$T_{Pyr} = V_{Pyr}^{ex} * \frac{Pyr_{SHB} - Pyr_{SH}}{K_m^{Pyr-ex} + Pyr_{SHB} + Pyr_{SH}}$
Fatty acids (palmitate) [simplified from Ashworth et al. (2016)]	$T_{FA} = V_{FA}^{ex} * \frac{FA_{SHB} - FA_{SH}}{K_m^{FA-ex} + FA_{SHB} + FFA_{SH}} + V_{active} * \frac{FA_{SHB}}{(K_m^{active} + FA_{SHB})} \left(1 + \frac{Ins}{Ins_{ref}^{active}}\right)$
Triglyceride [simplified from Ashworth et al. (2016)]	$T_{TG} = V_{TG}^{ex} * \frac{\left(TG_{SHB} - \frac{TG_{SH}}{TG_{ref}}\right)}{K_m^{TG-ex} + TG_{SHB} + \frac{TG_{SH}}{TG_{ref}}} - V_{out} * \frac{TG_{SH}}{(K_m^{out} + TG_{SH})}$

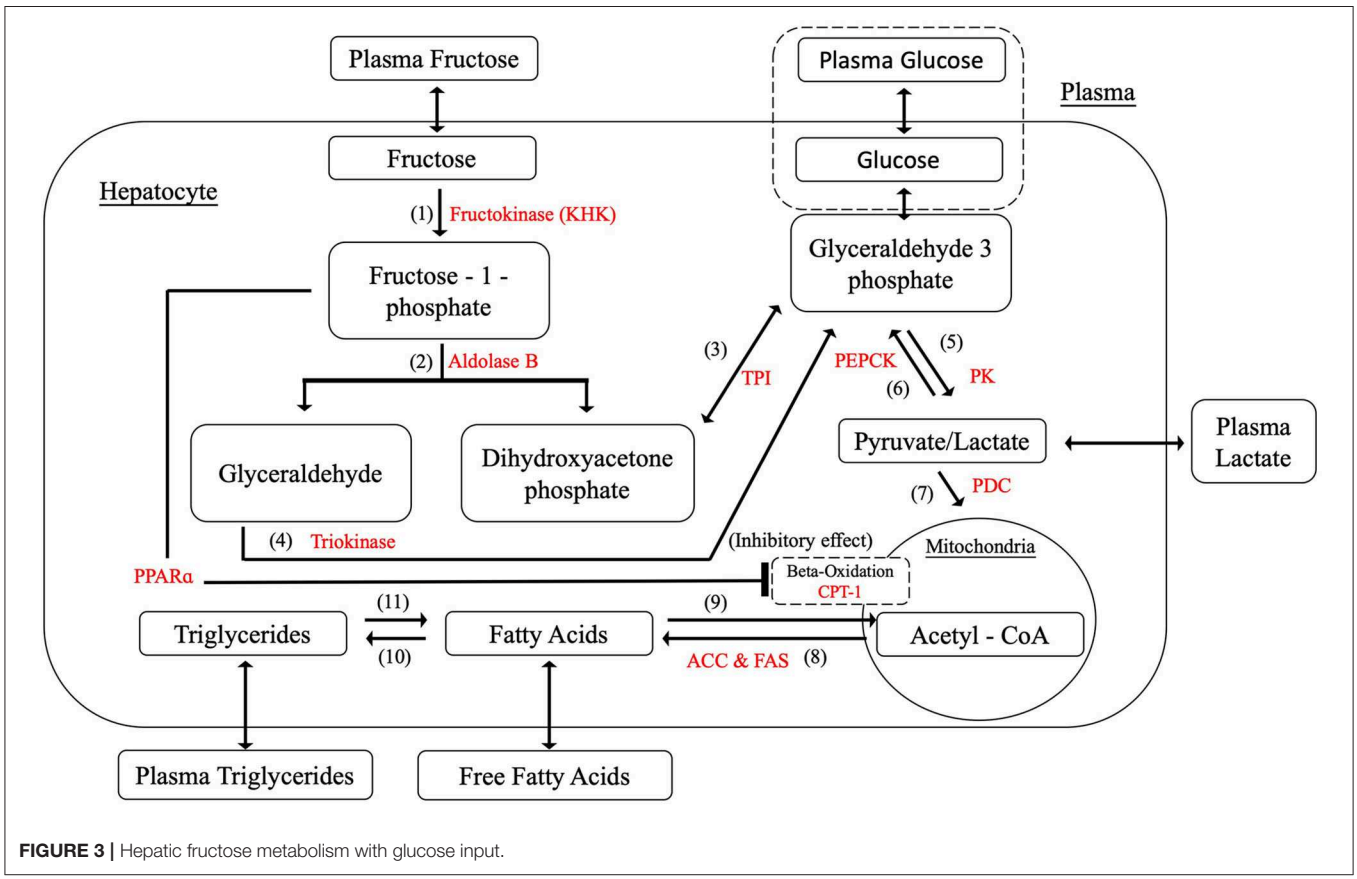

FIGURE 3 | Hepatic fructose metabolism with glucose input.

Dietary Inputs

After feeding, carbohydrates are processed in the digestive system and enter the hepatic portal system. According to the Dietary Guideline for Americans (2015–2020) (Health and Services, 2015), daily caloric intake of a healthy adult is in the range of 1,600–3,000 kcal, of which, 45–65% are derived from carbohydrates. Therefore, in this model, we set up the baseline to reflect a midpoint caloric consumption of 2,400 kcal per day and 50% of this energy source to be obtained from carbohydrates. A total amount of 300 g/day carbohydrates (4 kcal/g) was set to be taken up into the body from the diet. The remaining calorie intake would be comprised of proteins and fats. However, as the model has been set to examine the effects of carbohydrates in the liver, protein and fat inputs are not considered in this study.

After a mixed meal, dietary disaccharides and polysaccharides such as sucrose, HFCS and starches would be broken down into the various proportions of monosaccharides; hence, fructose and glucose as the principle simple sugars in the diet have been selected as the dietary inputs for the model. **Figure 3** shows that glucose was added to the model as an alternative dietary input to fructose and relevant equations are simplified from model constructed by Ashworth et al. (2016), as presented in **Table 4**.

Periodic simulation of the carbohydrate intake (shown below) is based on spiked inputs adapted from Ashworth et al. (2016), which provides three meals a day with 4-h breaks.

$$Dietary\ Input = v_{input} * \sin^6\left(\frac{pi}{4(hours)}\right)$$

Additional Settings

The settings for hormone regulation including insulin and glucagon secretion into the bloodstream (SBC) are based on the model constructed by Hetherington et al. (2012), while

TABLE 4 | The relevant equations of glucose feeding [simplified from Ashworth et al. (2016)].

Hepatic variables	Rate equations
Glucose (Glu)	$\frac{dGlu}{dt} = T_{Glu} - \mathbb{R}_{GK} + \mathbb{R}_{G6Pase}$
Glucose-6-phosphate (G6P)	$\frac{dG6P}{dt} = \mathbb{R}_{GK} - \mathbb{R}_{G6Pase} + \mathbb{R}_{FBP} - \mathbb{R}_{PFK}$
Key enzymes/reactions	
$\mathbf{T_{Glu}}$ – Glucose transportation	$T_{Glu} = V_{GLUTG}^{pump} * \frac{Glu_{SHB}}{K_m^{GLUTG-pump} + Glu_{SHB}} + V_{GLUTG}^{ex} * \frac{Glu_{SHB} - Glu_{SH}}{K_m^{GLUTG-ex} + Glu_{SHB} + Glu_{SH}}$
Glucokinase (GK)	$\mathbb{R}_{GK} = V_{GK} * \frac{Glu^{nGlu}}{Km_{Glu}^{nGlu} + Glu^{nGlu}} * \frac{ATP^{nATP}}{Km_{ATPgk}^{nATP} + ATP^{nATP}} * (1 - \frac{G6P}{G6P + k_i^{G6P}})$
Glucose-6-phosphatase (G6Pase)	$\mathbb{R}_{G6Pase} = V_{G6Pase} * \frac{G6P}{K_m^{G6Pase} + G6P}$
Fructose-bisphosphatase (FBP)	$\mathbb{R}_{FBP} = V_{FBP} * \frac{GA3P}{K_m^{FBP} + GA3P}$
Phosphofructokinase (PFK)	$\mathbb{R}_{PFK} = V_{PFK} * \frac{G6P}{K_m^{PFK} + G6P} * \frac{ATP}{Km_{ATPpfk} + ATP} * \left(1 - \frac{ATP}{ATP + k_i^{ATPfpk}} * \frac{ADP}{ADP + k_i^{ADPfpk}}\right) * (1 - \beta_{PFK} \frac{GA3P}{GA3P + k_i^{GA3Ppfk}})$

TABLE 5 | The rate equations in both Section Hepatic Bloodstream (SHB) and Section Bloodstream Circulation (SBC).

Exchanging variables	Rate equations in Section Hepatic Bloodstream (SHB)
Fructose	$\frac{dFru_{SHB}}{dt} = -T_{Fru} * R_{HE} + R_{BS} * (Fru_{SBC} - Fru_{SHB})$
Glucose [simplified from Ashworth et al. (2016)]	$\frac{dGlu_{SHB}}{dt} = -T_{Glu} * R_{HE} + R_{BS} * (Glu_{SBC} - Glu_{SHB})$
Pyruvate/lactate [simplified from Ashworth et al. (2016)]	$\frac{dPyr_{SHB}}{dt} = -T_{Pyr} * R_{HE} + R_{BS} * (Pyr_{SBC} - Pyr_{SHB})$
Fatty acids (palmitate) [simplified from Ashworth et al. (2016)]	$\frac{dFA_{SHB}}{dt} = -T_{FA} * R_{HE} + R_{BS} * (FA_{SBC} - FA_{SHB})$
Triglyceride [simplified from Ashworth et al. (2016)]	$\frac{dTG_{SHB}}{dt} = -T_{TG} * R_{HE} + R_{BS} * (TG_{SBC} - TG_{SHB})$
Exchanging variables	**Rate equations in Section Bloodstream Circulation (SBC)**
Fructose	$\frac{dFru_{SBC}}{dt} = Meal_{Fru} + C_{Fru}$
Glucose [simplified from Ashworth et al. (2016)]	$\frac{dGlu_{SBC}}{dt} = Meal_{Glu} + C_{Glu} - USE_{Glu} - UP_{FA} - UP_{TG}$
Pyruvate/lactate (simplified from Ashworth et al. (2016)]	$\frac{dPyr_{SBC}}{dt} = C_{Pyr}$
Fatty acids (palmitate) [simplified from Ashworth et al. (2016)]	$\frac{dFA_{SBC}}{dt} = C_{FA} - USE_{FA} + UP_{FA}$
Triglyceride [simplified from Ashworth et al. (2016)]	$\frac{dTG_{SBC}}{dt} = C_{TG} - USE_{TG} + UP_{TG}$

the hormonal equations in the liver blood flow (SHB) are simplified from the model built by Ashworth et al. (2016). In addition to the liver, the amount of each key variable (fructose, glucose, pyruvate/lactate, fatty acid, and triglyceride) generated ($USE_{variable}$) and used ($UP_{variable}$) by other body sections such as adipose tissues and muscle tissues are set to be the same as the equations described by Ashworth et al. (2016).

Overall, the final rate equations in both SHB and SBC are described in **Table 5**.

Model Simulations

Simulations were generated using MATLAB_R2019a (MATLAB, RRID:SCR_001622). Function "ode45" was used to solve all the ordinary differential equations in parallel. The units of metabolite concentration and reaction rate are presented in micromoles/liter (μM/L) and micromoles/second (μM/s), respectively. The time lengths of the simulations have been set to run over a 12-h period incorporating three meals. The Matlab code is provided in **Table S2**.

RESULTS AND DISCUSSION

To demonstrate the behavior of model, three scenario simulations were conducted. The first predicts lipid concentrations resulting from different dietary consumptions, the second explores the variability of biochemical reaction kinetics rate within the general population, and the third tests the effect of one specific inhibitor of lipid metabolism contributing to NAFLD that might be potentially administered.

Scenario One: The Effect of Changing Carbohydrate Intake on Lipid Accumulation

As described in section "Dietary Inputs," a dietary setup was created in which 100 g of carbohydrates were consumed by healthy subjects for each meal (3/day). Here we tested the effect of three different diets on lipid deposition, including: a 100% fructose meal, a mixed meal (50:50 fructose and glucose), and a 100% glucose meal, representing two extreme conditions and one more realistic setting. The results of these simulations are presented in **Figure 4**. The levels of hepatic fatty acids (FA), triglycerides (TG), plasma free fatty acids (FFA), triglycerides, as well as blood glucose were predicted after three meals at 8:00, 12:00, and 16:00, respectively. The model takes approximately an hour for the initial transient phrase before establishing a set of consistent predictions.

As shown in **Figure 4A**, hepatic fatty acids started decreasing after the first meal and reached a peak at around 13:00 in the fructose feeding group and ∼13:30 in both glucose and the mixed diet subjects. These decreasing patterns is because three fatty acids are required to generate one triglyceride molecule after meals during the triglyceride synthetic process. After the second meal, the subsequent peak time of fatty acid levels stimulated by all three diets was observed between 17:00 and 18:00, and again the fructose group took slightly less time to achieve the peak value. Even though the consumption of 50% glucose and 50% fructose resulted in the highest level of hepatic fatty acids for the first peak, a significantly higher concentration was induced by the fructose diet after the second

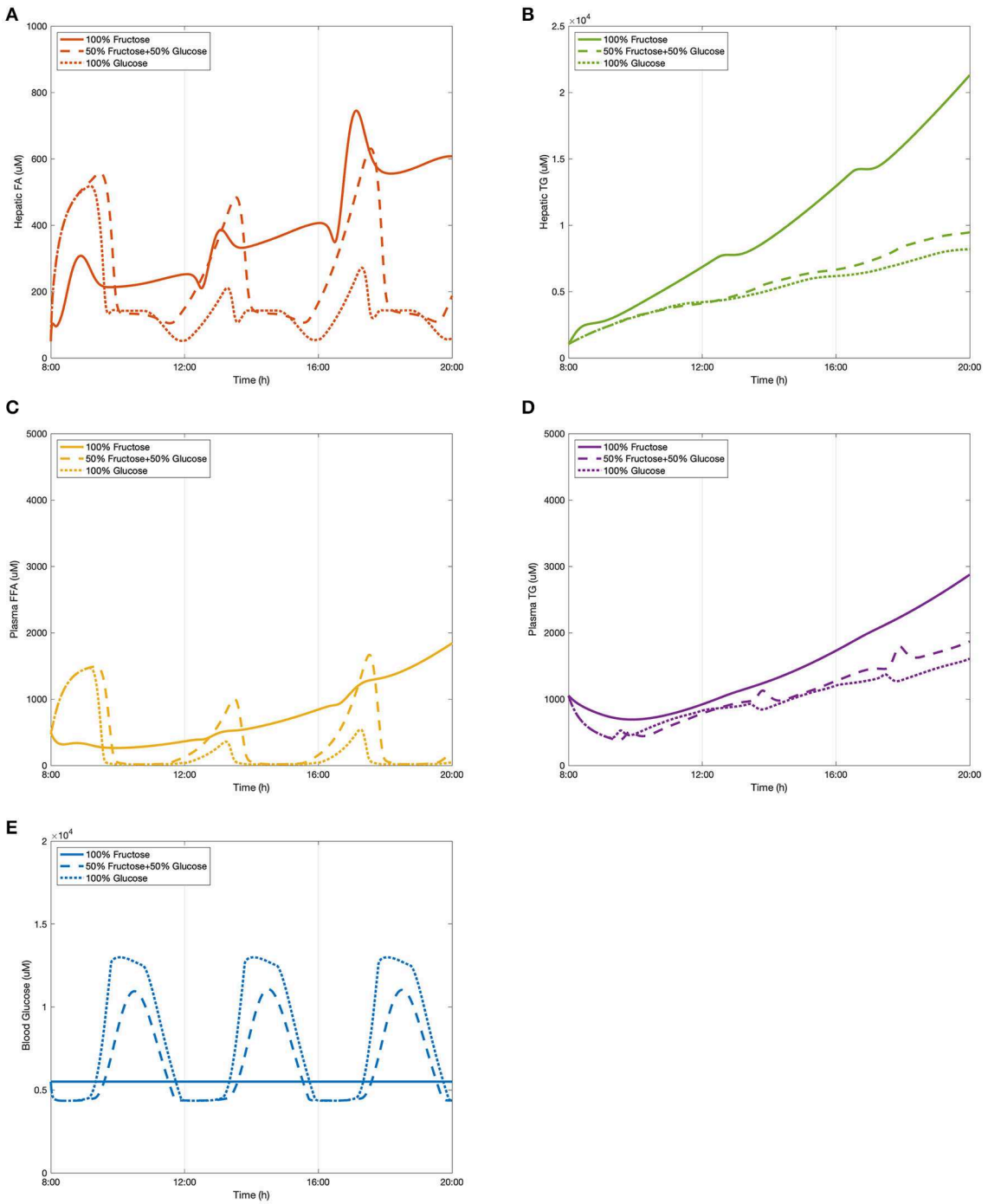

FIGURE 4 | The change of lipid accumulation after different dietary intakes. **(A)** Hepatic FA, **(B)** hepatic TG, **(C)** plasma FFA, **(D)** plasma TG, and **(E)** blood glucose.

meal. The glucose feeding group were found to have the lowest levels of fatty acids over the observation period. The concentration of hepatic FA in the mix-meal feeding group displayed stronger periodic behavior than in the other two extreme conditions. In terms of hepatic triglyceride (**Figure 4B**), the curves of the glucose group and the mix-carbohydrate group overlapped for several hours after breakfast. From around 13:00, the mix group started accumulating larger amounts of hepatic triglycerides than that of the glucose group. After consumption of the fructose-only diet, triglyceride concentration showed relatively dramatic increasing growth leading to the highest levels observed.

In addition to hepatic lipid concentrations, **Figures 4C,D** show the plasma levels of free fatty acids and triglycerides respectively. Similar to the periodic patterns of hepatic fatty acids, free fatty acids in the plasma declined over several hours before developing the first peak. For both mix-sugar feeding and glucose only groups, the levels of free fatty acids then returned to baseline after about 30 min. The second peaks of these two groups generated slightly higher values than the first peaks before again reducing to baseline. Regarding the 100% fructose model, this showed a smaller fluctuation than the other two diets and presented a flattened profile, and was not seen to drop back to the baseline level. Consistent with hepatic FA observations, plasma FFA peaked earlier in the fructose group than the others. Considering plasma triglyceride levels (**Figure 4D**), the fructose diet produced the highest concentrations throughout the model simulation. After the first meal, the glucose group contributed to greater triglyceride production than that induced by the mix group. However, this phenomenon shifted over during the 12:00–13:00 period where the mixed sugar group outgrew the glucose meal and continued increasing plasma triglyceride levels.

Blood glucose levels were also simulated after consuming different proportions of monosaccharides. A baseline normal blood glucose level was established within the model and the effects of the meals examined in addition to this. As presented in **Figure 4E**, the predicted peak values for each diet model throughout the period were equal in magnitude since the three meals were divided and induced equally. After pure fructose meals, blood glucose stayed relatively constant along the time period, while for the pure glucose group and the mix-sugar group, both of them caused dynamic periodic oscillations. It is apparent that blood glucose responded more strongly to the pure glucose diet than the mixed diet. As the models were considering healthy individuals, the effects of insulin in mediating cellular glucose uptake from the blood became more apparent once levels exceeded upper normal values (>1.2 mM), which can be observed as a blunting of the peak glucose levels in the figure.

Overall, it can be observed that it took ∼5 h on average to digest dietary meals containing 100 g carbohydrates to subsequently achieve peak values in lipid profiles. Compared to fatty acids, triglycerides in the liver and plasma progressively accumulated. The rate of accumulation was greater in the fructose diet than that of the mixed or glucose only models. For both fatty acids and triglyceride concentrations, glucose meals were observed to result in the lowest levels over the study period. Additionally, for the 50/50 glucose/fructose model, the fatty acid curves fluctuated more dramatically in comparison to the other dietary inputs.

Clinical data from Abraha et al. (1998), Chong et al. (2007), and Stanhope et al. (2008) were used to compare the model predictions. The research carried out by Chong et al. (2007) recruited 14 healthy individuals to have one test meal either containing 0.75 g/kg body weight fructose or glucose. Plasma composition was recorded over 6 h to investigate the acute effect of high-carbohydrate diets. In the study by Stanhope et al. (2008), a larger sample size and a larger time scale were applied with more abundant dietary carbohydrate forms. A total of 34 subjects were provided with three meals with sucrose or HFCS drinks. For this study eight men also participated in a sub-study that included pure glucose and pure fructose consumption. Blood samples of all participants were collected over 24-h. In contrast to these two studies, Abraha et al. (1998) also included diabetic patients as subjects of an investigation to explore the effect of fructose on post-prandial lipid profiles. Six healthy individuals and six diabetic individuals were provided a test meal with a fructose-enriched drink or starch-enriched bread. Plasma metabolites for both groups were recorded for 6 h. These data were chosen as they covered varying dietary carbohydrate compositions in both healthy and diabetic subjects, which were considerably suitable for testing the compatibility of the constructed model. It should be noted that since diabetic and NAFLD patients are considered to have similar insulin responses when inducing high-carbohydrate meals, the clinical values measured in these diabetic subjects were regarded as reference indices. Also, as hepatic lipid levels are difficult to measure in clinical studies, only plasma lipid profiles were employed to make comparisons with the data from the selected studies.

Our model concurred with the findings from these three studies in the following ways. Model predictions and literature data took roughly the same time to process fructose metabolism. Specifically, the plasma FFA concentrations in the simulated data dropped for roughly 90 min before they rose to reach a peak after ∼5 h. Also, consistent with results from these experimentally measured data, in healthy subjects the incremental plasma triglyceride concentration was higher after pure fructose meals than the other meal plans. The simulated results show that consumption of pure glucose can be attributed to the lowest triglyceride levels for the various diets, which is in keeping with the findings in Stanhope et al. (2008). Additionally, even though it is relatively difficult for computational models to make predictions matching the exact values of clinical measured data, the plasma triglyceride concentrations the model simulated here fitted within the range of 1,000–2,000 μmol for both glucose and mix-sugar feeding groups in the healthy subjects. Despite that pure fructose exposure produced values as high as 3,000 μmol plasma TG in the model predictions, this level was still lower than the plasma TG measured in the diabetic individuals after a fructose test meal (around 3,800 μmol). This result suggests that the model predictions are indicative of the normal range of plasma TG levels in a healthy population, even when considering two extreme conditions. Blood glucose predictions were also in agreement with the literature findings above. Furthermore, there are some discrepancies between the experimental figures and simulated numbers. We note that the peaks of plasma FFA induced by consumption of the mixed diet were higher than that of pure fructose diet. However, this inconsistency may be caused by the mechanism whereby fructose is able to enhance hepatic glucose uptake, hence indicating a synergistic effect of fructose and glucose in fatty acid synthesis.

TABLE 6 | Results for sensitivity analysis of rate constants in Section Hepatocytes (SH).

	Key enzymes/ reactions	Abbreviation	Δ Hepatic fatty acids (μM)		Δ Hepatic triglyceride (μM)		Δ Plasma fatty acids (μM)		Δ Plasma triglyceride (μM)	
			+10%	−10%	+10%	−10%	+10%	−10%	+10%	−10%
(1)	Fructokinase	KHK	3.44	–5.07	281.15	–325.16	22.24	–25.85	42.43	–49.38
(2)	Aldolase B	aldB	–18.87	17.80	152.01	–211.55	–6.23	1.98	13.24	–22.06
(3)	Triose phosphate isomerase	TPI	0.00	0.00	0.78	–0.94	0.00	–0.01	0.18	–0.19
(4)	Triokinase	Tri	0.00	0.00	0.03	–0.05	0.00	0.00	0.01	–0.01
(5)	Pyruvate kinase	PK	25.27	–25.88	320.09	–357.91	38.59	–37.67	74.51	–83.11
(6)	Phosphoenolpyruvate carboxykinase	PEPCK	–16.05	18.33	–222.74	241.06	–22.97	27.00	–52.58	57.29
(7)	Pyruvate oxidation	PDC	15.61	–16.73	217.04	–244.18	22.66	–23.67	52.77	–58.74
(8)	Fatty acid synthesis	FAS	12.14	–13.14	168.42	–190.44	19.23	–20.28	38.78	–43.83
(9)	Beta-oxidation	boxi	–0.45	0.47	–19.09	20.71	–0.64	0.68	–4.41	4.77
(10)	Triglyceride synthesis	TGS	–7.18	7.36	96.77	–112.67	1.07	–1.90	–25.38	26.82
(11)	Lipolysis	Lply	0.37	–0.36	–0.88	0.87	0.13	–0.12	0.71	–0.71

Scenario Two: The Effect of Varying Reaction Rate Constants on the Hepatic Metabolic Process

Rate constants indicate the maximum capacity of the enzymes in metabolic reactions, which are affected by numerous factors, e.g., age, diet, life style, and genetic predisposition. To explore the variability of these rate constants in the hepatic metabolic processes, an OAT (one at a time) sensitivity analysis was conducted by changing 11 key rate constants in the fructose pathway within the hepatocytes (SH). Since the normal range for healthy liver function can vary substantially between individuals, possibly by as much as 25% according to dye clearance measures designed to assess detoxification function (Vos et al., 2014), a mid-point 10% variation was applied to each rate constant to reflect the expected metabolic differences among healthy subjects. It is reasonable to choose this value as it is large enough to produce obvious changes on lipid levels that allow us to recognize the relative importance of metabolic reactions, but small enough to maintain within a healthy range. A 50/50 fructose/glucose diet was set as the standard input and the simulations were run for 12 h for acute effect consideration. Both hepatic and plasma concentrations of fatty acids and triglycerides were recorded as the end points for the analysis. The results are displayed in **Table 6**.

Hepatic TG levels were most sensitive to the reaction rate associated with pyruvate kinase, the rate-limiting enzyme that converts triose phosphate product GA3P to pyruvate for both fructose and glucose. Increasing the enzymatic activity of pyruvate kinase by 10% resulted in 320.09 μmol accumulation of hepatic TG and 74.51 μmol of plasma TG's while decreasing this rate by 10% caused a decline of 357.91 and 83.11 μmol in hepatic and plasma TG's, respectively. Secondly, an increase of 281.15 μmol in hepatic TG and 42.43 μmol in plasma TG levels were observed as the result of increasing the activity rate of KHK by 10%. A decrease of 325.16 μmol in hepatic TG and 49.38 was found when KHK was inhibited by 10%. The reason that the changes in hepatic TGs were greater than that of plasma TGs is because there is around 5% of body lipid stored in the liver under normal conditions, as such the triglyceride level in the liver is ordinarily much higher than that in the plasma. The two significant variations of pyruvate kinase and KHK activity suggests that they are likely to be the key determinants of individual responsiveness to the progression of simple lipid deposition in the liver. However, as KHK is exclusively contributing to the fructose metabolic pathway, it was selected for further investigation in Scenario Three. Apart from PK and KHK, PEPCK, PDC and FAS also expressed with high sensitivity to lipid levels, especially hepatic TG concentrations.

Scenario Three: Effect on NAFLD Through the Potential Interventional Target KHK

The early stages of NAFLD are identified by simple lipid accumulation within hepatocytes. Potentially, fructose enables an increase in hepatic *de novo* lipogenesis, thereby contributing to this build up within cells. As demonstrated in Scenario Two, in this process fructokinase (KHK) is of interest as a potential point of intervention. KHK is not limited by adenosine triphosphate (ATP) or citrate availability (as is the case of glucokinase in the glycolytic pathway) as part of the fructose phosphorylation process which potentially delivers a large amount of substrate for lipogenesis. In this scenario, the fructose only diet introduced in Scenario One (100 g/meal) was presented as a representation of a healthy subject. A very high fructose diet (150 g/meal) was employed to simulate the development of a simple pro-steatosis condition, in which a 18.34% increase in hepatic triglycerides was observed. This setting fitted in the criteria of mild steatosis (Petäjä and Yki-Järvinen, 2016). After feeding with the very high fructose diet, three degrees of KHK inhibition were simulated including 50% suppression, 70% suppression, and a full suppression of the enzyme. The results are presented in **Figure 5**. Inhibiting KHK expression by 50% was able to effectively reduce the hepatic lipid concentrations. Further suppression of KHK by 70% enables

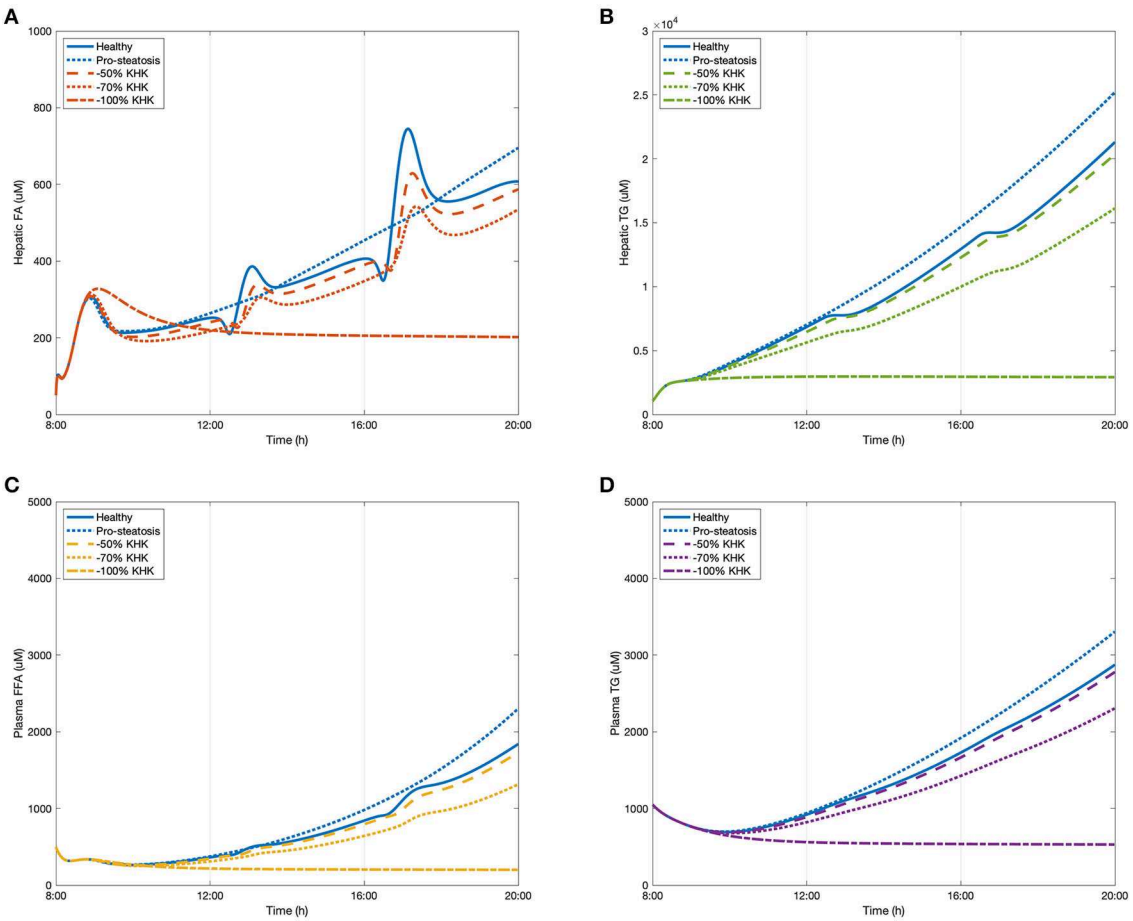

FIGURE 5 | The change of lipid accumulation after inhibiting KHK. **(A)** Hepatic FA, **(B)** hepatic TG, **(C)** plasma FFA, and **(D)** plasma TG.

lowering of plasma FFA concentration significantly (**Figure 5C**). When KHK was fully suppressed, hepatic FA, hepatic TG, plasma FFA, and plasma were maintained at a reduced steady-state. These complete inhibitory predictions are consistent with a recent study by Miller et al. (2018) who showed that, after feeding with a high fructose high fat diet, the plasma triglyceride level decreases dramatically in KHK knockout mice when compared to control wild-type animals.

Although we have confidence in the model, we recognize that further validation work is necessary in order to improve and expand the model. The simulations in three scenarios above suggest that the model is robust and it has sufficient detail to present the kinetic relationship between fructose and lipid in the liver. However, the model has its own limitations. Firstly, only acute effects of different carbohydrate diet could be represented by the current model. As the development of NAFLD is chronic and multifactorial, applying only one organ model to investigate the pathological mechanism over a long period may result in cumulative errors. Secondly, the actual dietary intake is more complicated than introduced in this model. The model is designed to give only the response to carbohydrate input. The prediction robustness may be improved if protein and fat consumptions were included for further model expansion. Furthermore, the structure of the liver is complex and the current simulations consider liver as a lumped model that neglects zonation across the liver plate. More comprehensive insight and more accurate information would be provided if the model could be further refined and expanded to include zonated effects.

CONCLUSIONS AND FUTURE WORK

In this study we introduced a computational model of the hepatic fructose metabolism. The model was validated against experimental data and shown to predict major trends, suggesting that fructose over-consumption leads to dyslipidaemia associated with NAFLD. The model was also used to identify and study a potential regulatory point for novel therapeutic intervention based on the reaction rate sensitivity. As fructokinase is recognized to be the key determinant within the fructose pathway, the effect of fructokinase activity suppression was simulated. When KHK expression was inhibited by 50%, an effective reduction in lipid deposition occurred alleviating simple steatosis while fully inhibited KHK expression induced a notable decrease in

lipid accumulation. These results match with experimental data from knock-out animals and should be further corroborated by cellular experimental studies, with the consideration that modification of fructose mediated lipogenesis rather than complete inhibition may be the preferred outcome. In addition, more potential regulatory targets could be tested as candidates for therapeutic treatment.

We believe that organ modeling *in silico* model systems will have numerous applications in developing future therapeutic strategies and represent a future growth area for disease modeling using the quantitative approaches applied by engineers to complex problems. These studies need to involve collaborations between engineers and clinical colleagues.

DATA AVAILABILITY STATEMENT

All datasets generated for this study are included in the article/**Supplementary Material**.

AUTHOR CONTRIBUTIONS

The computational model was constructed and analyzed by YL under the supervision of ND and IB. YL wrote the manuscript with support from ND and IB. All authors contributed to the article and approved the submitted version.

FUNDING

YL has been supported by UCL-CSC Joint Research Scholarship.

SUPPLEMENTARY MATERIAL

The Supplementary Material for this article can be found online at: https://www.frontiersin.org/articles/10.3389/fbioe.2020.00762/full#supplementary-material

Table S1 | Initial values of variables and parameter values used in the model.

Table S2 | Matlab code file of fructose metabolism.

REFERENCES

Abraha, A., Humphreys, S. M., Clark, M. L., Matthews, D. R., and Frayn, K. N. (1998). Acute effect of fructose on postprandial lipaemia in diabetic and non-diabetic subjects. *Br. J. Nutr.* 80, 169–175. doi: 10.1017/S000711459800107X

Allen, R. J., and Musante, C. J. (2017). Modeling fructose-load-induced hepatic *de novo* lipogenesis by model simplification. *Gene Regul. Syst. Biol.* 11, 1177625017690133. doi: 10.1177/1177625017690133

Allen, R. J., and Musante, C. J. (2018). A mathematical analysis of adaptations to the metabolic fate of fructose in essential fructosuria subjects. *Am. J. Physiol.-Endocrinol. Metabol.* 315, E394–E403. doi: 10.1152/ajpendo.00317.2017

Arias, M. I., Boyer, J. L., Fausto, N., Jakoby, W. B., Schachter, D. A., and Shafritz, D. A. (1994). *The Liver Biology and Pathology*. New York, NY: Raven Press.

Ashworth, W. B., Davies, N. A., and Bogle, I. D. L. (2016). A computational model of hepatic energy metabolism: understanding zonated damage and steatosis in NAFLD. *PLoS Comput. Biol.* 12:e1005105. doi: 10.1371/journal.pcbi.1005105

Basaranoglu, M., Basaranoglu, G., Sabuncu, T., and Senturk, H. (2013). Fructose as a key player in the development of fatty liver disease. *World J. Gastroenterol.* 19, 1166–1172. doi: 10.3748/wjg.v19.i8.1166

Beale, E. G., Harvey, B. J., and Forest, C. (2007). PCK1 and PCK2 as candidate diabetes and obesity genes. *Cell Biochem. Biophys.* 48, 89–95. doi: 10.1007/s12013-007-0025-6

Bray, G. A., Nielsen, S. J., and Popkin, B. M. (2004). Consumption of high-fructose corn syrup in beverages may play a role in the epidemic of obesity. *Am. J. Clin. Nutr.* 79, 537–543. doi: 10.1093/ajcn/79.4.537

Briggs, A. D., Mytton, O. T., Kehlbacher, A., Tiffin, R., Elhussein, A., Rayner, M., et al. (2017). Health impact assessment of the UK soft drinks industry levy: a comparative risk assessment modelling study. *Lancet Public Health* 2, e15–e22. doi: 10.1016/S2468-2667(16)30037-8

Chalhoub, E., Hanson, R. W., and Belovich, J. M. (2007a). A computer model of gluconeogenesis and lipid metabolism in the perfused liver. *Am. J. Physiol. Endocrinol. Metabol.* 293, E1676–E1686. doi: 10.1152/ajpendo.00161.2007

Chalhoub, E., Xie, L., Balasubramanian, V., Kim, J., and Belovich, J. (2007b). A distributed model of carbohydrate transport and metabolism in the liver during rest and high-intensity exercise. *Ann. Biomed. Eng.* 35, 474–491. doi: 10.1007/s10439-006-9217-2

Chong, M. F., Fielding, B. A., and Frayn, K. N. (2007). Mechanisms for the acute effect of fructose on postprandial lipemia. *Am. J. Clin. Nutr.* 85, 1511–1520. doi: 10.1093/ajcn/85.6.1511

Cohen, J. C., Horton, J. D., and Hobbs, H. H. (2011). Human fatty liver disease: old questions and new insights. *Science* 332, 1519–1523. doi: 10.1126/science.1204265

Critchley, L. A., and Critchley, J. A. (1999). A meta-analysis of studies using bias and precision statistics to compare cardiac output measurement techniques. *J. Clin. Monit. Comput.* 15, 85–91. doi: 10.1023/A:1009982611386

Davy, K. P., and Seals, D. R. (1994). Total blood volume in healthy young and older men. *J. Appl. Physiol.* 76, 2059–2062. doi: 10.1152/jappl.1994.76.5.2059

DeBosch, B. J., Chen, Z., Saben, J. L., Finck, B. N., and Moley, K. H. (2014). Glucose transporter 8 (GLUT8) mediates fructose-induced *de novo* lipogenesis and macrosteatosis. *J. Biol. Chem.* 289, 10989–10998. doi: 10.1074/jbc.M113.527002

Douard, V., and Ferraris, R. P. (2008). Regulation of the fructose transporter GLUT5 in health and disease. *Am. J. Physiol.*295, E227–E237. doi: 10.1152/ajpendo.90245.2008

Douard, V., and Ferraris, R. P. (2013). The role of fructose transporters in diseases linked to excessive fructose intake. *J. Physiol.* 591, 401–414. doi: 10.1113/jphysiol.2011.215731

Duarte, N. C., Becker, S. A., Jamshidi, N., Thiele, I., Mo, M. L., Vo, T. D., et al. (2007). Global reconstruction of the human metabolic network based on genomic and bibliomic data. *Proc. Nat. Acad. Sci. U.S.A.* 104, 1777–1782. doi: 10.1073/pnas.0610772104

Duarte, S. M. B., Stefano, J. T., Vanni, D. S., Carrilho, F. J., and Oliveira, C. P. M. S. D. (2019). Impact of current diet at the risk of non-alcoholic fatty liver disease (NAFLD). *Arquivos Gastroenterol.* 56, 431–439. doi: 10.1590/s0004-2803.201900000-67

Eipel, C., Abshagen, K., and Vollmar, B. (2010). Regulation of hepatic blood flow: the hepatic arterial buffer response revisited. *World J. Gastroenterol.* 16, 6046–6057. doi: 10.3748/wjg.v16.i48.6046

Estes, C., Anstee, Q. M., Arias-Loste, M. T., Bantel, H., Bellentani, S., Caballeria, J., et al. (2018). Modeling nafld disease burden in China, France, Germany, Italy, Japan, Spain, United Kingdom, and United States for the period 2016–2030. *J. Hepatol.* 69, 896–904. doi: 10.1016/j.jhep.2018.05.036

Ferraris, R. P., Choe, J.-Y., and Patel, C. R. (2018). Intestinal absorption of fructose. *Ann. Rev. Nutr.* 38, 41–67. doi: 10.1146/annurev-nutr-082117-051707

Garfinkel, D. (1971). Simulation of the Krebs cycle and closely related metabolism in perfused rat liver. I. Construction of a model. *Comput. Biomed. Res.* 4, 1–17. doi: 10.1016/0010-4809(71)90044-9

Gille, C., Bölling, C., Hoppe, A., Bulik, S., Hoffmann, S., Hübner, K., et al. (2010). HepatoNet1: a comprehensive metabolic reconstruction of the human hepatocyte for the analysis of liver physiology. *Mol. Syst. Biol.* 6:411. doi: 10.1038/msb.2010.62

Hashem, K. M., He, F. J., Alderton, S. A., and Macgregor, G. A. (2019). Cross-sectional survey of the amount of sugar and energy in chocolate confectionery sold in the UK in 1992 and 2017. *Nutrients* 11:1798. doi: 10.3390/nu11081798

Havel, P. J. (2005). Dietary fructose: implications for dysregulation of energy homeostasis and lipid/carbohydrate metabolism. *Nutr. Rev.* 63, 133–157. doi: 10.1111/j.1753-4887.2005.tb00132.x

Health and Services (2015). *US Department of Agriculture, 2015–2020 Dietary Guidelines for Americans*. Washington, DC.

Hetherington, J., Sumner, T., Seymour, R., Li, L., Rey, M. V., Yamaji, S., et al. (2012). A composite computational model of liver glucose homeostasis. I. Building the composite model. *J. R. Soc. Interface* 9, 689–700. doi: 10.1098/rsif.2011.0141

Hijmans, B. S., Grefhorst, A., Oosterveer, M. H., and Groen, A. K. (2014). Zonation of glucose and fatty acid metabolism in the liver: mechanism and metabolic consequences. *Biochimie* 96, 121–9. doi: 10.1016/j.biochi.2013.06.007

Jensen, T., Abdelmalek, M. F., Sullivan, S., Nadeau, K. J., Green, M., Roncal, C., et al. (2018). Fructose and sugar: a major mediator of non-alcoholic fatty liver disease. *J. Hepatol.* 68, 1063–1075. doi: 10.1016/j.jhep.2018.01.019

Jones, C. (2016). The UK sugar tax-a healthy start? *Br. Dent. J.* 221:59. doi: 10.1038/sj.bdj.2016.522

Kersten, S. (2014). Integrated physiology and systems biology of PPARα. *Mol. Metab.* 3, 354–371. doi: 10.1016/j.molmet.2014.02.002

König, M., Bulik, S., and Holzhütter, H.-G. (2012). Quantifying the contribution of the liver to glucose homeostasis: a detailed kinetic model of human hepatic glucose metabolism. *PLoS Comput. Biol.* 8:e1002577. doi: 10.1371/journal.pcbi.1002577

Koo, H.-Y., Wallig, M. A., Chung, B. H., Nara, T. Y., Cho, B. S., and Nakamura, M. T. (2008). Dietary fructose induces a wide range of genes with distinct shift in carbohydrate and lipid metabolism in fed and fasted rat liver. *Biochim. Biophys. Acta* 1782, 341–348. doi: 10.1016/j.bbadis.2008.02.007

Laughlin, M. R. (2014). Normal roles for dietary fructose in carbohydrate metabolism. *Nutrients* 6, 3117–3129. doi: 10.3390/nu6083117

Lim, J. S., Mietus-Snyder, M., Valente, A., Schwarz, J.-M., and Lustig, R. H. (2010). The role of fructose in the pathogenesis of NAFLD and the metabolic syndrome. *Nat. Rev. Gastroenterol. Hepatol.* 7, 251–264. doi: 10.1038/nrgastro.2010.41

Ma, H., Sorokin, A., Mazein, A., Selkov, A., Selkov, E., Demin, O., et al. (2007). The Edinburgh human metabolic network reconstruction and its functional analysis. *Mol. Syst. Biol.* 3:135. doi: 10.1038/msb4100177

Maldonado, E. M., Fisher, C. P., Mazzatti, D. J., Barber, A. L., Tindall, M. J., Plant, N. J., et al. (2018). Multi-scale, whole-system models of liver metabolic adaptation to fat and sugar in non-alcoholic fatty liver disease. *NPJ Syst. Biol. Appl.* 4, 1–10. doi: 10.1038/s41540-018-0070-3

Manolescu, A. R., Witkowska, K., Kinnaird, A., Cessford, T., and Cheeseman, C. (2007). Facilitated hexose transporters: new perspectives on form and function. *Physiology* 22, 234–240. doi: 10.1152/physiol.00011.2007

Mayes, P. A. (1993). Intermediary metabolism of fructose. *Am. J. Clin. Nutr.* 58, 754S−765S. doi: 10.1093/ajcn/58.5.754S

Miele, L., Valenza, V., La Torre, G., Montalto, M., Cammarota, G., Ricci, R., et al. (2009). Increased intestinal permeability and tight junction alterations in nonalcoholic fatty liver disease. *Hepatology* 49, 1877–1887. doi: 10.1002/hep.22848

Miller, C. O., Yang, X., Lu, K., Cao, J., Herath, K., Rosahl, T. W., et al. (2018). Ketohexokinase knockout mice, a model for essential fructosuria, exhibit altered fructose metabolism and are protected from diet-induced metabolic defects. *Am. J. Physiol. Endocrinol. Metabol.* 315, E386–E393. doi: 10.1152/ajpendo.00027.2018

Naftalin, R. J. (2016). A computer model simulating human glucose absorption and metabolism in health and metabolic disease states. *F1000Res.* 5:647. doi: 10.12688/f1000research.8299.1

Nomura, K., and Yamanouchi, T. (2012). The role of fructose-enriched diets in mechanisms of nonalcoholic fatty liver disease. *J. Nutr. Biochem.* 23, 203–208. doi: 10.1016/j.jnutbio.2011.09.006

Noorman, M., Allen, R., Musante, C. J., and Banks, H. T. (2019). Analysis of compartments-in-series models of liver metabolism as partial differential equations: the effect of dispersion and number of compartments. *Math. Biosci. Eng. MBE* 16:1082. doi: 10.3934/mbe.2019052

Ouyang, X., Cirillo, P., Sautin, Y., Mccall, S., Bruchette, J. L., Diehl, A. M., et al. (2008). Fructose consumption as a risk factor for non-alcoholic fatty liver disease. *J. Hepatol.* 48, 993–999. doi: 10.1016/j.jhep.2008.02.011

Patel, C., Sugimoto, K., Douard, V., Shah, A., Inui, H., Yamanouchi, T., et al. (2015). Effect of dietary fructose on portal and systemic serum fructose levels in rats and in KHK^{ff} and GLUT5^{-5n} mice. *Am. J. Physiol. Gastrointest. Liver Physiol.* 309, G779–G790. doi: 10.1152/ajpgi.00188.2015

Petäjä, E. M., and Yki-Järvinen, H. (2016). Definitions of normal liver fat and the association of insulin sensitivity with acquired and genetic NAFLD-a systematic review. *Int. J. Mol. Sci.* 17:633. doi: 10.3390/ijms17050633

Rutledge, A. C., and Adeli, K. (2007). Fructose and the metabolic syndrome: pathophysiology and molecular mechanisms. *Nutr. Rev.* 65, 13–23. doi: 10.1111/j.1753-4887.2007.tb00322.x

Softic, S., Cohen, D. E., and Kahn, C. R. (2016). Role of dietary fructose and hepatic *de novo* lipogenesis in fatty liver disease. *Dig. Dis. Sci.* 61, 1282–1293. doi: 10.1007/s10620-016-4054-0

Stanhope, K. L., Griffen, S. C., Bair, B. R., Swarbrick, M. M., Keim, N. L., and Havel, P. J. (2008). Twenty-four-hour endocrine and metabolic profiles following consumption of high-fructose corn syrup-, sucrose-, fructose-, and glucose-sweetened beverages with meals. *Am. J. Clin. Nutr.* 87, 1194–1203. doi: 10.1093/ajcn/87.5.1194

Sumner, T., Hetherington, J., Seymour, R. M., Li, L., Rey, M. V., Yamaji, S., et al. (2012). A composite computational model of liver glucose homeostasis. II. Exploring system behaviour. *J. R. Soc. Interface* 9, 701–706. doi: 10.1098/rsif.2011.0783

Sun, S. Z., and Empie, M. W. (2012). Fructose metabolism in humans-what isotopic tracer studies tell us. *Nutr. Metabol.* 9:89. doi: 10.1186/1743-7075-9-89

Tappy, L., and Lê, K.-A. (2010). Metabolic effects of fructose and the worldwide increase in obesity. *Physiol. Rev.* 90, 23–46. doi: 10.1152/physrev.00019.2009

Ventura, E. E., Davis, J. N., and Goran, M. I. (2011). Sugar content of popular sweetened beverages based on objective laboratory analysis: focus on fructose content. *Obesity* 19, 868–874. doi: 10.1038/oby.2010.255

Vos, J. J., Wietasch, J. G., Absalom, A. R., Hendriks, H. G., and Scheeren, T. W. (2014). Green light for liver function monitoring using indocyanine green? An overview of current clinical applications. *Anaesthesia* 69, 1364–1376. doi: 10.1111/anae.12755

Vos, M. B., and Lavine, J. E. (2013). Dietary fructose in nonalcoholic fatty liver disease. *Hepatology* 57, 2525–2531. doi: 10.1002/hep.26299

Wright, E. M., Sala-Rabanal, M., Loo, D. D. F., and Hirayama, B. A. (2012). "Chapter 58—sugar absorption," in *Physiology of the Gastrointestinal Tract*, *5th Edn*, eds L. R. Johnson, F. K. Ghishan, J. D. Kaunitz, J. L. Merchant, H. M. Said, and J. D. Wood (Boston, MA: Academic Press). doi: 10.1016/B978-0-12-382026-6.00058-0

Younossi, Z. M., Koenig, A. B., Abdelatif, D., Fazel, Y., Henry, L., and Wymer, M. (2016). Global epidemiology of nonalcoholic fatty liver disease-meta-analytic assessment of prevalence, incidence, and outcomes. *Hepatology* 64, 73–84. doi: 10.1002/hep.28431

Conflict of Interest: The authors declare that the research was conducted in the absence of any commercial or financial relationships that could be construed as a potential conflict of interest.

Copyright © 2020 Liao, Davies and Bogle. This is an open-access article distributed under the terms of the Creative Commons Attribution License (CC BY). The use, distribution or reproduction in other forums is permitted, provided the original author(s) and the copyright owner(s) are credited and that the original publication in this journal is cited, in accordance with accepted academic practice. No use, distribution or reproduction is permitted which does not comply with these terms.

frontiers in Physiology

ORIGINAL RESEARCH
published: 23 July 2020
doi: 10.3389/fphys.2020.00777

Chronic Undernutrition Differentially Changes Muscle Fiber Types Organization and Distribution in the EDL Muscle Fascicles

Erika E. Rodriguez-Torres[1], Jorge Viveros-Rogel[1], Kenia López-García[2], Enrique Vázquez-Mendoza[3], Gonzalo Chávez-Fragoso[4], Salvador Quiroz-González[5] and Ismael Jiménez-Estrada[3]*

[1] Center for Research in Mathematics, Hidalgo State Autonomous University (UAEH), Pachuca, Mexico, [2] Faculty of Health Sciences, Autonomous University of Tlaxcala, Tlaxcala, Mexico, [3] Department of Physiology, Biophysics and Neuroscience, Center for Research and Advanced Studies, National Polytechnic Institute, Mexico City, Mexico, [4] Department of Computer Science, Center for Research and Advanced Studies, National Polytechnic Institute, Mexico City, Mexico, [5] Department of Medical Acupuncture and Rehabilitation, State University of Ecatepec, Ecatepec, Mexico

OPEN ACCESS

Edited by:
Babatunde Ogunnaike, University of Delaware, United States

Reviewed by:
Debashis Sahoo, University of California, San Diego, United States
Wataru Mizunoya, Azabu University, Japan

***Correspondence:**
Erika E. Rodriguez-Torres
erikart@uaeh.edu.mx

Specialty section:
This article was submitted to Systems Biology, a section of the journal Frontiers in Physiology

Received: *10 September 2019*
Accepted: *15 June 2020*
Published: *23 July 2020*

Citation:
Rodriguez-Torres EE, Viveros-Rogel J, López-García K, Vázquez-Mendoza E, Chávez-Fragoso G, Quiroz-González S and Jiménez-Estrada I (2020) Chronic Undernutrition Differentially Changes Muscle Fiber Types Organization and Distribution in the EDL Muscle Fascicles. Front. Physiol. 11:777. doi: 10.3389/fphys.2020.00777

Fiber type composition, organization, and distribution are key elements in muscle functioning. These properties can be modified by intrinsic and/or extrinsic factors, such as undernutrition and injuries. Currently, there is no methodology to quantitatively analyze such modifications. On one hand, we propose a fractal approach to determine fiber type organization, using the fractal correlation method in software Fractalyse. On the other hand, we applied the kernel methodology from machine learning to build radial-basis functions for the spatial distribution of fibers (distribution functions), by dividing into square cells a two-dimensional binary image for the spatial distribution of fibers from a muscle fascicle and mounting on each cell a radial-basis function in such a way that the sum of all cell functions creates a smooth version of the fiber histogram on the cell grid. The distribution functions thus created belong in a reproducing kernel Hilbert space which permits us to regard them as vectors and measure distances and angles between them. In the present study, we analyze fiber type organization and distribution in fascicles (F2, F3, F4, and F5) of the *extensor digitorum longus* muscle (EDLm) from control and undernourished male rats. Fibers were classified according to the ATPase activity in slow, intermediate, and fast. Then, (x, y) coordinates of fibers were used to build binary images and distribution functions for each fiber type and both conditions. The fractal organization analysis showed that fast and intermediate fibers, from both groups, had a fractal organization within the four fascicles, i.e., the fiber assembly is distributed in clusters. We also show that chronic undernutrition altered the organization of fast fibers in the F3, although it still is considered a fractal organization. Distribution function analysis showed that each fiber type (slow, intermediate, and fast) has a unique distribution within the fascicles, in both conditions. However, chronic undernutrition modified the intra-fascicular fiber type distributions, except in the F2. Altogether, these results showed

that the methodology herein proposed allows for analyzing fiber type organization and distribution modifications. On the other side, we show that chronic undernutrition alters not only the fiber type composition but also the organization and distribution, which could affect the muscle functioning, and ultimately, its behavior (e.g., locomotion).

Keywords: fiber type, chronic undernutrition, fractal analysis, distribution functions, machine learning, ATPase, skeletal muscle

1. INTRODUCTION

Nature is ordered at all levels, from microscopic (atomic, molecular, and cellular) to macroscopic (individual and population levels), but when a disaster or disease occurs at any level such order changes. The application of mathematics and computer science in anatomical and/or physiological problems has allowed a better and deeper understanding of the fundamental processes of living beings. Cells, tissues, and organs in vertebrates present an organization which is mathematically similar to that observed in other biological systems (e.g., ecosystems) and manifests self-similarity (Mandelbrot, 1983). It is now possible to study the organization of particular biological systems (such as muscles) using fractal tools which have become essential in the work of physicists, chemists, biologists, physiologists, economists, among others. Such tools have allowed researches to reformulate old problems into novel terms, and address complex problems in simplified forms (Liebovitch et al., 1987; Jelinek and Fernandez, 1998; Reese et al., 2012; Hernández and Menéndez-Conde, 2013).

The skeletal muscle is a heterogeneous tissue composed of various fiber types, which can be classified according to their metabolic and contractile characteristics as glycolytic and oxidative or slow, intermediate, and fast fibers, respectively (Ariano et al., 1973). The organization of muscle fibers is relevant to maintain the homeostasis and muscle functioning. This organization can be altered by disease, inadequate nutrition, exercise or injury, modifying their contractile and structural properties. Yet we found practically no studies oriented to investigate the organization of fiber types in skeletal muscles and how natural or pathological conditions can modify it, specifically in the case of the *extensor digitorum longus* muscle (EDLm), which is composed in four fascicles (F2, F3, F4, and F5) with different fiber composition, metabolism, and size (Balice-Gordon and Thompson, 1988; Kissane et al., 2016; Vázquez-Mendoza et al., 2017). This particular muscle participates in the extension of toes (each fascicle extends a single toe, the F2 extends toe 2, the F3 extends toe 3, and so on) and in the dorsiflexion of the ankle in the rat.

Recently, it has been illustrated elsewhere that chronic undernutrition exerts a differential effect on the relative fiber type composition in the EDLm fascicles (Vázquez-Mendoza et al., 2017). Particularly, it was observed that the third fascicle (F3) was more affected than the others, being the sequential order of effects as follows: F3>F5>F4=F2. In that study, the authors suggested that those changes in the relative composition of fiber types in the EDLm fascicles could induce modifications in the intra-fascicle fibers organization. One way to analyze this is by mathematical methods such as fractal estimation analysis, which can determine whether a fiber phenotype group is organized in clusters or spread randomly over the whole muscle or fascicle.

Besides the organization, fiber types distribution within a muscle is crucial to its functioning (Burkholder et al., 1994). The visualization method that we developed consists in the application of the kernel methodology from machine learning to build distribution functions for the spatial localization of fiber types. In brief, on the reconstructed microphotograph of the stained section, we superimposed a square grid of size N and built a histogram for each fiber type. For each cell, we built a Gaussian kernel function that is mainly supported therein, by taking into account the number and localization of fiber types within the cell. The individual cell functions are then linearly superimposed to obtain a function whose graph resembles a smoothing of the histogram of the fiber type under study, we call it the distribution function (DF) of the fiber type shown in the histological image. DFs obtained in this way belong in a (finite-dimensional) reproducing kernel Hilbert space, which in effect enables us to treat each one of them (and thus each image) as vectors and thus measure distance and angle between any pair of them. We then use distance and angle measurements (which we call dissimilarity quantifiers) to differentiate data images from one another and in turn quantify the effects of undernutrition in EDLm fiber content.

In this study, we aimed to develop a methodology to evaluate changes in fiber type organization and spatial distribution due to alterations provoked by traumatic processes such as spinal cord injury, motor nerve damage, multiparity, or by metabolic diseases (undernutrition or obesity), among others. To this end, we applied fractal estimation analysis to analyze fiber type organization and we were able to make a quantitative analysis of changes in the structure of muscle fibers due to chronic undernutrition. On the other hand, we applied the kernel methodology from machine learning to build distribution functions for the spatial localization of fiber types and along with the dissimilarity quantifiers we were able to assess how chronic undernutrition alter the fiber type distribution within the EDLm fascicles.

2. MATERIALS AND METHODS

All experiments were performed in accordance with the Guide for the Care and Use of Laboratory Animals (National Research Council, 2010; National Institutes of Health, Bethesda, MD, USA; Animal Welfare Assurance #A5036-01). The animal protocols were approved by the Institutional Bioethical Committee for

the Care and Handling of Laboratory Animals (UPEAL-Protocol 013−02, CINVESTAV).

2.1. Animals

Chronic undernutrition protocol. We used nulliparous female Wistar rats (257.4 ± 16.3 g body weight), which were randomly allocated in two groups: control (C, $n = 16$) and undernourished (U, $n = 18$). Control group had free access to commercial food (Formulab 5008; LabDiet, Framingham, MA, USA); while the undernourished group was fed with 50% of the mean food intake given to control animals, both groups had access to water *ad libitum*. Two weeks after, female rats of both groups (C and U) were put together with a male for 1 week in the same cage to ensure mating and the consecutive pregnancy. After that, males were removed. The day females gave birth litters were adjusted to nine pups: five males and four females. During gestation, birth, and lactation all rats remained on the same feeding protocol to which they were subjected from the beginning (C or U). Each mother and her offspring were housed in large acrylic cages (43 × 53 × 20 cm). After weaning (postnatal day 21), pups remained on the same feeding protocol as their mothers (C or U) until the experimental proceeding. Later, male rats were housed individually in acrylic cages (32 × 47 × 20 cm) under the same conditions of light/dark cycle (12/12 h) and temperature (22–24°C). No supplementary mineral, trace elements or vitamins were added to the food supply of undernourished animals. Further details of these protocols can be found in Ruiz-Rosado et al. (2013) and Vázquez-Mendoza et al. (2017).

At 35 postnatal days, we randomly selected 6 males coming from each experimental group (C, $n = 6$; and U, $n = 6$), which weighed and anesthetized with urethane ($1.6\,g/kg$ of body weight). The EDL muscles were quickly removed and weighed (more details Vázquez-Mendoza et al., 2017). Subsequently, the four fascicles of each muscle ($F2$ to $F5$) were carefully separated and their length measured. After that, fascicles were immersed in 2−methylbutane, cooled to near freezing point with liquid nitrogen and stored at −80°C until their processing. At the end of tissue extraction, the animals were euthanized using an overdose of anesthetic (urethane). Subsequently, the middle segment of each fascicle was sectioned and mounted on a specimen holder in a cryoprotectant solution (Tissue−Tek® O.C.T Compound, Sakura® Finetek, Torrance, Ca). Serial transverse sections (10 μm thick) of each specimen tissue were obtained by means of a cryostat at −25°C (CM−1520; Leica Biosystems, Nussloch, Germany). The sections were subsequently mounted on glass coverslips for staining.

2.2. Histoenzymatic Analysis

EDLm fascicle sections were stained with the myofibrillar alkaline ATPase activity technique (pH = 9.4, modified from Guth and Samaha, 1970) to identify the fast, intermediate and slow fiber types. In brief, the muscle sections were submerged 20 min in a pre-incubation solution (0.01 M Tris base and 0.018 M $CaCl_2$, pH 10.3), then they were washed three times for 5 min with deionized water and subsequently incubated at 37°C for 60 min in the incubation solution (1.5% w/v of adenosine-5′-triphosphate in pre-incubation solution, pH 9.4). After incubation, slides were washed for 3 min with 0.2 M $CaCl_2$ and transferred to 2% w/v $CoCl_2$ solution for another 5 min. Subsequently, they were washed ten times with deionized water and finally transferred to 10% v/v ammonium sulfide for 3 min. Stained sections were washed, dehydrated with ascending alcohol solutions and mounted with glycerogel and coverslips. Photomicrographs of each muscle fascicle were taken by a digital camera (AxioCam MRc, Zeiss, Germany) mounted on a microscope (Olympus CX31, NY, US). The whole muscle fascicle was reconstructed with the photomicrographs using Photoshop CS4. After that, the spatial position (x, y coordinates) of each and the total number of the different fiber types was determined in control and undernourished muscles using ImageJ (Rasband, 2011). According to the alkaline ATPase technique, the fibers were identified as light = slow, Type I; gray = fast, Type IIb and dark = intermediate, Type IIa/IId (see section 7).

2.3. Experiments With Synthetic Data

In order to determine if the dissimilarity quantifiers (distance and angle) can differentiate between highly similar distribution, we generated synthetic data which we considered to be challenging to the quantifiers. Below is describe in detail how these distribution were constructed. This was implemented in a MatLab script available in https://github.com/GonzaloCin/DistributionFunctions.

2.3.1. Data Generation

Our synthetic data consists of four collections of randomly generated points and with very pronounced tendencies toward spreading and/or clustering. Each set has a geometric shape which we think should be challenging for the algorithm to discern one set from the another. The shapes are: a ball (uniform spread in all directions with no tendency toward clustering), a ring (uniform spread in all directions, with a pronounced tendency to cluster far from and uniformly around the global centroid of the set), a set in the shape of a sum sign (with pronounced spreading and clustering tendencies along the coordinate axes), a cross-shaped data set (same as the sum-shaped set but with a 45-degree rotation angle).

To generate each data set we first generated Q points (x, y) on a square $[-L/2, L/2] \times [-L/2, L/2]$, using a uniform distribution, then points were selected according to the following criteria:

Ball: only points satisfying $x^2 + y^2 \leq L^2/4$ were chosen to form part of the data set.
Ring: only points satisfying $(L^2/2 - \delta)^2 \leq x^2 + y^2 \leq L^2/4$ were chosen.
Sum sign: only points satisfying $-\delta/2 \leq x \leq \delta/2$ or $-\delta/2 \leq y \leq \delta/2$.
Cross: only points (ξ, η) satisfying $-\delta/2 \leq \xi \leq \delta/2$ or $-\delta/2 \leq \eta \leq \delta/2$ were chosen and then rotated a 45-degree angle: $x = (\xi - \eta)/\sqrt{2}$ and $y = (\xi + \eta)/\sqrt{2}$.

We chose $\delta = L/9$, and $Q = 500$, 1,000, 2,000, 3,000, 4,000 (**Figure 1**). For each value Q a collection of four data sets was

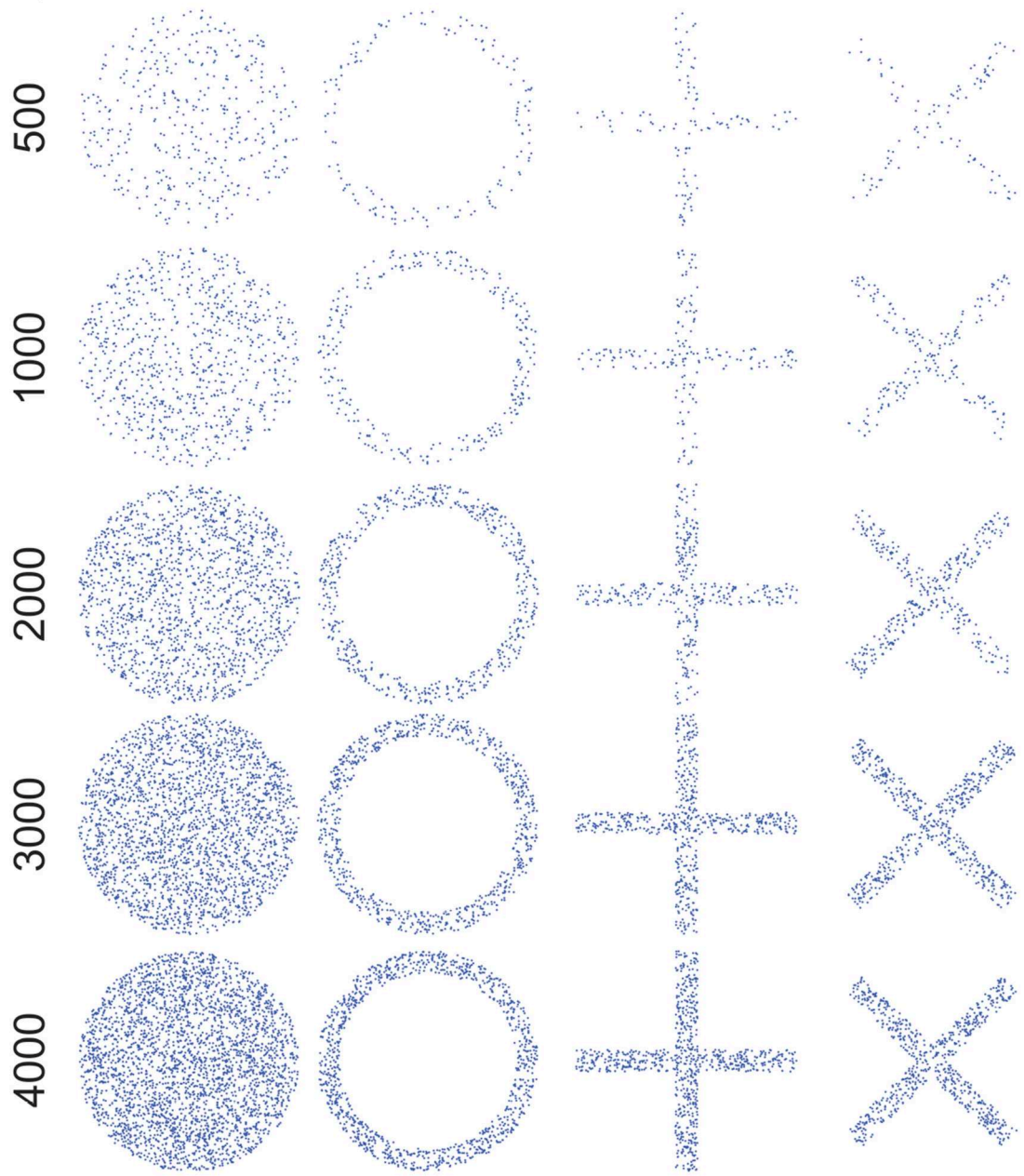

FIGURE 1 | Artificial data generated choosing $\delta =$, $L =$, and $Q = 500, 1{,}000, 2{,}000, 3{,}000, 4{,}000$. For each value of Q a collection of four data sets was generated (one for every shape: ball, ring, sum, cross) and for every one of them a distribution function was built. More details of experiments with synthetic data in section 2.3. Note that by increasing the number of points (Q), the shape of figures is more defined and, in dissimilarity quantifiers, induce an increase of distance, although angle is not affected, see text in section 7.2.

then generated (ball, ring, sum, cross) and for every one of them a distribution function was built using the methodology in 4. For every pair of distributions in each collection, distances and angles were calculated using formulae ($S19$) and ($S20$) from **Supplementary Material**, respectively. The results are reported in 7.2.

3. FRACTAL CORRELATION INTEGRAL METHOD

To determine the fractal structure of fiber types in fascicles we used the Fractalyse software (Thomas et al., 2008) and binary images constructed. This freeware program has been

developed by Frankhauser and colleagues and can be downloaded on the website http://www.fractalyse.org/. The original version of this software has been developed in the frame of the French research program "Ville émergente," financed by the PUCA (Plan Urbanisme Construction Architecture). Correlation analysis turned out to be the most reliable method as it introduces fewer artifacts compared to others, such as grid and dilation analysis. In fractal "correlation analysis," each fiber type pixel is surrounded by a small square window of size ε. The number of fibers pixels within each window is then counted. This allows the mean number of pair correlations per window $N(\varepsilon)$ to be computed. This step is repeated for windows of increasing size. It results in a series of points that can be represented on a Cartesian graph where the $X-axis$ refers to the size of the window $\varepsilon = (2i+1)$ (i being the iteration step), and the $Y-axis$ refers to the mean number of points per window. The next step consists in fitting this empirical curve to a theoretical curve that corresponds to a fractal law, i.e., a power law that links the number of correlations $N(\varepsilon)$ to the size of the window ε:

$$N = \varepsilon^D \tag{1}$$

The exponent D is the fractal dimension, or in this case, the correlation dimension. However, real-world patterns cannot strictly follow a fractal law. Therefore, it is useful to introduce a generalized fractal law, which contains two additional parameters:

$$N = a\varepsilon^D + c \tag{2}$$

The parameter a is called the "pre-form factor." It is giving a synthetic indication of local deviations from the estimated fractal law (Frankhauser, 1993, 1998; Thomas et al., 2007). For a mathematical fractal structure, is to be equal to 1 (Gouyet, 1996). Experience shows that when it goes 4 or less than 0.1, a fractal pattern is not confirmed (see Thomas et al., 2007). In real-world patterns, fractal behavior may change across scales. Changes often occur within rather small values of ε, i.e., for small distances, often corresponding to the clusters of fibers of the same type. In order to avoid local effects and hence wrong estimations, it is useful to introduce an additional parameter c that allows the correct estimation of D and a (Frankhauser, 1998; Thomas et al., 2008). The software Fractalyze was used to estimate the parameters mentioned above; it is mainly dedicated in this paper to the fractal analysis of fibers types and scaled in such a way that the pixel size is really the counting unit for ε. This ensures that the numbers $N(\varepsilon)$ are correctly counted in spatial structures like that illustrated further in this paper. Sensitivity analyses were performed to explore the role and the physiological meaning of a when estimating fractal dimensions for EDLm fibers under different conditions. The results were compared with a simplified version of the generalized law (2), where a is forced to one:

$$N = \varepsilon^D + c \tag{3}$$

D is often estimated by using a double logarithmic representation of the power law. Nonlinear regression was used to estimate the parameters that best fit the empirical curve since this avoids implicit assumptions about local deviations from the fractal law. Noise is assumed to be an independent additional effect. The fractal dimension D of fibers types can take any value between 0 and 2. When $D = 2$, the pattern of a fiber fiber type of EDLm is uniform, following a one-scale logic (Euclidian forms); $D = 0$ corresponds to a pattern made up of a single point (e.g., one or few muscle fibers); and finally, when D is between 1 and 2, the elements distributed in clusters over the space. Fractal dimension can be considered as a measure of an object's ability to fill the space in which it resides.

The quality of the estimation is measured by computing the ratio:

$$\frac{cov(N^{(est)}, N^{(obs)})}{\sqrt{var\left(N^{(est)}\right) var(N^{(obs)}}} \tag{4}$$

Where $N^{(est)}$ corresponds to the set of estimated values and $N^{(obs)}$ to the observed values. We here call this ratio R^{2*} by analogy with the determination coefficient. For values close to 1, $N^{(est)}(\varepsilon)$ and $N^{(obs)}(\varepsilon)$ curves tend to be equal, which means that the fractal model fits well to the observed data. If the fit between the two curves (empirical and estimated) is poor, we can conclude either that the pattern is not fractal or that it is multifractal (e.g., Tannier and Pumain, 2005). In our case, all analyzed patterns lead to R^{2*} values >0.99.

4. CONSTRUCTION OF DISTRIBUTION FUNCTIONS

4.1. Overview

The work discussed in this section is motivated by the old problem of extracting information about an underlying phenomenon from a collection of direct or indirect measurements or observations of the phenomenon itself, in order to estimate a functional dependency. Concrete examples of this type of problem are, determining which gene is responsible for a certain disease (microarray data classification; Cristianini and Shawe-Taylor, 2000; Schölkopf et al., 2004), and face and handwriting recognition (pattern classification; Duda et al., 2012; Devroye et al., 2013). The theory developed around this type of problems is nowadays known as Learning Theory (Vapnik, 1998; Cucker and Zhou, 2007) and its application was boosted thanks to the accessibility of modern computers capable of performing fast calculations.

Put plainly, the exact problem we are concerned here with is that of fitting a spatial distribution function to a finite set of points on the plane. The reader can think that the coordinates (x, y) of those points on the plane, give the location of muscle fibers in the histological image of a transverse muscle section. For distribution function, we will understand a smoothing of the histogram on the plane for the centered data, built on a square grid of given size N. N is a parameter specified by the user. If $\Phi : \mathbb{R}^2 \to \mathbb{R}$ is the distribution function of a set of points, $\Phi(z)$ gives the approximate count of points per unit square length at

the location $\mathsf{z} = (\mathsf{x}, \mathsf{y})$ on the plane. Our distribution functions will be linear superpositions of Gaussian kernel functions, one kernel function per each square of the grid. This section we will elaborate on it.

Gaussian kernel functions are a type of radial basis functions (RBFs). Aside from their ample use in classification problems in Bioinformatics, RBFs are also used in a variety of scenarios, such as approximation and interpolation problems (cf. Buhmann, 2003), or in the construction of Lyapunov functions for the determination of the stability of fixed points of certain dynamical systems (cf. Giesl, 2007). The RBF construction method we apply uses the so-called "kernel trick," which consists in taking advantage of properties of kernel functions to deal with the computational problem that entails high-dimensional data (which is not the case of our data), and to guarantee that the distribution functions so built will belong in an inner-product space which we denote by $\mathcal{L}_N$, and is the precursor of a Reproducing-Kernel Hilbert Space (the latter being the completion of the former under the norm induced by the inner product (cf. Schölkopf et al., 2004; Wendland, 2005). Working within an inner-product space will allow us to treat functions as vectors and thus measure distance and angle between two functions, we will then use these measurements to make a quantitative assessment of how distinct distribution functions associated to two fiber types are, which will directly translate into a semi-quantitative assessment of how two fiber types with distinct metabolic and myosin ATPase activities distribute across a muscle section.

Below we limit ourselves to presenting the methodology by which distribution functions are built for a single collection of finitely many points. The set of points is thought of as representing the spatial localization of fiber centroids in a given histological image of a muscle fascicle. In order to measure distance and angle between two functions (and thus between two collections of points or images), it is necessary to construct all distribution functions to be compared, simultaneously. The latter can be done by slightly tweaking the construction we present first.

In the next subsection, we briefly describe the construction of distribution functions. For a detail explanation on the mathematical framework of the construction and in what sense it is possible to speak of distance and angle between two distribution functions (see **Supplementary Material**).

Figure 2 shows a schematic representation of how distribution functions are constructed from the (x, y) coordinates of muscle fiber type. This method has already been implemented in a MatLab script for the construction of distribution function for a single and for a batch of images, which can be downloaded from https://github.com/GonzaloCin/DistributionFunctions.

4.2. Distribution Function for a Single Image

Let $\{\tilde{\mathsf{z}}_1, \ldots, \tilde{\mathsf{z}}_\nu\} \subset \mathbb{R}^2$, $\tilde{\mathsf{z}}_j = (\tilde{x}_j, \tilde{y}_j)$, be a collection of finitely many coordinate pairs of points within a sample image, each one of which represents a muscle fiber of the same type as all other fibers in the collection. Let $\bar{\mathsf{z}} = \nu^{-1} \sum_{j=1}^{\nu} \tilde{\mathsf{z}}_j$ be the centroid of the collection and $S = \{\mathsf{z}_1, \ldots, \mathsf{z}_\nu\}$ with $\mathsf{z}_j = \tilde{\mathsf{z}}_j - \bar{\mathsf{z}} = (x_j, y_j)$ be the centered collection of coordinate pairs. S is our data set and it is contained within a compact box $\mathcal{B} = [a, A] \times [b, B]$, where $a = -\varepsilon + \min x_j$ and $A = \varepsilon + \max x_j$, with ε a small, positive, chosen number (b and B defined similarly). $\mathcal{B}$ may as well be determined by the dimensions of the sample image, thus skipping the "cropping" just described.

Choose a fixed positive integer N and consider uniform partitions $P = \{a_0, \ldots, a_N\}$ and $Q = \{b_0, \ldots, b_N\}$ of $[a, A]$ and $[b, B]$, respectively. So $a_k = a + k(A-a)/N$ (b_k defined similarly). P and Q define a uniform rectangular grid over $\mathcal{B}$, composed of N^2 cells, $C_{ij} = [a_{i-1}, a_i] \times [b_{j-1}, b_j]$. We next describe a method to mount a bivariate Gaussian function on each cell C_{ij}. Such functions are then superimposed linearly so that the graph of the combined function will look like a smoothed version of the histogram defined on the grid.

Consider a cell C_{ij} and let S_{ij} be the subcollection of data points within it, $S_{ij} = \{\mathsf{z}_k \in C_{ij}\} \subseteq S$. Let $|S_{ij}|$ be the cardinality of S_{ij} and $\bar{\mathsf{z}}_{ij} = |S_{ij}|^{-1} \sum_{S_{ij}} \mathsf{z}_k$ be the centroid of the points in S_{ij}. The sample covariance matrix of points in C_{ij} is defined as (cf. Duda et al., 2012, p. 90),

$$\Sigma_{ij} = (|S_{ij}| - 1)^{-1} \sum_{S_{ij}} (\mathsf{z}_k - \bar{\mathsf{z}}_{ij})(\mathsf{z}_k - \bar{\mathsf{z}}_{ij})^t . \tag{5}$$

Assume for the moment Σ_{ij} is invertible (the case when Σ_{ij} is singular is discussed at the end of this section). The bivariate Gaussian function referred to above, also called *Gaussian kernel function* (see next section), is defined as

$$\phi_{ij}(\mathsf{z}) = \exp\Big(-2^{-1} (\mathsf{z} - \bar{\mathsf{z}}_{ij})^t \Sigma_{ij}^{-1} (\mathsf{z} - \bar{\mathsf{z}}_{ij}) \Big) , \tag{6}$$

We now associate to the collection S the following *distribution function,* where $R_{ij} = |S_{ij}|$,

$$\Phi(\mathsf{z}) = \sum_{i=1}^{N} \sum_{j=1}^{N} R_{ij} \phi_{ij}(\mathsf{z}) . \tag{7}$$

Φ is the main object of this section. We now mention three situations that must be sorted out when constructing Φ.

(*i*) If C_{ij} is empty, we set $\phi_{ij} = 0$ (indentically zero function).

(*ii*) If C_{ij} contains only one point $\mathsf{z}_p = (x_p, y_p)$, we compute its distance $\delta = \max\{a_j - x_p, b_j - x_p\}$ to the boundary of C_{ij}, redefine $\Sigma_{ij} = (\delta/3)^2 Id_2$ where Id_2 is the 2×2 identity matrix, and construct ϕ_{ij} as in Equation (6), that is $\phi_{ij}(\mathsf{z}) = \exp(-9 \cdot 2^{-1} \delta^{-2} \|\mathsf{z} - \mathsf{z}_p\|^2)$ ($\|\cdot\|$ denotes Euclidean distance). The unlikely case in which C_{ij} contains only one point which lies exactly on its boundary, can be treated in several ways. One way is to associate that point to the adjacent cell of shared boundary, assuming such cell has at least one other point. Another way is to arbitrarily set δ equal to a very small predefined positive number, so that the contribution of ϕ_{ij} to the sum Φ is highly localized for its double contribution to the sum in Equation (7) to be significant. We never incurred in this scenario in our experiments.

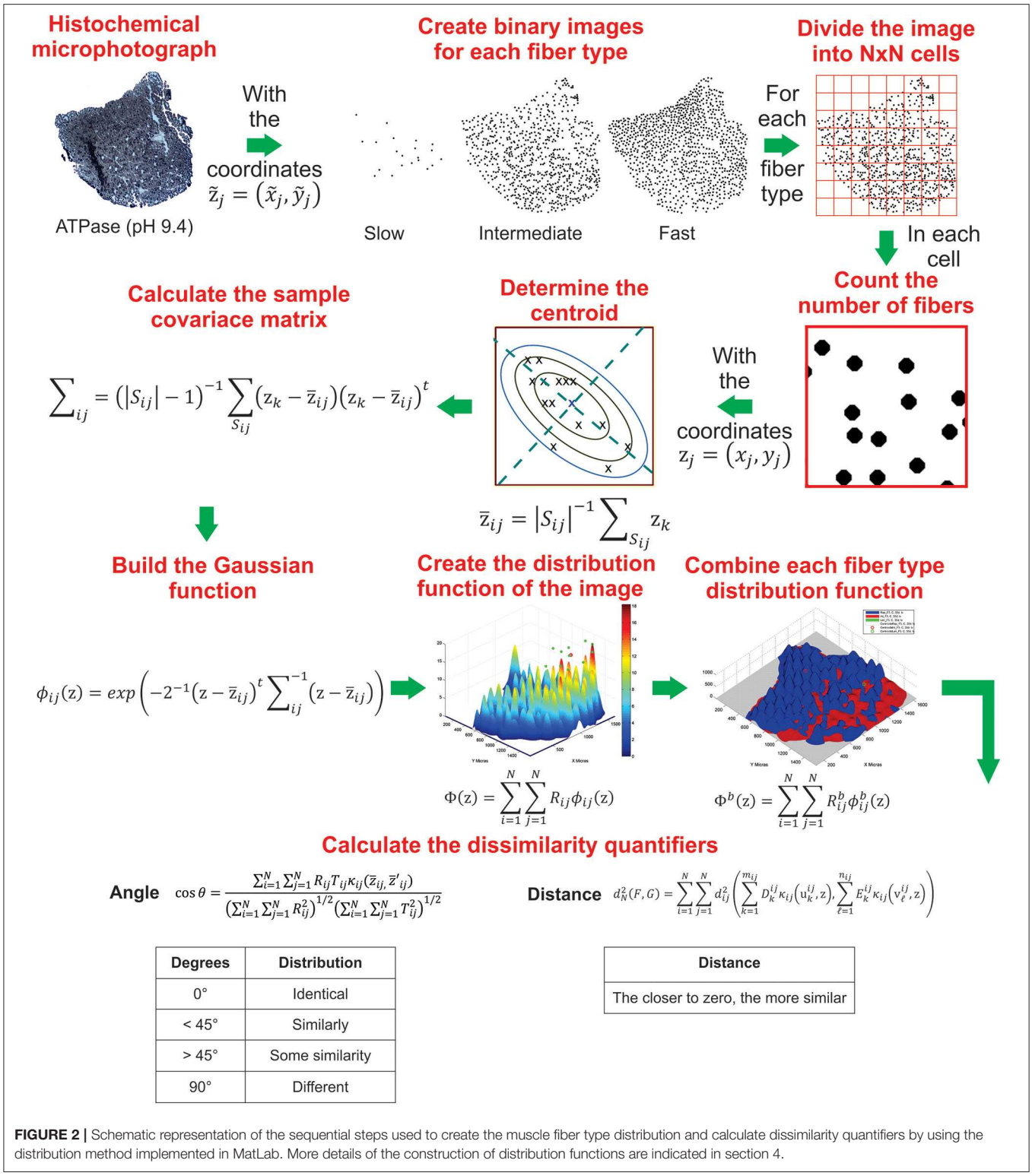

Degrees	Distribution
0°	Identical
< 45°	Similarly
> 45°	Some similarity
90°	Different

Distance
The closer to zero, the more similar

FIGURE 2 | Schematic representation of the sequential steps used to create the muscle fiber type distribution and calculate dissimilarity quantifiers by using the distribution method implemented in MatLab. More details of the construction of distribution functions are indicated in section 4.

(*iii*) If Σ_{ij} is singular or nearly so (its determinant is smaller than a pre-established number $\varepsilon_0 > 0$), we apply the following four steps:

(*a*) let $\lambda_1 = \max_{S_{ij}} \|z_k - \bar{z}_{ij}\|^2$, and $\lambda_2 = \lambda_1/9$.

(*b*) pick any z_k in C_{ij} and define $u_1 = (z_k - \bar{z}_{ij})\|z_k - \bar{z}_{ij}\|^{-1}$, then if $u_1 = (v, w)$ let $u_2 = (-w, v)$ so that $u_1^t u_2 = 0$.

(*c*) Let $M = [u_1\ u_2]$ be a 2×2 matrix with columns u_1 and u_2, in that order. and $\Lambda = \text{diag}(\lambda_1, \lambda_2)$ be a diagonal matrix.

(*d*) Redefine $\Sigma_{ij} = M\Lambda M^t$ and construct ϕ_{ij} as in (6).

In the next subsection, we establish that the function Φ in (7) belongs in an inner-product space.

For more details on the method of construction (see **Supplementary Material**).

4.3. Distribution Functions for a Batch of Images

In the previous subsection, we described a methodology to fit one distribution function to one single image. In this section, we show that with a slight modification the methodology can be applied to fit a distribution function for every image in a finite collection of r distinct images, in tandem, for cross comparison. The meaning of having a set of r images depends on the context. For instance, if the points z_k represent the location of muscle fibers, every image could represent muscle fibers of one of r different types. Once a distribution function has been obtained for every image, we wish to calculate distance and angle between pairs of them and assess if those measurements reflect the classification independently established.

The trick now is to make sure that the distribution functions of the images we want to compare, *belong in the same inner-product space* $\mathcal{L}_N$. In order to achieve that we only need to slightly change our definition of the functions ϕ_{ij} in (6). More precisely, we need to modify the definition of the covariance matrix Σ_{ij} in (5) as we now describe.

Similarly, as in the previous section, we divide every image into $N \times N$ cells. Let C^b_{ij} denote cell (i, j) of image b and z^b_k the kth point in that image. Let $S^b_{ij} = \{\mathsf{z}^b_k \in C^b_{ij}\}$ (set of points of image b in its cell C^b_{ij}), and let $|S^b_{ij}|$ represent the number of points in C^b_{ij}. We define the *global sample covariance matrix for cell* (i, j) as follows:

$$\Sigma_{ij} = (\mathcal{S}_{ij} - 1)^{-1} \sum_{b=1}^{r} \sum_{S^b_{ij}} (\mathsf{z}^b_k - \bar{\mathsf{z}}_{ij})(\mathsf{z}^b_k - \bar{\mathsf{z}}_{ij})^t \,, \tag{8}$$

where $\mathcal{S}_{ij} = \sum_{b=1}^{r} |S^b_{ij}|$ and $\bar{\mathsf{z}}_{ij}$ is the *global centroid for cell* (i, j),

$$\bar{\mathsf{z}}_{ij} = \mathcal{S}_{ij}^{-1} \sum_{b=1}^{r} \sum_{S^b_{ij}} \mathsf{z}^b_k \,. \tag{9}$$

Thus, if

$$\phi^b_{ij}(\mathsf{z}) = \exp(2^{-1}(\mathsf{z} - \bar{\mathsf{z}}^b_{ij})^t \Sigma^{-1}_{ij}(\mathsf{z} - \bar{\mathsf{z}}^b_{ij})) \,, \tag{10}$$

then

$$\Phi^b(\mathsf{z}) = \sum_{i=1}^{N} \sum_{j=1}^{N} R^b_{ij} \phi^b_{ij}(\mathsf{z}) \tag{11}$$

is the distribution function for sample image b, with $R^b_{ij} = |S^b_{ij}|$. The same observation as in equation (11) may be applied in this case for an alternate choice for the coefficients R_{ij}. We can also adapt cases (*i*), (*ii*), and (*iii*) in the first section to deal with the scenarios in which Σ^{-1} is singular or nearly so.

5. DATA ANALYSIS

In this work, we used the data obtained in a previous study from our group (Vázquez-Mendoza et al., 2017) corresponding to slow, intermediate, and fast fibers in the EDLm fascicles of control and undernourished young rats (35 days old).

5.1. Fiber Type Fractal Organization

In order to assess the fractal organization of the fiber types in the fascicles of the EDLm, we constructed binary images using the (x, y) coordinates of each fiber type with a MatLab program developed in our laboratory. These images were then analyzed using the fractal correlation method in Fractalyse, obtaining the fractal dimension (D), pre-form factor (a), and parameter c. From this analysis, we excluded the slow fibers because of their small number in muscle sections.

5.2. Fiber Type Distribution Functions

Intra-fascicle distribution of fiber types was determined applying the method described in the previous section (4), implemented in a MatLab script. In brief, this method requires the (x, y) coordinates of each fiber type, that are used to create a binary image, which is divided into $N \times N$ cells. In our case, we used an $N = 11$ because in a pilot study we observed that this number of cells allowed us to have cells with a few, many and a large number of fibers. This is relevant due to it lets us visualize the distribution of fibers in an optimal resolution, showing how the fibers form groups and how these groups are distributed within the muscle. Then in each cell, the number of fibers is counted in order to calculate the estimator covariance matrix and the centroid. Subsequently, a Gaussian function is built for each cell. Next, the distribution function of the fiber type is created by the lineal superposition of all Gaussian functions. Finally, the distribution function of each fiber type are merged to visualize them in a single image (**Figure 2**). Also, the (x, y) coordinates are used to calculate the dissimilarity quantifiers, distance (D), and angle (θ), which allows to compare two distribution functions. On one hand, the closer the distance to zero, the more similar are the distributions. On the other hand, angles $< 45°$ indicates similar distributions, whereas angles $> 45°$ indicates dissimilar distributions (**Figure 2**).

In order to determine differences between experimental condition (control and undernourished), we calculated the dissimilarity quantifiers for each pair of distributions within a fascicle (i.e., slow vs. fast, slow vs. intermediate, and intermediate vs. fast), which we called intra-fascicular fiber type distributions. Also, we calculated the dissimilarity quantifiers for synthetic data comparing between shapes (ring vs. ball, ring vs. cross, ring vs. sum, ball vs. cross, ball vs. sum, and cross vs. sum) and all quantities of points (500, 1,000, 2,000, 3,000, and 4,000 points).

6. STATISTICAL ANALYSIS

Dissimilarity quantifiers of fiber types distribution, as well as the fractal dimension (D), a, and c indexes between control and undernourished EDLm fascicles, were analyzed performing unpaired Student's t-test or Mann–Whitney test, depending on

its normality, evaluated with the Kolmogorov–Smirnov test. Dissimilarity quantifiers of synthetic data comparisons were analyzed using Person's correlation. Data analysis was performed in GraphPad Prism (v.6.00, GraphPad Sofware, Ca., USA). Significant differences were considered at $P \leq 0.05$. Data are showed as mean ± S.E.M.

7. RESULTS

The data obtained in this study was partially reported in Vázquez-Mendoza et al. (2017), where we found that chronic undernutrition reduces the percentage of intermediate fibers in the F4, increases this fiber type in the F5 and reduces the fast fibers in the F3 and F5, compared to control fascicles (**Table 1**). According to the changes in the proportion of fiber types it could be established the following sequence of fascicles affected by chronic undernutrition (most to less): $F3 > F5 > F4 = F2$. According to the later, Vázquez-Mendoza et al. (2017) proposed that chronic undernutrition evokes a differential effect on the relative proportion of fiber types in EDLm fascicles and suggested that such condition may provoke changes in the intra-fascicle distribution and organization of fiber types.

7.1. Fractal Analysis Results

In order to perform the fractal analysis, we first estimated the *a* index, which needs to be > 0.1 and < 4.0 to treat them as fractals. Fast and intermediate fibers in all fascicles (control and undernourished) showed an *a* in the range of a fractal (**Table 1**; only five values were excluded from the analysis because they showed $a < 0.1$). Although intermediate fibers in the fascicle F5 of the undernourished group showed a significant larger *a* value than the control one ($P < 0.01$) these fibers are still in range. With these results, we were able to treat the individual binary images of fast and intermediate fibers from the control and undernourished rats as fractals. In the case of slow fibers, these were excluded from the analysis due to the lower number of fibers.

Once established that the binary images can be treated as fractal, we estimated the dimension parameter (*D*), which gives us how the fibers are organized within the fascicles. The results showed that fast and intermediate fiber in all EDLm fascicles, of both conditions, had similar *D* values, varying between 1.5 and 1.84 (**Table 1**), indicating that both intermediate and fast fibers are distributed in clusters over the transverse area of each fascicle. Statistical analysis showed that chronic undernutrition only reduced the fractal dimension of fast fibers in the F3, as compared to control (C, 1.73 ± 0.03 vs. U, 1.50 ± 0.08; $P < 0.05$; **Table 1**). Nonetheless, this value still represents a distribution in clusters over the transverse area of the fascicle.

In real-world patterns, fractal behavior may change across scales. Changes often occur within rather small values of ε, i.e., for small distances, often corresponding to the clusters of fibers of the same type. In order to avoid local effects and hence wrong estimations, it is useful to introduce an additional *c* parameter that allows the correct estimation of *D* and *a* values (**Table 1**). Similar to the *a* index, the *c* parameter of fast and intermediate fibers in all fascicles was similar between the groups ($P > 0.05$; **Table 1**), except for the intermediate fibers in the undernourished F5, which showed a significant reduced *c* value as compared to control (C, 6.65 ± 0.90 vs. U, 0.11 ± 1.42; $P < 0.01$) that could be related with the reduction of the muscle CSA due to undernutrition.

TABLE 1 | Percentage fiber composition and fractal organization parameters [*a* index, fractal dimension (*D*), and *c* index] corresponding to the intermediate and fast fiber types present in the different EDLm fascicles (F2, F3, F4, and F5) of control (C) and undernourished (U) rats.

	Composition (%)			
	Intermediate		**Fast**	
	C	**U**	**C**	**U**
F2	57.6 ± 4.5	57.6 ± 5.2	31.7 ± 5.4	37.9 ± 5.4
F3	51.9 ± 5.4	67.2 ± 4.0	46.0 ± 5.5	29.7 ± 4.1*
F4	63.6 ± 2.3	53.6 ± 3.6*	33.3 ± 2.5	42.2 ± 4.0
F5	45.2 ± 2.0	54.4 ± 1.1*	53.7 ± 2.0	44.9 ± 1.1*
	***a* index**			
	C	**U**	**C**	**U**
F2	0.18 ± 0.03	0.22 ± 0.01	0.15 ± 0.03	0.21 ± 0.04
F3	0.20 ± 0.03	0.26 ± 0.03	0.22 ± 0.03	0.43 ± 0.11
F4	0.35 ± 0.10	0.26 ± 0.04	0.27 ± 0.09	0.25 ± 0.07
F5	0.16 ± 0.01	0.24 ± 0.07**	0.25 ± 0.07	0.28 ± 0.02
	Fractal dimension (*D*)			
	C	**U**	**C**	**U**
F2	1.77 ± 0.05	1.80 ± 0.01	1.75 ± 0.03	1.70 ± 0.05
F3	1.78 ± 0.02	1.75 ± 0.03	1.73 ± 0.03	1.50 ± 0.08*
F4	1.75 ± 0.04	1.78 ± 0.02	1.68 ± 0.04	1.74 ± 0.02
F5	1.84 ± 0.01	1.81 ± 0.01	1.80 ± 0.01	1.81 ± 0.01
	***c* index**			
	C	**U**	**C**	**U**
F2	6.54 ± 1.00	5.08 ± 1.01	7.48 ± 1.39	6.72 ± 0.54
F3	4.51 ± 2.18	0.30 ± 3.01	5.50 ± 1.22	6.62 ± 2.48
F4	−2.71 ± 4.87	2.02 ± 2.75	7.66 ± 3.07	4.98 ± 2.08
F5	6.65 ± 0.90	0.11 ± 1.42**	−1.81 ± 1.66	0.75 ± 1.01

*Mean ± S.E.M. Significant differences between C and U were determined using Student's t-test or Mann–Whitney test. *P < 0.05, **P < 0.01. n = 6, except in Intermediate F2C, F2U, F4U, and in Fast F3U, where n = 5, and in Fast F2 C, n = 4.*

Altogether, this analysis showed that intermediate and fast fibers in the four EDLm fascicles (F2, F3, F4, and F5) of the control rats present a fractal organization within the fascicle, i.e., the fiber assembly is distributed in clusters. Also, it showed that this organization is preserved during chronic undernutrition, except for the fast fibers in the F3, whose organization is reduced, but still conserve the distribution in clusters. This probably helps to preserve the optimal muscle functioning despite the alimentary condition.

7.2. Distribution Functions Results

Although the fractal organization was preserved in all fascicles of undernourished rats, the fiber types distributions could be

modified, in order to determine changes in the fiber types distribution we constructed the distribution function of slow, intermediate, and fast fibers of control and undernourished rats.

Before analyzing the distribution function of fiber type, we aimed to determine if our dissimilarity quantifiers could differentiate between very similar distributions. To achieved this, we calculated the dissimilarity quantifiers for synthetic data (**Figure 1**) that present distributions that could be a challenge to our quantifiers. **Tables 2**, **3** contain comparison results with synthetic data, angle measurements are displayed in degrees. In general, we observed an increase in distance values while increasing the number of points ($R^2 = 0.99$, $P < 0.001$, in all comparisons, except Ring vs. Ball, where $R^2 = 0.67$, $P > 0.05$), which did not happen with the angle values (Ring vs. Ball, $R^2 = 0.72$; Ring vs. Cross, $R^2 = 0.20$; Ring vs. Sum, $R^2 = 0.37$; Ball vs. Cross, R^2=0.75; Ball vs. Sum, R^2=0.75; Cross vs. Sum, R^2=0.48; $P > 0.05$, in all cases), of the shapes being compared. Our discussion of these results is given in section 8.2.

7.2.1. Intra-fascicle Distribution of Slow, Intermediate, and Fast Fiber Types

To visualize the intra-fascicle distribution of fibers types, binary density histograms from sections of EDLm fascicles of control and undernourished rats stained with the alkaline ATPase technique were constructed (**Figure 3**). Apparently, most of the undernourished EDLm fascicles (F2, F4, and F5) showed a similar distribution of fiber types as that of control fascicles (**Figures 3A,B,E–H**). In contrast, the internal distribution of fiber types in the F3 of undernourished rats (**Figure 3D**) completely differs from that determined in the control group (**Figure 3C**).

Once established that the dissimilarity quantifiers are robust to differentiate between distributions, we compared the fiber types distribution between fascicles of control and undernourished male rats, in order to obtain not just a qualitative comparison. Considering that our fascicles sections did not have anatomical orientation and in order to avoid misinterpretation of the results, we compared the intra-fascicular distribution of fiber types and then we compared this values between groups (**Table 4**).

F2 intra-fascicular distributions from the control animals showed distances lower than 60, and angles greater than 45 degrees, suggesting that each fiber type has a distinctive distribution within the fascicle (**Table 4**). And this was similar to the undernourished animals, suggesting that chronic undernutrition does not affect the fiber types distribution of the F2.

In the case of F3, in the control group, we found that distance was between 60 and 90, whereas angles were greater than 45 degrees, indicating that, as with F2, each fiber type distribution is dissimilar to the others (**Table 4**). In contrast, in the undernourished group showed distances smaller than the controls, particularly in the distribution between slow and fast fibers ($P < 0.001$; **Table 4**). In the case of angles, they were also greater than 45 degrees, but the angle between the distribution of intermediate and fast fiber was greater than the control ($P < 0.01$). These results suggest that chronic undernutrition modified the fiber type distribution in the F3, but maintaining differences among them.

For the F4 in the control group, distances were between 50 and 120, but all angles were greater than 45 degrees, suggesting that the fiber types distribution are dissimilar among them (**Table 4**). On the other hand, chronic undernutrition reduced the distances between the slow and intermediate fiber ($P < 0.05$; **Table 4**) and between the fast and intermediate fiber ($P < 0.05$; **Table 4**). Likewise, chronic undernutrition decreased the angles, especially between the fast and intermediate fibers ($P < 0.05$; **Table 4**). This suggests that chronic undernutrition affects the fiber type distribution of the F4, making them more similar among them.

Finally, the F5 of control animal showed distances between 80 and 130, but the angles were grater than 45 degrees between the distribution of slow and intermediate fibers and between slow and fast fibers (**Table 4**). In contrast, the angles between intermediate and fast fibers distribution were lower than 45 degrees, indicating that fast and intermediate fibers distribution is more similar between them than with the slow fiber distribution. Contrary to F4, in F5, chronic undernutrition increased the distance, especially between the slow and intermediate fibers distributions ($P < 0.01$) and between the slow and fast fibers distribution ($P < 0.05$; **Table 4**). Also, increased the angle values, notably between the slow and intermediate fibers distributions ($P < 0.01$; **Table 4**). This indicates that chronic undernutrition, also modifies the intra-fascicular fibers distribution in the F5, making the slow fiber

TABLE 2 | Distance (D) and angle (θ) for artificial data.

Synthetic data	Ring vs. Ball		Ring vs. Cross		Ring vs. Sum	
Points	***D***	***θ***	***D***	***θ***	***D***	***θ***
500	44.44	75.59	27.51	83.19	29.32	84.46
1,000	78.36	65.58	57.34	85.50	58.10	80.50
2,000	144.88	64.10	101.98	85.42	107.54	82.27
3,000	203.90	59.17	151.85	83.38	155.11	79.78
4,000	273.52	60.36	193.62	82.81	210.09	80.88
Mean	149.02	64.96	106.460	84.06	112.03	81.58
S.E.M.	92.82	6.50	67.68	1.30	72.87	1.85

500, 1,000, 2,000, 3,000, and 4,000 points. Ring vs. ball, ring vs. cross, and ring vs. sum.

TABLE 3 | Distance (D) and angle (θ) for artificial data.

Synthetic data	Ball vs. Cross		Ball vs. Sum		Cross vs. Sum	
Points	***D***	***θ***	***D***	***θ***	***D***	***θ***
500	42.91	73.19	44.89	77.61	27.77	83.37
1,000	81.59	70.73	84.05	72.62	56.61	82.33
2,000	145.53	65.04	145.22	64.35	99.69	83.08
3,000	214.80	64.81	209.16	61.80	135.39	79.66
4,000	285.31	65.06	283.28	63.85	192.16	82.63
Mean	154.03	67.77	153.32	68.05	102.32	83.01
S.E.M	98.23	3.93	95.69	6.76	64.84	2.78

500, 1,000, 2,000, 3,000 and 4,000 points. Ball vs. cross, ball vs. sum, cross vs. sum.

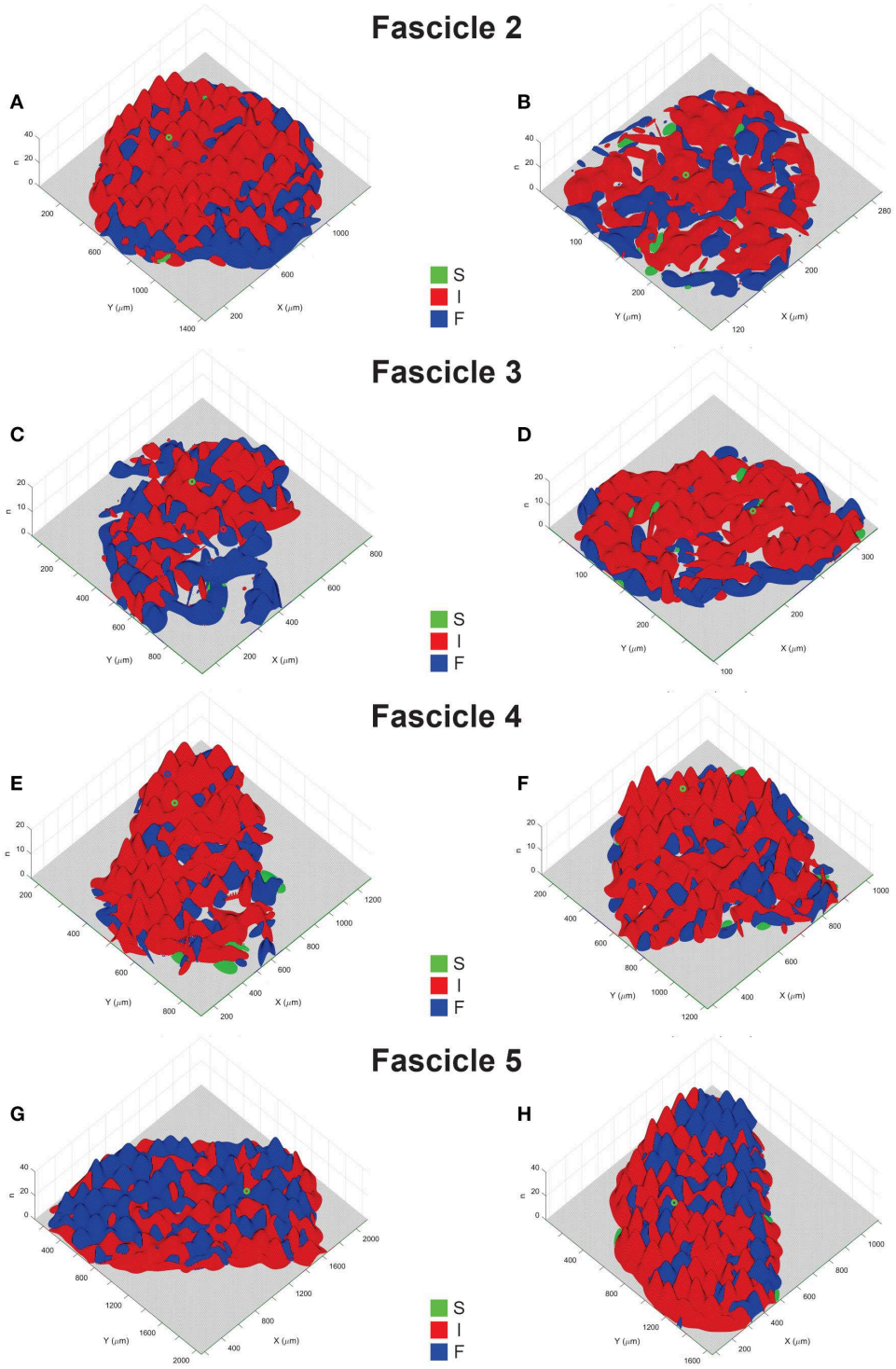

FIGURE 3 | Representative distribution functions maps of slow (S), intermediate (I) and fast (F) fibers in the EDLm fascicles (F2, F3, F4, and F5) from control **(A, C, E, G)** and undernourished **(B, D, F, H)** rats. The *X-axis Y – axis* represent the length and width of the cross-section of the fascicles, whereas the *Z – axis* represents the number of fibers (n). Qualitatively, we can observe that each fascicle present a characteristic distribution pattern of each fiber type, which is modified by chronic undernutrition, more evident in the F3. Quantitatively, dissimilarity quantifiers showed that, indeed, intra-fascicular distributions in F3, F4, and F5 are altered, becoming both, more similar and more dissimilar, for details see text.

TABLE 4 | Distance (*D*) and angle (θ) of the intra-fascicular fiber type distributions (slow vs. intermediate, *SvsI*; slow vs. fast, *SvsF*; intermediate vs. fast, *IvsF*) in the EDLm fascicles (F2, F3, F4, and F5) of control (C) and undernourished (U) rats.

		SvsI		SvsF		IvsF	
		D	θ	*D*	θ	*D*	θ
F2	**C**	59.20 ± 5.39	68.39 ± 0.72	38.95 ± 3.49	72.84 ± 0.93	57.58 ± 3.75	63.98 ± 1.32
	U	53.97 ± 1.97	71.46 ± 1.17	35.47 ± 1.32	75.38 ± 0.56	48.32 ± 137	55.05 ± 1.45
F3	**C**	82.20 ± 6.50	72.76 ± 1.39	68.09 ± 2.71	75.88 ± 0.68	71.75 ± 3.45	50.15 ± 1.16
	U	60.00 ± 3.42	75.98 ± 1.23	27.12 ± 0.84 ***	80.71 ± 0.91	56.89 ± 3.28	65.53 ± 0.96**
F4	**C**	105.01 ± 3.86	80.81 ± 0.74	55.72 ± 2.19	79.62 ± 0.32	116.64 ± 3.91	58.41 ± 1.25
	U	66.45 ± 4.03*	76.31 ± 1.80	53.57 ± 4.53	77.99 ± 1.09	49.60 ± 2.09 *	46.02 ± 1.61
F5	**C**	105.76 ± 4.87	74.07 ± 0.76	122.37 ± 2.31	78.67 ± 0.37	83.23 ± 2.65	40.27 ± 0.71
	U	167.50 ± 3.10**	81.24 ± 0.26**	143.62 ± 2.61 *	81.71 ± 0.46	95.07 ± 2.78	34.13 ± 0.80

*Mean ± S.E.M. Significant differences between C and U were determined using Student's t-test or Mann–Whitney test. *P < 0.05, **P < 0.01, ***P < 0.001. n = 6, except in F4U, where n = 5.*

distribution more dissimilar to the intermediate and fast fibers distributions.

Altogether, these results suggest that chronic undernutrition has a differential effect not just in the fiber type composition, but also in the organization and distribution of the fiber types. And these changes could affect the muscle function and ultimately the behavior (e.g., locomotion).

8. DISCUSSION

Here, we have developed a methodology to compare fiber types organization and distribution in the EDLm fascicles of control and undernourished rats. On one hand, we determined that intermediate and fast fibers in the EDLm fascicles present a fractal organization, i.e., they are distributed in clusters over the transverse area of each fascicle. Likewise, our results showed that chronic undernutrition reduces significantly the fractal organization of fast fibers in the F3, but preserving the organization in clusters. On the other hand, the distribution functions showed that each fiber phenotype has a unique spatial distribution pattern, but chronic undernutrition modifies the intra-fascicular fiber types distributions in the F3, F4, and F5.

8.1. Distribution Function Method

Before discussing the biological data, we make a detailed analysis regarding the methods developed by other authors in previous work on the spatial distribution, especially those based on the calculation of Dirichlet tessellations and adjacency matrices (cf. Venema, 1991, 1995; Grotmol et al., 2002) and correlation dimension (cf. Arsos and Dimitriu, 1995).

Methods based on Dirichlet tessellations (and variations of them) as well as adjacency matrices are particularly useful when one wants to distinguish between two or more classes of points, one of which is scarce in comparison to the others. Dirichlet tessellations provide a strictly *visual* tool when one wishes to establish clustering among two or more classes of points within one single image, as well as to *show* a tendency or pattern in the spread of those classes. However, this method is subjective in the sense that it is the user who decides whether or not there is clustering or spread, and in what direction. In other words, there is no established criterion or numerical parameter by which several users may all agree on the presence or absence of clustering or a pattern within the data sets. Moreover, such methods are mainly restricted to two-dimensional data.

On the other hand, calculation of the correlation dimension is a *quantitative* task which is not constrained to points on the plane. The concept of correlation dimension was introduced in Grassberger and Procaccia (1983a) within the context of dissipative dynamical systems whose phase space evolution is driven by the presence of a strange attractor. This type of attractors arise when the flow of the system is contracting in some directions, expanding in others, and confined within a compact region. This causes the volume element to fold on itself and acquire a multi-sheeted shape with a Cantor-like (self-similar) structure in certain directions, which is directly reflected on the attractor. The latter structures are typically associated to fractal sets (cf. Grassberger and Procaccia, 1983b).

To calculate the correlation dimension, one starts with a sequence of points on the attractor, $\{\mathsf{z}_j : j = 1, \ldots, M\}$, which ideally is a time series with fixed time increment time τ, i.e., $\mathsf{z}_j = \mathsf{z}(t + j\tau)$. A measure of the spatial correlation of the points is the quantity (cf. Grassberger, 1983; Grassberger and Procaccia, 1983b):

$$C(\ell) = \lim_{M\to\infty} \frac{1}{M^2} \times \left\{\text{number of pairs } (j,k) \text{ such that } \|\mathsf{z}_j - \mathsf{z}_k\| < \ell\right\}. \tag{12}$$

For small values of ℓ, it was established in Grassberger and Procaccia (1983b) that

$$C(\ell) \sim \ell^{\nu}, \tag{13}$$

where the constant ν is the correlation dimension or correlation exponent (cf. Grassberger, 1983; Grassberger and Procaccia, 1983b). The correlation dimension ν is related to Kolmogorov's capacity *D*, also called box-counting dimension or even "fractal dimension" after Mandelbrot (cf. Mandelbrot, 1977), but the

latter terminology is misleading as there is more than one way to define the dimension of a fractal set (cf. Grassberger, 1983). In Grassberger and Procaccia (1983b), D is identified as the Hausdorff dimension, but the latter has a more involved definition (cf. Farmer et al., 1983). Mandelbrot used the term fractal dimension in reference to the Hausdorff dimension and to the information dimension σ, as follows: $\nu \leq \sigma \leq D$. ν and D solely depend on the metric of the phase space for their calculation, whereas σ also requires defining a probability measure. ν should not exceed, for instance, the embedding dimension of the attractor (i.e., if the z_j's are p-dimensional vectors, then ν should not be greater than p).

In applications (e.g., measurements obtained from observations carried out in a laboratory), however, only a finite set of measurements will be available and thus considering the limit in Equation (12) is not possible. In that case Equation (12) is replaced by the following:

$$C(\ell) = \frac{2}{M(M-1)} \times \left\{\text{number of pairs } (j,k) \text{ such that } \|\mathsf{z}_j - \mathsf{z}_k\| < \ell\right\}; \tag{14}$$

observe that the coefficient $2/M(M-1)$ is the reciprocal of the maximum number of different pairs of data points. When using Equation (14) M is *expected* to be (sufficiently) large and the relation Equation (13) is still *assumed* to hold approximately for $\ell \in I$, where I is an open interval contained in $(\delta_{min}, \delta_{max})$ with δ_{min} the minimum distance between two data points and δ_{max} the maximum distance (the diameter of the point set). In the context of this work, which is the same as that of Arsos and Dimitriu (1995), these two hypotheses are important. Eckmann and Ruelle (1992) shows how to estimate the number of points necessary in order for Equation (14) to yield a meaningful result. Our method of construction of distribution functions does not need those hypotheses.

We now discuss the meaning of the exponent ν in Equation (13). Recall that Equation (13) is a law that is assumed to hold approximately for the right-hand side of (Equation 14), for ℓ values within a certain interval I. Even though the following two cases will not be meaningful to us, they are nonetheless convenient to discuss for the sake of clarity. If there is only one pair of points at a distance δ from each other, that is $M = 2$, then $C(\ell) = 0$ for $\ell \leq \delta$ and $C(\ell) = 1$ if $\ell > \delta$. In such case one can consider that $\nu = 0$ as $\ell^0 = 1$. When there is only one point in the data set, ν is *defined* as zero. Now, in general, when the data set is finite, but large (M large), it is customary to estimate ν by plotting $\log C(\ell)$ against $\log \ell$ and adjusting a line over the range of values of ℓ for which a linear tendency is observed, such tendency is expected to be easily detected for M sufficiently large. This, thus can be considered the criterion by which to consider that the size of the data set is adequate for purposes of the study. In this scenario, ν gives the growth rate of the number of data pairs at a distance no greater than ℓ. When $\nu = 1$, the growth is considered "neutral," that is, no clear tendency toward either spreading or clustering among data points can be declared. When $0 < \nu < 1$, this means a slower-than-linear growth in the number of pairs of points at a distance at most ℓ, in other words, one can speak of a tendency in the data toward clustering. On the contrary, when $\nu > 1$, it means an accelerated growth (greater than linear) in the number of points at a distance at most ℓ that is, the data points are spreading (no clustering). We think this interpretation is the most honest conclusion one can derive from the calculation of the correlation dimension alone, in the context of this work (and that of Arsos and Dimitriu, 1995), that is, outside of the dynamical systems context.

Pullen (1977a,b) uses a simple quantitative technique to analyze fiber composition and distribution of the adult tibialis anterior muscle in rats. The author considers complete cross-sections of the muscle in different specimens and sets deep-superficial and medial-lateral axes. Histological images are then projected on a counting grid. Only those cells of the grid along the axes are considered. The magnification of each image is set so that fifty to one hundred fibers are shown in each cell and their identification is possible. For each cell along the axes the fiber ratio (fiber type over total number of fibers in the cell) is determined for three different types of fibers which the authors name IIA, I, and IIB, and correspond to intermediate, slow and fast fibers, respectively, according to their oxidative, phosphorylase, and ATPase histochemistry. Then, for each cell, histograms are constructed to appreciate fiber distribution and muscle composition. The variance among histograms is then analyzed. The results obtained showed that, not only distribution of fiber histochemical types varies across an entire cross-section of the muscle, but also the histochemical technique employed seems to affect the quantitative analysis. Fiber cross-section area is also calculated, in an attempt to verify disparities found among classification of fibers based on different histochemical techniques. The author concludes with a few important observations such as fiber classification based on different histochemical techniques may produce different distributions profiles.

The relevance of Pullen (1977a,b) to our study comes from the fact that it considers a division of the cross-section of a muscle, by the deep-superficial and medial-lateral axes. Along these axes, cells of a counting grid are considered. Within each cell of this grid, a relative count of fiber types is performed and a profile of each fiber type distribution is revealed, by drawing histograms put together with the counts of all cells along each axis. The distribution profiles obtained by the author sweep along the perpendicular directions of the axes, not across the entire muscle. Our study is more focalized as it considers fascicles, but it does so entirely. We also construct distribution functions which we later use to be able to compare among fiber types and try to establish parameters for their distinction (distance and angle between pairs of them).

In another study, Henriksson-Larsén et al. (1983) focused on the importance of defining the biopsy depth when analyzing the distribution of different types of fibers of human skeletal muscle (tibialis anterior). Two types of fibers were considered based on enzyme histochemical classification criteria: type 1 (red, slow-twitch, and oxidative) and type 2 (white, fast-twitch, and glycolytic). The authors report significant variations in the relative number of fibers depending on the depth of the muscle biopsy (human tibialis anterior). There are two main

reasons why Henriksson-Larsén et al. (1983) seems relevant to our study:

1. It brings about the question of whether biopsy depth should be a factor to be taken into consideration. Given the size of the specimens used in our work, this point does not seem relevant.
2. In **Figure 2**, the authors have a histogram of fibers type 2, followed (**Figure 2D**) by a contour plot. For these figures, a grid was drawn on every mounted section of a muscle. Each cell of the grid drawn on the image had a side length of 1mm and was divided into nine sub-cells. The total number of fibers for each type was determined for the central sub-cell only (one-ninth of the whole cell). However, the authors do not detail how they determine the size of the grid or the method used to obtain the contour map (for the latter they used a computer program, but they did not mention which one). The authors use these contour plots to visually assess the distribution of fibers on a cross-section of the muscle, but they do not try to establish a method to compare two distributions (as we did in our work), nor do they attempt to give a more formal definition to the term distribution (as we did in our work).

In Wang and Kernell (2001), advantage is taken of the match between motoneuronal nerve endings and their muscle fibers, so that studying the spatial distribution of the latter will translate into properties of the spatial distribution of the former. To that end, the authors devise two methods for determining the position and the extent of muscle fibers within a muscle cross-section: the "mass vector method" and the "sector method." The authors developed these methods in order to get on the subject of degree and direction of what they call fiber type regionalization, something that had been missed by previous studies which are more focused on providing a detailed or pointwise description of the muscle fiber distributions (Johnson et al., 1973; Pullen, 1977a,b; Armstrong and Phelps, 1984). The specific questions that the methods developed by the authors address are: how much does the center for a given fiber type population differ from that for the muscle as a whole? (vector method) and, how much of the available cross-section space of a muscle is utilized by a given fiber type? (sector method). The vector method designed by the authors allows two things. On one hand, it allows pointing at a specific region within the muscle being observed, in which certain type of fibers are distributed. This is done by constructing the "mass vector," which is a vector that points from the centroid of the muscle section to the centroid of the fiber set. On the other hand, by scaling the mass vector by the diameter of a circle, whose area is that of the cross-section of the muscle, one obtains the "fiber target vector." The latter can be compared in length and in magnitude with other fiber target vectors from similar samples. Both, the mass and the fiber target vectors, account for the general location of the set of fibers as a whole, within the muscle. To account for the extent of the fiber set within the muscle cross-section, the authors designed the sector method. As in the case of the convex hull method, the section method determines what percentage of the total cross-section area of the muscle is being covered by the fibers under study. Unlike the convex hull method, the sector method tends to exclude regions of the cross-section that are not populated by fibers, and which would otherwise be included in the convex hull method due to the irregularity of the fiber set perimeter. However, the sector method has the disadvantage of being semi-automatic. The number of sectors to be considered must be determined by the experimenter. Too many sectors will tend to produce a fragmented picture of the occupied region, and too few sectors will cause that some fibers will fall outside of their region.

The relevance of Wang and Kernell (2001) to our work is in that, in essence, is the closest to the type of analysis we performed. More precisely, it tries to quantify the spatial localization of fibers and the region of the muscle cross-section they occupy. Like in the case of the sector method, our method is semi-automatic (the size of the counting grid must be determined by the experimenter). However, our method does provide a distribution function per se, which accounts for actual spatial location and number of fibers. The vector method provides a general direction in which fibers are located, but does not provide a sense of how fibers are distributed around the head of the mass vector. Our method specifically tells the experimenter where fibers are located within the muscle cross-section.

8.2. Dissimilarity Quantifiers

It is evident from our results that distance measurements show a tendency to increase as the number of points in the data set increases. In contrast, angle measurements seem to stabilize themselves as the number of data points increases, that is as more information is known about the data sets. Moreover, based on angle measurements alone we see that, as the data set increases (and thus becomes more defined), the pair ring vs. ball became the more similar pair among all, followed the ball vs. sum, and the ball vs. cross. Nonetheless, for these three pairs of shapes the angle between distributions is around or above 60 degrees which is two thirds of 90 degrees (maximum transversality) and four thirds of 45 degrees (halfway between colinearity and perpendicularity), therefore we think this is still clear evidence that the angle quantifier can serve as a tool to tell apart between two images. Note also that from the start the angle quantifier was able to distinguish the ring from the cross, the ring from the sum, and the cross from the sum, returning angles closer to 90 degrees.

The above discussion suggests that the angle quantifier is helpful in telling apart data sets which are uniformly distributed in all directions and highly localized (the ring), from data sets which are uniformly distributed and highly localized in specific directions (the sum and the cross), and even two data sets in the latter category so far as they are distributed along two distinct directions.

Currently, our distance quantifier depends strongly on the data size, but this can be fixed in the manner we suggest in the next paragraph. Right now, we want to make our point that angle and distance quantifiers are complementary dissimilarity quantifiers, in other words, they must both be used by the researcher who is trying to set apart two data sets based on the geometry of their spatial distributions. The argument is rather evident: based on **Tables 1**, **2**, we see that the angle quantifier did not perform so as well setting aside the ring from the ball, the ball from the cross, and the ball from the sum, as it did setting

apart the ring from the cross, the ring from the sum, and the cross from the sum. For instance, the angle value in the ring vs ball with 4,000 points is just above sixty degrees, whereas for a data set of the same size, the angle value in the ring vs sum is about 81 degrees, this amounts to a roughly 20 degree difference, and we perhaps "lose confidence" in the angle quantifier. But when we look at those same cases, the distance measurement for the ring vs. ball pair is 273, whereas for the ring vs. sum pair is 210, which tells us that the distance quantifier is better at distinguishing one data set from the other in the ring vs. ball pair, by a difference of over 60 units, so we "gain confidence" in this quantifier. In essence, when we think one quantifier is not performing to our standards, the other may be doing a better job.

To fix the scaling effect of the data set on the distance (larger data sets seem to yield larger values of the distance), we propose to modify our definition of the distance quantifier in the following way which completely eliminates that effect. Let

$$D = d/(1 + d),$$

where d is the distance as calculated by (Equation S19, **Supplementary Material**). D is bounded below by zero and above by one and it is well-known in functional analysis that it also satisfies the properties of a metric. We are currently testing this quantifier and our preliminary results suggest that it is more subtle to appreciate differences in distance readings with this quantifier.

These preliminary results on artificial data suggest that the method of construction of distribution functions, as well as their "measure of dissimilarity" (distance and angle), are adequate tools to distinguish among trends of spread and clustering within the data. The case presented here is that of two-dimensional data, but of course the methodology lends itself to study the case of higher-dimensional data, with straightforward modifications on the sample covariance matrix.

Lastly, we must note that, whereas the sample covariance matrix suffers from the effect of "high dimensionality of the data" (it is a square matrix of size d, where d is the dimension of the data vectors), distance and angle evaluations solely depend on kernel evaluations which are convenient from a computational standpoint.

8.3. Fiber Type Organization and Distribution on the EDLm Fascicles

It is well known that skeletal muscles actively participate in the extension and flexion of articular joints (Lindstedt, 2016) as well as during changes in position (muscle length) or during generation of force (muscle strength) (Schappacher-Tilp et al., 2015). Such muscle properties allow vertebrate organisms to perform changes in posture and locomotion (Frontera and Ochala, 2015). It has been considered that each muscle is constituted by a variable proportion of slow, intermediate, and fast fibers. In the rat, the EDL muscle, an extensor muscle involved in the extension of the toes (2nd to 5th) and dorsiflexion of the ankle, is mostly conformed by fast-twitch fibers, meanwhile the soleus muscle, one of the flexor muscles of the calf, mainly contains slow-fiber twitch fibers (Armstrong and Phelps, 1984; Soukup et al., 2002). In addition, it has been proposed that contractile properties of each individual muscle are closely related to the relative proportion of fibers types and to their intra-muscle distribution in the cross-sectional area, mainly in the medial part of the muscle (Myatt et al., 2011).

In this study, we analyzed the fractal organization of fiber types in fascicles of the EDLm from well-nourished and undernourished rats. Our previous results (Vázquez-Mendoza et al., 2017) indicate that each fascicle in the EDLm, from both well-nourished and undernourished rats, showed a particular composition of fibers types. The relative proportion of intermediate and fast fibers in undernourished fascicles F2 and F4 had no significant differences with that of control fascicles, while the relative proportion of fiber types in fascicles F3 and F5 showed notorious differences with respect to controls (see **Table 1**), being the sequential order of fascicles affected by chronic undernutrition as follows: F3>F5>F4=F2. In the present study, we found that the calculated values of a index, D and c parameters corresponding to intermediate and fast fiber types were practically similar between control and undernourished fascicles (F2, F3, F4, and F5), indicating that fibers are organized in clusters over the transverse area of each fascicle. Meanwhile, only fast fibers in the undernourished F3 showed significant differences in fractal parameter D, as compared to those of control muscles, suggesting that fast fibers in the undernourished F3 are slightly less organized in clusters than in control ones. Because of the latter, it could be proposed that such fiber type cluster-organization is used as a mechanism to increase muscle efficiency (Myatt et al., 2011). Then, this change in the organization of fast fiber in the F3 could imply a change in the efficiency of the EDLm.

Although fiber organization was similar between conditions, fiber type distribution analysis showed that chronic undernutrition modifies the intra-fascicular fiber type distribution in the fascicles F3, F4, and F5. As fiber types distributions within a muscle are crucial to its functioning (Burkholder et al., 1994), these changes could induce alterations in muscle functioning. Thus, chronic undernutrition could be changing the efficiency and functioning of the EDLm fascicles.

Altogether, our observations indicate that chronic undernutrition exerts a more complex effect that just on the fiber type composition, finding a differential effect among the EDLm fascicles. Also, there is a differential effect on the distribution of intermediate and fast fibers in the EDLm fascicles and only the fractal dimension or structure of fast fibers in F3 seems to be modified by chronic undernutrition. All these differential effects on the properties of EDLm fascicles could be related to their anatomical position within the muscle and the fiber type composition. The F2 is located in the anterior part, followed by the F3, then the F4, and finally, the F5 is in the posterior part (Balice-Gordon and Thompson, 1988). In our previous work (Vázquez-Mendoza et al., 2017), the F3 was the most affected by chronic undernutrition, in the fiber metabolism as well as in the fiber type, together with the F5 (in fiber type changes) in comparison with the F2 and F4. This probably is related to the similarities of fiber type percentages

composition (Vázquez-Mendoza et al., 2017). However, our data do not allow us to explain why a chronic food deprivation evoked such differential action on the EDLm fascicles, particularly on fascicles F3 and F5. In addition, it remains to be elucidated how the alterations provoked by undernutrition on the composition and fractal organization of fiber types in F3 affect the extension of the third toe and dorsiflexion of the ankle during a particular motor act (e.g., during gait locomotion).

9. CONCLUSION AND FUTURE APPLICATIONS

RBF distribution functions constitute not only a visual aid to, for example, assess muscle structure and organization in the form of fiber distribution, but they also provide quantitative means by which to distinguish spatial distribution of fiber types. Those means are our dissimilarity quantifiers, distance and angle, defined between pairs of distribution functions. The mathematics of these quantifiers rests soundly on learning theory, and ultimately on functional analysis. Our results on artificial data suggest that distance and angle are dissimilarity quantifiers that complement one another. The angle quantifier is able to set apart data sets that spread along definite linearly independent directions in space or sets that spread along definite directions from sets that are uniformly spread along all directions while forming a single coherent cluster pattern (e.g., a ring). However, the angle quantifier is less able to set apart sets that are uniformly spread say, in the ring or in the ball type-of patterns, it is in these circumstances when the distance quantifier may be a better tool to distinguish between the two sets.

Other scenarios where the proposed method can be used is in current research oriented to reveal possible structural alterations of muscles provoked by traumatic processes, such as spinal cord injury, motor nerve damage, multiparity, or undernutrition/obesity. Of course, one may also use other histochemical techniques.

Finally, we would like to mention that although the problem that motivated this work comes from physiology, we hope that, given the potential to use the distance and angle quantifiers with high-dimensional data, the mathematical tools herein developed can also serve in other fields of Computational Biology.

DATA AVAILABILITY STATEMENT

All datasets generated for this study are included in the article/**Supplementary Material**.

ETHICS STATEMENT

The animal study was reviewed and approved by All experiments were performed in accordance with the Guide for the Care and Use of Laboratory Animals (National Research Council, 2010; National Institutes of Health, Bethesda, MD, USA; Animal Welfare Assurance #A5036-01). The animal protocols were approved by the Institutional Bioethical Committee for the Care and Handling of Laboratory Animals (UPEAL-Protocol 013–02, CINVESTAV).

AUTHOR CONTRIBUTIONS

ER-T, JV-R, KL-G, SQ-G, and IJ-E conceived and designed the study. JV-R developed the theory for the distribution functions and dissimilarity quantifiers. EV-M carried out the experiments and analyzed the biological data. GC-F created the Matlab code for generating the synthetic data, binary images, distribution functions, and dissimilarity quantifiers. All authors contributed in writing the manuscript.

ACKNOWLEDGMENTS

The authors gratefully acknowledge partial support by grants Fundación Sofía Kovalevskaya (Sociedad Matemática Mexicana) to ER-T, Sistema Nacional de Investigadores to ER-T, KL-G, SQ-G, and IJ-E, and Programa para el Desarrollo Profesional Docente, PRODEP Convenio UAEHGO-103.5-14-10567 to ER-T.

SUPPLEMENTARY MATERIAL

The Supplementary Material for this article can be found online at: https://www.frontiersin.org/articles/10.3389/fphys.2020.00777/full#supplementary-material

REFERENCES

Ariano, M., Edgerton, V., and Armstrong, R. (1973). Hindlimb muscle fiber populations of five mammals. *J. Histochem. Cytochem.* 21, 51–55. doi: 10.1177/21.1.51

Armstrong, R. B., and Phelps, R. O. (1984). Muscle fiber type composition of the rat hindlimb. *Am. J. Anat.* 171, 259–272. doi: 10.1002/aja.1001710303

Arsos, G. A., and Dimitriu, P. P. (1995). A fractal characterization of the type ii fiber distribution in the extensor digitorum longus and soleus muscles of the adult rat. *Muscle Nerve* 18, 961–968. doi: 10.1002/mus.880180907

Balice-Gordon, R. J., and Thompson, W. J. (1988). The organization and development of compartmentalized innervation in rat extensor digitorum longus muscle. *J. Physiol.* 398, 211–231. doi: 10.1113/jphysiol.1988.sp017039

Buhmann, M. D. (2003). *Radial Basis Functions: Theory and Implementations, Vol. 12*. Cambridge, UK: Cambridge University Press. doi: 10.1017/CBO9780511543241

Burkholder, T. J., Fingado, B., Baron, S., and Lieber, R. L. (1994). Relationship between muscle fiber types and sizes and muscle architectural properties in the mouse hindlimb. *J. Morphol.* 221, 177–190. doi: 10.1002/jmor.1052210207

Cristianini, N., and Shawe-Taylor, J. (2000). *An Introduction to Support Vector Machines and Other Kernel-Based Learning Methods*. Cambridge, UK: Cambridge University Press. doi: 10.1017/CBO9780511801389

Cucker, F., and Zhou, D. X. (2007). *Learning Theory: An Approximation Theory Viewpoint, Vol. 24*. Cambridge, UK: Cambridge University Press. doi: 10.1017/CBO9780511618796

Devroye, L., Györfi, L., and Lugosi, G. (2013). *A Probabilistic Theory of Pattern Recognition, Vol. 31*. New York, NY: Springer Science & Business Media.

Duda, R. O., Hart, P. E., and Stork, D. G. (2012). *Pattern Classification*. New York, NY: John Wiley & Sons.

Eckmann, J.-P., and Ruelle, D. (1992). Fundamental limitations for estimating dimensions and lyapunov exponents in dynamical systems. *Phys. D* 56, 185–187. doi: 10.1016/0167-2789(92)90023-G

Farmer, J., Ott, E., and Yorke, J. A. (1983). The dimension of chaotic attractors. *Phys. D* 7, 153–180. doi: 10.1016/0167-2789(83)90125-2

Frankhauser, P. (1993). *La fractalité des structures urbaines* (Ph.D. thesis). Université Paris 1 Panthéon-Sorbonne, Paris, France.

Frankhauser, P. (1998). "The fractal Approach. A new tool for the spatial analysis of urban agglomerations," in *Population: An English Selection*, Vol. 10 (JSTOR), 205–240.

Frontera, W. R., and Ochala, J. (2015). Skeletal muscle: a brief review of structure and function. *Calcif. Tissue Int*. 96, 183–195. doi: 10.1007/s00223-014-9915-y

Giesl, P. (2007). *Construction of Global Lyapunov Functions Using Radial Basis Functions, Vol. 1904*. Heidelberg: Springer. doi: 10.1007/978-3-540-69909-5

Gouyet, J.-F. (1996). *Physics and Fractal Structures*. New York, NY: Springer Verlag.

Grassberger, P. (1983). Generalized dimensions of strange attractors. *Phys. Lett. A* 97, 227–230. doi: 10.1016/0375-9601(83)90753-3

Grassberger, P., and Procaccia, I. (1983a). Characterization of strange attractors. *Phys. Rev. Lett*. 50:346. doi: 10.1103/PhysRevLett.50.346

Grassberger, P., and Procaccia, I. (1983b). Measuring the strangeness of strange attractors. *Phys. D* 9, 189–208. doi: 10.1016/0167-2789(83)90298-1

Grotmol, S., Totland, G. K., Kryvi, H., Breistøl, A., Essén-Gustavsson, B., and Lindholm, A. (2002). Spatial distribution of fiber types within skeletal muscle fascicles from standardbred horses. *Anat. Rec*. 268, 131–136. doi: 10.1002/ar.10140

Guth, L., and Samaha, F. J. (1970). Procedure for the histochemical demonstration of actomyosin ATPase. *Exp. Neurol*. 28, 365–367. doi: 10.1016/0014-4886(70)90244-X

Henriksson-Larsén, K. B., Lexell, J., and Sjöström, M. (1983). Distribution of different fibre types in human skeletal muscles. I. Method for the preparation and analysis of cross-sections of whole tibialis anterior. *Histochem. J*. 15, 167–178. doi: 10.1007/BF01042285

Hernández, S. A., and Menéndez-Conde, F. (2013). "Explicit spectral decimation for a class of self-similar fractals," in *Abstract and Applied Analysis, Vol. 2013* (Hindawi). doi: 10.1155/2013/756075

Jelinek, H. F., and Fernandez, E. (1998). Neurons and fractals: how reliable and useful are calculations of fractal dimensions? *J. Neurosci. Methods* 81, 9–18. doi: 10.1016/S0165-0270(98)00021-1

Johnson, M., Polgar, J., Weightman, D., and Appleton, D. (1973). Data on the distribution of fibre types in thirty-six human muscles: an autopsy study. *J. Neurol. Sci*. 18, 111–129. doi: 10.1016/0022-510X(73)90023-3

Kissane, R., Egginton, S., and Askew, G. N. (2016). Contractile properties of the rat extensor digitorum longus muscle in relation to regional variation in fibre type composition. *FASEB J*. 30(1 Suppl.), 1245.10–1245.10. Available online at: https://faseb.onlinelibrary.wiley.com/doi/10.1096/fasebj.30.1_supplement.1245.10

Liebovitch, L. S., Fischbarg, J., and Koniarek, J. P. (1987). Ion channel kinetics: a model based on fractal scaling rather than multistate Markov processes. *Math. Biosci*. 84, 37–68. doi: 10.1016/0025-5564(87)90042-3

Lindstedt, S. L. (2016). Skeletal muscle tissue in movement and health: positives and negatives. *J. Exp. Biol*. 219, 183–188. doi: 10.1242/jeb.124297

Mandelbrot, B. (1977). *Fractals Form, Chance and Dimension*. WH Freeman and Co.

Mandelbrot, B. B. (1983). *The Fractal Geometry of Nature/Revised and Enlarged Edition*. New York, NY: WH Freeman and Co.

Myatt, J. P., Schilling, N., and Thorpe, S. K. S. (2011). Distribution patterns of fibre types in the triceps surae muscle group of chimpanzees and orangutans. *J. Anat*. 218, 402–412. doi: 10.1111/j.1469-7580.2010.01338.x

Pullen, A. (1977a). The distribution and relative sized of fibre types in the extensor digitorum longus and soleus muscles of the adult rat. *J. Anat*. 123(Pt 2):467.

Pullen, A. (1977b). The distribution and relative sizes of three histochemical fibre types in the rat tibialis anterior muscle. *J. Anat*. 123(Pt 1):1.

Rasband, W. S. (2011). *ImageJ, US National Institutes of Health*. Bethesda, MD. Available online at: http://imagej.nih.gov/ij/

Reese, T. M., Brzoska, A., Yott, D. T., and Kelleher, D. J. (2012). Analyzing self-similar and fractal properties of the *C. elegans* neural network. *PLoS ONE* 7:e40483. doi: 10.1371/journal.pone.0040483

Ruiz-Rosado, A., Cabrera-Fuentes, H. A., González-Calixto, C., González-López, L., Cázares-Raga, F. E., Segura-Alegría, B., et al. (2013). Influence of chronic food deprivation on structure-function relationship of juvenile rat fast muscles. *J. Muscle Res. Cell Motil*. 34, 357–368. doi: 10.1007/s10974-013-9357-6

Schappacher-Tilp, G., Leonard, T., Desch, G., and Herzog, W. (2015). A novel three-filament model of force generation in eccentric contraction of skeletal muscles. *PLoS ONE* 10:e117634. doi: 10.1371/journal.pone.0117634

Schölkopf, B., Tsuda, K., Vert, J.-P., Istrail, D. S., Pevzner, P. A., Waterman, M. S., et al. (2004). *Kernel Methods in Computational Biology*. MIT Press. doi: 10.7551/mitpress/4057.001.0001

Soukup, T., Zacharová, G., and Smerdu, V. (2002). Fibre type composition of soleus and extensor digitorum longus muscles in normal female inbred lewis rats. *Acta Histochem*. 104, 399–405. doi: 10.1078/0065-1281-00660

Tannier, C., and Pumain, D. (2005). Fractals in urban geography: a theoretical outline and an empirical example. *Cybergeo* doi: 10.4000/cybergeo.3275

Thomas, I., Frankhauser, P., and Biernacki, C. (2008). The morphology of built-up landscapes in wallonia (Belgium): a classification using fractal indices. *Landsc. Urban Plann*. 84, 99–115. doi: 10.1016/j.landurbplan.2007.07.002

Thomas, I., Frankhauser, P., and De Keersmaecker, M.-L. (2007). Fractal dimension versus density of built-up surfaces in the periphery of brussels. *Pap. Region. Sci*. 86, 287–308. doi: 10.1111/j.1435-5957.2007.00122.x

Vapnik, V. (1998). *Statistical Learning Theory, Vol. 3*. New York, NY: Wiley.

Vázquez-Mendoza, E., Rodríguez-Torres, E. E., López-García, K., Hinojosa-Rodríguez, C. X., and Jiménez-Estrada, I. (2017). Differential effect of chronic undernutrition on the fiber type composition of fascicles in the extensor digitorum longus muscles of the rat. *Acta Histochem*. 119, 364–371. doi: 10.1016/j.acthis.2017.03.005

Venema, H. W. (1991). Determination of nearest neighbours in muscle fibre patterns using a generalized version of the dirichlet tessellation. *Pattern Recogn. Lett*. 12, 445–449. doi: 10.1016/0167-8655(91)90343-K

Venema, H. W. (1995). Spatial distribution of muscle fibers. *Anat. Rec*. 241, 288–290. doi: 10.1002/ar.1092410216

Wang, L. C., and Kernell, D. (2001). Fibre type regionalisation in lower hindlimb muscles of rabbit, rat and mouse: a comparative study. *J. Anat*. 199, 631–643. doi: 10.1046/j.1469-7580.2001.19960631.x

Wendland, H. (2005). *Scattered Data Approximation Cambridge Monographs on Applied and Computational Mathematics, Vol. 17*. Cambridge: Cambridge University Press. doi: 10.1017/CBO9780511617539

Conflict of Interest: The authors declare that the research was conducted in the absence of any commercial or financial relationships that could be construed as a potential conflict of interest.

Copyright © 2020 Rodriguez-Torres, Viveros-Rogel, López-García, Vázquez-Mendoza, Chávez-Fragoso, Quiroz-González and Jiménez-Estrada. This is an open-access article distributed under the terms of the Creative Commons Attribution License (CC BY). The use, distribution or reproduction in other forums is permitted, provided the original author(s) and the copyright owner(s) are credited and that the original publication in this journal is cited, in accordance with accepted academic practice. No use, distribution or reproduction is permitted which does not comply with these terms.

frontiers in Genetics

ORIGINAL RESEARCH
published: 11 September 2020
doi: 10.3389/fgene.2020.00883

Progesterone Receptor Signaling Selectively Modulates Cytokine-Induced Global Gene Expression in Human Cervical Stromal Cells

Douglas A. Kniss[1,2]* *and Taryn L. Summerfield*[1]

[1] Division of Maternal-Fetal Medicine and Laboratory of Perinatal Research, Department of Obstetrics and Gynecology, The Ohio State University, College of Medicine and Wexner Medical Center, Columbus, OH, United States, [2] Department of Biomedical Engineering, College of Engineering, The Ohio State University, Columbus, OH, United States

OPEN ACCESS

Edited by:
Babatunde Ogunnaike,
University of Delaware, United States

Reviewed by:
Georges Nemer,
American University of Beirut, Lebanon
Debashis Sahoo,
University of California, San Diego, United States

***Correspondence:**
Douglas A. Kniss
kniss.1@osu.edu

Specialty section:
This article was submitted to Systems Biology, a section of the journal Frontiers in Genetics

Received: 24 December 2019
Accepted: 17 July 2020
Published: 11 September 2020

Citation:
Kniss DA and Summerfield TL (2020) Progesterone Receptor Signaling Selectively Modulates Cytokine-Induced Global Gene Expression in Human Cervical Stromal Cells. Front. Genet. 11:883. doi: 10.3389/fgene.2020.00883

Preterm birth (PTB) is the leading cause of morbidity and mortality in infants <1 year of age. Intrauterine inflammation is a hallmark of preterm and term parturition; however, this alone cannot fully explain the pathobiology of PTB. For example, the cervix undergoes a prolonged series of biochemical and biomechanical events, including extracellular matrix (ECM) remodeling and mechanochemical changes, culminating in ripening. Vaginal progesterone (P_4) prophylaxis demonstrates great promise in preventing PTB in women with a short cervix (<25 mm). We used a primary culture model of human cervical stromal fibroblasts to investigate gene expression signatures in cells treated with interleukin-1β (IL-1β) in the presence or absence of P_4 following 17β-estradiol (17β-E_2) priming for 7–10 days. Microarrays were used to measure global gene expression in cells treated with cytokine or P_4 alone or in combination, followed by validation of select transcripts by semiquantitative polymerase chain reactions (qRT-PCR). Primary/precursor (MIR) and mature microRNAs (miR) were quantified by microarray and NanoString® platforms, respectively, and validated by qRT-PCR. Differential gene expression was computed after data normalization followed by pathway analysis using Kyoto Encyclopedia Genes and Genomes (KEGG), Panther, Gene Ontology (GO), and Ingenuity Pathway Analysis (IPA) upstream regulator algorithm tools. Treatment of fibroblasts with IL-1β alone resulted in the differential expression of 1432 transcripts (protein coding and non-coding), while P_4 alone led to the expression of only 43 transcripts compared to untreated controls. Cytokines, chemokines, and their cognate receptors and prostaglandin endoperoxide synthase-2 (PTGS-2) were among the most highly upregulated transcripts following either IL-1β or IL-1β + P_4. Other prominent differentially expressed transcripts were those encoding ECM proteins, ECM-degrading enzymes, and enzymes involved in glycosaminoglycan (GAG) biosynthesis. We also detected differential expression of bradykinin receptor-1 and -2 transcripts, suggesting (prominent in tissue injury/remodeling) a role for the kallikrein–kinin system

in cervical responses to cytokine and/or P_4 challenge. Collectively, this global gene expression study provides a rich database to interrogate stromal fibroblasts in the setting of a proinflammatory and endocrine milieu that is relevant to cervical remodeling/ripening during preparation for parturition.

Keywords: cervix, inflammation, microRNA, preterm birth, transcriptomics

INTRODUCTION

Cervical integrity is crucial for a successful human pregnancy. Throughout most of an uncomplicated gestation, the cervix provides a physical and immune barrier between the interior of the uterus and the vaginal microbiome (Word et al., 2007; Akgul et al., 2014; Vink and Feltovich, 2016). The cervix prepares for parturition by first slow and then rapid transition from an elongated, closed, and rigid structure to an orifice sufficiently soft and dilated to facilitate delivery of the fetus.

Human and animal studies have yielded a working model for the biomolecular underpinnings of cervical remodeling/ripening (Elovitz and Mrinalini, 2004; Word et al., 2007; Timmons et al., 2010; Yellon, 2017). Broadly speaking, normal remodeling is the product of changes in the organization and composition of the extracellular matrix (ECM) during pregnancy, including a decrease in cross-linked collagens I and III, changes in the composition of glycosaminoglycans (GAGs), especially elevated hyaluronan (HA) production, increased tissue hydration, and leukocyte infiltration (Sakamoto et al., 2005; Myers et al., 2009; Akgul et al., 2012; Dubicke et al., 2016).

Progesterone receptor (PR, NR3C3) signaling underpins many of the physiological processes that oppose untimely cervical dilation (Word et al., 2007). Two separate protein isoforms, PR-A (90 kDa) and PR-B (130 kDa), are encoded by a single gene differentially expressed via alternate promoter usage (Kastner et al., 1990; Stjernholm-Vladic et al., 2004). In rodents, pregnancy maintenance requires continued synthesis of progesterone (P_4) by the corpus luteum. Systemic withdrawal of P_4 during luteolysis in rodents evokes cervical ripening and labor at term, while premature cervical ripening is prompted by ovariectomy (Gonzalez et al., 2009). Additionally, pharmacologic antagonism of the PR by mifepristone (RU-486) promotes cervical ripening in animal models (Chwalisz et al., 1994). Conversely, administration of vaginal P_4 reduces the incidence of preterm birth in women with a sonographically validated short cervix (Hassan et al., 2011).

There is strong evidence of the therapeutic utility of P_4 for the prevention of untimely cervical ripening and preterm labor in at-risk women (Conde-Agudelo and Romero, 2016). However, unanswered questions persist regarding the mechanisms by which P_4 influences the expression of inflammation-related genes, including cytokines and chemokines, extracellular matrix (ECM)-modifying enzymes, and bioactive lipid-generating enzymes (e.g., prostaglandin endoperoxidase synthase-2, PTGS-2; microsomal prostaglandin E synthase-1, mPGES; 5-lipoxygenase, 5-LOX) (Kniss, 1999; Sato et al., 2001; Ackerman et al., 2005) in gestational tissues, including the cervix. The overarching goal of the present study was to evaluate gene expression programs (including protein-coding and non-coding RNAs) executed in response to proinflammatory cytokine and/or PR:P_4 stimulation in cervical fibroblasts. Our results revealed a multifaceted profile of gene expression in the cervical stroma, including (1) genes that are cytokine-responsive/P_4-insensitive; (2) genes that are P_4-sensitive/cytokine-independent; (3) genes that are cytokine-responsive and suppressed by P_4; and (4) genes that are augmented by both cytokines and progesterone. These data provide a framework allowing us to construct gene networks involved in the manner by which PR signaling may prevent or delay inflammation-induced cervical ripening and consequent preterm labor. The ultimate goal of this work is that it allows us to identify and develop novel therapeutic targets for prevention and/or management of preterm labor, especially in at-risk women who manifest cervical insufficiency, a major cause of PTB.

MATERIALS AND METHODS

Cervical Stromal Fibroblast Culture

With institutional review board approval (OSU Biomedical IRB Protocol Number 2013H0046), de-identified cervical tissues were obtained from premenopausal women undergoing hysterectomy for benign gynecological conditions. Primary human cervical stromal fibroblasts were isolated via outgrowth from explanted cervical stromal tissues as previously described (Ackerman et al., 2016b). For experiments, cells were grown to confluence in complete Dulbecco's modified Eagle's medium (DMEM, high-glucose, 4.5 g/l) supplemented with 10% fetal bovine serum (FBS), 50 μg/ml gentamicin sulfate, and 0.5 μg/ml amphotericin B (all from Invitrogen, Carlsbad, CA, United States). Next, the cells were rinsed with Dulbecco's phosphate-buffered saline (DPBS) and then incubated in experimental medium containing phenol red-free DMEM/F12 (1:1) with 0.5% charcoal-stripped FBS (prepared in-house using charcoal-dextran extraction, clarification by centrifugation, and sterilization through a 0.2-μm filter) in the absence (0.001% ethanol vehicle control) or presence of 17β-estradiol (17β-E_2, 10^{-8} M; Sigma-Aldrich, St. Louis, MO, United States) for 7–14 days to promote the expression of nuclear progesterone receptors (PRs) (Ackerman et al., 2016b). Finally, cells were incubated for 24 h in the absence or presence of P_4 (10^{-7} M; Sigma-Aldrich), followed by challenge for 4 or 24 h with 0.2 ng/ml of human recombinant interleukin-1β (IL-1β; R&D Systems, Minneapolis, MN, United States) or an equivalent volume of vehicle (PBS with 0.1% bovine serum albumin, BSA). All experiments were performed between the 3rd and 7th passages

after primary explant cultures were prepared. To validate the expression patterns of select transcripts following high-dimensional profiling studies, biological replicate experiments were performed using treatment conditions identical to those described above using a separate set of cell cultures. Cell cultures were routinely tested for mycoplasma species using an in-house PCR-based assay (MycoAlert^{TM}, Lonza, Anaheim, CA, United States).

RNA Extraction

Total RNA was extracted from harvested cells using TRIzol (Invitrogen). Following the addition of chloroform and centrifugation, the aqueous phase was mixed with an equal volume of 100% ethanol, applied to a miRNeasy spin column (Qiagen, Valencia, CA, United States) and processed according to the manufacturer's protocol. The extraction procedure included on-column DNase I digestion using the RNase-Free DNase Set (Qiagen) to remove contaminating genomic DNA. RNA was quantified by absorbance at 260 and 280 nm using a NanoDrop 2000 spectrophotometer (Thermo Fisher, Hudson, NH, United States).

Microarray Analysis

Total RNA (250 ng per sample) was processed using the Ambion WT expression kit (Austin, TX, United States) and labeled with Affymetrix GeneChip (Santa Clara, CA, United States) whole-transcript sense target labeling assay, followed by hybridization to the Affymetrix Human Transcriptome 2.0 array according to the manufacturer's protocols. Following hybridization and scanning, quality control and robust multichip averaging were performed on the feature intensity files using the Affymetrix Expression Console software version 1.4. Gene-level differential expression analysis was subsequently performed using the Affymetrix Transcriptome Analysis Console software version 3.0 using the paired-sample analytical pipeline (one-way repeated-measure ANOVA), and the Benjamini–Hochberg false discovery rate (FDR)-controlling procedure (Reiner et al., 2003). For the default differential gene expression analysis, a linear fold-change threshold of $\pm$ 2 and an FDR of 10% was applied.

Mature MicroRNA Profiling

Multiplexed mature miRNAs were profiled using the Human v3 miRNA Expression Assay (NanoString® Technologies, Seattle, WA, United States). Total RNA (100 ng) was used as input for the nCounter® miRNA sample preparation reactions according to the manufacturer's instructions. Hybridization reactions were performed at 64°C for 18 h. Hybridized probes were analyzed using the nCounter digital analyzer. For each assay, a high-density scan (600 fields of view) was performed. The nSolver® Analysis Software version 3.0 was used for technical normalization. Probes with low levels of expression (defined as less than the mean 2 $\pm$ SD of counts assigned to negative control probes, which was 33.04 in our data set) were omitted from subsequent analyses. Differential expression analysis of the NanoString® data was performed using the edgeR (version 3.14.0) Bioconductor package (Robinson et al., 2010). The trimmed mean of *M*-value normalization was used together with the generalized linear model approach coupled with a paired-sample design matrix. Differential expression was determined using generalized linear model likelihood ratio tests. For FDR control, the Benjamini–Hochberg procedure was used (Reiner et al., 2003).

Quantitative Real-Time Polymerase Chain Reaction (qRT-PCR)

To validate the expression of select mRNAs, 1 μg of total RNA was reverse transcribed to complementary DNA (cDNA) using oligo(dT)$_{12-18}$ primers with SuperScript® III Reverse Transcriptase (Life Technologies, Grand Island, NY, United States). Quantitative PCR was performed using an equal amount of cDNA per sample on a LightCycler 480 II System (Roche Applied Science, Indianapolis, IN, United States) using the following TaqMan® primer/probe sets (Applied Biosystems, Foster City, CA, United States): *BDKRB1* (Hs00664201_s1), *BDKRB2* (Hs00176121_m1), *CXCL8* (Hs00174103_m1), *FKBP5* (Hs01561006_m1), *HAS2* (Hs00193435_m1), *HSD11B1* (Hs00194153_m1), *IL1B* (Hs01555413_m1), *IL6* (Hs00985639_m1), *IRAK3* (Hs00936103_m1), *MMP10* (Hs00233987_m1), *PTGES* (Hs00610420_m1), and *PTGS2* (Hs00153133_m1). The expression of *RPLP0* (4310879E) was used as a reference.

For primary/precursor miRNAs (pri-miRNAs), reverse transcription was performed using the high-capacity complementary deoxyribonucleic acid reverse transcription kit (Applied Biosystems), according to the manufacturer's instructions. Each reaction comprised 10 μl of master mix (10 × reverse transcription buffer, deoxynucleotide triphosphates, reverse transcription random primers, MultiScribe® reverse transcription enzyme (Thermo Fisher Scientific), ribonuclease inhibitor, and nuclease-free water) and 1 μg of RNA (in 10 μl reaction volume). For qRT-PCR, TaqMan® gene expression master mix and TaqMan Pri-miRNA assays (Applied Biosystems) were used. The assays were Hs03303259_pri (*MIR146A*) and Hs03303349_pri (*MIR155*). For mature miRNAs, reverse transcription was performed with total RNA using the TaqMan microRNA reverse transcription kit (Applied Biosystems), per the manufacturer's recommendations. Each reaction received 7 μl of TaqMan gene expression master mix, 5 μl of RNA (10 ng), and 3 μl of the reverse transcription primer appropriate for each target miRNA. TaqMan microRNA assays (Applied Biosystems) were used for qRT-PCR. The following assays were used: 000468 (hsa-miR-146a-5p) and 002623 (hsa-miR-155-5p). The relative abundance of each mRNA or miRNA was calculated by the comparative C_T method (Schmittgen and Livak, 2008).

Bioinformatics

Pathway Analysis

Pathway analysis for microarray data was performed using the Gene Set Enrichment Analysis (GSEA) Java desktop application (version 2.2.2[1]) (Subramanian et al., 2005). For a given gene set,

[1]http://software.broadinstitute.org/gsea

this algorithm calculates an enrichment score, which numerically reflects the degree to which a given dataset is overrepresented within a ranked list of gene expression data. The statistical significance of a given enrichment score is estimated using an empirical permutation test procedure, followed by correction for multiple-hypothesis testing. This analysis method tends to be more sensitive and robust than overrepresentation methods relying solely on differential expression with arbitrary cutoffs (Subramanian et al., 2005). Three databases of curated gene sets were obtained from an online repository[2] (Merico et al., 2010) and queried: 1. Kyoto Encyclopedia of Genes and Genomes (KEGG)[3]; 2. Panther[4]; and 3. Gene Ontology (GO) molecular function[5]. All gene sets with 1–500 members were evaluated using 1000 gene-set permutations (as recommended when fewer than seven samples in any phenotype are available for analysis) by applying the default weighted enrichment statistic, the signal-to-noise ratio metric for ranking genes, and the default method for enrichment score normalization. Additionally, the Ingenuity Pathways Analysis (IPA) upstream regulator algorithm (Qiagen) was employed to infer upstream signaling events potentially contributing to observed gene expression signatures.

Transcription Factor Binding Motif Overrepresentation Analysis

The promoter regions (i.e., FASTA sequences ± 1000 bp relative to each transcription start site) of differentially expressed genes in select conditions were programmatically retrieved from the University of California Santa Cruz hg38 human genome assembly via the TogoWS SOAP API website[6] (Katayama et al., 2010). The "multiple DNA sequences" algorithm of the Transcription Factor Affinity Prediction (Thomas-Chollier et al., 2011) (TRAP) Web Tools suite[7] was used to probe these regulatory regions for transcription factor binding affinities based on position-specific scoring matrices present in the non-redundant JASPAR core vertebrate database (Mathelier et al., 2014) using a background model of all human promoter regions.

Statistical Analysis

Statistical analyses were performed using the Kruskal–Wallis statistical test with *post hoc* testing using Dunn's multiple comparison test when appropriate. A p-value < 0.05 was considered significant. Microarray and qRT-PCR experiments were replicated three times in duplicate (i.e., $n = 6$ samples per treatment). The data were tested for Gaussian distribution, and, if normally distributed, they were expressed as mean ± SEM and evaluated by analysis of variance (ANOVA) followed by *post hoc* testing by the method of Tukey using GraphPad Prism 8.0 software (San Diego, CA, United States).

[2]http://baderlab.org/GeneSets

[3]http://www.genome.jp/kegg/pathway.html

[4]http://www.pantherdb.org/pathway

[5]http://geneontology.org

[6]http://togows.org

[7]http://trap.molgen.mpg.de/cgi-bin/home.cgi

RESULTS

Common and Unique Features of IL-1β and Progesterone Genomic Responses

The experimental design for the studies described throughout this work is shown in **Figure 1A**. Importantly, cervical stromal fibroblasts were stimulated to elicit the expression of progesterone receptors (**Figure 1B**). After carrying out experiments, total RNA from each study group was extracted and purified, quantified, and subjected to microarray analysis of differential gene (coding and non-coding RNAs) expression. To confirm these results, we also conducted follow-up experiments using the identical design with biological replicates (i.e., a separate set of cell cultures not used for microarray analysis) to measure by qRT-PCR transcripts induced by either IL-1β, P_4, or both agents incubated simultaneously. Extensive bioinformatics analysis was conducted using several publicly available genomic analytical tools (KEGG, Panther, and GO algorithms (**Figure 2**).

IL-1β Induces a Broad Array of Transcripts

Cervical fibroblasts cultured as described (Ackerman et al., 2016b) were pretreated for 7–14 days with 10^{-8} M 17β-E_2 to induce nuclear PR expression. Relative to vehicle-treated controls, microarray profiling of cells stimulated for 4 h with IL-1β (0.2 ng/ml) revealed changes in gene expression, with significant (minimum ≥two-fold change in expression and FDR <0.1) upregulation of 913 and downregulation of 519 transcripts (**Figure 2A** and **Supplementary Table S1**). As we observed previously in other intrauterine cell types, e.g., amnion mesenchymal fibroblasts (Li et al., 2011) and uterine decidual stromal cells (Ibrahim et al., 2016), highly IL-1β-induced transcripts included those encoding a wide array of cytokines and chemokines, enzymes involved in prostaglandin synthesis, bradykinin receptors-1 and -2, and matrix metalloproteinases, among others. Other prominent differentially expressed mRNAs included acute phase reactants, members of the complement family including tissue factor pathway inhibitor 2, and other proteases and their inhibitors (**Supplementary Table S1**). Intracellular signal transduction pathways differentially expressed following IL-1β treatment included the interferon (IFN), signal transducer and activator of transcription 5 (STAT5), and mitogen-activated protein kinase (MAP kinase)/phosphatase pathways (**Supplementary Table S1**).

Highly enriched pathways, as determined by the GSEA algorithms (KEGG, Panther, and GO, respectively), included those related to inflammatory signaling, apoptosis, blood coagulation, cell adhesion, and arachidonic acid metabolism (**Figures 2B–D** and **Supplementary Table S2**). Based on this gene expression signature, the IPA upstream regulator algorithm predicted activation of 65 and inhibition of 23 transcriptional regulators. As expected, following proinflammatory cytokine challenge, activation was inferred for nuclear factor-κB (NF-κB), components of the JAK-STAT signaling pathway, interferon regulatory factors (IRFs), activator protein-1 (AP-1) subunits, and Forkhead box (FOX) transcription factors, among many

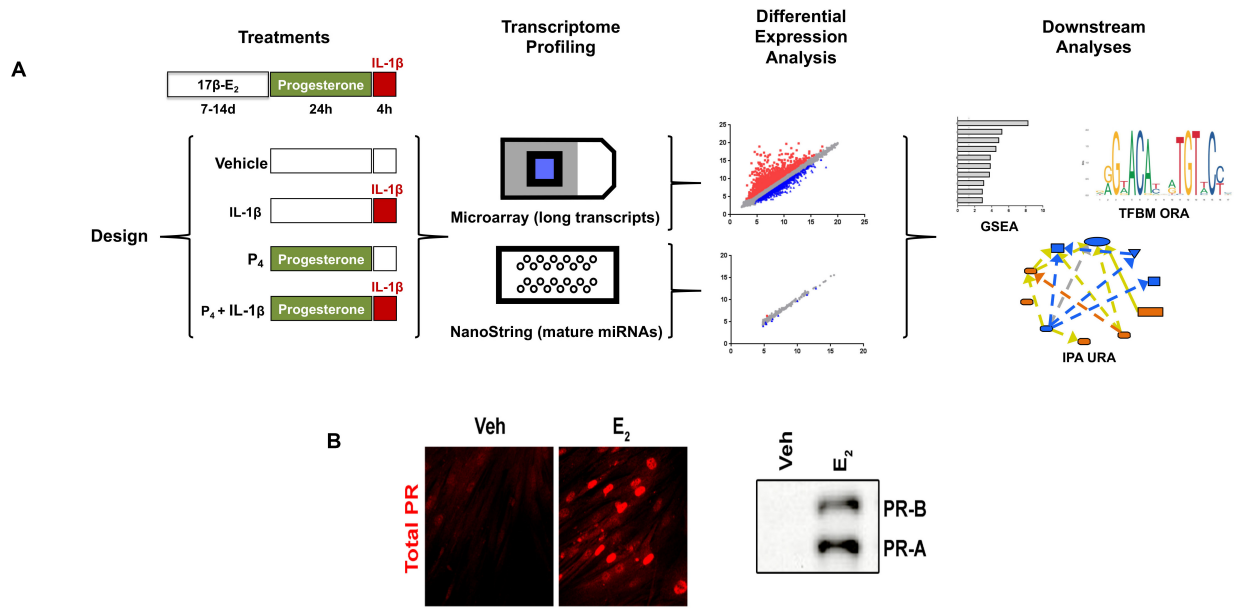

FIGURE 1 | Experimental design and workflow. **(A)** Primary cultures of cervical fibroblasts were primed with 10^{-8} M 17β-estradiol (17β-E2) or 0.001% ethanol vehicle for 7–14 days in F12/DMEM++0.5% charcoal-stripped FBS. Cells were then treated with 10^{-7} M progesterone (P4) or vehicle for 24 h followed by a 4-h stimulation with 0.2 ng/ml interleukin-1β (IL-1 *upbeta*) or vehicle (PBS/0.1% BSA). Total RNA was extracted to enrich for small RNAs and subjected to microarray analysis using the Affymetrix platform for long, coding transcripts and the NanoString® platform for small, non-coding RNAs. After normalization, the data were subjected to differential expression analysis was conducted using the Affymetrix Transcription Analysis Console. Downstream relationships were evaluated using Gene Set Enrichment Analysis (GSEA), Transcription Factor Binding Motif (TFBM) analysis, and Ingenuity Pathway Analysis. The relative expression data are the mean and FDR *p*-value from three separate sets of biological replicates. **(B)** depicts the expression of PR-A and PR-B using immunofluorescence (left panel) or immunoblotting (right panel) following priming with 17β-E2.

others (**Supplementary Table S3**). Confirming these predictions, a complementary promoter scanning analysis (TRAP analysis) of the differentially regulated genes revealed overrepresentation of canonical binding motifs corresponding to several of these transcription factors, including NF-κB (i.e., the NF-kappaB, NFKB1, REL, and RELA model matrices), FOX (i.e., the Foxq1, FOXF2, FOXO3, FOXD1, Foxa2, and FOXI1 matrices), IRF (i.e., the IRF1 and IRF2 matrices), STAT (i.e., the STAT1 and STAT3 matrices), and AP1 (**Supplementary Table S4**).

Although not prominently represented in the pathway analyses, given the importance of the ECM in cervical remodeling, we surveyed IL-1β-responsive transcripts for changes in genes responsible for ECM integrity, including proteoglycans, fibrous proteins, and genes associated with ECM biosynthesis and degradation. IL-1β induced the expression of three proteoglycan-related proteins (hyaluronan receptor/*CD44*, syndecan-4/*SDC4*, and serglycin/*SRGN*) and attenuated the expression of an additional two (decorin/*DCN* and structural maintenance of chromosome 3/chondroitin sulfate proteoglycan-6/*SMC3*) proteins. IL-1β also induced the expression of elastin (*ELN*), a basement membrane-associated procollagen (collagen type IV, α1 chain/*COL4A1*), and several genes involved in glycosaminoglycan (GAG) biosynthesis (β-1,4-galactosyltransferase-1/*B4GALT1*, carbohydrate sulfotransferase-11/*CHST11*, exostosin glycosyltransferase-/*EXT1*, fucosyltransferase-8/*FUT8*, hyaluronan synthase-2/*HAS2*, heparan sulfate-glucosamine 3-sulfotransferase-3B1/*HS3ST3B1*, and/ST3 β-galactosidase α-2,3-sialytransferase 1/*3GAL1*), while decreasing the expression of collagen type III, α1 chain/*COL3A1*, a major fibrillar procollagen in the cervical ECM **Supplementary Table S1**.

Progesterone Regulates a Modest Set of Genes

In contrast to the surfeit of differentially expressed genes observed following IL-1β stimulation, the transcriptional response to progesterone (10^{-7} M, a dose similar to the maternal circulating levels late in human gestation) (Word et al., 2007) was modest. Compared to cells receiving vehicle alone, cervical fibroblasts incubated with P_4 exhibited expression changes in only 52 genes, 34 of which were upregulated and 18 downregulated (**Figure 2E** and **Supplementary Table S5**).

Top-ranking pathways (analyzed by KEGG, Panther, and GO algorithms) associated with this gene expression signature included those related to the amino acid metabolism, xenobiotics, and fatty acid biosynthesis and catabolism, in addition to cortisol biosynthesis, insulin-like growth factor (IGF) signaling, and sodium reabsorption and the renin–angiotensin system (RAS) (**Figures 2F–H** and **Supplementary Table S6**). Based on this expression pattern, the IPA upstream regulator algorithm correctly predicted activation of the PR and inferred inhibition for a small number of inflammatory and growth regulators (**Supplementary Table S7**). Promoter scanning analysis revealed

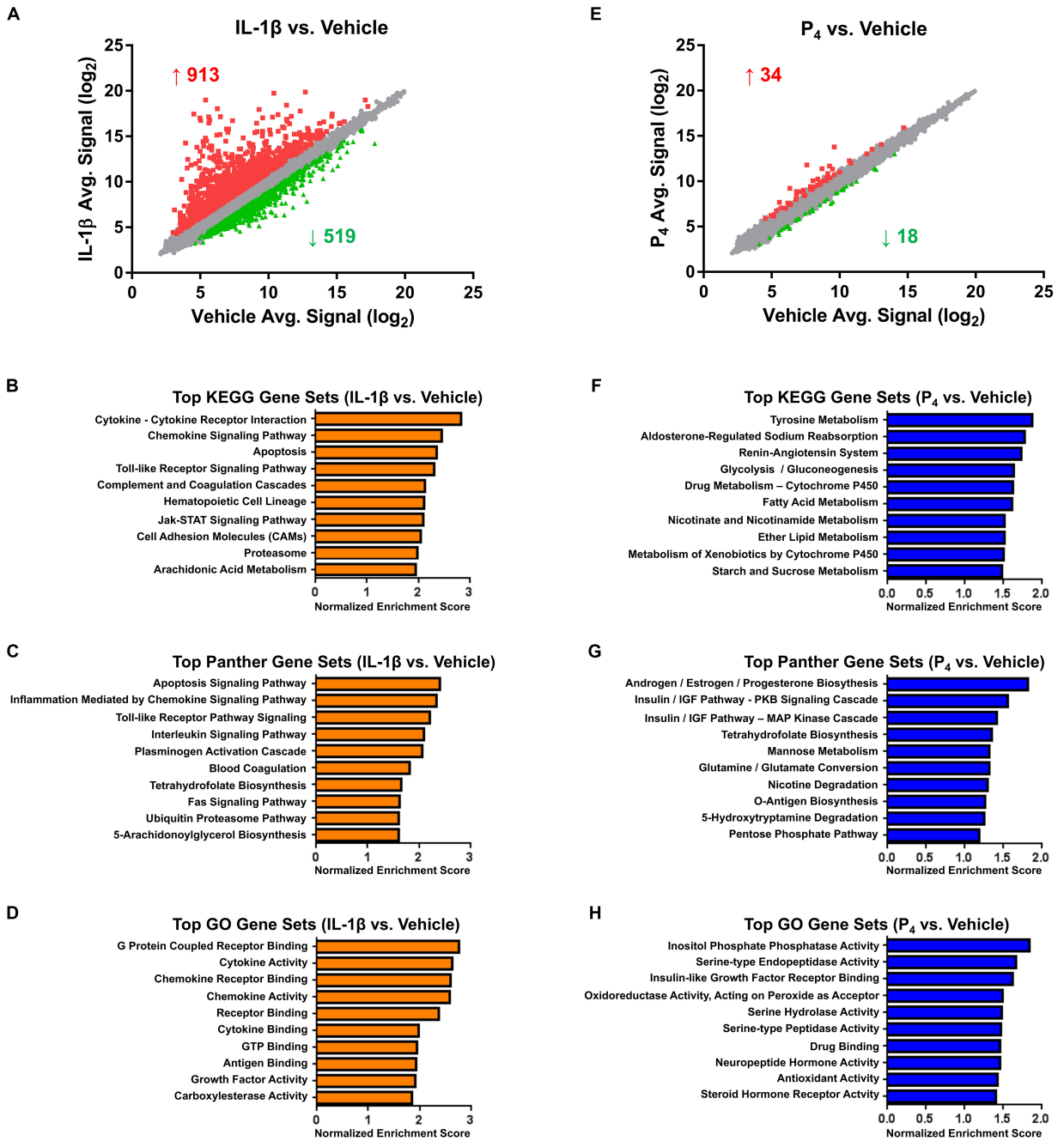

FIGURE 2 | Microarray and bioinformatics analysis of differentially expressed genes in cervical stromal fibroblasts stimulated with IL-1β (0.2 ng/ml) or P_4 (10^{-7} M) for hrs. Cells were primed with 17β-E2 (10^{-8} M) to induce progesterone receptors -A and -B and then challenged for 4 hrs with IL-1β **(A–D)** or P_4 for 4 h (after a 24-h preincubation with the steroid) **(E–H)**, total RNA isolated and quantified and differential gene expression by microarray analysis. The normalized data are expressed as mean signal intensity (log_2) and are from three separate experiments carried out in duplicate **(A,E)**. Bioinformatics analysis of differentially expressed transcripts using KEGG **(B,F)**, Panther **(C,G)** and GO **(D,H)** algorithms.

overrepresentation of the NR3C1 model matrix corresponding to the consensus binding motif of the glucocorticoid receptor (GRE: 5'RGRACANNNTGTYC3', where R = purine, Y = pyrimidine, N = any nucleic acid) (**Supplementary Table S8**). This was somewhat expected, inasmuch as the response elements for the glucocorticoid and progesterone receptors are quite similar (Lieberman et al., 1993; Nelson et al., 1999), and a separate PR response element model was not included in the non-redundant JASPAR vertebrate matrix database used for this query.

Unexpectedly, however, these promoter regions were also enriched for NF-κB-binding motifs. Given that we expected

NF-κB-responsive genes to be induced following cytokine challenge, we then compared the extent of overlap between the genes differentially expressed following IL-1β and P_4 co-stimulation. We found that a considerable proportion (31%) of the genes influenced by P_4 were also IL-1β responsive; specifically, nine genes were upregulated in both conditions. In addition, eight genes were downregulated following either treatment. Interestingly, most genes induced by either treatment were found to have roles in mitigating inflammation based on literature review (**Table 1**).

Progesterone Selectively Modulates Global Cytokine-Elicited Transcription

Relative to control cells, the global cellular response to IL-1β + P_4, like that following IL-1β exposure alone, was considerable: 889 genes exhibited induced expression, while 504 showed diminished expression (**Figures 3A–C** and **Supplementary Table S9**). The Jaccard similarity indices between these treatment groups were 0.79 and 0.62 for upregulated and downregulated genes, respectively. A minority (24 transcripts) of the genes differentially expressed by IL-1β + P_4 were also regulated by P_4 alone. Among the 17 genes responsive to both IL-1β and P_4 mentioned previously were ABI family member 3 binding protein/*ABI3BP*, collagen type VIII α1 chain/*COL8A1*, estrogen receptor 1/*ESR1*, osteomodulin/*OMD*, plexin domain containing 2/*PLXDC2*, prolactin receptor/*PRLR*, and secreted protein acidic and cysteine-rich-like 1/*SPARCL1*.

To assess the degree to which co-incubation with P_4 modified global IL-1β-inducible gene expression, we next compared the IL-1β and IL-1β + P_4 treatment groups. Of the 39 genes differentiating these two groups, 16 were downregulated by combined IL-1β + P_4 treatment relative to IL-1β alone

TABLE 1 | Characteristics of transcripts induced by both P4 and IL-1β based on microarray profiling.

Gene symbol	Description	IL-1β vs. vehicle fold change	P_4 vs. vehicle fold change	P_4 + IL-1β vs. vehicle fold change	Notes (references)
ALDH1A3	aldehyde dehydrogenase 1 family, member A3	2.25	2.57	4.43	Androgen-responsive gene in human prostate cancer epithelial cells (Trasino et al., 2007); participates in retinoic acid production and the metabolism of acetaldehyde, some amino acids, lipid peroxidation products, and exogenous chemicals (Duan et al., 2016).
CRISPLD2	cysteine-rich secretory protein LCCL domain containing 2	7.12	3.56	10.7	Progesterone receptor target gene in uterine cells (Yoo et al., 2014); blocks HMGB1-induced inflammation (Zhang et al., 2016); prevents lipopolysaccharide binding to target cells (Wang et al., 2009); responsive to both glucocorticoids and IL-1β in airway smooth muscle cells and negatively regulates pro-inflammatory cytokine function (Himes et al., 2014)
FKBP5	FK506 binding protein 5	2.18	4.13	4.2	Induced by glucocorticoids and progestins via hormone response elements (Hubler and Scammell, 2004); attenuates progestin responsiveness in cell models (Hubler et al., 2003).
HSD11B1	hydroxysteroid (11-beta) dehydrogenase 1	30.41	2.57	93.12	Reversibly reduces inactive cortisone to the active glucocorticoid receptor agonist cortisol (Oppermann et al., 1997); induced by progesterone in human endometrial stromal cells (Kuroda et al., 2013); responsive to IL-1α in human ovarian surface epithelium (Yong et al., 2002).
IRAK3	interleukin-1 receptor-associated kinase 3	6.77	2.5	19.75	Negative regulator of Toll/interleukin receptor signal transduction (Kobayashi et al., 2002); prevents neutrophil-dependent lung injury during influenza infection of the respiratory tract (Seki et al., 2010)
MMD	monocyte to macrophage differentiation-associated	5.42	2.48	9.64	Up-regulated during monocyte differentiation (Rehli et al., 1995); induced by lipopolysaccharide in macrophages (Liu et al., 2012); enhances cytokine and nitric oxide production in macrophages (Liu et al., 2012); plays a critical role in heart morphogenesis (Huang et al., 2012); inhibits growth of lung cancer cells (Li and He, 2014).
PLPP3	phospholipid phosphatase 3	4.16	2.93	4.86	Promotes anti-inflammatory phenotype and maintains vascular integrity of endothelial cells (Wu et al., 2015); promotes endothelial barrier function and limits sensitivity to inflammation-induced vascular leaks (Panchatcharam et al., 2014)
PPP4R4	protein phosphatase 4, regulatory subunit 4	4.39	3.47	8.18	Regulatory subunit for phosphoprotein phosphatase 4 PPP4C, modulates the latter's role in microtubule dynamics, DNA damage checkpoint recovery, apoptosis, and tumor necrosis factor alpha signaling (Chen et al., 2008); induced by preovulatory LH surge in ovarian steroidogenic cells (Christenson et al., 2013).
SLC39A8	solute carrier family 39 (zinc transporter), member 8	36.2	2.28	47.64	Functions in the cellular import of zinc at the onset of inflammation (Begum et al., 2002); NF-κB target gene that suppresses inflammatory signaling in zinc-dependent fashion (Liu et al., 2013).

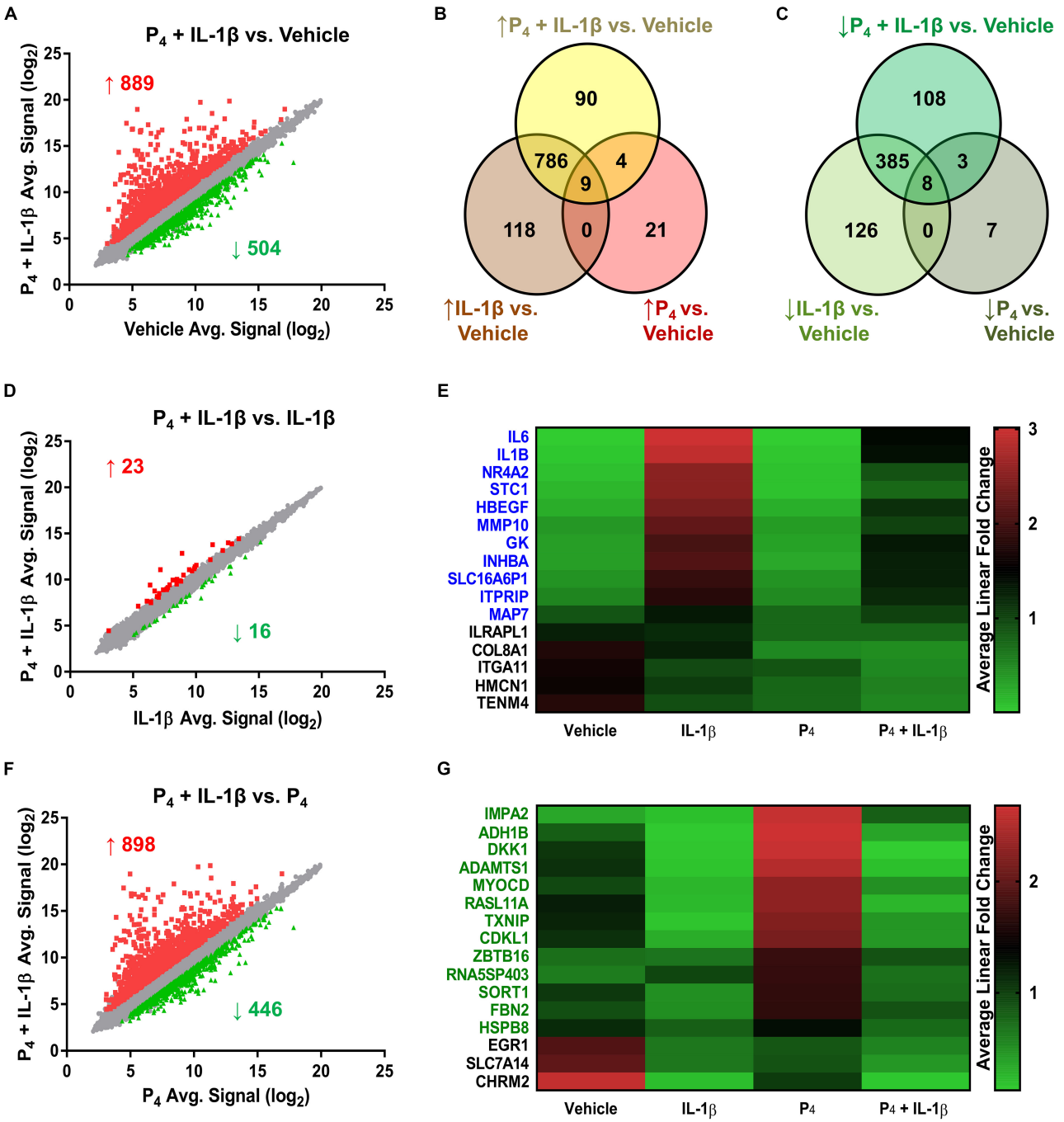

FIGURE 3 | Differential gene expression in cervical stromal fibroblasts stimulated with either IL-1β (0.2 ng/ml), P_4 (10^{-7} M) or both for 4 h followed by microarray analysis and data normalization. **(A)** shows the scatter plot and Venn diagrams comparing upregulated **(B)** and downregulated transcripts **(C)** in response to IL-1β +P_4 or vehicle. **(D)** Scatter plot and **(E)** heat map of differentially expressed genes in response to IL-1β or IL-1β + P_4. **(F)** Scatter plot and **(G)** heat map of differentially expressed genes in response to P_4 or IL-1β +P_4.

(**Figure 3B** and **Supplementary Table S10**). Of these, 11 genes were responsive when cells were incubated with IL-1β alone, including two proinflammatory interleukins (*IL1B*, *IL6*), a matrix metalloproteinase (*MMP10*), and the inhibin beta A subunit (*INHBA*) (**Figure 3E**). Finally, to determine how cytokine stimulation affected P_4-induced gene expression, we compared the P_4 and IL-1β + P_4 treatment groups (**Figure 3F** and **Supplementary Table S11**). Among the 446 genes downregulated by IL-1β under these conditions were 16 genes differentially regulated by P_4 alone. Among the 13 progestin-responsive

genes exhibiting diminished expression when incubated in the presence of IL-1β were those encoding the transcription factor myocardin (*MYOCD*), alcohol dehydrogenase 1B beta (*ADH1B*), the WNT signaling pathway inhibitor Dickkopf Inhibitor 1 (*DKK1*), and the ECM scaffold glycoprotein fibrillin 2 (*FBN2*) (**Figure 3G**).

To validate the initial profiling results, we performed qRT-PCR for select transcripts in experiments using separate biological replicates. These transcripts were categorized into three general expression patterns: (1) additive/synergistic expression in response to IL-1β + P_4 compared to either treatment alone (e.g., *IRAK3*, *HSD11B1*, and *FKBP5*) (**Figure 4A**); (2) induction by IL-1β with no significant response to P_4 in the absence or presence of IL-1β (e.g., *BDKRB1*, *BDKRB2*, *PTGES*, and *CXCL2*) (**Figure 4B**); and (3) IL-1β-inducible expression attenuated when co-incubated with P_4 (e.g., *HAS2*, *IL1B*, *IL6*, *MMP10*, and *PTGS2*) (**Figure 4C**).

Non-coding RNAs Are Induced by Cytokine and Progestin

The microarray chip analysis included both coding and non-coding RNA transcripts. We detected several miRNAs (host genes, pri-/pre-miRNAs, and mature miRNAs) and long, intergenic non-coding (LINC) RNAs in our microarray studies that were selectively upregulated by IL-1β stimulation. In addition, 12 non-coding RNAs, including five LINC RNAs, were downregulated when cells were challenged with the cytokine (**Supplementary Table S1**). In subsequent experiments, using biological replicates (samples separate from those used in the microarray studies), we used NanoString and qRT-PCR to further

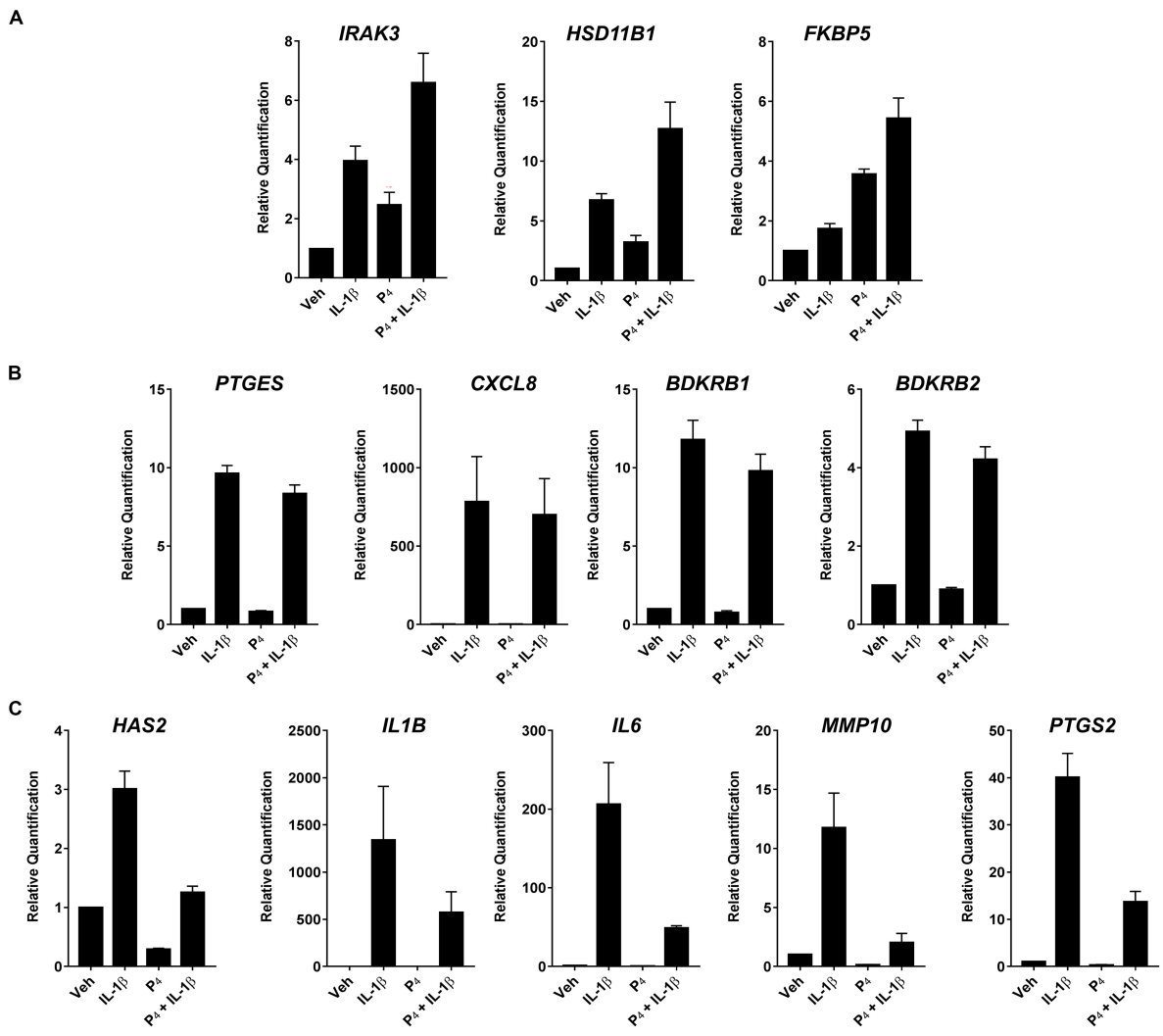

FIGURE 4 | Quantitative RT-PCR of select differentially expressed transcripts in cervical stromal fibroblasts stimulated with vehicle, IL-1β, P_4 or IL-1β+P_4 for 4 h. **(A)** Additive or synergistic relationship between P4 and IL-1 **(B)** No effect of P4 **(C)** Inhibitory effect of P4. After treatments, total RNA was isolated and quantified and primer sets were used to analyze individual transcripts in three separate experiments carried out in duplicate. Data are expressed as mean ± SEM of relative signal intensity (target/human acidic ribosomal protein).

assess non-coding RNA expression. Given the modest differential expression of LINC RNAs in our experiments, we did not pursue these transcripts in follow-up analyses.

We surveyed the expression of 800 mature miRNAs simultaneously using the non-amplification-based NanoString platform. Overall, the expression of individual miRNAs spanned five orders of magnitude, with 346 transcripts having average normalized counts above the threshold for detection (**Figure 5A**). The most highly expressed mature miRNAs under basal (vehicle treatment only) conditions were let-7a-5p, let-7b-5p, miR-125b-5p, miR-145-5p, and miR-4516. When subjected to differential gene expression analysis, nine mature miRNAs were differentially expressed under any treatment condition (**Figure 5B** and **Supplementary Table S12**), with expression changes on the order of two-fold or smaller. This was in striking contrast to the rather large fold changes in expression estimated at the level of miRNA host genes (i.e., immature pri-/pre-miRNA transcripts). For example, our microarray data indicated that the host gene for miR-155 changed by 20-fold in response to IL-1β (**Supplementary Table S1**), yet the corresponding mature miR-155-5p exhibited no discernible change in expression in the NanoString dataset (not shown). Using qRT-PCR, we found that the pri-/pre-miRNAs *MIR146A* and *MIR155* exhibited large changes in expression (166- and 32-fold, respectively) in response to IL-1β, yet the corresponding mature species changed only modestly (miR-146a-5p and miR-155-5p) (**Figure 5**).

In our studies of miRNA expression in response to IL-1β and/or P_4 exposure, we used the microarray platform to measure pri-/pre-miRNA transcripts while NanoString profiling was used to evaluate mature, fully processed miRNA species. We were surprised to learn that, while many pri-/pre-non-coding RNA host genes (including long non-coding and coding transcripts)

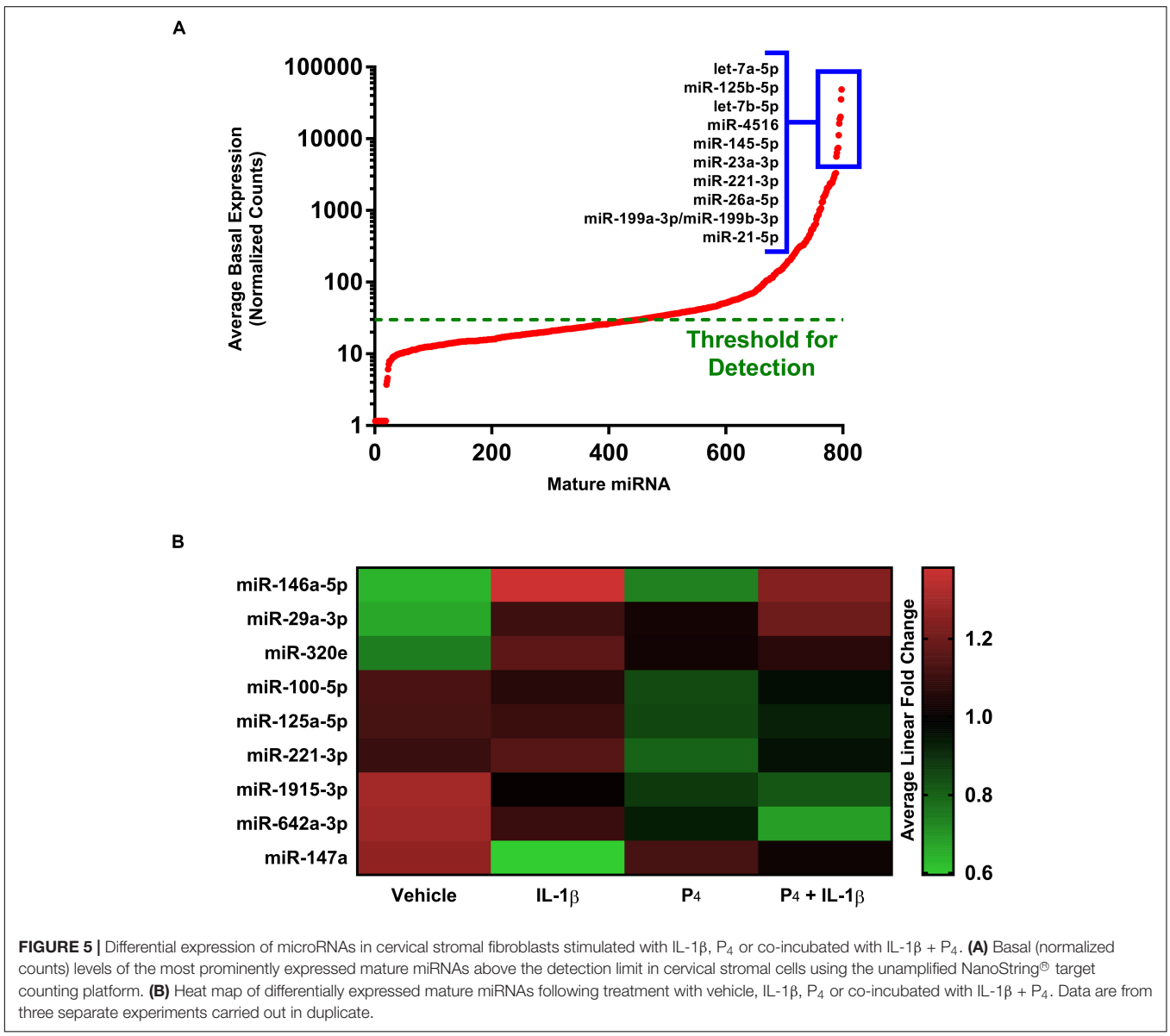

FIGURE 5 | Differential expression of microRNAs in cervical stromal fibroblasts stimulated with IL-1β, P_4 or co-incubated with IL-1β + P_4. **(A)** Basal (normalized counts) levels of the most prominently expressed mature miRNAs above the detection limit in cervical stromal cells using the unamplified NanoString® target counting platform. **(B)** Heat map of differentially expressed mature miRNAs following treatment with vehicle, IL-1β, P_4 or co-incubated with IL-1β + P_4. Data are from three separate experiments carried out in duplicate.

were differentially expressed in cytokine-stimulated cells, far fewer full-processed miRNAs were observed (**Supplementary Table S1** and **Figure 5**). This led us to postulate that this was due, at least in part, to the fact that while microarray analysis requires amplification of target transcripts, NanoString does not utilize a pre-amplification step prior to measurements.

To test this possibility, we compared directly two highly expressed miRNA transcripts (miR-146a and miR-155) using qRT-PCR of both immature and mature miRNAs. **Figure 6A** demonstrated that IL-1β stimulated robust upregulation of primary/precursors, MIR146a and MIR155, while co-incubation of IL-1β-treated cells with P_4 attenuated MIR146a and MIR155 expression. In contrast, when we used the same analytical platform (qRT-PCR) to evaluate mature miRNAs, we found that, while IL-1β induced miR-146a-5p and miR-155-5p, P_4 had no inhibitory effect on these two non-coding transcripts (**Figure 6B**).

DISCUSSION

Principal Findings

The current work investigated for the first time the modulation of cytokine-induced gene expression by P_4 using a simple, clinically relevant *in vitro* model of human cervical stromal fibroblasts. We chose to study the stroma based on the fact

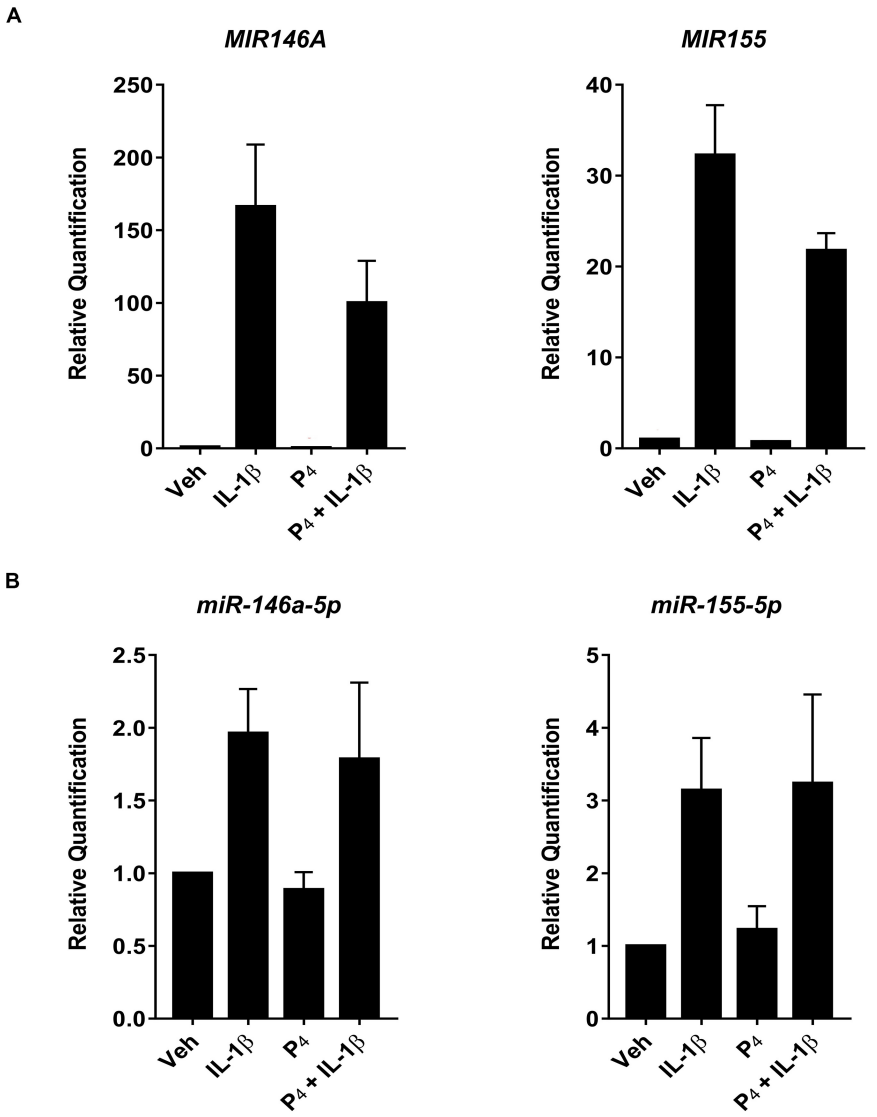

FIGURE 6 | Quantitative RT-PCR measurement of select primary/precursor and mature miRNA transcripts in cervical stromal fibroblasts from vehicle-, IL-1β-, P_4, or IL-1β + P_4-treated cells. Three separate experiments (carried out in duplicate) using biological replicates were incubated with the test agents listed above for 4 h, and then total RNA was isolated, quantified and subjected to RT-PCR using primers specific for either the primary/precursor or mature miRNA transcripts.
(A) Primary/precursor miRNA transcripts. **(B)** Fully processed, mature miRNAs. Data are expressed as mean ± SEM of relative intensity (target/human acidic ribosomal protein) and were analyzed by one-way ANOVA followed by Tukey's test for differences ($p < 0.05$, considered significant).

that the cervical stroma is the primary tissue that undergoes biochemical and biophysical remodeling allowing the fetus to descend the birth canal at the time of delivery (Malmstrom et al., 2007; Dubicke et al., 2016; Yellon, 2017; Shukla et al., 2018). Using a microarray platform and qRT-PCR-based validation, we demonstrated that IL-1β stimulation of stromal cells elicited changes in a panoply of genes encoding proinflammatory mediators, including cytokines and chemokines, arachidonic acid synthesizing enzymes, ECM-synthesizing enzymes, MMPs, and other proteases, and intracellular signaling proteins and transcription factors.

We also examined the regulation of genes in response to incubation with physiological levels of progesterone that are present at the end of pregnancy. In contrast to previous reports by DeMayo and colleagues (Jeong et al., 2005; Rubel et al., 2012), we detected relatively few genes that were directly controlled by P_4. With the exception of a few genes which were upregulated >four-fold (i.e., the matricellular protein SPARC-like 1/hevin, 18.66-fold; osteomodulin, 7.3-fold; inositol monophosphatase 2, 6.39-fold; alcohol dehydrogenase 1B, 5.36-fold; FK506-binding protein 5, 4.13-fold), most progestin-regulated genes were only modestly upregulated or downregulated in stromal cells.

Three Patterns of Progesterone Regulation of Cytokine-Driven Gene Expression

In contrast to gene expression in the context of progestin alone, co-incubation of cervical stromal cells with IL-1β and P_4 elicited three distinct patterns of regulation. One cohort of transcripts was profoundly upregulated by treatment with IL-1β but was unaffected by P_4 treatment alone (**Figure 4B**). A second set of transcripts exhibited IL-1β-stimulated upregulation that was almost completely suppressed by co-incubation with P_4 (**Figure 4C**). Notably, this set of genes was represented by proinflammatory cytokines (IL-1β and IL-6), the enzyme responsible for hyaluronan synthesis (i.e., HAS-2) (Garantziotis and Savani, 2019) and the rate-limiting enzyme in proinflammatory prostaglandin biosynthesis (i.e., PTGS-2) (Kniss, 1999). This can be interpreted as the subset of genes for which progestins exert anti-inflammatory actions.

Interestingly, there was a third set of IL-1β upregulated transcripts that was further elevated either additively or synergistically when cervical stromal cells were co-incubated with cytokine and progestin, including the steroid hormone receptor chaperone FK506-binding protein 5 (FKBP5) (Storer et al., 2011) and 11β-HSD1, the enzyme that converts biologically inert cortisone into bioactive cortisol (Tomlinson et al., 2004; Chapman K. et al., 2013; **Figure 4A**). Thus, the previously undescribed finding of three different patterns of gene expression exposed to cytokine and progestin in combination suggests that P_4 exerts complex regulatory control in the cervical stromal compartment and that, strictly speaking, it is not simply an anti-inflammatory steroid hormone. The suppression of proinflammatory genes induced by IL-1β by physiological concentrations of P_4 was predicted from previous studies in decidual stromal cells (Cakmak et al., 2005) and myometrial cells (Mendelson, 2009; Shynlova et al., 2013; Georgiou et al., 2016; Amini et al., 2019).

Regulation of Non-coding RNAs by Cytokine and Progestin

Analysis of the global expression of non-coding RNAs in cervical stromal cells treated with cytokine in the presence or absence of progestin revealed that miRNAs represent a relative minority of regulatory inputs to gene expression. Upregulated non-coding transcripts measured by microarray included both miRNAs encoded within host genes and LINC RNAs. The most highly upregulated miRNA transcript in IL-1β-treated cells was miR-155. MicroRNA-155 (hsa-mir155, coded within B-cell integration cluster (BIC) of non-coding transcripts located on chromosome 21, TargetScan, Release 7.1, June 2106; miRbase, Release 22.1, October 2018) (Madden et al., 2010; Kozomara and Griffiths-Jones, 2014) has been reported by many investigators to be induced in the setting of inflammation (O'Connell et al., 2007; Tili et al., 2007; Ceppi et al., 2009; Quinn and O'Neill, 2011; Xu et al., 2013) as a means to control tissue damage. We have recently demonstrated in decidual stromal cells that IL-1β causes the rapid and sustained upregulation of miR-155 (Ibrahim et al., 2016), and this was further confirmed using tissues isolated from patients who had a preterm delivery (Ackerman et al., 2016a). Thus, cytokine induction of miR-155 can be interpreted as a potential feedback loop to prevent tissue injury in the face of unrestrained acute inflammation (Baltimore et al., 2008; Contreras and Rao, 2012). One proposed mechanism by which miR-155 thwarts unwanted inflammation is by inhibition of the canonical inflammatory transcription factor NF-κB (Ma et al., 2011; Boldin and Baltimore, 2012).

Interestingly, in the NanoString platform, which does not amplify transcripts prior to their measurement, we were unable to detect significant differential expression of miR-155 following IL-1β stimulation, suggesting that, although induced by cytokine treatment the absolute abundance of this miRNA is quite low. When we analyzed miRNA expression using amplification-based qRT-PCR, we noted that, while the primary/precursor transcripts for miR-146a and miR-155 were substantially upregulated by IL-1β incubation, there was no significant induction of the corresponding mature miRNAs. These data further indicate that the regulation of miRNAs and their modulation of cytokine-induced gene expression can be quite modest (O'Neill et al., 2011; Ibrahim et al., 2016).

One of the most significantly downregulated miRNAs in IL-1β-treated cervical stromal cells was miR-143. This regulatory RNA transcript has been shown to target the COX-2 mRNA, suggesting that expression of this RNA in the basal state may prevent COX-2-mediated inflammatory prostaglandin biosynthesis (Kim et al., 2011; Pham et al., 2013).

Upregulation of BDKRs and HAS-2 Contributes to Cervical Remodeling

Among the transcripts that were upregulated by cytokine but unaffected by progestin were the bradykinin receptors

(BDKRB1 and BDKRB2). Bradykinin is a nonapeptide (H_2N–Arg–Pro–Pro–Gly–Phe–Ser–Pro–Phe–Arg–COOH) member of the kallikrein–kinin system (Burch et al., 1989) that is generated following the activation of plasma or tissue kallikrein and subsequent cleavage of kininogen into several smaller products (Moreau et al., 2005; Bryant and Shariat-Madar, 2009; Bjorkqvist et al., 2013). Bradykinin is implicated in several pathophysiological events, including coagulation (Del Rosso et al., 2011; Wu, 2015; Weidmann et al., 2017) and thrombosis, fibrinolysis (Del Rosso et al., 2008), and acute inflammation (Kaplan and Joseph, 2014; Wu, 2015; Schmaier, 2016). Among the physiological functions of bradykinin is vascular permeability (Bjorkqvist et al., 2013; Couture et al., 2014) and smooth-muscle contractility (Ricciardolo et al., 2018). It is possible that bradykinin, acting via BDKR-B1 and/or -B2, mediates increased tissue hydration in the cervix during ripening by altering endothelial cell junctions (Couture et al., 2014). HAS-2, the enzyme that catalyzes the synthesis of hyaluronan (hydrophilic GAG) that accumulates in the stroma during ripening, is upregulated by IL-1β, and the induction is attenuated by P_4. Thus, HAS-2- and BDKR-mediated functions of bradykinin may act in concert to orchestrate the softening that occurs during cervical ripening in preparation for parturition. To our knowledge, the current work is the first report of cytokine-induced bradykinin receptor expression in the cervical stroma. While P_4 had no effect on IL-1β induction of BDKR-B1 or -B2, HAS-2 transcripts were nearly abolished when IL-1β-treated cells were co-incubated with P_4. This observation provides a means by which progestins may prevent untimely hyaluronan synthesis and enhanced tissue hydration in the cervical stroma.

ECM Proteins and ECM-Modifying Enzymes

The regulation of ECM composition is a major determinant of the biomechanical features of cervical ripening in preparation for the onset of labor (Myers et al., 2008, 2009; House et al., 2009). During the initial phases of cervical remodeling in early pregnancy, collagens type I and III are highly organized and cross-linked via lysyl oxidase and lysyl hydroxylase (Hassan et al., 2009; Akins et al., 2011). This provides a rigid and closed cervix that resists the gravitational and contractile forces that would otherwise contribute to opening of the cervical os and premature delivery of the fetus (Danforth, 1983; Hao et al., 2018). Later in pregnancy, cross-linked collagens are replaced by randomly oriented fibers, increased hyaluronan accumulation, and tissue hydration (Garantziotis and Savani, 2019). Our *in vitro* studies demonstrated that treatment of cells with IL-1β downregulated collagen I and III and lysyl oxidase mRNA expression (**Supplementary Table S1**). Moreover, cytokine exposure of cervical stromal cells led to upregulated HAS-2 expression that was antagonized by simultaneous incubation with P_4. These results are consistent with previous findings by Elovitz's group that progestational agents act to maintain cervical integrity in a murine model of parturition (Xu et al., 2008).

We also showed that IL-1β caused the upregulation of several MMPs (i.e., MMP1/interstitial collagenase, 3/stromelysin 1, MMP10/stromelysin 2, and MMP12/macrophage elastase) by ≥five-fold. These data are consistent with previous reports using human cervical fibroblasts (Yoshida et al., 2002). Combined incubation of stromal cells with IL-1β and P_4 resulted in ∼60% reduction in MMP10 mRNA expression (see **Figure 4** and **Supplementary Tables S1, S9**). In contrast, co-incubation of cells with cytokine and progestin led to less pronounced diminution in MMP1 (∼15%) and MMP3 (∼42%) and no effect on MMP12 expression. These data suggest that P_4 has minimal effects on the key proteinases involved in tissue remodeling in the cervix.

We also detected the upregulation of several GAG synthases (i.e., B4GALT1, CHST11, EXT1, 3GAL1, FUT8, HS3STB1, and ST3) by IL-1β which was largely unaffected by P_4. Importantly, however, IL-1β-induced HAS-2 mRNA expression was strongly inhibited by P_4 co-incubation (see **Figure 4**), consistent with a previous report by Uchiyama et al. (2005). Taken together, these data indicate that, while inflammatory cytokines have wide-ranging effects on molecules involved in ECM biosynthesis and turnover, progestin treatment has a modest effect on these functions.

Synergistic Induction of 11β-HSD1 by Cytokine and Progestin

The expression of 11β-HSD1, the enzyme that converts biologically inert cortisone into bioactive cortisol in several tissues, was induced several folds in stromal cells incubated with IL-1β. In addition, P_4 treatment alone led to a 3-5-fold increase in 11β-HSD1 mRNA abundance, while 11β-HSD2, the enzyme that inactivates cortisol to cortisone, was unaffected by either cytokine or progestin exposure (data not shown) (Seckl, 2004). Surprisingly, when we combined exposure to IL-1β and P_4 in cervical stromal cells, we detected a very robust synergistic upregulation of the 11β-HSD1 gene and no change in 11β-HSD2 gene expression. Previous studies have reported that proinflammatory cytokines can induce 11β-HSD1 leading to local synthesis of cortisol (Chapman K. et al., 2013). Chapman and Seckl have suggested that local expression of 11β-HSD1 and conversion of cortisone to cortisol provides a means to dampen acute inflammation that could lead to chronic tissue injury if left unchecked (Seckl, 2004; Chapman et al., 2006; Chapman K.E. et al., 2013). Ahasan et al. (2012) reported that IL-1β caused upregulation of 11β-HSD1 as an anti-inflammatory response in mesenchymal stromal cells. Similarly, Hardy et al. (2008, 2016) demonstrated upregulation of 11β-HSD1 mRNA expression in acute inflammation in skeletal muscle and in the context of inflamed synovial tissue with patients with rheumatoid arthritis (Hardy et al., 2008).

CONCLUSION AND FUTURE DIRECTIONS

The current work has demonstrated that incubation of cervical stromal fibroblasts with a proinflammatory cytokine leads to a robust global gene expression profile that includes predicted inflammatory and anti-inflammatory transcripts (e.g., cytokines, chemokines, enzymes involved in bioactive lipid synthesis, signaling proteins, and transcription factors). In addition, we also demonstrated several other groups of genes expressed in

response to IL-1β, including ECM proteins and ECM-modifying enzymes (e.g., matricellular proteins, MMPs, other proteases, and glycosyltransferases driving the biosynthesis of GAGs). Finally, several non-coding RNAs were identified, including miRNAs and LINCRNAs.

A major objective of the study was to examine the role played by progesterone in governing cytokine-driven gene expression. In this regard, we were somewhat surprised to observe that a relatively modest cohort of stromal cell transcripts was regulated either positively or negatively by progestin. P_4 was found to inhibit only a subset of stromal cell genes following IL-1β treatment, suggesting that this hormone exerts only partial anti-inflammatory activity, at least in the cervical stroma. For example, while P_4 completely abolished cytokine-mediated IL-6 mRNA expression, it was ineffective at inhibiting CXCL8/IL-8 gene expression.

Finally, this work reported for the first time that IL-1β and P_4 conspired to upregulate a few genes, e.g., FKBP5, a steroid receptor chaperone and 11β-HSD1, the enzyme that converts inert cortisone into bioactive cortisol. In addition, we discovered for the first time that IL-1β upregulated the expression of bradykinin receptors B1 and B2 that mediate the actions of kallikrein products in vascular permeability and other events in the inflammatory cascade. These latter two observations open a new avenue for future investigations into the interaction of cytokines and progestins in governing the events leading to cervical ripening in preparation for parturition.

DATA AVAILABILITY STATEMENT

The microarray data is available at GEO (GSE154571).

ETHICS STATEMENT

The studies involving human participants were reviewed and approved by The Ohio State University Biomedical Institutional Review Board. The patients/participants provided their written informed consent to participate in this study.

AUTHOR CONTRIBUTIONS

DK conceived of the study, designed the experiments, analyzed the data, wrote the manuscript, and prepared the figures and tables. TS executed the experiments, assisted in data collection, and proofread the manuscript. All authors contributed to the article and approved the submitted version.

FUNDING

This work was supported by the March of Dimes Prematurity Research Collaborative of Ohio and The Ohio State University Perinatal Research and Development Fund.

ACKNOWLEDGMENTS

We gratefully acknowledge the excellent technical assistance of members of The Ohio State University Comprehensive Cancer Center (OSUCCC) Genomics Shared Resource who contributed to the microarray and mature high-dimensional miRNA profiling studies described herein. Specifically, we thank Sarah Warner for performing the Affymetrix microarray studies and Dr. Paolo Fadda for performing the NanoString miRNA profiling assays. We also thank the Comprehensive Cancer Center Human Tissue Cooperative Network for their assistance in procuring cervical tissue specimens. Following the embargo during the publication process, the gene expression database will be deposited in GenBank at the National Center for Biotechnology Information.

SUPPLEMENTARY MATERIAL

The Supplementary Material for this article can be found online at: https://www.frontiersin.org/articles/10.3389/fgene.2020.00883/full#supplementary-material

REFERENCES

Ackerman, W. E. IV, Buhimschi, I. A., Eidem, H. R., Rinker, D. C., Rokas, A., Rood, K., et al. (2016a). Comprehensive RNA profiling of villous trophoblast and decidua basalis in pregnancies complicated by preterm birth following intra-amniotic infection. *Placenta* 44, 23–33. doi: 10.1016/j.placenta.2016.05.010

Ackerman, W. E. IV, Summerfield, T. L., Mesiano, S., Schatz, F., Lockwood, C. J., and Kniss, D. A. (2016b). Agonist-dependent downregulation of progesterone receptors in human cervical stromal fibroblasts. *Reprod. Sci.* 23, 112–123. doi: 10.1177/1933719115597787

Ackerman, W. E. IV, Robinson, J. M., and Kniss, D. A. (2005). Despite transcriptional and functional coordination, cyclooxygenase-2 and microsomal prostaglandin E synthase-1 largely reside in distinct lipid microdomains in WISH epithelial cells. *J. Histochem. Cytochem.* 53, 1391–1401. doi: 10.1369/jhc.5a6710.2005

Ahasan, M. M., Hardy, R., Jones, C., Kaur, K., Nanus, D., Juarez, M., et al. (2012). Inflammatory regulation of glucocorticoid metabolism in mesenchymal stromal cells. *Arthritis Rheum.* 64, 2404–2413.

Akgul, Y., Holt, R., Mummert, M., Word, A., and Mahendroo, M. (2012). Dynamic changes in cervical glycosaminoglycan composition during normal pregnancy and preterm birth. *Endocrinology* 153, 3493–3503. doi: 10.1210/en.2011-1950

Akgul, Y., Word, R. A., Ensign, L. M., Yamaguchi, Y., Lydon, J., Hanes, J., et al. (2014). Hyaluronan in cervical epithelia protects against infection-mediated preterm birth. *J. Clin. Invest.* 124, 5481–5489. doi: 10.1172/jci78765

Akins, M. L., Luby-Phelps, K., Bank, R. A., and Mahendroo, M. (2011). Cervical softening during pregnancy: regulated changes in collagen cross-linking and composition of matricellular proteins in the mouse. *Biol. Reprod.* 84, 1053–1062. doi: 10.1095/biolreprod.110.089599

Amini, P., Wilson, R., Wang, J., Tan, H., Yi, L., Koeblitz, W. K., et al. (2019). Progesterone and cAMP synergize to inhibit responsiveness of myometrial cells to pro-inflammatory/pro-labor stimuli. *Mol. Cell. Endocrinol.* 479, 1–11. doi: 10.1016/j.mce.2018.08.005

Baltimore, D., Boldin, M. P., O'Connell, R. M., Rao, D. S., and Taganov, K. D. (2008). MicroRNAs: new regulators of immune cell development and function. *Nat. Immunol.* 9, 839–845. doi: 10.1038/ni.f.209

Begum, N. A., Kobayashi, M., Moriwaki, Y., Matsumoto, M., Toyoshima, K., and Seya, T. (2002). Mycobacterium bovis BCG cell wall and lipopolysaccharide

induce a novel gene, BIGM103, encoding a 7-TM protein: identification of a new protein family having Zn-transporter and Zn-metalloprotease signatures. *Genomics* 80, 630–645. doi: 10.1006/geno.2002.7000

Bjorkqvist, J., Jamsa, A., and Renne, T. (2013). Plasma kallikrein: the bradykinin-producing enzyme. *Thromb. Haemost.* 110, 399–407. doi: 10.1160/th13-03-0258

Boldin, M. P., and Baltimore, D. (2012). MicroRNAs, new effectors and regulators of NF-kappaB. *Immunol. Rev.* 246, 205–220. doi: 10.1111/j.1600-065x.2011.01089.x

Bryant, J. W., and Shariat-Madar, Z. (2009). Human plasma kallikrein-kinin system: physiological and biochemical parameters. *Cardiovasc. Hematol. Agents Med. Chem.* 7, 234–250. doi: 10.2174/187152509789105444

Burch, R. M., Connor, J. R., and Tiffany, C. W. (1989). The kallikrein-kininogen-kinin system in chronic inflammation. *Agents Actions* 27, 258–260. doi: 10.1007/bf01972790

Cakmak, H., Schatz, F., Huang, S. T., Buchwalder, L., Rahman, M., Arici, A., et al. (2005). Progestin suppresses thrombin- and interleukin -induced interleukin-11 production in term decidual cells: implications for preterm delivery. *J. Clin. Endocrinol. Metab.* 90, 5279–5286. doi: 10.1210/jc.2005-0210

Ceppi, M., Pereira, P. M., Dunand-Sauthier, I., Barras, E., and Reith, W., (2009). MicroRNA-155 modulates the interleukin-1 signaling pathway in activated human monocyte-derived dendritic cells. *Proc. Natl. Acad. Sci. U.S.A.* 106, 2735–2740. doi: 10.1073/pnas.0811073106

Chapman, K., Holmes, M., and Seckl, J. (2013). 11β−hydroxysteroid dehydrogenases: intracellular gate-keepers of tissue glucocorticoid action. *Physiol. Rev.* 93, 1139–1206. doi: 10.1152/physrev.00020.2012

Chapman, K. E., Coutinho, A., Gray, M., Gilmour, J. S., Savill, J. S., and Seckl, J. R. (2006). Local amplification of glucocorticoids by 11 hydroxysteroid dehydrogenase type 1 and its role in the inflammatory response. *Ann. N. Y. Acad. Sci.* 1088, 265–273. doi: 10.1196/annals.1366.030

Chapman, K. E., Coutinho, A. E., Zhang, Z., Kipari, T., Savill, J. S., and Seckl, J. R. (2013). Changing glucocorticoid action: 11β−hydroxysteroid dehydrogenase type 1 in acute and chronic inflammation. *J. Steroid Biochem. Mol. Biol.* 137, 82–92. doi: 10.1016/j.jsbmb.2013.02.002

Chen, G. I., Tisayakorn, S., Jorgensen, C., D'Ambrosio, L. M., Goudreault, M., and Gingras, A. C. (2008). PP4R4/KIAA1622 forms a novel stable cytosolic complex with phosphoprotein phosphatase 4. *J. Biol. Chem.* 283, 29273–29284. doi: 10.1074/jbc.m803443200

Christenson, L. K., Gunewardena, S., Hong, X., Spitschak, M., Baufeld, A., and Vanselow, J. (2013). Research resource: preovulatory LH surge effects on follicular theca and granulosa transcriptomes. *Mol. Endocrinol.* 27, 1153–1171. doi: 10.1210/me.2013-1093

Chwalisz, K., Benson, M., Scholz, P., Daum, J., Beier, H. M., and Hegele-Hartung, C. (1994). Cervical ripening with the cytokines interleukin 8, interleukin 1 beta and tumour necrosis factor alpha in guinea-pigs. *Hum. Reprod.* 9, 2173–2181. doi: 10.1093/oxfordjournals.humrep.a138413

Conde-Agudelo, A., and Romero, R. (2016). Vaginal progesterone to prevent preterm birth in pregnant women with a sonographic short cervix: clinical and public health implications. *Am. J. Obstet. Gynecol.* 214, 235–242. doi: 10.1016/j.ajog.2015.09.102

Contreras, J., and Rao, D. S. (2012). MicroRNAs in inflammation and immune responses. *Leukemia* 26, 404–413. doi: 10.1038/leu.2011.356

Couture, R., Blaes, N., and Girolami, J. P. (2014). Kinin receptors in vascular biology and pathology. *Curr. Vasc. Pharmacol.* 12, 223–248. doi: 10.2174/15701611126661402261216 27

Danforth, D. N. (1983). The morphology of the human cervix. *Clin. Obstet. Gynecol.* 26, 7–13. doi: 10.1097/00003081-198303000-00005

Del Rosso, M., Fibbi, G., Pucci, M., Margheri, F., and Serrati, S. (2008). The plasminogen activation system in inflammation. *Front. Biosci.* 13, 4667–4686. doi: 10.2741/3032

Del Rosso, M., Margheri, F., Serrati, S., Chilla, A., Laurenzana, A., and Fibbi, G. (2011). The urokinase receptor system, a key regulator at the intersection between inflammation, immunity, and coagulation. *Curr. Pharm. Des.* 17, 1924–1943. doi: 10.2174/138161211796718189

Duan, J. J., Cai, J., Guo, Y. F., Bian, X. W., and Yu, S. C. (2016). ALDH1A3, a metabolic target for cancer diagnosis and therapy. *Int. J. Cancer* 139, 965–975. doi: 10.1002/ijc.30091

Dubicke, A., Ekman-Ordeberg, G., Mazurek, P., Miller, L., and Yellon, S. M. (2016). Density of stromal cells and macrophages associated with collagen remodeling in the human cervix in preterm and term birth. *Reprod. Sci.* 23, 595–603. doi: 10.1177/1933719115616497

Elovitz, M. A., and Mrinalini, C. (2004). Animal models of preterm birth. *Trends Endocrinol Metab.* 15, 479–487. doi: 10.1016/j.tem.2004.10.009

Garantziotis, S., and Savani, R. C. (2019). Hyaluronan biology: a complex balancing act of structure, function, location and context. *Matrix Biol.* 7, 1–10. doi: 10.1016/j.matbio.2019.02.002

Georgiou, E. X., Lei, K., Lai, P. F., Yulia, A., Herbert, B. R., Castellanos, M., et al. (2016). The study of progesterone action in human myometrial explants. *Mol. Hum. Reprod.* 22, 877–889. doi: 10.1093/molehr/gaw037

Gonzalez, J. M., Xu, H., Chai, J., Ofori, E., and Elovitz, M. A. (2009). Preterm and term cervical ripening in CD1 Mice (*Mus musculus*): similar or divergent molecular mechanisms? *Biol. Reprod.* 81, 1226–1232. doi: 10.1095/biolreprod.108.075309

Hao, J., Yao, W., Harris, W. R., Vink, J. Y., Myers, K., and Donnelly, E. (2018). Characterization of collagen microstructural organization of human cervical tissue. *Reproduction* 156, 71–79. doi: 10.1530/rep-17-0763

Hardy, R., Rabbitt, E. H., Filer, A., Emery, P., Hewison, M., Stewart, P. M., et al. (2008). Local and systemic glucocorticoid metabolism in inflammatory arthritis. *Ann. Rheum. Dis.* 67, 1204–1210. doi: 10.1136/ard.2008.090662

Hardy, R. S., Doig, C. L., Hussain, Z., O'Leary, M., Morgan, S. A., Pearson, M. J., et al. (2016). 11β−Hydroxysteroid dehydrogenase type 1 within muscle protects against the adverse effects of local inflammation. *J. Pathol.* 240, 472–483. doi: 10.1002/path.4806

Hassan, S. S., Romero, R., Tarca, A. L., Nhan-Chang, C. L., Vaisbuch, E., Erez, O., et al. (2009). The transcriptome of cervical ripening in human pregnancy before the onset of labor at term: identification of novel molecular functions involved in this process. *J. Matern. Fetal Neonatal Med.* 22, 1183–1193. doi: 10.3109/14767050903353216

Hassan, S. S., Romero, R., Vidyadhari, D., Fusey, S., Baxter, J. K., Khandelwal, M., et al. (2011). Vaginal progesterone reduces the rate of preterm birth in women with a sonographic short cervix: a multicenter, randomized, double-blind, placebo-controlled trial. *Ultrasound Obstet. Gynecol.* 38, 18–31. doi: 10.1002/uog.9017

Himes, B. E., Jiang, X., Wagner, P., Hu, R., Wang, Q., Klanderman, B., et al. (2014). RNA-Seq transcriptome profiling identifies CRISPLD2 as a glucocorticoid responsive gene that modulates cytokine function in airway smooth muscle cells. *PLoS One* 9:e99625. doi: 10.1371/journal.pone.0099625

House, M., Kaplan, D. L., and Socrate, S. (2009). Relationships between mechanical properties and extracellular matrix constituents of the cervical stroma during pregnancy. *Semin. Perinatol.* 33, 300–307. doi: 10.1053/j.semperi.2009.06.002

Huang, H., Jin, T., He, J., Ding, Q., Xu, D., Wang, L., et al. (2012). Progesterone and adipoQ receptor 11 links ras signaling to cardiac development in zebrafish. *Arterioscler. Thromb. Vasc. Biol.* 32, 2158–2170. doi: 10.1161/atvbaha.112.252775

Hubler, T. R., Denny, W. B., Valentine, D. L., Cheung-Flynn, J., Smith, D. F., and Scammell, J. G. (2003). The FK506-binding immunophilin FKBP51 is transcriptionally regulated by progestin and attenuates progestin responsiveness. *Endocrinology* 144, 2380–2387. doi: 10.1210/en.2003-0092

Hubler, T. R., and Scammell, J. G. (2004). Intronic hormone response elements mediate regulation of FKBP5 by progestins and glucocorticoids. *Cell Stress Chaper.* 9, 243–252.

Ibrahim, S. A., Ackerman, W. E. IV, Summerfield, T. L., Lockwood, C. J., Schatz, F., and Kniss, D. A. (2016). Inflammatory gene networks in term human decidual cells define a potential signature for cytokine-mediated parturition. *Am. J. Obstet. Gynecol.* 214, 284.e1–284.e47. doi: 10.1016/j.ajog.2015.08.075

Jeong, J. W., Lee, K. Y., Kwak, I., White, L. D., Hilsenbeck, S. G., Lydon, J. P., et al. (2005). Identification of murine uterine genes regulated in a ligand-dependent manner by the progesterone receptor. *Endocrinology* 146, 3490–3505. doi: 10.1210/en.2005-0016

Kaplan, A. P., and Joseph, K. (2014). Pathogenic mechanisms of bradykinin mediated diseases: dysregulation of an innate inflammatory pathway. *Adv. Immunol.* 121, 41–89. doi: 10.1016/b978-0-12-800100-4.00002-7

Kastner, P., Krust, A., Turcotte, B., Stropp, U., Tora, L., Gronemeyer, H., et al. (1990). Two distinct estrogen-regulated promoters generate transcripts

encoding the two functionally different human progesterone receptor forms A and B. *EMBO J.* 9, 1603–1614. doi: 10.1002/j.1460-2075.1990.tb08280.x

Katayama, T., Nakao, M., and Takagi, T. (2010). TogoWS: integrated SOAP and REST APIs for interoperable bioinformatics Web services. *Nucleic Acids Res.* 38, W706–W711.

Kim, S. Y., Romero, R., Tarca, A. L., Bhatti, G., Lee, J., Chaiworapongsa, T., et al. (2011). miR-143 regulation of prostaglandin-endoperoxidase synthase 2 in the amnion: implications for human parturition at term. *PLoS One* 6:e24131. doi: 10.1371/journal.pone.0024131

Kniss, D. A. (1999). Cyclooxygenases in reproductive medicine and biology. *J. Soc. Gynecol. Invest.* 6, 285–292. doi: 10.1016/s1071-5576(99)00034-9

Kobayashi, K., Hernandez, L. D., Galan, J. E., Janeway, C. A. Jr., Medzhitov, R., and Flavell, R. A. (2002). IRAK-M is a negative regulator of Toll-like receptor signaling. *Cell* 110, 191–202. doi: 10.1016/s0092-8674(02)00827-9

Kozomara, A., and Griffiths-Jones, S. (2014). miRBase: annotating high confidence microRNAs using deep sequencing data. *Nucleic Acids Res.* 42, D68–D73.

Kuroda, K., Venkatakrishnan, R., Salker, M. S., Lucas, E. S., Shaheen, F., Kuroda, M., et al. (2013). Induction of 11beta-HSD 1 and activation of distinct mineralocorticoid receptor- and glucocorticoid receptor-dependent gene networks in decidualizing human endometrial stromal cells. *Mol. Endocrinol.* 27, 192–202. doi: 10.1210/me.2012-1247

Li, R., Ackerman, W. E. IV, Summerfield, T. L., Yu, L., Gulati, P., Zhang, J., et al. (2011). Inflammatory gene regulatory networks in amnion cells following cytokine stimulation: translational systems approach to modeling human parturition. *PLoS One* 6:e20560. doi: 10.1371/journal.pone.0020560

Li, W., and He, F. (2014). Monocyte to macrophage differentiation-associated (MMD) targeted by miR-140-5p regulates tumor growth in non-small cell lung cancer. *Biochem. Biophys. Res. Commun.* 450, 844–850. doi: 10.1016/j.bbrc.2014.06.075

Lieberman, B. A., Bona, B. J., Edwards, D. P., and Nordeen, S. K. (1993). The constitution of a progesterone response element. *Mol. Endocrinol.* 7, 515–527. doi: 10.1210/me.7.4.515

Liu, M. J., Bao, S., Galvez-Peralta, M., Pyle, C. J., Rudawsky, A. C., Pavlovicz, R. E., et al. (2013). ZIP8 regulates host defense through zinc-mediated inhibition of NF-kappaB. *Cell Rep.* 3, 386–400. doi: 10.1016/j.celrep.2013.01.009

Liu, Q., Zheng, J., Yin, D. D., Xiang, J., He, F., Wang, Y.-C., et al. (2012). Monocyte to macrophage differentiation-associated (MMD) positively regulates ERK and Akt activation and TNF-alpha and NO production in macrophages. *Mol. Biol. Rep.* 39, 5643–5650. doi: 10.1007/s11033-011-1370-5

Ma, X., Becker Buscaglia, L. E., Barker, J. R., and Li, Y. (2011). MicroRNAs in NF-kappaB signaling. *J. Mol. Cell Biol.* 3, 159–166.

Madden, S. F., Carpenter, S. B., Jeffery, I. B., Bjorkbacka, H., Fitzgerald, K. A., O'Neill, L. A., et al. (2010). Detecting microRNA activity from gene expression data. *BMC Bioinformatics* 11:257. doi: 10.1186/1471-2105-11-257

Malmstrom, E., Sennstrom, M., Holmberg, A., Frielingsdorf, H., Eklund, E., Malmstrom, L., et al. (2007). The importance of fibroblasts in remodelling of the human uterine cervix during pregnancy and parturition. *Mol. Hum. Reprod.* 13, 333–341. doi: 10.1093/molehr/gal117

Mathelier, A., Zhao, X., Zhang, A. W., Parcy, F., Worsley-Hunt, R., Arenillas, D. J., et al. (2014). JASPAR 2014: an extensively expanded and updated open-access database of transcription factor binding profiles. *Nucleic Acids Res.* 42, D142–D147.

Mendelson, C. R. (2009). Minireview: fetal-maternal hormonal signaling in pregnancy and labor. *Mol. Endocrinol.* 23, 947–954. doi: 10.1210/me.2009-\break0016

Merico, D., Isserlin, R., Stueker, O., Emili, A., and Bader, G. D. (2010). Enrichment map: a network-based method for gene-set enrichment visualization and interpretation. *PLoS One* 5:e13984. doi: 10.1371/journal.pone.0013984

Moreau, M. E., Garbacki, N., Molinaro, G., Brown, N. J., Marceau, F., and Adam, A. (2005). The kallikrein-kinin system: current and future pharmacological targets. *J. Pharmacol. Sci.* 99, 6–38. doi: 10.1254/jphs.srj05001x

Myers, K., Socrate, S., Tzeranis, D., and House, M. (2009). Changes in the biochemical constituents and morphologic appearance of the human cervical stroma during pregnancy. *Eur. J. Obstet. Gynecol. Reprod. Biol.* 144(Suppl. 1), S82–S89.

Myers, K. M., Paskaleva, A. P., House, M., and Socrate, S. (2008). Mechanical and biochemical properties of human cervical tissue. *Acta Biomater.* 4, 104–116. doi: 10.1016/j.actbio.2007.04.009

Nelson, C. C., Hendy, S. C., Shukin, R. J., Cheng, H., Bruchovsky, N., Koop, B. F., et al. (1999). Determinants of DNA sequence specificity of the androgen, progesterone, and glucocorticoid receptors: evidence for differential steroid receptor response elements. *Mol. Endocrinol.* 13, 2090–2107. doi: 10.1210/mend.13.12.0396

O'Connell, R. M., Taganov, K. D., Boldin, M. P., Cheng, G., and Baltimore, D. (2007). MicroRNA-155 is induced during the macrophage inflammatory response. *Proc. Natl. Acad. Sci. U.S.A.* 104, 1604–1609. doi: 10.1073/pnas.0610731104

O'Neill, L. A., Sheedy, F. J., and McCoy, C. E. (2011). MicroRNAs: the fine-tuners of Toll-like receptor signalling. *Nat. Rev. Immunol.* 11, 163–175. doi: 10.1038/nri2957

Oppermann, U. C., Persson, B., and Jornvall, H. (1997). Function, gene organization and protein structures of 11beta-hydroxysteroid dehydrogenase isoforms. *Eur. J. Biochem.* 249, 355–360. doi: 10.1111/j.1432-1033.1997.t01-1-00355.x

Panchatcharam, M., Salous, A. K., and Brandon, J. (2014). Mice with targeted inactivation of ppap2b in endothelial and hematopoietic cells display enhanced vascular inflammation and permeability. *Arterioscler. Thromb. Vasc. Biol.* 34, 837–845. doi: 10.1161/atvbaha.113.302335

Pham, H., Rodriguez, C. E., Donald, G. W., Hertzer, K. M., Jung, X. S., Chang, H. H., et al. (2013). miR-143 decreases COX-2 mRNA stability and expression in pancreatic cancer cells. *Biochem. Biophys. Res. Commun.* 439, 6–11. doi: 10.1016/j.bbrc.2013.08.042

Quinn, S. R., and O'Neill, L. A. (2011). A trio of microRNAs that control Toll-like receptor signalling. *Int. Immunol.* 23, 421–425. doi: 10.1093/intimm/dxr034

Rehli, M., Krause, S. W., Schwarzfischer, L., Kreutz, M., and Andreesen, R. (1995). Molecular cloning of a novel macrophage maturation-associated transcript encoding a protein with several potential transmembrane domains. *Biochem. Biophys. Res. Commun.* 217, 661–667. doi: 10.1006/bbrc.1995.2825

Reiner, A., Yekutieli, D., and Benjamini, Y. (2003). Identifying differentially expressed genes using false discovery rate controlling procedures. *Bioinformatics* 19, 368–375. doi: 10.1093/bioinformatics/btf877

Ricciardolo, F. L. M., Folkerts, G., Folino, A., and Mognetti, B. (2018). Bradykinin in asthma: modulation of airway inflammation and remodelling. *Eur. J. Pharmacol.* 827, 181–188. doi: 10.1016/j.ejphar.2018.03.017

Robinson, M. D., McCarthy, D. J., and Smyth, G. K. (2010). edgeR: a Bioconductor package for differential expression analysis of digital gene expression data. *Bioinformatics* 26, 139–140. doi: 10.1093/bioinformatics/btp616

Rubel, C. A., Lanz, R. B., Kommagani, R., Franco, H. L., Lydon, J. P., and DeMayo, F. J. (2012). Research resource: genome-wide profiling of progesterone receptor binding in the mouse uterus. *Mol. Endocrinol.* 26, 1428–1442. doi: 10.1210/me.2011-1355

Sakamoto, Y., Moran, P., Bulmer, J. N., Searle, R. F., and Robson, S. C. (2005). Macrophages and not granulocytes are involved in cervical ripening. *J. Reprod. Immunol.* 66, 161–173. doi: 10.1016/j.jri.2005.04.005

Sato, T., Michizu, H., Hashizume, K., and Ito, A. (2001). Hormonal regulation of PGE2 and COX-2 production in rabbit uterine cervical fibroblasts. *J. Appl. Physiol.* 90, 1227–1231. doi: 10.1152/jappl.2001.90.4.1227

Schmaier, A. H. (2016). The contact activation and kallikrein/kinin systems: pathophysiologic and physiologic activities. *J. Thromb. Haemost.* 14, 28–39. doi: 10.1111/jth.13194

Schmittgen, T. D., and Livak, K. J. (2008). Analyzing real-time PCR data by the comparative C(T) method. *Nat. Protoc.* 3, 1101–1108. doi: 10.1038/nprot.2008.73

Seckl, J. R. (2004). 11β—hydroxysteroid dehydrogenases: changing glucocorticoid action. *Curr. Opin. Pharmacol.* 4, 597–602. doi: 10.1016/j.coph.2004.09.001

Seki, M., Kohno, S., Newstead, M. W., Zeng, X., Bhan, U., Lukacs, N. W., et al. (2010). Critical role of IL-1 receptor-associated kinase-M in regulating chemokine-dependent deleterious inflammation in murine influenza pneumonia. *J. Immunol.* 184, 1410–1418. doi: 10.4049/jimmunol.0901709

Shukla, V., Barnhouse, V., Ackerman, W. E. IV, Summerfield, T. L., Powell, H. M., Leight, J. L., et al. (2018). Cellular mechanics of primary human cervical fibroblasts: influence of progesterone and a pro-inflammatory cytokine. *Ann. Biomed. Eng.* 46, 197–207. doi: 10.1007/s10439-017-1935-0

Shynlova, O., Lee, Y. H., Srikhajon, K., and Lye, S. J. (2013). Physiologic uterine inflammation and labor onset: integration of endocrine and mechanical signals. *Reprod. Sci.* 20, 154–167. doi: 10.1177/1933719112446084

Stjernholm-Vladic, Y., Wang, H., Stygar, D., Ekman, G., and Sahlin, L. (2004). Differential regulation of the progesterone receptor A and B in the human uterine cervix at parturition. *Gynecol. Endocrinol.* 18, 41–46. doi: 10.1080/09513590310001651777

Storer, C. L., Dickey, C. A., Galigniana, M. D., Rein, T., and Cox, M. B. (2011). FKBP51 and FKBP52 in signaling and disease. *Trends Endocrinol. Metab.* 22, 481–490. doi: 10.1016/j.tem.2011.08.001

Subramanian, A., Tamayo, P., Mootha, V. K., Mukherjee, S., Ebert, B. L., Gillette, M. A., et al. (2005). Gene set enrichment analysis: a knowledge-based approach for interpreting genome-wide expression profiles. *Proc. Natl. Acad. Sci. U.S.A.* 102, 15545–15550. doi: 10.1073/pnas.0506580102

Thomas-Chollier, M., Hufton, A., Heinig, M., O'Keeffe, S., Masri, N. E., Roider, H. G., et al. (2011). Transcription factor binding predictions using TRAP for the analysis of ChIP-seq data and regulatory SNPs. *Nat. Protoc.* 6, 1860–1869. doi: 10.1038/nprot.2011.409

Tili, E., Michaille, J. J., Cimino, A., Costinean, S., Dumitru, C. D., Adair, B., et al. (2007). Modulation of miR-155 and miR-125b levels following lipopolysaccharide/TNF-alpha stimulation and their possible roles in regulating the response to endotoxin shock. *J. Immunol.* 179, 5082–5089. doi: 10.4049/jimmunol.179.8.5082

Timmons, B., Akins, M., and Mahendroo, M. (2010). Cervical remodeling during pregnancy and parturition. *Trends Endocrinol. Metab.* 21, 353–361. doi: 10.1016/j.tem.2010.01.011

Tomlinson, J. W., Walker, E. A., Bujalska, I. J., Draper, N., Lavery, G. G., Cooper, M. S., et al. (2004). 11β−hydroxysteroid dehydrogenase type 1: a tissue-specific regulator of glucocorticoid response. *Endocr. Rev.* 25, 831–866. doi: 10.1210/er.2003-0031

Trasino, S. E., Harrison, E. H., and Wang, T. T. (2007). Androgen regulation of aldehyde dehydrogenase 1A3 (ALDH1A3) in the androgen-responsive human prostate cancer cell line LNCaP. *Exp. Biol. Med.* 232, 762–771.

Uchiyama, T., Sakuta, T., and Kanayama, T. (2005). Regulation of hyaluronan synthases in mouse uterine cervix. *Biochem. Biophys. Res. Commun.* 327, 927–932. doi: 10.1016/j.bbrc.2004.12.092

Vink, J., and Feltovich, H. (2016). Cervical etiology of spontaneous preterm birth. *Semin. Fetal Neonatal Med.* 21, 106–112. doi: 10.1016/j.siny.2015.12.009

Wang, Z. Q., Xing, W. M., Fan, H. H., Wang, K.-S., Zhang, H.-K., Wang, Q.-W., et al. (2009). The novel lipopolysaccharide-binding protein CRISPLD2 is a critical serum protein to regulate endotoxin function. *J. Immunol.* 183, 6646–6656. doi: 10.4049/jimmunol.0802348

Weidmann, H., Heikaus, L., Long, A. T., Naudin, C., Schluter, H., and Renne, T. (2017). The plasma contact system, a protease cascade at the nexus of inflammation, coagulation and immunity. *Biochim. Biophys. Acta Mol. Cell Res.* 1864, 2118–2127. doi: 10.1016/j.bbamcr.2017.07.009

Word, R. A., Li, X. H., Hnat, M., and Carrick, K. (2007). Dynamics of cervical remodeling during pregnancy and parturition: mechanisms and current concepts. *Semin. Reprod. Med.* 25, 69–79.

Wu, C., Huang, R. T., Kuo, C. H., Kumar, S., Kim, C. W., Lin, Y.-C., et al. (2015). Mechanosensitive PPAP2B regulates endothelial responses to atherorelevant hemodynamic forces. *Circ. Res.* 117, e41–e53.

Wu, Y. (2015). Contact pathway of coagulation and inflammation. *Thromb. J.* 13:17.

Xu, C., Ren, G., Cao, G., Chen, Q., Shou, P., Zheng, C., et al. (2013). miR-155 regulates immune modulatory properties of mesenchymal stem cells by targeting TAK1-binding protein 2. *J. Biol. Chem.* 288, 11074–11079. doi: 10.1074/jbc.m112.414862

Xu, H., Gonzalez, J. M., Ofori, E., and Elovitz, M. A. (2008). Preventing cervical ripening: the primary mechanism by which progestational agents prevent preterm birth? *Am. J. Obstet. Gynecol.* 198, 314–318.

Yellon, S. M. (2017). Contributions to the dynamics of cervix remodeling prior to term and preterm birth. *Biol. Reprod.* 96, 13–23. doi: 10.1095/biolreprod.116.142844

Yong, P. Y., Harlow, C., Thong, K. J., and Hillier, S. G. (2002). Regulation of 11beta-hydroxysteroid dehydrogenase type 1 gene expression in human ovarian surface epithelial cells by interleukin-1. *Hum. Reprod.* 17, 2300–2306. doi: 10.1093/humrep/17.9.2300

Yoo, J. Y., Shin, H., Kim, T. H., Choi, W.-S., Ferguson, S. D., Fazleabas, A. T., et al. (2014). CRISPLD2 is a target of progesterone receptor and its expression is decreased in women with endometriosis. *PLoS One* 9:e100481. doi: 10.1371/journal.pone.100481

Yoshida, M., Sagawa, N., Itoh, H., Yura, S., Takemura, M., Wada, Y., et al. (2002). Prostaglandin F, cytokines and cyclic mechanical stretch augment matrix metalloproteinase-1 secretion from cultured human uterine cervical fibroblast cells. *Mol. Hum. Reprod.* 8, 681–687. doi: 10.1093/molehr/8.7.681

Zhang, H., Liu, Z., and Liu, S. (2016). HMGB1 induced inflammatory effect is blocked by CRISPLD2 via MiR155 in hepatic fibrogenesis. *Mol. Immunol.* 69, 1–6. doi: 10.1016/j.molimm.2015.10.018

Conflict of Interest: The authors declare that the research was conducted in the absence of any commercial or financial relationships that could be construed as a potential conflict of interest.

Copyright © 2020 Kniss and Summerfield. This is an open-access article distributed under the terms of the Creative Commons Attribution License (CC BY). The use, distribution or reproduction in other forums is permitted, provided the original author(s) and the copyright owner(s) are credited and that the original publication in this journal is cited, in accordance with accepted academic practice. No use, distribution or reproduction is permitted which does not comply with these terms.

frontiers in Bioengineering and Biotechnology

REVIEW
published: 25 September 2020
doi: 10.3389/fbioe.2020.529365

An Introductory Overview of Image-Based Computational Modeling in Personalized Cardiovascular Medicine

*Thanh Danh Nguyen[1], Olufemi E. Kadri[1,2] and Roman S. Voronov[1,3]**

[1] Otto H. York Department of Chemical and Materials Engineering, Newark College of Engineering, New Jersey Institute of Technology, Newark, NJ, United States, [2] UC-P&G Simulation Center, University of Cincinnati, Cincinnati, OH, United States, [3] Department of Biomedical Engineering, Newark College of Engineering, New Jersey Institute of Technology, Newark, NJ, United States

OPEN ACCESS

Edited by:
David Bogle, University College London, United Kingdom

Reviewed by:
Yu Lin, Center for Devices and Radiological Health (CDRH), United States
Lucia Marucci, University of Bristol, United Kingdom

***Correspondence:**
Roman S. Voronov
rvoronov@njit.edu

Specialty section:
This article was submitted to Computational Genomics, a section of the journal Frontiers in Bioengineering and Biotechnology

Received: *24 January 2020*
Accepted: *31 August 2020*
Published: *25 September 2020*

Citation:
Nguyen TD, Kadri OE and Voronov RS (2020) An Introductory Overview of Image-Based Computational Modeling in Personalized Cardiovascular Medicine. Front. Bioeng. Biotechnol. 8:529365. doi: 10.3389/fbioe.2020.529365

Cardiovascular diseases account for the number one cause of deaths in the world. Part of the reason for such grim statistics is our limited understanding of the underlying mechanisms causing these devastating pathologies, which is made difficult by the invasiveness of the procedures associated with their diagnosis (e.g., inserting catheters into the coronal artery to measure blood flow to the heart). Likewise, it is also difficult to design and test assistive devices without implanting them *in vivo*. However, with the recent advancements made in biomedical scanning technologies and computer simulations, image-based modeling (IBM) has arisen as the next logical step in the evolution of non-invasive patient-specific cardiovascular medicine. Yet, due to its novelty, it is still relatively unknown outside of the niche field. Therefore, the goal of this manuscript is to review the current state-of-the-art and the limitations of the methods used in this area of research, as well as their applications to personalized cardiovascular investigations and treatments. Specifically, the modeling of three different physics – electrophysiology, biomechanics and hemodynamics – used in the cardiovascular IBM is discussed in the context of the physiology that each one of them describes and the mechanisms of the underlying cardiac diseases that they can provide insight into. Only the "bare-bones" of the modeling approaches are discussed in order to make this introductory material more accessible to an outside observer. Additionally, the imaging methods, the aspects of the unique cardiac anatomy derived from them, and their relation to the modeling algorithms are reviewed. Finally, conclusions are drawn about the future evolution of these methods and their potential toward revolutionizing the non-invasive diagnosis, virtual design of treatments/assistive devices, and increasing our understanding of these lethal cardiovascular diseases.

Keywords: image-based modeling, personalized cardiovascular medicine, cardio electromechanics, hemodynamics, thrombogenesis, simulation, biomechanics, heart

INTRODUCTION: IMAGE-BASED MODELING OF THE HEART

Heart disease is the leading cause of death in the U.S., with one person dying from it every 37 s, or about 647,000 each year (i.e., 1 in every 4 deaths), and amounting to a $219 billion per year burden to the public health system (CDC, 2019). Understanding it is very difficult, because it is a complex interaction of biomechanics, electrophysiology and non-Newtonian hemodynamics. This is further complicated by the interaction with external medical devices (pacemakers, pumps, etc.) that are commonly implanted in order to assist a failing or dysfunctional heart. Moreover, the heart's properties (e.g., shape, structure, stiffness, electrical conductivity) that play an important role in determining its pumping ability are patient specific. Finally, it is difficult to extract information about the physiological processes occurring in living hearts, due to its constant motion, and the fact that invasive probing can be life threatening. For these reasons, Image-Based Modeling (IBM) – a patient-specific experimentally constrained computational approach – is a lucrative way for gaining novel insight into the cardiovascular diseases and their treatments.

An illustrative example of the IBM's usefulness is HeartFlow Inc. – a company located in California, United States with about 300 employees and backed by $467 million capital investment (Craft, 2019). Their application is the diagnosis of Coronary artery disease (CAD) – an impairment of blood flow in the arteries that supply the heart, due to cholesterol plaque buildup. The disease is one of the most misdiagnosed: a recent study, which included data from more than 1,100 U.S. hospitals, found that over half of the more than 385,000 patients with suspected CAD underwent an invasive coronary angiography (ICA) only to find out that they did not have the disease (Patel et al., 2014). This is bad because ICA is an invasive technique that in itself could lead to mortality, because it uses catheters inserted into the femoral (groin) or radial (wrist) arteries to measure pressure difference across a coronary artery stenosis in order to check the likelihood of a blockage's presence.

Conversely, HeartFlow calculates pressure differences virtually by simulating the blood flow through the patients' own arteries, the structure of which is derived from a three-dimensional (3D) computerized tomography (CT) scan. This information is then used to calculate the fractional flow reserve (FFR), which is a statistic used to assess the hemodynamic significance of the stenosis by determining the ratio of the pressures before and after the narrowing. Therefore, this technology effectively serves as a non-invasive alternative to the ICA (**Figure 1**) (HeartFlow, 2019).

The HeartFlow's method has been evaluated in four large prospective clinical trials, enrolling a total of more than 1,100 patients at major medical centers worldwide. It received the European Economic Area CE mark in 2011 and U.S. FDA clearance in August 2019 (i.e., it is currently commercially available in the U.S.) (FDA, 2019). To date, clinicians have used the HeartFlow approach for over 30,000 patients in the diagnosis of heart disease (Kim, 2019). Therefore, it serves as the most mature IBM application in the context of cardiovascular disease. Yet, it is also one of the simplest in that it does not include the heart itself, and the blood assumed a homogeneous (i.e., no cells) fluid. At the same time, more advanced models are coming online as well. Yet, they are relatively unknown outside of this niche field.

Although many excellent reviews already exist in the image-based heart-modeling area, most of them are focused on just one or two specific aspects: for example, image acquisition and processing (Weese et al., 2013; Lamata et al., 2014; Wang et al., 2015; Watson et al., 2018), hemodynamic flow simulations (Tang et al., 2010; Mittal et al., 2016; Quarteroni et al., 2017; Zhong et al., 2018); electrical conduction and stimulation modeling (Trayanova, 2011, 2012; Tobon-Gomez et al., 2013; Lopez-Perez et al., 2015; Rodriguez et al., 2015; Beheshti et al., 2016; Gray and Pathmanathan, 2018; Ni et al., 2018); tissue mechanics computations (Trayanova, 2011, 2012; Sun et al., 2014; Wang et al., 2015; Chabiniok et al., 2016; Niederer et al., 2019a,b), ventricular thrombosis (Mittal et al., 2016) and the use of models in diagnostic procedures (Tang et al., 2010; Trayanova, 2012). Whereas, the goal of this manuscript is to provide a brief introductory overview of the entire cardiovascular IBM for a non-expert audience, in order to increase the broader exposure of this exciting topic and its numerous potential applications: CAD, Arrhythmias, Heart Failure (HF), Left-Ventricular Assist Devices (LVAD) and Pathogenic Thrombosis/Embolism.

To that end, this review is organized as follows: Section "Methods: Literature Search" describes our literature search methods; Section "Background: Cardio Electromechanics and Hemodynamics" provides a brief background of the relevant cardiovascular physiology that explains how the tissue electromechanics and blood biology are interrelated *in vivo*; Section "Geometry Module" reviews how the model geometry is obtained using imaging, in order to establish a connection with the individual's unique anatomy; Sections "Electrophysiology Module," "Biomechanics Module," "Simplified Hemodynamics Module," and "Hemodynamics with Thrombogenesis Module" illustrate the mathematical formulation of the simulation modules used by these models, such as electrophysiology, biomechanics, simplified hemodynamics with and without thrombogenesis, respectively. Finally, Section "Summary and Conclusion" presents our summary and conclusions regarding the inputs and outputs of all cardiac modules as well as the directions that the field of personalized cardiovascular IBM is expected to go into.

METHODS: LITERATURE SEARCH

In order to provide a "big picture" snapshot overview of the image-based cardiovascular modeling and its potential penetration into the clinical sector, we gathered works from the recent (i.e., approximately the last 5 years) proceedings of the

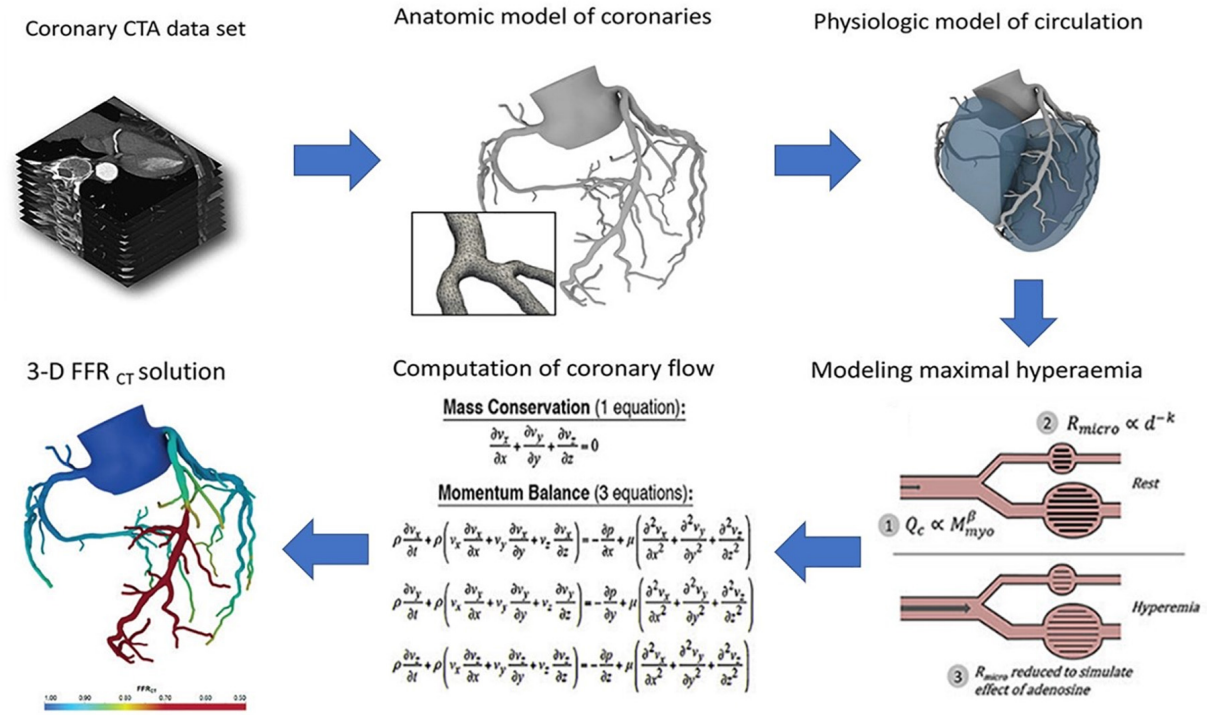

FIGURE 1 | Process flow diagram outlining the image-based computational pipeline of the HeartFlow's approach to calculating the fractional flow reserve computerized tomography (FFRCT). (Reproduced with permission from Nick Curzen, Professor of Interventional Cardiology/Consultant Cardiologist, University Hospital Southampton).

following meetings: Interagency Modeling and Analysis Group Consortium Meetings, National Institute for Mathematical and Biological Synthesis workshops, Personalized Medicine Coalition resources, International Workshop on Cancer Systems Biology meetings and conferences, Pacific Symposium on Biocomputing, Biomedical Engineering Society, American Institute of Chemical Engineers. Additionally, we performed manual searches with key words and terms including "image-based modeling of the heart," "patient-specific cardiovascular modeling," "cardio electrophysiology/biomechanics/electromechanics/hemodynamics image-based modeling" or "ventricular thrombosis modeling," etc. for both research and review articles on databases, such as PubMed central, Web of Science, Research Gate, and Google Scholar. Additionally, we relied on the corresponding author's own decade and a half long experience of working on biomedical image-based simulations. The obtained publication database was then screened by running citation reports to identify groups of researchers (typically led by a senior professor, who is joined by collaborators, postdocs, and students) that have established a track-record of being active within the various sub-areas of the cardiovascular modeling fields. Furthermore, to avoid bias (and to keep the work manageable) we tried to limit the literature sampling to just one most relevant publication from each of the groups. However, this was not always possible, because some of the researchers dominate their respective niches; and have published more than one article critical to our review.

BACKGROUND: CARDIO ELECTROMECHANICS AND HEMODYNAMICS

Macroscopic Overview of How the Three Physics Are Coupled With Each Other

Before going into the details of the computational models, it is first important to understand the three types of coupled physics occurring in the heart: electrical signal conduction, biomechanics of the contraction and hemodynamics (which could also include clot formation and embolism).

Figure 2A illustrates the cardiac conduction system (CCS) – a heterogeneous complex 3D network of highly specialized conductive cells (SA node, AV node, bundle of His, bundle branches, and Purkinje fibers) that transfer signals through the heart and cause it to contract. The electrical activity is initiated at the sinoatrial node (i.e., the natural pacemaker of the heart) where voltage signals called "action potentials" are produced periodically. Next the signals travel to the AV node, through the Bundle of HIS, down its branches and through the Purkinje Fibers. Ultimately, they are propagated to the myocardium (i.e., the muscular tissue of the heart) through discrete sites called Purkinje-Myocyte Junctions (not shown), causing the left and the right ventricles to contract independently of each other. This creates a double pumping action of the blood (see **Figure 2B**).

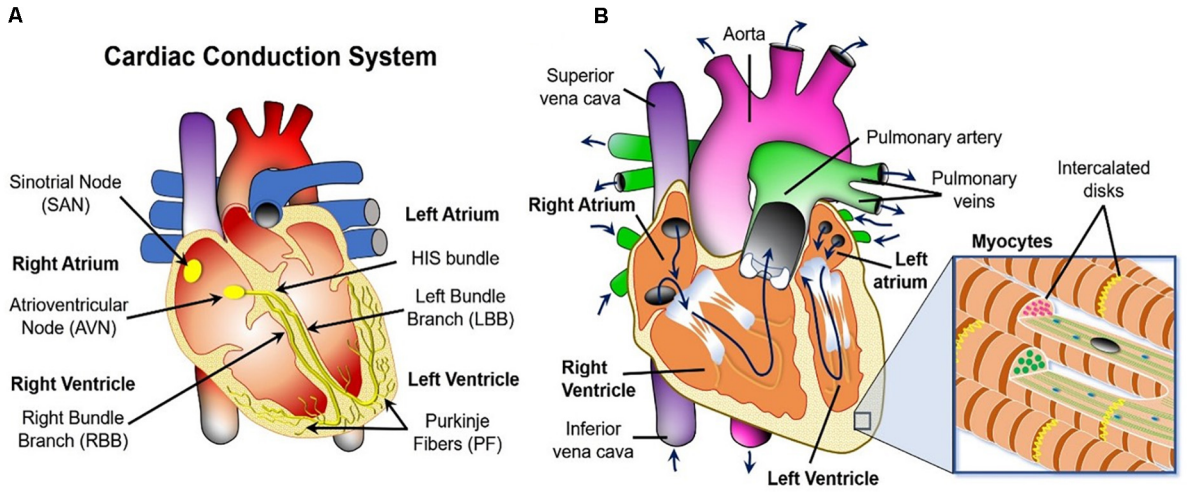

FIGURE 2 | Macroscopic overview of the three physics occurring in the heart. **(A)** Cardiac conduction system schematic. **(B)** Blood flow path (navy blue arrows) and the fibrous structure defining the biomechanics of the heart wall (inset).

Specifically, oxygen-poor blood returns from the body to the right side of the heart (i.e., atrium and ventricle), which then sends it to the lungs for re-oxygenation. Oxygen-rich blood from the lungs then enters the left side of the heart and is pumped through the aorta back to the body. The blood can also carry thrombi (or their embolized pieces) from other parts of the body, and/or the clots could be generated within the heart itself via activation of platelets (blood cells responsible for clot formation) and the coagulation cascade (a series of biochemical reactions that results in the formation of a polymer mesh that facilitates the structural integrity of the clot). The presence of these objects in the cardiovascular system can interfere with the mechanical action of the heart by creating rigid obstructions. Furthermore, the blood clots can also get stuck in the cardio-vasculature and block the delivery of metabolites to the heart tissue. This leads to necrosis of the latter, commonly referred to as an ischemia or a heart attack.

Structural Importance of the Myocardium

The organization of the cardiomyocyte fibers in the heart's walls is thought to be critical to both the conductive and to the mechanical properties of the organ. Specifically, the contractile myocytes cells that cause the heart ventricles to beat are arranged in fibers (see inset of **Figure 2B**). These fibers make up the walls of the heart, which are lined with collagen and elastin extracellular matrix on the inside (i.e., endocardium) and the outside (i.e., epicardium). Their thickness varies both spatially and temporarily throughout the cardiac cycle.

If one were to take a representative sample from the left ventricle (which pumps the most blood) as in **Figure 3A**, it would be possible to see that the 3D layered organization of the myocytes changes throughout the wall thickness from the epicardium to the endocardium. In fact, **Figure 3A** shows that the muscle fiber direction rotates from $+50°$ to $+70°$ (sub-epicardial region) to nearly $0°$ in the mid-wall region to $-50°$ to $-70°$ (sub-endocardial region) with respect to the circumferential direction of the left ventricle (Holzapfel and Ogden, 2009). Finally, **Figure 3B** show that the myocyte fibers (or myofibrils) are arranged into composite layers (or sheets), which are interconnected by collagen fibers. Therefore, for IBM to be physiologically representative, it must account for how this intricate structure affects the complex physics that occur in the heart.

GEOMETRY MODULE

The most common ways for obtaining a realistic macroscopic morphology of the heart and its surrounding blood vessels are computerized tomography (CT) and magnetic resonance imaging (MRI). However, the typical MRI/CT machines provide relatively coarse resolution datasets of the personalized cardiac geometry, with large gaps between slices (Schulte et al., 2001; Frangi et al., 2002; Appleton et al., 2005). This necessitates the use of interpolation procedures. Hence, the microscopic details (e.g., blood vessels, trabeculations, the Purkinje Fibers, the location and activity of the PMJs, the orientations of the myofibril sheets, etc.) are harder to resolve due to their small size. Yet, they strongly determine the electrophysiological and biomechanical properties of cardiac tissue (Watson et al., 2018). Consequently, there are three main methods for accounting for these fine details:

Rule-Based Heuristics

The most rudimentary approach is to generate these features mathematically, based on observed trends (see **Figure 4A**) (Streeter Daniel et al., 1969). Briefly, the longitudinal fiber direction is assumed to rotate clockwise from the endocardium to the epicardium. Specifically, it is made parallel to the long axis of the papillary muscles, trabeculae at these regions and parallel to the endocardial and epicardial surfaces at the ventricular

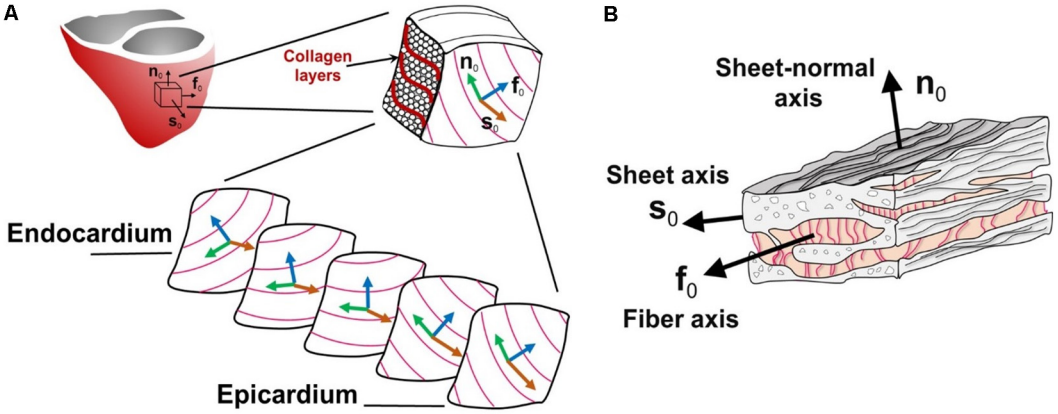

FIGURE 3 | Schematic diagram of the heart tissue microstructure. **(A)** The transmural configuration of the muscle fibers and laminar sheets. **(B)** The layered organization of myocytes and the collagen fibers between the sheets. f_0, fiber axis; s_0, sheet axis and n_0, sheet-normal axis. (Adopted with permission from Holzapfel and Ogden, 2009).

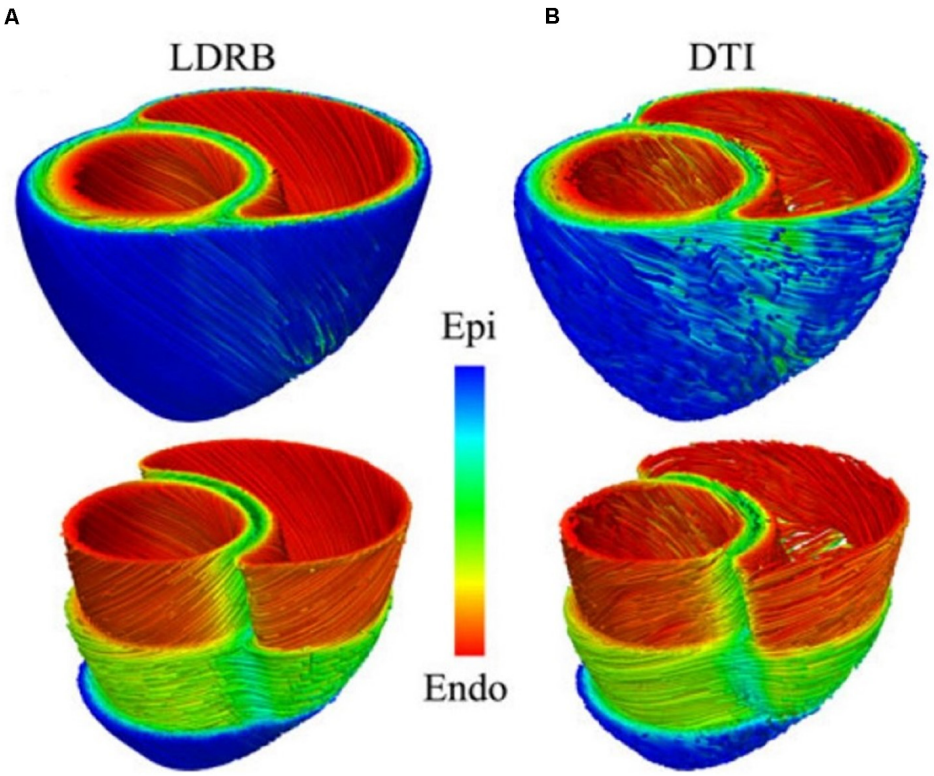

FIGURE 4 | Comparison between **(A)** rule-based method and **(B)** DTI-based estimation of the myocardial fiber orientation for a 3D model of canine ventricles. (Reproduced with permission from Bayer et al., 2012).

walls. Lastly, the fiber orientation in the septum is assumed to be running along the ventricular walls (Bayer et al., 2012). A popular way to personalize the algorithm to a patient specific structure of the heart is to use the minimal distance between the *imaged* endocardial and the epicardial surfaces to approximate orientation of the fibers. More stable and advanced rule based approaches, such as the Laplace-Dirichlet method also exist (Bayer et al., 2012). However, the heuristics are not guaranteed to be physiologically accurate, nor are they fully patient specific. Yet they remain the most common approach due to their low cost and ease of implementation, as well as due to the difficulty of imaging the microstructural details in a beating heart *in vivo*. And, as **Figure 4** shows, they yield results that are comparable with the best of the imaging techniques (which typically require

for the heart to be explanted and fixed in order to acquire such fine details).

Histology/Optical Microscopy

The fiber orientation can also be approximated from histology of explanted hearts (Vetter and McCulloch, 1998; Deng et al., 2012), where the tissue is sliced into very thin 2D sections and dyed using special agents that highlight the features of interest. Although it is possible to create a 3D reconstruction based on the 2D slices using this approach, manual sectioning of the tissue may result in uneven slice thicknesses and feature distortion (Burton et al., 2006). Additionally, confocal microscopy has been used to image the fine structure of the myocardium (Hooks et al., 2002, 2006). However, the light penetration depth into the sample is typically limited to ∼100 mm. Hence, imaging a whole heart using this technique is also impractical. Therefore, both histology and confocal are typically used to provide localized information on explanted samples only. However, this information is useful for validating the rule-based methods, the *in vivo* imaging, and the modeling results.

Diffusion-Tensor MRI, Micro-CT With Contrast and 3D Ultrasound Backscatter Tensor Imaging

Additional detail can be obtained from MRI images using a Gadolinium contrast agent (Bishop et al., 2010) and a special technique called Diffusion Tensor imaging (DTI) (see **Figure 4B**). The latter maps the diffusion of water molecules in the biological tissues, which is not free, but reflects the interactions with obstacles like macromolecules, fibers and membranes. For the cardiac DTI, it is well known that the direction of the primary eigenvector corresponding to each voxel of the received images matches the longitudinal axis of cardiac myocytes (Scollan et al., 1998; Holmes et al., 2000). This information can then be mapped onto the volumetric mesh of a 3D cardiac macro-geometry to include the microscopic fiber orientation (Plank et al., 2009; Vadakkumpadan et al., 2010). Likewise, micro-computed tomography (mCT) with iodine staining has also recently been used to assess the myocyte fiber orientation in the heart tissue (Aslanidi et al., 2013). However, both techniques are too slow to capture a beating heart in 3D without motion artifacts. Luckily, advanced ultrasound-based imaging techniques are coming online, which can map the myocardial fibers orientation and its dynamics with a temporal resolution of 10 ms during a single cardiac cycle, non-invasively and *in-vivo* in entire volumes (Papadacci et al., 2017). However, given the novelty, complexity and cost of these techniques, they are not yet widely available to the majority of the cardiovascular IBM researchers.

Imaging-to-Modeling Pipeline

Perhaps the most difficult aspect of the *in vivo* scanning of live hearts is the need to perform significant image alignment using "registration" techniques. Furthermore, once the images are aligned, they must be "segmented" to identify the various tissue types and structural features of interest within the data. The segmentation can be either based on contrast dyes and/or on morphological feature detection (both manual and automated). The images can also be enhanced using digital post-processing, such as deconvolution (i.e., minimizing noise caused by objects outside of the imaging plane) and structure tensor analysis (e.g., enhancing visibility of the structural features for the fiber orientation detection) (Burton et al., 2006; Zhao et al., 2013). Numerical interpolation and machine learning techniques can further enhance the apparent resolution of the images digitally. Finally, the cardiovascular geometry must be "meshed" (i.e., broken up into pieces) to discretize the objects obtained from the images as a set of finite elements for numerical analysis. The latter is a simulation necessity that enables solving systems of complex (e.g., partial differential) equations by recasting them as *algebraic* approximations of the true solution. The trade-off for the simplified math is that the solution accuracy must be increased by making the mesh finer. This grows the number of equations that must be solved simultaneously, and thus the computational resource and time requirements. Overall, the imaging pipeline procedures are often very complicated and necessitate manual labor. This is both cumbersome (e.g., due to the large size of the high-resolution images) and subjective (e.g., due to the lack of contrast agents which necessitate user input). Therefore, there is an on-going effort to automate the imaging-to-modeling pipeline (Bishop et al., 2010).

ELECTROPHYSIOLOGY MODULE

The simplest types of the heart models tend to be focused on cardiac arrhythmias. This is an "umbrella" term for irregularities in the conduction or pacing of the electrical signals that control the heartbeat rhythm. Given that some arrhythmias can lead to mortality, it is important to understand the underlying electrophysiological mechanisms of these disorders. Yet, electrocardiograms of the heart provide only limited information, which often fails to predict lethal outcomes (Goldberger et al., 2011). Therefore, computational modeling offers a better alternative for studying these diseases.

Most arrhythmia models focus on the electrophysiology of the heart, while assuming that it is isolated from the biomechanics of the contractions that lead to the pumping of the blood. As mentioned in Section "Methods: Literature Search," the contraction of cardiomyocytes is initiated by electrical impulses called "action potentials," which travel through the cardiac conduction system (see **Figure 2A**) into the myocardium. This electrical potential travels from one cell to another in the form of ions that pass through gap junctions between the cardiomyocytes (see **Figure 5**).

The cardiomyocytes are polarized, meaning that there is an electrical potential across the cell membrane: in the resting state the cells are more negative on the inside and positive on the outside, while the charge polarity is temporarily reversed as the action potential passes through them. This reversal occurs via the transport of Ca^{++} and Na^{+} ions from the outside of the cells to their inside, and K^{+} ions in the reverse direction (see **Figure 5**). The internalization of the Ca^{++} ion is especially important to the contraction of the cardiomyocytes, because it triggers a

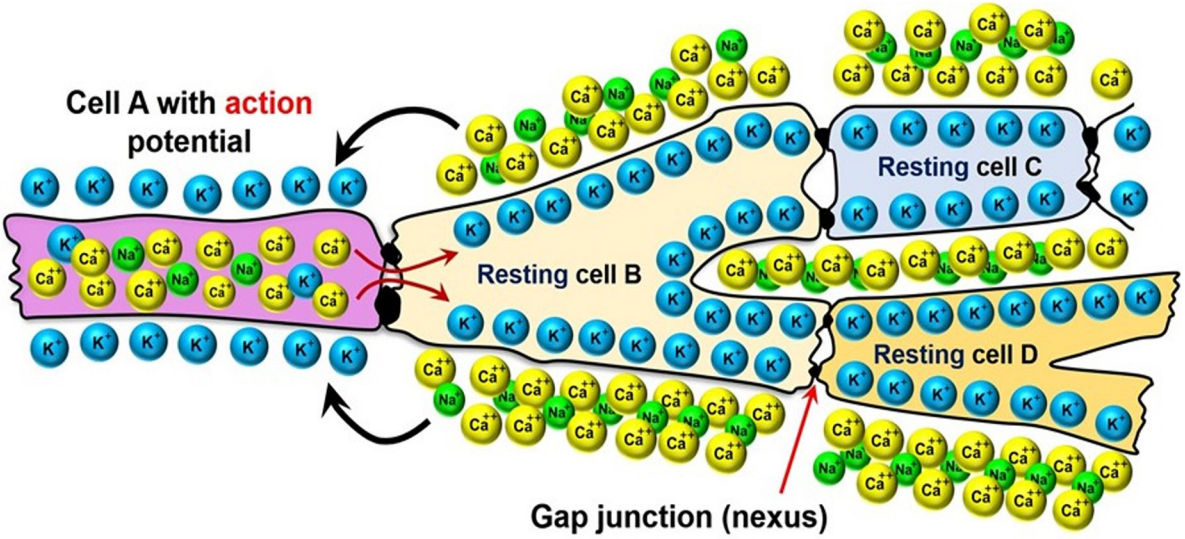

FIGURE 5 | Electrical coupling of the neighboring cardiomyocytes via the gap-junctions between their membranes.

sub-cellular signaling cascade that generates tension inside of the cells. Therefore, the electrophysiology models simulate the propagation of the ionic currents through the myocardium.

However, given that there are many cells in the heart, and each one of them has the ionic channels and transmembrane potentials, the problem is an inherently multiscale one (see **Figure 6**). On the subcellular scale (see **Figure 6**-LEFT), differential equations are used to model the transport of ionic species based on the Hodgkin–Huxley formulation (originally developed for the propagation of action potentials in neurons) (Hodgkin and Huxley, 1952). The subcellular models are then combined into cell scale models that can account for up to dozens of different ionic species and signaling intra-cellular cascades (see **Figure 6**, CENTER). Among these, the leading model is currently considered to be by O'Hara et al. (2011), which is based on experimental data from >150 undiseased human hearts. Finally, the individual ion currents are used to calculate the overall transmembrane potential, and its transport across the myocardium is treated as a diffusion across a homogenous medium (i.e., no discrete cells are considered by these models).

There are two types of formulations for the organ-level diffusion (which is related to the ionic conductivity) of the action potential across the myocardium: (1) the *bidomain* formulation, which considers different diffusivities inside and outside of the cell (Quarteroni et al., 2017) (see **Figure 6**, RIGHT):

$$\begin{aligned} \chi C_m(\partial_t v + i_{ion}(v,w,c)) - \nabla\cdot(D_i\nabla v_i) &= \chi i^i_{app}(t) \\ \chi C_m(\partial_t v + i_{ion}(v,w,c)) - \nabla\cdot(D_e\nabla v_e) &= \chi i^e_{app}(t) \\ \frac{dw}{dt} &= m_w(v,w,c) \\ \frac{dc}{dt} &= m_c(v,w,c) \end{aligned} \tag{1}$$

The bidomain formulation is used for simulating the action potential propagation throughout the myocardium in the intra- and the extra- domains separately. The myocardium is assumed to be a continuum in which the potential is considered to vary along the longitudinal direction of the conducting cells, while it is constant in the transversal (or radial) directions (Quarteroni et al., 2017). In this formulation, v_i, v_e and 'v' are intracellular, extracellular and transmembrane potentials, respectively; i^i_{app} and i^e_{app}stand for applied stimuli on the intra- and extracellular spaces, respectively; i_{ion} are the ionic currents following a Hodgkin–Huxley-type description for different ionic species (Hodgkin and Huxley, 1952); w are gating variables taking values in [0,1] that regulate the transmembrane currents and have a mutual relation with the intracellular concentrations c of different ionic species (which also vary depending on the values of transmembrane potentials v) (Quarteroni et al., 2017); C_m is the membrane capacitance; 'χ' is the ratio of membrane area per tissue volume; D_i and D_e are the conductivity tensors of the intra- and extracellular media, respectively.

and (2) the *monodomain* formulation, which simplifies the problem by considering only the transmembrane potential (Quarteroni et al., 2017):

$$\chi[C_m\partial_t v + i_{ion}(v,w,c) - i_{app}(t)] = \frac{1}{J}\nabla\cdot(D_0\nabla_v) \tag{2}$$

In this formulation, the cardiac tissue is also assumed to be a continuum, but the current conservation is written in terms of the transmembrane potential v only (i.e., not considering the intra- and extracellular potentials) (Quarteroni et al., 2017). Instead, the intracellular and extracellular diffusivities are assumed to be proportional to each other, and therefore can be represented by a single variable. Herein, D_0 is the conductivity tensor in a fixed reference state, J is the determinant of the deformation gradient tensor, which represents the volume change of a deformable object. The trade-off for the simplicity is that the monodomain model is unable to describe cardiomyocyte

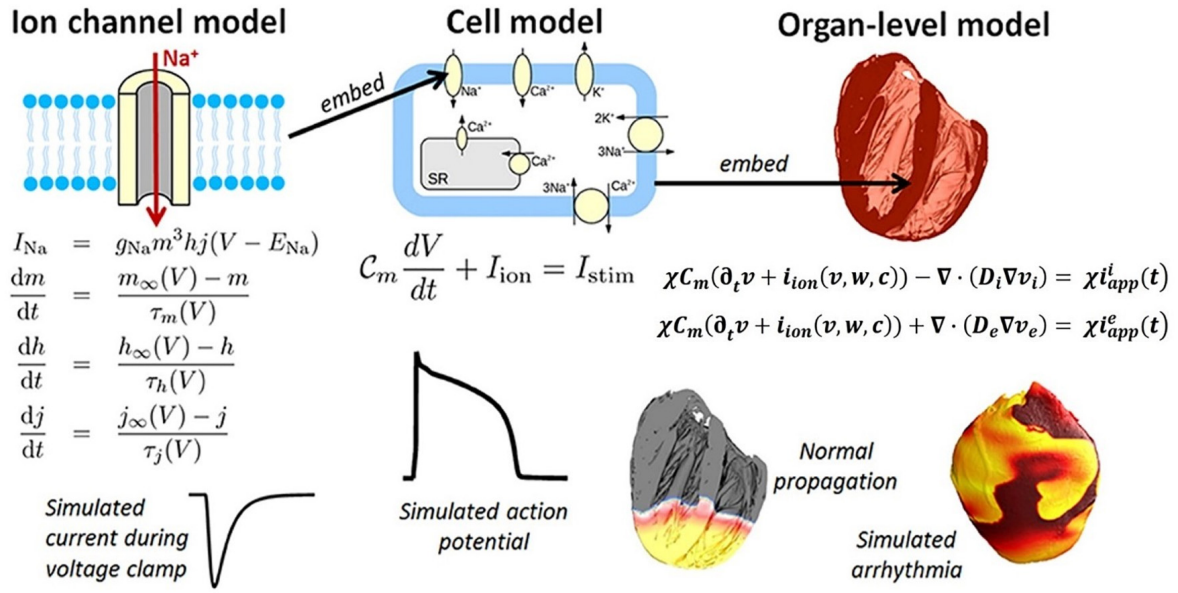

FIGURE 6 | Components of a multiscale cardiac electrophysiology model. **(Left)** Equations and sample output for a Hodgkin-Huxley formulation of the rapid sodium current through an ion channel. Multiple such sub-cellular models can be used to define a cell model. **(Center)** Schematic of sub-cellular processes included in a hypothetical cell model, together with the differential equation governing the transmembrane voltage, and sample output. Cell models differ in their formulation of the ionic current i_{ion} and can be made up of dozens of ordinary differential equations. **(Right)** Cell models can be incorporated into the bidomain equations and solved on a computational mesh of the heart (**top right:** high-resolution rabbit biventricular mesh of Bishop et al., 2010), to simulate normal or arrhythmic cardiac activity **(bottom right)**. (Adopted with permission from Pathmanathan and Gray, 2018).

repolarization patterns. For this reason, the bidomain model is more widely used (Bishop and Plank, 2011).

Module Personalization

Table 1 summarizes the most common electrophysiology module personalization approaches encountered in the recent IBM works, while **Figure 7** maps the relationships between the module's inputs, outputs and applications. In this, and in the subsequent modules, the heart's *macroscopic* anatomy can be personalized for a specific patient by acquiring its geometry from the *in vivo* imaging (see "Geometry Module" section). Furthermore, pathological tissue remodeling (e.g., locations and extension of infarct scars, diffuse fibrosis, etc.) can be accounted for via the imaging as well (Vadakkumpadan et al., 2009; Mewton et al., 2011; Dass et al., 2012; Ashikaga et al., 2013; Arevalo et al., 2016; Trayanova et al., 2017). However, there are two important types of *microscopic* structural information that cannot be completely personalized yet: the myocardial fiber orientation and the CCS.

Both are, unfortunately, still too difficult to image in a moving heart *in vivo*. Thus, typically an *approximated* personalization is performed to include these microscopic features using the rule-based algorithms (see "Geometry Module" section). Additional CCS approximation methods are based on: early activation points obtained from the literature (Durrer et al., 1970); manual delineation of CCS on the endocardial surfaces (Romero et al., 2010); *ex vivo* data obtained by means of histological studies of animal hearts (Sebastian et al., 2013); from *in vivo* electro-anatomical maps (EAMs) (Cardenes et al., 2014; Palamara et al., 2014). The EAMs data can provide the location of some of the PMJs, and can also be used to reconstruct patient-specific electrical activation patterns (Cardenes et al., 2014; Palamara et al., 2014).

Likewise, the conductivity values of different tissue zones (normal and abnormal/damaged) are typically too difficult to measure in living human patients, and are thus initialized based on accepted literature values: 2–3 m/s in the His-Purkinje system and 0.3–0.4 m/s in the conductive myocardial cells (Ideker et al., 2009). They are then either further adjusted to match the human myocardium conduction velocity (CV) (i.e., speed at which action potentials are distributed throughout the tissue) measured using explanted hearts (Arevalo et al., 2016; Trayanova et al., 2017; Lopez-Perez et al., 2019), or are tuned to fit patient-specific electrical activation patterns obtained from electrocardiograms (ECG), body surface potential maps (BSPM) or EAM (Sermesant et al., 2008; Lopez-Perez et al., 2015).

Unfortunately, at the cellular level, the patient-specific transmembrane current dynamics (i.e., i_{ion}) cannot yet be measured; and hence, the existing mathematical models are not personalized at such detail. Similarly, the electrical heterogeneity between the different regions (e.g., transmural heterogeneity in the ventricular walls), the electrical remodeling and the effects due to an individual's genetic mutations on the cardiac electrophysiology cannot yet be accounted for (Lopez-Perez et al., 2015). However, a cellular level electrophysiology model that best matches the patient's pathology can instead be chosen from either existing literature datasets that are representative of a patient-group (Krueger et al., 2013a,b) or from patch-clamp studies

TABLE 1 | A recent literature survey of how the Electrophysiology Module is typically personalized using image-based information.

Imaging method	Personalized information from imaging	Mapping of the personalized information from imaging to the module's inputs	Citation
MRI	Geometry with infarcted regions	Geometry was personalized and tissue conductivity values were adjusted to match the conduction velocity (CV) in human cardiac tissue.	Ashikaga et al., 2013
MRI	Geometry with infarcted regions	Geometry was personalized and tissue conductivity values were adjusted to match the CV in human cardiac tissue.	Arevalo et al., 2016
MRI	Geometry with infarcted regions	Geometry was personalized and tissue conductivity values were adjusted to match the CV in human cardiac tissue.	Trayanova et al., 2017
CT	Geometry	Geometry was personalized and tissue conductivities were adjusted to fit local activation times, which were obtained using electro-anatomical maps (EAMs).	Cardenes et al., 2014
CT and MRI	Geometry with infarcted regions	Geometry was personalized and tissue conductivities were adjusted to fit patient-specific electrical activation using EAMs.	Palamara et al., 2014
MRI	Geometry	Geometry was personalized; tissue conductivities were adjusted to fit patient-specific electrical activation and ECG; and ionic currents were also personalized (via blood electrolyte concentrations measurement).	Krueger et al., 2013a
MRI	Geometry with infarcted regions	Geometry was personalized; tissue conductivities were adjusted to fit a human cardiac tissue model; and ionic currents were personalized via blood electrolyte concentrations measurements.	Krueger et al., 2013b
Cardiac delayed enhancement-MRI	Geometry with infarcted regions, papillary muscles and main endocardial trabeculations	Geometry was personalized and tissue conductivity values were adjusted to match the CV in human cardiac tissue.	Lopez-Perez et al., 2019
MRI	Geometry	Geometry was personalized and tissue conductivities were adjusted to match clinically measured propagation times of the patient using EAMs.	Sermesant et al., 2008
MRI	Geometry with infarcted regions	Geometry was personalized and tissue conductivity values were adjusted to match the CV in human cardiac tissue.	Bruegmann et al., 2016
Cine MRI (with torso geometries)	Geometry with orientation and position of heart	Geometry was personalized and tissue conductivity values were adjusted to match patient-specific ECG data.	Kayvanpour et al., 2015
MRI (with torso geometries)	Geometry with orientation and position of heart	Geometry was personalized and tissue conductivity values were adjusted to match the CV in human cardiac tissue.	Mincholé et al., 2019
MRI	Geometry with infarcted regions	Geometry was personalized and tissue conductivity values were adjusted to match the CV in human cardiac tissue.	Deng et al., 2016
MRI	Geometry with infarcted regions	Geometry was personalized and tissue conductivity values were adjusted to match the CV in human cardiac tissue.	Prakosa et al., 2018
Late gadolinium enhancement MRI	Detailed geometry, including the atrial structure, mitral and tricuspid valves, coronary sinus, pulmonary veins, superior and inferior vena cava.	Geometry was personalized and tissue conductivity values were adjusted to match patient-specific activation mapping data using EAMs.	Roney et al., 2018
Cardiac magnetic resonance procedure	Detailed geometry, including the atrial structure, aortic arch, caval veins, torso surface, trabeculated myocardium between the wall and the intracavitary blood.	Geometry was personalized and tissue conductivity values were tuned to match patient-specific activation mapping using EAMs and ECG data.	Potse et al., 2014

of cells harvested from pathologic zones of the patient (Cabo and Boyden, 2003; Decker and Rudy, 2010). Additionally, the extracellular ion concentrations can be estimated and set into a model from personalized measurements of blood electrolyte concentrations (Krueger et al., 2013a,b).

Module Outputs and Applications

Overall, the electrophysiology modeling studies the normal conduction in the heart, as well as the pathological mechanisms that arise and cause cardiac arrhythmias. It is typically used to calculate physiological parameters (see **Figure 7**) like: the Mean firing rate (i.e., the number of spikes during a cardiac cycle divided by cycle duration, spike/s) (Behradfar et al., 2014); Re-entrant arrhythmias propagation (Arevalo et al., 2016; Deng et al., 2016; Trayanova and Chang, 2016; Prakosa et al., 2018) (i.e., a propagation of an impulse that fails to die out after normal activation of the heart and continues to re-excite it after the refractory period has ended, Antzelevitch, 2001); Phase singularities (Boyle et al., 2016; Pathmanathan and Gray, 2018; Roney et al., 2018) which represent the sites in which the activation state cannot be determined, because the particular location is surrounded by activation states ranging from fully activated to fully recovered (Valderrabano et al., 2003); Activation rate gradient which quantifies how fast the transmembrane

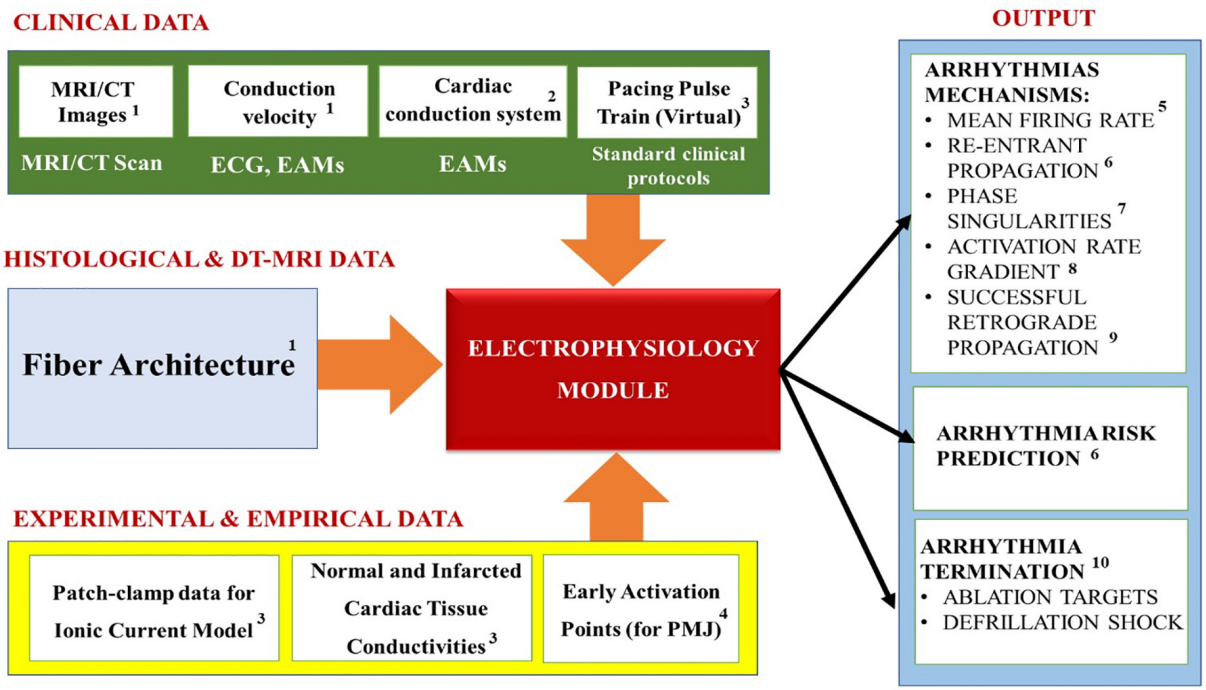

FIGURE 7 | Summary of the Electrophysiology module's inputs, outputs and applications. Superscripts in the figure correspond to the following references: [1]Cardenes et al., 2014; Kayvanpour et al., 2015; Lopez-Perez et al., 2015; [2]Cardenes et al., 2014; Palamara et al., 2014; [3]Arevalo et al., 2016; Trayanova et al., 2017; [4]Lopez-Perez et al., 2015; [5]Behradfar et al., 2014; [6]Arevalo et al., 2016; Deng et al., 2016; Trayanova and Chang, 2016; Prakosa et al., 2018; [7]Boyle et al., 2016; Roney et al., 2018; [8]Smith et al., 2011; Boyle et al., 2013; Potse et al., 2014; [9]Trayanova, 2011; Behradfar et al., 2014; [10]Arevalo et al., 2016; Trayanova et al., 2017; Deng et al., 2019.

voltage V_m changes in different cardiac regions (Smith et al., 2011; Boyle et al., 2013; Potse et al., 2014); Successful retrograde propagation which measures whether conduction at a terminal Purkinje node is successful or refractory (Trayanova, 2011; Behradfar et al., 2014); and the organization of electrical wavelets as they propagate through the myocardium (Starobin et al., 1996; Keldermann et al., 2009; Trayanova, 2014). In our experience, the majority of the electrophysiological modeling is used for elucidating the mechanisms of cardiac arrhythmia, especially for "reentrant propagation of complex waves" (e.g., effects of cardiac microstructure, spiral wave breakup, early afterdepolarizations, scroll-wave filaments, action potential duration, electrical alternans, etc.) (Trayanova, 2011); as well as for prediction of arrhythmia risks in specific patients. Furthermore, these models are also used to examine the mechanisms of defibrillation shock in the heart for terminating arrhythmia, as well as for increasing the understanding of ablation targets in the arrhythmia treatments (Trayanova et al., 2017).

Module Personalization Example

The following is a discussion of a representative example of the personalized electrophysiology modeling applied to an arrythmia risk assessment in post-infarcted hearts. Specifically, personalized 3D computer models of the post-infarction hearts was constructed based on clinical MRI of specific patients. First, an individualized geometric model of the postinfarction ventricles was reconstructed from late-gadolinium-enhanced-MRI (Arevalo et al., 2016), with representations of both the scar and the infarcted border zones. Due to the difficulty imaging the myocardial fiber orientation from a moving heart *in vivo*, an approximated personalization was performed using a rule-based algorithm (Bayer et al., 2012). Region-specific cell and tissue electrical properties were then assigned to the electrophysiological model based on literature data. After that, a virtual multi-site delivery of electrical stimuli from various bi-ventricular locations was conducted, in order to computationally determine all the ventricular tachycardia reentrant pathways that the infarct-remodeled ventricular substrate can sustain. This methodology was then validated in an arrhythmia risk prediction clinical study including 41 patients and significantly surpassed several existing clinical metrics in predicting upcoming arrhythmic events (Arevalo et al., 2016).

BIOMECHANICS MODULE

The next level of complexity are the models of myocardial abnormalities/heart failure (HF) and the blood pumping assist devices such as the Left-Ventricular Assist Device (LVAD). Since these models are interested in how the presence of abnormalities or assist devices affects the blood circulation, they must account for the contraction solid mechanics and the blood hemodynamics. However, if they are not interested in clot

formation, the models are simplified by homogenizing the blood flow. Therefore, they are not as complicated as the ones that do account for the thrombosis. Yet, they are still complex, because they include solving multiple different types of coupled physics (see **Figure 8**, LEFT) applied in different parts of the heart (see **Figure 8**, RIGHT).

Since the electrophysiology in these models is treated similarly to the arrhythmia models, the cardio biomechanics framework will be discussed next. Central to this physics type is the fact that the myocytes in the heart contain rod-like structures called myofibrils, which are composed of repeating contractile units called "sarcomeres" (see **Figure 9**, LEFT). Each sarcomere contains thin and thick filaments, made from actin and myosin proteins, respectively.

After depolarization, calcium enters the cardio-myocytes through the ion channels in their membrane, and triggers the release of cytosolic calcium stored in the sarcoplasmic reticulum (a storage compartment) of the cells through a cascade of intracellular signaling (see **Figure 9**, RIGHT). This release of the internal calcium leads to the binding of myosin heads to the actin filaments in the sarcomeres, which in turn causes the filaments to slide against each other and contract the entire cell (see bottom inset in **Figure 9**, LEFT). This process is called the "crossbridge mechanism" and it corresponds to the *active* tension in the biomechanical calculations of the heart.

The kinetics of this process have been modeled using Monte Carlo (Walcott and Sun, 2009) and partial differential equations (Huxley, 1957). However, both approaches are too computationally expensive to be calculated at the organ level. Consequently, the latter model has been simplified by considering a single cross bridge representative of the whole distribution (i.e., mean field theory) (Negroni and Lascano, 2008; Rice et al., 2008; Washio et al., 2012) or by averaging the distributions over a single cell (Bestel et al., 2001). Simpler yet is the assumption that the active contraction of the individual cells depends on the intracellular ionic concentrations and the local deformation gradient (Quarteroni et al., 2017). Ultimately, the microscopic sarcomere sliding velocity is related to the macroscopic strain along the myocardial fibers via a constitutive relationship (i.e., microscopic rate-of-strain depends on the macroscopic strain), such as the Hill-Maxwell rheological model which is a modification from Hill's force-velocity relation (Sainte-Marie et al., 2006). Herein, a specific choice of the attachment and detachment rates was modified so that they were not only dependent upon the sarcomere strain, but also on the strain rate.

The active contraction can be expressed by the following active stress formulation from Rossi et al. (2014):

$$P_A = \left(\frac{\partial W_A}{\partial I_1^E} + \frac{\partial W_A}{\partial I_{4,f}^E}\right)\hat{F}_A(c, I_{4,f}) f_0 \otimes f_0 + \frac{\partial W_A}{\partial F_A} \tag{3}$$

And the active strain formulation can be derived from Quarteroni et al. (2017):

$$\partial_t \gamma_f = \frac{1}{\eta_A}\left[\left(\frac{\partial W_A}{\partial I_1^E} + \frac{\partial W_A}{\partial I_{4,f}^E}\right)\left(\hat{F}_A(c, I_{4,f}) - \frac{2I_{4,f}}{(1+\gamma_f)^3}\right) - \frac{\partial W_A}{\partial F_A} : f_0 \otimes f_0\right] \tag{4}$$

Where, W_A is the *active* component of the free energy, F_A is the active deformation, 'c' is the intracellular calcium concentration, $I_{4,f}$ is the local deformation gradient invariant in the myofiber direction, ∂I_1^E and $\partial I_{4,f}^E$ are elastic invariants (described in more details in Rossi et al., 2014). The incorporation of the microscopic

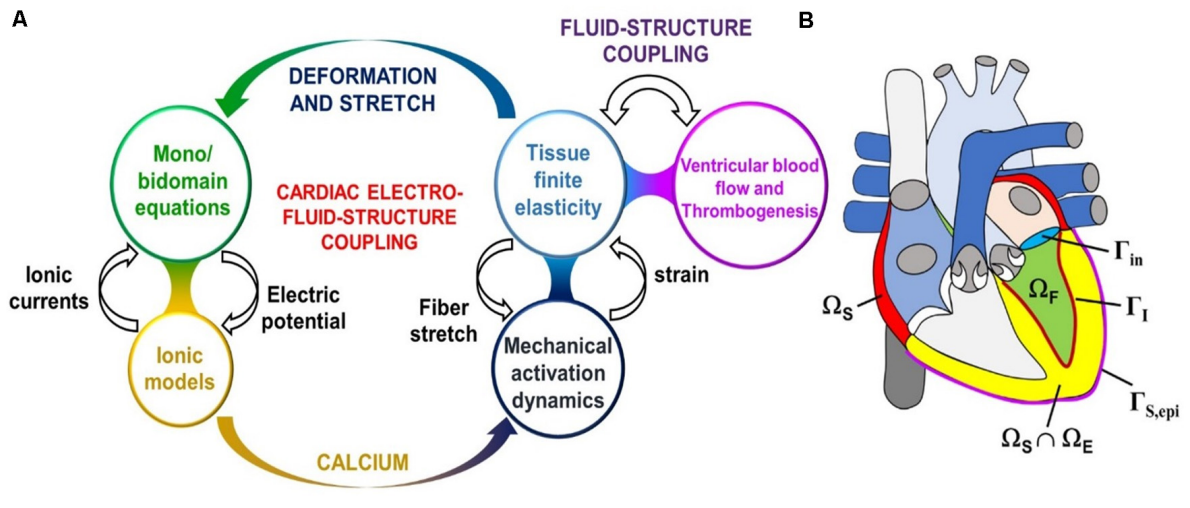

FIGURE 8 | (A) Sketch of the cardiac electro-fluid–structure coupling. **(B)** The three computational domains (fluid domain Ω_F, solid mechanics domain Ω_S, electrophysiology domain Ω_E) considered in the cardiac multiphysics problem. In this example the electrophysiology physics are only considered in the ventricles, whereas the solid mechanics physics applies to the atria also. Additionally pictured are the fluid–structure interface Γ_I inside the left ventricle, the epicardial surface $\Gamma_{S,epi}$, and the mitral valve inlet surface Γ_{in}. Lastly, the domains Ω_E and Ω_S overlap within the ventricular part of the heart. (Adopted with permission from Quarteroni et al., 2017).

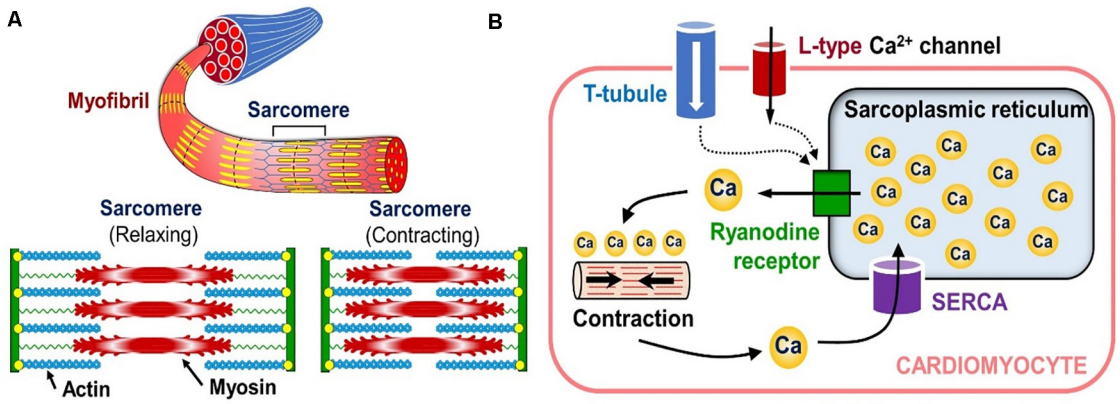

FIGURE 9 | Sub-cellular tension generation mechanisms. **(A)** Organization of the cardiac muscle cell's contraction mechanism (bottom inset shows the contraction-relaxation cycle of a single sarcomere). **(B)** Diagram showing how calcium release from internal cytosol storage causes cardiomyocyte contraction in response to the "outside-to-inside" calcium signaling.

active tension, $\hat{F}_A$, at the tissue level is a key aspect in the multi-scale framework of the cardiac function (Quarteroni et al., 2017) and can be derived by:

$$\hat{F}_A(c, I_{4,f}) = \alpha f(c) R_{F-L}(I_{4,f}) \tag{5}$$

where $R_{F-L}(I_{4,f})$ is a function that represents the force–length relationship of the cardiac cells (defined in Ruiz-Baier et al., 2014) which depends on $I_{4,f}$; f (c) specifies the amount of force generated by the cross-bridges in response to intracellular calcium release; and α is a positive parameter. Thus, the $\hat{F}_A$ represents the active tension generated within the sarcomeres, which then drives the macroscopic muscular contractions.

In addition to the active tension generated by the cross-bridge mechanism, the solid mechanics calculations must also account for the passive stiffness of the myocardium (e.g., when it is expanded by the blood flow entering the heart). This is modeled by assuming that the myocardium is an isotropic linear elastic tissue. The general formulation of passive stress (i.e., Cauchy stress) can be expressed by Avazmohammadi et al. (2019):

$$\sigma = J^{-1} F S F^T \tag{6}$$

Where, the second Piola–Kirchhoff stress tensor 'S' can be described in terms of the stored energy density function 'W' through: $S = 2\partial W/\partial C$, and '$W$' can be derived based on Holzapfel–Ogden constitutive law which is divided into three parts - the isotropic isochoric part, the isotropic volumetric part, and the orthotropic part:

$$\begin{aligned} W(F) = {} & \frac{a}{2b}\exp(b[\bar{I} - 3]) + \frac{\kappa}{4}[(J-1)^2 + (\ln J)^2] \\ & + \sum_{i=f,s} \frac{a_i}{2b_i}[\exp(b_i < \bar{I}_{4,i} - 1 >^2) - 1] \\ & + \frac{a_{fs}}{2b_{fs}}[\exp(b_{fs}\bar{I}^2_{8,fs}) - 1] \end{aligned} \tag{7}$$

where

$$\begin{gathered} J = \det(F),\ C = F^T F,\ I_1 = tr(C),\ \bar{I}_1 = J^{-2/3} I_1, \\ I_{4,f} = Cf_0 \cdot f_0,\ \bar{I}_{4,f} = J^{-2/3} I_{4,f},\ I_{4,s} = Cs_0 \cdot s_0,\ I_{4,s} = J^{-2/3} I_{4,s}, \\ I_{8,fs} = cf_0 \cdot s_0,\ \bar{I}_{8,f,s} = Cf_0 \cdot s_0,\ \bar{I}_{8,f,s} = J^{-2/3} I_{8,f,s} \end{gathered} \tag{8}$$

and the material parameters a, a_f, a_s, a_{fs}, b, b_f, b_s, b_{fs} are experimentally fitted (Quarteroni et al., 2017). The parameter 'κ' is the bulk modulus that "penalizes" local volume changes to enforce the incompressibility of the tissue.

Furthermore, since stretching a cell changes the distance between the gap junctions and their neighbors, this leads to changes in the ion channels, and consequently, in the conductivity of the action potential from cell to cell. This electromechanics coupling is typically included by modifying the conductivity tensor in the original equation of the electrophysiological propagation (see Equation 2). Specifically, the fixed reference state conductivity tensor 'D_0' is replaced with the spatial configuration conductivity tensor 'D'. Furthermore, an explicit dependence on the solid deformation tensor 'F' is included into the conductivity tensor in order to account for the geometric feedback, due to deformation of the tissue structure (Quarteroni et al., 2017):

$$\begin{aligned} & \chi[C_m \partial_t v + i_{ion}(v, w, c) + i_{SAC}(v, F) - i_{app}(t)] \\ & \quad = \frac{1}{J}\nabla \cdot (JF^{-1} D F^{-T} \nabla v) \end{aligned} \tag{9}$$

Moreover, an additional inward ionic current, induced by the stretch-activated channels, also contributes to the depolarization. This is commonly modeled as follows:

$$i_{SAC}(v, F) = g\left(\sqrt{I_{4,f}(F)} - 1\right)(v - E) \tag{10}$$

Where, 'E' and 'g' are the reversal potential and the maximal conductance of the channels.

Lastly, *in vivo* the heart is immersed in a pericardial fluid; and it is also loosely supported by a flexible double-layered

pericardium membrane. Therefore, spring-like external support enforced by Robin-type boundary conditions (Moireau et al., 2012) are typically tuned to mimic the global motion of the modeled heart. An explicit solution of the pericardium–heart contact problem has been proposed as well (Fritz et al., 2014).

Module Personalization

Table 2 summarizes the most common biomechanics module personalization approaches encountered in the recent IBM publications, while **Figure 10** the relationships between the module's inputs, outputs and applications. Before personalizing the modeling of the passive (i.e., resting) properties of the myocardium, the parameters of the Holzapfel and Ogden model (see Equations 7 and 8) are typically initialized using experimental data from biaxial (Krishnamurthy et al., 2013) and shear tests (Dokos et al., 2002; Sommer et al., 2015) of *explanted* myocardial tissue. The passive mechanics parameters are then further optimized to match the patient-specific end-diastolic pressure and volume (EDPV) relations (Krishnamurthy et al., 2013; Meoli et al., 2015; Finsberg et al., 2018; Palit et al., 2018). The EDPV relation is a graphical representation of the pressure-volume loop related to the passive filling of the left ventricle during diastole (i.e., relaxation), and is a measure of the passive ventricle stiffness. The chamber volume of the left ventricle at the end of the diastole is defined as the end-diastolic volume (EDV), which is used to estimate the preloading volume of the heart and indicate the stiffness of the ventricle.

The active contraction modeling, on the other hand, is coupled with the cardiac hemodynamics, so it is important to link it with the patient-specific hemodynamic metrics corresponding with the end-systolic condition. For example, the pumping ability of the heart is represented by the end-systolic pressure (ESP) and the end-systolic volume (ESV), which are the peak values of pressure and ventricular volume at the end of systole (i.e., contraction), respectively. The active contraction is also associated with ejection fraction (EF), which is defined as a measurement of the percentage of blood leaving out of the left ventricle with each contraction. Therefore, the optimization procedure is performed to find the patient-specific parameters that best replicate the clinical hemodynamics of the patient in terms of the mean, maximum and minimum values of the pressures, flows and the cardiac volumes (such as the clinically recorded values of the ESP, ESV, and EF).

Module Outputs and Applications

Overall, the biomechanics models tend to perform stress analysis, which is used to evaluate the effects that a defective myocardium structure has on the heart function, and design new therapies and treatment devices for reducing the abnormal stress (Guccione et al., 2003; Wall et al., 2006; Lee et al., 2013; Finsberg et al., 2018) (see **Figure 10**). Additionally, they calculate the stiffness of the heart, which strongly corresponds to its ability to function normally and can be used as an indicator for HF (e.g., heart attacks caused by a diastolic dysfunction that occurs when the ventricle becomes too stiff or weak to pump blood effectively). Ultimately, however, since the goal of these models is to obtain the relationship between the biomechanics of the myocardium tissue and the blood pumping ability of the heart, they also include a simplified (i.e., no discrete blood cells) hemodynamics module, which is discussed in the next section.

Module Personalization Example

The following is a discussion of a representative example of the personalized Biomechanics module applied to five HF failure patients from San Diego Veteran's Affairs Medical Center. Specifically, personalized 3D models of ventricular biomechanics in their failing hearts were derived from cardiac CT imaging. The human fiber orientation was modeled using DT-MRI data from an isolated (i.e., fixed) human organ-donor heart, and then transposed to the specific patient's geometric model. The biomechanics model was then developed for optimizing the passive material properties to match previous experimental results on cardiac tissues and patient-specific end-diastolic pressure and volume relations. The material properties of the active contraction were also optimized to match patient-specific measured peak left ventricular pressures and end-systolic volumes. These components were then integrated to generate a multi-scale computational approach for the patient-specific hearts. The simulation results in the patients demonstrated good agreement with their measured echocardiographic and cardiac output parameters, such as EF and peak cavity pressures. This model was developed for stress analysis in HF patients and could be further developed with the goal of predicting treatments for heart disease under different interventions.

SIMPLIFIED HEMODYNAMICS MODULE

In the cardiovascular models where clot formation is not considered, the blood flow is simulated using the incompressible Navier-Stokes equations. This means they do *not* account for discrete cells floating in the plasma. Instead the blood is treated as a *homogeneous* weakly non-Newtonian fluid (Shibeshi and Collins, 2005), which flows mostly in the laminar regime [though the strong vortices can create transition to turbulence with Reynolds numbers in the 1500–2500 range (Quarteroni et al., 2017)]. The fluid-structure interaction between the blood and the myocardium walls is typically modeled explicitly using moving mesh approaches: for example, Arbitrary Lagrangian-Eulerian (Cheng et al., 2005; Chnafa et al., 2014; Su et al., 2014), immersed boundary (Kohl et al., 2001; Vigmond et al., 2008) and level-set based methods (Mihalef et al., 2011). The heart valves, on the other hand, are commonly approximated using the Bernoulli equation for orifice flow (Flachskampf et al., 1990; Vandervoort Pieter et al., 1995; Donati et al., 2017).

Additionally, the myocardium hemodynamics are typically coupled to the rest of the body's circulation via the Windkessel circuit model, which mimics the arterial blood pressure's waveform. This is a relatively simple method used to obtain the relationship between the blood flow and the pressure in a modeled segment through the resistive '*R*' and the capacitance '*C*' properties of the arterial vasculature (see **Figure 11**) (Wall et al., 2006). Specifically, the heart and the systemic arterial system are treated as a closed hydraulic circuit, which, contains

a pump connected to a chamber partially filled with a liquid. As it is pumped, the latter compresses the air pocket in the chamber, which in turn pushes the liquid back out (i.e., creating a back-and-forth cycle). Consequently, the arterial compliance, the peripheral resistance, and the inertia are modeled as a capacitor, a resistor, and an inductor, respectively. In this model, the physiological variables such as pressure '*P*' and flow '*Q*' only vary as a function of time '*t*' (Morris et al., 2016). The relationship between the flow rate *Q(t)* and the pressure *P(t)* can be expressed by:

$$Q(t) = \frac{P(t)}{R} + C\frac{dP(t)}{dt} \tag{11}$$

It essentially states that the volumetric flowrate must equal to the sum of the volume stored in the capacitive element and the volumetric outflow through the resistive element. During the diastole there is no blood inflow ($Q = 0$), so the Windkessel equation can be solved for the *P(t)*:

$$P(t) = P(t_d)e^{\frac{-(t-t_d)}{(RC)}} \tag{12}$$

where t_d is the time of the start of the diastole and $P(t_d)$ is the blood pressure at that time. Due to its simplicity, the Windkessel equation is frequently used to approximate various components and boundary conditions in the cardiovascular system (Morris et al., 2016). However, this model is only a rough approximation

TABLE 2 | A recent literature survey of how the Biomechanics module is typically personalized using image-based information.

Imaging method	Personalized Information from Imaging	Mapping of the Personalized Information from the Imaging to the Module's Inputs	Citation
CT combined transthoracic 2D; and continuous-wave Doppler echocardiography	Geometry with Infarcted regions, ventricular dimensions including early diastolic volume, EDV, ESV and blood flow velocities	Geometry was personalized; passive mechanics parameters were fitted to match the previous experimental results on cardiac tissues and match patient-specific EDPV relations; active mechanics parameters were adjusted to match the patient-specific measured peak left ventricular pressures and ESV.	Krishnamurthy et al., 2013
DT-MRI from explanted heart	Fiber direction		
Cine cardiac MRI	Geometry with ventricular dimensions and ejection fraction (EF).	Geometry was personalized; passive mechanics parameters were fitted to match the previous experimental results and match the previous results of EDPV relations (due to the unavailability of subject-specific ventricular pressures that require invasive measurements).	Palit et al., 2018
Cine cardiac MRI	Geometry with ventricular dimensions and regional strain-time	Geometry was personalized; passive mechanics parameters were fitted to match patient-specific EDPV relations; active mechanics parameters were adjusted to match the patient-specific end-systolic state.	Finsberg et al., 2018
MRI flow tracing and echocardiographic Doppler velocity tracings	Geometry with ventricular dimensions and blood flow velocities.	Geometry was personalized; passive mechanics parameters were fitted to match the previous experimental results on cardiac tissues and match patient-specific EDPV relations; active mechanics parameters were adjusted to match the patient-specific measured peak left ventricular pressures.	Meoli et al., 2015
MRI	Geometry with ventricular dimensions	Geometry was personalized; passive parameters were tuned so that the resultant EDV matched the corresponding MRI-measured cavity volume; active parameters were adjusted so that the resultant ESV matched the corresponding MRI-measured cavity volume.	Lee et al., 2013
Cine MRI and Echocardiography	Geometry with ventricular dimensions and EF	Geometry was personalized; passive and active parameters were determined by minimizing the sum of the squared differences between computed and measured EF, stroke volume, EDV, ESV, end-diastolic pressure and end-systolic pressure.	Kayvanpour et al., 2015
Cine MRI	Geometry with ventricular volume waveforms	Geometry was personalized; biomechanics parameters were tuned along with hemodynamics parameters; passive parameters were adjusted to match the measured EDPV; active parameters were adjusted to match patient-specific volume and pressure waveforms.	Shavik et al., 2020
Phase-contrast MRI	Luminal area waveforms		

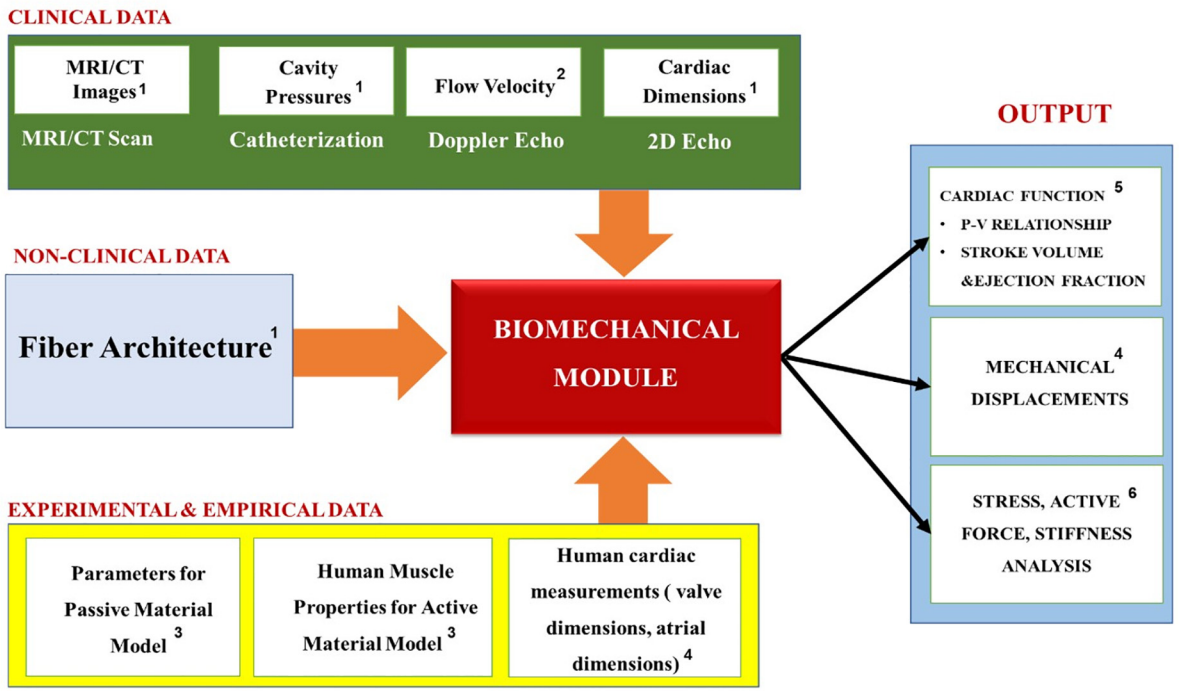

FIGURE 10 | Summary of the Biomechanics module's inputs, outputs and applications. Superscripts in the figure correspond to the following references: [1]Krishnamurthy et al., 2013; Meoli et al., 2015; Finsberg et al., 2018; [2]Krishnamurthy et al., 2013; Meoli et al., 2015; [3]Krishnamurthy et al., 2013; Kayvanpour et al., 2015; Meoli et al., 2015; Finsberg et al., 2018; Palit et al., 2018; Shavik et al., 2020; [4]Krishnamurthy et al., 2013; [5]Krishnamurthy et al., 2013; Palit et al., 2018; [6]Lee et al., 2013; Meoli et al., 2015; Finsberg et al., 2018.

of the arterial circulation. To that end, the next section covers the approaches to more detailed hemodynamic formulations.

HEMODYNAMICS WITH THROMBOGENESIS MODULE

The last class of the cardiovascular models is the one in which the hydrodynamics of the discrete blood cells, and the biochemistry associated with their physiological activity, are of interest. For example, such simulations could be focused on studying pathological clot formation inside of the heart (Choi et al., 2015; Mittal et al., 2016; Seo et al., 2016; Harfi et al., 2017), or embolism into it from other parts of the body. Therefore, these types of models must simulate the blood as a suspension of deformable cells (e.g., platelets and/or red blood cells), whose fate is intertwined with the mechanical motion of the myocardium (and by association with the electrophysiology of the heart). This is typically done using Stokesian Dynamics methods, Dissipative Particle Dynamics, Completed Double Layer Boundary Integration Equation Method and Lattice Boltzmann Method (Wang and King, 2012). These are mesoscopic off- and on- lattice frameworks that calculate trajectories of the cells under the influence of hydrodynamic and Brownian forces; while the deformation of the structure is typically simulated using continuum-based models that treat the cell membrane and intracellular fluids as homogeneous materials: some popular approaches are the Boundary Integral Method, the Immersed Boundary Method, and the Fictitious Domain Method (Li et al., 2017).

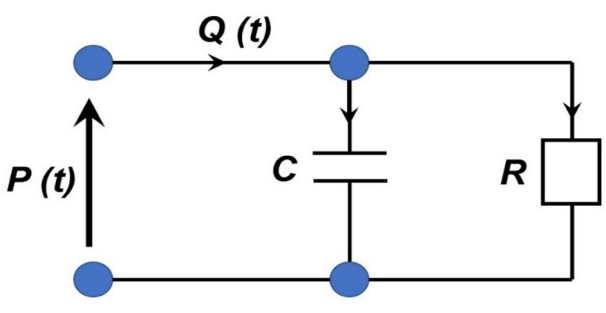

FIGURE 11 | Two-element Windkessel circuit analogy illustrated.

To make matters even more complicated, the mechanism of the blood clot formation strongly depends on the following three processes: Receptor-Ligand Binding, Platelet Activation and the Coagulation Cascade. Specifically, the initiation of thrombus development starts with tethering of circulating platelets onto the exposed subendothelial layer where a blood vessel is injured. This process involves bonding between the various receptors on the platelet surfaces to the extravascular proteins, such as the von Willebrand Factor. It is typically modeled using a Monte

Carlo approach called Adhesive Dynamics, while the rate of the receptor-ligand bond formation and breakage are determined by the Bell Model that calculates the probability of dissociation events occurring over a specific timespan.

Once the platelets have been recruited to the injury site, they undergo a metamorphosis that is generally described as "activation." During this process, the membrane receptors transmit signals to the inside of the cells, which results in the dumping of chemical agonists stored in the internal vesicles called lysosomes and granules (e.g., dense and alpha). The release of these molecules then activates other neighboring platelets, which ultimately leads them to becoming "stickier" and compacting into the blood clot's body. Unfortunately, the bottom-up description of the process contains numerous unknowns (Dolan and Diamond, 2014). For this reason, it has been instead described via a top-down Neural Network approach, which was trained on patient-specific experimental data (Flamm et al., 2012).

Lastly, the coagulation cascade is a system of coupled biochemical reactions with two different initiation pathways, which both ultimately lead to the polymerization of soluble fibrinogen (a blood plasma protein) into an insoluble fibrin mesh that holds the clot together. The kinetic portion of the cascade involves 34 differential equations, with 42 rate constants, that cumulatively account for 27 independent equilibrium expressions and fates of 34 chemical species (Hockin et al., 2002). Additionally, the mass transport of these species must be tracked under the flow conditions experienced in the cardiovascular system (which involves Knudsen diffusion within the porous clot). **Figure 12** summarizes the coupling of the various hemodynamics submodules, as well as the methods used to solve them.

Module Personalization

Table 3 summarizes the most common hemodynamics module personalization approaches encountered in the recent IBM works, while **Figure 13** maps the relationships between the module's inputs, outputs and applications. Similarly to the previous modules, the macroscopic geometry of the heart, and that of the surrounding blood vessels, is commonly obtained for use in the Hemodynamics modules via the *in vivo* imaging techniques (such as MRI and CT). Additionally, for the body's circulation, the parameters values for the Windkessel model (i.e. '*R*' and '*C*' elements) are typically chosen to match the patient specific cardiac output, flow waveforms and pressure pulses (Kim et al., 2009, 2010; Kung et al., 2014) obtained via contrast-enhanced CT scans, Doppler ultrasound scanning and invasive blood pressure measurements (IBPM). Particularly, the Doppler ultrasonography allows the measurement of the cardiac output and heart rate; and the IBPM allows to measure the systolic and diastolic pressures (Bonfanti et al., 2019). Specifically, they are first chosen based on literature data (Segers et al., 2002; Kim et al., 2009) and are then iterated until the calculated

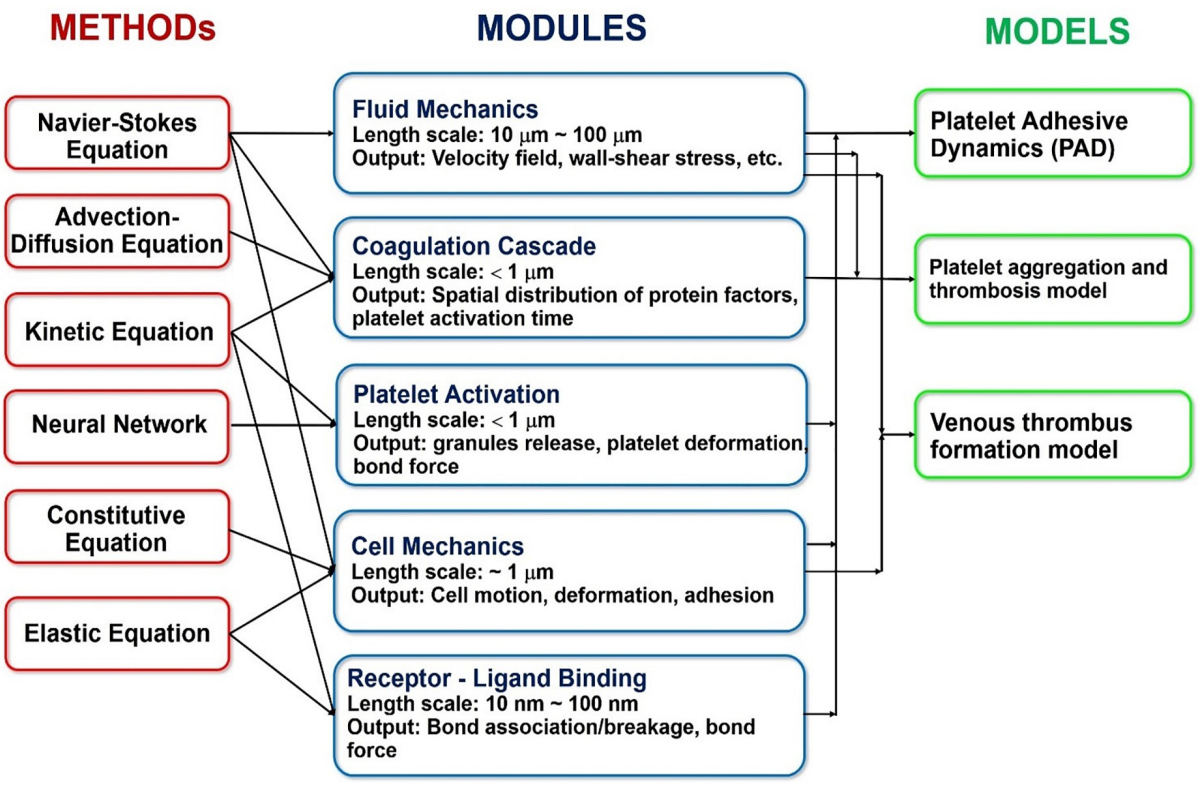

FIGURE 12 | Overview of the specific methods, modules and models commonly used in the state-of-the-art multiscale platelet hemodynamics and thrombus development studies. (Adopted with permission from Wang and King, 2012).

flow parameters match the subject's unique physiological profile (Kim et al., 2009).

Unfortunately, due to the enormous complexities and computational costs of the heart modeling, oversimplifications are common in the personalization of the blood properties within the Hemodynamics modules. Given that it is typically assumed to be a Newtonian (or weakly non-Newtonian) fluid, it effectively does not contain discrete blood cells, such as the platelets or the erythrocytes. This, in turn, means that only simple flow properties, like fluid viscosity can be personalized to the subject. Consequently, the patient-specific biology of these cells (e.g., thrombotic propensity, sickle cell anemia, etc.) are omitted. Yet, in the non-cardio blood modeling, attempts at personalizing such functionality and disorders have been made: for example, the application of the Neural Networks trained on the patient-specific experimental data in order to phenotype the platelet activation (Flamm et al., 2012). However, we could not find an example of such an extensive blood personalization in the cardiovascular modeling literature.

Module Outputs and Applications

Figure 13 summarizes the inputs, outputs and applications of the cardiac hemodynamics module. Overall, the models that use the simplified hemodynamics formulation tend to calculate the blood flow parameters, like the pressure-volume relationship of the cardiac cycle. These, in turn, help to elucidate quantities that are key to understanding the heart dysfunctions: such as the end-diastolic and the end-systolic pressure volume relationships. Additionally, Fractional Flow Reserve, which is defined as the pressure difference across a coronary artery stenosis (e.g., a narrowing due to atherosclerosis), can be calculated to determine the likelihood that the latter would impede oxygen delivery to the heart and lead to a myocardial ischemia. Furthermore, the biomechanical models measure "compliance," which is the ability of the blood vessel walls to stretch in order to accommodate an increasing amount of blood; and "resistance" (defined as the ratio of the pressure drop and the flow change across the segment) that the blood flow experiences due to viscous stresses and constrictions by the blood vessels. Most importantly, the biomechanics-hemodynamics modeling can be used to predict the left ventricular ejection fraction (LVEF) - a main indicator of HF, which is expressed as a percentage of how much blood the left ventricle pumps out with each contraction. Lastly, such models can be used to investigate the effects of the blood pumping assist devices (e.g., LVAD) on the cardiac function, which may otherwise be too difficult or costly to study experimentally.

TABLE 3 | A recent literature survey of how the Hemodynamics modules are typically personalized using image-based information.

Imaging method	Personalized Information from Imaging	Mapping of the Personalized Information from the Imaging to the Module's Inputs	Citation
CT	Coronary arteries geometry	Geometry was personalized; parameter values for coronary model were obtained from literature; parameter values of lumped heart model (for the inlet) and Windkessel models (for the outlet) were adjusted to match subject-specific cardiac output and pulse pressure.	Kim et al., 2010
MRI	Coronary arteries geometry	Geometry was personalized; parameter values of lumped heart model (for the inlet) and Windkessel models (for the outlet) were adjusted to match subject-specific flow distribution and measured brachial artery pulse pressure.	Kim et al., 2009
CT angiogram	Right coronary artery with aneurysmal region	Geometry was personalized; Windkessel model' parameters were adjusted to match subject-specific flow distribution and pressure at outlet boundary of the coronary artery.	Kung et al., 2014
Phase contrast MRI	3-component flow velocity at two slice locations in the coronary aneurysm geometry		
Contrast-enhanced CT	Aortic dissection geometry	Geometry was personalized; inlet flowrate was obtained by adjusting a typical ascending aorta blood flow waveform to match the patient-specific hemodynamic data including cardiac output, heat-rate and systolic-to-diastolic duration ratio; for the outlet, Windkessel models parameters were adjusted to achieve patient-specific physiological flow distribution at each outlet, and to obtain the measured systolic and diastolic pressures at the inlet.	Bonfanti et al., 2019
Doppler ultrasonography	Cardiac output and heart rate		
CT angiogram	Coronary arteries geometry	Geometry was personalized; parameter values of lumped heart model (for the inlet) and Windkessel models (for the outlet) were adjusted to match subject-specific flow distribution and measured aortic pressure.	Grande Gutierrez et al., 2017
4D cardiac CT images and echocardiogram	Whole-heart geometry with kinematics of left ventricle lumen: heart rate, EDV, ESV, EF, stroke volume.	Geometry was personalized; the immersed boundary-based method is used to match the patient-specific kinematics of the left ventricular lumen including heart rate, EDV, ESV, EF and stroke volume.	Harfi et al., 2017

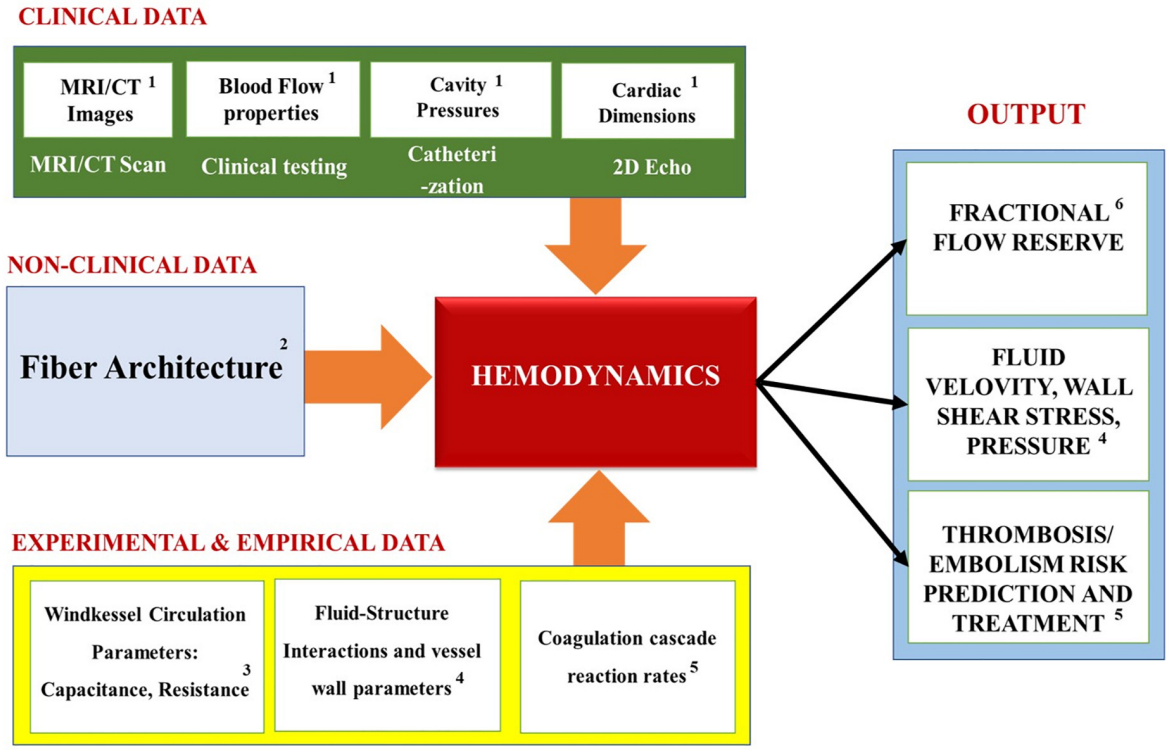

FIGURE 13 | Summary of the Hemodynamics modules' inputs, outputs and applications. Superscripts in the figure correspond to the following references: [1]Kim et al., 2009, 2010; Kung et al., 2014; Bonfanti et al., 2019; [2]Tang et al., 2010; Choi et al., 2015; [3]Kung et al., 2014; Grande Gutierrez et al., 2017; [4]Kim et al., 2010; Bonfanti et al., 2019; [5]Seo et al., 2016; Harfi et al., 2017; [6]Koo et al., 2011; Zhang et al., 2014; Min et al., 2015.

Conversely, the models that use the thrombogenesis hemodynamics module tend to try to assess the propensity of clot formation at (or near) the heart, based on parameters that are related to platelet activation: such as the Wall Shear Rate; the blood Residence Time Near a Damaged Tissue; the Ejection Fraction (i.e., the percentage of the blood leaving the left ventricle each time it contracts); Washout Ratio (i.e., the ratio of delayed ejection volume to the total ventricular blood at the beginning of the cycle). Additionally, some of these models simulate how drugs and clot breakup devices (e.g., Vena cava filters) help to protect the heart from pathogenic events. Overall, this is the most computationally expensive model type, due to the complexity of the thrombogenesis/embolism processes (which are themselves still being actively investigated) (Wang and King, 2012).

Module Personalization Example

The following is a discussion of a representative example of the personalized hemodynamics modeling applied to predicting the thrombosis risk in patients with Kawasaki disease (KD) (Grande Gutierrez et al., 2019). Thrombosis is a major complication associated with coronary artery aneurysms (CAAs) resulting from the KD. In this research, the aneurysm hemodynamics were investigated for thrombotic risk stratification in ten KD patients, and were compared to the standard clinical guidelines for anticoagulation therapy. The patient-specific models were generated from MRI data by performing an angiography of: the heart, the main coronary arteries (right, left main, left anterior descending and circumflex), and the aorta and its arch branches (the brachiocephalic artery, the left common carotid artery and the left subclavian artery). This was done via the injection of gadolinium-based contrast with a cardiac and respiratory-gated 3D TrueFISP sequence. Computational hemodynamic simulations were then performed in the reconstructed anatomical model using SimVascular software (Grande Gutierrez et al., 2019). The pulsatile flow, deformable arterial walls and Windkessel parameters were tuned to match the patient-specific arterial pressure and cardiac output. Local hemodynamics variables were derived from the simulation results, including the time-averaged wall shear stress, low wall shear stress exposure and blood residence time. These variables were then used to develop a framework for predicting the thrombosis risk. Although platelet activation and aggregation are typically associated with regions of higher fluid shear (Casa et al., 2015) and longer blood stagnation (Hathcock James, 2006), this study showed that a combination of low shear stress coupled with a high residence time correlated to thrombus formation in the KD CAAs patients. Furthermore, it was shown that the prediction of the thrombotic risk using the hemodynamic variables was validated with a higher sensitivity and specificity in comparison with the standard clinical metrics. In conclusion, this type of personalized computational modeling can be used to provide a non-invasive thrombotic risk stratification that is

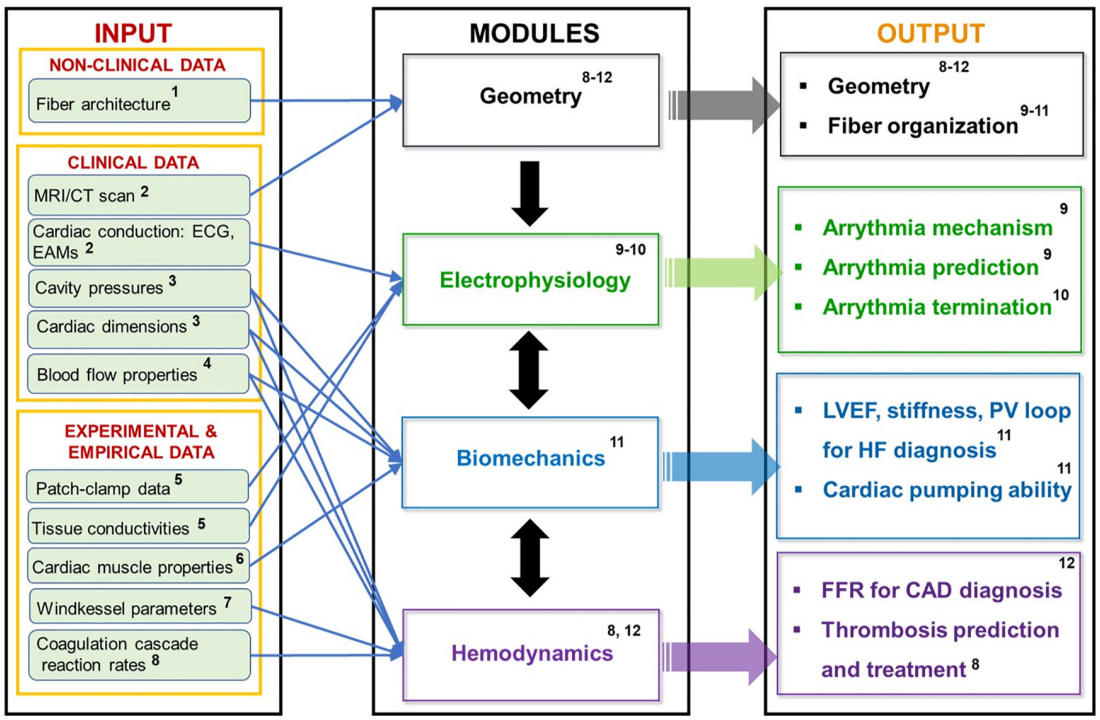

FIGURE 14 | Summary of cardiovascular IBM's modules and their respective inputs and outputs with corresponding references: [1]Krishnamurthy et al., 2013; Lopez-Perez et al., 2015; [2]Krishnamurthy et al., 2013; Cardenes et al., 2014; Kayvanpour et al., 2015; Lopez-Perez et al., 2015; [3]Krishnamurthy et al., 2013; Grande Gutierrez et al., 2017; Finsberg et al., 2018; [4]Meoli et al., 2015; Bonfanti et al., 2019; [5]Arevalo et al., 2016; Trayanova et al., 2017; Lopez-Perez et al., 2019; [6]Krishnamurthy et al., 2013; Finsberg et al., 2018; Palit et al., 2018; [7]Kung et al., 2014; Grande Gutierrez et al., 2017; Bonfanti et al., 2019; [8]Choi et al., 2015; Seo et al., 2016; Harfi et al., 2017; [9]Arevalo et al., 2016; Deng et al., 2016; Trayanova and Chang, 2016; Prakosa et al., 2018; [10]Arevalo et al., 2016; Trayanova et al., 2017; Deng et al., 2019; [11]Voorhees and Han, 2015; Walmsley et al., 2017; Lee et al., 2018; [12]Koo et al., 2011; Min et al., 2012, 2015; Zhang et al., 2014; Min et al., 2015.

more accurate than the current clinical approaches. This, in turn, can assist the long-term medical management of the KD patients with the CAAs.

SUMMARY AND CONCLUSION

Most of the published cardiovascular modeling reviews are typically oriented at an expert audience, which makes it difficult for the outsiders to understand the full medical potential of these methods. One of the barriers to penetrating the field is that these works tend to focus on just one or two specific aspects of the simulation approach at a time: such as imaging (Weese et al., 2013; Lamata et al., 2014; Watson et al., 2018), electrophysiology (Lopez-Perez et al., 2015; Rodriguez et al., 2015; Beheshti et al., 2016; Gray and Pathmanathan, 2018; Ni et al., 2018), biomechanics (Wang et al., 2015; Chabiniok et al., 2016), hemodynamics (Zhong et al., 2018), electro-biomechanical coupling (Trayanova, 2011, 2012; Tobon-Gomez et al., 2013; Niederer et al., 2019b), biomechanics-hemodynamics coupling (Tang et al., 2010; Sun et al., 2014), etc. In contrast, our manuscript provides a "big picture" overview of the components that these models are built from; their mechanisms, inputs, outputs and connecting pipelines; the underlying physiological processes that they represent; their image-based personalization to the individual patient's unique anatomy; and their applications to the different cardiovascular disease understanding and treatments.

As a part of our review, it was found that although this type of modeling holds a tremendous potential for revolutionizing personalized cardiovascular medicine, it is still in its infancy (with HeartFlow being the only commercially available product). Furthermore, due to the slow speed of high-resolution imaging, most of the IBM in academia still rely on scans of dead hearts (as opposed to beating ones). This, however, is expected to change, as the imaging speeds of mCT and MRI are increased. As far as the physics being modeled, the modules, their inputs and outputs are summarized in **Figure 14**. The simplest application of the cardiovascular IBM is to the study of arrythmias, which simulates the propagation of electrical impulses through the myocardium, while ignoring the biomechanics and hemodynamics. At the subcellular level, these models calculate transfer of ions across the cell membrane channels, while at the macro level the transfer of potential between the cells is modeled as a diffusive process. Conduction irregularities, ablation targets, and effects of defibrillation are just some of the outputs provided by the electrophysiological models.

The more complex models account for the biomechanical processes occurring in the myocardium. These models are focused on how abnormalities in the tissue morphology and stiffness affect the pumping efficiency of the heart. At the subcellular level, they simulate how the electrically driven calcium signaling governs the crossbridge mechanism of the active tension generation via the actin-myosin interactions in the cells' sarcomeres. Additionally, the solid mechanics calculation also involves the passive stress of the myocardium, which represents the stress-strain relationship of the cardiac fibers without the electrical stimulation. The resulting tissue deformation is then backwards-coupled to the electrophysiology, since the stretching of the cells can change the gap junction distance to their neighbors (which results in changes to the ionic conductivity).

Lastly, these models are coupled to the hemodynamics calculations via fluid-structure interactions. If only the blood flow without the clot formation is of interest, then the structure of the fluid is approximated to be homogeneous and Newtonian; while the rest of the body's circulation is introduced as an oscillating pressure boundary condition that is assumed to behave like a simple RC circuit. This type of model can provide insight into HF due to deformities and obstructions, as well as allow for virtual design and testing of assisted pumping devices. On the other hand, if clotting information is necessary, the blood must be treated as a suspension of deformable particles, with receptor ligand interactions, intra-cellular signaling, and coupled biochemical reactions representing the coagulation cascade. Although a lot more involved, this type of model can be useful for antithrombotic drug development and design of clot breakup devices (e.g., Vena cava filters) meant to protect the heart. However, for simplicity most cardiovascular IBM do not account for the hydrodynamics and biomechanics of the individual blood cells. Likewise, the coagulation cascade and the platelet activation, both of which are central to thrombogenesis, are oversimplified relative to the state-of-the-art within the non-cardiovascular blood modeling field.

Overall, the cardiovascular IBM is expected to become more mainstream as the computational and imaging technologies advance. This could potentially revolutionize how cardiovascular medicine is done in the future. Yet, significant improvements are still required to personalize the models more. For example, a common limitation across all of the modules is that the myocardium (e.g., conductivity and tissue stiffness) and the blood (e.g., hematocrit, coagulation cascade and platelet activation kinetics and deficiencies) properties that they use are typically estimated based on empirical measurements performed *ex vivo* and using samples that are not derived from the same individual (or even from the same species for that matter). Therefore, better imaging methods need to be developed, such that these properties could be estimated by scanning the individual patient. Furthermore, a finer image resolution is needed to capture the individualized variations in the conductive and contractile fibers, and their junctions. Likewise, the computational methods need to improve their modeling of the intra-cellular processes (e.g., the crossbridge mechanism) for the cardiovascular IBM to become more physiologically representative and adopted by the mainstream clinical market. However, given the fast pace of the technological progress, the near future impact of the IBM on the cardiovascular medicine is imminent.

AUTHOR CONTRIBUTIONS

TN and OK devised the manuscript, performed review of literature, and wrote the manuscript. RV provided the feedback and edits on all aspects of the manuscript. All the authors contributed to the article and approved the submitted version.

FUNDING

The study was financially supported by the New Jersey Health Foundation Grant #PC101-17 and the Gustavus and Louise Pfeiffer Research Foundation's Major Investment Grant.

ACKNOWLEDGMENTS

The authors would like to thank the copyright owners who allowed us to use their images in this manuscript. Additionally, Ms. Anh (Anne) Tong is graciously thanked for her useful discussions.

REFERENCES

Antzelevitch, C. (2001). Basic mechanisms of reentrant arrhythmias. *Curr. Opin. Cardiol.* 16, 1–7. doi: 10.1097/00001573-200101000-00001

Appleton, B., Qing, W., Crozier, S., Feng, L., Wilson, S., Ling, X., et al. (2005). "An electrical heart model incorporating real geometry and motion," in *Proceedings of the 27th Annual Conference IEEE Engineering in Medicine and Biology*, Shanghai, 345–348.

Arevalo, H. J., Vadakkumpadan, F., Guallar, E., Jebb, A., Malamas, P., Wu, K. C., et al. (2016). Arrhythmia risk stratification of patients after myocardial infarction using personalized heart models. *Nat. Commun.* 7:11437. doi: 10.1038/ncomms11437

Ashikaga, H., Arevalo, H., Vadakkumpadan, F., Blake, R. C., Bayer, J. D., Nazarian, S., et al. (2013). Feasibility of image-based simulation to estimate ablation target in human ventricular arrhythmia. *Heart Rhythm* 10, 1109–1116. doi: 10.1016/j.hrthm.2013.04.015

Aslanidi, O. V., Nikolaidou, T., Zhao, J., Smaill, B. H., Gilbert, S. H., Holden, A. V., et al. (2013). Application of micro-computed tomography with iodine staining to cardiac imaging, segmentation, and computational model development. *IEEE Trans. Med. Imaging* 32, 8–17. doi: 10.1109/TMI.2012.2209183

Avazmohammadi, R., Soares, J. S., Li, D. S., Raut, S. S., Gorman, R. C., and Sacks, M. S. (2019). A contemporary look at biomechanical models of myocardium. *Annu. Rev. Biomed. Eng.* 21, 417–442. doi: 10.1146/annurev-bioeng-062117-121129

Bayer, J. D., Blake, R. C., Plank, G., and Trayanova, N. A. (2012). A novel rule-based algorithm for assigning myocardial fiber orientation to computational heart models. *Ann. Biomed. Eng.* 40, 2243–2254. doi: 10.1007/s10439-012-0593-5

Beheshti, M., Umapathy, K., and Krishnan, S. (2016). Electrophysiological cardiac modeling: a review. *Crit Rev Biomed Eng.* 44, 99–122. doi: 10.1615/CritRevBiomedEng.2016016454

Behradfar, E., Nygren, A., and Vigmond, E. J. (2014). The role of Purkinje-myocardial coupling during ventricular arrhythmia: a modeling study. *PLoS One* 9:e88000. doi: 10.1371/journal.pone.0088000

Bestel, J., Clément, F., and Sorine, M. (2001). "A biomechanical model of muscle contraction," in *Medical Image Computing and Computer-Assisted Intervention – MICCAI 2001*, eds W. J. Niessen and M. A. Viergever (Berlin: Springer), 1159–1161. doi: 10.1007/3-540-45468-3_143

Bishop, M. J., and Plank, G. (2011). Bidomain ECG simulations using an augmented monodomain model for the cardiac source. *Proc. IEEE Trans. Biomed. Eng.* 58, 2297–2307. doi: 10.1109/TBME.2011.2148718

Bishop, M. J., Plank, G., Burton, R. A., Schneider, J. E., Gavaghan, D. J., Grau, V., et al. (2010). Development of an anatomically detailed MRI-derived rabbit ventricular model and assessment of its impact on simulations of electrophysiological function. *Am. J. Physiol. Heart Circ. Physiol.* 298, H699–H718. doi: 10.1152/ajpheart.00606.2009

Bonfanti, M., Franzetti, G., Maritati, G., Homer-Vanniasinkam, S., Balabani, S., and Díaz-Zuccarini, V. (2019). Patient-specific haemodynamic simulations of complex aortic dissections informed by commonly available clinical datasets. *Med. Eng. Phys.* 71, 45–55. doi: 10.1016/j.medengphy.2019.06.012

Boyle, P. M., Masse, S., Nanthakumar, K., and Vigmond, E. J. (2013). Transmural IK(ATP) heterogeneity as a determinant of activation rate gradient during early ventricular fibrillation: mechanistic insights from rabbit ventricular models. *Heart Rhythm* 10, 1710–1717. doi: 10.1016/j.hrthm.2013.08.010

Boyle, P. M., Zahid, S., and Trayanova, N. A. (2016). Towards personalized computational modelling of the fibrotic substrate for atrial arrhythmia. *Europace* 18(Suppl. 4), iv136–iv145. doi: 10.1093/europace/euw358

Bruegmann, T., Boyle, P. M., Vogt, C. C., Karathanos, T. V., Arevalo, H. J., Fleischmann, B. K., et al. (2016). Optogenetic defibrillation terminates ventricular arrhythmia in mouse hearts and human simulations. *J. Clin. Invest.* 126, 3894–3904. doi: 10.1172/JCI88950

Burton, R. A., Plank, G., Schneider, J. E., Grau, V., Ahammer, H., Keeling, S. L., et al. (2006). Three-dimensional models of individual cardiac histoanatomy: tools and challenges. *Ann. N. Y. Acad. Sci.* 1080, 301–319. doi: 10.1196/annals.1380.023

Cabo, C., and Boyden, P. A. (2003). Electrical remodeling of the epicardial border zone in the canine infarcted heart: a computational analysis. *Am. J. Physiol. Heart Circ. Physiol.* 284, H372–H384. doi: 10.1152/ajpheart.00512.2002

Cardenes, R., Sebastian, R., Berruezo, A., and Camara, O. (2014). "Inverse estimation of ventricular Purkinje tree pathways from sequences of depolarization," in *Proceedings of the 2014 Conference on Computing in Cardiology*, Cambridge, MA, 677–680.

Casa, L. D. C., Deaton, D. H., and Ku, D. N. (2015). Role of high shear rate in thrombosis. *J. Vasc. Surg.* 61, 1068–1080. doi: 10.1016/j.jvs.2014.12.050

CDC (2019). *Heart Disease Facts [Online]*. Available online at: https://www.cdc.gov/heartdisease/facts.htm (accessed on 26 December 2019)

Chabiniok, R., Wang, V. Y., Hadjicharalambous, M., Asner, L., Lee, J., Sermesant, M., et al. (2016). Multiphysics and multiscale modelling, data–model fusion and integration of organ physiology in the clinic: ventricular cardiac mechanics. *Interf. Focus* 6:20150083. doi: 10.1098/rsfs.2015.0083

Cheng, Y., Oertel, H., and Schenkel, T. (2005). Fluid-structure coupled CFD simulation of the left ventricular flow during filling phase. *Ann. Biomed. Eng.* 33, 567–576. doi: 10.1007/s10439-005-4388-9

Chnafa, C., Mendez, S., and Nicoud, F. (2014). Image-based large-eddy simulation in a realistic left heart. *Comput. Fluids* 94, 173–187. doi: 10.1016/j.compfluid.2014.01.030

Choi, Y. J., Constantino, J., Vedula, V., Trayanova, N., and Mittal, R. (2015). A new MRI-based model of heart function with coupled hemodynamics and application to normal and diseased canine left ventricles. *Front. Bioeng. Biotechnol.* 3:140. doi: 10.3389/fbioe.2015.00140

Craft (2019). *HeartFlow [Online]*. Available online at: https://craft.co/heartflow (accessed on 26 December 2019).

Dass, S., Suttie, J. J., Piechnik, S. K., Ferreira, V. M., Holloway, C. J., Banerjee, R., et al. (2012). Myocardial tissue characterization using magnetic resonance noncontrast t1 mapping in hypertrophic and dilated cardiomyopathy. *Circ. Cardiovasc. Imaging* 5, 726–733. doi: 10.1161/CIRCIMAGING.112.976738

Decker, K. F., and Rudy, Y. (2010). Ionic mechanisms of electrophysiological heterogeneity and conduction block in the infarct border zone. *Am. J. Physiol. Heart Circ. Physiol.* 299, H1588–H1597. doi: 10.1152/ajpheart.00362.2010

Deng, D., Arevalo, H. J., Prakosa, A., Callans, D. J., and Trayanova, N. A. (2016). A feasibility study of arrhythmia risk prediction in patients with myocardial infarction and preserved ejection fraction. *Europace* 18(Suppl. 4), iv60–iv66. doi: 10.1093/europace/euw351

Deng, D., Jiao, P., Ye, X., and Xia, L. (2012). An image-based model of the whole human heart with detailed anatomical structure and fiber orientation. *Comput. Math. Methods Med.* 2012:891070. doi: 10.1155/2012/891070

Deng, D., Prakosa, A., Shade, J., Nikolov, P., and Trayanova, N. A. (2019). Sensitivity of ablation targets prediction to electrophysiological parameter variability in image-based computational models of ventricular tachycardia in post-infarction patients. *Front. Physiol.* 10:628. doi: 10.3389/fphys.2019.00628

Dokos, S., Smaill, B. H., Young, A. A., and LeGrice, I. J. (2002). Shear properties of passive ventricular myocardium. *Am. J. Physiol. Heart Circ. Physiol.* 283, H2650–H2659. doi: 10.1152/ajpheart.00111.2002

Dolan, A. T., and Diamond, S. L. (2014). Systems modeling of Ca(2+) homeostasis and mobilization in platelets mediated by IP3 and store-operated Ca(2+) entry. *Biophys. J.* 106, 2049–2060. doi: 10.1016/j.bpj.2014.03.028

Donati, F., Myerson, S., Bissell, M. M., Smith, N. P., Neubauer, S., Monaghan, M. J., et al. (2017). Beyond Bernoulli: improving the accuracy and precision of noninvasive estimation of peak pressure drops. *Circ. Cardiovasc. Imaging* 10:e005207. doi: 10.1161/CIRCIMAGING.116.005207

Durrer, D., Van Dam, R. T. H., Freud, G. E., Janse, M. J., Meijler, F. L., and Arzbaecher, R. C. (1970). Total excitation of the isolated human heart. *Circulation* 41, 899–912. doi: 10.1161/01.CIR.41.6.899

FDA (2019). *510(k) Premarket Notification*. Silver Spring, MD: FDA.

Finsberg, H., Xi, C., Tan, J. L., Zhong, L., Genet, M., Sundnes, J., et al. (2018). Efficient estimation of personalized biventricular mechanical function employing gradient-based optimization. *Int. J. Numer. Method Biomed. Eng.* 34:e2982. doi: 10.1002/cnm.2982

Flachskampf, F. A., Weyman, A. E., Guerrero, J. L., and Thomas, J. D. (1990). Influence of orifice geometry and flow rate on effective valve area: an in vitro study. *J. Am. Coll. Cardiol.* 15, 1173–1180. doi: 10.1016/0735-1097(90)90260-V

Flamm, M. H., Colace, T. V., Chatterjee, M. S., Jing, H., Zhou, S., Jaeger, D., et al. (2012). Multiscale prediction of patient-specific platelet function under flow. *Blood* 120, 190–198. doi: 10.1182/blood-2011-10-388140

Frangi, A. F., Rueckert, D., Schnabel, J. A., and Niessen, W. J. (2002). Automatic construction of multiple-object three-dimensional statistical shape models: application to cardiac modeling. *IEEE Trans. Med. Imaging* 21, 1151–1166. doi: 10.1109/TMI.2002.804426

Fritz, T., Wieners, C., Seemann, G., Steen, H., and Dossel, O. (2014). Simulation of the contraction of the ventricles in a human heart model including atria and pericardium. *Biomech. Model. Mechanobiol.* 13, 627–641. doi: 10.1007/s10237-013-0523-y

Goldberger, J. J., Buxton, A. E., Cain, M., Costantini, O., Exner, D. V., Knight, B. P., et al. (2011). Risk stratification for arrhythmic sudden cardiac death: identifying the roadblocks. *Circulation* 123, 2423–2430. doi: 10.1161/CIRCULATIONAHA.110.959734

Grande Gutierrez, N., Kahn, A., Burns, J. C., and Marsden, A. L. (2017). Computational blood flow simulations in Kawasaki disease patients: insight into coronary artery aneurysm hemodynamics. *Glob. Cardiol. Sci. Pract.* 2017:e201729. doi: 10.21542/gcsp.2017.29

Grande Gutierrez, N., Mathew, M., McCrindle, B. W., Tran, J. S., Kahn, A. M., Burns, J. C., et al. (2019). Hemodynamic variables in aneurysms are associated with thrombotic risk in children with Kawasaki disease. *Int. J. Cardiol.* 281, 15–21. doi: 10.1016/j.ijcard.2019.01.092

Gray, R. A., and Pathmanathan, P. (2018). Patient-specific cardiovascular computational modeling: diversity of personalization and challenges. *J. Cardiovasc. Transl. Res.* 11, 80–88. doi: 10.1007/s12265-018-9792-2

Guccione, J. M., Salahieh, A., Moonly, S. M., Kortsmit, J., Wallace, A. W., and Ratcliffe, M. B. (2003). Myosplint decreases wall stress without depressing function in the failing heart: a finite element model study. *Ann. Thorac. Surg.* 76, 1171–1180. doi: 10.1016/s0003-4975(03)00731-8

Harfi, T. T., Seo, J. H., Yasir, H. S., Welsh, N., Mayer, S. A., Abraham, T. P., et al. (2017). The E-wave propagation index (EPI): a novel echocardiographic parameter for prediction of left ventricular thrombus. Derivation from

computational fluid dynamic modeling and validation on human subjects. *Int. J. Cardiol.* 227, 662–667. doi: 10.1016/j.ijcard.2016.10.079

Hathcock James, J. (2006). Flow effects on coagulation and thrombosis. *Arterioscl. Thromb. Vasc. Biol.* 26, 1729–1737. doi: 10.1161/01.ATV.0000229658.76797.30

HeartFlow (2019). *Transforming the Diagnosis and Management of Coronary Artery Disease Worldwide*. Available online at: https://www.heartflow.com/ (accessed on 13 December 2019)

Hockin, M. F., Jones, K. C., Everse, S. J., and Mann, K. G. (2002). A model for the stoichiometric regulation of blood coagulation. *J. Biol. Chem.* 277, 18322–18333. doi: 10.1074/jbc.M201173200

Hodgkin, A. L., and Huxley, A. F. (1952). A quantitative description of membrane current and its application to conduction and excitation in nerve. *J. Physiol.* 117, 500–544. doi: 10.1113/jphysiol.1952.sp004764

Holmes, A. A., Scollan, D. F., and Winslow, R. L. (2000). Direct histological validation of diffusion tensor MRI in formaldehyde-fixed myocardium. *Magn. Reson. Med.* 44, 157–161. doi: 10.1002/1522-2594(200007)44:1<157::aid-mrm22<3.0.co;2-f

Holzapfel, G. A., and Ogden, R. W. (2009). Constitutive modelling of passive myocardium: a structurally based framework for material characterization. *Philos. Trans. A Math. Phys. Eng. Sci.* 367, 3445–3475. doi: 10.1098/rsta.2009.0091

Hooks, D. A., Tomlinson, K. A., Marsden, S. G., LeGrice, I. J., Smaill, B. H., Pullan, A. J., et al. (2002). Cardiac microstructure: implications for electrical propagation and defibrillation in the heart. *Circ. Res.* 91, 331–338. doi: 10.1161/01.res.0000031957.70034.89

Hooks, D. A., Trew, M. L., Smaill, B. H., and Pullan, A. J. (2006). Do intramural virtual electrodes facilitate successful defibrillation? Model-based analysis of experimental evidence. *J. Cardiovasc. Electrophysiol.* 17, 305–311. doi: 10.1111/j.1540-8167.2006.00360.x

Huxley, A. F. (1957). 6 - Muscle structure and theories of contraction. *Prog. Biophys. Biophys. Chem.* 7, 255–318. doi: 10.1016/S0096-4174(18)30128-8

Ideker, R. E., Kong, W., and Pogwizd, S. (2009). Purkinje fibers and arrhythmias. *Pac. Clin. Electrophysiol. PACE* 32, 283–285. doi: 10.1111/j.1540-8159.2008.02232.x

Kayvanpour, E., Mansi, T., Sedaghat-Hamedani, F., Amr, A., Neumann, D., Georgescu, B., et al. (2015). Towards personalized cardiology: multi-scale modeling of the failing heart. *PLoS One* 10:e0134869. doi: 10.1371/journal.pone.0134869

Keldermann, R. H., ten Tusscher, K. H. W. J., Nash, M. P., Bradley, C. P., Hren, R., Taggart, P., et al. (2009). A computational study of mother rotor VF in the human ventricles. *Am. J. Physiol. Heart Circ. Physiol.* 296, H370–H379. doi: 10.1152/ajpheart.00952.2008

Kim, H. J., Vignon-Clementel, I. E., Coogan, J. S., Figueroa, C. A., Jansen, K. E., and Taylor, C. A. (2010). Patient-specific modeling of blood flow and pressure in human coronary arteries. *Ann. Biomed. Eng.* 38, 3195–3209. doi: 10.1007/s10439-010-0083-6

Kim, H. J., Vignon-Clementel, I. E., Figueroa, C. A., LaDisa, J. F., Jansen, K. E., Feinstein, J. A., et al. (2009). On coupling a lumped parameter heart model and a three-dimensional finite element aorta model. *Ann. Biomed. Eng.* 37, 2153–2169. doi: 10.1007/s10439-009-9760-8

Kim, J. (2019). *Fast Company Names HeartFlow One of the World's Most Innovative Companies [Online]*. Available online at: https://www.businesswire.com/news/home/20190220005218/en/Fast-Company-Names-HeartFlow-World's-Innovative-Companies/ (accessed on 13 December 2019)

Kohl, P., Noble, D., Hunter, P. J., Kovács, S. J., McQueen, D. M., and Peskin, C. S. (2001). Modelling cardiac fluid dynamics and diastolic function. *Philos. Trans. R. Soc. Lond. Ser. A Math. Phys. Eng. Sci.* 359, 1299–1314. doi: 10.1098/rsta.2001.0832

Koo, B. K., Erglis, A., Doh, J. H., Daniels, D. V., Jegere, S., Kim, H. S., et al. (2011). Diagnosis of ischemia-causing coronary stenoses by noninvasive fractional flow reserve computed from coronary computed tomographic angiograms. Results from the prospective multicenter DISCOVER-FLOW (Diagnosis of Ischemia-Causing Stenoses Obtained Via Noninvasive Fractional Flow Reserve) study. *J. Am. Coll. Cardiol.* 58, 1989–1997. doi: 10.1016/j.jacc.2011.06.066

Krishnamurthy, A., Villongco, C. T., Chuang, J., Frank, L. R., Nigam, V., Belezzuoli, E., et al. (2013). Patient-specific models of cardiac biomechanics. *J. Comput. Phys.* 244, 4–21. doi: 10.1016/j.jcp.2012.09.015

Krueger, M. W., Schulze, W. H., Rhode, K. S., Razavi, R., Seemann, G., and Dossel, O. (2013a). Towards personalized clinical in-silico modeling of atrial anatomy and electrophysiology. *Med. Biol. Eng. Comput.* 51, 1251–1260. doi: 10.1007/s11517-012-0970-0

Krueger, M. W., Seemann, G., Rhode, K., Keller, D. U. J., Schilling, C., Arujuna, A., et al. (2013b). Personalization of atrial anatomy and electrophysiology as a basis for clinical modeling of radio-frequency ablation of atrial fibrillation. *IEEE Trans. Med. Imaging* 32, 73–84. doi: 10.1109/TMI.2012.2201948

Kung, E., Kahn, A. M., Burns, J. C., and Marsden, A. (2014). In vitro validation of patient-specific hemodynamic simulations in coronary aneurysms caused by Kawasaki disease. *Cardiovasc. Eng. Technol.* 5, 189–201. doi: 10.1007/s13239-014-0184-8

Lamata, P., Casero, R., Carapella, V., Niederer, S. A., Bishop, M. J., Schneider, J. E., et al. (2014). Images as drivers of progress in cardiac computational modelling. *Prog. Biophys. Mol. Biol.* 115, 198–212. doi: 10.1016/j.pbiomolbio.2014.08.005

Lee, A. W. C., Costa, C. M., Strocchi, M., Rinaldi, C. A., and Niederer, S. A. (2018). Computational modeling for cardiac resynchronization therapy. *J. Cardiovasc. Transl. Res.* 11, 92–108. doi: 10.1007/s12265-017-9779-4

Lee, L. C., Wall, S. T., Klepach, D., Ge, L., Zhang, Z., Lee, R. J., et al. (2013). Algisyl-LVR with coronary artery bypass grafting reduces left ventricular wall stress and improves function in the failing human heart. *Int. J. Cardiol.* 168, 2022–2028. doi: 10.1016/j.ijcard.2013.01.003

Li, X., Li, H., Chang, H. Y., Lykotrafitis, G., and Em Karniadakis, G. (2017). Computational biomechanics of human red blood cells in hematological disorders. *J. Biomech. Eng.* 139, 0210081–02100813. doi: 10.1115/1.4035120

Lopez-Perez, A., Sebastian, R., and Ferrero, J. M. (2015). Three-dimensional cardiac computational modelling: methods, features and applications. *BioMed. Eng. Online* 14:35. doi: 10.1186/s12938-015-0033-5

Lopez-Perez, A., Sebastian, R., Izquierdo, M., Ruiz, R., Bishop, M., and Ferrero, J. M. (2019). Personalized cardiac computational models: from clinical data to simulation of infarct-related ventricular tachycardia. *Front. Physiol.* 10:580. doi: 10.3389/fphys.2019.00580

Meoli, A., Cutri, E., Krishnamurthy, A., Dubini, G., Migliavacca, F., Hsia, T. Y., et al. (2015). A multiscale model for the study of cardiac biomechanics in single-ventricle surgeries: a clinical case. *Interface Focus* 5:20140079. doi: 10.1098/rsfs.2014.0079

Mewton, N., Liu, C. Y., Croisille, P., Bluemke, D., and Lima, J. A. (2011). Assessment of myocardial fibrosis with cardiovascular magnetic resonance. *J. Am. Coll. Cardiol.* 57, 891–903. doi: 10.1016/j.jacc.2010.11.013

Mihalef, V., Ionasec, R. I., Sharma, P., Georgescu, B., Voigt, I., Suehling, M., et al. (2011). Patient-specific modelling of whole heart anatomy, dynamics and haemodynamics from four-dimensional cardiac CT images. *Interface Focus* 1, 286–296. doi: 10.1098/rsfs.2010.0036

Min, J. K., Koo, B. K., Erglis, A., Doh, J. H., Daniels, D. V., Jegere, S., et al. (2012). Usefulness of noninvasive fractional flow reserve computed from coronary computed tomographic angiograms for intermediate stenoses confirmed by quantitative coronary angiography. *Am. J. Cardiol.* 110, 971–976. doi: 10.1016/j.amjcard.2012.05.033

Min, J. K., Taylor, C. A., Achenbach, S., Koo, B. K., Leipsic, J., Norgaard, B. L., et al. (2015). Noninvasive fractional flow reserve derived from coronary CT angiography: clinical data and scientific principles. *JACC Cardiovasc. Imaging* 8, 1209–1222. doi: 10.1016/j.jcmg.2015.08.006

Mincholé, A., Zacur, E., Ariga, R., Grau, V., and Rodriguez, B. (2019). MRI-based computational torso/biventricular multiscale models to investigate the impact of anatomical variability on the ECG QRS complex. *Front. Physiol.* 10:1103. doi: 10.3389/fphys.2019.01103

Mittal, R., Seo, J. H., Vedula, V., Choi, Y. J., Liu, H., Huang, H. H., et al. (2016). Computational modeling of cardiac hemodynamics: current status and future outlook. *J. Comput. Phys.* 305, 1065–1082. doi: 10.1016/j.jcp.2015.11.022

Moireau, P., Xiao, N., Astorino, M., Figueroa, C. A., Chapelle, D., Taylor, C. A., et al. (2012). External tissue support and fluid-structure simulation in blood flows. *Biomech. Model. Mechanobiol.* 11, 1–18. doi: 10.1007/s10237-011-0289-z

Morris, P. D., Narracott, A., von Tengg-Kobligk, H., Silva Soto, D. A., Hsiao, S., Lungu, A., et al. (2016). Computational fluid dynamics modelling in cardiovascular medicine. *Heart* 102, 18–28. doi: 10.1136/heartjnl-2015-308044

Negroni, J. A., and Lascano, E. C. (2008). Simulation of steady state and transient cardiac muscle response experiments with a Huxley-based contraction model. *J. Mol. Cell Cardiol.* 45, 300–312. doi: 10.1016/j.yjmcc.2008.04.012

Ni, H., Morotti, S., and Grandi, E. (2018). A heart for diversity: simulating variability in cardiac arrhythmia research. *Front. Physiol.* 9:958. doi: 10.3389/fphys.2018.00958

Niederer, S. A., Campbell, K. S., and Campbell, S. G. (2019a). A short history of the development of mathematical models of cardiac mechanics. *J. Mol. Cell. Cardiol.* 127, 11–19. doi: 10.1016/j.yjmcc.2018.11.015

Niederer, S. A., Lumens, J., and Trayanova, N. A. (2019b). Computational models in cardiology. *Nat. Rev. Cardiol.* 16, 100–111. doi: 10.1038/s41569-018-0104-y

O'Hara, T., Virag, L., Varro, A., and Rudy, Y. (2011). Simulation of the undiseased human cardiac ventricular action potential: model formulation and experimental validation. *PLoS Comput. Biol.* 7:e1002061. doi: 10.1371/journal.pcbi.1002061

Palamara, S., Vergara, C., Catanzariti, D., Faggiano, E., Pangrazzi, C., Centonze, M., et al. (2014). Computational generation of the Purkinje network driven by clinical measurements: the case of pathological propagations. *Int. J. Numer. Methods Biomed. Eng.* 30, 1558–1577. doi: 10.1002/cnm.2689

Palit, A., Bhudia, S. K., Arvanitis, T. N., Turley, G. A., and Williams, M. A. (2018). In vivo estimation of passive biomechanical properties of human myocardium. *Med. Biol. Eng. Comput.* 56, 1615–1631. doi: 10.1007/s11517-017-1768-x

Papadacci, C., Finel, V., Provost, J., Villemain, O., Bruneval, P., Gennisson, J.-L., et al. (2017). Imaging the dynamics of cardiac fiber orientation in vivo using 3D ultrasound backscatter tensor imaging. *Sci. Rep.* 7:830. doi: 10.1038/s41598-017-00946-7

Patel, M. R., Dai, D., Hernandez, A. F., Douglas, P. S., Messenger, J., Garratt, K. N., et al. (2014). Prevalence and predictors of nonobstructive coronary artery disease identified with coronary angiography in contemporary clinical practice. *Am. Heart J.* 167, 846–852e842. doi: 10.1016/j.ahj.2014.03.001

Pathmanathan, P., and Gray, R. A. (2018). Validation and trustworthiness of multiscale models of cardiac electrophysiology. *Front. Physiol.* 9:106. doi: 10.3389/fphys.2018.00106

Plank, G., Burton, R. A. B., Hales, P., Bishop, M., Mansoori, T., Bernabeu, M. O., et al. (2009). Generation of histo-anatomically representative models of the individual heart: tools and application. *Philos. Trans. R. Soc. A Math. Phys. Eng. Sci.* 367, 2257–2292. doi: 10.1098/rsta.2009.0056

Potse, M., Krause, D., Kroon, W., Murzilli, R., Muzzarelli, S., Regoli, F., et al. (2014). Patient-specific modelling of cardiac electrophysiology in heart-failure patients. *Europace* 16(Suppl. 4), iv56–iv61. doi: 10.1093/europace/euu257

Prakosa, A., Arevalo, H. J., Deng, D., Boyle, P. M., Nikolov, P. P., Ashikaga, H., et al. (2018). Personalized virtual-heart technology for guiding the ablation of infarct-related ventricular tachycardia. *Nat. Biomed. Eng.* 2, 732–740. doi: 10.1038/s41551-018-0282-2

Quarteroni, A., Lassila, T., Rossi, S., and Ruiz-Baier, R. (2017). Integrated heart—coupling multiscale and multiphysics models for the simulation of the cardiac function. *Comput. Methods Appl. Mech. Eng.* 314, 345–407. doi: 10.1016/j.cma.2016.05.031

Rice, J. J., Wang, F., Bers, D. M., and de Tombe, P. P. (2008). Approximate model of cooperative activation and crossbridge cycling in cardiac muscle using ordinary differential equations. *Biophys. J.* 95, 2368–2390. doi: 10.1529/biophysj.107.119487

Rodriguez, B., Carusi, A., Abi-Gerges, N., Ariga, R., Britton, O., Bub, G., et al. (2015). Human-based approaches to pharmacology and cardiology: an interdisciplinary and intersectorial workshop. *EP Europace* 18, 1287–1298. doi: 10.1093/europace/euv320

Romero, D., Sebastian, R., Bijnens, B. H., Zimmerman, V., Boyle, P. M., Vigmond, E. J., et al. (2010). Effects of the purkinje system and cardiac geometry on biventricular pacing: a model study. *Ann. Biomed. Eng.* 38, 1388–1398. doi: 10.1007/s10439-010-9926-4

Roney, C. H., Williams, S. E., Cochet, H., Mukherjee, R. K., O'Neill, L., Sim, I., et al. (2018). Patient-specific simulations predict efficacy of ablation of interatrial connections for treatment of persistent atrial fibrillation. *Europace* 20(Suppl. 3), iii55–iii68. doi: 10.1093/europace/euy232

Rossi, S., Lassila, T., Ruiz-Baier, R., Sequeira, A., and Quarteroni, A. (2014). Thermodynamically consistent orthotropic activation model capturing ventricular systolic wall thickening in cardiac electromechanics. *Eur. J. Mech. A/Solids* 48, 129–142. doi: 10.1016/j.euromechsol.2013.10.009

Ruiz-Baier, R., Gizzi, A., Rossi, S., Cherubini, C., Laadhari, A., Filippi, S., et al. (2014). Mathematical modelling of active contraction in isolated cardiomyocytes. *Math. Med. Biol.* 31, 259–283. doi: 10.1093/imammb/dqt009

Sainte-Marie, J., Chapelle, D., Cimrman, R., and Sorine, M. (2006). Modeling and estimation of the cardiac electromechanical activity. *Comput. Struct.* 84, 1743–1759. doi: 10.1016/j.compstruc.2006.05.003

Schulte, R. F., Sands, G. B., Sachse, F. B., Dössel, O., and Pullan, A. J. (2001). Creation of a human heart, model and its customisation using ultrasound images. *Biomed. Eng.* 46, 26–28. doi: 10.1515/bmte.2001.46.s2.26

Scollan, D. F., Holmes, A., Winslow, R., and Forder, J. (1998). Histological validation of myocardial microstructure obtained from diffusion tensor magnetic resonance imaging. *Am. J. Physiol. Heart Circ. Physiol.* 275, H2308–H2318. doi: 10.1152/ajpheart.1998.275.6.H2308

Sebastian, R., Zimmerman, V., Romero, D., Sanchez-Quintana, D., and Frangi, A. F. (2013). Characterization and modeling of the peripheral cardiac conduction system. *IEEE Trans. Med. Imaging* 32, 45–55. doi: 10.1109/TMI.2012.2221474

Segers, P., Stergiopulos, N., and Westerhof, N. (2002). Relation of effective arterial elastance to arterial system properties. *Am. J. Physiol. Heart Circ. Physiol.* 282, H1041–H1046. doi: 10.1152/ajpheart.00764.2001

Seo, J. H., Abd, T., George, R. T., and Mittal, R. (2016). A coupled chemo-fluidic computational model for thrombogenesis in infarcted left ventricles. *Am. J. Physiol. Heart Circ. Physiol.* 310, H1567–H1582. doi: 10.1152/ajpheart.00855.2015

Sermesant, M., Peyrat, J.-M., Chinchapatnam, P., Billet, F., Mansi, T., Rhode, K., et al. (2008). Toward patient-specific myocardial models of the heart. *Heart Fail. Clin.* 4, 289–301. doi: 10.1016/j.hfc.2008.02.014

Shavik, S. M., Tossas-Betancourt, C., Figueroa, C. A., Baek, S., and Lee, L. C. (2020). Multiscale modeling framework of ventricular-arterial bi-directional interactions in the cardiopulmonary circulation. *Front. Physiol.* 11:2. doi: 10.3389/fphys.2020.00002

Shibeshi, S. S., and Collins, W. E. (2005). The rheology of blood flow in a branched arterial system. *Applied* 15, 398–405. doi: 10.1901/jaba.2005.15-398

Smith, N., de Vecchi, A., McCormick, M., Nordsletten, D., Camara, O., Frangi, A. F., et al. (2011). euHeart: personalized and integrated cardiac care using patient-specific cardiovascular modelling. *Interface Focus* 1, 349–364. doi: 10.1098/rsfs.2010.0048

Sommer, G., Schriefl, A. J., Andrä, M., Sacherer, M., Viertler, C., Wolinski, H., et al. (2015). Biomechanical properties and microstructure of human ventricular myocardium. *Acta Biomater.* 24, 172–192. doi: 10.1016/j.actbio.2015.06.031

Starobin, J. M., Zilberter, Y. I., Rusnak, E. M., and Starmer, C. F. (1996). Wavelet formation in excitable cardiac tissue: the role of wavefront-obstacle interactions in initiating high-frequency fibrillatory-like arrhythmias. *Biophys. J.* 70, 581–594. doi: 10.1016/S0006-3495(96)79624-8

Streeter Daniel, D., Spotnitz Henry, M., Patel Dali, P., Ross, J., and Sonnenblick Edmund, H. (1969). Fiber orientation in the canine left ventricle during diastole and systole. *Circ. Res.* 24, 339–347. doi: 10.1161/01.RES.24.3.339

Su, B., Zhong, L., Wang, X. K., Zhang, J. M., Tan, R. S., Allen, J. C., et al. (2014). Numerical simulation of patient-specific left ventricular model with both mitral and aortic valves by FSI approach. *Comput. Methods Prog. Biomed.* 113, 474–482. doi: 10.1016/j.cmpb.2013.11.009

Sun, W., Martin, C., and Pham, T. (2014). Computational modeling of cardiac valve function and intervention. *Annu. Rev. Biomed. Eng.* 16, 53–76. doi: 10.1146/annurev-bioeng-071813-104517

Tang, D., Yang, C., Geva, T., and Del Nido, P. J. (2010). Image-based patient-specific ventricle models with fluid-structure interaction for cardiac function assessment and surgical design optimization. *Prog. Pediatr. Cardiol.* 30, 51–62. doi: 10.1016/j.ppedcard.2010.09.007

Tobon-Gomez, C., Duchateau, N., Sebastian, R., Marchesseau, S., Camara, O., Donal, E., et al. (2013). Understanding the mechanisms amenable to CRT response: from pre-operative multimodal image data to patient-specific computational models. *Med. Biol. Eng. Comput.* 51, 1235–1250. doi: 10.1007/s11517-013-1044-7

Trayanova, N. A. (2011). Whole-heart modeling: applications to cardiac electrophysiology and electromechanics. *Circ. Res.* 108, 113–128. doi: 10.1161/CIRCRESAHA.110.223610

Trayanova, N. A. (2012). Computational cardiology: the heart of the matter. *ISRN Cardiol.* 2012:269680. doi: 10.5402/2012/269680

Trayanova, N. A. (2014). Mathematical approaches to understanding and imaging atrial fibrillation: significance for mechanisms and management. *Circ. Res.* 114, 1516–1531. doi: 10.1161/CIRCRESAHA.114.302240

Trayanova, N. A., and Chang, K. C. (2016). How computer simulations of the human heart can improve anti-arrhythmia therapy. *J. Physiol.* 594, 2483–2502. doi: 10.1113/JP270532

Trayanova, N. A., Pashakhanloo, F., Wu, K. C., and Halperin, H. R. (2017). Imaging-based simulations for predicting sudden death and guiding ventricular tachycardia ablation. *Circ. Arrhythm. Electrophysiol.* 10:e004743. doi: 10.1161/CIRCEP.117.004743

Vadakkumpadan, F., Arevalo, H., Prassl, A. J., Chen, J., Kickinger, F., Kohl, P., et al. (2010). Image-based models of cardiac structure in health and disease. *Wiley Interdiscip. Rev. Syst. Biol. Med.* 2, 489–506. doi: 10.1002/wsbm.76

Vadakkumpadan, F., Rantner, L. J., Tice, B., Boyle, P., Prassl, A. J., Vigmond, E., et al. (2009). Image-based models of cardiac structure with applications in arrhythmia and defibrillation studies. *J. Electrocardiol.* 42:e00151-10. doi: 10.1016/j.jelectrocard.2008.12.003

Valderrabano, M., Chen, P. S., and Lin, S. F. (2003). Spatial distribution of phase singularities in ventricular fibrillation. *Circulation* 108, 354–359. doi: 10.1161/01.CIR.0000080322.67408.B4

Vandervoort Pieter, M., Greenberg Neil, L., Pu, M., Powell Kimerly, A., Cosgrove Delos, M., and Thomas James, D. (1995). Pressure recovery in bileaflet heart valve prostheses. *Circulation* 92, 3464–3472. doi: 10.1161/01.CIR.92.12.3464

Vetter, F. J., and McCulloch, A. D. (1998). Three-dimensional analysis of regional cardiac function: a model of rabbit ventricular anatomy. *Prog. Biophys. Mol. Biol.* 69, 157–183. doi: 10.1016/S0079-6107(98)00006-6

Vigmond, E. J., Clements, C., McQueen, D. M., and Peskin, C. S. (2008). Effect of bundle branch block on cardiac output: a whole heart simulation study. *Prog. Biophys. Mol. Biol.* 97, 520–542. doi: 10.1016/j.pbiomolbio.2008.02.022

Voorhees, A. P., and Han, H.-C. (2015). Biomechanics of cardiac function. *Comprehens. Physiol.* 5, 1623–1644. doi: 10.1002/cphy.c140070

Walcott, S., and Sun, S. X. (2009). Hysteresis in cross-bridge models of muscle. *Phys. Chem. Chem. Phys.* 11, 4871–4881. doi: 10.1039/B900551J

Wall, S. T., Walker, J. C., Healy, K. E., Ratcliffe, M. B., and Guccione, J. M. (2006). Theoretical impact of the injection of material into the myocardium: a finite element model simulation. *Circulation* 114, 2627–2635. doi: 10.1161/CIRCULATIONAHA.106.657270

Walmsley, J., van Everdingen, W., Cramer, M. J., Prinzen, F. W., Delhaas, T., and Lumens, J. (2017). Combining computer modelling and cardiac imaging to understand right ventricular pump function. *Cardiovasc. Res.* 113, 1486–1498. doi: 10.1093/cvr/cvx154

Wang, V. Y., Nielsen, P. M. F., and Nash, M. P. (2015). Image-based predictive modeling of heart mechanics. *Annu. Rev. Biomed. Eng.* 17, 351–383. doi: 10.1146/annurev-bioeng-071114-040609

Wang, W., and King, M. R. (2012). Multiscale modeling of platelet adhesion and thrombus growth. *Ann. Biomed. Eng.* 40, 2345–2354. doi: 10.1007/s10439-012-0558-8

Washio, T., Okada, J. I., Sugiura, S., and Hisada, T. (2012). Approximation for cooperative interactions of a spatially-detailed cardiac sarcomere model. *Cell Mol. Bioeng.* 5, 113–126. doi: 10.1007/s12195-011-0219-2

Watson, S. R., Dormer, J. D., and Fei, B. (2018). Imaging technologies for cardiac fiber and heart failure: a review. *Heart Fail. Rev.* 23, 273–289. doi: 10.1007/s10741-018-9684-1

Weese, J., Groth, A., Nickisch, H., Barschdorf, H., Weber, F. M., Velut, J., et al. (2013). Generating anatomical models of the heart and the aorta from medical images for personalized physiological simulations. *Med. Biol. Eng. Comput.* 51, 1209–1219. doi: 10.1007/s11517-012-1027-0

Zhang, J. M., Zhong, L., Luo, T., Huo, Y., Tan, S. Y., Wong, A. S., et al. (2014). Numerical simulation and clinical implications of stenosis in coronary blood flow. *Biomed. Res. Int.* 2014:514729. doi: 10.1155/2014/514729

Zhao, J., Butters, T. D., Zhang, H., LeGrice, I. J., Sands, G. B., and Smaill, B. H. (2013). Image-based model of atrial anatomy and electrical activation: a computational platform for investigating atrial arrhythmia. *IEEE Trans. Med. Imaging* 32, 18–27. doi: 10.1109/TMI.2012.2227776

Zhong, L., Zhang, J.-M., Su, B., Tan, R. S., Allen, J. C., and Kassab, G. S. (2018). Application of patient-specific computational fluid dynamics in coronary and intra-cardiac flow simulations: challenges and opportunities. *Front. Physiol.* 9:742. doi: 10.3389/fphys.2018.00742

Conflict of Interest: The authors declare that the research was conducted in the absence of any commercial or financial relationships that could be construed as a potential conflict of interest.

Copyright © 2020 Nguyen, Kadri and Voronov. This is an open-access article distributed under the terms of the Creative Commons Attribution License (CC BY). The use, distribution or reproduction in other forums is permitted, provided the original author(s) and the copyright owner(s) are credited and that the original publication in this journal is cited, in accordance with accepted academic practice. No use, distribution or reproduction is permitted which does not comply with these terms.

GLOSSARY

Action Potential
A brief reversal (i.e., "depolarization" increase from a negative resting state followed by "repolarization" down to the original levels) in the voltage polarity of cardiomyocytes, which is generated by ion (e.g., Ca++, Na+, and K+) exchange across specialized channels in the cell membrane. The propagation of this electrical impulse through the heart tissue occurs via currents of the Ca++ and K+ ions moving through the gap junctions from the activated cells to their resting neighbors. This leads to the eventual contraction of the cardiac fibers along the conduction pathway.

Activation Rate Gradient
An arrythmia measure indicating a difference in the speed with which cardiomyocytes in the epicardial and in the endocardial tissues activate (i.e., depolarize/repolarize) in response to applied external stimuli (e.g., electrodes, needles, heat, blocking ion channels via medications, etc.) during Ventricular Fibrillation studies.

Bidomain Formulation
A mathematical framework that is used in Electrophysiology modeling to simulate the propagation of the *Action Potential* (see definition) through the myocardium. As opposed to the *Monodomain Formulation* (see definition), it considers both the intra- and the extra- cellular domains of the ion exchange across the cardiomyocyte membrane separately.

Cauchy–Green (Left and Right) Tensors
Rotation-independent measures of the material (e.g., myocardium tissue) deformation, in a spatial reference and in the object's coordinate systems, respectively. They are often used when describing the passive properties of hyperelastic materials, such as the diastolic cardiac dysfunction.

Conductivity Tensor
A mathematical quantity that describes the electrical conductivity of the myocardium. This property is highly dependent on the orientation of the fibers that the conductive heart cells are arranged into within the tissue. For this reason, the effective conductivity of the myocardium differs, depending on the direction of the current flow. Therefore, the tensor encompasses 9 total conductivity values: three of them represent directions along each of the principle axes, while the other six express the correlation of the conductivity between each pair of the principal directions.

Deformation Gradient Tensor
A mathematical quantity that describes a shape change (e.g., stretch), as well as overall rotation, relative to an initial state of a material (e.g., cardiac fiber structure). It holds information about the difference in the current locations of neighboring cardiomyocytes and is unity when they are displaced equally (i.e., for no deformation).

Diffusion Tensor
A mathematical quantity calculated in magnetic resonance imaging to visualize structural arrangements (e.g., fibers, sheets) of the cardiomyocytes within the myocardium. It is based on at least 6 unique (plus one baseline) measurements of how the diffusion of water molecules is restricted or biased in different directions by the structural obstructions that they encounter during their motion in the tissues of the hearts. Therefore, the tensor encompasses three main elements that represent diffusion coefficients along each of the principal axes, while the off-diagonal terms reflect the correlation of random motions between each pair of principal directions.

Determinant of the Deformation Gradient Tensor
A scalar value corresponding to the ratio of the deformed to the undeformed volume, which is computed from the elements of the *Deformation Gradient Tensor* (see definition) in order to quantify the amount of transformation occurring in the cardiac geometry.

Invariant
A property of a mathematical quantity which remains unchanged after an application of an operation or a transformation. For example, when calculating strain and stress of the cardiac fibers it is important that the resulting principal values remain the same, regardless of the coordinate system chosen for their calculation or measurement.

Membrane Capacitance
A constant that describes the relationship between the voltage across the membrane of a cell and the ionic charge that builds up on its interior and exterior surfaces. In cardiomyocytes it effectively determines how quickly the *Action Potential* (see definition) can travel through the myocardium. It is therefore useful for both modeling and understanding their excitability and pathological conditions.

Monodomain Formulation

A mathematical framework that is used in Electrophysiology modeling to simulate the propagation of the *Action Potential* through the myocardium. As opposed to the *Bidomain Formulation* (see definition), it does not consider both the intra- and the extra- cellular domains of the ion exchange across the cardiomyocyte membrane. Instead, the framework is expressed in terms of a transmembrane potential, which assumes that the intracellular and extracellular ion diffusivities are proportional to each other.

Neural Network

A set of artificial intelligence algorithms, modeled loosely after how the human brain learns, that are designed to recognize patterns within complex datasets. In cardiovascular modeling specifically, they are used to represent processes that are too difficult to describe mathematically using first-principle methods: for example, platelet "activation" – a cascade of cell membrane surface receptor activation, intracellular signaling, dumping of granules, etc. – in the context of thrombosis.

Stored (a.k.a., Strain) Energy Density Function

Energy per unit volume of a material temporarily deformed by an applied force, like a coiled spring or a stretched elastic band. This quantity is commonly used to formulate constitutive force-deformation relationships that characterize the spatial and temporal variations in the orthotropic (i.e., different in the axial, radial, and circumferential directions) properties of the myocardium. It is largely dominated by the structural arrangements of the myocardial fibers in the heart tissue.

frontiers in Bioengineering and Biotechnology

ORIGINAL RESEARCH
published: 26 November 2020
doi: 10.3389/fbioe.2020.539081

Effective Biophysical Modeling of Cell Free Transcription and Translation Processes

*Abhinav Adhikari, Michael Vilkhovoy, Sandra Vadhin, Ha Eun Lim and Jeffrey D. Varner**

Robert Frederick Smith School of Chemical and Biomolecular Engineering, College of Engineering, Cornell University, Ithaca, NY, United States

Transcription and translation are at the heart of metabolism and signal transduction. In this study, we developed an effective biophysical modeling approach to simulate transcription and translation processes. The model, composed of coupled ordinary differential equations, was tested by comparing simulations of two cell free synthetic circuits with experimental measurements generated in this study. First, we considered a simple circuit in which sigma factor 70 induced the expression of green fluorescent protein. This relatively simple case was then followed by a more complex negative feedback circuit in which two control genes were coupled to the expression of a third reporter gene, green fluorescent protein. Many of the model parameters were estimated from previous biophysical studies in the literature, while the remaining unknown model parameters for each circuit were estimated by minimizing the difference between model simulations and messenger RNA (mRNA) and protein measurements generated in this study. In particular, either parameter estimates from published studies were used directly, or characteristic values found in the literature were used to establish feasible ranges for the parameter estimation problem. In order to perform a detailed analysis of the influence of individual model parameters on the expression dynamics of each circuit, global sensitivity analysis was used. Taken together, the effective biophysical modeling approach captured the expression dynamics, including the transcription dynamics, for the two synthetic cell free circuits. While, we considered only two circuits here, this approach could potentially be extended to simulate other genetic circuits in both cell free and whole cell biomolecular applications as the equations governing the regulatory control functions are modular and easily modifiable. The model code, parameters, and analysis scripts are available for download under an MIT software license from the Varnerlab GitHub repository.

Keywords: systems biology, synthetic biological circuits, cell free, mathematical modeling, simulation

OPEN ACCESS

Edited by:
Robert Parker,
University of Pittsburgh, United States

Reviewed by:
Pavel Loskot,
Swansea University, United Kingdom
Mohit Kumar Jolly,
Indian Institute of Science (IISc), India

***Correspondence:**
Jeffrey D. Varner
jdv27@cornell.edu

Specialty section:
This article was submitted to Computational Genomics, a section of the journal Frontiers in Bioengineering and Biotechnology

Received: *28 February 2020*
Accepted: *02 November 2020*
Published: *26 November 2020*

Citation:
Adhikari A, Vilkhovoy M, Vadhin S, Lim HE and Varner JD (2020) Effective Biophysical Modeling of Cell Free Transcription and Translation Processes. Front. Bioeng. Biotechnol. 8:539081. doi: 10.3389/fbioe.2020.539081

1. INTRODUCTION

Cell free systems are a widely used research tool in systems and synthetic biology and a promising platform for the manufacturing of proteins and chemicals (Vilkhovoy et al., 2020). A distinctive feature of cell free systems is the absence of cellular growth and maintenance, thereby allowing the direct allocation of carbon and energy resources toward a product of interest. Cell free systems are also more amenable than living systems to observation and manipulation, hence allowing rapid

tuning of reaction conditions. Arguably, the most widely used cell free technology is cell free protein synthesis (CFPS), an *in vitro* platform for protein transcription (TX) and translation (TL). Transcription and translation, the processes by which information stored in DNA is converted to a working protein, are at the center of metabolism and signal transduction programs important to biotechnology and human health. For example, evolutionarily conserved developmental programs such as the epithelial to mesenchymal transition (EMT) (Thiery, 2003), or retinoic acid induced differentiation (Nilsson, 1984), rely on multiple rounds of highly coordinated gene expression. From the perspective of biotechnology, even relatively simple industrially important organisms such as *Escherichia coli*, have intricate transcriptional regulatory networks which control the metabolic state of the cell in response to changing nutrient conditions (Orth et al., 2010; Vilkhovoy et al., 2016). Understanding the dynamics of regulatory networks can be greatly facilitated by mathematical models. A majority of these models fall into three categories: logical, continuous, and stochastic models (Karlebach and Shamir, 2008). Logical models such as Boolean networks (Glass and Kauffman, 1973) developed using a variety of approaches and data (Pratapa et al., 2020) represent the state of each network entity as a discrete variable, provide a quick but qualitative description of the behavior of the regulatory network. Linear and non-linear ordinary differential equation (ODE) models fall into the second category, and they generally provide a detailed picture of the network dynamics, although they can be non-physical models, e.g., relying on a gene signal perspective (Bonneau et al., 2006). Lastly, stochastic models describe the interactions between individual molecules, and discrete reaction events (McAdams and Arkin, 1997; Mettetal et al., 2006; Kaufmann and van Oudenaarden, 2007; Raj and van Oudenaarden, 2008). Model choice depends on criteria such as speed, the level of detail required and the quantity of experimental data available to estimate the model parameters. While the end goal of the models might be to accurately predict *in vivo* behavior, living systems do not necessarily provide an ideal experimental platform. For example, although there have been significant advancements in metabolomics (e.g., Park et al., 2016), the rigorous quantification of intracellular messenger RNA (mRNA) copy number or protein abundance remains challenging. Toward this challenge, cell free systems offer several advantages for the study of transcription and translation processes.

Cell free biology has historically been an important tool to study the fundamental biological mechanisms involved with gene expression. In the 1950s, cell free systems were used to explore the incorporation of amino acids into proteins (Borsook, 1950; Winnick, 1950a,b), and the role of adenosine triphosphate (ATP) in protein production (Hoagland et al., 1956). Further, *E. coli* extracts were used by Nirenberg and Matthaei in 1961 to demonstrate templated translation (Matthaei and Nirenberg, 1961; Nirenberg and Matthaei, 1961), leading to a Nobel Prize in 1968 for deciphering the codon code. More recently, as advancements in extract preparation and energy regeneration have extended their durability, the usage of cell free systems has also expanded to both small- and large-scale biotechnology and biomanufacturing applications (Swartz, 2018; Silverman et al., 2019). Today, cell free systems have been implemented for therapeutic protein and vaccine production (Ng et al., 2012; Jaroentomeechai et al., 2018; Stark et al., 2019), biosensing (Soltani et al., 2018), genetic part prototyping (Moore et al., 2017) and minimal cell systems (Yue et al., 2019). The versatility of cell free systems offers a tremendous opportunity for the systems-level experimental and computational study of biological mechanism. For example, a number of ordinary differential equation based cell free models have been developed (Stögbauer et al., 2012; Mavelli et al., 2015; Matsuura et al., 2017; Doerr et al., 2019; Marshall and Noireaux, 2019). However, despite the obvious advantages offered by a cell free system, experimental determination of the kinetic parameters for these models is often challenging. For instance, the cell free modeling study of Horvath and coworkers (which included a description of transcription and translation, and the underlying metabolism supplying energy and precursors for transcription and translation), had over 800 unknown model parameters (Horvath et al., 2020). Moreover, the construction, identification and validation of the Horvath model took well over a year to complete. Thus, constructing, identifying and validating biophysically motivated cell free models, which are simultaneously manageable, is a key challenge. Toward this challenge, effective modeling approaches which coarse grain biological details but remain firmly rooted in a biophysical perspective, could be an important tool.

In this study, we developed an effective biophysical modeling approach to simulate cell free transcription and translation processes. The model used classical biophysical arguments to formulate kinetic expressions for the rates of transcription and translation. These rates were then used in material balance equations (ordinary differential equations) to simulate the mRNA and protein concentration as a function of time for different cell free genetic circuits. The model was effective as it neglected potentially important mechanistic factors, and the integration of transcription and translation with metabolism. For example, the model did not consider how the transcription and translation rate was influenced by the availability of metabolic resources, e.g., energy or building block concentration. Nor did the model consider potentially important biology, for example the role of elongation factors or protein folding chaperones (among many other potentially important factors). We tested this approach by comparing simulations of two cell free synthetic circuits with messenger RNA (mRNA) and protein measurements (deGFP) generated in this study using the *E. coli* based myTXTL cell free system. First, we considered a simple circuit ($\mathcal{C}1$) in which endogenous sigma factor 70 (σ_{70}) induced the expression of a fast maturing dual emission green fluorescent protein variant (deGFP). This relatively simple case was then followed by a more complex negative feedback circuit ($\mathcal{C}2$) where two control genes were coupled to the expression of deGFP. The second circuit is an extension of the first, with the presence of additional regulatory elements. Characteristic values for many of the model parameters were estimated from published biophysical studies or took the form of corrections to order of magnitude literature estimates, while the remaining unknown model parameters for each circuit were estimated by minimizing the difference between simulated and measured mRNA and protein concentrations. In particular,

either parameter estimates from published studies were used directly, or characteristic values found in the literature were used to establish feasible ranges for the parameter estimation problem. Next, in order to provide a detailed insight into the influence of individual model parameters on the expression dynamics of each circuit, Morris sensitivity analysis was employed. For $\mathcal{C}1$, the sensitivity results were informative, but expected. However, for $\mathcal{C}2$, the analysis hierarchically stratified the parameters (and associated model species) into local vs. global categories. For example, parameters that controlled the abundance of lambda phage repressor protein (cI-ssrA), a master circuit regulator in $\mathcal{C}2$, were globally important as they influenced all other species. On the other hand, the parameters that influenced deGFP levels (the endpoint of both circuits) were only locally important to deGFP. Taken together, the effective biophysical modeling approach captured the expression dynamics, including the transcription dynamics, for two synthetic cell free circuits. While, we considered only two circuits here, this approach could potentially be extended to simulate other genetic circuits in both cell free and whole cell biomolecular applications. The model code, parameters, and analysis scripts are available under an MIT software license from the Varnerlab GitHub repository[1].

2. MATERIALS AND METHODS

2.1. Cell Free Protein Synthesis Reactions

The cell free protein synthesis (CFPS) reactions were carried out using the myTXTL Sigma 70 Master Mix (Arbor Biosciences) in 1.5 mL Eppendorf tubes. The working volume of all the reactions was 12 μL, composed of the Sigma 70 Master Mix (9 μL) and the plasmids (3 μL total): P70a-deGFP (5 nM) for the single-gene system; P70a-deGFP-ssrA (8 nM), P70a-S28 (1.5 nM), and P28a-cI-ssrA (1 nM) for the negative feedback circuit. The plasmids were bought in lyophilized form (Arbor Biosciences) and purified using QIAprep Spin Miniprep Kit (Qiagen) using cell lines DH5-Alpha (for P28a-cI-ssrA) or KL740 (for P70a-deGFP, P70a-deGFP-ssrA, and P70a-S28). The CFPS reactions were incubated at 29°C.

2.2. mRNA and Protein Quantification

Following each CFPS run, the total RNA was extracted from 1 μL of the reaction mixture using PureLink RNA Mini Kit (Thermo Fisher Scientific) and stored at −80°C. The quantitative RT-PCR reactions were done using Applied Biosystems™ TaqMan™ RNA-to-CT™ 1-Step Kit and Custom TaqMan Gene Expression Assays (Thermo Fisher Scientific). An mRNA standard curve was used to determine absolute mRNA concentrations for each of the samples. The mRNA standards were prepared as follows: separate CFPS reactions for 5 nM of plasmids (P70a-S28, P70a-deGFP, and P70a-deGFP-ssrA) were carried out for 2 h. Total RNA was extracted using the full reaction volume. This was followed by the removal of 16S and 23S rRNA using the MICROBExpress™ Bacterial mRNA Enrichment Kit (Life Technologies Corporation). Lastly, the MEGAclear™ Kit (Life Technologies Corporation) was used to further purify the mRNA. The mRNA concentrations were determined using the Qubit™ RNA assay kit (ThermoFisher Scientific). At least three technical replicates were performed for each standard. The concentration of cI-ssrA mRNA was quantified using the deGFP-ssrA mRNA standard. Green fluorescent protein (deGFP) fluorescence was measured using the Varioskan Lux plate reader at 488 nm (excitation) and 535 nm (emission). At the end of the CFPS run, 3 μL of the reaction mixture was diluted in 33 μL phosphate buffered saline (PBS) and stored at −80°C. The fluorescence was measured in triplicate with 10 μL each of this mixture. For all measurements, at least three biological replicates were performed.

2.3. Synthetic Circuit Architecture

The two genetic circuits ($\mathcal{C}1$ and $\mathcal{C}2$) used in this study were based upon the bacterial sigma factor regulatory system (**Figure 1**). Sigma factor 70 (σ_{70}), endogenously present in the extract, was the primary driver of each circuit. In $\mathcal{C}1$, σ_{70} induced green fluorescent protein (deGFP) expression was explored in the absence of additional regulators or protein degradation (**Figure 1A**). In $\mathcal{C}2$, σ_{70} induced the expression of sigma factor 28 (σ_{28}) and deGFP-ssrA (**Figure 1B**). Sigma 28 induced the expression of the lambda phage repressor protein cI-ssrA, which was under the σ_{28} responsive P28 promoter. The cI-ssrA protein repressed the P70a promoter, thereby down-regulating σ_{28} and deGFP-ssrA transcription (Marshall and Noireaux, 2018). Simultaneously, the C-terminal ssrA degradation tags present on the deGFP and cI proteins were recognized by the endogenous ClpXP protease system in the cell free extract, thereby promoting the degradation of these proteins into peptide fragments (Flynn et al., 2003; Garamella et al., 2016). In addition, messenger RNAs (mRNAs) were always subject to degradation due to the presence of degradation enzymes in the extract (Karzbrun et al., 2011; Garamella et al., 2016). Taken together, the interactions of the components manifested in an accumulation of deGFP protein for $\mathcal{C}1$, and a pulse signal of deGFP-ssrA in $\mathcal{C}2$. Studying $\mathcal{C}1$ allowed us to estimate parameters governing the interaction of σ_{70} with the P70a promoter. Whereas, the $\mathcal{C}2$ allowed us to characterize the interaction of σ_{28} with the P28 promoter, the strength of the transcriptional repression by cI-ssrA, and the kinetics of protein degradation by the endogenous ClpXP protease system. Finally, both circuits tested the effective model formulation for the transcription and translation rates.

2.4. Formulation and Solution of Model Equations

Consider a cell free synthetic circuit composed of the genes $\mathcal{G} = 1, 2, \ldots, \mathcal{N}$. Each gene in the circuit is described by two differential equations, one for mRNA (m_j) and a second for the corresponding protein (p_j):

$$\dot{m}_j = r_{X,j} u_j(\ldots) - \theta_{m,j} m_j \quad j = 1, 2, \ldots, \mathcal{N} \tag{1}$$

$$\dot{p}_j = r_{L,j} w_j(\ldots) - \theta_{p,j} p_j \tag{2}$$

The term $r_{X,j} u_j(\ldots)$ in the mRNA balance, which denotes the regulated rate of transcription for gene j, is the product of a kinetic limit $r_{X,j}$ (nM h^{-1}) and a transcription control function $0 \leq u_j(\ldots) \leq 1$ (dimensionless). Similarly, the rate of translation

[1]Varnerlab. Github repository for tx/tl model code. Available online at https://github.com/varnerlab/Biophysical-TXTL-Model-Code.

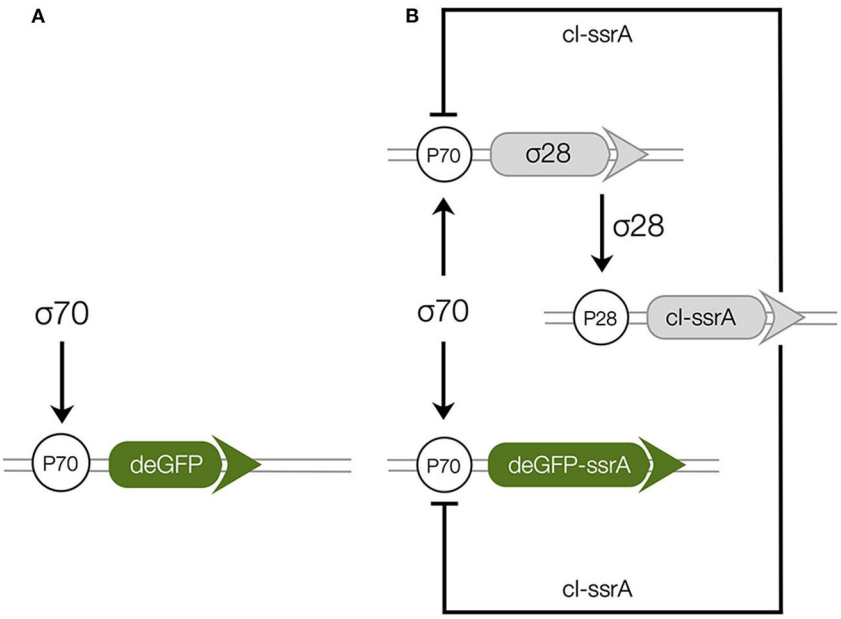

FIGURE 1 | Schematic of the cell free gene expression circuits used in this study. **(A)**: Sigma factor 70 (σ_{70}) induced expression of deGFP. **(B)**: The circuit components encode for a negative feedback loop motif. Sigma factor 28 and deGFP-ssrA genes on the P70a promoters are expressed first because of the endogenous presence of sigma 70 factor in the extract. Sigma factor 28, once expressed, induces the P28a promoter, turning on the expression of the cI-ssrA gene which represses the P70a promoter. The circuit is modified from a previous study (Garamella et al., 2016) by including an ssrA degradation tag on the cI gene.

of mRNA j, denoted by $r_{L,j}w_j$, is also the product of the kinetic limit of translation (nM h^{-1}) and a translational control term $0 \leq w_j(\ldots) \leq 1$ (dimensionless). Lastly, $\theta_{\star,j}$ denotes the first-order rate constant (h^{-1}) governing degradation of protein and mRNA. The model equations, encoded in the Julia programming language (Bezanson et al., 2017), were automatically generated using the JuGRN tool[2]. The model equations were solved numerically using the `Rosenbrock23` routine of the `DifferentialEquations.jl` package (Rackauckas and Nie, 2017).

2.4.1. Transcription and Translation Kinetic Limits

The key idea behind the transcription and translation kinetic limit expressions is that the polymerase (or ribosome) acts as a pseudo-enzyme; it binds a gene (or message), reads the gene (or message), and then dissociates. Thus, we used a strategy similar to classical enzyme kinetics to derive expressions for $r_{X,j}$ (or $r_{L,j}$); we proposed a set of elementary reactions for transcription and translation, one of which we assumed was rate limiting, and then invoked the pseudo state assumption for each intermediate complex to develop the overall rate expression. Following this approach, the details of the derivation of $r_{X,j}$ (or $r_{L,j}$) are given in the **Supplementary Materials**. The transcription kinetic limit $r_{X,j}$ is given by:

$$r_{X,j} = V_{X,j}^{max}\left(\frac{\mathcal{G}_j}{\tau_{X,j}K_{X,j} + \left(1+\tau_{X,j}\right)\mathcal{G}_j + \mathcal{O}_{X,j}}\right) \tag{3}$$

[2]Varnerlab. Gene Regulatory Network Generator in Julia (JuGRN). Available online at https://github.com/varnerlab/JuGRN-Generator.

where $V_{X,j}^{max}$ denotes the maximum transcription rate (nM/h) of gene j, $\mathcal{G}_j$ denotes the concentration of gene j (nmol/L), $K_{X,j}$ denotes the saturation constant for transcription of gene j (nmol/L), $\tau_{X,j}$ denotes the time constant for transcription (dimensionless) and:

$$\mathcal{O}_{X,j} = \sum_{i=1,j}^{\mathcal{N}} \frac{K_{X,j}\tau_{X,j}}{K_{X,i}\tau_{X,i}}\left(1+\tau_{X,i}\right)\mathcal{G}_i \tag{4}$$

denotes the coupling of the transcription of gene j with the other genes in the system through competition for RNA polymerase.

In a similar way, we developed an expression for the translational kinetic limit:

$$r_{L,j} = V_{L,j}^{max}\left(\frac{m_j}{\tau_{L,j}K_{L,j} + \left(1+\tau_{L,j}\right)m_j + \mathcal{O}_{L,j}}\right) \tag{5}$$

where $V_{L,j}^{max}$ denotes the maximum translation rate (nM/h), $K_{L,j}$ denotes the saturation constant for translation of mRNA message j (nmol/L), $\tau_{L,j}$ denotes the time constant for translation of message j (dimensionless) and:

$$\mathcal{O}_{L,j} = \sum_{i=1,j}^{\mathcal{N}} \frac{K_{L,j}\tau_{L,j}}{K_{L,i}\tau_{L,i}}\left(1+\tau_{L,i}\right)m_i \tag{6}$$

describes the coupling of the translation of mRNA j with other messages in the system because of kinetic competition for available ribosomes. The saturation and time constants for

each case (which are unknown and must be estimated from experimental data) are defined in the **Supplementary Materials**. Lastly, in this study, the $\mathcal{O}_{X,j}$ and $\mathcal{O}_{L,j}$ terms were neglected as both circuits had either only one, or a small number of genes.

The maximum transcription rate $V_{X,j}^{max}$ was formulated as:

$$V_{X,j}^{max} \equiv R_{X,T}\left(\frac{\dot{\nu}_X}{l_{G,j}}\right) \tag{7}$$

where $R_{X,T}$ denotes the total RNA polymerase concentration (nM), $\dot{\nu}_X$ denotes the RNA polymerase elongation rate (nt/h) and $l_{G,j}$ denotes the length of gene j in nucleotides (nt). Similarly, the maximum translation rate $V_{L,j}^{max}$ was formulated as:

$$V_{L,j}^{max} \equiv K_P R_{L,T}\left(\frac{\dot{\nu}_L}{l_{P,j}}\right) \tag{8}$$

where $R_{L,T}$ denotes the total ribosome pool, K_P denotes the polysome amplification constant, $\dot{\nu}_L$ denotes the ribosome elongation rate (amino acids per hour), and $l_{P,j}$ denotes the length of protein j (aa).

2.4.2. Control Functions *u* and *w*

Values of the control functions $u(\ldots)$ and $w(\ldots)$ describe the regulation of transcription and translation. Ackers et al., borrowed from statistical mechanics to recast the $u(\ldots)$ function as the probability that a system exists in a configuration which leads to expression (Ackers et al., 1982). The idea of recasting $u(\ldots)$ as the probability of expression was also developed (apparently independently) by Bailey and coworkers in a series of papers modeling the *lac* operon (see Lee and Bailey, 1984). More recently, Moon and Voigt adapted a similar approach when modeling the expression of synthetic circuits in *E. coli* (Moon et al., 2012). The $u(\ldots)$ function is formulated as:

$$u(\ldots)_j = \frac{\sum_{i\in\{\chi\}} W_i f_i(\ldots)}{\sum_{j\in\mathcal{C}_j} W_j f_j(\ldots)} \tag{9}$$

where W_i (dimensionless) denotes the weight of configuration i, while $f_i(\cdots)$ (dimensionless) is a binding function (taken to be a hill-type function) describing the fraction of bound activator/inhibitor for configuration i. The summation in the numerator of Equation (9) is over the set of promoter configurations leading to expression (denoted as χ), while the summation in the numerator is over the set of all possible configurations for gene j (denoted as $\mathcal{C}_j$). Thus, $u(\ldots)_j$ can be thought of as the fraction of all possible configurations that lead to expression. The weights W_i are related to the Gibbs energy of configuration i: $W_i = \exp(-\Delta G_i/RT)$ where ΔG_i denotes the molar Gibbs energy for configuration i (kJ/mol), R denotes the ideal gas constant (kJ mol^{-1} K^{-1}), and T denotes the system temperature (Kelvin) (Ackers et al., 1982). The value of the binding function depends on the concentrations of the different transcriptional elements and their dissociation constants. The temporal evolution of u, therefore, is tied to the dynamics of its transcriptional elements, and its value lies between 0 and 1. In the case of circuit $\mathcal{C}1$, u did not vary during the course of the reaction because the concentration of its activator, σ_{70}, was fixed. For this case, u approximately equalled 0.95. However, in the second circuit, $\mathcal{C}2$, u varied with time because of the change in levels of σ_{28} and cI-ssrA proteins.

We accounted for the experimentally observed loss of translational activity through the translational control function $w(\ldots)$. Loss of translational activity could be a function of many factors, including depletion of metabolic resources. However, in this study, we modeled the loss of translational activity as an exponential decay process with half-life $\tau_{L,1/2}$:

$$\dot{\epsilon} = -\left(\frac{0.693}{\tau_{L,1/2}}\right)\epsilon \tag{10}$$

where ϵ denotes the fraction of remaining translational activity. Initially we assumed translation to be fully active, $\epsilon(0) = 1$. Solving equation (10) yields $\epsilon(t) = \exp\left(-0.693 \cdot t/\tau_{L,1/2}\right)$. Over time, as the cell free reaction progressed, the translational activity decreased with a half-life $\tau_{L,1/2}$ which was estimated from experimental data. The translational control variable was then given by $w_i = \epsilon$ for all translation processes.

2.5. Estimation of Model Parameters

Model parameters were estimated from published studies, were specified by experimental conditions (**Table 1**) or were estimated by minimizing the squared difference between model simulations and messenger RNA (mRNA), or protein measurements generated in this study. For the P70-deGFP model ($\mathcal{C}1$), 11 parameters were estimated, while 33 parameters were estimated for the negative feedback model ($\mathcal{C}2$).

The minimization problem to estimate the unknown model parameters was structured as a multiobjective optimization problem in which each measured mRNA or protein trajectory was treated as a separate objective. The minimization problem was solved using the Pareto Optimal Ensemble Technique in the Julia programming language (JuPOETs) (Bassen et al., 2017). JuPOETs is a multiobjective optimization approach which integrates simulated annealing with Pareto optimality to estimate parameter values on or near the optimal tradeoff surface between N potentially competing objectives (squared difference between model simulations and experimental measurements). JuPOETs minimized a problem of the form:

$$\min_k \mathcal{E}_j = \sum_{i=1}^{\mathcal{T}_j}\left(\hat{\mathcal{M}}_{ij} - x_{ij}(k)\right)^2 \qquad j = 1, 2, \ldots, N \tag{11}$$

subject to

$$\dot{x} = f(x, k) \tag{12}$$

$$\mathcal{L} \leq k \leq \mathcal{U} \tag{13}$$

$$x(t_o) = x_o \tag{14}$$

where Equation (12) denotes the model equations, Equation (13) denotes the parameter bounds, and Equation (14) denotes

TABLE 1 | Characteristic parameters for TX/TL model equations.

Description	Parameter	Value	Units	Reference
RNA polymerase concentration	$R_{X,T}$	0.06–0.075	μM	*a*
Ribosome concentration	$R_{L,T}$	< 2.3	μM	*a,b*
σ_{70} concentration	σ_{70}	<35	nM	*a*
initial σ_{28} concentration	σ_{28}	<20	nM	*a*
Transcription elongation rate	$\dot{\nu}_X$	12–30	nt/s	*a,d*
Translation elongation rate	$\dot{\nu}_L$	1–2	aa/s	*a,b*
Transcription saturation coefficient	K_X	0.036	μM	*i*
Polysome amplification constant	K_P	10.0	constant	*e*
Transcription initiation time	k_l^X	22	s	*i*
Translation initiation time	k_l^L	1.5	s	*e*
Default mRNA degradation coefficient	θ_m	3.75	h^{-1}	*a*
Default protein degradation coefficient	θ_p	0.462–1.89	h^{-1}	*f,g*
Gene concentration σ_{28}		1.5	nM	*c*
Gene concentration cI-ssrA		1.0	nM	*c*
Gene concentration deGFP-ssrA		8.0	nM	*c*
Gene length σ_{28}		811	nt	*h*
Gene length cI-ssrA		850	nt	*h*
Gene length deGFP-ssrA		782	nt	*h*
Protein length σ_{28}		240	aa	*h*
Protein length cI-ssrA		248	aa	*h*
Protein length deGFP-ssrA		237	aa	*h*

Key to references used in the table: (a) Garamella et al. (2016), (b) Underwood et al. (2005), (c) set by experiment, (d) Kassavetis and Chamberlin (1981), (e) estimated in this study, (f) Niederholtmeyer et al. (2015) and Vilkhovoy et al. (2018), (g) Grilly et al. (2007), (h) calculated from plasmid sequence, (i) McClure (1980).

the initial conditions. The objective function(s) $\mathcal{E}_j$ measured the squared difference between model simulations and experiment j (either a protein or mRNA trajectory). The symbol $\hat{\mathcal{M}}_{ij}$ denotes an experimental observation at time index i from experiment j, while the symbol x_{ij} denotes the model simulation output at time index i from experiment j. The quantity i denotes the sampled time-index and $\mathcal{T}_j$ denotes the number of time points for experiment j. For the P70-deGFP model ($\mathcal{C}1$), $\mathcal{E}_1$ corresponded to mRNA deGFP, while $\mathcal{E}_2$ corresponded to the deGFP protein concentration. On the other hand, for the negative feedback model ($\mathcal{C}2$), $\mathcal{E}_1$ corresponded to mRNA deGFP-ssrA, $\mathcal{E}_2$ to mRNA σ_{28}, $\mathcal{E}_3$ to mRNA cI-ssrA and $\mathcal{E}_4$ to the deGFP-ssrA protein concentration. Lastly, we penalized accumulation of the cI-ssrA protein (unmeasured) reaching unrealistically high levels with a term of the form: $\mathcal{E}_5 = C \times \max(0, x_{cI} - U_{cI})$ where C denotes a penalty parameter ($C = 1{\times}10^5$), x_{cI} denotes the maximum simulated cI-ssrA protein concentration, and U_{cI} denotes a concentration upper bound ($U_{cI} = 100\mu M$). This bound was chosen to be approximately five-fold higher than the protein levels observed in an uninhibited circuit (e.g., $\mathcal{C}1$).

The lower and upper bounds for unknown model parameters were established from previously published studies, or from previous model analysis; parameter values estimated for the P70-deGFP model were also used to establish ranges for the negative feedback model. JuPOETs searched over ΔG_i, K_L, and $\tau_{L,1/2}$ values directly, while other unknown parameter values took the form of corrections to order of magnitude characteristic literature estimates. For example, we set the mRNA degradation rate constant (θ_m) to a characteristic value taken from literature. Then, the degradation constant for any particular mRNA was represented as: $\theta_{m,i} = \alpha_i \theta_m$, where α_i was an unknown (but bounded) modifier. In this way, we guaranteed the parameter search (and the resulting estimated parameters) were within a specified range of literature values. We used this procedure for all degradation constants (both mRNA and protein) and all time constants (for both transcription and translation). The baseline parameter values are given in **Table 1**. JuPOETs was run for 20 generations for both models, and all parameters sets with Pareto rank less than or equal to two were collected for each generation. The JuPOETs parameter estimation routine is encoded in the `sa_poets_estimate.jl` script in the model repositories.

JuPOETs uses a simulated annealing approach to generate candidate parameter solutions whose Pareto rank is then evaluated; ranks below a threshold are kept while higher rank solutions are discarded. Thus, all the advantages (and disadvantages) associated with simulated annealing have been inherited by JuPOETs; for example, the time required to generate a family of low rank solutions will be significantly longer than a derivative based approach. Beyond these specific performance issues, a unique pathology of JuPOETs is the use of Pareto rank as a surrogate for training error. JuPOETs attempts to find low rank solutions, but rank is a relative measure of the quality of a solution. Thus, during the early iterations, low rank solutions often have large errors. As the iteration count increases the approach tends to find low error solutions with low rank, however, for complex models the rate of convergence to these

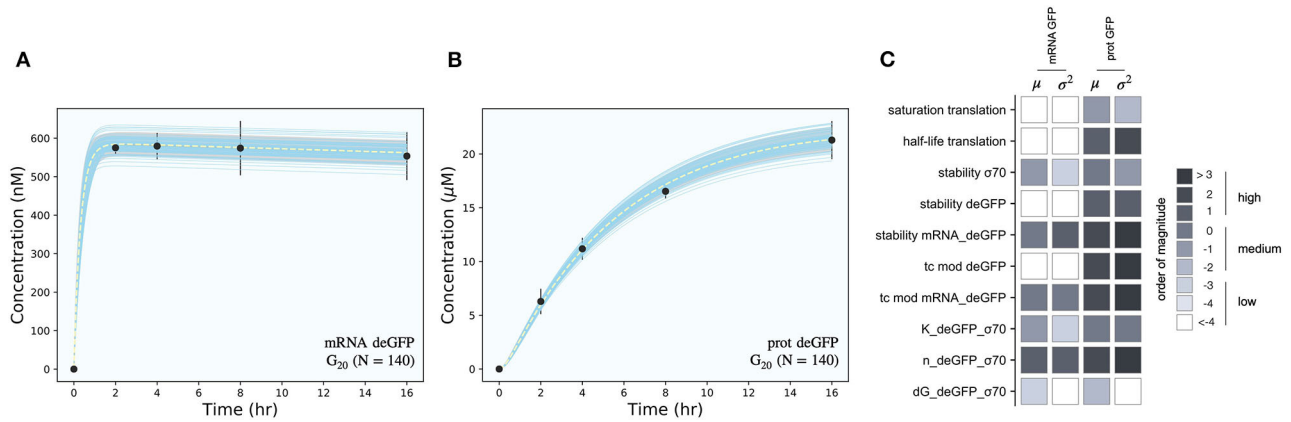

FIGURE 2 | Model simulations vs. experimental measurements for σ_{70} induced deGFP expression. **(A)**: Simulated and measured deGFP mRNA concentration vs. time using the small circuit G_{20} ensemble ($N = 140$). **(B)**: Simulated and measured deGFP protein concentration vs. time using the small circuit G_{20} ensemble ($N = 140$). **(C)**: Global sensitivity analysis of the P70-deGFP circuit parameters. Morris sensitivity coefficients were calculated for the unknown model parameters, where the range for each parameter was established from the ensemble. Uncertainty: Simulations and uncertainty quantification are shown for the generation 20 (G_{20}) ensemble which yielded $N = 140$ parameter sets that were rank two or below. The parameter ensemble was used to calculate the mean (dashed line) and the 95% confidence estimate of the simulation (gray region). Additionally, the 99% confidence estimate of the mean simulation is shown in orange. Individual parameter set trajectories are shown in blue. Points denote the mean experimental measurement while error bars denote the 95% confidence estimate of the experimental mean computed from at least three replicates.

low rank low error solutions is slow. To address this concern, we periodically switch to single objective mode where we minimize the total training error (summation of all objective functions) instead of finding low rank solutions. The best solutions from single objective mode can then be used to restart the multi-objective calculation. This hybrid approach, which was used in this study, has previously been shown to increase the rate of finding low rank and low error solutions (see Bassen et al., 2017).

2.6. Morris Sensitivity Analysis

Morris sensitivity analysis was used to understand which model parameters were sensitive (Morris, 1991). The Morris method is a global method that computes an elementary effect value for each parameter by sampling a model performance function, in this case the area under the curve for each model species in their respective timeplots, over a range of values for each parameter; the mean of elementary effects measures the direct effect of a particular parameter on the performance function, while the variance of each elementary effect indicates whether the effects are non-linear or the result of interactions with other parameters (large variance suggests connectedness or non-linearity). The Morris sensitivity coefficients were computed using the `DiffEqSensitivity.jl` package (Rackauckas and Nie, 2017). The parameter ranges were established by calculating the minimum and the maximum value for each parameter in the parameter ensemble generated by JuPOETs. Each range was then subdivided into 10,000 samples for the sensitivity calculation. Elementary effect values were then calculated one at a time by measuring the perturbation in the AUC on changing one parameter, where the AUC was calculated by solving the set of ODEs for each change. In order to calculate the mean and variance, the top 1000 perturbations with the highest spread in parameter values were used. In total, the model was evaluated $10000n$ times, where n is the number of parameters varied. The Morris sensitivity coefficients are calculated using the `compute_sensitivity_coefficients.jl` script in the model repositories.

3. RESULTS

3.1. Modeling and Analysis of the $\mathcal{C}1$ Circuit

The effective biophysical transcription and translation model captured σ_{70} induced deGFP expression at the mRNA and protein level within the experimental error for $\mathcal{C}1$ (**Figure 2**). JuPOETs produced an ensemble ($N = 140$) of the 11 unknown model parameters which captured the transcription of mRNA (**Figure 2A**) and the translation of deGFP protein (**Figure 2B**). The mean and standard deviation of key parameters is given in **Table 2**. The deGFP mRNA reached its steady state concentration of approximately 580 nM within 2 h, and stayed at this level for the remainder of the reaction. Thus, the cell free reaction maintained continuous transcriptional activity with an average mRNA lifetime of 27 min; Garamella et al. (2016) reported a similar lifetime of 17–18 min. On the other hand, deGFP protein concentration increased more slowly, and began to saturate between 8 and 10 h at approximately 15 μM. Given there was negligible protein degradation (the mean deGFP half-life was estimated to be ∼11 days, which was similar to the value of 6 days estimated by Horvath et al., albeit in a different cell free system, Horvath et al., 2020). The saturating protein concentration suggested that the translational capacity of the cell free system decreased over the course of the reaction. The decrease in translational capacity, which could stem from several sources, was captured in the simulations using a monotonically decreasing

TABLE 2 | Estimated parameter values for the P70-deGFP model ($\mathcal{C}1$).

Description	Parameter	Value ($\mu \pm \sigma$)	Units
Translation saturation coefficient	K_L	483.13 ± 10.10	μM
Half-life translation	$\tau_{L,1/2}$	4.03 ± 0.031	h^{-1}
Time constants			
deGFP transcription	$\tau_{X,GFP}$	0.61 ± 0.04	dimensionless
deGFP translation	$\tau_{L,GFP}$	0.16 ± 0.003	dimensionless
mRNA and protein half-life			
mRNA deGFP	$\ln(2)/\theta_{m,GFP}$	13.5 ± 2.47	min
Protein deGFP	$\ln(2)/\theta_{p,GFP}$	10.86 ± 0.78	days
Protein σ_{70}	$\ln(2)/\theta_{p,\sigma_{70}}$	3.65 ± 0.17	days
Free energies			
RNAP + deGFP gene	$\Delta G_{GFP,RX}$	28.82 ± 1.75	kJ mol^{-1}
RNAP + σ_{70} + deGFP gene	$\Delta G_{GFP,\sigma_{70}}$	–20.38 ± 1.91	kJ mol^{-1}
Binding parameters			
Hill coefficient deGFP gene + σ_{70}	$n_{GFP,\sigma_{70}}$	1.12 ± 0.06	dimensionless
Dissociation constant deGFP gene + σ_{70}	$K_{GFP,\sigma_{70}}$	24.19 ± 2.18	μM

The mean and standard deviation of each parameter value was calculated over the ensemble of parameter sets meeting the rank selection criteria (N = 139).

translation capacity state variable ϵ, and the translational control variable $w(\ldots)$. In particular, the mean half-life of translational capacity was estimated to be $\tau_{L,1/2} \sim 4$ h in the $\mathcal{C}1$ experiments. Taken together, JuPOETs produced an ensemble of model parameters that captured the experimental training data. Next, we considered which $\mathcal{C}1$ model parameters were important to the model performance using Morris sensitivity analysis, a global sensitivity analysis method.

The importance of $\mathcal{C}1$ model parameters was quantified using Morris sensitivity analysis (**Figure 2B**). The Morris method computes the influence of each parameter, known as the elementary effect, on a model performance function. The mean of elementary effects measures the direct effect of a particular parameter, while the variance indicates whether the effects are non-linear or the result of interactions with other parameters (large variance suggests non-linearity). The performance function was defined as the integrated area under the curve (AUC) for each mRNA and protein species in their respective timeplots, calculated for each parameter value range. The Morris sensitivity measures (mean and variance) were binned into categories based upon their relative magnitudes, from no influence (white) to high influence (black). Only four parameters (translation saturation coefficient K_L, translational capacity half-life $\tau_{L,1/2}$, translation time constant, and protein degradation constant) influenced the protein level. On the other hand, six parameters influenced both mRNA and protein abundance; all six of these parameters were either directly or indirectly associated with transcription. Thus, these parameters influenced the production or stability of mRNA which in turn influenced the protein level. In particular, the mRNA degradation constant and the cooperativity of σ_{70} in the P70a promoter function had the largest direct effect and variance. Surprisingly, the ΔG of σ_{70}/RNAP/promoter configuration was the least influential of the six parameters and had a small elementary effect variance. Taken together, Morris sensitivity analysis of the $\mathcal{C}1$ model parameters highlighted the hierarchical structure of the transcriptional and translational model, suggesting experimentally tunable parameters such as mRNA stability were globally important. Next, we used the ensemble of P70a, time constant and degradation parameters estimated for $\mathcal{C}1$ to constrain the analysis of $\mathcal{C}2$.

3.2. Modeling and Analysis of the $\mathcal{C}2$ Circuit

The effective biophysical transcription and translation model captured the deGFP-ssrA expression dynamics in the negative feedback circuit $\mathcal{C}2$ (**Figure 3A**). JuPOETs produced an ensemble ($N = 498$) of the 33 unknown model parameters which captured transcription and translation dynamics for σ_{28}, cI-ssrA and deGFP-ssrA. The mean and standard deviation of key parameters is given in **Table 3**. Compared with the estimated parameters for $\mathcal{C}1$, the $\mathcal{C}2$ model had almost a two fold change in the half life of translation and the translation saturation coefficient. Similarly, there were variations in the values of the transcription and translation time constants for the two systems. However, for both circuits, the small values of the transcription and translation time constants qualitatively suggested elongation limited reactions; the exception was σ_{28} translation which was closer to initiation limited. Unlike $\mathcal{C}1$, the mRNA expression pattern for σ_{28} and deGFP-ssrA both showed an initial spike, to a concentration similar with the previous pseudo steady state, before the cI-ssrA regulator protein could be expressed. However, once cI-ssrA began to accumulate, the concentrations of the regulated mRNAs dropped by approximately an order of magnitude compared with the unregulated case. Again, as shown with $\mathcal{C}1$, the regulated mRNA concentrations reached an approximate steady-state. This further confirmed continuous transcription and mRNA degradation throughout the cell free reaction. The mean estimated mRNA lifetime for cI-ssrA and deGFP were similar (approximately 16 min), while the degradation of σ_{28} mRNA was predicted to be slower (mean mRNA lifetime

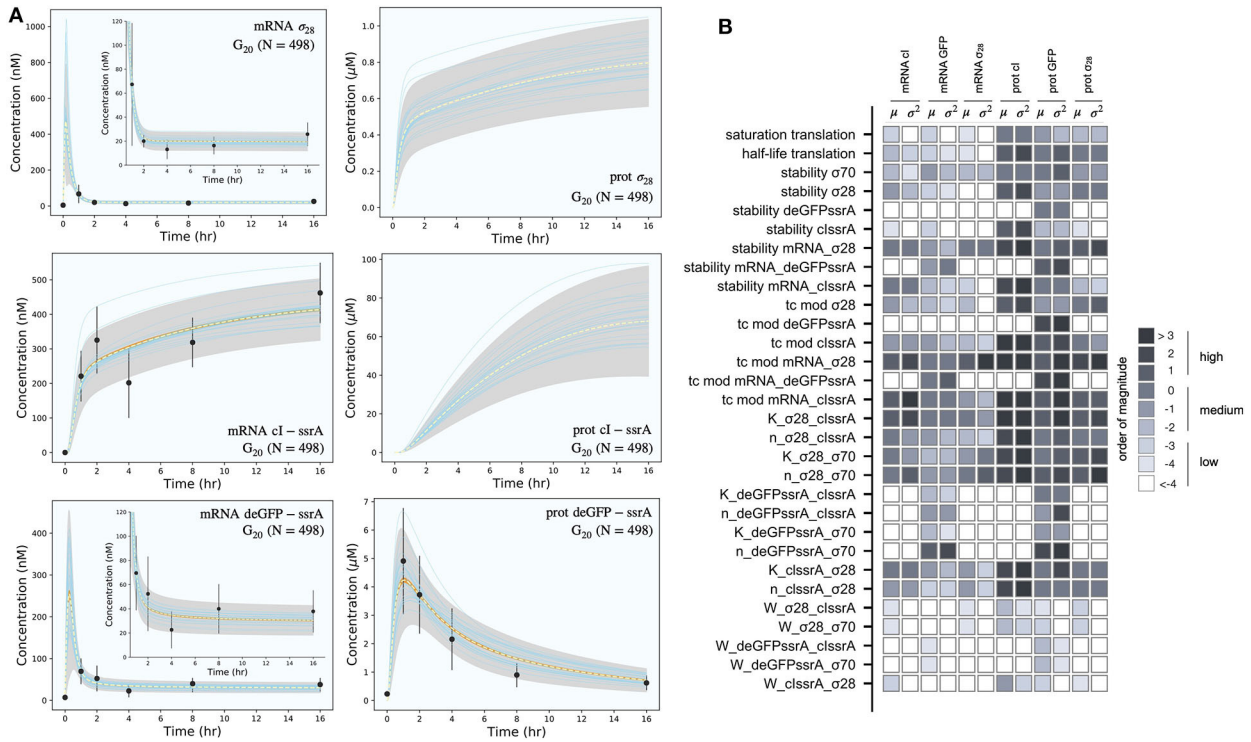

FIGURE 3 | Model simulations vs. experimental measurements for the negative feedback deGFP-ssrA circuit. **(A)**: Model simulations of the negative feedback deGFP-ssrA circuit using the G_{20} ensemble ($N = 498$). Uncertainty: Simulations and uncertainty quantification are shown for the generation 20 (G_{20}) ensemble which yielded $N = 489$ parameter sets (rank two or below). The parameter ensemble was used to calculate the mean (dashed line) and the 99% confidence estimate of the simulation (gray region). Additionally, the 99% confidence estimate of the mean simulation is shown in orange. Individual parameter set trajectories are also shown in blue. Points denote the mean experimental measurement while error bars denote the 95% confidence estimate of the experimental mean computed from at least three replicates. **(B)**: Global sensitivity analysis of the negative feedback deGFP-ssrA circuit parameters. Morris sensitivity coefficients were calculated for the unknown model parameters, where the range for each parameter was established from the ensemble.

was estimated to be approximately 30 min). Lastly, the mean peak degradation rate for GFP was approximately 47 nM/min, while the mean peak cI-ssrA degradation rate was predicted to be approximately 63 nM/min; both of these degradation rate estimates were consistent with the previously reported range of 15–150 nM/min measured by Garamella et al. (2016).

The secondary effect of cI-ssrA repression was visible in the cI-ssrA mRNA expression pattern. The expression of cI-ssrA was induced by σ_{28}, however, σ_{28} expression was repressed by cI-ssrA, thereby completing a negative feedback loop. Initially, before appreciable levels of cI-ssrA had been translated, the cI-ssrA transcription rate was maximum (approximately 200 nM/h). However, the transcription rate decreased to approximately 12 nM/h after 2 h and remained constant for the remainder of the cell free reaction. Similarly, transcription rates for σ_{28} (approximately 1,200 nM/h) and deGFP-ssrA (approximately 750 nM/h) were initially at a maximum due to the presence of endogenous σ_{70}, but then quickly dropped as cI protein accumulated. Protein synthesis followed a similar trend, with the translation rates for σ_{28} and deGFP-ssrA initially present at their maximum values before quickly dropping. After 1 h, deGFP levels reached a peak and decayed due to the ClpXP-mediated degradation, whereas σ_{28} protein levels continued to slowly rise at a steady rate (approximately 15 nM/h). The $\mathcal{C}2$ model also predicted the expected lag present during the initial phase of cI-ssrA protein synthesis due to the need for σ_{28} protein to reach appreciable levels. Moreover, the combination of high cI-ssrA mRNA abundance (expressed because σ_{28} does not have a degradation tag) and ClpXP-mediated degradation led to the saturation of the cI-ssrA protein concentration. However, the cI-ssrA protein concentration could not be verified because we did not have an experimental measurement for this species. Taken together, the effective model simulated cell free expression dynamics for $\mathcal{C}2$. Next, we considered which $\mathcal{C}2$ model parameters were important using Morris sensitivity analysis.

Morris sensitivity analysis of the negative feedback circuit $\mathcal{C}2$ stratified the parameters into locally and globally important groups (**Figure 3B**). The influence of 33 parameters was computed using the AUC of each mRNA and protein species as the performance function. The Morris sensitivity metrics (mean and variance) were binned into categories based upon their relative magnitudes, from no influence (white) to high influence (black). Some parameters affected only their respective mRNA or protein target, whereas others had widespread effects. For example, the time constant (tc) modifiers, stability of deGFP-ssrA protein and mRNA, and the binding dissociation constant (K) and cooperativity parameter (n) of cI-ssrA and σ_{70} for the deGFP-ssrA promoter affected only the values of deGFP-ssrA

TABLE 3 | Estimated parameter values for the negative feedback circuit ($\mathcal{C}2$).

Description	Parameter	Value ($\mu \pm \sigma$)	Units
Translation saturation coefficient	K_L	253.75 ± 14.12	μM
Half-life translation	$\tau_{L,1/2}$	8.86 ± 0.85	h^{-1}
Time constants			
cI-ssrA transcription	$\tau_{X,cI}$	< 0.001	dimensionless
deGFP transcription	$\tau_{X,GFP}$	0.045 ± 0.003	dimensionless
σ_{28} transcription	$\tau_{X,\sigma_{28}}$	0.0018 ± 0.0003	dimensionless
cI-ssrA translation	$\tau_{L,cI}$	0.054 ± 0.004	dimensionless
deGFP translation	$\tau_{L,GFP}$	0.058 ± 0.007	dimensionless
σ_{28} translation	$\tau_{L,\sigma_{28}}$	1.1 ± 0.13	dimensionless
mRNA and protein half-life			
mRNA cI-ssrA	$\ln(2)/\theta_{m,cI}$	8.1 ± 0.60	min
mRNA deGFP	$\ln(2)/\theta_{m,GFP}$	7.74 ± 1.13	min
mRNA σ_{28}	$\ln(2)/\theta_{m,\sigma_{28}}$	14.96 ± 1.60	min
Protein cI-ssrA	$\ln(2)/\theta_{p,cI}$	0.46 ± 0.043	days
Protein deGFP-ssrA	$\ln(2)/\theta_{p,GFP}$	0.051 ± 0.002	days
Protein σ_{28}	$\ln(2)/\theta_{p,\sigma_{28}}$	7.65 ± 0.91	days
Protein σ_{70}	$\ln(2)/\theta_{p,\sigma_{70}}$	14.86 ± 2.30	days
Free energies			
RNAP + cI gene	$\Delta G_{cI,RX}$	46.57 ± 4.28	kJ mol^{-1}
RNAP + σ_{28} + cI gene	$\Delta G_{cI,\sigma_{28}}$	−1.10 ± 0.04	J mol^{-1}
RNAP + deGFP gene	$\Delta G_{GFP,RX}$	41.94 ± 1.80	kJ mol^{-1}
RNAP + σ_{70} + deGFP gene	$\Delta G_{GFP,\sigma_{70}}$	−27.67 ± 1.79	kJ mol^{-1}
RNAP + cI + deGFP gene	$\Delta G_{GFP,cI}$	−7.21 ± 1.14	kJ mol^{-1}
RNAP + σ_{28} gene	$\Delta G_{\sigma_{28},RX}$	46.67 ± 3.18	kJ mol^{-1}
RNAP + σ_{70} + σ_{28} gene	$\Delta G_{\sigma_{28},\sigma_{70}}$	−10.46 ± 1.15	kJ mol^{-1}
RNAP + cI + σ_{28} gene	$\Delta G_{\sigma_{28},cI}$	−12.89 ± 1.44	kJ mol^{-1}
Hill coefficients			
cI gene + σ_{28}	$n_{cI,\sigma_{28}}$	1.88 ± 0.28	dimensionless
deGFP gene + σ_{70}	$n_{GFP,\sigma_{70}}$	1.53 ± 0.14	dimensionless
deGFP gene + cI	$n_{GFP,cI}$	0.698 ± 0.133	dimensionless
σ_{28} gene + σ_{70}	$n_{\sigma_{28},\sigma_{70}}$	1.10 ± 0.10	dimensionless
σ_{28} gene + cI	$n_{\sigma_{28},cI}$	1.51 ± 0.25	dimensionless
Dissociation constants			
cI gene + σ_{28}	$K_{cI,\sigma_{28}}$	1.09 ± 0.088	μM
deGFP gene + σ_{70}	$K_{GFP,\sigma_{70}}$	86.87 ± 7.13	μM
deGFP gene + cI	$K_{GFP,cI}$	3.83 ± 0.41	μM
σ_{28} gene + σ_{70}	$K_{\sigma_{28},\sigma_{70}}$	1.35 ± 0.26	μM
σ_{28} gene + cI	$K_{\sigma_{28},cI}$	0.0389 ± 0.0068	μM

The mean and standard deviation for each parameter was calculated over the ensemble of parameter sets (N = 498).

protein and mRNA. On the other hand, the tc, stability, K and n parameters for σ_{70}, σ_{28}, or cI-ssrA influenced mRNA and protein expression globally. The σ_{70} and σ_{28} proteins acted as inducers or repressors for more than one gene product: σ_{70} induced both deGFP-ssrA and σ_{28}, and cI-ssrA protein repressed both of these genes. Degradation constants (denoted as stability) affected the half-lives of the transcribed messages or the translated proteins in the mixture, while the time constant modifiers changed the time required to form the open gene complex (or translationally active complex). Dissociation and cooperativity constants affected the binding interactions of the inducer (or repressor in the case of cI-ssrA) in the promoter control function. Varying these parameters, therefore, had a strong effect on their respective targets. Similarly, the translation saturation and its half-life, which captured the depletion in the translation activity over the course of the reaction, not only affected protein levels but also mRNA levels. This is because these parameters tuned the rate of formation of cI-ssrA, which in turn affected the mRNA levels of its gene targets. Given that cI-ssrA was the main regulator (repressor) of the circuit, the parameters that dictated the levels of cI-ssrA mRNA and protein had a global effect. We also observed high sensitivity variance for several parameters, in particular involving cI-ssrA. For example, the time constant modifiers for cI-ssrA mRNA and protein had a two-pronged effect. On the one hand, they positively influenced the transcription/translation rates of the gene and mRNA products, directly increasing the cI-ssrA protein. On the other hand, increased cI-ssrA expression reduced the level of σ_{28}, in turn reducing the cI-ssrA levels

over time. Taken together, Morris sensitivity analysis of the $\mathcal{C}2$ model stratified that parameters into local and globally important groups, with the parameters governing the synthesis rates of the cI-ssrA mRNA and protein being globally important. The sensitivity analysis also gave insight into the organization of the circuit, suggesting cI to be highly connected within the circuit.

4. DISCUSSION

In this study, we developed an effective biophysical modeling approach to simulate transcription (TX) and translation (TL) processes occurring in a cell free system. We tested this approach by simulating the dynamics of two cell free synthetic circuits ($\mathcal{C}1$ and $\mathcal{C}2$).

The model formulation, and parameter values were mechanistic and largely derived from literature. For example, characteristic values for τ_X and K_X, the time and saturation constants for transcription, were approximated from *in vitro* experiments using an abortive initiation assay (McClure, 1980). The RNAP and ribosome elongation rates were taken from Garamella et al. (2016), while other parameters were estimated from BioNumbers (Milo et al., 2010). Similarly, the weights appearing in the transcription control function $u(\dots)$ were based upon the Gibbs energies of the respective promoter configurations, while the form of the transcriptional control functions was derived from a statistical mechanical treatment of promoter activity (Ackers et al., 1982; Lee and Bailey, 1984; Moon et al., 2012). However, there were parameters that were not available from literature; in these cases multiobjective optimization was used to estimate these parameters from mRNA and protein measurements. For $\mathcal{C}1$, sigma factor 70 (σ_{70}) induced expression of green fluorescent protein (deGFP), the time constants, degradation rates, and other parameters governing deGFP expression were estimated from measurements of deGFP mRNA and protein. These estimates were then used to constrain the parameter search for $\mathcal{C}2$, which involved deGFP expression subject to negative feedback and programmed protein degradation. We estimated which model parameters were important to the performance of $\mathcal{C}1$ and $\mathcal{C}2$ using Morris sensitivity analysis. Sensitivity analysis results for $\mathcal{C}1$ were expected; the time constant for transcription, the stability of the deGFP message and the cooperativity of σ_{70} were all important parameters. On the other hand, the sensitivity analysis results for $\mathcal{C}2$ were more nuanced, with parameters (and associated species) being stratified into locally and globally important groups; the performance of $\mathcal{C}2$ was most sensitive to the parameters controlling the cI-ssrA mRNA and protein abundance.

The effective TX/TL modeling approach described here has several potential applications. For example, a challenge of *in vivo* constraint based modeling is the description of gene expression (Covert and Palsson, 2002). Boolean and probabilistic approaches (Covert et al., 2001, 2004; Chandrasekaran and Price, 2010) have been developed to address this challenge. However, the transcriptional state of a boolean gene is either on or off based on the state of its regulators, thus, gene expression is coarse-grained. The current modeling approach could be an interesting mechanistic alternative to the boolean framework that utilizes a continuous description of gene expression dynamics and transcriptional regulation. In particular, the rules encoding typical boolean gene expression networks are easily translatable into the rational promoter functions described here, however, the estimation of the parameters appearing in these promoter functions, especially in an *in vivo* context, remains an open question. Another application could be the extension of the current model to other prokaryotic or eukaryotic systems with a few changes. For example, in order to adopt it for an *in vivo* system, the dilution of resources due to growth (proportional to the cellular doubling time) would be added as a first order term to the mRNA and protein balance equations. Additionally, the competition for RNAP and ribosomes, denoted respectively as $\mathcal{O}_{X,j}$ and $\mathcal{O}_{L,j}$ in the study, and assumed to be negligible due to the presence of only three genes in the system, would need to be taken into account; this term would serve to change the rates of transcription and translation of the added genes because of the presence of a large amount of endogenous genes in the *in vivo* system. Moreover, characteristic literature-based parameter values would be different for cellular processes compared to the *in vitro* ones used in this study, and they would thus need to be adjusted accordingly. For the case of a mammalian or a yeast *in vivo* system, a few more changes to the current model are necessary because the mechanistic processes of gene expression and regulation are different in these two types of systems. For example, a key difference present in eukaryotes is the addition of an intron splicing step during the synthesis of a mature mRNA from a pre-mRNA. In addition, the gene regulation mechanisms are vast and composed of numerous elements in eukaryotes. Finally, especially in *in vivo* systems, addition of exogenous genes often leads to a tug-of-war of carbon and energy resources between cellular growth processes and the expression of these genes, driving cellular resources away from the latter. Synthetic biology studies often neglect the role that metabolism plays in the expression of synthetic circuits. Ultimately, metabolism is centrally important to the operation of any synthetic circuit; gene expression is strongly dependent upon the metabolic resources provided by catabolic processes. It is imperative that this metabolic burden by the addition of exogenous genes be incorporated in the *in vivo* model description to accurately capture the expression behavior. We have recently started to explore this question by integrating effective transcription and translation models with metabolic networks in cell free reactions e.g., Vilkhovoy et al., 2018; Horvath et al., 2020, and also developing experimental tools to measure metabolite concentrations in cell free systems (Vilkhovoy et al., 2019). However, these previous transcriptional and translational models (and similar precursor models simulating eukaryotic processes, Gould et al., 2016; Tasseff et al., 2017) were less developed than those presented here. Taken together, the effective modeling approach described here can potentially be used to simulate transcription and translation processes in a variety of applications.

There have been many studies looking into oscillatory and other dynamic behavior of synthetic circuits (see Prangemeier et al., 2020). A negative feedback loop, such as the one explored here, has the potential to give rise to oscillations. Yelleswarapu et al. carried out TX/TL reactions, with a circuit similar to $\mathcal{C}2$, in both batch and continuous conditions (Yelleswarapu et al., 2018).

Similar to our study, no oscillations were observed in the batch reaction. However, oscillations were observed in the continuous reaction. There are several possible reasons why no oscillations were seen in our (or the Yelleswarapu et al.) batch study; as it was carried out in batch, dilution of the expressed protein or mRNA species due to an inlet feed was not possible. Thus, mRNA species reached a pseudo steady state (after approximately 2 h) because of ribonuclease degradation (Garenne et al., 2019). On the other hand, in general protein species were not at steady-state; only proteins tagged with a ssrA tag were able to be degraded by the ClpXP system, thereby allowing a steady-state. Thus, the batch system likely evolved dynamically through a set of concentration profiles that were not consistent with oscillations.

The effective TX/TL model described the experimental mRNA and protein training data. However, there were several important questions to be addressed by future studies. First, the model formulation described the data, but did not predict dynamics outside of the training set. If this approach is to be useful to the synthetic biology community, or more broadly as an effective biophysical technique to model *in vivo* gene expression dynamics for applications such as regulatory flux balance analysis, we need to have confidence that the modeling approach is predictive. Thus, while we have established a descriptive model, we have yet to establish a predictive model. Next, there were several technical or mechanistic questions that should be explored further. For example, cI-ssrA represses the activity of the P70a promoter via interaction with its OR2 and OR1 operator sites; in this study we considered only a single operator site suggesting that we potentially underestimated the potency of cI repression in the deGFP and σ_{28} promoter functions, see the multiplication rule (Lucks et al., 2011). Further, we used a first order approximation of ClpXP mediated protein degradation, while Garamella et al. (2016) described this degradation as zero order. Similarly, we did not establish the concentration of ClpXP in the commercially available cell free reaction mixture. The levels of this protein complex could be an important factor controlling protein degradation. Next, we should compare the current modeling approach, and the values estimated for the model parameters, with the study of Marshall and Noireaux (2019). For example, one of the potential limitations of the current study (that was addressed by Marshall and Noireaux, 2019) is that we did not consider a separate species for dark GFP. In our previous RNA circuit modeling (Hu et al., 2015), we did include this term, but failed to do so here. We expect inclusion of a dark vs. light GFP species could influence the values for the estimated parameters, particularly the translation time constants. However, previous reports suggested the *in vitro* maturation time of deGFP was approximately 8 min (Shin and Noireaux, 2010), much faster than the typical maturation times for GFP of 1 h *in vivo* (Sniegowski et al., 2005; Iizuka et al., 2011). Thus, the impact of including a dark vs. light GFP species may not be worth the increased model complexity. Lastly, we should validate the values estimated for the binding function parameters and the promoter configuration free energies. Maeda et al. measured the binding affinities of the seven *E. coli* σ factors with RNAP (Maeda et al., 2000); while not directly comparable, these measurements give an order of magnitude characteristic value for the dissociation constants appearing in the promoter binding functions. Further, there have been several studies that have quantified the binding energies of promoter configurations (e.g., Ackers et al., 1982; Brewster et al., 2012; Tapia-Rojo et al., 2012, 2014). A perfunctory inspection of the values estimated in this study suggested our estimated free energy values, while the same order of magnitude as previous studies in many cases, did have values that were off by a factor of up to an order of magnitude compared with literature (albeit for different promoters). In particular, the positive Gibbs energy estimated for free RNAP binding leading to transcription was likely too large, while the magnitude of other values such as the energy of cI repression of σ_{28} expression was likely too small. Thus, these other studies could serve as a basis to validate our estimates, and perhaps more importantly constrain the parameter search space for future studies.

DATA AVAILABILITY STATEMENT

Model code is available under an MIT software license from the Varnerlab GitHub repository for TXTL model code (https://github.com/varnerlab/Biophysical-TXTL-Model-Code). The mRNA and protein measurements presented in this study are available in the data directory of the model repositories in comma separated value (CSV) and Microsoft Excel format.

AUTHOR CONTRIBUTIONS

JV directed the study. MV, SV, HL, and AA conducted the cell free experimental measurements. JV, MV, and AA developed the reduced order models and the parameter ensemble. MV, AA, and JV analyzed the model ensemble, and generated figures for the manuscript. The manuscript was prepared and edited for publication by AA, MV, SV, and JV. All authors reviewed this manuscript.

FUNDING

The work described was also supported by the Center on the Physics of Cancer Metabolism through Award Number 1U54CA210184-01 from the National Cancer Institute. The content is solely the responsibility of the authors and does not necessarily represent the official views of the National Cancer Institute or the National Institutes of Health.

ACKNOWLEDGMENTS

We gratefully acknowledge the suggestions from the reviewers to improve this manuscript.

SUPPLEMENTARY MATERIAL

The Supplementary Material for this article can be found online at: https://www.frontiersin.org/articles/10.3389/fbioe.2020.539081/full#supplementary-material

REFERENCES

Ackers, G. K., Johnson, A. D., and Shea, M. A. (1982). Quantitative model for gene regulation by lambda phage repressor. *Proc. Natl. Acad. Sci. U.S.A.* 79, 1129–33. doi: 10.1073/pnas.79.4.1129

Bassen, D. M., Vilkhovoy, M., Minot, M., Butcher, J. T., and Varner, J. D. (2017). Jupoets: a constrained multiobjective optimization approach to estimate biochemical model ensembles in the Julia programming language. *BMC Syst. Biol.* 11:10. doi: 10.1186/s12918-016-0380-2

Bezanson, J., Edelman, A., Karpinski, S., and Shah, V. B. (2017). Julia: a fresh approach to numerical computing. *SIAM Rev.* 59, 65–98. doi: 10.1137/141000671

Bonneau, R., Reiss, D. J., Shannon, P., Facciotti, M., Hood, L., Baliga, N. S., et al. (2006). The inferelator: an algorithm for learning parsimonious regulatory networks from systems-biology data sets *de novo*. *Genome Biol.* 7:R36. doi: 10.1186/gb-2006-7-5-r36

Borsook, H. (1950). Protein turnover and incorporation of labeled amino acids into tissue proteins *in vivo* and *in vitro*. *Physiol. Rev.* 30, 206–219. doi: 10.1152/physrev.1950.30.2.206

Brewster, R. C., Jones, D. L., and Phillips, R. (2012). Tuning promoter strength through rna polymerase binding site design in *Escherichia coli*. *PLoS Comput. Biol.* 8:e1002811. doi: 10.1371/journal.pcbi.1002811

Chandrasekaran, S., and Price, N. D. (2010). Probabilistic integrative modeling of genome-scale metabolic and regulatory networks in *Escherichia coli* and *Mycobacterium tuberculosis*. *Proc. Natl. Acad. Sci. U.S.A.* 107, 17845–50. doi: 10.1073/pnas.1005139107

Covert, M. W., Knight, E. M., Reed, J. L., Herrgard, M. J., and Palsson, B. O. (2004). Integrating high-throughput and computational data elucidates bacterial networks. *Nature* 429, 92–6. doi: 10.1038/nature02456

Covert, M. W., and Palsson, B. Ø. (2002). Transcriptional regulation in constraints-based metabolic models of *Escherichia coli*. *J. Biol. Chem.* 277, 28058–64. doi: 10.1074/jbc.M201691200

Covert, M. W., Schilling, C. H., and Palsson, B. (2001). Regulation of gene expression in flux balance models of metabolism. *J. Theor. Biol.* 213, 73–88. doi: 10.1006/jtbi.2001.2405

Doerr, A., de Reus, E., van Nies, P., van der Haar, M., Wei, K., Kattan, J., et al. (2019). Modelling cell-free rna and protein synthesis with minimal systems. *Phys. Biol.* 16:025001. doi: 10.1088/1478-3975/aaf33d

Flynn, J. M., Neher, S. B., Kim, Y.-I., Sauer, R. T., and Baker, T. A. (2003). Proteomic discovery of cellular substrates of the ClpXP protease reveals five classes of ClpX-recognition signals. *Mol. Cell* 11, 671–683. doi: 10.1016/S1097-2765(03)00060-1

Garamella, J., Marshall, R., Rustad, M., and Noireaux, V. (2016). The all *E. coli* TX-TL toolbox 2.0: a platform for cell-free synthetic biology. *ACS Synth. Biol.* 5, 344–55. doi: 10.1021/acssynbio.5b00296

Garenne, D., Beisel, C. L., and Noireaux, V. (2019). Characterization of the all-*E. coli* transcription-translation system myTXTL by mass spectrometry. *Rapid Commun. Mass Spectrom.* 33, 1036–1048. doi: 10.1002/rcm.8438

Glass, L., and Kauffman, S. A. (1973). The logical analysis of continuous, non-linear biochemical control networks. *J. Theoret. Biol.* 39, 103–129. doi: 10.1016/0022-5193(73)90208-7

Gould, R., Bassen, D. M., Chakrabarti, A., Varner, J. D., and Butcher, J. (2016). Population heterogeneity in the epithelial to mesenchymal transition is controlled by NFAT and phosphorylated Sp1. *PLoS Comput. Biol.* 12:e1005251. doi: 10.1371/journal.pcbi.1005251

Grilly, C., Stricker, J., Pang, W. L., Bennett, M. R., and Hasty, J. (2007). A synthetic gene network for tuning protein degradation in *Saccharomyces cerevisiae*. *Mol. Syst. Biol.* 3, 1–5. doi: 10.1038/msb4100168

Hoagland, M. B., Keller, E. B., and Zamecnik, P. C. (1956). Enzymatic carboxyl activation of amino acids. *J. Biol. Chem.* 218, 345–358.

Horvath, N., Vilkhovoy, M., Wayman, J., Calhoun, K., Swartz, J., and Varner, J. (2020). Toward a genome scale sequence specific dynamic model of cell-free protein synthesis in *Escherichia coli*. *Metab. Eng. Commun.* 10:e00113. doi: 10.1016/j.mec.2019.e00113

Hu, C. Y., Varner, J. D., and Lucks, J. B. (2015). Generating effective models and parameters for RNA genetic circuits. *ACS Synth. Biol.* 4, 914–26. doi: 10.1021/acssynbio.5b00077

Iizuka, R., Yamagishi-Shirasaki, M., and Funatsu, T. (2011). Kinetic study of *de novo* chromophore maturation of fluorescent proteins. *Anal. Biochem.* 414, 173–8. doi: 10.1016/j.ab.2011.03.036

Jaroentomeechai, T., Stark, J. C., Natarajan, A., Glasscock, C. J., Yates, L. E., Hsu, K. J., et al. (2018). Single-pot glycoprotein biosynthesis using a cell-free transcription-translation system enriched with glycosylation machinery. *Nat. Commun.* 9:2686. doi: 10.1038/s41467-018-05620-8

Karlebach, G., and Shamir, R. (2008). Modelling and analysis of gene regulatory networks. *Nat. Rev. Mol. Cell Biol.* 9, 770–780. doi: 10.1038/nrm2503

Karzbrun, E., Shin, J., Bar-Ziv, R. H., and Noireaux, V. (2011). Coarse-grained dynamics of protein synthesis in a cell-free system. *Phys. Rev. Lett.* 106:048104. doi: 10.1103/PhysRevLett.106.048104

Kassavetis, G., and Chamberlin, M. (1981). Pausing and termination of transcription within the early region of bacteriophage t7 DNA *in vitro*. *J. Biol. Chem.* 256, 2777–2786.

Kaufmann, B. B., and van Oudenaarden, A. (2007). Stochastic gene expression: from single molecules to the proteome. *Curr. Opin. Genet. Dev.* 17, 107–12. doi: 10.1016/j.gde.2007.02.007

Lee, S. B., and Bailey, J. E. (1984). Genetically structured models forlac promoter-operator function in the *Escherichia coli* chromosome and in multicopy plasmids: Lac operator function. *Biotechnol. Bioeng.* 26, 1372–1382. doi: 10.1002/bit.260261115

Lucks, J. B., Qi, L., Mutalik, V. K., Wang, D., and Arkin, A. P. (2011). Versatile RNA-sensing transcriptional regulators for engineering genetic networks. *Proc. Natl. Acad. Sci. U.S.A.* 108, 8617–22. doi: 10.1073/pnas.1015741108

Maeda, H., Fujita, N., and Ishihama, A. (2000). Competition among seven *Escherichia coli* sigma subunits: relative binding affinities to the core RNA polymerase. *Nucleic Acids Res.* 28, 3497–503. doi: 10.1093/nar/28.18.3497

Marshall, R., and Noireaux, V. (2018). "Synthetic biology with an all E. coli TXTL system: quantitative characterization of regulatory elements and gene circuits," in *Synthetic Biology*, ed. J. C. Braman (New York, NY: Humana Press), 61–93. doi: 10.1007/978-1-4939-7795-6_4

Marshall, R., and Noireaux, V. (2019). Quantitative modeling of transcription and translation of an all-*E. coli* cell-free system. *Sci. Rep.* 9:11980. doi: 10.1038/s41598-019-48468-8

Matsuura, T., Tanimura, N., Hosoda, K., Yomo, T., and Shimizu, Y. (2017). Reaction dynamics analysis of a reconstituted *Escherichia coli* protein translation system by computational modeling. *Proc. Natl. Acad. Sci. U.S.A.* 114, E1336–E1344. doi: 10.1073/pnas.1615351114

Matthaei, J. H., and Nirenberg, M. W. (1961). Characteristics and stabilization of DNAase-sensitive protein synthesis in *E. coli* extracts. *Proc. Natl. Acad. Sci. U.S.A.* 47, 1580–8. doi: 10.1073/pnas.47.10.1580

Mavelli, F., Marangoni, R., and Stano, P. (2015). A simple protein synthesis model for the pure system operation. *Bull. Math. Biol.* 77, 1185–1212. doi: 10.1007/s11538-015-0082-8

McAdams, H. H., and Arkin, A. (1997). Stochastic mechanisms in gene expression. *Proc. Natl. Acad. Sci. U.S.A.* 94, 814–9. doi: 10.1073/pnas.94.3.814

McClure, W. R. (1980). Rate-limiting steps in RNA chain initiation. *Proc. Natl. Acad. Sci. U.S.A.* 77, 5634–8. doi: 10.1073/pnas.77.10.5634

Mettetal, J. T., Muzzey, D., Pedraza, J. M., Ozbudak, E. M., and van Oudenaarden, A. (2006). Predicting stochastic gene expression dynamics in single cells. *Proc. Natl. Acad. Sci. U.S.A.* 103, 7304–9. doi: 10.1073/pnas.0509874103

Milo, R., Jorgensen, P., Moran, U., Weber, G., and Springer, M. (2010). Bionumbers-the database of key numbers in molecular and cell biology. *Nucleic Acids Res.* 38, D750–D753. doi: 10.1093/nar/gkp889

Moon, T. S., Lou, C., Tamsir, A., Stanton, B. C., and Voigt, C. A. (2012). Genetic programs constructed from layered logic gates in single cells. *Nature* 491, 249–53. doi: 10.1038/nature11516

Moore, S. J., MacDonald, J. T., and Freemont, P. S. (2017). Cell-free synthetic biology for *in vitro* prototype engineering. *Biochem. Soc. Trans.* 45, 785–791. doi: 10.1042/BST20170011

Morris, M. D. (1991). Factorial sampling plans for preliminary computational experiments. *Technometrics.* 33, 161–174. doi: 10.1080/00401706.1991.10484804

Ng, P. P., Jia, M., Patel, K. G., Brody, J. D., Swartz, J. R., Levy, S. et al. (2012). A vaccine directed to b cells and produced by cell-free protein synthesis generates potent antilymphoma immunity. *Proc. Natl. Acad. Sci. U.S.A.* 109, 14526–14531. doi: 10.1073/pnas.1211018109

Niederholtmeyer, H., Sun, Z. Z., Hori, Y., Yeung, E., Verpoorte, A., Murray, R. M., et al. (2015). Rapid cell-free forward engineering of novel genetic ring oscillators. *eLife* 4:e09771. doi: 10.7554/eLife.09771

Nilsson, B. (1984). Probable *in vivo* induction of differentiation by retinoic acid of promyelocytes in acute promyelocytic leukaemia. *Br. J. Haematol.* 57, 365–71. doi: 10.1111/j.1365-2141.1984.tb02910.x

Nirenberg, M. W., and Matthaei, J. H. (1961). The dependence of cell-free protein synthesis in *E. coli* upon naturally occurring or synthetic polyribonucleotides. *Proc. Natl. Acad. Sci. U.S.A.* 47, 1588–1602. doi: 10.1073/pnas.47.10.1588

Orth, J. D., Fleming, R. M. T., and Palsson, B. Ø. (2010). Reconstruction and use of microbial metabolic networks: the core *Escherichia coli* metabolic model as an educational guide. *EcoSal Plus* 4,1–47. doi: 10.1128/ecosalplus.10.2.1

Park, J. O., Rubin, S. A., Xu, Y.-F., Amador-Noguez, D., Fan, J., Shlomi, T., et al. (2016). Metabolite concentrations, fluxes and free energies imply efficient enzyme usage. *Nat. Chem. Biol.* 12, 482–9. doi: 10.1038/nchembio.2077

Prangemeier, T., Lehr, F.-X., Schoeman, R. M., and Koeppl, H. (2020). Microfluidic platforms for the dynamic characterisation of synthetic circuitry. *Curr. Opin. Biotechnol.* 63, 167–176. doi: 10.1016/j.copbio.2020.02.002

Pratapa, A., Jalihal, A. P., Law, J. N., Bharadwaj, A., and Murali, T. M. (2020). Benchmarking algorithms for gene regulatory network inference from single-cell transcriptomic data. *Nat Methods* 17, 147–154. doi: 10.1038/s41592-019-0690-6

Rackauckas, C., and Nie, Q. (2017). DifferentialEquations.jl—A performant and feature-rich ecosystem for solving differential equations in Julia. *J. Open Res. Soft.* 5:15. doi: 10.5334/jors.151

Raj, A., and van Oudenaarden, A. (2008). Nature, nurture, or chance: stochastic gene expression and its consequences. *Cell* 135, 216–26. doi: 10.1016/j.cell.2008.09.050

Shin, J., and Noireaux, V. (2010). Study of messenger rna inactivation and protein degradation in an *Escherichia coli* cell-free expression system. *J. Biol. Eng.* 4:9. doi: 10.1186/1754-1611-4-9

Silverman, A. D., Karim, A. S., and Jewett, M. C. (2019). Cell-free gene expression: an expanded repertoire of applications. *Nat. Rev. Genet.* 38, 7364–7377. doi: 10.1093/nar/gkq617

Sniegowski, J. A., Lappe, J. W., Patel, H. N., Huffman, H. A., and Wachter, R. M. (2005). Base catalysis of chromophore formation in arg96 and glu222 variants of green fluorescent protein. *J. Biol. Chem.* 280, 26248–55. doi: 10.1074/jbc.M412327200

Soltani, M., Davis, B. R., Ford, H., Nelson, J. A. D., and Bundy, B. C. (2018). Reengineering cell-free protein synthesis as a biosensor: biosensing with transcription, translation, and protein-folding. *Biochem. Eng. J.* 138, 165–171. doi: 10.1016/j.bej.2018.06.014

Stark, J. C., Jaroentomeechai, T., Moeller, T. D., Dubner, R. S.,Hsu, K. J., Stevenson, T. C., et al. (2019). On-demand, cell-free biomanufacturing of conjugate vaccines at the point-of-care. *bioRxiv*. 1–41. doi: 10.1101/681841

Stögbauer, T., Windhager, L., Zimmer, R., and Rädler, J. O. (2012). Experiment and mathematical modeling of gene expression dynamics in a cell-free system. *Integr. Biol.* 4, 494–501. doi: 10.1039/c2ib00102k

Swartz, J. R. (2018). Expanding biological applications using cell-free metabolic engineering: an overview. *Metab. Eng.* 50, 156–172. doi: 10.1016/j.ymben.2018.09.011

Tapia-Rojo, R., Mazo, J. J., Hernández, J. Á., Peleato, M. L., Fillat, M. F., and Falo, F. (2014). Mesoscopic model and free energy landscape for protein-DNA binding sites: analysis of cyanobacterial promoters. *PLoS Comput. Biol.* 10:e1003835. doi: 10.1371/journal.pcbi.1003835

Tapia-Rojo, R., Prada-Gracia, D., Mazo, J. J., and Falo, F. (2012). Mesoscopic model for free-energy-landscape analysis of DNA sequences. *Phys. Rev. E Stat. Nonlinear Soft Matter Phys.* 86(2 Pt 1):021908. doi: 10.1103/PhysRevE.86.021908

Tasseff, R., Jensen, H. A., Congleton, J., Dai, D., Rogers, K. V., Sagar, A., et al. (2017). An effective model of the retinoic acid induced hl-60 differentiation program. *Sci. Rep.* 7:14327. doi: 10.1038/s41598-017-14523-5

Thiery, J. P. (2003). Epithelial-mesenchymal transitions in development and pathologies. *Curr. Opin. Cell Biol.* 15, 740–6. doi: 10.1016/j.ceb.2003.10.006

Underwood, K. A., Swartz, J. R., and Puglisi, J. D. (2005). Quantitative polysome analysis identifies limitations in bacterial cell-free protein synthesis. *Biotech. Bioeng.* 91, 425–35. doi: 10.1002/bit.20529

Vilkhovoy, M., Adhikari, A., Vadhin, S., and Varner J. D. (2020). The evolution of cell free biomanufacturing. *Processes* 8:675. doi: 10.3390/pr8060675

Vilkhovoy, M., Dai, D., Vadhin, S., Adhikari, A., and Varner, J. D. (2019). Absolute quantification of cell-free protein synthesis metabolism by reversed-phase liquid chromatography-mass spectrometry. *J. Vis. Exp.* 152,e60329 doi: 10.3791/60329

Vilkhovoy, M., Horvath, N., Shih, C.-H., Wayman, J. A., Calhoun, K., Swartz, J., et al. (2018). Sequence specific modeling of *E. coli* cell-free protein synthesis. *ACS Synth. Biol.* 7, 1844–1857. doi: 10.1021/acssynbio.7b00465

Vilkhovoy, M., Minot, M., and Varner, J. D. (2016). Effective dynamic models of metabolic networks. *IEEE Life Sci. Lett.* 2, 51–54. doi: 10.1109/LLS.2016.2644649

Winnick, T. (1950a). Studies on the mechanism of protein synthesis in embryonic and tumor tissues. I. evidence relating to the incorporation of labeled amino acids into protein structure in homogenates. *Arch. Biochem.* 27, 65–74.

Winnick, T. (1950b). Studies on the mechanism of protein synthesis in embryonic and tumor tissues. II. inactivation of fetal rat liver homogenates by dialysis, and reactivation by the adenylic acid system. *Arch. Biochem.* 28, 338–47.

Yelleswarapu, M., Linden, A. J. V. D., Sluijs, B. V., Pieters, P. A., Dubuc, E., Greef, T. F. A. D., et al. (2018). Sigma factor-mediated tuning of bacterial cell-free synthetic genetic oscillators. *ACS Synth. Biol.* 7, 2879–2887. doi: 10.1021/acssynbio.8b00300

Yue, K., Zhu, Y., and Kai, L. (2019). Cell-free protein synthesis: chassis toward the minimal cell. *Cells* 8:315. doi: 10.3390/cells8040315

Conflict of Interest: The authors declare that the research was conducted in the absence of any commercial or financial relationships that could be construed as a potential conflict of interest.

Copyright © 2020 Adhikari, Vilkhovoy, Vadhin, Lim and Varner. This is an open-access article distributed under the terms of the Creative Commons Attribution License (CC BY). The use, distribution or reproduction in other forums is permitted, provided the original author(s) and the copyright owner(s) are credited and that the original publication in this journal is cited, in accordance with accepted academic practice. No use, distribution or reproduction is permitted which does not comply with these terms.

frontiers in Bioengineering and Biotechnology

ORIGINAL RESEARCH
published: 16 February 2021
doi: 10.3389/fbioe.2020.536957

Metabolic Modeling Combined With Machine Learning Integrates Longitudinal Data and Identifies the Origin of LXR-Induced Hepatic Steatosis

Natal A. W. van Riel[1,2,3]*, *Christian A. Tiemann*[1], *Peter A. J. Hilbers*[1] and *Albert K. Groen*[2,4]

[1] Department of Biomedical Engineering, Eindhoven University of Technology, Eindhoven, Netherlands, [2] Department of Vascular Medicine, Amsterdam UMC, Amsterdam, Netherlands, [3] Maastricht Centre for Systems Biology, Maastricht University, Maastricht, Netherlands, [4] Department of Laboratory Medicine, University Medical Center Groningen, Groningen, Netherlands

OPEN ACCESS

Edited by:
Babatunde Ogunnaike,
University of Delaware, United States

Reviewed by:
Hamed Bostan,
National Institute of Environmental Health Sciences (NIEHS), United States
David Bogle,
University College London, United Kingdom

***Correspondence:**
Natal A. W. van Riel
n.a.w.v.riel@tue.nl

Specialty section:
This article was submitted to Computational Genomics, a section of the journal Frontiers in Bioengineering and Biotechnology

Received: 21 February 2020
Accepted: 16 December 2020
Published: 16 February 2021

Citation:
van Riel NAW, Tiemann CA, Hilbers PAJ and Groen AK (2021) Metabolic Modeling Combined With Machine Learning Integrates Longitudinal Data and Identifies the Origin of LXR-Induced Hepatic Steatosis. Front. Bioeng. Biotechnol. 8:536957. doi: 10.3389/fbioe.2020.536957

Temporal multi-omics data can provide information about the dynamics of disease development and therapeutic response. However, statistical analysis of high-dimensional time-series data is challenging. Here we develop a novel approach to model temporal metabolomic and transcriptomic data by combining machine learning with metabolic models. ADAPT (Analysis of Dynamic Adaptations in Parameter Trajectories) performs metabolic trajectory modeling by introducing time-dependent parameters in differential equation models of metabolic systems. ADAPT translates structural uncertainty in the model, such as missing information about regulation, into a parameter estimation problem that is solved by iterative learning. We have now extended ADAPT to include both metabolic and transcriptomic time-series data by introducing a regularization function in the learning algorithm. The ADAPT learning algorithm was (re)formulated as a multi-objective optimization problem in which the estimation of trajectories of metabolic parameters is constrained by the metabolite data and refined by gene expression data. ADAPT was applied to a model of hepatic lipid and plasma lipoprotein metabolism to predict metabolic adaptations that are induced upon pharmacological treatment of mice by a Liver X receptor (LXR) agonist. We investigated the excessive accumulation of triglycerides (TG) in the liver resulting in the development of hepatic steatosis. ADAPT predicted that hepatic TG accumulation after LXR activation originates for 80% from an increased influx of free fatty acids. The model also correctly estimated that TG was stored in the cytosol rather than transferred to nascent very-low density lipoproteins. Through model-based integration of temporal metabolic and gene expression data we discovered that increased free fatty acid influx instead of *de novo* lipogenesis is the main driver of LXR-induced hepatic steatosis. This study illustrates how ADAPT provides estimates for biomedically important parameters that cannot be measured directly, explaining (side-)effects of pharmacological treatment with LXR agonists.

Keywords: longitudinal trajectory modeling, regularization, cholesterol, LXR agonist, systems biology, machine learning, mechanistic modeling, uncertainty quantification

1. INTRODUCTION

Dynamic responses contain important information about the behavior of biological systems. For example, data from continuous glucose monitoring has been used to identify characteristic patterns in glucose dynamics (Hall et al., 2018). Statistical modeling of time-series data using machine learning works well if the number of samples (individuals) in the dataset is large and the number of outcome variables is (relatively) small. For example, Latent Class Trajectory Analysis has been applied for time-series modeling of glucose measurements obtained during an oral glucose tolerance test (Hulman et al., 2018), thyroid hormones during gestation (Pop et al., 2018) and troponin levels after cardiac surgery (Deneer et al., 2020). The application of omics technologies, such as transcriptomics and metabolomics, to study the dynamics of biological systems results in high-dimensional time-series data, in which the number of gene expression values or small molecules detected in biological fluids is larger than the number of samples. Statistical analysis of high-dimensional time-series data is challenging. Mechanistic modeling offers a complementary approach to study the dynamics of biological systems (van Riel, 2006). Differential equation models can be used to describe disease progression. For example, the model by de Winter et al. (2006) is composed of three differential equations to simulate glucose, insulin and HbA1c (glycated hemoglobin) over time in patients with diabetes. Dynamic metabolic models calibrated to time-series data have been developed for biological systems such as yeast (e.g., Rizzi et al., 1997; van Riel et al., 1998) and human metabolism (e.g., Rozendaal et al., 2018a; O'Donovan et al., 2019). *In silico* dynamic models often lack the multi level layers of regulation that control metabolism. This impedes their application in disease modeling because causes of disease can be located at multiple levels, and also molecular therapies can be targeted to genes, proteins and metabolites. To overcome current limitations in statistical analysis and mechanistic modeling we combine metabolic modeling with machine learning techniques to integrate longitudinal metabolic and transcriptomic data. Previously we developed the computational approach called ADAPT (Analysis of Dynamic Adaptations in Parameter Trajectories) (Tiemann et al., 2011; van Riel et al., 2013). ADAPT combines mechanism-based differential equation models with machine learning to model temporal metabolic data (Tiemann et al., 2013; Rozendaal et al., 2018b). ADAPT functions as a so-called state observer (or state estimator), which is a system that provides an estimate of the internal state of a given real system from measurements of the input and output of the real system. Here, we aimed to extend ADAPT to include both metabolic and transcriptomic time-series data. Hereto we added a new regularization function to the learning algorithm that is used to estimate model parameters. The new version of ADAPT uses the metabolite data as input to estimate trajectories of metabolic parameters and takes the gene expression data as additional information to refine the trajectories.

ADAPT has been applied to a model of hepatic lipid and plasma lipoprotein metabolism (HepaLip2) to predict which metabolic adaptations are induced upon pharmacological treatment of mice by Liver X receptor (LXR) agonist T0901317. LXR agonists exert potent antiatherosclerotic actions but simultaneously induce excessive triglyceride (TG) accumulation in the liver. Using the new version of ADAPT we reveal that both input and output fluxes to hepatic TG content are considerably induced on LXR activation and that in the early phase of LXR agonism, hepatic steatosis results from only a minor imbalance between the two. It is generally believed that LXR-induced hepatic steatosis results from increased *de novo* lipogenesis (DNL). In contrast, ADAPT predicts that the hepatic influx of free fatty acids is the major contributor to hepatic TG accumulation in the early phase of LXR activation. This prediction is tested *in vivo* by a metabolic tracer experiment.

2. RESULTS

2.1. HepaLip2: Model of Hepatic Lipid and Plasma Lipoprotein Metabolism

Fundamental in ADAPT is a mathematical model of the (molecular) pathways of interest. We developed a mathematical multi-compartment model describing triglyceride and cholesterol metabolism (*HepaLip*2). The mathematical model contains three compartments representing the liver cytosol, liver endoplasmic reticulum (ER) and blood plasma (**Figure 1**). The liver includes the production, utilization and storage of triglycerides (TG) and cholesterols. Triglycerides are produced in the ER and can be transferred to the cytosol where they are stored in lipid droplets or catabolized. TG produced in the ER are also incorporated into nascent produced very low density lipoprotein (VLDL) particles. These VLDL particles are subsequently secreted in the blood plasma where they provide nutrients for peripheral tissues. The model also includes the hepatic uptake of free fatty acids (FFA) from plasma that predominantly originate from adipose tissue. Finally, the model includes the reverse cholesterol transport pathway, i.e., the net transport of cholesterol from peripheral tissues back to the liver via high density lipoproteins (HDL). The model is composed of 11 differential equations, (**Table 1**) 29 fluxes and 22 parameters. The flux equations are based on mass-action kinetics. Each flux equation introduces a parameter with unknown *in vivo* value. Collectively these parameters are referred to as the 'metabolic parameters'. A detailed description of the mathematical model including an overview of the state variables, parameters, fluxes, and differential equations is presented in the **Supplementary Material** (section 2).

2.2. Pharmacological Treatment With LXR Agonists

The liver X receptor (LXR) plays a central role in the control of cellular lipid and cholesterol metabolism and is

Abbreviations: ADAPT, analysis of dynamic adaptations in parameter trajectories; apo, apolipoprotein; C, cholesterol; CE, cholesterylester; DNL, *de novo* lipogenesis; ER, endoplasmic reticulum; FC, free cholesterol; FFA, free fatty acid; FPLC, fast protein liquid chromatography; HDL, high density lipoprotein; LXR, liver X receptor; ODE, ordinary differential equation; SSE, sum of squared errors; TG, triglyceride; VLDL, very low density lipoprotein.

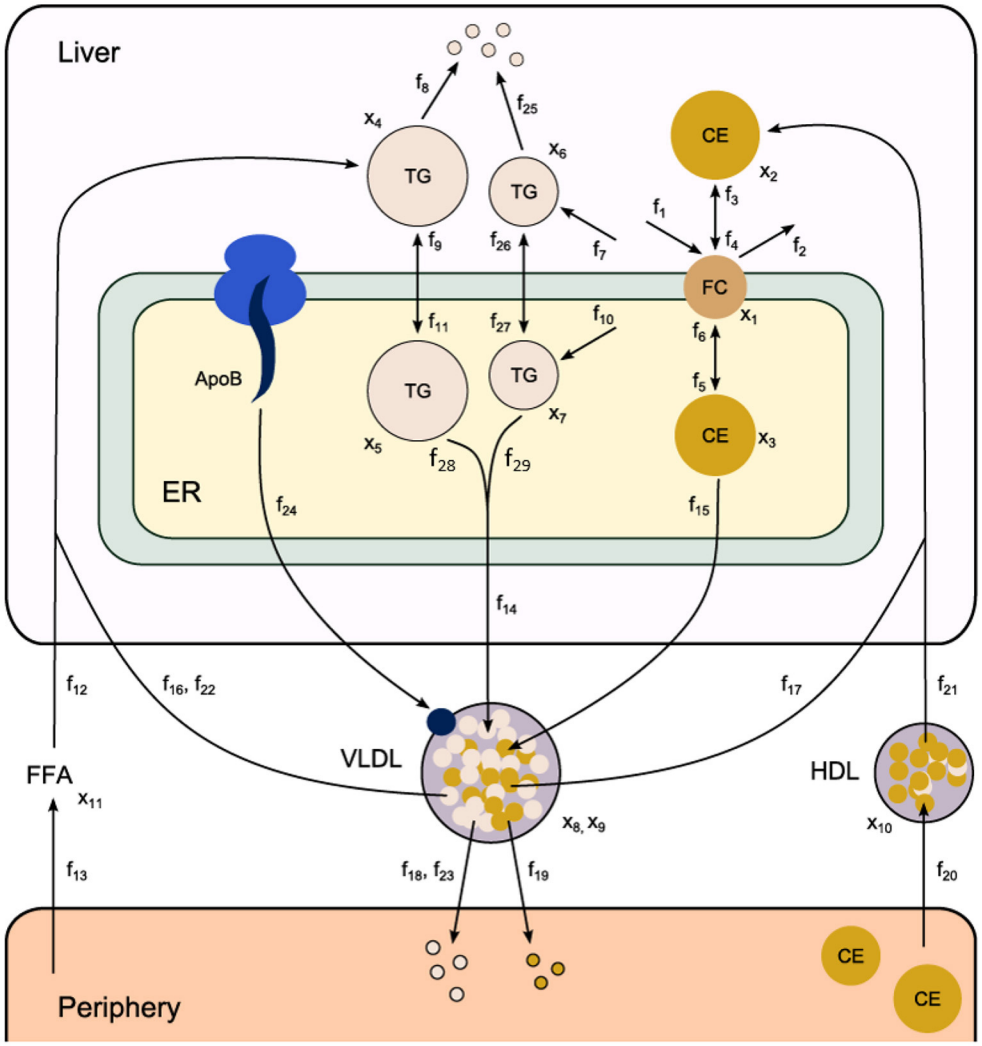

FIGURE 1 | Computational model of hepatic lipid and plasma lipoprotein metabolism (HepaLip2), under fasting conditions. The HepaLip2 model is composed of three compartments representing the liver cytosol, liver endoplasmic reticulum, and blood plasma. The liver compartment includes reactions comprising the production, utilization, and storage of triglycerides and cholesterols, and the mobilization of these metabolites to the endoplasmic reticulum, where they are incorporated into nascent VLDL particles. The VLDL particles are secreted in the plasma compartment where they serve as energy source for peripheral tissues. Remnant particles are taken up and cleared by the liver. The model furthermore includes the hepatic uptake of free fatty acids as well as HDL-mediated reverse cholesterol transport. The model is composed of 11 differential equations (and 11 corresponding state variables *x*), 29 fluxes *f* and 22 (unknown) parameters. ApoB, apolipoprotein B; CE, cholesterylester; ER, endoplasmic reticulum; FFA, free fatty acid; FC, free cholesterol; HDL, high density lipoprotein; TG, triglyceride; VLDL, very low density lipoprotein.

considered a potential target to treat or prevent atherosclerosis. However, a serious complication of LXR activation is the excessive accumulation of triglycerides in the liver, which finally results in the development of hepatic steatosis. The underlying molecular mechanisms inducing these adaptations are not fully understood, which complicates the clinical application of LXR agonists (Grefhorst et al., 2002; Grefhorst and Parks, 2009; Cave et al., 2016). We used data obtained from pharmacological treatment of mice by LXR agonist T0901317 up to 3 weeks. Quantitative experimental data at different stages of the treatment intervention were collected to study the dynamics of induced molecular adaptations. All the experiments were performed in the fasting state. Details about the experimental procedures can be found in section 5.

An overview of the quantities that were experimentally observed and their relation to corresponding model components is presented in **Table 2**. A model output y_i ($i = 1, \ldots, 15$) was coupled to experimental data d_i. Some model outputs are equal to state variables, other outputs are a combination (summation) of state variables. The data also includes fluxes, such as the synthesis rate of triglycerides secreted in VLDL particles, and the size and composition of VLDL particles and the corresponding variables in the model were also selected as outputs. Data was collected at 0, 1, 2, 4, 7, 14, and 21 days of treatment with T0901317 (**Figure 2**).

TABLE 1 | State variables included in the HepaLip2 model (**Figure 1**).

State	Name	Description	Units
x_1	x_{FC}	Hepatic free cholesterol	μ mol/liver
x_2	$x_{CE_{cyt}}$	Hepatic cholesteryl ester (cytosol)	μ mol/liver
x_3	$x_{CE_{ER}}$	Hepatic cholesteryl ester (ER)	μ mol/liver
x_4	$x_{TG_{cyt}}$	Hepatic triglyceride (cytotol)	μ mol/liver
x_5	$x_{TG_{ER}}$	Hepatic triglyceride (ER)	μ mol/liver
x_6	$x_{TGdnl_{cyt}}$	Hepatic *de novo* triglyceride (cytosol)	μ mol/liver
x_7	$x_{TGdnl_{ER}}$	Hepatic *de novo* triglyceride (ER)	μ mol/liver
x_8	$x_{TG_{VLDL}}$	Plasma VLDL-triglyceride	μ mol/L
x_9	$x_{C_{VLDL}}$	Plasma VLDL-cholesterol	μ mol/L
x_{10}	$x_{C_{HDL}}$	Plasma HDL-cholesterol	μ mol/L
x_{11}	x_{FFA}	Plasma free fatty acid	μ mol/L

*The differential equations, parameters and fluxes are presented in **Supplementary Material** (section 2).*

TABLE 2 | Measured quantities and their relation to model components.

Measurement	Model output	Equation	Unit
Hepatic triglyceride	y_1	$[x_4]+[x_5]+[x_6]+[x_7]$	μ mol/liver
Hepatic cholesteryl ester	y_2	$[x_2]+[x_3]$	μ mol/liver
Hepatic free cholesterol	y_3	$[x_1]$	μ mol/liver
Plasma total cholesterol	y_4	$[x_9]+[x_{10}]$	μ mol/L
HDL-cholesterol	y_5	$[x_{10}]$	μ mol/L
Plasma triglyceride	y_6	$[x_8]$	μ mol/L
Plasma free fatty acid	y_7	$[x_{11}]$	μ mol/L
VLDL TG/C ratio	y_8	TG_{cnt}/CE_{cnt}	[-]
VLDL diameter	y_9	D_{VLDL}	nm
VLDL-TG production	y_{10}	f_{14}	μ mol/h
VLDL catabolic rate	y_{11}	CR_{VLDL}	[-]
de novo lipogenesis	y_{12}	FC_{DNL}	[-]
Hepatic HDL-C uptake	y_{13}*	f_{21}	μ mol/h
Ratio cyt-TG / ER-TG concentration	y_{14}*	$R_{cTGcyt,TGer}$	[-]
Ratio cyt-TG / ER-TG production	y_{15}*	$R_{pTGcyt,TGer}$	[-]

**Only for the untreated phenotype ($t = 0$).*

Most measurements were available for all the seven time points, but y_{13} to y_{15} were experimentally observed for the untreated phenotype ($t = 0$) only.

2.3. Calibrating the Model to the Untreated Phenotype

First the HepaLip2 model was used to describe the untreated phenotype. Model parameters at baseline (start of simulation and experiment) are estimated from metabolic data and flux information. ADAPT estimates the model parameters by applying a least squares algorithm that minimizes the sum of squared errors (SSE) between the metabolic data $d_{m,i}$ of the untreated phenotype and corresponding model outputs y_i. To account for experimental and biological uncertainties different random samples of the data were generated assuming a data error model based on Gaussian distributions, with means and standard deviations according to the experimental data. A global scatter search was used to initialize a multi-start, gradient-based, interior point local optimization method, resulting in a collection of parameter sets that describe the untreated phenotype. These parameter sets served as a starting point from which ADAPT iteratively learns and updates the parameters to describe the transition between experimental data obtained during different stages of the treatment, as is described next.

2.4. Linking the Computational Model to Time-Series Data

HepaLip2 and ADAPT have been employed to generate insight in the LXR agonism response. The T0901317-induced perturbation starts at the proteome level and subsequently induces adaptations at the other levels. During the 3 week treatment the metabolic parameters and fluxes are expected to change over time. ADAPT captures adaptations or modulating effects on metabolic pathways by introducing time-dependent descriptions of model parameters. Parameter trajectories are constrained by experimental data. To enable the estimation of dynamic trajectories of metabolic parameters and fluxes, continuous dynamic descriptions of the experimental data are used as input for ADAPT. For this purpose, cubic smoothing splines were calculated that describe the experimental data, taking into account experimental and biological uncertainties. A collection of splines was calculated using a Monte Carlo approach as follows. For all time points in the data the same data model and sampling approach were used as described above for the untreated phenotype (the first time point in the time-series). Subsequently, for each generated set of time samples a cubic smoothing spline was fitted, which is used as input for the next step of the ADAPT algorithm. The experimental data and splines are presented in **Figure 2**.

2.5. Estimating Time-Dependent Changes of the Model Parameters

The HepaLip2 model mechanistically describes the kinetics of metabolic pathways (**Figure 1**). ADAPT is based on the assumption that during disease development and treatment response, changes in kinetic metabolic parameters are caused by changes in corresponding enzymes that catalyze conversion or transport of metabolites. Adaptations in metabolic processes are identified by inferring which metabolic parameters and consequently metabolic fluxes necessarily have to change to describe the experimental data. To this end, a simulation of the full treatment period was divided into a number N_t of time segments Δt. First, the simulation is started using the parameters and model state of the untreated phenotype. Next, for each subsequent segment n, the system is simulated (using a variable step integration method) for a time-period Δt using the parameters and model state of the previous step $n-1$ as a starting point. The parameters for segment n are re-estimated by minimizing the difference between the data interpolants

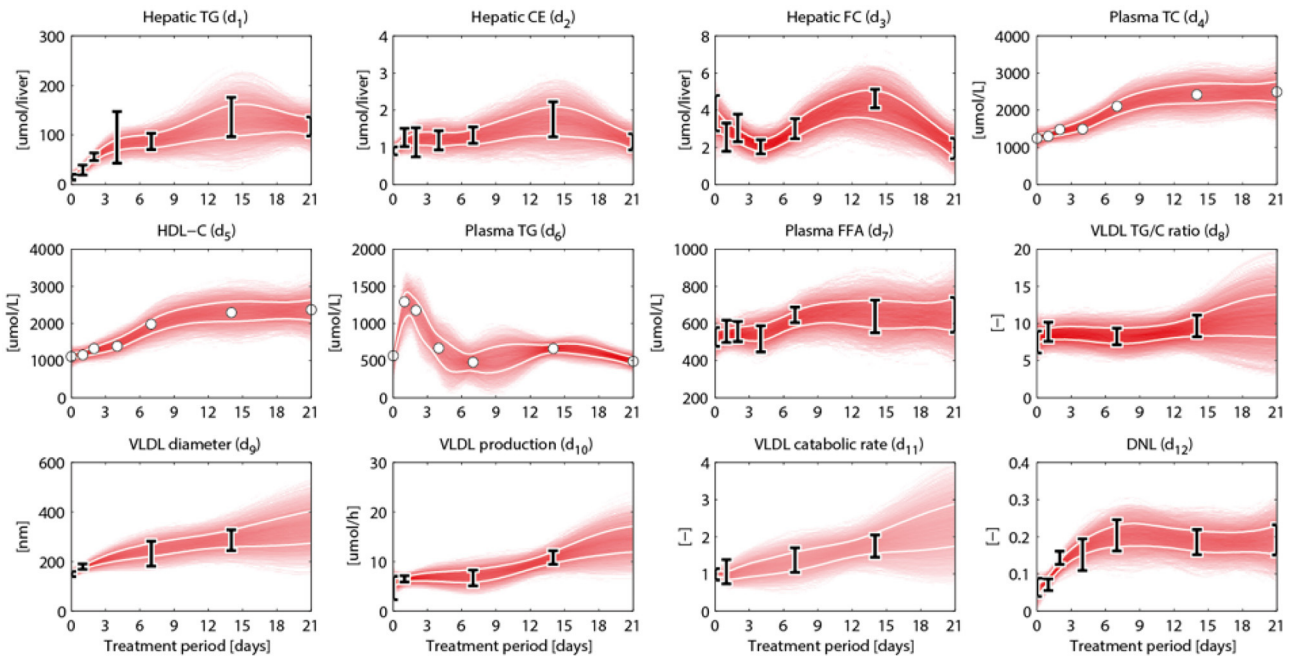

FIGURE 2 | Metabolic data and interpolants. Metabolic time-series data and 2D histograms of the splines that were used as input for ADAPT (included in χ_d^2, Equation 2). A darker color represents a higher density of trajectories in that specific region and time point. The white lines enclose the central 67% of the interpolant density at each time point. Data is represented as means ± standard deviations (N = 5–6), with an exception for the experimental data obtained via FPLC measurements. These measurements were performed on pooled mice plasma and are represented by the white dots. Measures of variance used for the Monte Carlo sampling of these quantities were estimated based on similar experiments that were performed in Grefhorst et al. (2012).

and corresponding model outputs for that time segment. This procedure is repeated for all segments and as a result parameter trajectories are inferred by minimizing the objective function χ^2 over the time segments through numerical optimization:

$$\hat{\vec{p}}(n\Delta t) = \arg\min_{\vec{p}(n\Delta t)} \chi^2(\vec{p}(n\Delta t)) \;\; n = 1, \ldots, N_t \tag{1}$$

$\hat{\vec{p}}(n\Delta t)$ represents the optimized parameter set for the nth time segment. The objective function χ^2 is the weighted sum of squared differences between model outputs and data:

$$\chi^2(\vec{p}(n\Delta t)) = \sum_{i=1}^{N_y} \left(\frac{Y_i(n\Delta t) - d_{m,i}(n\Delta t)}{\sigma_{m,i}(n\Delta t)} \right)^2 \doteq \chi_d^2(\vec{p}(n\Delta t)) \tag{2}$$

where N_y is the number of measured model variables (outputs), $Y_i(n\Delta t)$ are the discrete time model outputs, $d_{m,i}(n\Delta t)$ are the interpolants of the metabolic data with standard deviation $\sigma_{m,i}$. The optimization procedure is repeated for all data interpolants, starting from the state and parameter set of the untreated phenotype. An ADAPT solution was considered acceptable if model outputs were within the 95% confidence interval of the data. In this study $N_y = 15$, and $N_t = 200$ was used.

ADAPT simulation of HepaLip2 provides estimates for system variables that were not experimentally observed, such as the synthesis rate and composition of VLDL particles (**Supplementary Figure 7**). As observed before (Tiemann et al., 2013), VLDL particle secretion is reduced upon LXR activation. Although the secretion of VLDL particles decreased, an increased release of VLDL-TG to the plasma was experimentally observed (**Supplementary Figure 7B**). Similarly, the computational analysis showed an increased production of VLDL-CE to the plasma (**Supplementary Figure 7C**). According to the model the progressive increase of these fluxes was facilitated by an increased loading of triglycerides and cholesterol onto VLDL particles (**Supplementary Figures 7D,E**). These predictions were obtained using only the metabolic data as input for ADAPT.

2.5.1. Integration of Gene Expression Data

Until here ADAPT connected metabolic parameters to activity of enzymes (protein level). Next, gene expression was added as a third layer of information. ADAPT has been extended to include a potential functional relationship between metabolic parameters and gene expression levels. Variables in the mechanistic (metabolic) part of the model can be directly linked to metabolic data, which is used to fit the model to that experimental data. Pathways at the transcriptome level were not modeled mechanistically due to the lack of sufficient quantitative information about these systems. Gene expression data does not have an one-to-one connection with the metabolic variables and, therefore, cannot be included in the error function (Equation 2). Therefore, a different approach was used to integrate gene expression data in the parameter trajectory estimation algorithm.

The transcriptomic data is implicitly used to constrain the dynamic behavior of parameter trajectories, by including a regularization function. Time-course data of relative expression levels of 23 genes was available (**Figure 3**). **Table 3** provides an overview of the parameters and genes that were coupled. The optimization problem was extended as follows. First, for each time segment Δt, parameter adaptations are preferred such that resulting parameter trajectories and corresponding gene expression profiles display temporal correlation. This was implemented by including an additional component ($\chi^2_{g_1}$) in the objective function which maximizes the Pearson correlation between these profiles. Secondly, the gene expression data was also used to find parameter trajectories that are steady and smooth (enforcing temporal sparsity in the solutions). It was assumed that parameters are less likely to change when corresponding gene expression levels remain unchanged over time, compared to data indicating that expression of the genes is induced or repressed. Therefore, when transcriptomics data indicate that expression of genes changes over time parameter adaptations will be less penalized compared to genes with constant expression. This was implemented by including a third component ($\chi^2_{g_2}$) in the objective function which utilizes the time derivative of gene expression profiles to penalize parameter fluctuations. The higher the derivative of the gene expression profile, the lower the penalty on changes in parameter values will be. The resulting objective function $\chi^2(\vec{p})$ is written as:

$$\chi^2(\vec{p}) = \chi^2_d(\vec{p}) + \lambda_{g_1}\chi^2_{g_1}(\vec{p}) + \lambda_{g_2}\chi^2_{g_2}(\vec{p}) \tag{3}$$

in which χ^2_d is the (weighted) sum of squared errors (SSE) of metabolic data and model outputs (Equation 2), $\chi^2_{g_1}$ maximizes the temporal correlation between parameter trajectories and gene expression profiles, and $\chi^2_{g_2}$ penalizes parameter fluctuations. λ_{g_1} and λ_{g_2} are regularization constants (also referred to as weighting coefficients) that determine the relative importance of the components. Further details are provided in section 5 and in the **Supplementary Material**.

2.6. Setting the Regularization Constants

In multi-objective optimization and regularized regression approaches, like Equation (3), the weights of the different components in the objective function are important hyper-parameters of the algorithm that are problem dependent and need to be tuned for adequate performance. First, the influence of the regularization constants for gene correlation (λ_{g_1}) and damping of unnecessary parameter fluctuations (λ_{g_2}) on the estimation of the parameter trajectories was investigated using a Monte Carlo approach. ADAPT was performed for 20,000 random combinations for λ_{g_1} and λ_{g_2} and the values of the three components in the objective function were analyzed. Results are reported in the **Supplementary Material** (section 3.1). We found combinations of regularization constants for which $\lambda_{g_1}\chi^2_{g_1}$ becomes effective: when λ_{g_1} is larger than 10^{-6} and λ_{g_2} is smaller than 10^{-8} parameter-gene couples displayed temporal correlation. For these combinations λ_{g_2} is sufficiently large for $\lambda_{g_2}\chi^2_{g_2}$ to reduce unnecessary parameter trajectory fluctuations, and the data error χ^2_d is always small (**Supplementary Figure 3**).

Secondly, the characteristics of parameter trajectory solutions corresponding to a specific combination of gene regularization constants was investigated. In some cases parameter-gene couples already displayed (high) temporal correlation without including gene expression data (**Supplementary Figure 4**, bottom panel). As expected, in many cases an increase in temporal correlation between the assigned parameter-gene couples was obtained when gene expression data was included (**Supplementary Figure 4**, bottom panel). Interestingly, couple $c_{5,1}$ showed a predominantly negative correlation for all solution groups. Couple $c_{5,1}$ links the expression of *Apob* encoding for the apolipoprotein B to VLDL particle secretion (flux f_{24}, parameter p_{22}, **Table 3**). This can be explained when inspecting the VLDL particle secretion, described in detail in the **Supplementary Material** (section 3).

After these verification steps, we concluded the proposed method works as designed for Hepalip2 in combination with the experimental data: ADAPT provides a data-driven approach to incorporate the multi level layers of regulation in a dynamic model of metabolism. In the following sections we analyze the applicability of gene expression data to constrain model predictions, and ADAPT is applied to study: (1) the compartmentalization of hepatic triglycerides, (2) adaptations in the hepatic lipid loading capacity, and (3) the quantitative contribution of the different metabolic routes to the increased hepatic triglyceride level.

2.7. Integration of Gene Data Constrains Metabolic Predictions

We introduce the following notation: A group of trajectory solutions is denoted by G_i where i ($0.05 \leq i \leq 1$) represents the fraction of all solutions with the highest temporal correlations of parameter trajectories with gene expression over the entire treatment period (hence lowest $\chi^2_{g_1}$). For example, group $G_{0.05}$ contains 5% of the 20,000 trajectory solutions with the lowest values for $\chi^2_{g_1}$ summed over time. Furthermore, G^0 is defined as the group of solutions corresponding to $\lambda_{g_1} = \lambda_{g_2} = 0$ (solutions obtained without regularization). The effect of integration of gene expression data on model performance was expressed as reduction in variance in model estimations (Equation 7 in the **Supplementary Material**). **Figure 4** shows the variance reduction of $G_{0.05}$ compared to G^0 at each time point for all state variables (left panel), parameters (middle panel), and fluxes (right panel). The (dark-)gray parts clearly display model predictions that were effectively constrained by the gene expression data. Note that in multiple cases also a reduction in variance was obtained for parameters that were not coupled to genes.

2.8. Compartmentalization of Hepatic Triglycerides

A reduction in the variance (estimation uncertainty) was observed for many of the model components when gene expression was included (**Figure 4**). One example concerns the hepatic storage of triglycerides in cytosolic ($x_4 + x_6$) and endoplasmic reticulum ($x_5 + x_7$) fractions. The cytosolic fraction represents the TG pool stored in lipid droplets and the ER

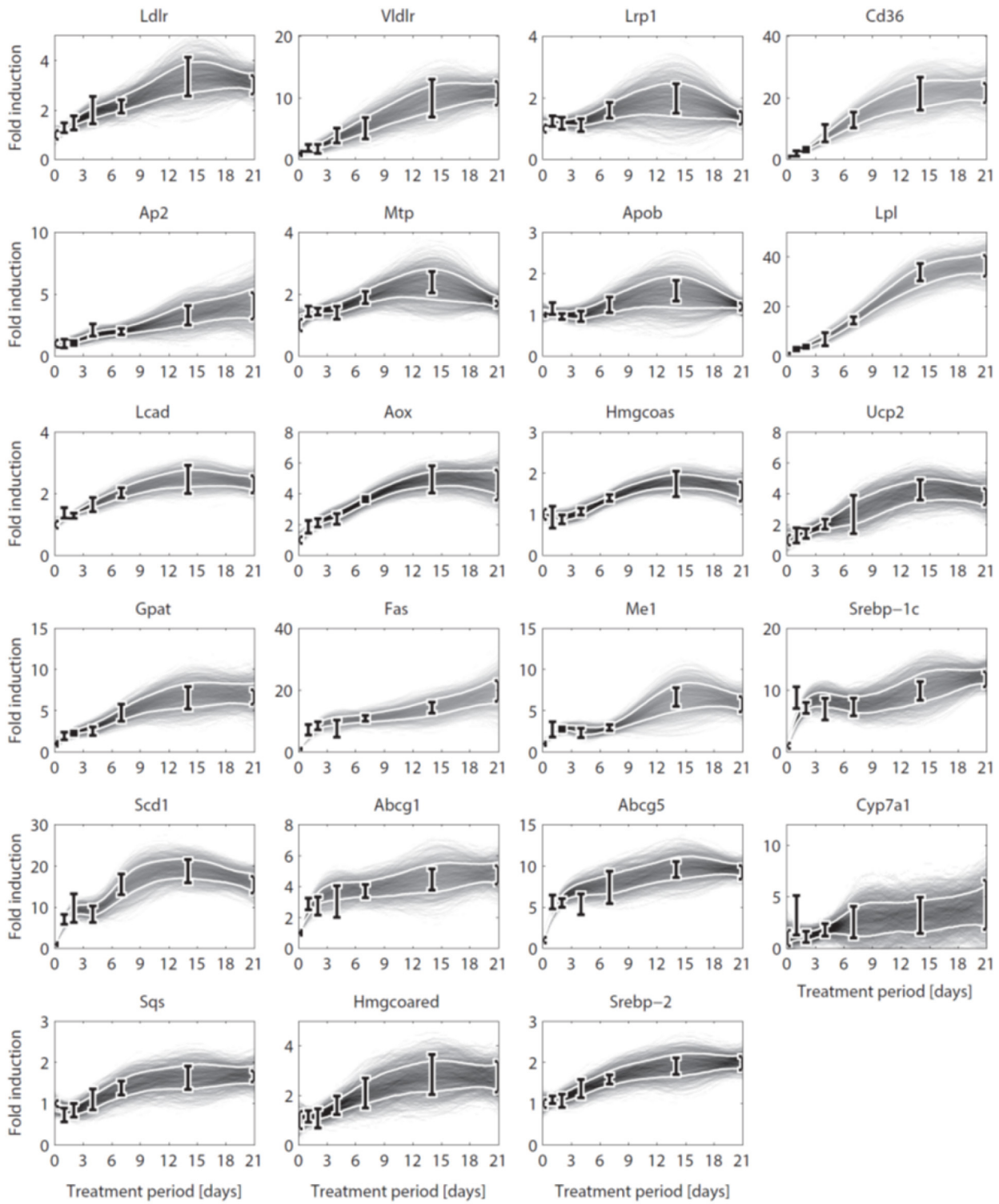

FIGURE 3 | Gene expression data and interpolants. Temporal expression data for 23 genes and 2D histograms of the corresponding cubic splines that were used as input for ADAPT (included in $\chi^2_{g_1}$ and $\chi^2_{g_2}$). The experimental data is represented as means ± standard deviations (N = 5-6). The white lines enclose the central 67% of the interpolant density at each time point. (see **Table 3** for the gene names).

TABLE 3 | Parameter-gene couples, linking 23 genes to 11 model parameters.

Couple	Parameter	Gene	Description
$c_{1,1}$	p_{16}	Ldlr	Low-density lipoprotein receptor
$c_{1,2}$	p_{16}	Vldlr	Very-low-density lipoprotein receptor
$c_{1,3}$	p_{16}	Lrp1	Low-density lipoprotein receptor-related protein 1
$c_{2,1}$	p_{12}	Cd36	Cluster of differentiation 36
$c_{2,2}$	p_{12}	Ap2	Adipocyte protein 2
$c_{3,1}$	p_{14}	Mtp	Microsomal triglyceride transfer protein
$c_{4,1}$	p_{15}	Mtp	Microsomal triglyceride transfer protein
$c_{5,1}$	p_{22}	Apob	Apolipoprotein B
$c_{6,1}$	p_{18}	Lpl	Lipoprotein lipase
$c_{7,1}$	p_{8}	Lcad	Long chain acyl-CoA dehydrogenase
$c_{7,2}$	p_{8}	Aox	Aldehyde oxidase
$c_{7,3}$	p_{8}	Hmgcoa	Hydroxymethylglutaryl-CoA
$c_{7,4}$	p_{8}	Ucp2	Uncoupling protein 2
$c_{8,1}$	p_{7}	Gpat	Glycerol-3-phosphate acyltransferase
$c_{8,2}$	p_{7}	Fas	Fatty acid synthase
$c_{8,3}$	p_{7}	Me1	NADP-dependent malic enzyme 1
$c_{8,4}$	p_{7}	Srebp-1c	Sterol regulatory element binding transcription factor 1c
$c_{8,5}$	p_{7}	Scd1	Stearoyl-CoA desaturase 1
$c_{9,1}$	p_{10}	Gpat	Glycerol-3-phosphate acyltransferase
$c_{9,2}$	p_{10}	Fas	Fatty acid synthase
$c_{9,3}$	p_{10}	Me1	NADP-dependent malic enzyme 1
$c_{9,4}$	p_{10}	Srebp-1c	Sterol regulatory element binding transcription factor 1c
$c_{9,5}$	p_{10}	Scd1	Stearoyl-CoA desaturase 1
$c_{10,1}$	p_{2}	Abcg1	ATP-binding cassette subfamily G member 1
$c_{10,2}$	p_{2}	Abcg5	ATP-binding cassette subfamily G member 5
$c_{10,3}$	p_{2}	Cyp7a1	Cytochrome P450, family 7, subfamily A, polypeptide 1
$c_{11,1}$	p_{1}	Sqs	Squalene synthase
$c_{11,2}$	p_{1}	Hmgcoared	HMG-CoA reductase
$c_{11,3}$	p_{1}	Srebp-2	Sterol regulatory element-binding protein 2

A description of the parameters and corresponding fluxes is presented in ***Supplementary Material*** *(section 2).*

fraction the TG contained in nascent VLDL particles. **Figure 5** shows the 95% intervals of these model quantities for group G_1 (**Figure 5**, left column), $G_{0.1}$ (**Figure 5**, middle column), and $G_{0.05}$ (**Figure 5**, right column). The experimental data only includes measurements of the total hepatic triglyceride content (y_1) and the model provides more detailed information on where these lipids reside inside the hepatocyte. Experimental data of the total hepatic triglyceride content ($y_1 = x_4 + x_5 + x_6 + x_7$) was included in the optimization procedure and all solution groups describe this data adequately. Before the inclusion of gene expression data, it was not possible to accurately predict how the total triglyceride content is distributed between cytosolic and VLDL fractions (**Figure 5**, left column). However, when the gene expression data was included, the model estimates that the increased triglyceride fluxes are especially stored in the cytosol, rather than transferred to nascent VLDL (**Figure 5**, middle and right column). This estimation was more precise for the 5% of the trajectory solutions with the lowest values for $\chi^2_{g_1}$ (highest temporal correlation with gene expression) compared to when the number of trajectories in the analysis was increased to include 10% of the trajectories with the lowest values for $\chi^2_{g_1}$ ($G_{0.05}$ vs. $G_{0.1}$).

Subsequently, additional independent measurements were performed to validate this model result. Fractionation experiments were performed on livers from untreated C57BL/6J mice and C57BL/6J mice treated with T0901317 for 14 days, to separate the cytosolic triglyceride fraction from the microsomal fraction, containing VLDL. A description of the experimental materials and procedures is available in section 5. Indeed, the experimental data shows that the increased triglyceride fluxes are predominantly stored in the cytosolic fraction compared to the microsomal fraction (**Figure 6**), confirming the model prediction.

The parameter and flux trajectories were investigated to determine which processes are responsible for the observed compartmentalization of hepatic triglycerides between cytosolic and ER fractions (**Supplementary Material**, section 4). It appeared that the calculation of constrained estimations for the nascent VLDL triglyceride content was determined by two factors. First, the nascent VLDL triglyceride content is co-determined by the hepatic capacity to load these triglycerides onto nascent produced VLDL particles (fluxes f_{14} and f_{15}). A second factor is the VLDL-TG production flux which increases progressively during the treatment (**Supplementary Figure 7**). Mathematically, this compartmentalization was enforced by a predicted increase of the hepatic lipid loading capacity of lipoproteins, as described before (**Figure 5**). The lipid loading capacity is co-determined by the activity of microsomal triglyceride transfer protein Mtp. Expression of Mtp is linked to parameters p_{14} and p_{15} in the HepaLip2 model. The expression level of the *Mtp* gene was increased upon LXR activation (**Figure 3**). Furthermore, a significant increase of the activity of Mtp was experimentally observed in mice treated with T0901317 for 1 week (Grefhorst and Parks, 2009).

2.9. Hepatic Triglyceride Accumulation

Pharmacological activation of LXR induces the excessive accumulation of triglycerides in the liver (**Figure 7**). **Figure 7A** shows that the sum of all fluxes contributing to the hepatic triglyceride pool increased rapidly during the first 3 days of the intervention, and remained at this elevated level upon prolonged treatment. In the mathematical model the additive fluxes (F_a) include: *de novo* lipogenesis, hepatic FFA uptake from plasma, and clearance of lipoproteins via lipases and whole-particle uptake (Equation 8 in the **Supplementary Material**). **Figure 7B** shows that the increased F_a was closely accompanied by an increase of the fluxes that catabolize hepatic triglycerides (F_s, Equation 9 in the **Supplementary Material**). The subtractive fluxes include the secretion of triglycerides to nascent produced VLDL particles and the hepatic catabolism of triglycerides (the hydrolysis of triglyceride into fatty acids and glycerol which are subsequently used in processes such as β-oxidation, gluconeogenesis,

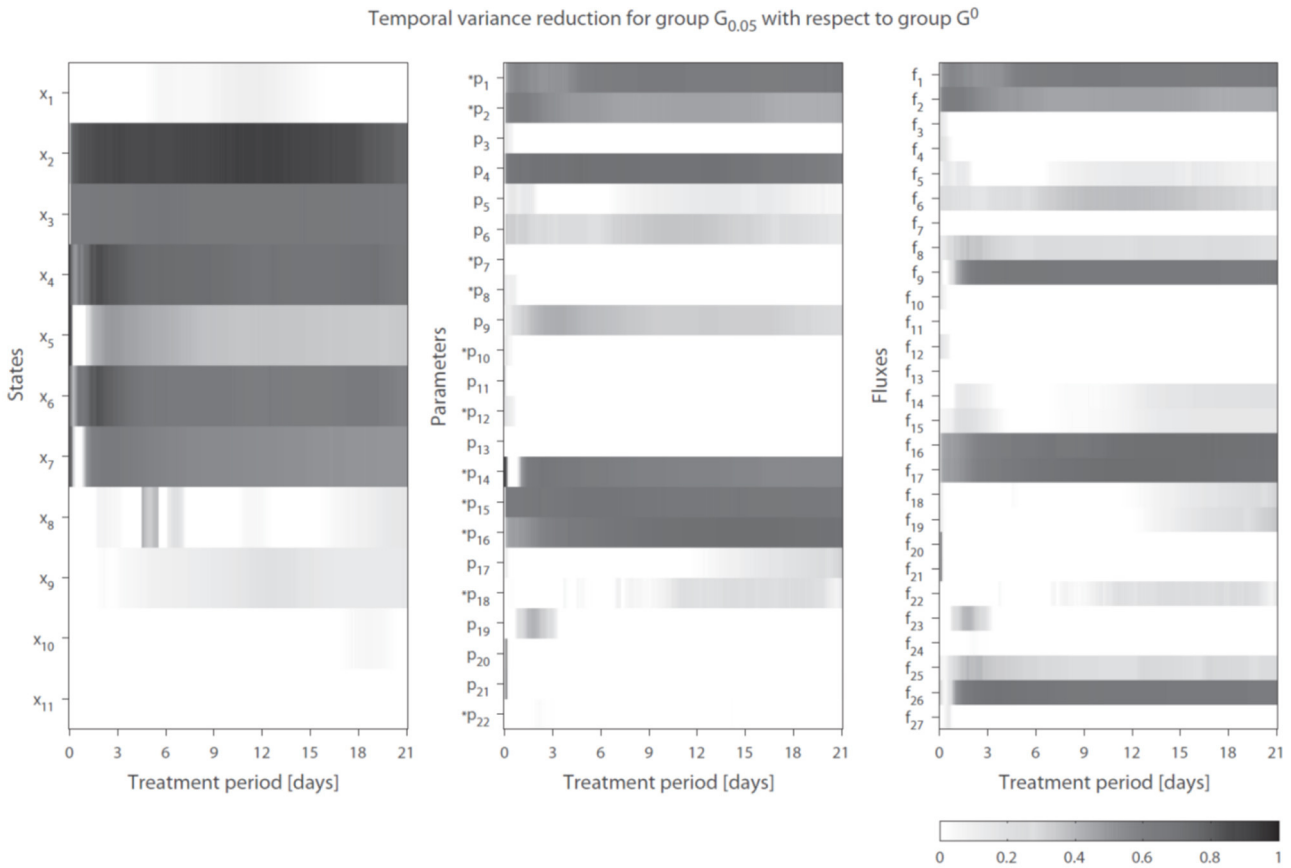

FIGURE 4 | Temporal variance reduction by incorporating gene expression data. The gray-intensity indicates reduction in variance for estimated state variables **(left)**, parameters **(middle)**, and fluxes **(right)**. The asterisk signs (*) indicate parameters that were coupled to one or multiple genes. The (dark-)gray parts display model estimates that were effectively constrained by the gene expression data. Results shown for group $G_{0.05}$, containing 5% of the trajectory solutions with the highest temporal correlation between parameter trajectories and gene expression (lowest penalty by $\chi^2_{g_1}$). Compared to G0, which are the solutions obtained without regularization Note $f_{14} = f_{28} + f_{29}$.

ketogenesis, sterol- and phospholipid synthesis). The difference between additive and subtractive triglyceride fluxes is displayed in **Figure 7C**. An imbalance between these fluxes can be observed during the first days of the intervention, which stabilizes gradually during the treatment. One process that contributes to the hepatic triglyceride accumulation is *de novo* lipogenesis. LXR induces the expression of lipogenic genes such as *Fas* (fatty acid synthase) and *Scd1* (stearoyl-CoA desaturase 1) (**Figure 3**), resulting in an increased fractional contribution of *de novo* lipogenesis (**Figure 2**). A question remained whether *de novo* lipogenesis is the sole process being responsible for the triglyceride accumulation. Experimental data and model simulations showed that the hepatic triglyceride level was already increased within 1 day of treatment, while no significant change in the fractional contribution of *de novo* lipogenesis was observed. This suggests that other processes are involved during the initial phase of the treatment (and perhaps also upon prolonged treatment). Therefore, we quantified the contribution of all metabolic routes included in the mathematical model that influence the hepatic triglyceride level. **Figure 7D** shows how the fractional contribution of the various fluxes included in F_a changes during treatment with T0901317. The analysis shows that plasma FFA provided a major contribution to the supply of hepatic triglycerides, whereas the clearance of lipoproteins played merely a minor role. Furthermore, the figure shows a peak contribution of hepatic FFA uptake at $t \approx 1$ day, while the contribution of *de novo* lipogenesis increased gradually up to one week of treatment. **Figure 7E** shows the time to peak (time to maximal fractional contribution) of the various processes. The results clearly indicate that an increased uptake of FFA precedes the induction of *de novo* lipogenesis. The hepatic influx of FFA contributes for roughly 80% to the accumulation of TG in the liver.

To establish whether the flux of FFA from plasma to the liver is indeed increased in the initial phase of LXR activation, as suggested by the model, experiments were performed in which ^{13}C-palmitate was infused into C57Bl/6J mice that were treated

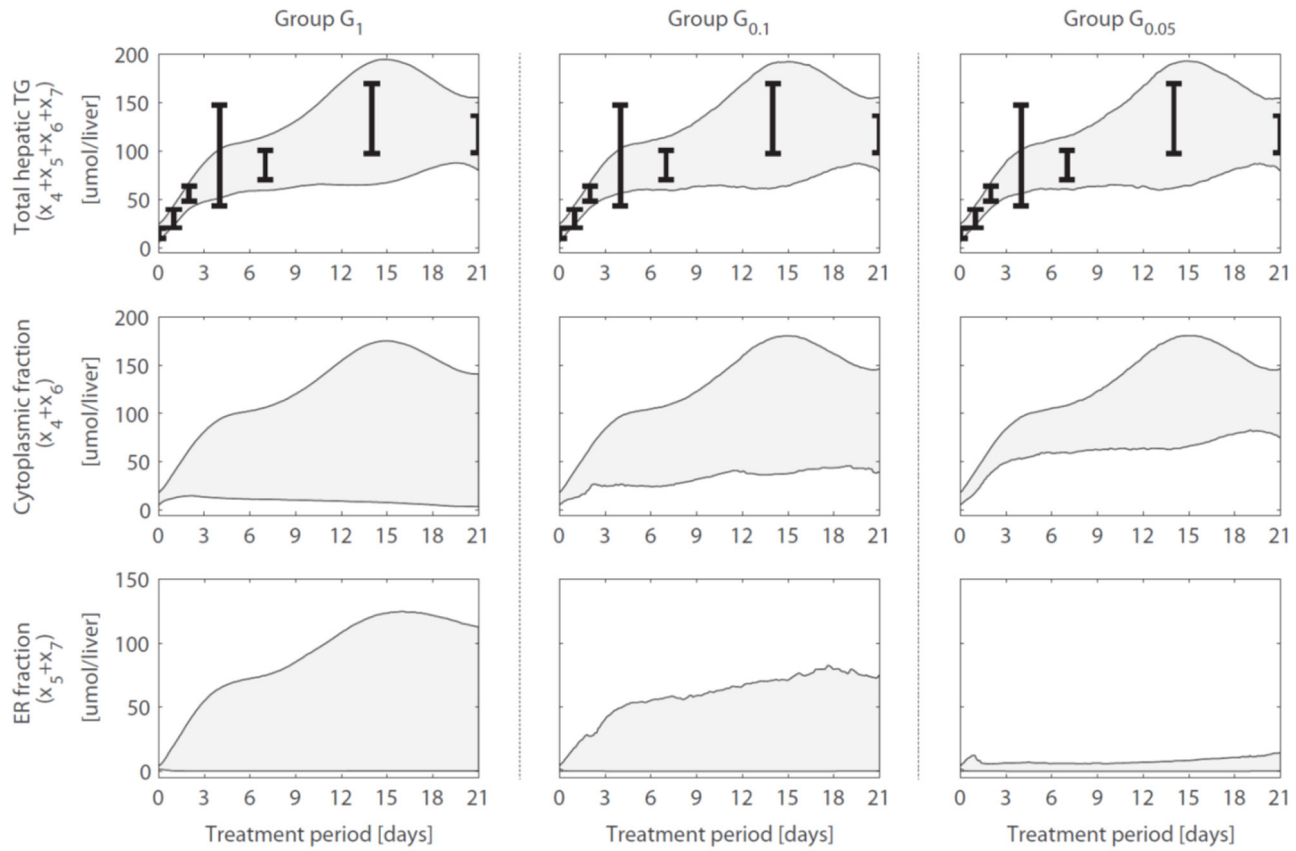

FIGURE 5 | Hepatic triglyceride fluxes are increased and especially stored in the cytosolic fraction. Trajectories of the total hepatic TG content ($y_1 = x_4 + x_5 + x_6 + x_7$), as well as its subdivision into cytosolic ($x_4 + x_6$) and endoplasmic reticulum ($x_5 + x_7$) fractions, are displayed for different groups of solutions. The experimental data of the total hepatic TG content (the error bars represent the standard deviation of the data) was included in the optimization procedure (linked to output y_1) and all groups describe this data adequately. When only the metabolic data was used to calibrate the model (group G_1), the distribution of the total TG content between the cytosolic fraction (TG in lipid droplets) and ER fraction (TG transferred to nascent VLDL could not be estimated precisely (left column). When including the gene expression data, model results showed that the increased TG pool is especially stored in the cytosol, rather than transferred to nascent VLDL (middle and right column). The solutions with the highest correlation between parameter trajectories and temporal gene expression ($G_{0.05}$, right column) yielded the most precise estimates. The shaded areas indicate the 95% confidence intervals of the model estimates.

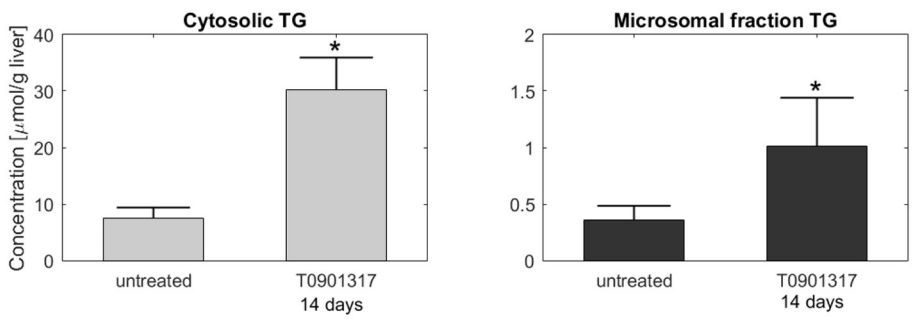

FIGURE 6 | Fractionation of hepatic triglycerides. Additional measurements were performed on livers from C57BL/6J mice treated with T0901317 for 14 days and untreated controls to separate the cytosolic TG fraction from the microsomal fraction, containing VLDL particles. The experimental data shows that hepatic TG is predominantly stored in the cytosolic fraction, which confirmed the model estimations presented in **Figure 5**. Note the 20-fold scale difference in both y-axis. The bars indicate mean + standard deviation, $^*p < 0.05$, Mann-Whitney *U*-test.

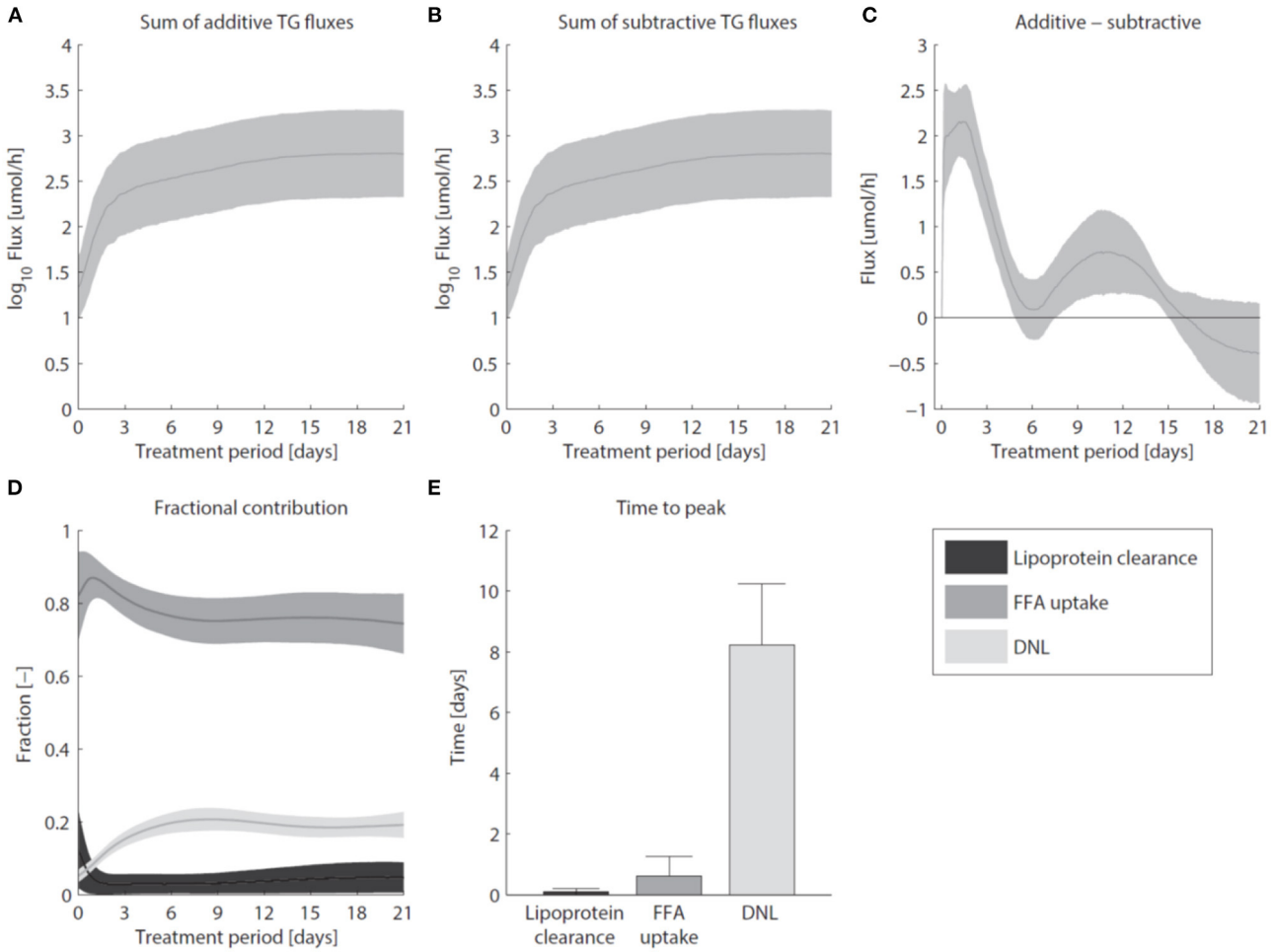

FIGURE 7 | Hepatic accumulation of triglycerides. **(A)** The sum of fluxes contributing to the hepatic TG pool. **(B)** The sum of fluxes that catabolize hepatic TG. **(C)** The difference between additive and subtractive TG fluxes. Note the 10-fold smaller scale of the y-axis in **(C)** compared to **(A,B)**. **(D)** The fractional contribution of the various fluxes included in F_a. **(E)** The time to peak (time to maximal fractional contribution) of the various processes. The areas and bars represent median ± median absolute deviation. The solutions of group $G_{0.05}$ are displayed.

with T0901317 for 1 day, and untreated controls (Hijmans et al., 2015). A description of the experimental materials and procedures is available in section 5. The contribution of plasma palmitate to hepatic palmitate and stearate were unchanged after 1 day of LXR activation (**Figures 8A,B**). However, LXR activation increased the flux from plasma palmitate to liver palmitoleate and oleate (**Figures 8C,D**), thereby confirming the model prediction obtained via ADAPT that FFA uptake increases within 1 day of treatment with T0901317.

3. DISCUSSION

Biomedical applications of systems biology require to consider the complexity of the physiological system in humans or in the animals used to study human disease, including its highly interconnected structure and nonlinear dynamic behavior. The study of progressive adaptations during disease or intervention is complicated by the multilevel characteristics (metabolome, proteome, and transcriptome) of the underlying biological systems and the timescales on which these occur (seconds to years). Physiological parameters with diagnostic value are hidden in complicated, multivariate datasets. Time-series measurements of the metabolome provide information-rich data about the status of a biological system (Smilde et al., 2010). Gene expression data is abundant in literature and online repositories. However, it is not trivial to integrate multi-omics data, and hence to exploit the full potential of the information contained in these data. Multi-omics data is high-dimensional because the number of features and outcome variables is larger than the number of samples. Despite developments in machine/deep learning methods, data-driven approaches have fundamental limitations to model high-dimensional time series data. Mathematical modeling can construct computer simulation models from expert-based domain knowledge that can make transparent and explainable predictions of biological systems (mechanism-based systems biology models, van Riel, 2006). We proposed a combination of mathematical models and machine learning,

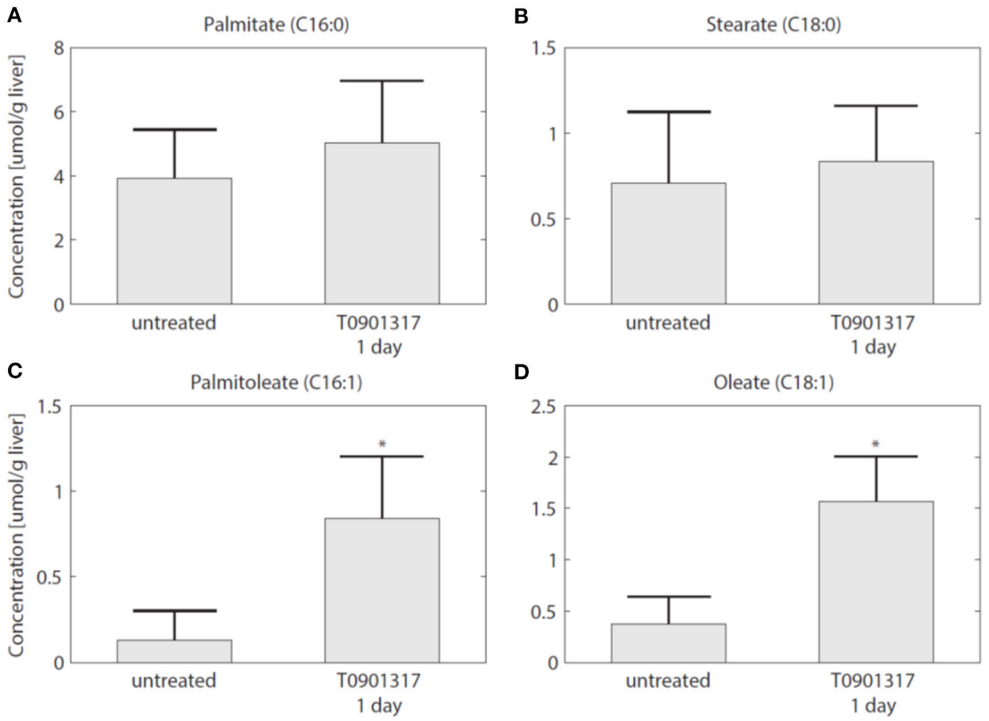

FIGURE 8 | The hepatic uptake of FFA is increased. Additional experiments were performed in which ^{13}C-palmitate was infused into C57Bl/6J mice that were treated with T0901317 for 1 day, and untreated controls. The different graphs present the contribution of plasma palmitate to hepatic palmitate **(A)**, stearate **(B)**, palmitoleate **(C)**, and oleate **(D)**. The contribution of plasma palmitate to hepatic palmitoleate and oleate was increased after 1 day of LXR activation, thereby confirming the model estimation presented in **Figure 7**. The bars represent mean + standard deviation, $^{*}p<0.05$, Mann–Whitney *U*-test.

implemented in ADAPT. ADAPT is less susceptible to data bias than data-driven, machine learning methods. Moreover, ADAPT quantifies uncertainty in the model and its predictions.

ADAPT is rooted in methods and techniques like system identification (from systems theory, Ljung, 1998), state-estimators (such as the Kalman filter, currently applied in navigation and positioning technology; Kalman, 1960) and data assimilation (in geosciences, such as weather forecasting, Asch et al., 2016). Characteristic is the use of a dynamical model of the system being analyzed in combination with statistical methods to incorporate measured data. Like a state-estimator, ADAPT combines dynamic models based on system knowledge with measurements and statistical models of uncertainties and variation in the process. The computer simulation model contains the elements and the dynamics of how the (complex) biological system operates. ADAPT connects the real biological system and the corresponding virtual model by different types of data, and the model updates ("learns") as the biological counterparts changes. The algorithm requires time-series data to execute the model. It provides estimates for unobserved system variables and at time points for which data is not available. These state estimates are the "predictions" that can be made with ADAPT. In studies in humans and animals it is relatively easy to collect blood to perform measurements in. Via these measurements one often aims to get information about processes in organs and tissues. ADAPT enables the translation of plasma time-series metabolomics data to information about metabolic processes in tissues and between organs. In dedicated experiments with metabolic tracers and liver tissue was collected we have been able to validate estimates (predictions) of metabolic pools and fluxes to explain the development of hepatic steatosis as side-effect of treatment with a synthetic LXR agonist.

The application of advanced simulation models in (biomedical) systems biology and systems medicine requires credible models, that have been scrutinized on verification, validation and uncertainty quantification (Viceconti et al., in press). ADAPT addresses two major types of uncertainty in model estimation that impact model credibility and applicability: parametric uncertainty and structural uncertainty. First, *parametric uncertainty* concerns the problem of parameter identifiability. Values of model parameters are inferred from experimental data, but not all parameters might be identifiable from the available data (Raue et al., 2009; Vanlier et al., 2013). Since model parameters are estimated by calibrating the model to experimental data, uncertainty in the data (noise, errors) will propagate into the parameter estimates. Uncertainty in the parameter estimates subsequently will limit the accuracy of the model predictions. We used a stochastic data model from which samples were generated using a Monte Carlo approach. ADAPT was run for all samples hereby quantifying confidence in the estimated parameter trajectories. Parameter estimation in nonlinear dynamic models remains a computationally

challenging task due to its non-convexity (presence of local optima) and ill-conditioning (Gábor and Banga, 2015). ADAPT uses a global scatter search to initialize a multi-start, gradient-based, interior point local optimization method. This approach was shown to be a successful strategy with a good performance in a benchmark study (Villaverde et al., 2019). A local solver (lsqnonlin in Matlab) is started from multiple start points to sample multiple basins of attraction associated with possible local minima in the cost function (the negative log-likelihood). The scatter search was made more efficient by only selecting the 10% of the most promising sampled parameters sets (lowest SSE) as start values for the local solver to estimate the model for the untreated condition (multistart with preselection).

Second, lack of knowledge about components and their quantitative interactions introduces uncertainty about the model structure. *Structural uncertainty* resides in simplifications that are inherent to the process of model building and assumptions that are made in case the nature and/or kinetic details of certain interactions are unknown (or disputed). The network topology of metabolic pathways is (relatively) well-known. Network structures impose strong constraints on the solution space of mathematical models, a characteristic that is employed in constraint-based simulation and analysis of (genome-scale) metabolic network models (Orth et al., 2010). Mathematical modeling of signal transduction and gene regulatory networks is more difficult. Insufficient information is available to formulate accurate mathematical descriptions of these networks. Making wrong and/or too strong assumptions about interactions and their kinetics could largely bias the model. Instead of adding equations with structural uncertainty, ADAPT introduces freedom in model parameters to compensate for unmodeled regulation.

ADAPT combines differential equation models of the network topology and mass fluxes in metabolic pathways with machine learning to model temporal metabolic data (Tiemann et al., 2013; Rozendaal et al., 2018b). A more complete understanding of underlying biological adaptations requires integration of other molecular data, such as transcriptomics and proteomics. Here we have extended ADAPT to integrate metabolic and transcriptomic time-series data. ADAPT uses numerical optimization for learning and updating of model parameters, to estimate the current state of the system and forecast its future trajectory. A new regularization function was added to the learning algorithm that is used to estimate model parameters. The new version of ADAPT uses the metabolite data as input to estimate trajectories of metabolic parameters and takes the gene expression data as additional information to refine the trajectories. The gene expression data was included implicitly in the model by incorporation in the regularization function (composed of two components $\chi^2_{g_1}$ and $\chi^2_{g_2}$), where it was implicitly used to guide and constrain the dynamic variations in the parameter trajectories. First, parameter adaptations were preferred such that resulting parameter trajectories and corresponding gene expression profiles display temporal correlation. Secondly, the gene expression data was used to prevent unnecessary (random) fluctuations in parameter trajectories, that could be the result of poor identifiability of certain parameters. The importance (weight) of each objective function component is determined by the corresponding regularization constant. The penalty function is a refinement of the regularization function described in Tiemann et al. (2013). $\chi^2_{g_2}$ effectuates that changing a parameter is costly, which will therefore be avoided unless it is required to describe the metabolic data. This results in parameter trajectories that are steady and smooth (enforcing temporal sparsity in the solutions). However, in the present study, the penalty of changing a parameter is reduced when corresponding gene expression level changes.

Regularization is a key component of ADAPT. It provides the possibility to extend the biological realism of the simulations by including post-transcriptional control that was not accounted for in the mathematical model. Regularization also improves numerical performance by resolving ill-conditioning of the estimation problem. Regularization is known to be beneficial for inverse problems, of which parameter estimation is an example. Regularized regression, like LASSO, is used to prevent overfitting and perform feature selection in computational statistics and machine learning (e.g., Imangaliyev et al., 2018). Regularization for estimating models of dynamical systems has been investigated in much lesser extent (Chen, 2013). We and others have shown that regularization can be very effective to mitigate ill-conditioning when estimating dynamic systems biology models (van Riel et al., 2013; Gábor and Banga, 2015). In ADAPT regularization is extended beyond so-called ridge regression (also known as Tikhonov regularization), in which the regularization function penalizes deviations of the parameter estimates from their reference (nominal) values or *a priori* defined target values (Cedersund and Roll, 2009; Dolejsch et al., 2019). Regularized estimations ensure a trade-off between bias and variance, reducing overfitting, and allowing the incorporation of prior knowledge in a systematic way.

Previously we had applied a model of hepatic lipid and plasma lipoprotein metabolism using an earlier version of ADAPT and discovered how pharmacological activation of LXR induced the reverse cholesterol pathway, but with counter-intuitive behavior of scavenger receptor class B1 (SR-B1), a receptor that facilitates the hepatic uptake of cholesterol from HDL particles (Tiemann et al., 2013). Here we have included gene expression data that was not available in the previous work to study the development of hepatic steatosis, which is a serious side effect of pharmacological activation of LXR. Results from the computational analysis showed that the additional integration of gene expression data effectively constrained and improved estimations (model predictions). of the hepatic storage of triglycerides in cytosolic and nascent VLDL fractions (**Figure 5**). Without the gene expression data it was not possible to accurately estimate how the total triglyceride content is distributed between these fractions. Interestingly, when the gene expression data was included, model predictions indicated that the increased triglyceride fluxes are predominantly stored in the cytosol, rather than being transferred to nascent VLDL. Hepatic fractionation experiments were subsequently performed that confirmed this prediction, providing an independent validation of the model.

As LXR induces the expression of lipogenic genes, such as *Fas* and *Scd1*, it was expected that *de novo* lipogenesis would be the major metabolic route contributing to development of hepatic steatosis. Experimental data shows that the hepatic triglyceride level was already increased within 1 day of treatment. The parameter and flux trajectories obtained with ADAPT were used to quantitatively analyze the contribution of all metabolic routes included in the mathematical model to the accumulation of hepatic triglycerides. Remarkably, the computational analysis revealed that plasma FFA provided a major contribution to the supply of hepatic triglycerides. Moreover, a peak contribution of hepatic FFA uptake was observed at 1 day of treatment, while the contribution of *de novo* lipogenesis increased gradually up to 1 week of treatment. The computational results clearly indicated that an increased uptake of FFA precedes the induction of *de novo* lipogenesis. This prediction was validated in an independent experiment with a metabolic tracer. To establish whether the flux of FFA from plasma to the liver is increased upon LXR activation, ^{13}C-palmitate was infused via jugular vein catheter into C57Bl/6J mice that were treated with T0901317 for 1 day, and untreated controls. Indeed, an increased incorporation of ^{13}C was observed in the hepatic triglyceride levels of palmitoleate and oleate confirming plasma as main source, as predicted by the model. Our findings might also be relevant to understand the development of steatosis, non-alcoholic fatty liver disease (NAFLD) and non-alcoholic steatohepatitis (NASH) associated with Metabolic Syndrome (Rozendaal et al., 2018b). Increased flux of FFA and glycerol from lipolysis of white adipose tissue (O'Donovan et al., 2019) has been associated with liver steatosis and NAFLD, also contributing to impaired postprandial repression of endogenous glucose production occurring in Type 2 Diabetes (Perry et al., 2015; Roden and Shulman, 2019).

ADAPT can be used to extract information on disease development and effects of medication that cannot be directly observed from the data. The computational model functions as a state-estimator applied to monitor the effect of therapeutic interventions and detect critical transitions of the system. Future developments include applications in so-called digital twinning in which computer simulation models are connected to their biological counterparts by different types of data and the model automatically updates as the biological counterpart changes (van Riel et al., 2020).

4. CONCLUSIONS

The development of computational models and techniques to study molecular adaptations during disease or intervention are important challenges in the field of biomedical systems biology and systems medicine. ADAPT combines the data-driven power of machine learning with that of knowledge-based, mechanistic simulation models. We presented an extension of ADAPT to integrate metabolomic and transcriptomic time-series data using a novel regularization approach. The gene expression data effectively constrained and improved model predictions, providing new insights in triglyceride metabolism related to drug-induced development of hepatic steatosis.

5. MATERIALS AND METHODS

The computational workflow of ADAPT is described. First, the mathematical modeling of metabolic pathways and the identification of molecular adaptations are discussed. Second, the methodology to integrate gene expression data is presented.

5.1. Continuous Descriptions of the Experimental Data

Progressive diseases affect multiple processes operating at different levels (metabolome, proteome, and transcriptome) and different timescales (seconds to years). During disease development metabolic parameters (and consequently metabolic fluxes and concentrations) can be expected to change over time. The concept of time-dependent model parameters is introduced to study these adaptations. ADAPT identifies necessary dynamic changes in the model parameters to describe the transition between experimental data obtained during different stages (time points) of the disease. To estimate dynamic trajectories of model parameters, continuous dynamic descriptions of the experimental data were used as input for ADAPT. Cubic smoothing splines were calculated to describe the dynamics of the experimental data. To account for experimental variance and biological variation a collection of splines was calculated using a Monte Carlo approach. Different random samples of the experimental data were generated assuming Gaussian distributions with means and standard deviations according to the data. Subsequently, for each generated sample a cubic smoothing spline was calculated (**Figure 9**).

In the present study, a distinction between two types of data was made. First, metabolic data was acquired, e.g., concentrations and fluxes of metabolites in plasma and tissue compartments. The splines describing this data are denoted by $\vec{d}_m(t)$. Secondly, experimental data derived from the transcriptome level was considered, e.g., mRNA expression levels of genes. Corresponding splines are denoted by $\vec{d}_t(t)$.

5.2. Mathematical Modeling of the Metabolome Level

Mathematical modeling was centered on metabolic pathways. Pathways at the proteome and transcriptome levels that modulate the metabolic processes were not modeled explicitly as insufficient information of the underlying network structure and interaction mechanisms was available. The metabolic model is defined by a set of (non)linear ordinary differential equations (state-space structure):

$$\begin{aligned} \dot{\vec{x}}(t) &= \mathbf{N}\vec{f}(\vec{x}(t),\vec{p},\vec{u}) \quad \text{with} \quad \vec{x}(t_0) = \vec{x}_0 \\ \vec{y}(t) &= \vec{g}(\vec{x}(t),\vec{p},\vec{u}) \end{aligned} \tag{4}$$

where $\dot{\vec{x}}$ is a vector of first derivatives of molecular species (or state variables) $\vec{x}$ with respect to time. The right-hand side of the equation is given by the topology of the network (stoichiometric matrix $\mathbf{N}$) and a set of functions $\vec{f}$ that describe the interactions between the species. The initial concentrations of $\vec{x}$ are given by $\vec{x}_0$. The vector $\vec{y}$ represents the model outputs, which are given by a set of functions $\vec{g}$ that map the model states to specific

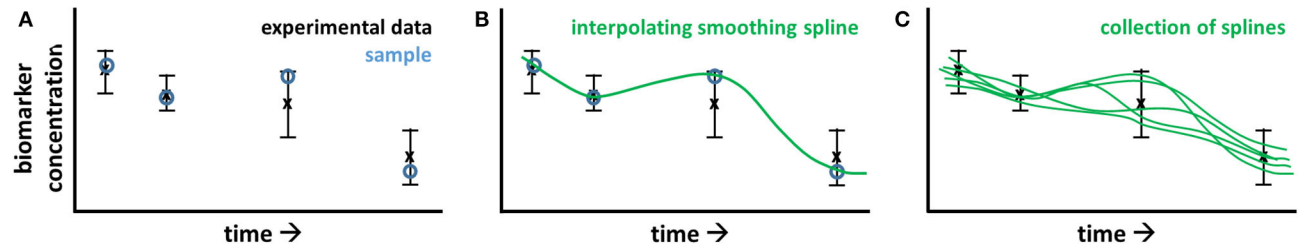

FIGURE 9 | Pre-processing of experimental data for ADAPT. The experimental data consists of time course, longitudinal data obtained at multiple, discrete points in time, describing the transition of the biological system. In **(A)**, the black error bars represent mean and standard deviation of the data at each point in time. A time continuous description of the data is obtained by spline interpolation. To account for experimental and biological uncertainties, a Monte Carlo approach is used. The data is randomly sampled assuming a data error model based on Gaussian distributions with means and standard deviations according to the experimental data (**A**; blue circles). A cubic smoothing spline (**B**; green line) is fitted through these samples. This process is repeated, obtaining a collection of splines **(C)**.

quantities of interest. The outputs usually are quantities that have been experimentally measured. Both functions $\vec{f}$ and $\vec{g}$ depend on kinetic parameters $\vec{p}$ and optional external inputs $\vec{u}$. In principle, the generic set of equations in (4) can be used to describe any biomolecular reaction network. Here we use the system of ordinary differential equations to describe metabolic networks.

5.3. Dynamic Parameters to Describe Metabolic Adaptations

Details of the ADAPT methodology have been described in Tiemann et al. (2013) and are repeated here briefly for consistency. Dynamic adaptations in metabolic processes are identified by inferring necessary dynamic changes in the model parameters which are therefore time-dependent. To this end, a simulation of the treatment was divided in N_t steps of Δt time period using the following discretization:

$$\begin{aligned} \vec{X}(n\Delta t) &= \vec{x}(\Delta t, \vec{p}(n\Delta t)) \\ \vec{Y}(n\Delta t) &= \vec{g}(\vec{X}(n\Delta t), \vec{p}(n\Delta t)) \\ \vec{X}(0) &= \vec{x}_0(\vec{p}(0)) \end{aligned} \tag{5}$$

with $0 \leq n \leq N_t$ and $N_t \Delta t$ the time period of the entire experiment. The simulation is initiated ($n = 0$) using the initial values of the model states $\vec{x}_0$ obtained with parameter set $\vec{p}(0)$ representing the untreated phenotype. Subsequently, for each step $n > 0$ the system is simulated for a time period of Δt using the final values of the model states of the previous step $n - 1$ as initial conditions. Parameters $\vec{p}(n\Delta t)$ are estimated by minimizing the difference between the data interpolants $\vec{d}_m(n\Delta t)$ and corresponding model outputs $\vec{Y}(n\Delta t)$. Here, the previously estimated parameter set $\vec{p}((n-1)\Delta t)$ is provided as initial set for the optimization algorithm. The parameter optimization problem is given by:

$$\hat{\vec{p}}(n\Delta t) = \arg\min_{\vec{p}(n\Delta t)} \chi_d^2(\vec{p}(n\Delta t)) \tag{6}$$

$$\chi_d^2(\vec{p}(n\Delta t)) = \sum_{i=1}^{N_y} \left(\frac{Y_i(n\Delta t) - d_{m,i}(n\Delta t)}{\sigma_{m,i}(n\Delta t)} \right)^2 \tag{7}$$

where $\hat{\vec{p}}(n\Delta t)$ represents the optimized parameter set and χ_d^2 is the weighted sum of squared errors (SSE), with N_y the number of model outputs (equal to the number of measured variables). Parameter trajectories were estimated using 200 time steps ($N_t = 200$).

A Monte Carlo approach was employed to account for methodological and experimental uncertainties. First, a global scatter search was used to initialize a multi-start local optimization method (Tiemann et al., 2011). 2×10^5 parameter vectors were sampled from a widely dispersed range of initial parameter values (10^{-6} to 10^6). For each parameter vector $\chi_d^2|_{n=0}$ was computed (SSE at $t = 0$). 2×10^4 (10%) of the best performing parameter sets (with lowest $\chi_d^2|_{n=0}$) were selected and used to initiate the optimization procedure and estimate $\hat{\vec{p}}(0)$, using a gradient-based, interior point local optimization method (lsqnonlin in Matlab). This resulted in a collection of parameter sets that describe the untreated phenotype. Secondly, in each optimization series a different spline function for $\vec{d}_m$ was used. Finally, distributions of parameter trajectories (and consequently state and flux trajectories) are obtained that describe the transition of the phenotype during the disease or intervention.

5.4. Implicit Integration of the Transcriptome Level

Time-course data of relative gene expression levels was used as an additional source of information to constrain the dynamic behavior of parameter trajectories. However, note that pathways at the transcriptome level were not modeled explicitly due to the lack of sufficient quantitative information about the gene regulatory networks regulating the response to LXR activation. Therefore, the parameter trajectory estimation protocol, as formulated in Equations (6) and (7), was modified to integrate gene expression data. ADAPT is based on the assumption that changes in metabolic parameters are reflected by changes in corresponding enzymes, which in turn are reflected by changes in corresponding gene expression levels. This implies there is a functional relationship between a metabolic parameter p_i and corresponding gene expression level $d_{t,i}$.

5.4.1. Maximization of the Temporal Correlation

The optimization problem presented in Equation (6) was extended as follows. For clarity we introduce the following definitions: $\vec{p}[\cdot n] = \vec{p}[0, \Delta t, \cdots n\Delta t]$ and $\vec{d}_t[\cdot n] = \vec{d}_t[0, \Delta t, \cdots n\Delta t]$, which represents the parameter trajectories from time step 0 to n and corresponding gene expression data, respectively. During a re-optimization of the metabolic parameters $\vec{p}$ from step $n-1$ to step n, a $\Delta\vec{p}$ is preferred such that resulting parameter trajectories $\vec{p}[\cdot n]$ and corresponding gene expression profiles $\vec{d}_t[\cdot n]$ display temporal correlation.This was effectuated by including an additional component $\chi^2_{g_1}$ in the objective function which maximizes the temporal correlation between these profiles:

$$\chi^2_{g_1}(\vec{p}(n\Delta t)) = \sum_{i=1}^{N_p} V_i(n\Delta t) \tag{8}$$

where N_p is the number of parameters, and $V_i(n\Delta t)$ is given by:

$$V_i(n\Delta t) = \begin{cases} \dfrac{1}{N_{ci}} \displaystyle\sum_{j=1}^{N_{ci}} \left(1 - \rho_{ij}(n\Delta t)\right)^2 & \text{if } N_{ci} > 0 \\ 0 & \text{otherwise} \end{cases} \tag{9}$$

where N_{ci} is the number of genes assigned to parameter i, and $\rho_{ij}(n\Delta t)$ is given by:

$$\rho_{ij}(n\Delta t) = \frac{\mathrm{Cov}(\vec{p}_i[\cdot n], \vec{d}_{t,ij}[\cdot n])}{\sigma(\vec{p}_i[\cdot n])\sigma(\vec{d}_{t,ij}[\cdot n])} \tag{10}$$

Equation (10) represents the Pearson correlation coefficient between a parameter trajectory and corresponding gene expression data, which is bounded between -1 (maximal negative correlation) and 1 (maximal positive correlation). Note that multiple genes can be assigned to a parameter, which could be useful for instance when a cascade of molecular processes is integrated in a single mathematical reaction equation.

5.4.2. Constraining the Magnitude of Dynamic Variations in Trajectories

The gene expression data was also used to constrain the magnitude of dynamic variations in the parameter trajectories. It was assumed that parameters are less likely to change when corresponding gene expression levels remain unchanged, compared to scenarios when expression of the genes is induced or repressed. Therefore, in latter cases parameter adaptations are less penalized compared to former cases. This was effectuated by including an additional objective function $\chi^2_{g_2}$ which utilizes the time derivative of gene expression profiles to penalize parameter fluctuations:

$$\chi^2_{g_2}(\vec{p}(n\Delta t)) = \sum_{i=1}^{N_p} W_i(n\Delta t) \tag{11}$$

with $W_i(n\Delta t)$ given by:

$$W_i(n\Delta t) = \begin{cases} \dfrac{1}{N_{ci}} \displaystyle\sum_{j=1}^{N_{ci}} \left(\frac{P_i(n\Delta t)}{G_{ij}(n\Delta t)}\right)^2 & \text{if } N_{ci} > 0 \\ P_i(n\Delta t) & \text{otherwise} \end{cases} \tag{12}$$

with $P_i(n\Delta t)$ and $G_{ij}(n\Delta t)$ defined as:

$$P_i(n\Delta t) = \frac{1}{p_i(0)} \frac{p_i(n\Delta t) - p_i((n-1)\Delta t)}{\Delta t} \tag{13}$$

$$G_{ij}(n\Delta t) = \frac{1}{d_{t,i,j}(0)} \frac{d}{dt} d_{t,i,j}(t)\Big|_{t=n\Delta t} \tag{14}$$

where $P_i(n\Delta t)$ represents the normalized derivative of parameter i at time step n. Relative derivatives were used to assign equal relevance to all parameters and to avoid domination of the optimization by large absolute values. Furthermore, $G_{ij}(n\Delta t)$ represents the normalized derivative of the spline function (evaluated at time step n) that describes corresponding gene expression data. To avoid division by zero (when $G_{ij}(n\Delta t) = 0$), the minimal absolute value of $G_{ij}(n\Delta t)$ was truncated at 10^{-6}. Note that $P_i(n\Delta t)$ effectuates that changing a parameter is costly, which will therefore be avoided unless it is required to describe the experimental data. However, when accompanied by a change in gene expression level, the penalty of changing corresponding parameter is reduced (because P is divided by G).

Objective functions $\chi^2_{g_1}$ and $\chi^2_{g_2}$ were formulated as soft constraints by introducing constants λ_{g_1} and λ_{g_2}, which determine the contribution strengths of the functions. This implies that metabolic parameters and corresponding gene expression levels do not necessarily have to display temporal correlation when this is in contradiction to the metabolic data. This provides the possibility to account for post-transcriptional control. In summary, an optimized parameter set is defined as follows:

$$\hat{\vec{p}}(n\Delta t) = \arg\min_{\vec{p}(n\Delta t)} \Big(\chi^2_d(\vec{p}(n\Delta t)) + \lambda_{g_1}\chi^2_{g_1}(\vec{p}(n\Delta t)) + \lambda_{g_2}\chi^2_{g_2}(\vec{p}(n\Delta t))\Big) \tag{15}$$

The determination of the regularization constants is discussed in **Supplementary Material** (section 3.1).

5.5. Implementation Details

The mathematical model and ADAPT were implemented in MATLAB (The Mathworks, Natick, Massachusetts, USA). The code is available on GitHub (https://github.com/nvanriel/ADAPT, https://github.com/rcqsnel/adapt-modeling-framework, and https://github.com/yvonnerozendaal). The ordinary differential equations were solved with compiled MEX files using numerical integrators from the SUNDIALS CVode package (2.6.0, Lawrence Livermore National Laboratory, Livermore, California) (Hindmarsh et al., 2005). An absolute and relative tolerance of 10^{-6} were used. The MATLAB nonlinear least-squares solver lsqnonlin (from the Optimization

Toolbox), which uses an interior reflective Newton method (Coleman and Li, 1996), was used to estimate model parameters. The termination tolerances for the objective function and the parameter estimates were set to 10^{-10}, the maximum number of iterations allowed was set to 10^3 and the maximum number of function evaluations allowed to 10^5. Parameter trajectories were estimated using 200 time steps. The MATLAB function csaps (from the Curve Fitting Toolbox) was used to calculate cubic smoothing splines using the default smoothness setting (= 1) and the roughness dependent on the variation in the data: $(1/std)^2$ (std: standard deviation).

5.6. Experimental Procedures

The experimental procedures have been described previously (Tiemann et al., 2013; Hijmans et al., 2015). Information about the fractionation experiments is provided in the **Supplementary Material**. Experimental procedures were approved by the Ethics Committee for Animal Experiments of the University of Groningen.

DATA AVAILABILITY STATEMENT

All datasets generated for this study are included in the article/ **Supplementary Material**.

ETHICS STATEMENT

The animal study was reviewed and approved by Institutional Animal Care and Use Committee of the University of Groningen.

AUTHOR CONTRIBUTIONS

NR and AG conceived and designed the study. NR, AG, and PH supervised the research. CT developed the software and performed the simulations. CT and NR analyzed the results and wrote the paper. NR, PH, and AG read and revised the paper. All authors contributed to the article and approved the submitted version.

FUNDING

This research was funded by the European Union FP7-HEALTH (Grant 305707): A systems biology approach to RESOLVE the molecular pathology of two hallmarks of patients with metabolic syndrome and its co-morbidities; hypertriglyceridemia and low HDL-cholesterol, and supported by the NWO Complexity in Health and Nutrition program (project nr. 645.001.003).

ACKNOWLEDGMENTS

We want to acknowledge multiple people who contributed to the development of ADAPT in the past years: Joep Vanlier, Fianne Sips, Yvonne Rozendaal, Roderick Snel, Pascal van Beek, and Yared Paalvast. We also thank Maaike Oosterveer and Brenda Hijmans for providing the experimental data.

SUPPLEMENTARY MATERIAL

The Supplementary Material for this article can be found online at: https://www.frontiersin.org/articles/10.3389/fbioe.2020.536957/full#supplementary-material

REFERENCES

Asch, M., Bocquet, M., and Nodet, M. (2016). *Data Assimilation: Methods, Algorithms, and Applications*. SIAM. doi: 10.1137/1.9781611974546

Cave, M. C., Clair, H. B., Hardesty, J. E., Falkner, K. C., Feng, W., Clark, B. J., et al. (2016). Nuclear receptors and nonalcoholic fatty liver disease. *Biochim. Biophys. Acta* 1859, 1083–1099. doi: 10.1016/j.bbagrm.2016.03.002

Cedersund, G., and Roll, J. (2009). Systems biology: model based evaluation and comparison of potential explanations for given biological data. *FEBS J.* 276, 903–922. doi: 10.1111/j.1742-4658.2008.06845.x

Chen, L. L. T. (2013). What can regularization offer for estimation of dynamical systems? *IFAC Proc. Vol.* 46, 1–8. doi: 10.3182/20130703-3-FR-4038.00155

Coleman, T., and Li, Y. (1996). An interior trust region approach for nonlinear minimization subject to bounds. *SIAM J. Optimiz* 6, 418–445. doi: 10.1137/0806023

de Winter, W., DeJongh, J., Post, T., Ploeger, B., Urquhart, R., Moules, I., et al. (2006). A mechanism-based disease progression model for comparison of long-term effects of pioglitazone, metformin and gliclazide on disease processes underlying type 2 diabetes mellitus. *J. Pharmacokinet. Pharmacodyn.* 33, 313–343. doi: 10.1007/s10928-006-9008-2

Deneer, R., Boxtel, A. G. M. V., Boer, A.-K., Hamad, M. A. S., van Riel, N. A. W., and Scharnhorst, V. (2020). Detecting patients with PMI post-CABG based on cardiac troponin-T profiles: a latent class mixed modeling approach. *Clin. Chim. Acta* 504, 23–29. doi: 10.1016/j.cca.2020.01.025

Dolejsch, P., Hass, H., and Timmer, J. (2019). Extensions of $\ell 1$ regularization increase detection specificity for cell-type specific parameters in dynamic models. *BMC Bioinformatics* 20:395. doi: 10.1186/s12859-019-2976-1

Gábor, A., and Banga, J. R. (2015). Robust and efficient parameter estimation in dynamic models of biological systems. *BMC Syst. Biol.* 9:74. doi: 10.1186/s12918-015-0219-2

Grefhorst, A., Elzinga, B., Voshol, P., Plösch, T., Kok, T., Bloks, V., et al. (2002). Stimulation of lipogenesis by pharmacological activation of the liver X receptor leads to production of large, triglyceride-rich very low density lipoprotein particles. *J. Biol. Chem.* 277, 34182–34190. doi: 10.1074/jbc.M204887200

Grefhorst, A., Oosterveer, M. H., Brufau, G., Boesjes, M., Kuipers, F., and Groen, A. K. (2012). Pharmacological LXR activation reduces presence of SR-B1 in liver membranes contributing to LXR-mediated induction of HDL-cholesterol. *Atherosclerosis* 222, 382–389. doi: 10.1016/j.atherosclerosis.2012.02.014

Grefhorst, A., and Parks, E. (2009). Reduced insulin-mediated inhibition of VLDL secretion upon pharmacological activation of the liver X receptor in mice. *J. Lipid Res.* 50, 1374–1383. doi: 10.1194/jlr.M800505-JLR200

Hall, H., Perelman, D., Breschi, A., Limcaoco, P., Kellogg, R., McLaughlin, T., et al. (2018). Glucotypes reveal new patterns of glucose dysregulation. *PLoS Biol.* 16:e2005143. doi: 10.1371/journal.pbio.2005143

Hijmans, B. S., Tiemann, C. A., Grefhorst, A., Boesjes, M., Dijk, T. H. v., Tietge, U. J. F., et al. (2015). A systems biology approach reveals the physiological origin of hepatic steatosis induced by liver x receptor activation. *FASEB J.* 29, 1153–1164. doi: 10.1096/fj.14-254656

Hindmarsh, A., Brown, P., Grant, K., Lee, S., Serban, R., Shumaker, D., et al. (2005). SUNDIALS: Suite of nonlinear and differential/algebraic equation solvers. *ACM Trans. Math. Softw.* 31, 363–396. doi: 10.1145/1089014.1089020

Hulman, A., Witte, D. R., Vistisen, D., Balkau, B., Dekker, J. M., Herder, C., et al. (2018). Pathophysiological characteristics underlying different glucose response curves: a latent class trajectory analysis from the prospective EGIR-RISC study. *Diabetes Care* 41, 1740–1748. doi: 10.2337/dc18-0279

Imangaliyev, S., Prodan, A., Nieuwdorp, M., Groen, A. K., van Riel, N. A. W., and Levin, E. (2018). Domain intelligible models. *Methods*. 149, 69–73. doi: 10.1016/j.ymeth.2018.06.011

Kalman, R. E. (1960). A new approach to linear filtering and prediction problems. *J. Basic Eng.* 82, 35–45. doi: 10.1115/1.3662552

Ljung, L. (1998). *System Identification: Theory for the User*. Pearson Education.

O'Donovan, S. D., Lenz, M., Vink, R. G., Roumans, N. J. T., Kok, T. M. C. M. d., Mariman, E. C. M., et al. (2019). A computational model of postprandial adipose tissue lipid metabolism derived using human arteriovenous stable isotope tracer data. *PLoS Comput. Biol.* 15:e1007400. doi: 10.1371/journal.pcbi.1007400

Orth, J. D., Thiele, I., and Palsson, B. Ø. (2010). What is flux balance analysis? *Nat. Biotechnol.* 28, 245–248. doi: 10.1038/nbt.1614

Perry, R. J., Camporez, J.-P. G., Kursawe, R., Titchenell, P. M., Zhang, D., Perry, C. J., et al. (2015). Hepatic acetyl CoA links adipose tissue inflammation to hepatic insulin resistance and type 2 diabetes. *Cell* 160, 745–758. doi: 10.1016/j.cell.2015.01.012

Pop, V., Broeren, M., Wijnen, H., Endendijk, J., van Baar, A., Wiersinga, W., et al. (2018). Longitudinal trajectories of gestational thyroid function: a new approach to better understand changes in thyroid function. *J. Clin. Endocrinol. Metab.* 103, 2889–2900. doi: 10.1210/jc.2017-02556

Raue, A., Kreutz, C., Maiwald, T., Bachmann, J., Schilling, M., Klingmüller, U., et al. (2009). Structural and practical identifiability analysis of partially observed dynamical models by exploiting the profile likelihood. *Bioinformatics* 25, 1923–1929. doi: 10.1093/bioinformatics/btp358

Rizzi, M., Baltes, M., Theobald, U., and Reuss, M. (1997). In vivo analysis of metabolic dynamics in Saccharomyces cerevisiae: II. Mathematical model. *Biotechnol. Bioeng.* 55, 592–608. doi: 10.1002/(SICI)1097-0290(19970820)55:4<592::AID-BIT2>3.0.CO;2-C

Roden, M., and Shulman, G. I. (2019). The integrative biology of type 2 diabetes. *Nature* 576, 51–60. doi: 10.1038/s41586-019-1797-8

Rozendaal, Y. J., Maas, A. H., van Pul, C., Cottaar, E. J., Haak, H. R., Hilbers, P. A., et al. (2018a). Model-based analysis of postprandial glycemic response dynamics for different types of food. *Clin. Nutr. Exp.* 19, 32–45. doi: 10.1016/j.yclnex.2018.01.003

Rozendaal, Y. J. W., Wang, Y., Paalvast, Y., Tambyrajah, L. L., Li, Z., Dijk, K. W. V., et al. (2018b). *In vivo* and *in silico* dynamics of the development of Metabolic Syndrome. *PLoS Comput. Biol.* 14:e1006145. doi: 10.1371/journal.pcbi.1006145

Smilde, A. K., Westerhuis, J. A., Hoefsloot, H. C. J., Bijlsma, S., Rubingh, C. M., Vis, D. J., et al. (2010). Dynamic metabolomic data analysis: a tutorial review. *Metabolomics* 6, 3–17. doi: 10.1007/s11306-009-0191-1

Tiemann, C., Vanlier, J., Hilbers, P., and van Riel, N. (2011). Parameter adaptations during phenotype transitions in progressive diseases. *BMC Syst. Biol.* 5:174. doi: 10.1186/1752-0509-5-174

Tiemann, C., Vanlier, J., Oosterveer, M., Groen, A., Hilbers, P., and van Riel, N. (2013). Parameter trajectory analysis to identify treatment effects of pharmacological interventions. *PLoS Comput. Biol.* 9:e1003166. doi: 10.1371/journal.pcbi.1003166

van Riel, N. (2006). Dynamic modelling and analysis of biochemical networks: mechanism-based models and model-based experiments. *Brief. Bioinformatics* 7, 364–374. doi: 10.1093/bib/bbl040

van Riel, N. A., Giuseppin, M. L., TerSchure, E. G., and Verrips, C. T. (1998). A structured, minimal parameter model of the central nitrogen metabolism in *Saccharomyces cerevisiae*: the prediction of the behavior of mutants. *J. Theor. Biol.* 191, 397–414. doi: 10.1006/jtbi.1997.0600

van Riel, N. A., Mueller, R., and Dall'Ara, E. (2020). The Digital Mouse: why computational modelling of mouse models of disease can improve translation. *bioRxiv*. doi: 10.1101/2020.05.04.075812

van Riel, N. A., Tiemann, C. A., Vanlier, J., and Hilbers, P. A. (2013). Applications of analysis of dynamic adaptations in parameter trajectories. *Interface Focus* 3:20120084. doi: 10.1098/rsfs.2012.0084

Vanlier, J., Tiemann, C., Hilbers, P., and van Riel, N. (2013). Parameter uncertainty in biochemical models described by ordinary differential equations. *Math. Biosci.* 246, 305–314. doi: 10.1016/j.mbs.2013.03.006

Viceconti, M., Pappalardo, F., Rodriguez, B., Horner, M., Bischoff, J., and Musuamba Tshinanu, F. (in press). *In silico* trials: verification, validation and uncertainty quantification of predictive models used in the regulatory evaluation of biomedical products. *Methods*. doi: 10.1016/j.ymeth.2020.01.011

Villaverde, A. F., Fröhlich, F., Weindl, D., Hasenauer, J., and Banga, J. R. (2019). Benchmarking optimization methods for parameter estimation in large kinetic models. *Bioinformatics* 35, 830–838. doi: 10.1093/bioinformatics/bty736

Conflict of Interest: The authors declare that the research was conducted in the absence of any commercial or financial relationships that could be construed as a potential conflict of interest.

Copyright © 2021 van Riel, Tiemann, Hilbers and Groen. This is an open-access article distributed under the terms of the Creative Commons Attribution License (CC BY). The use, distribution or reproduction in other forums is permitted, provided the original author(s) and the copyright owner(s) are credited and that the original publication in this journal is cited, in accordance with accepted academic practice. No use, distribution or reproduction is permitted which does not comply with these terms.

Advantages of publishing in Frontiers

OPEN ACCESS
Articles are free to read for greatest visibility and readership

FAST PUBLICATION
Around 90 days from submission to decision

HIGH QUALITY PEER-REVIEW
Rigorous, collaborative, and constructive peer-review

TRANSPARENT PEER-REVIEW
Editors and reviewers acknowledged by name on published articles

Frontiers
Avenue du Tribunal-Fédéral 34
1005 Lausanne | Switzerland

Visit us: www.frontiersin.org
Contact us: frontiersin.org/about/contact

REPRODUCIBILITY OF RESEARCH
Support open data and methods to enhance research reproducibility

DIGITAL PUBLISHING
Articles designed for optimal readership across devices

FOLLOW US
@frontiersin

IMPACT METRICS
Advanced article metrics track visibility across digital media

EXTENSIVE PROMOTION
Marketing and promotion of impactful research

LOOP RESEARCH NETWORK
Our network increases your article's readership